

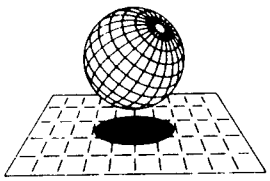
EDITOR: C. DOPAZO

EDITORIAL ADVISORY COMMITTEE: T. BOHR, I. CASTRO, Y. COUDER, H. FERNHOLZ, D. HENNINGSON, L. KLEISER, R. PIVA, D. RONNEBERGER, G.J. VAN HEIJST, A. LOZANO, L. VALIÑO, E. OÑATE, J.A. PICAZO, J.M REDONDO

ADVANCES IN TURBULENCE VIII



ADVANCES IN TURBULENCE VIII presents an updated sample of the research being performed world wide in the study of turbulence, with some inevitable bias towards work in Europe. It contains an almost complete collection of the papers delivered and the posters discussed at the Eighth European Turbulence Conference (ETC-8). The event is organized, under the auspices of the European Mechanics Society (EUROMECH), by the Universidad de Zaragoza and the Consejo Superior de Investigaciones Científicas (CSIC), with the collaboration of CIMNE (Spanish ERCOFTAC Pilot Center) and the Universidad Politécnica de Cataluña (Barcelona). The topics covered include instabilities and transition, DNS/LES, compressible turbulence, vortex dynamics, wall-free and wall-bounded turbulence, geophysical and environmental flows, transport and mixing, high Reynolds number turbulence and intermittency, magnetohydrodynamics, flow control, turbulent reacting flows, two-phase flows and modelling. The volume is thus geared towards specialists in the area of flow turbulence who could not attend ETC-8 as well as to anybody who would like to quickly assess the most active current research topics and the groups associated with them.



International Center
for Numerical Methods in Engineering

www.cimne.upc.es

REPORT DOCUMENTATION PAGE

Form Approved OMB No. 0704-0188

Public reporting burden for this collection of information is estimated to average 1 hour per response, including the time for reviewing instructions, searching existing data sources, gathering and maintaining the data needed, and completing and reviewing the collection of information. Send comments regarding this burden estimate or any other aspect of this collection of information, including suggestions for reducing this burden to Washington Headquarters Services, Directorate for Information Operations and Reports, 1215 Jefferson Davis Highway, Suite 1204, Arlington, VA 22202-4302, and to the Office of Management and Budget, Paperwork Reduction Project (0704-0188), Washington, DC 20503.

1. AGENCY USE ONLY (Leave blank)	2. REPORT DATE	3. REPORT TYPE AND DATES COVERED
	28 August 2000	Conference Proceedings

4. TITLE AND SUBTITLE

Eighth European Turbulence Conference (ETC8)

5. FUNDING NUMBERS

F61775-00-WF020

6. AUTHOR(S)

Conference Committee

7. PERFORMING ORGANIZATION NAME(S) AND ADDRESS(ES)

Universidad de Zaragoza
Maria de Luna, 3
Zaragoza 50015
Spain

8. PERFORMING ORGANIZATION REPORT NUMBER

N/A

9. SPONSORING/MONITORING AGENCY NAME(S) AND ADDRESS(ES)

EOARD
PSC 802 BOX 14
FPO 09499-0200

10. SPONSORING/MONITORING AGENCY REPORT NUMBER

CSP 00-5020

11. SUPPLEMENTARY NOTES

12a. DISTRIBUTION/AVAILABILITY STATEMENT

Approved for public release; distribution is unlimited.

U.S. Government Rights License
This work relates to Department of the Air Force Grant/rContract issued by the European Office Aerospace Research and Development (EOARD). The United States Government has a royalty-free license throughout the world in all copyrightable material contained herein

12b. DISTRIBUTION CODE

A

13. ABSTRACT (Maximum 200 words)

The Final Proceedings for Eighth European Turbulence Conference (ETC8), 27 June 2000 - 30 June 2000

This is an interdisciplinary conference. Topics are related to fundamental aspects of Turbulence Physics and include the following fields: Instabilities and transition; Experimental techniques; Direct Numerical Simulation/Large Eddy Simulation; Compressible turbulence; Transport and mixing; Geophysical and environmental flows; Vortex dynamics; Intermittence and scaling; and Turbulent reacting flows.

14. SUBJECT TERMS

EOARD, Turbulence, Vortex flows, Mixing, Compressible Flows

15. NUMBER OF PAGES

1006

16. PRICE CODE

N/A

17. SECURITY CLASSIFICATION OF REPORT	18. SECURITY CLASSIFICATION OF THIS PAGE	19. SECURITY CLASSIFICATION OF ABSTRACT	20. LIMITATION OF ABSTRACT
UNCLASSIFIED	UNCLASSIFIED	UNCLASSIFIED	UL

Advances in Turbulence VIII

Advances in Turbulence VIII

Proceedings of the Eighth European Turbulence Conference,
Held in Barcelona, Spain, June 27-30, 2000

Editor:
C. Dopazo

Editorial Advisory Committee:
T. Bohr, I. Castro, Y. Couder, H. Fernholz,
D. Henningson, L. Kleiser, R. Piva,
D. Ronneberger, G.J. van Heijst, A. Lozano,
L. Valiño, E. Oñate, J.A. Picazo, J.M Redondo

DISTRIBUTION STATEMENT A
Approved for Public Release
Distribution Unlimited

20011203 226

A publication of CIMNE

International Center for Numerical Methods
in Engineering (CIMNE)
Barcelona, Spain

AQ F02-02-0281

U.S. Government Rights License
This work relates to Department of the Air Force Grant/rContract issued by the European Office Aerospace Research and Development (EOARD). The United States Government has a royalty-free license throughout the world in all copyrightable material contained herein

Advances in Turbulence VIII.
Proceedings of the Eighth European Turbulence Conference.
C. Dopazo at al. (Eds.)

First edition, June 2000

© International Center for Numerical Methods in Engineering (CIMNE)
Gran Capitán s/n, 08034 Barcelona, Spain

Cover design by Jordi Pallí

Printed by Artes Gráficas Torres S.A., Morales 17, 08029 Barcelona, Spain

Depósito legal: B-28.562-2000

ISBN: 84-89925-65-8

TABLE OF CONTENTS

PREFACE xxxv

Special Keynote Lecture

A Century of Turbulence 3
J. L. Lumley and A. M. Yaglom

I. Instabilities and Transition

Three-dimensional instability of two merging vortices 15
P. Meunier, T. Leweke and M. Abid

Zigzag instability and the origin of the pancake turbulence 19
Paul Billant and Jean-Marc Chomaz

Hysteretic transition from laminar to vortex shedding flow in soap films 23
V.K. Horváth, J.R. Cressman, W.I. Goldburg and X.L. Wu

A resonance principle for spatially developing wakes 27
Benoît Pier and Patrick Huerre

Experimental Characterization of Polymer Effects on Two- and Three-Dimensional Shear Instabilities 31
O. Cadot and S. Kumar

On steady-state flow solutions and their nonparallel global linear instability 35
V. Theofilis

II. Magnetohydrodynamics

Laminar-Turbulent Transition in an Electromagnetically-Levitated Molten Metal Droplet 41
B. Abedian, R. W. Hyers, C. Bullard and G. Trapaga

Bifurcation analysis of an electrically driven fluid layer 45
N. Seehafer and J. Schumacher

The Nonlinear Evolution of Disturbances to a Subsonic Mixing Layer with Transverse and Coplanar Magnetic Fields 49
R. Mallier

Simulations of turbulence subjected to gravitational and magnetic fields 53
S. Kenjereš and K. Hanjalić

On certain features of helical turbulent flows 57
H. Branover, O. Chkhetiani, A. Eidelman, E. Golbraikh and S. Moiseev

Helical turbulence properties in the laboratory and in nature 61
A. Eidelman, H. Branover and S. Moiseev

III. Instabilities and Transition

Hydrodynamic fluctuations in Couette flow 67
G. D. Chagelishvili, G. R. Khujadze and J. G. Lominadze

Dynamics of perturbations in plane Couette flow 71
H. Faisst, A. Schmiegel and B. Eckhardt

Modeling transitional plane Couette flow 75
Paul Manneville

Laminar-Turbulent Coexistence following a Subcritical Transition to Turbulence 79
O. Dauchot and A. Prigent

Uncertainty of the transition threshold for Poiseuille flows 83
C. M. Casciola, A. Olivieri and R. Piva

Direct numerical simulations of subsonic plane Poiseuille flows undergoing transition 87
Y. Mocz , H. Maekawa and K. Yamamoto

IV. Turbulence Control

Instabilities and control of transition in round and coaxial jets 93
C. B. da Silva and O. Métais

The Manipulation of Small-Scale Mixing in Coaxial Jets Using Synthetic Jet Actuators 97
S. A. Davis, B. D. Ritchie, J. M. Seitzman and A. Glezer

Identification and Control of Unstable Modes in an Isothermal and Reacting Swirling Jet 101
C. O. Paschereit, E. Gutmark and L. Haber

Large eddy simulation of turbulent flow over an open cavity 105
Haecheon Choi, Seonghyeon Hahn and Joonhyuk Choi

Response of Turbulent Channel Flow to Sudden Wall Suction and Blowing 109
Yongmann M. Chung, Hyung Jin Sung and Kai. H. Luo

On the Use of Thermal MEMS-Sensors for Wall-Shear-Stress Measurements 113
P. Johansson, L. Löfdahl, A. Bakchinov, M. Sen and M. Gad-el-Hak

Control of laminar-turbulent transition in three-dimensional boundary layer 117
Sergei V. Manuilovich

Control by Stationary and Nonstationary Streaky Structures and Their Secondary Instability 121
V.V. Kozlov and G.R. Grek

Invited Lectures

Cryogenic turbulence experiments 125
B. Castaing, B. Chabaud, B. Hébral , X. Chavanne, O. Chanal and P. Roche

Turbulent transport and mixing 133
F.T.M. Nieuwstadt and G. Brethouwer

V. Instabilities and Transition

Secondary instability of streaks in boundary layers 141
L. Brandt , P. Andersson and D. S. Henningson

On early stage instability of separated boundary layer transition 145
Z.Y. Yang and P.R. Voke

Experimental study of tuned and detuned resonant interactions of instability waves in self-similar boundary layer with an adverse pressure gradient 149
V.I. Borodulin, Y.S. Kachanov and D.B. Koptsev

Investigation of hypersonic boundary layer stability on cone with the help of artificial disturbances 153
D. A. Bountin, A. A. Maslov, A. N. Shiplyuk and A. A. Sidorenko

Sensitivity Analysis Using Adjoint Parabolized Stability Equations for Compressible Flows 157
J. O. Pralits, C. Airiau, A. Hanifi and D. S. Henningson

Numerical simulation of the spatial evolution of the instabilities in a supersonic plane jet 161
A. Kudryavtsev and D. Khotyanovsky

VI. Transport and Mixing

Kinematic Simulation for particle pair diffusion 167
F. Nicolleau, J. C. Vassilicos, D. J. Thomson

Relative dispersion in fully developed turbulence 171
G. Boffetta

Turbulent mixing of a passive tracer in the Batchelor regime 175
M.-C Jullien, P. Castiglione and P. Tabeling

The Kinetics and Geometry of Turbulent Mixing 179
E. Villermaux and J. Duplat

Averaged dynamics in the phase planes of a scalar field using DNS data 183
J. Martín, C. Dopazo and L. Valiño

Inclusion of the effect of turbulent production in a generalization of Yaglom's equation 187
L. Danaila and L. Mydlarski

VII. Instabilities and Transition

A Naimark-Sacker route to turbulence in a periodically forced flow 193
F. Marques, J. M. Lopez and J. Shen

The influence of streamwise modulation on the evolution of three-dimensional wavetrains 197
Marcello A. F. Medeiros

On Flow Reattachment By Periodic Excitation 201
A. Darabi, L. Lourenco and I. Wygnanski

Optimal control of bypass transition 205
M. Högberg, D. S. Henningson and M. Berggren

On harmonic perturbations in turbulent shear flows 209
N. Reau and A. Tumin

The Extension of CFD-Friendly Turbulence Modelling to Include Transition 213
J. Vicedo, S. Vilmin, W. N. Dawes, H. P. Hodson and A. M. Savill

VIII. Transport and Mixing

PDF computation of thermal mixing layer in grid turbulence 219
T. Bukasa, J. Pozorski and J. P. Minier

Application of an Eulerian Monte Carlo Field Method to the Simulation of the Filtered PDF in LES 223
C. Jiménez, C. Dopazo and L. Valiño

Large Eddy Simulation of Flow in Lean Premixed Prevapourised Combustor Geometries 227
G. Tang, Z. Yang and J.J. McGuirk

Turbulence Statistics and Scalar Transport in an Open-Channel Flow 231
Y. Yamamoto, T. Kunugi and A. Serizawa

Scalar Flux Measurements and Models of a Plume Emitting from a Wall Line Source Downstream of an Obstacle on the Wall of a Turbulent Boundary Layer 235
J.-Y. Vinçont, S. Simoëns, M. Ayrault and J.M. Wallace

Simultaneous measurements of scalar and velocity in variable density turbulent jets 239
M. Amielh , L. Pietri and F. Anselmet

IX. Boundary Layers and Free Shear Flows

Multi-scale structures in a turbulent near-wake 245
Hui Li and Yu Zhou

Topological Features of a Turbulent Wake 249
G.A. Kopp, Francesc Giralt and A. Vernet

Active control of the flow downstream of a swept fence 253
A. Huppertz and H.-H. Fernholz

Numerical simulation of forced turbulent flow over a fence 257
A. Orellano and H. Wengle

Experimental investigation of two-point correlations in a separated flow 261
Lars Sætran and Bård Venäs

Study of a turbulent separated flow using HPIV 265
K. von Ellenrieder, J. Kostas and J. Soria

Recovery of a turbulent boundary layer behind a swept, rearward-facing step 269
Hans-J. Kaltenbach

Karhunen–Loève expansion (POD) of the flow behind a swept, rearward-facing step 273
Werner Jürgens and Hans–Jakob Kaltenbach

Unilateral-Average Based Study of Incompressible Turbulent Mean Flow and Coherent Flow 277
Ge Gao and Yan Yong

X. Geophysical Turbulence

Three-dimensional instability of columnar cyclone-anticyclone pairs 283
Y. Afanasyev

High Rayleigh and Taylor Number Convection in Spherical Shells 287
Anil E. Deane, Paul F. Fischer and Henry M. Tufo

Buoyancy effect and universal structure of a stably stratified turbulence field 291
K. Sassa, S. Matsunaga and H. Makita

Kinematic Simulation for stably stratified and rotating turbulence 295
F. Nicolleau and J. C. Vassilicos

Pressure/Potential-Temperature Covariance in Free and Rotating Convection 299
Dmitrii V. Mironov

Turbulence universality in laboratory and atmospheric observations and its theoretical investigation 303
S. Gordienko, S. Moiseev, A. Eidelman and H. Branover

Spectra of turbulence in boundary layers near the ground 307
P. Carlotti and J.C.R. Hunt

Non-Local Turbulence in Stably Stratified Boundary Layers 311
Prof. S. Zilitinkevich

Analysis of the pdf of the vertical velocity in the buoyancy-driven atmospheric boundary layer 315
S. Alberghi, F. Tampieri, S. Argentini, G. Mastrantonio and A. Viola

XI. Boundary Layers and Free Shear Flows

Mixing enhancement in turbulent wall jets 321
M. Schober and H.-H. Fernholz

Turbulence characteristics in pipe flow with swirl 325
M. Schmidts and V. Vasanta Ram

LES of Turbulent Flows through 90°-Pipe Bends 329
F. Rütten, M. Meinke and W. Schröder

Visualization and PIV measurements of the near wall structure in a turbulent pipe flow 333
Zhang Zhaoshun, Feng Binchun, Cui Guixiang and Michel Ayrault

Characteristics of Internal Vortical Structures in a Merged Turbulent Spot 337
H. Makita and A. Nishizawa

Investigation of wall structures in a turbulent channel flow using stereo PIV 341
G. Ciraolo and G.P. Romano

DPIV Studies of Turbulent Boundary Layers 345
M. Onorato, G. M. Di Cicca, G. Iuso and P. G. Spazzini

PIV measurements in a high Re turbulent boundary layer 349
Kristian Angele and Barbro Muhammad-Klingmann

XII. Geophysical Turbulence

Direct numerical simulation of mixing in geophysical flows 355
Wolfgang Gerlinger, Kai Schneider and Henning Bockhorn

Algebraic parametrizations for the triple correlations in modelling the shearless turbulence mixing layer 359
V. Grebenev and B. Ilyushin

PDF Construction for Modeling the Pollutant Dispersion in Convective Atmospheric Boundary Layer 363
B. B. Ilyushin

Turbulent transport across a sheared inversion at the convective boundary layer top 367
E. Fedorovich and J. Thäter

On the generation of turbulence by baroclinic instability in the upper ocean 371
P. Ripa

Sensitivity of rhythmic oblique bar generation to wave-driven turbulence in the surf-zone 375
F. Ribas, A. Montoto and A. Falqués

Invited Lectures

Laboratory modeling of geophysical turbulence 379
P. F. Linden, J. N. Hacker, B. M. Boubnov and S. B. Dalziel

Large eddy simulation of turbulent, nonpremixed combustion 385
Parviz Moin, Charles Pierce and Heinz Pitsch

XIII. Boundary Layers and Free Shear Flows

High Reynolds number turbulent boundary-layer experiments 395
Jens M. Österlund and Arne V. Johansson

Flow structures in high Reynolds number turbulent boundary-layers 399
B. Lindgren, J. Österlund and A.V. Johansson

Structure of Turbulence in the Logarithmic Layer and its Mechanism 403
Y. Miyake, K. Tsujimoto, N. Sato and Y. Suzuki

Kinetic energy, enstrophy and strain rate in near-wall turbulence 407
N.D.Sandham and A.Tsinober

On order and accuracy of the stochastic estimation of the flow structure associated with surface pressure events in a turbulent boundary layer 411
A. Naguib and C. Wark

Reynolds-stress budgets from a wall-bounded adverse-pressure-gradient flow 415
G. N. Coleman, J. Kim and P. R. Spalart

Scaling of the near-wall layer beneath a three-dimensional turbulent separation bubble 419
P.E. Hancock and J.R. Hardman

XIV. Turbulent Reacting Flows

A geometric criterion for non-equilibrium and triple flame domains 425
W. Kollmann , J. H. Chen and H. G. Im

Edge flame and partially premixed flamelets in nonpremixed combustion . 429
Valérie Favier and Luc Vervisch

The effects of combustion on turbulence in high speed mixing layers 433
F. Ladeinde, E. E. O'Brien and W. Liu

Compressibility Effects on Scalar Mixing in the Turbulent Reacting Shear Layer 437
C. Pantano and S. Sarkar

Subgrid Scale Variance and Dissipation of a Scalar Field in Large Eddy Simulation Combustion Models 441
C. Jiménez, F. Ducros and B. Cuenot

Large Eddy Simulation of a Counterflow Configuration with and without Combustion: Mixing and Flowfield 445
A. Kempf, H. Forkel, J.-Y. Chen, A. Sadiki and J. Janicka

Large eddy simulation of a turbulent premixed V-shaped flame 449
M. Boger and D. Veynante

XV. Boundary Layers and Free Shear Flows

The surface region of rough-wall boundary layers 455
Alison Ploss, Ian Castro and Hong Cheng

Space-Time Characteristics of the Wall Shear-Stress Fluctuations in a Turbulent Boundary Layer with Transverse Curvature 459
Dongshin Shin and Haecheon Choi

The Influence Of Wall-Porosity Upon The Near-Wall Turbulence Dynamics 463
M. Uhlmann, A. Pinelli, J. Jiménez and G. Kawahara

Similitudes in turbulent near-wall flows with injection and suction 467
I. I. Vigdorovich

Impact of localized unsteady blowing on the near wall turbulence 471
S. Tardu

Changes in turbulent structure in a boundary layer due to local injection 475
P.-Å. Krogstad

Receptivity of boundary layers under centrifugal forces 479
N. Yurchenko

The effect of long chain polymers on the structure of wall turbulence 483
E. De Angelis, C. M. Casciola and R. Piva

Direct interaction between highly-entangled polymers and small-scale coherent structures in a turbulent polymer-solution flow 487
Y. Hagiwara, T. Imamura, S. Takagaki and M. Tanaka

XVI. Turbulent Reacting Flows

Modeling of Mixing Processes in non–Isothermal and Combusting Flows 493
R. P. Lindstedt and E. M. Váos

Probability Density Function Modelling of an Axisymmetric Combustion Chamber 497
W.P. Jones and R. Weerasinghe

Implementation and Validation of an Adaptive Particle PDF Transport Method 501
M. Pfitzner and I. Romaschov

Simulation of turbulent spray combustion in a full-scale gas turbine combustor 505
S. Menon

The Impact of Buoyancy and Flame Structure on Soot and Radiation Emissions from a Turbulent Flame 509
W. Kollmann, J. Auston, R.L. Vander Wal and I.M. Kennedy

XVII. DNS / LES

A generalised view on mixed models 515
J. Meyers, M. Baelmans and C. Lacor

Assessment of subgrid-scale models in dissipative vortical structures 519
Kiyosi Horiuti

Multifractal Scale-Similarity in Subgrid-Scale Turbulence Modeling 523
G.C. Burton, W.J.A. Dahm, D.R. Dowling and K.G. Powell

A LES model based on the spectral decay of the kinetic energy 527
F. Bouchon and T. Dubois

On energy and pressure backscatter in incompressible isotropic turbulence 531
S. Ossia and M. Lesieur

Large-eddy simulation of turbulent mixing layers 535
Elias Balaras, Ugo Piomelli and James M. Wallace

Rapid and slow contributions to the turbulent stress tensor and inverse modeling in a turbulent mixing layer 539
B.J. Geurts, I.C.C. de Bruin and S. Sarkar

Spatial development of a 3D compressible turbulent mixing layer 543
L. Doris, C. Tenaud and L. Ta Phuoc

A-Posteriori Tests of a New SGS Model: LES of Fully Developed Pipe Flow 547
C. Brun, T. J. Hüttl and R. Friedrich

XVIII. Two Phase Flows

Settling velocity and clustering of particles in an homogeneous and isotropic turbulence 553
F. Hainaux, A. Aliseda, A. Cartellier and J. C. Lasheras

Two-way coupling effect on settling velocity of small heavy particles in homogeneous turbulence 557
M. Tanaka, N. Komai, Y. Maeda and Y. Hagiwara

Direct numerical simulation of particle dispersion in a spatial mixing layer 561
Z. W. Hu, K. H. Luo and X. Y. Luo

Measurements and LES Modeling of Dispersion in a Turbulent Two phase round Jet 565
I.M. Kennedy, P.J. Santangelo and W. Kollmann

Initial distribution of bubbles injected into a turbulent water jet and its effect on the final bubble size PDF 569
C. Martínez-Bazán, J.L. Montañes and J.C. Lasheras

The Breakup Time of a Droplet in a Fully-Developed Turbulent Flow 573
C. Eastwood, A. Cartellier and J. C. Lasheras

Experiments on Particle-Turbulence Interaction in a Backward-Facing Step Flow 577
T. Vogt and U. Renz

Partially premixed turbulent combustion in spray 581
J. Réveillon and L. Vervisch

Modelling inter-particle collisions in Lagrangian approaches 585
P. Achim, A. Berlemont and Z. Chang

XIX. DNS / LES

Application of Optimal LES 591
J.A. Langford, S. Völker, P. Venugopal and R.D. Moser

Large Eddy Simulation of High Reynolds Number Flows 595
C. Fureby and F.F. Grinstein

Lagrangian methods for the tensor-diffusivity subgrid model 599
Piet Moeleker and Anthony Leonard

Wavelet Cross-Correlation Analysis of Turbulent Mixing from Large-Eddy-Simulations 603
S. Sello and J. Bellazzini

Sidewall boundary layer instabilities in confined swirling flow 607
H. M. Blackburn

Convective turbulence of gaseous helium in a closed domain: a look inside the cell 611
R. Verzicco and R. Camussi

XX. Modelling

Low-order models derived from POD-Galerkin approximations for separated turbulent flows 617
A. Lombard, P. Sagaut, J.P. Bonnet and J. Delville

Geometry and statistics in Lagrangian dispersion 621
A. Pumir, B. Shraiman and M. Chertkov

Using Rapid Distortion Theory to interpret experiments on stably stratified turbulent shear flows 625
D. D. Stretch, J. W. Rottman, K. H. Keller and C. W. Van Atta

Nonlinear RDT theory of near wall turbulence 629
S.V. Nazarenko, N.K.-R. Kevlahan and B. Dubrulle

Decaying two-dimensional turbulence in a bounded domain 633
H.J.H. Clercx and G.J.F. van Heijst

Invited Lectures

Some Open Computational Problems in Wall-Bounded Turbulence 637
Javier Jiménez

Low-Pressure Vortex: The Role in Turbulence Dynamics 647
S. Kida

XXI. DNS / LES

Appearance and Alignment with Strain Rate of Coherent Fine Scale Eddies in Turbulent Mixing Layer 655
M. Tanahashi, S. Iwase and T. Miyauchi

DNS of flow around a circular cylinder at a subcritical Reynolds number with cartesian grids 659
F. Tremblay, M. Manhart and R. Friedrich

Reynolds number effect on turbulent structures in a pipe flow via DNS 663
S. Satake and T. Kunugi and R. Himeno

The directional dissipation scale: a criterion for grid resolution in direct numerical simulations 667
M. Manhart

Analysis of coherent structures in turbulent channel flow using the orthogonal wavelet representation. 671
D. C. Dunn and J. F. Morrison

Near-wall structures in turbulent rotor-stator flow 675
M. Lygren and H. I. Andersson

Triadic interaction of vorticity, strain rate, and scalar gradient in stably stratified homogeneous sheared turbulence 679
K.K. Nomura and P.J. Diamessis

XXII. Modelling

Spectral reduction: a statistical description of turbulence 685
John C. Bowman, B. A. Shadwick and P. J. Morrison

A spectral closure applied to anisotropic inhomogeneous turbulence 689
H. Touil, J.P. Bertoglio and S. Parpais

A numerical algorithm for efficiently solving spectral closure equations 693
T. Gotoh and Y. Kaneda

Local Energy Transfer theory in forced and decaying isotropic turbulence 697
W.D. McComb and A.P. Quinn

Consolidated expansions used in modeling anisotropic turbulence in a channel flow 701
S. T. Smith and K. Santy-Ateyaba

XXIII. Compressible Turbulence

Compressibility effects in grid generated turbulence 707
Yiannis Andreopoulos

Large Eddy Simulation of a Mach 0.9 turbulent jet 711
B.J. Boersma and S.K. Lele

LES of Shock-Boundary-Layer Interaction with the Approximate Deconvolution Model 715
S. Stolz, N. A. Adams and L. Kleiser

Relaxation of super/hypersonic boundary layer behind interaction with shock wave/expansion fan 719
A.V. Starov and M.A. Goldfeld

XXIV. Vortex Dynamics

Multipolar instability of a vortex in a deformed cylinder 725
C. Eloy, P. Le Gal and S. Le Dizès

Decay of perturbations near the centre of a strong vortex 729
K. Bajer, A. P. Bassom and A. D. Gilbert

Energy dissipation in spiral vortex layers wrapped around a diffusing straight vortex tube 733
G. Kawahara, S. Kida, S. Yanase and M. Tanaka

Vortex-wave conversion in high shear flows 737
G. D. Chagelishvili, A. G. Tevzadze, G. Bodo, P. Rossi and G. T. Gogoberidze

Experimental study of large-scale coherent structures with helical symmetry of vorticity 741
S.V. Alekseenko, I.S. Cherny and S.I. Shtork

Coherent Vortex Simulation (CVS) of a two-dimensional mixing layer 745
Kai Schneider and Marie Farge

XXV. Intermittency and Scaling

The structures which cause intermittency 751
Adrian Daniel Staicu and Willem van de Water

Remarkable features of multiplier distributions in turbulence 755
P. Chainais, E. Lévêque, P. Abry and Ch. Baudet

On the complete statistical characterization of velocity increments in turbulence 759
St. Lück, Ch. Renner, J. Peinke and R. Friedrich

Exit time of turbulent signals. 763
L. Biferale, M. Cencini, D. Vergni and A.Vulpiani

A Langevin equation for turbulent velocity increments 767
P. Marcq and A. Naert

Intermittent structure functions and coherent structures in fully developed turbulence 771
R. Camussi and R. Verzicco

Disentangling Scaling Properties in Anisotropic and Inhomogeneous Turbulence 775
Irene Mazzitelli, Itai Arad, Luca Biferale and Itamar Procaccia

Scaling laws and vortical structures in homogeneous shear flow 779
P. Gualtieri, C. M. Casciola, G. Amati and R. Piva

Self similarity and intermittency in a turbulent non-homogeneous wake 783
O.B. Mahjoub, J.M. Redondo and A. Babiano

Asymmetry of Velocity Increments in a Turbulent Channel Flow 787
G. Iuso and M. Onorato

XXVI. Vortex Dynamics

Alignment properties in Fourier and wavelet filtered forced two-dimensional turbulence 793
Bartosz Protas, Kai Schneider and Marie Farge

Vortex tube extraction in three–dimensional turbulence using orthogonal wavelets 797
Marie Farge, Kai Schneider and Giulio Pellegrino

Flow and Reynolds Number Dependencies of Turbulent Vorticity Fluctuations 801
R. A. Antonia and T. Zhou

Two-dimensional breakdown of a Burgers vortex subject to a rotating strain field 805
S. Le Dizès

The Axisymmetric Vortex Breakdown Phenomenon 809
Z. Rusak

Confined Vortex Breakdown in a Conical Cavity 813
R. K. M. Seah, T. T. Lim, B. C. Khoo and J. M. Lopez

Modelling of the turbulent vortex breakdown as a transition from column to conical helical vortices 817
T.O. Murakhtina and V.L. Okulov

DNS of vortex breakdown in swirling jets 821
W. Kollmann, A. Ooi, M. S. Chong and J. Soria

Lagrangian LES and vortex dynamics of forced unsteady round jets and colliding vortices 825
H. Ishikawa, S. Izawa and M. Kiya

XXVII. Intermittency and Scaling

Intermittency in turbulent boundary layers 831
F. Toschi, E. Levêque and G. Ruiz-Chavarria

Turbulent mixing of a passive scalar: Statistics of the cliffs 835
F. Moisy, H. Willaime, J. S. Andersen and P. Tabeling

Velocity-acceleration structure function and Kolmogorov's 4/5 law 839
Søren Ott and Jakob Mann

Scaling behavior of the vertical velocity field and of the intensity field in the solar photosphere 843
F. Lepreti, B. Bavassano, F. Berrilli, R. Bruno, V.Carbone, G. Consolini and E. Pietropaolo

An inner scale for dissipation of helicity in turbulence 847
P. D. Ditlevsen and P. Giuliani

A universal law for tails of density pdf's in multi-dimensional Burgers turbulence 851
J. Bec, U. Frisch, K. Khanin and B. Villone

XXVIII. Miscellaneous

Fossils of turbulence and non-turbulence in the primordial universe: the fluid mechanics of dark matter 857
Carl H. Gibson

Power fluctuations in confined turbulence, analogy with finite size critical phenomena 861
J.-F. Pinton, P.C.W. Holdsworth, R. Labbé, S.T. Bramwell and J.-Y. Fortin

Reduction and long time behaviour of homogeneous turbulence under spatially constant mean-velocity gradient 865
M. Oberlack and M. Barakat

Interaction of worm-like micelles with turbulent flow 869
Z. Chara and J. Myska

Numerical Simulations and DPIV Measurements of Pulsatile Flow in Large Stenosed Arteries 873
A. Borg and L. Fuchs

Quantification of anisotropy in an oscillating grid flow 877
Jakob Mann and Søren Ott

Invited Lectures

Anomalous Scaling Laws in Turbulence 881
R. Benzi

Nonlinear self-sustained structures in shear flows 889
Patrick Huerre

XXIX. Small Scale Features

Geometrical statistics in the atmospheric turbulent flow at $Re_\lambda=10^4$ 895
M. Kholmyansky, A. Tsinober and S. Yorish

Improvements to hot-wire measurementsof turbulence energy dissipation . 899
J.-J. Lasserre, M. Coantic and F. Anselmet

Turbulent energy scale–budget equations in a fully developed channel flow 903
L. Danaila, F. Anselmet, T. Zhou and R.A. Antonia

Energy and Temperature Dissipation Rates in a Cylinder Wake and Grid Turbulence 907
T. Zhou and R. A. Antonia

XXX. Miscellaneous

Oscillatory binary fluid convection in finite containers 913
O. Batiste, M. Net, I. Mercader and E. Knobloch

From Hard Turbulence to the Ultimate Regime in a Rough Rayleigh-Bénard cell 917
P.M. Roche, B. Castaing, B. Chabaud and B. Hébral

The phase diagram of Rayleigh-Benard turbulence 921
Siegfried Grossmann and Detlef Lohse

Cryogenic Ultra-High Rayleigh Number Turbulence 925
J.J. Niemela, L. Skrbek, K.R. Sreenivasan and R.J. Donnelly

Turbulence in liquid helium 929
D. Kivotides, C.F. Barenghi and D.C. Samuels

Decay of Grid Generated Classical and Superfluid Turbulence 933
L. Skrbek and Steven R. Stalp

Modeling of quantum turbulence in superfluid ^{4}He 937
Tomasz Lipniacki

POSTERS

Instabilities and Transition

Numerical study of bifurcations for the two-dimensional Poiseuille flow 943
Pablo S. Casas and Àngel Jorba

Nonlinear dynamics in a rapidly rotating annulus 943
D. Pino, I. Mercader, J. Sánchez and M. Net

Reentrant squares in Rayleigh-Bénard convection 944
A. Demircan and N. Seehafer

The research of laminar–turbulent transition in hypersonic three-dimensional boundary layer 944
M.A. Goldfeld

Stability of a helium II flow 945
S. P. Godfrey, C. F. Barenghi and D. C. Samuels

Interactions of Three-dimensional Instabilities in Plane Mixing Layers 945
Jordi Estevadeordal

Holographic flow visualization for study of 3D vortex and flow instabilities 946
J. Estevadeordal , S. Gogineni , L. Goss , H. Meng and M. Roquemore

Magnetohydrodynamics

Anisotropic zero-modes for a kinematic MHD model 947
A. Lanotte and A. Mazzino

Helical and Chiral Dynamo 947
O. Chkhetiani, E. Golbraikh, V. Pungin and S. Moiseev

Vortex evolution in helical turbulence flow 948
A. Kapusta, B. Mikhailovich, E. Golbraikh

Characterization of the intermittency in 2–D magnetohydrodynamic through the scaling properties of the PDFs of the turbulent fluctuations .. 948
L. Sorriso-Valvo , V. Carbone , P. Veltri , H. Politano and A. Pouquet

Response of the solar wind to incoming thermal or magnetic perturbations 949
R. Grappin, J. Léorat and A. Buttighoffer

Turbulence Control

Modification of a two-dimensional vortex street by a polymer additive 950
W.I. Goldburg, J.R. Cressman and Q. Bailey

Controlling a Separating Flow using Piezoelectric-Actuators 950
Y. Yokokawa , Y. Fukunishi and S. Kikuchi

Transport and Mixing

The numerical solution of the equation for one-point probability density function of a scalar in homogeneous turbulence 951
A.D. Chorny, V.A. Sosinovich

New development of the LMSE mixing model with accounting for intermittency 951
M.Gorokhovski and V.Sabel'nikov

Iso-scalar surfaces in a Direct Numerical Simulation of isotropic turbulence with scalar injection 952
M. Elmo , J. P. Bertoglio and V. A. Sabel'nikov

Mean-field theory of a passive scalar advected by a random velocity field with finite renewal time 952
T. Elperin , N. Kleeorin , I. Rogachevskii and D. Sokoloff

Effects of compressibility and finite renewal time of a random velocity field to intermittency of passive scalar fluctuations 953
T. Elperin , N. Kleeorin, I. Rogachevskii and D. Sokoloff

Two-particle dispersion in Kinematic Simulations 953
J.Dávila , E. Bravo-León , and J.C. Vassilicos

Measurement of Passive Scalar Statistics through Use of Compensated Cold Wires 954
J. Lemay , J. S. Blais , A. Benaïssa and B. Fleck

Statistics of a high Schmidt number passive scalar in the far-wake 954
H. Rehab, R. A. Antonia and L. Djenidi

Mixing and coherent structures in jets in crossflow 955
A. Rivero, J.A. Ferré, F. Giralt

A Comparative Study of Heat and Mass Transfer by Impinging Jets on Flat and Curved Surfaces 955
H. Stapountzis, D. Tsipas,and A. Stamatellos

Characterization of trailing vortex structures in stirred tanks 956
Jos Derksen,John McLaughlin and Konstantinos Kontomaris

Boundary Layers and Free Shear Flows

Experimental assessment of stress-strain relation for coaxial jets 957
F. Schmitt, Ch. Hirsch and B. K. Hazarika

Effect of an accelerating co-flow on a turbulent jet 957
A. Califano, A.K. Prasad and J. Westerweel

A Comparative Experimental Investigation of a Turbulent Axisymmetric Zero-Net-Mass Flux Jet and a Continuous Jet 958
J. Cater and J. Soria

Development of large-scale structures in confined jet shear layer 958
S. Alekseenko, A. Bilsky, D. Markovich and V. Vasechkin

Experimental investigation of wall effects on the initial region of turbulent round jets 959
A. Benaissa , B. A. Fleck , A. Pollard , and J.F. Morrison

Evaluating the accuracy of the LSE-POD technique in an axisymmetric shear layer. 959
D. Ewing and S. Woodward

A study of turbulent transport processes in the near wake of cylinder under controlled inflow oscillation 960
A. Jarża , M. Podolski

A numerical investigation of momentumless turbulent wake dynamics in a linearly stratified medium 960
G. G. Chernykh , B. B. Ilyushin , O. F. Voropayeva

A spatial structure of a flow in a axisymmetric sudden expansion 961
Noriyuki Furuichi , Yasushi Takeda and Yasuhiro Ozaki

Instability waves in separated swirling flows at bluff bodies 961
S. P. Bardakhanov

Enstrophy and Dissipation Within Flow Regions of a Turbulent Channel Flow 962
S. Wade , J. Soria , A. Ooi and M. S. Chong

Flow visualization of turbulent flow in an open channel with 2D fixed bed forms 962
Joselina Espinoza and Jorge Rojas

Experimental Investigation of Secondary Currents Using High-Temporal Resolved PIV 963
J. von Lukowicz, T. Rosenstein, T. Baur and J. Köngeter

Scaling the outer profiles of turbulent boundary layers 963
L. Castillo and W.K. George

Simulation of the intrusion of coherent free-stream perturbations in a subsonic boundary layer 964
H.C. de Lange and R.J.M. Bastiaans

Analysis of the Interactions between Large-Scale Streamwise EHD Structures and a Turbulent Boundary Layer 964
C. Marchioli, A. Soldati and M.V. Salvetti

Interaction of Endothermic and Exothermic Regions with a Turbulent Hypersonic Boundary Layer 965
M. Pino Martín and Graham V. Candler

Geophysical Turbulence

Correlation intervals of sea turbulence velocity field 966
G. A. Fedotov

Turbulence structure and mixing near gas-liquid interface 966
Derek Stretch and Mosa Chaisi

On Tracers And Potential Vorticities In Ocean Dynamics 967
Michael V. Kurgansky and Ettore Salusti

Large Eddy Simulation of Flow Phenomena in Lakes and Reservoirs 967
K. Rettemeier , O. Bergen and J. Koengeter ,

GOTM, a model for simulating dissipation measurements in estuaries and open ocean 968
M. R. Villarreal , H. Burchard , K. Bolding and P. P. Mathieu

Experiments on flow characteristics and resistance in vegetated channels 968
A. Bateman, J.M. Redondo, D. Velasco and J.P. Martín Vide

SAR Observations of the Gibraltar Oceanographic and Environmental Features 969
J.J. Martinez Benjamin, A. Platonov and J.M. Redondo

Turbulent Reacting Flows

Mixing Regimes in Gaseous Diffusion Flames 970
A. Cavaliere , D. Pappa and R. Ragucci

Effect of chemical reactions and phase transitions on turbulent transport 970
T. Elperin, N. Kleeorin and I. Rogachevskii

Reduced Kinetic Mechanisms in Time Dependent Numerical Simulations of Nonpremixed Flames 971
J. Hsu and S. Mahalingam

Direct Numerical Simulation Large Eddy Simulation

DNS of turbulent Couette flow and its comparison with turbulent Poiseuille flow 972
K. Shingai, H. Kawamura, and Y. Matsuo

Generation of Turbulent Inflow Data without Temporal Correlations 972
A. Spille and H.-J. Kaltenbach

A priori and a posteriori tests of subgrid scale models for scalar transport 973
C. Jiménez, C. Dopazo and L. Valiño

A-posteriori test of LES closure models for free surface flows. 973
R. Broglia, L. Bognetti, A. Di Mascio and B. Favini

Large Eddy Simulations of the flow around a square cylinder 974
E. Védy and P. R. Voke

Large-eddy simulation of flow around a rectangular obstacle in fully developed turbulent boundary layer – The effects of turbulence on a separation bubble – 974
K. Nozawa and T. Tamura

Large Eddy Simulation of a turbulent flow in a heated duct 975
M. Salinas Vázquez and O. Métais

A Multi-domain/Multi-resolution Method with Application to Large-eddy Simulation 975
P. Quéméré, P. Sagaut, V. Couaillier and F. Leboeuf

Large-Eddy Simulation of an oscillatory boundary layer 976
V. Armenio and G. Vittori

On the relation between coherent structures and grid/subgrid-scale energy transfer in transitional and turbulent shear flows 976
C. B. da Silva

Two Phase Flows

Turbulence modification by particles; Experimental verification of a theoretical model 977
G. Ooms, J. Pietryga, C. Poelma and J. Westerweel

Near wall effects on particles in a turbulent channel flow 977
P. Rambaud, A. Tanière, B. Oesterlé and M.L. Riethmuller

Modelling

Optimisation of two-equation turbulence models 978
H. Bézard

A $k-\omega$ /Rapid Distortion Model applied to unsteady wall flows 978
P. da Costa and S. Tardu

Effect of inlet turbulence on convective flow between two vertical walls : k-ϵ low Reynolds turbulence model 979
R. Bennacer, T. Hammami and A.A. Mohamad

Thermodynamically Consistent Turbulence Modeling of Turbulent Flows with Variable Mass-density 979
A. Sadiki

Prediction of the Reynolds stresses and higher moments in a developed turbulent flow in an axially rotating pipe 980
B. B. Ilyushin and S. N. Yakovenko

Predictions of higher moments by a transported pdf model 980
D. Lentini

Full velocity-scalar PDF approach for wall-bounded flows and computation of thermal boundary layers 981
J. Pozorski and and J. P. Minier

Asymptotic models for slow dynamics and anisotropic structure of turbulence in a rotating fluid 981
F.S. Godeferd, J.F. Scott and C. Cambon

Assessment of turbulence models of second order for the prediction of near-field aircraft plumes 982
A. Sadiki, A. Maltsev and J. Janicka

Influences of Buoyancy on Turbulence for Conditions of Heat Transfer by Combined Forced and Free Convection to Air in a Vertical Tube 982
J.D. Jackson and Jiankang Li

Compressible Turbulence

Validation of the subgrid modelling by simulating a compressible turbulent flow in a 3D channel 983
L. Coquart, C. Tenaud and L. Ta Phuoc

Study of wake, vortex-shedding, and shock in a Transonic Compressor 983
J. Estevadeordal , S. Gogineni , L. Goss , W. Copenhaver and S. Gorrell

Intermittency and Scaling

Anisotropic Scaling Anomaly in Isotropic Turbulence 984
B. R. Pearson and W. v. d. Water

Effects of shear on small-scale properties in a Kolmogorov flow 984
I. San Gil , S. Chen and K. R. Sreenivasan

Fractal skins of turbulence 985
D. Queiros-Conde

Turbulent wakes of 3-D fractal grids 985
D. Queiros-Conde and J.C. Vassilicos

Temporal structures in Shell Models 986
F. Okkels

Wavelet Analysis of Intermittent Behavior of Pressure Fluctuations in Separated and Reattaching Flows 986
Inwon Lee and Hyung Jin Sung

The Scalings of Scalar Structure Functions in a Velocity Field with Coherent Vortical Structures 987
Md. Amirul Islam Khan and J. Christos Vassilicos

Coherent structures in shell models for passive scalar advection 987
L. Biferale, I. Daumont, T. Dombre and A. Lanotte

Passive temperature pdf's in fully developped turbulence 988
C. Auriault, Y. Gagne and B. Castaing

From a Vortex Gas Model of Turbulence to Mellin Functions 988
P. Borgnat, O. Michel, C. Baudet and P. Flandrin

The Scalings of Scalar Structure Functions in a Velocity Field with Coherent Vortical Structures 989
Md. Amirul Islam Khan and J. Christos Vassilicos

Vortex Dynamics

The definition and identification of a vortex revisited 990
B. Herrera, F.X. Grau and Francesc Giralt

Inhomogeneous turbulence near a large scale vortex 990
C. Simand, F. Chillà and J.-F. Pinton

Computation of equilibria between two corotating nonuniform vortices. .. 991
U. Ehrenstein and M. Rossi

Experiments on the vortex structure of a wake behind a torus 991
S. Yamashita and Y. Inoue

Topological complexity of a vortex tangle 992
C. F. Barenghi, A. Marsden and D. C. Samuels

Length scales in turbulent superfluid vortex line tangles 992
D. C. Samuels and D. Kivotides

Coherent Vortex Simulation (CVS) to compute two-dimensional turbulent flows using wavelets 993
M. Farge, K. Schneider and N. Kevlahan

Miscellaneous

Dimension of the Attractor of Turbulence revisited: statistical mechanics considerations 994
E. Segre and L. Rondoni

Self-amplification of the field of velocity derivatives in quasi-isotropic turbulence 994
B. Galanti and A. Tsinober

On the calculation of streamwise derivatives from single-point measurements 995
C.F. Stein , A. Bakchinov, J. Bergh and L. Löfdahl

Instantaneous frequency of the near wall singularities 995
S. Tardu

Large scales features of the flow induced by precession of a rotating cylinder 996
J. Léorat , P. Lallemand , J.L. Guermond and F. Plunian

Mean field hydrodynamics for turbulent flows subjected rotation 996
A.S. Petrosyan and D.V. Tsygankov

Computation of turbulent flow around periodic obstacles using a Krylov-spectral method based on Brinkman penalization 997
A. Cherhabili and N. K.-R. Kevlahan

Buoyancy generated turbulent flows in semi-enclosed regions: applications to oil-production technology 997
M.K. Neophytou, R.E. Britter

On the role of the divergence of the velocity for variable density flows in mixed or natural convection 998
C. Rey

Cryogenic High Reynolds Experiment 998
B. Chabaud, B. Hebral, S. Pietropinto, P. Roche, C. Baudet, Y. Gagne, E. Hopfinger, C. Poulain, B. Castaing, Y. Ladam, O. Michel, A. Naert, A. Bezaguet, J.-P. Dauvergne, P. Lebrun and R. Van-Weelderen

Experimental and numerical investigation of the transition convective motion in a cylinder 999
Minerva Vargas, Fernando Sierra, Andrey Avramenko and Eduardo Ramos

Experimental investigation and numerical simulation of the flow around a high speed train 999
N. Paradot, C. Talotte, H. Garem, J. Delville and J.-P. Bonnet

AUTHOR INDEX 1001

Preface

Advances in Turbulence VIII presents an updated sample of the research being performed world wide, with some inevitable bias towards work in Europe. It contains an almost complete collection of the papers delivered and the posters discussed at the Eighth European Turbulence Conference (ETC-8). The event is organized, under the auspices of the European Mechanics Society (EUROMECH), by the University of Zaragoza and the Consejo Superior de Investigaciones Científicas (CSIC), with the collaboration of CIMNE (Spanish ERCOFTAC Pilot Center) and the Universidad Politécnica de Cataluña (Barcelona), where the conference will be held from June 27 to 30, 2000. As for ETC-6 (Lausanne) and ETC-7 (Nice), the present volume is being produced before the conference in order to assure timely dissemination of the latest research results and replaces the usual collection of abstracts which is generally accessible only to participants. The volume is thus geared towards specialists in the area of flow turbulence who could not attend ETC-8 as well as to anybody who would like to quickly asses the most active current research topics and the groups associated with them.

The papers presented and the posters discussed at ETC-8 have been selected by the international EUROMECH Turbulence Conference Committee (ETCC). Besides the organizer, this committee, chaired by D. Henningson, was composed by T. Bohr, I. Castro, Y. Couder, H. Fernholz, L. Kleiser, R. Piva, D. Ronneberger and G. J. van Heijst; for this occasion the ETCC was extended to include A. Lozano, J.M. Redondo and L. Valiño from the Regional Organizing Committee. I wish to express my most sincere gratitude to all of them for their hard and efficient work. Their highly qualified judgment made possible the difficult task of evaluating 478 extended abstracts submitted to ETC-8 in a limited time span, accepting over 70% for either oral presentation or poster discussion.

ETC-8 reflects the original EUROMECH philosophy for establishing the European Turbulence Conferences of bringing together mathematicians, physicist and engineers working both on fundamental aspects of turbulent flows as well as on their applications and interactions with several physical and chemical processes. Today, probably better than ever before, the thoughts of Leonardo da Vinci (Those who are endowed with practical skills with no scientific knowledge are like a sailor who goes on board with neither a rudder nor a compass; he would never know precisely where he is heading for) are pertinent. Admitting the undisputed validity of da Vincis ideas, the precision, however, should be made that tools (modellling, CFD, diagnostic techniques, etc.) and a well defined destination (engineering applications) are indispensable travel companions

of the rudder and compass (basic understanding). In this respect, the European Turbulence Conferences seem to have had a distinct flavour compared to similar events over the world, combining fundamental aspects and applied state-of-the-art instead of keeping them apart and within separate niches.

The papers have been grouped in the order to be presented under the different sessions of ETC-8, as this volume is intended as a guideline of the conference development. New ideas and insights on classical topics such as hydrodynamic instability and transition, numerical simulations and modelling, vortex dynamics, high Reynolds number turbulence and intermittency, geophysical flows, compressibility effects, transport and mixing and multiphase flows are discussed along these pages, as they have been sources of interest since the first conference. Only minor changes have been introduced in comparison with ETC-6 and ETC-7; the ETCC made the sensible decision to embed into different topics (e.g., wall-free and wall-bounded turbulent shear flows) those previously included under the umbrella of Experiments and Experimental Techniques. What was perceived as Industrial Applications by previous organizers ranged from algebraic stress models to the DNS of transonic flow around a wing; this heading has been supressed in this volume. A small number of contributions dealing with different aspects of combusting flows had been presented in previous conferences; a significant number of abstracts, emphasizing the interaction between turbulence and chemical kinetics, were submitted to ETC-8 and made the organization of a session on Turbulent Reacting Flows possible. Similarly, the topic of turbulent flow Control made its way into an independent scene.

After these remarks, I would like to thank all the contributors for keeping to the tight schedule for submission of manuscripts and for synthesizing in four pages the work of years. Thanks are also due to CIMNE for agreeing to produce this volume in a very short time and at an unbeatable price.

I would also like to express my gratitude to the members of the Regional Organizing Committee, A. Babiano, J. Ferré, F. Giralt, J. Jiménez, A. Lozano, E. Oñate, J. M. Redondo, M. R.Soler and L. Valiño for their help. In particular, the continuous and efficient assistance of A. Lozano and L. Valiño has been the key to streamlined solutions of multiple problems and they should share with the organizer the credits for the success of ETC-8. The in-site collaboration of E. Oñate and J. M. Redondo made the organization from a distance possible.

Mr. J. A. Picazo should also be thanked for keeping in touch with the authors as well as for receiving the flood of papers, checking their compliance with the prescribed ETC-8 format and making the required corrections and conversions; he has done a great co-editorial work.

Administrative matters were very professionally handled by Mrs. P. Ezquerra, M. Idelsohn and L. Zielonka. The assistance of Mrs. E. Ramos, M.C. Ramos and A. Blanco at different chores along the organization is gratefully acknowledged. Finally, thanks go to all the financial sponsors (listed separately) who made the conference and this volume possible. Special recognition is due to the European Comission for contributing to this event under the "Competitive and Sustain-

able Growth Programme, CE Reference GMA1-1999-2003. This conference and this volume is also supported by the European Office of Aerospace Research and Development, Air Force Office of Scientific Research, Air Force Laboratory, under Contract No. F61775-00-WF020.

As this Preface was being drafted, Uriel Frisch informed the organizer of the death of George K. Batchelor. The sound possibility of somebody presenting at ETC-8 the work of G. K. Batchelor was suggested by Uriel. Due to the lack of time it was unfeasible to prepare and include such a presentation in this volume. The organizer senses to interpret the feeling of all the authors of this volume, in dedicating it to the memory of G. K. Batchelor for his gigantic contribution to the field of Fluid Mechanics, at large, and of Turbulence, in particular, which has great and lasting influence on many of us.

May 2000, César Dopazo

Sponsoring Organizations

- CIMNE
- CSIC/LITEC Combustion Research Laboratory
- Electricité de France (EDF)
- European Office of Aerospace Research and Development (EOARD)
- European Comission (Competitive and Sustainable Growth Programme)
- ERCOFTAC
- EUROMECH
- Generalitat de Cataluña
- Kemira - Kemwater
- Ministerio de Educación y Cultura
- NASA
- Universidad de Barcelona
- Universidad Politécnica de Cataluña
- Universidad Politécnica de Madrid
- Universidad Rovira i Virgili
- Universidad de Zaragoza/IBERCAJA/CAI

Special Keynote Lecture

ADVANCES IN TURBULENCE VIII
Proceedings of the Eighth European Turbulence Conference
C. Dopazo et al. (Eds.)
© CIMNE, Barcelona 2000

A Century of Turbulence

J. L. Lumley[1] and A. M. Yaglom[2]

[1]Cornell University
Ithaca, NY 14853, USA
[2]Massachusetts Institute of Technology
Cambridge, MA 02139, USA

Contact e-mail: JLL4@Cornell.edu

1 Introduction

To begin with, we wanted to accumulate some statistics about the field. We decided that the number of significant papers published per year might be useful. The easiest way to do this is to count papers in five-year intervals in the bibliography of Monin and Yaglom's massive work *Statistical Fluid Mechanics* ([24]) from 1900 to 1965, where the bibliography stops. Although AMY is revising this work, and will eventually bring the bibliography up to date, this is not yet available.

On the basis of this data, necessarily highly selective (representing only those papers that Monin and Yaglom thought to be significant), we can say that the number $N(t)$ of turbulence papers published per unit time (measured in years) is given by

$$N(t) = 0.434e^{t/11.8} \tag{1}$$

where t is the number of years since 1900. That is, the number of papers published between t_1 and t_2 is the integral of $N(t)$ over that interval. The fluctuations begin in the neighborhood of $\pm 22\%$ near 1900, and fall steadily to $\pm 2.5\%$ near 1965.

We should consider the possibility that the exponential curve exists for other reasons. The further in the past an event took place, the more perspective we have, and the more critical we can be. Hence, we probably regard as noteworthy a smaller and smaller number of papers, the greater has been the time lag between their writing and the present. Even if the output of papers were constant, this would creat an exponential growth. Recent papers are more difficult to evaluate, and there would be a tendency to include a larger fraction as possibly noteworthy. So, too much reliance should not be placed on Equation (1). The exponential growth is probably a little slower than it suggests.

The question is, where is the beginning? If the beginning is estimated from a linear extrapolation to zero based on the current slope, the beginning always

appears to be 11.8 years in the past. This probably explains the natural human tendency to pay attention only to recent papers.

A slightly better estimate of the beginning could be obtained as that point after which 99% of all existing papers were published. This always appears to be 54 years in the past. So, from this point of view, turbulence currently appears to have started about the end of the second world war, corresponding very approximately with our professional careers.

Equation (1) suggests that there were only about five papers from the beginning of time until 1900, or 4.5 from 1874 to 1900. In fact, [24] list thirteen, one each by Hagen, Darcy and Helmholtz (in 1839, 1858 and 1869), two by Boussinesq (in 1877 and 1897), three by Reynolds (1874, 1883 and 1894) and five by Rayleigh (1880, 1887, 1892, 1894 and 1895). This level of fluctuation is considerably above (by a factor of six) the fluctuation level extrapolated from that observed between 1900 and 1965. It does suggest that the last quarter of the 19th century was an exceptional time, and that these men, Rayleigh in particular, were exceptional people. In fact, it is well known that this period was extraordinary [7]. If we take the period from 1864 to 1894, and limit ourselves to the physical sciences, we have Hamilton, Maxwell, Curie, Faraday, Kelvin, Haber, Millikan, Galton, Mendelyev, Rutherford, Westinghouse, Bosch, Marconi, Bell, Rayleigh, Wimshurst, and Hertz (in chronological order), and these are just the ones whose names are instantly recognizable. [Wimshurst may not be instantly recognizable - he invented the Wimshurst generator, a machine that accumulates static charge]. All these people did something noteworthy in this period, and some (e.g.- Kelvin) more than one thing.

On a non-statistical basis, it is probably fair to date the beginning of the field from 1874. Leonardo da Vinci, of course, also wrote some interesting things about turbulent flows, and we are neglecting him. In addition, Monin & Yaglom [24] refer in their introduction to several unspecified papers in the first half of the 19th century which remark on the existence of two distinct states of flow.

Please note, that we do not yet know what the field has been doing since 1965. It seems doubtful that it has continued to grow exponentially. Based on Equation (1), the doubling time for the number of papers is 8.2 years. When G. I. Taylor wrote Diffusion by Continuous Movements in 1921, there were 2.6 papers per year. When JLL started graduate school, there were 36 papers per year, which could still be easily read by one person. If we can believe Equation (1), there are currently 2000. We doubt this - we believe that the number has ceased to climb exponentially, and the curve is leveling off a bit. Still, there are probably more papers in a year than one person can comfortably absorb.

In fact, of course, we know something about the mechanisms at work here. We know that in 1965 we were still in the initial phase of growth, since the increase in publications was still exponential. Presumably, the working out of a single major idea (say, the statistical approach to turbulence) would produce first an exponential increase in publications, then a gradual saturation, a leveling off, and finally an exponential decay. We have not seen statistics on this canonical

life-cycle. However, most fields benefit from the infusion of new ideas at various times, which would upset this simple statistical picture. In turbulence, the idea of coherent structures might be regarded as a new idea that reinvigorated the field. There is no reason other than pessimism to suppose that new ideas will dry up any time soon.

Public support of research in engineering and the hard sciences did not begin until just after the Second World War, which is to say, about half-way through our century of turbulence. We tend to think of current research as being inextricably tied to this public support, and find it difficult to imagine maintaining the present research establishment without this support. Yet, examination of the production of papers during the period 1900-1965 (by which time public support had been in place for 20 years) shows absolutely no effect. The exponential growth in number of papers continues as though nothing had happened. Considering the current parlous state of public support for turbulence, we might find this encouraging - perhaps we will be able to keep on quite nicely without support. On the other hand, perhaps the growth would have leveled off without the start of public support. That suggests that we may be in trouble due to the drying up of support.

In addition, in 1956, the Soviet Union placed Sputnik in orbit, and the US research establishment was galvanized. Money poured into US universities, which expanded their engineering and hard science faculties substantially. JLL was just about to receive his Ph.D. His thesis advisor (Stanley Corrsin) said (roughly) that if we all could hang in there, we would all be department heads. In fact, looking at the record (which cuts off nearly ten years later) there is no indication that anything happened.

The curve of paper output dips slightly for the two world wars, but the dips are no larger than the general statistical variability, and have no lasting effect on the curve. If the reader did not know there had been a war at that time, s/he would not conclude from the data that anything extraordinary had happened.

The appearance of promising new ideas and methods that seem significant to us (Kolmogorov's 1941 theory, coherent structures, DNS, chaos, fractals, strange attractors) cannot be identified from the data.

2 A few threads

From the very beginning, there have been two major threads in turbulence research. The first concerned the calculation of the practical effects of turbulence, primarily the momentum, heat and mass transfer, associated with the design of devices and their interaction with their environment. The other concerned the physics of the turbulence phenomenon. Both these threads were present in the initial work of Boussinesq and of Reynolds. They are still with us. The practical thread really was two threads - one is technological, and the other geophysical. The geophysical branch might well be called atmospheric and oceanic engineering, since it is motivated by a desire to calculate the effects of turbulence in

order to predict the behavior of atmospheric and oceanic phenomena, in which turbulence is only one of many players. A fundamental desire to understand turbulence is not always a basic motivation.

Another long thread concerned the establishment of the mathematical basis for the treatment of stochastic fields. There is, of course, much work on this that has no explicit connection to turbulence. The part that is explicitly related to turbulence probably began with Keller and Friedmann's paper in 1924 ([11]).

We may also mention the advent of large-scale computing of turbulent flows, which began in 1972 with the work of Orszag and Patterson ([26]), and which has surely grown exponentially since then (we have not done a statistical analysis). Although the Reynolds numbers attainable are still quite limited, direct numerical simulation of turbulence has taken the place of experiment for some simple flows, since it permits access to quantities that are difficult to measure, such as pressure fluctuations.

We have already mentioned the early work on the semi-empirical approach, associated with the names of Prandtl ([27]), von Kármán ([34],) and G. I. Taylor ([32],). High-speed digital computers, of course, did not yet exist, so that the flows that could be computed using these simple models were few. The beginnings of modern turbulence models, with the work of Chou [3], Kolmogorov [15] (who proposed a two-equation model) and a little later, Rotta [28] were still impeded by the general unavailability of high-speed computation. Finally, with Daly & Harlow ([4]) we come to the arrival of large-scale computing on the scene, and the beginning of the modern period of turbulence modeling.

2.1 The mathematical basis

The modern mathematical theory of stochastic processes of one variable was originated by Wiener[35] who had been stimulated by the works of G.I.Taylor on turbulence, but who considered only one scalar function of time, and applied his results to Brownian motion. Then Kolmogorov [12] developed the rigorous axiomatic foundations of probability theory which included the strict definition of the notion of a stochastic function of any number of variables. Kolmogorov also began with application of his results to Brownian motion but he was looking simultaneously for possible applications of his new theory of random fields. This search attracted his attention to turbulence. He gave full credit to the early attempt by Keller and Friedmann [11] to develop a probabilistic theory of turbulent fields but was mainly interested in investigating the physical mechanism of small-scale turbulent fluctuations. His two short notes [13], [14] on the statistical theory of turbulence included a rigorous statistical description of the fields of turbulent variables as random fields in the sense presented in [12], as well as the definition of a new important class of random fields which had been unknown. Primarily, however, they were devoted to a remarkable attempt to explain the mechanism of small-scale turbulence. To achieve this Kolmogorov stated two general statistical hypotheses (based on non-rigorous but convincing

heuristic physical arguments) which describe the universal equilibrium regime of small-scale components in any turbulent flow at high enough Reynolds number (the existence of such a universal regime was predicted by Kolmogorov). Then he considered the application of these hypotheses to the determination of the shapes of some specific characteristics of turbulent fluctuations. Kolmogorov's theory of 1941 (which is now expounded and discussed in many monographs and surveys) cardinally changed the state of turbulent investigations and is basic to all subsequent developments of turbulent studies during the second half of the 20th century. Publications devoted to turbulence which were stimulated by Kolmogorov's theory at first involved mainly the Moscow and Cambridge research groups (in Cambridge G.K. Batchelor discovered Kolmogorov's papers shortly after their appearance and at once understood their importance) but then enveloped all developed countries.

The first attempt to compare the predictions of Kolmogorov's theory with the results of specially posed experiments were quite favorable. However, measurements of small-scale turbulent fluctuations made in the atmospheric surface layer by the Moscow group in the late 1950s revealed data clearly contradicting Kolmogorov's predictions. This showed that Kolmogorov's similarity hypotheses of 1941, which at first seemed quite convincing, in fact are only approximately true. In 1962 Obukhov [25] sketched some arguments which explained the contradictions by the influence of the spatial variation of the rate of energy dissipation $\epsilon(x,t)$. He produced a crude quantitative estimate of this influence, while Kolmogorov [16], expanding on Obukhov's argument, formulated a generalized version of his two hypotheses of 1941, and supplemented them by a third hypothesis, the three forming the new theory of small-scale turbulence. Kolmogorov's theory of 1962 was consistent with new experimental data and implied a number of additional consequences which could be experimentally verified.

The new Kolmogorov theory at once attracted attention and produced new activity in small-scale turbulence studies. Many results may be found in books by Monin and Yaglom [24], Hunt, Phillips and Williams [10], and Frisch [6] and in research papers which continue to appear regularly.

2.2 Large Eddies / Coherent Structures

The last twenty-five years have coincided with an enormous explosion of interest in the more-or-less organized part of turbulent flows. To be sure, it has been recognized for some fifty-five years that turbulent flows have both organized and apparently disorganized parts. Liu ([20]) has documented the first appearance of this idea around the outbreak of the second world war. The idea was probably first articulated by Liepmann ([19]), and was thoroughly exploited by Townsend ([33]), but all within the context of the traditional statistical approaches. However, in ([1], [2]), Brown and Roshko presented visual evidence that the mixing layer, in particular, was dominated by coherent structures, and this captured the imagination of the field, which was ready for a new approach. Within two

years, the number of citations in this area had gone up by a factor of four, and within two decades had risen by a factor of ten. A lot of immoderate things have been said about coherent structures, and the statistical approaches that were previously popular; a discussion of this, and a current position on why coherent structures are present in turbulent flows, and why they are present in different strengths in different flows, and how they can be calculated, and when they need to be calculated, and what to do with them once you have them, are all discussed at length in ([8]). Briefly, the coherent structures appear to be the result of an instability of (what must be an imaginary) flow with turbulence but without coherent structures, and they can be calculated approximately by using stability arguments of various sorts. It is not always necessary to take them into account explicitly, depending on the particular purpose of the calculation; on the other hand, it can be, for some purposes, very profitable to model the flow as coherent structures plus a parameterized turbulent background, and so construct a low-dimensional model of the flow. Such models can be used whenever an inexpensive surrogate of the flow is needed, and have been very helpful in shedding light on the basic physical mechanisms.

2.3 Chaos / Dynamical Systems Theory

The early investigations of instability and transition were mostly based on classical nonlinear dynamical systems theory, originated by Poincaré at the end of the 19th century. Therefore, transition to turbulence was modeled by a sequence of simple Hopf bifurcations [or Poincaré-Andronov-Hopf bifurcations; see e.g. [23]]. Every such bifurcation increases by one the dimension of the phase space of the dynamical system, making its behavior more and more complicated and disordered. This scenario of transition was proposed by Landau [17], illustrated by some mathematical examples by Hopf [9] and for many years was considered as the unique plausible scenario; in particular, it was the only scenario considered in the early editions of Landau and Lifshitz [18] and in Monin and Yaglom [24].

However, the rapid development of dynamical systems theory in the second half of the last century, well illustrated by the paper by Smale [30], showed that in fact the Landau scenario often is far from typical or cannot be realized [see, e.g., the last edition of [18]]. Smale showed that for many dynamical systems a more probable scenario involves the appearance in phase space of a 'strange attractor', a set of very complicated topological structure, to which the system trajectories are gradually attracted. This implies chaotic behavior of the system, and the exponential divergence of neighboring trajectories. Ruelle and Takens [29] were the first to assume that the Navier-Stokes equations have a strange attractor, appearing after a few elementary Hopf bifurcations, and that the resulting chaotic behavior described transition.

So far, these ideas have been successfully applied only to turbulence near transition, or near a wall, so that a relatively small number of degrees of freedom will have been excited, and the turbulence will be relatively simple, and can be

described by a mechanical system of relatively few degrees of freedom. As the system moves farther from transition, or from a wall, more and more degrees of freedom are excited, until the structure of the attractor becomes so complex that the system must be treated statistically. The ideas from dynamical systems theory have been successfully used to analyze the low-dimensional models that have been constructed of turbulence near a wall or near transition. See also ([8]), ([5]).

2.4 Traditional Problems

Of course, the problems on which people worked before the attractive new approaches came on the scene (above) are still with us. ([24]) is an excellent source for a survey of such problems, although it does not contain the most recent results. The following list is intended to be illustrative, not exclusive:

- the asymptotic behavior of turbulence for large Reynolds number, which is beyond the reach of experiment or computation, has been a source of fascination ([21]).
- The asymptotic behavior of jets, wakes and shear layers at great distances from the origin is also beyond the reach of experiment or computation, and exerts a strange attraction - there is evidence that these flows remember their initial conditions far longer than we had suspected. Is there a universal state to which these flows tend (as was once believed), even if slowly, or is there not?
- It has been an article of faith for fifty years that the small scales were more nearly isotropic than the large scales, and while that does appear to be true, we have found that they are often a great deal less isotropic than we might have expected, especially for a scalar. The mechanisms for this are being investigated.
- We have found that there is a certain residual anisotropy in the small scales even at infinite Reynolds number, associated with intercomponent energy transfer.
- While it is clear that in three-dimensional turbulence, if averages are taken over a sufficient region or a long enough time, energy is transferred from large scales to small, it is also now clear that for short times, or small regions, energy can flow the other way. This is known as back-scatter, a term that we feel was poorly chosen, but it is too late now.

There are also many fundamental questions connected with geophysics.

As a result of the construction of low-dimensional models for the wall region of the turbulent boundary layer, we are coming to have some understanding for the dynamical role of the secondary instabilities that occur in the wall region, which lead to what are called bursts. Some light has been shed on the interaction

between these phenomena and adverse and favorable pressure gradients ([31]). The time is now ripe to extend this understanding to flows on concave and convex walls, and as influenced by a non-inertial rotating frame. This would have interesting applications in axial flow turbomachines.

The fundamental study of turbulent combustion, or even of turbulent reacting flows without heat release, is still in its infancy.

3 Acknowledgments

We are grateful to the following Cornell students: Louise Parsons, Cem Albukrek, Sheng Xu, Vejapong Juttijudata, Peter Blossey, Gadi Reinhorn and Kiran Bhaganagar; who took on the thankless task of counting publications.

Supported in part by Contracts No. F49620-92-J-0287 and F49620-97-1-0203 jointly funded by the U. S. Air Force Office of Scientific Research (Control and Aerospace Programs), and the U. S. Office of Naval Research, in part by Grants No. F49620-92-J-0038, F49620-99-1-0012 and F49620-96-1-0329, funded by the U. S. Air Force Office of Scientific Research (Aerospace Program), in part by Grant Number CTS-9613948 funded by the U. S. National Science Foundation and in part by the Physical Oceanography Programs of the U. S. National Science Foundation (Contract No. OCE-901 7882) and the U. S. Office of Naval Research (Grant No. N00014-92-J-1547).

Some of this material previously appeared in [22].

References

[1] G. Brown and A. Roshko. The effect of density difference on the turbulent mixing layer. In *A.G.A.R.D. Conference on Turbulent Shear Flows, Conf. Proceedings No. 93*, pages 23/1–23/12. NATO Advisory Group for Aerospace Research and Development, 1971.

[2] G. L. Brown and A. Roshko. On density effects and large structure in turbulent mixing layers. *Journal of Fluid Mechanics*, 64:775–816, 1974.

[3] P.-Y. Chou. On an extension of Reynolds' method of finding apparent stress and the nature of turbulence. *Chinese Journal of Physics*, pages 1–53, 1940.

[4] B. J. Daly and F. H. Harlow. Transport equations in turbulence. *Phys. Fluids*, 13:2634–2649, 1970.

[5] M. Farge. Wavelet transforms and their applications to turbulence. *Ann. Rev. Flu. Mech.*, 24:395–457, 1992.

[6] U. Frisch. *Turbulence. The Legacy of A. N. Kolmogorov*, Cambridge, UK: Cambr. Univer. Press. 1995.

[7] B. Grun. *The Timetables of History.* Simon & Schuster, Inc., New York, NY, 1982. A Touchstone Book.

[8] P. J. Holmes, G. Berkooz, and J. L. Lumley. *Turbulence, Coherent Structures, Dynamical Systems and Symmetry.* Cambridge University Press, 1996.

[9] E. Hopf. A mathematical example displaying features of turbulence, *Comm. Pure Appl. Math.*, 1:303-322. 1948.

[10] J. C. R. Hunt, O. M. Phillips and D. Wiliams (eds). *Turbulence and Stochastic Processes: Kolmogorov's Ideas 50 Years on*, London: Royal Society. 240pp. 1991.

[11] L. V. Keller and A. A. Friedmann. Differentialgleichung für die turbulente Bewegung einer kompressiblen Flüssigkeit. *Proceedings of 1st International Congress of Applied Mechanics*, pages 395–405, 1924. Delft.

[12] A. N. Kolmogorov.*Grundbegriffe der Wahrscheinlichkeitsrechnung*, Berlin: Springer. 1933.

[13] A. N. Kolmogorov. Local structure of turbulence in an incompressible fluid at very high Reynolds numbers. *Dokl. Akad. Nauk SSSR*, 30:299-303. 1941.

[14] A. N. Kolmogorov. Energy dissipation in locally isotropic turbulence, *Dokl. Akad. Nauk SSSR*, 32:19-21. 1941.

[15] A. N. Kolmogorov. Equations of turbulent motion of an incompressible fluid, *Izv. Akad. Nauk SSSR, Ser. Fiz.*, 6:56-58. 1942.

[16] A. N. Kolmogorov. A refinement of previous hypotheses concerning the local structure of turbulence in a viscous incompressible fluid at high Reynolds numbers. *J. Fluid Mech.*, 13:82-85. 1962.

[17] L. D. Landau. On the problem of turbulence, *Dokl. Akad. Nauk SSSR*, 44:339-342. 1944 (Engl. transl. in *C. R. Acad. Sci. URSS*, 44:311-314, and in *Collected Papers*, pp. 387-391, Oxford: Pergamon Press and New York: Gordon and Breach, 1965).

[18] L. D. Landau and E.M. Lifshitz. *Mechanics of Continuous Media*, Moscow: Gostekhisdat (1st Rusian edition) 1944; *Mechanics of Continuous Media*, Moscow: Gostekhisdat, (2nd Russian edition) 1953; *Fluid Mechanics*, London: Pergamon Press (1st English edition) 1958; *Fluid Mechanics*, London: Pergamon Press (revised English edition) 1987.

[19] H. W. Liepmann. Aspects of the turbulence problem. Part II. *Z. Angew. Math. Phys.*, 3:407–426, 1952.

[20] J. T. C. Liu. Contributions to the understanding of large-scale coherent structures in developing free turbulent shear flows. *Advances in Applied Mechanics*, 26:183–309, 1988.

[21] J. L. Lumley. Some comments on turbulence. *Physics of Fluids A*, 2:203–211, 1992.

[22] J. L. Lumley, A. Acrivos, L. G. Leal, and S. Leibovich, editors. *Research Trends in Fluid Dynamics.* American Institute of Physics, Woodbury, NY, 1996.

[23] J. E. Marsden and M. McCracken. *The Hopf Bifurcation and its Applications*, New York: Springer. 1976.

[24] A. S. Monin and A. M. Yaglom. *Statistical fluid mechanics.* The MIT press, Volume I, 1971; Volume II, 1975. Translation editor J. L. Lumley.

[25] A. M. Obukhov. Some specific features of atmospheric turbulence. *J. Fluid Mech.*, 13:77-81. 1962.

[26] S. A. Orszag and G. S. Patterson. Numerical simulation of three-dimensional homogeneous isotropic turbulence. *Physical Review Letters*, 28:76–79, 1972.

[27] L. Prandtl. Über die ausgebildete Turbulenz. *ZAMM*, 5:136–139, 1925.

[28] J. C. Rotta. Statistische Theorie nichthomogener Turbulenz. *Z. Phys.*, 129:547–572, 1951.

[29] D. Ruelle and F. Takens. On the nature of turbulence, *Comm. Math. Phys.*, 20:167-192. 1971,

[30] S. Smale. Differential dynamical systems. *Bull. Amer. Math. Soc.*, 73:747-817. 1967.

[31] E. Stone. *A Study of Low Dimensional Models for the Wall Region of a Turbulent Layer.* PhD thesis, Cornell University., 1989.

[32] G. I. Taylor. Eddy motion in the atmosphere. *Phil. Trans. Roy. Soc.*, A215:1–26, 1915.

[33] A. A. Townsend. *The Structure of Turbulent Shear Flow.* Cambridge University Press, 1956.

[34] T. von Kármán. Mechanische Änlichkeit und Turbulenz. *Proceedings 3rd International Congress of Applied Mechanics, Pt. I*, pages 85–105, 1930. Stockholm.

[35] N. Wiener. Differential space, *J. Math. Phys. Mass. Inst. Techn.*, 2:131-174. 1923.

I

Instabilities and Transition

ADVANCES IN TURBULENCE VIII
Proceedings of the Eighth European Turbulence Conference
C. Dopazo et al. (Eds.)
© CIMNE, Barcelona 2000

Three-dimensional instability of two merging vortices

P. Meunier, T. Leweke and M. Abid

IRPHE, CNRS/Universités Aix-Marseille
12 avenue Général Leclerc, F-13003 Marseille, FRANCE

Contact e-mail: meunier@marius.univ-mrs.fr

1 Introduction

We investigate experimentally and numerically the three-dimensional dynamics of a pair of corotating laminar vortices. A well-known feature of such a flow is the merging of the two vortices into a single one. It has been established by numerous studies, mostly of 2D inviscid flows [1, 2], that merging occurs whenever the size of the vortex cores, scaled on their separation distance, exceeds a certain limit. Recent experiments [3] have shown that the viscous evolution of the pair can be decomposed into three distinct phases: 1) the viscous growth of the cores up to a critical radius of about 25% of the separation distance, 2) the convective merging of the vortices into a single core with spiral arms, and 3) the axisymmetrisation and viscous diffusion of the final vortex. However, such a description does not take into account the possibility of 3D instabilities, which may significantly change this picture.

2 Description of the flow

In our experiments, the vortices are generated in a water tank using two flat plates with sharpened edges, impulsively started from rest. Visualization is achieved using fluorescent dyes. Direct numerical simulations (DNS) were performed by solving the 3D Navier-Stokes equations using a spectral code with second-order accuracy in time. The vortex pair is characterized by the circulation Γ of each vortex, the separation b between vortex centers, and a characteristic core radius a, defined by the approximately Gaussian distribution of the vortices:

$$\omega = \frac{\Gamma}{\pi a^2} e^{-r^2/a^2} \qquad (1)$$

These parameters are determined from flow field measurements using Particle Image Velocimetry. The (initial) conditions for the cases discussed in the following were $Re = \Gamma/\nu = 4100$, $a_o/b_o = 0.15$ for the experiment, and $Re = 1000$, $a_o/b_o = 0.10$ plus an initial perturbation for the DNS.

3 Three-dimensional instability

Two point vortices of the same circulation Γ and separated by a distance b rotate around each other with a turnover period $t_c = 2\pi^2 b^2/\Gamma$. It was shown theoretically [4] that this system is stable with respect to 3D perturbations. However, Fig. 1(a) shows a clear observation of a short-wavelength instability, which is due to the non-vanishing size of the vortex cores. The pair is seen from the side, and the initially straight vortex center lines, marked by bright dye filaments, are subject to wavy perturbations, whose axial wavelength is about one vortex spacing b. The contours of axial vorticity in Fig. 1(b), obtained by DNS, show the associated distortion of the initially symmetric distribution.

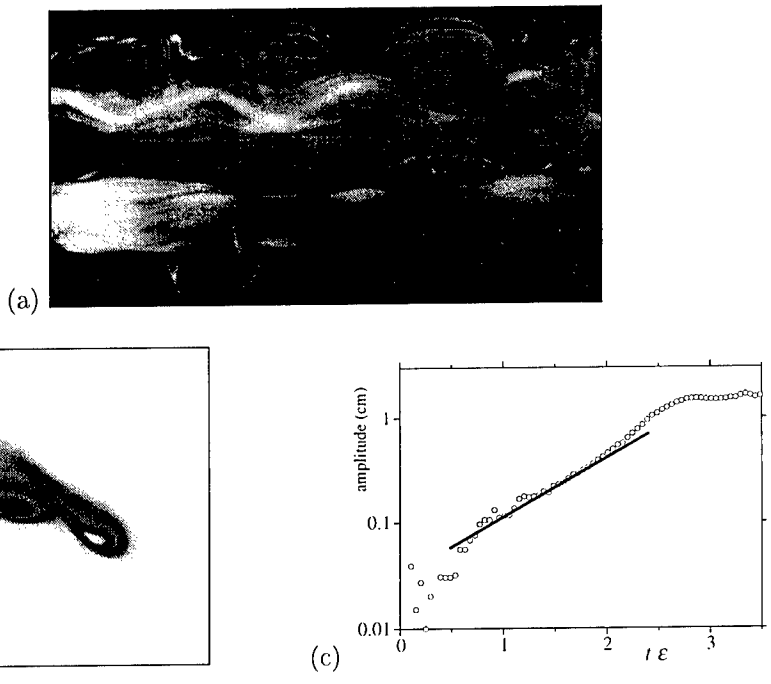


Figure 1: Elliptic instability of corotating vortices. (*a*) Dye visualization (side view). (*b*) Axial vorticity from DNS. (*c*) Growth of centerline deformation: experiment (symbols) and theory [6] (line). ε: mutually induced external strain in the cores.

The instability mode is stationary in the rotating frame of reference of the pair, and the perturbations on the two vortices are found to be in phase. In the experiment, this instability was observed for $Re \gtrsim 2000$, *i.e.* when the initial phase before merging is sufficiently long.

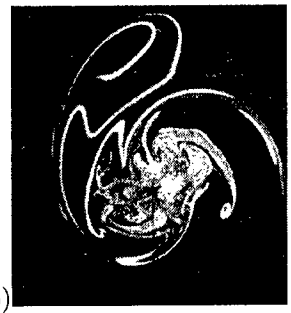
The characteristic spatial structure of the instability is very similar to that of the cooperative elliptic instability of a counterrotating pair [5]. Precise measurements of the growth of the centerline deformations (Fig. 1(c)), show very good agreement with the predictions of elliptic instability theory for a single Gaussian vortex in a uniform strain [6].

4 Turbulent vortex merging

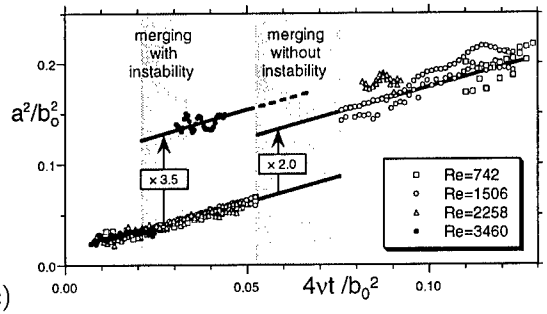
When the perturbation amplitude gets sufficiently large, layers of fluid initially orbiting one vortex are drawn around the respectively other vortex in a periodic interlocking fashion. The corresponding tongues of dye are faintly visible in Fig. 1(a). These tongues contain vorticity, which is reoriented and stretched into perpendicular secondary vortices wrapping around the primary pair. This



(a)



(b)



(c)

Figure 2: Sideview (a) and cross-cut section (b) of the turbulent vortex after merging of two corotating vortices in the presence of a 3D instability. (c) Evolution of the non-dimensional core size a/b_o with and without instability. Solid lines: Theoretical viscous growth of a Gaussian vortex defined by (1).

exchange of fluid (and vorticity) between the vortices has two consequences: 1) the vortices are drawn closer together, initiating a premature merging, and 2) the interaction between primary and secondary vortices leads to the almost explosive breakdown of the flow into small-scale motion during this merging (see Fig. 2(a,b)). Eventually, the flow relaminarizes, and one finds again a single viscous vortex at the end. The non-dimensional core size a/b_o of the two initial vortices before merging and of the final vortex after merging is plotted as a function of time in Fig. 2(c). It shows that, in the presence of the instability, merging sets in much earlier, and that the final vortex appears to be bigger than in a two-dimensional laminar flow.

5 Conclusion

We have presented experimental results concerning the interaction between two identical, parallel, initially laminar vortices. A three-dimensional instability is discovered, showing the characteristic features of a cooperative elliptic instability of the vortex cores. The subsequent stage of small-scale turbulent flow makes the vortices merge for smaller core sizes than in a 2D laminar flow. The final vortex seems to be larger and more turbulent than in the absence of instability. Experiments are presently underway to quantify in more detail this effect of three-dimensional instability on vortex merging.

References

[1] P. G. Saffman and R. Szeto. Equilibrium of a pair of equal uniform vortices. *Phys. Fluids*, 23: 2339–2342, 1980.

[2] E. A. Overman and N. J. Zabusky. Evolution and merger of isolated vortex structures. *Phys. Fluids*, 25: 1297–1305, 1982.

[3] P. Meunier and T. Leweke. Influence of a three-dimensional instability on vortex merging. *submitted to Phys. Rev. Lett.*, 2000.

[4] J. Jimenez. Stability of a pair of co-rotating vortices. *Phys. Fluids*, 18: 1580–1581, 1975.

[5] T. Leweke and C. H. K. Williamson. Cooperative elliptic instability of a vortex pair. *J. Fluid Mech.*, 360: 85–119, 1998.

[6] C. Eloy and S. Le Dizès. Three-dimensional instability of Burgers and Lamb-Oseen vortices in a strain field. *J. Fluid Mech.*, 378: 145–166, 1999.

ADVANCES IN TURBULENCE VIII
Proceedings of the Eighth European Turbulence Conference
C. Dopazo et al. (Eds.)
© CIMNE, Barcelona 2000

Zigzag instability and the origin of the pancake turbulence

Paul Billant[1] and Jean-Marc Chomaz[2]

[1]LadHyX, CNRS, Ecole Polytechnique, F–91128 Palaiseau Cedex, France
[2]CNRM Météo-France, 42 avenue Coriolis, F–31057 Toulouse , France

Contact e-mail: paul.billant@meteo.fr, jmarc@ladhyx.polytechnique.fr

1 Introduction

A prominent feature of strongly stratified turbulence observed in laboratory experiments, numerical simulations and field observations in the oceans and in the atmosphere is the emergence of coherent horizontal pancake vortices organized in decoupled horizontal layers[1].

To understand the mechanism responsible for the emergence of such layers and the thickness selection, we have studied the dynamics of a prototype flow: a columnar vertical vortex pair in a strongly stratified fluid. This basic flow is initially uniform along the vertical but we have observed experimentally that an instability, which we name zigzag instability, slices the vortex pair into thin horizontal layers. We describe experimental, theoretical and numerical investigations on this new instability. Potential implications for the dynamic of pancake turbulence are discussed in the concluding section.

2 Experimental evidence for the zigzag instability

A 60 cm long columnar vertical vortex pair is created by computer-controlled flaps, i.e. two rotating vertical plates. When the horizontal Froude number F_h ($F_h = U/L_hN$, where U is the dipole traveling velocity, L_h is the horizontal lengthscale taken as the dipole radius R and N is the Brunt–Väisälä frequency) is below 0.21, the vortex pair is subjected to the zigzag instability (figure 1) which is distinct from the Crow and elliptic three-dimensional instabilities known to occur on vortex pairs in a homogeneous fluid[2]. The zigzag instability consists of a vertically modulated rotation and a translation of the columnar vortex pair perpendicularly to the traveling direction with almost no change of the dipole's cross-sectional structure. Ultimately the vortex pair is sliced into thin horizontal layers of independent pancake dipoles (figure 1). This is to be contrasted with the

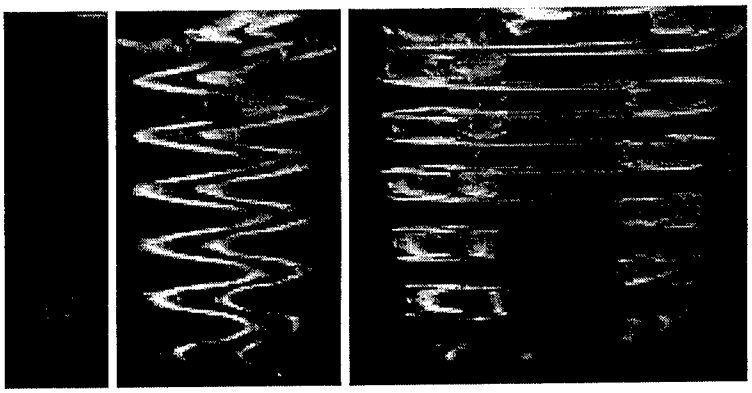


Figure 1: Front views showing the development of the zigzag instability for $F_h = 0.17$ and $Re = 233$ at $t = 7$ s (a), 75 s (b) and 176 s (c).

elliptic instability which develops for $F_h \geq 0.21$ and distorts the inner structure of each vortex[2].

3 Phase dynamics of the zigzag instability

A striking characteristic of the zigzag instability is that the horizontal dipole structure is only weakly perturbed. This observation suggests that the vortex pair can be described by "macroscopic" or phase variables such as location and orientation of the dipole in the horizontal plane and that a long-wavelength linear stability analysis can be carried out in the spirit of phase dynamic approaches. The relevant phase variables for the zigzag instability are η, the y-coordinate of the dipole along the axis perpendicular to the initial travelling direction and ϕ, the angle of propagation. By considering that η and ϕ vary slowly with the vertical coordinate and with time, and that $F_h \ll 1$, we have found by a multiple-scale perturbation analysis in the inviscid limit that η and ϕ are governed by

$$\frac{\partial \eta}{\partial t} = \phi, \tag{1}$$

$$\frac{\partial \phi}{\partial t} = (D + F_h^2 g_1) F_h^2 \frac{\partial^2 \eta}{\partial z^2} + g_2 F_h^4 \frac{\partial^4 \eta}{\partial z^4}, \tag{2}$$

up to the fourth order in F_h and $\partial/\partial z$. The coefficients $D = -3.67$, $g_1 = -56.4$, $g_2 = -16.1$ have been exactly calculated from solvability conditions using the Lamb-Chaplygin dipole as basic state. Inserting three-dimensional disturbances of the form $(\eta, \phi) \propto \exp(\sigma t + i k_z z)$ yields the dispersion relation

$$\sigma^2 = -D F_h^2 k_z^2 + g_2 F_h^4 k_z^4 - g_1 F_h^4 k_z^2, \tag{3}$$

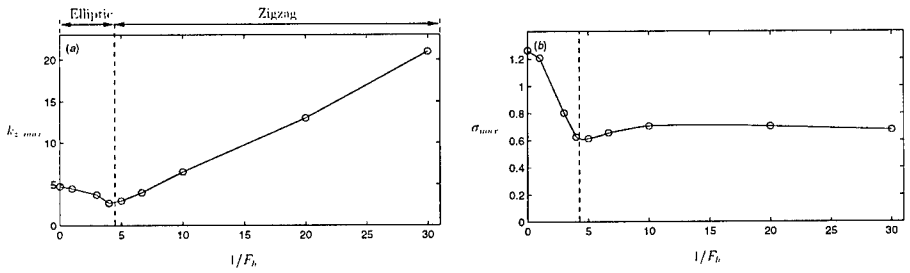


Figure 2: (*a*) Wavenumber $k_{z\ max}$ and (*b*) growth rate σ_{max} of the fastest growing perturbation as a function of the inverse Froude number for $\{Re = 10000, Sc = 1\}$.

which is an expansion for small Froude number and small wavenumber of the exact dispersion relation. Since D and g_1 are negative, this dispersion relation indicates the existence of a long-wavelength instability which consists of of a vertically modulated rotation $\phi(z,t)$ and translation $\eta(z,t)$ of the vortex pair perpendicularly to the propagation direction in qualitative agreement with the behaviour of the zigzag instability observed in the experiment. It is also particularly noteworthy that the first two terms in the rhs of (3) are of the form $(F_h k_z)^m$ implying that the most amplified wavenumber scales as $k_{z\ max} \propto 1/F_h$ when $F_h \to 0$ since the third term is then negligible. The corresponding maximum growth rate σ_{max} is thus independent of F_h. In dimensional form, this corresponds to a growth rate scaling like the turnover time scale U/L_h and a wavelength λ scaling like U/N. Physically, this means that the zigzag instability survives in the limit of strong stratification but the thickness of the ensuing layers becomes thinner and thinner as F_h decreases.

4 Three-dimensional stability analysis

In order to check these theoretical scaling laws, we have carried out a numerical stability analysis of the Lamb-Chaplygin dipole. Figure 2 shows the maximum growth rate σ_{max} and the associated wavenumber $k_{z\ max}$ as a function of the inverse Froude number for Reynolds-Schmidt numbers $\{Re = 10000, Sc = 1\}$ approaching the non-diffusive limit. Two distinct regimes can be clearly identified. For $F_h \geq 0.25$, the instability is of elliptic type and stratification effects are stabilizing. In contrast, when $F_h \leq 0.2$, the instability is of zigzag type and $k_{z\ max}$ is growing with $1/F_h$ while σ_{max} is almost constant as predicted theoretically. The agreement with the theory is not only qualitative but also quantitative: as seen from figure 3, the analytical and numerical zigzag eigenmodes are in striking agreement. There is also a quite good agreement between the numerically calculated wavelength for Reynolds numbers typical of experimental conditions

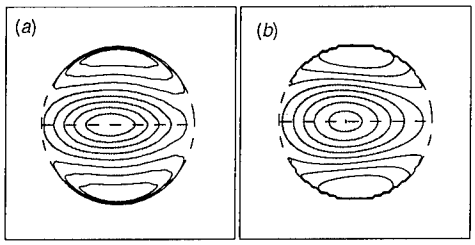


Figure 3: Comparison between the numerical (a) and analytical (b) vertical vorticity of the zigzag eigenmode in the horizontal plane for $F_h = 0.033$, $k_z = 8.25$, $Re = 10000$.

and experimental measurements.

5 Conclusions

These results demonstrate that an instability can be responsible for the emergence of layered pancake-shaped vortices with a typical thickness scaling like U/N. On the basis of a self-similarity of the equations of motion when $F_h \ll 1$, this scaling law can be extended to any strongly stratified inviscid flow. For such a fine vertical scale, the leading order governing equations of strongly stratified flows are not two-dimensional in contradiction with a previous conjecture[1, 3]. This scaling law implies also that the vertical spectrum of horizontal kinetic energy of pancake turbulence should be of the form $E(k_z) \propto N^2 k_z^{-3}$, giving an alternative explanation for the observed vertical spectra in the atmosphere and oceans[4].

References

[1] J. J. Riley and M.-P. Lelong. Fluid motions in the presence of strong stable stratification. *Ann. Rev. Fluid Mech.*, To appear, 2000.

[2] T. Leweke and C. H. K Williamson. Cooperative elliptic instability of a vortex pair. *J. Fluid Mech.*, 360:85–119, 1998.

[3] D. K. Lilly. Stratified turbulence and the mesoscale variability of the atmosphere. *J. Atmos. Sci.*, 40:749–761, 1983.

[4] S. A. Smith, D. C. Fritts and T. E. VanZandt. Evidence for a saturated spectrum of atmospheric gravity waves. *J. Atmos. Sci.*, 44:1404–1410, 1987.

ADVANCES IN TURBULENCE VIII
Proceedings of the Eighth European Turbulence Conference
C. Dopazo et al. (Eds.)
© CIMNE, Barcelona 2000

Hysteretic transition from laminar to vortex shedding flow in soap films

V.K. Horváth*, J.R. Cressman, W.I. Goldburg, and X.L. Wu

Department of Physics and Astr., Univ. of Pittsburgh, Pittsburgh, PA 15260, USA

*Contact e-mail: vhorvath@pitt.edu

1 Introduction

Studies of flow behind a single cylinder have greatly contributed to our understanding of the development of complex flows like the Kármán vortex street[1] or turbulent flows. At the first instability in such a system the laminar flow (LF) becomes time dependent and vortices appear. It has been shown that this transition to the vortex shedding phase (VS) is well described by the supercritical Hopf bifurcation[2].

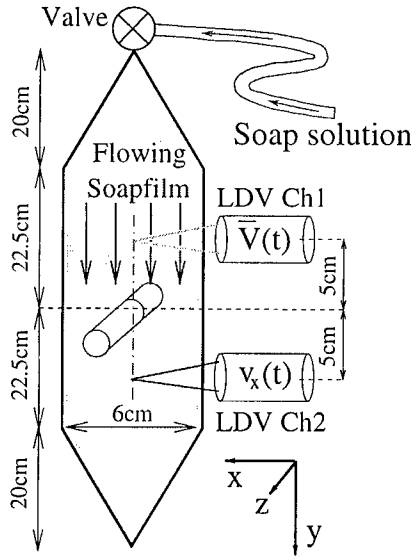


Figure 1: Schematic of the experimental setup. The diameter d of the rod is 1mm. The 0.2mm thick nylon lines are tied to a weight at the bottom.

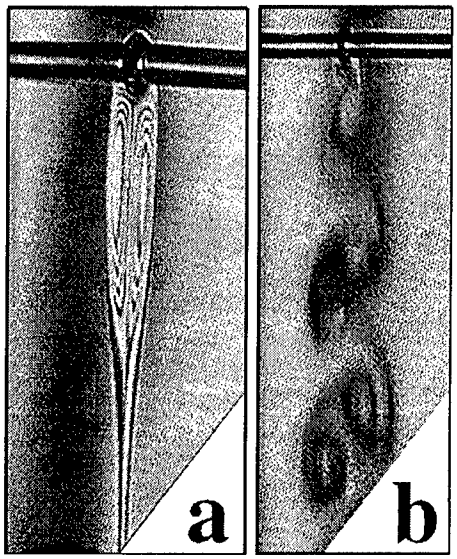


Figure 2: Interference pictures of the flowing soap film below the rod in (a) the laminar state and (b) the vortex shedding state.

2 Hysteretic Primary Instability in Soap Films

Soap films have been shown to be a particularly useful for the study of two dimensional flows[3]. Here we present measurements demonstrating that the LF→VS transition can be hysteretic in a (quasi-two dimensional) soap film penetrated by a glass cylinder[4]. Our experimental setup consists of a rapidly flowing soap film formed between two vertically positioned thin nylon lines (see Fig. 1). The film is fed continuously from the top through a valve. To investigate the flow at different Reynolds numbers $Re = \overline{V}d/\nu$ we changed the mean velocity $\overline{V}$ by either opening and closing the valve at different rates or by changing the separation of the nylon lines, using computer controlled stepping motors (here ν is the kinematic viscosity). At the center of the parallel segment of the set-up, a glass rod penetrates the film in the z direction. The velocity measurements were made using a dual head laser Doppler velocimeter (LDV). The fluctuating horizontal component $V_x(t)$ and $\overline{V}$ were measured simultaneously below and above the rod respectively.

On increasing the flow rate a transition appears from the LF state to the VS state. Below the transition, the flow is characterized by two counter-rotating vortices underneath the rod (Fig. 2a). In the VS state these recirculating vortices peel off the rod and flow downstream. The continuously generated counter-rotating vortices form the Kármán vortex street (Fig. 2b). All experiments start with slowly increasing $\overline{V}$ in the LF regime. The critical velocity, where VS commences, is called V_c^{up}. After some waiting time in the VS state, $\overline{V}$ is slowly decreased. At V_c^{down} the system undergoes a reverse transition, i.e. from VS into LF. This cycle was repeated several times in each run with $V_x(t)$ and $\overline{V}$ being recorded simultaneously.

In order to determine the transition velocities, we have calculated the velocity probability distribution function $P(V_x)$ from $V_x(t)$ by a standard binning procedure. In Fig. 3 the magnitude of $P(V_x, t)$ is mapped into gray scale values and is shown as a function of V_x and t. It can be seen that sharp changes in $P(V_x, t)$ precisely indicate the transition times t_d^* and t_u^* and therefore $V_c^{down} = \overline{V}(t_d^*)$ and $V_c^{up} = \overline{V}(t_u^*)$ too. It is apparent in Fig. 3 that V_c^{up} is not equal to V_c^{down}, that is, there is no unique critical velocity for the transition. The Reynolds number is roughly 50 in the hysteretic gap. A large uncertainty in this value comes from the poorly determined two-dimensional soap film viscosity ν, which depends on the film thickness.

It is worth pointing out that if we keep the mean flow rate constant in the interval $[V_c^{down}, V_c^{up}]$, then the laminar state can persist for an indefinite length of time. However applying sufficiently large acoustic or pulse-like mechanical perturbations, the system could be driven into the VS state. The system remains in this state even if the perturbation is turned off. Applying similar perturbations, VS→LF transition was never observed at constant $\overline{V}$. As a result we can conclude that the observed static hysteresis is *not* a result of some delay in the response of the system to the bifurcation. Auxiliary experiments were also

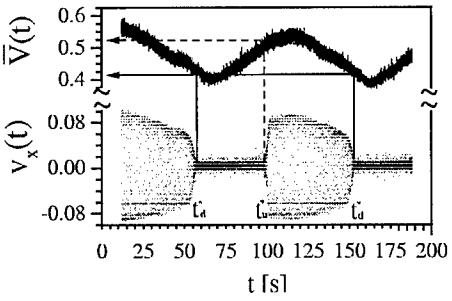


Figure 3: Here the function $\overline{V}(t)$ is shown together with the $P(v_x, t)$ map at $|d\overline{V}/dt|$=0.004 m/s^2. The gray scale corresponds to the probability density of v_x. The solid and dashed lines are intended to guide the eye for the transitions VS→LF and LF→VS.

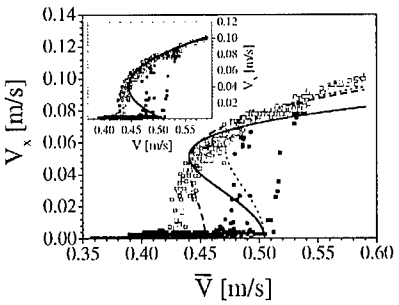


Figure 4: This figure shows our experimental data together with different fits (see text). The circles and squares represent two different experimental run. Closed and opened symbols are used for data taken at increasing and decreasing $\overline{V}$ respectively.

performed to exclude wetting properties and the effect of the air boundary near the film as possible sources of hysteresis.

In the absence of any available theory, we consider a fifth order Landau equation[5] $d\tilde{v}(t)/dt = \tilde{a}\tilde{v} + 2\tilde{b}v^2\tilde{v} - \tilde{c}v^4\tilde{v}$, for the complex velocity $\tilde{v}$=$v_x + iv_y$. Here all variables denoted by tilde are complex and $v_i = V_i - < V_i >_t$ (i=x or y). The complex velocity can also be written as $\tilde{v}$=$ve^{i\phi}$, where v is the amplitude. The real part of this equation describes the evolution of v. Its non-trivial positive stationary solution describes the VS state:

$$v_{VS}{}^2 = \frac{b_r}{c_r}(1 + \sqrt{1 + a_r c_r / b_r^2}, \qquad (1)$$

where the subscript r is used to designate the real part of complex numbers.

Although the application of this model for data fitting purposes is not obvious (the relationship between the parameters a_r, b_r, c_r and the control parameter of the experiment is unknown), typically a_r is considered to be proportional to $(\overline{V} - V_c^{up})$. As one can see in Fig. 4, this generic model of the hysteresis is in qualitative agreement with our observations. However none of our 3 best fits are very satisfactory. It is interesting to note that a simple three-parameter phenomenological equation $P_0(\overline{V} - V_c) + 2P_1 v - P_2 v^2 = 0$ provides a surprisingly good fit to our data in the VS state (see inset of Fig. 4.). Using least square fitting to the solution of this equation provides the following result: $v_x = 0.04 \pm \sqrt{\overline{V}/39.06 - 0.0113}$, where the velocities are in units of m/s.

Auxiliary experiments suggest that the hysteresis may be connected with the fact that the film may become very thin in the recirculating region. Recognizing

that the viscosity of a soap film depends on its thickness, the observed hysteresis effect can be qualitatively understood; the Reynolds number can now take different values at the same value of $\overline{V}$, when the parameter is lowered than when it is raised.

3 Conclusions

- We have observed unexpected hysteresis at the onset of the Kármán vortex street in a quasi two-dimensional soap film.
- The fifth order amplitude equation is in qualitative agreement with our observations, but a simple phenomenological equation provides a better numerical fit to the experimental data in the vortex shedding regime.
- A phenomenological picture is suggested to explain the origin of the hysteresis.

This material is based upon work supported by the NATO under a Grant DGE-9804461 awarded to W.I. Goldburg and V.K. Horváth. The work was also supported by NSF grant DMR-9622699, NASA grant 96-HEDS-01-098 and by additional support from the Hungarian Science Foundation grant OTKA F17310.

References

[1] T. von Karman, Gott. Nachr., 24 (1911).

[2] M. Provansal, C. Mathis, and L. Boyer, J. Fluid Mech. **182**, 1 (1987); K. R. Sreenivasan, P. J. Strykowski, and D. Olinger, in *ASME Forum on Unsteady Separation*, edited by K. N. Ghia, volume 52, page 1, 1986.

[3] Y. Couder and C. Basdevant, J. Fluid Mech. **173**, 225 (1986); M. Gharib and P. Derango, Physica D **3**, 406 (1989).

[4] V.K. Horváth, J.R. Cressman, W.I. Goldburg, and X.L. Wu, *to appear in* Phys. Rev. E, Rapid Comm., (2000).

[5] S. H. Strogatz, *Nonlinear Dynamics and Chaos*, Addison Wesley, New York, 1994.

ADVANCES IN TURBULENCE VIII
Proceedings of the Eighth European Turbulence Conference
C. Dopazo et al. (Eds.)
© CIMNE, Barcelona 2000

A resonance principle for spatially developing wakes

Benoît Pier and Patrick Huerre

Laboratoire d'Hydrodynamique (LadHyX)
CNRS - École polytechnique
F-91128 Palaiseau cedex, France

Wakes behind bluff-bodies are well known [8, 3] to undergo a transition to periodic vortex shedding at moderate Reynolds numbers. These finite-amplitude self-sustained intrinsic oscillations are shown to be governed by an internal resonance principle derived from the local properties of the basic flow.

Frequency selection criteria have so far been obtained in the linear approximation: first for one-dimensional model equations [1] and then for the complete Navier–Stokes equations [4]. Recently nonlinear selection criteria have been derived in the framework of the complex Ginzburg–Landau equation [5, 6]. The present investigation demonstrates that the steep frequency selection principle [6] also applies to *fully nonlinear vortex streets* sustained by spatially developing wake flows.

The formulation essentially relies on the assumption of slow spatial variations characterized by the slow streamwise variable $X = \epsilon x$, where $\epsilon \ll 1$ is a small non-uniformity parameter. This assumption is fulfilled by construction in the model studies [5, 6]. In the present context of real flows, the basic wake is chosen such as to strictly enforce this condition over the entire domain.

Two-dimensional incompressible flows are conveniently studied in terms of the streamfunction $\Psi(x, y, t)$ governed by the vorticity equation

$$\left(\frac{\partial}{\partial t} + \frac{\partial \Psi}{\partial y}\frac{\partial}{\partial x} - \frac{\partial \Psi}{\partial x}\frac{\partial}{\partial y}\right)\Delta\Psi = \frac{1}{\mathrm{Re}}\Delta^2\Psi, \tag{1}$$

where x and y denote streamwise and cross-stream coordinates respectively. The Reynolds number Re is based on the characteristic width and velocity of the wake profile. The steady basic flow is subjected to viscous spreading which takes place on a scale of $1/\mathrm{Re}$. Hence the order of magnitude of the weak streamwise nonuniformity is then effectively defined as $\epsilon = 1/\mathrm{Re} \ll 1$, which is the *only small parameter* of the present investigation.

Under this quasiparallel flow assumption, the leading-order basic flow approximation Ψ_0 is then readily shown to obey the Prandtl boundary layer equation

$$\left(\frac{\partial \Psi_0}{\partial y}\frac{\partial}{\partial X} - \frac{\partial \Psi_0}{\partial X}\frac{\partial}{\partial y}\right)\frac{\partial \Psi_0}{\partial y} = -\frac{dP}{dX} + \frac{\partial^3 \Psi_0}{\partial y^3}, \tag{2}$$

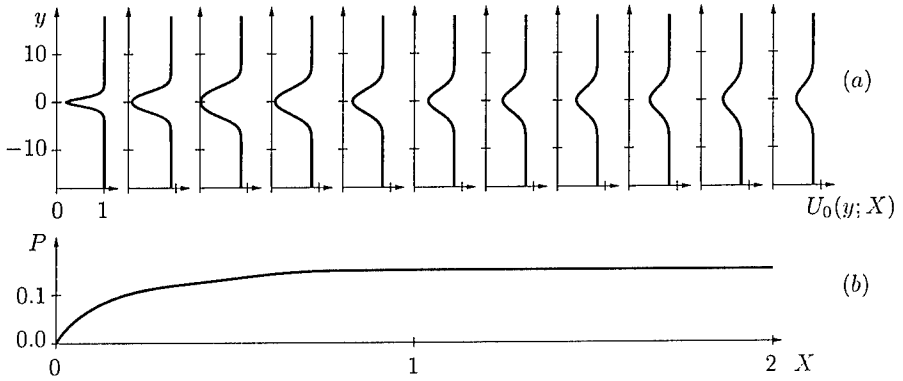


Figure 1: Streamwise development of the basic flow. (*a*) Velocity profiles $U_0(y;X)$ at different streamwise X locations. (*b*) Basic pressure field $P(X)$.

where the given streamwise pressure gradient dP/dX is the integration "constant" arising in the integration of the leading-order vorticity equation. The externally applied pressure field $P(X)$ effectively allows to taylor the streamwise evolution of the basic wake flow profiles $U_0(y;X)$ as shown in figure 1.

Small-amplitude perturbations are governed by the local linear dispersion relation $\omega = \Omega^\ell(k,X)$ derived from the Orr–Sommerfeld equation applied to the velocity profiles prevailing at each streamwise station X. The dispersion Ω^ℓ yields in particular the local absolute frequency $\omega_0(X)$ defined as the frequency of a wave packet of vanishing group velocity. The local absolute growth rate $\omega_{0,i}(X) \equiv \mathrm{Im}\,\omega_0(X)$ is of primary importance since small perturbations grow in place in absolutely unstable (AU) regions (characterized by $\omega_{0,i}(X) > 0$) whereas they are swept away in convectively unstable (CU) regions (characterized by $\omega_{0,i}(X) < 0$). The evolution of $\omega_0(X)$ for the basic flow of figure 1, sketched in figure 2, is seen to reproduce the essential features of experimental wake flows: a central region of absolute instability ($X^{ca} < X < X^{ac}$) and convective instability in the far downstream and upstream domains.

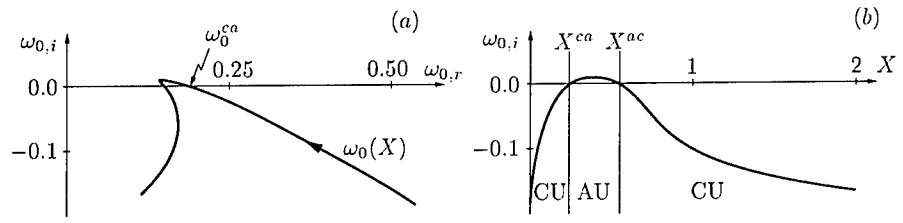


Figure 2: (*a*) Locus of local absolute frequency $\omega_0(X)$ in the complex plane. (*b*) Local absolute growth rates $\omega_{0,i}(X)$ as a function of streamwise station.

In this situation, the resonance principle derived in [6] predicts a globally synchronized state oscillating at the real absolute frequency

$$\omega_0^{ca} \equiv \omega_0(X^{ca}) = 0.190 \tag{3}$$

prevailing at the upstream boundary of the AU domain. Direct numerical simulations of the Navier–Stokes equation (1) with Re = 100 confirm that this wake gives rise to a finite-amplitude vortex street tuned at a well defined global frequency

$$\omega_g = 0.186, \tag{4}$$

in excellent agreement with the predicted value ω_0^{ca} derived from the local instability characteristics of the basic flow.

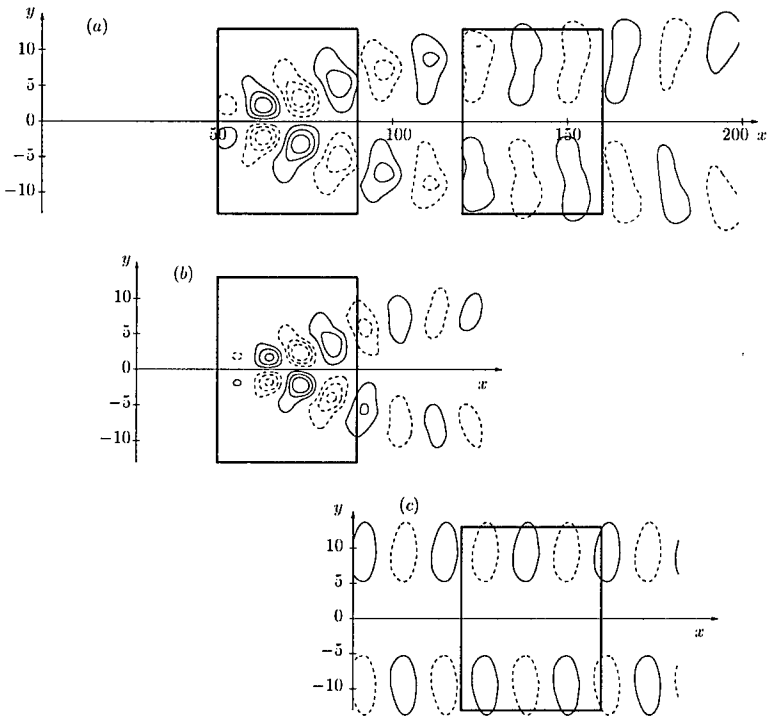


Figure 3: Interpretation of self-sustained vortex street (a) as a steep global mode triggered by a stationary front (b) sending out nonlinear travelling wave trains (c). (a) Streamwise fundamental velocity component of global vortex street living in the spatially developing wake. (b) Front structure obtained by harmonic forcing of parallel wake profile prevailing near the upstream marginal absolutely unstable station. (c) Nonlinear travelling wave obtained in a temporal evolution problem of given wave number for the parallel wake prevailing at the corresponding downstream station.

The periodic vortex street (figure 3*a*) may be interpreted in terms of a *steep global mode* [6] exhibiting a sharp Dee–Langer [2] type front at the upstream station of marginal absolute instability. The front acts as a wavemaker which sends out nonlinear travelling waves in the downstream direction, the global frequency being imposed by the real absolute frequency prevailing at the front station. This front is located at the transition station X^{ca} from local convective to absolute instability which is the only stable stationary front location of the entire flow. Following the procedure of [7] developed in the framework of a complex Ginzburg–Landau equation, the front configuration may be approached via a spatial harmonic response problem of parallel CU wakes. When $X < X^{ca}$, the response of the local wake profiles to forcing of frequency ω_0^{ca} yields the spatial structure of a stationary front in the limit $X \to X^{ca}$ (figure 3*b*). The nonlinear travelling waves prevailing further downstream are found to be governed by the local nonlinear dispersion relation as resulting from a temporal evolution problem (figure 3*c*) on a local parallel wake profile. An asymptotic WKBJ matching scheme shows that each of these constitutive elements consistently assemble to form a uniformly valid approximation of the global vortex street.

Thus, a *globally* synchronized *nonlinear* vortex shedding structure obeys a *local* resonance principle derived from the *linear* characteristics of the underlying basic flow. This frequency selection criterion is likely to hold whenever a spatially developing flow exhibits an AU region embedded within a CU region, as in separated flows.

References

[1] J.-M. Chomaz, P. Huerre and L.G. Redekopp, Stud. Appl. Math. **84**, 119–144 (1991).

[2] G. Dee and J.S. Langer, Phys. Rev. Lett. **50**, 383–386 (1983).

[3] D. Hammond and L. Redekopp, J. Fluid Mech. **331**, 231–260 (1997).

[4] P.A. Monkewitz, P. Huerre and J.M. Chomaz, J. Fluid Mech. **251**, 1–20 (1993).

[5] B. Pier and P. Huerre, Physica D **97**, 206–222 (1996).

[6] B. Pier, P. Huerre, J.-M. Chomaz and A. Couairon, Phys. Fluids **10**, 2433–2435 (1998).

[7] B. Pier, P. Huerre and J.-M. Chomaz, Bifurcation to fully nonlinear synchronized structures in slowly varying media, submitted to Physica D (2000).

[8] M. Provansal, C. Mathis and L. Boyer, J. Fluid Mech. **182**, 1–22 (1987).

ADVANCES IN TURBULENCE VIII
Proceedings of the Eighth European Turbulence Conference
C. Dopazo et al. (Eds.)
© CIMNE, Barcelona 2000

Experimental Characterization of Polymer Effects on Two- and Three-Dimensional Shear Instabilities

O. Cadot [1] and S. Kumar [2]

[1]Laboratoire de Mécanique, Universite du Havre
25 rue Philippe Lebon, BP 540 76058 Le Havre cedex, FRANCE
[2]Department of Chemical Engineering, University of Michigan
2300 Hayward, 3074 H.H. Dow Building. Ann. Arbor, MI 48105 USA

Contact e-mail: Olivier.Cadot@univ-lehavre.fr

1 Introduction

The effect of polymer additives on the formation of vorticity filaments [1], [2] in fully turbulent flow has been a subject of recent investigations. Bonn *et. al* [3] injected a polymer solution and found that filament formation was partially inhibited. This observation was found to be valid only during the time that the semi-dilute polymer solution was being mixed into the turbulent flow [4]. Thus, the effect of filament inhibition is a form of heterogeneous drag reduction [5], where the injected polymer solution behaves like a coherent viscoelastic thread. The aim of the present work is to gain insight into the inhibition mechanisms by studying the effect of local injection of a polymer solution on 2D and 3D hydrodynamic instabilities which occur in water flow past a circular cylinder. In the present experiment, the polymer solution is directly injected through rows of holes pierced in the cylinder as displayed by figures 1 and 3 (see [6] and [7] for details.)

The semi-dilute polymer solution results from the dilution of 0.25 g to 1 g of polyethyleneoxide (WSR 303 of molecular weight $7 \times 10^6 g/mol$) in 1 liter of water. For these moderately high concentrations (from 250 wppm to 1000 wppm) the solutions exhibit viscoelastic properties: shear thinning together with high elongational viscosity. The relaxation times (see [7] for rheological data of these solutions) associated with these effects increase with concentration from 0.1s (at 100 wppm) to 1 s (at 1000 wppm.) Thus, the Weissenberg number of the cylinder experiment, which provides a ratio of elastic forces (due to the presence of polymers) to inertial forces, is of order of magnitude 1.

2 2D and 3D stabilizations

In figures 1(a) and 1(b), we can see how the polymers delay the development of the 2D instability as displayed by the large zone of slow motion behind the cylinder. Also, the instability is shifted to much longer wavelengths. In figure 1(b), the shapes of the vortices in the street are flattened and the braid regions are thickened.The following figures are velocity fields with and without polymer solution injection (built from a PIV technique). We see that elasticity modifies the structure of the vortex street. The vortices are elliptical and a large sinuous flow takes place between them. It then appears that the shear instability is inhibited during the roll-up process. The scenario of inhibition of the 2D shear instability we observe with polymers is very similar to an inhibition scenario due to surface tension in the Kelvin-Helmholtz instability.

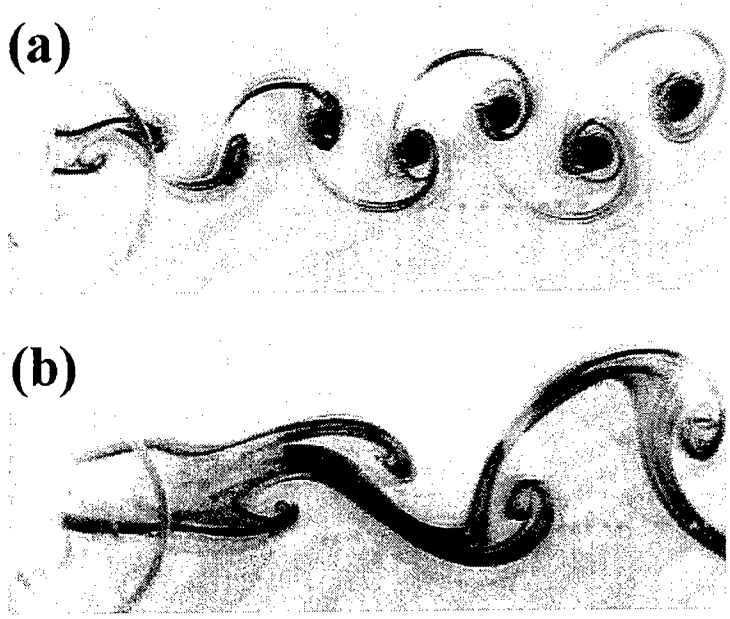


Figure 1: Side views of the cylinder wake at Re = 150. In (a) simple colored water is injected. In (b) the viscoelastic polymer solution is injected under exactly the same experimental conditions as the previous picture (a)

The 3D instabilities of the wake produce small scale streamwise structures. We find that polymer injection also stabilizes their production as displayed by figures 3(a) and 3(b). We think that the main underlying inhibition mechanism is related to the modification of the basic 2D flow (partial roll-up of the Karman

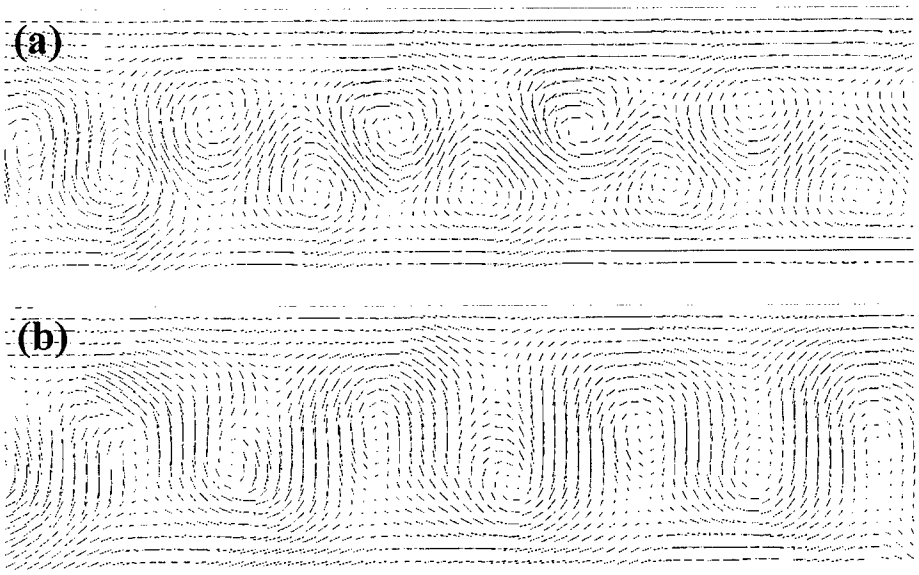


Figure 2: Velocity field in the frame of the vortex centres at Re = 150. (a) represents the case of the Newtonian wake (no injection). In (b), a polymer solution is injected

vortices.) This idea is supported by the recent numerical simulations of Kumar and Homsy [8] on a viscoelastic mixing layer.

3 Implications for turbulent flows

In turbulent flows, the local shear stresses can have a broad range of values, the smallest occurring at large scales and the largest at the Kolmogorov scale. Since the filaments are produced by the large scale structures of the turbulence, similar stabilization mechanisms as those present in the wake would occur only if the injected solution has a relaxation time comparable to the large scale turnover time. This is exactly the case in the experiments cited in the introduction. During the mixing of the solution, the coherent viscoelastic thread is degraded and finally the polymers become highly diluted. At this stage the relaxation time is considerably decreased, shifting the large scale Weissenberg number to very small values. Hence, at the beginning of the mixing, there is a modification of the large scale properties of the turbulence. Other consequences (in addition to the filament inhibition), such as a power dissipation reduction in the bulk, could be expected.

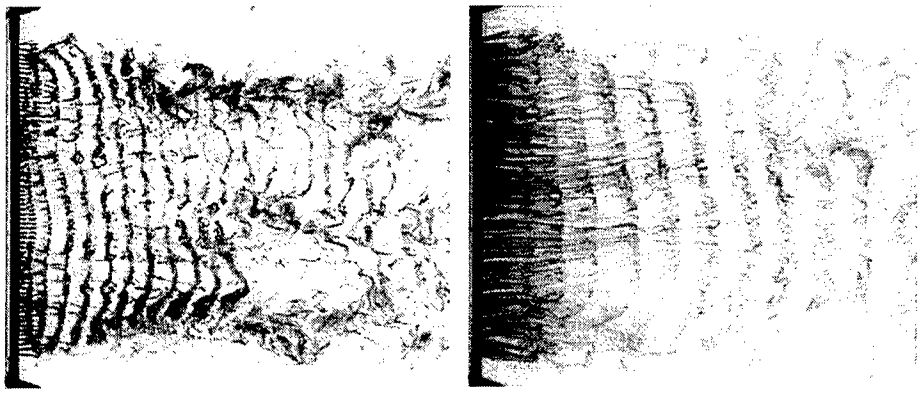


Figure 3: Top views of the cylinder wake at Re = 250. In (a) simple colored water is injected. In (b) the viscoelastic polymer solution is injected under exactly the same experimental conditions as the previous picture (a)

References

[1] S. Douady, Y. Couder and M.-E Brachet. *Phys. Rev. Lett.*, 67:982, 1991.

[2] O. Cadot, S. Douady and Y. Couder, *Phys. Fluids*, 7:630, 1995.

[3] D. Bonn,Y Couder, P. H. J. van Dam and S. Douady, *Phys. Rev. E*, 47:R28, 1993.

[4] O. Cadot, D. Bonn, S. Douady, *Phys. Fluids*, 10:426, 1998.

[5] J. Vleegaar, and M. Tels, *Chem. Eng. Sci.*, 28:965, 1973.

[6] O. Cadot and M. Lebey *Phys. Fluids*, 11:494, 1999.

[7] O. Cadot and S. Kumar *J. Fluid Mech.*, accepted, 2000.

[8] S. Kumar, and G.M. Homsy, *J. Non-Newtonian Fluid Mech.*, 83:251, 1999.

ADVANCES IN TURBULENCE VIII
Proceedings of the Eighth European Turbulence Conference
C. Dopazo et al. (Eds.)
© CIMNE, Barcelona 2000

On steady-state flow solutions and their nonparallel global linear instability

V. Theofilis

DLR Institute of Fluid Mechanics,
Bunsenstraße 10, D-37073 Göttingen, GERMANY

Contact e-mail: Vassilios.Theofilis@dlr.de

Introduction

Global three-dimensional linear instability analysis of a laminar two-dimensional steady-state flow reveals that what is commonly known as 'residuals' in direct numerical simulations (DNS) which aim at recovery of steady-state fluid-flow solutions is associated with a small number of the least-stable two-dimensional linear global flow eigenmodes. The eigenmodes are obtained by solving the partial-derivative eigenvalue problem which governs three-dimensional nonparallel (global) linear instability of the two-dimensional steady-state. Both the frequency and the damping rates of the global eigenmodes have been identified and are in excellent agreement with the DNS results as the latter approaches convergence to a steady-state; it is the least damped of these modes which determines the ultimate behaviour of the flow near convergence. On the other hand, the inability to obtain a steady-state solution using DNS may be explained within the framework of the present non-parallel global linear instability theory as a deterministic consequence of the diminishing damping rates of the linear global eigenmodes as the flow Reynolds number increases. A worked example of the well-known lid-driven cavity flow is presented.

The partial derivative eigenvalue problem

Motivation for the present analysis is offered by our desire to embed a number of observations regarding the transient behaviour of DNS solutions for the recovery of laminar two-dimensional steady-states within a unified theoretical framework. In particular we are interested in the physical mechanism which underlies exponential monotonic or oscillatory decay of residuals near convergence to a steady state. The diminishing of the rate of decay of residuals as the Reynolds number increases and the ultimate inability to obtain converged steady-state solutions of the equations of motion is another intriguing universal behaviour, the origin

of which is not understood presently in a satisfactory manner. These questions have been posed and answered within the unifying framework of *linear* global instability of the two-dimensional laminar steady-state solution; two distinct paths have been followed. Firstly, at conditions favouring the existence of laminar two-dimensional steady-states $\bar{\mathbf{q}}$, these have been recovered by marching the equations of motion in time until convergence. The DNS signal is processed in order for information on the damping rate of residuals to be obtained; discrete Fourier transforms (DFT) have delivered the frequencies at play. Secondly, steady-state solutions obtained have been analysed using non-parallel global linear instability theory in which $\bar{\mathbf{q}}$ forms the two-dimensional variable coefficients in the complex nonsymmetric generalised eigenvalue problem [1]. Near convergence every flow quantity $\mathbf{q}$ is decomposed into

$$\mathbf{q}(x,y,z,t) = \bar{\mathbf{q}}(x,y) + \varepsilon\ \hat{\mathbf{q}}(x,y)\ \mathrm{e}^{\mathrm{i}\ [\beta z - \omega t]} + c.c. \qquad (1)$$

The decomposition is substituted into the incompressible equations of motion, the $O(1)$ terms are subtracted out as an exact solution of these equations and the resulting system is linearised, taking $\varepsilon \ll 1$. Here $\bar{\mathbf{q}} = (\bar{u},\bar{v},0,\bar{p})^{\mathrm{T}}$ is the two-dimensional steady-state and $\hat{\mathbf{q}} = (\hat{u},\hat{v},\hat{w},\hat{p})^{\mathrm{T}}$ are three-dimensional linear perturbations superimposed upon $\bar{\mathbf{q}}$. Complex conjugation is introduced in (1) since $\mathbf{q}$ and $\bar{\mathbf{q}}$ are real while all three of $\hat{\mathbf{q}}, \beta$ and ω may be complex. In the framework of a temporal linear nonparallel instability analysis used presently we write the linearised system in the form of an eigenvalue problem for the complex quantity ω, while β is taken to be a real wavenumber parameter describing an eigenmode in the third spatial direction z. The frequency of the instability mode is associated with $\omega_{\mathrm{r}} \equiv \Re\{\omega\}$ while the imaginary part of ω is the growth/damping rate of the global disturbance; a positive value of $\omega_{\mathrm{i}} \equiv \Im\{\omega\}$ indicates exponential growth of the global instability mode $\tilde{\mathbf{q}} = \hat{\mathbf{q}}\mathrm{e}^{\mathrm{i}\ [\beta z - \omega t]}$ in time t while $\omega_{\mathrm{i}} < 0$ denotes decay of $\tilde{\mathbf{q}}$ in time. It should be clearly stressed that although a two-dimensional $\bar{\mathbf{q}}$ is sought, physical space is three-dimensional and is treated as such within the framework of the global linear instability analysis. Linear disturbances having wavenumbers $\beta \neq 0$ correspond to a periodicity length $L_z = 2\pi/\beta$ in the $z-$direction while only two-dimensional ($\beta = 0$) global linear disturbances enter the dynamics of a two-dimensional DNS. The key idea in this paper is that the existence of a laminar two-dimensional steady-state $\bar{\mathbf{q}}$ is synonymous with stability of *all* $\beta = 0$ global flow eigenmodes if a two-dimensional DNS is used[1] for the recovery of $\bar{\mathbf{q}}$.

Results

Non-parallel flow in the square lid-driven cavity serves as a demonstrator of the relationship between residuals in the two-dimensional DNS and global linear eigenmodes of the converged steady-state solution $\bar{\mathbf{q}}$. The least stable part of

[1] and of all $\beta \neq 0$ global flow eigenmodes $\tilde{\mathbf{q}}$ if a 3D DNS is used

the two-dimensional ($\beta = 0$) global eigenspectrum of the respective converged steady states has been calculated at $Re \in [0, 10^4]$. Residuals in the DNS were defined either globally (using some integral measure) or locally as the difference between the transient and the converged solution of *any* flow variable, e.g. $\psi^t \equiv \psi(x_0, y_0, t) - \bar{\psi}(x_0, y_0)$ with ψ denoting the streamfunction and (x_0, y_0) an arbitrary location in the flow field. The rate of decay of the residuals in the DNS was compared with the damping rates of one of the least stable global flow eigenmodes. Excellent agreement was obtained at low Reynolds numbers, as shown in Fig. 1 at $Re = 500$ and 1000.

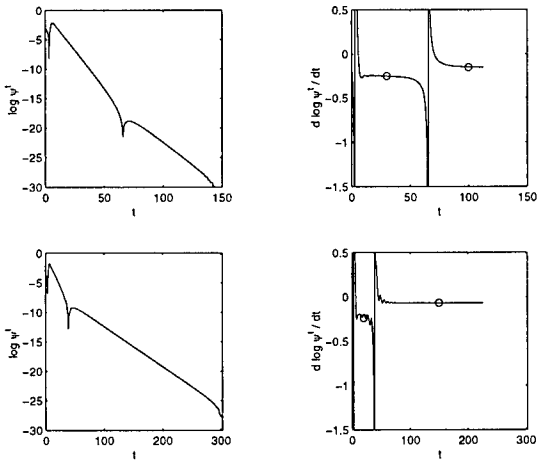


Figure 1: Local behaviour of residuals (left) and their time-derivative (right) as delivered by the DNS at $Re = 500$ (upper) and $Re = 1000$ (lower). Symbols denote the damping-rates of the least-damped two-dimensional global flow eigenmodes at the respective Reynolds numbers.

Further, the frequencies of the global eigenmodes in question were compared with the frequencies f delivered by power spectral analysis of the DNS signal; again an one-to-one correspondence between the results of the two independent approaches was established, as may be seen in Fig. 2 where flow at $Re = 2500$ is monitored; analogous results were obtained at all Reynolds numbers examined. The progressive destabilisation of the flow as Re increases is shown in terms of diminishing damping rates ω_i at $Re = 2500, 5000$ and 7500 in Fig. 3.
The conclusion which may be drawn from the global linear instability theory results at low Reynolds numbers is that the different forms in which residuals manifest themselves in the DNS are associated with either stationary or travelling two-dimensional ($\beta = 0$ in (1)) linear global instabilities superimposed upon the converged steady state. The increasingly long integration times necessary in order for a converged steady state to be obtained as the Reynolds number increases may now be explained by reference to the diminishing damping rates of

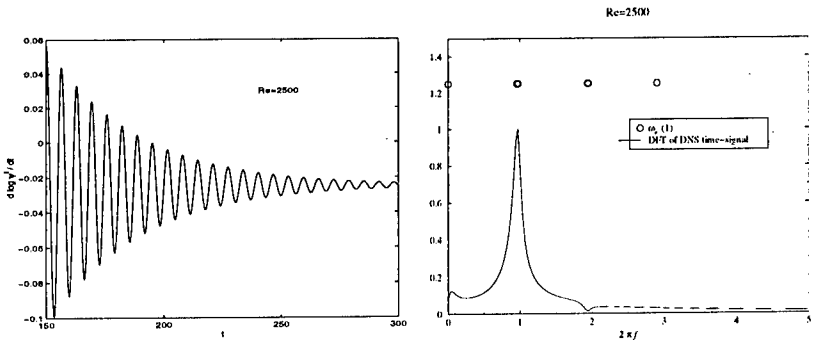


Figure 2: Left: Time-history of the residual obtained in the DNS at $Re = 2500$; right: power spectral analysis of the DNS signal and arbitrarily placed on the vertical axis, denoted by symbols, global eigenmode frequencies ω_r.

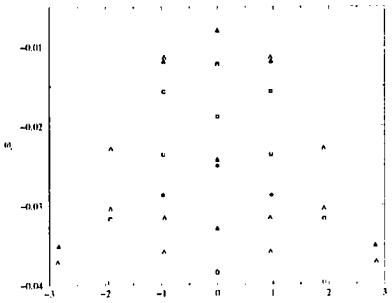


Figure 3: Eigenvalues (ω_r, ω_i) in the least-stable part of the global spectrum at $Re = 2500$ (diamond), $Re = 5000$ (square) and $Re = 7500$ (triangle).

the least stable ($\beta = 0$) global flow eigenmodes; ultimately, the latter approach a state of neutral stability and interact nonlinearly to the effect that no steady-state solution may be obtained. Additional details of this work-in-progress may be found in [2].

This material is based upon work supported by the European Office of Aerospace Research and Development, Air Force Office of Scientific Research, Air Force Research Laboratory, under Contracts No. F61775-99-WE049 and F61775-99-WE090.

References

[1] V. Theofilis. Linear instability in two spatial dimensions. In: *Fourth European Computational Fluid Dynamics Conference ECCOMAS'98*. Chichester, N. York, 547–552, 1998.

[2] V. Theofilis. On numerical residuals and physical instabilities in incompressible steady-state fluid flow calculations. *Technical Report IB 223-99 A 25, DLR*, 1999.

II

Magnetohydrodynamics

ADVANCES IN TURBULENCE VIII
Proceedings of the Eighth European Turbulence Conference
C. Dopazo, L. Valiño, A. Lozano, E. Oñate and J. M. Redondo (Eds.)
© CIMNE, Barcelona 2000

Laminar-Turbulent Transition in an Electromagnetically-Levitated Molten Metal Droplet

B. Abedian[1], R. W. Hyers[2], C. Bullard[1], and G. Trapaga[3]

[1]Department of Mechanical Engineering, Tufts University
Medford, Massachusetts USA
[2]NASA Marshall Space Flight Center
Huntsville, AL USA
[3]Department of Materials Science and Engineering, Massachusetts Institute of Technology
Cambridge, Massachusetts USA

Contact e-mail: babedian@tufts.edu

1 Introduction

This work reports experimental observations made on the MSL-1 (First Microgravity Science Laboratory) mission of the Space Shuttle (STS-83 and STS-94) regarding flow transition in spheroidal palladium-silicon droplets and compares them to a theoretical prediction of transition in electromagnetically levitated droplets using conventional boundary-layer type approximations. The droplet represents a new geometry in which transition has not previously been described, and it is one for which there are important applications in materials science.

In an EML system, the induced electric current in the material heats up the sample. The electromagnetic body force, known as the Lorentz force, is often used for levitation. Under microgravity conditions, the net electromagnetic body force on the sample is small compared to the overall force and used primarily for positioning and maintaining the sample at a prescribed location. By contrast, the heating coil(s) induce a Lorentz force that is much stronger than the positioning force, symmetric with respect to the equatorial plane and give rise to a dominant fluid motion inside the molten droplet. The axisymmetric body force in the experiments produces two toroidal flow enclosures immediately above and below the equatorial plane inside the droplet.

2 Experiments

The droplets of interest in this study were Pd82-Si18 spheroids approximately 7 mm in diameter, levitated in TEMPUS, a two-frequency microgravity electromagnetic levitator. The experiments were performed on the MSL-1 (First Microgravity Science Laboratory) mission of the Space Shuttle (STS-83 and STS-94). The temperature of the sample was measured by optical pyrometry. A viscosity-temperature relation used in the analysis of these experiments is obtained experimentally under microgravity conditions using the oscillating drop technique and provided elsewhere [1]. The temperature dependence in the other properties was neglected, as the correction would be insignificant relative to the uncertainty of approximately 20% in these viscosity data. The distribution of the electromagnetic forces on the sample was calculated by the method of mutual inductances7,9. The magnetic fields of both the positioning coils and the heating coils were held constant from the initial heating of the solid sample, through the melt plateau, until the maximum operating temperature was reached.

Equilibrium laminar flow patterns are established once the samples are fully molten. The flow pattern can be deduced from the accumulation of solid particles on the surface of the drop in the equatorial stagnation point. However, as the sample is heated under constant magnetic conditions, this stable equilibrium is disrupted, and the particles show the flow's progression to a turbulent state. The evolution of the flow pattern is detailed in Figure 1, which shows a side view of the droplet. The top and bottom of the drop are not visible because they are obscured by the levitation coils. Throughout this sequence, the forces on the sample are constant; only the temperature of the sample is changing. Figure 3a shows the particles on the surface of the sample in the stagnation point of the equilibrium laminar flow. This frame was taken when the sample was at a temperature of 1211 K, which corresponds to a viscosity of 22 mPa-s. 1.7 seconds later, however, the temperature is 1250 K (viscosity of 19 mPa-s), and the stagnation point is no longer static, but oscillating about the equator. Upon further heating, the amplitude of these oscillations increases. Finally, by the time of Figure 3c, at 1312 K (viscosity of 15 mPa-s), the flow is fully turbulent.

3 Analysis

The flow structure inside each of the two axisymmetric toroidal enclosures is explained in terms of two-dimensional active and passive flow loops. Active loops are formed by the circulating fluid that crosses the magnetized region inside the droplet. They form an enclosed band of thickness of order of the skin depth of the Lorentz force in the droplet. By contrast, there is no magnetic field in the region enclosed by a passive loop. Passive loops are set into motion via viscous interactions with the active loops. The onset of turbulence is obtained by considering the shear interactions between passive and active loops and making an analogy with other flows.

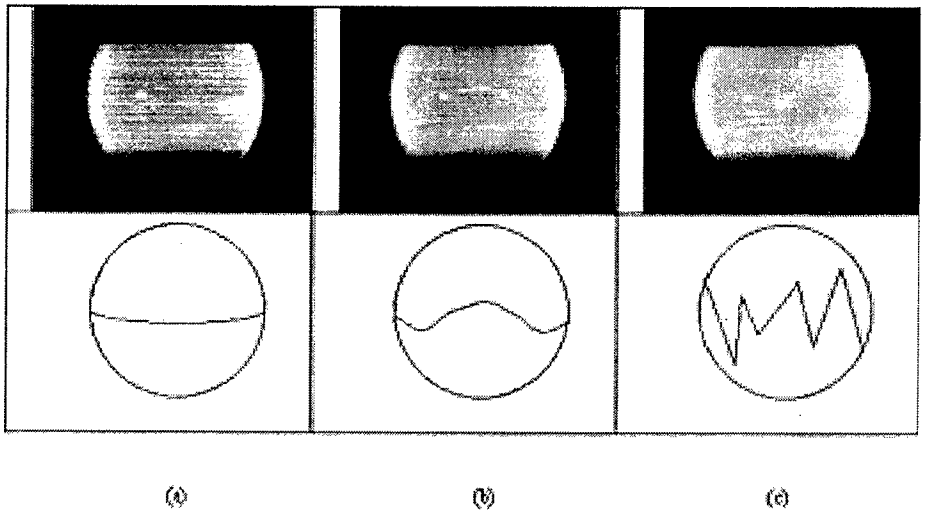


Figure 1: Video images of the tracer patterns on the Pd82-Si18 sample. (a) equilibrium laminar flow at $T = 1211K(\mu = 22mPa - s)$, (b) oscillatory flow at $T = 1250K(\mu = 19mPa - s)$, and (c) turbulent flow at $T = 1312K(\mu = 15mPa - s)$.

In the presentation, it is shown that the flow in the droplet can be characterized by a dimensionless magnetic force which can be described as a magnetic Rayliegh number and defined as

$$F^+ = \frac{F_o R^3}{\rho \nu^2}, \tag{1}$$

where F_0 is the characteristic Lorentz force (force/vol.) in the drop, ρ and ν the fluid density and kinematic viscosity and R the drop radius. Conservation of angular momentum is applied to the active loops and the shear interactions between active and passive loops estimated from classical boundary layer theory. In the limit of small magnetic Prandtl number flows and when $\delta/R \ll 1$, with δ being the thickness of the skin depth, the onset of turbulence in the droplet is expressed in terms of F_c^+, the critical value for F^+.

$$F_c^+ \sim 2.0 \times 10^4 \left(\frac{R}{\delta}\right), \tag{2}$$

A comparison between the experimentally-observed transition and this semi-empirical correlation is presented in the table below. Electomagnetic force calculations inside the drop are carried out according to Schwartz [3]. The good

agreement between the theoretical approach and the experimental data provides the first piece of evidence that transition in this system is shear layer type. A corresponding particle tracking analysis of the observed instability of the drop along with comparisons with a recent analysis on transitional behavior of two corotating tori [4] are included in the discussion of the experimental data.

$\mu = 13.4 - 18.4mPa - s$ [1]
ρ =11,650 − 11,670kg/m^3 [2]
$R = 3.610 - 3.612mm$
$\delta = 0.594 - 1.88mm$
$F_\circ = 5.5x10^4 - 1.14x10^5 N/m^3$
$F^+_{c,exp} = 9.3x10^4 - 3.5x10^5$
$F^+_{c,the} = 3.8x10^4 - 1.2x10^5$

Table 1: A comparison between theory and experimental observations.

References

[1] R. W. Hyers. Modeling of and Experiments on Electromagnetic Levitation for Materials Processing. *Ph.D. Thesis*, Massachusetts Institute of Technology,1998.

[2] B. Damaschke, K. Samwer. Private communications. 1998.

[3] E. M. Schawrtz Measurement of the Surface Tension of Electromagnetically-Levitated Droplets in Microgravity *Ph.D. Thesis*, Massachusetts Institute of Technology,1995.

[4] J. Herrero, F. F. Giralt, and J. A. C. Humphery. Influence of the geometry on the structure of the flow between a pair of corotating disks. *Physics of Fluids*, 11:88–96, 1999.

ADVANCES IN TURBULENCE VIII
Proceedings of the Eighth European Turbulence Conference
C. Dopazo et al. (Eds.)
© CIMNE, Barcelona 2000

Bifurcation analysis of an electrically driven fluid layer

N. Seehafer[1] and J. Schumacher[2]

[1]Institut für Physik, Universität Potsdam
PF 601553, 14415 Potsdam, GERMANY
[2]Fachbereich Physik, Philipps-Universität Marburg
35032 Marburg, GERMANY

Contact e-mail: seehafer@agnld.uni-potsdam.de

1 Introduction

The equilibrium states of electrically conducting fluids or plasmas have been a subject of intense study for a long time, motivated in particular by the interest in controlled thermonuclear fusion, as well as that in space and astrophysical phenomena such as plasma loops in the solar corona. If high temperatures prohibit solid walls, a conducting fluid can be held together by the action of an electric current passing through it with the pressure gradients being balanced by the Lorentz force. The resultant configuration is known as a pinch. In this paper we report on studies of the pinch in the geometry of a plane sheet.

2 Equations and Static Equilibrium

We use the nonrelativistic, incompressible magnetohydrodynamic (MHD) equations,

$$\rho\left(\frac{\partial \mathbf{v}}{\partial t}+(\mathbf{v}\cdot\nabla)\mathbf{v}\right)=\rho\nu\nabla^2\mathbf{v}-\nabla p+\mathbf{J}\times\mathbf{B},\quad \nabla\cdot\mathbf{v}=0, \tag{1}$$

$$\frac{\partial \mathbf{B}}{\partial t}=-\nabla\times(\eta\mu_0\mathbf{J}-\mathbf{v}\times\mathbf{B}),\quad \eta(\mathbf{x})=\eta_0\tilde{\eta}(\mathbf{x}),\quad \nabla\cdot\mathbf{B}=0, \tag{2}$$

where $\mathbf{v}$ is the fluid velocity, $\mathbf{B}$ the magnetic induction, μ_0 the magnetic permeability in a vacuum, $\mathbf{J}=\nabla\times\mathbf{B}/\mu_0$ the electric current density, ρ the mass density, p the thermal pressure, ν the kinematic viscosity, and η the magnetic diffusivity, which is connected with the electrical conductivity σ by the relation $\eta=1/\mu_0\sigma$. While ρ and ν are assumed to be uniform, η is allowed to vary spatially: η_0 is a dimensional constant and $\tilde{\eta}(\mathbf{x})$ a dimensionless function of position.

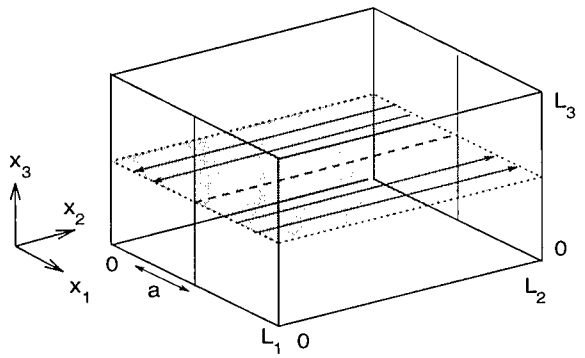


Figure 1: Geometry of the magnetohydrodynamic sheet pinch. Arrows in the shaded plane indicate the direction of the equilibrium magnetic field.

Using Cartesian coordinates x_1, x_2, x_3, we consider our magnetofluid in the slab $0 < x_1 < 1$, see Fig. 1. In the x_2 and x_3 directions periodic boundary conditions with periods L_2 and L_3, respectively, are used. The boundary planes are assumed to be impenetrable and stress-free, and the system is driven by an electric field in the x_3 direction prescribed on the boundary. We further assume that there is no magnetic flux through the boundary.

For the case of a uniform η, it is found that the quiescent basic state, in which the current density is uniform and the magnetic field profile across the sheet linear, remains stable, no matter how strong the driving electric field [4]. By contrast, in the voltage-driven cylindrical pinch the basic state is known to become unstable. The situation is reminiscent of the difference between plane and rotating hydrodynamic Couette flow (only for the latter one the laminar ground state becomes unstable).

The quiescent basic state of the sheet pinch can become unstable, however, if η varies across the sheet, due, for instance, to temperature differences between the sheet center and the walls. This results in profiles of the equilibrium magnetic field deviating from linear behavior. We have studied in detail the Harris equilibrium

$$\tilde{\eta} = \cosh^2[(x_1 - 0.5)/a], \quad \mathbf{B} = \mathbf{B}^e = \left(0, \frac{\tanh[(x_1 - 0.5)/a]}{\tanh(1/2a)} + \overline{B_2^e}, \overline{B_3^e}\right). \quad (3)$$

Here a is an effective current sheet half width, and all quantities have been made appropriately nondimensional with, for instance, the distance between the boundary planes as the unit of length [3]. The main system parameters are the two Reynolds-like numbers $M = v_A L/\nu$ and $S = v_A L/\eta_0$, where $v_A = B_0/\sqrt{\mu_0 \rho}$ is the Alfvén velocity associated with the magnetic field strength B_0 on the boundary planes when $\overline{B_2^e} = 0$ (symmetric profile).

3 Instability and Bifurcation

A Squire's theorem could be proven [2] stating that, as M or S are raised, the basic state becomes first unstable to two-dimensional (2D) perturbations, with velocity and magnetic field vectors lying completely in the x_1-x_2 plane and having no x_3 dependence. Furthermore, the instability is nonoscillatory and the stability boundary depends only on the Hartmann number $Ha = \sqrt{M\,S}$ (and not on M and S separately). It is found that instability is only possible for $a < 0.4$ [3]. The most unstable eigenmode is the 2D tearing mode, which is characterized by a magnetic island structure with a chain of X and O points, fluid motion in the form of convection-like rolls, and a filamentation of the original current sheet (Fig. 2). Restricting the whole problem to two spatial dimensions, this mode

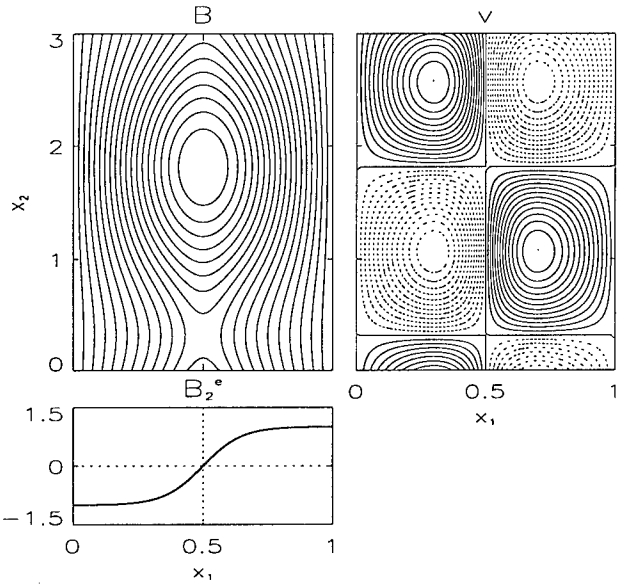


Figure 2: Magnetic field lines and velocity stream lines of an unstable mode for $a = 0.15$, $\overline{B_2^e} = 0$, $L_2 = 3$, and $Ha = 100$. Solid (dashed) velocity stream lines correspond to clockwise (counterclockwise) motion. A mixture of 20% perturbation $\mathbf{b}$ and 80% equilibrium field $\mathbf{B}^e$ was taken for the magnetic field. The lower left panel shows the undisturbed cross-sheet equilibrium profile $B_2^e(x_1)$.

was followed up to a time-asymptotic steady state (Fig. 3, left panel). This state proves to be sensitive to three-dimensional (3D) perturbations even close to the point where the primary instability sets in [1]. The instability with respect to 3D perturbations is suppressed by a sufficiently strong magnetic field in the invariant direction of the equilibrium. For a special choice of the parameters, the unstably perturbed state was followed up in its nonlinear evolution and was found to approach a 3D steady state (Fig. 3, right panel). Although velocity

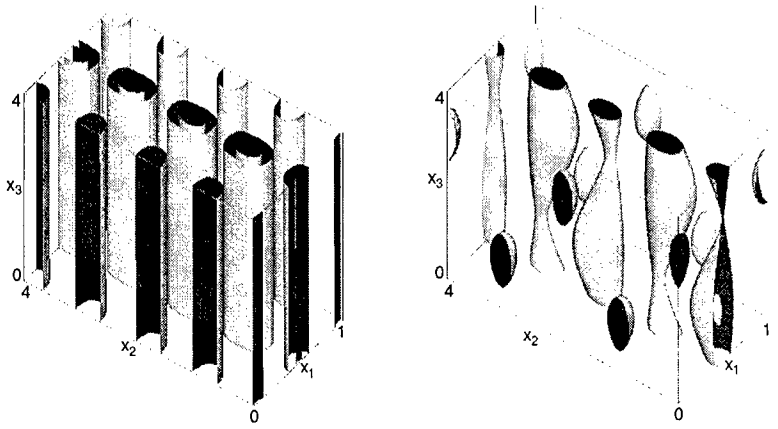


Figure 3: Isosurfaces $|\mathbf{v}|=0.03$ and $|\mathbf{v}|=0.016$ for the time-asymptotic 2D state (left) and the time-asymptotic 3D state (right). The values of the parameters are $L_2 = L_3 = 4$, $\overline{B_2^c} = \overline{B_3^c} = 0$, and $Ha = 67.0$. The maximum and minimum values of $|\mathbf{v}|$ are 0.0384 and 0.0017, respectively, in the 2D case and 0.0311 and 0.0, respectively, in the 3D case.

and magnetic field have now components in the invariant direction of the 2D state and are modulated in this direction, there is still some resemblance to the 2D tearing-mode state. This suggest that the unstable 3D perturbations to the 2D state do not drive the system to a completely different solution, but that 2D and 3D solutions originate simultaneously in the primary bifurcation of the basic state. Since our calculations were made very close to the primary bifurcation point, we suppose that a supercritical bifurcation leads directly from the basic state to a 3D attractor.

References

[1] J. Schumacher and N. Seehafer. Bifurcation analysis of the plane sheet pinch. *Phys. Rev. E*, 2000. In press.

[2] N. Seehafer and J. Schumacher. Squire's theorem for the magnetohydrodynamic sheet pinch. *Phys. Plasmas*, 4:4447–4449, 1997.

[3] N. Seehafer and J. Schumacher. Resistivity profile and instability of the plane sheet pinch. *Phys. Plasmas*, 5:2363–2369, 1998.

[4] N. Seehafer, E. Zienicke, and F. Feudel. Absence of magnetohydrodynamic activity in the voltage-driven sheet pinch. *Phys. Rev. E*, 54:2863–2869, 1996.

ADVANCES IN TURBULENCE VIII
Proceedings of the Eighth European Turbulence Conference
C. Dopazo et al. (Eds.)
© CIMNE, Barcelona 2000

The Nonlinear Evolution of Disturbances to a Subsonic Mixing Layer with Transverse and Coplanar Magnetic Fields

R. Mallier

Department of Applied Mathematics, University of Western Ontario
London ON N6A 5B7, CANADA

Contact e-mail: mallier@julian.uwo.ca

1 Introduction

A small, nearly neutral two-dimensional disturbance superimposed on a mixing layer initially grows linearly. However, eventually its amplitude will become large enough that nonlinear effects become important, first entering inside the critical layer, and the theory of nonlinear critical layers has been developed to deal with this. Typically, one poses both an outer expansion in the main body of the fluid and an inner expansion near the critical layer, and matching these together leads to an amplitude equation. Using nonlinear critical layers for unsteady two-dimensional shear layers, Goldstein & Leib [3] were the first to derive an evolution equation of the form that is now widely accepted as correct. They considered an incompressible shear layer, and found that if a disturbance was $\mathcal{O}(\varepsilon)$, then the evolution remains linear provided $\varepsilon^{1/2} \ll \mu$, where μ is the order of the departure of the phase velocity c of the disturbance from its neutral value and thus the lengthscale upon which the disturbance develops. Goldstein & Leib found that the evolution first became nonlinear when $\mu \sim \varepsilon^{1/2}$, with the amplitude governed by a set of nonlinear equations.

While Goldstein also considered compressible flows [4], he considered only the three-dimensional case, arguing that for high enough Mach numbers, oblique modes can grow faster than plane modes, although later [5], he did examine two-dimensional hypersonic flow, a very different limit from that studied here. However while oblique disturbances can be more important than plane disturbances, this does not mean that the latter are unimportant.

For low Mach numbers, plane disturbances are still the most linearly unstable. Sandham & Reynolds [8] suggested that the Mach number range should be split into three regimes with different instability and physical characteristics.

For low values, $0 < M < 0.6$, plane disturbances were linearly the most unstable. For higher, but still subsonic, values, $0.6 < M < 1$, the flow was increasing three-dimensional with, however, the plane waves still having an effect. Finally, for supersonic modes, $M > 1$, the oblique modes were linearly the most unstable. Sandham & Reynolds[8] tested this by running simulations and found results consistent with their hypothesis. Three-dimensionality appears important in the second regime, $0.6 < M < 1$, since two-dimensional simulations in this range [6] tended to develop weak shock waves absent in the three-dimensional simulations. However, for lower Mach numbers, $0 < M < 0.6$, the two-dimensional problem remains important, and the present study is relevant to that parameter range.

A related reason for studying the two dimensional problem is that there have been several numerical simulations of this problem and theoretical work is needed to accompany these, as well as related simulations in plasma physics [7].

In this study, we look at a plane disturbance to a compressible shear layer, considering the range $0 < M < 0.6$, the regime in which plane disturbances are important. As a starting point for our analysis, we will use the linear solution of Blumen [1], which is valid for $M < 1$. We will consider flows in the presence of a transverse magnetic field, and separately with a coplanar field. Both linear stability and simulations of compressible shear layers have shown that, to first order, the linear results are described by a single parameter, the convective Mach number, and our results will show that this holds true for the nonlinear problem in the absence of viscosity also. Indeed, we will find that the flow with a transverse magnetic field collapses onto the problem of a flow in the absence of a magnetic field with a modified Mach number.

2 Formulation and Outer Expansion

We consider plane waves of magnitude $\mathcal{O}(\varepsilon) \ll 1$ of the form $e^{\pm i\alpha(x-ct)}$ superimposed on a compressible $\tanh y$ mixing layer. Following [7], for an ideal magnetohydrodynamic gas, the governing equations of a two-dimensional inviscid compressible gas with a transverse magnetic field can be written

$$\begin{aligned} \frac{D}{Dt}\{\rho, B, p^{1/\Gamma}\} &= -(\nabla \bullet \underline{u})\{\rho, B, p^{1/\Gamma}\} \\ \rho\frac{D\underline{u}}{Dt} &= -\nabla\left[p - B^2/(2\mu_0)\right] \end{aligned} \tag{1}$$

where $\underline{u} = (u, v, 0)$ is the velocity, ρ the density, p the pressure, $\underline{B} = (0, 0, B)$ the magnetic field, and Γ the ratio of specific heats. We consider the base flow $(u_0, 0, 0)$, with $u_0(y) = 1 + \tanh y$, while the base pressure p_0, density ρ_0 and magnetic field B_0 are assumed constant. Our outer expansion will be of the form

$$u = u_0(y) + \varepsilon\left[(A(X)u_{10}(y) + \mu u_{11}(y, X) + \cdots)e^{i\xi} + c.c.\right] + \mathcal{O}\left(\varepsilon^2\right), \tag{2}$$

where we have introduced the small parameter $\mu \ll 1$ and phase $\xi = \alpha(x - ct)$. The wave number $\alpha = \alpha_0$ is neutral while the phase velocity is perturbed slightly

from neutral, $c = c_0 - \mu c_1$, giving rise to the long length-scale $X = \mu x$. At leading order, we find that the modified Mach number

$$\tilde{M} = \sqrt{\rho_0 \mu_0 / \left(B_0^2 + \Gamma \mu_0 P_0\right)} = M \left[1 + B_0^2 M^2 / \left(\rho_0 \mu_0\right)\right]^{-1/2}, \tag{3}$$

lets us use Blumen [1], and we have a neutral mode with $c = 1$, $\alpha_0 = \sqrt{1 - \tilde{M}^2}$, and $v_{10} = \mathrm{sech}^{\alpha_0^2} y$. Numerical simulations [8] would suggest that this is the mode of interest here, while two others [2] become important at higher $\tilde{M}$. The relation between α_0 and $\tilde{M}$ above restricts our analysis to subsonic modes, $0 \leq \tilde{M} < 1$, and physical considerations would seem to limit us still further to $0 < \tilde{M} < 0.6$.

At the next order, there is a jump across the critical layer,

$$[u_{11}]_{0-}^{0+} = -2A' B\left(1/2, \alpha_0^2\right), \tag{4}$$

where B is the beta function. In the early stages, we know that the jump is

$$[u_{11}]_{0-}^{0+} = 2i\pi\alpha_0^{-2} A' - 2\pi\alpha_0^{-1} c_1 A, \tag{5}$$

so early on, the amplitude $A(X)$ obeys $A' = \sigma X$, and we have an initial condition $A \to a_0 e^{\sigma X}$ as $X \to -\infty$, where σ is the growth rate,

$$\sigma = \pi\alpha_0 c_1 \left[\alpha_0^2 B\left(1/2, \alpha_0^2\right) - i\pi\right] / \left[\pi^2 + \alpha_0^4 B\left(1/2, \alpha_0^2\right)^2\right]. \tag{6}$$

3 Inner Expansion

As in [3], near the critical layer, we use the rescaled variable, $Y = y/\mu$, and set $\epsilon = \mu^2$, the balance for which the amplitude equation first becomes nonlinear. The outer solution suggests that the inner expansion will take the form

$$u = 1 + \mu Y - \mu^3 Y^3/3 + 2\mu^5 Y^5/15 + \cdots + \mu^3 U_3(Y, X, \xi) + \cdots. \tag{7}$$

Substituting this into the governing equations (1), we arrive at a single PDE for the streamwise velocity component U_3, and defining $\tilde{Y} = Y + c_1$ and $Q = U_{3Y} + i\alpha_0^{-1}\left(Ae^{i\xi} - A^* e^{-i\xi}\right)$, this can be written

$$\left[\partial_X + \left(Ae^{i\xi} + A^* e^{-i\xi}\right)\partial_{\tilde{Y}} + \alpha_0 \tilde{Y} \partial_\xi\right] Q = 2\left(i\alpha_0^{-1} A' - c_1 A\right) e^{i\xi} + c.c., \tag{8}$$

together with the boundary condition that $Q \to 0$ as $\tilde{Y} \to \pm\infty$, and a jump condition across the critical layer,

$$(2\pi)^{-1} \int_0^{2\pi} \int_{-\infty}^{\infty} e^{-i\xi} Q \, d\tilde{Y} \, d\xi = [u_{11}]_{0-}^{0+} = -2A' B\left(1/2, \alpha_0^2\right). \tag{9}$$

We also have the initial condition that as $X \to -\infty$, $A \to a_0 e^{\sigma X}$ and

$$Q \to 2\alpha_0^{-2}\left(\sigma + i\alpha_0 c_1\right) A e^{i\xi} / \left(\tilde{Y} - i\sigma/\alpha_0\right) + c.c.. \tag{10}$$

The only place that the transverse magnetic field enters into these inviscid equations is through the Mach number $\tilde{M}$ (and also the wave number α_0 which depends on $\tilde{M}$). These equations are very similar to those found for the incompressible problem [3], essentially differing only in the coefficients, and this was to have been expected.

For a coplanar field $\underline{B} = (B_1, B_2, 0)$ with a weak base field $\left(\mu^{1/2} B_0, 0, 0\right)$, we arrive at coupled equations involving the magnetic potential χ,

$$\begin{aligned} & \left[\partial_X + \left(Ae^{i\xi} + A^* e^{-i\xi}\right) \partial_Y + \alpha_0 \left(Y + c_1\right) \partial_\xi\right] Q \\ = \; & 2\left(i\alpha_0^{-1} A' - c_1 A\right) e^{i\xi} + c.c. + \left[\chi_{YYY} \chi_\xi - \chi_{YY\xi} \chi_Y\right] / \left(\alpha_0 P_0 \Gamma \mu_0\right) \quad (11) \end{aligned}$$

and

$$\left[\partial_X + \left(Ae^{i\xi} + A^* e^{-i\xi}\right) \partial_Y + \alpha_0 \left(Y + c_1\right) \partial_\xi\right] \chi = -B_0 A e^{i\xi} + c.c. \quad (12)$$

References

[1] W. Blumen. Shear layer instability of an inviscid incompressible fluid. *J. Fluid Mech.*, 40:769–781, 1970.

[2] W. Blumen, P. G. Drazin and D. F. Billings. Shear layer instability of an inviscid incompressible fluid. Part 2. *J. Fluid Mech.*, 71:305–316, 1975.

[3] M. E. Goldstein and S. J. Leib. Nonlinear roll-up of externally exited shear layers. *J. Fluid Mech.*, 191:481–515, 1988.

[4] M. E. Goldstein and S. J. Leib. Nonlinear evolution of oblique waves on compressible shear layers. *J. Fluid Mech.*, 207:73-96, 1989.

[5] M. E.Goldstein and D. W. Wundrow. Spatial evolution of nonlinear acoustic mode instabilities on hypersonic boundary layers. *J. Fluid Mech.*, 236:635–664, 1990.

[6] S. Lele. Direct numerical simulation of compressible free shear flows. *AIAA Paper* 89-0374, 1989.

[7] A. Miura. Compressible magnetohydrodynamic Kelvin-Helmholtz instability with vortex pairing in the two-dimensional transverse configuration. *Phys. Plasmas*, 4:2871–2885, 1997.

[8] N. D. Sandham and W. C.Reynolds. Three-dimensional simulations of large eddies in the compressible mixing layer. *J. Fluid Mech.*, 224:133-158, 1991.

ADVANCES IN TURBULENCE VIII
Proceedings of the Eighth European Turbulence Conference
C. Dopazo et al. (Eds.)
© CIMNE, Barcelona 2000

Simulations of turbulence subjected to gravitational and magnetic fields

S. Kenjereš and K. Hanjalić

Department of Applied Physics, Delft University of Technology
Lorentzweg 1, 2628 CJ Delft, The Netherlands

Contact e-mail: kenjeres@ws.tn.tudelft.nl; hanjalic@ws.tn.tudelft.nl

1 Introduction

In many turbulent flows of industrial and environmental relevance large eddy structures are the major carrier of momentum, heat and concentration. In such flows the transport processes can be best controlled by affecting the coherent eddy structure. This can be done by imposing an external force, or by control of boundary topology or its physical conditions. We argue that for flows with a dominant eddy structure, the application of time-dependent RANS ('TRANS') can be a powerful tool for identifying the organized motion and its response to the imposed external force or specific boundary conditions. In order to demonstrate the TRANS approach, we investigate several cases of classical and magnetic Rayleigh-Bénard convection in which large scale coherent structure has been detected both by DNS and by experimental studies.

2 Results

2.1 Classical Rayleigh-Bénard convection (RB)

First, the classical Rayleigh-Bénard convection is presented. The available DNS simulation results of Wörner [5] have been used as reference for comparison, Ra=6.5×10^5, Pr=0.71. The LES approach is based on the subgrid model where the effect of thermal stratification is taken into account in buoyancy-extended Smagorinsky-type turbulent viscosity/diffusivity formulation, Eidson [1], Wong and Lilly [4]:

$$\nu_t = C_s \Delta^2 \left(|\overline{S}| + \frac{1}{Pr_t} \frac{\partial T}{\partial x_j} \beta g_k \delta_{kj} \right)^{1/2} \tag{1}$$

where C_s=0.21, Pr_t=0.4 and $|\overline{S}| = \sqrt{2 \overline{S_{ij} S_{ij}}}$. The TRANS approach is based on the triple-decomposition where the large scale periodic-like motion is fully resolved in time and space, whereas the unresolved stochastic contribution is modeled by using algebraic flux expressions:

$$\overline{\theta u_i} = -C_\theta \frac{k}{\varepsilon} \left[\overline{u_i u_j} \frac{\partial \tilde{T}}{\partial x_j} + \xi \overline{\theta u_j} \frac{\partial \tilde{U}_i}{\partial x_j} + \eta \beta g_i \overline{\theta^2} \right] \tag{2}$$

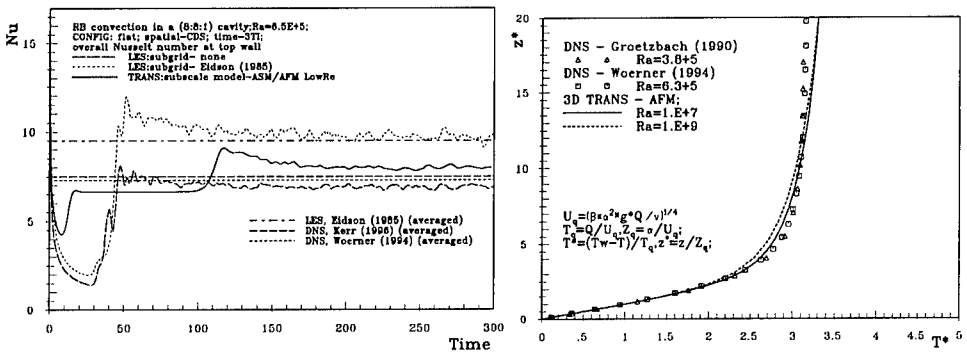


Figure 1: (a.) Assessment of fully resolved DNS, underresolved DNS, LES and TRANS approach in reproduction of the integral heat transfer time evolution for RB convection at Ra=6.5×10^5; (b.) scaling of the main vertical temperature profile (TRANS and DNS);

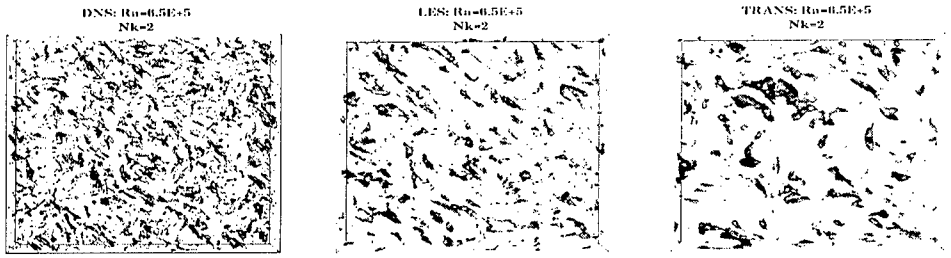


Figure 2: RB convection at Ra=6.5×10^5;DNS-Wörner [5], LES- Eidson [1] subgrid model, TRANS-LowRe ASM/AFM subscale model, Kenjereš and Hanjalić [2]: capturing of large coherent structures in DNS, LES and TRANS realization;

closed with the low-Re $k-\varepsilon-\overline{\theta^2}$ three-equation model, Kenjereš and Hanjalić [2]. In contrast to LES, in the TRANS approach the contribution of both modes (resolved and modeled) to the turbulence fluctuations are of the same order of magnitude. In the horizontal wall boundary layers the TRANS model accounts almost fully for the turbulence statistics, with a marginal contribution of resolved ones. This proved to be the key of success for accurate near-wall mean temperature and wall heat transfer predictions (verified by the DNS), whereas the LES yielded serious overprediction, attributed to inadequate wall treatment by subgrid scale model, Fig.1. Very recently Kimmel and Domaradzki [3] applied a new subgrid scale estimation model for RB convection, but again their simulations overpredicted the wall heat transfer. A direct comparisons of captured eddy structure by the three simulation techniques is also presented. Two structure identification methods have been used for this purpose: the classical vorticity/helicity approach and the critical point theory (the kinematic vorticity number, the second invariant of the velocity gradient tensor, the discriminant of characteristic equation). Fig.2 shows the contours of the identical value of the

structure identification parameter obtained from single DNS, LES and TRANS realizations. Both, LES and TRANS capture only the large structure while the smaller ones are filtered out. The filtering process is defined by mesh size in LES approach and by specific length scale emerging from the subscale model in the TRANS approach.

2.2 Magnetic Rayleigh-Bénard convection (MRB)

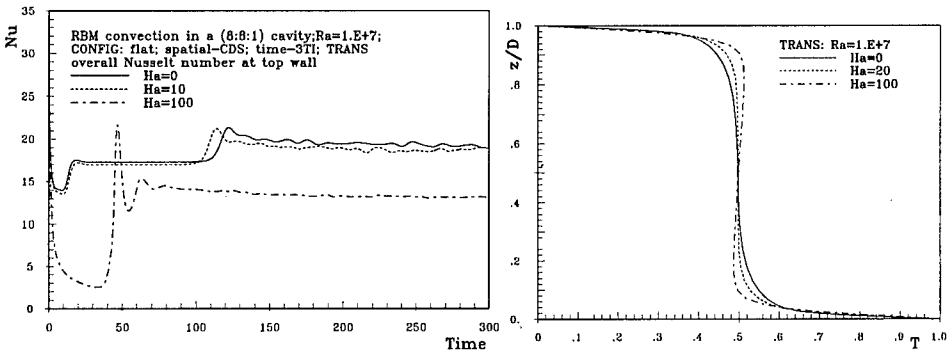


Figure 3: Influence of imposed transversal magnetic field ($B_i||g_i$) of different strength (Ha=0, 20, 100) on time evolution of integral Nu number and the mean vertical temperature

The second case considered was the magnetic RB convection. Two situations have been analyzed: when the gravitational vector and imposed magnetic field are aligned ($g_i||B_i$) and when they are orthogonal ($g_i \perp B_i$). In both situations, the different intensities of imposed magnetic field, defined by the Hartmann number (weak, Ha=20 and strong, Ha=100) have been applied. Beside the direct effect through Lorentz force in momentum equations:

$$\hat{F}_i^L = \sigma \left(\epsilon_{ijk} \hat{B}_k \frac{\partial \hat{\Phi}}{\partial x_j} + \hat{U}_k \hat{B}_i \hat{B}_k - \hat{U}_i \hat{B}_k^2 \right) \tag{3}$$

the additional 'magnetic' source terms representing the effects of magnetic field are included in subscale model equations for k and ε of the TRANS approach:

$$G_k^L = -\frac{\sigma}{\rho} B_0^2 k \exp\left(-C_L \frac{\sigma}{\rho} B_0^2 \frac{k}{\varepsilon} \right); \quad G_\varepsilon^L = G_k^L \frac{\varepsilon}{k} \tag{4}$$

In this paper, due to limited space, we presented only situation where the gravitational vector and imposed magnetic field are aligned. The presence of magnetic field significantly damps the heat transfer, as shown by the time evolution of the Nusselt number, Fig. 3. The long-time averaged vertical temperature profiles show a visible temperature inversion as the magnetic field strength increase. Due to presence of Lorentz force in the horizontal plane (for $g_i||B_i$ case), the horizontal movement of thermal plumes is significantly reduced. These plumes are

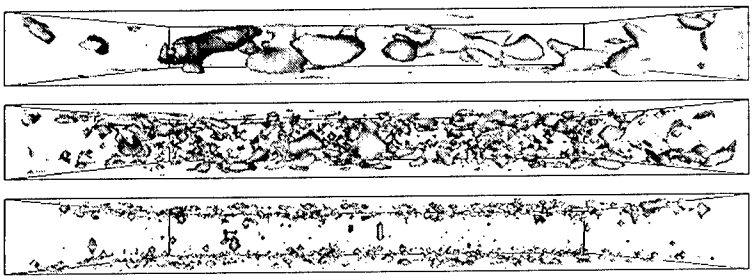


Figure 4: The spatial reorganization of the large coherent structures (defined by kinematic vorticity number $\mathcal{N}_k = \left(|\omega_i|^2/2S_{ij}S_{ij}\right)^{1/2}$=3 under influence of imposed transversal magnetic field of different strength ($Ha = 0, 20, 100$)

smaller and more extended in vertical direction compared to situation without magnetic field. The large coherent structures show a similar behavior, Fig.4. With an increase in Ha, they become smaller with a more pronounced orientation in vertical direction. This confirms the general view that vortical structures are modified with a tendency to align the major vortex axis with the magnetic field vector.

3 Conclusions

Turbulence confined between two infinite horizontal plates and subjected to combined thermal buoyancy and magnetic fields has been studied using two simulation techniques: large eddy simulation (LES) and time-dependent RANS (TRANS) methods. It is demonstrated that TRANS techniques compared to LES reproduced the heat transfer in much closer accordance with DNS results. It is argued that TRANS method can reproduce the major flow features and turbulence statistics, as well as to capture the coherent structures, much in accord with DNS and LES results, but with substantially smaller computational effort.

References

[1] T. M. Eidson. Numerical simulation of the turbulent Rayleigh-Bénard problem using subgrid model. *J. Fluid Mech.*, 158:245–268, 1985.

[2] S. Kenjereš and K. Hanjalić. Transient analysis of Rayleigh-Bénard convection over flat and wavy walls with a RANS model. *Int. J. Heat and Fluid Flow*, 20:329–340, 1999.

[3] S. J. Kimmel and J. A. Domaradzki. LES of Rayleigh-Bénard convection using subgrid scale estimation model. *Phys. Fluids*, **(12)**1:169–184, 2000.

[4] V. C. Wong and D. K. Lilly. A comparison of two dynamical subgrid closure methods for turbulent thermal convection. *Phys. Fluids*, 6:1016–1023, 1994.

[5] M. Wörner. Direkte Simulation turbulenter Rayleigh-Bénard Konvektion in flüssigem Natrium. *Dissertation, Uni. of Karlsruhe*, KfK 5228, Kernforschungszentrum Karlsruhe, Germany, 1994.

ADVANCES IN TURBULENCE VIII
Proceedings of the Eighth European Turbulence Conference
C. Dopazo et al. (Eds.)
© CIMNE, Barcelona 2000

On certain features of helical turbulent flows

H. Branover[1], O. Chkhetiani[2], A. Eidelman[1],
E. Golbraikh[1] and S. Moiseev[2]

[1]Center for MHD Studies, Ben-Gurion University of the Negev, Beer-Sheva, Israel
[2]Space Research Institute, RAS, Moscow, Russia

Contact e-mail: golbref@bgumail.bgu.ac.il

Self-organization of large-scale structures in turbulent and chaotic flows is one of important problems of hydrodynamics. Helical turbulence occupies a special position among these flows. Helicity $H = \int_V (\mathbf{u} \cdot rot\mathbf{u}) dV$ (here $\mathbf{u}$ is the velocity), being a second invariant of Euler's equation, just as energy [10], exerts a great influence on the evolution and stability of turbulent and laminar flows [8, 2, 7, 5]. Apparently, helicity is one of the main sources of magnetic fields generation and maintaining in astrophysical objects [13]. Possibly, helical mechanism is responsible for the generation of intense large–scale geophysical vortices, such as typhoons [11, 4].

Numerous investigations of the properties of helical turbulence (see, for example, [8]) also demonstrate that non-zero helicity leads to the decrease in the energy flux from large to small scales. One of principal parameters connected with the energy flux from larger to smaller scales is turbulent viscosity. Hence, its magnitude should decrease with decreasing direct energy cascade. Additionally, a decrease in energy transfer should lead to another energy redistribution between different scales involved in turbulent motions. At the initial (linear) stage of such redistribution the process can be unstable [2, 7].

In the present work we dwell on the main characteristics of helical turbulent flows. We briefly discuss how mean helisity can be generated in a medium and how small-scale and large-scale characteristics of the flow change if the mean helicity is non-zero.

Helicity generation

The problem of mean helicity generation is connected with mirror symmetry violation in hydrodynamic flows. It is known that mean helicity is generated in a rotating stratified atmosphere[13]. Other situations where helicity can also be generated were studied in [6, 9, 12] for the Eckman boundary layers and convective flows. The dissipative mechanism of mean helicity generation was proposed first in [1]. This mechanism is the cause of a helical "fur-coat" of secondary vortices "worn" by interacting vortical structures. Here we dwell

on the process of mean helicity generation in an electroconductive fluid shear flow in an external homogeneous magnetic field. As it was shown in [5] in the equation for helicity first-order terms appear, which are proportional to $(\mathbf{\Omega}_o^2\mathbf{B}_o^2 - (\mathbf{\Omega}_o\mathbf{B}_o)^2 + \mathbf{\Omega}_o(\mathbf{B}_o\nabla)[\mathbf{B}_o \times \mathbf{U}_o])$(where $\mathbf{\Omega}_o = \mathbf{rot}\overline{\mathbf{u}}$ and $\mathbf{B}_o$ is an external magnetic field). These terms lead to an intense generation of mean helicity.

Thus, we can assume that non-zero mean helicity exists in turbulence flows practically always. This helicity is generated in different processes which violate the mirror symmetry in a flow.

Inverse cascade and helical spectrum

To study helicity influence on the turbulent energy cascade, we consider the stability of helical turbulence with respect to weak large-scale inhomogeneous disturbances of the velocity field[2]. In this case turbulent part of the velocity has a form $\mathbf{u}' = \mathbf{u}^0 + \mathbf{u}^1$. Let a two-point correlator of undisturbed turbulence have the following form

$$\begin{aligned} Q_{ij}^{00}(\mathbf{x},t,\xi,\tau) &= \overline{\mathbf{u}_i^0(\mathbf{x},t)\mathbf{u}_j^0(\mathbf{x}',t')} = A(\xi,\tau)\delta_{ij} + B(\xi,\tau)\xi_i\xi_j + C(\xi,\tau)\varepsilon_{ijk}\xi_k \\ \xi &= |\mathbf{x}-\mathbf{x}'|, \tau = |t-t'|. \end{aligned}$$

Then the equation for a two-point correlator of disturbance $Q_{ij}^{10}(\mathbf{x},t,\xi,\tau) = \overline{\mathbf{u}_i^1(\mathbf{x},t)\mathbf{u}_j^0(\mathbf{x}',t')}$ has the form [2]:

$$\left[(\frac{\partial}{\partial\tau} - (\nu+\nu_t^0)\Delta)\delta_{ik} - \alpha\varepsilon_{ipk}\nabla_p\right] Q_{kj}^{10}(\xi,\tau,\mathbf{x},t) =$$

$$\mathbf{D}(\overline{\mathbf{u}(\mathbf{x},t)}, Q_{ij}^{00}(\xi,\tau,\mathbf{x},t), Q_{kp}^{10}(\mathbf{x},t,0,0), \tau^*)$$

where $\mathbf{D}$ is a function of average velocity $\overline{\mathbf{u}(\mathbf{x},t)}$ and correlators $Q_{ij}^{00}(\xi,\tau,\mathbf{x},t)$, $Q_{kp}^{10}(\mathbf{x},t,0,0)$; $\nu_t^0 = A(0,0)\tau^*$, $\alpha = |C(0,0)|\,\tau^*$, and τ^* is the relaxation time in Orszag's approximation model. As follows from this system, the parameter of instability (or increment) $\gamma = -i\omega$ is defined by the condition: $\gamma = -\nu' k^2 \pm \alpha k$, where $\nu' = \nu + \nu_t^0$.

At $k < \alpha/\nu'$ experiences instability arises in the system. In fact, at large-scale disturbances of the correlational tensor with $k < k_{tur} = \alpha/\nu'$, the system is unstable (at the linear stage); energy growth take place over these scales. Turbulent energy in the linear mode is redistributed with an exponential growth over the scales $k < k_{tur}$. On the other hand, within the range of $k > k_{tur}$, helicity increases the characteristic dissipation time $\tau_{\text{diss}} \sim \frac{1}{\gamma} = 1/(-\nu' k^2 + |C|\tau^* k)$. This implies an increase in the lifetime of vortices of the given scale which, in turn, increases the probability of their merging, thus slowing down the energy transfer over the spectrum and leading to an inverse transfer from small to large scales.

The same situation takes place in MHD turbulent flows in laboratory experiments [7]. A modified parameter of instability has a form: $\gamma = -\nu_H k^2 -$

$N\cos^2\theta \pm \tilde{\tau}|C|k$, where N is the Stuart number; θ is an angle between the directions of an external magnetic field and wave vector, and $\tilde{\tau} = \left(\frac{1}{\tau^*} + N\cos^2\theta\right)^{-1}$. For $\dot{\gamma} > 0$:

$$\frac{1}{2}k_{tur}\left(1 - (1 - \frac{4N\cos^2\theta}{k_{tur}^2\nu'})^{1/2}\right) < k < \frac{1}{2}k_{tur}\left(1 + (1 - \frac{4N\cos^2\theta}{k_{tur}^2\nu'})^{1/2}\right),$$

here $\nu_t^0 = A(0,0)\tilde{\tau}$, and when a magnetic field is absent ($N \to 0$), this inequality transforms into $k < \alpha/\nu'$. We can see that turbulent modes grow in a limited interval whose size depends on the magnitude of the magnetic field.

Let $\cos\theta = 0$, i.e., we consider the modes for which $\mathbf{k} \perp \mathbf{B}_0$. In this case $0 < k < k_{tur}$. On the other hand, at $\cos\theta = 1$, i.e., in the modes for which $\mathbf{k} \parallel \mathbf{B}_0$.

$$\frac{1}{2}\left(k_{tur} - \left(k_{tur}^2 - \frac{4N}{\nu'}\right)^{1/2}\right) < k < \frac{1}{2}\left(k_{tur} + \left(k_{tur}^2 - \frac{4N}{\nu'}\right)^{1/2}\right),$$

With growing magnetic field the instability interval is reduced and vanishes at the magnetic fields described by $4N/\nu' = k_{tur}^2$.

Note that when the instability vanishes with growing external magnetic field, the value of $\cos\theta$ decreases and tends to zero at $\mathbf{B}_0 \Rightarrow \infty$. Hence, at large scales $k < k_{tur}$ in a strong magnetic field turbulence is quasi-two-dimensional. At $k > k_{tur}$ turbulence remains three-dimensional and helical, as shows, in particular, the dependence of energy density on the wave vector [3, 4]. Thus, the behavior of helical turbulence (and it is helical practically always) in an external homogeneous magnetic field is three-dimensional. It can be quasi-two-dimensional at the large scales in a strong magnetic field only. But it is not only the magnitude of a magnetic field that determines the transition in this regime, but also the intrinsic parameters of the flow, such as kinematic viscosity, characteristic relaxation time, density, conductivity etc.

As we have noted above, mean helicity changes energy transfer in a turbulent flow. It is well known that the spectral energy density has the form $E(k) \propto k^{-5/3}$ in Obuchov-Kolmogorov's model of the direct cascade, and the energy transfer rate plays the principal role. On the other hand, if the mean helicity transfer rate $\eta \equiv dH/dt$ is a determining parameter, the dependence of $E(k)$ on k changes and transform into $E(k) \propto k^{-7/3}$[12]. The transition from one regime to another is connected with the magnitude of helicity in the flow. The Kolmogorov's spectrum exists when the influence of helicity transfer is weak.

Turbulent viscosity

A special influence of mean helicity on the flow characteristics manifests itself in the turbulent viscosity change. Turbulent viscosity decreases, and its dependence on the helicity has the form[4]:

$$\nu_t = \left[1 + \frac{\tau^*}{15}\int\limits_{k_{tur}}^{\infty}\int\limits_{0}^{\infty}\exp(-\nu_t^0 k^2\tau)(2E_f(k,\tau)\mathrm{Ch}(\alpha k\tau) + \frac{H_f(k,\tau)}{k}\mathrm{Sh}(\alpha k\tau))dkd\tau\right]^{-1} \times$$

$$\frac{2}{5}\int_{k_{tur}}^{\infty}\int_{0}^{\infty}\exp(-\nu_t^0 k^2\tau)\{[E_f(k,\tau)+\frac{k}{3}\frac{\partial E_f(k,\tau)}{\partial k}]\mathrm{Ch}(\alpha k\tau)-$$

$$-[\frac{2}{3}\frac{H_f(k,\tau)}{k}-\frac{1}{6}\frac{\partial H_f(k,\tau)}{\partial k}]\mathrm{Sh}(\alpha k\tau)\}dkd\tau$$

where $E_f(k,\tau)$ and $H_f(k,\tau)$ are related to symmetric and antisymmetric parts of the Fourier-transform of the undisturbed turbulence correlator. Turbulent viscosity ν_t in the presence of an external magnetic field decreases strongly[7, 4].

Conclusion

In conclusion, we list mean features of a helical flow. The process of mean helicity generation exists practically always in any flows. If the determining parameter of the turbulent system is mean helicity transfer rate, the spectral density of energy has a non-Kolmogorov's dependence on k ($E(k) \propto k^{-7/3}$). There is an inverse cascade of turbulent energy from small to large scales, which is connected with the life-time growth of eddies in small scales. Turbulent viscosity of a helical flow decreases, and this effect can be intensified in an external magnetic field. Turbulent viscosity decrease in a helical flow can play an appreciable role in solving the drag reduction problem.

References

[1] Andre, J.C. and Lesieur, M.,(1977), J. Fluid Mech., **81**, 187.

[2] Belian, A., Chkhetiani, O., Golbraikh, E., and Moiseev, S. (1998). *Physica A*, **258**(1/2), 55.

[3] Eidelman A., Branover, H. and Moiseev S., (2000)., Proc. 8th European Turbulence Conference, Barcelona, Spain, June 27-30.

[4] Branover H., Eidelman A., Golbraikh E., Moiseev S., (1999), *Turbulence and Structures,* Academic Press, Boston.

[5] Chkhetiani, O., Moiseev, S., and Golbraikh, E. (1998). *Zh. Eksp. Teor. Fiz.* **114**, 946.

[6] Hide, R. ,(1989),Geophys. Astrophys. Fluid Dynamics, **48**, 69

[7] Golbraikh, E., Chkhetiani, O., and Moiseev, S. (1998). , *JETP* **87**(1), 95.

[8] Levich, E., Shtilman, L.and Tur, A.V. 1991, Physica A, **176**, 241.

[9] Lilly, D.K.,(1986), J. Atmos. Sci., **43**, 126 .

[10] Moffatt, H.K. 1969, J. Fluid Mech., **35**, 1117

[11] Moiseev, S.S., Sagdeev, R.Z., Tur, A.V., Khomenko, G.A. and Yanovskii, V.V. (1983), Sov. Phys. JETP, **58**, No 6, 1149.

[12] Moiseev, S.S. and Chkhetiani, O.G., (1996),Helical scaling in turbulence. JETP, **83**, No.1, 192 .

[13] Vainshtein, S.I., Zeldovich, Ya.B., and Ruzmaikin, A.A. (1980). *Turbulent Dynamo in Astrophysics.* Nauka, Moscow.

ADVANCES IN TURBULENCE VIII
Proceedings of the Eighth European Turbulence Conference
C. Dopazo et al. (Eds.)
© CIMNE, Barcelona 2000

Helical turbulence properties in the laboratory and in nature

A. Eidelman[1], H. Branover[1] and S. Moiseev[2]

[1]Center for MHD Studies, Ben-Gurion University of the Negev, Beer-Sheva, Israel
[2]Space Research Institute, RAS, Moscow, Russia

Contact e-mail: eidel@bgumail.bgu.ac.il

Our experimental studies of magnetohydrodynamic (MHD) turbulence have revealed its different modes corresponding to the interaction parameter N value which describes the ratio of electromagnetic to inertial forces. Particularly, Kolmogorov's mode with the velocity spectral slope -5/3 in the inertial range transforms into a mode with the slope close to -7/3 with the growth of N. Such turbulence has been called helical, since in this scale range helicity transfer determines its properties [1]. Main properties of helical turbulence defined by the instability of large-scale motions and by the arising inverse energy transfer, as well as by turbulent diffusivity drop are described in detail in [2]. Here we examine velocity spectra which allow us to reveal the helical turbulence mode and to establish its quantitative characteristics.

Our further studies have shown that spectra with the slope close to -7/3 are also obtained in the atmosphere. In the laboratory studies such spectral slope as in MHD helical turbulence was revealed under the conditions of convection, rotation, stratification, as well as in numerical studies of such flows. The helical turbulence mode is widespread since it appears when the motion is affected by factors of various physical origin causing symmetry violation [3].

A brief review of helical turbulence cases demonstrates that this phenomenon exists in turbulent flows under various conditions. Thus, velocity spectra with slopes -2.3 and -2.46 were obtained for turbulence generated by unstable density front in stratified fluid experiments under rotation [4]. Similar results have been obtained in a rotationally dominated turbulent flow where spectral slope was evaluated as -2.5 [5]. The experiments in stably stratified turbulence have revealed spectra with a slope "...slightly greater than -2" [6]. Authors note that the observed reverse energy cascade is similar to the predictions for two-dimensional turbulence, but the velocity spectra do not show any evidence that the collapsed turbulence has become purely two-dimensional. In this experiment a velocity spectrum was obtained in a flow of salt-stratified water streamdown of an array of vertical rods. We estimate a spectral slope in the section $\frac{x}{M} = 60$ ($M = 3.81$ cm) as rather close to -7/3 within the range of scales covering a

decade. Besides, there is an adjacent range covering a decade in larger scales, where the spectral slope is close to -5/3.

Wind spectra computed for the FGGE-IIIa global data set display a power law "...with slopes somewhat shallower than -3 " at high global wave-numbers [7]. Authors note a strong up-scale energy flux towards low wave-number range which they also cannot interpret within the theory of two-dimensional turbulence. Our estimation of the slope of these spectra is -7/3 within the range of global wave numbers above 7.5. Twenty six tapes of wind obtained during long distance flights were studied in [10], and the corresponding wind spectral slope was about -2.2. The slope of 130 stratospheric wind spectra obtained during Global Atmospheric Sampling Program (GASP) was estimated as -2.2 and -2.5 for the synoptic scale range [8]. Our estimation of GASP spectra for 1670 flights at the latitudes from 30°S to 60°N [9] gives a slope close to -7/3 for the meridional wind component in the range of synoptic scales from 3 to 0.3 thous. km [3]. Here the adjacent mesoscale range can be satisfactorily approximated by -5/3 slope. Wind spectra characterizing in more detail the mesoscale range of GASP data are given in [12] for three different regions - over plains, mountains and ocean. The authors note that steepened spectral slopes (-7/3 as we estimated) correspond to velocity fluctuations scales below 15-23 km.

Thus, we can summarize the main properties of spectra presented here as well as other helical turbulence spectra that are not mentioned in this brief report. Spectra include adjacent ranges with slopes close to -5/3 and -7/3 and a characteristic scale L of their matching. Besides, there can be several ranges with such alternating slopes and respective characteristic scales. Figure 1a shows a complex wind spectrum illustrating the properties of helical turbulence. The large-scale synoptic spectrum with -7/3 slope becomes below $L_S \simeq 300$ km a spectrum with -5/3 slope in the mesoscale. Then a spectrum with -7/3 slope is formed on the scales below $L_m = 15$ km. For the scales below 2 km we applied spectra obtained in [13] for the atmospheric boundary layer. The slope of these spectra is close to -7/3 within the scale range from the boundary layer altitude ($\backsim$1.5-2 km) to $L_t \simeq 250$ m, and to -5/3 - on the scales < 250 m. Note another transition from -5/3 to -7/3 slope at still smaller scales ($\backsim$ 1 m) in spectra [14] obtained under a strong wind forcing in the overflow of a hill.

Let us describe main features of helical turbulence spectra. Helicity H, just as kinetic energy, is an inviscid invariant and a basic characteristic of turbulent motion. For certain turbulence modes both the energy transfer rate $\varepsilon = du^2/dt$ and the helicity transfer rate $\eta = dH/dt$ are crucial parameters defining spectra formation. Helical turbulence spectrum (see Fig. 1a) includes Kolmogorov's -5/3 range determined by the energy transfer rate ε : $E(k) = C_1\varepsilon^{2/3}k^{-5/3}$, and -7/3 range determined by the helicity transfer rate η : $E(k) = C_2\eta^{2/3}k^{-7/3}$, where $C_2 = (2\pi)^{2/3}C_1$. Therefore, $C_2 = 1.7$ for the horizontal velocity spectrum $E_u(k_h)$ and $C_2' = 2.2$ for the vertical one $E_u(k_z)$, since $C_1 = 0.5$; $C_1' = 0.65$ [11]. Since C_2, generally speaking, can differ from the mentioned value by a constant factor, we have independently estimated η on the Earth rotation basis.

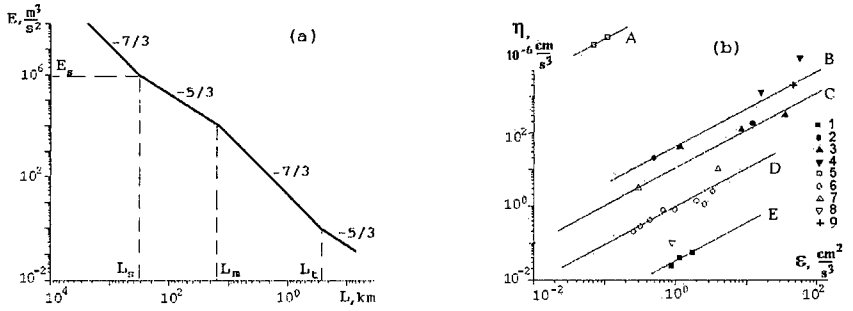


Figure 1: Compound wind spectrum characterizing helical turbulence (a) and transfer rates of energy ε and helicity η established for various laboratory and atmospheric conditions (b): 1 - [9], 2 - [13], 3 - [15], 4 - [16], 5 - [1], 6 - [12], 7 - [17], 8 - [10], 9 - [18]. Straight lines indicate the scales of spectral range conjugations: A - 3 cm, B - 0.1 km, C - 1 km, D - 15 km, E - 300 km.

For synoptic scales in the troposphere, estimation of the helicity transfer rate $\eta = 2u\Omega \sin\phi/t = 5.5 \cdot 10^{-8} cm/s^3$, where the latitude $\phi = 45^o$; $\Omega = 7.27 \times 10^{-5}$ rad/s is angular velocity; $u = 2$ m/s - vertical velocity; $t = 100$ hours is the synoptic spectral maximum. For atmospheric boundary layer scales, estimation of $\eta = 10^{-4} cm/s^3$, where t= 200 s is the atmospheric boundary layer spectral maximum. The above value of the coefficient C_2 may be applied until it will be defined more precisely in experiments requiring direct η measurements.

In the case of helical turbulence, a helicity scale $L_\eta = \varepsilon/\eta$ divides the spectrum into two ranges. As observations show, under atmospheric conditions there are several values of the scale L_η. They characterize the situation of several inputs of energy and helicity generating a complex wind spectrum (Fig. 1a). If the range scale is limited, as in laboratory flows or in the atmospheric boundary layer, only one scale or even one range is observed.

Energy and helicity transfer ($\eta = \varepsilon/L_\eta$) rates estimated on the basis of velocity spectra in flows of various scales are shown in Fig. 1b. In particular, within L_η range from 100 m to 300 km in the atmosphere, ε varies within $0.3 \div 30$ cm^2/s^3, whereas helicity transfer rate - within $(0.03 \div 3000)$ 10^{-6} cm/s^3. A much larger range of the variation of helicity transfer rate (10^6) than that of energy transfer rate (10^2) points to a much higher topological variability of turbulence in comparison with its energy variability. Helical turbulence possessing a partial order represents a mode of turbulent flow which determines the similarity of turbulent characteristics noted under various external conditions in the laboratory and in nature.

References

[1] Branover, H., Eidelman, A., Nagorny, M. and Kireev, M. 1994. In: Progress in Turbulence Research, Eds. H. Branover and Y. Unger., v. 162, 64-79.

[2] Branover, H., Chkhetiani, O., Eidelman, A., Golbraikh, E., Moiseev, S. 2000. Proc. 8th European Turbulence Conf., Barcelona, Spain, June 27-30.

[3] Branover, H., Eidelman, A., Golbraikh, E., and Moiseev, S. 1999. Turbulence and Structures. Academic Press, N.Y., 269 pp.

[4] Griffiths, R.W., Hopfinger, E.J. 1984. Deep-Sea Res., v. 31, No 3, 245-269.

[5] Mory, M. and Hopfinger, E.J. 1986. Phys. Fluids, v. 29, No 7, 2140-2146.

[6] Itsweire, E.C. and Helland, K.N. 1985. 7th Symp. on Turbulence and Diffusion. November 12-15, 1985, Boulder, Colorado, 172-175.

[7] Boer, G.J. and Shepherd, T.G. 1983. J. Atmosph. Sci., v. 40, 164-184.

[8] Nastrom, G.D., Gage, K.S. 1983. Tellus, v. 35A, No 5, 383-388.

[9] Nastrom, G.D., Gage, K.S. 1985. J. Atm. Sci., v. 42, No 9, 950-960.

[10] Lilly, D.K. and Petersen, E.L. 1983. Tellus, v. 35A, 379-382.

[11] Monin, A.S., Yaglom, A.M. 1975. Statistical fluid mechanics: Mechanics of turbulence. Ed. Lumley, J. MIT Press, Cambridge, Mass.

[12] Nastrom, G.D., Fritts, D.C. and Gage, K.S. 1987. J. Atm. Sci., v. 44, No 20, 3087-3096.

[13] Caughey, S.J., Palmer, S.G. 1979. Quart. J. R. Met. Soc., v. 105, 811-827.

[14] Mason, P.J., King, J.C. 1985. Quart. J. R. Met. Soc., v. 111, 617-640.

[15] Endlich, R.M., Singleton, R.C. and Kaufman, J.W. 1969. J. Atm. Sci., v. 26, 1030-1041.

[16] Dewan, E.M., Grossbard, N., Quesada, A.F. and Good, R.E. 1984. Geophys. Res. Let., v.11, No 1, 80-83.

[17] Vinnichenko, N.K., Dutton, J.A. 1969. Radio Sci., v. 4, No 12, 1115-1126.

[18] Lenschow, D.H. 1970. J. Appl. Meteorol., v. 9, No 12, 874-884.

III

Instabilities and Transition

ADVANCES IN TURBULENCE VIII
Proceedings of the Eighth European Turbulence Conference
C. Dopazo et al. (Eds.)
© CIMNE, Barcelona 2000

Hydrodynamic fluctuations in Couette flow

G. D. Chagelishvili,[1,2] G. R. Khujadze[1,3] and J. G. Lominadze[1]

[1] Abastumani Astrophysical Observatory, Kazbegi Ave.2[a], 380060, Tbilisi, Georgia
[2]Space Research Institute, Str. Profsoyuznaia 84/32, 117810, Moscow, Russia
[3]Center for Plasma Astrophysics, K.U.Leuven,Celestijnenlaan 200B, 3001, Heverlee, Belgium

Contact e-mail: georgech@mx.iki.rssi.ru

1 Introduction

In 90-s has been formulated a conception of so-called bypass transition to turbulence that is able to explain subcritical transition in shear flows [1-5]. According to this conception transient growth of disturbances is a key element in the subcritical transition process. (All normal modes of the system are exponentially stable.) At the same time, trigger of nonlinear (energy conserving mixing) regeneration process of the disturbances that are able to draw mean flow energy is the necessary step to the transition. This fact necessitates the existence of finite initial vortex disturbance in the system for the transition. It is obvious, that the finite disturbance can be produced at extrinsic forcing. For instance, in the paper [6] a pair of small but finite amplitude oblique waves were used as initial condition in numerical simulations of transition to turbulent flow. However, the question arises: whether or not the intrinsic, stochastic forces can generate the finite vortex perturbations in shear flows, i.e. does this nonequilibrium system give birth to the sufficiently high level of the background of vortex fluctuation? The question is the motivation of our exploration of the fluctuation background. The background of hydrodynamic fluctuations in a stochastically forced, laminar, Couette flow is described and analysed. It is shown that in the nonequilibrium open system under study it exists subspace $\mathcal{D}_{\mathbf{k}}$ in the wave-number space ($\mathbf{k}$-space) where the spatial Fourier harmonics of vortex as well as acoustic wave fluctuations are strongly subjected by flow shear: The fluctuation backgrounds of both the vortex and the acoustic wave modes are anisotropic and non-markovian; The spatial spectral density of the energy of the vortex fluctuations by far exceeds the white-noise; The fluctuation background of the acoustic waves should be completely different at low and moderate/high shear rates.

2 Formalism

Consider Couette flow with the velocity shear parameter A: $\mathbf{U} = \mathbf{U}(Ay, 0, 0)$. Numerical calculations are performed for three-dimensional vortex fluctuations at small deviation from the macroscopic equilibrium state. I.e., for stochastically driven Navier-Stokes equations *linearized* about the mean shear flow:

$$\frac{\partial u_x(\mathbf{r},t)}{\partial x} + \frac{\partial u_y(\mathbf{r},t)}{\partial y} + \frac{\partial u_z(\mathbf{r},t)}{\partial z} = 0, \tag{1}$$

$$\left(\frac{\partial}{\partial t} + Ay\frac{\partial}{\partial x}\right) u_x(\mathbf{r},t) + Au_y(\mathbf{r},t) = -\frac{1}{\rho_0}\frac{\partial p(\mathbf{r},t)}{\partial x} + \nu\Delta u_x(\mathbf{r},t) + \frac{1}{\rho_0}\frac{\partial s_{xj}(\mathbf{r},t)}{\partial x_j}, \tag{2}$$

$$\left(\frac{\partial}{\partial t} + Ay\frac{\partial}{\partial x}\right) u_y(\mathbf{r},t) = -\frac{1}{\rho_0}\frac{\partial p(\mathbf{r},t)}{\partial y} + \nu\Delta u_y(\mathbf{r},t) + \frac{1}{\rho_0}\frac{\partial s_{yj}(\mathbf{r},t)}{\partial x_j}, \tag{3}$$

$$\left(\frac{\partial}{\partial t} + Ay\frac{\partial}{\partial x}\right) u_z(\mathbf{r},t) = -\frac{1}{\rho_0}\frac{\partial p(\mathbf{r},t)}{\partial z} + \nu\Delta u_z(\mathbf{r},t) + \frac{1}{\rho_0}\frac{\partial s_{zj}(\mathbf{r},t)}{\partial x_j}, \tag{4}$$

Here ρ_0 is uniform flow density; $p(\mathbf{r},t)$, $v_x(\mathbf{r},t)$, $v_y(\mathbf{r},t)$, $v_z(\mathbf{r},t)$ – perturbations of pressure and velocity components respectively; $s_{ij}(\mathbf{r},t)$ – the spontaneous strain tensor $(i,j = x,y,z)$; The statistical properties of $s_{ij}(\mathbf{r},t)$ are modeled in accordance with the Fluctuation-Dissipation theory [7]:

$$\langle s_{ij}(\mathbf{r},t)s_{kl}(\mathbf{r}',t')\rangle = 2T\rho_0\nu\left[\delta_{ik}\delta_{jl} + \delta_{il}\delta_{kj} - \frac{2}{3}\delta_{ij}\delta_{kl}\right]\delta(\mathbf{r}-\mathbf{r}')\delta(t-t') \tag{5}$$

Here ν is the kinematic viscosity; T – temperature; The calculations are based only on Eqs.(1-5) and no other assumptions are made at all. Define the Fourier transform by

$$\{\mathbf{u}(\mathbf{r},t); p(\mathbf{r},t); s_{ij}(\mathbf{r},t)\} = \int d\mathbf{k}\,\{\mathbf{u}(\mathbf{k},t); p(\mathbf{k},t); s_{ij}(\mathbf{k},t)\}\, exp(i\mathbf{kr}). \tag{6}$$

So-called nonmodal mathematical analysis is used and the linear dynamics of spatial Fourier harmonics (SFH) of disturbances without spectral expansion in time is analyzed. Finally, the energy spectral density of vortex fluctuations in the stationary limit ($e(\mathbf{k}) = \frac{1}{2}\rho_0|u_x(\mathbf{k})|^2 + |u_y(\mathbf{k})|^2 + |u_z(\mathbf{k})|^2$) and the correlation functions of the fluctuations of physical quantities ($\langle p(\mathbf{k}',t')p(\mathbf{k}'',t'')\rangle$, $\langle u_i(\mathbf{k}',t')u_j(\mathbf{k}'',t'')\rangle$.) are described.
The nonmodal analysis makes it possible to represent the fluctuation background in *a new light* (see Refs. [8, 9]) and provides insight into physics of its formation.

3 Results

There are itemized the main results of our exploration:
• Decisive role in the formation of the background of hydrodynamic fluctuations,

besides the (i) stochastic and (ii) dissipation processes, play two other physical phenomena: (iii) linear drift of the SFH in the wave-number space (**k**-space) and (iv) energy exchange between the mean flow and the SFH of vortices;
• It exists a certain subspace $\mathcal{D}_{\mathbf{k}}$ in the **k**-space, limited externally by spherical surface with radius $k \leq k_\nu \equiv (A/\nu)^{1/2} \sim Re^{1/2}$ (where ν is the kinematic viscosity, $Re \equiv AL_0^2/\nu$ – Reynolds number, L_0 – channel width). The SFH (vortex and acoustic ones) are strongly subjected by the velocity shear at wave numbers $k^2 \equiv k_x^2 + k_y^2 + k_z^2 < k_\nu^2$ (in the nondimensional variables $K \equiv k_i/k_\nu$, the latter condition may by rewrite as $K^2 \equiv K_x^2 + K_y^2 + K_z^2 < 1$). I.e. in $\mathcal{D}_{\mathbf{k}}$ the open character of the system - action of the processes (iii) and (iv) - is manifested. The last circumstance determines the peculiar character of the fluctuation background under study;
• The energy spectral density of vortex fluctuations in the **k**-space in the stationary limit ($e(\mathbf{k})$) by far exceeds the white-noise in $\mathcal{D}_{\mathbf{k}}$ (see Figs.1,2). The peak is the greater the larger is Reynolds number $(e(\mathbf{k})|_{peak} \sim Re^{\gamma/2}, \gamma > 1)$;
• Action of the processes (iii) and (iv) leads to the anisotropy of the fluctuation background of vortex fluctuation in $\mathcal{D}_{\mathbf{k}}$ (see Fig.1). Maximum value $lg(E_{\mathbf{K}})_{peak}$ ($E_{\mathbf{K}} \equiv e(\mathbf{k})/T$) is significantly displaced in the region $K_y/K_x < 0$;
• Cross transport of momentum arises due to the shear: X component of momentum is transported along the axis Y;
• New, indirect way of mean flow energy conversion to heat in the nonequilibrium steady state is revealed: there is the permanent transformation of mean flow energy to the spatial Fourier harmonics of vortex perturbations and at last to thermal energy. The efficiency of this channel of energy conversion should increase (and not decrease) with Reynolds number. On the transition to turbulence (which occurs at high Reynolds numbers) the revealed channel of the mean flow energy conversion to heat is transformed to the turbulent viscosity;
The fluctuation background of acoustic wave is also estimated that is determined by shear parameter $R \equiv A/k_x C_s$, where C_s is the sound speed. (As it has been found in [10] recently, vortex and acoustic wave disturbances are coupled even in linear theory: acoustic waves are always eventually excited, even if the initial conditions are of nondivergent form. This phenomenon is strong at $R > 0.3$.)
• The fluctuation background of acoustic wave should be completely different in $\mathcal{D}_{\mathbf{k}}$ at low ($R < 0.1$) and moderate/high ($R > 0.3$) shear rates:
– It should be reduced in comparison to the uniform (non-shear) flow at low shear rates,
–it should be comparable to the background of the vortex fluctuations at moderate /high shear rates.

According to the results of our study, the finite perturbations should have the intrinsic, fluctuation origin – fluctuation background of vortices in the region of small wave-numbers is quite strong, by far exceeds the white-noise at high Reynolds numbers. This, in turn, should trigger nonlinear processes – energy conserving mixing – and should lead to the flow transition to turbulence in the case of the "positive feedback".

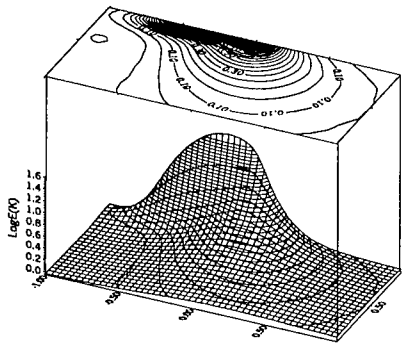


Figure 1: Plot of $lgE_{\mathbf{K}}$ in the plane $K_x 0 K_y$ at: $K_x > 0.06$, $K_z = 0.05$, $Re \approx 300$. Maximum $(lg(E_{\mathbf{K}}))_{peak} = 1.79$ is reached at $K_y = -0.18$.

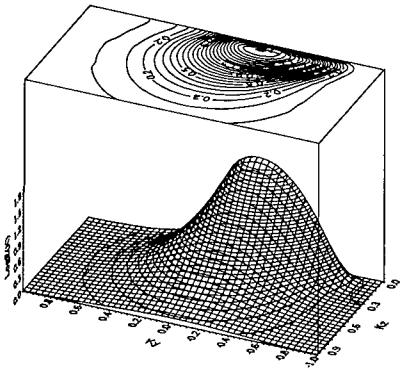


Figure 2: $lg(E_{\mathbf{K}})$ in the plane $K_y O K_z$ at $K_x = 0.06$, $Re \approx 300$. Maximum $(lg(E_{\mathbf{K}}))_{peak} = 1.91$ is reached at $K_y = -0.22$, $K_z = 0.09$.

This research has been supported in part by the INTAS grant GE97-0504. G. Khujadze acknowledges hospitality of C.P.A./K.U.Leuven, where a part of this work was done.

References

[1] Boberg L. and Brosa, U. *Z. Naturforschung Teil*, 43a:697, 1988.

[2] Chagelishvili G.D., Chanishvili R.G. and Lominadze J.G. *in: High Energy Astrophysics: American and Soviet Perspectives, Washington, National Academy Press*, :55–64, 1991.

[3] Reddy S. C. and Henningson D. S. *J. Fluid Mech,*, 252: 209–238, 1993.

[4] Gebhardt T., Grossmann S. *Phys. Rev. (E)*, 50: 3705–3711, 1994.

[5] Baggett J.S., Driscoll T.A., Trefethen L.N. *Phys. Fluids*, 7: 833–838, 1995.

[6] Schmid P.J. and Henningson D.S. *Phys.Fluids*, A4: 1986–1989, 1992.

[7] Landau L.D. and Lifshitz E.M. Pergamon Press, New York, 1980.

[8] Chagelishvili G.D. and Khujadze G.R. *JETP*, 85: 907–913, 1997.

[9] Chagelishvili G.D., Khujadze G.R. and Lominadze J.G. Hydrodynamical fluctuations in smooth shear flows ICTP Preprint # IC/99/173.

[10] Chagelishvili G.D., Tevzadze A.G., Bodo G. and Moiseev S.S., *Phys.Rev.Lett.*, 79: 3178–3181, 1997.

ADVANCES IN TURBULENCE VIII
Proceedings of the Eighth European Turbulence Conference
C. Dopazo et al. (Eds.)
© CIMNE, Barcelona 2000

Dynamics of perturbations in plane Couette flow

H. Faisst, A. Schmiegel, and B. Eckhardt

Fachbereich Physik, Philipps Universität Marburg, D-35032 Marburg, Germany

Contact e-mail: holger.faisst@physik.uni-marburg.de

We have analyzed the dynamics of perturbations in plane Couette flow (pCf) from a probabilistic and dynamical system point of view. In the absence of a sharp transition border we use a probabilistic approach to the definition of a transitional Reynolds number. We find that more than half the initial conditions stay turbulent for the full integration time if Re exceeds a value of about 320 [1]. In numerical annealing experiments [2] it was possible to follow the turbulent state down to Reynolds numbers of about 240. This is much lower than the previous number but also much higher than the value of 120 near which the first steady states originate from saddle node bifurcations [5, 6, 7]. A promising approach for further investigation is the embedding of plane Couette flow into Couette-Taylor flow between concentric cylinders. The planar case emerges in the limit of large radii and shows similar behaviour in an experimentally accessible parameter range [8].

Transition in plane Couette flow

A transition to turbulence has two prerequisites: the first one is the presence of some turbulent state in phase space and the second one is the stimulation of initial conditions that go to that part of phase space. In linearly unstable systems both elements are very often obtained in a single step: the instability assures that just about every perturbation is driven away from the laminar flow and the new state that emerges is often a global attractor. In many shear flows the behaviour is different: the flows are linearly stable so that only perturbations of sufficient amplitude and pointing 'in the right direction' escape from the basin of attraction. And the new states that carry the turbulent behaviour are difficult to identify, since they are not suggested by linearly unstable modes.

However, it still remains a fact that unless there are three-dimensional stationary or periodic solutions no turbulence can be sustained. Therefore, following up previous work of Busse et al. we have searched for 3-d stationary states in the plane Couette flow. Fig. 1 shows all the states we could find in the NBC symmetry. The lowest one is indeed the NBC state, created in a saddle

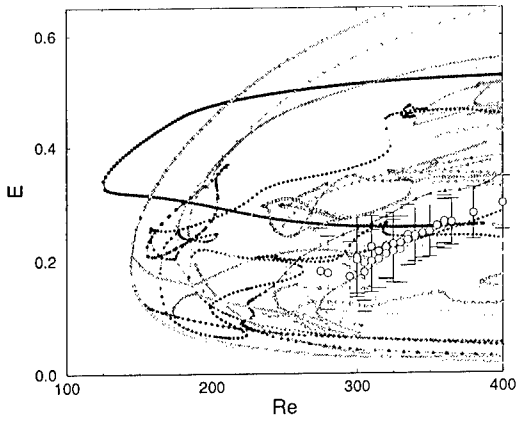


Figure 1: Stationary states in plane Couette flow, characterized by their energy. The open symbols and error bars mark the mean and variance of the energy fluctuations in a turbulent state.

node bifurcation at $Re = 120$. The next main bifurcation is near $Re = 150$ and thereafter the number of states increases rapidly.

Experiments with a variety of initial conditions of different shape and amplitude show that they do not begin to sense the presence of the stationary states until Reynolds numbers of the order of 300. Specifically, more than half the initial conditions decay if the Reynolds number is below about $Re = 320$. However, once a turbulent state forms it can be followed down to a Reynolds number of about 240 by slowly reducing Re (a process we call 'annealing' in analogy to the slow reduction of temperature used in thermodynamics) (Fig. 2).

The values for the mean and the variance of the kinetic energy show that the turbulent state lies within reach of the stationary states (Fig. 1). While it is clear that the stationary states themselves cannot sustain the turbulent state, the tangle of homoclinic and heteroclinic connections between them can. Numerical studies of the phase space flow between the states show that for low Re there are few connections and that their number increases with Re. As the number of connections grows the escape rate from the turbulent state decreases (Fig. 3). Note that the relaxation to the turbulent state is much faster, so that indeed after a short transient period the same turbulent state is reached from all initial conditions.

Couette-Taylor system in the limit of large radii

A promising way to further investigations into the origins and phase space structures connected with the transition to turbulence in plane Couette flow is to consider it as a limit of Couette-Taylor flow between concentric cylinders. For large radii the curvature and centrifugal effects become minor and the behaviour

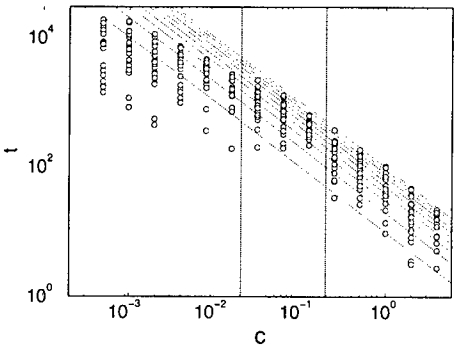


Figure 2: Lifetimes and final Reynolds number observed in annealing experiments with $Re(t) = Re_0 - ct$. The dotted lines are lines of constant Re, decreasing in steps of 10 from Re = 310 for the left line down to Re = 220 at the right end. See text.

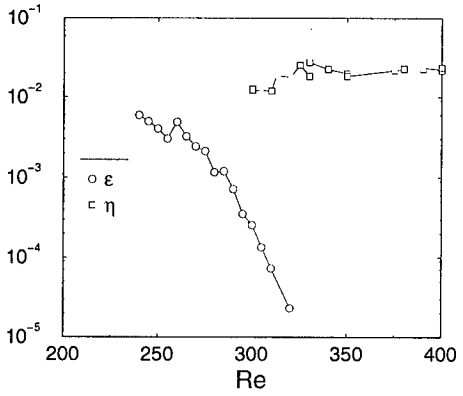


Figure 3: Escape rates ϵ and relaxation rates η extracted from lifetime measurements for different vortex-rings as initial perturbation and from relaxation experiments [2].

should approach that of plane Couette flow. In this limit the linear instability of Couette flow to Taylor vortices moves out to higher Reynolds number and disappears. As shown first by Nagata, the wavy vortex flow, which appears as a secondary instability of Taylor vortex flow for small radii, persists as a finite amplitude, finite Reynolds number saddle-node bifurcation in the Couette-Taylor system for large radii. In a parameter range where the wavy-vortex flow state is already present but the laminar profile still stable the behaviour of the system should be similar to that observed in plane Couette flow.

In order to be able to compare to plane Couette flow the Reynolds number is based on half the gap width and half the velocity difference between cylinders. The ratio between radii of inner and outer cylinder is denoted by η. For counterrotating cylinders the above mentioned overlap between existence of wavy vortex flow and linear stability appears $\eta > 0.93$, as is indicated in Fig. 4. In this regime the dynamics of the system is similar to plane Couette flow and shows also irregular fluctuations in life times (Fig. 5). Experiments in such a parameter range of Couette-Taylor flow should allow to study the characteristics of shear flow turbulence in a closed flow geometry and provide valuable insight into the mechanisms of this transition.

Numerical methods

We used Fourier-Legendre spectral methods with periodic boundary conditions in stream- and spanwise direction. With d as the wallnormal height of the box the fluid volume was $2\pi d$ long and πd wide, which was chosen so as to contain one pair of vortices created in the Nagata-Busse-Clever bifurcation. Up to

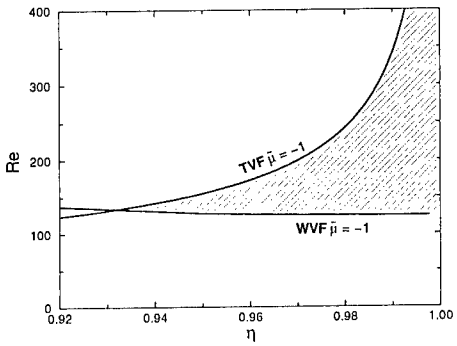


Figure 4: Bifurcation diagram for Taylor vortices (TVF) and wavy vortices (WVF) in a Couette-Taylor cell with counterrotating cylinders.

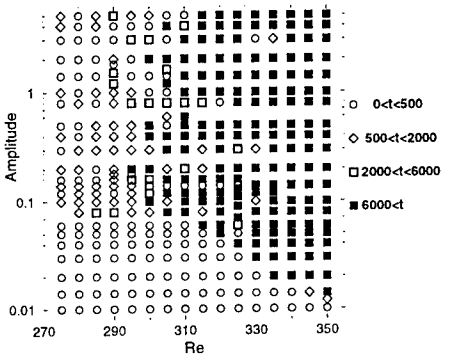


Figure 5: Life time distribution in Couette-Taylor flow at radius ratio $\eta = 0.993$ and counterrotating cylinders as a function of Reynolds number and the disturbance amplitude.

83 Fourier modes in the plane and 16 Legendre polynomials in the wall normal direction were used. The numerical code is energy preserving in the Eulerian limit and reproduces the characteristic parameters identified by Busse and Clever within a few percent.

References

[1] A. Schmiegel, B. Eckhardt. Dynamics of perturbations in plane Couette flow. *submitted.*

[2] A. Schmiegel, B. Eckhardt. Persistent turbulence in annealed plane Couette flow. *submitted*

[3] N. Tillmark, P.H. Alfredsson. *J. Fluid Mech.*, **235**, 89, (1992).

[4] S. Bottin, O. Dauchot, F. Daviaud. *Phys. Rev. Lett.*, **79**(22), 4377, (1997).

[5] M. Nagata. *J. Fluid Mech.*, **217**, 519, (1990).

[6] R.M. Clever, F.H. Busse. *J. Fluid Mech.*, **344**, 137, (1997).

[7] A. Schmiegel; PhD thesis, Philipps Universität Marburg, 1999.

[8] H. Faisst, B. Eckhardt. Transition from the Couette-Taylor system to the plane Couette system. *submitted*

[9] A. Cherhabili, U. Ehrenstein. *J. Fluid Mech.*, **342**, 159, (1997).

[10] A. Schmiegel, B. Eckhardt. *Phys. Rev. Lett*, **79** (26), 5250, (1997).

[11] P. Balakumar. *Theoret. Comput. Fluid Dynamics*, **9**, 103, (1997).

ADVANCES IN TURBULENCE VIII
Proceedings of the Eighth European Turbulence Conference
C. Dopazo et al. (Eds.)
© CIMNE, Barcelona 2000

Modeling transitional plane Couette flow

Paul Manneville

Laboratoire d'Hydrodynamique, École polytechnique
91128 Palaiseau, France

Contact e-mail: paul.manneville@ladhyx.polytechnique.fr

1 Introduction

The transition to turbulence is easier to understand for systems that experience a globally supercritical scenario, such as Rayleigh–Bénard convection. By contrast, the plane Couette flow (PCF), the shear flow achieved between two walls in relative parallel motion, is perhaps the most dramatic example of subcritical system since it is stable against infinitesimal perturbations for all Reynolds numbers R whereas a direct transition to turbulence *via* the nucleation of turbulent spots is observed at intermediate R [1]. On the one hand, the mechanism sustaining turbulence inside the spots involves the breakdown and regeneration of streamwise structures called "streaks" observed in laboratory and computer experiments [2], also possibly connected to nonlinear nontrivial solutions of the Navier–Stokes equations [3]. On the other hand, *space-time intermittency* (STI), as introduced Pomeau [4], is supposed to account for the statistics of the coexistence of the turbulent flow within the spots and the laminar flow outside them. Up to now, the latter phenomenon has been studied in the context of critical phenomena using spin-like models [5]. Here we derive a simplified, semi-realistic model that could help filling the gap between the STI paradigm and the actual processes at work in the PCF.

2 The model

Within a "minimal box" assumption, Waleffe [6] derived a simple differential dynamical system thought to account for the couplings that govern the streaks' dynamics. However, only transient complex behavior seems possible and no sustained (temporal) chaos is observed [7] in his Lorenz-like model that freezes the spatial structure by periodic boundary conditions at distances of the order of the gap between the walls. Unfreezing the in-plane space dependence seems thus necessary to better understand the transition to turbulence and especially the microscopic mechanisms of STI. In line with the Swift–Hohenberg approach [8] that does the job in convection problems, yielding a consistent description of

patterning, we develop here a Galerkin strategy in which the cross-stream (y) dependence is eliminated, yielding partial differential equations governing the in-plane (x, z) dependence [9].

In dimensionless form the Navier–Stokes equations relevant to the Couette problem read

$$\partial_t \mathbf{v} + \mathbf{v}\cdot\boldsymbol{\nabla}\mathbf{v} = -\boldsymbol{\nabla}p + R^{-1}\boldsymbol{\nabla}^2\mathbf{v} + \mathbf{f}\,, \tag{1}$$

$$\boldsymbol{\nabla}\cdot\mathbf{v} = 0\,, \tag{2}$$

where $R = U_{\rm w}h/\nu$ is the Reynolds number, h is the half-gap, $U_{\rm w}$ is the speed of the walls, and ν is the kinematic viscosity of the fluid. For simplicity we assume, as Waleffe did, that the no-slip boundary conditions at the walls are replaced by stress-free conditions, which allows the y dependence to be expanded using trigonometric functions. The bulk force $\mathbf{f}$ in (1) is adjusted so as to generate the basic flow $\mathbf{v}_{\rm b} = u_{\rm b}\mathbf{x}$ with $u_{\rm b} = \sin(\pi y/2)$ and the model is directly written for the perturbation $\mathbf{v}'$ in $\mathbf{v} = \mathbf{v}_{\rm b} + \mathbf{v}'$ taken as $\mathbf{v}' = u'\mathbf{x} + v'\mathbf{y} + w'\mathbf{z}$ with $u' = U_0(x,z,t) + U_1(x,z,t)\sin(\pi y/2)$, $v' = V_1(x,z,t)\cos(\pi y/2)$, $w' = W_0(x,z,t) + W_1(x,z,t)\sin(\pi y/2)$. Accordingly, the pressure perturbation reads $p' = P_0(x,z,t) + P_1(x,z,t)\sin(\pi y/2)$. This truncated expansion is further inserted Eqs. (1–2) and a projection onto the corresponding reduced basis is performed. The model reads

$$\partial_x U_0 + \partial_z W_0 = 0\,, \qquad \partial_x U_1 + \partial_z W_1 = \tfrac{1}{2}\pi V_1 \tag{3}$$

$$\partial_t U_0 + N_{U_0} = -\partial_x P_0 - \tfrac{1}{2}\partial_x U_1 - \tfrac{1}{4}\pi V_1 + R^{-1}\Delta_2 U_0\,, \tag{4}$$

$$N_{U_0} = U_0\partial_x U_0 + W_0\partial_z U_0 + \tfrac{1}{2}U_1\partial_x U_1 + \tfrac{1}{4}\pi V_1 U_1 + \tfrac{1}{2}W_1\partial_z U_1\,,$$

$$\partial_t W_0 + N_{W_0} = -\partial_z P_0 - \tfrac{1}{2}\partial_x W_1 + R^{-1}\Delta_2 W_0\,, \tag{5}$$

$$N_{W_0} = U_0\partial_x W_0 + W_0\partial_z W_0 + \tfrac{1}{2}U_1\partial_x W_1 + \tfrac{1}{4}\pi V_1 W_1 + \tfrac{1}{2}W_1\partial_z W_1\,,$$

$$\partial_t U_1 + N_{U_1} = -\partial_x P_1 - \partial_x U_0 + R^{-1}(\Delta_2 - \tfrac{1}{4}\pi^2)U_1\,, \tag{6}$$

$$N_{U_1} = U_1\partial_x U_0 + U_0\partial_x U_1 + W_1\partial_z U_0 + W_0\partial_z U_1\,,$$

$$\partial_t V_1 + N_{V_1} = -\tfrac{1}{2}\pi P_1 + R^{-1}(\Delta_2 - \tfrac{1}{4}\pi^2)V_1\,, \tag{7}$$

$$N_{V_1} = U_0\partial_x V_1 + W_0\partial_z V_1\,,$$

$$\partial_t W_1 + N_{W_1} = -\partial_z P_1 - \partial_x W_0 + R^{-1}(\Delta_2 - \tfrac{1}{4}\pi^2)W_1\,, \tag{8}$$

$$N_{W_1} = U_1\partial_x W_0 + U_0\partial_x W_1 + W_1\partial_z W_0 + W_0\partial_z W_1\,,$$

where (3) derives from the continuity equation by projection onto "y = cst" and "$\sin(\pi y/2)$" and (4–8) from the Navier–Stokes equations by projection onto "y = cst", "$\sin(\pi y/2)$," or "$\cos(\pi y/2)$" where appropriate. The pressure field can further be eliminated in the usual way by introducing appropriate streamfunctions and potentials:

$$U_0 = -\partial_z\Psi_0\,, \quad W_0 = \partial_x\Psi_0\,, \quad U_1 = \partial_x\Phi_1 - \partial_z\Psi_1\,, \quad W_1 = \partial_z\Phi_1 + \partial_x\Psi_1\,. \tag{9}$$

The space-time evolution of the three-dimensional plane Couette flow velocity is thus governed by a system of three coupled partial differential equations for the three two-dimensional fields Ψ_0, Ψ_1, and Φ_1 appearing in (9).

3 Preliminary results

It is easily checked that our model preserves the linear stability of the basic flow for all R, while containing non-normal terms at the origin of transient energy growth. Also, the nonlinear terms in the model conserve the kinetic energy, as the Navier–Stokes equations themselves do.

Here we present the results of preliminary numerical simulations with limited computing power. A pseudo-spectral Fourier code with $N_x = 256$ and $N_z = 128$ modes on a rectangular domain with periodic boundary conditions at $L_x = 32$ and $L_z = 16$ (hence $\delta x = \delta z = 0.125$) has been implemented on a PC using MatLab FFTs. The evolution is achieved by exact evaluation of diagonal linear terms, and second order, Adams–Bashford, evaluation of all other terms (linear off-diagonal and nonlinear). The time step is adjusted according to empirical nonlinear stability requirements depending on R and the spatial resolution ($\delta t = 0.001$ for $R = 180$). When R becomes large, the space resolution must be refined in order to avoid a finite time blow-up of the solution. This might be due to an insufficient leakage of energy *via* viscous dissipation in the cross-stream direction y, which can be corrected by continuing the expansion of the velocity field and adding terms generated by $\sum_{k\geq 1} U_{2k}(x,z,t)\cos(2k\beta y) + U_{2k+1}\sin((2k+1)\beta y)$, at the expense of complicating the model.

Figure 1 displays the evolution of the total energy contained in the perturbation $K = K_0 + K_1 = (U_0^2 + W_0^2) + \frac{1}{2}(U_1^2 + V_1^2 + W_1^2)$, as a convenient diagnostic of the PCF's state. A sustained turbulent regime is obtained for $R = 180$. At $t = 200$ the Reynolds number is either kept equal to 180, or decreased down to $R = 100$, $R = 50$ (apparently still sustained or very long-lived transient), $R = 40$ (chaotic transient) or $R = 30$ (direct relaxation towards laminar flow). This behavior is similar to that observed in experiments except for lower Reynolds numbers, which is easily understood when recalling the stress-free assumption.

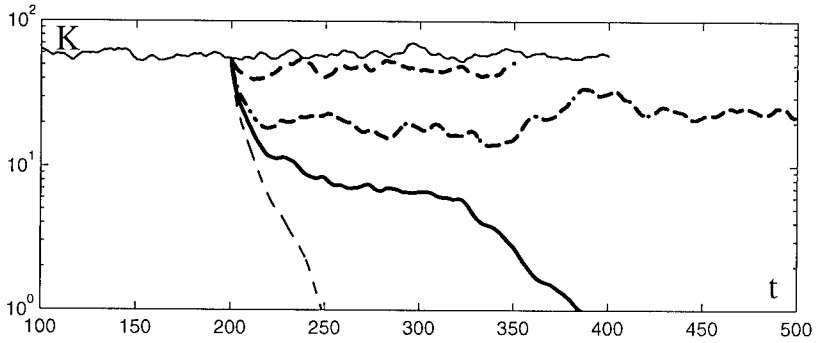


Figure 1: Evolution of the total kinetic energy K (per unit surface): solid thin: $R = 180$; dashed thick: $R = 100$; mixed thick: $R = 50$, solid thick: $R = 40$; dashed thin: $R = 30$.

4 Perspectives

Focusing on the space-time behavior, our approach appears to be complementary to that followed by Eckhardt *et al.* [10] who pointed out the existence of transient and sustained chaos in a dynamical system modeling PCF in a periodic "minimal box" with refined cross-stream resolution. The preliminary results presented here are an encouragement to develop large scale numerical simulations on domains of sizes relevant to experiments where STI is observed. Our model can also be the starting point of a tractable analytical approach of the phenomenon, possibly after some further simplification of the nonlinear terms. Improved models involving a more fields or using polynomials appropriate to no-slip boundary conditions are also under development.

We believe that our modeling strategy is promising and could be developed also for other shear flows in extended geometry where turbulent spots play a key role, the Taylor–Couette flow between counter-rotating cylinders, the Poiseuille channel flow, or the Blasius boundary layer flow.

Interesting discussions with O. Dauchot and Y Pomeau, and the participation of F. Locher to early developments of the present study are deeply acknowledged.

References

[1] see, e.g. O. Dauchot & F. Daviaud, Phys. Fluids **7** (1995) 335–343.

[2] (a) S. Bottin *et al.*, Phys. Fluids **10** (1998) 2597–2607. (b) J.M. Hamilton *et al.*, J. Fluid Mech. **287** (1995) 317–348;

[3] (a) M. Nagata, J. Fluid Mech. **217** (1990) 519–527; (b) R.M. Clever & F.H. Busse, J. Fluid Mech. **234** (1992) 511–527.

[4] Y. Pomeau, Physica D **23** (1986) 3–11; see also Chapter IV of: P. Bergé, Y. Pomeau & Ch. Vidal, *L'espace chaotique* (Hermann, 1998).

[5] H. Chaté & P. Manneville, "Spatio-temporal intermittency," in *Turbulence, a tentative dictionary*, P. Tabeling & O. Cardoso, eds. (Plenum Press, 1995).

[6] F. Waleffe, Phys. Fluids **9** (1997) 883–900.

[7] O. Dauchot & N. Vioujard: Phase space analysis of a dynamical model for subcritical transition to turbulence in plane Couette flow, EPJB, in press.

[8] (a) J. Swift & P.C. Hohenberg, Phys. Rev. A **15** (1977) 319; (b) P. Manneville, J. de Physique **44** (1983) 759–765.

[9] P. Manneville, F. Locher, C.R. Acad Sc. Paris, Série IIb, vol. 328, in press.

[10] A. Schmiegel & B. Eckhardt, Phys. Rev. Lett. **79** (1997) 5250–5253. B. Eckhardt & A. Mersmann, Phys. Rev. E **60** (1999) 509–517.

ADVANCES IN TURBULENCE VIII
Proceedings of the Eighth European Turbulence Conference
C. Dopazo et al. (Eds.)
© CIMNE, Barcelona 2000

Laminar-Turbulent Coexistence following a Subcritical Transition to Turbulence

O. Dauchot 1[1], and A. Prigent [1]

[1]Group Instabilities and Turbulence, SPEC
CEA-Saclay, L'Orme des Merisiers
91191 Gif sur Yvette, FRANCE

Contact e-mail:olivier.dauchot@cea.fr

1 Introduction

In shear flows such as pipe flow or plane Couette flow, the transition to turbulence occurs for Reynold numbers much smaller than the linear instability threshold, or even when there is no linear instability at all. This kind of transition, driven by finite amplitude disturbances called *subcritical* exhibits a coexistence of turbulent and laminar domains, which we have experimentally studied in both plane Couette and contra-rotating Taylor-Couette flow (pCf and TCf).

We first shortly describe our experimental devices, especially the new large aspect-ratios Taylor-Couette apparatus. Second, after reviewing several characteristics features of the transition in the pCf case, we present a new flow regime obtained when increasing the aspect ratios. Then, since our pCF apparatus is not adapted for quantitative large aspect ratios experiments, we consider the Taylor-Couette system, which in the contra-rotating regime and in the limit of equal radii cylinders is a formal equivalent to the pCf. This allows us to perform a quantitative analysis for the emergence of a long range ordered state, periodic in space and time. We would like to propose a new way of considering these observations.

2 Experimental set-up

Our pCf apparatus [3](b) used to be run with a spanwise aspect ratio $\Gamma_z^{pCf} = 35$. For the purpose of the present study, reducing the gap down to $d = 1$ mm, we obtain $\Gamma_z^{pCf} = 250$. For the moment, the Reynolds number accuracy is not better than 10% and does not allow quantitative analysis.

The Taylor-Couette apparatus consists of two counter-rotating coaxial cylinders. The useful length of the apparatus is $L = 380 \pm 0.1$ mm. The glass outer

cylinder has an inner radius $r_o = 49.95 \pm 0.005$ mm. The inner cylinder has an outer radius $r_i = 49.09 \pm 0.005$ leading to a gap $d = 0.86 \pm 0.01$, a radius ratio $\eta = 0.983$ and aspect ratios $\Gamma_z^{TCf} = 442$ and $\Gamma_\theta^{TCf} = 362$. The flow is governed by the inner (resp. outer) Reynolds numbers, $R_{i,o} = r_{i,o}\Omega_{i,o}d/\nu$. A constant temperature water is circulated inside the core of the inner cylinder to insure isothermal conditions of the system at the room temperature. The visualization is achieved by seeding the flow with kalliroscope. The inner cylinder is covered by a fluorescent film and the entire apparatus is lighted with two long UV neon lights parallel to the cylinder. Two plane mirrors reflect the two-third of the flow hidden to the camera and the full flow image is reconstructed, (see [1] for more details).

3 Emergence of a long range ordered state

For the past few years a number of experimental and numerical studies have lead to the formulation of several characteristic features of the transition to turbulence in the pCf. First, a general picture of the transition has emerged underlying the role plaid by unstable finite amplitude solutions in drawing the structure of the phase space [2]. Second, various observations have outlined the emergence of turbulent domains coexisting with the laminar flow. These domains move, grow, decay, split and merge leading to a disordered spatio-temporal intermittency, that is a coexistence dynamics in which active/turbulent regions may invade absorbing/laminar ones, where turbulence cannot emerge spontaneously. Some statistical characterizations of this dynamics could be achieved but were limited by the small number of domains observed simultaneously [3]. Increasing the spanwise aspect ratio from $\Gamma_z^{pCf} = 35$ to $\Gamma_z^{pCf} = 250$, one could observe up to a dozen turbulent domains following the same kind of disordered dynamics for Reynolds numbers slightly above 325. For Reynolds number of the order of 350 these turbulent domains lead to stationary turbulent strips (figure 1). These strips are inclined by about 30° with the streamwise direction, and form a periodic pattern, whose length-scale is between one and two orders of magnitude larger than the gap. When increasing further the Reynolds number, the flow becomes fully turbulent.

Lets consider now the Taylor-Couette system. The flow regimes diagram in the (R_o, R_i) parameter space have been determined in the contra-rotating regime and compared to the one obtained by Andereck et al. for a radius ratio $\eta = 0.878$ [4]. Apart from the fact that the linear instabilities thresholds increase, we also notice a strong enlargement of the parameters range where laminar-turbulent coexistence occurs.

Figure 2 displays several snapshots of the whole flow for $R_o = 700$. When increasing R_i from 600 to 750 one observes (on the upper row) how the turbulent spots merge and progressively lead to a turbulent spiral pattern, propagating along the axial direction, and (on the lower line) how this turbulent spiral evolves towards the turbulent state. Precise measurements could be performed, varying

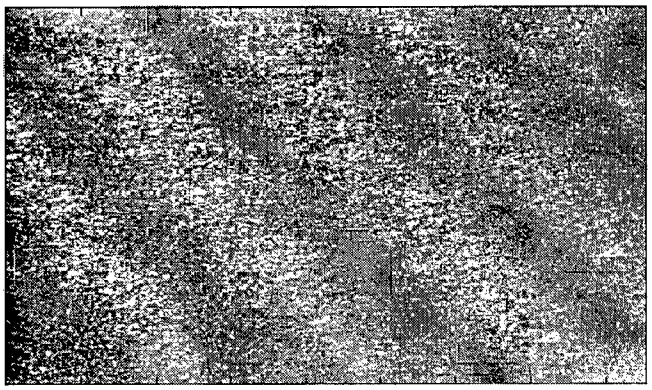


Figure 1: *Turbulent strips in pCf,* $R = 345$

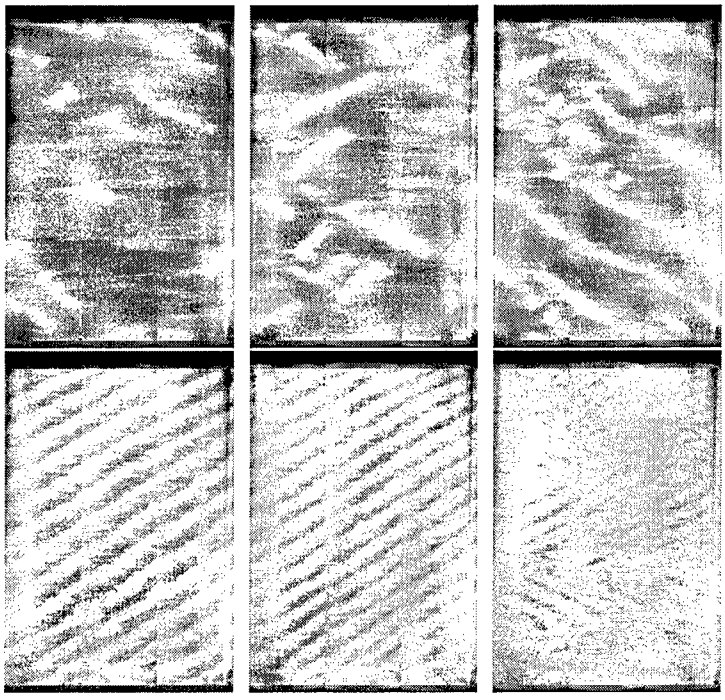


Figure 2: *Turbulent spots and turbulent spiral in TCf* ($R_o = 700$, $R_i = 600; 610; 625; 662; 697; 744$)

both R_o and R_i [5]. The main results concern the spiral geometry. In the present system, the spiral pitch, the angle ϕ between the spiral branch and the azimuthal direction, constant along the axial direction, decreases between 40° and 20° when R_i increases and is independent from R_o in the range $[-900; -600]$, which we explore. The azimuthal wavenumber of the pattern is quantified because of the azimuthal periodicity of the flow : $k_\theta = n_\theta \frac{2\Pi}{P}$, where P is the mean perimeter

and $n_\theta = 6$, the number of branches is constant in our range of observation. The axial wavenumber k_z increases linearly with R_i, according to the geometrical relation $k_z = k_x/atan(\phi)$. Finally in the laboratory frame, the spiral propagates with a well define frequency ω, proportional to the mean angular velocity.

Altogether our results call for a description of the turbulent spiral as a wave, which emerges from the homogeneous turbulent regime, with a well defined critical wavenumber and a well defined frequency, when following the inverse transition from the turbulent flow to the laminar one. In this perspective the spot regimes appears as a disordered regime resulting from the multiplication of defects in this spiral pattern.

4 Conclusions

Investigating the subcritical transition to turbulence in plane Couette and Taylor Couette flows, we notice strong similarities, which call for a unique modelisation. This modelisation should be able to describe how a long range ordered pattern (strips or turbulent spiral) emerges from the turbulent state, develops in amplitude, and finally breaks into defects when following the inverse transition.

Further work will deal with a full characterization of the turbulent spiral (long term dynamics, default dynamics ...) as well as with the statistical characterization of the spot regime (lifetime, size...).

References

[1] Prigent A., Dauchot O., *submitted to Phys. Fluids.*

[2] (a) Nagata N., J. Fluid Mech., **217** (1990) 519-527. (b) Clever R. M. and Busse F. H., J. Fluid Mech., **234** (1992) 511-527. (c) Henningson D. S., Lundbladh A., Johansson A. V., *J. Fluid Mech.* **250**, (1993), 169-207. (d) Hamilton J. M., Kim J., Waleffe F., *J. Fluid Mech.* **287**, 317-348 (1995). (e) Cherhabili A. and Ehrenstein U., J. Fluid Mech., **342** (1997) 159-177. (f) Bottin S., Dauchot O., Daviaud F., *Phys. Fluids***10**(10),(1998) 2597-2607. (g) Schmiegel A., Eckhardt B., *Phys. Rev. Lett.* **79**(26) 5250–5253 (1997). (h) Eckhardt B., Mersmann A., *Phys. Rev. E* **60** (1999), 509-517.

[3] (a) Lundbladh A.,Johansson A. V., *J. Fluid Mech.* **229**, (1991) 499-516. (b) Daviaud F., Hegseth J. and Bergé P., *Phys. Rev. Lett.* **69**(17), (1992) 2511-2514. (c) Tillmark N., Alfredsson P. H., *J. Fluid Mech.* **235**, (1992) 89. (d) Dauchot O., Daviaud F., *Phys. Fluids* **7**(2), (1995) 335-343. (e) Bottin S., Daviaud F., Manneville P., Dauchot O., *Europhys. Lett.* **43**(2) 171–176 (1998). (f) Bottin S., Chaté H., *Eur. Phys. J. B* **6**, (1998) 143-155.

[4] Andereck C. D., Liu S. S., Swinney H. L., *J. Fluid Mech.* **164**, (1986) 155-183.

[5] Prigent A., Dauchot O., *submitted to Phys. Rev. Lett.*

ADVANCES IN TURBULENCE VIII
Proceedings of the Eighth European Turbulence Conference
C. Dopazo et al. (Eds.)
© CIMNE, Barcelona 2000

Uncertainty of the transition threshold for Poiseuille flows

C. M. Casciola*, A. Olivieri+ and R. Piva*

*Dipartimento di Meccanica e Aeronautica Università di Roma *La Sapienza*
Via Eudossiana 18 00184 Roma, Italy
+INSEAN, Italian ship model basin
Via di Vallerano 139 00128 Roma Italy

Contact e-mail: cm.casciola@dma.ing.uniroma1.it

In wall-bounded shear flows, the evolution equation for the perturbation field, u, is characterized by a non-normal linear operator, $\mathcal{L}$, and a conservative nonlinear term, $\mathcal{N}$,

$$\frac{du}{dt} = \mathcal{L}(u) + \mathcal{N}(u)\,.$$

For toy models of this kind (Trefethen) the attraction basin of a given solution (the base flow) may be shown to become narrower and narrower as the amount of non-normality is increased. Moreover, we do not have, in general, complete control on either the initial or the boundary conditions. This introduces noise in the system and originates some fuzziness, particularly noticeable when a stochastic response (formation of turbulent spots) is going to take over the purely deterministic laminar behavior. It follows a certain level of uncertainty in the threshold amplitude for breakdown to turbulence. This effect is clearly seen in fig. (1), which refers to a Poiseuille flow perturbed by a short duration injection of fluid issuing in the normal direction from one of the walls. By measuring the perturbation at a fixed station downstream, we evaluate, as a function of the disturbance amplitude, a, and of the Reynolds number of the base flow, R, the ensemble average of the energy contained in the high frequency band of the spectrum,

$$E_t = \frac{1}{2T}\int_0^T < (\mathcal{F}\,u)^2 > dt\,, \qquad (1)$$

where $\mathcal{F}$ stands for a filtering operator, in actual conditions a sharp hi-pass filter at $100\,Hz$. In the experiments, R spans a subcritical range, $1500 < R < 2500$ ($R_c = 5772$), to explicitly exclude the classical modal amplification associated to growing TS-waves.

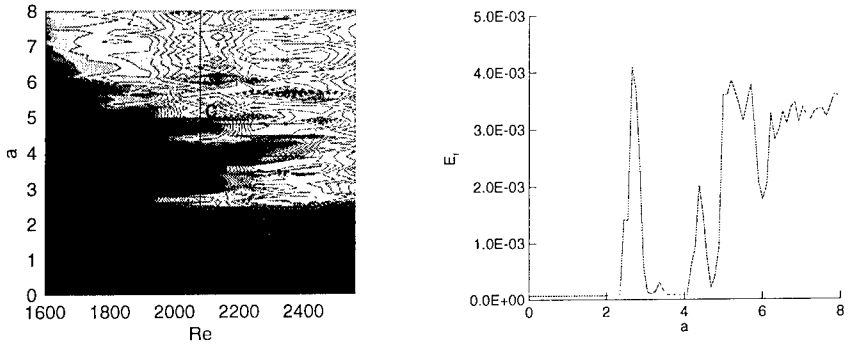


Figure 1: Left: Isolevels of the energy content in the high frequency band, E_t, vs Reynolds number, R, and amplitude of the disturbance, a. Right: E_t as a function of a at $Re = 2100$.

Beyond the fuzzy boundary between laminar and turbulent region, a further characteristic of the diagram are the multiple thresholds, seen, e.g., in the cut at $Re = 2100$. For this Reynolds number, by increasing the intensity of the disturbance we enter first the turbulent region of the parameter space. Then the response returns laminar, until a further increase eventually leads to turbulence.

We claim all these features as related strictly to the dynamics of the vortical structures which are originated by the injection. Specifically, the DNS results, obtained from a largely validated code based on a fully de-aliased Fourier ×

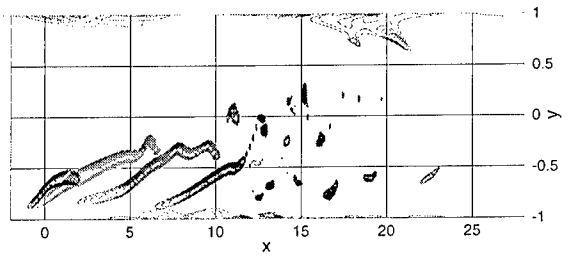


Figure 2: DNS results: evolution of the shear-layer originated by the injection. Symmetry plane $z = 0$ (x, flow direction, y, wall-normal) flow from left to right.

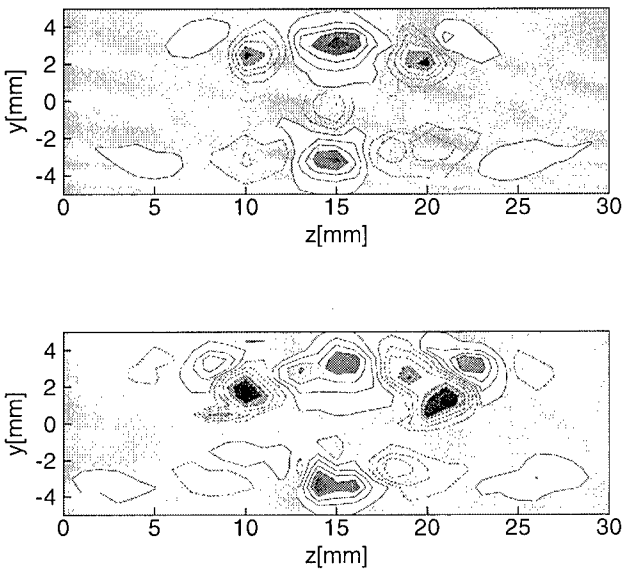


Figure 3: Iso-contours of streamwise perturbation velocity, $Re = 2100$, $x = 30$. Top, $a = 2.6$, bottom, $a = 4.8$.

Chebyshev $\times$ Fourier spectral method [1], show the formation of an intense shear-layer in correspondence with the injection, fig. (2). From its instability, a complex system of hairpins is formed, which, depending on the amplitude of the perturbing jet, may remain close to the injection wall, or travel up to the opposite wall. The streamwise component of the perturbation velocity, as determined from the experiments, fig. (3), seems to confirm the behavior obtained by DNS. The transition is initiated at the injection wall for small amplitude of the perturbing jet (lower threshold). For larger amplitudes the structures tend to travel in the central region of the channel, and no transition is observed. By increasing further the amplitude, the structures reach the opposite wall and transition to turbulence is observed again.

The present analysis suggests that near the transition thresholds the dynamics is highly sensitive to the external noise, which, although maintained at a reasonably low level (incoming fluctuation level less then .1 %), cannot be avoided altogether. As a first step to investigate the effect of background disturbances on the uncertainty of the threshold curve, highly reproducible artificial noise is introduced in the apparatus by a vibrating ribbon, fig. (4). Our preliminary results actually confirm that the addition of noise alters the thresholds. This is presumably associated with a combination of events, the most important of which takes places during the phase of formation of the hairpins. Actually, during this phase, small changes in the shape and small deviations from symmetry

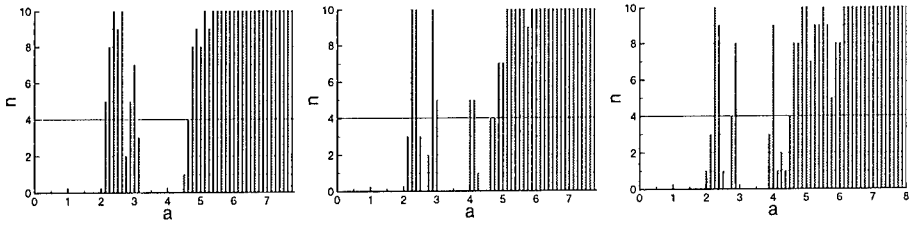


Figure 4: Number of turbulent realizations, n, vs amplitude of the injection, a. Controlled noise introduced by a vibrating ribbon, at rest (left), driven at $60\,Hz$ (center) and with an added sub-harmonic component (right).

seem to alter dramatically the successive evolution, originating the stochastic behavior detected at the observation station downstream.

Acknowledgments: A. Olivieri has been supported by *Ministero dei Trasporti e della Navigazione* through *INSEAN Research Program 1997-99.*

References

[1] Lundbladh A., Henningson D.S., Johansson A.V. *An efficient spectral integration method for the solution of the time-dependent Navier-Stokes equations* FFA-TN-28, Aeronautical Research Institute of Sweden 1992

[2] Casciola C.M., Olivieri A., Piva R. *Formation of turbulent spots from localized disturbances in Poisuille flows* 2nd ERCOFTAC SIG33 Workshop, Late stages of transition in internal flows versus boiundary layer flows, Delft (NL), 20-22 October 99.

[3] Darbyshire A.G., Mullin T. *Transition to turbulence in constant mass-flux pipe flow* J. Fluid Mech. **289** 83-114, 1995

[4] Draad A.A., Kuiken G.D.C., Nieustadt F.T.M. *Laminar-turbulent transition in pipe flow for Newtonian and non-Newtonian fluids* J. Fluid Mech. **377** 267-312, 1998

[5] Eliahou S., Tumin E.A., Wygnanski I. *Laminar-turbulent transition in Poiseuille pipe flow subject to periodic perturbation emanating from the wall* J. Fluid Mech. **361** 333-349, 1998

[6] Schmiegel A., Eckhardt, B. *Fractal stability border in plane Couette flow* Phys. Rev. Lett. **79** 26, 5250-5253, 1997

ADVANCES IN TURBULENCE VIII
Proceedings of the Eighth European Turbulence Conference
C. Dopazo et al. (Eds.)
© CIMNE, Barcelona 2000

Direct numerical simulations of subsonic plane Poiseuille flows undergoing transition

(Effects of compressibility and disturbances on the transition)

Y. Moez [1], H. Maekawa [1] and K. Yamamoto [2]

[1]Department of Mechanical Engineering and Intelligent Systems
The University of Electro-Communications, Chofu-shi, Tokyo, JAPAN
[2]The National Aerospace Lab. of Japan
Chofu-shi, Tokyo, JAPAN

Contact e-mail: moez@maekawa.mce.uec.ac.jp
ctr@maekawa.mce.uec.ac.jp

1 Introduction

Recent interest in transatmospheric flight has promoted renewed research efforts in laminar-turbulent wall/free shear flow transition. The subject of this work is the numerical simulation of laminar-turbulent wall shear flow transition (case of plane channel flow). As transition is evolving in the streamwise direction, it is natural to simulate this process with the spatial approach. Due to the enormous computer requirements (and hence cost) of three-dimensional spatial simulations, most published spatial simulations are two-dimensional and thus confined to linear and non-linear primary instability stages of transition. Fasel *et. al* [1] investigated the non-linear disturbance development in incompressible plane Poiseuille flow for both sub-critical and super-critical Reynolds numbers. Henningson *et. al* [2] investigated the bypass transition and transition thresholds in incompressible wall bounded shear flows. The first compressible D.N.S studies were of flows in open-domains. These open-domain studies, which are reviewed in Lele [3], provide a useful reference in the attempt to isolate compressibility effects unique to wall-bounded flows. Of more relevance are the recent supersonic boundary layer simulation of Guo, Kleiser and Adams [4] who used DNS to investigate transition of temporally and spatially evolving Mach 4.5 layers.

2 Governing Equations

The three dimensional time-dependent compressible Navier-Stokes equations are numerically solved to study spatially developing plane Poiseuille flows undergo-

ing transition. All distances are non-dimensionalized by the half channel width, L, and all velocities by the centerline streamwise velocity, U. (summation convention is used with $\mathbf{x}_1 = x$, $\mathbf{x}_2 = y$ and $\mathbf{x}_3 = z$)

$$\frac{\partial \rho}{\partial t} + u_j \frac{\partial \rho}{\partial x_j} + \rho \frac{\partial u_j}{\partial x_j} = 0 \tag{1}$$

$$\frac{\partial u_i}{\partial t} + u_j \frac{\partial u_i}{\partial x_j} + \frac{1}{\rho} \frac{\partial p}{\partial x_i} = \frac{\partial \tau_{ij}}{\partial x_j} \tag{2}$$

$$\frac{\partial p}{\partial t} + u_j \frac{\partial p}{\partial x_j} + \gamma . p \frac{\partial u_j}{\partial x_j} = -\frac{\partial q_i}{\partial x_i} + (\gamma - 1)\tau_{ij} \frac{\partial u_i}{\partial x_j} \tag{3}$$

$$\tau_{ij} = \frac{\mu}{Re}\left(\frac{\partial u_i}{\partial x_j} + \frac{\partial u_j}{\partial x_i} - \frac{2}{3}\delta_{ij}\frac{\partial u_k}{\partial x_k}\right) \tag{4}$$

$$q_i = -\lambda \frac{\partial T}{\partial x_i}, \quad with \quad \lambda = \frac{\mu}{M^2 Re Pr} \tag{5}$$

3 Numerical Schemes and Boundary Conditions

In the present simulations, NSCBC (Navier-Stokes Characteristic Boundary Conditions) are used in the streamwise and the vertical directions. The outlet pressure condition proposed by Rudy and Strikwerda [5] is employed.
As for the numerical schemes, the choice was made on compact finite difference scheme [6] in the (x) and (y) directions, however, a classical Fourier method [7] is used in the treatment of the periodic (z) direction.

4 Numerical Results

In any numerical simulation, the various parts of the code must be tested by solving some problems with analytical or independently-known solutions. The code and the boundary conditions were validated by simulating a steady Poiseuille flow at relatively low Reynolds and Mach numbers [8].

4.1 Laminar flow simulations

The Reynolds number was fixed to a relatively high value, Re=2500, then three laminar simulations, with isothermal walls, for M=0.25, M=0.5 and M=0.7 were executed. The numerical results of each simulation show the effect of compressibility on the temperature and density, however, the increase of Mach number doesn't affect much the streamwise velocity component.

4.2 Perturbed flow simulations

The main subject of this numerical study is to investigate the effects of varying the Mach number and the disturbance amplitudes on the flow fields. The three subsonic laminar Poiseuille flows (mentioned above) were perturbed at the inlet with random disturbances equal to 1%, 2.5%, 5% and 10%, respectively. Figures 1, 2 and 3 show the evolution in time and space of the vertical vorticity and the low/high speed streaks near the wall, for Re=2500, M=0.25, 0.5 and 0.7, respectively. ($\omega_y^+ = 0.06(red)$, $\omega_y^- = -0.06(blue)$, $U_f^+ = 0.01(yellow)$ *and* $U_f^- = -0.01(green)$)

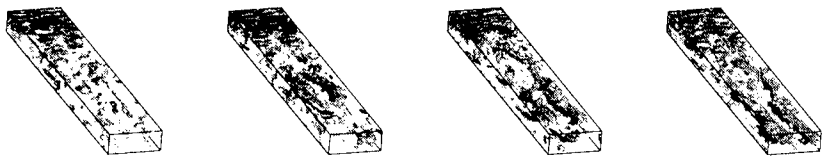


Figure 1: Evolution of near-wall structure from t=183(left) to t=189(right), for Re=2500 and M=0.25 (x from 0 to 10L, y from -L to -2L/3 and z from 0 to 2L).

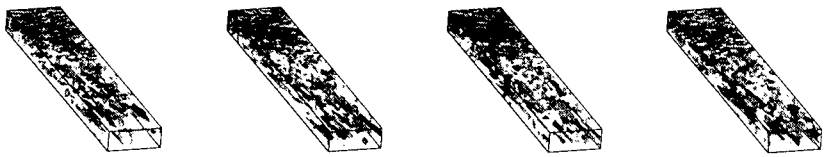


Figure 2: Evolution of near-wall structure from t=142(left) to t=148(right), for Re=2500 and M=0.5 (x from 0 to 10L, y from -L to -2L/3 and z from 0 to 2L).

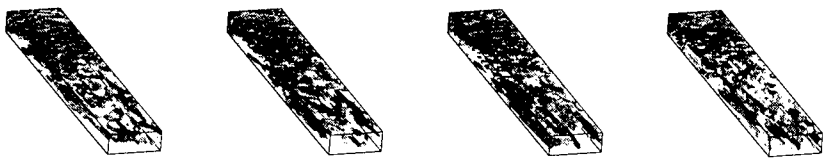


Figure 3: Evolution of near-wall structure from t=142(left) to t=148(right), for Re=2500 and M=0.7 (x from 0 to 10L, y from -L to -2L/3 and z from 0 to 2L).

5 Conclusions

Direct numerical simulations of subsonic Poiseuille flows have been performed. The numerical tests have shown a good agreement with the theoretical results of laminar flow. As a result of the forced simulations, an early transitional state scenario can be imagined; After reaching the laminar regime, flows were perturbed at the inlet with random disturbances, therefore, near-wall low/high speed streaks and vortical structure are generated. These vortical and streaky structures are elongated longitudinally with a quasi-periodicity in the spanwise direction. For numerical simulations executed with disturbance amplitudes less than 5% (2.5% and 1% cases), these structures were not reproduced, suggesting the existence of threshold amplitudes for the disturbances to onset and generate the transitional near wall structure. Work will be continued to uncover the reason behind this near-wall structure generation, and hopefully, to complete simulating the later stages of transition.

References

[1] H. Fasel and H. Bestek. Investigation of non-linear spatial disturbance amplification in plane Poiseuille flow. *In Laminar-Turbulent Transition*, pp. 173–185, 1980.

[2] 2. A. Lundbladh and D. S. Henningson. Threshold amplitudes for transition in channel flows. *Transition, Turbulence and Combustion*, Vol.I:309–318, 1994.

[3] S. K. Lele. Compressibility effects on turbulence. *Ann. Rev. Fluid Mech.*, 26:211–254, 1994.

[4] Y. Guo, L. Kleiser, and N. A. Adams. A comparison study of an improved temporal DNS and spatial DNS of compressible boundary layer transition. *AIAA. No. 94-2371*, 1994.

[5] D. H. Rudy and J. C. Strikwerda. *J. Comput. Phys.*, 36:55, 1980.

[6] S. K. Lele. Compact finite difference schemes with spectral-like resolution. *J. Comput. Phys.*, 103:16–42, 1992.

[7] C. Canuto, M. Y. Hussaini, A. Quarteroni and T. A. Zang. *Spectral Methods in Fluid Dynamics*, 1988.

[8] Y. Moez, H. Maekawa, and K. Yamamoto. Effects of compressibility and disturbances on subsonic Poiseuille flows undergoing transition. *Proceedings of CFD13 Symp. Tokyo*, Dec. 1999.

IV

Turbulence Control

ADVANCES IN TURBULENCE VIII
Proceedings of the Eighth European Turbulence Conference
C. Dopazo, L. Valiño, A. Lozano, E. Oñate and J. M. Redondo (Eds.)
© CIMNE, Barcelona 2000

Instabilities and control of transition in round and coaxial jets

C. B. da Silva and O. Métais *

* LEGI, Institut de Mécanique de Grenoble, B.P. 53, 38041 Grenoble Cedex 09, FRANCE

Contact e-mail: Carlos.Silva@hmg.inpg.fr

1 Introduction

Coherent structures present in transitional round jets have been studied both experimentally and numerically. Most experimental works have focused in the study of the primary modes of instabilty. Numerical studies although dealing with secondary instabilities have been restricted to low Reynolds numbers. Urbin and Métais [?] while studying the possibility of controlling a high Reynolds number jet found what they called the "alternated pairing" mode. However, their computations were performed using dissipative numerical methods, which somehow could put in question the validity of their conclusions for high Reynolds number flows. For the round jet case, the goal of the present work was to study in detail, using LES and an highly accurate code, the eventual formation of this original "alternated pairing" mode, in a spatially evolving high Reynolds number round jet. After this, several ways of controlling the jet were investigated.

Most studies concerning coaxial jets are experimental works that deal with the several regimes of transition and their dependence upon the global parameters of the flow [?]. Numerical studies of coaxial jets are very rare and often restricted to 2D cases, although coannular jets were recently studied with LES in a fully turbulent configuration [?]. Here we focused on studying (with DNS) the coherent structures present in a spatially evolving low Reynolds number transitional coaxial jet. To the Authors knowledge this the first DNS of coaxial jets ever done.

2 Direct and Large-Eddy simulations

All the simulations were performed with the same numerical code. It is an highly accurate solver of the incompressible Navier-Stokes equations which combines pseudo-spectral and high-order compact finite difference schemes. In the round jet case, the inflow mean velocity profile was given by $U = \frac{U_2+U_3}{2} -$

$\frac{U_2-U_3}{2}\tanh\left[\frac{1}{4}\frac{R}{\theta}\left(\frac{r}{R}-\frac{R}{r}\right)\right]$. For the coaxial jet case, it was made up of two tangent hyperbolic profiles centered at each gradient *i.e.* $U=\frac{U_1+U_2}{2}+\frac{U_1-U_2}{2}\tanh\left(\frac{r}{2\theta_1}\right)$ for $r<R_m$ and $U=\frac{U_2+U_3}{2}+\frac{U_2-U_3}{2}\tanh\left(\frac{r}{2\theta_2}\right)$ for $r>R_m$. Here U_1 is the jet/inner jet centerline velocity, U_2 is the outer jet's velocity and U_3 is a very small co-flow. R_1, R_2 and R_m are the jet's inner, outer and mean radius respectively and θ_i is the momentum thickness of the i'th initial shear layer. At each time step, a three component fluctuating velocity field (with statistical characteristics of isotropic turbulence) was superimposed to the stream-wise mean velocity profiles. The noise is set to be located mainly in the shear layers gradients. The outflow condition was of a non-reflective (Orlansky) type. All the lateral boundaries were taken as periodic. It is clear that such boundary conditions, although permitting the use of very accurate pseudo-spectral schemes, do not allow the entrainment naturally expected in free jets/coaxial jets. However, if the lateral boundaries are placed sufficiently far away, we have checked that those do not perturb the flow with spurious reflections. Furthermore, as was previously shown, a very small co-flow (less than 1%) superimposed to the inlet does not perturb the flow dynamics and allows the natural growth of the jet by entraiment.

The round jet simulation consists of an LES at Reynolds number $Re_D=\frac{U_2D}{\nu}=25000$ using the filtered structure fnction subgrid-scale model proposed by Lesieur and Métais [?]. The grid used has $201\times96\times96$ points and the computational domain extends to $12D\times6D\times6D$. As in Urbin and Métais [?] the ratio R/θ was set to 10 and the maximum amplitude of the incoming noise was 0.5%. The coaxial jet simulation is a DNS at Reynolds number $Re_{D_1}=\frac{U_2D_1}{\nu}=3000$. The ratio $\beta=\frac{D_2}{D_1}$ was set to 2 and the grid consists of $231\times256\times256$ points to allow a domain size of $10.8D_1\times7.1D_1\times7.1D_1$. We here choose $\frac{D_1}{\theta_1}=\frac{D_1}{\theta_2}=20$ and the maximum noise amplitude is limited to 3.0%. For the coaxal jet simulation, a deterministic perturbation of fixed frequency correponding to a Strouhal number $S_{tr}=\frac{U_m f}{D_1}=0.33$ is added to the inlet noise. Finally, the velocities chosen for both simulations are such that $\frac{U_1}{U_2}=0.33$ and $\frac{U_3}{U_2}$=0.091. The co-flow is then very small ($\frac{U_3}{U_2}<1\%$) and does not influence the jet dynamics.

3 Results and Discussion

The code has been extensively validated in the round jet configuration. First for the laminar jet, the numerical results were compared with the analytical predictions. Second for the turbulent jet, DNS were compared to recent experimental measurements. Visualizations of the high Reynolds number LES round jet are shown in Figure 1. As expected by linear stability analysis based on the prescribed inlet profile, at early stages of transition i.e. near $2<\frac{x}{D}<3$ (x axial direction), one sees vortex rings appearing with a frequency corresponding to a

Strouhal number of $S_{tr} = \frac{U_2 f}{D_1} = 0.35$. Following the apparition of vortex rings one sees that they have a tendency to become inclined (making angles greater than 30^o) with the axis of the jet. This is due to the growth of a sub-harmonic mode which yields an alternated inclination of consecutive vortex rings. Further downstream, strong stream-wise vortex tubes appear, mainly in the regions where the two consecutive rings are brought closer and where stretching mechanisms are very strong. The rings subsequently undergo a localized pairing. This way alternated pairings [?] appear in the flow around $3 < \frac{x}{D} < 5$. Further downstream the flow becomes highly three-dimensional with a lot of small scale activity and for $x/D > 8$ the field exhibits statistical characteristics of fully developed turbulence.



Figure 1: Large-eddy simulation of a natural, spatially evolving round jet. Isosurfaces of pressure (grey) and positiv Q (green). The entire simulated jet (left). Idem, region between $2 < x < 6D$ (center). Pressure isosurfaces in the region $2 < x < 6D$ (right).

We now turn to the case of the spatially developing coaxial jet (see Figure 2). The first stages of transition ($\frac{x}{D_1} < 5$) are characterized by the emergence of vortex rings in the regions of the inner and outer velocity gradients. The rings soon begin to exhibit azimuthal instabilities. We have checked that the inner rings are unstable to an azimuthal mode of 7 while outer rings are unstable to a mode 9. Both numbers correspond fairly well with Widnall's prediction [?] for the instability of an isolated vortex ring based upon the radii of the ring and of its core. This seems to indicate that vortex ring interactions do not significantly affect the stability characteristics at least for this initial stage. Notice that the inner rings move downstream faster than the outer ones since we have $r_u = \frac{U_2}{U_1} > 1$. An interesting phenomemum is the formation, in the jet core and for a distance $\frac{x}{D_1} > 5$, of a region of strong backflow of size $\frac{L_b x}{D_1} = 1$ and $\frac{L_b r}{D_1} = 0.5$. At a downstream distance $5 < \frac{x}{D_1} < 8$, pairs of stream-wise counter-rotating vortices form between each two consecutive outer rings. They are associated with a typical longitudinal vorticity of about twice the vorticity of their originating vortex rings. Pairs of longitudinal vortices can also be observed in the inner region of the coaxial jet, but surprisingly these are much longer and do not connect two consecutive inner rings. Their length may reach 2.5 the average distance between two consecutive inner rings and their vorticity 8

times the one of the corresponding inner vortex rings. These vortices may be attributable to the presence of the strong backflow which may yield a strong stretching of longitudinal vorticity. This point deserves further investigation. Finally, merging of the rings (both inner and outer) is seen to happen around $6 < \frac{x}{D_1} < 8$, and soon after the flow turns abruptly to fully developed turbulence.

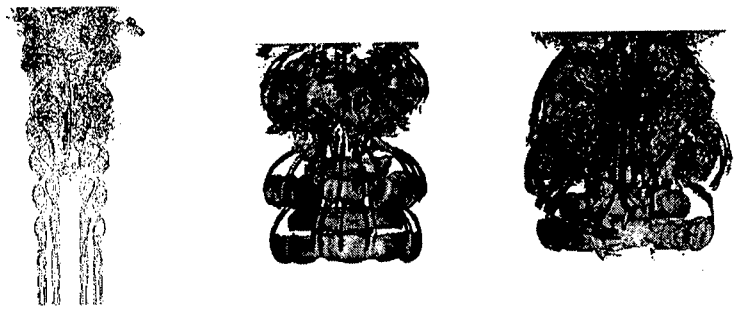


Figure 2: Direct numerical simulation of a forced spatially evolving coaxial jet. Isosolines of vorticity modulus (left). Isosurfaces of positiv Q colored by streamwise vorticity. Zoom of the region around $5 < \frac{x}{D_1} < 8$ (center). Idem, inside the coaxial jet (right).

References

[1] K. Akeselvoll and P. Moin. Large-eddy simulation of turbulent confined coannular jets. *J. Fluid Mech.*, 351:387–411, 1996.

[2] E. Villermaux H. Rehab. and J. Hopfinger. Flow regimes of large-velocity-ratio coaxial jets. *J. Fluid Mech.*, 345:345–281, 1997.

[3] M. Lesieur and O. Métais. New trends in large-eddy simulations of turbulence. *Annu. Rev. Fluid Mech.*, 28:45–00, 1996.

[4] D. B. Bliss S. E. Widnall and C. Y. Tsai. The instability of short waves on a vortex ring. *J. Fluid Mech.*, 66:35–47, 1974.

[5] G. Urbin and O. Métais. *Large-eddy simulations of the three-diemnsional spatially-developing round jets.* in Direct and Large Eddy Simulation II, Edited by Jean-Pierre Chollet, Peter R. Voke and Leonhard Kleiser, KLUWER ACADEMIC PUBLISHERS, 1997.

ADVANCES IN TURBULENCE VIII
Proceedings of the Eighth European Turbulence Conference
C. Dopazo, L. Valiño, A. Lozano, E. Oñate and J. M. Redondo (Eds.)
© CIMNE, Barcelona 2000

The Manipulation of Small-Scale Mixing in Coaxial Jets Using Synthetic Jet Actuators

S. A. Davis[1], B. D. Ritchie[2], J. M. Seitzman[2] and A. Glezer[1]

[1]Woodruff School of Mechanical Engineering, Georgia Institute of Technology
Atlanta, GA 30332-0405, USA
[2]School of Aerospace Engineering, Georgia Institute of Technology
Atlanta, GA 30332-0150, USA

Contact e-mail: ari.glezer@me.gatech.edu

1 Introduction

The traditional approach to small-scale mixing enhancement in free shear flows has been *indirect* and has relied primarily on the manipulation of large-scale, global instability modes of the base flow upstream of mixing transition. More efficient control of mixing in fully turbulent shear flows might be achieved by direct (rather than hierarchical) control of both the large-scale entrainment *and* the small-scale mixing processes. The present work focuses on mixing enhancement based on concurrent manipulation of *both* the small- and large-scale dynamical processes and the coupling between the large- and small-scale motions in the shear layers of coaxial round air jets. Excitation is effected by fluidic actuators based on synthetic (zero net mass flux) control jets. These jets are formed from the ambient fluid near the flow boundary by a time-periodic train of vortical structures induced by the motion of a diaphragm that is operated at resonance within a shallow cavity. The vortical structures that synthesize each control jet scale with the membrane frequency and can be adjusted to match, and directly interact with, small-scale eddies within the equilibrium range of the embedding flow. Large-scale flow structures and global entrainment are affected by amplitude modulation of the diaphragm's excitation waveform.

2 Experimental Apparatus and Procedure

The coaxial jet is formed by a nozzle (tube in the mixing facility) with $D_o = 2.54cm$ and a central tube with $D_i = 1.4cm$ (wall thickness $t = 1mm$), yielding an area ratio $A_i/A_o = 0.5$. Three velocity ratios U_i/U_o =0.35, 0.65, and 1.4 are

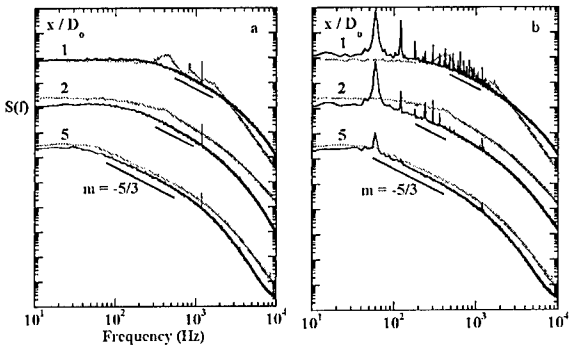


Figure 1: Power spectra of the streamwise velocity at the radial location where $U(x,r)/U_{max}(x) = 0.5$ with $U_i/U_o = 0.65$ for forcing with carrier only (a) and amplitude modulated excitation at 60 Hz (b). Corresponding power spectra of the unforced flow are plotted using gray curves.

investigated (some results for $U_i/U_o = 0.65$ are presented here). The combined volume flow rate is nominally constant and is equivalent to an $11m/s$ uniform jet ($Re_{D_H} = 7700$). The exit plane of the primary jet nozzle is equipped with an insert housing nine individually controlled jet actuators equally spaced around the circumference. Each control jet issues from an arc-shaped orifice ($w = 0.5mm$, $l = 9mm$). The carrier waveform of the actuators is $1180Hz$, and the amplitude, duty cycle, and relative phase of each of the modulating waveforms of the individual actuators are computer controlled. The effects of the actuation on the flow structure and mixing are investigated in two parallel experiments. The flow mechanisms induced by the excitation are inferred from detailed phase-locked measurements of the velocity field using two-component hot wire anemometry, and the resultant mixing of a passive scalar is studied using planar laser-induced fluorescence (PLIF) of acetone. In the mixing experiments, acetone is seeded into the annular air stream by bubbling the air through a pressurized cylinder containing liquid acetone.

3 Results

The flow scales that are induced by the high-frequency forcing (at the resonance frequency of the actuators) and pulse modulated forcing are apparent in power spectra of the streamwise velocity measured in the jet shear layer (Figures 1a and b, respectively). High-frequency forcing results in spectral peaks at the forcing frequency and some of its higher harmonics. The amplitude of the spectral peak at the forcing frequency decays with downstream distance, but is still discernible at $x/D_o = 5$. Amplitude modulation of the excitation waveform using a modified square wave function results in spectral peaks at the carrier and modulation

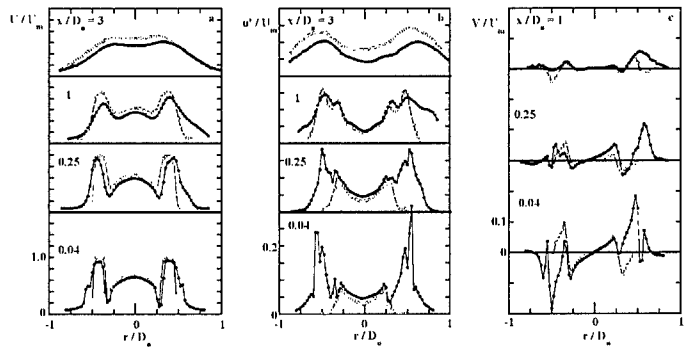


Figure 2: Radial distributions of U (a), u' (b), and V (c) for $U_i/U_o = 0.65$: unforced (o), forcing with carrier frequency (•).

frequencies (and several higher harmonics). In the presence of modulation, the carrier frequency decays faster with streamwise distance but the spectral peak at the modulation frequency is still present at $x/D_o = 5$.

Cross-stream distributions of the streamwise and radial velocity components are measured in a plane that includes the jet centerline and passes through the azimuthal center of an actuator at the edge of the jet on one side and between two actuators on the other side. The measurement domain is $x/D_o \leq 5$ with increments of $\Delta x/D_o = 0.25$ and $\Delta r/D_o = 0.025$. For the amplitude-modulated cases, data are acquired phase locked to the modulation waveform at 72 equal phase increments. The effect of unmodulated excitation input on radial distributions of U, u', and V at several streamwise stations is shown in Figures 2a-c. Since the jet actuators are placed near the radial edges of the outer jet ($r/D_o \sim 0.55$), they lead to a radial expansion of the jet flow field (more than $0.1D_o$ at $x/D_o = 0.04$). The asymmetry mentioned above is apparent at $x/D_o = 0.25$ and 1 where the jet spreads radially towards the active actuator on the right. Similar spreading was shown by Davis and Glezer [1] as a result of azimuthal non-uniform forcing having a three-fold symmetry of a single jet. The forcing leads to an increase in u' throughout the entire width of the annular flow for $x/D_o < 1$ but does not increase the turbulent fluctuations in the core flow. By $x/D_o = 1$, the differences between distributions of U and u' in the forced and unforced flows are reduced and by $x/D_o = 3$ the unforced and forced flows are quite similar with lower turbulent intensity in the forced flow. The reduction in u' downstream with forcing is ostensibly due to increased dissipation in the near field. It is expected that mixing enhancement due to small-scale forcing would occur upstream of $x/D_o = 3$. The radial velocity is especially significant to the mixing of the two streams because it is a measure of the radial penetration between the two flow domains. In Figure 2c the radial velocity away form the jet centerline is taken to be positive to the right of the centerline and vice versa on the left. The strongest effect of the forcing occurs near the jet exit plane

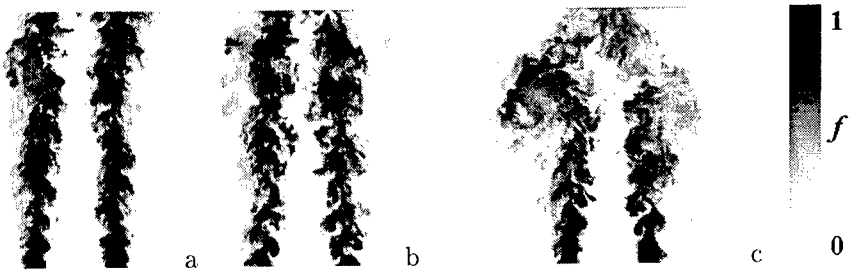


Figure 3: Jet mixture fraction, f, for $U_i/U_o = 0.65$: unforced (a), forcing with carrier only (b), and amplitude modulated excitation at 60 Hz (c).

($x/D_o = 0.04$). In the unforced flow, the radial velocities in the core and annular flows are directed towards the wake region of the pipe wall. In the presence of forcing, the mean radial velocity in both the core and annular flows is directed outward except within the wake and near the jet actuators. This mean outward radial velocity results from the time-periodic entrainment by the synthetic jets. Time series of the radial velocity (not shown), indicate that in the wake region, while the mean radial velocity is nearly zero, the instantaneous velocity oscillates at the forcing frequency resulting in the formation of vortical structures in the mixing region.

The impact of forcing on the scalar field is seen in Figure 3, which shows PLIF images acquired in a plane through the jet centerline with height $3D_o$. The intensity of each pixel is converted to a local mixture fraction (f), defined as the fraction of the pixel's fluid mass that originated in the annular fluid. With high-frequency forcing (Figure 3b), mixing increases between the annular jet and both the ambient fluid and inner jet (compared to the unforced case, Figure 3a). Regular structures at the jet's outer edge correspond to the individual, high frequency pulses. Amplitude modulation (Figure 3c) leads to a further increase in mixing during a large portion of the duty cycle, primarily through increased entrainment from the associated large-scale structures. Radial and azimuthal integration of the results shows that there is essentially no unmixed annular fluid (defined as $f > 0.95$) for the amplitude modulated case by $x/D_o = 0.5$, while in the unforced case this is not achieved until just beyond $x/D_o = 2$.

This work has been supported by ARO-MURI DAAH04-96-1-0008.

References

[1] S. A. Davis and A. Glezer. Mixing Control of Fuel Jets using Synthetic Jet Technology: Velocity Field Measurements. AIAA Paper 99-0447, 37th Aerospace Sciences Meeting, Reno, NV, 1999.

ADVANCES IN TURBULENCE VIII
Proceedings of the Eighth European Turbulence Conference
C. Dopazo, L. Valiño, A. Lozano, E. Oñate and J. M. Redondo (Eds.)
© CIMNE, Barcelona 2000

Identification and Control of Unstable Modes in an Isothermal and Reacting Swirling Jet

C. O. Paschereit[1], E. Gutmark[2] and L. Haber[1]

[1]ABB ALSTOM POWER Technology Ltd, 5405 Baden, Switzerland
[2]University of Cincinnati, Aerospace Engineering and Engineering Mechanics Department, Cincinnati, OH 45221-0070, USA

Contact e-mail: oliver.paschereit@ch.abb.com

1 Introduction

Flow instabilities play an important role in combustion and heat release processes by controlling the mixing between the fresh fuel/air mixture and hot combustion products in premixed combustors. The evolution of these structures in nonreacting flows was extensively studied in mixing layers [1, 2, 3] and flows over backward facing steps. However, the evolution of flow instability waves in more complex flows such as swirling flows and their interaction with combustion is not as well understood. Interaction between large scale structures related to flow instabilities, acoustic resonant modes in the combustion chamber and the heat release process can potentially give rise to undesired thermoacoustic instabilities in the combustor. To suppress swirl induced instability controlling the large scale vortices is of critical importance [4].

2 Experimental Setup, Results and Discussion

The instability structure was investigated in a water test rig as well as in a combustor test-rig [4]. The water test facility was built as a companion to the combustion test facility and therefore designed to operate at the same flow parameter range as the combustion test rig at Reynolds number of $Re = 80000$ and swirl number of $S = 0.7$. Measurement of the swirling jet in water showed that the flow pattern near the axis was similar to wake flow behind a bluff-body. The other region receptive to flow instabilities was the sudden expansion area at the jet's (burner's) exit plane. The flow at this area exhibited features of an annular jet. The inner shear layer exhibited primarily one fundamental unstable mode at a normalized frequency of $St = fD/U = 1.2$. The outer shear layer

was unstable to an axisymmetric mode at a normalized frequency of $St = 0.58$ and to high frequency helical modes.

Linear stability analysis was used to investigate the stability properties of the swirl-stabilized burner. The basic flow $\underline{U}$ under consideration is assumed to be incompressible, axisymmetric and independent of axial direction such that $\underline{U} = \{U(r), V(r), W(r)\}$, where $\{U, V, W\}$ denote the axial, radial, and azimuthal velocity components in the $\{x, r, \theta\}$ cylindrical coordinate system. The linear dispersion relation is derived by splitting the flow field into mean and perturbation components.The perturbation components are decomposed into normal modes of the form $\{u', v', w', p'\} = \{iF(r), G(r), H(r), P(r)\} \exp[i(\alpha z + n\theta - \omega t)]$, where α is the wavenumber in the axial direction, n is the wavenumber in the azimuthal direction, and ω is the temporal frequency. Linearizing the Navier–Stokes equations around the basic flow $\underline{U}$ results in the disturbance equations.

For a semi-infinite domain, this set of equations is completed by boundary conditions that are derived from requiring azimuthal and radial derivatives to vanish on the centerline $r = 0$, and that all perturbations vanish at $r = \infty$,

$$\begin{aligned} r = 0: &\quad nF + G = 0; F + nG = 0; nH = 0; nP = 0, \\ r = \infty: &\quad F = G = H = P = 0. \end{aligned} \tag{1}$$

The resulting set of equations was solved using a standard Chebychev collocation method which is known for rapid convergence as the number of discretization points is increased, evenly distributed errors, and straightforward treatment of boundary conditions. Here, the eigenfunctions $\{F, G, H, P\}$ are approximated by a truncated series of Chebychev polynomials. Gauss–Lobatto points were chosen for the collocation points of the polynomials. As the Chebychev polynomials are defined on the interval $\xi \in [-1, 1]$, the numerical coordinate ξ needs to be mapped onto the physical coordinate r. For the semi-infinite interval $r \in [0, \infty[$ investigated here, $r = a(1 - \xi)/(b + \xi)$ was used where a fixes the stretching of the grid and $b = 1 + 2a/r_{max}$ is determined by the physical domain size. The discretized equations could then be written as a generalized eigenvalue problem which was solved either for spatial (α) or temporal (ω) eigenmodes. For the spatial analysis, all terms that are quadratic in α were additionally linearized using a companion matrix method and the singularity that may appear in the eigenvalue coefficient matrix was eliminated with an artificial compressibility.

The resulting calculated modes of instability are shown in Fig. 1. The axisymmetric mode $m = 0$ is most unstable at $St = 1.0$. The frequency of the axisymmetric instability observed in the test rig is mainly determined by the acoustic feedback which acts as a forcing mechanism to the flow instabilities is somewhat lower ($St = 0.58$). Changing the flow speed shows the instability to increase towards $St = 1.0$. The helical mode, $m = -1$, which is opposite to the swirling direction, was the dominant one. This mode corresponded to a $St = 1.3$, which was also identified as the dominant instability in the flow measurements.

The vortices shedding at the burner's exit lip were visualized during combustion and in a water tunnel (Fig. 2). The instantaneous images of the vortex

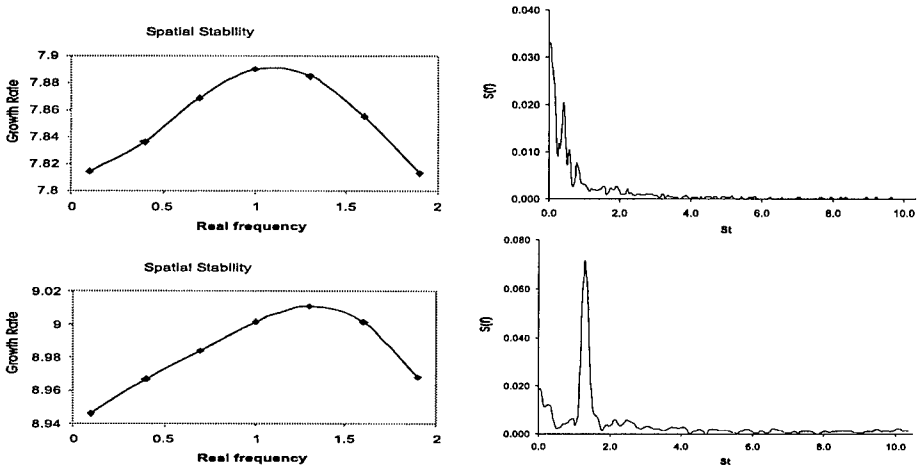


Figure 1: Instabilities in the swirling jet. **left:** stability analysis, upper: $m = 0$. lower: $m = -1$. **right:** spectra measured in water tunnel, upper: outer shear layer $r/D = 1.14$. lower: inner shear layer $r/D = 0.5$.

were captured at different phases during its formation, revealing a strong coherent structure despite the high swirl number. In reacting flow, as these coherent structures evolve from small incipient vortices at the burner's lip to large-scale vortices in the shear layer, they mix fuel, air and combustion products and thus dominate the pattern of heat release. The subsequent interaction between heat release and acoustic pressure waves set up the conditions that may lead to stable or unstable thermoacoustic behavior of the combustor.



Figure 2: Visualization of vortex shedding at the burner's exit lip.

In order to modify the combustion process by controlling the swirling jet, a special arrangement was added to the burner's exit to enable direct excitation of the separating jet's circumferential shear layer to control the shear layer and thus the vortex formation. Symmetric and antisymmetric excitation was tested (Figs. 3-4). A closed loop feedback controller determined the timing of the modulation. The effects of parameters as phase, amplitude and duty cycle of the modulation as well as combustion output power and equivalence ratio on the pressure oscillations during combustion and on NO_x and CO emissions were studied.

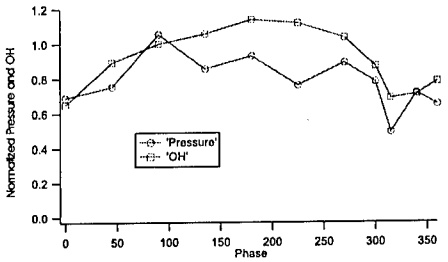


Figure 3: Closed loop control. Symmetric excitation at $F/F_{max} = 1.9\%$ and $St = 0.67$.

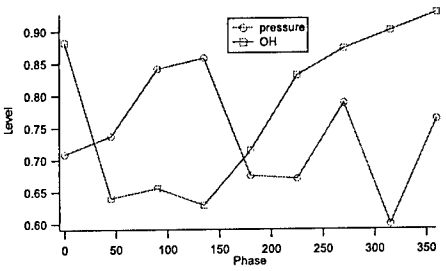


Figure 4: Closed loop control. Antisymmetric excitation at $F/F_{max} = 1.9\%$ and $St = 0.67$.

3 Conclusions

Linear stability analysis and experimental investigation were performed to identify unstable modes and the ensuing coherent structures in a highly swirling jet, discharged downstream of a backward facing step into an axisymmetric chamber. The axisymmetric mode $m = 0$ is most unstable at $St = 1.0$. The frequency of the axisymmetric instability observed in the test rig is mainly determined by the acoustic feedback which acts as a forcing mechanism to the flow instabilities is somewhat lower ($St = 0.58$). Changing the flow speed shows the instability to increase towards $St = 1.0$. The helical mode, $m = -1$, which is opposite to the swirling direction, was the dominant one. This mode corresponded to a Strouhal number of 1.3, which was also identified as the dominant instability in the flow measurements. This instability causes the shear layer to roll-up into vortical coherent structures which affect the jet's growth rate by entraining ambient fluid and by mixing it with the jet's flow. Therefore, these vortices play an important role in the combustion and heat release processes by controlling the mixing between fuel, air and hot combustion products. Active control of the flow and combustion instabilities was achieved by direct excitation of the shear layer at the burner exit.

References

[1] C. Ho and Patrick Huerre. Perturbed free shear layers. *Ann. Rev. Fluid Mech.*, **16**:365–424, 1984.

[2] C. O. Paschereit, I. Wygnanski, and H. E. Fiedler. Experimental investigation of subharmonic resonance in an axisymmetric jet. *Journal of Fluid Mechanics*, **283**:365–407, 1995.

[3] A. Michalke. Survey on jet instability theory. *Prog. Aerospace Sci*, **21**:159–199, 1984.

[4] C. O. Paschereit, E. Gutmark, and W. Weisenstein. Coherent structures in swirling flows and their role in acoustic combustion control. *Physics of Fluids*, **9**:2667–2678, 1999.

ADVANCES IN TURBULENCE VIII
Proceedings of the Eighth European Turbulence Conference
C. Dopazo, L. Valiño, A. Lozano, E. Oñate and J. M. Redondo (Eds.)
© CIMNE, Barcelona 2000

Large eddy simulation of turbulent flow over an open cavity

Haecheon Choi, Seonghyeon Hahn and Joonhyuk Choi

Center for Turbulence and Flow Control Research
School of Mechanical and Aerospace Engineering
Seoul National University
Seoul 151-742, KOREA

Contact e-mail: choi@socrates.snu.ac.kr

1 Introduction

For a long time, a cavity has been regarded as what must be removed on the surface of a body because it significantly increases drag and flow-induced noise. However, recently some experimental results showed that skin-friction drag can be reduced by using a small-size cavity ([1], [2]), which provides a possibility of using a cavity as a passive device for drag reduction. Therefore, the objectives of this study are to understand the effect of cavity on the turbulence characteristics of boundary layer flow and to investigate the possibility of reducing the skin-friction drag in a turbulent boundary layer using an open cavity.

2 Computational Details

The large eddy simulation technique with Germano *et al.* [3]'s dynamic subgrid-scale model is used for the analysis of turbulent boundary layer flow over a cavity. The filtered Navier-Stokes equations are discretized using the second-order accurate central difference in space. As for time integration, a third-order accurate Runge-Kutta method is used for nonlinear terms and the Crank-Nicolson method is used for viscous terms. A fractional step method is used to split the implicit coupling between velocity and pressure. The Reynolds number is $\mathrm{Re} = u_\infty \theta/\nu = 1520$, where u_∞ is the free-stream velocity and θ is the momentum thickness at the backward-facing corner of the cavity. Six different cavity configurations are examined: $(D/\theta,\ L/D)$=(0.93, 4), (1.46, 1), (1.46, 2), (1.46, 4), (3.44, 1) and (3.44, 2), where D and L are the depth and length of the cavity.

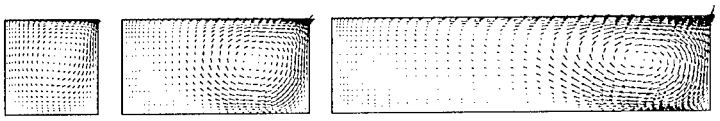


Figure 1: Mean velocity vectors inside the cavity ($D/\theta = 1.46$): (a) $L/D = 1$; (b) 2; (c) 4.

3 Results and Discussion

Figure 1 shows mean velocity vectors inside the cavities with three different cavity lengths ($L/D = 1$, 2 and 4) and a fixed cavity depth ($D/\theta = 1.46$). A large recirculating vortex generated inside the cavity is clearly identified and it becomes much stronger as the cavity length increases. This vortex plays an important role in the drag characteristics around a cavity. First, this vortex exists near the forward-facing wall, while the flow near the backward-facing wall is very weak. Thus, it is expected that the pressure drag, caused by the wall pressure difference between the two cavity walls, should increase as the cavity length increases. On the other hand, the skin friction is negative at the bottom of the cavity near the forward-facing wall due to the reverse flow generated by the recirculating vortex and it contributes to reduction of the friction drag.

Figure 2 shows the wall-pressure distributions along the forward- and backward-facing walls of the cavity in all three cases presented in Figure 1. As mentioned above, it is observed that the pressure drag increases as the cavity length increases because the recirculating vortex inside the cavity becomes stronger (Figure 1). Another reason for the increase of pressure drag is related to the shear layer passing over the cavity: As the cavity length increases, the shear layer obtains more momentum from the cavity and it impinges against near the forward-facing corner much stronger. Therefore, the wall pressure near the forward-facing corner is greatly increased. Moreover, the pressure drag increases with increasing cavity depth D/θ (not shown here), because the size of the recirculating vortex is proportional to the cavity depth.

Figure 3 shows the distribution of the skin-friction coefficient around the cavity in all three cases presented in Figures 1 and 2. Here, the coordinate $x = 0$ denotes the location of backward-facing wall of the cavity and rapid increase of the skin-friction coefficient denotes the location of the forward-facing wall. At the bottom of the cavity, negative skin friction is observed due to the recirculating vortex generated inside the cavity. As expected in Figure 1, the skin friction decreases further as the cavity length increases. On the other hand, the skin friction significantly increases behind the cavity due to the impingement of the shear layer. In cases of $L = D$ and $L = 2D$, the skin friction recovers to that of the flat-plate boundary layer at a downstream location from the cavity. Therefore, it is expected that the friction drag decreases as the cavity length

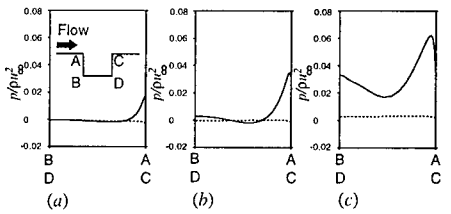


Figure 2: Wall pressure distribution along the cavity walls in case of $D/\theta = 1.46$: (*a*) $L/D = 1$; (*b*) 2; (*c*) 4. ——, for the forward-facing walls; – – – –, for the backward-facing walls.

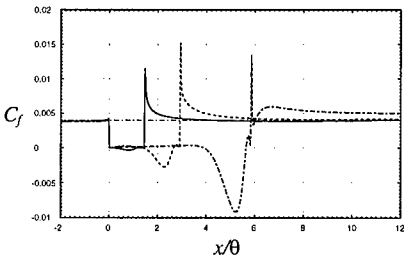


Figure 3: Distribution of skin-friction coefficient in case of D/θ=1.46: ——, $L/D = 1$; – – – –, 2; ———, 4; —·—, flat plate.

increases. However, in case of $L = 4D$, the skin friction behind the cavity shows one more local peak and does not recover to that of the flat plate boundary layer even far downstream of the cavity. This behavior occurs in case of $L = 2D$ when the cavity size is large ($D/\theta = 3.44$), while it does not even in case of $L = 4D$ when the cavity size is small ($D/\theta = 0.93$). The second local peak of C_f is related to the existence of strong streamwise vortices. Figure 4 shows the iso-surfaces of streamwise vorticity in case of $(D/\theta, L/D) = (1.46, 4)$. Strong streamwise vortices are observed after the mid-plane of the cavity due to complex interaction between the shear layer and recirculating vortex, resulting in the significant increase of the skin friction.

One of the most conspicuous dynamic features of turbulent flow over a cavity is the interaction between the recirculating vortex inside the cavity and the shear layer over the cavity: a recirculating vortex inside the cavity continually pushes and pulls the shear layer over the cavity (Figure 5), which causes the turbulence intensities above the cavity to be larger than those above the flat plate. A similar phenomenon can be found in the flow visualization of Djenidi *et al* [4]. Turbulence intensities inside the recirculating vortex also become larger as the cavity length increases. The pressure fluctuations are maximum right below the corner of the forward-facing wall, which is believed to be the main source of flow-induced noise.

Total-drag increase or decrease is determined by the combination of pressure drag and friction drag. About 2% and 6% of drag reductions are achieved in cases of (D/θ, L/D)=(1.46, 1) and (1.46, 2), respectively. However, in case of (D/θ, L/D)=(1.46,4), total drag increases due to the increase of both the form drag inside the cavity and skin-friction drag downstream of the cavity. In case of a deeper cavity ($D/\theta = 3.44$), the increase of pressure drag becomes dominant and total drag increases in all cases ($L/D = 1$ and 2). In case of a shallower cavity ($D/\theta = 0.93$, $L/D = 4$), about 9% of drag reduction is achieved. Two-dimensional simulations of laminar flow over an open cavity at the same Reynolds number were also performed in this study. In case of laminar flow, the

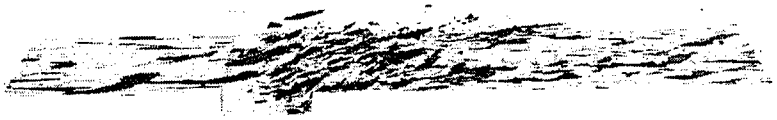


Figure 4: Iso-surfaces of the streamwise vorticity ω_x in case of $(D/\theta, L/D) = (1.46, 4)$.



Figure 5: Time sequence of the spanwise vorticity ω_z in an (x, y) plane in case of $(D/\theta, L/D) = (1.46, 4)$.

magnitude of pressure drag was much smaller than that in turbulent flow and the total drag decreased in all six cases.

4 Conclusions

- Total-drag increase or decrease mainly depends on the depth of the cavity, while there exists a limitation of the length of the cavity to achieve drag reduction.
- The interaction between the vortex and the shear layer passing over the cavity plays an important role in the changes in drag and turbulence characteristics around the cavity.

This work is supported by Creative Research Initiatives of the Korean Ministry of Science and Technology.

References

[1] I. Tani, H. Munakata, A. Matsumoto and K. Abe. Turbulence management by groove roughness. *Turbulence Management and Relaminarisation. H. W. Liepman and R. Narasimha* (eds.), Berlin: Springer-Verlag, 161–172, 1987.

[2] K.-S. Choi and N. Fujisawa. Possibility of drag reduction using d-type roughness. *Appl. Sci. Res.*, 50:315–324, 1993.

[3] M. Germano, U. Piomelli, P. Moin and W. H. Cabot. A dynamic subgrid-scale eddy viscosity model. *Phys. Fluids* A, 3: 1760–1765, 1991.

[4] L. Djenidi, R. Elavarasan and R. A. Antonia. The turbulent boundary layer over transverse square cavities. *J. Fluid Mech.*, 395: 271–294, 1999.

ADVANCES IN TURBULENCE VIII
Proceedings of the Eighth European Turbulence Conference
C. Dopazo et al. (Eds.)
© CIMNE, Barcelona 2000

Response of Turbulent Channel Flow to Sudden Wall Suction and Blowing

Yongmann M. Chung[1,2], Hyung Jin Sung[1], and Kai. H. Luo[2]

[1]Department of Mechanical Engineering
Korea Advanced Institute of Science and Technology (KAIST)
373-1 Kusong-dong, Yusong-gu, Taejon 305-701, SOUTH KOREA
[2]Department of Engineering
Queen Mary and Westfield College (University of London)
Mile End Road, London E1 4NS, UNITED KINGDOM

Contact e-mail: Y.M.Chung@QMW.ac.uk or Yongmann@KAIST.ac.kr

1 Introduction

Many studies have been made to delineate the effect of uniform wall suction and blowing on wall-bounded turbulent flows. It was found that wall suction and blowing has significant effects on mass, momentum and consequently heat transfer rates of turbulent flows. However, most previous studies focused on the asymptotic behavior of turbulent flow with uniform suction and blowing both in experiments and numerical simulations [1, 6].

When wall suction and blowing is applied to a turbulent channel flow from a certain downstream location, there is an *initial relaxation* of the flow from the upstream impermeable wall boundary condition to the wall suction and blowing [5]. As the flow goes downstream farther, the flow adjusts itself to its asymptotic state corresponding to the uniform suction and blowing. The main objective of the present study is focused on the initial relaxation of turbulent flow to wall suction and blowing with direct numerical simulation.

2 Results and Discussion

In the present paper, a direct numerical simulation is performed to investigate the response of turbulent channel flow to sudden wall suction and blowing. A uniform blowing is applied at the lower wall of the channel and a suction at the upper wall. Suction and blowing is applied for $x > 5$. The Reynolds number based on the friction velocity at inlet $u_{\tau_{in}}$ and the channel half-width h, is Re_τ = 100. The computational domain are set (25.6×2×4) with the present grid system (256×97×64) in the x, y, z directions, respectively.

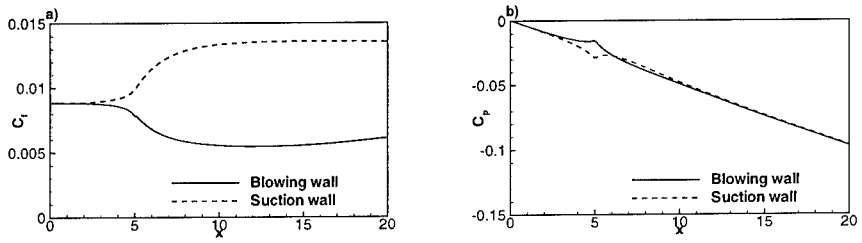


Figure 1: Downstream variations of turbulent stresses. a) C_f, b) C_p.

The numerical method used for this study is originally due to Yang & Ferziger [7]. As inflow boundary conditions, instantaneous flow data from an auxiliary inflow simulation of a fully-developed turbulent channel flow are used [2, 3].

After wall suction and blowing is applied, the pressure field as well as the skin-friction coefficient converges to the asymptotic state very quickly as shown in Figure 1. Time-mean velocity field in Figure 2 approaches the asymptotic state much faster than that of turbulent kinetic energy k, showing the quicker response of the lower order statistics.

When the velocity profiles are plotted in terms of $u^+ = U/u_\tau$ and $y^+ = yu_\tau/\nu$ based on the local friction velocity u_τ (not shown here), wall blowing results in an upward-shift of the velocity profile while suction makes a downward-shift. The upward- and downward-shift of the velocity profile are also found in the uniform wall suction and blowing [6].

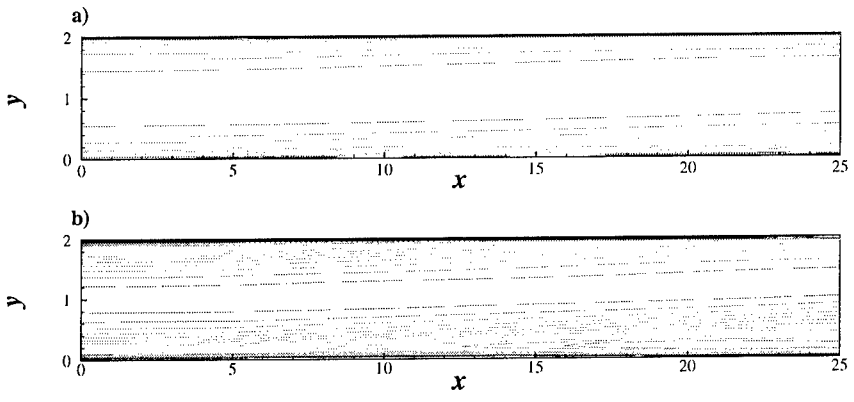


Figure 2: Downstream variations of mean velocity. a) U, b) k.

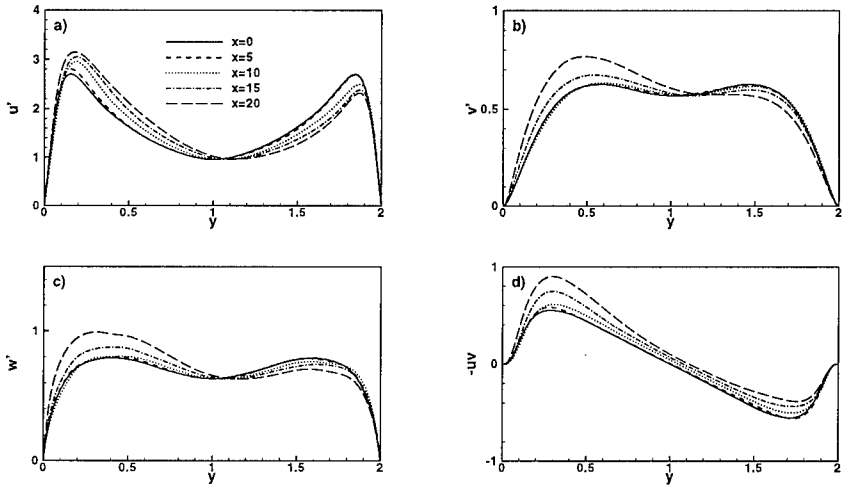


Figure 3: Downstream variations of turbulent stresses. a) u', b) v', c) w', d) $-\overline{uv}$.

Figure 3 shows the profiles of turbulent stresses at several downstream locations. The results are normalized based on the friction velocity at inlet, $u_{\tau_{in}}$. The initial relaxation of each component of Reynolds stress is different from each other [4]. u' component shows faster response than other normal components ($x = 10$), while the response of v' and w' is quite slow.

3 Concluding Remarks

The initial relaxation of turbulent channel flow to sudden wall suction and blowing was investigated with a direct numerical simulation. The response of time mean and fluctuating velocity field shows various degrees of adjustment. Each component of Reynolds stress has a different characteristics from each other.

Support from the UK EPSRC under grant no. GR/L56237 is gratefully acknowledged.

References

[1] R. A. Antonia, L. Fulachier, L. V. Krishnamoorthy, T. Benabid, and F. Anselmet. Influence of wall suction on the organized motion in a turbulent boundary layer. *J. Fluid Mech.*, 190:217–240, 1988.

[2] Y. M. Chung and H. J. Sung. Comparative Study of Inflow Conditions for Spatially Evolving Simulation. *AIAA Journal*, 35:269–274, 1997.

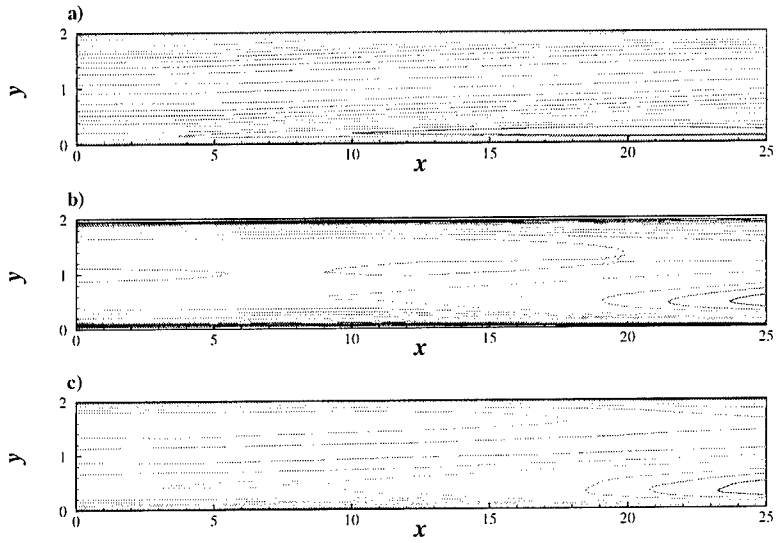


Figure 4: Downstream variations of turbulent stresses. a) u', b) v', c) w'.

[3] Y. M. Chung and H. J. Sung. Asymmetric response of turbulent channel flow to wall suction and blowing. In *Proceedings of the First International Symposium on Turbulence and Shear Flow Phenomena*, Santa Barbara, USA, September 12–15, 1999, pp. 423–428.

[4] M. Schildknecht, J. A. Miller, and G. E. A. Meier. The influence of suction on the structure of turbulence in fully developed pipe flow. *J. Fluid Mech.*, 90:67–107, 1979.

[5] A. J. Smits and D. H. Wood. The response of turbulent boundary layers to sudden perturbations. *Annual Review of Fluid Mechanics*, 17:321–358, 1985.

[6] Y. Sumitani and N. Kasagi. Direct numerical simulation of turbulent transport with uniform wall injection and suction. *AIAA Journal*, 33:1220–1228, 1995.

[7] K. S. Yang and J. H. Ferziger. Large-eddy simulation of turbulent obstacle flow using a dynamic subgrid-scale model. *AIAA Journal*, 31:1406–1413, 1993.

ADVANCES IN TURBULENCE VIII
Proceedings of the Eighth European Turbulence Conference
C. Dopazo et al. (Eds.)
© CIMNE, Barcelona 2000

On the Use of Thermal MEMS-Sensors for Wall-Shear-Stress Measurements

P. Johansson[1], L. Löfdahl[1], A. Bakchinov[1],
M. Sen[2] and M. Gad-el-Hak[2]

[1]Thermo and Fluid Dynamics
Chalmers University of Technology, SE-412 96 Göteborg, Sweden
[2]Aerospace and Mechanical Engineering
University of Notre Dame, Notre Dame, IN 46556, USA

Contact e-mail: jope@tfd.chalmers.se

1 Introduction

Wall-shear stress is an essential quantity to compute, measure or infer in a wall bounded turbulent flow. The time averaged values of this quantity are indicative of the global state of the flow along a surface and can be used to determine for instance body-averaged properties like the skin-friction. The time resolved part is a measure of the unsteady structures in the flow, which are responsible for the individual momentum transfer events, and an indicator of the coherent portion of the turbulent activities. The latter signifying that spatially distributed values of the instantaneous wall-shear stress may be used in a feed-forward or feedback control-loop to effect coherent structures in the boundary layer, for instance in drag reduction or separation delay, see e. g. Löfdahl and Gad-el-Hak [4].

2 The Thermal Principle

One way of determining the time resolved part of the wall-shear stress is to use the in-direct thermal method. Through the years, it has been argued and shown that conventional thermal sensors suffer from large heat losses to the substrate, yielding a larger active sensor area which adversely affects the temporal and spatial response of the probe. A knowledge and control of these issues is of utmost importance in measurements of the time resolved wall-shear stress.

The thermal principle in context is shown in Figure 1. The ohmic (Joule) heating in the device Q_J is transferred both to the fluid and to the surrounding substrate, which can be expressed:

$$Q_J = Q_f + Q_s \tag{1}$$

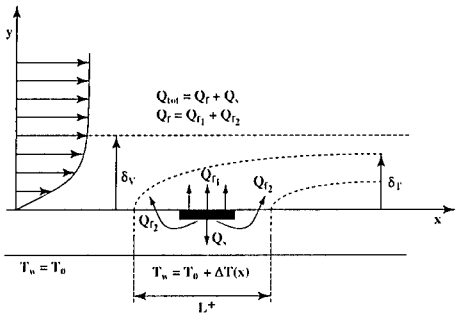


Figure 1: Schematic of a thermal sensor.

where Q_f represents the heat transferred to the fluid directly from the heated surface (Q_{f_1}) and indirectly through the heated portion of the substrate (Q_{f_2}). Q_s represents the heat lost irretrievably to the substrate.

From en experimental perspective, it is not possible to measure Q_{f1}. Instead, the total heating power Q_J is measured, and a calibration curve is then fitted to the measured points. The calibration function has traditionally been on the form:

$$Q_J = A\tau^{1/n} + B \tag{2}$$

where A is directly related to the heat convected from the hot-film to the fluid, Q_{f1}. The calibration constant B represents the heat loss to the substrate, e.g. the part associated to Q_s. To account for situations where Q_{f2} is important, n is also treated like a calibration constant. (For a laminar flow over an adiabatic wall, $n = 1/3$. See e. g. Löfdahl and Gad-el-Hak [4].)

Noteworthy here is that Eq. 2 does not stand on a solid theoretical ground. The assumption that the heat conduction to the substrate is independent of the flow velocity (and totally represented by a constant, B) is highly questionable, especially if B is large.

3 MEMS-based sensors and experiments

MEMS(Micro-Electro-Mechanical Systems)-based thermal sensors reveal some interesting properties, which put them in a group of utmost interest, both for measuring fluctuating flow quantities and for detecting coherent structures in reactive control purposes. The MEMS technology makes it feasible to fabricate miniature sensors in such a small scale that even high wave-number-range eddies in technically interesting turbulent flows can be resolved. The significant benefits of MEMS are the possibility to operate sensors at low overheat temperatures and improved methods for insulation of the heated sensing parts. Other general features of the MEMS technology are the possibilities to fabricate closely spaced multi-sensor probes integrated on one chip, high accuracy in the manufacturing process, and once the design and fabrication method has been developed,

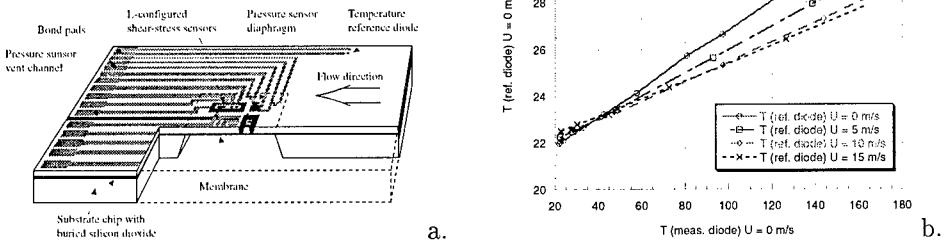


Figure 2: a) Schematic and b) measured heating of the Kälvesten *et al.* [2] MEMS-sensor.

production of sensors in a large quantity at a low cost. Since the mid-nineties, MEMS-based wall-shear-stress sensors have been presented, e. g. Kälvesten *et al.* [2], Jiang *et al.* [1] and Liu *et al.* [3].

A schematic drawing of a MEMS-based wall-shear stress sensor by Kälvesten *et al.* [2] is shown in Fig. 2a. Instead of using a bridge balance, the operation relies on a voltage difference between two temperature sensitive diodes. The chip is divided into a hot and a cold part, thermally separated through polyimide filled trenches. On the hot part, a heating resistor is located together with a diode which monitor the temperature. To measure the ambient temperature, another diode is placed on the cold part. The overheat temperature is then controlled to force the voltage difference between the diodes to remain constant.

Jiang *et al.* [1] have developed an array of wall-shear stress sensors based on the thermal principle. It consists of polysilicon resistor wire located on a diaphragm. Below the diaphragm is vacuum cavity so that the device will have a reduced heat conduction loss to the substrate. Recently, Liu *et al.* [3] presented a further development of the Jiang *et al.* [1] sensor, also with a diaphragm located on top of a vacuum-sealed cavity. The major advantage of both the Jiang *et al.* [1] and the Liu *et al.* [3] sensors is claimed to be the good insulation from the surrounding substrate, and thereby a minimization of the heat conduction.

The principle of operation of the Kälvesten *et al.* [2] sensor made an investigation of the surface temperature distribution possible by feeding the heating resistor independently of the diodes. The temperatures of the reference and measuring diode, respectively, were then measured. In Fig. 2b, the result of such a measurement at different free-stream velocities is shown.

As the temperature of the measuring diode increases, there is also a significant temperature raise of the reference diode. Due to effects of heat convection to the flow, the heating of the reference diode shows a velocity dependence. Hence, a substantial amount of heat is conducted through the metal conductors and the substrate out to the whole chip resulting in an increased heated area. For

measurements of the time averaged part of the wall-shear stress this may not be considered as a serious effect, since the whole chip operates more or less like a hot-film and the voltage difference between the two diodes is some kind of measure of the supplied energy. However, for the time-resolved part of the wall-shear stress it is devastating, since the heated area is totally uncontrolled.

The effect of heat loss to the substrate can be further examined by studying the static calibration coefficients in Eq. (2). Typical values for the sensors by Kälvesten *et al.* [2] are $A = 1.09$, $B = 42.6$ and $n = 2.0$. For the sensors made by Liu *et al.* [3], the reported values are $A = 0.5698$, $B = 42.593$ for $n = 3$.

These expressions are surprisingly similar, since the probes are differently designed. From these curve fits, it is obvious that the heat conduction effects are severe since B is one order of magnitude larger then A. This clearly implies that the reduction in heat conduction achieved by insulating polyimide ditches or vacuum cavities have a very small effect.

4 Concluding Remarks

Using MEMS-based sensors for wall-shear stress measurements have been considered as a possibility to circumvent some classical problems associated with hot-films. By examining the performance of such a MEMS-sensor, which is based on the detection of the voltage difference between two temperature diodes and has a good thermal insulation between the heated and cooled part of the chip, the following conclusions may be drawn. For this particular sensor, the problem of enlarged area of the heated part of the chip has not been solved, since most of the energy supplied is still conducted to the substrate. Neither polyimide insulation's or vacuum cavities underneath the heated part seem to have any significant influence on the minimization of the heat conduction to the substrate.

References

[1] Jiang, F., Tai, Y., Gupta, B., Goodman, R., Tung, S., Huang, J. and Ho, C. A surface micromachined shear-stress imager. *Proc. IEEE, 9th Int. Workshop on MEMS, Amsterdam, The Netherlands*, 110-115, 1996.

[2] Kälvesten, E., Vieider, C., Löfdahl, L. and Stemme, G. An integrated pressure-velocity sensor for correlation measurements in turbulent gas flows. *Sensors and Actuators A*, 52:51–58, 1996.

[3] Liu, C., Huang, J.-B., Zhu, Z., Jiang, F., Tung, S., Tai, Y.-C. and Ho, C.-M. A micromachined flow shear-stress sensor based on thermal transfer principles. *IEEE J. Microelectromech. Syst.*, 8(1):90–99, 1999.

[4] Löfdahl, L. and Gad-el-Hak, M. MEMS Applications in Turbulence and Flow Control. *Progress in Aerospace Sciences*, 35:101–203, 1999.

ADVANCES IN TURBULENCE VIII
Proceedings of the Eighth European Turbulence Conference
C. Dopazo et al. (Eds.)
© CIMNE, Barcelona 2000

Control of laminar-turbulent transition in three-dimensional boundary layer

Sergei V. Manuilovich

Central Aero-Hydrodynamics Institute (TsAGI),
Zhukovsky, Moscow region, 140160, Russia.
Fax: (095) 556-4337, e-mail: manu@recp.aerocentr.msk.su

Abstract

New methods for the laminarization of the boundary layer flow on swept wings are offered. The laminar-turbulent transition is assumed to be due to acoustic influence and random roughness of wing surface. The basis for the methods is in mutual cancellation of unstable eigenmodes excited in the vicinity of the leading edge of the wing and over the boundary-layer flow irregularity generated by the artificial spanwise-periodic roughness or the selective suction.

1 Introduction

The first stage of laminar-turbulent transition consists in transformation of external disturbances into spatially growing unstable eigenmodes. This process is referred to as the boundary-layer receptivity. The most important factors resulting in unstable mode generation are free-stream disturbances and roughness of wing surface. Once generated, unstable modes undergo linear amplification and nonlinear interactions and then destroy the laminar flow.

Two main types of methods for the attenuation of unstable oscillations exist. The first type contains methods based on stabilization of the boundary-layer mean flow. Classical example of these methods is distributed suction. The second type of methods, first proposed by Milling [1], applies the principle of Tollmien-Schlichting (TS) wave cancellation by means of the formation of artificial wave with the same frequency and amplitude but opposite phase.

This paper is devoted to theoretical investigation of the laminarization of low-speed 3D boundary layer using receptivity control. It is shown that both acoustic TS wave and crossflow instability vortices generated by random roughness can be canceled by the artificial spanwise-periodic irregularity.

2 Cancellation of acoustic TS wave over 2D irregularity

The basic advantage of laminarization method using 2D vibrating part of wing surface [1] is its versatility. Whatever is the cause of TS wave excitation, this wave may be canceled by the above method. However, the grave drawback of this method is the need to use the control system for unsteady generator of artificial TS wave. To overcome this disadvantage for the case of unstable wave generated by sound, the usage of 2D roughness under the same acoustic field as the generator of the "artificial" unstable wave was offered in [2]. The amplitude and the phase of artificial TS wave can be controlled by means of varying of the height and the location of the roughness. Being excited by the same acoustic wave, the natural TS wave and artificial one are synchronized automatically.

In this paper two types of artificial irregularities are considered, namely roughness and local suction. The processes of cancellation of acoustic TS wave over these two irregularities are illustrated in Figures 1 and 2 respectively (the main flow is Blasius boundary layer $U_x(\infty) = 1$; Reynolds number $R = 500$ and sound frequency $\omega = 0.05$ are calculated using boundary-layer thickness; the real and imaginary parts of complex amplitude τ of wall shear stress disturbance describing the cancellation process $\partial v_x/\partial y = \tau(x)\exp(-i\omega t) + c.c.$ are shown by solid and dashed lines correspondingly). The outlined results show that the disturbance really presents the incoming TS wave in upstream region $\tau \sim \exp(i\alpha_{TS}x)$, $\alpha_{TS} = 0.140 - i0.003$, with the location of the most intensive flow oscillations corresponding to the middle of controlling inhomogeneity. The amount of the disturbance is quickly damped downstream from the irregularity.

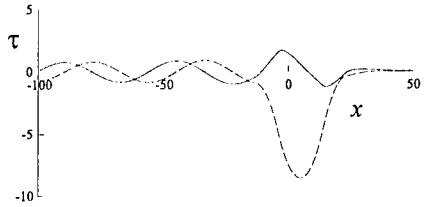


Figure 1: Cancellation of Tollmien-Schlichting wave over 2D roughness in monoharmonic acoustic field

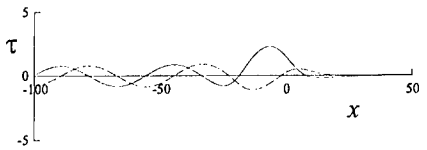


Figure 2: Cancellation of acoustic Tollmien-Schlichting wave by 2D suction

3 Cancellation of crossflow instability vortices by spanwise-periodic inhomogeneity

Up to this point the methods of for TS wave cancellation have been considered. These methods are applicable for laminarization of boundary layer on a wing of small sweep angle. Except TS instability, in 3D boundary layer a crossflow instability occurs. The importance of the last type of instability in laminar-turbulent transition increases with increase of the sweep angle. One of the main cause of crossflow instability vortex generation is roughness of wing surface. The initial amplitude of these vortices may be large even in the case of random roughness with small height because the steady eigenmodes are excited via a direct scattering of main flow by surface roughness. Thus, random roughness leads to formation of system of crossflow instability vortices. This system of natural origin can be canceled by spanwise-periodic artificial roughness of the same spanwise period. The cancellation condition may be achieved by special choice of height and spanwise phase of the roughness [3].

The process of cancellation of crossflow instability vortices over artificial sinusoidal roughness is illustrated in Figure 3 (the main flow is boundary layer in the vicinity of attachment line of swept wing $U_x(\infty) = U_z(\infty) = 1$; Reynolds number $R = 400$ and spanwise wavenumber $\gamma = 0.8$ are calculated using boundary-layer thickness; the real and imaginary parts of complex amplitude P of pressure disturbance on the wall $p = P(x)\exp(i\gamma z) + c.c.$ are shown by solid and dashed lines respectively). In upstream region one can see the incoming crossflow instability mode $P \sim \exp(i\alpha_{cf}x)$, $\alpha_{cf} = -0.658 - i0.008$. The amount of the disturbance is quickly damped downstream from the roughness.

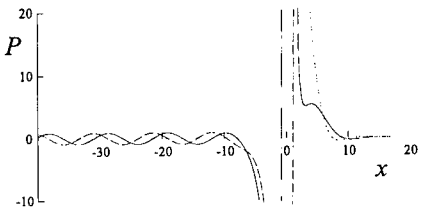


Figure 3: Cancellation of crossflow instability vortices by spanwise-periodic roughness

Note that the level of the disturbance over the roughness is 200 times greater than the amplitude of the incoming crossflow instability vortices. This may lead to by-pass transition immediately over the roughness if the amplitude of the canceled vortices is large enough. To avoid this problem, one can use another type of spanwise-periodic irregularity generated by distributed suction-blowing. In this case the amplitude of disturbance over the controlling irregularity is 30 times less than in the above case (see Figure 4).

Up to now the problems of suppression of TS waves and crossflow instability

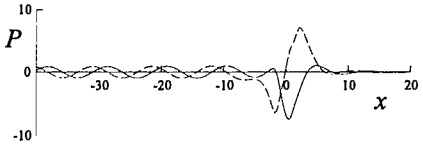


Figure 4: Cancellation of crossflow instabilities by sinusoidal suction-blowing

vortices were considered separately. Nevertheless, these unstable modes can be canceled by unique artificial inhomogeneity, which is local in longitudinal direction and periodic in spanwise direction. Zeroth Fourier harmonic of spanwise modulation should be tuned for cancellation of TS wave generated by sound on natural inhomogeneity of boundary layer in the vicinity of leading edge. First harmonic is used for suppression of crossflow instability vortices generated by "natural" roughness of wing surface.

Note that application of spanwise-periodic suction for formation of the controlling inhomogeneity is preferable. In contrast to the case of the sinusoidal suction-blowing, Fourier decomposition of spanwise-periodic suction contains both zeroth and first harmonics, which can be tuned for cancellation of TS wave and crossflow instability, respectively. In addition to the reduction of the disturbance amplitude immediately over the region of the controlling influence, the suction makes the overall stabilizing effect on boundary-layer flow. The last method of the receptivity reduction can be applied as modification of the classical method of boundary-layer laminarization by suction.

Finally note that the suppression of crossflow instability mode by selective suction observed in experiment [4] can be explained using the superposition principle described here.

References

[1] Milling, R.W. (1981) Tollmien-Schlichting wave cancellation, *Phys.Fluids* **24**, No. 5, 979-981.

[2] Manuilovich, S.V. (1994) On new methods for boundary-layer flow laminarization, *Journal of Theoretical and Computational Fluid Dynamics* **6**, No. 1, 31-47.

[3] Manuilovich, S.V. (1994) Laminarization of three-dimensional compressible boundary-layer flow using receptivity control. In *Laminar-Turbulent Transition. IUTAM Symp., Senday/Japan. September 5-9, 1994*, 129-136.

[4] Egami, Y. & Kohama Y. (1996) Control of crossflow dominant boundary layer by distributed suction system. In *XIXth International Congress of Theoretical and Applied Mechanics, Kyoto/Japan. August 25-31, 1996, Abstracts*, 782.

ADVANCES IN TURBULENCE VIII
Proceedings of the Eighth European Turbulence Conference
C. Dopazo et al. (Eds.)
© CIMNE, Barcelona 2000

Control by Stationary and Nonstationary Streaky Structures and Their Secondary Instability

V.V. Kozlov, and G.R. Grek

Institute of Theoretical and Applied Mechanics, Siberian Branch,
Russian Academy of Sciences, Novosibirsk 630090, RUSSIA

Contact e-mail: kozlov@itam.nsc.ru

The review of our last results with respect to the experimental study on control of secondary instability of the streaky structure (*puffs*) and crossflow vortices is presented here. Stationary (*Görtler-like and crossflow*) and nonstationary (*puffs, lambda-structures and etc.*) vortices and were generated into the flat plate and swept wing boundary layer. The transition was initiated by the growth of small amplitude traveling waves (secondary disturbances) generated in these boundary layers by means of different methods (sound, localized suction-blowing and *etc.*). It is shown, that the riblets, localized and continuous suction, and spanwise-wall oscillation are effectively methods by control of development of the stationary and nonstationary vortices and traveling waves developed on their. The use of different passive and active control techniques and experimental results on swept wing transition control indicate some possible schemes of the MEMS actuators as well as place and time of their application. Coherent structures of laminar sublayer of the turbulent boundary layer are similar with the vortex structures of a transitional boundary layer and, hence, the methods of control by them presented here may be used also for this case.

It is good known, a favorable influence on drag reduction in a turbulent boundary layer of the different devices such as riblets [1] and spanwise-wall oscillation [2]. One possible explanation of drag reduction, for example by riblets, is due to changes in the near-wall coherent structures. The coherent structures of the turbulent boundary later seem similar to the vortex structures that appear at laminar- turbulent transition. The laminar boundary layer investigations showed, that the surface manipulation in the form of *triangular riblets* allows one to suppress the intensity streamwise vortices, the same as in a case longitudinal lambda-vortices which appear at nonlinear stage of Blasius boundary layer transition, and thereby stabilize them with respect to the high-frequency traveling

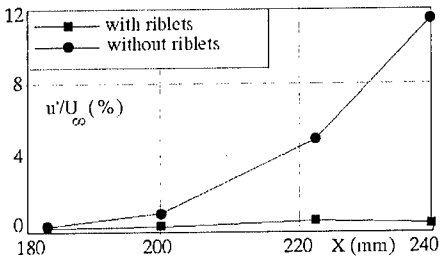


Figure 1: Riblets effect on the disturbances development in flow with crossflow vortices.

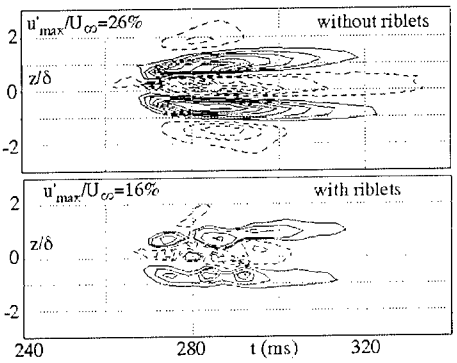


Figure 2: Riblets effect on the nonstationary streaky structure (*Puff*) in a flat plate boundary layer.

waves and delay the transition to turbulence. The effect was definitely observed for the lambda-vortices [3], wake behind an isolated roughness element [4] as well as for the element arrays [5]. According to the hot-wire measurements, this large influence is related to changes in the pattern formation and inner vortex structures. The studies described below were carried out with the intention to look at the *riblets effect* on transition in flows with the stationary (*crossflow*) vortices and nonstationary vortices (*puffs*). Other methods of the transition control for these flows were also considered and, on the basis of these researches, attempt to consider an opportunity of application for transition control of modern technologies (MEMS control system) was made.

An isolated and arrays of stationary crossflow-like vortices were generated by means of specially designed vortex generators in a swept wing boundary layer. Growing waves were introduced in the vortices by sound and through excitation from a small hole in the wing surface. It was shown that waves modes excited through the hole and by sound are similar, having the close cross-section amplitude distributions and amplification rates. Devices such as *riblets* may be placed in the boundary layer in a attempt to suppress the formation or interaction of organized flow structures. It was found that *triangular riblets* (see [3, 4, 5]) located along the laminar vortex reduce its intensity that in its turn prolong the laminar flow [6] (see Fig.1.).

Intensity decreasing of the streaky structure (*puff*) up to sixty percent by means of the same riblets was obtained in a flat plate boundary layer experiment (see Fig.2.). In this case, the transwerse velocity gradient ($\partial u/\partial z$) decreased and it resulted in delay of the secondary high-frequency disturbances development. Probability of the turbulent spot origination due to this reason reduced or it at all occurred absolutely.

Some conclusions are derived concerning optimal *riblet* position and their geometric parameters. The possibility to use such experiments for modelling

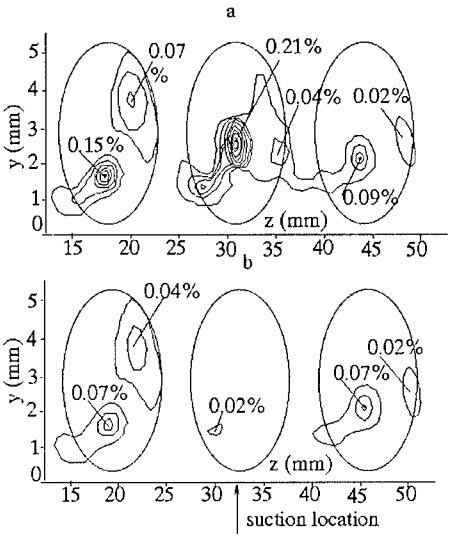


Figure 3: Comparison of the oscillations distributions for the few crossflow vortices both without (a) and with (b) localized suction.

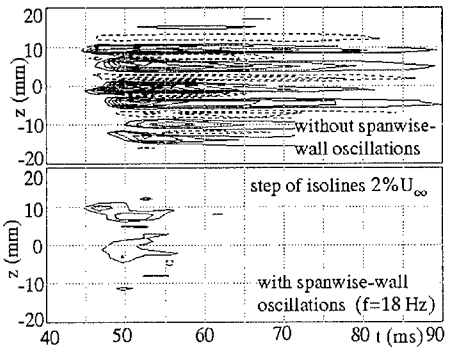


Figure 4: Spanwise wall oscillation effect on the disturbance development in the boundary layer modulated by streaky-structures (*Puffs*).

effects of miniature actuators of a MEMS control system at larger spatial scales is discussed. Based on our experimental results [6] it is shown in some details where and how small-size suction devices could be applied for the localized control at an early stage of transition in a 3D boundary layer. Namely, in a specific case, the transition in a swept-wing boundary layer occurs through the development of wave packets localized inside strong streamwise vortices excited behind quite large obstacles of different forms. Traveling 3D waves constituting the packets having a linear amplification range could be directly and effectively suppressed by the waves of a similar amplitude, but the opposite phase excited with a low-intensity suction-blowing, provided that the operating orifice is located in a certain position in respect to the vortex cross-section (see Fig.3.).

Moreover, an indirect wave suppression could be achieved by a continuous suction through its stabilizing effect on the vortex stability characteristics. The last experiments [7] (see Fig.4.) demonstrated also that spanwise-wall oscillation suppressed both the intensity of longitudinal structures such as nonstationary vortices (*puffs*) and high-frequency wave packets developed on their.

Thus, it is shown that the riblets, localized and continuous suction, and the spanwise-wall oscillation significantly reduce the stationary and nonstationary vortices intensity, which is accompanied by inhibition of the amplification of natural and forced disturbances, leading to prolongation of the laminar regime. The use of different passive (e.g., *riblets*), *quasi-passive* (e.g. *riblets* which adapts

their forms and sizes only with considerable general changes in the flow), and active (e.g., localized suction) control techniques and experimental results on swept wing and flat plate transition control indicate some possible schemes of the MEMS actuators as well as place and time of their application. Some estimations are given showing the possibility to transfer the data of the laboratory test to the sub-millimeter range.

The study was supported by the Russian Basic Sciences Foundation (96-15-96310 and 99-01-00591).

References

[1] D.W. Bechert, M. Bartenwerfer, and G. Hoppe. The viscous flow on surfaces with longitudinal ribs. *J. Fluid Mech.*, 206:105–129, 1989.

[2] K.-S. Choi, J.-R. De Bisschop, and B.R. Clayton. Turbulent boundary layer control by spanwise-wall oscillation. Theoretical and applied mechanics: XIXth INTERN. Congress, Kyoto, Japan, August 25–31, 1996, P.376.

[3] G.R. Grek, V.V. Kozlov, and S.V. Titarenko. An experimental study of the influence of riblets on transition. *J. Fluid Mech.* 315:31–49, 1996.

[4] G.R. Grek, V.V. Kozlov, and S.V. Titarenko. Effects of riblets on vortex development in the wake behind a single roughness element in the laminar boundary layer. *La Recherche Aerospatiale*, 1:1–9, 1996.

[5] G.R. Grek, V.V. Kozlov, S.V. Titarenko, and B.G.B. Klingmann. The influence of riblets on a boundary layer with embedded streamwise vortices. *Phys. Fluids*, 7(10):2504–2506, 1995.

[6] A.V. Boiko, V.V. Kozlov, V.V. Syzrantsev, and V.A. Scherbakov. Transition control by riblets in swept wing boundary layer with embedded streamwise vortex. *Eur. J. Mech., B/Fluids*, 16(1):465–482, 1997.

[7] M.M. Katasonov, and V.V. Kozlov. Boundary layer longitudinal localized structures control by means of riblets and spanwise-wall oscillation. *Proceedings of 9th ICMAR Conference*, Novosibirsk, Russia [Part 1], P. 99–104, 1998.

ADVANCES IN TURBULENCE VIII
Proceedings of the Eighth European Turbulence Conference
C. Dopazo et al. (Eds.)
© CIMNE, Barcelona 2000

Cryogenic turbulence experiments

B. Castaing[1,2], B. Chabaud[1], B. Hébral [1],
X. Chavanne[3], O. Chanal[1] and P. Roche[1]

[1]Centre de Recherches sur les Très Basses Températures
BP 166, 38042 Grenoble Cedex 9, FRANCE
[2]École Normale Supérieure de Lyon,
46 Allée d'Italie, 69364, Lyon Cedex 07, FRANCE
[3]Laboratoire de Physique Statistique
24 rue Lhomond, 75231, Paris Cedex 05, FRANCE

Contact e-mail: Bernard.Castaing@ens-lyon.fr

1 Overview

Since the pioneering work of Threlfall [1] on the Rayleigh-Bénard convection, gaseous Helium progressively became a classical fluid for turbulence studies. Its main interests are:

i) Large control parameters (Rayleigh, Reynolds numbers) within small, laboratory sized, set ups.

ii) Decades of variation of these control parameters at constant geometry.

iii) Small characteristic times, allowing large statistics for measurements.

These points, indeed, could be common to all gases, but the advantage of Helium is the accessibility of its critical point (0.22MPa, 5.2K). Close to the critical point, every fluid reaches the smallest values of its diffusivity constants, the heat diffusivity κ or the kinematic viscosity ν. But the critical pressure of ordinary gases is rather large. Large pressure conditions can be at least as difficult to manage as the now standard Helium temperatures. As it will be seen later, low temperature can also be an advantage for measurements.

Let us take a few examples. For a cylindrical cell, 20cm high for 10cm in diameter, with acetone as working fluid, Rayleigh numbers up to $Ra = 4.10^{10}$ can be reached [2]. Within the same dimensions, and the same Prandtl number ($Pr = \frac{\nu}{\kappa} = 4$) we [3] could reach $Ra > 10^{13}$. X.Z. Wu et al. [4] could obtain $Ra = 10^{14}$ with a double sized cell (40cm high for 20cm in diameter). We could get also $Ra = 2.10^{14}$ closer to the critical point, for larger Pr. For the same conditions and a 1m high cell, Niemela et al. [5] recently get $Ra = 10^{17}$, characteristic of atmospheric Rayleigh numbers. With the same dimensions one could only reach $Ra = 10^{12}$ with water.

The same is true for Reynolds numbers. A laboratory jet in air can reach a Taylor scale based Reynolds number $R_\lambda = 800$ with a typical nozzle of 10cm

and a 40m/s velocity for the air [6]. We [7] could reach $R_\lambda = 1200$ in a gaseous helium jet, with a 2mm nozzle. Tabeling et al. [8] could reach a R_λ larger than 2500 with a Von Kàrmàn flow, the same R_λ as obtained in the Modane [9] tunnel flow, 24m in diameter. Presently, in collaboration with the CERN, we develop a Helium jet experiment which should reach $R_\lambda = 5500$.

Small characteristic times directly come from the small dimensions. For instance, in the Rayleigh-Bénard turbulent convection, velocity U is of the order of the " free fall " value with the renormalised acceleration $g\alpha\Delta$ (α being the isobar thermal dilatation, Δ the temperature difference between plates). Thus the characteristic times goes like:

$$\frac{h}{U} = (\frac{h}{g\alpha\Delta})^{1/2} = \frac{\nu^{1/3}}{(g\alpha\Delta)^{2/3}} \left(\frac{Ra}{Pr}\right)^{1/6}$$

with $Ra = \frac{g\alpha\Delta h^3}{\nu\kappa}$ $Pr = \frac{\nu}{\kappa}$ and h is the height of the cell. For the same Ra and Pr conditions, the kinematic viscosity of Helium gas can be 20 times smaller than the water one, and $\alpha\Delta$, 10 times bigger. This gives a factor 13 in the characteristic times.

Obviously, there are drawbacks. Short characteristic times also means high frequencies, which is not really a problem with low temperatures, since specific heat of solid materials is typically more than 10^3 times smaller than at room temperature. This is not true for Helium itself, however, and the specific heat of the boundary layer around probes can play an important role [10].

Small dimensions are a more serious problem. In a turbulence experiment (jet for instance), the Kolmogorov length goes like:

$$\eta = \frac{\nu}{U} Re Re^{-3/4} = \frac{\nu}{c} \frac{Re^{1/4}}{Ma}$$

where c is the velocity of sound and Ma the Mach number. In the same conditions of Re and Ma, the dissipation length η can be 10^2 smaller in Helium than in air. The typical value 0.1mm which is obtained in classical experiments becomes 1μm for cryogenic ones. Adapting probes is not obvious. In particular, it completely rules out Laser Doppler Anemometry, at least with visible light. The classical hot wire is less limited. This will be discussed in the following section.

2 A jet experiment

2.1 Experimental details

The experimental set up has been described elsewhere [7]. In this talk we concentrate on peculiar aspects as the structure of the probes, their calibration, or the correction of spurious effects due to the noise.

The sensitive part of the probe is a AuGe alloy layer sputtered on a glass fiber and annealed up to close to its metal-insulator transition. It is bypassed by a Au layer except on a very small length in the middle of the fiber. In the present experiment the fiber is 1.5μm in diameter and the AuGe spot in the middle is 0.5μm long. The resistivity of the AuGe alloy is temperature dependent with:

$$\sigma = \frac{T}{R}\frac{dR}{dT} = -0.45$$

and gives typically 200Ω at 15K as the resistance of the probe. A higher sensitivity (larger σ) would give too high a resistance for the probe.

The difficulty, which prevents using the modern microfabrication processes, lies in the frame on which the probe is fixed. It must be widely opened to avoid perturbing the flow and this is what modern technics cannot yet make.

The probe is operated at constant resistance (constant temperature) and the measurement is the Joule heating power necessary to maintain this probe temperature in the flow. For these very short wires, cooling occurs through the wire itself. Heat expands along the wire on a typical length that depends on the coupling to the gas through the boundary layer, thus on the velocity. The usual King's law is thus not verified. Also [11], the probe is sensitive to all components of the velocity, not only those perpendicular to the wire.

Calibration can be made as usual, positioning the probe in the potential cone of the jet, or through the average velocity at the operating point, according to what is usually found in litterature on jets. We can also go further and remark that the distribution of velocities is well known through this litterature, and close to a Gaussian one [6]. The calibration can be obtained from this knowledge: if the instantaneous signal is such that, say, 10% of the recorded points are lower, the corresponding velocity is the one for which 10% of the model Gaussian distribution is lower. This method gives an accurate calibration, which can be checked by comparison with the other records, at different Reynolds numbers. It limits the problems due to aging of the probe, which are well known in classical, room temperature, experiments.

Let us now say a few words about noise. As the noise is a priori uncorrelated with the physical signal, we can correct statistical quantities, such as structure functions, from it. If the noise b can be considered as small compared to the velocity difference δv, then:

$$\langle(\delta v + \delta b)^p\rangle = \langle(\delta v)^p\rangle + \frac{p(p-1)}{2}\langle(\delta b)^2\rangle\langle(\delta v)^{p-2}\rangle$$

as $\langle\delta b\rangle = 0$ and $\langle\rangle$ stands for ensemble average. Non integer p are possible only using absolute value moments. Then a formula such as:

$$\langle|\delta v|^p\rangle = \langle|\delta v + \delta b|^p\rangle - \frac{p(p-1)}{2}\langle(\delta b)^2\rangle\langle|\delta v + \delta b|^{p-2}\rangle$$

is valid only for even integer p, but gives an interpolation formula for all p.

Now, the noise can be recorded independently as a signal noise n, not directly related to the velocity noise b. If $v(s)$ is our calibration function, we can approximate: $v(s+n) = v(s) + n(dv/ds) = v(s) + b$.

Thus, using the noise record and our velocity file, we can construct for each point a model noise: $b = n(dv/ds)$ whose statistical characteristics, in particular the second moment of differences $\langle(\delta b)^2\rangle$ should be identical to the real noise which affects our file [12].

2.2 Stretching of the cascade

Let us now concentrate on an effect showing the interest in accessing to a wide range of Reynolds numbers. Turbulent flows present velocity intermittency. It can be defined as the progressive change of shape of the probability density function of velocity differences at distance r, as r goes from the correlation length L down to the dissipation length η. In the multiplicative cascade models of intermittency, velocity differences at distance r appear as those at distance L multiplied by a factor α [9]. The statistics of these factors can be experimentally approached through the moments:

$$< \alpha^p >_r = \frac{< |\delta v|^p >_r}{< |\delta v|^p >_L}$$

These moments fit as power law of each other: this is the Extended Self Similarity [13]. As $< \alpha^p >$ is also the characteristic function of the distribution of $ln\alpha$:

$$< \alpha^p > = < exp(p ln\alpha) > = exp[C_1 p + C_2(p^2/2!) + ...]$$

a fine check of ESS can be obtained by looking at the proportionality between cumulants C_i. It is generally found that C_3 is very small, so C_2, which is the mean squared deviation of $ln\alpha$, can be reliably estimated through the flatness:

$$\frac{< (\delta v)^4 >}{< (\delta v)^2 >^2} = 3exp(4C_2)$$

The physical multiplicative cascade picture has consequences on the behaviour of C_2 versus r. The cascade should stop and the signal should become smooth when the local Reynolds number crosses a critical value close to 1. Large α regions should become smooth for smaller scales than small α ones. Above this dissipation threshold, in the inertial range, α roughly goes as $r^{1/3}$. Under the threshold, α goes like r. This change of "velocity" $dln\alpha/dlnr$ occurs first for small α, then for large ones, and thus stretches the distribution of $ln\alpha$, increasing its width $\sqrt{C_2}$.

Thus the smoothing effect of the viscosity is completely different from that of low pass filtering the signal. In the later case, the change of $dln\alpha/dlnr$ occurs for all α at the same r. The distribution of α is not stretched and C_2 is not increased. To check this effect, we obtained a filtered $\{y_i\}$ file from the $\{x_i\}$ one

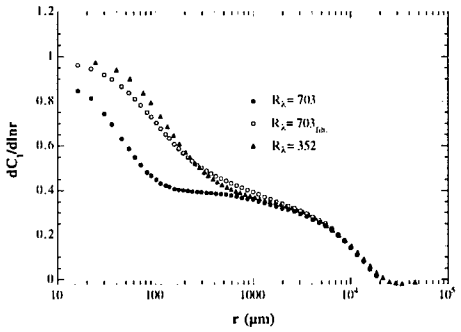


Figure 1: Filtering affects C_1 the same way as viscous damping

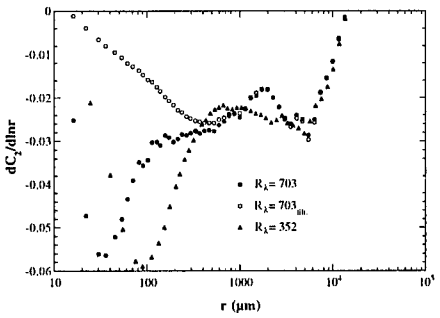


Figure 2: Stretching is visible on unfiltered files, but not on the filtered one

(for $R_\lambda = 703$) through the exponential average: $y_i = \theta x_i + (1-\theta)y_{i-1}$, with $\theta = 0.1$. It is equivalent to averaging at the scale 10η.

As shown on figure 1 the behaviour of $dC_1/dlnr$ for the low pass filtered $R_\lambda = 703$ file, is very similar to the $R_\lambda = 352$ case. However, the corresponding behaviours of $dC_2/dlnr$ are completely different (figure 2). The filtered file does not show the peak close to the dissipation scale, predicted from the physical interpretation, and observed on unfiltered files. This gives support to the physical origin of the cascade and to the physical significance and soundness of the mean squared deviation C_2.

On the other hand, this peak in $dC_2/dlnr$ make it looking as proportional to $dC_1/dlnr$ down to small, dissipative scales. This is ESS, which appears as fortuitous and probably wrong at larger R_λ. Indeed, in this limit, the relative width of the distribution of $ln\alpha$: $\sqrt{C_2}/C_1$ goes down, making the peak stronger.

3 Rayleigh-Bénard cell

3.1 Essential experimental features

Again we refer to a previous paper [14] for a complete description of the experiment. We focus here on peculiar points.

The cold part of the apparatus is shown on figure 3. A thermocouple measures the temperature difference between the plates. Ten pairs of AuFe alloy and superconductive wires were used giving a sensitivity of 130μV/K. Due to the large difference between Helium and room temperatures, the copper wires used for the voltage measurements contribute for a few 100nV depending on the Helium bath level. This contribution was measured, shortening the wires at low temperature by a superconductive wire. Once heated above its transition temperature, this wire is 500Ω in resistance, well above the thermocouple resistance (a few ohms). With superfluid Helium inside the cell, we verified that the

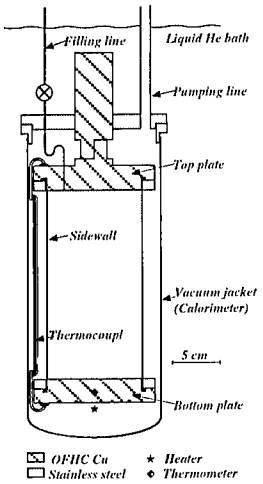


Figure 3: Sketch of the cell

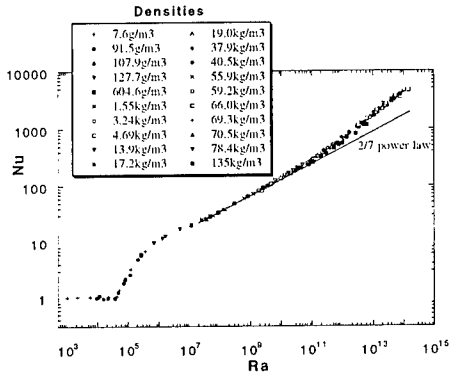


Figure 4: Nu versus Ra diagram for different Helium densities

difference in voltage is zero within 2nV, with 1mW heating on the bottom plate.

The absolute temperature of Helium was obtained through a home calibrated Ge resistance. We checked in situ its calibration, looking when possible at the condensation point corresponding to the density we worked with. In particular we obtained within 1mK the accepted value for the critical point temperature (5.194K) looking at the maximum conductance of the cell at a density close to the critical one. We discovered indeed that direct density measurement was far more accurate than pressure measurements for determining Helium properties [14], especially for densities more than half the critical one. We proceeded by filling the cell from a calibrated volume at room temperature. The large range in Δ we can cover allows to obtain the same Ra and Pr with different densities, giving further cross-checks of these properties.

A final point of interest is the heat conductivity of the plates. We choose rather thick plates, 2.5cm for 10cm in diameter. Indeed, we search for a uniform, constant value of the temperature in contact with the fluid. This does not mean uniform heat fluxes. Exchange of heat with the fluid is known to occur via rather localised plumes. Then the uniformity of the temperature is ensured by the transverse heat conductivity of the plates, which must be compared to the effective heat conductivity of the cell. The relevant parameter is:

$$\Lambda = (\lambda_{Cu} e)/(Nu \lambda_{He} \phi^2/h) = \frac{4}{Nu} \frac{\lambda_{Cu}}{\lambda_{He}} \frac{e}{h}$$

where ϕ is the diameter of the plate, e its thickness, h the height of the cell, λ_{Cu} (resp λ_{He}) the copper (resp Helium) conductivity. Note that the superfluid test and the maximum conductivity at the critical point, discussed above, both

give a lower bound to the conductivity of the plates. It would not be lower than 50W/K. Precise in situ measurement of this conductivity is under progress.

3.2 Ultimate regime-A controversy

One of the results of the experiments performed with this cell is the evidence of a new, high Rayleigh, convection regime which could be interpreted as the ultimate regime predicted by Kraichnan [3]. Our goal in this paragraph is not to discuss of this interpretation, but of the controversy about the data themselves.

Indeed, our result is that the Nusselt versus Rayleigh relation changes its logarithmic slope for $Ra > 10^{11}$ (figure 4). Two other experiments, with the same cell shape, have been performed with low temperature Helium gas. They disagree both with us and between them. The Wu experiment [4] (40cm high, twice ours) is in good agreement with us up to $Ra = 10^{11}$. For larger Ra, the rise in logarithmic slope they observe, if any, is very small. The recent Niemela experiment [5] (1m high, 5 times ours) gives, from $Ra = 10^6$ to $Ra = 10^{17}$, a constant slope higher than Wu's one but smaller than our final slope.

A remarkable point, in this controversy, is that an experimental mistake can hardly be invoked. The differences in Nusselt numbers at the extreme points approaches a factor of 2. There is no way to miss a factor of 2 on temperature differences of typically 100mK or Joule heating power of a fraction of a Watt. Thus we have to consider that the flows are really different, despite the fact that aspect ratio, Rayleigh and Prandtl numbers are the same.

The only possibility is that the boundary conditions are different. If the transverse conductivity of the plate is too low, heat flux cannot accomodate for the presence of a plume. The bottom plate, for instance will locally lower its temperature, stoping the developement of the plume. The free raising time of the plume is then limited to the diffusion time in the boundary layer δ, which allows it to go up to a height d:

$$\frac{d}{g\alpha\Delta} = \frac{\delta^4}{\kappa^2}$$

A similar equation was obtained by Kadanoff [15] for his intermediate distance on which plumes develop. In any case this relation implies $Nu < Ra^{1/3}$ $(d > \delta)$.

Note that this condition of high conductivity of the plates (large Λ) stands for low temperatures where the specific heat of the plates is very low. At room temperature, the available specific heat is that of the thermal skin depth in the plates at the frequency κ/δ^2. In laboratory experiments, it is generally sufficient to ensure the stability of the plate temperature.

As a general comment and concluding remark, we hope to have shown both the possibilities of fluid mechanics with Helium, and the complementary role it has versus classical experiments.

References

[1] D. C. Threlfall. Free Convection in Low Temperature Gaseous Helium *J. Fluid Mech.*, 67:17–28, 1975

[2] X. Xu, K. M. S. Bajaj, G. Ahlers. Heat Transport in Turbulent Rayleigh-Bénard Convection. *preprint*, january 2000

[3] X. Chavanne, F. Chillà, B. Castaing, B. Chabaud, B. Hébral, J. Chaussy. Observation of the Ultimate regime in Rayleigh-Bénard Convection. *Phys. Rev. Letters*, 78:3648–3651, 1997

[4] X. Z. Wu, A. Libchaber. Scaling Relations in Thermal Turbulence: The Aspect Ratio Dependence. *Phys. Rev. A*, 45:842–845

[5] J. J. Niemela, L. Skrbek, K. R. Sreenivasan, R. J. Donnelly. Turbulent Convection at very High Rayleigh Numbers. *Nature*, To be published, 2000

[6] F. Anselmet, Y. Gagne, E. Hopfinger, R. A. Antonia. High order velocity structure functions in turbulent shear flows *J. Fluid Mech.*, 140:63–89, 1984

[7] O. Chanal, B. Baguenard, O. Bethoux, B. Chabaud. Micronic-size Cryogenic Thermometer for Turbulence Measurements. *Rev. Sc. Inst.*, 68:2442–2446, 1997

[8] P. Tabeling, G. Zocchi, F. Belin, J. Maurer, H. Willaime. Probability density functions, skewness and flatness in large Reynolds number turbulence. *Phys. Rev. E*, 53:1613–1621, 1996

[9] B. Castaing, Y. Gagne, E. Hopfinger. Velocity probability density function of high Reynolds number turbulence. *Physica D*, 46:177–200, 1990

[10] S. Grossmann, D. Lohse. Characteristics scales in Rayleigh-Bénard turbulence *Phys. Letters A*, 173:58–62, 1993

[11] V. Emselem. Simulation of the flow around a hot wire anemometer. *C. R. Acad. Sc. (Paris)*, 322:11–18, 1996

[12] O. Chanal, B. Chabaud, B. Castaing, B. Hébral. Intermittency in a turbulent low temperature gaseous Helium jet. *to be published* 2000

[13] R. Benzi, S. Ciliberto, R. Tripicione, C. Baudet, F. Massaioli, S. Succi. Extended Self Similarity in Turbulent Flows. *Phys. Rev. E*, 48:R29–32, 1993

[14] X. Chavanne, B. Castaing, B. Chabaud, F. Chillà, B. Hébral. Rayleigh-Bénard Convection at very high Ra close to the ^{4}He critical point. *Cryogenics*, 38:1191–1198, 1998

[15] B. Castaing, G. Gunaratne, F. Heslot, L. Kadanoff, A. Libchaber, S. Thomae, X. Z. Wu, S. Zaleski, G. Zanetti. Scaling of Hard Thermal Turbulence in Rayleigh-Bénard Convection. *J. Fluid Mech.*, 204:1–30, 1998

ADVANCES IN TURBULENCE VIII
Proceedings of the Eighth European Turbulence Conference
C. Dopazo et al. (Eds.)
© CIMNE, Barcelona 2000

Turbulent transport and mixing

F.T.M. Nieuwstadt and G. Brethouwer

J.M. Burgers Centre, Delft University of Technology, 2628 AL Delft, the Netherlands

Contact e-mail: f.nieuwstadt@wbmt.tudelft.nl

1 Introduction

Mixing is usually considered to be one of the important characteristics of turbulence where the objective of mixing is to blend a scalar admixture into the flow until a uniform concentration is reached. On the molecular scale mixing takes place by diffusion but if this would be the only process to cause mixing, it would in general take a very long time to reach a uniform concentration. Turbulence can greatly speed up this process. Namely, turbulence generates large concentration gradients which are susceptible to fast mixing by molecular diffusion. The mechanism by which these large concentration gradients are formed, is advection and deformation by the turbulent flow field such as stretching and folding. So the combined action of turbulent transport and molecular diffusion makes mixing an efficient process in turbulence.

A turbulent flow can be characterized by the length scale ℓ and the velocity scale $\mathcal{U}$ of the large-scale turbulence structure. These scales for instance determine the dissipation $\varepsilon \cong \mathcal{U}^3/\ell$ by which the turbulent energy of the large-scale motions is transferred to the small-scale motions where it is eventually dissipated by viscosity. These smallest scales can be estimated from the ε together with the kinematic viscosity ν. For their length scale which is also known as the Kolmogorov scale η_K, we find

$$\eta_K = \left(\frac{\nu^3}{\varepsilon}\right)^{1/4}. \tag{1}$$

From the expression of ε in terms of ℓ and $\mathcal{U}$ mentioned above, it follows that $\eta_K/\ell = \mathrm{Re}_\ell^{3/4}$ with $\mathrm{Re}_\ell = \mathcal{U}\,\ell/\nu$.

Apart from Re_ℓ the process of mixing is also characterized by the Schmidt number $\mathrm{Sc} = \nu/\kappa$ where κ is the molecular diffusivity. This number determines the magnitude of concentration micro-scale in relation to the micro-structure of the turbulent velocity field. For instance for $\mathrm{Sc} \gg 1$ it follows [10]

$$\frac{\eta_B}{\eta_K} = \mathrm{Sc}^{1/2}. \tag{2}$$

where the so-called Batchelor scale η_B denotes the smallest scale of the concentration field. An example of the concentration field for the case Sc = 144 is illustrated in figure 1. It clearly illustrates the process of turbulent stretching of folding by which layers of concentration are formed together with large concentration gradients in between these layers. These results have been obtained with help of a direct-numerical simulation of isotropic turbulence with a constant concentration gradient. For the numerical solution we have used a spectral code with 64^3 - 324^3 modes for the velocity field leading to a value of $\mathrm{Re}_\lambda = U\,\lambda/\nu = 15.8 - 92.5$ where λ is the Taylor micro scale. For the resolution of the scalar field we have used $96^3 - 192^3$ modes. For further details we refer to [3]



Figure 1: Isocontours of the concentration field generated by a constant mean concentration gradient in isotropic turbulence with $\mathrm{Re}_\lambda = 15.8$ and Sc = 144.

In the following we shall present some further results based on our direct numerical simulation in order to analyze and explain the structures in the concentration field that we observe in figure 1.

2 Scalar spectra

The scalar admixture concentration c is governed by the following conservation equation

$$\frac{\partial c}{\partial t} + u_j \frac{\partial c}{\partial x_j} = \kappa \frac{\partial^2 c}{\partial x_j \partial x_j} \tag{3}$$

where $u_j(\mathbf{x},t)$ is the turbulent velocity field which we take here to be homogeneous and isotropic. The mean concentration field consists of a constant gradient Γ in the z-direction so that we can write: $c(\mathbf{x},t) = \Gamma z + \vartheta(\mathbf{x},t)$ where ϑ satisfies the equation

$$\frac{\partial \vartheta}{\partial t} + w\Gamma + u_j \frac{\partial \vartheta}{\partial x_j} = \kappa \frac{\partial^2 \vartheta}{\partial x_j \partial x_j}. \tag{4}$$

Although it has not been formally proven [5], the mean gradient Γ together with the velocity field is usually assumed to result in a stationary and homogeneous field of concentration fluctuations $\overline{\vartheta^2}$ governed by the equation

$$0 = -\overline{w\vartheta}\,\Gamma - \kappa \overline{\left(\frac{\partial \vartheta}{\partial x_j}\right)^2} \tag{5}$$

from which it becomes clear that Γ acts as a source of concentration fluctuations. The last term on the right-hand side of this equation, denoted as χ, is the molecular destruction of concentration fluctuations.

The scalar spectrum $E_\vartheta(k)$ gives the distribution of the variance $\overline{\vartheta^2}$ as a function of the wave number k. When $\mathrm{Sc} \gg 1$, the small-scale scalar fluctuation are caused by straining motions at the scale of the Kolmogorov eddies which have a magnitude $\sim \varepsilon/\nu$. For this case Batchelor [1] and Kraichnan [8] have derived expressions for the spectrum which read, respectively

$$\frac{kE_\vartheta(k)}{\chi(\varepsilon/\nu)^{1/2}} = q \exp\left(-\frac{\kappa k^2}{\varepsilon/\nu}\right) \tag{6}$$

$$\frac{kE_\vartheta(k)}{\chi(\varepsilon/\nu)^{1/2}} = q\left(1 + (6q)^{1/2}\, k\eta_B\right) \exp\left(-(6q)^{1/2}\, k\eta_B\right) \tag{7}$$

where q is a constant, which should follow from experiments. The difference between these expressions is the assumption made by Batchelor that the local small-scale straining motions which create the smallest concentration fluctuations, are steady while Kraichnan assumed the correlation time of the straining motions to be small. Both expressions agree on the behaviour of $E_\vartheta(k)$ for small values of k for which they state $E_\vartheta(k) \sim k^{-1}$.

For $\mathrm{Sc} < 1$ the assumption concerning the straining rate generating the smallest scale concentration fluctuations no longer applies. In that case Batchelor *et al.* [2] derive for the spectrum

$$E_\vartheta(k) = q\chi\kappa^{-3}\varepsilon^{2/3}k^{-\frac{17}{3}} \tag{8}$$

while Gibson [6] proposes

$$E_\vartheta(k) = q\chi^2\kappa^{-1}k^{-3} \tag{9}$$

where in both equations q is again a constant.

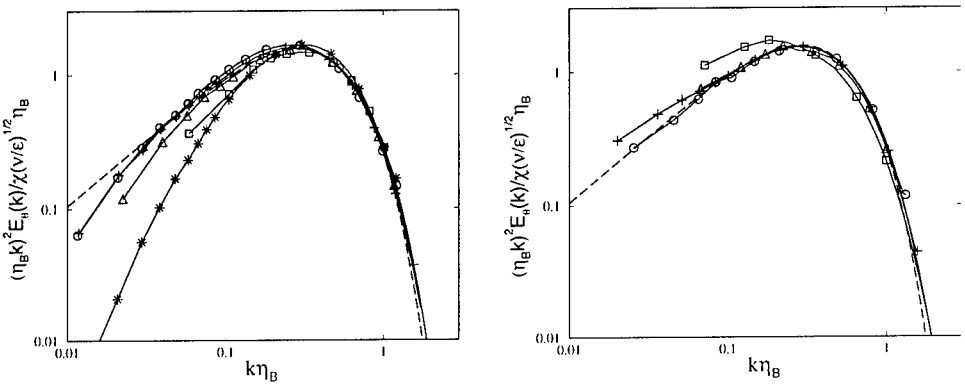


Figure 2: Scalar spectra, dashed line, Kraichnan model; Left figure: $\circ$, Sc = 144; $+$, Sc = 25; $\triangle$, Sc = 7; $\square$, Sc = 1; and $*$, Sc = 144 for the case of decaying concentration fluctuations; Right figure: Sc = 0.7; $+$, Sc = 0.5; $\triangle$, Sc = 0.1; $\square$, Sc = 0.04.

In figure 2 we show the scalar spectra for various values of Sc as computed from our direct numerical simulations. The spectra are scaled in terms of η_B which is also known as the Batchelor scaling. In the left figure of 2 we have plotted the results for Sc > 1. We find that for $k\eta_B \gtrsim 0.1$ all spectra collapse more or less on a single curve which confirms the Batchelor scaling. Moreover, in this range of $k\eta_B$ all the spectra agree very well with the Kraichnan spectrum (7) and not with the Batchelor spectrum (6) (not shown). For small values of k all computed spectra for the constant gradient case show a behaviour like $E_\vartheta(k) \sim k^{-1}$ which agrees with both the Kraichnan and the Batchelor spectrum. For the case of decaying concentration fluctuations also shown in the left figure of 2 the spectrum behaves differently and rather as $E_\vartheta(k) \sim k^{-0}$. For a further discussion on this latter behaviour we refer to [4]. In the right figure of 2 we illustrate the scalar spectra for the case Sc < 1. The spectra for $k\eta_B > 0.1$ seem still to scale according to Batchelor scaling and moreover they are again well described by the Kraichnan spectrum. A clear range where the spectra behave either as $E_\vartheta(k) \sim k^{-3}$ or $E_\vartheta(k) \sim k^{-17/3}$ is not apparent. This seems to be in contradiction with the assumption formulated in [10] that for Sc < 1 the strain rate at the Kolmogorov scale is no longer relevant. Instead we find that the spectrum remains dependent on the strain rate ε/ν.

3 Lagrangian statistics

Given the important role of the small-scale strain rate in the spectrum of the scalar fluctuations, we consider here the dynamics of concentration fluctuations and its relation to the strain rate in somewhat more detail.

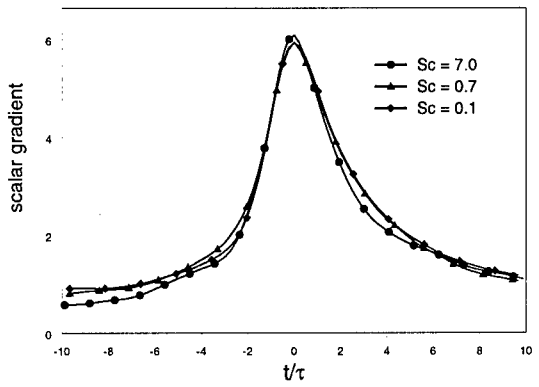


Figure 3: The ensemble-averaged absolute value of the scalar gradient normalised with the mean gradient Γ as a function of time normalized with the Kolmogorov time scale τ along the path of a fluid element. The cases shown are Sc = 0.1, Sc = 0.7 and Sc = 7

The equation for the concentration fluctuations (5) shows that these are destroyed in regions of a large scalar gradient. Therefore, we have selected in our simulation locations where the scalar gradient is large with respect to the mean gradient Γ. The turbulent dynamics which leads to this large gradient, can be best studied in a Lagrangian frame work because until molecular diffusion becomes important, the scalar concentration is advected with the flow. To this end we consider the fluid particles that are at the positions where we have found the large values of concentration gradient and for each particle we set the time equal to $t = 0$. Next we compute the trajectories of these particles both going backward, i.e. $t < 0$, and forward in time, i.e. $t > 0$. In other words we consider fluid particle trajectories conditioned on reaching a large value of the concentration gradient at the position of the particle for $t = 0$. In figure 3 we show the results for ensemble averaged behaviour of the concentration gradient as a function of travel time following these particles and for several values of Sc. These results are based on 4000 to 24000 trajectories. The time has been normalized with the Kolmogorov time scale $\tau = (\nu/\varepsilon)^{1/2}$. We see that the increase of the concentration gradient to its maximum value scales on the time scale τ and is moreover independent of Sc. In other words the destruction of concentration fluctuations, or the molecular mixing, takes place in short and intense bursts. This has for instance direct implications for processes that depend on mixing such as chemical reactions. Moreover, the process of mixing in intermittent, local events can be taken as a point of departure in modelling [7].

Let us next consider how these bursts of molecular mixing are formed. For

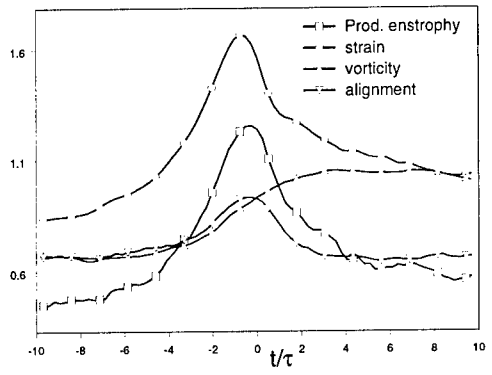


Figure 4: The ensemble-averaged values along a particle trajectory conditioned on a large value of the concentration gradient at $t = 0$ for the strain $(2s_{ij}s_{ij})^{1/2}$, the vorticity fluctuation or enstrophy $(\omega_i\omega_i)^{1/2}$, the production of enstrophy $(\omega_i s_{ij}\omega_j)$ and the alignment of the concentration gradient $\partial\vartheta/\partial x_j$ with the direction of the largest compressive strain for the case Sc = 0.7.

this we consider that evolution of some other statistics as they develop along the fluid particle trajectories that we have selected above. In particular we consider the behaviour of the strain $(2s_{ij}s_{ij})^{1/2}$, the vorticity fluctuation or enstrophy $(\omega_i\omega_i)^{1/2}$, the production of enstrophy $(\omega_i s_{ij}\omega_j)$ and the alignment of the concentration gradient $\partial\vartheta/\partial x_j$ and the direction of the largest compressive strain. The results are shown in figure 4 for the case Sc = 0.7 (for the other values of Sc the results are qualitatively the same).

If we compare the results shown in figures 3 and 4 we see that the strain rate mimics the behaviour of the concentration gradient, i.e. there is a short burst in which the strain rate increases strongly with a maximum value reached at $t = 0$, i.e. at the time instant where the maximum concentration gradient is reached. The time scale of this burst is again proportional to the Kolmogorov time scale and this fact seems to be independent of the value of Sc. This fact is consistent with the results of the previous section where we found that the spectra scale in terms of Batchelor scaling irrespective of the Schmidt number.

Simultaneously with the increase in the strain rate we see that the alignment of the concentration gradient with the direction of the largest compressive strain improves (a value 0.5 implies non-alignment and a value 1.0 perfect alignment). At the point of maximum strain rate and maximum concentration gradient we find a almost perfect alignment. It has been found that at this location the other eigenvalues of the strain rate tensor are positive which imply stretching. Therefore, locally the topology of the concentration can be visualized as a thin

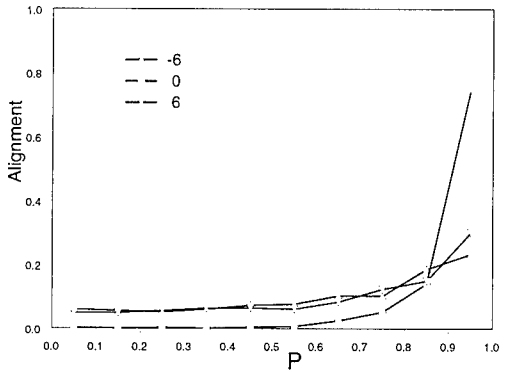


Figure 5: The probability density function of the alignment of the concentration gradient with the direction of the largest compressive strain for Sc = 0.7 for the times $t/\tau = -6$, $t/\tau = 0$ and $t/\tau = 6$.

sheet with its gradient parallel to the direction of strongest compression. This picture agrees with the contour plot shown in figure 1. This almost perfect alignment at $t = 0$ is further illustrated in figure 5 where we show the probability density distribution of the alignment with the largest compressive strain at $t/\tau = -6$, $t/\tau = 0$ and $t/\tau = 6$. For both values $t/\tau = -6$ and $t/\tau = 6$ the probability distribution is almost flat implying no alignment. In contrast at $t/\tau = 0$ the distribution has a large peak at the value 1 which means perfect alignment.

The value of the vorticity also shown in figure 4 is initially rather small and increases somewhat during the process in which the strain rate goes through its maximum. This is consistent with the behaviour of the production of enstrophy which goes through a maximum at about $t = 0$. This result leads us to conclude that the burst of strong molecular mixing are not connected to the strong small scale vortices which have been observed in turbulent flow. This fact is in agreement with the results of Ruetsch and Maxey [9]. The process of vorticity increase after $t = 0$ is possibly due to the roll up of the strong strain region.

4 Conclusions

- We have found that the spectra of scalar fluctuations collapse when plotted in terms of Batchelor scaling irrespective of the value of the Schmidt number with $0.04 < \mathrm{Sc} < 144$. Moreover for all values of the Schmidt number the spectrum agrees well with the expression derived by Kraichnan [8].
- Based on ensemble average of properties sampled along particle trajectories which are conditioned on reaching a large value of the scalar gradient at

$t = 0$, we find that the molecular mixing takes place in bursts which scale on the small-scale Kolmogorov time scale. The large concentration gradients which accompany these bursts are caused by a strong small-scale compressive strain which results in a local topology of the concentration in the form of a sheet. The vorticity during this process is small.

The authors are grateful to drs. J.C.R. Hunt and A. Tsinober for some inspiring discussions. In addition the authors are indebted to dr. A. Kerstein for his advice and to dr. T. Dubois for using his spectral code.

References

[1] G.K. Batchelor. (1959) Small scale variance of convected quantities like temperature in a turbulent fluid. *J. Fluid Mech.*, **5**, 113-133

[2] G.K. Batchelor, I.D. Howells and A.A. Townsend. (1959) Small scale variance of convected quantities like temperature in a turbulent fluid. *J. Fluid Mech.*, **5**, 134-139.

[3] G. Brethouwer and F.T.M. Nieuwstadt. (1999) Mixing of weakly and strongly diffusive passive scalars in isotropic turbulence. Direct and Large Eddy Simulation III (eds. P.R. Voke N.D. Sandham and L. Kleiser), Kluwer Acad. Publ., 311-322.

[4] J.R. Chasnov (1998) The viscous-convective subrange in non-stantionary turbulence. *Phys. Fluids.*, **11**, 1191-1205.

[5] P.A. Durbin (1980) A stochastic model of two-particle dispersion amd concentration fluctuations in homogeneous turbulence. *J. Fluid Mech.*, **100**, 2, 279-302

[6] C.H. Gibson. (1968) Fine structure of scalar fields mixed by turbulence II spectral theory. *Phys. Fluids.*, **11**, 2316-2327.

[7] S. Komori, J.C.R. Hunt, T. Kanzaki and Y. Murakami (1991) The effects of turbulent mixing on the correlation between two species and on concentration fluctuations in non-premixed reacting flows. *J. Fluid Mech.*, **228**, 629-659

[8] R.H.Kraichnan. (1974) Convection of a passive scalar by a quase-uniform random straining field. *J. Fluid Mech.*, **64**, 737-762.

[9] G.R.Ruetsch and M.R. Maxey (1992) The evolution of small-scale structures in homogeneous isotropic turbulence. *Phys. Fluids.*, **A4**, 2747-2760.

[10] H. Tennekes and J.L. Lumley. (1972)A First Course in Turbulence. The MIT press., p. 285.

V

Instabilities and Transition

ADVANCES IN TURBULENCE VIII
Proceedings of the Eighth European Turbulence Conference
C. Dopazo et al. (Eds.)
© CIMNE, Barcelona 2000

Secondary instability of streaks in boundary layers

L. Brandt [1], P. Andersson [1], and D. S. Henningson [1,2]

[1]Department of Mechanics, Royal Institute of Technology (KTH)
S–100 44 Stockholm, SWEDEN
[2]FFA, the Aeronautical Research Institute of Sweden,
P.O. Box 11021, S–161 11 Bromma, SWEDEN

Contact e-mail: luca@mech.kth.se

A scenario for bypass transition to turbulence likely to occur in natural transition in a flat plate boundary layer flow is studied. The disturbances at the leading edge of the flat plate that show the highest potential for transient energy growth consist of streamwise aligned vortices. Due to the lift-up mechanism these optimal disturbances are transformed downstream into elongated streamwise streaks with significant spanwise modulation. The initial disturbance that yields the maximum spatial transient growth in a non-parallel flat plate boundary layer flow was determined by Andersson, Berggren & Henningson [2] by applying the boundary layer approximations to the three-dimensional steady incompressible Navier-Stokes equations and linearising around the Blasius base flow. If the disturbance energy of the streaks becomes sufficiently large, secondary instability can take place and provoke early breakdown and transition, overruling the theoretically predicted modal decay. A possible secondary instability is caused by inflectional profiles of the base flow velocity, a mechanism which does not rely on the presence of viscosity. Experiments with flow visualisations by for example Alfredsson & Matsubara [1] have considered the case of transition induced by streaks formed by the passage of the fluid through the screens of the wind-tunnel settling chamber. They report on the presence of a high frequency "wiggle" of the streak with a subsequent breakdown into a turbulent spot.

Direct Numerical Simulations (DNS), using a numerical code described in [5], are used to follow the nonlinear saturation of the optimally growing streaks in a spatially evolving boundary layer. The complete velocity vector field from the linear results by Andersson *et al.* [2] is used as input close to the leading edge and the downstream nonlinear development is monitored for different initial amplitudes of the perturbation. To be able to quantify the size of the primary disturbance field an amplitude A is defined as

$$A = \frac{1}{2}\left[\max_{y,z}(U - U_B) - \min_{y,z}(U - U_B)\right]. \qquad (1)$$

Using linear Floquet theory we study the temporal, inviscid secondary instability of these streaks to determine the characteristic features of their breakdown. The linear secondary stability calculation are carried out on the basis of the boundary layer approximation, i.e. the mean field to leading order will consist only of the streamwise velocity component (here denoted U), consistent with the scaling hypothesis which led to the definition of the streak. Such a mean field varies on a slow streamwise scale, whereas the secondary instability varies rapidly in the streamwise direction x, as observed in the visualisations [1]. Hence, our leading order stability problem is the parallel flow problem, with perturbation mode shapes dependent only on the cross-stream coordinates y (wall-normal) and z (spanwise).

The equations governing the stability of the streak are obtained by substituting $\mathbf{U}+\mathbf{u}$, where $\mathbf{u}(x,y,z,t)=(u,v,w)$ is the perturbation velocity and $\mathbf{U}$ is the streak profile above, into the Navier–Stokes equations and dropping nonlinear terms in the perturbation. If viscosity is neglected it is possible to find an uncoupled equation for the pressure by taking the divergence of the momentum equations and introducing continuity (see [4]). These manipulations yield

$$(\frac{\partial}{\partial t} + U\frac{\partial}{\partial x})\Delta p - 2U_y p_{xy} - 2U_z p_{xz} = 0. \tag{2}$$

The pressure is expanded in an infinite sum of Fourier modes and only perturbation quantities consisting of a single wave component in the streamwise direction are considered, i.e.

$$p(x,y,z,t) = Real\{e^{i\alpha(x-ct)} \sum_{k=-\infty}^{\infty} \hat{p}_k(y) e^{i(k+\gamma)\beta z}\},$$

where α is the real streamwise wavenumber and $c = c_r + ic_i$ is the phase speed. Here β is the spanwise wavenumber of the primary disturbance field and γ is the (real) Floquet exponent. Because of symmetry it is sufficient to study values of γ between zero and one half, with $\gamma = 0$ corresponding to a *fundamental* instability mode, and $\gamma = 0.5$ corresponding to a *subharmonic* mode. The most commonly used definitions of *sinuous* or *varicose* modes of instability are adopted with reference to the visual appearance of the motion of the *low-speed streaks*; the symmetries of the subharmonic sinuous/varicose fluctuations of the low-speed streaks are always associated to staggered (x) varicose/sinuous oscillations of the high-speed streaks.

We show that the linear and nonlinear spatial development of optimal streamwise streaks are both well described by the boundary layer approximations and as a consequence Reynolds number independent for large enough Reynolds numbers. This results in a boundary layer scaling property that couple the streamwise and spanwise scales, which implies that the same solution is valid for combinations of the streamwise position, x, and spanwise wavenumber, β, such that the product $x\beta^2$ stays constant. The parameter study of streak's instability is

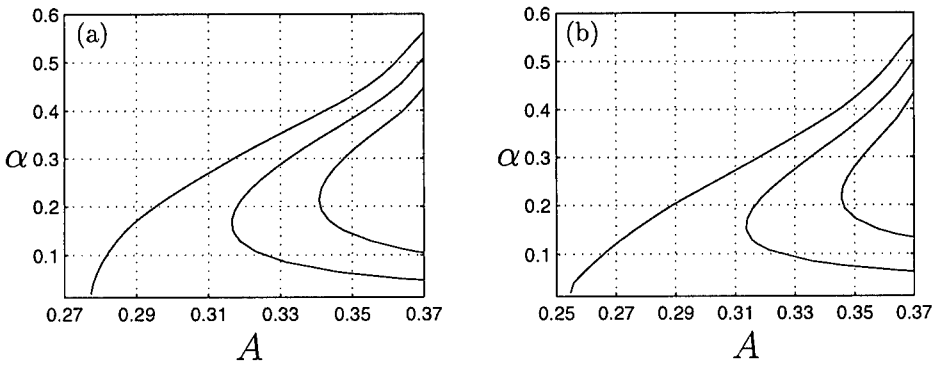


Figure 1: Neutral curves for streak instability in the A-α plane for (a) fundamental sinuous mode, (b) subharmonic sinuous mode. (contour levels: ω_i=0, 0.0046, 0.0092)

therefore representative of a wide range of intermediate values of β for which saturation occurs at a reasonable x; large enough so that the boundary layer approximation may still be valid and small enough so that Tollmien–Schlichting waves may not play a significant role.

The parameter study was conducted also to identify the neutral stability curves calculated for a range of α's. These results are displayed in figures 1 for the two sinuous symmetries, together with contour levels of constant growth rates. It can immediately be observed that a streak amplitude of about 26% of the free-stream speed is needed for an instability to occur. One can also notice that the subharmonic mode is unstable for lower amplitudes than the fundamental mode and that the growth rates for larger amplitudes are quite close for the two symmetries.

No results for the varicose instabilities are presented here. In fact, both the varicose fundamental and the subharmonic symmetries result in weak instabilities for amplitudes larger than A=0.37 with growth rates smaller than one fifth of the corresponding sinuous growth rates. Therefore a breakdown scenario triggered by a varicose instability seems unlikely.

Numerical experiments on streak's instability are also carried out using DNS and the results are compared with the linear stability calculations. The secondary disturbances are triggered using a harmonic volume force with frequency ω=0.211, while linear temporal stability calculations, using the real part of the streamwise wavenumber obtained from the direct numerical simulations, α_r=0.260, are also performed, employing mean fields extracted at different streamwise positions from the DNS. In order to compare the spatial results to the growth rates obtained from the temporal inviscid stability problem Gaster's transformation is used [3]. The results are shown in figure 2, where the u_{rms} distribution of the fundamental sinuous mode at x=2 is also displayed.

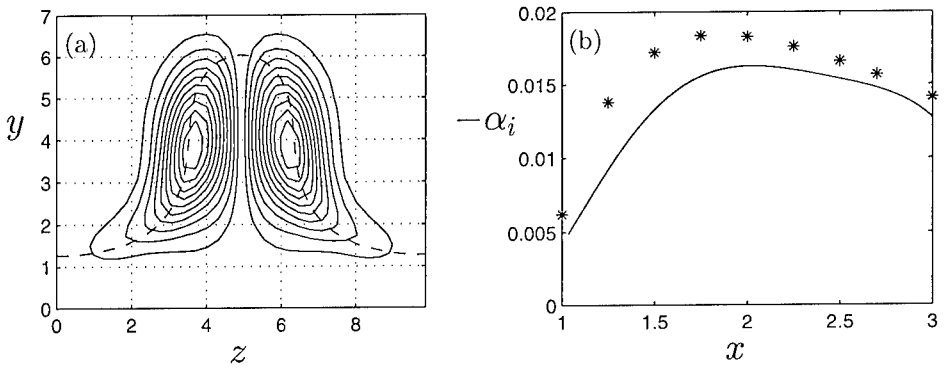


Figure 2: (a) Isocontours of rms values of the streamwise velocity component of the secondary disturbance (ω_r=0.211) for the fundamental sinuous mode at x=2, obtained from the DNS. The dashed line represents the contour of the constant value of the mean field corresponding to the phase speed of the disturbance ($U = c_r = 0.80$). (b)Spatial growth rates, α_i versus x; —– DNS data with Re_δ=430 and β=0.45; $*$ linear temporal inviscid stability calculations using mean fields at each corresponding x position and streamwise wavenumber α_r=0.260.

References

[1] ALFREDSSON, P. H. & MATSUBARA, M. 1996 Streaky structures in transition In *Proc. Transitional Boundary Layers in Aeronautics.* (ed. R. A. W. M. Henkes & J. L. van Ingen), pp. 373-386, Royal Netherlands Academy of Arts and Sciences. Elsevier Science Publishers.

[2] ANDERSSON, P., BERGGREN, M. & HENNINGSON, D. S. 1999 Optimal disturbances and bypass transition in boundary layers. *Phys. Fluids* **11**, 134.

[3] GASTER, M. 1962 A note on the relation between temporally-increasing and spatially-increasing disturbances in hydrodynamic stability *J. Fluid Mech.* **14**, 222.

[4] HALL, P. & HORSEMAN, N. J. 1991 The linear inviscid secondary instability of longitudinal vortex structures in boundary-layers. *J. Fluid Mech.* **232**, 357.

[5] LUNDBLADH, A., BERLIN, S., SKOTE, M., HILDINGS, C., CHOI, J., KIM, J. & HENNINGSON, D. S. 1999 An efficient spectral method for simulation of incompressible flow over a flat plate. *TRITA-MEK Technical Report* 1999:11, Royal Institute of Technology, Stockholm, Sweden

ADVANCES IN TURBULENCE VIII
Proceedings of the Eighth European Turbulence Conference
C. Dopazo et al. (Eds.)
© CIMNE, Barcelona 2000

On early stage instability of separated boundary layer transition

Z.Y. Yang[1] and P.R. Voke[2]

[1]Department of Aeronautical and Automotive Engineering
Loughborough University, Loughborough LE11 3TU, U.K.
[2]School of Mechanical and Materials Engineering
University of Surrey, Guildford GU2 5XH, U.K.

Contact e-mail: z.yang@lboro.ac.uk

1 Abstract

A feature of laminar separated flows is that they become unstable at relatively low Reynolds numbers. As a result, the mean-flow pattern and unsteady behaviour is then governed, largely, by instability and transition. We report the use of large-eddy simulation to study the early stage instability of separated boundary layer transition induced by a change of curvature of the surface. The geometry is a flat plate with a semi-circular leading edge. The Reynolds number based on the uniform inlet velocity and the leading edge diameter ($d = 10mm$) is 3450. It is shown from the simulation that transition starts with the primary 2D instability originating from the free shear in the bubble as the free shear layer is inviscidly unstable via the Kelvin-Helmholtz mechanism.

2 Introduction

Laminar boundary layer separation and transition is a fundamental flow phenomenon and occur in many important engineering flows. Despite intensive research over the past several decades our understanding is still far from complete [1, 3, 4, 7]. A free shear layer is formed as a laminar boundary layer separates owing to curvature changes in the present study. When a laminar boundary layer separates, its instability increases since the free shear layer formed in the separation bubble could be inviscidly unstable. Kiya and Sasaki [5] indicate from their separated boundary layer study that the large-scale vortices originate from a successive amalgamation of vortices formed in the separated shear layer through the Kelvin-Helmholtz instability. However, sufficient and detailed evidence has not been given in separated boundary layer transition studies to show that the instability mechanism at work is indeed the Kelvin-Helmholtz instability. The main objective of this paper is to demonstrate that the free shear

layer in the separation bubble is inviscidly unstable via the Kelvin-Helmholtz instability mechanism by analysing the LES data and comparing the results with those of the inviscid linear stability analysis.

3 Numerical methods

The fully covariant general incompressible Navier-Stokes equations are discretised on a staggered mesh using finite volume methods, together with a generalised dynamic subgrid scale model. The explicit second order Adams-Bashforth is used for the momentum advancement except for the pressure term. The Poisson equation for pressure is solved using a efficient hybrid Fourier multigrid method with the periodic boundary conditions applied in spanwise dimension. Details of the mathematical formulation and numerical methods in general coordinates used in the present study have been reported elsewhere [6].

4 Results and discussion

Figures 1 shows the mean and rms fluctuating parts of the streamwise velocity compared with the experimental data at seven streamwise stations. The simulated mean bubble length is about $2.56d$, slightly shorter than the experimental one ($2.75d$). The profiles are plotted as functions of y/l at corresponding values of x/l where l is the mean reattachment length. As can be seen from figure 1 very good agreement between the experimental data and the simulated results has been obtained for the mean streamwise velocity profiles. The agreement for the rms fluctuations is also good except that the simulation shows higher peaks of u' occurring closer to the wall at two stations in the bubble, especially at $x/l = 0.66$ where the discrepancy between the peak values is about 22%. After the reattachment the agreement is much better.

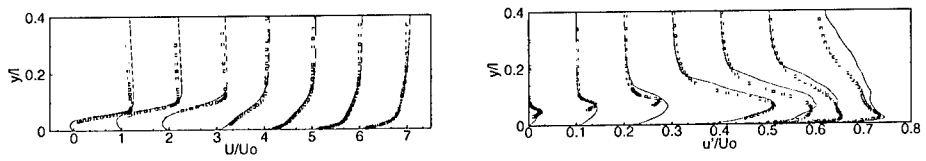


Figure 1: Mean axial velocity at seven streamwise positions measured from the blend point. Left to right, x/l = 0.22, 0.44, 0.66, 1.09, 1.27, 1.64, 2.55. Line—LES; Symbols—Exp. data

The transition process can be clearly seen in figure 2 which shows a snapshot of the instantaneous spanwise vorticity in the (x, y) plane at an arbitrary z (spanwise) position. In the first half of the bubble a free shear layer develops and spanwise vortices forms; these are inviscidly unstable and any small disturbances present grow downstream with a amplification rate larger than that in the case

of viscous instabilities. Further downstream the initial spanwise vortices are distorted severely and roll up, leading to streamwise vorticity formation associated with significant 3D motions, eventually breaking down at about the reattachment point and developing into a turbulent boundary layer rapidly afterwards.

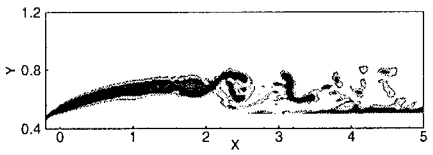


Figure 2: Instantaneous spanwise vorticity in the (x, y) plane

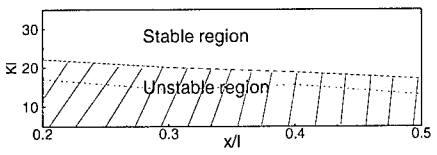


Figure 3: Stable and unstable wave numbers; dashed line—LES

In order to clarify whether the instability of the free shear layer in the present study is the Kelvin-Helmholtz instability. Let us consider the Kelvin-Helmholtz mechanism in more detail. The Kelvin-Helmholtz instability was originally derived considering two uniform incompressible inviscid fluids of densities ρ_1, ρ_2 and velocity U_1, U_2 separated by a horizontal boundary at y=0. Let the density ρ_1 of the upper fluid be less than the density ρ_2 of the lower fluid so that the arrangement is a stable one when U_1 and U_2 are zero. For a given difference in velocity $U_2 - U_1$, no matter how small it is, instability occurs for all wave numbers larger than a critical value (for disturbances of sufficiently small wavelengths) or it can be stated that for a given wave number instability occurs if the velocity difference $U_2 - U_1$ is larger than a critical value. This is the Kelvin-Helmholtz instability [2]. What remains to be clarified is whether the Kelvin-Helmholtz instability occurs due to the sharp discontinuities in ρ and U which has been assumed in its derivation. Chandrasekhar [2] considered the case of continuous variation of U and certain distribution of ρ (characterized by the Richardson number) and concluded from the inviscid linear stability analysis that, for any values of the Richardson number, there are always bands of wavelengths for which the Kelvin-Helmholtz instability occurs. In particular, when the Richardson number is zero, i.e. for constant density, the condition for the Kelvin-Helmholtz instability to occur is $0 < Kh < 1.2785$ where K is the wave number and h is the shear layer thickness. In the present study the shear layer thickness in the region where the unsteadiness first becomes apparent at about $x/l = 0.2$ (l is the mean separation bubble length) is $0.0577l$ and hence the unstable region for K is $0 < K < 22.16/l$. In other words, the Kelvin-Helmholtz instability will not occur in the present study for wave numbers larger than $22.16/l$, or wavelength smaller than $2\pi/K = 0.2836l$. The characteristic frequency in the present study varies from about 100 to 220Hz (obtained from spectra of u' in the separation bubble) and the wave speed c is equal to the velocity at the critical layer, $U(y_c)$ i.e., the streamwise velocity at the inflection point where $d^2U(y_c)/dy^2 = 0$ which is about $0.42U_0$ at $x/l = 0.2$. Therefore the maximum wave number from the simulated results is $K_{max} = 2\pi f_{max}/c = 17.05/l$, corresponding to a wavelength

of $0.368l$, which satisfy the Kelvin-Helmholtz instability criterion for the present study ($0 < K < 22.16/l$). Several locations between $0.2 < x/l < 0.45$ have also been checked and the maximum wave numbers are all within the unstable region according to the Kelvin-Helmholtz instability criterion for constant density and continuous variation of U velocity [2] as shown in figure 3. Thus it can be concluded that the free shear layer in the separation bubble is likely to become inviscidly unstable via the Kelvin-Helmholtz instability mechanism.

5 Conclusions

The study of separated boundary layer transition on a flat plate with a semi-circular leading edge has been carried out numerically and the predicted mean and turbulence quantities compare well with the experimental data. From detailed analysis of the LES data, it has been shown that transition starts with the 2D instability of the free shear layer formed in the separation bubble which is inviscidly unstable via the Kelvin-Helmholtz instability mechanism.

The authors gratefully acknowledge the support of EPSRC, DERA and Rolls-Royce plc who funded this research. We thank Dr. Mark Savill and Dr. John Coupland for their advice.

References

[1] F. K. Browand. An experimental investigation of the instability of an incompressible, separated shear layer *J. Fluid Mech.*, 26:281–307, 1966.

[2] S. Chandrasekhar. Hydrodynamic and hydromagnetic stability. , Clarendon Press, Oxford, 1961.

[3] A. V. Dovgal, V. V. Kozlov, and A. Michalke. .Laminar boundary layer separation: instability and associated phenomena *Prog. Aerospace Sci.*, 30:61–94, 1994.

[4] M. E. Goldstein. Generation of instability waves in flows separating from smooth surfaces. *J. Fluid Mech.*, 145:71–94, 1984.

[5] M. Kiya and K. Sasaki. Structure of large-scale vortices and unsteady reverse flow in the reattaching zone of a a turbulent separation bubble. *J. Fluid Mech.*, 154:463–491, 1985.

[6] Z. Y. Yang and P. R. Voke. Large-eddy simulation of separated leading-edge flow in general co-ordinates. Accepted to be published in *Int. J. for Num. Methods in Eng.*, 2000

[7] Z. Y. Yang and P. R. Voke. Large-eddy simulation of boundary-layer separation and transition at a change of surface curvature. Submitted to *J. Fluid Mech.*, 2000

ADVANCES IN TURBULENCE VIII
Proceedings of the Eighth European Turbulence Conference
C. Dopazo et al. (Eds.)
© CIMNE, Barcelona 2000

Experimental study of tuned and detuned resonant interactions of instability waves in self-similar boundary layer with an adverse pressure gradient

V.I. Borodulin, Y.S. Kachanov and D.B. Koptsev

Institute of Theoretical and Applied Mechanics, Russian Academy of Sciences,
Siberian Division, 630090, Novosibirsk, Russia

Contact e-mail: danil@itam.nsc.ru

1 Introduction

The first strict experimental evidence of the enhancement of the instability wave growth in presence of an adverse pressure gradient (APG) has been obtained in the classical experiments by Schubauer and Skramstad [1]. Probably first strong evidence of an important role of the subharmonic resonance in the process of the laminar-turbulent transition in the APG boundary layer was obtained experimentally in [2]. The only available at present direct experimental study of the subharmonic resonant interactions in the APG boundary layer was performed in [3] for rather small values of the Hartree parameter ($\beta_H = -0.06$ and -0.09). In agreement with the theoretical prediction the rapid growth and subsequent saturation of the subharmonic amplitudes was found at controlled disturbance conditions. However, the double-exponential growth and the explosive amplification have not been found. Moreover, some important properties of the resonant interactions were not investigated.

The goal of the present experiments was to fill the gaps existing in this area, in particular to investigate in more detail both the properties of the tuned and detuned subharmonic resonances in the APG boundary layer and to clear up the subsequent destiny of the transition process including its essentially nonlinear stages.

2 Experimental Setup and Basic Flow

Experiments were conducted in the low-turbulence subsonic wind tunnel T-324 of the ITAM at the free-stream velocity $U_o \approx 9$ m/s. The APG was induced over a flat plate (equipped with a flap and installed horizontally) with the help of

an adjustable wall-bump. In general the experimental setup was similar to that used in [4]. A special disturbance source was used for excitation of the 2D and 3D instability modes in a controlled way. The source was mounted at a distance $x_s = 300$ mm ($Re = 770$) from the leading edge of the plate and consisted of a set of "point-like sources" aligned with the model span. Main features of such generator are described in [5].

The basic flow under investigation was a self-similar boundary layer with Hartree parameter $\beta_H = -0.115$. All measurements were carried out by means of a hot-wire anemometer.

3 Generation of Disturbances

In the present work the disturbance source was used in a number of regimes. In main regimes the following modes were excited: (i) a large-amplitude 2D fundamental wave ($f_1 = 109.1$ Hz, $\beta = 0$) and a pair of small-amplitude 3D subharmonics ($f = f_{\frac{1}{2}} = f_1/2 = 54.6$ Hz, $\beta = \pm\beta_{\frac{1}{2}}$) simultaneously, (ii) the 2D fundamental mode only (regime F), (iii) the pair of subharmonics only (regime S), (iv) the fundamental mode introduced simultaneously with a small-amplitude continuous-spectrum ('noise-like') disturbance that simulated some background boundary-layer perturbations (regime NR), and (v) the 'noise-like' disturbance only (regime N). In regime (i) three sub-regimes were investigated, namely: regime MR (Main Resonant regime) – with an initial fundamental (Fun) amplitude $A_{01} = A_{m01}$ and an initial subharmonic (Sub) amplitude $A_{0\frac{1}{2}} = A_{m0\frac{1}{2}}$ and with a 'resonant' phase relationship between the Sub and Fun modes; regime 2FR – with two times greater initial Fun amplitude $A_{01} = 2A_{m01}$ and Sub amplitude $A_{0\frac{1}{2}} = A_{m0\frac{1}{2}}$; and regime AR (Anti-Resonant regime) – with initial Fun and Sub amplitudes the same as in regime MR but with a phase shift between the Fun and Sub modes orthogonal to the resonant one (ϕ_{01} was shifted by π). In addition a dependence of the disturbance behavior on initial phase relationship was studied for various initial phases. An influence of Sub frequency detuning on the resonant interaction was also studied at conditions of regime MR but at excitation of quasi-subharmonic wave at frequencies $f = f_{\frac{1}{2}} + \Delta f$, where Δf varied from $-0.9f_{\frac{1}{2}}$ to $+0.9f_{\frac{1}{2}}$ (regimes MRD).

In order to satisfy the resonance phase synchronism conditions the pair of Sub waves with a spanwise wavelength of $\lambda_{z\frac{1}{2}} = 48$ mm $\approx 2\pi/\beta_{\frac{1}{2}}$ and with the wavenumbers $\beta_{\frac{1}{2}} = \pm 0.134$ rad/mm, $\alpha_{r\frac{1}{2}} = 0.103$ rad/mm has been chosen in all studied regimes when the Sub or quasi-Sub waves were excited.

4 Subharmonic Resonance and Its Properties

An exponential growth of the Fun wave is observed both in regime MR and F (Figure 1). In regime F the Sub waves grow also exponentially. However, during the resonant interaction (regime MR in Figure 1) the Sub-waves growth

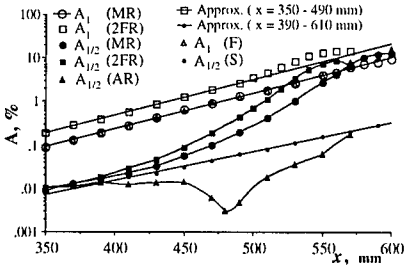


Figure 1: Amplification curves for Fun and Sub waves.

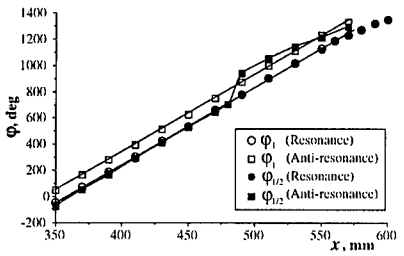


Figure 2: Evolution of the phases in MR and AR regimes.

increases. It was found that this growth is double exponential. The phase behavior (Figure 2) observed in regime MR has shown a satisfaction of the phase synchronism conditions that is necessary for the resonant amplification of subharmonics.

The difference of the AR regime from MR is in a phase shift of Fun wave by 180 degrees. In this case the Sub wave attenuates initially because the phase relationship is orthogonal to the resonant one (see Figure 2). In the end (beyond the $x \approx 470$ mm) the subharmonics starts to amplify because a very small component of the Sub wave with the resonant phase shift survives, while the component with the orthogonal phase is disappeared.

The dependence of the subharmonics amplitude at $x = 510$ mm (far from the source) on initial phase shift has shown both a very strong amplification of the subharmonic when the resonant component is present and even its suppression when the phase shift is orthogonal ($\Delta\phi \approx 240°$).

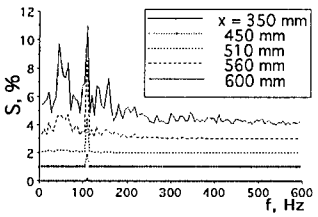


Figure 3: Amplitude spectra in NR regime

Variation of the initial frequency of quasi-subharmonic waves has shown that the subharmonic resonance has a great width in the frequency spectrum and can amplify even waves with frequencies $0.1f_{\frac{1}{2}}$ and $1.9f_{\frac{1}{2}}$!

In regime 2FR the increment of the double-exponential growth of subharmonic increases (see Figure 1). An additional growth of the Fun wave is observed at late stages due to an essentially non-linear interaction with the subharmonics. This growth is called in weakly-nonlinear theory an 'explosive growth'.

It is seen from Figure 3 that the resonance amplifies a wide continuous spectrum of perturbations, which are shown to be 3D ones with a dominant spanwise wavenumber close to that studied in resonant regimes with deterministic Sub waves. The amplification curves measured in regime NR has shown that start-

ing from $x \approx 450$ mm the random quasi-subharmonic perturbations start to be amplified with the same double-exponential growth rate as in regime MR. The resonant phase synchronism condition was found to be also satisfied in regime NR in the range of the resonant amplification of continuous-spectrum perturbations.

5 Conclusions

- The subharmonic resonance is studied using an advanced methods of measurements and data processing. Similar to the Blasius case the resonance is found to be very strong.
- The resonance is shown to be very wide in the frequency spectrum and very sensitive to the phase shift between the subharmonic and fundamental waves.
- The resonance is found to lead to a very rapid amplification of background continuous-spectrum perturbations.
- The double-exponential resonant growth of the subharmonic (tuned and detuned) waves, predicted by weakly-nonlinear theory, is found experimentally.
- An experimental evidence of the "explosive" (at least "additional") amplification of the fundamental wave under the influence of the subharmonic waves is found at late stages of the resonant interaction (following after the stage of parametric resonance).

The work was supported by Russian Foundation for Basic Research (grant 0001-00835).

References

[1] G. B. Schubauer, H. K. Skramstad. Laminar boundary layer oscillation and stability of laminar flow. NACA Rep. No 909, 1948.

[2] F. J. M. Wubben, D. M. Passchier, J. L. Van Ingen. Experimental investigation of Tollmien-Schlichting instability and transition in similar boundary layer flow in an adverse pressure gradient. *In: Laminar-Turbulent Transition (D. Arnal, R. Michel, eds)*, pp. 31–42. Berlin: Springer-Verlag, 1989.

[3] T. Corke , S. Gruber. Resonant growth of three-dimensional modes in Falkner-Skan boundary layers with adverse pressure gradients. *J. Fluid Mech.*, 320: 211–233. 1996.

[4] Y. S. Kachanov , D. B. Koptsev. Three-dimensional stability of self-similar boundary layer with negative Hartree parameter. 1. Wave trains. *Thermophysics and Aeromechanics*, 6, No 4, 463–477. 1997.

[5] V. I. Borodulin, V. R. Gaponenko, Y. S. Kachanov. Investigation of normal instability modes in a three-dimensional boundary layer. *Thermophysics and Aeromechanics*, 5, No 1, 21–31. 1998.

ADVANCES IN TURBULENCE VIII
Proceedings of the Eighth European Turbulence Conference
C. Dopazo et al. (Eds.)
© CIMNE, Barcelona 2000

Investigation of hypersonic boundary layer stability on cone with the help of artificial disturbances

D. A. Bountin, A. A. Maslov, A. N. Shiplyuk and A. A. Sidorenko

Institute of Theoretical and Applied Mechanics SB RAS
Institutskaya 4/1, Novosibirsk, 630090, Russia

Contact e-mail: sindr@itam.nsc.ru

1 Introduction

Investigations of stability and transition of hypersonic boundary layers are critical for design of high-velocity vehicles because the state of boundary layer determines drag and heat transfer. Besides, these researches form a part of more common fundamental problem of transition to turbulence. The studies in this field either numerical or experimental were conducted actively over last decades. The latest achievements are published in [1],[2]. So as a rule in these experiments development of natural disturbances was studied. The progress of computational methods and the necessity of their verification call for information about structure of disturbances developing in the boundary layer. This information may be obtained through the application of artificial wave packet method.

2 Experiments

The experiments were carried out in blowdown wind tunnel T-326, ITAM SB RAS at free stream Mach number M_∞=5.92 and Re_1=12.5·10^6 m^{-1}. The stability of hypersonic boundary layer with reference to both natural and artificial disturbances was studied on a sharp and blunted cones with half angle of 7 degree. The length of model was 500 mm, nose bluntness radius was R_n=2 mm.

A high frequency point glow discharge situated at a distance of 70 mm from model nose of sharp cone was used to generate the artificial wave packets [3]. Such a packet consists of many inclined waves. The development of this wave train in the boundary layer was registered by a constant temperature hot wire anemometer in frequency band up to 500 kHz. Hot wire was moved in longitudinal and vertical direction at the same time the model was rotated. As a result,

three-dimensional distributions of pulsations were obtained, which were decomposed into a Fourier series. Investigation of natural disturbances was executed in ordinary manner.

The measured cross distributions of natural and artificial disturbance amplitudes on the sharp cone are typical for laminar hypersonic boundary layers (Figure 1). For all frequencies fluctuation amplitude maxima are grouped in the narrow layer approximately at $0.75 \div 0.8\delta$. It is evident that maximum value of disturbances amplitude decreases as nose radius rises. Such a decrease of fluctuation amplitude may be explained through the decrease of boundary layer receptivity to free stream disturbances when nose radius increases. Distribution of artificial disturbances amplitude agree with natural one and LST calculation.

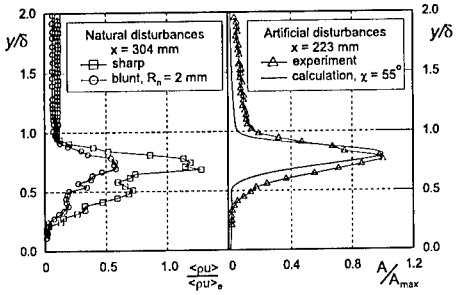


Figure 1: Cross distribution of disturbance amplitude.

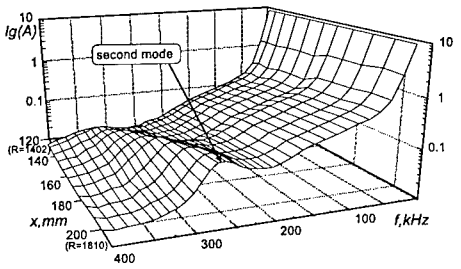


Figure 2: Pulsation spectra at maximum energy location for sharp cone.

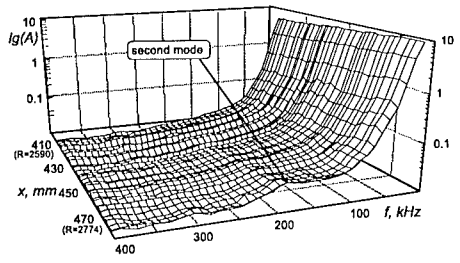


Figure 3: Pulsation spectra at maximum energy location for blunted (R_n=2 mm) cone.

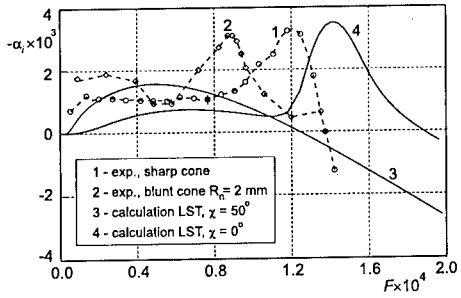


Figure 4: Amplification rates.

The measurements in maximum energy location were carried out for determination of amplification rates of instability waves. The longitudinal distributions of fluctuation spectra for natural disturbances are presented in Figures 2,3. It is possible to observe a peak on high frequencies ($F = 2\pi f/Re_1 U_e = 1 \div 1.5 \cdot 10^{-4}$) which corresponds second mode of instability waves. The amplitude increase and shift of fluctuation maximum to low frequencies side is seen clearly. The

estimation of wave length of these fluctuations (with use of theoretical phase velocity) shows that it is approximately equal to the two boundary layer thicknesses. Such a behavior is typical for the second disturbances mode: mode wavelength is approx 2δ, and that is why wave length increases and thus frequency decreases. The amplitudes distributions versus R=$\sqrt{Re_x}$ are smoothed and approximated with polynomial. Then the amplification rates are calculated by the following formula: $-\alpha_i = 0.5(\partial \ln A_f / \partial R)$. The results of processing and numerical calculations are given in Figure 4. In the area of frequencies corresponding with the second disturbances mode, the peak is seen clearly. Though the main energy of fluctuations is accounted for low frequency fluctuations, corresponding with the first mode, the second mode waves are more unstable, as the theory predicts. A good qualitative and quantitative coincidence of calculated and experimental α_i values is seen. It is seen from Figure 3 and 4 that on blunted cone just only low-frequency disturbances exist but increase in the area of high frequencies is observed. Comparison of spectra and amplification rates shows that disturbances rises slower on bluntned cones. At the same time second mode disturbances have great amplification in pre-transitional zone.

Frequency range of generated artificial disturbances for sharp cone was chosen in view of results of natural disturbances development studying and LST. From the obtained fluctuation spectra distributions in the maximum fluctuations layer (Figure 2) two frequencies were chosen f_1=78.125 kHz (F=0.38·10^{-4}) and f_2=266 kHz (F=1.29·10^{-4}); they conform to the most unstable disturbances of the first and second mode correspondingly. As the value of a phase velocity C_x weakly depends on wave inclination angle, the measurements of C_x were realized in center of wave packet in the maximum fluctuations layer. Measured phase velocity is equal to 0.89 and 0.9 for first and second mode correspondingly.

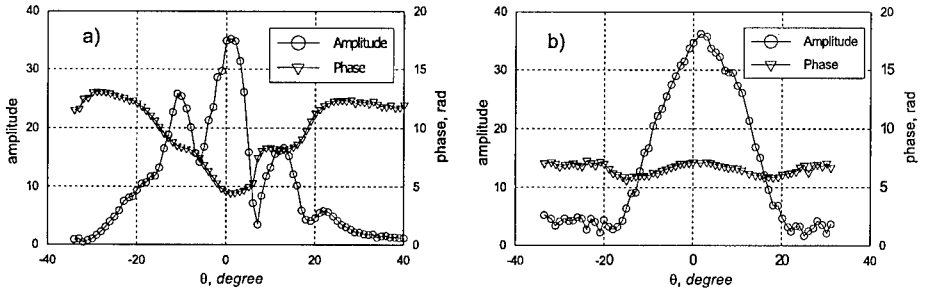


Figure 5: Spanwise distribution of amplitude for first (a) and second (b) modes.

In Figure 5 there are the examples of distributions of amplitude A and phase Φ of artificial disturbances on angle of model rotation θ. Small asymmetry caused by the source was found out in each section on x. The spatial amplitude spectra obtained after Fourier decomposition are presented in Figure 6. The spanwise wave number β has the scale rad/(deg of θ). It is viewed that two peaks with

β=±0.28 rad/deg stand out on the spectra for the first mode. Depending on position of section they are correspond to pair of inclined waves with χ=40÷49° which predominate in wave packet. Amplification rates of these inclined waves obtained from spectra are in range $-\alpha_i$=0.9÷1.7·10^{-3}. Calculation in terms of LST result in $-\alpha_i$=1.6·10^{-3} for the most unstable waves of χ=57°. The amplitude β spectrum (Figure 6b) for second mode has the narrow peak when β=0; it means that two-dimensional wave prevail in the packet. Measured amplification rate for second mode is $-\alpha_i$=3.4·10^{-3} and theoretical value is $-\alpha_i$=2.1·10^{-3}. So waves of second mode are two-dimensional and their amplification rates are greater than for first mode. This result corresponds with the results of research of natural disturbances development, presented above.

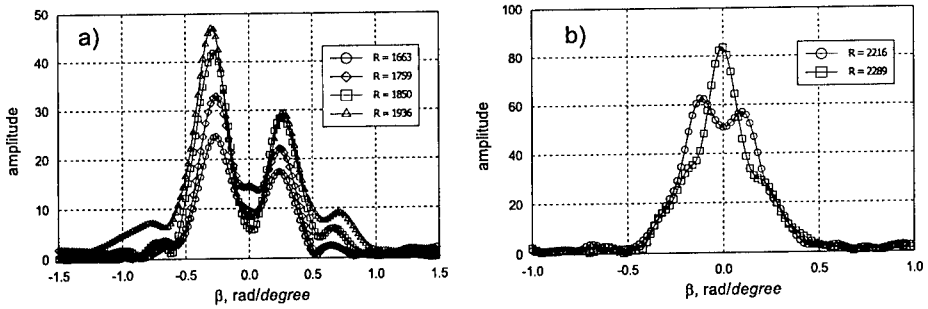


Figure 6: Amplitude and phase spectra of first (a) and second (b) mode artificial disturbances versus transversal wave number β.

This research has been supported in part by the project 128 of the International Science Technology Center, and by project 98-01-00735 of Russian Foundation of Basic Research.

References

[1] H. Reed, R. Kimmel, S. Schneider, D. Arnal. Drag Prediction and Transition in Hypersonic Flow. *AIAA Paper N 97-1818*, 1997.

[2] K. Stetson, R .Kimmel. On Hypersonic Boundary-Layer Stability. *AIAA Paper N 92-0737*, 1992.

[3] A. A. Maslov, A. D. Kosinov, S. G. Shevelkov. Experiments on the stability of supersonic laminar boundary layers. *J. Fluid Mech.*, 219:621–633, 1990.

ADVANCES IN TURBULENCE VIII
Proceedings of the Eighth European Turbulence Conference
C. Dopazo et al. (Eds.)
© CIMNE, Barcelona 2000

Sensitivity Analysis Using Adjoint Parabolized Stability Equations for Compressible Flows

J. O. Pralits[1], C. Airiau[2], A. Hanifi[3] and D. S. Henningson[1,3]

[1]Department of Mechanics, KTH SE-100 44 Stockholm, Sweden
[2]Institut de Mécanique des Fluides de Toulouse Allée du professeur Camille Soula, F31400 Toulouse, France
[3]The Aeronautical Research Institute of Sweden Box 11021, SE-161 11 Bromma.

Contact e-mail: jpralits@mech.kth.se

1 Introduction

Transition from laminar to turbulent flow is usually triggered by unstable disturbances inside the boundary layer. The growth of such disturbances are sensitive to different type of forcing inside the boundary layer and on the boundaries. The knowledge about the response of disturbances to such forcing is of great importance when one wishes to predict or control the transition. The receptivity and sensitivity analysis have been investigated by different authors, *e.g.* Crouch [2] and Hill [3]. Here we investigate the sensitivity of disturbances to wall conditions and source of momentum in a compressible boundary layer in the framework of the non-local stability theory using Parabolized Stability Equations, PSE. The main tool developed here is based on the adjoint equations. With this technique the sensitivity of a disturbance can be obtained with a single adjoint calculation.

We start by deriving the non-local stability equations. The idea is to model convectively unstable disturbances with curved or divergent wave-rays in a non-uniform flow in an orthogonal curvilinear coordinate system. In such coordinate system an arc length element is expressed as $(ds)^2 = \sum_{i=1}^{3} (h_i\, dx^i)^2$. The disturbances are divided into an amplitude function and a wave function

$$\tilde{q}(x^i,t) = \hat{q}(x^1,x^3)\Theta, \quad \Theta = \exp\, i\,(\int_{X_0}^{x^1} \alpha(x')dx' + \beta x^2 - \omega t). \qquad (1)$$

where x^3, x^2 and x^1 are the normal, spanwise and streamwise directions respectively, α is the streamwise wavenumber, β the spanwise wavenumber and ω the frequency. According to the boundary layer approximation we assume the streamwise derivatives of $\hat{q}$ and α as well as the normal mean velocity to be of

$\mathcal{O}(1/Re_x)$. Introducing Eq. 1 and scalings above into the linearized conservation equations of mass, momentum and energy for a compressible flow and keeping terms up to $\mathcal{O}(1/Re_x)$, result in a set of parabolic equations. In a general case, when the flow is subjected to sources, $\mathcal{S}$, of mass, momenta and energy, the non-local disturbance equations can be written as

$$\Theta\ (\mathcal{A} + \mathcal{B}D_3 + \mathcal{C}D_{33} + \mathcal{D}D_1)\ \hat{q} = \mathcal{S}, \quad \hat{q} = (\hat{u}, \hat{v}, \hat{T}, \hat{w}, \hat{\rho})^T. \tag{2}$$

The boundary conditions are $\hat{\mathbf{u}}(x^1, 0) = \hat{\mathbf{u}}_W(x^1)$ and $\hat{T}(x^1, 0) = \hat{T}_W(x^1)$. Moreover, disturbances vanish in the far field. The operators $\mathcal{A}, \mathcal{B}, \mathcal{C}$ and $\mathcal{D}$ are functions of the mean flow and D_i are derivatives w.r.t. x^i. Eq. 2 is solved by a marching procedure in the downstream direction using an initial condition of $\tilde{q}$ at X_0. The streamwise wavenumber α is derived such that the auxiliary condition

$$\int_0^\infty \bar{\hat{q}} \cdot \frac{\partial \hat{q}}{\partial x^1}\, dx^3 = 0. \tag{3}$$

is satisfied. Here, the overbar denotes complex conjugate. Eq. 3 also ensures that the streamwise variation of the amplitude function $\hat{q}$ remains small. For details on the non-local stability theory see Bertolotti [1].

2 Adjoint formulation

The adjoint equations are derived using an appropriately defined inner product, the Lagrange identity and the generalized Greens theorem. This can be written

$$\langle \tilde{q}^*, \mathcal{L}\tilde{q} \rangle - \langle \mathcal{L}^* \tilde{q}^*, \tilde{q} \rangle = \int_{X_0}^{X_1} \int_{Z_0}^{Z_1} \int_0^{+\infty} \nabla \mathbf{J}(\tilde{q}^*, \tilde{q})\ h_1 h_2 h_3\ dx^3\ dx^2\ dx^1 \tag{4}$$

Here $\tilde{q}^* = (\tilde{u}^*, \tilde{v}^*, \tilde{T}^*, \tilde{w}^*, \tilde{\rho}^*)^T$ is the adjoint vector of the disturbance vector $\tilde{q}$ and $\mathbf{J}$ are bilinear combinations of $\tilde{q}$ and $\tilde{q}^*$, see Hill [3]. We make an ansatz for $\tilde{q}^*$ similar to that for $\tilde{q}$ as

$$\tilde{q}^*(x^i, t) = \hat{q}^*(x^1, x^3)\Theta^*, \quad \Theta^* = \exp\ i\ (\int_{X_1}^{x^1} \alpha^*(x')dx' + \beta^* x^2 - \omega^* t) \tag{5}$$

We choose $\beta^* = \beta$ and $\omega^* = \omega$. The adjoint equations are obtained by applying integration by parts to the inner product between Eq. 2 and $\tilde{q}^*$. The adjoint equations can now be written

$$(\tilde{\mathcal{A}}\ +\ \tilde{\mathcal{B}}\ D_3\ +\ \tilde{\mathcal{C}}\ D_{33}\ +\ \tilde{\mathcal{D}}\ D_1)\ \hat{q}^*\ =\ 0. \tag{6}$$

with homogeneous boundary conditions for $\hat{u}^*$ and $\hat{T}^*$ on the wall and in the far field. Here H denotes conjugate transpose. The operators $\tilde{\mathcal{A}}, \tilde{\mathcal{B}}, \tilde{\mathcal{C}}$ and $\tilde{\mathcal{D}}$ are functions of the mean flow and. Eq. 6 is integrated in the upstream direction.

The initial field at $x^1 = X_1$ is obtained from the local adjoint equations. The adjoint streamwise wavenumber α^* is solved such that

$$\frac{\partial}{\partial x^1}\left[\Theta\bar{\Theta}^* \int_0^\infty h_2 h_3 \hat{q}^{*H} \mathcal{D}\hat{q}\, dx^3\right] = 0, \tag{7}$$

is satisfied. Details on the above derivations are given in Pralits *et al.* [4].

3 Sensitivity analysis

Introducing the boundary and auxiliary conditions for $\hat{q}$ and $\hat{q}^*$ and using the definition of adjoint equations, Eq. 4 reduce to a relation between input and output quantities. Here, input is the forcing and output is the disturbance amplitude at X_1. Now we introduce $\tilde{A}(x^1)$ which denotes the complex amplitude of the disturbance defined such that

$$\tilde{q}(x^1) \;=\; \tilde{A}(x^1)\, \hat{q}_0(x^1, x^3)\, \exp\, i(\beta x^2 - \omega t). \tag{8}$$

Here $\hat{q}_0$ is the amplitude function normalized with the maximum amplitude of the velocity, mass flow or energy. Further, the source $\mathcal{S}$, $\hat{\mathbf{u}}_W(x^1)$ and $\hat{T}_W(x^1)$ are modeled as point forcing using a Dirac delta function. If Eq. 8 is introduced into the right hand side of Eq. 4, the changes in amplitude $\tilde{A}$ at $x^1 = X_1$ can be written in a simplified form as

$$\Delta\tilde{A}(X_1) = \sum_{\xi} \tilde{\Lambda}_W^{\xi} \hat{q}_W^{\xi} \;+\; \sum_{\zeta} \tilde{\Lambda}_S^{\zeta} \mathbf{s}^{\zeta}, \quad \xi = (u, v, w, T), \quad \zeta = (u, v, w, T, \rho). \tag{9}$$

The coefficients $\tilde{\Lambda}_W^{\xi}$ and $\tilde{\Lambda}_S^{\zeta}$ will now provide the response to point forcing on the wall and inside the boundary layer, respectively. Each coefficient depends on the solution of the forward and adjoint equations. For example, the response to a streamwise and normal velocity disturbance on the wall is obtained as

$$\tilde{\Lambda}_W^u = \frac{h_1 h_2 \bar{\theta}^*}{\tilde{J}(X_1)} \left\{\frac{\mu}{R} D_3(\bar{\tilde{u}}^*)\right\}_{(x^1 = x_W, x^3 = 0)}, \tilde{\Lambda}_W^w = \frac{h_1 h_2 \bar{\theta}^*}{\tilde{J}(X_1)} \left\{\rho \bar{\tilde{\rho}}^*\right\}_{(x^1 = x_W, x^3 = 0)} \tag{10}$$

Here $\tilde{J}(x^1) = \bar{\theta}^*(x^1) \int_0^\infty h_2 h_3 \hat{q}^{*H} \mathcal{D}\hat{q}_0\, dx^3$, $\theta^*(x^1) = \exp i \int_{X_1}^{x^1} \alpha^*(x')dx'$ and $R = \sqrt{U^\star x^{1\star}/\nu^\star}$. Here $\star$ denotes the physical quantities. In a similar manner we can write the response to forcing by streamwise momentum as

$$\tilde{\Lambda}_S^u = \frac{1}{\tilde{J}(X_1)} h_1 h_2 h_3 \bar{\theta}^* \left\{\bar{\tilde{u}}^*\right\}_{(x^1 = x_s, x^3 = y_s)}. \tag{11}$$

Some typical results are given in Figure 1. Here, X_0 corresponds to $R = 250$ and X_1 to $R = 760$. In Figure 1a. $|\tilde{\Lambda}_S^u|$ is plotted for an incompressible flow, $M = 0$. The maximum response corresponds to forcing at branch I of the neutral stability

curve and in the vicinity of the critical layer. Compared to the other components of $\tilde{\Lambda}_S^{\zeta}$, the magnitude of the streamwise component is at least 10 times larger. This is also true for higher Mach numbers. In Figure 1b, $|\tilde{\Lambda}_W^{\zeta}|$ is plotted for the streamwise and wall normal velocity component for different Mach numbers. Here it should be noted that the maximum for all curves are close to branch I of the neutral stability curve. The branch points are marked with + signs. Further, the magnitude of the wall normal component is approximately 15 times that of the streamwise component. This indicates that the most efficient way of affecting the growth of disturbance is to use the normal velocity. The results in Figure 1b show also that the forcing at the wall becomes less efficient as the Mach number increases.

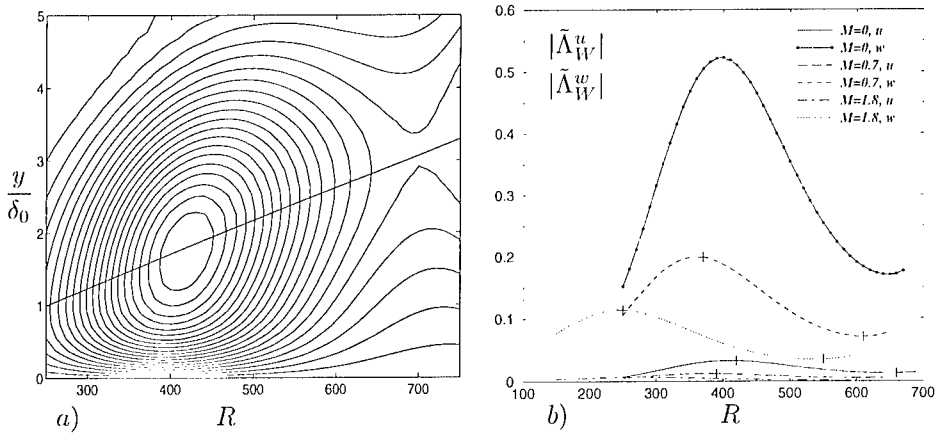


Figure 1: a) $|\tilde{\Lambda}_S^u|$, $M = 0$, $\beta = 0$. The straight line denotes the critical layer. Branch locations: I at $R = 430$, II at $R = 730$. b) $|\tilde{\Lambda}_W^u|$, $|\tilde{\Lambda}_W^w|$ $M = 0, 0.7, 1.8$, $F = 2\pi f^\star \nu_c^\star / U_c^{\star 2} = 100 \times 10^{-6}$ $\beta = 0.05$. Branch locations are marked with +.

References

[1] F. P. Bertolotti. Linear and Nonlinear Stability of boundary layers with streamwise varying properties. *PhD thesis, Ohio State University, Columbus*, 1991.

[2] J. D. Crouch. Localized receptivity of boundary layers. *Phys. Fluids A*, 4:1408–1414, 1992.

[3] D. C. Hill. Adjoint Systems and their role in the Receptivity Problem for Boundary Layers. *J. Fluid Mech.*, 292:183–204, 1995.

[4] J. O. Pralits, C. Airiau, A. Hanifi, D. S. Henningson. Sensitivity Analysis Using Adjoint Parabolised Stability Equations for Compressible Flow. Submitted to *Journal of Flow, Turbulence and Combustion*, 1999

ADVANCES IN TURBULENCE VIII
Proceedings of the Eighth European Turbulence Conference
C. Dopazo et al. (Eds.)
© CIMNE, Barcelona 2000

Numerical simulation of the spatial evolution of the instabilities in a supersonic plane jet

A. Kudryavtsev [1], and D. Khotyanovsky [1]

[1]Computational Aerodynamics Lab, Institute of Theoretical & Applied Mechanics
4/1 Institutskaya str. , Novosibirsk 630090, Russia

Contact e-mail: dima@itam.nsc.ru

1 Introduction

In this study we have performed the numerical simulation of the nonlinear evolution of the unstable disturbances in a plane perfectly expanded supersonic jet exhausting into the co-flowing stream. This kind of flow is of interest due to its practical importance in such problems of jet propulsion as mixing, supersonic combustion, and jet noise generation.

Linear stability analysis reveals multiple-mode character of the jet instability. Betchov & Criminale [1] showed that two unstable modes exist for an incompressible plane jet, one of those modes has symmetrical pressure eigenfunction, which is usually referred to as a varicose mode, and another is anti-symmetrical one (sinuous mode). The compressibility also greatly influences the stability properties of the jet flow: the top-hat jet analysis performed by Gill [2] reveals a number of unstable modes in supersonic case, which is believed to be associated with the transfer of energy across the jet by sound waves.

We are primarily focused here on the differences between the spatial evolution of the instabilities of different modes, and also on the effects of the compressibility. As will be shown in the following, the nonlinear evolution of the jet instabilities appears to be essentially different at subsonic and supersonic relative speeds of the jet and the co-flowing stream, and for the different instability modes.

2 Numerical techniques

To simulate spatial evolution of the instability waves in supersonic plane jet we solve numerically two-dimensional Navier-Stokes equations of compressible

gas. The viscosity is assumed to be linearly proportional to temperature. The Prandtl number is unity.

For the spatial discretization of convective terms of Navier-Stokes equations weighted essentially non-oscillatory (WENO) scheme of the 5th order by Jiang & Shu [3] is used. This scheme represents a new generation of high-order shock-capturing schemes providing high accuracy at smooth solutions, which is necessary when modelling wave processes, and capture shock waves inherent in high-speed flows without oscillations. Diffusive terms in Navier-Stokes equations were approximated with the central differences of the 4th order. Time integration was made with low-storage Runge-Kutta-Gill scheme of the fourth order. The details of our numerical method can be found in [5]

All calculations were performed in the rectangular computation domain. The size of the domain was typically 50×10 jet widths. Number of grid nodes used was 800×160. The grid was uniform in streamwise direction, and stretched along the normal coordinate according to algebraic mapping in order to enhance resolution in the jet shear layers.

At the top and bottom boundaries, and at the outflow we impose non-reflecting characteristic boundary conditions by Thompson [4] to prevent undesired reflections which could affect the flow. The inflow conditions were imposed in the following way. At the first stage of the computations we have at the inflow co-flowing supersonic top-hat jet and the ambient supersonic stream of smaller velocity. The pressures in the jet and in the ambient streams are equal. The computed Navier-Stokes stationary profiles of streamwise velocity and temperature in some downstream location were then used in the linear stability analysis. The computed linear stability eigenfunctions were imposed on the stationary mean flow as the inflow forcing.

3 Results and discussion

We consider here two cases with different relative velocities of the jet and the ambient stream. The influence of the compressibility on the stability characteristics is characterized by so-called convective Mach number $M_c = (U_1 - U_2)/(a_1 + a_2)$, where U_1, U_2 are streamwise velocities, a_1, a_2 are speeds of sound in the corresponding stream (index 1 corresponds to the parameters of the jet, index 2 corresponds to the co-flowing stream).

First case corresponds to subsonic relative speeds, and the Mach numbers of the jet and the ambient stream are $\mathrm{M}_1 = 2.5$, $\mathrm{M}_2 = 1.5$. Temperatures of the jet and the ambient stream were chosen to be equal, and the convective Mach number determined across the jet shear layer is in this case $\mathrm{M}_c = 0.5$. Reynolds number based on the width of the jet and the velocity difference is $\mathrm{Re} = 5000$ in our computations.

The results of computations for subsonic sinuous and varicose modes are shown in Fig. 1. In early stages of the evolution the instability waves in two shear layers develop independently and are quite similar to the well-known Kelvin-

Helmholtz vortices. Farther downstream the neighboring vortices in each shear layer are no longer independent and interact in a complex way. In case of

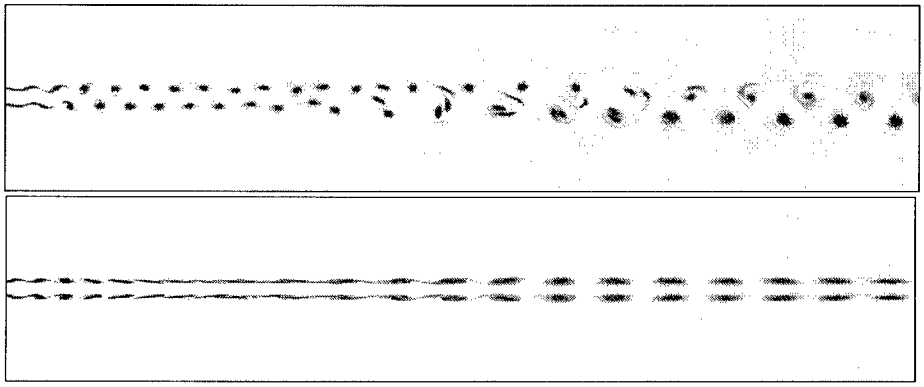


Figure 1: Subsonic sinuous (upper image) and varicose (lower image) modes. Entropy

sinuous mode, the neighbouring vortices merge rolling around each other, and the vortical movement gradually involves the fluid in the whole jet column. It is interesting to note that in the case of varicose instability the rolling interaction of the neighbouring vortices is replaced with shredding interaction, which is known from the studies on mixing layer dynamics [6].

In the second considered case we increase the velocity difference between the jet and the ambient stream. The corresponding Mach numbers are $M_1 = 4.5$, $M_2 = 1.5$, so the convective Mach number is $M_c = 1.5$. The results of compu-

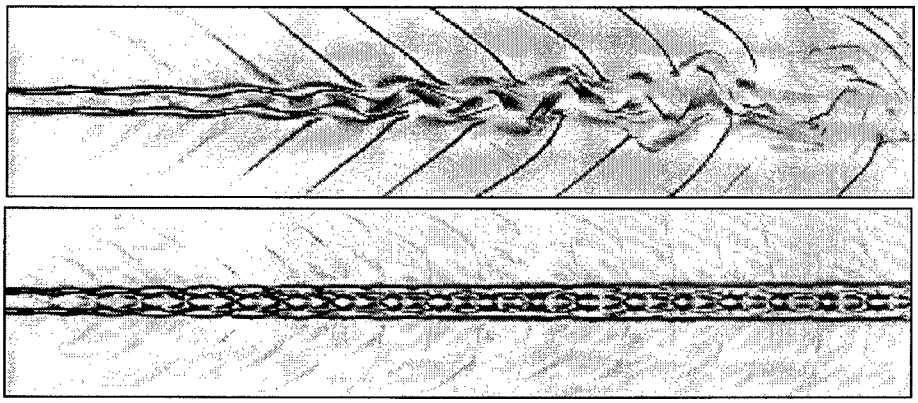


Figure 2: Supersonic sinuous (upper image) and varicose (lower image) modes. Density gradient

tations in supersonic case (see Fig. 2) show the essentially different instability

evolution. Vortical structures in the shear layer are very slender and flattened. In case of supersonic sinuous mode Mach waves are emitted into the ambient stream. Farther downstream these Mach waves transform into weak inclined shock waves. As the instability grows, the shock waves and expansions appear in the jet core, and the jet breaks up. On the contrary, the varicose instability mode seems to remain confined in the jet core up to the outflow. The flow evolves as a sequence of complex periodic patterns containing shock and expansions. These patterns are somewhat similar to steady cell structure typical for non-isobaric jets. This is not surprising because the pressure in the jet core at the inflow is changing in time due to the forcing, and this could correspond to the situation when the jet becomes locally overexpanded or underexpanded at different moments. Of course, in our simulations we have travelling waves, not steady state structure.

4 Conclusions

The early non-linear stages of the transition to turbulence were simulated numerically for the perfectly expanded supersonic planar jet, exhausting into the co-flowing stream. Results of Navier–Stokes simulations show essentially distinct patterns of the jet instability in subsonic and supersonic cases, and for different instability modes. The computations show that sinuous instability is mainly responsible for the jet break-up in both subsonic and supersonic cases.

The authors would like to acknowledge the support of RFBR (Grant No. 98-01-00723) and INTAS (Open Call 1999 Proposal No. 785).

References

[1] R. Betchov and W. O.Criminale Jr. Spatial instability of the inviscid jet and wake. *Physics of Fluids*, 9(2):359–362, 1966.

[2] A. E. Gill Instabilities of "Top-Hat" jets and wakes in compressible fluid. *Physics of Fluids*, 8(8):1428–1430, 1965.

[3] G. Jiang and C.-W. Shu Efficient implementation of weighted ENO schemes. *J. Comput. Phys.*, 126:202–208, 1996.

[4] K. W. Thompson Time-Dependent Boundary Conditions for Hyperbolic Systems. *J. Comput. Phys.*, 68(1):1–24, 1987.

[5] A. N. Kudryavtsev and D. V. Khotyanovsky Numerical Simulation of Compressible Shear Layers Development with Weighted ENO Schemes. *Proc. 4th European CFD Conf., Athens, Greece*, 1(2): 900-905, 1998.

[6] P. C. Patnaik, F. S. Sherman, and G. M.Corcos A numerical simulation on Kelvin—Helmholtz waves of finite amplitude. *J. Fluid Mech.*, 73(2):215–240, 1976.

VI

Transport and Mixing

ADVANCES IN TURBULENCE VIII
Proceedings of the Eighth European Turbulence Conference
C. Dopazo et al. (Eds.)
© CIMNE, Barcelona 2000

Kinematic Simulation for particle pair diffusion

F. Nicolleau[1], J. C. Vassilicos[2], D. J. Thomson[3]

[1]University of Sheffield, Department of Mechanical Engineering
[2]University of Cambridge, DAMTP
[3]The Meteorological Office, Bracknell, UK

1 Introduction

Kinematic Simulation (KS) is a unified Lagrangian model of one- and two- and indeed multi-particle turbulent diffusion. In practice it relies on the integration of

$$\frac{d\mathbf{x}}{dt} = \mathbf{u}(\mathbf{x}, t) \tag{1}$$

where $\mathbf{x}$ is the position of the fluid particle and $\mathbf{u}$ a turbulent-like Eulerian velocity field. Statistics are then performed on the trajectories. Incompressibility is enforced in every single realisation of $\mathbf{u}$ and the energy spectrum is prescribed according to the type of turbulence considered. As such, KS should be contrasted with Lagrangian stochastic models of turbulent diffusion which do not explicitly incorporate structural aspects of the flow by means of full realisations of Eulerian velocity fields and which are by construction different models for one- and two-particle statistics. However, as demonstrated by [1], and [3], two-particle statistics are very significantly influenced by small-scale spatio-temporal flow structures.

In this paper we only study the case of a $k^{-5/3}$ energy spectrum. In KS we need to introduce an explicit time dependence based on turn-over frequencies proportional to $\sqrt{k^3 E(k)}$.

Comparisons with Direct Numerical Simulation results of two-particle statistics in stationary isotropic turbulence have shown good agreement with KS [3]. Compared to Lagrangian integration of DNS data KS is a much less time consuming method. Here, we are able to run many different cases corresponding to different values of the turbulence parameters and different initial particle pair separations in a KS with two velocity components, i.e. in the 2-D plane (same KS as in [2]).

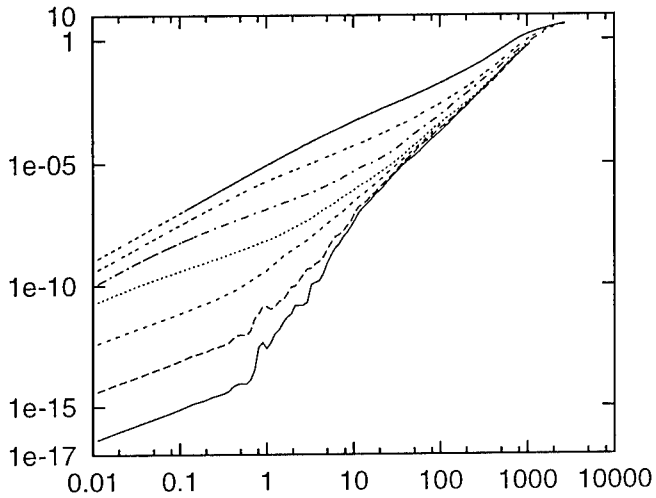


Figure 1: Two particle diffusion in 2-D turbulence : $< |\Delta\mathbf{x}(t) - \Delta\mathbf{x}(0)|^2 > /L^2$ as a function of $\frac{t}{\tau_\eta}$. $\Delta\mathbf{x}(t)$ is the two particle vector difference and here $\frac{L}{\eta} = 11180$. From top to bottom $\frac{\Delta_0}{\eta} = 1000, 100, 10, 1, 0.1, 0.01, 0.001$.

2 Investigation of Richardson's range

Because of computing constraints we have been able to assess the limits of Richardson's law in the 2-D plane, and are only currently investigating the 3-D case.

Our most important result is that Richardson's law seems to hold only for initial particle-pair separations Δ_0 between η and 0.1η where η is the Kolmogorov length scale of the turbulence. Figure 1 shows for different initial separations Δ_0, the two-particle diffusion $< |\Delta\mathbf{x}(t) - \Delta\mathbf{x}(0)|^2 > /L^2$ as a function of $\frac{t}{\tau_\eta}$ where L is an integral length scale and τ_η the Kolmogorov time scale.

The different curves collapse only at large times, at the end of the inertial range. Two-particle diffusion is affected by its initial condition (i.e. $\Delta\mathbf{x}(0)$) much longer than predicted by Richardson's law. At small times, two-particle diffusion grows at a faster rate than Richardson's prediction when $\Delta\mathbf{x}(0) < \eta$ and at a slower rate when $\Delta\mathbf{x}(0) > \eta$.

This result is confirmed in Figure 2 which shows $< |\Delta\mathbf{x}(t) - \Delta\mathbf{x}(0)|^2 > / \frac{u'^3}{L} t^3$ as a function of $t\frac{u'}{L}$. Clear evidence of a t^3 régime is only observed for $\Delta\mathbf{x}(0)$ between 0.1η and η

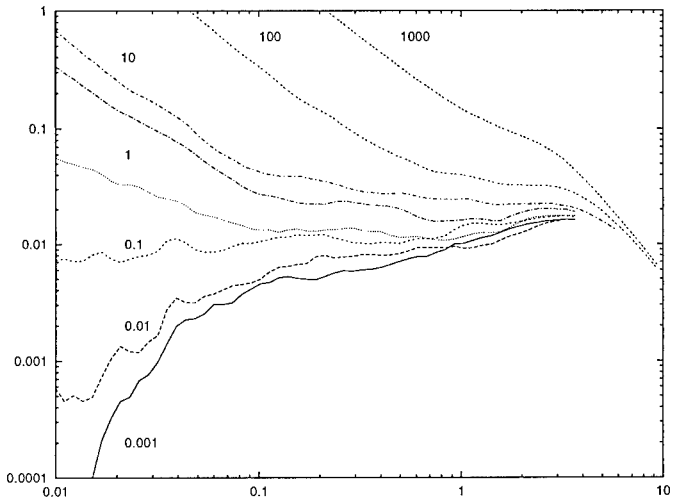


Figure 2: Two particle diffusion in 2-D turbulence : $< |\Delta\mathbf{x}(t) - \Delta\mathbf{x}(0)|^2 > / \frac{u'^3}{L} t^3$ as a function of $t\frac{u'}{L}$. $\Delta\mathbf{x}(t)$ is the two particle vector difference and here $\frac{L}{\eta} = 11180$. From top to bottom $\frac{\Delta_0}{\eta} = 1000, 100, 10, 5, 1, 0.1, 0.01, 0.001$.

3 Investigation of diffusion at small times

We are also able to give accurate scalings for the initial diffusion when $t \to 0$ namely:

$$< \Delta x_1{}^2(t) > \simeq \frac{\Delta_0{}^2}{L^2} \left(\frac{L}{\eta}\right)^{\frac{4}{3}} u'^2 t^2 \tag{2}$$

when $\Delta_0 \leq \eta$ and

$$< \Delta x_1{}^2(t) > \simeq u'^2 \left(\frac{\Delta_0}{L}\right)^{\frac{2}{3}} t^2 \tag{3}$$

when $\Delta_0 \geq \eta$, where L is the integral length scale and u' the rms velocity fluctuation of the turbulence.

Relations (2) and (3) can be summarised as

$$< \Delta x_1{}^2(t) > = \Delta v_0{}^2 t^2 \tag{4}$$

where $\Delta v_0 = \lim_{t\to 0} < \Delta x_1{}^2(t) > /t^2$. Figure 3 shows $\frac{\Delta v_0}{v_\eta}$ as a function of $\frac{\Delta_0}{\eta}$ where Δ_0 is the initial separation of the particle pair, η and v_η the Kolmogorov length and velocity scales. The spectra used for obtaining Figure 3 are all $k^{-5/3}$ in shape; only the range $\frac{L}{\eta}$ has been varied and the data collapse on the same curve.

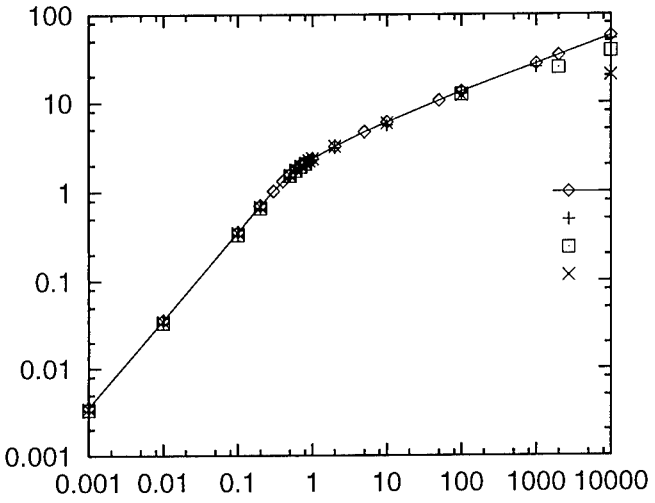


Figure 3: $\frac{\Delta v_0}{v_\eta}$ as a function of $\frac{\Delta_0}{\eta}$ for four different spectra: *Diamond* $\frac{L}{\eta} = 250000$, $+$ $\frac{L}{\eta} = 38748$, *Box* $\frac{L}{\eta} = 11180$, $\times$ $\frac{L}{\eta} = 1691$.

References

[1] Fung, J. C. H., J. C. R. Hunt, N. A. Malik, and R. J. Perkins: 1992, 'Kinematic Simulation of homogeneous turbulence by unsteady random Fourier modes'. *J. Fluid Mech.* **236**, 281–317.

[2] Fung, J. C. H. and J. C. Vassilicos: 1998, 'Two-particle dispersion in turbulentlike flows'. *Phys. Rev. E* **52**(2), 1677–1690.

[3] Malik, N. A. and J. C. Vassilicos: 1999, 'A Lagrangian model for turbulent dispersion with turbulent-like flow structure: comparison with DNS for two-particle statistics'. *Phys. Fluids* **11**(6).

ADVANCES IN TURBULENCE VIII
Proceedings of the Eighth European Turbulence Conference
C. Dopazo et al. (Eds.)
© CIMNE, Barcelona 2000

Relative dispersion in fully developed turbulence

G. Boffetta

[1]Dipartimento di Fisica Generale and INFM, Università di Torino
via Pietro Giuria 1, 10125 Torino, ITALY

Contact e-mail: boffetta@to.infn.it

1 Introduction

Understanding the statistics of particle pairs dispersion in turbulent velocity fields is of great interest for both theoretical and practical implications. Since fully developed turbulence displays well known, non-trivial universal features in the Eulerian statistics of velocity differences, pair dispersion represents a starting point for the investigation of the general problem of the relationship between Eulerian and Lagrangian properties. Moreover, a deep comprehension of relative dispersion mechanisms is of fundamental importance from an applicative point of view, for a correct modelization of small scale diffusion and mixing properties.

In this Paper we present a detailed investigation of the statistics of relative dispersion from extensive numerical simulations of particle pairs. In the first part we will consider the advection of particles by a fully developed turbulent flow obtained by means of direct numerical simulation of two–dimensional inverse energy cascade. This flow is known to be well described by Kolmogorov self-similarity theory [1] with no detectable intermittency corrections [2]. In this case we expect a confirm of the Richardson-Obukhov predictions on relative dispersion statistics. In the second part we will investigate the effects of Eulerian intermittency on Lagrangian statistics by replacing the DNS Eulerian flow with a synthetic flow with prescribed statistical features. We find deviations of the scaling exponents from the Richardson's values, i.e., "Lagrangian intermittency". These effects cannot be captured by dimensional arguments alone. The simplest step beyond dimensional analysis is the extension of the multifractal description successfully used for Eulerian statistics to Lagrangian quantities [3].

The intermittency corrections to relative dispersion are however small. Moreover, they can be hidden by the finite scaling rangei, expecially in the case of direct numerical simulated Eulerian flow. To partially overcome this difficulty we propose a new methodology for the analysis of relative dispersion data based on Lagrangian statistics at fixed spatial particle separation [4].

2 Relative dispersion in two-dimensional turbulence

Pair dispersion statistics has been investigated by direct numerical simulation of the inverse energy cascade in two-dimensional turbulence. The 2D Navier-Stokes equations for the vorticity

$$\partial_t \omega + J(\omega, \psi) = \nu \Delta \omega - \alpha \omega + \phi, \tag{1}$$

are integrated by a standard pseudospectral method on a doubly periodic square domain of $N^2 = 2048^2$ grid points [2]. The friction linear term $-\alpha\omega$ extracts energy from the system to avoid Bose-Einstein condensation at the gravest modes. The forcing is active only on a typical scale l_f and is δ-correlated in time to ensure the control of the energy injection rate. In Figure 1 we plot relative dispersion $R^2(t)$ obtained after averaging over 64000 particle pairs for two different initial conditions $R^2(0)$. The Richardson t^3 law is observed in a limited time interval, especially for the largest $R^2(0)$ run. It is remarkable that the relative separation law displays such a strong dependence on the initial conditions even in this high resolution runs.

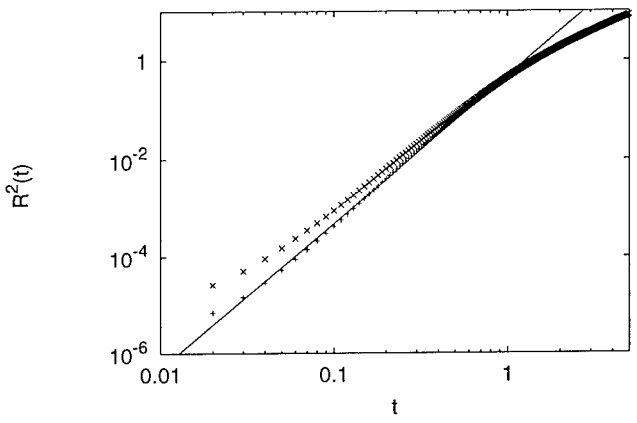


Figure 1: Relative dispersion $R^2(t)$ for two initial separation $R(0) = 1.5 \times 10^{-3}$ (+) and $R(0) = 3 \times 10^{-3}$ (×). The continuous line is the Richardson law $R^2(t) \simeq t^3$.

To overcome the difficulty to observe the Richardson scaling law, we use an alternative approach based on "doubling time" $T_r(R)$ defined as the time it

takes for the particle pair separation to grow by a factor r from R. The method has been successfully applied to the analysis of relative dispersion in laminar flow [4]. The scaling property of the doubling time statistics in fully developed turbulence is obtained by a simple dimensional argument. The time it takes for the particle pair separation to grow from R to rR can be dimensionally estimated as $T_r(R) \sim R/\delta v_{\|}^{(L)}(R)$; we thus expect for the inverse doubling times the scaling

$$\langle T_r(R) \rangle \simeq R^{2/3} \tag{2}$$

In Figure 2 it is shown the doubling time for the same simulation of Figure 1. At small scales $R < 0.01$ there appears a constant plateau corresponding to exponential particle separation [3]. At larger R, we observe the scaling (2) on a range of scales.

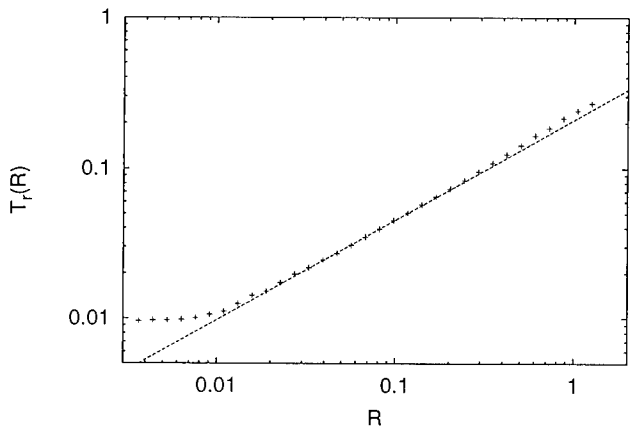


Figure 2: Average doubling time for particle pairs in DNS of two–dimensional turbulence. The line is the theoretical Richardson scaling $R^{-2/3}$.

3 The effect of Eulerian intermittency

We now consider the case of an intermittent velocity field with scaling exponents $\zeta_p \neq p/3$. We can extend the dimensional argument for the Richardson law to the intermittent case by using the multifractal representation [3]. For the doubling time statistics the prediction is very simple and can be summarize as follows. A dimensional estimate of the doubling time is $T(R) \sim R/\delta v(R)$ thus, after

averaging over many realizations we can write

$$\langle T^p(R) \rangle \simeq R^{p-\zeta_p} \tag{3}$$

As reported in Figure 3 prediction (3) is well verified in our simulations. As for the Eulrian statistics, also for the Lagrangian statistics there is an exponent $3 - \zeta_3 = 2$ unaffected by intermittency.

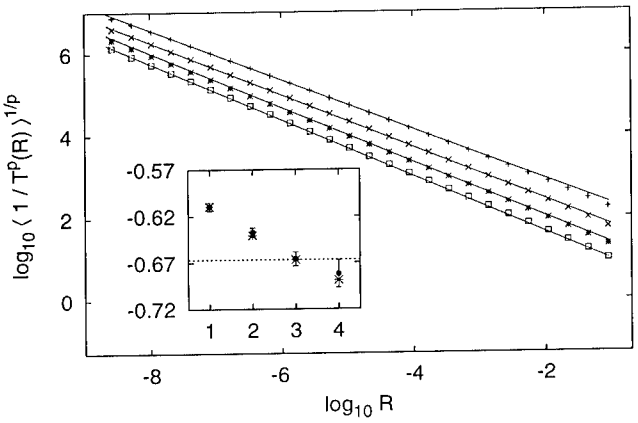


Figure 3: Inverse doubling time moments $\langle 1/T^p(R) \rangle^{1/p}$ for the intermittent velocity field. Continuous lines represent the theoretical scaling. In the inset we plot the theoretical and numerical exponents as a function of the moment p (the dashed line is the non-intermittent prediction).

References

[1] R. H. Kraichnan and D. Montgomery. Two-dimensional turbulence. *Rep. Prog. Phys.*, 43:547–619, 1980.

[2] G. Boffetta, A. Celani and M. Vergassola. Inverse cascade in two-dimensional turbulence: deviations from Gaussianity. *Phys. Rev. E*, 61:R29–R32, 2000.

[3] G. Boffetta, A. Celani, A. Crisanti and A. Vulpiani. Pair dispersion in synthetic fully developed turbulence *Phys. Rev. E*, 60:6734–6741, 1999.

[4] V. Artale, G. Boffetta, A. Celani, M. Cencini and A. Vulpiani. Dispersion of passive tracers in closed basin: beyond the diffusion coefficient. *Phys. Fluids*, A9:3162–3171–6741, 1997.

ADVANCES IN TURBULENCE VIII
Proceedings of the Eighth European Turbulence Conference
C. Dopazo et al. (Eds.)
© CIMNE, Barcelona 2000

Turbulent mixing of a passive tracer in the Batchelor regime

M.-C Jullien[1], P. Castiglione[1,2] and P. Tabeling[1]

[1]Laboratoire de Physique Statistique, Ecole Normale Suprieure
24 rue Lhomond, 75005 Paris, FRANCE
[2]INFM sezione Roma I,
Piazzale Aldo Moro 2, 00185 Roma, ITALY

Contact e-mail: jullien@physique.ens.fr

Turbulent dispersion of passive tracers is involved in an extremely large number of situations, pertaining to industrial, environmental, astrophysical contexts [1, 2]. In two dimensions, the Batchelor regime [3] refers to a situation where the tracer is simply dispersed by a smooth two-dimensional, chaotic, velocity field, characterized by a single large scale L [4]. The two-point statistics of the scalar field has been calculated under controlled approximation in [6, 7, 8], where a scalar variance spectrum, $E_\theta(k)$, decreasing as k^{-1}, logarithm like behaviour for the second order structure function [6] and exponential tails for both fluctuations and increments scalar distributions (PDF) [7, 8] are predicted. In this paper we report results on the spreading of a low diffusivity colorant in a two-dimensional turbulent flow, forced at large scales. The experimental set-up we use has been described in [9]. The flow is generated in a square PVC cell, 15 cm × 15 cm. The bottom of the cell is made of a thin (1 mm) glass plate, below which permanent magnets, 5×8×4 mm in size are placed. In order to ensure two dimensionality, the cell is filled with two layers of NaCl solutions, each 3 mm thick, with different densities, $\rho_1 = 1030$ gl^{-1} and $\rho_2 = 1060$ gl^{-1}, placed in a stable configuration, *i.e.* the heavier underlying the lighter. The interaction of an electrical current driven across the cell with the magnetic field produces local stirring forces. In the experiments we describe here, the experimental conditions of [9] have been exactly reproduced : the flow develops, after a short transient, a direct enstrophy cascade with Kolmogorov-Kraichnan scaling, $E(k) \sim k^{-3}$. The passive scalar is a mixture of fluorescein and water, of density $\rho = 1002$ gl^{-1}, and diffusivity $\kappa = 10^{-6}$ cm^{2}s^{-1}. The "molecular" Péclet number UL/κ (where U and L are typical velocity and length scales) is typically on the order of 10^8. In these experiments, the flow is statistically stationary, while the concentration field is in a freely decaying regime. Additionally, we have simulated the concentration field in order to mimick the experiment [10]. We will incorporate the results of this work in the discussion of the physical experimental results. Fig.1 shows a typical evolution of a spot of fluorescein 5 cm in diameter, released in the system

at time t=0. At early time, the blob is localized in the center of the cell, and is slightly distorted. It is further vigorously advected and strained, under the action of the velocity field, undergoing a random sequence of baker's transforms. At this stage, the striations display a broad range of sizes; it would be hard to extract a simple characteristic length from the inspection of the turbulent fields displayed in Fig.1.

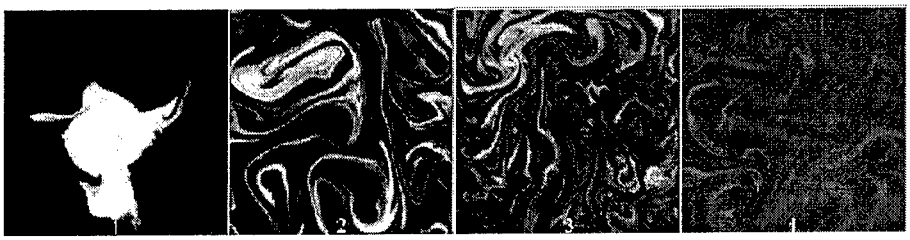


Figure 1: Time evolution of a blob of fluoresceine in a 16 cm×16 cm region, at times $t = 1$, 12, 20, and 40s.

The existence of a range of time, comprised between 8 and 18 s, where the concentration field seems to reach a quasi-stationary state is confirmed by the inspection of the total dissipation $\int k^2 E(k)$, which displays a broad maximum in this range of time . We further concentrate ourselves on the analysis of this region, we call "quasi-stationary domain" [10].

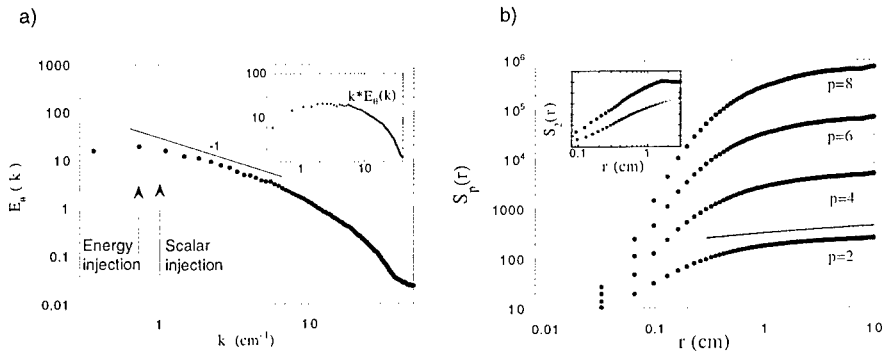


Figure 2: a) Variance scalar spectra, the straight line has ak^{-1} slope. The insert shows the compensated spectra $E_\theta(k) \times k$. b) Even structure functions up to order eight. Straight line is a logarithmic fit for $S_2(r)$, $S_2(r) \approx 300 + 55 \ln(r/L)$. The passive scalar used has the density ρ= 1002 gl^{-1}. The numerical result for $S_2(r)$ (full circles) is shown in insert with lin-log axis, compared with the experimental ones (empty circles).

The scalar variance spectra $E_\theta(k)$ is expected to evolve as $E_\theta(k) \approx -\chi/\gamma k$, where γ is a mean rate of strain, and $\chi = \kappa\langle(\nabla\theta)^2\rangle$ is the scalar dissipation. The

spectrum displays a range of wave-number, comprised between 1 and 7 cm^{-1}, where a k^{-1} law fairly holds (Fig.2.a). The range of scale in which the power law is observed is consistent with the scaling range developed by the enstrophy cascade. We now turn to the measurement of the probability density functions (PDF) of scalar fluctuations $P(\theta(\mathbf{x}) - \langle\theta(\mathbf{x})\rangle)$, a crucial quantity to consider for comparing with theory. The PDFs of the quasi stationary domain are non symmetric and non Gaussian, they develop exponential tails, on the positive size and Gaussian behavior, on the negative one (Fig.3.a). The tails seem controlled by the fronts, located at the edges of the tracer filaments. These characteristics for the PDFs of the concentration field are in good qualitative agreement with the theoretical analysis of [7, 8].

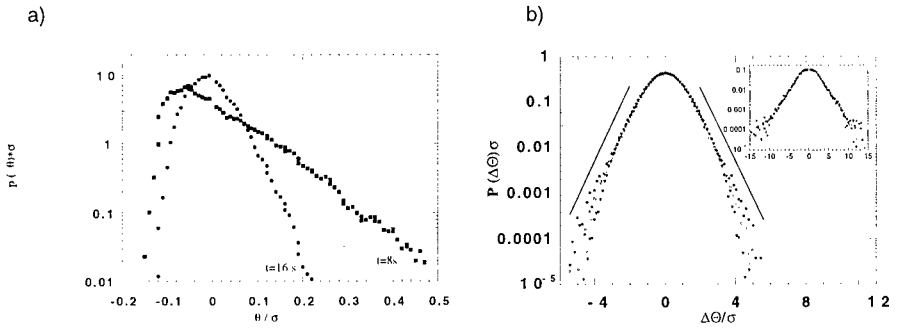


Figure 3: a) Rescaled distributions of the fluctuations of concentration at time t=8 s and t=16 s. b) Rescaled distributions of the concentration increments at time t=16 s for three different increments in the Batchelor range. The insert shows the numerical result for the same increments at the same time.

Another quantity of interest is the standardized (*i.e.* rescaled so as the variance be unity) PDFs of the concentration increments defined by:

$$\Delta\theta = \theta(\mathbf{x} + \mathbf{r}) - \theta(\mathbf{x})$$

where r is the scale. These PDFs appear self-similar in space, and roughly symmetric (Fig.3.b); the small increment region looks Gaussian while the tails, defined for increments above one standard type deviation, may be fitted by exponential functions. We thus have here a Gaussian bump with exponential tails, which agrees well with the theoretical predictions of [6, 7, 8]. The analyse of the structure function of the concentration increments defined by

$$S_p = \langle(\theta(\mathbf{x} + \mathbf{r}) - \theta(\mathbf{x}))^p\rangle$$

shows that there is no clear power law, and one may propose a logarithmic law for representing $S_2(r)$ (Fig.2.b). The fit formula for $S_2(r)$ turns out to be consistent with the early proposals of Batchelor [3] and Kraichnan [5]. In the framework of

Chertkov *et al.* [6] theory our fit formula corresponds to the case where, in the enstrophy cascade, the logarithmic corrections are small (which appears to be the case in our experiment [9]). We thus have consistency between the theory and the experiment. We will also present new observations on intermittent concentration fields, obtained in the inverse cascade of energy. This experiment reveals a situation where the tracer field is intermittent while the underlying velocity field is close to gaussian at all scales; this provides a physical support to recent theoretical developments based on the Kraichnan model. This work was supported by the Centre National de la Recherche Scientifique, the Ecole Normale Supérieure and the Universités Paris 6 and Paris 7.

References

[1] H. L. Grant, B. A. Hugues, R. B. Williams and A. Moillet. The spectrum of temperature fluctuations in turbulent flow. *J. Fluid Mech.*, 34:423, 1968.

[2] N. S. Oakey. Determination of the rate of dissipation of turbulent energy from simultaneous temperature and velocity shear measurements. *J. Phys. Oceanogr.*, 12:256, 1982.

[3] G. K. Batchelor. Small-scale variation of convected quantities like temperature in turbulent fluid. *J. Fluid Mech.*, 5:113, 1959.

[4] A. Crisanti, M. Falcioni, G. Paladin and A. Vulpiani. Role of lagrangian chaoticity and the small scale structure of passive scalars in fluids. *Physica A*, 166:305, 1990.

[5] R. Kraichnan. Small-scale structure of a scalar field convected by turbulence. *Phys. Fluid.*, 11:945, 1968.

[6] M. Chertkov, G. Falkovich, I. Kolokolov and V. Lebedev. Statistics of a passive scalar advected by a large-scale two-dimensionnal velocity field: Analytic solution. *Phys. Rev. E*, 51:5609, 1995.

[7] G. Falkovich, I. Kolokolov, V. Lebedev and A. Migdal. Instantons and intermittency. *Phys. Rev. E*, 54:4896, 1996.

[8] E. Balkovsky and A. Fouxon. Universal long-time properties of Lagrangian statistics in the Batchelor regime and their application to the passive scalar problem. *Phys. Rev. E*, 60:4164, 1999.

[9] J. Paret, M.-C. Jullien and P. Tabeling. Vorticity statistics in the two-dimensional enstrophy cascade. *Phys. Rev. Lett.*, 83:3418, 1999.

[10] M.- C. Jullien, P. Castiglione and P. Tabeling. Experimental observation of the Batchelor dispersion of passive tracers. *Phys. Rev. Lett.*, submitted.

ADVANCES IN TURBULENCE VIII
Proceedings of the Eighth European Turbulence Conference
C. Dopazo et al. (Eds.)
© CIMNE, Barcelona 2000

The Kinetics and Geometry of Turbulent Mixing

E. Villermaux and J. Duplat

IRPHE, Université de Provence,
Centre de Saint Jérôme
Service 252, 13397 Marseille Cedex 20, France.

Contact e-mail: villerma@lrc.univ-mrs.fr

1 Introduction

Mixing, as suggested by our common sense, is the operation by which a system evolves from one state of simplicity (the initial segregation of the constituents) to another state of simplicity (the complete uniformity of the mixture). Between these extremes, complex patterns birth, and die. Questions arise : how can the complex patterns geometry be characterized, what is the clock of the process and what are the structures involved in the flow ? Indeed mixing is, in the strict sense, a transient process from the initial segregation to the ultimate homogeneity. Transients call for the understanding of the kinetics, and time scales. We first focus on the kinetics of mixing from an isolated scalar source in a turbulent flow. Then, we show how a complex mixture results from the superposition of elementary sources. Both the statistical signature of a single source, and the composition law between multiple sources are established experimentally.

2 The single source response

Experiments are conducted allowing to follow an initially smooth and compact blob of dye released in a turbulent flowalong its transient evolution, from the initial segregation, in its route to uniformity. We inject continuously in the far field and on the axis of a turbulent jet the scalar to be mixed via a small tube whose diameter d is smaller than the local integral scale L (typically $d/L \approx 1/10$, see figure 1) and we record the concentration signal at different locations x downstream of the injection point, up to a distance of the order of the integral scale. The injection point behaves neither as a source, nor as a sink of momentum, in the mean, and the properties of the flow (stirring scale L, r.m.s. velocity u') are constant in the range of observation of the mixing process. These experiments



Figure 1: Instantaneous planar cuts of the scalar field (disodium fluorescein in water, $Sc = 2000$) downstream of the injection point illustrating how a scalar blob, initially compact and smooth, is progressively converted into disjointed sheets with broad fluctuations in thickness and concentration. $d = 1$ cm. *Left*: the picture covers the region just downstream of the injection tube $0 < x/d < 4$. *Right*: farther downstream $4 < x/d < 8$.

involve three types of scalars, temperature in air ($Sc = \nu/D = 0.7$), temperature in water ($Sc = 7$) and the concentration of disodium fluorescein in water ($Sc = 2000$) thus allowing the quantitative study of the process sensivity to the intrinsic diffusive molecular properties of the scalar being mixed (Villermaux et al. 1998 [1]). The concentration fluctuations Probability Density Function (PDF) $P(C)$ resulting from the transient turbulent mixing of the blob exhibits rapidly a decreasing exponential shape, sharpening in time

$$P(C) \sim (\gamma t_s)^{-1/2} \exp\left(-\frac{t}{t_s}C\right) \qquad \text{where} \qquad t_s \sim \frac{d}{u'}\ln(5Sc) \qquad (1)$$

and is parametrised by a mixing time t_s which depends solely on the injection time of the blob in the medium $\frac{d}{u'}$, on the Schmidt number Sc, independently of the Reynolds number. C denotes the scalar concentration normalized to the injection concentration. The geometry of the concentration field is studied by a laser induced fluorescence technique on plane cuts through the medium. Global features such as the scalar dispersion from the source, as well as the fine structure of the scalar field are analyzed. In particular, we define the volume occupied by the regions whose concentration is larger than a given concentration threshold (support of the scalar field) and the surface in which this volume is embodied (boundary of the support). The volume and surface extents, their respective fractal dimensions are measured as a function of time t, and concentration threshold

normalized to the initial concentration C_s for different injection sizes d. All of these quantities display a clear dependence on t, d and C_s, and their evolutions rescale with the variable

$$\xi = \frac{u't}{d} C_s, \tag{2}$$

consistently with the dependencies of the mixing time (1) on d and u'. The fractal dimension is, in addition, scale dependent. The surface to volume ratio and the fractal dimension of both the volume and the surface tend towards unity at large ξ, reflecting the sheet-like structure of the scalar at small scale (Villermaux and Innocenti 1999 [2]).

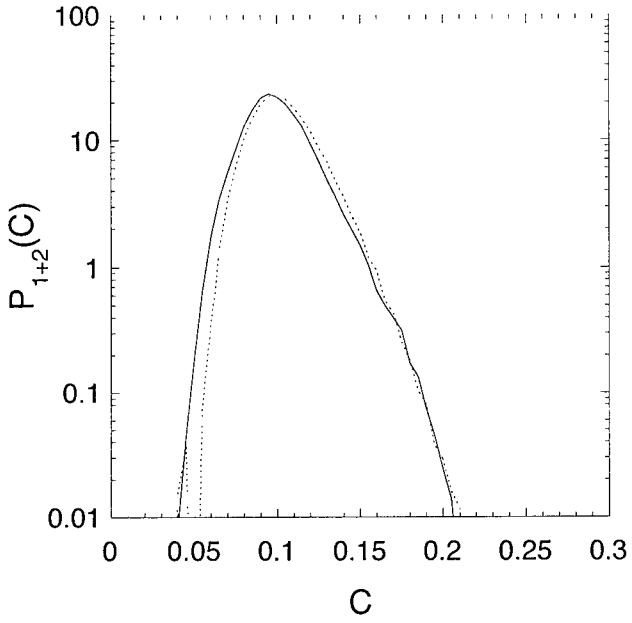


Figure 2: Two sources disposed in the vicinity of each other, and their individual response are identical, given by equation (1), with $Sc = 2000$, $ut/d = 17$. The continuous line represents the experimental compound PDF, and the dashed line represents the convolution of the original two PDF's, each associated to one of the sources.

3 Multiple sources

The response of one scalar source being established, the interaction of multiple sources is also considered. Indeed, scalar fluctuations in a real flow, such as those found in a hot turbulent jet discharging in a quiescent cold environment are the result of cumulated contributions from different parcels of cold fluid entrained at the boundary of the jet in the course of its development. If $P_1(C)$ and $P_2(C)$ are the PDF's of two sources disposed in the vicinity of each other, the compound PDF $P_{1+2}(C)$ is established experimentally (figure 2). In the dilluted limit, the compound PDF is very close to the convolution of the two original sources i.e.

$$P_{1+2}(C) = P_1(C) \otimes P_2(C), \tag{3}$$

consistently with the linear character of the scalar evolution equation. We extend this result to the turbulent jet problem, for which we show that the scalar fluctuation PDF on the centerline can be decomposed in well defined elementary contributions.

4 Conclusions

These findings, which offer an original picture of the kinetics of turbulent mixing, also suggest that a complex mixture can be understood as the superposition of the contributions of sources, whose spatial distribution reflects the entrainment properties of the flow.

References

[1] E. Villermaux, C. Innocenti and J. Duplat. Scalar fluctuations PDF's in transient turbulent mixing. *C. R. Acad. Sci. Paris*, t. 326:21–26, 1998.

[2] E. Villermaux and C. Innocenti On the geometry of turbulent mixing. *J. Fluid Mech.*, 393:123–145, 1999.

ADVANCES IN TURBULENCE VIII
Proceedings of the Eighth European Turbulence Conference
C. Dopazo et al. (Eds.)
© CIMNE, Barcelona 2000

Averaged dynamics in the phase planes of a scalar field using DNS data

J. Martín[1], C. Dopazo[1] and L. Valiño[2]

[1]Fluid Mechanics Group, University of Zaragoza. C. María de Luna s/n. 50015 Zaragoza. SPAIN
[2] Laboratorio de Investigación en Tecnologías de la Combustión (LITEC). CSIC. C. María de Luna s/n. 50015 Zaragoza. SPAIN

Contact e-mail: jjmartin@posta.unizar.es

1 Introduction and Mathematical Formulation

Scalar mixing in a turbulent flow is characterized by a wide range of time and length scales, over which a variety of physical mechanisms take place[1]. The scalar evolution is driven by the velocity field and involves convection, random straining and rotation, and molecular transport.

Much effort has been invested in the past years to describe and understand the scalar phenomena in turbulent flows using data from Direct Numerical Simulations (DNS)[2, 3, 4]. That work has been generally focused on the scaling of intermittency of the scalar-related magnitudes, the study of statistical correlations between the scalar and velocity fields and also in the description of the effect of the velocity field coherent structures on the scalar features.

The work presented here intends to introduce a new point of view to study the scalar mixing processes. Given a pair of variables of interest, the method consists in using conditional averages of their transport equations to obtain an *averaged dynamical system* in the 2-D phase space associated to these variables. This idea, introduced by Martn *et al*[5] for the study of the velocity gradient invariants, permits to describe the joint evolution of any pair of variables in a simple, direct way. The technique is also useful to isolate the effect of each equation term on the global dynamics, enabling to understand the role of its corresponding physical mechanism. The mathematical formulation of this method follows: given a pair of variables X and Y, the time derivatives $\dot{X} = dX/dt$ and $\dot{Y} = dY/dt$, at each point of the phase space (X, Y), are calculated from the DNS data. This is carried out taking conditional averages of the right hand sides of the corresponding transport equations. This is expressed as

$$\dot{X}(X,Y) = \left\langle \frac{dX}{dt} \middle| X, Y \right\rangle \tag{1}$$

$$\dot{Y}(X,Y) = \left\langle \frac{dY}{dt} \middle| X,Y \right\rangle \tag{2}$$

The vector $(\dot{X}(\mathrm{X,Y}), \dot{Y}(\mathrm{X,Y}))$ is the *velocity* at each point of the phase space. Eqs. (1) and (2) constitute a dynamical system, since the velocity depends solely on the coordinates (X, Y). It must be noticed at this point that this dynamical system is time dependent, since the statistics of the scalar field is evolving with time. This fact raises the need of further investigation on how the resulting scalar dynamics changes with time and also suggests to search for self-similarity and universal behavior.

2 Numerical experiments and Results

Data fields from 128^3 DNS runs for an inert scalar have been used in this work. The velocity field is forced and a Reynolds number $Re_\lambda \simeq 47$ is reached. This low Re_λ has been taken to guarantee a proper numerical resolution of the high order scalar derivatives required for the calculations. The value of the Schmidt number, Sc, is 1.0. The initial scalar distribution is a double Dirac delta with peaks at the boundaries 0 and 1. The results presented here correspond to a time when the scalar pdf has relaxed to a nearly uniform distribution, but still with two peaks near the extreme values, 0 and 1.

Figure 1 displays the dynamical system resulting for the phase plane scalar fluctuation-diffusion term, $(c, D\nabla^2 c)$. Figure 2 shows the result for the square scalar fluctuation-scalar dissipation rate phase plane, (c^2, ϵ_c). The joint pdfs are also depicted using isocontours in log-scale. Mean trajectories can be calculated from the vector fields. These trajectories, not shown here, indicate the most probable evolution for the variables, given the initial values. The $(c, D\nabla^2 c)$ plane presents a stable focus at the origin, with points moving clockwise spirally until they reach the center. It can be observed that points with large values of diffusion change the sign of the scalar fluctuation before it becomes zero. The (c^2, ϵ_c) plane shows that points with large initial square fluctuations strongly increase a moderately small value of the dissipation; the larger the values of the scalar fluctuation and of the dissipation rate, the larger that increment is. On the contrary, for small values of c^2 the scalar dissipation is a monotonically decreasing magnitude.

The quantity $-2DS_{i,j}c_{,i}\,c_{,j}$, which appears in the transport equation of ϵ_c, is a production term responsible for amplification of the local scalar dissipation rate. It is well known[3] that this fact is due to the alignment of the scalar gradient vector with the principal axis of the strain corresponding to its negative eigenvalue γ. Similarly to the stretching rate $\sigma = S_{ij}\omega_i\omega_j/\omega^2$, used for the vorticity dynamics, a "scalar gradient stretching rate" can be defined as $\sigma_{\nabla c} \equiv S_{ij}c_{,i}\,c_{,j}\,/c_{,k}\,c_{,k}$. This magnitude indicates the (positive or negative) rate of change of the local scalar dissipation due to the turbulence straining action. It should be noticed here that a negative value of $\sigma_{\nabla c}$ implies amplification of ϵ_c,

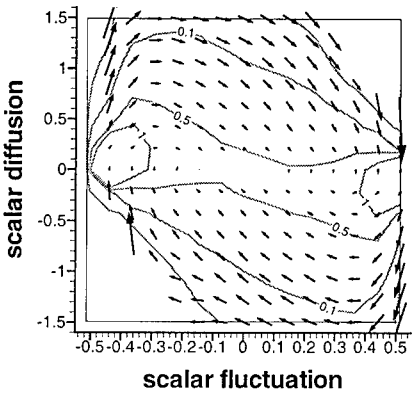


Figure 1: Averaged dynamical system resulting in the phase plane$(c, D\nabla^2 c)$

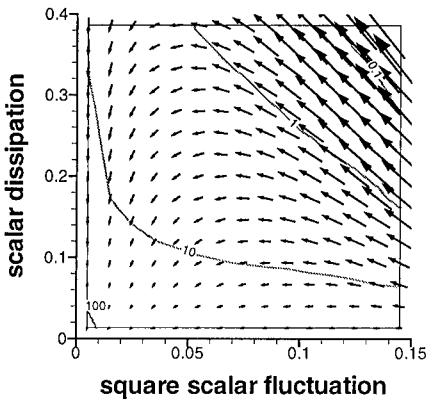


Figure 2: Result in the plane (c^2, ϵ_c)

while positive values imply a reduction. Figure 3 shows the dynamics in the plane $(\sigma_{\nabla c}, \epsilon_c)$ from the DNS data. The result indicates that in almost any case, the magnitude of $\sigma_{\nabla c}$ increases, this effect being larger for negative values than for positive ones. The scalar dissipation increases in a slow but systematic way in all points of the semiplane $\sigma_{\nabla c} < -6.0$, and has a fast decay in the right semiplane.

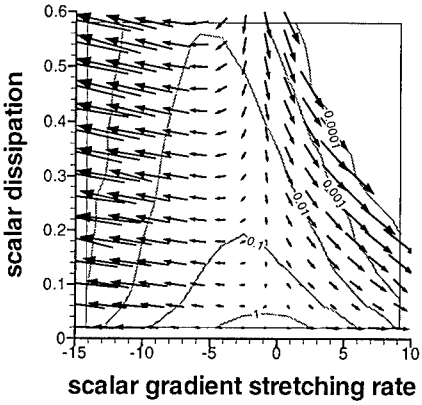


Figure 3: Phase plane $(\sigma_{\nabla c}, \epsilon_c)$

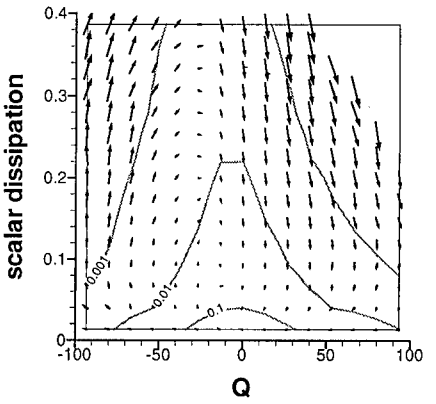


Figure 4: Phase plane (Q, ϵ_c)

The effects of vorticity and strain on the scalar mixing have been studied considering the phase planes (Q, c^2) and (Q, ϵ_c). The second invariant of the velocity gradient tensor, $Q = Q_W + Q_S$, gives a quantitative estimation of the

local balance between rotation ($Q_W = \omega^2/4$) and strain ($Q_S = -S_{ij}S_{ij}/2$). The result in the plane (Q, c^2), not shown, indicates that the square scalar fluctuations decrease for all values of Q, being this process enhanced in the left semiplane ($Q < 0$) corresponding to high strain and low vorticity regions of the flow. This is consistent with the result in Figure 4, where ϵ_c is found to increase strongly for large strain values ($Q < 0$), while it is progressively reduced as the strain diminishes and the vorticity dominates the balance ($Q > 0$). Both processes, the increase of the scalar dissipation in the left semiplane and the reduction in the right one, are enhanced for large values of ϵ_c.

3 Conclusions

- A new method for the study of the scalar mixing in turbulence has been introduced. The averaged joint dynamics of any pair of variables results from their transport equations by the use of conditional averages.
- The method permits the analysis of different mechanisms in the scalar evolution. The effects of the local motions topology along the mixing process can be also described and visualized in an explicit way.
- The averaged dynamical systems obtained are time-dependent due to the non-stationary nature of the scalar field. Further work is needed to analyze the implications of this time evolution.

References

[1] Dopazo, C. 1994. "Recent Developments in PDF methods", In *Turbulent reacting flows*, Eds. Libby, P.A. and Williams, F.A., Ch 7, 375, Academic Press.

[2] Kerr, R.M. 1985. "Higher-order derivative correlations and the alignment of small-scale structures in isotropic numerical turbulence", *J. Fluid Mech.* **153**(31).

[3] Arhurst, W.T., Kerstein, A.R., Kerr, R.M., and Gibson, C.H. 1987. "Alignment of vorticity and scalar gradient with strain rate in simulated Navier-Stokes turbulence", *Phys. Fluids A*, **8**(30), 2343-2353.

[4] Ruestch, G.R. and Maxey, M.R. 1991. "Small-scale features of vorticity and passive scalar fields in homogeneous isotropic turbulence", *Phys. Fluids A*, **3**(6), 1587-1597.

[5] Martín, J., Ooi, A., Chong, M.S. and Soria, J. 1998. "Dynamics of the velocity gradient tensor invariants in isotropic turbulence", *Phys. Fluids*, **10**(9), 2336-2346.

ADVANCES IN TURBULENCE VIII
Proceedings of the Eighth European Turbulence Conference
C. Dopazo et al. (Eds.)
© CIMNE, Barcelona 2000

Inclusion of the effect of turbulent production in a generalization of Yaglom's equation

L. Danaila[1] and L. Mydlarski[2]

[1]I.R.P.H.E.
12 Avenue Général Leclerc, 13003 Marseille, FRANCE
[2]McGill University – Department of Mechanical Engineering
817 Sherbrooke Street West, Montréal, Québec, H3A-2K6, CANADA

Contact e-mail: laurentm@mecheng.mcgill.ca

1 Introduction

In 1949, Yaglom[1] derived an equation for the passive scalar field (analogous to that derived by Kolmogorov for the velocity field) relating the third-order mixed structure function, the second-order scalar structure function and the rate of destruction of temperature half variance:

$$-\langle \Delta u_1 (\Delta\theta)^2 \rangle + 2\kappa \frac{d}{dr} \langle (\Delta\theta)^2 \rangle = \frac{4}{3} \langle \epsilon_\theta \rangle r, \tag{1}$$

where θ is the fluctuating temperature field, $\langle \cdot \rangle$ denotes time averaging, the longitudinal velocity increment $\Delta u_1 = u_1(x_1 + r) - u_1(x_1)$ is measured along the stream-wise direction, x_1, $\langle \epsilon_\theta \rangle = \kappa \langle (\frac{\partial \theta}{\partial x_i})^2 \rangle$ includes temperature derivatives in all directions and κ is the scalar molecular diffusivity.

Yaglom's equation can be considered to be a scale-by-scale budget of the temperature variance. It is of capital importance to the study of turbulence, being the only relationship directly deduced from the advection-diffusion equation for temperature. Recently, Danaila *et al.*[2] derived a generalized form of Yaglom's equation which accounts for the effects of the non-stationarity of second-order moments in decaying flows such as grid turbulence, jets and wakes. This new equation was tested and well verified ($\pm 10\%$) in heated grid turbulence.

The aim of the present work is to account for the effect of turbulent production of temperature fluctuations (arising from the presence of a mean temperature gradient) in an equation of the form (1). The flow under consideration is decaying grid turbulence with an imposed mean temperature gradient (Mydlarski and Warhaft [3]). Temperature fluctuations are created by the (large-scale) mean temperature gradient, G, in the x_3 direction.

To this end, a further generalized form of Yaglom's equation (incorporating the effects of decay *and* production) is developed and compared with experimental data. The philosophical approach consists of studying the role played by the mean temperature gradient, a large-scale anisotropy, in the scale-by-scale budget of the temperature variance (Yaglom's equation).

2 Theory and Results

For the flow under consideration, we start from the advection-diffusion equation, written at a point in space, $\vec{x}$:

$$\frac{\partial \theta}{\partial t} + \vec{u}\vec{\nabla}\theta + Gu_3 = \kappa \nabla^2 \theta, \tag{2}$$

where the gradient vector $\vec{\nabla} \equiv (\partial/\partial x_1, \partial/\partial x_2, \partial/\partial x_3)$ and ∇^2 is the Laplacian. G is in the x_3 direction. We then write the same equation for another point in space, $\vec{x}^+ (= \vec{x} + \vec{r})$. By subtracting (2) from the equation at $\vec{x}^+$, multiplying the result by $2\Delta_{\vec{r}}\theta (= 2(\theta(\vec{x}+\vec{r}) - \theta(\vec{x})))$ and spatially averaging, one obtains:

$$\frac{\partial}{\partial t}\langle(\Delta_{\vec{r}}\theta)^2\rangle + \vec{\nabla}_{\vec{r}}\langle\Delta_{\vec{r}}\vec{u}(\Delta_{\vec{r}}\theta)^2\rangle + 2G\langle\Delta_{\vec{r}}u_3\Delta_{\vec{r}}\theta\rangle = 2\kappa\nabla^2\langle(\Delta_{\vec{r}}\theta)^2\rangle - 4\langle\epsilon_\theta\rangle, \tag{3}$$

where $\Delta_{\vec{r}}$ denotes a difference between a value measured at $\vec{x}+\vec{r}$ and its value at $\vec{x}$. Note that Eq. (3) assumes homogeneity of the passive scalar field when transforming spatial derivatives $\vec{\nabla}$ to $\vec{\nabla}_{\vec{r}} = (\partial/\partial r_i)$. In an isotropic passive scalar field, $\langle\Delta_{\vec{r}}u_3\Delta_{\vec{r}}\theta\rangle$ should be zero, whereas in the flow investigated here, both the non-stationary term $\partial/\partial t\langle(\Delta_{\vec{r}}\theta)^2\rangle$ and the production term $2G\langle\Delta_{\vec{r}}u_3\Delta_{\vec{r}}\theta\rangle$ are non-zero. In the limit of $\vec{r}\to\infty$, Eq. (3) reduces to the one-point temperature variance budget, where the temperature dissipation $\langle\epsilon_\theta\rangle$ is balanced by both the decay ($\frac{\partial}{\partial t}\langle\theta^2\rangle$) and the production ($G\langle u_3\theta\rangle$) of temperature variance.

We proceed to consider the turbulent advection and molecular diffusion terms. Since they correspond to the small-scale motions, we assume they are locally isotropic and will therefore only depend on the modulus $r = |\vec{r}|$. For simplicity, we measure r along the x_1-axis. The decay term is a large–scale, non-homogeneous term (see [2] for further physical explanations), but can also be considered as depending solely on r (since it involves second-order structure functions). The production term $\mathcal{P} = 2G\langle\Delta_{\vec{r}}u_3\Delta_{\vec{r}}\theta\rangle$ is not isotropic. However, in the limit of large scales, the directional differences in this term disappear, since $\lim_{|r|\to\infty}\mathcal{P}(\vec{r}) = 4G\langle u_3\theta\rangle$, regardless of the orientation of $\vec{r}$. For small scales, the value of $\mathcal{P}$ depends slightly on the spatial direction. However, the contribution of $\mathcal{P}$ to equation (3) decreases with scale size. Therefore, it is a reasonable approximation to evaluate $\mathcal{P}(\vec{r})$ using only one spatial direction (x_1), since its contribution is significant only at large scales.

A derivation similar to that of Yaglom[1] (see also Danaila *et al.*[2]) then

results in a generalized form of Yaglom's equation:

$$-\langle \Delta u_1 (\Delta\theta)^2 \rangle + 2\kappa \frac{d}{dr}\langle (\Delta\theta)^2 \rangle - \frac{1}{r^2}\int_0^r y^2 \cdot [2G\langle \Delta u_3 \cdot \Delta\theta \rangle (y)]\, dy$$
$$-\frac{1}{r^2}\int_0^r y^2 \cdot \left[U_1 \frac{d}{dx_1}\langle (\Delta\theta)^2 \rangle (y)\right] dy = \frac{4}{3}\langle \epsilon_\theta \rangle r, \qquad (4)$$

where y is a dummy variable representing the separation in the longitudinal direction, x_1. All terms are then obtained using simultaneous measurements of two–velocity components (u_1, u_3) and of temperature.

This equation includes the effects of the non-stationarity of second-order moments and the large-scale anisotropy (*viz.* the mean temperature gradient in the x_3-direction). We rewrite (4) in the form:

$$A + B + S_1 + S_2 = C, \qquad (5)$$

where the terms A, B and C are the terms from Yaglom's equation $(A+B=C)$, S_1 is a source term arising from the mean temperature gradient and S_2 is a source term arising from the non-stationarity of the second-order moments. Figure 1

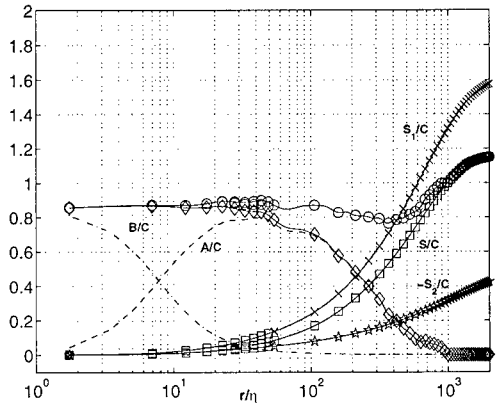


Figure 1: Non-dimensionalized measurements of the terms in the generalized form of Yaglom's equation (4) $((A + B + S_1 + S_2)/C = 1)$. The sum of A/C (dashed line) and B/C (dot-dashed line) – Yaglom's original equation – is represented by $\diamond$. The S_1/C source term is given by $\times$, $-S_2/C$ by $\star$ and their sum $(S/C = (S_1 + S_2)/C)$ by $\square$. The sum of all the terms $((A + B + S)/C)$ is given by $\circ$.

displays the terms comprising (4) as determined from the grid turbulence data of Mydlarski and Warhaft[3] for $R_\lambda \approx 200$. It can be seen that Yaglom's equation $(A/C + B/C = 1)$ is poorly verified for $r/\eta \geq 40$, while the generalized form of Yaglom's equation (4) is verified over a much larger range of scales. The

difference between experiment and theory of about 15% (below the theoretical prediction of 1.0) is due to the anisotropic nature of the scalar dissipation rate in flows with mean temperature gradients[3, 4].

The source terms S_1 and S_2 are significant at large scales (and decrease in magnitude with decreasing scale size). The production term S_1 (which results from the mean temperature gradient) is about 3 times more important than S_2 at the largest scales. (However, in decaying grid turbulence (heated without a mean gradient by means of a mandoline) a term such as S_2 is the only "source term" present.) Here, term S_2 is negative, since temperature fluctuations, under the effect of G, continuously increase in x_1.

3 Conclusions

We have derived a generalized form of Yaglom's equation for the case of decaying grid turbulence with an imposed mean temperature gradient. The large-scale motion is characterized by two phenomena: the decaying effect behind the grid and the production of temperature fluctuations due to the presence of the mean temperature gradient, G. These physical effects are mathematically expressed as two new terms in Yaglom's equation. Equation (4) is well satisfied over an extended range of scales, particularly so for the very large scales. This result emphasizes the role played by the large-scale motion, decomposed, here, into two different effects. However, it is obvious that the persistent anisotropy already noticed at very small scales in such a flow can not be "solved" nor explained by such an approach, and this problem requires further efforts.

Funding for this work was provided by FCAR, NSERC and the USDOE (Basic Energy Sciences). L. D. gratefully acknowledges support received by means of a "Bourse d'Excellence du Gouvernement du Québec." F. Anselmet, A. Pumir, R. Antonia, Z. Warhaft and E. Lindborg are also thanked for fruitful discussions.

References

[1] A. M. Yaglom. On the local structure of a temperature field in a turbulent flow. *Dokl. Akad. Nauk. SSSR* , 69:743–746, 1949.

[2] L. Danaila, F. Anselmet, T. Zhou and R. A. Antonia. A generalization of Yaglom's equation which accounts for the large-scale forcing in heated decaying turbulence. *J. Fluid Mech.*, 391:359–372, 1999.

[3] L. Mydlarski and Z. Warhaft. Passive scalar statistics in high-Péclet-number grid turbulence . *J. Fluid Mech.*, 358:135–175, 1998.

[4] S. T. Thoroddsen and C. W. Van Atta. Experiments on density-gradient anisotropies and scalar dissipation of turbulence in a stably stratified fluid. *J. Fluid Mech.*, 322:383–409, 1996.

VII

Instabilities and Transition

ADVANCES IN TURBULENCE VIII
Proceedings of the Eighth European Turbulence Conference
C. Dopazo et al. (Eds.)
© CIMNE, Barcelona 2000

A Naimark-Sacker route to turbulence in a periodically forced flow

F. Marques[1], J. M. Lopez[2], and J. Shen[3]

[1]Universitat Politecnica de Catalunya, Barcelona, Spain
[2]Arizona State University, Tempe AZ 85287-1804, USA
[3]Pennsylvania State University, State College PA 16802, USA

Contact e-mail: marques@fa.upc.es, lopez@math.la.asu.edu, shen@math.psu.edu

Recent experiments of Weisberg et al. (1997) have demonstrated that the onset of the centrifugal instability leading to Taylor vortex flow can be delayed by harmonic oscillations of the inner cylinder in the axial direction. Marques & Lopez (1997, 2000) used Floquet analysis to describe the observed control of the instability over a wide range of frequencies and amplitudes of this oscillation; the dynamics remained axisymmetric and the response to the applied periodic control mechanism was synchronous over an extensive range of parameters. Here we implement an accurate and efficient spectral-projection scheme for solving the fully nonlinear axisymmetric Navier-Stokes equations to examine the effects of endwalls on the flow dynamics and the breaking of space-time symmetries.

We present a numerical study of a periodically forced centrifugally unstable flow, well into the nonlinear regime. For the physically realistic case of finite length annulus, the endwalls and the finite aspect ratio of the annulus are dynamically important. These nonlinear effects are investigated with a very efficient and accurate spectral-projection method for solving the fully nonlinear axisymmetric Navier-Stokes equations. Attention is focused on the axisymmetric states, guided by the results of the fully three-dimensional Floquet analysis, and two scenarios are considered: the forcing amplitude Re_a or the Couette flow Reynolds number Re_i are varied while keeping other parameters fixed.

1 Multiple solutions

At a set value of $Re_i = 200$ and reducing Re_a from 100 to 50, the nonlinear response of the system was synchronous with the forcing frequency. The flow undergoes a smooth transition from a flow with essentially no axial variation, other than near the endwalls, for $Re_a > 80$, to a state with Taylor cells for $Re_a <$

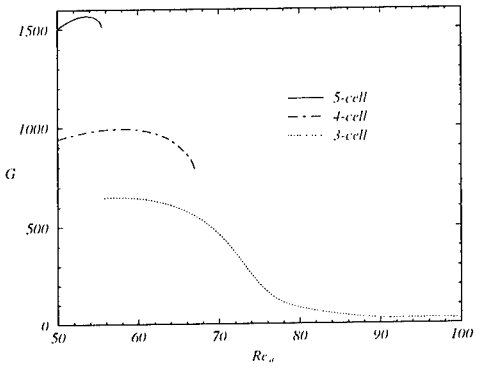


Figure 1: Bifurcation diagram showing multiple solution branches as Re_a is varied, for $Re_i = 200$ and $\omega_f = 30$. The quantity G is a measure of the flow state's axial variation.

70. As Re_a is further reduced, additional solution branches, all synchronous with the forcing, are encountered (see Fig. 1). The existence of multiple flow states with differing length scales is typical of pattern forming systems in enclosed regions.

2 Naimark-Sacker route to chaos

When Re_a was fixed and Re_i increased, we encountered a Naimark-Sacker bifurcation leading to flow on a 2-torus. The solution subsequently followed a Ruelle-Takens route to chaos, in this case through a 1:9 resonance horn. A separate stable branch of 3-tori solutions that appear via a global bifurcation has also been found. Over a range of parameters, there co-exist at least three distinct quasiperiodic stable states (see Fig. 2). The numerical results suggest that these bifurcation sequences are physically related to the the coupling between the Taylor-Stokes vortices and the endwall Ekman vortices.

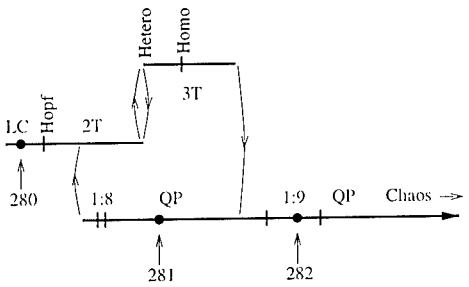


Figure 2: Bifurcation diagram as Re_i is varied with $Re_a = 80$ and $\omega_f = 30$.

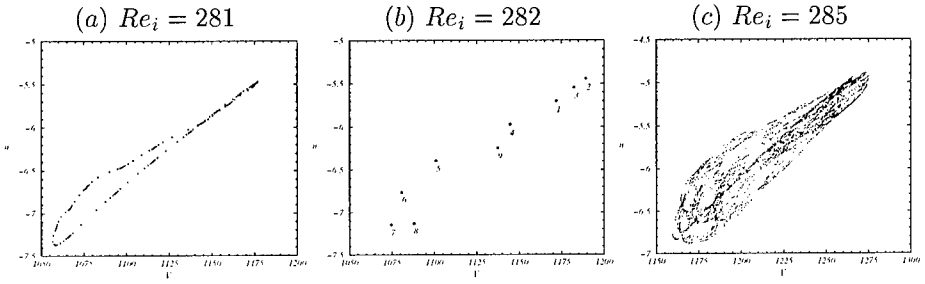


Figure 3: Poincaré maps for $Re_a = 80$, $\omega_f = 30$, $e = 0.905$, $\Lambda = 10$, and Re_i as indicated. For the locked case of $Re_i = 282$, the order in which the trajectory passes through the Poincaré map is indicated.

By $Re_i = 281$, a Naimark-Sacker bifurcation has occurred. The limit cycle behavior observed at the lower Re_i has given way to a 2-torus. The corresponding Poincaré map (Fig. 3*a*) clearly shows the presence of an invariant circle. Note that the trajectory on the circle is not uniform, but shows the typical bottleneck behavior associated with a nearby saddle-node bifurcation. The two frequencies ω_s and ω_f are close to a 1:9 resonance, and hence the bottleneck behavior. Increasing Re_i to 282, the solution branch undergoes a saddle-node bifurcation as it enters a 1:9 resonance horn (see Fig. 3*b*, where the order in which the iterates of the map appear is indicated). The ordering is a strong indication that the locking is 1:9, rather than n:9 with $n > 1$. Increasing Re_i beyond 282, the solution leaves the 1:9 resonance horn, and by $Re_i = 285$ behavior characteristic of chaos is observed. The Poincaré map shows clear evidence of the breakup of the 2-torus (Fig. 3*c*).

3 Three-tori solutions

We have located a range ($Ri \in [280.89, 281.26]$) where stable 3-tori solutions co-exist (with $\omega_{VLF} << \omega_s, \omega_f$). Over the range of Ri where 3-tori solutions exist the period associated with the third frequency, $T_{VLF} = 2\pi/\omega_{VLF}$, experiences dramatic changes over this range, as shown in Fig. 4. There are two Ri values where T_{VLF} becomes unbounded. Infinite-period bifurcations are usually associated with homoclinic or heteroclinic behavior.

The range of Ri where 3-tori exist consisting of two branches; for $Ri_{het} < Ri < Ri_{hom}$ there is a single symmetric 3-torus and for $Ri > Ri_{hom}$ a pair of non-symmetric, but symmetrically related, 3-tori. The first branch starts in a heteroclinic bifurcation and is related to the second branch via a homoclinic bifurcation at $Ri = Ri_{hom}$. In this homoclinic bifurcation a symmetric 3-torus splits in two symmetrically related 3-tori. We have found for the first time a gluing bifurcation of 3-tori in a real fluid system. This bifurcation sequence is

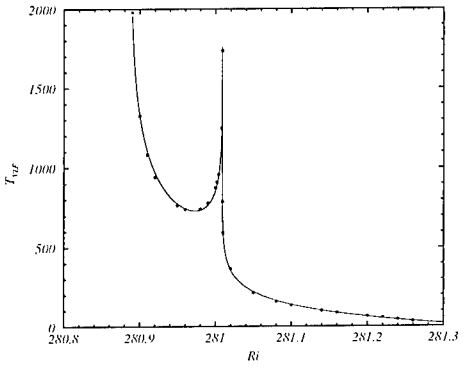


Figure 4: Variation of $T_{VLF} = 2\pi/\omega_{VLF}$ with Ri.

shown in Fig. 5.

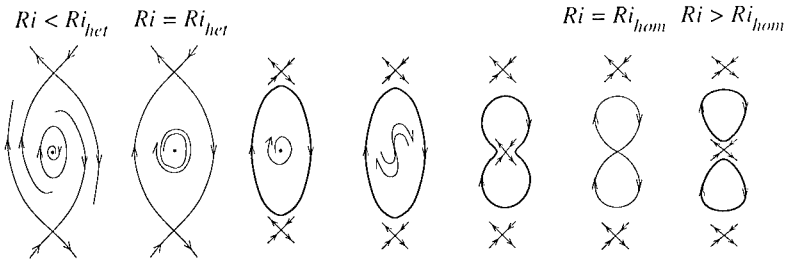


Figure 5: Schematic of the bifurcation sequence for the 3-tori solutions. In this schematic, 2-tori are represented as fixed points and 3-tori as cycles.

This work was supported by NSF grants DMS-9706951 and INT-9732637, and SEEUID grants PB97-0685 and PR1999-0272.

References

[1] F. Marques and J. M. Lopez. Taylor–Couette flow with axial oscillations of the inner cylinder: Floquet analysis of the basic flow. *J. Fluid Mech.*, 348:153–175, 1997.

[2] F. Marques and J. M. Lopez. Spatial and temporal resonances in a periodically forced extended system. *Physica D*, 136:340–352, 2000.

[3] A. Y. Weisberg, I. G. Kevrekidis, and A. J. Smits. Delaying transition in Taylor–Couette flow with axial motion of the inner cylinder. *J. Fluid Mech.*, 348:141–151, 1997.

ADVANCES IN TURBULENCE VIII
Proceedings of the Eighth European Turbulence Conference
C. Dopazo et al. (Eds.)
© CIMNE, Barcelona 2000

The influence of streamwise modulation on the evolution of three-dimensional wavetrains

Marcello A. F. Medeiros

Departamento de Engenharia Mecânica
Pontifícia Universidade Católica de Minas Gerais
Av. D. José Gaspar, 500, Belo Horizonte, 30535-610, MG, BRAZIL

Contact e-mail: marcello@pucminas.br

1 Introduction

Previous works [1] have shown that the nonlinear evolution of wavepackets in boundary layers involves the appearance of modes with frequency close to the subharmonic frequency of the fundamental waves. More recent work has also shown that, in the case of the wavepackets, subharmonic resonance alone cannot explain the experimental observations [2]. The current paper presents an experimental investigation of the effect of different degrees of streamwise modulation on the nonlinear evolution of wavetrains.

2 Experimental Set-Up and Precedures

The experiments were carried out in the low turbulent wind tunnel of the University of Cambridge [1]. The free-stream velocity was set to 17.4m/s. The disturbances were introduced by an acoustic point source located on the centreline of the plate at 203mm from the leading edge. The R_δ at that location was about 800. Measurements of the streamwise velocity were taken with a constant-temperature hot-wire anemometer mounted on a three-dimensional traverse gear. The last downstream station was at R_δ about 2000. The signal to noise ratio was improved by repeating the disturbance 128 times for each measuring position and taking the ensemble average of the hot-wire records.

[1] Now located at the Queen Mary and Westfield College, London

3 Experimental Results and Discussion

Figure 1 (top frame) displays hot-wire records taken along the centerline of the plate at a number of distances from the leading edge. The figure shows a comparison of the evolution of wavetrains subjected to different degrees of modulation. The different degrees of modulation are indicated by a letter from A to F. Signal A corresponds to a three-dimensional wavetrain long enough that its central part behaved like a continuous one. In the nonlinear regime the wavetrain A displays a large mean flow distortion. This mean flow distortion has also been observed in numerical experiments with harmonic point sources [3]. It displays a three-dimensional pattern in the form of longitudinal streaks. This phenomenon has been linked to the production of longitudinal vorticity via Reynolds stress interaction. In Fourier space, figure 2 (top frame), the mean flow distortion appears as a very low frequency signal.

In figure 1 (top frame), signal (F) is a wavepacket generated from a pulse. In the physical space the nonlinearity of the packet is characterized by the loss of a ripple. In Fourier space, figure 2, this corresponds to the appearance of modes close to the subharmonic.

When a small degree of modulation is introduced to the wavetrain, signals B, C and D, a mean flow distortion is still observed, albeit only very localized. The results tend to suggest that increasing degrees of modulation produce an increasingly localized mean flow distortion. The picture displays a pattern linking the mean flow distortion of the wavetrain to the loss of a ripple in the wavepacket. In Fourier space the more localized mean flow distortion is represented by a broader band of low frequency components, figure 2.

It is plausible that a highly localized mean flow distortion would include spectral modes with frequencies close to the subharmonic of the fundamental frequencies of the packet. This led to the conjecture that the mean flow distortion observed in three-dimensional wavetrains might provide the seed for the subharmonic resonance in the packet.

Medeiros and Gaster [1] have shown that the nonlinearity in the packet is affected by the phase of the ripples relative to the envelope. The bottom frame of both figures 1 and 2 display signals which are shifted by 180^o with respect to the signals of the top frame. They were produced by driving the acoustic source with an excitation identical to that of the top frames, but negative. The pictures confirm previous results [1] and suggest that the packets of opposite sign display different degrees of nonlinearity. It is also conjectured that this is linked to the fact the phase relation between the subharmonic seed and the fundamental oscillations is be different in each case. The phase relation is known to have an important effect on the resonant interaction.

Aknowledgedments: part of the work was supported by CNPq/Brazil and an ORS Award from UK.

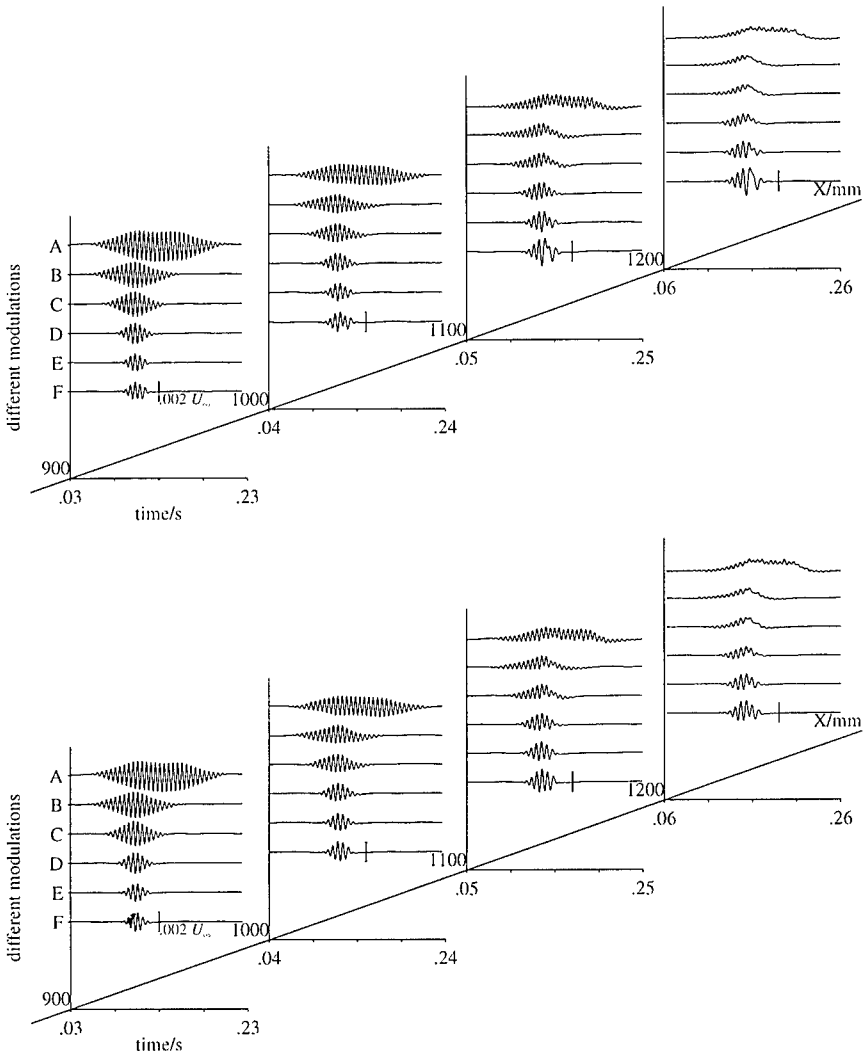


Figure 1: Evolution of waves with different degrees of modulation. Measurements taken along the centerline of the plate at $y = 0.6\delta^*$.Top frame corresponds to a positive excitation and bottom frame to a negative one.

References

[1] M. A. F. Medeiros and M. Gaster. The influence of phase on the nonlinear evolution of wavepackets in boundary layers. *J. Fluid Mech.*, 399:259–283, 1999.

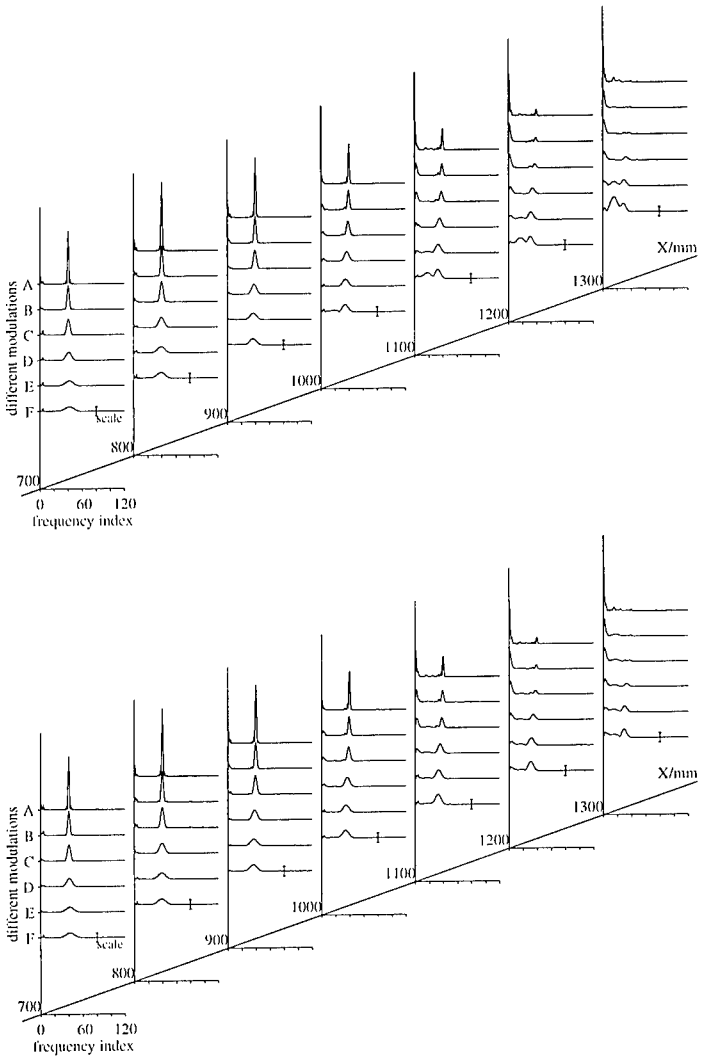


Figure 2: Signals of figure 1 in Fourier space.

[2] M. A. F. Medeiros and M. Gaster. The production of sub-harmonic waves in the nonlinear evolution of wavepackets in boundary layers. *J. Fluid Mech.*, 397:301–318, 1999.

[3] C. Stemmer, K. Kloker, and S. Wagner. DNS of harmonic point source distarbances in an airfoil boundary layer flow. In *29th AIAA Fluid Dynamics Conference*, Albuquerque, NM, June 1998.

ADVANCES IN TURBULENCE VIII
Proceedings of the Eighth European Turbulence Conference
C. Dopazo et al. (Eds.)
© CIMNE, Barcelona 2000

On Flow Reattachment By Periodic Excitation

A. Darabi, L. Lourenco* and I. Wygnanski†

Faculty of Engineering, Tel-Aviv University
Tel-Aviv 69978, ISRAEL

Abstract

The process of forced flow reattachment to an adjacent inclined surface (a "generic flap") was investigated. The flap deflection was set at angles that exceeded the natural separation angle and then periodic perturbations were introduced into the flow at the flap shoulder. This caused the separated mixing layer to progressively adhere to the flap surface. The primary objective of the study was to investigate the transient process and to assess the role of its governing parameters, such as: flap deflection angle in excess of natural reattachment $\triangle \equiv (\delta_f - \delta_{re})$; reduced frequency of the periodic perturbations, $F^+ = fU/L_f$; and perturbation amplitude defined in terms of oscillatory momentum coefficient $< c_\mu >$. It was found that reattachment involves an incremental decrease in the pressure coefficient along the flap due to the passage of discrete vortices induced by the oscillatory forcing. The shortest time required for reattachment is achieved by forcing at $1.2 < F^+ < 1.6$. This is comparable to the most efficient F^+ in attaching the flow with minimum $< c_\mu >$. The forcing intensity did not appear to affect the minimum attachment time provided a threshold value of $< c_\mu >$ was exceeded. The number of perturbation cycles, N_{att}, required to reach a steady state, depends upon the reduced frequency and the flap angle but it was always greater than 10. A positive pressure perturbation associated with the first impingement of the rolled-up vortex onto the surface was observed. Its scale was almost independent of the excitation frequency.

1 Results and Discussion

The experimental setup is described by Nishri & Wygnanski ("The Effect of Periodic Excitation on Turbulent Flow Separation from a Flap", *AIAA J.*, 36:547-556, 1998).

*Professor at Florida State University
†Also Professor at The University of Arizona

The normal aerodynamic force C_n acting on the flap does not reflect the detailed nature of reattachment. However, it is a good indicator of the different stages of reattachment and is used to define the final reattachment time T_{att}, described below. Figure 1 represents a typical evolution of the ensemble-averaged C_n throughout the reattachment process, starting from the initiation of the excitation ($t = 0$), when the latter was not synchronized with the phase of the excitation. For all data presented in this paper, time was non-dimensionalized by the free stream velocity (U) and the flap-chord (L_f), as $\tau = tU/L_f$. The prevailing conditions were: $Re = 165,000$, $< c_\mu >$=0.05 % and $\triangle$=4^o.

It is apparent that the initial stage during which the normal force is being built up is independent of the excitation frequency. At this initial stage, a decrease in C_n is observed and its temporal record is independent of the frequency for all cases measured. However, as τ exceeds a value of about 5, the rate at which the flow reattaches, and therefore C_n increases, becomes lower with increasing F^+. Apart from a peculiarity observed at the lowest frequency considered (i.e. in the F^+=0.64 case), where the build up in C_n occurred in two distinct steps, all higher frequencies exhibit an almost linear increase in C_n with time.

The distinction between the two stages of reattachment and the role of F^+ in this process may be deduced from Figures 2a-d, that show the dimensionless pressure (C_P) distributions for two of the cases considered in figure 1. The transient decrease in C_n after the initiation of the disturbance is the result of a roll-up of the coherent structures, generated (or amplified) in the separated mixing layer, which had been strengthened by the introduction of the periodic excitation. These structures may have paired or undergone a "collective-interaction" to form a larger eddy that impinged onto the inclined flap. This impingement temporarily increases the pressure near the impingement (stagnation) location and it is responsible for the "spike" in C_n (Figure 1). This spike occurs only once during the reattachment process (though it might be modulated by the excitation frequency) and it may intensify as it propagates downstream along the flap. It is followed by a low-pressure oscillation that is most pronounced in the F^+=0.64 case and it attains its maximum amplitude just upstream of the trailing edge (figures 2a & 2c).

At times τ >5, the ensemble averaged C_P, that is conditioned only to the initiation of the periodic perturbations, decreases steadily over most of the flap until it attains a steady state. Only at the trailing edge, the ambient pressure that existed while the flow was separated persists. One may note that for F^+=0.64, the maximum pressure gradient (dC_p/dx) in the aft region of the flap is attained very quickly (i.e. during the third time step drawn on figure 2c), while the negative C_P near the leading edge builds up rather slowly. One would deduce from this distribution of pressure that the flow contains a long bubble that spans most of the flap chord. For the F^+=1.28 case, C_P evolves more gradually in time but its evolution takes place over the entire flap (figure 2d) and it does not appear to contain as long a bubble.

When the periodic excitation is always initiated at the same phase of the excitation-period, the ensemble-averaged pressures are oscillatory (figures 3a-b). The data therefore, preserve the imprints of the traveling vortices generated by the periodic excitation. These vortices undergo amplification and decay process because of the sensitivity of the separated mixing layer to the imposed oscillations. However, the reattached boundary layer maintains a similar sensitivity because the mean velocity profile retains its inflection point. The amplitudes of the local pressure signatures after the completion of the reattachment process (e.g. at τ >30 in figure 3) bear witness to this fact. By doubling the forcing frequency from F^+=0.64 to F^+=1.28 the location of the maximum amplitude of the pressure oscillations was halved (compare the amplitudes in figures 3a & b). This is a very familiar observation in excited mixing layers that spread-out linearly in the direction of streaming. There is no simple relation between the size of the vortices and their respective role in the reattachment process. Nevertheless, a gradual decrease in C_P is observed after every passage of a vortex near the leading edge of the flap during the process. The rate of change of the local pressure with time ($dC_p/d\tau$) depends in general on F^+, $< c_\mu >$ and on Δ. However, many weak vortices scouring the surface may have a similar effect on the mean pressure as fewer but stronger ones.

By defining the mean reattachment time from the intersection of the maximum slope $dC_p/d\tau$ (for τ >5) with the extension of the steady state value of C_n (figure 1), one may obtain the optimum frequency for minimum reattachment time. This frequency corresponds to $1.2 < F^+ > 1.6$ and it is equal to $\tau_{att,min} \approx 16$ for a fixed flap deflection angle of Δ=4^o (figure 4). It is interesting to note that τ_{att} is not sensitive to the input amplitude, $< c_\mu >$, provided the latter exceeds a certain threshold required for reattachment that in this case is $< c_\mu >$=0.02 % (figure 4). The number of cycles required for reattachment is almost directly proportional to F^+ although the relationship is not linear and is again dependent on the threshold amplitude of the excitation.

2 Concluding Remarks

Entrainment of fluid by the large coherent structures in a mixing layer forces the flow to reattach to the adjacent surface. Stability considerations play an important role in speeding up the process and enabling it at small input amplitudes. PIV measurements that are not discussed in the written version of the paper described the evolution of the rolled up vortices at various stages of the transient. They revealed that initially the mixing layer bends toward the surface near the flap shoulder while further downstream it lifts off from it leaving a stagnant region next to the surface. This is followed by a collective interaction among the large eddies that bends the mixing layer toward the surface, enclosing a much larger vortex (akin to the dynamic stall vortex) whose length is initially comparable with the length of the flap. This dimension decreases with each passing vortex that is generated by the periodic excitation and finally the entire mix-

ing layer flows next to the solid surface. Therefore, the forced periodic vortices may be regarded as moving pumps that sweep the surface regularly lowering the pressure near it during the transient reattachment process.

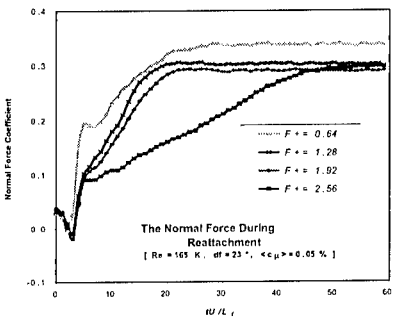


Figure 1: The average normal force during reattachment.

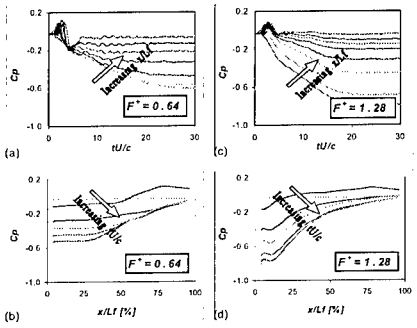


Figure 2: The pressure coefficient during the reattachment process.

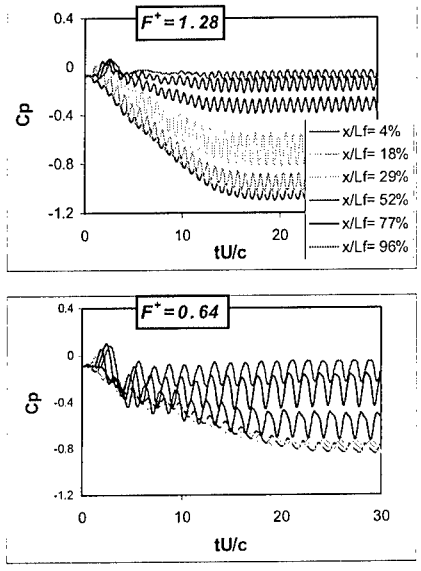


Figure 3: The phase-Locked pressure coefficient.

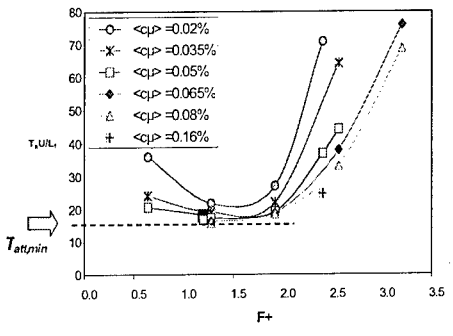


Figure 4: Reattachment time vs the reduced frequency.

ADVANCES IN TURBULENCE VIII
Proceedings of the Eighth European Turbulence Conference
C. Dopazo et al. (Eds.)
© CIMNE, Barcelona 2000

Optimal control of bypass transition

M. Högberg[1], D. S. Henningson[1,2] and M. Berggren[2,3]

[1]Department of Mechanics KTH
S-100 44 Stockholm , SWEDEN
[2] The Aeronautical Research Institute of Sweden FFA
S-161 11 Bromma, SWEDEN
[3]Department of Scientific computing, Uppsala University
Uppsala, SWEDEN

Contact e-mail: markush@mech.kth.se

1 Introduction

Transition to turbulence is an ambiguous process, and since knowledge about the underlying non-linear mechanism is limited, it is difficult to design an efficient control. Successful attempts have been made to control the linear mechanisms involved in transition scenarios such as the growth of Tollmien-Schlichting waves. More complicated processes leading to transition such as the bypass transition scenarios with non-linear effects are not as intuitive and therefore more difficult to control. The goal of the current work is to determine how to control such processes in the optimal way given the method of controlling the flow, and an objective function describing the features of the flow to be controlled. There are several different possibilities to affect the flow. The method chosen here is blowing and suction at the walls, since it is a fairly simple way of acting on the flow, and also because it is a technique that is widely used. Blowing and suction has successfully been used for similar problems, namely control of turbulence, where complete relaminarization was obtained [1]. The blowing and suction is applied to flow in a channel, where we can find many of the interesting bypass transition scenarios. Optimization of the control is not a trivial issue. Direct search methods are costly, requiring a lot of computations, and often inefficient for non-linear processes. Methods where one can access the gradient of the objective function are more efficient, and there are several algorithms developed for this type of optimization. To compute gradients of the objective function the adjoint equation approach is used. It is an efficient method in the sense that only two computations are required for each optimization iteration independent of the number of degrees of freedom of the control. First the state equation (Navier–Stokes) is solved and then this solution is used as input to the adjoint equation that is solved next and gives the gradient of the objective function. There is no need to have any knowledge of the underlying physics nor

of the functional behavior of the control. After computing the optimal control for a specific transition scenario, it is possible to analyze the computed control and perhaps gain some insight to the physics of the transition process. The transition scenario we study here is oblique transition in channel flow, since it contains many different stages, and is highly nonlinear. The transition threshold for this scenario has been thoroughly studied in [5]. Optimization is performed with a limited memory quasi Newton method described in [2].

2 Control problem

For the purpose of studying the non-linear stages of bypass transition an adjoint DNS code has been developed based on a existing spectral channel flow code [4]. The derivation of the adjoint equations is done by a perturbation analysis, starting from the Navier–Stokes equation in velocity–pressure formulation. The resulting equations are then reformulated to a form suitable for the discretization approach we use, similarly as in the existing DNS code. This facilitates the implementation by allowing re-use of code. However, this approach introduces inaccuracies in the objective-function gradient directions. This issue has been investigated in a previous study [3], where we concluded that the approach nevertheless can be used, particularly for instability control. Temporal direct numerical simulations (DNS) are performed using this code with the modification for the ability to solve the associated adjoint equations. Fourier modes are used for the span-wise and stream-wise directions and chebyshev collocation in the wall normal direction. The modification necessary to solve the adjoint equations involves a change in what corresponds to the non-linear terms for the Navier–Stokes solver to forcing terms depending on the choice of objective function. Solution of the adjoint equation requires full information about the solution of the Navier–Stokes equation in space and time. The flow geometry is

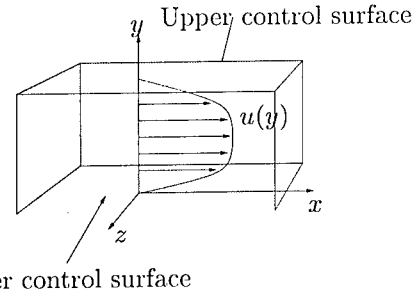


Figure 1: Geometry for control of channel flow.

the one in figure 1 with blowing and suction applied at both walls of the channel and periodic boundary conditions on the stream-wise and span-wise directions. For the optimization the objective function J is,

$$J = \frac{\varepsilon}{2} \int_{T_{C0}}^{T_{CF}} \varphi^2(x,z,t)\, d\Gamma + \frac{1}{2} \int_{T_{E0}}^{T_{EF}} (u(x,y,z,t) - u_{lam}(y))^2\, d\Omega$$

where the control φ is applied from time $t = T_{C0}$ to T_{CF} on the boundary Γ and the energy of the deviation from the laminar profile u_{lam} is measured from time $t = T_{E0}$ to T_{EF} in the computational domain Ω. The regularisation parameter ε is chosen to be 10^{-7} in all simulations. The spatial resolution of the control is the same as for the simulation and temporally the control is linearly interpolated with 20 points over the control time.

3 Transition scenario

The oblique transition scenario in channel flow involves different stages. (i) Transient growth of the oblique waves such that they (ii) interact non-linearly and produce stream-wise vorticity that then induce (iii) streaks that experience additional transient growth. If some noise is present and the streak amplitude is sufficiently large we get streak breakdown and possibly transition to turbulence. In this initial study there will not be any noise present, and the initial amplitude of the disturbance and the Reynolds number are chosen not to result in transition within the simulation. The initial condition will always be a pair of oblique waves, and then control is applied at different stages of the transient growth process.

4 Simulations, results and discussion

Five different simulations are performed using the same initial condition. The objective is to minimize the integral of the deviation from the laminar flow profile from time T_{E0} to $T_{EF} = 100$. The Reynolds number is 1500 and the box size is $2\pi \times 2 \times 2\pi$ in x, y, z. In case 1a,b,c the control is applied from time $T_{C0} = 0$ until $T_{CF} = 50$ in a,b and $T_{CF} = 25$ in c. The objective function is measured from $T_{E0} = 50$ in case 1a and from $T_{E0} = 0$ in cases 1b and 1c. For cases 2 and 3 the control is applied from $T_{C0} = 25$ and $T_{C0} = 50$ respectively, and the objective function from $T_{E0} = 50$. The resulting control velocity in all cases is of the order 2% of the centerline velocity. And the reduction of the gradient norm is about 3 orders of magnitude after 10-15 optimization iterations.

The growth of the oblique waves is efficiently hindered by the control formulation in 1a,b,c and the growth of streaks is eliminated. In figure 2B the differences between the formulations are shown. In case 1a the energy is not penalized by the objective function initially as it is in 1b and this results in lower energy after $t = 50$ than in case 1b. A higher temporal resolution of the control is applied during a shorter time in case 1c. The result is a smoother energy curve but not as low energy at a later time as in the other two cases.

In case 2 the control is applied during the formation of the streaks. Initially the energy is allowed to grow but then the growth is hindered by the control and energy decays as seen in figure 2A.

In case 3 the streaks have formed and are growing when control is applied. In figure 2A we see that the streak growth is immediately eliminated by the

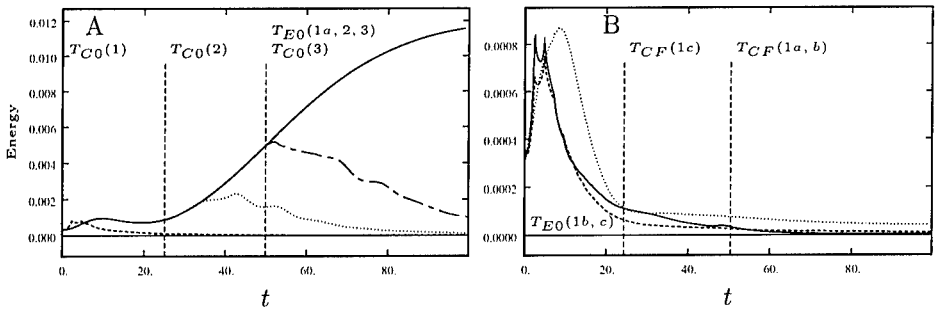


Figure 2: [A] solid: The energy growth without control ; dashed: case 1a ; dotted: case 2 ; dash-dot: case 3. [B] solid: case 1a ; dashed: case 1b ; dotted: case 1c.

control and the energy decays.

- The temporal extent of the control appear to be more important than the resolution.
- Allowing a higher energy initially can result in lower energy at a later time.
- It appears that there is enough control authority using blowing and suction on the wall to handle all the different stages of the oblique transition scenario. From the work in [1] its evident that this type of actuation is powerful enough to relaminarize a turbulent flow.
- The choice of objective function is very important for the performance of the resulting control.

References

[1] Bewley, T. R. , Moin, P. , Temam, R. DNS-based predictive control of turbulence: an optimal target for feedback algorithms. *Submitted to J. Fluid Mech.* 1999.

[2] Byrd, R. H. , Peihuang, L. , Nocedal, J. & Zhu, C. A limited memory algorithm for bound constrained optimization *Technical Report NAM-08* Northwestern University. 1994.

[3] Högberg, M., Berggren, M., Henningson, D. S. Numerical investigation of different discretization approaches for optimal control. *FFA TN 1999-74*

[4] Lundbladh, A. Henningson, D.S. , Johansson A.V. An Efficient Spectral Integration Method for the Solution of the Navier-Stokes Equations *FFA TN 1992-28*

[5] Reddy, S. C. , Schmid, P. J. , Baggett, J. S. & Henningson, D. S. On stability of streamwise streaks and transition tresholds in plane channel flows. *J. Fluid Mech. vol. 365, pp 269-303* Cambridge University Press 1998.

ADVANCES IN TURBULENCE VIII
Proceedings of the Eighth European Turbulence Conference
C. Dopazo et al. (Eds.)
© CIMNE, Barcelona 2000

On harmonic perturbations in turbulent shear flows

N. Reau and A. Tumin

Faculty of Engineering, Tel-Aviv University
Tel-Aviv 69978, ISRAEL

Contact e-mail:tumin@eng.tau.ac.il

1 Introduction

An appropriate method for analysis of a coherent signal in a turbulent flow is the triple decomposition method. The instantaneous velocities and pressure are considered as sums of three distinctive components: mean (time averaged), coherent (phase averaged) and random (incoherent turbulent) motion. Reynolds and Hussain [1] derived the equations for a coherent signal in a turbulent flow. The equations contain new unknown terms that correspond to oscillations of the background Reynolds stresses caused by the organized wave. These terms reflect the existence of an interaction between the coherent signal and the random field. To a first approximation, the interaction may be neglected and the linearized problem may be reduced to the Rayleigh equation with the mean velocity profile (the effect of molecular viscosity is considered as negligible).

As the free shear flows (such as jets, wakes and mixing layers) spread rapidly, it is necessary to take into account the flow divergence for a correct comparison of theoretical and experimental data for growth rates and overall amplification. Gaster *et al.* [2] carried out the analysis of coherent perturbations in a mixing layer within the scope of the Rayleigh equation. They included the flow divergence into the consideration in attempt to predict the overall growth. Nevertheless, the theory overpredicted the amplification by $2-3$.

The effect of two-dimensional periodic disturbances of high amplitude on the development of turbulent mixing layers and wakes was investigated experimentally in [3], [4], [5]. It was revealed that coherent perturbations can significantly change dynamics of the flow. A theoretical model of the phenomenon is still in question. The foregoing serves as a motivation for the present work.

2 Governing equations

We consider a two-dimensional turbulent flow disturbed by a harmonic two-dimensional wave. To analyze the dynamics of the organized wave, we apply the

triple decomposition method [1]. It is assumed that the instantaneous velocities and pressure consist of the three distinct components

$$\mathbf{q}(x,y,z,t) = \overline{\mathbf{q}}(x,y) + \widetilde{\mathbf{q}}(x,y,t) + \mathbf{q}'(x,y,z,t); \tag{1}$$

where $\overline{\mathbf{q}}$ stands for the mean (time averaged) values of the velocities and pressure; $\widetilde{\mathbf{q}}$ is the coherent (phase averaged) contribution corresponding to the organized wave; $\mathbf{q}'$ stands for the random (turbulent) motion. After substituting (1) in Navier-Stokes equations, phase and time averaging, the equations for the mean flow and for the organized wave [1] can be obtained. We assume that effects of molecular viscosity are negligible, and the equations for the mean values are considered in the boundary-layer approximation. They contain random and coherent Reynolds stresses as well, $-\rho\overline{u'v'}$ and $-\rho\widetilde{\widetilde{u}\widetilde{v}}$ correspondingly. We invoke closure of the equations by means of the eddy viscosity $\nu_t(x)$ of the undisturbed flow $\overline{u'v'} = -\nu_t(\partial\overline{u}/\partial y)$. The equations for the coherent part contain new terms $\widetilde{r}_{ij} = \widetilde{u_i'u_j'} - \overline{u_i'u_j'}$ corresponding to oscillation of the background Reynolds stresses caused by the organized wave [1]. The term is responsible for the interaction of a coherent signal with the random field, and we need to choose a hypothesis to close the equations. We adopt the Newtonian eddy viscosity model [1]

$$\widetilde{r}_{ij} = -\nu_t\left(\frac{\partial\widetilde{u}_i}{\partial x_j} + \frac{\partial\widetilde{u}_j}{\partial x_i}\right). \tag{2}$$

Thus, we arrive at the system of governing equations. The equations for the coherent signal are considered in linear approximation with slowly diverging mean flow, and they are solved by invoking the method of multiple scales. In the main order, we obtain the Orr-Sommerfeld equation (instead of the Rayleigh equation used in [2]). The mean velocity profile is obtained from simultaneous solving of the corresponding equations including coherent Reynolds stresses.

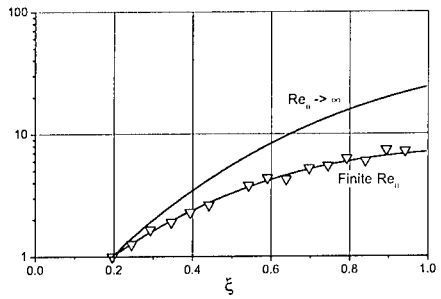


Figure 1: The overall amplification $\int_{-\infty}^{+\infty} |\widetilde{u}|\, dy$. Solid lines - theory; symbols - experimental data [2] .

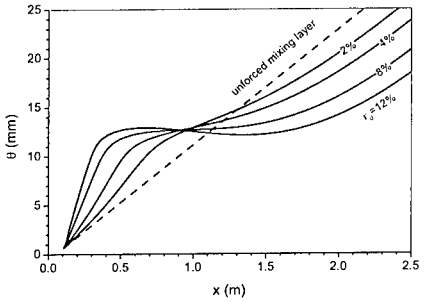


Figure 2: Momentum thickness of the mixing layer in the presence of a coherent signal.

3 Results

Figure 1 shows comparison of the calculated and experimental data [2] for a coherent signal of small amplitude. The new theoretical element in the comparison is the interaction of the coherent signal with the random field that is incorporated by the closure (2). The results correspond to $U_1 = 10$ m/s, $U_2 = 4$ m/s, the frequency of the coherent signal $f = 20$ Hz. The Reynolds number $Re_\theta = 14.5$ is defined with the momentum thickness θ and the eddy viscosity ν_t extracted from the experimental data. The solid line with $Re_\theta \to \infty$ corresponds to the model based on the Rayleigh equation [2] that neglects the interaction of the coherent signal with the random field. The coordinate ξ in figure 1 is the dimensionless streaming coordinate defined in [2]. The result indicates importance of the interaction between the coherent signal and the random field.

The feedback to the mean flow becomes important at high amplitude of the coherent signal. The momentum thickness θ versus streaming coordinate x is presented in figure 2 for a disturbance of frequency 20 Hz in a mixing layer between two flows with $U_1 = 5$ m/s and $U_2 = 3$ m/s. The amplitude parameter ε_0 is defined as ratio of the normal velocity disturbance $v(y = 0)$ at the starting point $x_0 = 0.106$ m to the velocity difference $U_1 - U_2$. One can see that at $\varepsilon_0 = 12\%$ there is an interval with a negative derivative $\mathrm{d}\theta/\mathrm{d}x$. The physical meaning is the following: far downstream from the disturbance source, the coherent Reynolds stress becomes negative (figure 3). If the disturbance amplitude is sufficiently high, the coherent Reynolds stress (that represents a term in the mean flow equations) accelerates the flow and overcome the turbulent diffusion. As the coherent disturbance decays, further downstream, the effect of the coherent Reynolds stress is reduced and the turbulent diffusion process regains its dominance and the mixing layer starts spreading again. A similar

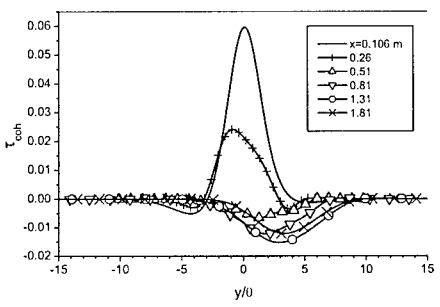


Figure 3: Coherent Reynolds stresses in the mixing layer at $\varepsilon_0 = 12\%$.

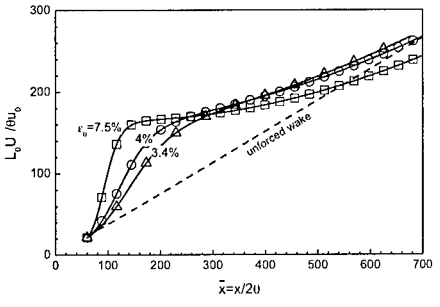


Figure 4: The wake growth parameter in the presence of a coherent signal.

effect may be obtained for a turbulent wake. Figure 4 shows calculations of the growth parameter of a turbulent wake, defined in [6]. The parameter describes the spreading of the mean flow. The disturbance amplitude ε_0 is defined as the

ratio of the normal velocity component v at the wake axis at $x/2\theta = 60$. The disturbance frequency $f = 80$ Hz was chosen in accordance with the experimental data analyzed in [6].

One can see from figures 2 and 4 that the feedback to the mean flow may cause a significant change in the shear layer thickness.

4 Conclusion

A theoretical model of periodic disturbances in turbulent mixing layers and turbulent wakes was proposed. The model includes instability analysis of the mean flow with the non-parallel effects. The interaction of the coherent signal with incoherent turbulent fluctuations is incorporated by the Newtonian eddy viscosity. The feedback of the disturbances to mean flow is taken into account through the coherent Reynolds stresses. The results are in agreement with experimental observations.

The authors thank Professor I. Wygnanski for attracting their interest to the problem and for useful discussions of the results. This research was supported by a Grant from the G.I.F., the German-Israeli Foundation for Scientific Research and Development.

References

[1] W. C. Reynolds, and A. K. M. F. Hussain, The mechanics of an organized wave in turbulent shear flow. Part 3. Theoretical models and comparisons with experiments. *J. Fluid Mech.*, 54:263–288, 1972.

[2] M. Gaster, E. Kit, and I. Wygnanski, Large-scale structures in a forced turbulent mixing layer. *J. Fluid Mech.*, 150:23–39, 1985.

[3] D. Oster, and I. Wygnanski, The forced mixing layer between parallel streams. *J. Fluid Mech.*, 123:91–130, 1982.

[4] I. Weisbrot, and I. Wygnanski, On coherent structures in a highly excited mixing layer. *J. Fluid Mech.*, 195:137–159, 1988.

[5] B. Marasli, F. H. Champagne, and I. Wygnanski, Effect of traveling waves on the growth of a plane turbulent wake. *J. Fluid Mech.*, 235:511–528, 1992.

[6] B. Marasli, F. H. Champagne, and I. Wygnanski, On linear evolution of unstable disturbances in a plane turbulent wake. *Phys. Fluids A*, 3:665–674,1991.

ADVANCES IN TURBULENCE VIII
Proceedings of the Eighth European Turbulence Conference
C. Dopazo et al. (Eds.)
© CIMNE, Barcelona 2000

The Extension of CFD-Friendly Turbulence Modelling to Include Transition

J. Vicedo, S. Vilmin, W. N. Dawes,
H. P. Hodson and A. M. Savill

Department of Engineering, University of Cambridge
Trumpington St., Cambridge CB2 1PZ, UK

1 Introduction

The transition region is fundamentally characterised by an intermittent behaviour of the flow such that an indicator function, $I(x,y,z,t)$, defined as

$$I(x,y,z,t) \equiv \begin{cases} 0 & laminar \\ 1 & turbulent \end{cases} \tag{1}$$

can be applied locally at each point in the flow. Time averaging this function introduces the so-called intermittency factor ($\gamma = \langle I \rangle$) which can be interpreted as the probability that a turbulent fluid occurs at the point (x,y,z).

Two-equation turbulence models are well known to imply a lack of physical model particularly on the inset of the turbulent regime at the initial stages of transition. In order to improve these predictions, several researchers have proposed modifying the existing models by simply scaling the eddy viscosity formulation by means of the intermittency factor [1]. It is the scope of the present paper to explore the capabilities of two methods derived from such approach.

2 PUIM

The Prescribed Unsteady Intermittency Model (PUIM) aims to simulate the evolution in time of the laminar, transitional and turbulent patches characteristic of bypass transition. The laminar-turbulent transition onset is determined using experimental correlations and the intermittent feature of the transitional flow is modelled by the intermittency factor [2]. Based on the characteristics of the development of turbulent spots, the latter can be computed either using the concentrated breakdown concept (Narasimha, 1957), or using a continuous breakdown of the turbulent spots taking account of the laminar-flow calmed

region which immediately trails a spot, as observed by Schubauer and Klebanoff in 1956.

3 The Intermittency Equation

Based on the approach of modelling the transition region through means of the intermittency factor, and based on the work by Cho and Chung [3], we suggest the following transport equation for γ

$$\begin{aligned} \frac{\partial}{\partial t}\int_{\mathbf{V}} \rho\gamma \mathbf{dV} &= -\oint_{\mathbf{S}} (\rho \mathbf{v}\gamma)\cdot \mathbf{dS} + \oint_{\mathbf{S}} (\mu_L + (1-\gamma)\,\mu_T/\sigma_\gamma)\,\nabla\gamma \cdot \mathbf{dS} \\ &\quad + \int_{\mathbf{V}} \left(C_{\gamma 1}\rho\gamma\,(1-\gamma)\left(\tfrac{1}{2}P_k/k\right) + C_{\gamma 2}\rho\left(k^2/\varepsilon\right)\nabla^2\gamma\right)\mathbf{dV} \\ &\quad - \int_{\mathbf{V}} \left(\rho\gamma\,(1-\gamma)\,(\varepsilon/k)\,(C_{\gamma 3} + C_{\gamma 4}\Gamma)\right)\mathbf{dV} \end{aligned} \quad (2)$$

where $\Gamma = -\left(k^{\frac{5}{2}}/\varepsilon^2\right)(\nabla p/\rho)\,(\nabla\gamma)\,/\,|U|$ has been defined as the amount of intermittency entrained by the interaction between the mean velocity gradient and the intermittency field per unit volume of fluid.

The constants read $\sigma_\gamma = 1.0; C_{\gamma 1} = 2.2; C_{\gamma 2} = 0.6; C_{\gamma 3} = 0.1; C_{\gamma 4} = 0.16$.

4 Solution Method

The solution method is a 2D solution adaptive unstructured mesh, Reynolds Averaged Navier Stokes solver, UNNEWT [4]. Equations are formulated with a finite volume vertex store strategy and integrated with a classical multi-step Runge-Kutta scheme with residual smoothing and industry standard second and fourth difference artificial viscosity.

Closure is achieved via the two equation model of Yang and Shih [5], and the time scale was limited locally by adopting the approach proposed Durbin [6], in order to avoid unrealistic high values of kinetic energy close to points near which the flow stagnates. To take account of the so-called 'interaction effect', the term $C_{\varepsilon\gamma}\left(\varepsilon^2/k\right)\Gamma$ with $C_{\varepsilon\gamma} = 0.1$ introduced by Cho and Chung was included in the transport equation governing the turbulent dissipation rate.

Both PUIM and the Intermittency Equation interact with the flow by means of the eddy viscosity $\mu_T = \gamma\mu_T^*$, where μ_T^* is the eddy viscosity from the $k-\varepsilon$ model of Yang and Shih.

5 Results and Discussion

The flow over a long horizontal body with semi-circular leading edge was computed for a free-stream turbulence level of 2.3% 6mm after the leading edge and a Reynolds number of 3293. Results were compared to the experimental test case T3L3 of the Ercoftac database [7]. Turbulence decay is well predicted in the free-stream as shown by Figure 1, whereas discrepancy between the two

transition models arises when predicting both length and strength of separation inside the boundary layer (Figure 2).

Boundary layer integral parameters are better predicted when employing any of the intermittency-based treatments, specially evidenced by the accuracy in the of the results obtained when using PUIM as shown by Figures 3-5. Skin friction values, on the other hand, are better predicted using the so-called $k - \varepsilon - \gamma$.

Overall, results shown considerable improvement in the prediction of transitional behaviour by the inclusion of any of the intermittency-based models proposed.

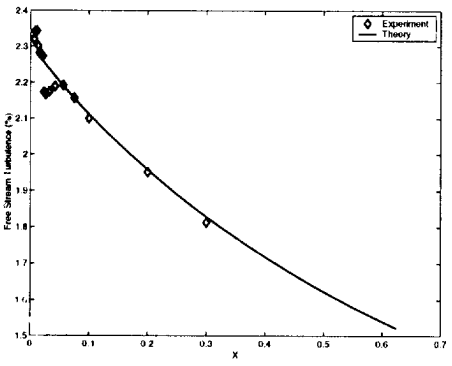


Figure 1: Freestream turbulence against the axial coordinate from the leading edge.

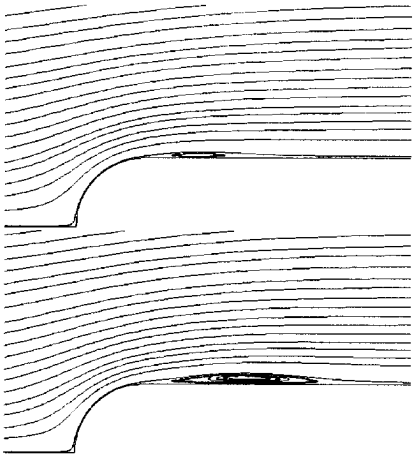


Figure 2: Streamlines of the flow around the plate: $k - \varepsilon$ model (top); $k - \varepsilon$-PUIM (bottom).

References

[1] Savill, A.M., "One-Point Closures Applied to Transition", in "Turbulence and Transition modelling", Ercoftac Series, Hallbäck, M., Henningson, D.S., Johansson, A.V., and Alfredsson, P.H., 233-268, 1996.

[2] Schulte, V.S. and Hodson, H.P., "Unsteady wake-induced boundary layer transition in high lift LP turbines", Transactions of the ASME, J. Turbomachinery, Vol. 120, 28-35, 1998.

[3] Cho, J.R. and Chung, M.K., "A $k - \varepsilon - \gamma$ equation turbulence model", J. Fluid Mech., 237, 301-322, 1992.

[4] Dawes, W.N., "The Practical Application of Solution-Adaption to the Numerical Simulation of Complex Turbomachinery Problems", Prog. Aero. Sci., 29:221-269, 1992.

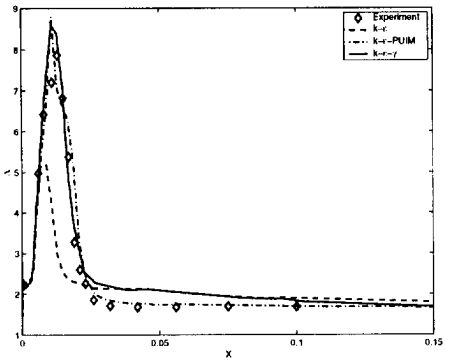


Figure 3: Shape factor distribution against the axial coordinate from the leading edge.

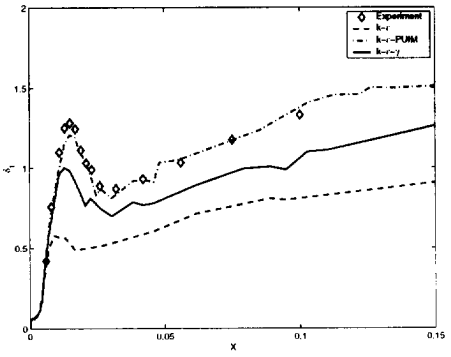


Figure 4: Displacement thickness.

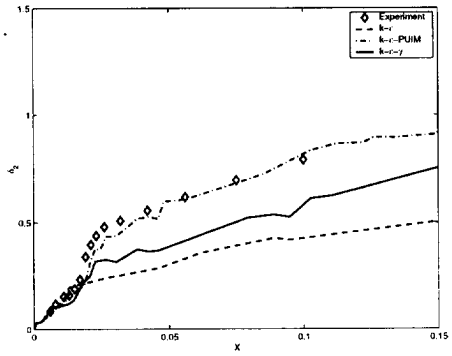


Figure 5: Momentum thickness

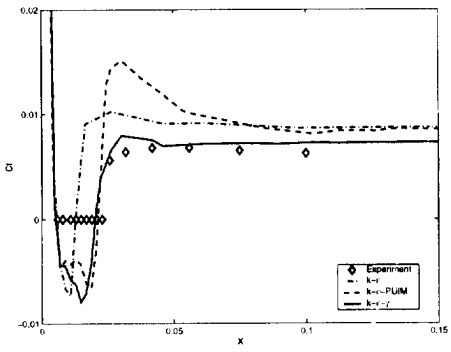


Figure 6: Skin friction coefficient.

[5] Yang, Z. and Shih, T.H., " A Galilean and Tensorial Invariant $k-\varepsilon$ Model for Near Wall Turbulence", AIAA Paper 93-3105, 1993.

[6] Durbin, P.A., "On the k-3 Stagnation Point Anomaly", Int. J. Heat and Fluid Flow, 17:89-90, 1996.

[7] Coupland, J., "Transition Modelling for Turbomachinery Flows", ERCOF-TAC Bulletin, 24:5-8, 1995.

VIII

Transport and Mixing

ADVANCES IN TURBULENCE VIII
Proceedings of the Eighth European Turbulence Conference
C. Dopazo et al. (Eds.)
© CIMNE, Barcelona 2000

PDF computation of thermal mixing layer in grid turbulence

T. Bukasa[1], J. Pozorski[1] and J. P. Minier[2]

[1]Institute of Fluid Flow Machinery, Polish Academy of Sciences
Fiszera 14, 80952 Gdańsk, POLAND
[2]Groupe Mécanique des Fluides et Transferts Thermiques, Electricité de France
6 quai Watier, 78400 Chatou, FRANCE

Contact e-mail: jp@imp.pg.gda.pl

1 Introduction

The modelling and computation of turbulent flows with additional scalar variables remains an active area of research [1]. This is due to numerous technical applications of reacting flows (including combustion) or flows with temperature variations (including geophysical flows and heat transfer). The probability density function (PDF) method is well suited for use in such flows, because reaction and convection terms are exact and do not require modelling. The main idea of the PDF method (for a review see [5]) is to propose a closed evolution equation for the one-point joint pdf of velocity, turbulent energy dissipation rate and scalar variables (as chemical composition, temperature, etc.) However, in all one-point statistical descriptions of turbulent flows with scalars, the so-called micro-mixing term remains unclosed. Many mixing models have been proposed to date (cf. [1, 2] for recent reviews); among them, the CD (coalescence/dispersion) model of Curl and the IEM (interaction by exchange with the mean) of Dopazo are a solution of choice (mostly because of their simplicity and robustness) in many computational codes. Another recent proposals are the BL (binomial Langevin) model of Valiño & Dopazo, the mapping closure model originally due to Kraichnan, the linear eddy modelling of Kerstein and the Fokker-Plank closure developed by Fox.

The purpose of this paper is to test three well-known micro-mixing models (IEM, CD and BL) in a given test case and to present computational results from a complete stand-alone joint velocity-turbulent frequency-scalar PDF code (Pozorski & Minier 1998). Numerical results are obtained for transport of an inert passive scalar in grid turbulence.

2 Case studied

The flow simulated here is a thermal mixing layer generated by a temperature step in a grid turbulence, studied experimentally by Ma & Warhaft [3]. The thermal step was set at $x_0 = 20M$ downstream the grid of the mesh size M. The computations were carried to the distance $x = 120M$. The initial variance of temperature fluctuations (not reported in Ma & Warhaft paper, unfortunately) was assumed different at the hot and the cold side and obtained after many tests (using trial and error procedure). Periodic velocity conditions were applied on both upper and lower boundary, as well as constant scalar values, because the temperature field is undisturbed there. It has to be noted that the statement of different boundary conditions is also possible (as for the case of heated/cooled channel flow), by analogy to the formulation proposed for the instantaneous flow velocity [4]. First computations of this kind of flow are currently underway.

For all tested mixing models of passive scalars, the dynamics of the flow remains obviously identical. It was obtained using the standard version of the PDF algorithm and program developed by Pozorski & Minier [6]. The computations were carried out with various numbers of particles, different grids and time steps. The independence of the results of different conditions was verified.

In our PDF computation of grid turbulence, turbulent kinetic energy k and its dissipation rate ϵ decay with the distance from the grid, following power-law formulae. The mean temperature profile (Fig. 1a) is scaled by the temperature step value ΔT_0. The cross-stream coordinate y equals zero at the center of the thermal mixing layer and is scaled by the half-width of the mean temperature profile L. Temperature profiles at several x-stations, scaled this way, collapse reasonably well into a single curve. The rms of the temperature field is shown in Fig. 1b.

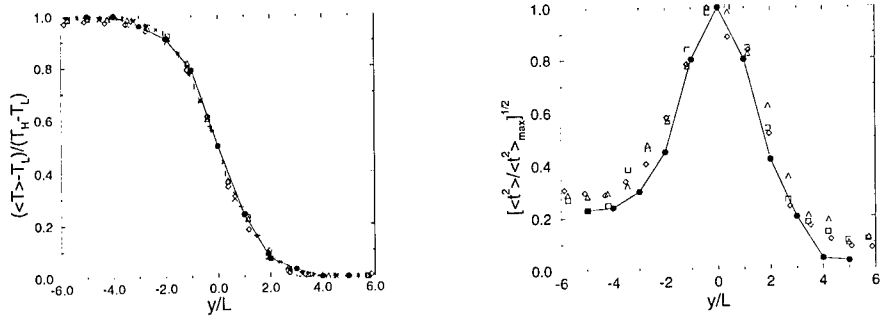


Figure 1: a) Mean temperature profiles plotted as a function of a normalised cross-stream coordinate; b) temperature rms scaled by its maximum. Experiment: solid line with (•); computation for various molecular mixing models at a location $x/M = 120$ from the grid:(□) CD, (△) IEM, (◇) BL; IEM for various locations: (x) $x/M = 32.5$, (+) $x/M = 62.5$, (∗) $x/M = 92.5$.

The PDF method for turbulent flow computation readily gives also higher moments of velocity and scalar fields, such as the correlation of the temperature fluctuations and cross-stream velocity component (normalised heat flux, Fig. 2a), the flux of temperature variance (Fig. 2b), third moments as the correlation of square temperature fluctuations with the normal velocity component and the skewness of the temperature profile, as well as the fourth moment (the kurtosis) of the temperature fluctuations (Fig. 3). The results are in good agreement with experimental data.

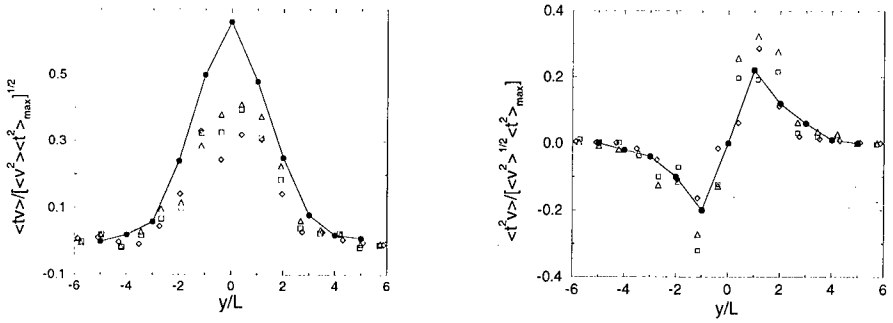


Figure 2: Correlations of temperature and cross-stream velocity component: a) correlation normalised by the maximum temperature variance; b) normalised flux of temperature variance. Symbols as in Fig. 1.

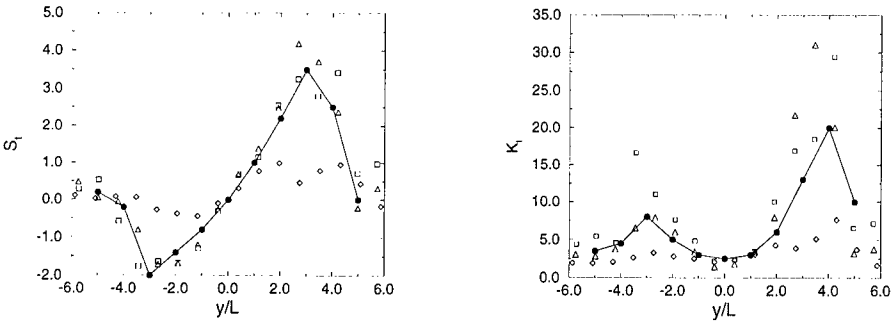


Figure 3: Higher moments of the temperature distribution: a) skewness; b) kurtosis. Symbols as in Fig. 1.

The level of the initial scalar fluctuations has a great impact on the final results; specially, higher order moments such as skewness and flatness of scalar distribution are affected. Fig. 4 presents the temperature variance and skewness for various values of the initial temperature variance. The results obtained with the inlet step in the variance of scalar fluctuations yield the closest match with respect to the experimental values.

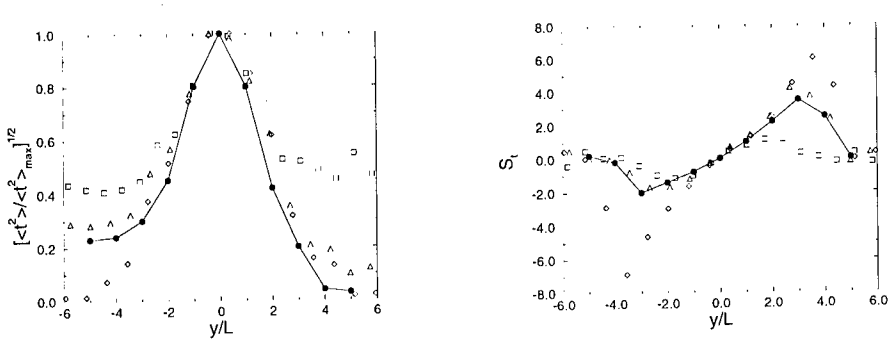


Figure 4: The influence of the inlet fluctuations on the temperature variance (plot a) and skewness (plot b). Experiment: solid line with (•). Computation for the step in initial variance (△): $0.089(\Delta T_0)^2$ (hot side), $0.0089(\Delta T_0)^2$ (cold side); constant value $2.2 \cdot 10^{-2}(\Delta T_0)^2$ (□); constant value $2.2 \cdot 10^{-4}(\Delta T_0)^2$ (◇).

3 Conclusion

The aim of this paper was to perform computations of transport and mixing of temperature as a passive inert scalar in a grid-generated turbulent flow. The velocity and scalar fields were calculated using the full (stand-alone) PDF method; three different scalar micro-mixing models were tested. Computed statistics include moments (up to the fourth order) of the temperature distribution and velocity-temperature correlations. High sensitivity to the inflow scalar variance was stated. The overall agreement with experimental data is satisfactory.

References

[1] C. Dopazo. Recent developments in PDF methods In *Turbulent reacting flows* (Libby, P.A., Williams, F.A., eds.), Academic Press, New York, 1994.

[2] R. O. Fox. Computational methods for turbulent reacting flows in the chemical process industry. *Rev. Inst. Français du Pétrole* 51:215–243, 1996.

[3] B. K. Ma and Z. Warhaft. Some aspects of the thermal mixing layer in grid turbulence' *Phys. Fluids* 29:3114-3120, 1986.

[4] J. P. Minier and J. Pozorski. Wall boundary conditions in PDF methods and application to a turbulent channel flow. *Phys. Fluids*, 11:2632–2644, 1999.

[5] S. B. Pope. Lagrangian PDF methods for turbulent flows. *Annu. Rev. Fluid Mech.*, 26:23–63, 1994.

[6] J. Pozorski and J. P. Minier. Development of theoretical and numerical models for the computation of turbulent flows with the PDF method. Rep. No. 93/98, IMP PAN, Gdańsk, 1998.

ADVANCES IN TURBULENCE VIII
Proceedings of the Eighth European Turbulence Conference
C. Dopazo et al. (Eds.)
© CIMNE, Barcelona 2000

Application of an Eulerian Monte Carlo Field Method to the Simulation of the Filtered PDF in LES

C. Jiménez[1,*], C. Dopazo[1,2] and L. Valiño[2]

[1] Fluid Mechanics Area. University of Zaragoza. Spain.
[2] LITEC-CSIC. Zaragoza. Spain.
[*] Present Affiliation: CERFACS. Toulouse. France

Contact e-mail:carmen@cerfacs.fr

1 Introduction

Once subgrid scale transport (SGS) models are introduced, the only open term in the LES equations of a filtered reacting scalar $\overline{Y}$ is the chemical term, that for a reaction rate given by $w(Y)$ is $\overline{w(Y)}$. No algebraic or simple model can be expected for such a term, due to its highly non linear, system dependent and coupled to dynamics character. But if the values $\overline{Y^2}$, $\overline{Y^3}$,... were known the problem would be closed. The filtered probability density function (PDF) [3]:

$$\overline{\mathcal{P}}_Y(\Gamma;\vec{x}) = \int \mathcal{G}(\vec{x},\vec{x}')\delta(\Gamma - Y(\vec{x}'))d\vec{x}', \tag{1}$$

contains that information and its evolution equation:

$$\frac{\partial \overline{\mathcal{P}}}{\partial t} + \frac{\partial \overline{u_i}\overline{\mathcal{P}}}{\partial x_i} = \frac{\partial}{\partial x_i}\left[(D+D_T)\frac{\partial \overline{\mathcal{P}}}{\partial x_i}\right] - \frac{\partial}{\partial \Gamma}\left(w(\Gamma)\overline{\mathcal{P}} + D\overline{\left.\frac{\partial^2 Y}{\partial x_i^2}\right|_{Y=\Gamma}}\,\overline{\mathcal{P}}\right), \tag{2}$$

presents a closed chemical term. An additional term representing SGS mixing appears, thought, which has to be modeled.

The simplest and most widely used mixing model is the Linear Mean Square Estimation (LMSE) [2]. Tests of this model for the evolution of a scalar PDF in homogeneous isotropic turbulence have shown that while it reproduces the evolution of the mean and variance of the PDF, it is unable to change its shape towards an asymptotic gaussian shape. Alternative models have been proposed, among them the Binomial Langevin (BL) [6], which by addition of a stochastic term can account for that shape change, but which results much more complex and costly. In this work, the performance of BL and LMSE in LES are compared, with the hope that LMSE can reproduce the correct PDF evolution when combined with the other terms of equation 2, even if when acting alone on a PDF it cannot.

2 An eulerian Monte Carlo method

To be able to isolate the effects of mixing models from effects of SGS transport models and numerical schemes, the approach adopted here is to perform direct numerical simulations (DNS) together with the LES, so that individual terms can be explored. Two test cases were selected that fulfilled the following conditions: (1) a DNS of the same case was feasible and affordable and (2) a statistically homogeneous direction existed so that comparison of mean values of the DNS and LES was possible at low cost. DNS of:

- A scalar mixing and reacting in homogeneous isotropic turbulence.
- A scalar mixing in a temporal mixing layer.

were performed in a 64^3 grid and a $64 \times 64 \times 128$ grid resp., by a pseudo-spectral code with a 6th order compact difference scheme in the transverse direction for the mixing layer case. Turbulent Reynolds numbers were in the order of 100. The same code was used for LES after adding SGS models.

A fundamental difficulty was found in the selection of a numerical method to simulate the evolution of the filtered PDF. Monte Carlo particle methods [4], typically used in RANS+PDF calculations, resulted inadequate for the simulation of the filtered PDF in the context of LES. Two major problems were identified:

- The discrete representation of convection and diffusion by exchanges of particles between cells produces a distorsion in the instantaneous large scale fields preventing a reliable non-stationary simulation of scalars (see figure 1)
- First order upwind methods have to be used to discretize the PDF equation in cells where convection dominates. That led in the present study cases to a numerical diffusion of scalars bigger than laminar/turbulent diffusion and numerical dissipation of the variance bigger than dissipation by mixing (see figure 2).

In general, Monte Carlo particle methods present practical problems for direct implementation in LES calculations, as they can not be implemented in combination with high order methods or in non–structured grids.

A new method has been recently proposed [5], based on the representation of the PDF by stochastic fields, continuously varying in space and time, whose values in the cells of the grid evolve according to a stochastic equation reproducing the evolution of the PDF. It was adapted in this work to the simulation of the filtered PDF evolution For the present LES case the stochastic evolution equation of the fields stochastic fields $y^{(n)}$ if a LMSE model is used for mixing is:

$$\frac{\partial y^{(n)}}{\partial t} + \frac{\partial \overline{u_i} y^{(n)}}{\partial x_i} = \frac{\partial}{\partial x_j}\left[(D + D_T)\frac{\partial y^{(n)}}{\partial x_j}\right] + \left[2\,(D + D_T)\right]^{1/2}\frac{\partial y^{(n)}}{\partial x_i} dW_i - \\ - \frac{\overline{\omega}}{2}\left(y^{(n)} - \overline{Y}\right) + w(y^{(n)}), \qquad (3)$$

where the last three terms represent stochastic diffusion, mixing modeled by LMSE (with $\overline{\omega}$ the SGS mixing frequency) and reaction, that appears closed as

in equation 2. This equation can be discretized in a purely eulerian way, with any high or low order method in any grid. Implementation is straightforward in a LES code, as just a stochastic and a mixing term have to be added to an otherwise typical filtered scalar evolution equation. In figures 1 and 2 some advantages of this method as compared to particle methods can be seen: the continuous nature of evolution avoids the distorsion effects and the possibility of using non–dissipative schemes, can prevent numerical diffusion/dissipation.

3 Results and conclusions

The new stochastic fields method allowed the study of mixing models, whose effect were hindered by numerical errors when the particle method was used. Equation 3 was implemented with a high order non dissipative finite-difference scheme for 64 stochastic fields, in combination with the LES for filtered velocity fields. After validation of SGS transport models for both momentum and transport [1], an independent test of mixing models was feasible.

Global resolved scalar mean and variance results are a good test of mixing in reacting situations and were used in the first test case (figure 3). In the mixing layer case, the PDF in planes parallel to the initial mixing layer at the final time in simulation is used for that purpose (figure 3), as in a non-reacting case this is the hardest test for mixing. Results of runs in which the LMSE and the BL models were used are compared in those figures to DNS results, showing that both models give very similar results and reproduce accurately enough the DNS results. The SGS mixing frequency was taken as constant both in time and space along the simulation and such a simple model is the reason of slight discrepancies between DNS and LES results. But the performances of LMSE and BL models appear as identically good, a very encouraging result for the extension of PDF transport simulations to LES, given the simplicity and low cost of LMSE,

References

[1] C. Dopazo C.Jiménez and L. Valiño. *Poster session in ETC8.*

[2] C. Dopazo. *Acta Astronautica*, 1:1239–1266, 1974.

[3] F. Gao and E.E. O'Brien. *Physics of Fluids A*, 5:1282–84, 1993.

[4] S.B. Pope. *Combustion Science and Technology*, 25:159–174, 1981.

[5] L. Valiño. *Flow, Turbulence and Combustion*, 60:157–172, 1998.

[6] L. Valiño and C. Dopazo. *Phys Fluids*, 3:3034, 1991.

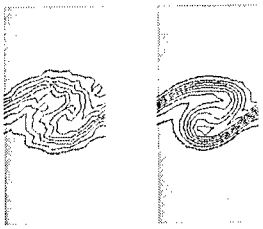


Figure 1: $\overline{Y}$ isosurfaces in the LES+PDF calculation of a mixing layer with a particle method (left) and the present method (right).

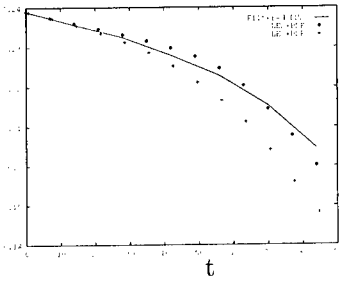
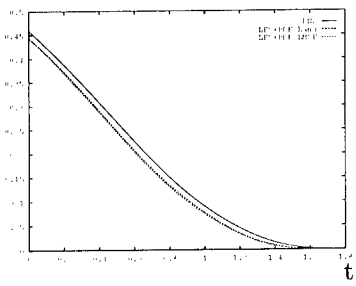


Figure 2: SGS variance decay in the mixing layer from DNS and LES + PDF with a particle (+) and the stochastic fields method ($\diamond$).



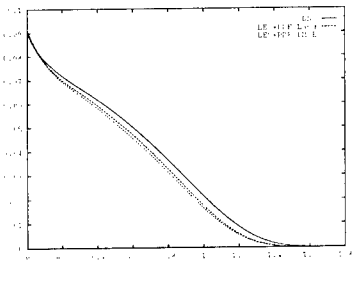


Figure 3: Mean value of $\overline{Y}$ (left) and SGS variance (right) from DNS and LES+PDF of a scalar reacting in homogeneous isotropic turbulence with LMSE and BL models

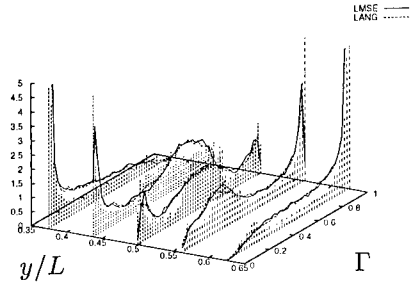


Figure 4: PDF of the scalar Y across the mixing layer. Vertical bars represent the PDF obtained in DNS, continuous lines LES+PDF calculations

ADVANCES IN TURBULENCE VIII
Proceedings of the Eighth European Turbulence Conference
C. Dopazo et al. (Eds.)
© CIMNE, Barcelona 2000

Large Eddy Simulation of Flow in Lean Premixed Prevapourised Combustor Geometries

G. Tang, Z. Yang and J.J. McGuirk

Dept. of Aeronautical and Automotive Engineering, Loughborough University, Loughborough LE11 3TU, UK

Contact e-mail: j.j.mcguirk@lboro.ac.uk

1 Introduction

As environmental pollution issues, particularly NO_x emissions, become an ever more important design driver for gas-turbine combustors, the aerospace industry is placing increasing research emphasis on combustors which operate under lean premixed prevapourised (LPP) conditions, rather than the liquid-spray diffusion flame designs which have predominated to date. In LPP combustors, in addition to problems associated with auto-ignition and flashback, the achievement of controlled, lean fuel air ratios (FAR) which, in the flame zone, are as homogeneous as possible in both space and time, is absolutely crucial to low emissions perfomance. Consequently, methods for predicting mixing processes to a high accuracy in the turbulent swirling flow premix zones of LPP combustors is a topic of much current interest.

Whilst RANS-based CFD methods have been used for some time, the importance of predicting time-resolved large-scale unsteady flow features is sufficiently important in LPP combustors that a RANS approach will be inadequate. Capture of time-resolved features will be necessary in terms of emissions performance, but also from the viewpoint of combustion/acoustic instabilities, to which gas-fuelled LPP combustors are particularly prone. Large Eddy Simulation (LES) methods are probably the only completely satisfactory CFD route for accurate prediction. The paper described here constitutes work underway to apply LES methods to LPP systems.

2 Numerical Features and Results

The numerical method used in the present LES method has the following main features: use of conservation form of the governing equations, the orthogonal

block-structured grids, a staggered variable arrangement with grid-oriented velocity components, a central differencing discretization of both convection and diffusion terms, the explicit Adams-Bashforth scheme for time-stepping and a 3D multigrid method for accelerating the solution of the Poisson equation for pressure. The sub-grid scale stresses are simulated by the Smagorinski model and a wall function approach was employed for the treatment of the wall layer. Figure 1 shows the geometry of the LPP combustor currently under consideration. The combustor geometry consists of a central non-swirling axial jet nozzle, two radially-inflowing swirling streams, a convergent-divergent section to act as a flame trap, and a large diameter dump region which constitutes the main combustion zone. The geometry is axisymmetric and only a single radial plane is shown in Figure 1. However, all grids generated, and all LES calculations are of course fully 3D (i.e. cover the entire 360° sector). This geometry is much more complicated than the one used in another LES calculation [1].

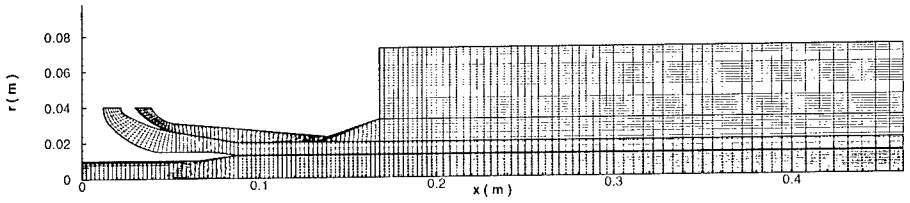


Figure 1: Grids for LPP Combustor (side view)

In the calculations presented here, only isothermal(air) flow has initially been considered. The Reynolds number of a parallel experimental study conducted on this geometry at Cranfield University was 68,000 [2]. The LES computation used a mesh of 12 blocks with around 480,000 cells. The presence of a centreline with the associated small cell size in the present grid, in combination with the use of an explicit method has placed a severe time-step restriction in the calculation; the time step used was only 0.25 microsecond.

Figures 2 and 3 show two examples of instantaneous axial velocity contours from the LES calculation, after 2,000 and 120,000 time steps respectively. At present flat axial and swirl velocity profiles have been presented at all flow inlets with a superimposed random forcing; these random fluctuations decayed very quickly and the flow unsteadiness observed is essentially due to the instability of the shear layers between swirling streams and between the central axial jet and the annular merged swirling flow. The early time picture (Figure 2) indicates the rapid growth of large scale oscillation in the mixing duct, leading to the rapid cross-stream mixing of the central jet fluid. At this time the flow has not penetrated to the end of the combustion zone and no clear negative velocity regions are observed. At a later time (Figure 3) central jet mixing has proceeded further and the central recirculation zones have begun to form. Although the flow is still not fully statistically stationary after the 30 msec developing time, it

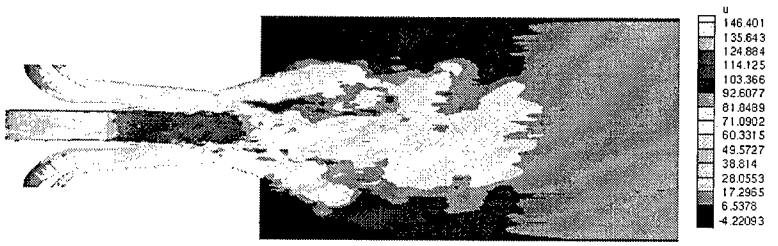


Figure 2: Instantaneous Axial Velocity Contours, t=5ms

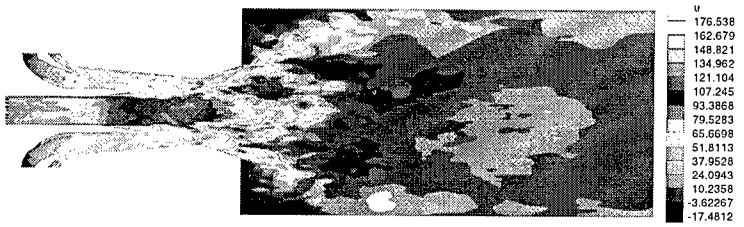


Figure 3: Instantaneous Axial Velocity Contours, t=30ms

is worthwhile examining some mean flow characteristics. Figures 4 shows mean streamlines obtained by averaging over the last 6 msec of the calculation; corner and central recirculation zones are evident. The central recirculations are still growing in size but upstream the flow has settled down sufficiently to allow time

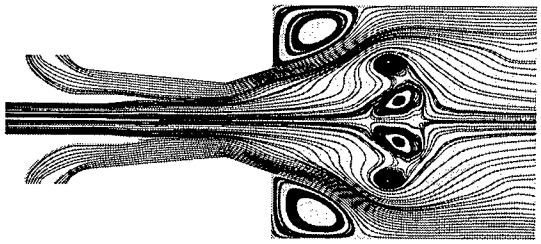


Figure 4: Mean Stream Lines

average to be carried out. Figure 5 presents a comparison with time-averaged LDA data taken in the Cranfield University study in the upstream mixing duct. The agreement is reasonable indicating that the LES method is representing the mixing processes in the premix part of the duct quite accurately. The levels of

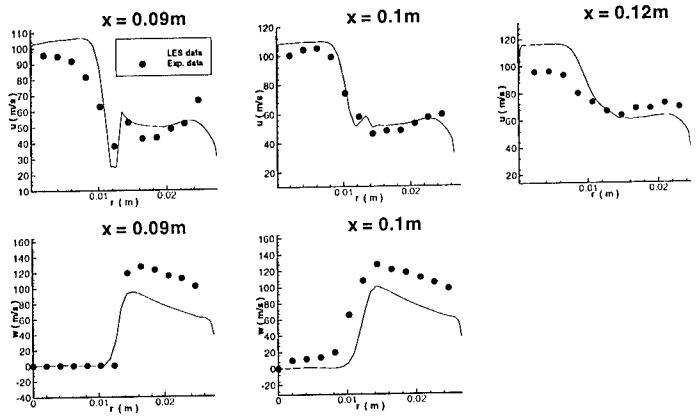


Figure 5: Mean Velocity Profiles

swirl are underpredicted, but this may be due to the inadequacies in the inlet profiles.

3 Conclusions

- A multi-block curvilinear mesh LES code incorporating a simple Smagorinski SGS model has been successfully applied to analyze the flow in a geometry typical of that proposed for LPP combustion systems.
- Although the calculations have not at present reached a statistically stationary state throughout the whole domain, comparison with LDA velocity profiles in the upstream premixing duct have shown reasonable agreement with measurements - the LES approach seems a promising methodology for predicting the mixing in LPP geometries.

The authors would like to acknowledge: (i)the contribution made to the original development of the LES code used in this work by Dr A.P.Manners and Dr S.Zeng, (ii)discussion with collegues at Cranfield University and the experimental measurements.

References

[1] K. Akselvoll, and P. Moin. Large-eddy Simulation of Turbulent Confined Coannular Jets. *J Fluid Mech.*, 315:387–411, 1996.

[2] Large Eddy Simulation Modelling for Lean Prevapourised Premixed Combustion. *Technical Report*, LES4LPP-BE95-1953, 1999.

ADVANCES IN TURBULENCE VIII
Proceedings of the Eighth European Turbulence Conference
C. Dopazo et al. (Eds.)
© CIMNE, Barcelona 2000

Turbulence Statistics and Scalar Transport in an Open-Channel Flow

Y. Yamamoto[1], T. Kunugi[1] and A. Serizawa[1]

[1]Department of Nuclear Engineering, Kyoto University
Yoshida, Sakyo, Kyoto, 606-8501, Japan

Contact e-mail: kunugi@nucleng.kyoto-u.ac.jp

1 Introduction

Free-surface turbulent flows are very often found in the industrial devices. To investigate the turbulent structures near free-surface is very important to understand the heat and mass transport phenomena across the free-surface. The interesting information about the relationship between turbulent motion [1], and scalar transport have obtained via DNS [2],[3]. However, in both calculations, molecular diffusivity of scalar was comparable to that of momentum, it is questionable whether these results can be used for the higher Prandtl or Schmidt number fluid. The aims of this study are to clarify the turbulence structures near free-surface and to estimate the effect of the turbulent structure on scalar transport near free-surface for various Schmidt numbers.

2 Numerical Procedures

Governing equations are incompressible Navier-Stokes equations, the continuity equation and the convective diffusion equation of passive scalar. The numerical integration method is based on a fractional step method [4], time integration is a 2nd Adams-Bashfort scheme for the convective terms and Crank-Nicholson scheme for the viscous terms as well as those for the scalar fields. For the spatial discretization, a second order central differencing scheme is adapted. Numerical conditions are shown in Table 1. As the boundary conditions for fluid motion, free-slip condition at the free-surface, no-slip condition at the bottom wall, and as for passive scalar, constant concentration at the free-surface and the bottom wall, the cyclic condition in stream and spanwise directions are imposed, respectively.

The transport equations for the time-averaged Reynolds stresses of a 2D fully-developed turbulent open-channel flow are given by

$$\frac{D\overline{u_i u_j}}{Dt} = 0 = P_{ij} + TD_{ij} + VD_{ij} + \Pi_{ij}(= \phi_{ij} + PD_{ij}) - \epsilon_{ij}, \qquad (1)$$

where is u_i i th-component turbulent velocity (i=1,2,3), and the terms on the right-hand side of Eq.(1) denote the rate of production, turbulent diffusion (P_{ij}), viscous diffusion (VD_{ij}), velocity pressure-gradient (Π_{ij}) (=Pressure strain (ϕ_{ij}) + Pressure diffusion (PD_{ij})) and dissipation (ϵ_{ij}), respectively. All quantities normalized bythe friction velocity, kinetic viscosity and mean scalar flux at the free-surface, were denoted by the super script +.

3 Results and Discussion

Figures 1-5 show the budgets of the turbulent kinetic energy $k=\overline{u_i u_i}/2$ and Reynolds stresses. Near wall turbulence structure is as well as the wall turbulence, and fairly agree with other DNS data [6] of closed channel flow by a spectral method. This verifies the accuracy of the present numerical simulation. Near the free-surface, that is to say, approximately 5 percent region of the flow depth, typical turbulence structures caused by the presence of free-surface were existed and these results were in good agreements with Handler et al [6]. Figure 6 shows the turbulent viscosity estimated by the present DNS results. This indicates that turbulence models are required to be modified at the free-surface for representing the anisotropic turbulent statistics behaviors.

Mean scalar profiles, scalar fluxes and fluctuation profiles are shown in Figs.7 and 8. It can be seen that the scalar fluctuation is produced by both mean velocity gradient near wall and mean scalar gradient near free-surface, but these profiles are distinct from each other. Especially, in the case of Sc= 5.0, the turbulent scalar statistics depict the maxima at near free-surface where typical turbulence structures are existed. These mean that if the Schmidt number is higher, the mass transfer is enhanced by turbulent structures at near free-surface, and indicate that *Reynolds analogy* between momentum and scalar transport couldn't be applied. Instantaneous turbulent scalar fields near free-surface are shown in Fig.9. Scalar transport is gone with surface renewal vortex, but in the case of Sc= 5.0, the filamentous high concentration fragments are kept, because the time scale of the fluid motion is so fast compared with the scalar diffusion time scale.

4 References

[1] Nagaosa and Saito, AIChE. J. vol.43, 1997. [2] Handler et al, Physics of fluids., vol.11, No.9, pp.2607-2625, 1999. [3] Komori et al., Int.J.Heat and Mass Transfer, 25, pp.513-522, 1982. [4] Kim and Moin, J. Comput. Phys. 59, pp.308-323, 1985. [5] Gilbert and Kleiser, Proc, 8th Symp. Turbulent shear flows, Paper 26-1, 1991. [6] Handler et al., AIAA J., vol.31, pp.1998-2007, 1993.

Table 1 Numerical conditions

R_τ	Grid number $(x \times y \times z)$	Computional Domain (L_x, L_y, L_z)	Spatial resolution $(\Delta x^+, \Delta y^+, \Delta z^+)$	S_c
200	$128 \times 108 \times 128$	$6.4h, h, 3.2$	$10, 0.5 \sim 4, 5$	1.0
200	$256 \times 131 \times 256$	$6.4h, h, 3.2$	$5, 0.5 \sim 2, 2.5$	5.0

where $R_\tau = u_\tau h/\nu$ is Reynolds number, u_τ is friction velocity, h is flow depth, ν is kinetic viscosity, $x_1(x)$:streamwise direction, $x_2(y)$:vertical direction, $x_3(z)$:spanwise direction $S_c = \nu/D$ is Schmidt number, D is mass diffusivity

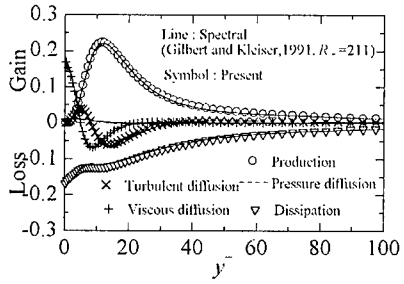


Fig. 1 Budget of turbulent kinetic energy (Near Wall)

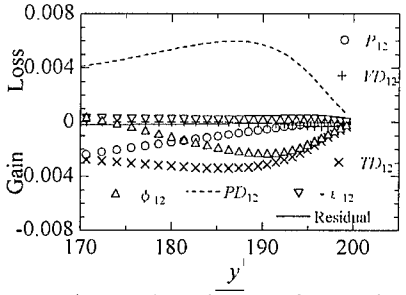


Fig.2 Budget of $\overline{uv}$ near free-surafce

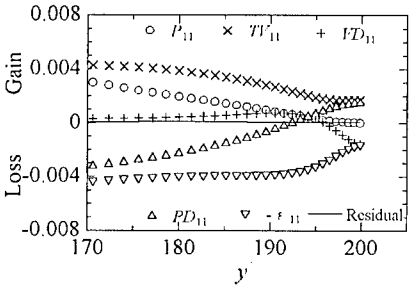


Fig. 3 Budget of $\overline{uu}$ near free-surface

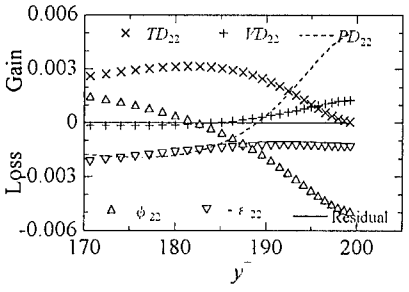


Fig. 4 Budget of $\overline{vv}$ near free-surface

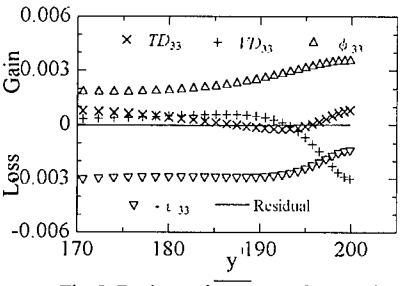


Fig.5 Budget of $\overline{ww}$ near free-surface

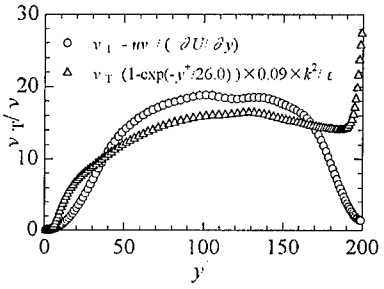


Fig. 6 Turbulent visocity profiles

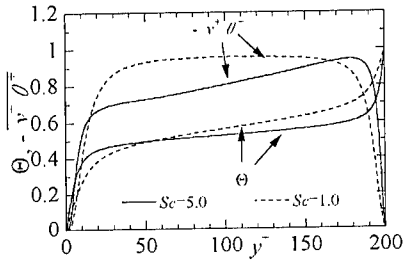


Fig.7 Mean scalar and wall-normal scalar flux profiles

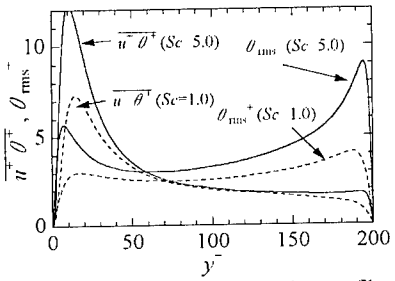
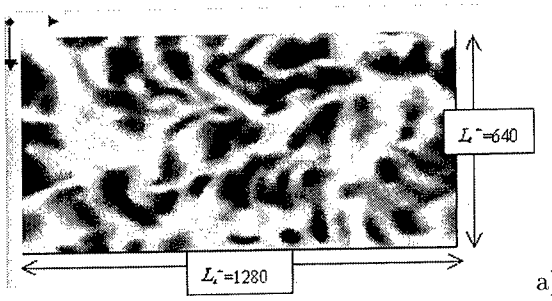
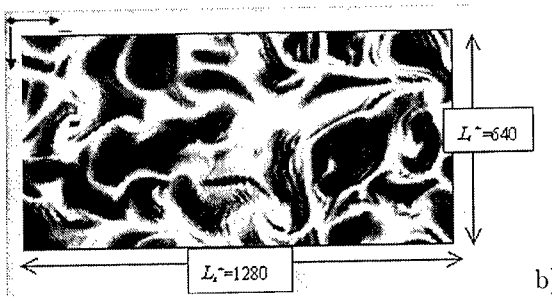


Fig.8 Scalar flux and fluctuation profiles

where $\theta^* = \Theta + \theta$ is defined as , $\theta^* = (C^* - C_b)/(C_s - Cb), C^*$is mass concentration, C_s and C_b and are the mass concentration at the free-surface and the wall, Θ is mean scalar, θ is scalar fluctuation, respectively.



a)$S_c = 1.0$



b)$S_c = 5.0$

Fig9 Turbulent scalar fields near free-surface (Top view)
a)$S_c = 1.0$,b)$S_c = 5.0$
$-0.27(Black) < \theta < 0.27(White)$

ADVANCES IN TURBULENCE VIII
Proceedings of the Eighth European Turbulence Conference
C. Dopazo et al. (Eds.)
© CIMNE, Barcelona 2000

Scalar Flux Measurements and Models of a Plume Emitting from a Wall Line Source Downstream of an Obstacle on the Wall of a Turbulent Boundary Layer

J.-Y. Vinçont [1], S. Simoëns [1], M. Ayrault [1], and J.M. Wallace [2]

[1]Ecole Centrale de Lyon, FRANCE
[2]Department of Mechanical Engineering
University of Maryland, College Park, MD 20742, USA

Contact e-mail: wallace@eng.umd.edu

1 Introduction

Simultaneous measurements of the velocity and scalar concentration fields have been made in the plume emitting from a two-dimensional line source at the wall (see Vinçont [1] for additional details). The source is one obstacle height, h, downstream of a two-dimensional square obstacle located on the wall of a turbulent boundary layer. The obstacle height is 1/7th the boundary layer thickness. These measurements were made in two fluid media: water and air, as illustrated in Fig. 1. In both media particle image velocimetry (PIV) was used for the velocity field measurements. For the scalar concentration measurements laser induced fluorescence (LIF) was used for the water flow and Mie scattering diffusion (MSD) for the air flow. In the water flow this was done with iriodine particles for the PIV measurements and rhodamine B fluorescent dye for the LIF. In the air flow incense smoke was used both for the PIV and the MSD.

2 Conditional analysis of the mass fluxes

At 4h and 6h downstream, the scalar flux values were sorted into eight categories (octants) given by sign combinations of the variables: $\pm u$, $\pm v$ and $\pm c$. Three levels above the wall, 1.9h, 1.3h and 0.7h, were studied because they are representative of the three major zones: the outer flow, mixing and recirculation zones. At all three levels the octants that correspond to types of scalar concentration flux motions that can be approximated by mean gradient scalar transport models are the octants that make the dominant contributions to $\overline{uc}$ and $\overline{vc}$.

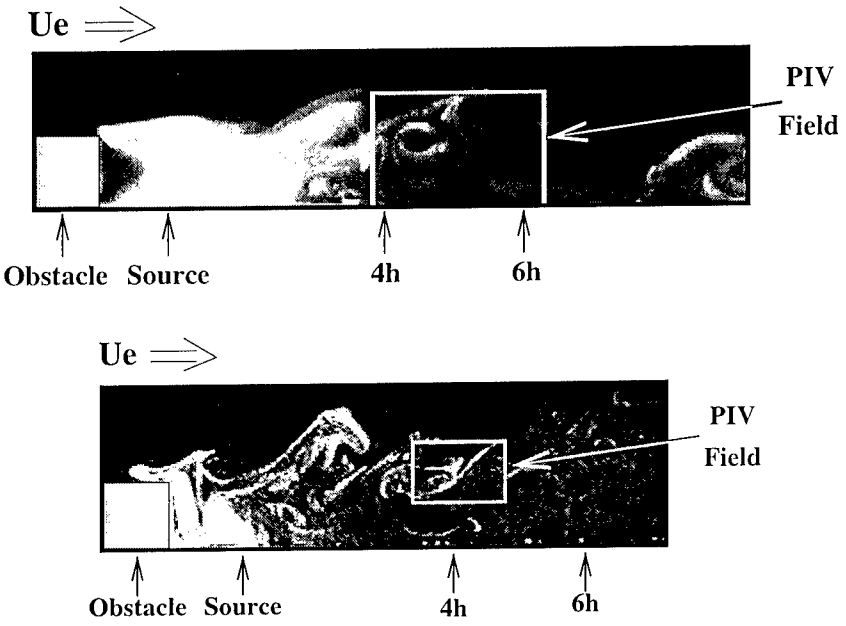


Figure 1: Images of fluorescine dye in water (above) and incense smoke in air (below) plumes downstream of the obstacle. The full fields of view are used for the concentration measurements; the smaller boxes in the images are the fields of view for the PIV measurements.

3 Mass fluxes models

Based on this conditional analysis and following arguments of Wyngaard [2] second order mean gradient models of the momentum and scalar fluxes, $\overline{uv}$, $\overline{vc}$, and $\overline{uc}$ have been constructed:

$$\overline{uv} = -K_v \frac{\partial \overline{U}}{\partial y} \equiv -\tau_1 \overline{v^2} \frac{\partial \overline{U}}{\partial y}, \tag{1}$$

$$\overline{vc} = -K_s \frac{\partial \overline{C}}{\partial y} \equiv -\tau_2 \overline{v^2} \frac{\partial \overline{C}}{\partial y}, \tag{2}$$

and

$$\overline{uc} = \tau_3 \left(K_s + K_v\right) \frac{\partial \overline{U}}{\partial y} \frac{\partial \overline{C}}{\partial y} \equiv D_1 \frac{\partial \overline{U}}{\partial y} \frac{\partial \overline{C}}{\partial y}, \tag{3}$$

where the transport coefficient, D_1, is the product of the sum of the eddy diffusivity coefficients in (1) and (2) with the time scale τ_3, and τ_1 and τ_2 represent large-eddy turnover times. The $\overline{uc}$ model, which requires the $\overline{vc}$ and $\overline{uv}$ models, captures in great detail all aspects of the experimental measurements at the two

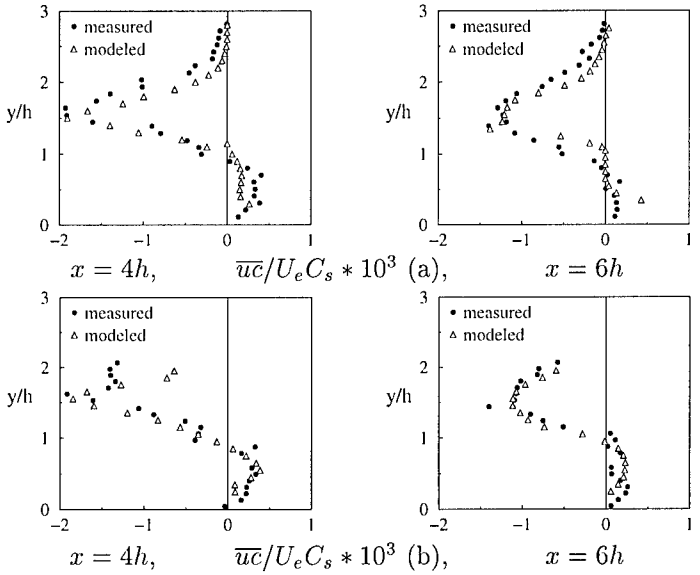


Figure 2: Vertical profiles of streamwise scalar flux downstream of the obstacle. Comparisons between direct measurements and 2nd order gradient model equation (3). Filled circles, $\overline{uc}$ from measurements; open triangles from model. (a) Rhodamine B dispersion in water, $Sc \simeq 2500$, $Re_h \simeq 700$ and (b) smoke dispersion in air, $Sc \simeq 10^6$, $Re_h \simeq 1500$. C_s is the source mean concentration and U_e is the external flow velocity.

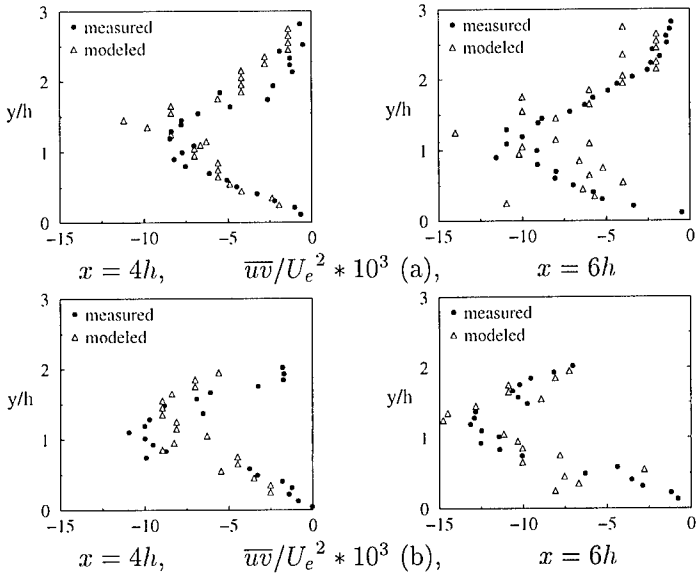


Figure 3: Vertical profiles of Reynolds shear stress downstream of the obstacle. Comparisons between direct measurements and 2nd order gradient model equation (1). Filled circles, $\overline{uv}$ from measurements; open triangles from model. See Fig. 2 caption for other information.

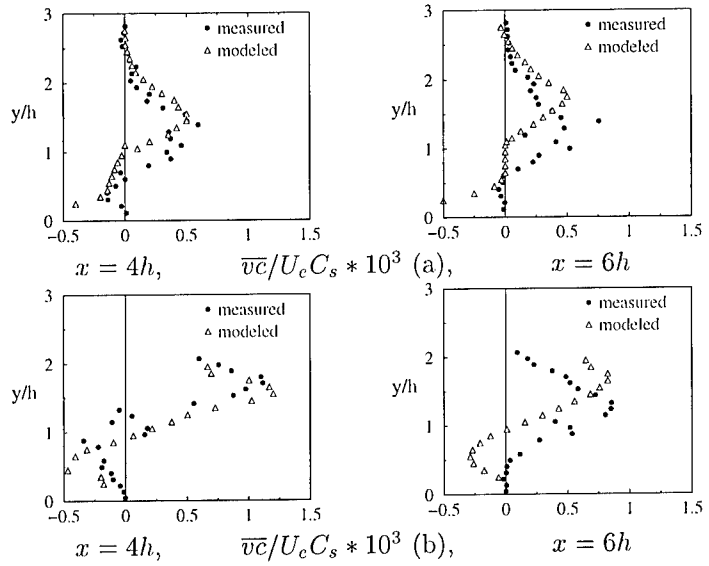


Figure 4: Vertical profiles of cross-stream scalar flux downstream of the obstacle. Comparisons between direct measurements and 2nd order gradient model equation (2). Filled circles, $\overline{vc}$ from measurements; open triangles from model. See Fig. 2 caption for other information.

measurement locations. The $\overline{uv}$ model also agrees quite well with the measured data except below $y/h \approx 0.4$. The $\overline{vc}$ model does not compare as well in every detail to the measurements, but the shapes of the measured and modeled profiles are quite similar. Constant turbulent eddy diffusivity coefficients were chosen at each measurement location to give the best fit of the models to the measured data.

The authors are grateful for the financial support of the CNRS of France. Support of JMW while in France was provided by Ministère de l'Enseignment Superieur et de la Recherche as well as by DOE grant DE-FG02-94ER14441 and NSF grant INT-9726632. We thank J.-N. Gence for his help and comments about the models.

References

[1] J.-Y. Vinçont. Détermination des flux turbulents de masse dans le sillage d'un obstacle : Application à l'écoulement à l'intérieur de la canopée urbaine. *These de Doctorat* , Ecole Centrale de Lyon, France, 1999.

[2] J.C.Wyngaard. Atmospheric Turbulence and Air Pollution Modelling, *Niewstadt F.T.M. and Van Dop H. eds.*, D. Reideil Publishing Co., 69 - 106, 1981.

ADVANCES IN TURBULENCE VIII
Proceedings of the Eighth European Turbulence Conference
C. Dopazo et al. (Eds.)
© CIMNE, Barcelona 2000

Simultaneous measurements of scalar and velocity in variable density turbulent jets

M. Amielh [1], L. Pietri [2] and F. Anselmet [1]

[1] IRPHE, 12 Avenue Général Leclerc, 13003 Marseille, FRANCE
[2] GMAI - CEF, 52 Avenue de Villeneuve, 66680 Perpignan Cedex, FRANCE

Contact e-mail: amielh@marius.univ-mrs.fr

1 Introduction

Variable density jets are associated [1,2] with a much more efficient mixing with the ambient air when the jet density ρ_j is smaller than the air density ρ_e. In particular, to quantify the centreline evolutions of the mean longitudinal velocity U_c and concentration C_c, the downstream location X must be normalized by an efficient diameter D_{eff} such that $D_{eff} = D_j(\rho_j/\rho_e)^{1/2}$. However, although the turbulent field also reaches its fully developed stage more rapidly when $\rho_j < \rho_e$, the asymptotic centreline levels of the velocity turbulence intensity and third order moments almost do not depend on $R_\rho = \rho_j/\rho_e$ [3,4]. Due to measurement difficulties, turbulence data associated with the concentration field are rather scarce [3,5], and this is especially true for mixed moments involving velocity and concentration (or density) fluctuations. The objective of the present study is to analyze the linkage between the scalar and dynamic fields in order to better understand the physical processes involved in variable density turbulent mixing.

2 Experimental set-up

Experiments are performed in a facility [4] where a fully developed turbulent vertical pipe flow ($D_j = 26mm$) of pure air or pure helium discharges into ambient air ($R_\rho = 0.14$) in a slightly confined configuration (velocity $U_e = 0.9m/s$, square section $285 \times 285mm^2$). In the basic nominal configuration, jets are compared at the same exit momentum flux M_j so that, for air and helium respectively, U_j is then 12 m/s and 32 m/s while the Reynolds number Re_j is 21000 and 7000. The air jet can be slightly heated ($T_j - T_e = 20K$) so that temperature is then a passive marker of the flow ($R_\rho = 0.94$). Velocity measurements are performed with a two component laser Doppler system (Argon 4W) fitted with fibre optics and Burst Spectrum Analysers. Concentration is inferred from simultaneous

measurements with a $5\mu m$ hot wire separately calibrated [6] in terms of both velocity and helium mass fraction. Temperature fluctuations are obtained with a $0.6\mu m$ cold wire. For the spectral analysis, the velocity signal is resampled with a 01-order interpolation which is a mixing of the zero order and the linear interpolations. The chosen resampling frequencies are 100kHz for measurements at $X/D_j = 5$ and $37.5kHz$ at $X/D_j = 15$.

3 Results and discussion

For temperature (Fig. 1.a) and helium concentration (Fig. 1.b), the axial evolutions of the longitudinal velocity u' and scalar (θ' or c') rms values are shown together with those for the velocity-scalar covariance and the associated correlation coefficient. The faster development of the helium jet is here illustrated by the fact that the position of the maxima of the u', c' and $\langle uc \rangle$ distributions are attained at the station $X/D_j \approx 3$, whereas the heated jet distributions attain their maxima at $X/D_j \approx 7$. The values of these maxima are larger in the helium jet, which is in good agreement with the fact that the mean velocity and scalar gradients are stronger than in the slightly heated jet. But the most interesting new feature is associated with the significantly smaller value of the correlation coefficient R_{uc} (about 0.35 the in self-similar region) in comparison with $R_{u\theta}$ (about 0.5, a commonly reported value, see Pietri et al. [7]).
On the axis of the helium jet (Fig. 2, left, f_λ is the frequency associated with the Taylor micro-scale), velocity and concentration spectra at $X/D_j = 5$ are shifted with respect to those at $X/D_j = 15$, in agreement with the very different local mean velocities ($U_c(5D_j) = 21.3m/s$ and $U_c(15D_j) = 5.96m/s$). At a given station, the concentration spectrum extends over a higher frequency range compared to the longitudinal velocity spectrum, a usual observation in slightly heated flows which is related to the influence of the two other velocity components [8]. The spectral correlation coefficients between scalar and velocity (Fig. 2, right, f_λ and f_η are almost the same for the two sets of data) show a negative contribution to R_{uc} which is likely to explain why R_{uc} is lower than $R_{u\theta}$.
Figures 3 present the skewness factors, $S_{\delta q}$, of the longitudinal velocity and concentration increments, $\delta q = q(x+r) - q(x)$, on the helium jet axis at $X/D_j = 5$ and 15. At $X/D_j = 5$, a plateau, typical of an inertial subrange, is obtained for velocity between 40 and 100η. For smaller r, $S_{\delta u}$ keeps a stagnant value around 0.2 due to the noise associated with the resampling method for the LDV measurements. Comparison with similar results obtained at the same station from hot-wire measurements in the air jet shows that such a plateau is not at all observable in the air jet. The close to zero values of $S_{\delta q}$ for large r are in good agreement with the zero limit value independent of the skewness factor of the quantities u and c. For the air jet, $S_{\delta u}$ remain at a zero value for a large range of r, up to 100η, which is a consequence of the very small Reynolds number value (R_λ about 30) since the air jet is only initiating its development at this station (see Fig. 1). At $X/D_j = 15$, the developments of the helium and air jets

are similar, with an inertial subrange between 20 and 150. The plateau level of -0.28, characteristic of homogeneous isotropic turbulence (H.I.T.), is not exactly reached for $S_{\delta u}$ because of the low value of the turbulent Reynolds number (R_λ about 150 in both jets at this station). The limitation due to the low mean data rate of LDV measurements ($4.5kHz$, to be compared with $f_\eta = 7kHz$) does not allow us to reach the value of -0.5, typical of the vortex stretching at small r, as obtained from the hot-wire measurements of Ould-Rouis [9]. The non-zero value of $S_{\delta c}$ in the helium jet and for small r is the signature of large scale ramps in the scalar signal, as previously described for temperature in slightly heated jets [10]. This important new result for variable density turbulent jets is also a validation of our measurement technique which combines LDV and hot wire to deduce the concentration fluctuations.

We are very grateful to L. Fulachier, J.F. Lucas and S. Mucini for their contribution to the present measurements and to EDF/LNH for financial support.

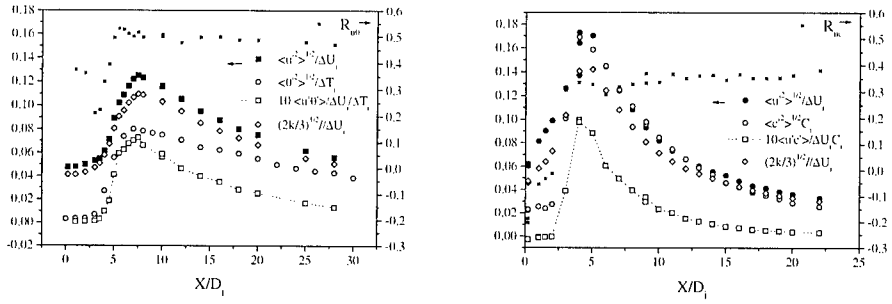


Figure 1: Velocity and scalar second order moments in the slightly heated (left) and helium (right) jets.

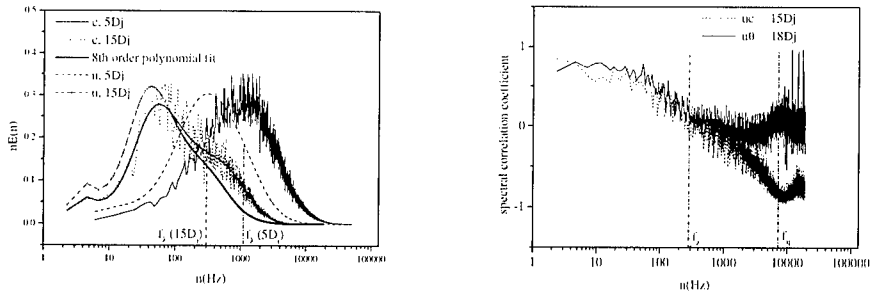


Figure 2: Velocity and concentration spectra in helium (left) and spectral correlation coefficients (right).

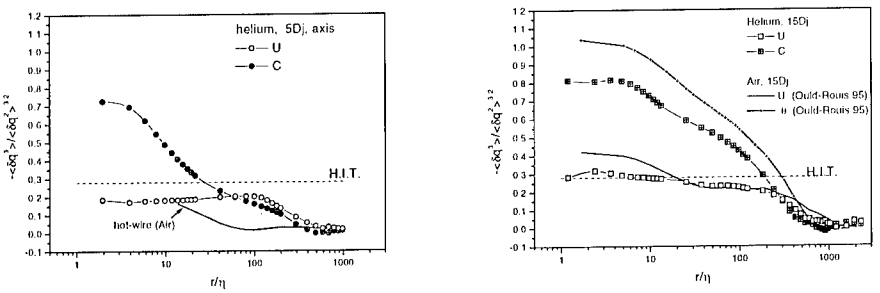


Figure 3: $S_{\delta u}$ and $S_{\delta c}$ on the helium jet axis at $X/D_j = 5$ (left) and 15 (right).

References

[1] M.W. Thring and N.P. Newby. Combustion length of enclosed turbulent jet flames. *4–th International Symposium on Combustion, Pittsburg,* 1952.

[2] C.J. Chen and W. Rodi. Vertical turbulent buoyant jets. *A review of experimental data*, Pergamon Press, New York, 1980.

[3] N.R. Panchapakesan and J.L. Lumley. Turbulence measurements in axisymmetric jets of air and helium. *J. Fluid Mech.*, 246:197-247, 1993.

[4] T. Djeridane, M. Amielh, F. Anselmet, and L. Fulachier. Velocity turbulence properties in the near-field region of axisymmetric variable density jets. *Physics of Fluids* , 8:1614-1630, 1996.

[5] R.M.C. So, J.Y. Zhu, M.V. Otügen, and B.C. Hwang. Some measurements in a binary gas jet. *Experiments in Fluids*, 9:273-284, 1990.

[6] J.F. Lucas. Analyse du champ scalaire dans un jet turbulent axisymétrique à densité variable. *Ph. D. Thesis*, IRPHE-Univ. Aix Marseille II, 1998.

[7] L. Pietri, M. Amielh, and F. Anselmet. Simultaneous measurements of temperature and velocity in a slightly heated jet combining a cold wire and laser Doppler anemometry. *Int. J. Heat Fluid Flow*, 21:22-36, 2000.

[8] L. Fulachier and R.A. Antonia. Spectral analogy between temperature and velocity fluctuations in several turbulent flows. *Int. J. Heat and Mass Transfer* , 27:987-997, 1984.

[9] M. Ould-Rouis. Intermittence interne pour un scalaire passif en turbulence pleinement développée . *Ph. D. Thesis*, IRPHE-Univ. Aix Marseille II, 1995.

[10] R.A. Antonia and C.W. Van Atta. Structure functions of temperature fluctuations in turbulent shear flows. *J. Fluid Mech.*, 84:561-580, 1978.

IX

Boundary Layers and Free Shear Flows

ADVANCES IN TURBULENCE VIII
Proceedings of the Eighth European Turbulence Conference
C. Dopazo et al. (Eds.)
© CIMNE, Barcelona 2000

Multi-scale structures in a turbulent near-wake

Hui Li[1] and Yu Zhou[2]

[1]Department of Mechanical Engineering, Kagoshima University
1-21-40, Korimoto, Kagoshima 890-0065, JAPAN
[2]Department of Mechanical Engineering, The Hong Kong Ploytechnic University
Hung Hom, Kowloon, Hong Kong, CHINA

Contact e-mail: li@mech.kagoshima-u.ac.jp

1 Introduction

The turbulent near-wake of a circular cylinder has a high degree of organization and is dominated by spanwise vorticity. It is therefore attractive for the purpose of identifying turbulent organized structures and clarifying their contribution to turbulent transfer process. However, it is difficult to use traditional techniques to deduce relatively small scale structures. As a result, this affects our understanding of turbulent structures of various scales. In the past decade, there has been a growing interest in the use of wavelet analysis for turbulent flow data (Li, 1998) [1]. This technique allows time-space and frequency-space analyses to be combined and produces a potentially clearer picture of time-frequency localization of turbulent structures. The present work firstly develops a new signal processing technique, called vector multiresolution analysis based on a two-dimensional orthogonal wavelet transform. Then the technique is applies to experimental data of the near-wake of a circular cylinder for identifying the turbulent structures of various scales and extracting information on the intermediate-scale and relatively small-scale turbulent structures.

2 Orthogonal Vector Wavelet Transform

Let us consider a two-dimensional vector field $\vec{f}(x_1, x_2)$ and a two-dimensional orthogonal wavelet basis

$$\Psi_{m_1,n_1;m_2,n_2}(x_1, x_2) = 2^{-(m_1+m_2)/2}\psi(2^{-m_1}x_1 - n_1)\psi(2^{-m_2}x_2 - n_2), \qquad (1)$$

where $\psi(x)$ is an one-dimensional orthogonal wavelet basis. The two-dimensional discrete vector wavelet transform is defined as

$$\overrightarrow{Wf}_{m_1,n_1;m_2,n_2} = \sum_i \sum_j \vec{f}(x_1^i, x_2^j)\Psi_{m_1,n_1;m_2,n_2}(x_1^i, x_2^j) \qquad (2)$$

The reconstruction of the original vector field can be achieved by using

$$\overrightarrow{f}(x_1^i, x_2^j) = \sum_{m_1}\sum_{m_2}\sum_{n_1}\sum_{n_2} \overrightarrow{Wf}_{m_1,n_1;m_2,n_2} \Psi_{m_1,n_1;m_2,n_2}(x_1^i, x_2^j) \qquad (3)$$

In this paper a new signal processing technique, called the vector multiresolution analysis, is proposed. The procedure can be summarised in two steps: (1) Wavelet coefficients of vector data are computed based on the discrete vector wavelet transform of Eq.2. (2) Inverse vector wavelet transform of Eq.3 is applied to wavelet coefficients at each wavelet level, and vector components are obtained at each level or scalein the wavelet space.

The vector multiresolution analysis may process fewer data by selecting the relevant details that are necessary to perform an extraction of the multi-scale structures and coherent structures, and may decompose the vector data in both Fourier and physical spaces. The technique is unique in terms of its capability to separate turbulence structures of different scales. In this paper, we use the Daubechies family with index $N = 20$ as orthogonal wavelet basis.

3 Experimental Setup and Results

Experiments were carried out in a low turbulence wind tunnel with a $2.4m$ long working section ($0.35m \times 0.35m$). A circular cylinder ($d = 12.5mm$) was installed in the mid-plane and spanned the full width of the working section. Two orthogonal arrays, each of eight X-wires, were used. Eight X-wires were aligned in the (x, y)-plane, i.e. the plane of mean shear, and eight in the (x, z)-plane, which is parallel to both the cylinder axis and the streamwise direction. The sixteen X-wires allow velocity fluctuations u and v in the (x, y)-plane and u and w in the (x, z)-plane to be obtained simultaneously with a sampling frequency of $f_s = 3.5kHz$. The nominal spacing between X-wires was about $5mm$. Measurements were made at $x/d = 20$ and a constant free stream velocity ($U_\infty = 6.7m/s$). The corresponding Reynolds number Re was 5600. More details of the data have been given in Zhou *et. al* (1999) [2]

The spanwise and lateral components of vorticity can be defined in terms of the derivatives of the instantaneous velocity components $U = \overline{U} + u$, $V \cong v$ ($\overline{V} \cong 0$), and $W \cong w$ ($\overline{W} \cong 0$), where an overbar denotes time averaging, viz.

$$\omega_z = \frac{\partial V}{\partial x} - \frac{\partial U}{\partial y} = \frac{\partial v}{\partial x} - \frac{\partial(\overline{U}+u)}{\partial y} \approx \frac{\Delta v}{\Delta x} - \frac{\Delta(\overline{U}+u)}{\Delta y} \qquad (4)$$

$$\omega_y = \frac{\partial U}{\partial z} - \frac{\partial W}{\partial x} = \frac{\partial u}{\partial z} - \frac{\partial w}{\partial x} \approx \frac{\Delta u}{\Delta z} - \frac{\Delta w}{\Delta x} \qquad (5)$$

In above equations, $\Delta y \approx \Delta z$ ($\approx 5.0mm$) is spacing between two X-wires; $\Delta x = -U_c \Delta t$, where $\Delta t = 1/f_s$ and $U_c = 0.87U_\infty$ is the average convection velocity.

The velocity vector data were decomposed into nine wavelet levels. Figure 1 (plates 1 - 3) presents the decomposed velocity vectors overlapping on the

corresponding vorticity data for wavelet levels 6 to 8 in the (x, y)-plane. The frequency range of the three levels is $100 \sim 200$, $200 \sim 400$ and $400 \sim 800Hz$, respectively, representing different scales of turbulence structures. The data is compared with the measured velocity vectors and vorticity (plate 4). Plate 1 exhibits four vortical structures at tU_c/d=1.4, 4.8, 7.0 and 9.0. These structures correspond quite well to the large-scale structures in plate 4, which occur at frequencies around the average frequency ($108Hz$) of Karman vorticies. They are apparently the uppermost and energy-containing structures. The agreement between the measured velocity and the decomposed data of the $100 \sim 200Hz$ range provides a validation for the present data analysis technique. Both velocity vectors and vorticity in plate 2 show a number of structures that are smaller than those in plate 1. Some of them correspond to Karman vortices in plate 4, e.g. at $tU_c/d \approx$1.4, 4.8 and 9.0. Others correspond to the saddle regions, e.g. at $tU_c/d \approx$2.2 and 5.7, between the vortices. These are consistent with the occurrence of rib structures. As the wavelet level is increased to 8 (plate 3), a number of even smaller scale structures are identifiable. These structures seem to occur all over the space. However, their occurrence is rather periodical. It should be pointed out that, as indicated by the vorticity data, the structures decrease in strength as their scales reduce. This is consistent with the concept of the energy cascade. Note that it is difficult to identify the structures smaller than Karman vortices in the original velocity vectors (plate 4).

Figure 2 shows the data corresponding to Fig 1 in the (x, z)-plane. The structures of $100 \sim 200Hz$ (plate 1) tend to occur simultaneously with Karman vortices, e.g. at $tU_c/d \approx$4.8, 7.0 and 9.0, and are probably due to the three-dimensionality of Karman vortices. Some correspond to the saddle region, for example, the one at $tU_c/d \approx 1.8$. The structures of $200 \sim 400Hz$ (plate 2) also appear corresponding to either the Karman vortices such as those $tU_c/d \approx$1.0, 4.8 and 7.0 or the saddle regions, e.g. the one at $tU_c/d \approx 3.2$. The small structures in plate 3 behave quite similarly to their counterparts in the (x, y)-plane. They occur regularly and at approximately the same periodicity as in the (x, y)-plane. Although preliminary, the results presented here demonstrate that the orthogonal vector wavelet transform technique can be used reliably and effectively for decomposition and analysis of multi-scale turbulent structures. The technique is unique that turbulent structures of different scales can be separated and characterized.

References

[1] H. Li. Identification of Coherent Structure in Turbulent Shear Flow with Wavelet Correlation Analysis. *ASME Journal of Fluids Engineering*, 120:778–785, 1998.

[2] Y. Zhou, W. K. Tsang, and R. A. Antonia. Vortical structures in a turbulent far-wake. *Fluid Dynamics Research*, 25:293–314, 1999.

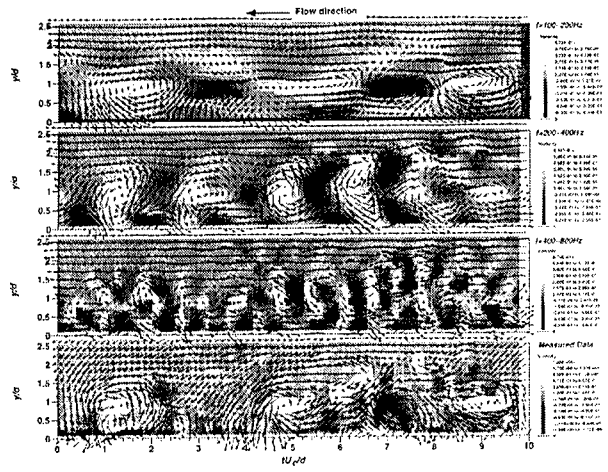


Figure 1: Distribution of velocity vector and vorticity in the (x, y)-plane.

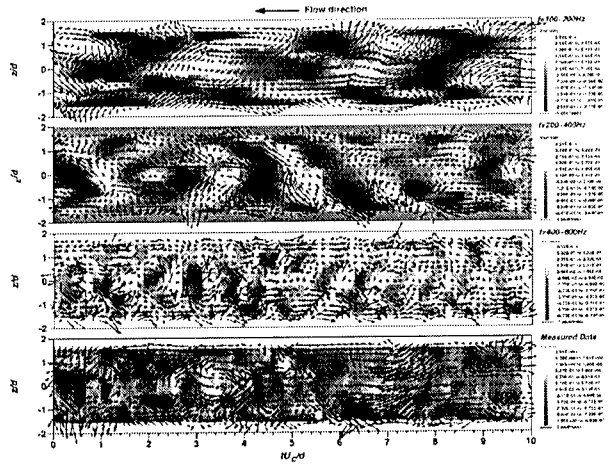


Figure 2: Distribution of velocity vector and vorticity in the (x, z)-plane.

ADVANCES IN TURBULENCE VIII
Proceedings of the Eighth European Turbulence Conference
C. Dopazo et al. (Eds.)
© CIMNE, Barcelona 2000

Topological Features of a Turbulent Wake

G.A. Kopp[1], Francesc Giralt[2] and A. Vernet [2]

[1]1Boundary Layer Wind Tunnel Laboratory, Faculty of Engineering Science, University of Western Ontario, London, ON, N6A 5B9, CANADA
[2] Escola Tecnica Superior d'Enginyeria Quimica, Universitat Rovira i Virgili, Carretera de Salou, s/n, 43006 Tarragona, Catalunya, SPAIN

Contact e-mail: gak@blwtl.uwo.ca

1 Introduction

Many engineering processes require the detailed understanding of mixing and entrainment. Since overall rates of mixing and entrainment are governed, to a large extent, by large-scale coherent motions, obtaining details of these motions has been the focus of a great deal of research. Vernet *et. al* [1] recently identified the complete three-dimensional large-scale structure of the turbulent far wake of a circular cylinder at Re = 7000. They found it to be horseshoe-like structure, as originally speculated by Theodorsen. Townsend and Grant's double rollers were found to be a horizontal slice of these horseshoes. Vernet *et. al* [1] also discussed the upstream and downstream saddle points that appear, though not always, in the events identified with pattern recognition. They related these motions to the momentum transfer in the far wake. Giralt *et. al* [2] also found that upstream of the horseshoe structure and the saddle point were very large rollers (or foci), with lateral vorticity. Neither the origin of these motions, nor their impact on entrainment and mixing, is clear.

There has been debate in the literature about the origins of the far wake structures with two points of view generally put forward; (i) instability of the mean velocity profile, and (ii) evolution from the near wake structures. Hayakawa and Hussain [3] and others have favoured the latter point of view, while, for example, Cimbala *et. al* [4] considered the former. The main objective of this work is to investigate how a very large roller with lateral vorticity might exist upstream of the horseshoe structure. The present approach is to identify the wake topology as it evolves downstream from the vortex street.

2 Experiments

The experimental data were obtained in the Low Turbulence Wind Tunnel of Universitat Rovira i Virgili. This wind tunnel has a test section of 600 mm x 600 mm by 3 m long. A circular cylinder was placed horizontally near the beginning of the test section at mid-height, spanning the full width. A uniform free stream velocity of U_o = 9.0 m/s was used so that the Reynolds number, based on the nominal diameter, D=11.6 mm, was Re=7000. Two orthogonal rakes of 4 X-wire probes each were located at downstream position x* = 29, as shown in Figure 1.

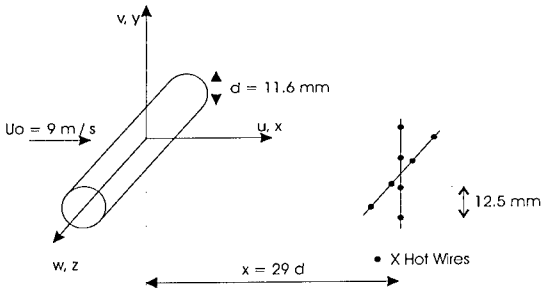


Figure 1: Definition sketch for the experiments.

The horizontal rake was positioned at y* = -0.86. Thus, only the lower half of the wake was analyzed. Here, and in the remainder of this paper, the spatial coordinates are normalized as y* =y/D, z* = z/D and $x^* = -U_{ot}/D$. Taylor's hypothesis of frozen turbulence was used to transform time coordinate to streamwise coordinate. The spacing between adjacent probes is 12.5 mm. A convection velocity of $U_c = 0.9U_o$ has been used to obtain the streamwise component of the velocity from the measured u signal. Both, vertical and horizontal planes were sampled simultaneously at 5000 samples per second per channel during 40 seconds. Additional measurements were taken at x/D = 60, 90 and 170, although space limitations do not allow the discussion of the results from these locations.

3 Analysis

Figure 2 shows the u-autospectrum at x/D = 29 near the location of maximum shear. There is only weak evidence for the vortex street (at the shedding frequency of 159 Hz) at this downstream location since it has already become significantly randomised (see, for example, ref. [3]). The autospectra of the lateral velocity and coherence functions indicate that vortex streets may persist until about x/D = 60.

The time series data were also analysed with the fuzzy clustering pattern recognition technique developed by Kopp and Vernet [5]. This technique was developed for the identification of critical points in coarsely-spaced experimental data such as that obtained from hot-wire probes. The advantage of the fuzzy clustering approach is that multiple patterns can be simultaneously identified without the need for the templates used in "traditional" pattern recognition. With the current data, the approach is to identify the critical points in one plane and examine simultaneously what occurs in the other. Figure 3a shows the ensemble average of saddle points centred on y* = -1.4 in the vertical plane while Figure 3b shows the resulting velocity pattern in the horizontal plane, averaged at the same instants.

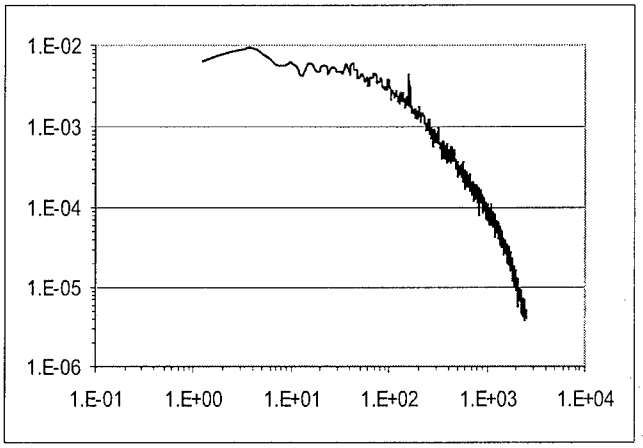


Figure 2: The streamwise velocity autospectrum at x/D = 29 near the lateral location of maximum shear.

About 1400 saddle points and 1400 foci were identified in the vertical plane. This represents about 22% of the originally shed vortices. Figure 3 accounts for about half of the identified saddle points, those centred on the third probe from the top of the rake. The passage frequency of the observed critical points was very broadband, consistent with the autospectrum presented in Figure 2. A saddle point is also observed in the horizontal plane, corresponding to the saddle point in the vertical plane. Downstream of this saddle is a double roller structure with two foci, or at least what appears to be the beginning of such motions. This is the same topological pattern that exists in the far wake (cf.ref [2]), although the present ensemble-average is not particularly symmetrical, since one of the foci in the double roller is observed to be rather weak. This could be due to the rather coarse probe spacing.

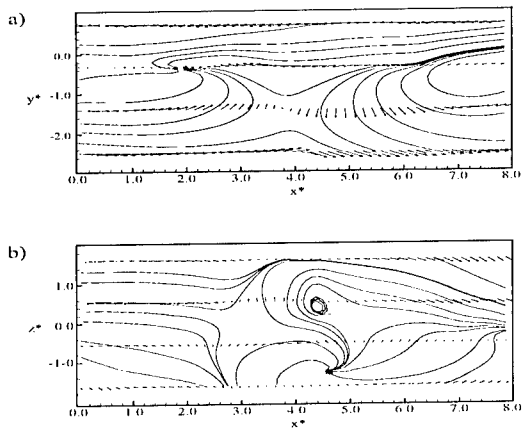


Figure 3: (a) Ensemble averages of (u,v) for clusters identified as saddle points in the vertical plane at x/D = 29; (b) ensemble averages of (u,w) in the horizontal plane, corresponding to the events identified in the vertical plane.

This work was supported by NSERC (Canada) and DGICYT project PB96-1011 (Spain). The third author gratefully acknowledges the support of Universitat Rovira i Virgili during the portion of the investigation carried out in Canada. Thanks to Mr. Seifu Bekele for preparing the latex format of this paper.

References

[1] Vernet A., Kopp, G.A., Ferre, J.A. and Giralt, F., Three-dimensional structure and momentum transfer in a turbulent cylinder wake, *J. Fluid Mech.*, vol. 394, pp. 303-337, 1999.

[2] Giralt, F., Arenas, A., Ferre-Gine, J., Rallo, R. and Kopp, G.A., The simulation and interpretation of turbulence with a cognative neural system, *Phys. Fluids* (to appear), 2000.

[3] Hussain, A.K.M.F. and Hayakawa, M., Three-dimensionality of organized structures in a plane turbulent wake, *J. Fluid Mech.*,vol. 206, pp. 375-404, 1987.

[4] Cimbala, J.M., Nagib, H.M. and Roshko, A., Large structure in the far wakes of two-dimensional bluff bodies, *J. Fluid Mech.*, vol. 190, pp. 265-298, 1988.

[5] Kopp, G.A. and Vernet A., A fuzzy clustering technique for identifying critical points in coarsely-spaced experimental, turbulent flow data, *submitted to Exp. Fluids.*, 2000.

ADVANCES IN TURBULENCE VIII
Proceedings of the Eighth European Turbulence Conference
C. Dopazo et al. (Eds.)
© CIMNE, Barcelona 2000

Active control of the flow downstream of a swept fence

A. Huppertz and H.-H. Fernholz *

Hermann-Föttinger-Institut für Strömungsmechanik
Technische Universität Berlin;
Straße des 17. Juni 135;
10623 Berlin, Germany

Contact e-mail: huppertz@pi.tu-berlin.de

1 Introduction

Many separating and reattaching flows are three-dimensional and the understanding of their behaviour can be important for the design of engineering devices. However, only few experimental investigations are available of three-dimensional flows such as a swept backward-facing step [1] and [3] or a swept fence with a splitter plate [2], especially if control of the turbulent structure is applied to change the flow behaviour, e.g. to enhance mixing. The aim of this study is to investigate the flow over a swept fence in order to improve the understanding of its dynamics and to influence the size of the separation bubble downstream of the fence by enhancing the entrainment of the shear-layer via forcing.

2 Experimental facility

The model consists of an elliptical nose followed by a flat plate section (length 480mm) and the swept fence (fig. 1). The fence height ($H = 10mm$) is chosen such that the flow field parallel to the fence is nearly homogeneous up to an angle of 30° which was proved by wall-streamline visualisations and LDV measurements. The coordinate system is therefore orientated on the fence (fig. 1). The sweep angles were $\alpha = 0°$ and 20°. Forcing of the flow is achieved by means of a slot mounted flush in the flate plate upstream of the fence (fig. 1). Distance and sweep angle of the slot could be varied with respect to the fence. The forcing array consisted of a slot and a chamber connected via PVC tubes to six loudspeakers. The loudspeakers were driven by power amplifiers and controlled by a

*The authors gratefully acknowledge the financial support by the Deutsche Forschungsgemeinschaft (DFG) and the help of S. Reitebuch during the experiments.

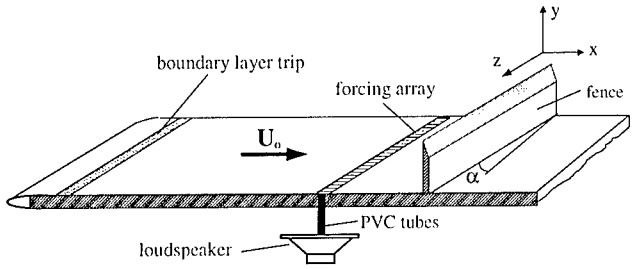


Figure 1: experimental set-up

multi-channel arbitrary-signal generator. At high amplitudes forcing produced an oscillating jet with zero net mass flux. The amplitude of the forcing level was determined by phase-averaged LDV measurements above the slot. For a comparison of the flow field at different sweep angles the Reynolds number, based on step height and free stream component normal to the step $Re_H = U_o cos\alpha H/\nu$, was kept constant, and the bulk of the measurements was performed at a Reynolds number $Re_H = 5300$. The Reynolds number Re_θ at the fence location was 1050 and the ratio of boundary layer thickness δ to fence height h was 2 (measured with the fence removed). The mean velocity profiles and the Reynolds stresses of the turbulent boundary layer showed good agreement with the DNS data of Spalart.

3 Results

The unforced flow. The streamlines of the swept fence ($\alpha = 20°$) projected onto the (x,y) plane are shown in figure 2 . Due to the crossflow the closed streamlines form nonintersecting helicals in z direction and there are the two reverse flow regions up- and downstream of the swept fence with wall-parallel velocity components normal and parallel to the fence. The characteristic length

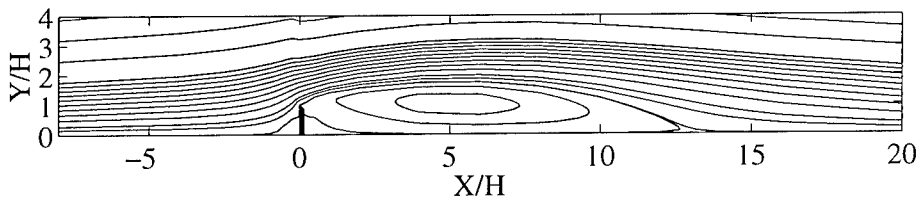


Figure 2: Projection of streamlines onto the (x,y) plane

scale of the flow regime downstream of the fence is the reattachment length x_R, measured as the distance between the fence and reattachment ($c_{fx} = 0$). In

parameter studies the ratio δ_{99}/h was varied between 2 and 4 and the Reynolds number Re_H between 3400 and 8400. For a constant sweep angle none of the two parameters affected the length x_R of the downstream reverse-flow region. If the sweep angle was increased, however, x_R was reduced as for the swept backward-facing step [1]. Measurements of the Reynolds shear stresses $\overline{u'v'}$ and of the turbulence production showed that these quantities were larger than in the unswept case. For both cases the vortical structures in the shear layer are orientated perpendicular to the incoming flow in agreement with the flow over a swept step [3].

The forced flow. The efficiency of forcing was determined by the length of the reverse-flow region visualized by a suspension of petroleum and TiO_2. The forced flow showed a significant reduction of the reattachment length at high amplitudes and for a constant amplitude of $A \equiv v'/U_o = 88\%$ the separation bubble was shortened by 30% for both angles α in a frequency range of $0.03 < St_H \equiv (fH)/U_o < 0.1$ (fig. 3).

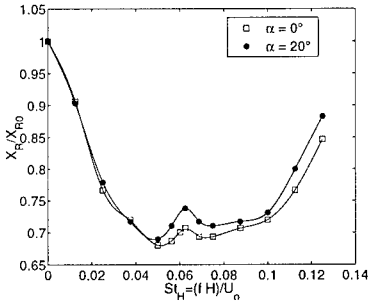


Figure 3: Reattachment length x_R vs. forcing frequency St_h

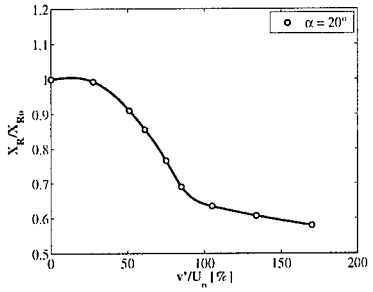


Figure 4: Reattachment length x_R vs. forcing amplitude A

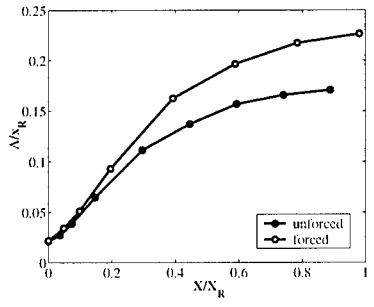


Figure 5: Gradient thickness Λ

The largest reduction of the reattachment length was achieved when the forcing slot was parallel to the fence at a distance of approximately 1.5 fence heights upstream. The effect of the excitation amplitude for constant Strouhal number $St_H = 0.05$ is presented in figure 4. The largest changes of x_R were observed at forcing levels between $25\% < A < 100\%$. A further increase of the forcing amplitude required a disproportionaly large energy input and had little further effect, indicating saturation. The flow manipulation enhanced the spreading of the shear-layer over the fence. Spreading is often described by the gradient thickness $\Lambda \equiv (\bar{u}_{max} - \bar{u}_{min})/(\partial\bar{u}/\partial y)_{max}$ which is

shown in figure 5. Further, all fluctuation levels and the production of turbulent energy were significantly higher with forcing. This means that forcing changes the turbulence structure of the flow field and increases the mixing in the whole reverse-flow region, but at the same time enhances the loss of the mean motion. In order to gather information about the dynamics of the forced flow ($\alpha = 20°$) phase-averaged velocity, vorticity and streamline fields are shown in figure 6 for $St_H = 0.07$ and $A = 88\%$ at two different phase angles. The vorticity is presented as a grey-coded color map whereas the streamlines are viewed from a moving frame. Large vortices are generated downstream of the fence during the suction phase (fig. 6a). At the blowing phase (fig. 6b) these vortices were convected downstream of the fence. The excitation produces a periodical incoming flow which generates vortices similar to those in a starting flow.

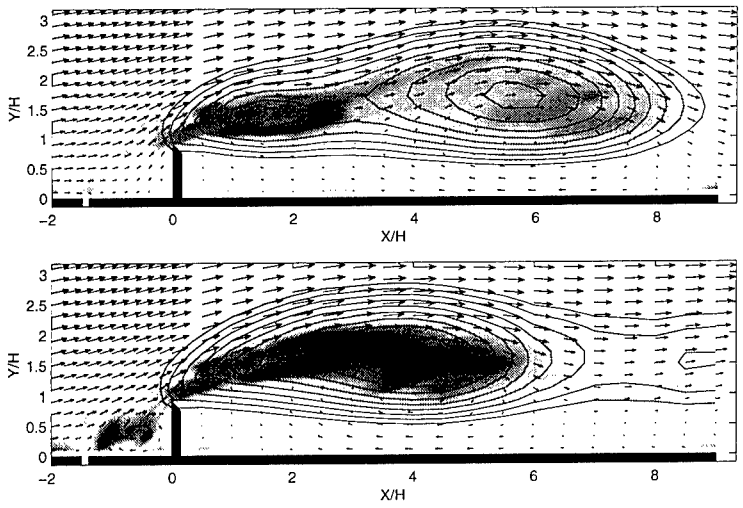


Figure 6: Phase averaged velocity, streamlines and vorticity, a) $\phi = 225°$, b) $\phi = 75°$

References

[1] Fernholz, H.H., Janke, G., Kalter, M., Schober, M., 1993. On the separated flow behind a swept backward-facing step.in: Physics of Separated Flows - Numerical, Experimental and Theoretical Aspects. Editor: K. Gersten, NNFM **14**, Vieweg, Braunschweig.

[2] Hancock, P.E. & McCluskey, F.M., 1997. Spanwise-invariant three-dimensional separated flow. *Experimental Thermal and Fluid Science.* **14**, 25–34.

[3] Kaltenbach, H. & Janke, G., 1999. Direct numerical simulation of flow separation behind a swept rearward facing step at $Re_H = 3000$. *submitted to Physics of Fluids A.*

ADVANCES IN TURBULENCE VIII
Proceedings of the Eighth European Turbulence Conference
C. Dopazo et al. (Eds.)
© CIMNE, Barcelona 2000

Numerical simulation of forced turbulent flow over a fence

A. Orellano and H. Wengle

Institut für Strömungsmechanik und Aerodynamik, LRT WE 7
Universität der Bundeswehr München, 85577 Neubiberg, Germany

Contact e-mail: hans.wengle@unibw-muenchen.de

1 Introduction

In a flow case with a re-attaching shear layer bounding a separation region behind a flow obstacle there are two different instabilities involved: the Kelvin-Helmholtz instability of the free shear layer and a 'shedding'-type instability of the entire separation bubble [1]. We investigate the case of a turbulent boundary layer flow over a surface-mounted fence, for a Reynolds number of $Re_h = 3000$ (based on fence height, h, and maximum inflow velocity, U_∞). The flow is manipulated by time-periodic blowing/suction forcing through a narrow slot upstream of the obstacle, see Figure 1. The purpose of the control is to increase the exchange of fluid from the separated flow regime across the bounding shear layer to the outer flow, and vice versa, thereby reducing the size of the mean separation bubble behind the obstacle. There is an optimum forcing frequency for a maximum reduction of the re-attachment length.

2 Discussion of results

First, a reference data set was provided from a Direct Numerical Simulation (DNS), using 51.6 million grid points, to resolve all the relevant spatial scales of the flow. A Large-Eddy Simulation (LES), using 1.67 million grid points, was validated with this reference solution and compared with experimental data for the same Reynolds number [2]. Then, manipulated flow cases were investigated applying time-periodic forcing with an amplitude of $A = 0.5U_\infty$. High-frequency forcing, with $Str_1 = f_1 h/U_\infty = 0.60$, leads to about 10% reduction of the mean re-attachment length. A much stronger reduction of about 36% could be achieved by low-frequency forcing with $Str_2 = f_2 h/U_\infty = 0.08$.

Figure 2 shows selected time-spectra for three typical regions of the flow: upstream of the fence (X X X), immediately at and after separation (* * *), before and at re-attachment and further downstream (+ + +). Note, the range

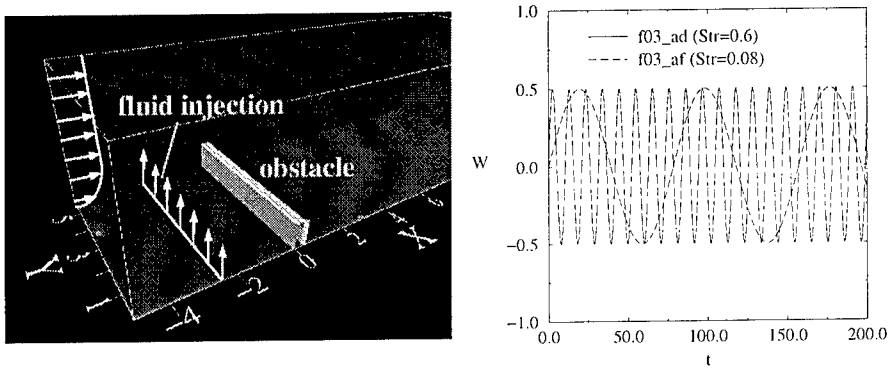


Figure 1: Computational domain with manipulation slot at X=-3 (left) and disturbance velocity W(t) at the slot for the two different Strouhal numbers used in the simulations (right).

of the Strouhal number shown in Figure 2 is smaller than actually used in the evaluation of the time records ($Str_{cutoff} = 12.5$).

In *the non-manipulated case* (see Figure 2a, uppermost row of spectra) the flow domain in front of the obstacle (X X X) shows spectra which reflect the properties of the incoming boundary layer, in particular at the location X=-2.1. The spectra at the other two locations closer to the fence seem to be influenced by processes related to the shear layer bounding the separation region in front of the fence, i.e. low frequency processes are amplified. The flow region at and after separation (* * * *) shows at X=0.6 an amplification of frequencies in the range ($0.3 < Str < 1.8$) with a peak at Str=1.2, (in our case the fundamental frequency of the primary roll-up of the shear layer). Between X=0.6 and X=2.0 energy is transferred to lower frequencies, first to Str=0.6 and then to Str=0.3, signalizing two pairing events in the shear layer. Around re-attachment (X=13.0) most of the energy is contained in the low frequencies. Further downstream ($X \approx 20.0$) there is a peak visible at Str=0.08 (in all three flow cases).

In *the high-frequency forcing case* (see Figure 2b, middle row of spectra) the flow in front of the fence (X X X) is characterized by the forcing frequency and, in addition, by higher levels of energy for all frequencies. After separation (* * * *), the spectra between X=1.0 and X=2.0 only exhibit peaks at the fundamental frequency, $Str = 1.2$, in addition to the peaks at the (sub-harmonic) forcing frequency, $Str = 0.6$. Around and after re-attachment (+ + +) the spectra are quite similar to those of the non-manipulated case.

In *the low-frequency forcing case* (see Figure 2c, bottom row of spectra) all the spectra are dominated by the low-frequency forcing with $Str = 0.08$, and its higher harmonics also contain large amounts of energy. The flow around and

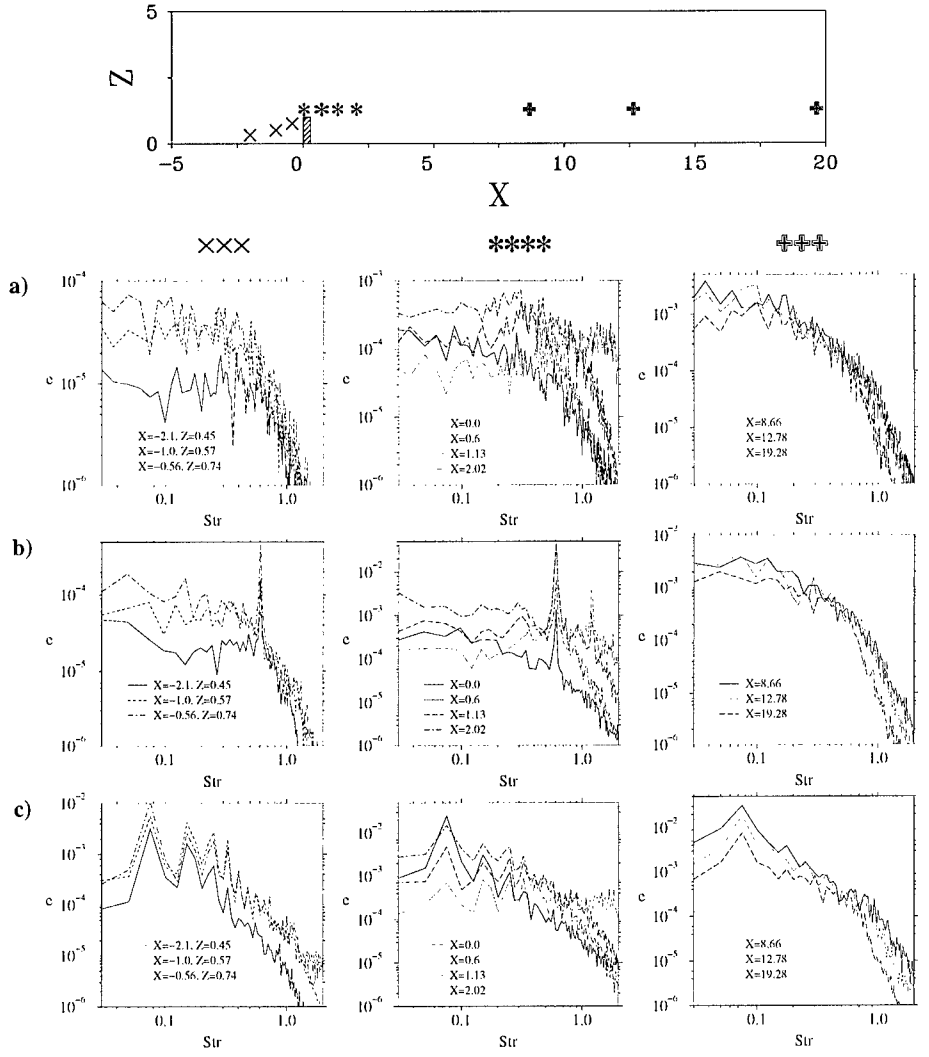


Figure 2: Energy spectra at selected locations in typical flow regions of the non-manipulated case (a), the manipulated cases, Str=0.60 (b) and Str=0.08 (c): left column (XXX): flow region in front of fence, middle column (****): flow region at and after separation (Z=1.287), right column (+++): flow region before, at and after re-attachment (Z=1.287). Note, this figure does not show the total range of Strouhal numbers used in the evaluation of the spectra ($Str_{cutoff} = 12.5$).

after re-attachment is dominated by large structures with a typical frequency $Str = Str_2 = 0.08$. This is also the case in the two other flows but in this case the energy of these structures is significantly amplified. In all three flow cases these large-scale structures leave the separation zone behind the flow obstacle and they are the first dominant structures in the newly developing turbulent boundary layer.

3 Conclusions

Manipulated flow cases were investigated by LES applying time-periodic forcing through a narrow slot upstream of the flow obstacle. High-frequency forcing, with $Str_1 = f_1 h/U_\infty = 0.60$ (the sub-harmonic of the primary roll-up frequency of the separated shear layer), leads to about 10% reduction of the mean re-attachment length. A much stronger reduction of about 36% could be achieved by low-frequency forcing with $Str_2 = f_2 h/U_\infty = 0.08$. In the latter case, large-scale coherent structures are created between the location of the disturbance and the fence, they roll over the flow obstacle (nearly unaffected) and in rolling downstream they still grow in size until they fill out the entire height of the separation zone behind the fence. In agreement with corresponding experiments of Siller and Fernholz [3] for a higher Reynolds number ($Re_h = 10500$) the optimum forcing Strouhal number seems to be related to the low-frequency movement of the entire separation bubble and not to the instability mode of the separating shear layer. More detailed results of this investigation shall be presented in Orellano and Wengle [4].

References

[1] L.W. Sigurdson. The structure and control of a turbulent reattaching flow. *J. Fluid Mech.*, 298:139–165, 1995.

[2] P.S. Larsen. Database on tc-2c and tc-2d fence-on-wall and obstacle-on-wall test cases. Report AFM-ETMA 95-01, ISSN 0590-8809, TU Denmark, 1995.

[3] H.A. Siller and H.H. Fernholz. Control of the separated flow downstream of a two-dimensional fence by low-frequency forcing. *Applied Scientific Research*, 57:309–318, 1997.

[4] A. Orellano and H. Wengle. Numerical simulation (DNS and LES) of manipulated turbulent boundary layer flow over a surface-mounted fence. *Eur.J.Mech. B/Fluids*, accepted for publication in 2000.

Acknowledgments This research was supported by the Deutsche Forschungsgemeinschaft (DFG) under grant number We 705/4+6. We also gratefully acknowledge the support by the Leibniz Computing Center (LRZ) of the Bavarian Academy of Sciences, and by the computing center of the Federal Armed Forces University Munich.

ADVANCES IN TURBULENCE VIII
Proceedings of the Eighth European Turbulence Conference
C. Dopazo et al. (Eds.)
© CIMNE, Barcelona 2000

Experimental investigation of two-point correlations in a separated flow

Lars Sætran and Bård Venås

Department of Mechanics, Thermo- and Fluid Dynamics
Norwegian University of Science and Technology, N-7491 Trondheim, Norway

1 Introduction

We study the flow past a sharp edged surface mounted obstacle with very thin inflow boundary layers, and want to look into the temporal and spatial structure of the flow - including the highly turbulent separated region, where such information is rare. Features under investigation are periodicities in separated flows; a low frequency 'oscillation' have been found [1] in the outer shear layer, and at frequencies much lower than those characterized by the vortex shedding in the separated shear layer. We further wanted to try finding whether, or how, this behavior was linked to large-scale motions in the backflow region. To provide information on spatial relationships in the separation zone one has to resort to multi-point measurements.

2 Experimental details

The experiment was performed in a 1m x 0.5m test section closed return wind tunnel. The triangular shaped model has a height of 100mm measuring 153mm horizontally from leading edge to apex and 113mm from there to the trailing edge (figure 1, see [2] for details). Pulsed hot-wire anemometry was used in regions of the flow containing reverse flow. Conventional constant temperature hot-wire anemometry was used in regions of lower turbulence intensity (turbulence intensities of, say, less than 30%).

3 Correlations

Since the flow is highly inhomogeneous in the x-y-plane, two-point correlations R are presented as functions of both probe positions, (x_1, y_1) and (x_2, y_2), i.e. $R(x_1, y_1, x_2, y_2, \Delta t) = \overline{u(x_1, y_1, t)u(x_2, y_2, t + \Delta t)}$ where overline represents the time mean value. The correlation coefficients Q are normalized in the standard manner, by the fluctuation intensities at both probes. To search for a coupling between the backflow region and the rest of the flow, two-point measurements

were conducted with probe 1 stationary in the position, x/H=6, y/H=0.1. Probe 2 was traversed in a grid comprising of 11 x-positions and 8 y-positions ($y/H = 0.1 - 2.9$ in steps of $\Delta y/H = 0.4$).

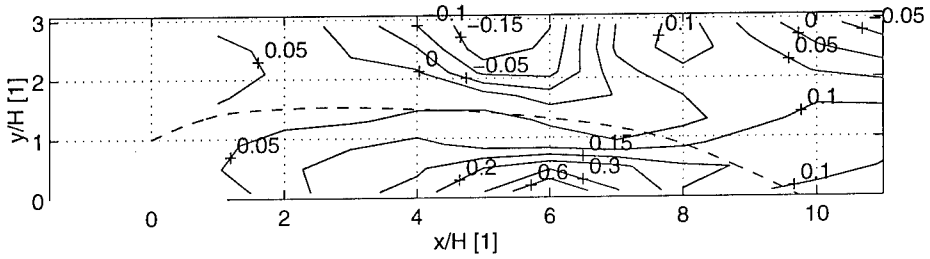


Figure 1: Isocontours for (zero time lag) 2-point correlations.

Figure 2 shows iso-contours of Q for eight different time lags (the lower left figure corresponds to figure 1). Looking at the zero time lag case, one may conclude that the length scale is close to equal to H in the x-direction, and a little less than half this value in the y-direction. This is based on a typically correlation value for the time scale, being $Q \approx 0.3$ for an exponentially decaying correlation. One further notices quite significant negative correlation along the roof; having one center at $x/H \approx 5$ and possibly another somewhere aft of $x/H \approx 11$, with a positive region in-between.

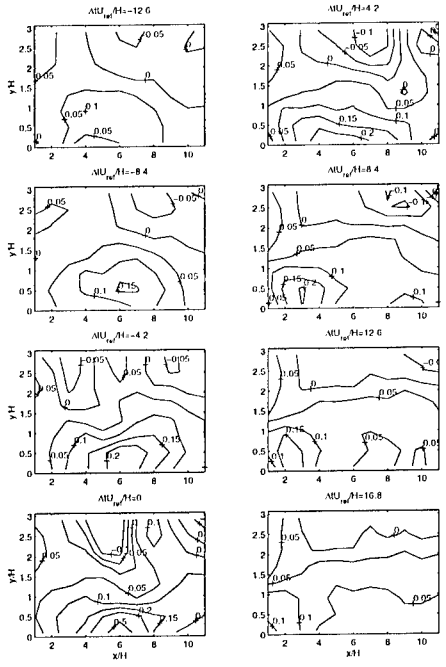


Figure 2: 2-point correlations for different time lags.

The negative correlations indicate that there is a tendency (i.e. in the mean)

for the upper flow to fluctuate in the opposite direction of the flow near the floor. The correlation says nothing about the mechanism behind this, but remembering the normalization - the value of the correlation is quite low compared to the fluctuations in the backflow, but high compared to the fluctuations near the roof. The magnitude of an effect of the outer flow (e.g. the vortex shedding) on the inner flow is rather low. The coupling is very significant for the upper flow. This may be, either or both, correlation between vortices shed in the separation process and the backflow region (strictly speaking: x/H=6, y/H=0.1), or that fluctuations in the backflow perturbs the outer flow.

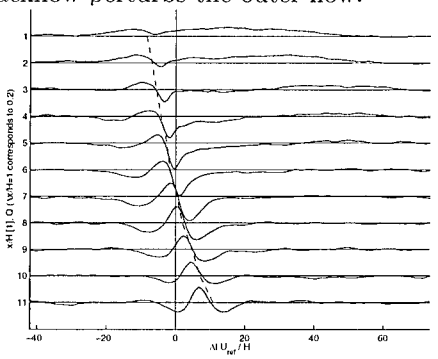


Figure 3: 2-point correlations for measurements along y/H=2.9.

In a 'convective flow' the locus of the correlation should move downstream with the local mean velocity. In the separated flow this can clearly not be seen for negative time lags: the correlation here seems to be quite low in value, widespread, stationary, and centered near the origin (by definition the case for $\Delta t = 0$). For positive time lags a maximum correlation point moves with the mean velocity, that is to say, in the upstream direction. This locus, however, has a low value, meaning that it can not be said to be a convective motion - merely that there is a tendency for structures to move in this direction. Along the roof one can recognize the negative correlation regions mentioned earlier, moving downstream with time. The downstream locus is located above the lower wall probe for the first time lag, and leaves the measuring domain just after $\Delta t = 0$. The second locus first appears at x/H=3 for $\Delta t/H = -4.2$, and moves to the end of the domain during the time span covered in the figure.

A better understanding of this structure can be provided by plotting the cross correlation as function of time, as is done in figure 3 for the points along y/H=2.9. One can here see very large scale correlations at the forward-most measuring stations, which are the same as the constant '0.05' iso-contour in this region in figure 2. From x/H=1, and all the way downstream, a dip is found in the correlation, which grows somewhat larger and moves along the time axis for downstream measurements. The dashed line in the figure corresponds to a convection velocity 0.6 times the local mean velocity.

The fact that the vortices, and the convection of them, are identified by two-point measurements means that the same vortex system influences both the

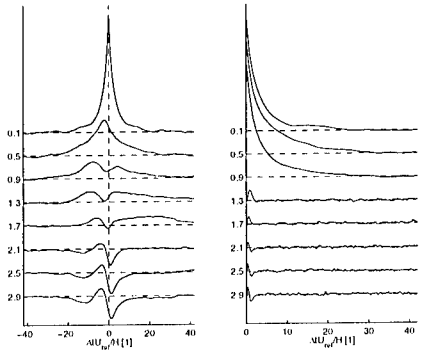


Figure 4: Left: 2-point correlations along x/H=6. Right: autocorrelations.

fluctuations along the roof and the backflow. The oscillations in the outer flow show periodicity based on one-point measurements [2]. However, oscillations are not identified from one-point measurements in the backflow, probably since the effect is small compared to the general fluctuation level here. This can be studied more closely in figure 4, where two-point and auto correlations are plotted beside each other, along x/H=6. The oscillations are visible from y/H=0.9 in the two-point correlation, but not for the lower positions. It seems as that the correlation is a summation of a general exponentially decaying fluctuation, and a (wave-like) oscillation. In the auto correlations oscillations are seen only for the highest y-positions, while correlations at large time scales are found in both types of measurements. It is noticed that the large-scale fluctuations at this x-position are comparable with the oscillations, i.e. in frequency. This oscillation frequency, found towards the reattachment position is close to values reported from other separated flows, e.g. (Driver et al. [3]) and (Cherry et al. [4]), reporting values of ca. 0.06-0.07.

4 Conclusions

Oscillations (partially periodic) and large time scale fluctuations (non-periodic) have been identified from one- and two-point measurements. Vortices shed in the separation process are found to influence the whole flow downstream. The mechanisms behind the large scale fluctuations may be linked to a coupling with the oscillations in the latter part of the separation zone (comparable in frequency) or perturbation from fluctuations in the separated flow zone (comparable in time scale).

5 REFERENCES

[1] Heist, DK, and Gouldin, FC, JFM, **331**, 107-125, (1977)
[2] Venås, B, and Sætran, LR, Proc. TSFP1 (eds. S. Banerjee and J. Eaton), pp 1149-1154, ISBN 1-56700-135-1, (1999)
[3] Driver, D, Seegmiller, H, and Marvin, J, AIAA J, **25**, 7, 914-919, (1987)
[4] Cherry, NJ, Hillier, R, and Latour, MEMP, JFM, **144**, 13-46, (1984)

ADVANCES IN TURBULENCE VIII
Proceedings of the Eighth European Turbulence Conference
C. Dopazo et al. (Eds.)
© CIMNE, Barcelona 2000

Study of a turbulent separated flow using HPIV

K. von Ellenrieder, J. Kostas, and J. Soria

Mechanical Engineering, Monash University
Melbourne, Victoria, AUSTRALIA

Contact e-mail: karl.ellenrieder@eng.monash.edu.au

1 Introduction

In this work, a lens-less, off-axis, HPIV system is employed to study the flow at the leading-edge of a flat plate. Multiple two dimensional velocity maps within a three dimensional region of interest (at a single instant in time) are presented. The out of plane vorticity is extracted from the velocity fields. Owing to the small effective aperture of the holographic image it is not possible to measure the third component of velocity using a stereoscopic scanner. The limitations of the stereoscopic scanning method for HPIV and some potential solutions are discussed.

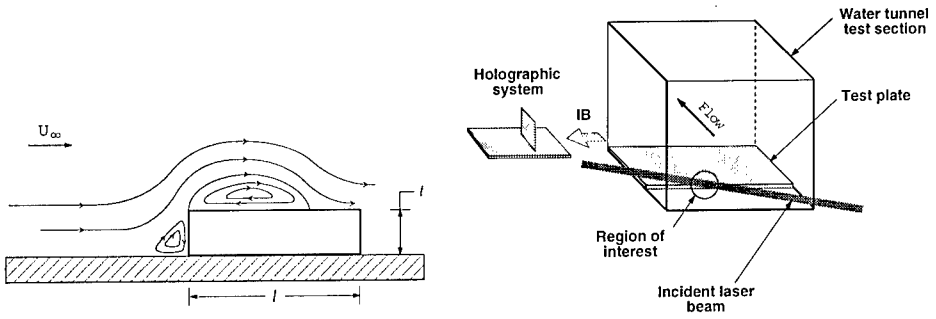
2 Experimental Apparatus and Technique

2.1 Flow facility and seed particles

The experiments were conducted on the flow through a 500mm × 375mm × 5m test section of a closed-circuit, horizontal water tunnel. A perspex test plate spanned the test section, was mounted on the tunnel floor, and had a chord-to-thickness ratio of $l/t = 4.5$ (figure 1a). A Reynolds number of $Re_t \approx 1650$, based on test plate thickness and freestream velocity, was used.

2.2 Holographic Technique

The details of the holographic recording and reconstruction technique are presented in von Ellenrieder et al. (1999). A cylindrical volume of fluid, 25 mm in diameter, was illuminated with a laser beam set at approximately 21° to the normal axis of the hologram plate (figure 1b). The laser beam was aligned so that it was parallel to the top surface of the test plate and intersected the leading-edge 160 mm from the side of the test section. The plane of the hologram plate was located 335 mm from the region of interest.



(a) (b)

Figure 1: (a) Flow configuration, (b) experimental setup.

Two holograms were recorded, at separate times, on a single film plate by using two independent reference beams. The virtual image of each hologram was reconstructed and a set of several cross-correlation image pairs were digitised using a CCD camera. The resulting data was analysed with a multigrid cross-correlation algorithm (Soria et al. 1999) to find the velocity in multiple 2D planes. The vorticity corresponding to each plane was extracted from the velocity data with a 13 point χ^2 vorticity calculation method.

3 Results

Regions of reversed flow are clearly visible in the vector plots (figure 2). The separating shear layer appears as a concentrated band of vorticity extending from the separation point. Since the incident laser beam was not parallel with the leading edge of the plate (figure 1b) every successive slice in the cross stream direction is further from the separation point than the previous one.

4 Stereoscopic Scanning

The error analysis of Lawson & Wu (1998) for stereoscopic systems reveals that the optimum angle of a stereoscopic system is 20°– 30° depending on the magnification, f-stop and lens size of the cameras.

For a system such as the one shown in figure 3 the scanning angle ϕ_3 differs slightly from the camera angle ϕ_1 because the light rays leaving the region of interest traverse media with different indices of refraction. The size of the reference beam spot on the hologram minus the size of a camera lens (figure 3) is the effective aperture of the hologram. The maximum ϕ_1 for such a system is the inverse tangent of the ratio of 1/2 the maximum aperture to the effective distance (refractive index varies) from the region of interest to the film plate.

For the conditions in our flat plate experiment, when $\phi_3 = 20°$, $\phi_1 = 27°$. If cameras with a 55 mm focal length lens set to $f\# = 2.8$ are used, the maximum

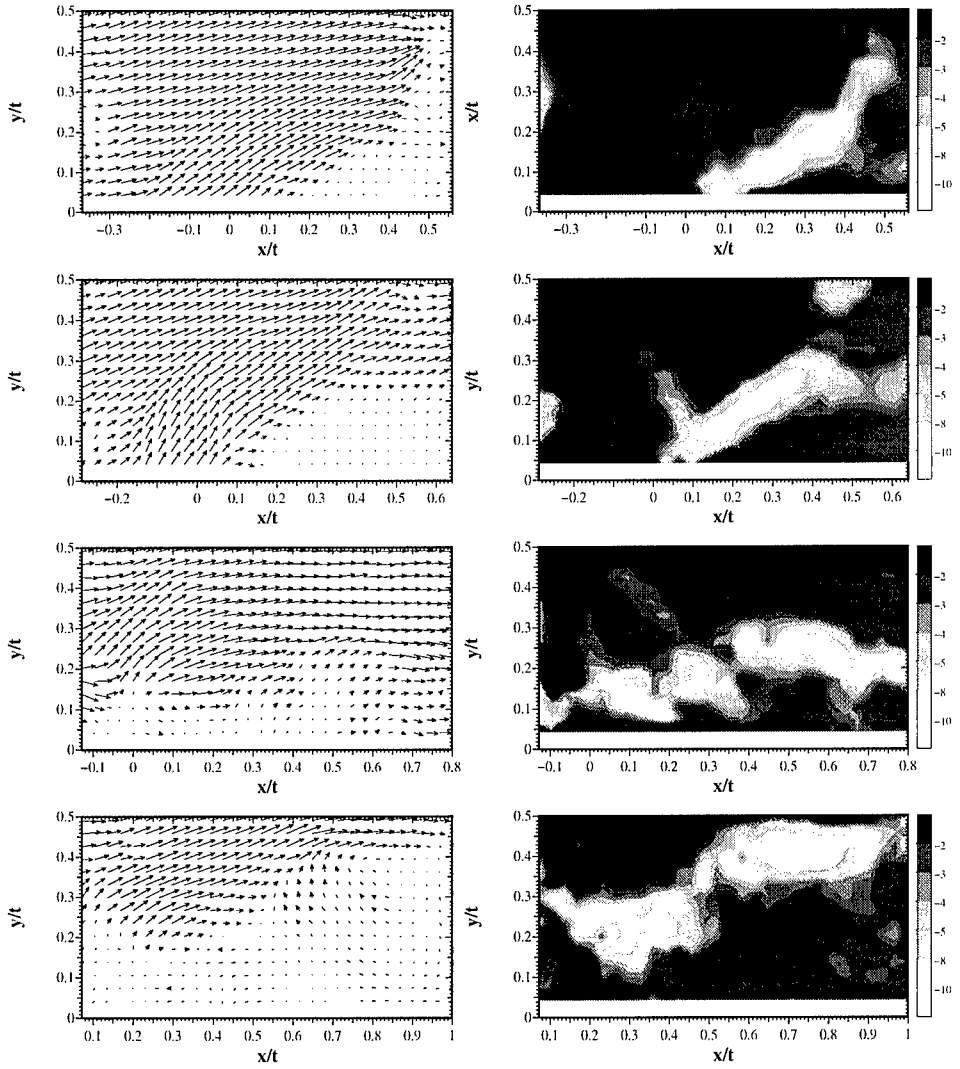


Figure 2: Instantaneous velocity (left column) and corresponding vorticity (right column) fields within the region of interest; raw data is shown with velocity in units of m s^{-1} and vorticity in s^{-1}. Coordinates are scaled by the test plate thickness t, x is the distance from leading edge of the plate, and y is the height above its surface — the leading-edge of the plate is located at $(x/t, y/t) = (0, 0)$. The top-to-bottom sequence of images shows successive slices of the flow spaced 10mm apart in the cross stream direction.

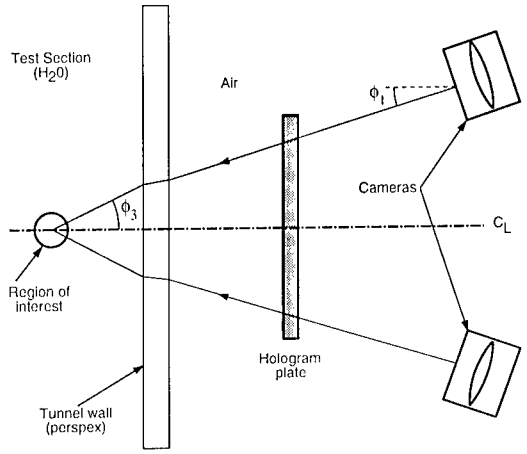


Figure 3: Stereoscopic scanning.

ϕ_1 attainable is 3°. Hence, stereoscopic scanning of our holograms is not feasible. Possible ways of circumventing this difficulty include scanning the hologram in three dimensions and applying a 3D cross-correlation technique to determine the spanwise velocity or to restrict the use of the method to flow regions very near the hologram plate.

5 Concluding Remarks

The use of HPIV coupled with stereoscopic scanning to image flows in large test sections is complicated by the effective aperture of the holographic image. However, the method still enables one to simultaneously acquire several 2D slices of a flow's velocity and vorticity fields.

References

[1] N. J. Lawson & J. Wu. Three-dimensional particle image velocimetry: error analysis of stereoscopic techniques. *Meas. Sci. Technol.*, 8:894–900, 1997.

[2] J. Soria, J. Cater, & J. Kostas. High resolution multigrid cross-correlation digital PIV measurements of a turbulent starting jet using half frame image shift film recording. *Optics & Laser Technology*, 31:3–12, 1999.

[3] K. von Ellenrieder, J. Kostas, & J. Soria. Holographic PIV measurements of the flow over the blunt leading-edge of a flat plate. 2^{nd} *Australian Conference on Laser Diagnostics in Fluid Mechanics and Combustion*, Melbourne, Australia, 1999.

ADVANCES IN TURBULENCE VIII
Proceedings of the Eighth European Turbulence Conference
C. Dopazo et al. (Eds.)
© CIMNE, Barcelona 2000

Recovery of a turbulent boundary layer behind a swept, rearward-facing step

Hans-J. Kaltenbach

Hermann-Föttinger-Institut für Strömungsmechanik,
Technische Universität Berlin, Sekr. HF 1, D-10623 Berlin

Background

By means of direct numerical simulation the development of an initially laminar shear layer behind a swept, backward facing step has been studied. Transition occurs prior to reattachment. The sweep angle α defined in Fig. 1 is varied between 0° and 60°, resulting in a three-dimensional mean flow with a maximum cross-flow $\mathcal{O}(0.4C_\infty)$ ahead of the reattachment region. Here, C_∞ denotes the edge-velocity of the boundary layer of thickness $\delta_{99}/H \approx 0.2$ at the step.

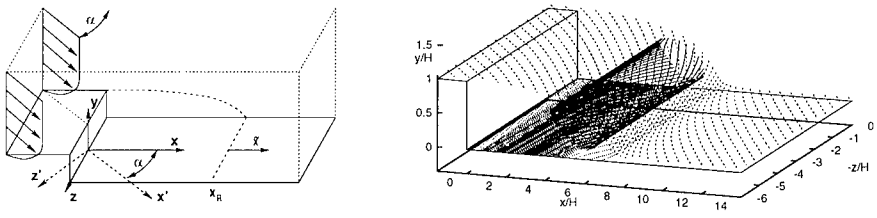


Figure 1: **Left:** Sketch of the configuration and definition of coordinate systems. Results for different sweep angles α will be compared at the same distance $\widetilde{x} = (x - x_R)/H$ from the reattachment location. **Right:** Streamlines along the wall, near the surface defining the separated flow, and in the recirculation zone.

Results were obtained with a finite-difference code of second order spatial accuracy with staggered variable configuration on a rectangular domain with dimensions $L_x \times L_y \times L_z = 21.5H \times 12H \times 6H$ using a non-equidistant mesh with $560 \times 128 \times 128$ cells. The adequacy of the resolution was confirmed by grid refinement and examination of spectra [2].

Up to sweep angles of 40° the influence of sweep on shear layer transition and reattachment length $x_R = \mathcal{O}(6H)$ is weak [3]. For higher sweep angles an upstream shift of the transition location is observed, resulting in a reduction of x_R by more than 40% for $\alpha = 60°$ when compared to the planar case.

In this contribution, we focus on the boundary layer development downstream of the reattachment location. The "recovery" towards a canonical 2D

boundary layer is twofold since the upstream flow history includes both three-dimensionality and separation. Results are from a simulation series where the Reynolds number based on the step height and C_∞ were kept constant at $Re_\infty = HC_\infty/\nu = 3000$. At the domain inlet located at $x/H = -1.5$, isotropic freestream disturbances of magnitude $u' = 0.0011/C_\infty$ were superimposed onto steady profiles derived from measurements of [8].

Results

In Figs. 2 and 3 results are scaled based on wall variables. Downstream of $\widetilde{x} = 3.6$, the skewing of the mean flow profile is weak and the flow develops gradually in a 2D boundary layer. Near reattachment, the direction of the mean flow vector (U, W), of the shear vector $(dU/dy, dW/dy)$, and of the shear stress vector $(-\overline{uv}, -\overline{vw})$ differ considerably across the shear layer. However, very close to the wall the misalignment is small. Therefore, the rms-value with respect to the direction of the wall-streamline normalized with u_τ can serve as an indicator to what degree the characteristic process of near-wall turbulence generation [1] has been established.

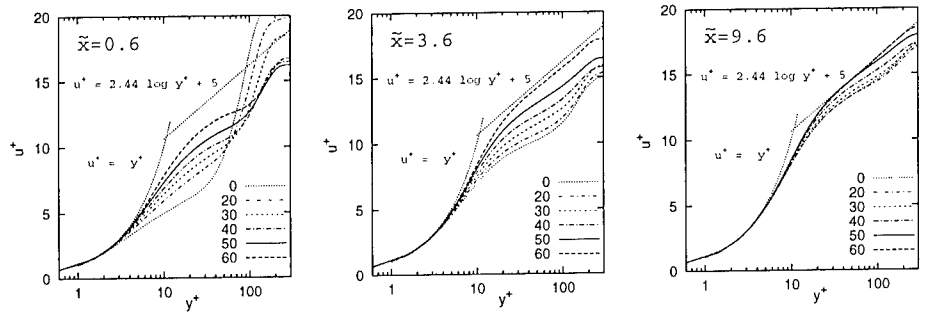


Figure 2: Magnitude of mean flow $(\sqrt{U^2 + W^2})/u_\tau$ versus yu_τ/ν at locations $\widetilde{x} = 0.6, 3.6$ and 9.6 downstream of reattachment.

For the same step-normal distance $\widetilde{x}$ from the reattachment location, both mean flow and rms-profiles indicate that recovery of the flow towards a canonical boundary layer proceeds faster with increasing sweep angle. This corroborates results of [7] for flow of a turbulent boundary layer over a swept step. The apparently good agreement of the normalized rms-value at $\widetilde{x} = 3.6$ for different sweep angles is deceiving since the characteristic peak value $u'/u_\tau \approx 2.8$ has not yen been established at this station. As in [6] we observe a strong under-prediction of the log-law intercept close to the reattachment location.

Part of the earlier recovery might be contributed to the fact that for the same location $\widetilde{x}$ the development length of the boundary layer grows approximately with $1/\cos\alpha$ with increasing sweep angle. However, close examination of the near-wall region reveals substantial differences among individual cases even

upstream of reattachment.

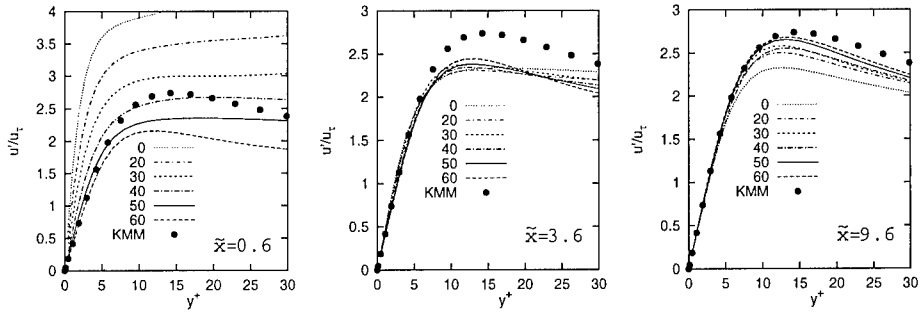


Figure 3: Rms of the velocity fluctuation corresponding to the direction of the wall-streamline scaled in wall variables. Symbols denote channel flow results from [4].

Near reattachment, the velocity-pressure gradient $\Pi_{ii} = -\overline{u_i' \frac{\partial p'}{\partial x_i}}$ is a source term in the budget of the kinetic energy (TKE) $q^2/2 = 0.5(\overline{u'^2 + v'^2 + w'^2})$. It scales approximately with U_∞^3/H rather than C_∞^3/H, see Fig. 4. A similar scaling is observed for pressure and skin-friction fluctuations [2, 3]. For small sweep angles, shear-production $P_i = -\overline{u_i' u_j'} \frac{\partial U_i}{\partial x_j}$ is small in the vicinity of $x = x_R$, but it becomes the dominant source term for cases with high sweep angles. The relative magnitude of other terms such as convection, dissipation, turbulent and molecular diffusion of TKE does not change much with sweep angle. Thus, the observed acceleration of boundary layer recovery with increasing α is related to the step-parallel mean flow component $W(y)$ which provides the mean shear necessary for establishing the autonomous cyscle of near-wall turbulence generation [1].

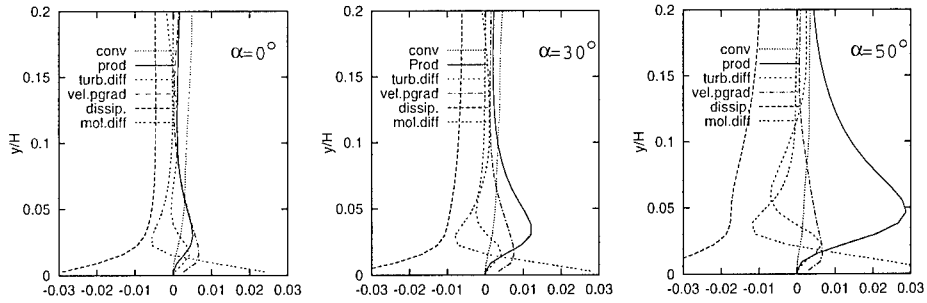


Figure 4: Balance of turbulent kinetic energy normalized by $(C_\infty \cos\alpha)^3/H$ for $\alpha = 0°, 30°, 50°$ at the location $\widetilde{x} = 1.6$.

For high sweep angles we observe a characteristic streaky pattern in the wall-streamline direction throughout the reattachment region [2]. It turns out that the dimensionless shear parameter $\sqrt{(dU/dy)^2 + (dW/dy)^2}(q^2/\epsilon)$ is not a useful

criterion for prediction of streaks in this situation. However, the alternate shear parameter proposed by [5] may be generalized as

$$S = \frac{|\overline{uv}\frac{\partial U}{\partial y} + \overline{vw}\frac{\partial W}{\partial y}|}{\epsilon}$$

to make it applicable for 3D flows. Streaks are observed when the maximum of this parameter in the near wall region is close to one.

Profiles of the second invariant II of the Reynolds stress anisotropy tensor $b_{ij} = \overline{u_i' u_j'}/q^2 - \delta_{ij}/3$ are found to be another useful indicator for the state of recovery in the near-wall region. For high sweep angles, profiles of $II(y)$ exhibit a characteristic peak *off* the wall even ahead of reattachment whereas the peak occurs *at* the wall for sweep angles below $\alpha = 40°$, see Fig. 5.

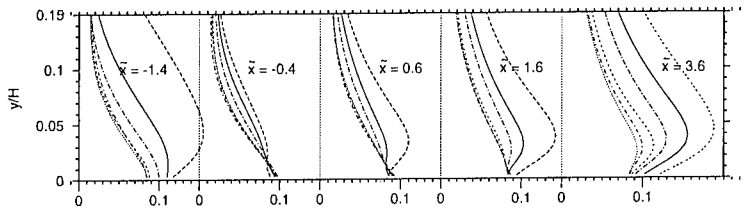


Figure 5: Profiles of the second invariant of the Reynolds stress anisotropy tensor at selected locations near reattachment. Line coding as in Fig. 2.

Acknowledgments: Part of this work was funded by DFG within Sfb 557. Computing time on the CRAY T3E-1200 was provided by the Konrad-Zuse-Zentrum Berlin.

References

[1] J. Jimenez, and A. Pinelli. The autonomous cycle of near-wall turbulence. *J. Fluid Mech.* 389: 335-359, 1999.

[2] H.-J. Kaltenbach. Direct numerical simulation of flow over a swept rearward-facing step. In: P.R. Voke, N.D. Sandham, L. Kleiser (eds.) *Direct and Large-Eddy Simulation III.* Kluwer Acad. Publ., 393-404, 1999.

[3] H.-J. Kaltenbach, and G. Janke. Direct numerical simulation of flow separation behind a swept, rearward facing step at $Re_H = 3000$. *submitted to Phys. Fluids*

[4] J. Kim, P. Moin, and R. Moser. Turbulence statistics in fully developed channel flow at low Reynolds number. *J. Fluid Mech.* 177: 133–166, 1997.

[5] K. Lam, and S. Banerjee. On the condition of streak formation in a bounded turbulent flow. *Phys. Fluids* A4: 306–320, 1992.

[6] H. Le, P. Moin, and J. Kim. Direct numerical simulation of turbulent flow over a backward-facing step. *J. Fluid Mech.* 330: 349–374, 1997.

[7] D. J. Weber, and J. E. Danberg. Correlation of mean velocity measurements downstream of a swept backward-facing step. *AIAA J.*, 30:2701–2706, 1992.

[8] H. Wengle, G. Bärwolff, G. Janke, and A. Huppertz. The manipulated transitional backward-facing step flow: an experimental and direct numerical simulation investigation. *submitted to EJM B/Fluids.*

ADVANCES IN TURBULENCE VIII
Proceedings of the Eighth European Turbulence Conference
C. Dopazo et al. (Eds.)
© CIMNE, Barcelona 2000

Karhunen–Loève expansion (POD) of the flow behind a swept, rearward-facing step

Werner Jürgens and Hans–Jakob Kaltenbach

Hermann-Föttinger-Institut für Strömungsmechanik,
Sekretariat HF 1, Technische Universität Berlin, D-10623 Berlin, Germany

Contact e-mail: juergens@pi.tu-berlin.de

1 Background

Our goal is to analyse the dominating dynamic structures of the separating flow behind a swept, backward-facing step using the Karhunen–Loève expansion (proper orthogonal decomposition; see for example [1]) of velocity fields. A database was generated by direct numerical simulation for sweep angles α between 0° (planar case) and 60° [3]. The Reynolds number based on the step height H and the step-normal component $C_{\max}\cos\alpha$ of the incoming flow is kept constant at $\mathrm{Re}_\alpha = H(C_{\max}\cos\alpha)/\nu = 3180$, ($C_{\max} := \max_y\{\sqrt{U^2(y)+W^2(y)}\}$ at $x = -0.05H$). The inflow consists of a laminar boundary layer with a thickness of $\delta_{99}/H = 0.195$.

The computational domain is: $x \in [-1.5H, 20H]$ (step-normal), $y \in [0, 11.9H]$ (wall-normal), and $z \in [0, 6H = L_z]$ (spanwise). The step is located at $x = 0$. The numerical scheme consists of a finite-difference, incompressible NS solver of second order spatial accuracy with staggered variable configuration on a non-equidistant mesh with $560 \times 128 \times 128$ cells. In order to reduce the size of the Karhunen–Loève (KL) problem, the results are filtered onto the cell centers of a mesh, which is coarser by a factor 2 in x and y. In addition, the spatial domain is reduced to $x \in [0.1H, 19.4H]$, $y \in [0, 2.7H]$. This yields 256×52 points in the x-y-plane.

Because of the spanwise homogeneity of the flow, a KL expansion will result in eigenfunctions of the form $\hat{\phi}_j^{k_z}(x,y)\exp(2\pi i k_z z/L_z)$, ($k_z \in \mathbb{N}_0$, $j = x, y, z$). Thus, the velocity fields were Fourier transformed in the spanwise direction prior to the KL decomposition. The fields have been sampled every 15 time steps of the simulation, which yields a sampling rate of $\Delta t = 0.27H/C_{\max}$.

2 Energy spectra

Fig. 1 displays the energy spectra for the $\alpha = 0°$ case and for the sweep angle $\alpha = 40°$. The database consists of 1325 time samples for the 0° case, and 1000 time samples for the 40° case.

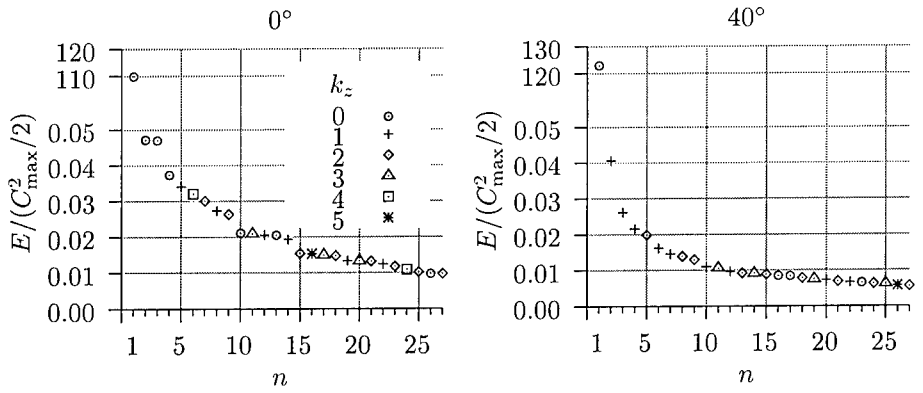


Figure 1: Spectra of kinetic energy $E = 0.5 \iiint \phi_j^{(n)} \phi_j^{(n)} \, dx \, dy \, dz$ of eigenfunctions for sweep angles $\alpha = 0°$ and 40°.

We did not subtract the mean flow prior to the KL expansion. Hence, a strong first eigenfunction appears in the mode $k_z = 0$, which is approximately equal to the mean flow. Neglecting this eigenfunction, the next 6 functions represent approximately 10% of the energy present in the functions $n > 1$. This holds for both cases. Up to $n = 31$, the eigenfunctions contain 28% of the energy (0°), respectively 23% (40°).

In the 0° case, the second and third eigenfunction have almost identical energy, and are part of the mode $k_z = 0$. Their velocity components are sinusoidal in the streamwise direction with a phase shift of 90° between the two eigenfunctions. The same applies to their temporal coefficients, such that the combination of the two eigenfunctions represents a structure which travels downstream. In the 40° case, the second most energetic eigenfunction appears for $k_z = 1$. Being a complex eigenfunction, its complex temporal coefficient determines its amplitude and phase. The phase corresponds to its spanwise location. Thus, moving structures can be represented by a single complex eigenfunction.

3 Eigenfunctions

Fig. 2 shows the second most energetic mode of the KL expansion for 40° sweep angle. Vortices appear which get amplified up to $x = 5H$. They originate in the skewed shear layer which forms behind the step. Although other eigenfunctions with relevant velocity magnitudes in that region exist, we analyse to what degree the displayed eigenfunction represents the shear layer instability.

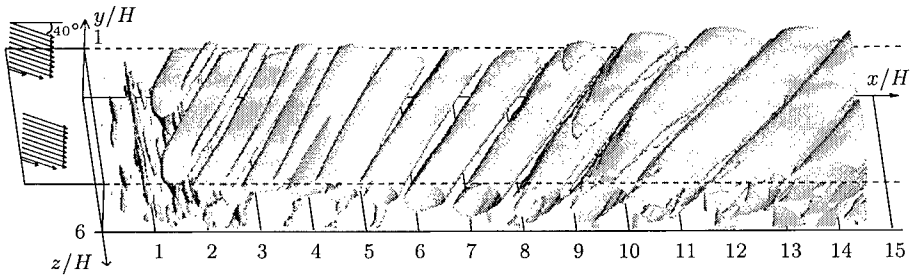


Figure 2: The second most energetic KL mode of the 40° sweep case is represented by the isosurface $Q = 10^{-7}(C_{\max}/H)^2$ of the second invariant Q of its velocity gradient tensor.

Because of the homogeneity along the spanwise axis, spatial amplification is restricted to the x-direction. The displayed instability wave exhibits exponential growth in the region $1 < x/H < 4$, $y \approx 1H$. From the x-wise growth of the amplitudes $|\hat{\phi}_j(x,y)|$, we derive a spatial amplification rate of $-\alpha_i = 2.5/H$. Free shear layers exhibit a maximum amplification rate $-\alpha_i\theta/R \approx 0.10$ (θ: momentum thickness, R: velocity ratio) over a range of velocity ratios [2]. The linear stability analysis of [5] showed, that the amplification rate $-\alpha_i$ scales with the *effective* velocity ratio R_{eff} in the case of skewed mean profiles. This yields in our case a range of $-\alpha_i\theta/R_{\text{eff}} = 0.084$ ($x/H = 1$) up to 0.15 ($x/H = 4$), see [4].

In the region $1.5 < x/H < 3.5$, $y \approx 1H$, the velocity components of the eigenfunction behave like planar waves travelling in a direction which forms an angle of 17° with the step-normal. According to [5], the most amplified wave travels in the direction of the *effective shear*. This angle is found to vary between 26° ($x/H = 1.5$) and 20° ($x/H = 3.5$) for the present case.

The complex temporal coefficient of the displayed eigenfunction exhibits a phase progression which is linear in time. The corresponding frequency yields a Strouhal number based on the momentum thickness of $\text{St} = f\theta/U_{c,x} = 0.032$ at $x/H = 1$. Here, the x-component $U_{c,x}$ of the mean convection velocity vector $\mathbf{U}_c$ is used, because spatial amplification is restricted to the x-direction. At the end of the exponential growth ($x/H = 4$), the Strouhal number reaches $\text{St} = 0.059$. For parallel, planar flows, the Strouhal number of the most amplified wave is known to be $\text{St} = f\theta/U_c = 0.032$, see [2].

The results indicate that the displayed eigenfunction is related to the shear layer instability. The quantitative agreement of instability properties with *parallel* shear flows is quite good, if the shear layer parameters are computed at the beginning of the exponential growth.

In the turbulent boundary layer downstream of the reattachment location, the relationship between eigenfunctions and physical processes is more complicated [6]. Fig. 3 shows the third most energetic mode of the KL expansion, which is strong downstream of the reattachment location ($x_r = 6.8H$ for 40°). Its phase speed in the z-direction $c_{\mathbf{e}_z} = \omega/(2\pi k_z/L_z) = -0.090C_{\max}$ differs strongly from

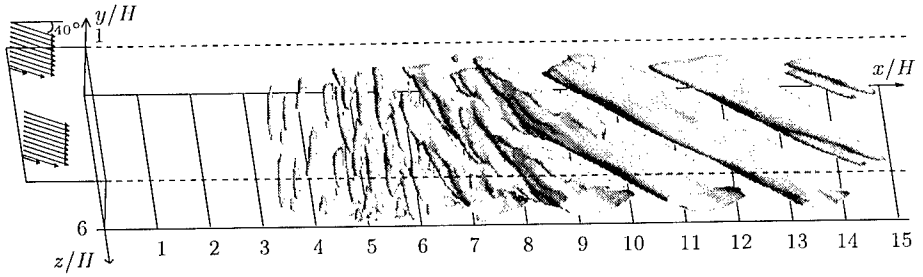


Figure 3: The third most energetic KL mode of the 40° sweep case is represented by the isosurface $Q = 5 \cdot 10^{-4}(C_{\max}/H)^2$ of the second invariant Q of its velocity gradient tensor.

the value $c_{\mathbf{e}_z} = 1.8C_{\max}$ of the second eigenfunction. Other eigenfunctions exist which exhibit structures with different orientation and propagation velocity. They all contribute comparable energy to the region downstream of reattachment.

Acknowledgements: This work was supported by the German Research Council (DFG) in the scope of the research program Sfb 557 of the TU Berlin. Computing time was provided by the Konrad Zuse Center Berlin (ZIB).

References

[1] G. Berkooz, P. Holmes, and J. L. Lumley. The proper orthogonal decomposition in the analysis of turbulent flows. *Ann. Rev. of Fluid Mech.*, 25:539–575, 1993.

[2] C.-M. Ho and P. Huerre. Perturbed free shear layers. *Ann. Rev. of Fluid Mech.*, 16:365–424, 1984.

[3] H.-J. Kaltenbach. Direct numerical simulation of flow over a swept rearward-facing step. In P. R. Voke, N. D. Sandham, and L. Kleiser, eds., *Direct and Large-Eddy Simulation III*, 393–404. ERCOFTAC Series, Kluwer Acad. Publ., 1999.

[4] H.-J. Kaltenbach and G. Janke. Direct numerical simulation of flow separation behind a swept, rearward facing step at $\mathrm{Re}_H = 3000$. *submitted.*

[5] G. Lu and S. K. Lele. Inviscid instability of a skewed compressible mixing layer. *J. of Fluid Mech.*, 249:441–463, 1993.

[6] L. Sirovich, K. S. Ball, and L. R. Keefe. Plane waves and structures in turbulent channel flow. *Phys. Fluids A*, 2(12):2217–2226, 1990.

ADVANCES IN TURBULENCE VIII
Proceedings of the Eighth European Turbulence Conference
C. Dopazo et al. (Eds.)
© CIMNE, Barcelona 2000

Unilateral-Average Based Study of Incompressible Turbulent Mean Flow and Coherent Flow*

Ge Gao[1] and Yan Yong[2]

[1]Beijing University of Aeronautics and Astronautics, China
[2]Florida Atlantic University, USA

1 Introduction

This paper presents a new set of equations of incompressible turbulent flow for both statistical mean flow and intermittent coherent flows. Unlike the traditional approach, the statistical average is only taken on one group of turbulent fluctuations. This nonzero average provides valuable first-order statistical information of the fluctuation field and gives rise to additional conditions much needed for solving the closure problem.

2 Analysis

For a large Reynold's number, the nonlinearity of N-S equations usually leads to infinite number of solutions for a set of given initial conditions. Let u_i be one of the random samples in the solution space. The corresponding fluctuating velocity is defined as $u_i' = u_i - \bar{u}$. The mean velocity is obtained from the following ensemble average

$$\bar{u} = \lim_{N\to\infty} \frac{1}{N} \sum_{i=1}^{N} u_i \tag{1}$$

in which N is the number of possible solutions of Navier-Stokes equations. Now, we divide the solutions into two groups according to the projections of their fluctuation components onto the mean flow direction. Those solutions with fluctuations having positive projections are belonging to the first group, or the forward group. The remaining solutions are belonging to the second group, called the backward group. The fluctuation components in these two groups are denoted by u_i^F and u_i^B. The ensemble averages of these fluctuations

$$\bar{u}^F = \lim_{N_F\to\infty} \frac{1}{N_F} \sum_{i=1}^{N_F} u_i^F, \; \bar{u}^B = \lim_{N_B\to\infty} \frac{1}{N_B} \sum_{i=1}^{N_B} u_i^B \tag{2}$$

*The two authors of this paper have made equal contributions to this work.

are called forward and backward drift velocities, respectively. N_F and N_B are the numbers of solutions in each group. It is important to point out that the unilateral averages given in Eq. 2 are both nonzero. As the ensemble average of all fluctuations is zero, we can prove that $M_F\bar{u}^F + M_B\bar{u}^B = 0$, in which $M_F(x,t) = N_F/N$ and $M_B(x,t) = N_B/N$ are weighting functions of drift flows. Although the two drift flows are not symmetric, their weighted values $\tilde{u}^F = M_F\bar{u}^F$ and $\tilde{u}^B = M_B\bar{u}^B$ are symmetric. So are their weighted average pressures $\tilde{p}^F$ and $\tilde{p}^B$. As a result, only one weighted drift flow (in short, drift flow), say $\tilde{u}^F$, is needed for the present analysis. It can be proved that the Reynolds averaged N-S equation and the unilateral averaged N-S equation are

$$\frac{D\bar{u}}{Dt} = -\frac{1}{\rho}\nabla\bar{p} + \nu_L\nabla^2\bar{u} - \overline{(u'\cdot\nabla)u'} \tag{3}$$

$$\frac{D\tilde{u}^F}{Dt} = -\frac{1}{\rho}\nabla\tilde{p}^F + \nu_L\nabla^2\tilde{u}^F - (\tilde{u}^F\cdot\nabla)\bar{u} + M_F\overline{(u'\cdot\nabla)u'} - M_F\overline{(u^F\cdot\nabla)u^F} \tag{4}$$

As usual, we name $\overline{(u'\cdot\nabla)u'} = -\nabla\cdot\bar{\tau}_T$. The momentum equation of the mean flow is, therefore, written as

$$\frac{D\bar{u}}{Dt} = -\frac{1}{\rho}\nabla\bar{p} + \nu_L\nabla^2\bar{u} + \nabla\cdot\bar{\tau}_T \tag{5}$$

We now model correlation term

$$M_F\overline{(u^F\cdot\nabla)u^F} = \nu_L\nabla^2\bar{u} + M_B\nabla\cdot\bar{\tau}_T - \nabla\cdot\tilde{\tau}_T^F \tag{6}$$

such that the momentum equation of the forward drift flow can be written as

$$\frac{D\tilde{u}^F}{Dt} = -\frac{1}{\rho}\nabla\tilde{p}^F + \nu_L\nabla^2(\tilde{u}^F - \bar{u}) + \nabla\cdot(\tilde{\tau}_T^F - \bar{\tau}_T) - (\tilde{u}^F\cdot\nabla)\bar{u} \tag{7}$$

The rationale behind the modeling equation 6 can be depicted by Eq. 5 and Eq. 7 as a momentum transfer chain [1]. Eq. 5 and Eq. 7 together with $\nabla\cdot\bar{u} = 0$ and $\nabla\cdot\tilde{u}^F = 0$ constitute equations of incompressible turbulent flows.

It is reasonable to argue that the fluctuation field constitutes an orthotropic environment for the mean flow. The corresponding material principal axes are tangent and normal to the mean streamline, respectively. Such a flow appears to be anisotropic because 21 constitutive coefficients (6 for two-dimensional flow) vary with coordinates. When stresses and strains are expressed in the material principal coordinate system, only 6 constitutive coefficients (3 for two-dimensional flow) are nonzero. In the two-dimensional case, for instance, one can construct eddy viscosity coefficients in the material principal coordinate system using mean drift displacement l, such that $\sigma_1^T = \tilde{u}_1^F l_1\epsilon_1^T$, $\sigma_2^T = \tilde{u}_2^F l_2\epsilon_1^T$, $\tau_{12}^T = \epsilon_{12}^T(\tilde{u}_1^F l_2 + \tilde{u}_2^F l_1)/2$. To determine the mean drift displacement l, we consider the difference of kinetic energies at two

locations x and $x+l$, $\Delta T = [\bar{x}(x+l) + \tilde{u}_F(x+l)]^2/2 - [\bar{u}(x) + \tilde{u}_F(x)]/2$. Expanding ΔT into a Tayler's series and using the principle of work and energy, we obtain the following energy equation:

$$\frac{1}{2}\sum_{j=1}^{J}\frac{1}{j!}(l\cdot\nabla)^j(\bar{u}+\tilde{u}^F)^2 = l\cdot[-\frac{1}{\rho}\nabla(\bar{p}+\tilde{p}) + \nu_L\nabla^2\tilde{u}^F + \nabla\cdot\tilde{\tau}_T^F - (\tilde{u}^F\cdot\nabla)\bar{u}] \quad (8)$$

The right hand of the above equation is the work done by the force applied to the drift flow that undergoes displacement l. With the assumption that the mean drift displacement always points to the direction of the maximum stress of the mean flow, we can solve the above equation for $|l|$. Integer J represents a coherent flow up to J-th level of structure.

3 Discussions

In order to verify the merit of the derived equations, we consider two benchmark flows, namely, boundary layer flow (transition flow on flat plate) and separation flow (backward-facing step). Figure 1 shows a simulated flat-plate boundary layer (solid curve) and velocity profiles (broken curves). The velocity distribution at the inlet has a laminar profile. Transition takes place at the location where $Re = 3.8 \times 10^5$. A fully developed turbulence profile is compared with experimental data [2] in Figure 2. Figure 3 show the mean flow pattern of the backward-facing step. It was obtained by using a second-order Taylor's series in the energy equation. The length of the re-circulation vortex is seven-times of the step height, again, within the range of experimental data 6.5 7.5 [3]. To simulate a coherent flow, we use only a first-order Taylor's series in the energy equation. The result shows a series of quasi-periodic vortex shedding. Figure 4 is just a snap shot of one of them. In summary, the unilateral average scheme is a powerful tool to extract the first-order statistical information (precisely, the first moment) of turbulence fluctuations. The results shown here were obtained by using the same equations given above without using any empirical coefficients and wall functions. All the numerical computations were performed on a Pentium 200 personal computer. The grid sizes for the three flows are 81X41, 41X41, and 101X61, respectively.

References

[1] Gao,G. and Yong,Y."The United Modeling Theory for both of Mean Flow and Coherent Flow of Incompressible Turbulence",Journal of Aerospace Power (ISSN 1000-8055 CODEN HDOXE5), Vol.15,No.1,pp1-11,Jan. 2000.

[2] Klebanoff, P.S, NASA Report 1247. 1956.

[3] 1980-81 AFOSR-HTTM-STANDFORD Conference on Complex Turbulent Flows.

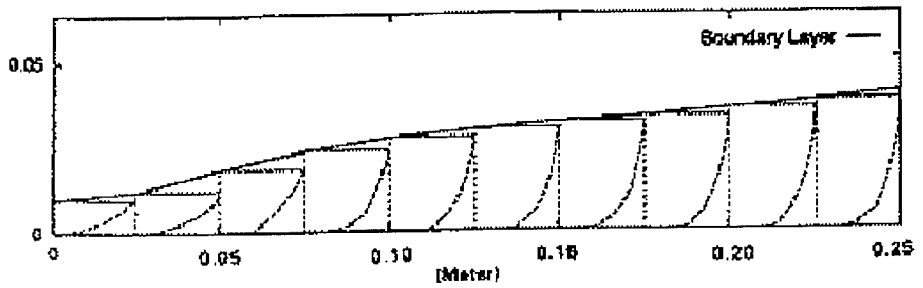


Figure 1. Calculated velocity profiles in the boundary layer of flat plate.

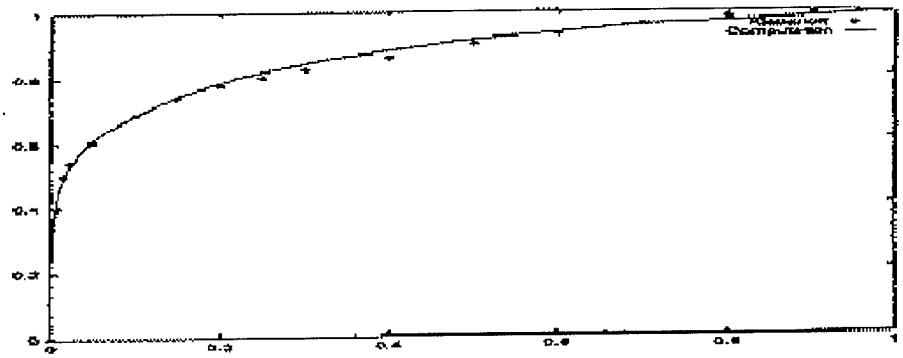


Figure 2. Dimensionless velocity profile of fully developed turbulence in the boundary layer.

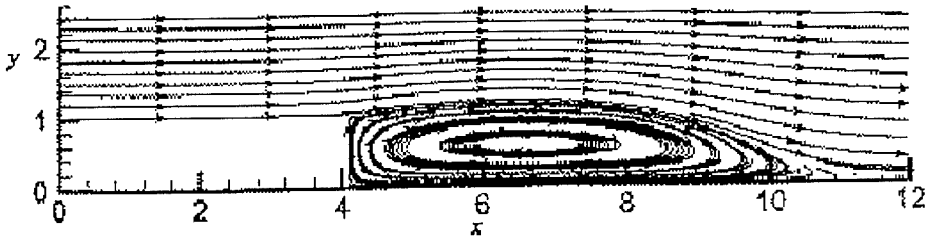


Figure 3. Streamlines of backward-facing step flow.

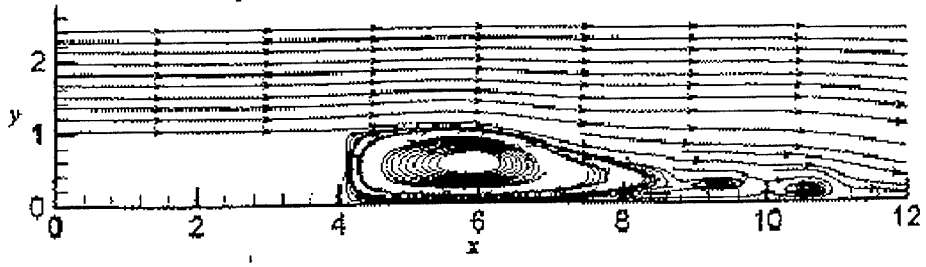


Figure 4. A school of vortexes shed toward downstream.

X

Geophysical Turbulence

ADVANCES IN TURBULENCE VIII
Proceedings of the Eighth European Turbulence Conference
C. Dopazo et al. (Eds.)
© CIMNE, Barcelona 2000

Three-dimensional instability of columnar cyclone-anticyclone pairs

Y. Afanasyev

Memorial University of Newfoundland,
Dept. of Physics and Physical Oceanography,
St. John's, NF, Canada A1B 3X7

Contact e-mail: yakov@physics.mun.ca

1 Introduction

The Earth's rotation may be a crucial factor in determining the stability characteristics of columnar (barotropic) vortices in both the atmosphere and the oceans. Small and mesoscale columnar vortices may, in particular, be subject to the centrifugal (inertial) instability due to the background rotation although this fact has only been realized rather recently due to 3-D DNS analysis and numerical stability analysis [1], [2]. Theoretical analyses by Smyth and Peltier [1] have demonstrated that in the case of elliptic vortices in shear created as a result of Kelvin-Helmholtz instability, the growth rate of a mode of instability associated with centrifugal destabilization reaches a maximum for the value of the Rossby number, $Ro = \omega/f$, that is $O(1)$, when the vortices are anticyclonic. The difference in the behavior of cyclones and anticyclones has also been demonstrated in the numerical experiments of Carnevale *et al.* [2]. Our recent results [4] present the attempt to demonstrate such instability in controlled laboratory conditions. Besides clear demonstration of inertial instability these experiments showed the appearance of secondary 2-D Kelvin-Helmholtz instability due to finite amplitude development of the primary inertial instability. This effect has an important dynamical consequences. It is this secondary instability that destroys the core of the vortex. This result allowed us to explain also the results of previous laboratory experiments of Kloosterziel and van Heijst [3] on isolated vortices.

The main aim of the present work is to extend our recent results in demonstrating the destabilizing effect of rotation on anticyclonic vortices to "free" vortices (rather than vortices generated by a rotating cylinder as in the experiments of Afanasyev and Peltier [4]) and vortex structures, namely vortex pairs (dipoles).

2 Laboratory apparatus and technique

The experiments were carried out in a Perspex tank of dimensions 80x80x15 cm mounted on a rotating turntable. The tank itself was filled with a homogeneous fluid and rotated until a nearly solid-body rotation was established. The flows in the tank were then generated by a narrow plate rotated about its vertical axis for a short interval of time. The rotation rate and the time interval were varied between the experiments. Vortex pairs (in some cases with asymmetric distribution of vorticity) were generated by the rotating plate. The horizontal velocity field in the resulting flow was measured using a PIV technique. Seeding particles were polyamid spheres of mean diameter 50 μm. For flow visualization a solution of pH indicator thymol-blue was employed (see e.g. [5]).

3 Experimental results

Two typical examples of the evolution of the unstable flow are illustrated by the photographs shown in Figure 1. In the first case the cyclone is approximately two times stronger than the anticyclone thus providing a strong straining field. The core of the anticyclone becomes unstable. The vortex tube bends forming dipole-like structures in a vertical cross section. The deformed vortex tube then wraps around the stable cyclonic vortex so that the anticyclonic vortex eventually ceases to exist. The initial stage of the evolution of the anticyclone can be compared qualitatively with the results of numerical simulations of Carnevale *et al.* [2] for their case of large Rossby number and strong perturbations where similar form of the perturbation was observed. In the second case the dipole is symmetric initially and the Rossby number of the flow based on the peak value of vorticity in the vortex is equal to $Ro = 2.2$. This value is approximately two times less than that in the previous case. As a result, the instability develops slower and initially has an axisymmetric form of rib vortices of alternating sign. During the finite amplitude stage of the instability development the flow in the horizontal plane is characterized by strong jet-like (dipolar) perturbations of the anticyclonic vortex with peak values of vorticity 3-5 times greater that the mean vorticity in the vortex (Figure 2). The perturbations eventually decay when the Rossby number based on the evolving mean vorticity falls to a level below the threshold for centrifugal instability ($Ro < 1$). Restabilized anticyclone has a new Rossby number of approximately 0.8 (Figure 3). This result agrees well with the results of numerical simulations [2]. It is interesting to note that the vortex pair keeps its translational motion with approximately constant speed during the development of the instability in the anticyclone and afterwards during the relaxation stage when the peak values of vorticity fall in both anticyclone and the cyclone. Thus the flow corresponds to the inviscid Lamb dipole which propagates with constant speed in an irrotational environment. The perturbations only effectively redistribute vorticity in the vortex while the integral dipolar moment of vorticity distribution (see e.g. [5]) and hence the total impulse of the flow

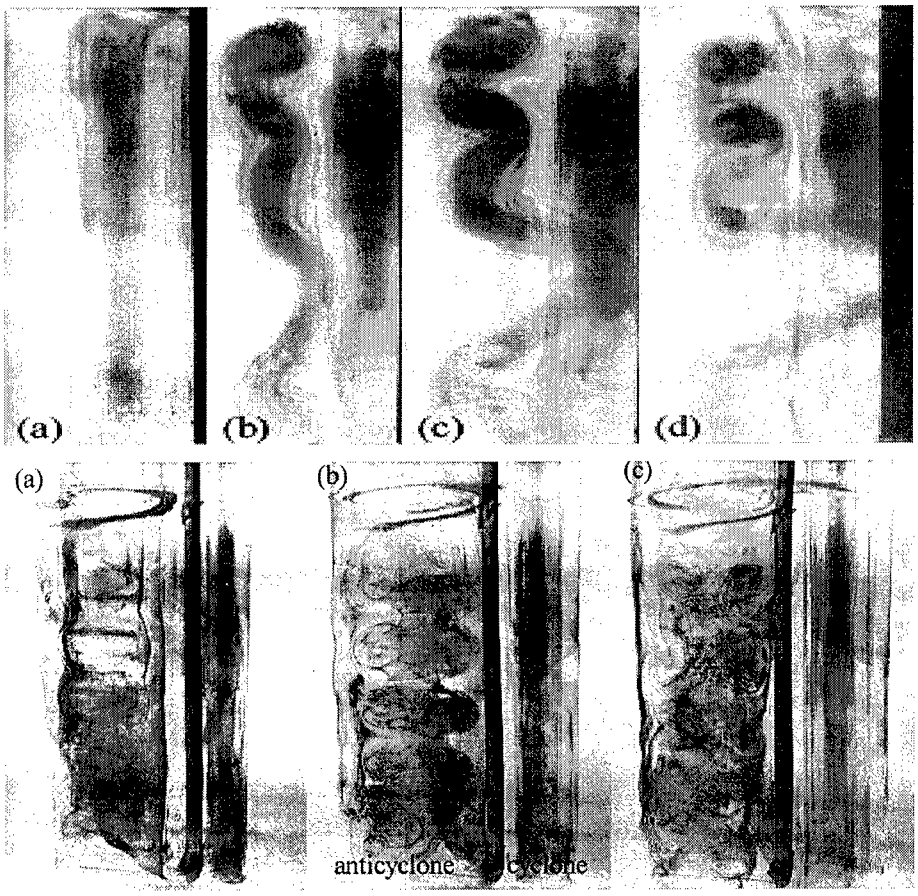


Figure 1: A sequence of photographs showing the evolution of the centrifugal instability. Side view. Asymmetric dipole (upper plate), symmetric dipole for smaller value of the Rossby number (lower plate).

remains constant as one can expect.

References

[1] W.D. Smyth and W.R. Peltier. Three-dimensionalization of barotropic vortices on the f-plane. *J. Fluid Mech.*, 265:25–64, 1994.

[2] G.F. Carnevale, M. Briscolini, R.C. Kloosterziel and G.K. Vallis. Three-dimensionally perturbed vortex tubes in a rotating flow. *J. Fluid Mech.*, 341:127–163, 1997.

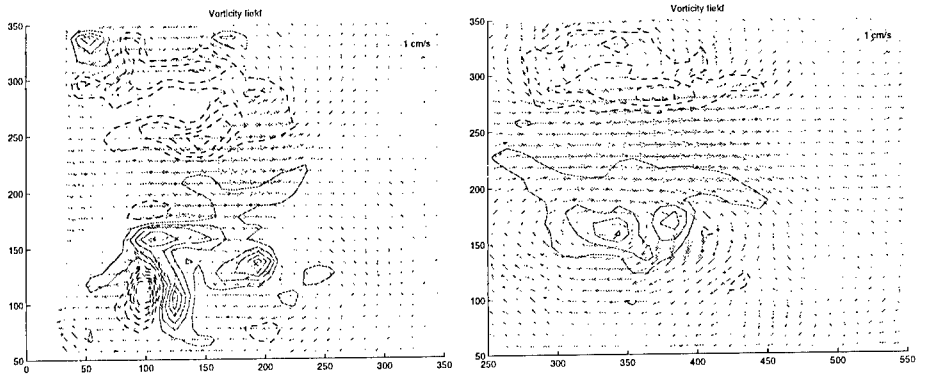


Figure 2: Velocity and vorticity fields in the flow during the development of strong perturbations ($t/T = 0.9$) and at later time ($t/T = 3.6$) during the relaxation of the flow at subcritical values of the Rossby number. Vorticity is nondimensonalized by the Coriolis parameter f. Contours are given with the increment of 0.25 starting from 0.25. Solid/dashed line shows the anticyclonic/cyclonic vorticity. Distance is in pixels, 1 pixel = 0.034 cm.

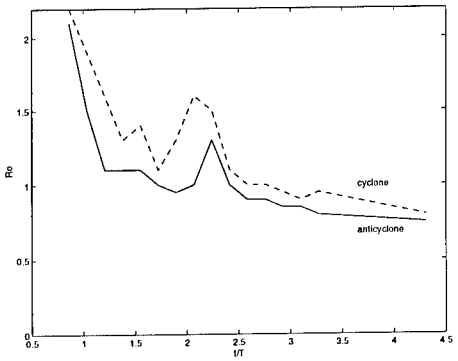


Figure 3: Evolution of the Rossby number estimated by the mean values of vorticity in cyclonic and anticyclonic vortices. Time is nondimensionalized by the period of rotation of the turntable.

[3] R.C. Kloosterziel and G.J.F.van Heijst. An experimental study of unstable barotropic vortices in a rotating fluid. *J. Fluid Mech.*, 223:1–24, 1991.

[4] Y.D. Afanasyev and W.R. Peltier Three-dimensional instability of anticyclonic swirling flow in rotatting fluis: Laboratory experiments and related theoretical predictions. *Physics of Fluids A*, 10:3194–3202, 1998.

[5] S. Voropayev and Y. Afanasyev. *Vortex Structures in a Stratified Fluid*, Chapman and Hall, 1994.

ADVANCES IN TURBULENCE VIII
Proceedings of the Eighth European Turbulence Conference
C. Dopazo et al. (Eds.)
© CIMNE, Barcelona 2000

High Rayleigh and Taylor Number Convection in Spherical Shells

Anil E. Deane[1], Paul F. Fischer[2] and Henry M. Tufo[2]

[1]Institute for Physical Science and Technology
University of Maryland, College Park, MD 20742, USA.
[2]Mathematics and Computer Science Division
Argonne National Laboratory, Argonne, IL 60439, USA.

Contact e-mail: deane@ipst.umd.edu

1 Introduction

The deep atmospheres of the planets such as Jupiter and Saturn and rotating stars such as our Sun are strongly influenced by buoyancy and Coriolis forces. In addition the giant planets also feel the effects of differential heating (North-South temperature gradients). The latitudinal variation of Coriolis forces is crucial to understanding large-scale motions (scales comparable to the curvature of the body) that are manifested in diverse phenomena such as the differential rotation of the Sun, and the cloud bands on Jupiter.

We describe the results of a numerical model based on the spectral element method[6, 7, 5] that we have developed to study these competing forces. The present simulations are motivated by a space-laboratory experiment in rotating convection as an analog of the geophysical environment[3]. During its missions this experiment obtained large quantities of data in a wide variety of parameter ranges. The data has shown many interesting flow features that are poorly understood[4].

Using the spectral element method we are able to obtain highly accurate solutions corresponding to the geometry and parameter regime of this experiment. Among the observed phenomena are cellular convection, wave motions, turbulence and its onset, and mode competition.

This paper presents simulation results for a range of heating and rotation rates and focuses primarily on mean energetics.

2 Results

Figure 1 shows a high Ra and Ta simulation. For this case the rotation is sufficiently high that structures generally align themselves to the rotation direction

(as evidenced by the figure on the left). The temperature field obtains a vortical structure and small scale features are evident. In Figure 2, at a slightly lower Ra, where the rotational effects are even more dominant, we have computed the azimuthally-averaged mean fields of velocity and temperature. Focusing on the temperature and in-plane velocity fields we see that the mean field consists of roughly four rolls. A small polar roll, a slightly larger high-latitude roll, a broader mid-latitude roll, and an equatorial roll. The last is a consequence of the artificial equatorial boundary necessary in the space-laboratory experiment. The other rolls show confinement to the tangent cylinder and conform to the expected picture from theory (although in a mean-field sense)[2]. The confinement to the tangent cylinder is underscored by the center figure of the azimuthal velocity, which shows Taylor-Proudman column-like behavior. As we have noted this is visible in the full field as well (Figure 1).

Figure 3 (left) shows the time-dependent heat flux at the inner surface and illustrates one of our typical computations. The transport of heat in this system occurs because of correlations of $< u_r T >$. As the Taylor number is increased, the vigor of convection is reduced, with attendant decrease in Nusselt number (Figure 3, right). This figure shows Nu for both the inner and outer surfaces, as well as error bars corresponding to the error of computing time-averages from the finite computations. (Note that in this figure and in Figure 4, this error is better represented by the difference between time-averaged values at the inner and outer surfaces since the system does not heat up in a net sense)

Figure 4 shows the increase in heat flux at moderate and high Taylor numbers. Note the change in the Ra scales. It is possible that there is slope difference between these regimes which we are currently investigating with more simulations. We note that the overall error appears negligible, except for the extreme Ra at the lower Ta.

3 Conclusions

We have performed high Rayleigh and Taylor number simulations in an arrangement motivated by a space laboratory experiment in rotating convection. We have shown the variation of Nusselt number with these parameters and results for mean field dynamics. Ignoring the effects of the artifical equatorial boundary the results are in general agreement with theoretical ideas, and previous computations in full shells [2, 1, 8]. Fuller results will be reported elsewhere.

Acknowledgments AED acknowledges support from NASA Microgravity Fluid Physics grant NAG3-2139 to University of Maryland. PFF and HMT acknowledge support by the Mathematical, Information, and Computational Sciences Division subprogram of the Office of Advanced Scientific Computing Research, U.S. Department of Energy, under Contract W-31-109-Eng-38. The computations were performed at the High Performance Computing Research Facility, Mathematics and Computer Science Division, Argonne National Laboratory.

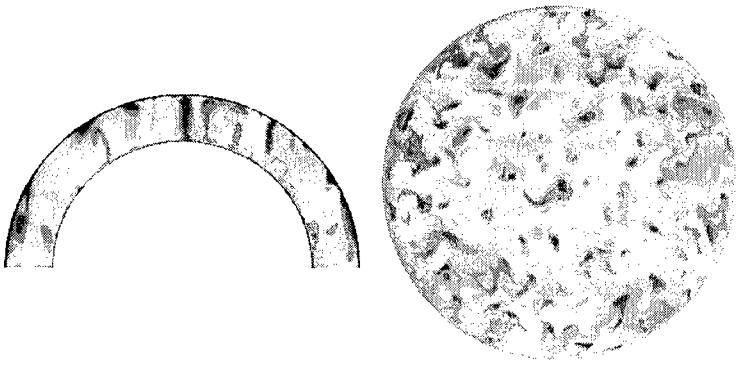


Figure 1: Two views of the temperature field for $Ra = 1.7 \cdot 10^6$ and $Ta = 8.9 \cdot 10^6$. Shown on the left is a cut through the hemispherical shell. Shown on the right is the temperature field at the radius corresponding to mid-gap viewed from the pole.

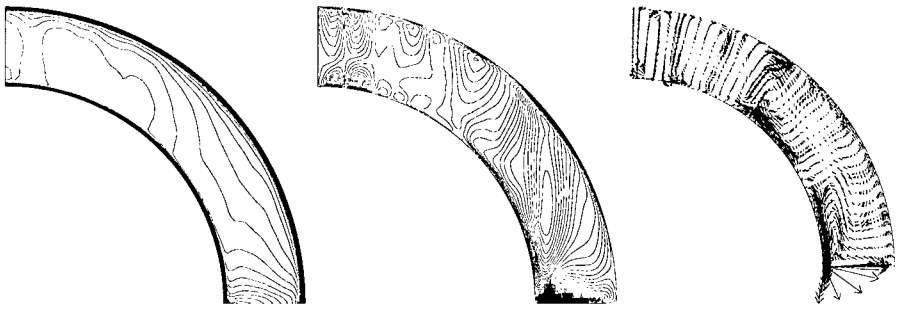


Figure 2: Three views of the azimuthally-(in the longitudinal direction) and time-averaged fields for $Ra = 1.1 \cdot 10^6$ and $Ta = 8.9 \cdot 10^6$. On the left is the temperature field. In the center the azimuthal velocity (in/out of the plane of the paper). On the right are velocity vectors corresponding to velocity in the plane of the paper.

References

[1] Ardes, M., Busse, F.H., and Wicht, J., "Thermal convection in rotating spherical shells," Phys. Earth and Planet. Interiors **99** pp. 55-67 (1997).

[2] Busse, F.H.,"Convection driven zonal flows and vortices in the major planets," Chaos **4** pp. 1054-1500 (1994).

[3] Hart, J., Glatzmaier, G., and Toomre, J., J. Fluid Mech. **173**, 519 (1986).

[4] Hart, J., Ohlsen, D., Kittleman, S., Leslie, F., and Miller, T. "The Geophysical Fluid Flow Cell Experiment on USML2," (preprint).

[5] Maday, Y. and Patera, A.T., "Spectral element methods for the Navier-Stokes

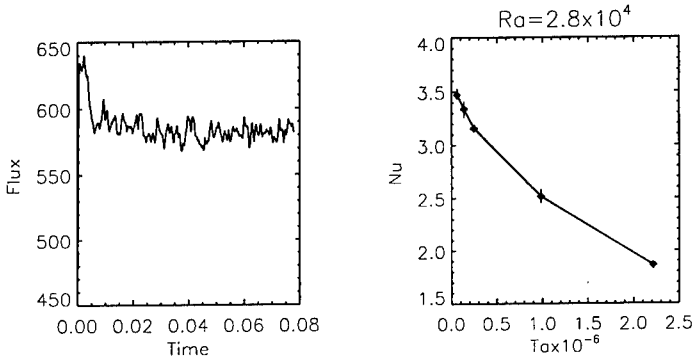


Figure 3: Shown on the left is the time variation of the heat flux at the inner surface for $Ra = 1.1 \cdot 10^6$ and $Ta = 8.9 \cdot 10^6$. On the right is the Nusselt number shown as a function of $Ta \times 10^{-6}$ for $Ra = 2.8 \cdot 10^4$.

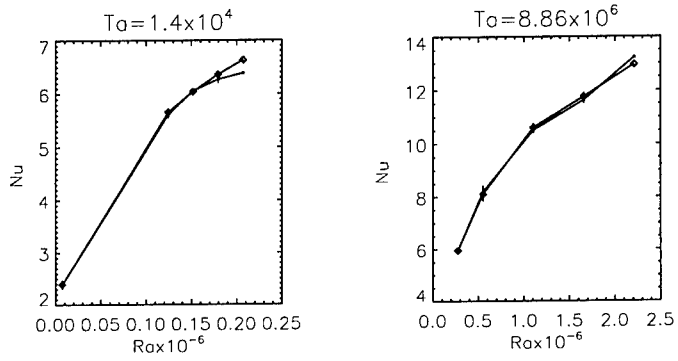


Figure 4: Shown is the variation of Nusselt number with $Ra \times 10^{-6}$ at moderate, $Ta = 1.4 \cdot 10^4$ and high, $Ta = 8.86 \cdot 10^6$. Note the different ranges of the Ra for these figures.

equations," in *State of the Art Surveys in Computational Mechanics* (Ed. A.K. Noor), ASME, New York, (1989).

[6] Patera, A.T.,"A spectral element method for fluid dynamics; Laminar flow in a channel expansion," J. Comput. Phys., **54** (1984), 468-488.

[7] Fischer, P.F.,"An overlapping Schwarz method for spectral element solution of the incompressible Navier-Stokes equations", J. of Comp. Phys., **133**, pp. 84–101 (1997).

[8] Tilgner, A. and Busse, F.H., "Finite-Amplitude convection in rotating spherical fluid shells," J. Fluid Mech. **332** pp. 359-376 (1997).

ADVANCES IN TURBULENCE VIII
Proceedings of the Eighth European Turbulence Conference
C. Dopazo et al. (Eds.)
© CIMNE, Barcelona 2000

Buoyancy effect and universal structure of a stably stratified turbulence field

K. Sassa[1], S. Matsunaga[1], and H. Makita[2]

[1]Dept. of Natural Environmental Science, Kochi University
Akebono-cho, Kochi 780-8520, JAPAN
[2]Dept. of Mech. Eng., Toyohashi University of Technology
Tempaku-cho, Toyohashi 441-8580, JAPAN

Contact e-mail: sassa@cc.kochi-u.ac.jp

1 Introduction

Atmospheric and oceanic turbulence fields provide very interesting objects to investigate universal structure of fully-developed turbulence as well as the buoyancy effects on it by their inseparable nature of density stratification. Most of the experiments on stably-stratified turbulence were made at small turbulence Reynolds numbers [2, 8]. Their results clarified the buoyancy effect on weak turbulence but could not demonstrated the universal structures of turbulence affected by the buoyancy. Sreenivasan [7] pointed out that a homogeneous turbulence field of $R_\lambda > 250$ is needed to examine the universal structure of scalar fields. Such a passive scalar field was experimented only by Mydlarski and Warhaft [5], however, an active scalar field at large R_λ have never been realized experimentally yet. We aim to examine the universal structure of a quasi two-dimensional field where the vertical component of fluctuating velocity is suppressed by the buoyancy effect by realizing a stably-stratified turbulence field with the large Reynolds number of $R_\lambda \approx 300$.

2 Experiment

Figure 1 shows the wind tunnel used in the present experiment. It has a test section of 0.35×0.45 m^2 in cross section and about 3.1 m long. A thermal stratification generator and an active turbulence generator were installed just upstream of the test section. The thermal stratification generator is composed of 20 layers of heater arrangements having two coiled heaters. The active turbulence generator [4] is a kind of biplane grid with mesh size, $M = 25$ mm, composed of 32 agitator rods with many triangular wings. The agitator rods are randomly oscillated by stepping motors and induce strong turbulence in the flow passing

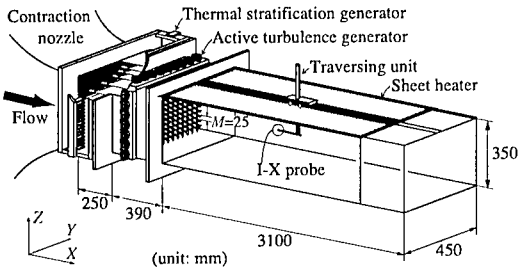


Figure 1: Sketch of a small wind tunnel

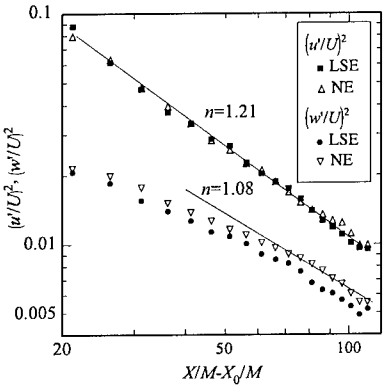


Figure 2: Streamwise evolution of turbulence energy

through them. Sheet heaters were attached on the ceiling in order to prevent the effect of heat conduction through it.

Four cases were examined; actively excited turbulence (LSE) and grid turbulence (LSG) with the stable stratification, and excited (NE) and grid (NG) turbulence in the neutral condition. Mean flow velocity, U, was 5 m/s in each case. Linear mean temperature profiles were given for the two stratified fields, LSE and LSG, of which the gradients, $d\theta/dZ$, were fixed at about 30 K/m. Turbulence Reynolds numbers, R_λ, were about 300 for the excited cases and about 20 for the grid cases, respectively. Simultaneous measurements of fluctuating velocity and temperature were made by using a thermo-anemometer [3] and an I-X probe made of tungsten wires of 2.5 μm in diam. The spatial resolution of the probe is about $0.6\times0.6\times0.4$ mm^3. The error in measured signal arising from the gap between the cold wire and the X hotwire was compensated by a digital delay circuit. Its S/N ratio is better than 60 dB and the frequency response is flat from DC to about 5 kHz.

3 Result and Discussion

In the present experiment, turbulence intensities in LSE and NE were one order of magnitude larger than those in LSG, NG and the other grid turbulence fields [2, 8]. Figure 2 shows the decay of turbulence energy for the excited cases. The vertical component, $(w'/U)^2$, decreases more rapidly in LSE than in NE for $X/M > 60$. It shows the collapse of w' by the buoyancy. The heat flux coefficient of LSE begins to decrease from $X/M = 30$ as shown in Fig.3. According to Lienhard and Van Atta [2], such turning point of the decay corresponds to the onset of the collapse of turbulence. The onset in the present experiment, however, occurred fairly faster than their results [2], as shown by the nondimen-

sional time based on Brunt-Väisälä frequency, $Nt/2\pi \approx 0.03$. The decay rate of the heat flux is larger in LSE than in LSG and the buoyancy is found to more drastically act on the turbulence structure in LSE. If the heat flux is assumed to decay downstream at the same gradient, the quasi 2-D turbulence with zero heat flux may be realized at $X/M \approx 300$ in LSE.

In spite of such evident buoyancy effect in LSE, the disturbance Froude number [1], $Fr_u = u'/LN$ is slightly larger than the critical value, $Fr_u = 1$, see Fig.4. The difference may be introduced by the anisotropy of the initial turbulence field. Actually, Fr_w, evaluated from the vertical component directly suppressed by the buoyancy, is close to unity. In addition, the integral scale, L, may be underestimated in LSE. If not, the other appropriate stability parameters must be derived to describe the buoyancy effect more accurately.

Figure 5 shows the velocity spectra in LSE and LSG. The energy level of velocity spectrum in LSE is evidently elevated in small wavenumber range and the inertial subrange is clearly observed in it. The strong anisotropy due to the buoyancy effect, in addition to the initial anisotropy, appears only in the small wavenumber range and the universal structure exists over the wide wavenumber range. Then, the Kolmogorov constant was about 0.5 for both cases of LSE and NE. The temperature spectrum also has wide inertial subrange in LSE as shown in Fig.6. Unlike the result of Mydlarski and Warhaft [5], the bump of the spectral distribution is not observed in large wavenumber range. The present experiment gave the Obukhov-Corrsin constant of the temperature spectrum of about 1.0 which is larger than the mean value arranged by Sreenivasan [7]. Such differences in the results may be caused by the intrinsic inequality between the active scalar and the passive scalar as suggested by Monin and Yaglom [6].

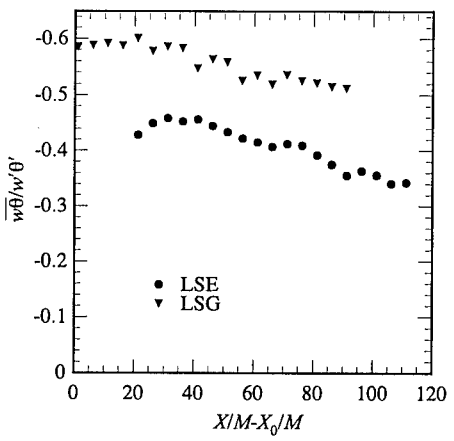


Figure 3: Streamwise evolution of heat flux coefficient

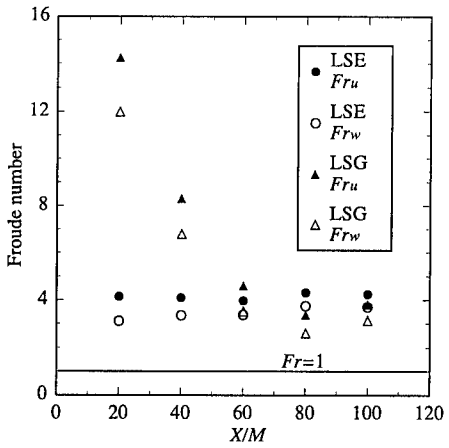


Figure 4: Streamwise evolution of disturbance Froude number

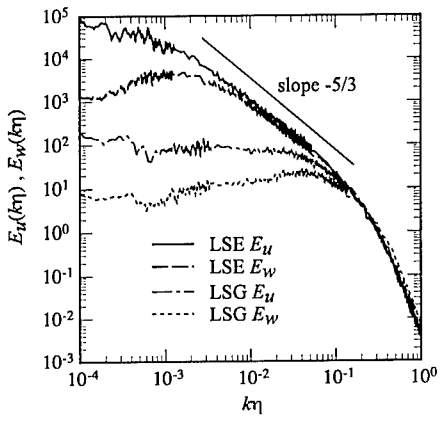


Figure 5: Turbulence energy spectra at $X/M = 60$

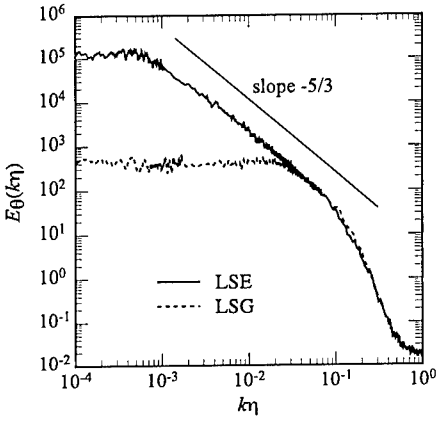


Figure 6: Temperature variance spectra at $X/M = 60$

4 Conclusions

A stably-stratified turbulence field at $R_\lambda \approx 300$ was realized in a small wind tunnel. The buoyancy effect directly acted on the aspect of the streamwise decay of w' and the heat flux. The universal spectrum was observed in wide wavenumber range though its small wavenumber range was apparently affected by the buoyancy. The present turbulence field is capable of providing the essential experimental data to verify the universal structure of the stratified turbulence.

This work has been supported in part by the Grant-in-Aid for Scientific Research from the Ministry of Education of Japan.

References

[1] E. J. Hopfinger. *J. Geophys. Res.*, 92-C5: 5287–5303, 1987.

[2] J. H. Lienhard and C. W. Van Atta. *J. Fluid Mech.*, 210: 57–112, 1990.

[3] H. Makita, S. Mori, and A. Yahagi. in Stably Stratified Flows: 81–91, 1994.

[4] H. Makita and K. Sassa. in Advances in Turbulence 3: 497–505, 1991.

[5] L. Mydlarski and Z. Warhaft. *J. Fluid Mech.*, 358: 135–175, 1998.

[6] A. S. Monin and A. M. Yaglom. in Statistical fluid mechanics. vol.2: 387-393, 1975.

[7] K. R. Sreenivasan. *Phys. Fluids.*, 8-1: 189–196, 1996.

[8] K. Yoon and Z. Warhaft. *J. Fluid Mech.*, 215: 601–638, 1990.

ADVANCES IN TURBULENCE VIII
Proceedings of the Eighth European Turbulence Conference
C. Dopazo et al. (Eds.)
© CIMNE, Barcelona 2000

Kinematic Simulation for stably stratified and rotating turbulence

F. Nicolleau[1] and J. C. Vassilicos[2]

[1]University of Sheffield, Department of Mechanical Engineering
[2]University of Cambridge, DAMTP

1 Introduction

We present a Lagrangian model of both one-particle and two-particle turbulent diffusion in high Reynolds number non-decaying turbulence that is stably stratified and/or rotating with small Froude and Rosby numbers. This model is a Kinematic Simulation (KS) that satisfies both incompressibility and the linearised Boussinesq equations with Coriolis force induced by a rotation around a vertical axis. Hence, turbulent diffusion is anisotropic and is studied in all three directions concurrently with incompressibility satisfied at the level of every single trajectory.

2 One-particle vertical diffusion

Horizontal one-particle and two-particle diffusions are found to be independent of the buoyancy (Brünt-Väissälä) frequency N and of the rotation frequency Ω. However, along the vertical axis, we observe a capping of the particle diffusion (as in [1]).

$$< (x_3(t) - x_3(t_0))^2 > \simeq \frac{u'^2}{N^2} \qquad \text{for } \frac{2\pi}{N} \ll t - t_0 \tag{1}$$

in the case of pure stratification and, to some lesser extent, a capping of particle diffusion in the case of pure rotation (see Figure 1) with similar scalings,

$$< (x_3(t) - x_3(t_0))^2 > \simeq \frac{u'^2}{\Omega^2} \qquad \text{for } \frac{2\pi}{\Omega} \ll t - t_0 \tag{2}$$

where u' and L are a rms velocity and a length-scale of the energy containing motions respectively and t_0 is the time of release of the particles. The conjunction of both effects, rotation superimposed on stratified turbulence, increases dramatically the oscillations around the mean plateau (dash curve in Figure 1). These cappings of one-particle vertical diffusion requires the consideration of the entire 3-D flow to be explained.

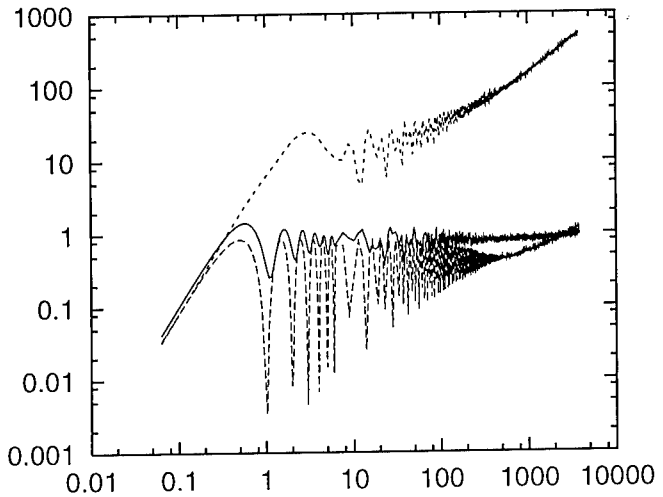


Figure 1: One particle diffusion: solid line $2\Omega = 0$, $N = 200$, $< (x_3(t) - x_3(t_0))^2 > \frac{N^2}{u'^2}$ as a function of $(t - t_0)\frac{N}{2\pi}$. Dotted line $2\Omega = 200$, $N = 0$, dashed line $2\Omega = 200$, $N = 200$ $< (x_3(t) - x_3(t_0))^2 > \frac{2(\Omega)^2}{u'^2}$ as a function of $(t - t_0)\frac{2\Omega}{2\pi}$.

3 Horizontal diffusion

KS is a relatively low time consuming method and we have run many computations varying the values of the turbulence stratification and rotation parameters. We have enough data to discuss the scalings of one and two particle diffusions in the presence of strong stratification, rotation and stratification with rotation. In particular when $t - t_0 \to 0$ we observe the same scalings in the horizontal plane with and without rotation and/or stratification (see Figure 2). For all values of N and Ω we get:

$$< (x_i(t) - x_i(t_0))^2 > \simeq {u'}^2 (t - t_0)^2 \tag{3}$$

for one-particle diffusion and

$$< (\Delta x_i(t) - \Delta x_i(t_0))^2 > \simeq {\Delta v_0}^2 (t - t_0)^2, \tag{4}$$

for two-particle diffusion, where $i = 1, 2$ and Δv_0 is the initial difference of velocity between the pair of particles (see [2]). For large times $t - t_0 > \frac{L}{u'}$ the two particles become independent and we retrieve the classical random walk behaviour,

$$< (x_i(t) - x_i(t_0))^2 > \simeq u' L (t - t_0). \tag{5}$$

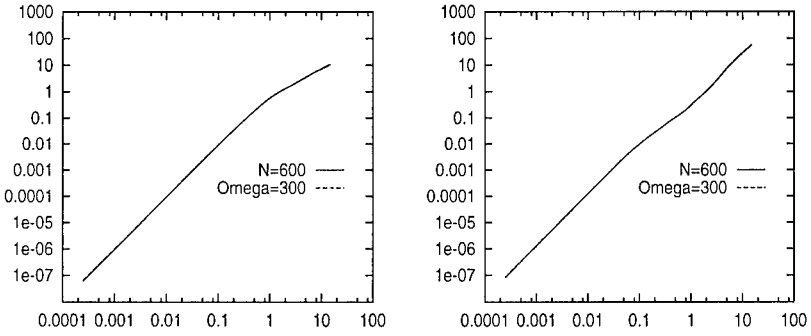


Figure 2: Comparison between Froude number and Rosby number effects. One- and two-particle diffusions in the horizontal plane for $\Omega = 300$, $N = 0$ and $\Omega = 0$, $N = 600$. Plot on the left: one particle diffusion $< (x_i(t) - x_i(t_0))^2 > /L^2$ as a function of $(t - t_0)\frac{u'}{L}$. Plot on the right: two-particle diffusion in the horizontal plane $< (x_i(t) - x_i(t_0))^2 > \frac{1}{L^2}\left(\frac{L}{\Delta_0}\right)^{2/3}$ as a function of $(t - t_0)\frac{u'}{L}$ (see Nicolleau et al., 2000 for an explanation of these scalings), with $\frac{\Delta_0}{\eta} = 3.18$ where Δ_0 is the initial separation between the two particles. In both plots the two curves, corresponding to pure stratification and pure rotation, are indistinguishable.

4 Two-particle vertical diffusion

Whereas two-particle horizontal diffusion is unaffected by the stratification and rotation, two-particle vertical diffusion is very significantly affected and exhibits a plateau at a much lower value than the one obtained for one particle diffusion. Figure 3 shows the two-particle vertical diffusion for pure rotation, pure stratification and rotation superimposed on stratification. With pure rotation the caping is less extended than when there is stratification.

Relation (4) is still valid for two-particle vertical dispersion except that Δv_{03} has a different value along the vertical axis. But we observe the same scalings for Δv_{03} and Δv_0 and we do *not* observe $\Delta v_{03} \to 0$ when $N$and/or $\Omega \to \infty$ which can therefore not be the explanation for the vertical capping. As can been seen from the dashed curve in Figure 3 superposition of rotation on stratification decreases the value of Δv_{03} and enhances oscillations in the diffusion curve.

With rotation superimposed on stratification we can generalise the results of [1] concerning the two-plateau structure of two-particle vertical diffusion. The first plateau's scaling depends on Δv_{03} The second plateau is reached when the two particles become statistically independent. The transition between the two plateaux coincides with the time when the two particles start moving significantly apart in the horizontal plane.

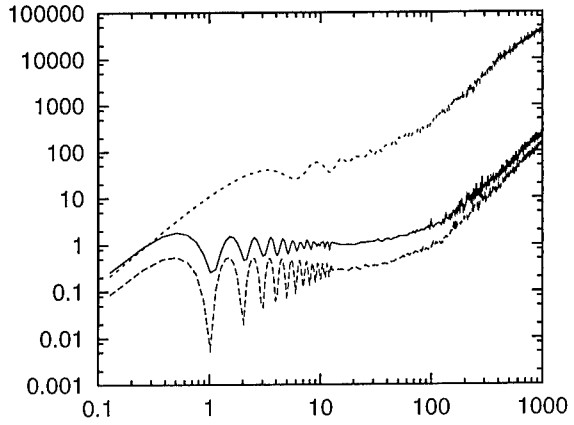


Figure 3: Two-particle diffusion along the vertical axis. Solid line pure stratification, dotted line pure rotation, dashed line rotation superimposed on stratification. $< (\Delta x_i(t) - \Delta x_i(t_0))^2 > \frac{1}{2}\frac{N^2}{u'^2}\left(\frac{L}{\Delta_0}\right)^2\left(\frac{\eta}{L}\right)^{4/3}$ as a function of $(t-t_0)\frac{N}{2\pi}$ for pure stratification, $< (\Delta x_i(t) - \Delta x_i(t_0))^2 > \frac{1}{2}\frac{\Omega^2}{u'^2}\left(\frac{L}{\Delta_0}\right)^2\left(\frac{\eta}{L}\right)^{4/3}$ as a function of $(t-t_0)\frac{\Omega}{\pi}$ otherwise (in the case of stratification with rotation here we chose $N = 2\Omega$), η is the Kolmogorov length scale and $\Delta_0 = 0.032\eta$.

References

[1] Nicolleau, F. and J. C. Vassilicos: 2000, 'Kinematic simulation for sably stratified non-decaying turbulence: one- and two-particle diffusion'. *Accepted for publication in J. Fluid Mech.* **409**.

[2] Nicolleau, F., J. C. Vassilicos, and D. J. Thomson: 2000, 'Kinematic Simulation for particle pair diffusion'. In: *ETC8*. Barcelona, Spain.

ADVANCES IN TURBULENCE VIII
Proceedings of the Eighth European Turbulence Conference
C. Dopazo et al. (Eds.)
© CIMNE, Barcelona 2000

Pressure/Potential-Temperature Covariance in Free and Rotating Convection

Dmitrii V. Mironov

Deutscher Wetterdienst, Abt. Meteorologische Analyse und Modellierung
Postfach 10 04 65, Frankfurter Str. 135, D-63067 Offenbach am Main, Germany
Fax +49-69-8062 3721, phone +49-69-8062 2705, e-mail: Dmitrii.Mironov@dwd.de
and
Alfred-Wegener-Institut für Polar- und Meeresforschung, Bremerhaven, Germany

1 Introduction

The pressure/potential-temperature covariance in free and rotating turbulent convection with no mean velocity shear is analysed, using a data set generated through large-eddy simulation (LES). Rotating convection is encountered in many geophysical and astrophysical fluid systems and in some technical applications. A prominent geophysical example is open-ocean deep convection. As it was shown by Mironov et al. (2000), the potential-temperature/pressure-gradient covariance, $\langle \theta \partial p/\partial x_i \rangle \equiv \Pi_i$, is one of the dominating terms in the budget equation for the potential temperature flux, $\langle u_i \theta \rangle$, in convective flows affected by rotation (we omit primes and use small letters to denote turbulent fluctuations; the ensemble means are denoted by angle brackets). This places heavy demands on the accuracy of parameterisation of the pressure term. A standard approach nowadays is to decompose Π_i into the contributions due to the nonlinear turbulence-turbulence interactions, Π_i^T, mean shear, Π_i^S, buoyancy, Π_i^B, and the Coriolis effects, Π_i^C, and to model these contributions separately. We use LES data to resolve the fluctuating pressure field into turbulence-turbulence, buoyancy and Coriolis components, to evaluate contributions from these components to Π_i, and to test the performance of closure models for Π_i^T, Π_i^B and Π_i^C. An attempt is made to develop an improved model for the Coriolis contribution, Π_i^C.

2 Π_i^T, Π_i^B and Π_i^C from LES data and closures

Four convective flows are generated and analysed. Two cases are simulations of the surface-heating-driven convective boundary layers (one with strong rotation and the other rotation-free) that grow into a quiescent stably stratified fluid. The other two cases are simulations of convection between the two rigid boundaries (one with strong rotation and the other rotation-free), where the lower boundary is heated at the same rate as the upper is cooled. The Rossby number, $Ro_* = (B_s)^{1/2} (2\Omega)^{-3/2} h^{-1}$, in our simulations with rotation is small, $Ro_* = 0.02$, indicating that convection is strongly affected by rotation. Here, B_s is the surface buoyancy flux, $\Omega = (\Omega_i \Omega_i)^{1/2}$ is the magnitude of the angular velocity of rotation, and h is the convective boundary layer (CBL) depth. Potential temperature is used as the only thermodynamic variable, the equation of state is linear, and the rotation vector is aligned with the vector of gravity. The turbulence statistics are built by averaging the LES fields over horizontal planes and over a number of large-eddy turnover times.

The slow part of Π_i in free convection is well approximated by the Rotta-type return-to-isotropy model, $\Pi_i^T = C_T \langle u_i \theta \rangle / \tau$, C_T being a dimensionless constant, with the relaxation time scale, τ, set equal to the turbulence energy dissipation time scale, $\langle u_i u_i \rangle / 2 \langle \epsilon \rangle$. In convection with rotation, neither the simplest Rotta-type model with $\tau = \langle u_i u_i \rangle / 2 \langle \epsilon \rangle$, nor more sophisticated two-component-limit (TCL) non-linear model of Craft et al. (1996) is able to accurately describe the LES data. A somewhat better agreement is found when a limitation is imposed on the relaxation time scale in the asymptotic case of rapid rotation, $\tau = \Omega^{-1}$, as proposed by Hassid and Galperin (1994). If one of the models considered is to be used for practical applications, one should put up with possible large uncertainties.

In non-rotating convection, the buoyancy contribution compensates about one half of the buoyant production term in the flux budget equation, $\Pi_i^B = C_B \beta_i \langle \theta^2 \rangle$ with $C_B = 0.5$ (β_i is the buoyancy parameter in direction x_i). In convection with rotation, this simple linear model fares poorly. A reasonably good fit to data throughout the CBL cannot be obtained by simply varying the value of C_B. The TCL model of Craft et al. (1996), $\Pi_i^B = \left(\frac{1}{3}\delta_{ij} - a_{ij}\right) \beta_j \langle \theta^2 \rangle$, where $a_{ij} = 2\frac{\langle u_i u_j \rangle}{\langle u_i u_i \rangle} - \frac{2}{3}\delta_{ij}$ is the departure-from-isotropy tensor, shows better agreement with LES data although some uncertainties remain. The relative importance of the buoyancy contribution to Π_i decreases with the increasing rotation rate.

In contrast, Π_i^C becomes more important as the rotation rate increases. Neither the simplest linear model for the Coriolis contribution, $\Pi_i^C = C_C \epsilon_{ijk} \Omega_j \langle u_k \theta \rangle$, where C_C is a dimensionless constant, nor a more complex model, where C_C is not a constant but a non-linear function of a_{ij}, is adequate. Neither model appropriately accounts for the component of the angular velocity of rotation that is parallel to the component of the pressure gradient in question. In the seemingly simplest case considered in the present paper, where the rotation vector is

aligned with the vector of gravity, these models yield Π_i^C that is identically zero.

3 Proposed formulation for Π_i^C

In an attempt to develop a more realistic model of Π_i^C, we basically adhere to the TCL approach of Craft et al. (1996). Π_i^C is represented in the form $\Pi_i^C = -2b_{kji}\epsilon_{jlk}\Omega_l$, where the tensor b_{kji} should satisfy the conditions of symmetry, $b_{kji} = b_{kij}$, continuity, $b_{kki} = 0$, and normalisation, $b_{kjj} = \langle u_k\theta\rangle$. We assume that in turbulent flows strongly affected by the background rotation the tensor b_{kji}, apart from being a function of $\langle u_i\theta\rangle$ and a_{ij}, explicitly depends on the rotation tensor $r_{ij} = 2\epsilon_{ilj}\Omega_l\tau$, where τ is the turbulence time scale, which can be set equal either to the turbulence energy dissipation time scale, $\tau = \langle u_iu_i\rangle / 2\langle\epsilon\rangle$, or to the time scale of the dissipation of the temperature variance, $\tau = \langle\theta^2\rangle / \langle\epsilon_\theta\rangle$. With due regard for the linearity principle, suggesting that b_{kji} should be linear in $\langle u_i\theta\rangle$, we consider an expression for b_{kji} of the third order in a_{ij} and of the first order in r_{ij}. Dimensionless constants in that expression are determined by applying the above symmetry, continuity and normalisation constraints, and the TCL constraint. The TCL constraint requires that, when one of the velocity components vanishes, the net Coriolis contribution to the transport equation for the corresponding component of the temperature flux also vanishes. For Π_3^C, this gives $b_{kj3}\epsilon_{jlk}\Omega_l - \epsilon_{3lk}\Omega_l\langle u_k\theta\rangle = 0$. As a result, we obtain an expression for Π_i^C that contains only one extra empirical coefficient as compared to models that are linear in $\epsilon_{ijk}\Omega_j$. In the case considered in the present study, where only the vertical component of the angular velocity of rotation is present, it greatly simplifies to give

$$\Pi_3^C = \tilde{C}_C\Omega^2\tau\left(1 + \frac{3}{8}a_{33}\right)\langle u_3\theta\rangle\,, \tag{1}$$

where $\tilde{C}_C$ is a dimensionless constant.

As seen from Fig. 1, the proposed formulation with $\tau = \langle\theta^2\rangle / \langle\epsilon_\theta\rangle$ appears to satisfactorily compare with the LES data in the core of the CBL. The model fails in the entrainment layer at the CBL outer edge. The entrainment layer requires special consideration.

4 Conclusions

- The pressure-potential temperature covariance in free and rotating convection is analysed through large-eddy simulation.
- Using the framework of the two-component-limit model of Craft et al. (1996), an improved formulation for the Coriolis part of Π_i is developed and checked against LES data.

Acknowledgements. Thanks are due to Tim Craft, Vladimir Gryanik and Dirk Olbers for many helpful suggestions. This work was supported by the Ger-

man Co-ordinating Office of the World Ocean Circulation Experiment (Grant 03F0157A), and partially supported by the EU Projects CARTUM (EC Contract Mas3-CT98-0172) and INTAS 97-0734. It is the contribution No. 1769 of the Alfred Wegener Institute for Polar and Marine Research.

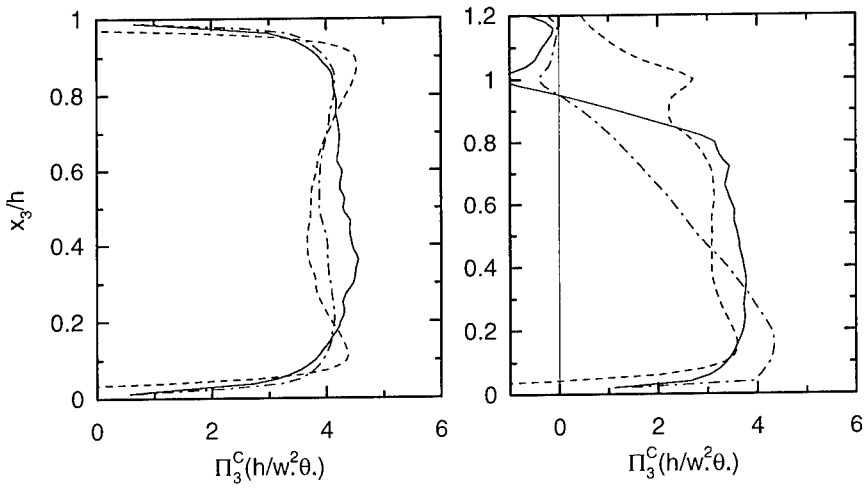


Figure 1. Vertical profiles of the Coriolis component of the potential-temperature/pressure-gradient covariance in convection between the two rigid boundaries, left panel, and in the CBL growing into a quiescent stably stratified fluid, right panel. Dashed curves show Π_3^C from the LES data. Dot-dashed curves are computed from Eq. (1) with $\tilde{C}_C = 0.16$ and $\tau = \langle u_i u_i \rangle / 2 \langle \epsilon \rangle$. Solid curves are computed from Eq. (1) with $\tilde{C}_C = 0.16$ and $\tau = \langle \theta^2 \rangle / \langle \epsilon_\theta \rangle$. Curves are normalised with $h^{-1} w_*^2 \theta_*$, where $w_* = (B_s h)^{1/3}$ and $\theta_* = Q_s / w_*$ are the Deardorff convective velocity and temperature scales (Q_s is the surface potential temperature flux).

References

[1] Craft, T. J., N. Z. Ince, and B. E. Launder. Recent developments in second-moment closure for buoyancy-affected flows. *Dyn. Atmos. Oceans*, 23:99–114, 1996.

[2] Hassid, S., and B. Galperin. Modeling rotating flows in neutral and unstable stratification. *J. Geophys. Res.*, 99:12,533–12,548, 1994.

[3] Mironov, D. V., V. M. Gryanik, C.-H. Moeng, D. J. Olbers, and T. H. Warncke. Vertical turbulence structure and second-moment budgets in convection with rotation: a large-eddy simulation study. *Quart. J. Roy. Meteor. Soc.*, 126:477–516, 2000.

ADVANCES IN TURBULENCE VIII
Proceedings of the Eighth European Turbulence Conference
C. Dopazo et al. (Eds.)
© CIMNE, Barcelona 2000

Turbulence universality in laboratory and atmospheric observations and its theoretical investigation

S. Gordienko[2], S. Moiseev[2], A. Eidelman[1] and H. Branover[1]

[1]Center for MHD Studies, Ben-Gurion University of the Negev, Beer-Sheva, Israel
[2]Space Research Institute, RAS, Moscow, Russia

Contact e-mail: eidel@bgumail.bgu.ac.il ; moiseev@mx.iki.rssi.ru

The basic result of turbulence theory is the Kolmogorov spectrum experimentally confirmed both in laboratory studies and atmospheric observations [1]. It was derived from the hypothesis that the only dimensional constant of the developed turbulence in the inertial range is the rate of energy dissipation per unit mass. Attempts to justify this spectrum theoretically have not yielded entirely satisfactory results yet. Meanwhile, the Kolmogorov spectrum is not the only spectrum that has been observed experimentally in turbulent incompressible fluids [2]. We study universal spectral ranges and parameters governing their onset when the finite correlation time of the force that drives fluid motion is taken into account. Turbulent flows were found for which Kolmogorov's theory is valid and those that cannot be described by it [3], [4].

To describe large Reynolds numbers flows, the Euler equation with external force $\mathbf{f}(\mathbf{r},t)$ is applied

$$\frac{\partial \mathbf{v}}{\partial t} + (\mathbf{v}\nabla)\mathbf{v} = -\nabla p + \mathbf{f}(\mathbf{r},t), \quad div\mathbf{v} = 0 \tag{1}$$

$$< \mathbf{f}(\mathbf{r},t) >= 0, \quad < \mathbf{f}(\mathbf{r}_1,t_1)\mathbf{f}(\mathbf{r}_2,t_2) >= f_0^2 K\left(\frac{t_1-t_2}{\tau_0}, \frac{\mathbf{r}_1-\mathbf{r}_2}{r_0}\right) \tag{2}$$

Here K describes correlational properties of the force $\mathbf{f}$ sustaining media in motion, and $\int K\left(\frac{t}{\tau_0}, \frac{\mathbf{r}}{r_0}\right) d\mathbf{r}dt = r_0^3\tau_0$ by the definition of f_0^2 (r_0 and τ_0 are spatial and time scales of the acting force). The last integral converges and is nonzero; it constitutes the only limit imposed on the force that brings the liquid into motion. Without any loss of generality, we consider the force $\mathbf{f}$ as purely solenoidal and include potential part in the pressure gradient.

In order to study the spectral properties of the problem stated by Eq. (1), a kinetic equation for the Lagrangian particles of an incompressible fluid in the

limit $Re \to +\infty$ was used and the generalized two-particle distribution function $F_2(t,1,2)$ was obtained [5]. If that function is a solution of the kinetic equation, then the function

$$F_2^{(\Delta,\lambda)}(t,1,2) = \lambda^{-18\Delta-6} F_2(\lambda^{1+\Delta}t, \lambda\mathbf{r}_1, \lambda^{-\Delta}\mathbf{v}_1, \lambda^{-1-2\Delta}\mathbf{a}_1, \lambda\mathbf{r}_2, \lambda^{-\Delta}\mathbf{v}_2, \lambda^{-1-2\Delta}\mathbf{a}_2) \tag{3}$$

as can be easily shown, is also its solution, if an external force is

$$\mathbf{f}^{(\Delta,\lambda)}(\mathbf{r},t) = \lambda^{2\Delta+1}\mathbf{f}(\lambda\mathbf{r}, \lambda^{1+\Delta}t), \tag{4}$$

where $\lambda > 0$ and Δ are arbitrary numbers [3]. The kinetic equation formalism makes it possible to describe turbulence in terms of an evolution problem.

In order to study the large-scale structure of a flow, we choose the number Δ so that in the limit $\lambda \to +\infty$ the function $F_2^{(\Delta,\lambda)}(t,1,2)$ approaches a finite limit. This requires that the correlator of the force (4) has a finite limit as $\lambda \to +\infty$, and therefore it can be shown that $\Delta = \Delta_\infty = 2/3$ and the relation

$$< \mathbf{v}(\mathbf{r},t) \cdot \mathbf{v}(0,t) >= C_1 \left(\frac{f_0^2 r_0^3 \tau_0}{r^2} \right)^{2/3} \quad \text{for } r >> \max\left(r_0, \left(\frac{f_0 \tau_0^2}{r_0} \right)^{2/5} r_0 \right) \tag{5}$$

holds, where C_1 is a universal constant. The governing parameter in the large-scale range is $\varepsilon_0' = f_0^2 r_0^3 \tau_0$. We can confirm that the correlator (5) is propoprtional to $1/r^{4/3}$ at large distances. The power law character of the right hand side of Eq. (5) was not postulated, but proven. The correlator (5) leads to a spectrum $E(k) \propto k^{1/3}$ in the large-scale range, as confirmed experimentally.

The universality of large-scale turbulence was detected in our magnetohydrodynamic (MHD) experiments, where mercury flow was placed into a transverse magnetic field [6]. The peculiarities of the behavior of large-scale turbulence lead to the appearance of a spectral range with the slope of 1/3. A phenomenological model [6] developed for the description of large-scale range of such turbulence spectra involved total dissipation $\varepsilon_0 = \int\limits_R \varepsilon(r) d\mathbf{r}$ in the spatial region R as a governing parameter similar to ε_0' derived above from the kinetic equation. Therefore, a well-grounded assumption can be made that the revealed universality obtained rigorously for the case without intermittency also exists in intermittent flows.

Our experimental results show that it is large-scale turbulence that possesses the feature of universality even under the condition of different self-similar small-scale fluctuation modes. In fact, there exist spectra obtained in various turbulent flows which have the slope 1/3 in the large-scale range, whereas their slopes in small scales are different. Thus, MHD turbulence spectra have -7/3 slope in the small-scale range. With increasing interaction parameter and turbulence transition into intermittent mode, the slope in this range becomes close to -4. However, despite this, the spectral slope in the large-scale range remains close to 1/3 in both cases. The spectral slope 1/3 also is observed in a stable atmospheric

boundary layer [7] and in such an excited dynamic system as cirrus [8], where spectral slope in small-scale range is also close to helical one [9]. There are also observed turbulence spectra where the large-scale spectral slope 1/3 conjugates with Kolmogorov's spectrum -5/3 in the small-scale range. Such velocity spectra are observed in the atmospheric boundary layer [10], [11]. Both atmospheric and MHD turbulence spectra discussed above clearly demonstrate large-scale spectral slope 1/3. Now we can think that formal difficulties in the validation of Kolmogorov's spectrum connected with infrared divergence were hiding a new physical phenomenon, namely, the universality of large-scale turbulence.

The examination of the small-scale structure of the flow is reduced to choosing $\Delta = \Delta_0 = -1/2$ in Eq. (4), which ensures the existence of a finite homogeneous function $\lim_{\lambda\to+0} F_2^{(-1/2,\lambda)}$. This implies that

$$< (\mathbf{v}(\mathbf{r},t) - \mathbf{v}(0,t))^2 >= C_2 f_0 r \text{ for } r << \min\left(r_0, f_0\tau_0^2\right), \tag{6}$$

where C_2 is a universal constant. A numerical study has been made of turbulent flows driven by a constant force applied to the fluid [12]. It was found that in certain directions (in the simulations the external force was chosen to have a spatial period and not depend on time) a spectrum $E(k) \sim 1/k^2$ is formed, rather than the Kolmogorov spectrum $E(k) \sim 1/k^{5/3}$. This is in accord with Eq. (6) and, we believe, validates the ideas developed here.

To study the flow at scales from r_0 to $f_0\tau_0^2$, we will discuss a limiting case $\gamma = f_0\tau_0^2/r_0 << 1$. If $\gamma << 1$ and $|\mathbf{r}_1 - \mathbf{r}_2| << r_0$ the force correlator (2) can be set equal to

$$< \mathbf{f}(\mathbf{r}_1,t_1)\cdot\mathbf{f}(\mathbf{r}_2,t_2) >= f_0^2 K\left(\frac{t_1-t_2}{\tau_0},0\right) \tag{7}$$

Eq. (7) allows the discussion for distances $|\mathbf{r}_1 - \mathbf{r}_2| << r_0$, while the limit $\lambda \to +\infty$ ensures it for $|\mathbf{r}_1 - \mathbf{r}_2| >> \gamma r_0$. Thus, for $\gamma r_0 << |\mathbf{r}_1 - \mathbf{r}_2| << r_0$, the flow can be described by a uniform function $\lim_{\lambda\to+\infty} F_2^{(-1/3,\lambda)}$, and

$$< (\mathbf{v}(\mathbf{r},t) - \mathbf{v}(\mathbf{0},t))^2 >= C_3(f_0^2\tau_0 r)^{2/3} \text{ for } \gamma r_0 << r << r_0 \tag{8}$$

holds, i.e., the Kolmogorov-Obukhov law is satisfied within this scaling interval. Therefore, for the discussed method of exciting turbulence, Kolmogorov spectrum develops only when the condition $\gamma << 1$ is imposed on the external force. Only in this case does a constant with the dimensions of power dissipated per unit mass stops to be the determining parameter within a certain spectral range.

The energy dissipated per unit time per unit mass (specific power dissipation ϵ), is determined by the new dimensionless parameter $\Gamma = \gamma^{4/3}\,\mathrm{Re}$, where Re $= r_0(f_0^2 r_0\tau_0)^{1/3}/\nu$ for $\gamma << 1$ and Re $= r_0(f_0 r_0)^{1/2}/\nu$ for $\gamma >> 1$. There are three cases that can occur in turbulent flows (Re $>> 1$). For $\gamma << 1$ and $\Gamma << 1$, according to Eq. (6), the viscous length exceeds $f_0\tau_0^2$, i.e., the Kolmogorov spectrum is immediately adjacent to the viscous range. The specific power dissipation in this case can be estimated as $\epsilon \sim f_0^2\tau_0$ (the viscous loss

over scale lengths on the order of the viscous length), and it is independent of the viscosity (cf. Eq. (8)). This result is entirely consistent with the, by now, classical statement that viscous losses in a turbulent fluid are independent of the viscosity value. However, as we shall now verify, this case is only valid as long as the Kolmogorov range is immediately adjacent to the viscous range and therefore a spectrum range with $E(k) \sim 1/k^2$ is absent.

One of the main results of this study is a proof that the concepts of the universality of developed turbulence in incompressible fluids arising from the classical work of Kolmogorov do need substantial refinement. An important new result obtained by taking the finite correlation time of the driving source into account is some nontrivial physics of the energy transfer over the spectrum. Namely, several universal ranges actually appear in the turbulent spectrum, whose appearance, relative position and wavenumber interval are determined by the parameters of the source that drives the fluid into motion. The universality of large-scale turbulence, as the theoretical study and the experiment show, is independent of small-scale turbulence modes. Classification of turbulent flows established here for the first time may be of interest in a number of geophysical and technological problems.

References

[1] Monin, A.S. and Yaglom, A. M. Statistical Fluid Mechanics, vols. 1 and 2, MIT Press, Cambridge, MA (1971, 1975).

[2] Branover, H., Eidelman, A., Golbraikh, E., and Moiseev, S. Turbulence and Structures. Academic Press, N.Y., 269 pp. (1999).

[3] Gordienko, S. N. and Moiseev, S. S. JETP Lett. 68, 204 (1998).

[4] Gordienko, S. N. and Moiseev, S. S. JETP, 89, 5, 880 (1999).

[5] Gordienko, S. N. Plasma Phys. Rep. 25,119 (1999).

[6] Branover, H., Eidelman, A., Nagorny, M. and Kireev, M. In: Progress in Turbulence Research, AIAA 162,64 (1994).

[7] Caughey, S.J. Boundary-Layer Met. 11, 3-14 (1977).

[8] Gultepe, I. and Starr, D. O'C. J. Atmosph. Sci. 52, 4159-4182 (1995).

[9] Eidelman, A., Branover, H., Moiseev, S.S., and Gordienko, S.N. Phys. Chem. Earth (B), v. 25, No. 1, 35-38 (2000).

[10] Tjernstrom, M. and Friehe, C.A. J. Atmosph. Ocean. Technol. 8, 19-40 (1991).

[11] Kaimal, J.C. et al. J. Atmosph. Sci. 39, 1098 -1114 (1982).

[12] Borue, V. and Orszag, S. J. Fluid Mech. 306, 293 (1995).

ADVANCES IN TURBULENCE VIII
Proceedings of the Eighth European Turbulence Conference
C. Dopazo et al. (Eds.)
© CIMNE, Barcelona 2000

Spectra of turbulence in boundary layers near the ground

P. Carlotti [1,2] and J.C.R. Hunt [3,4]

[1] Dept of Applied Mathematics and Theoretical Physics,
University of Cambridge, Silver street, Cambridge, UK
[2] Centre National de Recherches Météorologiques, Météo France, Toulouse
[3] Depts of Space Climate Physics and Geological Sciences,
University College, Gower Street, London WC1, UK
[4] J.M. Burgers centre, Delft University of Technology, Delft, Netherlands

Contact e-mail : P.Carlotti@damtp.cam.ac.uk

abstract In the high Reynolds number boundary layer, although the shear stress is constant and the mean velocity profile is logarithmic throughout the surface layer, the turbulence structure changes near the wall in a lower 'eddy surface layer'. It is shown that measurements of spectra and correlations are consistent with the mechanisms of mean shear distortion, blocking and shear stresses acting on the largest eddies as they impinge from the outer layer onto the wall (top-down concept) and with the new results of Rapid Distortion Theory applied to these inhomogeneous flows, using the hypothesis of a finite shear strain.

1 Introduction

Recent atmospheric and high Reynolds number laboratory turbulent boundary layer measurements have shown how the one-dimensional spectra and cospectra E_{11}, E_{22}, E_{33}, E_{13} of the three velocity components (u_1, u_2, u_3) vary rapidly and in quite different ways near the ground (where $z = 0$) (fig. 1) (Fuehrer & Friehe [1], Kim & Adrian [5]). Moreover, the characteristic streamwise length of the eddies near the ground, Λ, can be as large as three times the boundary layer depth h (even extending to $17h$ for pipe flow (Kim & Adrian [5])).

The conceptual analysis of such a high Reynolds number boundary layer is made in Hunt & Morrison [4], who showed that the main mechanism is a top-down behaviour, where eddies formed in a layer above the surface impinge onto the wall. The atmospheric boundary layer can be divided into three sublayers (see fig. 2), the middle layer (ML) where the effects of shear (and of the Coriolis forces in the case of the atmospheric boundary layer) dominate , the surface layer (SL) where the eddy motions are dominated by the effects of shear and blocking by the wall and which is characterised by a logarithmic velocity profile, and the eddy surface layer (ESL) where the main effects are blocking of the eddies and the creation of internal boundary layers within the eddies (Hunt & Carlotti [3]). If we denote by h the height of the boundary layer, the surface layer is typically

of height $h/10$ and the eddy surface layer of height $h/100$. Note that in the usual terminology the surface layer and eddy surface layer are the same, because the latter needs a very high Reynolds number to exist.

2 Flow calculations

In the SL and the ESL the dominant distorting mechanisms are the blocking of the eddies by the wall (B), the shearing of the eddies by the mean flow (S) and the non-linear deformation of the eddies (NL). We can sort these mechanism from the faster to the slower : (B), (S), (NL). Because they act on different time scales, these processes can be analysed separately. More precisely, the slope of the spectra is due to (NL). However, the distribution of energy between the components is controlled by fast processes, and primarily by (B). The approach we take here is therefore to analyse the effects of (B) and (S) using Rapid Distortion Theory (RDT) (i.e. the linearisation of the Navier-Stokes equations with a fully turbulent state as initial condition), in the idealised cases of a uniform mean flow U_0 and shear flow $U = U_0(1+\alpha z)$ above a rigid surface, generalising the work of Lee & Hunt [6] and Mann [7] to account for different form of the spectra. The turbulence is assumed to be homogeneous far away from the rigid boundary.

Analysis of the SL. In the SL, we have to consider both (S) and (B). The form of the spectrum well above the ground is taken as $E(k) \approx k^{-2p}$, where $2p = 5/3$ in the case of a Kolmogorov spectrum. We concentrate on the calculation of the length scales

$$L_{33}^{(x_j\pm)} = \frac{\int_0^\infty \overline{u_3(\underline{x})u_3(\underline{x} \pm r\underline{e}_j)}dr}{\overline{u_3^2}(\underline{x})} \qquad (1)$$

The main result of this analysis is shown on fig. 3. For $2p > 2$, the length scales behave quite differently, in particular $L_{33}^{(z+)}$ which goes to a singular limit when $z \to 0$. This can be explained as follows : the faster the spectrum roll-off is, the smoother is the velocity field, and therefore the stronger the remote correlations are. The effect of (S) in addition to (B) is only a small change in the numerical constants as far as u_3 only is concerned. On the other hand, in the case of u_1 and u_2, the governing process is (S), as shown by Mann [7].

The case $2p > 2$ can originate not only from a low Reynolds number, but also from a subgrid model in Large Eddy Simulation (LES). Obviously, the singular limit is a matching condition for the ESL below. Since the ESL is nearly always parametrised in LES, a LES having a too fast roll-off of the spectrum above the ground needs a parametrisation of the ESL taking into account this singularity.

Analysis of the ESL. The problem in the ESL is more complex, since the non-linear effects change the behaviour of the spectrum (see fig. 1) through the creation of substructures within the eddies (see fig. 2 and Hunt & Carlotti [3] and references in it). However, as explained earlier, (B) is a fast elliptical process, which controls the distribution of energy between the components. A dimensional analysis show that

$$E_{ij}(k_1, z) = \frac{1}{2\pi}\frac{E_0}{4\pi}k_1^{-2p}\widetilde{E}_{ij}(z') \qquad \text{with } z' = k_1 z, \qquad (2)$$

and RDT is used to get the expression of $\widetilde{E}_{ij}(z')$. This calculation can be made analytically in the cases (B) and (S+B). However, only the former leads to a tractable expression. As a result of the slow (NL) processes, the exponent $2p$ of the energy spectrum is 1 if $k_1 \ll 1/z$ and 5/3 if $k_1 \ll 1/z$, we derive the result plotted on fig. 4. Note that $E_{11}(k_1)$ behaves as the energy spectrum $E(k)$ but $E_{33} \approx u_*^2 z$ for $k_1 < 1/z$, u_* being the friction velocity. However, the case (B) has some strong limitation, the main one being that E_{13} (and therefore the Reynolds stress $-\overline{u_1 u_3}$) remains equals to zero. We can introduce (S) in the case $1/L^H < k_1 < 1/z$ using directly the simplified Fourier-tranformed Navier-Stokes equations, to get $E_{13} = -\beta E_{33}$, where β is the non-dimensional shear. Hence the case (S+B) can be understood as a perturbation of the case (B) ; this leads to $E_{13} \approx u_*^2 z$ as observed.

Obviously these results can only be valid in the range $k_1 \gg 1/L^H$, L^H being the size of the large eddies well above the boundary. Therefore, the magnitude of Λ can not be predicted by RDT. The actual value of the slope of the spectrum, $2p$, can not be predicted by RDT either. However, physical and statistical arguments can be given (cf. Hunt & Carlotti [3]) for these two facts.

3 Conclusion

The way that spectra change in the SL depends quite critically on the form of the spectrum well above the ground, so that the changes for a Kolmogorov ($-5/3$) spectrum differ significantly from those at low Reynolds number ($\approx k^{-2p}$ where $2p > 2$) (fig. 3). Between the SL and the ESL, E_{11} and E_{22} change dramatically while E_{33}, E_{13} and therefore the Reynolds stresses do not, because E_{33} is determined by u_* and z only. This is the reason why the mean velocity profile remains logarithmic in the ESL even if the structure of the horizontal component of turbulence changes dramatically.

References

[1] P.L. Fuehrer and C.A. Friehe. A physically-based turbulent velocity time series decomposition *Boundary Layer Meteorology* 90(2):241-295, 1999.

[2] J.C.R. Hunt. Turbulence structure in thermal convection and shear-free boundary layers. *J. Fluid Mech.* 138:161-184, 1984.

[3] J.C.R. Hunt and P. Carlotti. Statistical structure of the high Reynolds number turbulent boundary layer. *Flow, turbulence and combustion* X:xx-xx, 2000

[4] J.C.R. Hunt and J.F. Morrison. Eddy structure in turbulent boundary layers. *Euro. J. Mech.* X,xx-xx, 2000

[5] K.C. Kim and R.J. Adrian. Very large scales motion in the outer boundary layer. *Phys. Fluids* 11(2):417-422, 1999.

[6] M.J. Lee and J.C.R. Hunt. The structure of sheared turbulence near a plane boundary. in *7th symposium on turbulent shear flows,* Stanford University, pp. 8.1.1-8.1.6, 1989.

[7] J. Mann. The spatial structure of of neutral atmospheric surface layer turbulence. *J. Fluid Mech.* 273:141-168, 1994

[8] A.A Townsend. The structure of turbulent shear flow *Cambridge University Press,* 1976.

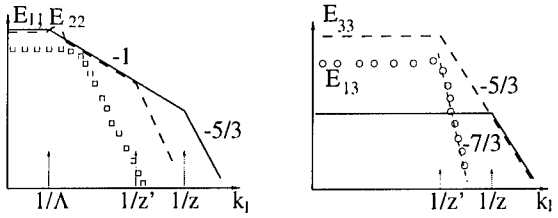


Figure 1: measured spectrum in atmosphere and pipe ; □ : spectra above the surface layer ; solid and dashed lines : E_{11}, E_{22} and E_{33} in the surface layer ; ∘ : E_{13} in the surface layer

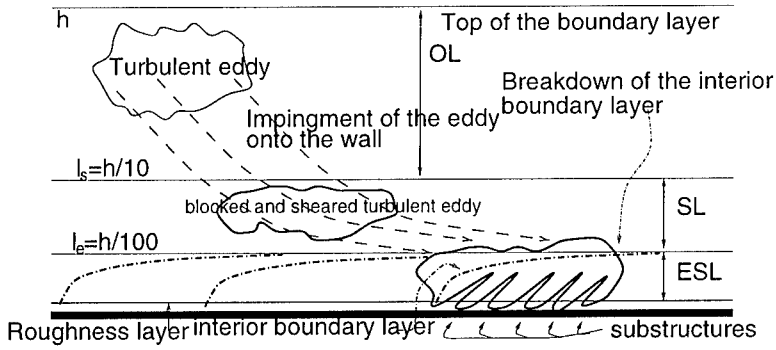


Figure 2: sketch of a typical high Reynolds number boundary layer ; $h \approx 1-2km$, $\ell_s \approx 100 - 200m$, $\ell_e \approx 10 - 20m$, the roughness length is less than $0.1m$ over a field, less than $3m$ over a typical city

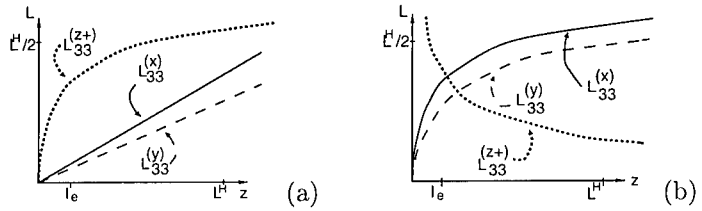


Figure 3: $L_{33}^{(x_i)}$; (a) : $2p = 5/3 < 2$; (b) $2p > 2$.

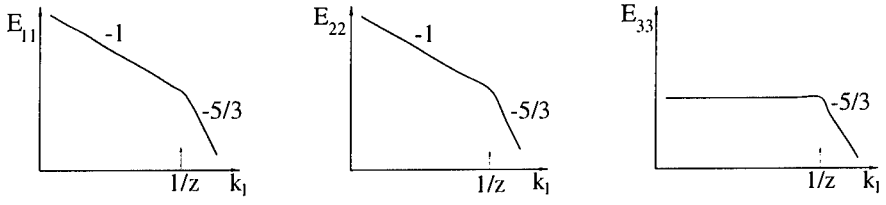


Figure 4: spectra calculated with RDT, assuming the existence of k^{-1} and $k^{-5/3}$ ranges for the energy spectrum

ADVANCES IN TURBULENCE VIII
Proceedings of the Eighth European Turbulence Conference
C. Dopazo et al. (Eds.)
© CIMNE, Barcelona 2000

Non-Local Turbulence in Stably Stratified Boundary Layers

Prof. S. Zilitinkevich[1]

[1]Department of Earth Sciences, Meteorology, Uppsala University
Villavagen 16, SE-752 36 Uppsala, Sweden

Contact e-mail: Sergej.Zilitinkevich@met.uu.se

Traditional theory of the atmospheric stably stratified boundary layers (SBLs) includes the following known formulations.

(i) The Monin and Obukhov (MO) similarity theory of the surface layer based on the length scale $L = -u_*^3/\beta F_{\theta_s}$, where u_* is the friction velocity, β is the buoyancy parameter, and $F_{\theta s}$ is the flux of virtual potential temperature.

(ii) The equilibrium SBL depth scale formulation, $h \propto u_*^2/|f\beta F_{\theta_s}|^{1/2}$, where f is the Coriolis parameter (Zilitinkevich, 1972).

(iii) The SBL bulk resistance and heat/mass transfer laws based on the A, B, C and D similarity functions of the dimensionless stratification parameter $\mu = u_*/|fL|$ (Zilitinkevich, 1967; 1975).

(iv) Conventional turbulence closure models applied to SBLs, such as "k-closure" employing the budget equation for the turbulence kinetic energy k, or "k/ϵ-closure" employing also the budget equation for the energy dissipation rate ϵ, together with turbulent diffusivities [e.g., the Nieuwstadt (1971) analytical k-model neglecting the third-order transport, the Brost and Wyngaard (1973) k-model, and the Lykossov (1998) k/ϵ-model].

Explicitly or implicitly, all these formulations employ the concept of local correspondence between turbulence fluxes and mean gradients,

$$Turbulence \quad Flux \quad = \quad -(Eddy \quad Diffusivity) \times (Mean \quad Gradient). \quad (1)$$

Here, all terms are taken at a given height, z, and moreover, it is supposed that the eddy diffusivity is fully determined by properties of the flow in the vicinity of this height. This concept is nothing other but formal analogy with the molecular diffusion, where Eq. (1) is well grounded by the fact that the molecule free pass is much less than the basic length scale of the flow. Traditional reasoning for applicability of Eq. (1) to stably stratified turbulent flows is as follows. Stable stratification prevents development of large eddies, which is why turbulence transport is performed basically by small eddies. Their length scales are small compared to the mean-flow length scales and the above analogy is justified.

A number of theoretical models employing the local transport concept, including the formulations (i)-(iv), agree quire well with data from measurements in nocturnal SBLs typical of mid latitudes. The MO theory (i) has been very well supported by data in the conditions when the density stratification deviates not too strongly from neutral stratification (e.g., Chapter 4 in Monin and Yaglom, 1971). Some data support the SBL depth formulation (ii) and SBL models employing the turbulence closure schemes (iv). More or less successful efforts were made to specify empirically the similarity functions in the resistance and heat/mass transfer laws (iii).

At the same time there are data, which evidently contradict to the above formulations. Pronounced turbulent fluxes are quite often observed in the conditions when the Richardson number is so large that the conventional MO theory predicts no turbulence (e.g., Larsen et al., 1990; Sempreviva et al., 1992). Recent tracer studies with radon 222 using the global climate model ECHAM4 have disclosed insufficient vertical diffusion in strongly stable stratification at high latitudes (Roeckner and Jacob, 1998). What this means is that the MO-theory-based parameterization employed in ECHAM4 underestimates the turbulence transport. The SBL depth formulation (ii) is not applicable to shallow SBLs typical of the Arctic and Antarctic regions. Here, h strongly depends on the Brunt-Väisälä frequency in the free flow, N (e.g., Zilitinkevich and Mironov, 1996). Empirical plots of the A, B, C and D functions exhibit enormously wide spread of data indicating that other arguments, besides μ, should be taken into account (e.g., Zilitinkevich, 1989a,b).

Recent empirical evidence and theoretical reasoning (Zilitinkevich et al., 1998; Zilitinkevich and Calanca, 2000) suggest that the nature of the SBL is essentially distinguished by the conditions in which the stable stratification is developed. The conventional nocturnal SBLs at mid latitudes usually develop on the background of a deep residual layer, which keeps near-neutral stratification as a memory of convective mixing in the daytime. In such SBLs both shear-generated turbulence and static stability sharply decrease towards the SBL top. Typical SBLs represent comparatively shallow stable layers separated from the stably stratified free atmosphere by a-few-hundred-meter deep neutrally stratified residual layer. Then the SBL turbulence is not affected by internal-wave interactions with the free atmosphere. This explains why the concept of local transport, Eq. (1), and consequently, the formulations (i)-(iv) represent reasonable approximations when applied to mid-latitudinal SBLs.

By contrast, at high latitudes and in coastal regions, the static stability is often kept strongly stable throughout the troposphere both by day and at night. Here, the SBL and the free atmosphere are essentially linked, first of all, through the vertical transport of kinetic energy and potential temperature variance by internal waves. Then the local transport concept is by no means applicable. In particular, the Brunt-Väisälä frequency in the free atmosphere, N, becomes an important parameter governing the structure of the SBL. It affects mean profiles and turbulence statistics in the surface layer, the SBL depth and the

near-surface resistance and heat/mass transfer. First attempts to revise the traditional similarity-theory formulations (i)-(iii) accounting for possible effects of the free-flow stability on "high latitudinal" SBLs are made by Zilitinkevich et al. (1998) and Zilitinkevich and Calanca (2000).

The present paper presents further advance along this line. It is understood that traditional type turbulence closure schemes (iv) employing Eq. (1) are inconsistent with new empirical evidence. To overcome this drawback, the effect of internal waves is incorporated in a more advanced turbulence closure scheme. Some consequences of the new approach are given below.

The most obvious is the revised formulation for the wind and temperature gradients, $\partial u/\partial z$ and $\partial\Theta/\partial z$, in the surface layer,

$$\frac{\partial u}{\partial z} = \frac{u_*}{kz}\left[1 + C_{u1}(1 + C_{u2}S)\frac{z}{L}\right], \frac{\partial\Theta}{\partial z} = \frac{\Theta_*}{k_T z}\left[1 + C_{\theta 1}(1 + C_{\theta 2}S^3)\frac{z}{L}\right], \qquad (2)$$

where $S = NL/u_*$ is a dimensionless parameter characterising the extent to which the surface layer is affected by the free-flow stability, $\Theta_* = -F_{\theta_s}/u_*$, $C_{u1} = 2.1$ and $C_{\theta 1} = 3.2$ are known empirical constants, which appear in the classical formulation, whereas C_{u2} and $C_{\theta 2}$ are new constants (~ 0.4). At $S = 0$, these expressions reduce to the classical ones. However, when the free flow stability is strong ($S > 1$), the classical theory fails. Then the so-called "slope factors" $s_u = (kL/u_*)\partial u/\partial z - L/z$ and $s_\theta = (k_T L/\Theta_*)\partial\Theta/\partial z - L/z$ exhibit essential dependence on S in correspondence with the new theory (Figure 1).

Other advance is a revised formulation for the equilibrium SBL depth, accounting for the effect of the free-flow stability. For the Ekman layer it reads

$$h_E = \frac{C_R u_*}{|f|}\left[1 + \frac{C_R^2 u_*(1 + C_{u2}S)}{C_S^2 |f| L}\right]^{-1/2} \qquad (3)$$

where, $C_R \sim 0.5$ and $C_S \sim 0.7$ are known empirical constants, and $C_{u2} \sim 0.4$ is a new constant, which already appeared in Eq. (2). Eq. (3) covers the whole range of the static stability regimes from neutral to strongly stable and better fits to experimental data than earlier formulations. In particular cases it reduces to the depth scales proposed by Rossby-Montgomery (1935) for the neutrally stratified boundary layer, Zilitinkevich (1972) for the SBL capped by the residual layer ($S \ll 1$), and Pollard et al. (1973) for the upper mixed layer in the ocean dominantly affected by static stability in the thermocline ($S \gg 1$).

For the slope wind driven by the buoyancy force in stable stratification, the proposed theory suggests a new expression for the boundary layer depth,

$$h_{SW} = {C_1}^4 \sqrt{\frac{(u_* L)^2}{(1 + C_{u2})(1 + C_{\theta 2}S^3)(\alpha N)^2}}, \qquad (4)$$

where α is the slope inclination angle, and C_1 is a dimensionless constant to be determined empirically. P. Calanca (private communication) applied this

formula to the height, $z(U_{max})$, of the wind maximum in the low-level jet characteristic of the slope wind. He disclosed a reasonably good correlation between measured $z(U_{max})$ and calculated h_{SW} with $C_1 = 27$ (Figure 2).

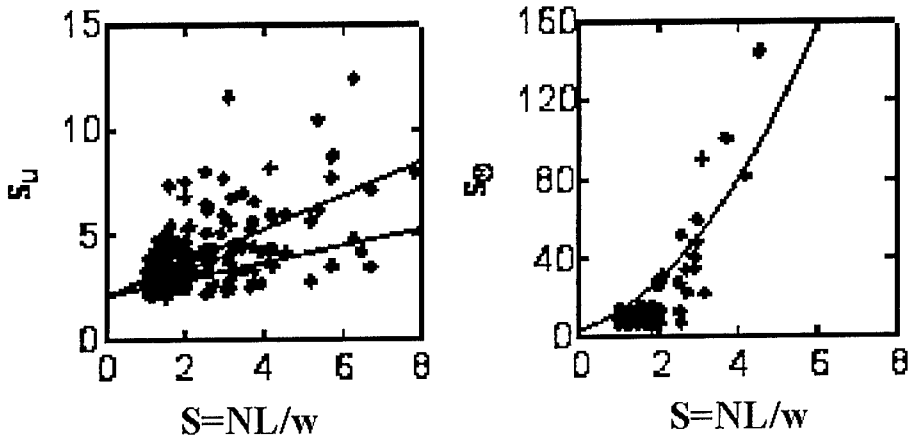


Figure 1: Empirical data on slope factors, s_u and s_θ (Zilitinkevich and Calanca, 2000). In the classical theory, s_u and s_θ are constants.

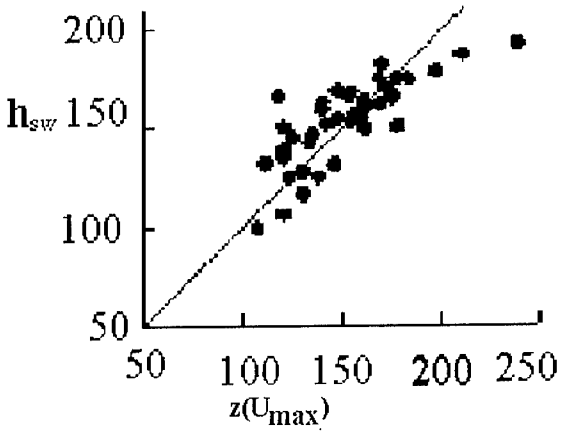


Figure 2: Empirical validation of Eq.(4) as applied to the height of the low-level jet in the slope-wind flow over Greenland (Calanca, private communication).

ADVANCES IN TURBULENCE VIII
Proceedings of the Eighth European Turbulence Conference
C. Dopazo et al. (Eds.)
© CIMNE, Barcelona 2000

Analysis of the pdf of the vertical velocity in the buoyancy-driven atmospheric boundary layer

S. Alberghi[1], F. Tampieri[1],
S. Argentini[2], G. Mastrantonio[2] and A. Viola[2]

[1]ISAO—CNR Bologna (Italy)
[2]IFA—CNR Roma (Italy)

Contact e-mail: f.tampieri@isao.bo.cnr.it

Introduction Improving the knowledge of the statistical properties of the atmospheric boundary layer has an interest for the basic understanding of high Reynolds number flow turbulence and quite relevant practical applications, from numerical modelling of atmospheric processes to environmental issues, to enginnering applications. In this work we examine some statistical properties of time-series of vertical velocity in the Convective Boundary Layer (CBL). In particular the total integral time scale of velocity correlation has been calculated, the probability density function (pdf) has been analysed and a relationship between Kurtosis and Skewness is then proposed.

Data analysis Sodar data were collected at various sites around and in the center of Rome (Italy), during breeze summer days and winter nights. Coherent structures (fig. 1) have been identified in two different situations: 1)in the case of well developed CBL (upward plumes) and 2) in case of negative buoyancy (descending plumes). The sodar systems are triaxial and provide the profiles of radial wind velocity and echo intensity, one for each antenna. A signal to noise (S/N) related parameter (see [9]) and a spurious data evaluation method are used to reject unreliable data. They have been replaced by a linear interpolation in the Fourier analysis and in the autocorrelation coefficient calculation.

As far as situation 1 is concerned, the stationarity of CBL is recognized from the analysis of horizontal wind (constant in modulus and direction below a certain height—typically 400m—and in a certain time interval), and from the analysis of steadyness of mean, variance, skewness and kurtosis of vertical velocity at various heights. Tipically these conditions identify steady periods between 10:00 and 16:30 LT.

The data relative to these periods have been used to calculate the vertical profile of mean ($\simeq 0$ at all heights), variance (which shows a maximum approximately at the center of the Mixed Layer), Skewness and Kurtosis (which increase

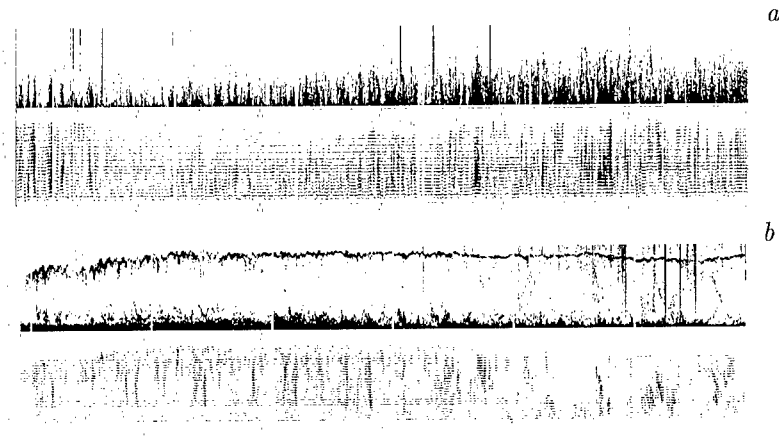


Figure 1: Fac-simile and Vertical velocity data showing: a)updrafts; b)downdrafts (Vertical scale: hundreds of meters).

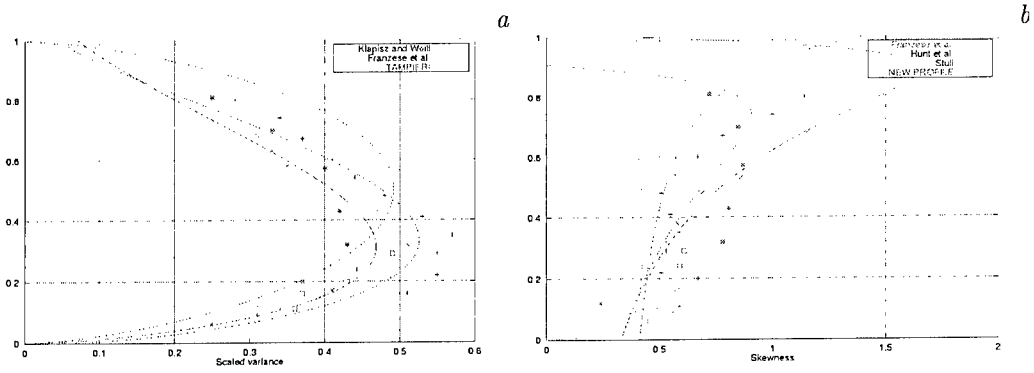


Figure 2: a)Variance and b)Skewness vertical profiles scaled by w_* and z_i (Data shown are the same as in Fig. 3).

with height till 80% of the CBL width, with most values between 0.4 and 1.2 in skewness, and between 3 and 7 in kurtosis). The CBL height z_i and the vertical velocity scale w_* has been estimated fitting data with Stull ([10]) variance profile with the method described in [13]. z_i results to be $\approx 500m$ and $w_* \approx 1.5m/s$. The resulting vertical profiles of variance and skewness are reported in fig. 2, together with previously proposed curves ([3],[5],[6],[10],[11]).

A Skewness–Kurtosis (S–K) relationship can be proposed by fitting the data as in fig. 3. It has been derived according to the idea of a family of parabolic curves of the type $K = \alpha S^2 + \alpha$: the $\alpha = 1$ curve represents a statistical limiting value in the S–K plane, while the $\alpha = 2.43$ curve is our data best-fitting quadratic reltionship. It can be compared with other measurements of

vertical and horizontal velocity in case of shear turbulence: the formers dispose themeselves in a compact zone, different from those in CBL, the latters on a nearly parabolic curve (see also [2]).

An estimate of the value of the typical Eulerian time scale τ_E has been deduced both from the direct evaluation of the integral of the correlation and from the limit for $\omega \to 0$ of the energy spectral density. They both give $\tau_E \approx 40s$ (within a 5%) at all heigths. The corresponding Lagrangian time scale τ_L may be derived (according to [1],[4]) from $\tau_L = C\frac{U}{\sigma_w}\tau_E$ where $C = 0.44$ and the mean wind $U \approx 4m/s$ (approximately constant with height). This evaluation of τ_L is also consistent with that derived from $\tau_L = 0.17 z_i/\sigma_w$ (see [4]).

As far as situation 2 is concerned, repeated downdraughts have been identified and a similar statistical analysis has been performed. It must be noted that such downdraughts are observed during night when a marine well mixed layer moves inland and produces a positive jump of potential temperature and a negative jump in the mixing ratio at its top (fig. 4).

Discussion The results obtained for the CBL allows to make a documented hypotesis about a possible closure for the pdf of vertical velocity, accounting for skewness and kurtosis. In terms of mmi pdf we suggest the choice: $f(w,z) = \exp(-\sum_{k=0}^{4}\lambda_k(z)w^k)$ where $\lambda_k(z)$ are calculated from the selected moment profiles. The actual shapes differ from other ones proposed by previous authors for use in Lagrangian dispersion models (e.g.[7],[12]).

The downdraft case has been investigated on phenomenological bases. Some statistics are presented, without pretending a systematic approach. It is however important to observe that the presence of such structures may alter in a relevant way the dispersive behaviour of the nocturnal boundary layer.

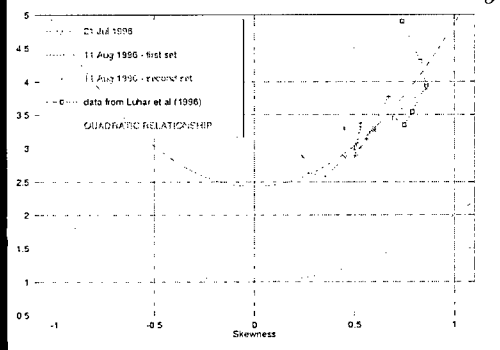


Figure 3: Relationship between Skewness and Kurtosis as a function of z/z_i. The lower curve represents a Skewness-Kurtosis statistical limit.

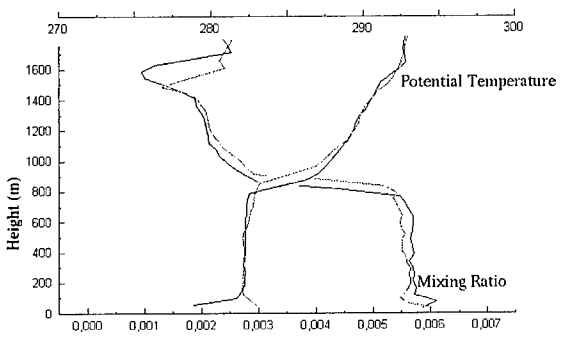


Figure 4: Mixing ratio and Potential Temperature during downdrafts.

References

[1] Degrazia G., Anfossi D., Fraga de Campos Velho H. and Ferrero E., A lagrangian decorrelation time scale for non-homogeneous turbulence, B.L.Met., 86, 525-534, 1998

[2] Durst F., Jovanovic J. and Kanevce Lj., Probability Density Distribution in Turbulent Wall Boundary-Layer Flows, Turbulent Shear Flows 5, 197-220, Springer-Verlag 1987.

[3] Franzese P., Luhar A.K. and Borgas M.S., An efficient Lagrangian stochastic model of vertical dispersion in the convective boundary layer, Atm.Env., 33, 2337-2345, 1999

[4] Hanna S.R., Lagrangian and Eulerian time-scale relations in the daytime boundary layer, J.Appl.Met., 20, 242-249, 1981

[5] Hunt J.C.R., Kaimal J.C. and Gaynor J.E., Eddy structure in the convective boundary layer—new measurements and new concepts, Q.J.R. Meteorol.Soc., 114, 827-858, 1988

[6] Klapisz C. and Weill A., Modèle semi-empirique d'évolution matinale du profil de vent entre le sol et le sommet de l'inversion, J. de Recherches Atmosph., 12, 113-117, 1978

[7] Luhar A.K. and Britter R.E., A random walk model for dispersion in inhomogeneous turbulence in a convective boundary layer, Atm.Env., 23, 1911-1924, 1989

[8] Luhar A.K., Hibberd M.F. and Hurley P.J., Comparison of closure schemes used to specify the velocity pdf in lagrangian stochastic dispersion models for convective conditions, Atm.Env., 30, 1407-1418, 1996

[9] Mastrantonio G. and Fiocco G., Accuracy of wind velocity determinations with Doppler Sodar, J.Appl.Met., 21, 820-830, 1982.

[10] Stull R.B., An introduction to Boundary Layer Meteorology, 370-372, Kluwer Academic Publishers 1988

[11] Tampieri F., Lecture notes on turbulence in the planetary boundary layer, unpublished report, 1994

[12] Thomson D.J., Criteria for selection of stochastic models of particle trajectories in turbulent flows, J.Fl.Mech., 180, 529-556, 1987

[13] Weill A., Klapisz C., Strauss B., Baudin F., Jaupart C., van Gruderbeek P. and Goutorbe J.P., Measuring heat flux and structure Functions of Temperature Fluctuations with an acoustic Doppler sodar, J.Appl.Met., 19, 199-205, 1980

XI

Boundary Layers and Free Shear Flows

ADVANCES IN TURBULENCE VIII
Proceedings of the Eighth European Turbulence Conference
C. Dopazo et al. (Eds.)
© CIMNE, Barcelona 2000

Mixing enhancement in turbulent wall jets

M. Schober and H.-H. Fernholz

Hermann-Föttinger-Institut für Strömungsmechanik
Technische Universität Berlin;
Straße des 17. Juni 135;
10623 Berlin, FRG

Contact e-mail: schober@pi.tu-berlin.de

1 Introduction

A wall jet is a flow that has features of both a boundary layer and a jet. It is often used in mixing devices. The present experimental investigation describes two methods that enhance the mixing of the wall jet with the ambient fluid. The first method uses an oscillating wire near the wall-jet exit to stimulate the formation of large scale coherent structures, the second one the interaction of a wall jet blown into a counter flow, as shown in figure 1.

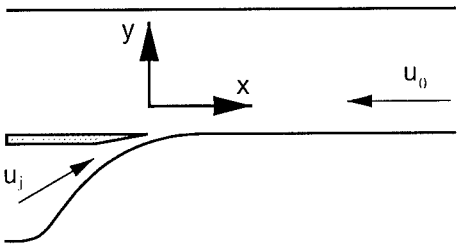


Figure 1: Flow configuration

The investigation was carried out in a low-speed wind tunnel with a cross-section of $0.5 \times 0.5m^2$. Measurements of the mean and fluctuating velocity have been made using Laser-Doppler-anemometry (LDA) and hot-wire anemometry. The surface skin-friction was determined using calibrated wall pulsed-wire probes in regions with flow reversal and wall hot-wires elsewhere. Flow visualisation was performed to give an overall impression of the wall-streamlines. The Reynolds number, based on wall jet slot width b and exit velocity u_j, was $Re_j = 10000$.

2 Mixing enhancement by an oscillating wire

Vandsburger & Ding (1995) noted that an oscillating "music" wire stimulated the energy transfer in a free shear layer. The wire performed flow-induced vibrations, i.e. no external additional input was required. In the present investigation, a

wire was placed into the shear layer originating at the wall-jet nozzle. The flow visualisation study by Schober, Grewe & Fernholz (1999) showed that the wire generates large-scale vortical structures in the wall-jet.

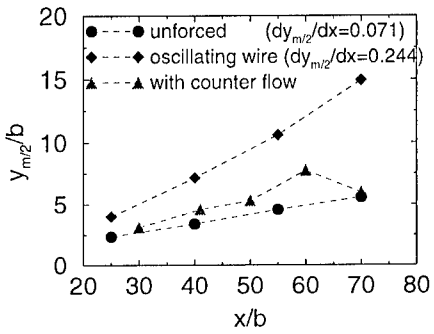


Figure 2: Development of the half width

Figure 2 shows the development of the wall-jet half-width $y_{m/2}/b$ versus the streamwise distance. The half-width $y_{m/2}$ denotes the distance from the wall at which $u(y_{m/2})/u_m = 0.5$, where u_m is the local velocity maximum. The oscillating wire significantly increases the spreading and thus enhances the mixing compared with the unforced case. The skin friction (not shown) in the wall jet was significantly reduced. The two dimensionality of the flow is, however, lost due to the three-dimensional nature of the oscillation.

3 Mixing enhancement by a counter flow

The wall jet in a counter flow is a flow phenomenom which has drawn little attention from fluid dynamicists. This seems to be surprising, since the strong mixing of the wall jet with the counter flow makes it interesting for applications in combustion chambers of aero engines, for example. The flow field contains regions where the velocity and the skin friction change sign, similar to separated flows. It is therefore a special case for the study of separated flow fields with variable height and length, since the ratio of the velocity of the wall jet and the counter flow u_j/u_0, and thus the size of the interaction region can easily be varied.

A first overview of the flow field in the parameter range $3 \leq u_j/u_0 \leq 8$ is given by visualisations of the wall streamlines (figure 3). The Reynolds number of the wall jet was kept constant at $Re_j = 10000$. The aspect ratio of the flow, i.e. the ratio of tunnel width to the wall jet slot width, was $b/B_k = 125$. The separation line is almost straight in the central part of the tunnel for $u_j/u_0 = 3$, becomes convex/concave for 4 and remains concave for higher ratios of u_j/u_0 as seen from the direction of the windtunnel main flow. The three-dimensionality of the flow was increased by the standing vortices near the tunnel side walls once the wall jet had become stronger relative to the boundary layer, forming an increasing obstacle. This is similar to the flow downstream of a normal plate with a long splitter plate (Ruderich & Fernholz 1986). This strong three-dimensionality was not anticipated, since the wall jet and the counter flow both were two-dimensional individually.

Figure 4 shows the velocity vectors and the stream function for the case of

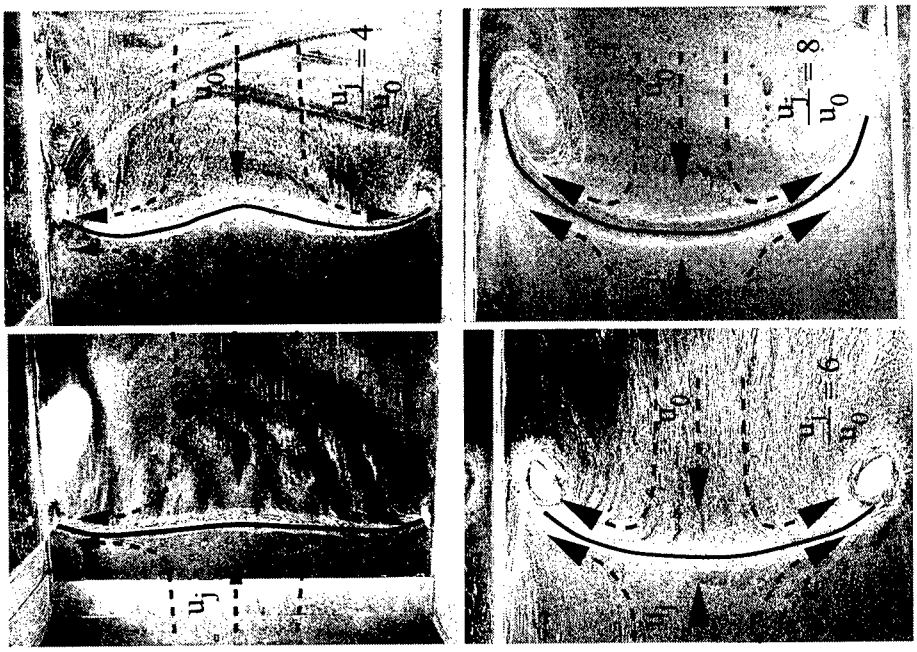


Figure 3: Visualisation of wall streamlines at different velocity ratios $u_j/u_0 =$ 3, 4, 6, 8

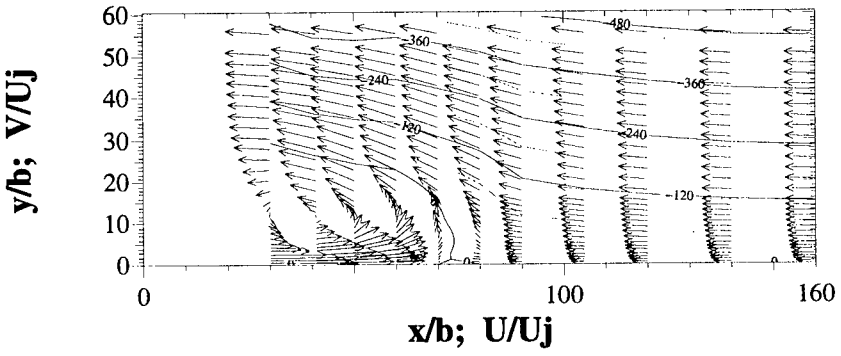


Figure 4: Velocity and stream function ($u_j/u_0 = 4$)

$u_j/u_0 = 4$. The wall jet exhibits a strong upward v-component of the velocity as it approaches the separation line. The counter flow causes a free stagnation point, deflects the wall jet away from the wall and then into the direction of the counter flow. The velocity within the potential core of the counter flow, that is

for $y/b > 30$, is larger near the wall jet exit than far away from it. This is due to the displacement of the counter flow by the the wall jet.

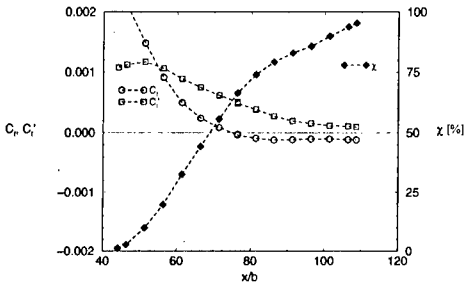


Figure 5: Skin-friction coefficients c_f, c_f' and reverse flow factor χ for $u_j/u_0 = 4$ (wall pulsed wire probe)

Figure 5 shows the skin friction coefficient c_f, the fluctuating friction coefficient $c_f' = (\overline{\tau_w'^2})^{0.5}/0.5\rho u_j^2$ and the reverse flow factor χ which is defined as the number of samples in the direction of the free stream divided by the total number of samples. The position at which $\chi = 50\%$ and $c_f = 0$ do normally coincide in separated flows (Dengel & Fernholz 1990). Here, however, $\chi = 50\%$ at $x/b = 69$ and $c_f = 0$ at $x/b = 74$. This means, that at separation ($c_f = 0$) there are few but strong events from the wall jet and more but weak events from the counter flowing boundary layer. This relative strength of the wall jet also explains why the fluctuating friction coefficient c_f' reaches its maximum of 0.0012 at $x/b \approx 50$, upstream of separation.

The development of the half-width $y_{m/2}/b$ in figure 2 is not as large as for the case with the oscillating wire, but still larger as for the unforced case. Furthermore, mixing takes places upstream of the injection of the wall jet, if viewed from the boundary layer point of view. It thus leads to shorter mixing regions.

References

DENGEL, P. & FERNHOLZ, H. H., 1990. An experimental investigation of an incompressible turbulent boundary layer in the vincinity of separation. *J. Fluid Mech.* **212**, 615–636.

RUDERICH, R. & FERNHOLZ, H. H., 1986. An experimental investigation of the structure of a turbulent shear flow with separation, reverse flow, and reattachment. *J. Fluid Mech.* **163**, 283–322.

SCHOBER, M., GREWE, F. & FERNHOLZ, H. H., 1999. Turbulence control in wall jets: a visualisation study. *Int. J. Fluid Dyn.* **3**. Article 1.

VANDSBURGER, U. & DING, C., 1995. Self-excited wire method for the control of turbulent mixing layers. *AIAA Journ.* **33**, 1032–1037.

ADVANCES IN TURBULENCE VIII
Proceedings of the Eighth European Turbulence Conference
C. Dopazo et al. (Eds.)
© CIMNE, Barcelona 2000

Turbulence characteristics in pipe flow with swirl

M. Schmidts [1] and V. Vasanta Ram [1]

[1]Institut fuer Thermo- und Fluiddynamik, Ruhr-Universität Bochum
D-44780 Bochum, Germany

Contact e-mail: schmidts@lstm-ruhr-uni-bochum.de

1 Abstract

The present work is an experimental study of the evolution of swirl introduced at an initial station into the turbulent flow in a pipe. The swirl is generated by a specially designed device based on the principle of a rotating tube bundle so that the experimentally realized flow exhibits the characteristic of solid-body rotation over essentially the entire pipe cross section at the initial station. The evolution of all the components of the mean velocity vector and Reynolds stress tensor in this flow is measured by 3-D LDV employing the refractive index matching technique at rotation numbers of up to one. The measured data have been analyzed to yield insight into some outstanding features of turbulence behaviour in the flow that are important for turbulence modelling.

2 Introduction and scope of the work

Swirl in a flow, a term which we use here to denote a flow with streamlines wound in the shape of a helix, is a common phenomenon occuring both in nature and in engineering. The helical winding of the streamlines in a flow with swirl implies the streamline curvature not lying entirely in one plane, and this is a salient topological feature of these flows. A consequence of this topological feature of importance to the modelling of turbulence in the flow is that the principal axes of the rate of strain tensor and of the Reynolds stress tensor need not align with each other in the entire flow region. High swirl rates also tend to suppress turbulence in the core. To be able to answer some of the fundamental questions raised in these flows it is desirable to generate flows with a well defined swirl distribution in experiments, measure all the components of the Reynolds stresses therein, analyze the measured data in a sound theoretical framework, and establish the properties of turbulence in this flow. This is the goal of the present work.

3 Experiments

The experimental facility and the experiments are described in Vasanta Ram *et al* [1].

3-D LDV measurements have been conducted in a specially designed facility in which a "rotating tube bundle" generates at an initial station a swirling flow with solid-body rotation to a high degree of accuracy over a wide range of rotation numbers. This flow evolves downstream under the influence of turbulence that establishes itself in the flow. In order to circumvent the difficulties associated with carrying out 3-D LDV measurement of flows in geometries with curved walls, the facility operates on the principle of refractive-index matching of the fluid and the surroundings.

4 Results and discussion

In this paper the data of our measurements have been analyzed from the following points of view:

1) the relation between the evolution of swirl and the Reynolds stresses and
2) the terms of production of the Reynolds stresses.

A part of the theoretical framework for data analysis is the Reynolds-averaged equation for the moment of the azimuthal velocity, $\overline{C} = r\overline{v}_\theta$, which is

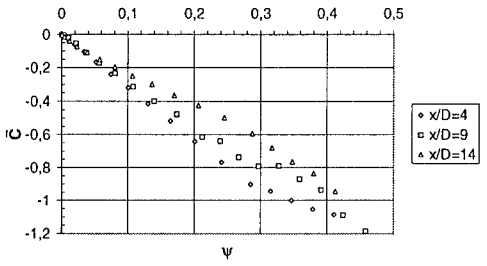
$$\overline{v}_x \frac{\partial \overline{C}}{\partial x} + \overline{v}_r \frac{\partial \overline{C}}{\partial r} + \frac{\overline{v}_\theta}{r} \frac{\partial \overline{C}}{\partial \theta} = -r \frac{\partial}{\partial x} \left(\overline{v'_x \, v'_\theta} \right) + r \frac{\partial}{\partial r} \left(\overline{v'_r \, v'_\theta} \right) - 2 \left(\overline{v'_r \, v'_\theta} \right). \qquad (1)$$

In the absence of Reynolds stresses the well known result that $\overline{C}$ is constant along a stream surface ψ = const. is recoverable from the equation (1). The presence of Reynolds stresses leads to $\overline{C}$ not being preserved along a stream surface and this is evident in the plots of $\overline{C}$ vs. ψ (figure 1). The plots at the different rotation numbers $Ro \left(= \frac{\Omega \frac{D}{2}}{v_{xm}} \right)$ of figure 1 show that at the higher rotation numbers the Reynolds stresses do not act to change $\overline{C}$ along ψ in the core. This conclusion is substantiated by examination of the production terms in the equation for the Reynolds stress components $\overline{v'_r \, v'_\theta}$ and $\overline{v'_x \, v'_\theta}$ in which the dominant terms are $\overline{v'_r \, v'_r} \frac{\partial v_\theta}{\partial r}$ and $\overline{v'_x \, v'_r} \frac{\partial v_\theta}{\partial r}$. The plots in figure 2 show the distribution of these terms along the radius.

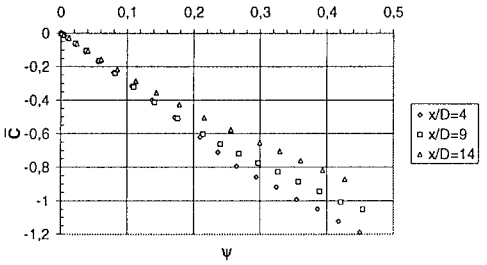
References

[1] V. I. Vasanta Ram, G. Rocklage-Marliani, T. Demmer and M. Schmidts. 3-D LDV measurement in swirling turbulent pipe flow. *Proceedings of the International Symposium on Turbulence and Shear Flow Phenomina*, September 12-15, Santa Barbara, USA, pp. 811-815, 1999.

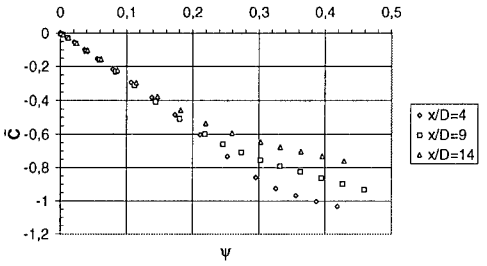
Ro=0.25



Ro=0.50



Ro=0.75



Ro=1.00

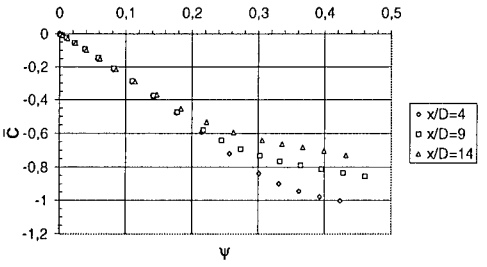


Figure 1: Moment of azimuthal velocity $\bar{C}$ vs. streamfunction Ψ

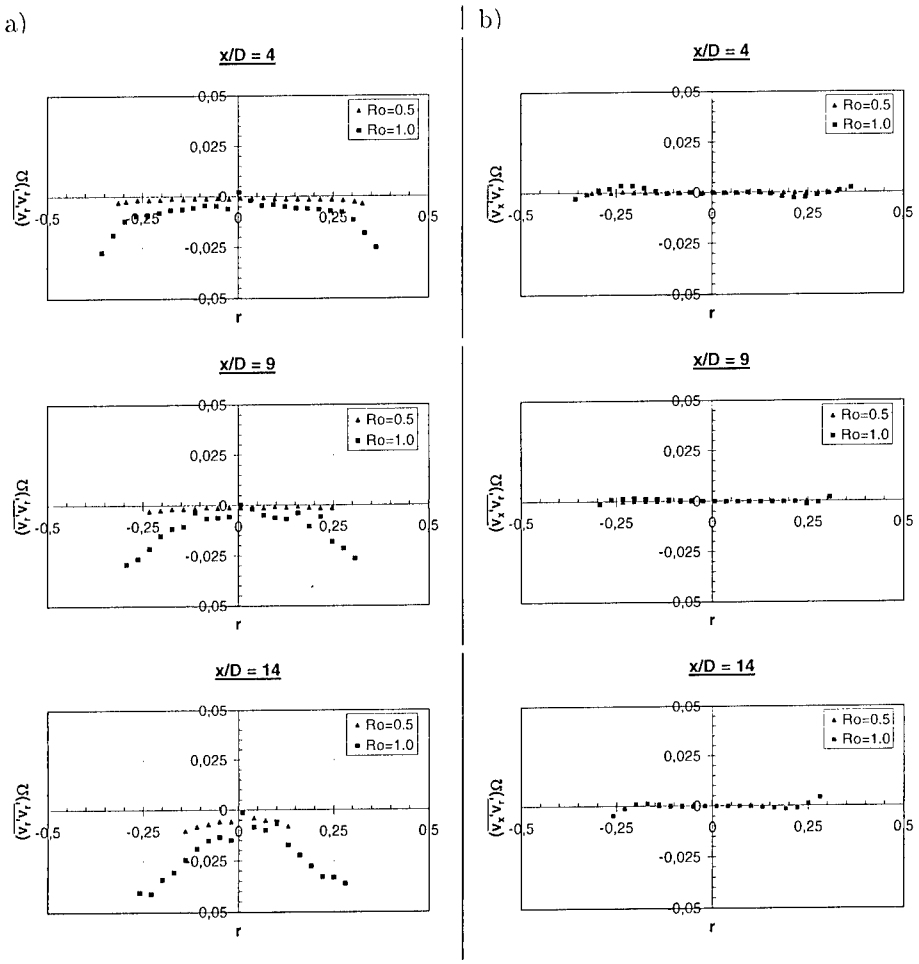


Figure 2: Dominant production terms a) in the equation for $\overline{v_r' v_\theta'}$ and b) in the equation for $\overline{v_x' v_\theta'}$

ADVANCES IN TURBULENCE VIII
Proceedings of the Eighth European Turbulence Conference
C. Dopazo et al. (Eds.)
© CIMNE, Barcelona 2000

LES of Turbulent Flows through 90°-Pipe Bends

F. Rütten, M. Meinke and W. Schröder

Aerodynamisches Institut der RWTH Aachen
Wüllnerstr. zw. 5 u. 7, 52062 Aachen, Germany

Contact e-mail: frank@aia.rwth-aachen.de

1 Introduction

The characteristic secondary flow pattern, the so called Dean vortices, that develops in laminar flow through pipe bends is well known and equally well understood. The turbulent flow through pipe bends, however, is more complicated, which is the reason why only a few numerical simulations have been carried out to investigate this flow, e.g. [1]. An interesting flow phenomenon in a 90°-bend is the so called swirl switching, observed by TUNSTALL & HARVEY [5], which, to the authors' knowledge, has not yet been studied using numerical methods. TUNSTALL & HARVEY report a tangential flow in alternating directions with a low frequency at the inner side of the curved pipe. This paper investigates numerically such oscillatory phenomena in pipe bends.

2 Numerical Methods

A Large-Eddy Simulation (LES) enables a detailed insight into the unsteady mechanisms of bend flows. A full description of the LES-method used here to compute compressible flows can be found in [2]. For completeness it is briefly outlined in the following. The LES equations are obtained by convolution of the Navier-Stokes equations for an ideal gas by a low-pass filter of width Δ which corresponds in this study to a local average in each grid cell (box filter). The resulting subgrid-scale (SGS) stresses have been modelled with SGS-models following SMAGORINSKY or GERMANO. However, the SGS based results of the computations showed hardly any influence on the solution in comparison to findings without any SGS model. Therefore, in this investigation no SGS model was incorporated. A modified AUSM-scheme, that is a variation of the work by LIOU & STEFFEN [3], is used to discretize the convective terms on a collocated grid to second-order accuracy. Written in tensor notation the vector of the convective fluxes $\boldsymbol{F}_\beta^C$ is:

$$\boldsymbol{F}_{\beta}^{C} = \begin{pmatrix} F_1^C \equiv \frac{M_\beta}{2}((\rho a)^L + (\rho a)^R) + \frac{|M_\beta|}{2}((\rho a)^L - (\rho a)^R) \\ \frac{F_1^C}{2}(u_\alpha^L + u_\alpha^R) + \frac{|F_1^C|}{2}(u_\alpha^L - u_\alpha^R) + (\frac{p^L+p^R}{2} + \chi(p^L u_\alpha^L - p^R u_\alpha^R))\delta_{\alpha\beta} \\ \frac{F_1^C}{2}(\frac{(\rho c)^L+p^L}{\rho^L} + \frac{(\rho c)^R+p^R}{\rho^R}) + \frac{|F_1^C|}{2}(\frac{(\rho c)^L+p^L}{\rho^L}) - \frac{(\rho c)^R+p^R}{\rho^R}) \end{pmatrix}.$$

The superscripts L and R denote left and right interpolated variables which are obtained via a quadratic MUSCL interpolation of the primitive flow variables. The quantity $M_\beta = \frac{u_\beta}{a}$ is the average of the left and right interpolated Mach number. The speed of sound a represents an average of the left and right interpolated values. The parameter χ is used to control the amount of numerical dissipation of the scheme and should be that small that a stable scheme on the body-fitted grid results without supressing the development of the turbulent structures. χ was set to zero for $Re = 5000$ and 10000, and a value of $\frac{1}{40}$ was used for $Re = 22000$. A central discretization of the viscous stresses and an explicit time stepping scheme, both of which are of second-order accuracy, are applied.

The turbulent inflow condition is generated by extracting solutions from a simultaneously performed LES of a fully developed turbulent pipe flow. The solutions are prescribed at the inflow boundary at each time step such that physically meaningful instantaneous values of the mass flow can be provided. Following POINSOT & LELE [4] a non-reflecting boundary condition is used at the outflow plane. The computational grids are sufficiently fine ($y_{min}^+ = 2$) to resolve the near-wall coherent structures.

3 Results

Simulations of turbulent bend flows are conducted for diameter based Reynolds numbers of 5000, 10000, and 22000. The radii of the 90°-bends are $r/D = 1$ and 3 such that the corresponding Dean number ranges from 1000 to 8800. The comparison of the turbulence intensities of the pipe flow with reference data (Fig. 1, left) shows the accuracy of the turbulent inflow condition. An example of the solutions is given in Fig. 1 (right), where the instantaneous flow field is visualized. It is dominated by a large separation region downstream of the bend. A small backflow region due to a strong adverse pressure gradient can also be observed at the outer side of the bend. The instantaneous flow pattern in the cross section is strongly asymmetric, as illustrated in Fig. 1, whereas a time-averaged solution shows only two counter-rotating Dean vortices. A comparison of numerical and experimental results is presented in Fig. 2 using time-averaged values and turbulence intensities of the axial velocity. The profiles are determined by the strong separation resulting in low axial velocities at the inner side and an accelerated flow at the outer side. The highest turbulence intensities are reached in the shear layer between the separated and the outer flow. The agreement of the numerical results and the data from PIV measurements is good.

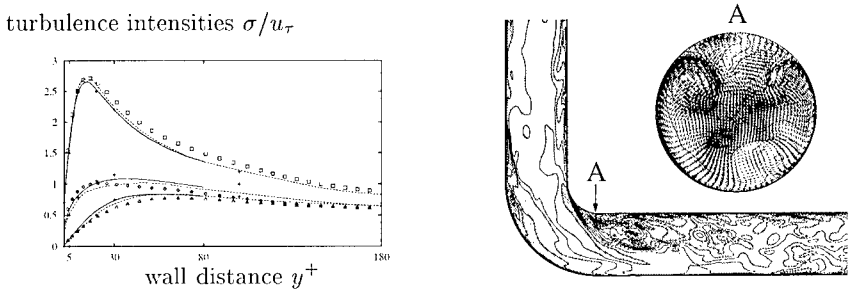


Figure 1: Bend flow at $Re = 5000$ and $r/D = 1$. Turbulence intensities of the straight pipe flow used as inflow condition (left). Computational results (□ axial, ◇ circumferential, △ radial) in comparison to reference data (+ Exp. by DURST 1995, --- DNS by UNGER 1994, — DNS by KIM ET AL. 1987). Instantaneous velocity field in the plane of symmetry and in cross section A (right).

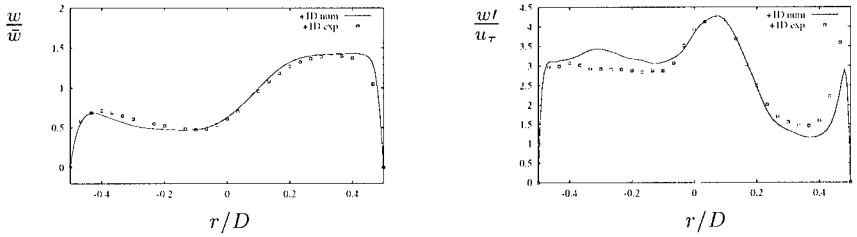


Figure 2: Bend flow at $Re = 5000$ and $r/D = 1$. Comparison of numerical (—) and experimental (□, PIV) results in the plane of symmetry at one diameter downstream of the curved part. Time-averaged axial velocity (left) and axial turbulence intensities (right). The inner (outer) side is at $r/D = -0.5$ (0.5).

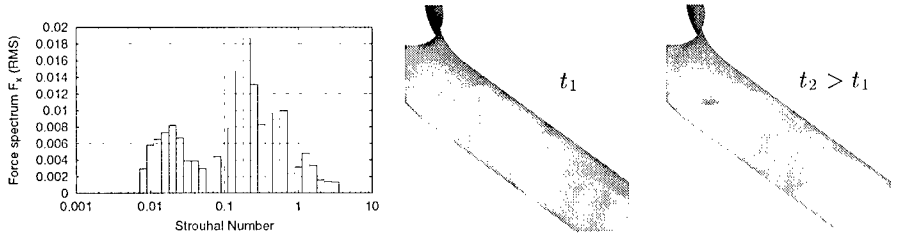


Figure 3: Bend flow at $Re = 22000$ and $r/D = 1$. Power spectrum of the integrated force onto the wall in the outflow direction with a distinct peak at $Sr = 0.2$ (left). Instantaneous pressure distribution on the bend wall at different time levels $t_2 - t_1 = 1.35$ dimensionless time units (right).

To study the oscillatory phenomena a spectral analysis of the force integral on the surface of the bends is performed. The obtained spectra are bimodal, i.e. they are characterized by a distinct peak at a Strouhal number $Sr = 0.2$ on the one hand (Fig. 3), and higher amplitudes in the low frequency range at about $Sr = 0.01$ on the other hand (Fig. 4). The high frequency peak is linked to a

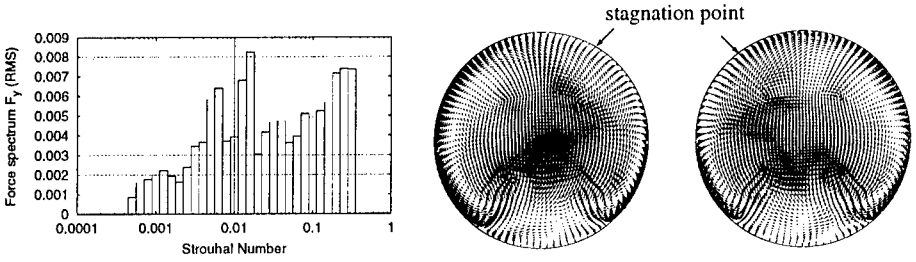


Figure 4: Bend flow at $Re = 22000$ and $r/D = 1$. Power spectrum of the integrated force onto the wall perpendicular to the plane of symmetry with distinct peaks in the low frequency range at $Sr = 0.0055$ and 0.014 (left). Different flow patterns at the end of the curved section with vector fields averaged over a dimensionless time of $\Delta t = 30$ (right).

periodic roll-up of the shear layer between the separation and the outer region. Areas of alternately high and low pressure move along the bend and cause an oscillating force onto the bend walls (Fig. 3, right). The low frequency peaks are related to an oscillation of the Dean vortices, that is the flow pattern at the end of the curved part is alternately dominated by the left or right Dean vortex, resulting in an oscillation of the stagnation point (Fig. 4, right). This is confirmed by a spectral analysis of the position signal of the stagnation point which shows the same two peaks as the force signal. The amplitude of the high frequency peak generally decreases and that of the low frequency peak grows with increasing Reynolds number.

4 Conclusion

An LES-method was applied to swirling, separated turbulent bend flows. The numerical results agree well with experiments with regard to time-averaged and statistical data. In the force spectra distinct frequencies are observed that are related to vortex shedding and a low frequency oscillation of the Dean vortices.

References

[1] BOERSMA, B.J., NIEWSTADT, F.T.M.: Large-eddy simulation of turbulent flow in a curved pipe. *J. Fluids Eng.*, **118**:248-254 (1996).

[2] MEINKE, M., KRAUSE, E.: Application of LES to Jets and Internal Turbulent Flows, *IUTAM Summer School on Advanced Turbulent Flow Simulation*, 1999, edited by W. Schneider, Kluwer, to be published.

[3] LIOU, M.-S., STEFFEN JR., C.: A new flux splitting scheme. JCP **107**, pp. 23–39 (1993).

[4] POINSOT, T. AND LELE, S., Boundary Conditions for Direct Simulations of Compressible Viscous Flows. *J. Comput. Phys.*, 101:104–129, 1992.

[5] TUNSTALL, M.J., HARVEY, J.K.: On the effect of a sharp bend in a fully developed turbulent pipe-flow. JFM (1968), vol. **34**, part 3, pp. 595–608.

ADVANCES IN TURBULENCE VIII
Proceedings of the Eighth European Turbulence Conference
C. Dopazo et al. (Eds.)
© CIMNE, Barcelona 2000

Visualization and PIV measurements of the near wall structure in a turbulent pipe flow

Zhang Zhaoshun[1], Feng Binchun[1], Cui Guixiang[1] and Michel Ayrault[2]

[1]Department of Engineering Mechanics, Tsinghua University, Beijing 100084
[2]Lab of Fluid Mechanics and Acoustics, Ecole Centrale de Lyon, FRANCE

1 Abstract

This paper investigates the near wall structures of a turbulent pipe flow at Reynolds numbers ranged from 5000 to 10000. The LIF technique is used for the visualization of the flow patterns which are recorded by a CCD camera at the speed of 25 frames per second. The longitudinal vortices and bursting rates are evaluated from the time series of the images. The results show that both average spacing of the longitudinal vortices and mean time interval of the bursts are greater than those at plate wall of turbulent flows. The conditional average of the local velocity field in the near-wall region by PIV technique shows that there are greater turbulent fluctuations in the ejection event.

2 Introduction

The target of this study is aimed at the characteristics of the burst phenomenon in the near wall region of a turbulent pipe flow. The flow structures are well known at the turbulent boundary layer, e.g. Head et al (1981) [1], however the effect of the transverse curvature on the structures has not been explored in details. In the paper both visualization technique and PIV measurements are used to investigate the near-wall structures of a turbulent pipe flow. The results show that the bursting phenomenon occurs at the near-wall region of the pipe flow as similar as that in the near-wall region of turbulent boundary layer, however the bursting frequency is lower in turbulent pipe flow.

3 Visualization results

The experiments were performed in a circular smooth water pipe flow of inner diameter 40mm at Reynolds number 5000 and 10000, based on the bulk velocity and the diameter of the pipe. The LIF technique was used for the visualization of the flow patterns and PIV technique was used for measurements of velocity field in the near wall region. Fluorescent dye was sucked into the pipe flow tangentially through a circular slot which has a width of 0.3mm at the pipe wall. The flow rate of the dye was low enough to ensure that it would not disturb the turbulent pipe flow. Both longitudinal and cross planes were illuminated by a 1mm laser light sheet. The time series of the flow pictures were stored in the videotape by means of a standard CCD camera. The frames of pictures were then digitized into images and processed on a Work Station.

Figure 1 shows the typical pictures of the near wall structures on longitudinal planes. The flow structure on the longitudinal plane clearly show the lifting and ejection events as well as the spanwise vortices which are similar to those of plate wall turbulence [1]. The flow picture on the cross plane, shown in Figure 2, reveals the longitudinal vortices near the wall and the mushroom type structure indicates the longitudinal vortex pairs.

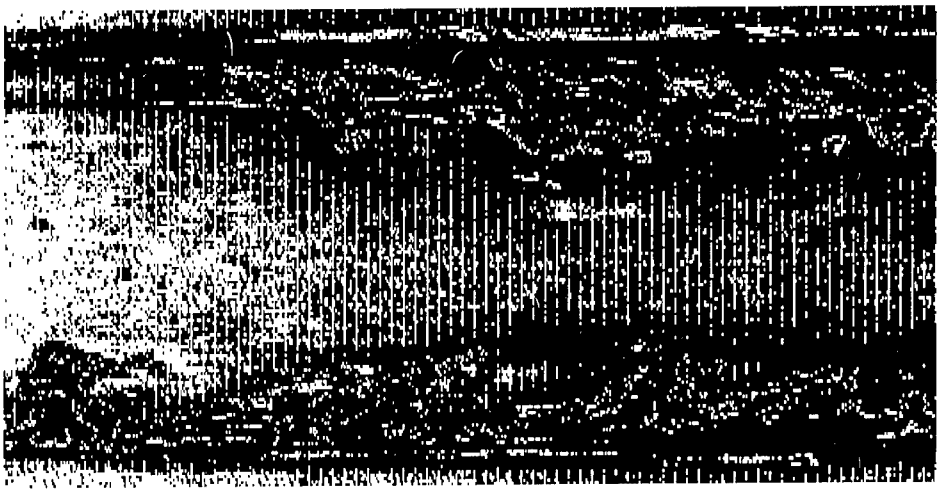
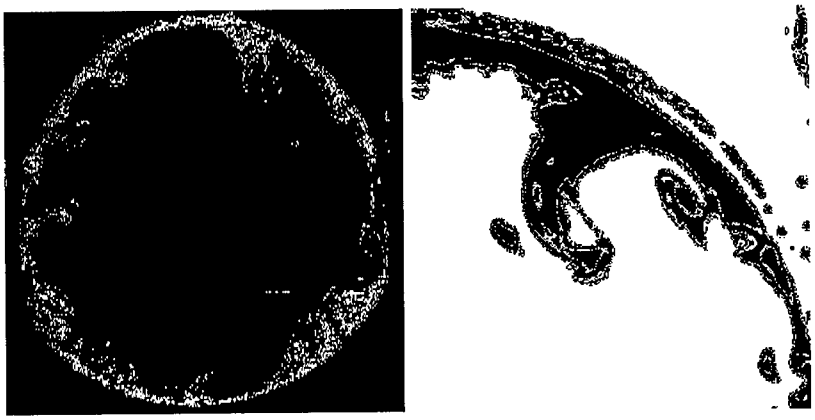


Figure 1: Flow structure on longitudinal plane at Re=6000

Based on the 400 hundred successive frames of images on the longitudinal and cross planes, the mean time interval of bursting and the average spacing of the longitudinal vortices are evaluated. The criterion of the burst events is borrowed from Bogard (1986) [2] and the mean time interval of bursts is estimated as $T = (8 - 10)R/U_m$, in which R is the pipe radius and U_m is the bulk velocity of the pipe flow. The mean time interval is comparable but greater than that in the plate turbulent boundary layer [3]. The average spacing of the



(a) Global view (b) Local view

Figure 2: Flow structure on cross plane at Re=6000

streaks is estimated from the images on the cross plane, it is about $140\nu/u_\tau$ and is slightly larger than that at the flat bounded turbulent flow in which $100\nu/u_\tau$ is usually accepted as the average spacing of longitudinal streaks.

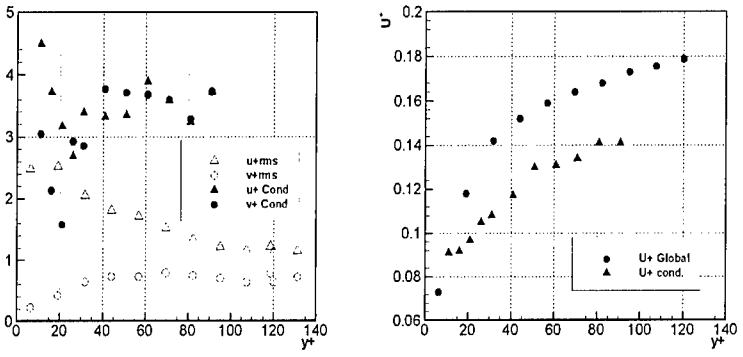
4 Conditional average of a local structure

To investigate the flow properties during lifting process of the bursting event the PIV technique was utilized. The fine particles were fed into the pipe and a shutter was used for adjusting the exposure time. The particle images were recorded on the videotape by standard CCD camera and then they were transferred into a Work Station for processing. When we investigated the flow structures in the near wall region we only take the images in near-wall region, i.e. within a quarter of radius from the wall. The particles were fed from the circular slot at the wall in the same way as we did in visualization described before.

The statistics were calculated from the 400 hundred images. The global mean values were taken as usual time and streamwise average, the local mean values inside the lifting structures were taken as the conditional average. The results are shown in Figure 3. The global average of the turbulent pipe flow is in good agreements with previous well-known measurements. The conditional average velocity profile show that the flow in the lifting structures is slower than the mean flow while the turbulence intensity profile demonstrates the high intensity in the region where a group of particles bulging in the near wall region.

5 Concluding remarks

The burst phenomena occur at the wall of a turbulent pipe flow but the bursting characteristics are different from those in the plate turbulent boundary layer. The reason for the difference results from the centrifugal constraints of the lon-



(a) mean velocity (b) turbulent intensity

Figure 3: Global and conditional mean velocity and turbulent intensity profiles

gitudinal vortices. The local measurements of the lifting structures confirm that there is a group of particles bulging in the near wall region with high intensity in the near-wall region.

Acknowledgements

The Chinese authors express them gratitude to the Natural Science Foundation of China (Grant-19732005) and Ministry of Science and Technology for their financial support. All of the authors thank the Sino-French Laboratory LIAMA for the financial support for the collaborative project between Tsinghua University and Ecole Centrale de Lyon.

References

[1] HEAD, M.R. and BANDYOPADHYAY, P. 1981 New aspects of turbulent boundary-layer structure. JFM, 107:297

[2] BOGARD, D.G. and TIEDERMAN, W.G. 1987 Characteristics of ejection in turbulent channel flow JFM, 179:1

[3] LUCHIK, T.S. and TIEDERMAN, W.G. 1987 Timescale and structure of ejections and bursts in turbulent flows. JFM, 174 :520

ADVANCES IN TURBULENCE VIII
Proceedings of the Eighth European Turbulence Conference
C. Dopazo et al. (Eds.)
© CIMNE, Barcelona 2000

Characteristics of Internal Vortical Structures in a Merged Turbulent Spot

H. Makita[1] and A. Nishizawa[2]

[1]Department of Mechanical Engineering, Toyohashi University of Technology
1-1 Tenpaku-cho, Toyohashi, Aichi 441-8580, Japan
[2]Fluid Science Research Center, National Aerospace Laboratory
7-44-1 Jindaiji Higashi-machi, Chofu, Tokyo 182-8522, Japan

Contact e-mail: makita@mech.tut.ac.jp

1 Introduction

Occurrence of turbulent spots characterizes the final stage of laminar to turbulent transition of the boundary layer and their geometrical similarity to the turbulent bulge in a downstream turbulent boundary layer was also suggested in [1]. Then, the flow visualization [5] revealed that the turbulent spot was an assemblage of many small-scale coherent vortices. But, no attention has been paid on the vortex interaction phenomena in the merging process of turbulent spots. The present work aims to clarify the behavior of the small-scale vortices inside the turbulent spot during the merging process of two simultaneously generated spots in a laminar boundary layer. It also discusses about the possibility of the resultant large-scale coherent vortices growing up into the turbulent bulges.

It is difficult to inspect the interaction phenomena among the small-scale vortices only by applying the ensemble average method to the data of a single hotwire, because their fine-scale configuration differs for each occurrence [6]. In the present study, two types of multi-hotwire systems are employed to get detailed instantaneous configurations of the internal small-scale vortices.

2 Experimental procedure

As shown in Fig. 1, the experiment was conducted in a zero pressure-gradient laminar boundary layer developed on a flat plate of 0.75 m 7.7 m in a low turbulence and low noise wind tunnel. A pair of turbulent spots was simultaneously generated by issuing small jets from two holes ($X = 0$); 1 mm in diam. and spaced 40 mm apart from each other, at 700 mm downstream of the leading edge. The Reynolds number, Re_{δ^*} was about 744 at $X = 0$, based on the free stream velocity U_∞=5.0 m/s and the displacement thickness δ^*=2.2 mm.

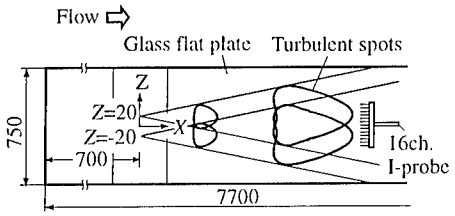


Figure 1: Schematic of experimental setup (unit: mm).

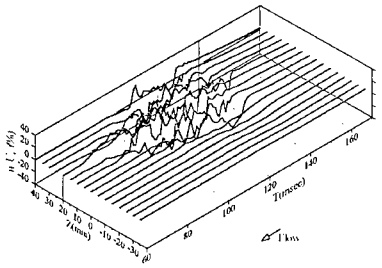


Figure 2: Instantaneous velocity perturbation u/U_∞ of the single spot at X = 300 mm and $Y/\delta = 0.4$.

The side wall contamination was removed by venting on both sides of the flat plate. Two types of hotwire rakes were employed. For 16-channel I-probe, wires were arranged every 5 mm and had a 75-mm total measuring span and gave the macroscopic instantaneous views in the Z–T plane of the spots. A 30-channel X-probe, composed of alternatively inclined 32 wires placed at every 0.5 mm, gave 30 points u and v components in detail over the limited span of 14.5 mm.

3 Results and discussion

Figure 2 shows an instantaneous velocity field when a single spot passes through the 16 hotwires. It gives a typical configuration of a single spot with an arrow-shaped turbulent region followed by a laminar-like calmed region [7]. Then, the instantaneous contours of u of a single and merged spots in the Z–T plane are obtained at X = 300 mm and $Y/\delta = 0.4$ as shown in Figs. 3(a),(b), which give detailed structures of the turbulent spots different from those given by the ensemble-average method [1]. A number of small-scale velocity excess and defect regions appear alternatively along the leading edge. Their streamwise scale, TU_∞, is 30~80 mm and 5~8 times larger than their spanwise scale of 5~15 mm, suggesting that the turbulent spot is composed of many longitudinal vortices. Possibly, these vortices compose the legs of horseshoe (hairpin) vortices inside the spot, as visualized by Matsui [5]. The streamwise growth of the turbulent spot, keeping its similarity in the three-dimensional configuration, is brought about by the increase in number of the longitudinal vortices [3]. It must be noted that the spot always accompanies a negative u region at its each wing tip where an upwash of low-momentum fluid is induced. When two spots begin to merge, as shown in Fig. 3(b), the interaction occurs around their inside wing tips and the upwash is enhanced in the merged region. The longitudinal vortices in each spot seem not to intrude into the other spot across the ejection.

Figure 4 shows instantaneous contours of u and v for a single spot given by the 30-channel X-wire array. Symmetrically arranged longitudinal streaky structures

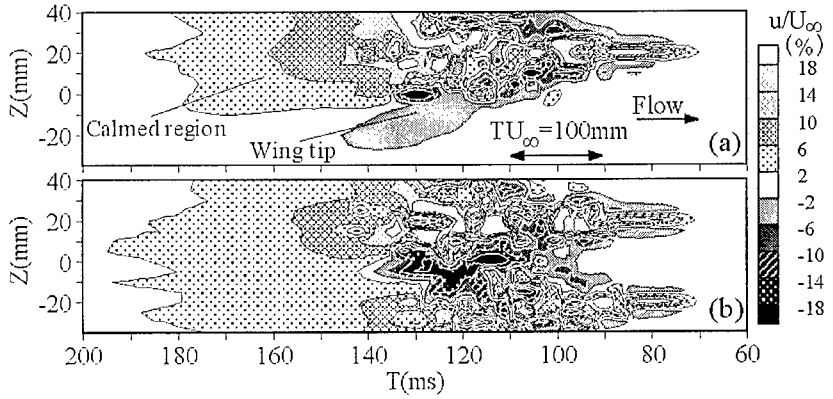


Figure 3: Contours of u/U_∞ (%)in the Z–T plane at X= 300mm and Y/δ = 0.4 given by the 16 channel I-probe. (a) single spot, (b) merged spot.

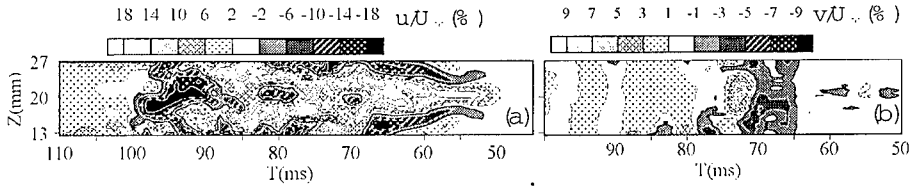


Figure 4: Contours of instantaneous velocity perturbation of the single spot in the Z–T plane at X = 200 mm given by the 30 channel X-probe. (a) u/U_∞ (%) at Y/δ = 0.4, (b) v/U_∞ (%) at Y/δ = 1.0.

are clearly observed near the arrow head at Y/δ = 0.4, i.e., the counter-rotating longitudinal vortex pairs exist in the lower part of the single spot. On the other hand, the instantaneous plane view of v at Y/δ = 1.0 shows the existence of several spanwise vortical structures around its top.

Figure 5 compares the ensemble-averaged velocity profile, $\langle U \rangle/U_\infty$, at Z = 0 of X = 300 mm between the single and merged spot. The merging process enhances the velocity defect and induces a stronger inflectional velocity profile in the merged region. The velocity inflection induces spanwise vortices in the upper merged region as shown in Fig. 6(b) and conform the heads of horseshoe vortices connecting the longitudinal vortex pairs in the lower merged region. At the further downstream of X = 600 mm, the merged spot grows higher and a far stronger velocity defect region appears around its head as shown in Fig. 7. Different from Elder's result [2], the present results suggest that the vortex interaction in the merged spot gives significant influences on the aspect of the boundary layer transition. The horseshoe vortices generated by the vortical interaction in the merging process may develop downstream keeping their geo-

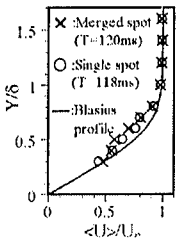


Figure 5: Profile of $\langle U\rangle/U_\infty$ at X=300mm and $Z = 0$.

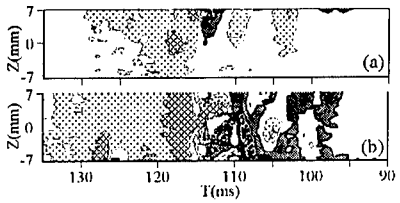


Figure 6: Contours of v/U_∞ (%) at $X = 300$ mm and $Y/\delta = 1.2$. Contour levels are the same as Fig. 4b. (a) single spot, (b) merged spot.

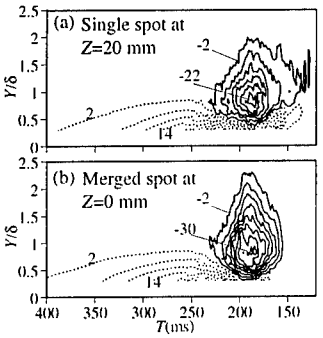


Figure 7: Contours of $\langle u\rangle/U_\infty$ (%) at $X = 600$mm.

metric identity and become to have a stronger configuration, which initiate the turbulent bulge in the fully developed turbulent boundary layer [4].

4 Conclusions

A turbulent spot is composed of many small-scale horseshoe vortices. When two turbulent spots begin to merge, strong interaction occurs at their wing tips and induces a strong upwash in the merged region. The unstable velocity profile there enhances spanwise vortices at the top of the merged spot connecting the longitudinal vortices beneath. The resultant horseshoe vortex with a stronger configuration may grow into the turbulent bulge: a large-scale vortical motion in the turbulent boundary layer.

References

[1] D. Coles and S.J. Barker. *Turbulent Mixing in Nonreactive and Reactive Flows*, 285–293 , 1975.

[2] J. W. Elder. *J. Fluid Mech.*, 9:235–245 , 1960.

[3] H. Makita and A. Nishizawa. *Trans.JSME(in Jap.)*, 65-632:1283–1290 , 1999.

[4] H. Makita and K. Sassa. *Turbulent Shear Flows 8*, 277:23–36 , 1994.

[5] T. Matsui. *Laminar-Turbulent Transition* , 288–296 , 1980.

[6] R. Sankaran, R. A. Antonia, D. K. Bisset and M. Sokolov. *Physics of Fluids A*, 3:1560–1571 , 1991.

[7] G. B. Schubauer and P. S. Klebanoff. *NACA TN 3489* , 1955.

ADVANCES IN TURBULENCE VIII
Proceedings of the Eighth European Turbulence Conference
C. Dopazo et al. (Eds.)
© CIMNE, Barcelona 2000

Investigation of wall structures in a turbulent channel flow using stereo PIV

G. Ciraolo and G.P. Romano

Dept. Mechanics and Aeronautics, University "La Sapienza", Roma
Via Eudossiana 18, 00184 Roma, ITALY

Contact e-mail: andrea@dits.ing.uniroma1.it

1 Introduction

The modelling of near-wall turbulence is still debated either from the point of view of the small intermittent structures, either for what concerns the large "coherent" structures. Regarding the latter, several euristical models have been proposed to describe the generation (or regeneration), the interaction and the dissipation of wall structures (Hussain, 1994; Adrian 1996; Adrian 1999). Although there is a general agreement on the behaviour of the structures aligned along the streamwise direction ("hairpin legs"), the flow structures connecting them, if exist, are modelled diffently. These are expected to leave a trace, on a plane orthogonal to the wall, in the form of a transverse rotating structure ("hairpin head"), but the exact shape of such a head and the related velocity and vorticity fields are dependent on the specific model. For example, Hussain (1994) described these connecting structures as filaments where low velocity and vorticity fields are present, whereas in the regeneration model by Adrian (1996) the strenght of the connection is much higher. Therefore, the open question concerns with the spanwise velocity component, orthogonal to the wall normal plane and usually indicated as w, which is rarely obtained either numerically or experimentally. As a matter of fact, real three-dimensional data are required to solve the problem. Despite the large amount of data from Direct Numerical Simulation (DNS) available for low Reynolds number turbulent channel flows, the spatial and temporal resolutions at the distance from the wall where heads are observed (well inside the log-region, i.e. for $y^+ > 30$, where $+$ denotes normalization by the friction velocity, u^*, and the kinematic viscosity) is not well enough: this is especially true along the streamwise and spanwise directions and in time. Therefore, high resolution three-dimensional experiments are required to investigate the previous questions. The aim of this paper is to measure the three-dimensional velocity field on a plane orthogonal to the wall in a turbulent

channel flow in order to point out the behaviour of the spanwise velocity related to wall structures. The experimental technique used is the Particle Image Velocimetry (PIV) and namely a stereo version of this technique which enables all the three velocity components on a plane to be determined (Adrian, 1996).

2 Experimental Set-up and Image Analysis

Measurements are taken in a horizontal water channel containing a fully developed turbulent flow. The coordinates x,y and z refer to the streamwise, wall-normal and spanwise directions respectively and the related velocity components are denoted as u,v and w. Measurements are made in the test section (y = 2 cm, z = 20 cm) at about 160 cm downstream of the inlet (x/h = 80, where h is the channel half-width). Most of the measurements were performed at a Reynolds number, based on h and U (the mean velocity at the centreline), equal to 4000 (h^+ = 170). This value was selected to compare the obtained results with the available DNS by Kim et al. (1987). Images of the flow field on the (x, y) plane are acquired by means of different experimental methods based on PIV:

(i) a planar PIV to measure the u and v components

(ii) a stereo PIV using one CCD camera to measure the u, v and w components

(iii) a stereo PIV using two CCD cameras to measure the u, v and w components

The second method was used with mirrors and prism to acquire images from two views on one half of the CCD sensor (the horizontal resolution is decreased), whereas the last method has been used with two videocameras tilted of about 30 one to each other. For the present measurements the time interval between images is about $1/250s$ (and this represents the obtained temporal resolution), which can be extended up to $1/2000s$ for measurements in high Reynolds number flows. The size of the acquired region is about $(2 \times 2)cm^2$, corresponding to (340×340) wall units in the plane (x, y). To derive the spatial resolution, it should be considered that the CCD of the videocameras has about (500×500) elements so that the minimum detectable displacement is about 0.5 wall units. The thickness of the light sheet (obtained from an Ar-ion laser using a rotating mirror) is less than 1 mm (about 15 wall units). The images are processed (using an improved non-standard PIV software, Romano et al. (1999)) to derive the two velocity components on each plane. The third velocity component (for methods (ii) and (iii)) is obtained by comparing the results from the two planes: the two horizontal components are rearranged to give the streamwise and spanwise velocities, whereas the two wall-normal components are used for validation purposes (Adrian, 1996).

3 Presentation of the Results

Several thousands of images are acquired to form a large data base for further analysis. The first four moments of u, v and w components and the $u'v'$, $u'w'$ and $v'w'$ cross moments are derived from such data. They are compared to the well known previous results by Kim et al (1987) (DNS) and Johansson et al.(1986) (LDA) nearly at the same Reynolds number: the agreement is very good down to the minimum measured distance from the wall ($y^+ = 15$). Measured rms values of the three velocity components are compared on Figure 1 with the DNS data by Kim et al (1987). The Reynolds stress $u'v'$ is given in Figure 2 for the three PIV acquisition methods together with the DNS data. All three sets of measurements agree between them with a slight overestimation in comparison to the DNS for $y^+ > 80$. This could depend on the slightly different Reynolds number. The results support the conclusion that both the one-camera and the two-cameras configurations can be employed. The former allows to have a simpler optical set-up and analysis procedure, whereas the latter attains a higher spatial resolution.

The attention is then focused on the detection of wall structures to identify "hairpin heads" in the (x, y) plane. Hairpin heads are mostly observed (about 80%) between $y^+ \simeq 30$ and $y^+ \simeq 130$ in agreement with the literature on the argument. In Figure 3 an instantaneous plot of the three velocity components is given (the mean flow velocity was subtracted from the longitudinal u component). It should be observed that the largest values of the spanwise velocity ($0.3u^*$) are observed for $y^+ < 70$, just where most of the hairpin heads form. In the region from the wall to $y^+ \simeq 70$, the number of such hairpins decreases as the Reynolds number, whereas in the outer region it slightly increases.

The spanwise velocity w (measured at the center of each hairpin head), is computed and averaged. In Figure 4 it is plotted as a function of the distance from the wall. The measured maximum value ($w \simeq 0.3u^*$) is of the same order of magnitude of those obtained for the u and v (in-plane) fluctuating velocity components, thus confirming a strong spanwise velocity field related to those heads. The spanwise velocity (almost equal to zero for $y^+ < 30$) increases from the wall up to $y^+ \simeq 70$ and then again decreases vanishing at $y^+ \simeq 140$. This means that a fundamental role for the spanwise field is effective within the layer ($40 < y^+ < 120$), where the value of w is at least one third of the other velocity components ($0.1u^*$). This is an experimental evidence that should be considered by the existing models of near-wall structures.

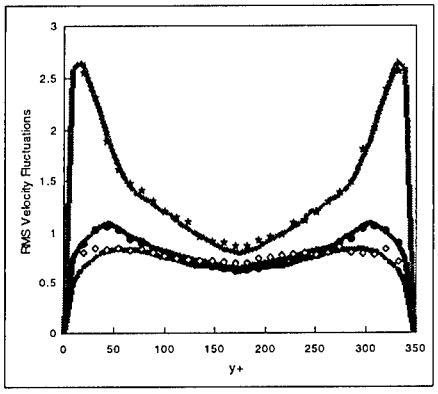


Figure 1: Measured rms velocities (symbols) compared with DNS by Kim et al (1987) (lines).

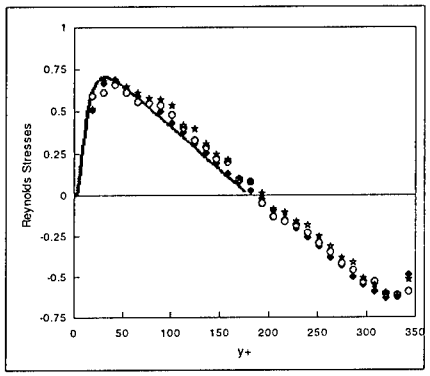


Figure 2: Measured Reynolds stress (symbols) compared with DNS by K im et al (1987) (lines). diamonds, PIV 2D; stars, Stereo-PIV (1 camera); circles, Stereo-PIV (2 cameras).

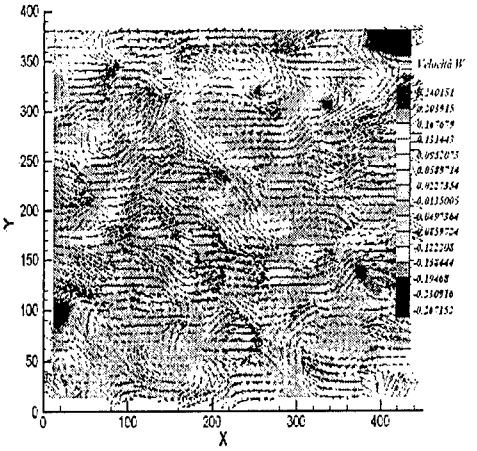


Figure 3: Instantaneous plot of the three velocity components in the channel flow.

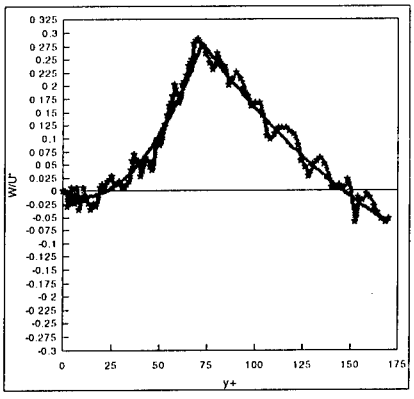


Figure 4: Spanwise velocity within hairpin heads. The line is a fit to data.

ADVANCES IN TURBULENCE VIII
Proceedings of the Eighth European Turbulence Conference
C. Dopazo et al. (Eds.)
© CIMNE, Barcelona 2000

DPIV Studies of Turbulent Boundary Layers

M. Onorato[1], G. M. Di Cicca[1], G. Iuso [1] and P. G. Spazzini [2]

[1]Department of Aerospace Engineering (DIASP), Politecnico di Torino
C.so Duca degli Abruzzi, 24, I-10129 Torino, ITALY
[2]CSDF-CNR, Department of Aerospace Engineering (DIASP), Politecnico di Torino
C.so Duca degli Abruzzi, 24, I-10129 Torino, ITALY

Contact e-mail: Onorato@polito.it

1 Introduction

Recently, Jimenez & Pinelli [1] performed a numerical experiment showing that the organization of the buffer layer in quasi-longitudinal low and high speed streaks is responsible for the regeneration of the streamwise vortices and demonstrated the principle that the turbulence production cycle may be interrupted through the weakening of the streaks by some external perturbation. Schoppa & Hussain [2], using DNS of a turbulent channel flow, suggested a promising new skin friction drag reduction technique based on large scale vortices or colliding spanwise wall jets control. They showed that both techniques may break the boundary layer vortex regeneration cycle by disrupting the unstable low speed wall streaks generated by previous (or pre-existing) streamwise vortices.

In order to clarify the mechanisms of near-wall turbulence regeneration and to examine the possibility of turbulence control in the future, it appears thus interesting to investigate the responses of the turbulent wall structures to external perturbations. The investigation presented here deals with the turbulence characteristics of the flow in the buffer layer of a flat plate boundary layer in presence of streamwise embedded large scale vortices; the main objective is to observe the direct influence of the disturbances on the wall organized motions.

2 Experimental Technique

The experiment was carried out in the Hydra Water Tunnel of CNR-CSDF. This facility is a closed loop, open flow channel with 350x500x1800 mm test section. Measurements were taken over a flat plate 2050 mm long, spanning the whole test section, with imposed transition at the leading edge. An array of longitudinal vortices is generated by water jets, injected at x=0 through 6 holes (2mm diameter), drilled at pitch angles of alternatively 45 and -45 degrees, through the plate along its span. The jet configuration produces three couples of counter-rotating vortices. The distance between two adjacent holes is 30

mm, corresponding to about 500 viscous lengths at the natural test condition. The ratio between the mass flow rate of the 6 jets and the mass flow rate of the boundary layer is 0.003. The evolution of the vortices is described in Di Cicca et al. [3]. Measurements have been carried out by digital particle image velocimetry (DPIV). The flow field is seeded with spherical solid paricles, 2 micron nominal diameter. Seeding concentration is about 10^{-7}. A double-pulsed light sheet is provided by a Nd-YAG laser source (200 mJ and 8 ns per pulse). Images are captured by a digital CCD video camera Kodak MEGAPLUS ES 1.0 (1008 × 1012 pixels) and analyzed via cross-correlation technique. Results obtained lighting a plane (x,z) parallel to the flat plate will be commented in this paper. The dimension of the measurement volume Δ^3 are determined by the laser light sheet thickness, about 0.5 mm, and by the interrogation spot size. For the present data the interrogation window is 32 × 32 pixels (with 50% overlapping); the physical dimension Δ is then 0.9 mm (about 13 wall units, 8 Kolmogorov scale lengths). The natural boundary layer at the measurement section is characterized by $Re_\theta = 1010$ and $U_e/u_\tau = 21.3$.

In Fig. 1, from [3], the rear end view ((y,z) plane) of the flow field is shown in a section upstream of the present measurement section. The vectors represent the mean velocity obtained by averaging over 100 couples of PIV images and show the two counter-rotating vortices in the central part ($-30\text{mm} \leq z \leq 30\text{mm}$) of the flat plate. The vortices appear to be completely immersed in the boundary layer, whose thickness there is about 40mm.

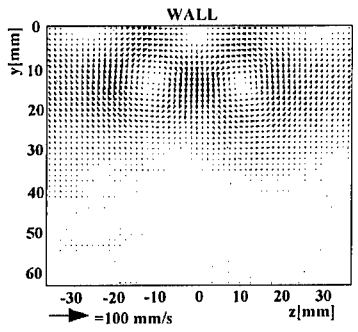


Figure 1: Rear-end view of the averaged flow field at x=130 mm.

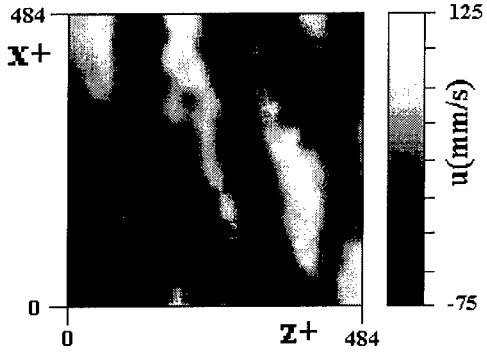


Figure 2: Fluctuating streamwise velocity component map. Jets off; $y^+ = 15$.

3 Results and Comments

Results obtained in a plane parallel to the plate, in the buffer layer, at a distance from the wall that was estimated to be 15 viscous lengths ($y^+ = 15$) are here shown. With reference to Fig. 1, the analyzed flow extends from about z=0 to z=30 mm, covering a planar flow field of about 500 × 500 wall units. In this region the secondary vortical flow appears as a spanwise jet parallel to the wall, colliding with an opposite jet at z=0. The center of the observed flow section is

at 250 mm downstream from the vortex generator jets. The maximum spanwise disturbance velocity induced by the vortices in this region is less than 5% of the external flow velocity.

A grey level map of the instantaneous fluctuating longitudinal component of the velocity, u, is reported in Fig. 2 for the case without control jets. The organization of the buffer layer flow in low and high speed streaks is evident. A similarly organized flow field can be observed for the case of vortex manipulated boundary layer, although the streaks' edges are more blurred in the spanwise direction, indicating that transversal shear is reduced. A statistical analysis performed over 25 images like the ones in Fig. 2, for the natural wall flow and for the manipulated one, gives a reduction of 14% for the variance of the u velocity and a reduction of 40% for the variance of the fluctuating component of the spanwise velocity w, due to the flow control. It should be observed that 25 images are not enough to completely characterize statistically the flow under consideration, due to low frequency unsteadiness present in the vortex controlling flow. Similar velocity fluctuation reduction has been observed in [3] in the buffer layer region, where statistical convergence was reached.

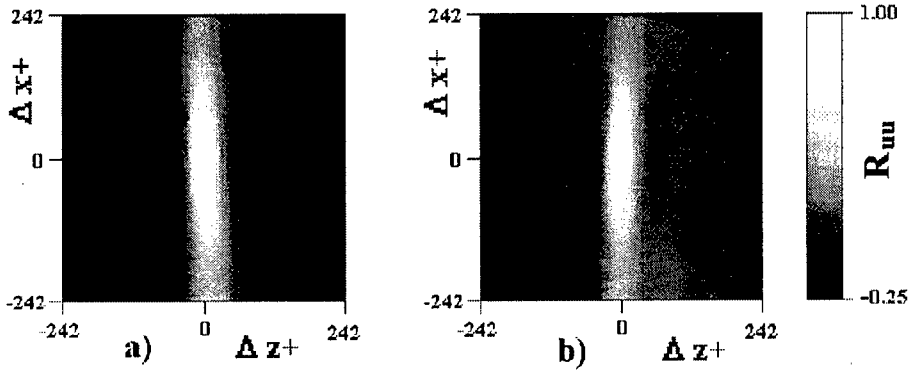


Figure 3: Double spatial correlation function R_{uu} maps.

In Fig. 3 a) the double spatial correlation function, relative to the longitudinal fluctuating velocity R_{uu} is shown, for the natural boundary layer. The results, in very good agreement with those of Carlier et al. [4], show an elliptical shape of about 100 wall units in width and more than 500 wall units in length (scales are not resolved in the x direction). The correlogram in Fig. 3 b) refers to the case of vortex manipulated flow. Comparison with Fig. 3 a) shows strong similarities between the two cases, which suggests that, in spite of the observed reduction in turbulence, due to the superimposed vortical flow field, the global organization of the flow is not affected by the manipulation, at least for this weak level of the introduced disturbance. Similar results have been found by Soldati et al. [5] in their study of turbulence control simulating numerically large scale Electro-Hydrodynamic streamwise vor tical flows superimposed to a plane Poiseuille flow. In Fig. 4 the probability density functions of $\partial u/\partial z$ are compared for the natural and manipulated boundary layer. For the vortex controlled flow, at values larger

than $(\partial u/\partial z)_{RMS}$ and lower than $-(\partial u/\partial z)_{RMS}$, the PDF shows lower values (reductions up to 30%). This is in agreement with the visual observation of the u velocity maps. The value of $(\partial/\partial z)$ is significative of the vorticity component normal to the wall, ω_y. The importance of ω_y in the turbulence production cycle has been stressed, among others, by Jimenez & Pinelli [1] and Schoppa & Hussain [2]. According to them the inviscid instability of the vorticity sheet (mainly provided by ω_y) flanking the streak is the basic regeneration mechanism of the streamwise vortices populating the buffer layer region.

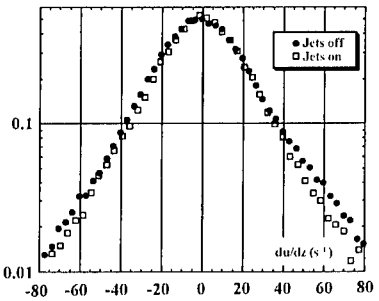


Figure 4: Spanwise derivatives $(\partial u/\partial z)$ probability density functions; natural flow, $(\partial u/\partial z)_{RMS} = 27s^{-1}$; manipulated flow, $(\partial u/\partial z)_{RMS} = 25s^{-1}$.

In conclusion, the weak control imposed by the embedded longitudinal vortices has produced, in the measurement plane at $y^+ = 15$, a sensible reduction of turbulence. The exam of the flow organization shows no evidence of disruption of the velocity streaky pattern or differences in the velocity bands spacing. PDF analysis of $(\partial u/\partial z)$ has indicated a reduction in transversal shear, that may imply a reduction in velocity turbulent fluctuations.

References

[1] J. Jimenez and A. Pinelli. Wall turbulence: How it works and how to damp it. In *Proceedings of the 28th AIAA Fluid Dynamics Conference/4th AIAA Shear Flow Control Conference, AIAA-97-2112*, Snowmass Village, Co., USA, 1997.

[2] W. Schoppa and F. Hussain. A large-scale control strategy for drag reduction in turbulent boundary layers. *Physics of Fluids*, 10(5):1049–1051, 1998.

[3] G. M. Di Cicca, M. Onorato, G. Iuso, A. Bollito, and P. G. Spazzini. DPIV study of a non canonical turbulent boundary layer flow. In *Proceedings of the 3rd International Workshop on Particle Image Velocimetry*, Santa Barbara, CA., USA, 1999.

[4] J. Carlier, J. M. Foucault, P. Dupont, and M. Stanislas. Experimental study of near wall turbulence using Particle Image Velocimetry. In *Proceedings of the 3rd International Workshop on Particle Image Velocimetry*, Santa Barbara, CA., USA, 1999.

[5] A. Soldati, M. Fulgosi, and S. Banerjee. On the use of large scale vortical streamwise structures to control turbulence in channel flow. In *Proceedings of the 1st International Symposium on Turbulence and Shear Flow*, Santa Barbara, CA., USA, 1999.5

ADVANCES IN TURBULENCE VIII
Proceedings of the Eighth European Turbulence Conference
C. Dopazo et al. (Eds.)
© CIMNE, Barcelona 2000

PIV measurements in a high Re turbulent boundary layer

Kristian Angele and Barbro Muhammad-Klingmann

Department of Mechanics, Royal Institute of Technology (KTH),
S-100 44 Stockholm, Sweden.

1 Introduction

Due to the recent technical development, digital PIV (Particle Image Velocimetry) has become a widespread tool for overall flowfield measurements. One of the limitations of the digital technique is its poor spatial resolution. However, the present study shows that accurate near wall measurements can also be obtained with digital PIV, provided the image size is small enough and sufficient care is taken to eliminate optical disturbances. This is also the first time that PIV-measurements have been made in a boundary layer at high Reynolds numbers with a sufficiently large data set to form a statistically safe average. The present study also shows the use of digital PIV for studying coherent structures in turbulent flows, making use of the fact that instantaneous values in a whole plane of the flowfield are available.

2 Experimental setup

Experiments were performed in a turbulent boundary layer with zero pressure gradient developing on a flat plate. PIV-measurements were made in the wall normal and spanwise directions. A large number of images were captured and processed statistically and the results were compared to those obtained with hotwire anemometry.

The experiment was carried out in the MTL wind tunnel at KTH. The tunnel has a 7 meter long test section with cross section area 0.8 m x 1.2 m, and an exceptionally good flow quality. Measurements were done on a flat aluminum plate at a distance x=5.5 m from the leading edge, and a free stream velocity U_∞=13.2 m/s. The Reynolds number based on x-position, Re_x, was 4.8 millions and based on momentum loss thickness Re_θ was 8300. The reference measurements, made with CTA hot wire anemometry were made in the same setup [2].

The PIV equipment consists of a 400 mJ double pulsed Nd:Yag laser and a digital Kodak ES1.0 CCD camera, containing 1018 x 1008 pixels. Figure 1

shows the setup for the wall normal measurements. The flow was seeded by means of a smoke generator using either paraffin oil or glycol. The presented

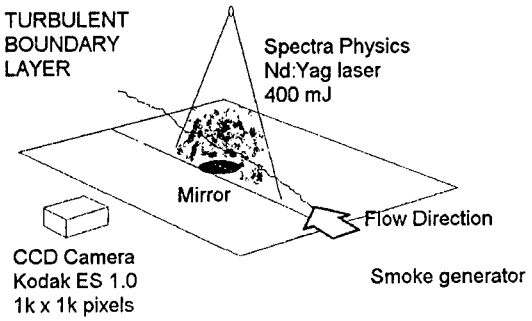


Figure 1: *Setup in the xy-plane experiment.*

data are ensemble averages of 2700 and 1300 image pairs respectively which were submitted to validation and statistical processing. The interrogation area size was 32 x 32 pixels with an overlap of 50%.

A mirror was mounted in the plate in order to avoid reflexions of the light sheet from the surface which might corrupt the data in the near wall region.

3 Results

3.1 Comparison between PIV and hotwire

Figure 2 shows the boundary layer profile of the the streamwise velocity component (U) and its fluctuations (u_{rms}) compared to hot wire data. The data are plotted in wall units, defined using a wall shear stress determined by means of oil film interferometry, see [3], giving a viscous length scale 31 μm. The dashed line in the figure shows the logarithmic law and a linear scaling $u^+=y^+$ for $y^+\leq 10$.

The total boundary layer thickness was 70 mm and the PIV image size was 11.2 mm x 11.1 mm giving an interrogation area size of 0.35 mm, i.e 11.4 viscous units. The agreement between PIV and hot wire measurements is fair all the way down to the measurement point at $y^+=8$, see [5]. Also the profile of u_{rms} shows the correct behavior. The inner peak at $y^+=17$ is well captured, however, the overall level of the u_{rms} values is higher than those measured with the hotwire.

With use of the mirror the wall distance could accurately be determined and optical disturbances were efficiently eliminated. It is possible to measure all the way down to the innermost point at $y^+=4.5$ but due to the large velocity gradient close to the wall the velocity is underestimated in the averaging over a rather large area. The hot wire has a much smaller extent normal to the wall than can be achieved with PIV, however, it is affected by heat convection into the wall.

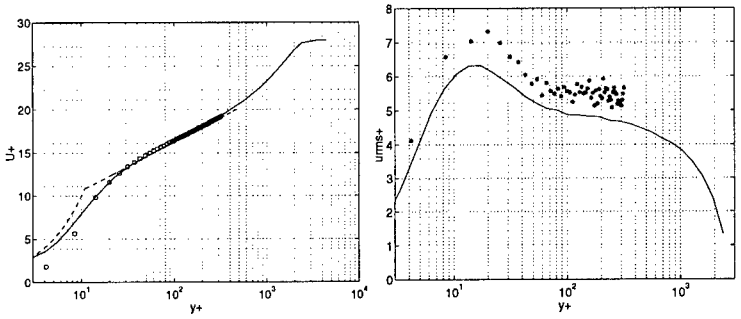


Figure 2: *Boundary layer profile in inner variables, comparison between PIV (symbols) and hot wire anemometry (line) Left: mean, right: rms of the streamwise velocity.*

3.2 Spanwise structures

It is well known that low speed streaks exist in the viscous sublayer with a characteristic spanwise spacing of 100 viscous units. According to [1], such structures

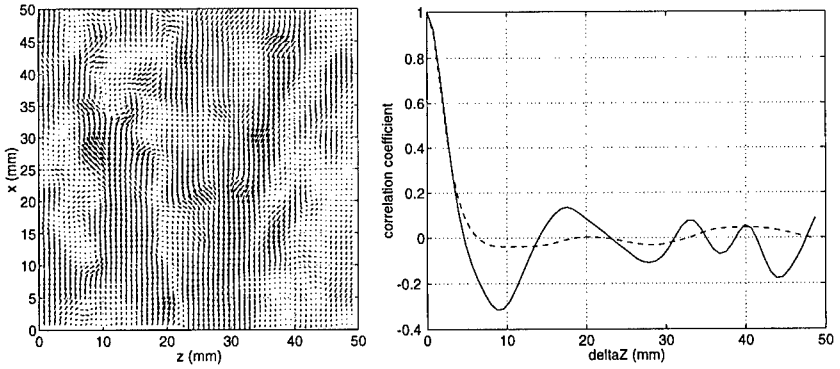


Figure 3: *Left: Instantaneous fluctuations in the xz-plane, right: spanwise correlation of u'.*

can still be observed as far out as y^+=100. PIV measurements were made in the x-z plane and images of 50 mm x 50 mm were captured at a distance of approximately y^+=100 from the wall. Since the laser sheet has a thickness of about 1 mm, corresponding to about 32 viscous units, velocities represent an average over a finite region. A mean velocity was computed as the ensemble average from the data set and this mean velocity was then subtracted from each instantaneous flow field, in order to obtain the fluctuating velocity components u' and w'. Figure 3 (left) shows an example of the instantaneous velocity fluctuations in the xz-plane. Visual inspection of such pictures reveal coherent structures.

Spanwise correlation functions were derived and averaged in images where u′ was predominantly negative, indicating presence of low speed streaks. The result is shown in Figure 3 (right), where the dashed line is the average of 200 image pairs, and the full line is the correlation obtained from the instantaneous flow field in the left figure. The graph clearly indicates that there is an alternating positive and negative correlation at a spanwise peak-to-peak distance of about 20 mm, which corresponds to 620 viscous units. This is substantially larger than 100 suggesting that emerging of sublayer streaks may take place in the logarithmic region. The size of the interrogation area, 26 viscous units, might be to small to capture streaks with a spacing of 100 viscous units, but a reprocessing with half the interrogation area size did not have any effect on the measured streak spacing. Similar observations have been made in [4].

4 Summary

In summary, the present experiments show that PIV can give accurate results for the mean velocity in the near wall region of a turbulent boundary layer, provided the image is focused in this region, reflexions are eliminated, and sufficiently large data sets are used. Accurate measurements are made down to $y^+=8$ in a high Reynolds number turbulent boundary layer. This is comparable to what can be achieved with hotwire.

Coherent structures can be clearly seen in these pictures, however, their spacing is substantially larger than 100 viscous units.

References

[1] J. Westerweel, "Digital Particle Image Velocimetry: theory and application", Doctoral Thesis, (1993)

[2] Österlund, J. M., "Experimental Studies of Zero Pressure-Gradient Turbulent Boundary-Layer Flow", (1999)

[3] Österlund, J. M. and Johansson, A. V. and Nagib, H. M. and Hites, M. H., "Wall Shear Stress Measurements in High Reynolds Number Boundary Layers from Two Facilities", AIAA paper 99-3814 (1999)

[4] K. C. Kim and R. J. Adrian, "Very large-scale motion in the outer layer", Physics of Fluids vol.11, 417-422 (1999).

[5] K. Angele , B. Muhammad Klingmann, "The use of PIV in turbulent boundary layer flows", to be published in Proceedings of IUTAM Symposium on Geometry and Statistics of Turbulence, (2000).

XII

Geophysical Turbulence

ADVANCES IN TURBULENCE VIII
Proceedings of the Eighth European Turbulence Conference
C. Dopazo et al. (Eds.)
© CIMNE, Barcelona 2000

Direct numerical simulation of mixing in geophysical flows

Wolfgang Gerlinger, Kai Schneider, and Henning Bockhorn

Institut für Chemische Technik,
Universität Karlsruhe,
Kaiserstr. 12, 76131 Karlsruhe, Germany.

Contact e-mail: gerlinger@ict.uni-karlsruhe.de

1 Introduction

Turbulent mixing can be observed in a lot of geophysical flows. The turbulent flow conditions guarantee accelerated mixing of all transported quantities, like momentum, mass, and energy, and lead to an enhanced diffusion. Furthermore, there is a wide range of active scales present in the flow which involves a large number of degrees of freedom. In this paper we present high resolution direct numerical simulation of the mixing in two-dimensional turbulent flows to get fundamental insights into the transport processes. As the dynamics of such flows is mainly dominated by coherent vortices [1], they are of primordial importance for the mixing of scalars. The aim of our work is to study the influence of coherent vortex structures and of the transport coefficients on the mixing of passive and reactive scalars.

2 Conceptual formulation

We use a classical pseudo-spectral scheme to integrate numerically the Navier–Stokes equations together with the convection–diffusion equations of the scalars [2]. The semi-implicit time scheme consists of an Euler backwards treatment for the linear terms and an Adams–Bashforth extrapolation for the non-linear terms. The governing equations read

$$\partial_t \vec{v} + \vec{v}\cdot\nabla\vec{v} - \frac{1}{Re}\nabla^2\vec{v} + \frac{1}{\rho}\nabla p = 0\,, \tag{1}$$

$$\nabla\cdot\vec{v} = 0\,, \tag{2}$$

$$\partial_t c_i + \vec{v}\cdot\nabla c_i - \frac{1}{Re\,Sc}\nabla^2 c_i = -Da\,c_A c_B\,, \tag{3}$$

with the velocity $\vec{v}$, the pressure p, the concentration c_i of species $i = A, B$. The density ρ is set to 1. As non-dimensional parameters, the Reynolds number

Re, the Schmidt number Sc and the Damköhler number Da are introduced. We consider a system of two species in a two-dimensional isothermal incompressible flow imposing periodic boundary conditions. In the reactive case, we implement a second order reaction between the species.

We calculate the time evolution of the physical quantities in a domain of $\Omega = [2\pi]^2$ using 600^2 grid points for the computation of about 10 eddy turnover times with a time step of 10^{-3}. The physical parameters are $Re = 10^4$, $Sc = 1$, and $Da = 0$ in the non-reactive case and $Da = 0.2$ in the reactive case, respectively.

3 Results

In [3], we mainly examined typical coherent vortex structures in order to show how vortices affect the mixing of species. Here, we present the evolution of a fully developed turbulent flow (cf. figure 1), and show the two identified mechanisms which enhance the mixing process:

(a) the merging of co-rotating vortices, and

(b) the creation of quasi-singular structures, i.e. the formation of spirals.

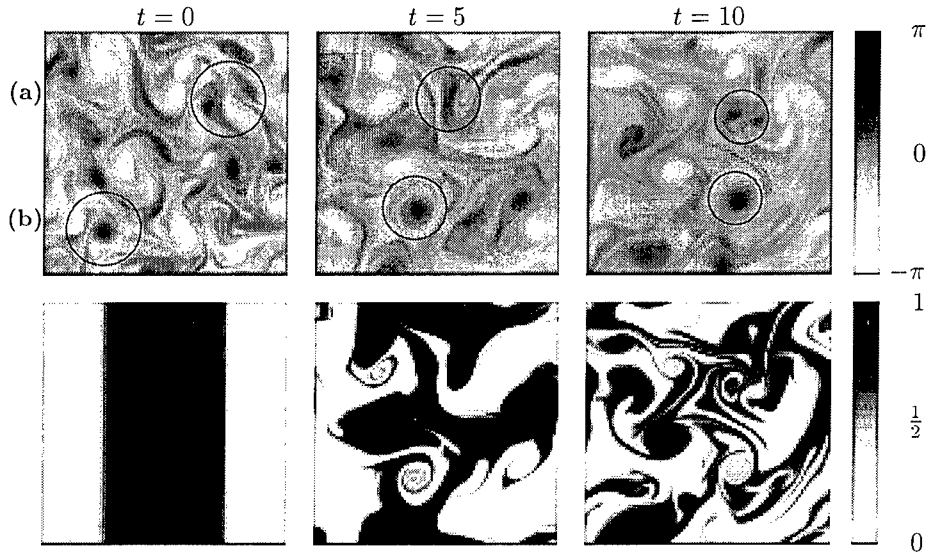


Figure 1: Time evolution of a fully developed, freely decaying turbulence at $t = 0, 5, 10$ eddy turnover times. Top: Vorticity fields. The marked regions denote two main mixing processes: **(a)**: merger, **(b)**: spirals' formation. Bottom: Scalar concentration.

In order to quantify the mixing, we consider local mixing time scales which describe the early variance decay. By asymptotic analysis for a one-vortex flow,

the following evolution of the variance of a passive scalar $\sigma^2(t)$ is predicted by [4]:

$$\sigma^2(0) - \sigma^2(t) \sim t^{3-3D'_k} + t^{0.5} \tag{4}$$

For the case of a fully developed turbulent flow, the evolution of the scalar variance is depicted in figure 2. In the early beginning the variance evolves similar to pure diffusive scalars described by the second term in (4), whereby after some eddy turnover times an enhanced (anomalous) diffusion can be observed. This enhancement can be correlated to the Kolmogorov capacity D'_k, i.e. a fractal dimension of the flow, which is here $D'_k = 0.33$ and agrees with the first term in (4).

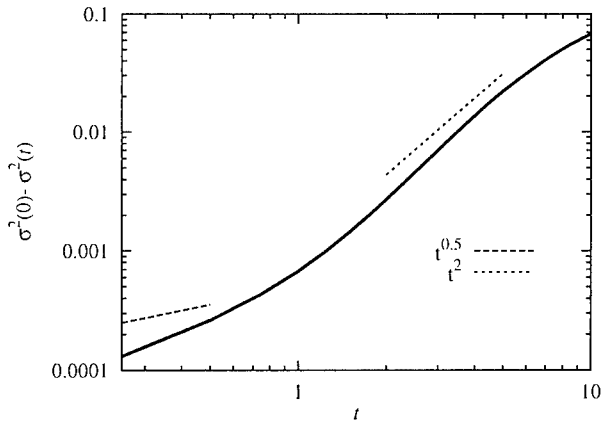


Figure 2: Evolution of the variance of a passive scalar with $Sc = 1$.

Figure 3 shows the histograms of c_A in the non-reactive and reactive case after about 30 vortex turnover times. A comparison with fitted β-functions, which are used in classical presumed shape PDF-models [5] for computing turbulent flows shows a good accordance.

4 Conclusions

The present paper is concerned with the direct numerical simulation of the mixing in freely decaying, incompressible homogeneous isotropic turbulence in two dimensions. We compared the fractal dimension of the passive scalar in the flow with theoretical predictions and showed the agreement. We conclude that the spiral formation and the vortex merging are important features to model turbulent flows. This impact will increase with the Reynolds number which enhances the intermittency of the flow. Also, we showed the agreement of the histograms of passive and reactive scalars with commonly used β-PDF's.

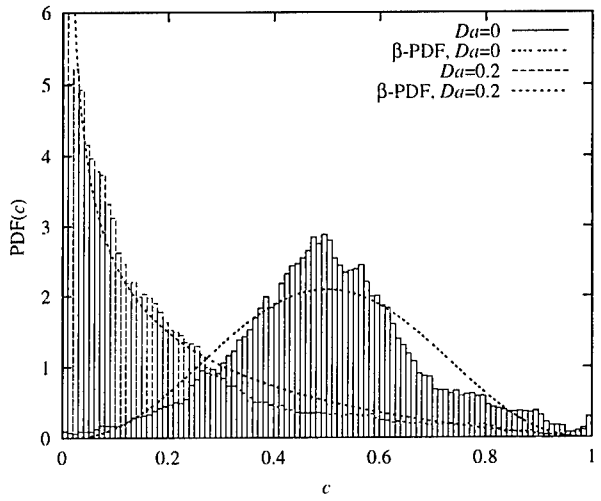


Figure 3: Histograms and approximated β-PDF's for a non-reactive ($Da = 0$) and a reactive ($Da = 0.2$) simulation after 30 eddy turnover times.

5 Acknowledgements

We gratefully acknowledge the financial support through the Deutsche Forschungsgemeinschaft (Contract DFG Bo 693/8-2)

References

[1] J.C. Mc Williams. The emergence of isolated coherent vortices in turbulent flows, *J. Fluid Mech.* 146:21–43, 1984.

[2] C. Canuto, M.Y. Hussaini, A. Quarteroni, and T.A. Zang. *Spectral Methods in Fluid Dynamics*, Berlin, 1988.

[3] W. Gerlinger, K. Schneider, L. Falk, and H. Bockhorn. Numerical Simulation of the Mixing of Passive and Reactive Scalars in Two-Dimensional Flows Dominated by Coherent Vortices, *Chem. Eng. Sci.*, 2000, to appear.

[4] P. Flohr and J.C. Vassilicos. Accelerated scalar dissipation in a vortex, *J. Fluid Mech.*, 348:295–317, 1997.

[5] R.O. Fox. Computational methods for turbulent reactive flows in the chemical process industry, *Revue de l'Institut Francais du Pétrole* 51(2):215–242, 1996.

ADVANCES IN TURBULENCE VIII
Proceedings of the Eighth European Turbulence Conference
C. Dopazo et al. (Eds.)
© CIMNE, Barcelona 2000

Algebraic parametrizations for the triple correlations in modelling the shearless turbulence mixing layer

V. Grebenev [1] and B. Ilyushin [2]

[1]Institute of Computational Technologies, Russian Academy of Science SD,
Lavrentjev ave. 6, Novosibirsk 630090, Russia
[2]Institute of Thermophysics, Russian Academy of Science SD,
Lavrentjev ave. 1, Novosibirsk 630090, Russia

Contact e-mail: vova@lchd.ict.nsc.ru

1 Introduction

The method of differential constraints advanced by Yanenko [1], for constructing explicit solutions to different kinds of nonlinear partial differential equations makes it possible to obtain the gradient–type algebraic expressions for unknown functions. This provides us a concept for examining the closure procedure for momentum equations in Turbulence Models. Moreover, the method gives a reasonable tool for obtaining algebraic expressions. The exposition is demonstrated on an example chosen from Free Turbulence Flow Theory. The analysis has been carried out in the article shows that a concept of differential constraints allows us to interpret algebraic expressions as the equations of invariant sets (manifolds) generated by corresponding differential equations.

The plan of the article is as follows. In Section 2 we expose a new third-order closure model of turbulence based on using an approach which was developed in [2]. This approach has been employed in [2] to obtain a closed model of turbulence that does not imply equality to zero of the fourth-order cumulants. The closer procedure was performed at level of the fifth moments. We apply the model to study a classical problem on the dynamics of the shearless turbulence mixing layer. Our next result is devoted to examining an algebraic expression for the triple correlation of the vertical velocity fluctuations $\langle w^3 \rangle$. In Section 3 we show that the set of smooth functions:

$$D = \{\langle w^2 \rangle, \langle w^3 \rangle, \hat{\tau} \, : \, \mathcal{H}^1(\langle w^2 \rangle, \langle w^3 \rangle, \hat{\tau}) \equiv \langle w^3 \rangle + \delta \hat{\tau} \langle w^2 \rangle \langle w^2 \rangle_z = 0\}$$

is invariant under the flow generated by the differential equation for $\langle w^3 \rangle$. As a consequence, it is established that the differential constraint $\mathcal{H}^1$ coincides with

the algebraic expression for $\langle w^3\rangle$ or the so-called tensor-invariant model [3]. In Section 4 we discuss the existence of selfsimilar solutions.

2 Modelling the turbulent transport in a shearless mixing layer

The subject of the study is the problem on interaction and mixing between two semi-infinite homogeneous turbulent flow fields of different scales. The starting point is the following system of average equations:

$$\frac{\partial e_h}{\partial t} = -\frac{\partial\langle e_h w\rangle}{\partial z} - \frac{c_1}{\tau}\left[e_h - \frac{2}{3}E\right] - \frac{2}{3}\epsilon,\quad \frac{\partial \epsilon}{\partial t} = \frac{\partial}{\partial z}\left[c_d\tau\langle w^2\rangle\frac{\partial\epsilon}{\partial z}\right] + \frac{c_{\epsilon_1}}{\tau}\beta g\langle w\theta\rangle - c_{\epsilon_2}\frac{\epsilon}{\tau},$$

$$\frac{\partial\langle w^2\rangle}{\partial t} = -\frac{\partial\langle w^3\rangle}{\partial z} + 2\beta g\langle w\theta\rangle - \frac{c_1}{\tau}\left[\langle w^2\rangle - \frac{2}{3}E\right] - \frac{2}{3}\epsilon.$$

As usual, $\langle w^2\rangle$ is the one-point velocity correlation of the second-order, $\tau = E/\epsilon$ the time scale of turbulence. Here E, ϵ are the kinetic energy and spectral flux of the turbulent kinetic energy. The volumetric expansion coefficient is $\beta = 1/\Theta$, where Θ and θ are the mean and variance potential temperature respectively. The constants involved in the model with lower case letters are denoted by c_{**}. We complete the system by the transport equation:

$$\frac{\partial\langle w^3\rangle}{\partial t} = -\frac{\partial C}{\partial z} - 3\langle w^2\rangle\frac{\partial\langle w^2\rangle}{\partial z} + 3\beta g\langle w^2\theta\rangle - c_2\frac{\langle w^3\rangle}{\tau}.$$

Algebraic parametrizations for the fourth-order cumulant C, the triple correlation $\langle w^2\theta\rangle$ and the vertical heat flux $\langle w\theta\rangle$ can be written as [2]:

$$C = -\frac{\tau}{c_3}\left[6\langle w^3\rangle\frac{\partial\langle w^2\rangle}{\partial z} + 4\langle w^2\rangle\frac{\partial\langle w^3\rangle}{\partial z}\right],$$

$$\langle w^2\theta\rangle = -\frac{\tau}{c_4}\left[\langle w^3\rangle\frac{\partial\Theta}{\partial z} - 2\beta g\langle w\theta^2\rangle\right],\qquad \langle w\theta^2\rangle = -\frac{\tau}{c_5}\langle w^2\rangle\frac{\partial\langle\theta^2\rangle}{\partial z},$$

$$\langle w\theta\rangle = -\frac{\tau}{c_{\theta_1}}\langle w^2\rangle\frac{\partial\Theta}{\partial z} \equiv -\frac{\tau N^2}{\beta g c_{\theta_1}}\langle w^2\rangle,\quad N^2 = \beta g\frac{\partial\Theta}{\partial z}$$

$$\langle\theta^2\rangle = -\frac{\tau}{c_r}\langle w\theta\rangle\frac{\partial\Theta}{\partial z} = -\frac{\tau N^2}{\beta g r}\langle w\theta\rangle = \left(\frac{\tau N^2}{\beta g}\right)^2\frac{\langle w^2\rangle}{c_{\theta_1} r},$$

where $r = \tau/\tau_\theta$, τ_θ is the time scale of potential temperature variance, N the Brunt-Vaisala frequency. Using the balance approximation between exchange mechanism and dissipation, the equation for e_h is simplified. It follows from the formula for C [2] that the contribution of the second term in the algebraic model for the cumulant C is leading. Thus the governing equations are:

$$\frac{\partial\langle w^2\rangle}{\partial t} = -\frac{\partial\langle w^3\rangle}{\partial z} - \alpha\frac{\langle w^2\rangle}{\hat\tau}, \tag{2.1}$$

$$\frac{\partial\langle w^3\rangle}{\partial t} = \frac{\partial}{\partial z}\left[\kappa\hat{\tau}\langle w^2\rangle\frac{\partial\langle w^3\rangle}{\partial z}\right] - 3\langle w^2\rangle\frac{\partial\langle w^2\rangle}{\partial z} - \gamma\frac{\langle w^3\rangle}{\hat{\tau}}, \tag{2.2}$$

$$\frac{\partial\epsilon}{\partial t} = \frac{\partial}{\partial z}\left[\delta\hat{\tau}\langle w^2\rangle\frac{\partial\epsilon}{\partial z}\right] - \varrho\frac{\epsilon}{\hat{\tau}}, \tag{2.3}$$

where $\alpha = 2/3$, $\kappa = 6c_1/c_3(c_1+2)$, $\gamma = 2c_2(c_1+1)/3c_1$, $\delta = 3c_1c_d/2(c_1+2)$, $\varrho = 2c_{\epsilon_2}(c_1+2)/3c_1$, $\hat{\tau} = \langle w^2\rangle/\epsilon$.

3 Invariant sets

By using the theory of Symmetry Analysis [4] we prove

Theorem 3.1 *Let the triple $\langle w^2\rangle$, $\langle w^3\rangle$, ϵ be a sufficiently smooth solution of (2.1)-(2.3) and let $\kappa = \delta$. Assume also that $\hat{\tau}_z = 0, \hat{\tau}_t = (2\alpha\delta - \gamma\delta + 3)/\delta$, then* (i) *the equation (2.2) admits the invariant set D;* (ii) *the system (2.1)-(2.3) on the invariant set D is equivalent to:*

$$\langle w^2\rangle = (2\alpha\delta - \gamma\delta + 3)\epsilon/\delta, \qquad \langle w^3\rangle = -\delta\hat{\tau}\langle w^2\rangle\langle w^2\rangle_z, \tag{3.1}$$

$$\frac{\partial\epsilon}{\partial t} = \frac{\partial}{\partial z}\left[\delta\hat{\tau}^2\epsilon\frac{\partial\epsilon}{\partial z}\right] - \varrho\frac{\epsilon}{\hat{\tau}}. \tag{3.2}$$

Theorem 3.1 has a special interest in view of its application to Turbulence Models.

Corollary 3.1 *The equation $\mathcal{H}^1(\langle w^2\rangle, \langle w^3\rangle, \hat{\tau}) = 0$ that defines an invariant set of (2.1)-(2.3) coincides with the algebraic triple correlation model or the tensor-invariant model* [3].

Other words, the algebraic expression represents the equation of an invariant set (manifold) generated by the differential equation for the triple correlation.

Corollary 3.2 *There no exists differential constraints of the form*

$$\mathcal{H}^n \equiv \langle w^3\rangle - H^n(\langle w^2\rangle, \langle w^3\rangle, \langle w^3\rangle_1, \ldots \langle w^3\rangle_n, \hat{\tau}) = 0$$

for $n > 1$ where $\langle w^3\rangle_n$ denotes the n-order derivative, H^n is a sufficiently smooth function.

4 Selfsimilar solutions

Theorem 3.1 enables us to reduce (2.1)-(2.3) to the algebraic differential expressions (3.1), (3.2) which are more simple system for analyzing. Using the obtained reduction we give the selfsimilar description for (2.1)-(2.3). Appropriate selfsimilar solution to our problem is a solution of the form:

$$\epsilon_a = \frac{h(\xi)}{(t+t_0)^{3\mu+\nu}}, \quad \langle w_a^2\rangle = \frac{f(\xi)}{(t+t_0)^{2\mu}}, \quad \langle w_a^3\rangle = \frac{q(\xi)}{(t+t_0)^{3\mu}}, \tag{4.1}$$

$$\xi = \frac{z - z_0}{L}, \quad L = \lambda(t + t_0)^{\nu}, \quad z_0 = \lambda_0 L + \lambda_1, \quad t_0 > 0,$$

where λ, λ_i are model constants and t_0 is a parameter. A straightforward calculation yields that if we choose $\nu = 1 - \mu$, then the original system is transformed to the system of ordinary differential equations for the profiles f, q and h. The free similarity exponent μ has to be determined from a solution of the obtained nonlinear eigenvalue problem. This is a typical situation appearing in nonlinear diffusion problems where a conservation law does not exist. The boundary conditions are determined by the physical model: the functions $f(\xi)$, $q(\xi)$, $h(\xi)$ tend to given positive limits as ξ tends to $\pm\infty$.

To solve the problem we use the existence of an invariant set obtained in Theorem 3.1. For this purpose, we study the equation for $\hat{\tau}$ and show that $\hat{\tau} = (\varrho - \alpha)(t + t_0)$ is a solution to the equation. As the result, the system admits a reduction. Therefore we have the following boundary value problem:

$$\delta(w_c^2 h h_\xi)_\xi + (1 - \mu)(\xi + \lambda_0)h_\xi = 0, \quad w_c = \varrho - \alpha, \quad \mu = \frac{\alpha}{2(\varrho - \alpha)}, \tag{4.2}$$

$$h(-\infty) = a_- t_0^{2\mu+1}, \quad h(+\infty) = a_+ t_0^{2\mu+1}, \tag{4.3}$$

where $a_\pm = \lim_{z \to \pm\infty} \epsilon(z, 0), a_\pm > 0$. We prove the existence and uniqueness results to (4.2), (4.3), expose in details the qualitative properties of the solution. As a remark we note that this solution is essentially different from the well-known Barenblatt's solutions.

Theorem 4.1 *Let $\kappa = \delta$, $\delta = 3/(\rho - \gamma)$ and $\gamma = (3/2)\alpha$, assume that $\rho - \gamma > 0$. Then there exists a solution $\langle w_a^2 \rangle$, $\langle w_a^3 \rangle$, ϵ_a of system (2.1)–(2.3) which represents the selfsimilar description of the shearless turbulence mixing layer.*

Acknowledgments
This research was partially supported by the Russian Foundation of Basic Research (grant no. 98-01-00719). This work was financially supported by INTAS (proposal no. 97-2022)

References

[1] N. N. Yanenko. Selected works. Nauka, Moscow, 1991 (in Russian).

[2] B. B. Ilyushin. Model of fourth-order cumulants for prediction of turbulent transport by large-scale vortex structures. *J. Appl. Mechan. Tech. Phys.*, 40(5): 871–876, 1999.

[3] K. Hanjalic, B. Launder. A Reynolds stress model of turbulence and its application to thin shear flows. *J.Fluid Mech.*, 52:609–638, 1972.

[4] N. H. Ibragimov. Transformation groups applied to mathematical physics. Reidel, 1985.

ADVANCES IN TURBULENCE VIII
Proceedings of the Eighth European Turbulence Conference
C. Dopazo et al. (Eds.)
© CIMNE, Barcelona 2000

PDF Construction for Modeling the Pollutant Dispersion in Convective Atmospheric Boundary Layer

B. B. Ilyushin [1]

[1]Institute of Thermophisics, Russian Academy of Science SD,
Lavrentjev ave. 1, Novosibirsk 630090, Russia

Experimental and theoretical investigations confirm the formation of Coherent Large Scale Eddy Structure (CS) in convective atmospheric boundary layer (CABL). They contain the main part of the turbulence energy and the turbulent transfer is achieved mainly by the action of CS. Such non-local turbulent transfer cannot be described within "standard" turbulent diffusion models of gradient type. The turbulent transport models of third- and second- order closure are presented in the paper (Ilyushin and Kurbatskii, 1997). These models describe the statistic structure of CABL adequately of the experimental data. In this paper the results of modeling of the pollutant turbulent transfer in CABL are presented. The approach based on accounting the influence of the CS by accentuation of the periodic properties of motions, which is analogous to VLES is used. But in this paper the accentuation of periodic motions are obtained for the pdf of vertical velocity field.

The pdf of turbulent fluctuations of the vertical velocity is represented as a superposition of two independent distributions: inertial interval of turbulent spectrum (background turbulence) $P_b(u)$ and large-wave region of pdf spectrum $P_c(v)$ (u and v are the vertical velocity fluctuations of background turbulence and the vertical velocity field of CS, correspondingly)

$$P(u,v) = P_b(u)P_c(\nu) = \frac{1}{2\pi\sigma_b}\exp\left\{-\frac{u^2}{2\sigma_b^2}\right\}\left[\frac{a^+}{\sigma_c^+}\exp\left\{-\frac{(m^+-\nu)^2}{2(\sigma_c^+)^2}\right\}+ \right. \quad (1)$$
$$\left. +\frac{a^-}{\sigma_c^-}\exp\left\{-\frac{(m^--\nu)^2}{2(\sigma_c^-)^2}\right\}\right],$$

where σ_b is the dispersion of background turbulence; a^+ and a^- are the weight coefficients, σ_c^+ and σ_c^- are the dispersions, m^+ and m^- are the centers of distributions of upflow and downflow of CS, correspondingly. Considering the total turbulent velocity fluctuation w as the sum of u and ν, one can obtain the total pdf:

$$P(w) = \int_R P(u,v)\delta(w-u-\nu)dud\nu = \frac{a^+}{2\pi\sigma_+}\exp\left\{-\frac{(m^+-w)^2}{2\sigma_+^2}\right\}+ \quad (2)$$

$$+\frac{a^-}{2\pi\sigma_-}\exp\left\{-\frac{(m^- - w)^2}{2\sigma_-^2}\right\},$$

where $\sigma_+^2 = (\sigma_c^+)^2 + \sigma_b^2$, $\sigma_-^2 = (\sigma_c^-)^2 + \sigma_b^2$. From the conditions

$$\int P(w)dw = I, \qquad \int_R wP(w)dw = 0, \tag{3}$$

$$\int_R w^2 P(w)dw = \sigma^2, \qquad \int_R w^3 P(w)dw = S_w\sigma^3,$$

($\sigma = \langle w^2\rangle^{1/2}$ is the dispersion and $S_w = \langle w^3\rangle/\langle w^2\rangle^{3/2}$ is the skewness factor) the relations for a^+, a^-, σ_+^2, σ_-^2, m^+ and m^- are the following:

$$a^+ + a^- = I, \quad a^+m^+ + a^-m^- = 0, \quad a^+\left[(m^+)^2 + \sigma_+^2\right] + a^+\left[(m^+)^2 + \sigma_-^2\right] = \sigma^2,$$
$$a^+\left[(m^+)^3 + 3m^+\sigma_+^2\right] + a^-\left[(m^-)^3 + 3m^-\sigma_-^2\right] = S_w\sigma^3. \tag{4}$$

The conditions for σ_+^2 and σ_-^2 are found from the assumption (Anne et al., 1986) that the square of dispersions σ_+^2 and σ_-^2 can be equal to the square of centers of distribution $(m^+)^2$ and $(m^-)^2$ correspondingly:

$$\sigma_+^2 = (m^+)^2, \qquad \sigma_-^2 = (m^-)^2. \tag{5}$$

This assumption means that flux directed positively (negatively) remains mainly positive (negative) taking into account a possible scatter. Necessary condition for closure of the equations set (for σ_b) is found from the wavelet model (Tennekes and Lumley, 1972). We suppose here that the main part of the energy-containing interval of the fluctuations spectrum is defined by a single main wavelet with the typical wave number corresponding to the spectrum maximum. The horizontal size of LSES ($\lambda_{\max} = 2\pi(2a/E)^{-3/2}/\epsilon$, a is the Kolmogoroff coefficient) and the ratio $(\sigma_b^2/\langle w^2\rangle)$ are determined from second-order moment distributions with using of this approach. Equations (4), (5) with distribution of ratio $\sigma_b^2/\langle w^2\rangle$ and with accounting the condition for the values place $m^+ > 0$ and $m^- < 0$ have exclusive solution. The results of reconstruction of pdf using the calculated distributions of the second– and third–order moments are shown in Fig.1 for time 3 p.m. It can be seen that the results of reconstruction of pdf correspond to the observed data: an upflow within a CS with larger turbulent energy (σ_c^+) and larger velocity (m^+) occupy smaller region (of size $\approx P_c(m^+) < P_c(m^-)$) than a downflow with smaller energy $(\sigma_c^- < \sigma_c^+)$ and smaller velocity $(m^- < m^+)$. Such a structure of the CABL is conditioned by vertical asymmetry of the mechanism of turbulent fluctuations generation: in the near-ground layer an influx of the turbulence energy is provided by the mean velocity shear whereas in the upper (stably stratified) part of CABL turbulent fluctuations are strongly suppressed so the dispersion of vertical velocity fluctuations in upflows appear to be larger than that in downflows. For horizontally homogeneous CABL the size of horizontal region of the LSES (where the vertical velocity is equal to $\tilde{w}$) is taken to be

proportional to the probability $P_c(\tilde{w})$: $P_c(\tilde{w})d\tilde{w} = dx/(\lambda_{\max}/2)$. The vertical velocity field of the coherent structures $\tilde{w}(x,z)$ can be found from this differential equation. The horizontal velocity field $\tilde{u}(x,z)$ is determined from the equation of mass conservation. The result of reconstruction of the coherent structures velocity field $(\tilde{u},\tilde{w})$ in the convective PBL is shown in Fig 2. For describing the process of substance dispersion in the convective PBL, it is used the model which takes into account directly an effect of the substance transfer by LSES (in advection terms of the equation for the crosswind integrated concentration) is used. For accounting of the substance turbulent diffusion under the effect of background turbulence, the "standard" gradient diffusion model is applied:

$$\frac{\partial C_y}{\partial t} + (U+\tilde{u})\frac{\partial C_y}{\partial x} + \tilde{w}\frac{\partial C_y}{\partial z} = \frac{\partial}{\partial}\left[\nu_t \frac{\partial C_y}{\partial z}\right]. \qquad (6)$$

The results of simulation of the pollutant jet spreading from sources placed both on the CABL ground surface and in the middle of the mixed layer are presented. The averaging (over one period $\lambda_{\max}/U$) crosswind integrated concentration fields are shown in Figs.3, 4. The calculated behavior of the plume centerline with a source situated both near the ground and in the middle of the mixing layer corresponds to the Willis and Deardorff's tank experiments.

Acknowledgments
This research was partially supported by the Russian FBR (98-01-00719), (00-15-96810). This work was financially supported by INTAS (97-2022)

References

[1] Anne F. De Baas, Han van Dop and Frans T. M. 1986. An application of Langevin equation for inhomogeneous conditions to dispersion in a convective boundary layer. *Quart. J. R. Met. Soc.*, 112: 165-180, 1986.

[2] Ilyushin B. B., Kurbatskii A. F. Modeling of turbulent transport in PBL with third-order moments. *roc. Symposium on Turbulent Shear Flows. Grenoble, France.* 2: 2019–2024.

[3] Monin A. S., Yaglom A. M. Statistical Hydromechanics (Part 1,2). Moscow, Science, 1967.

[4] Tennekes H., Lumley J. L. A First Course in Turbulence. MIT Press, Cambridge, Massachusetts, 1972.

[5] Willis G. E., Deardorff J. W. A laboratory model of diffusion into the convective boundary layer. *Quart. J. Roy. Meteor. Soc.* 102: 427–445, 1976.

[6] Willis G. E., Deardorff J. F. A laboratory study of dispersion from a source in the middle of the convective boundary layer. *Atmos. Environ.* 15: 109–117, 1981.

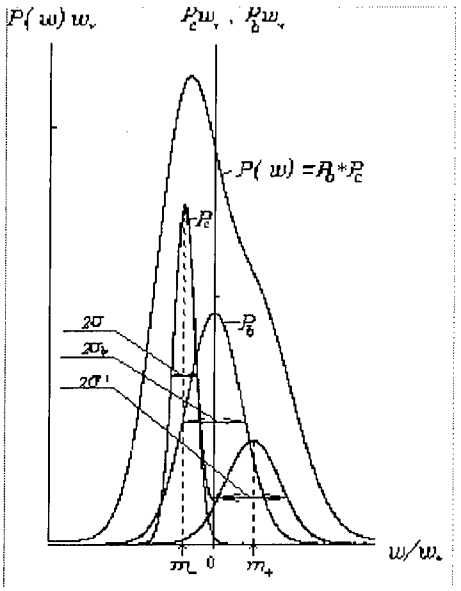


Figure 1: The constructed profile of pdf of the vertical velocity fluctuations for $z/z_i = 0.5$.

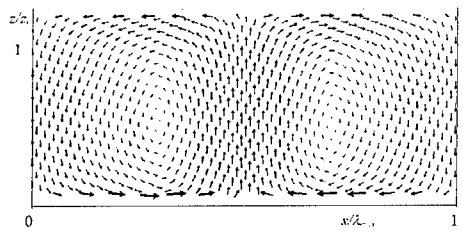


Figure 2: The velocity field of CS in CABL.

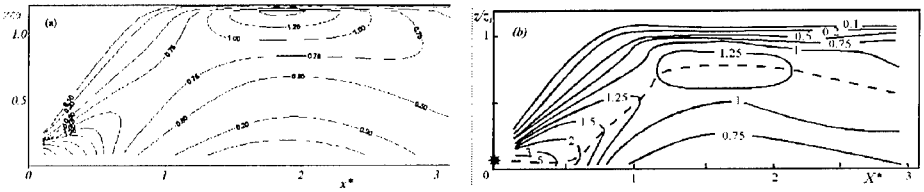


Figure 3: Calculated (a) (left) and measured (Willis and Deardorff, 1976) (b) (right) non-dimensional crosswind integrated concentration $C_y z_i U_x / q_0$ for point sources of height $z/z_i = 0.067$.

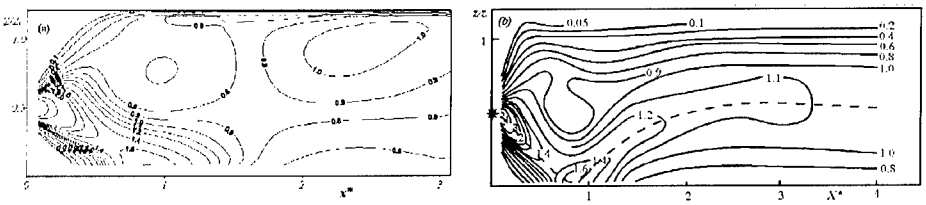


Figure 4: Calculated (a) (left) and measured (b) (right) (Willis and Deardorff, 1981) non-dimensional crosswind integrated concentration for point sources of height $z/z_i = 0.5$.

ADVANCES IN TURBULENCE VIII
Proceedings of the Eighth European Turbulence Conference
C. Dopazo et al. (Eds.)
© CIMNE, Barcelona 2000

Turbulent transport across a sheared inversion at the convective boundary layer top

E. Fedorovich[1,2] and J. Thäter[2]

[1]School of Meteorology, University of Oklahoma
100 East Boyd, Norman OK 73019, USA
[2]Institute for Hydromechanics, University of Karlsruhe
Kaiserstrasse 12, 76128 Karlruhe, GERMANY

Contact e-mail: fedorovich@ou.edu

1 Introduction

Two principal forcing mechanisms determine turbulence regime in the atmospheric convective boundary layer (CBL) driven by buoyant heat transfer from the warm underlying surface. The main of them is associated with turbulence production by buoyancy forces, and the secondary one is the turbulence generation due to the surface wind shears and shears across the density interface at the CBL top (the elevated shears). Density interface in the atmospheric CBL is marked by sharp temperature gradients and usually referred to as the capping inversion layer (or simply the capping inversion). Interaction of the CBL with the free atmosphere aloft is characterized by the entrainment of heat through the capping inversion layer down into the convectively mixed core of the CBL. The entrainment, which is the essential mechanism of the CBL deepening, is primarily caused by convective updrafts (thermals) that rise from the heated surface and penetrate into stably stratified fluid above the CBL.

Experimental and model studies of CBL conducted during the last several decades were mainly focused on the turbulence structure and entrainment dynamics in the case of pure buoyantly driven CBL (the so-called shear-free CBL) and on the role of surface wind shear in the CBL turbulence production. The effects of elevated wind shear on the turbulent transport across the capping inversion and on the CBL evolution have not been sufficiently studied so far.

In this paper we show results of numerical simulation of the CBL with sheared capping inversion and present new wind tunnel model data on the dispersion in the atmospheric CBL with elevated shear. We also discuss a possible physical mechanism of the directional effect of shear on the turbulent exchange at the CBL top.

2 Simulation Results

For the numerical part of our study, a modified version of large eddy simulation (LES) code by Nieuwstadt and Brost [3] has been employed. The original code was designed for simulating the turbulence regime of a temporally evolving, horizontally homogeneous atmospheric CBL in a rectangular domain with periodic lateral boundary conditions. The code was modified in order to match requirements of simulating quasi-stationary, horizontally inhomogeneous CBL.

As the reference case for the present study, the CBL with shear-free upper interface has been used. This CBL case was comprehensively studied in the stratified wind tunnel of the University of Karlsruhe (UniKa). It has been also simulated numerically, using the aforementioned LES code, and a fairly good agreement has been found between the numerical and experimental results. The configuration of flow at the tunnel inlet in the reference case is as follows: the lower portion of the flow with a uniform temperature is separated from the stably stratified flow aloft by a temperature jump; above the jump, the temperature is growing linearly with height; the flow velocity has value 1 m/s everywhere. The bottom heat flux is kept constant over the entire wind tunnel floor area.

Two CBL cases with velocity shears across the capping inversion layer have been investigated. In the case with positive elevated shear (PS), the flow velocity was kept 1 m/s below the temperature jump (inversion) and increased in the jump-like way to 1.5 m/s above the inversion. In the case of negative elevated shear (NS), the mean velocity was 1 m/s below the inversion and reduced to 0.5 m/s above it. The remaining flow parameters in the both test cases were same as in the reference case.

With present operating ranges of the UniKa wind tunnel, the NS case cannot be reproduced there. For the PS case, the wind tunnel study of Fedorovich and Kaiser [1] has shown that positive elevated shear obstructs the entrainment and vertical turbulent transport across the inversion. As a first guess, this effect could be explained by the so-called shear sheltering of turbulence (Hunt and Durbin [2]). Our recent wind tunnel experiments on gaseous tracer dispersion in the CBL with sheared inversion have provided additional evidence concerning suppression of the vertical diffusion at the CBL top in the PS case.

From the comparison of concentration patterns presented in Figure 1 one can see how elevated positive shear inhibits the diffusion of tracer at the CBL top in addition to the blockage of diffusion by stable stratification inside the inversion layer. The resulting concentration values in the upper portion of the CBL with sheared capping inversion (PS) are thus noticeably smaller than in the CBL with shear-free upper interface (RC). Numerical simulation of the PS case has provided additional data on turbulence statistics at the CBL top. These statistics have been found in fair quantitative agreement with their counterparts obtained in the wind tunnel model.

Turbulence regime in the CBL with negative shear across the inversion (the NS case) was also investigated numerically. This investigation yielded rather

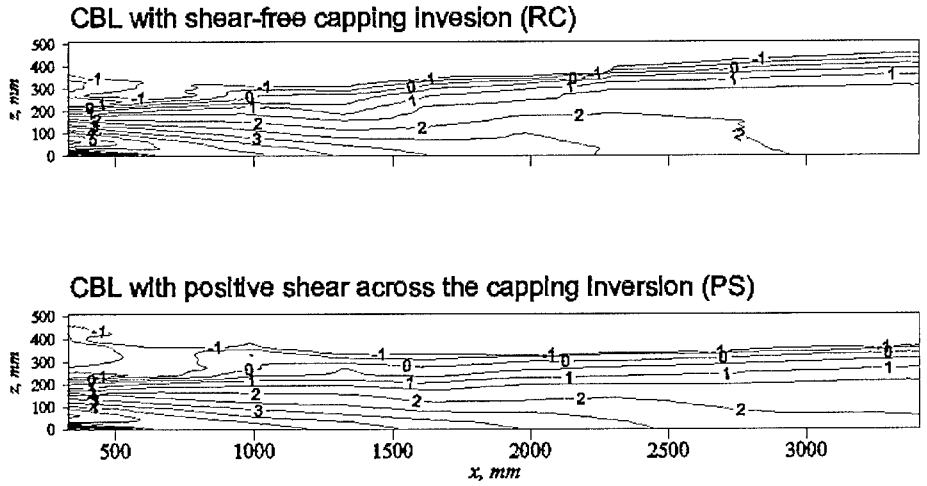


Figure 1: Distribution of logarithm of normalized concentration along the CBL in the RC and PS cases. The source elevation is 100mm.

surprising result. It turned out that damping of thermals in the inversion layer with negative shear is weakened compared to the case of the CBL with shear-free inversion (RC) and as a result the entrainment and the CBL growth are activated in the NS case. In other words, the effect of negative elevated shear on the CBL evolution appeared to be opposite to that of positive elevated shear.

This opposite effect of positive and negative elevated shear on the CBL development is clearly seen in the vertical distribution of the temperature variance presented in Figure 2. In the PS case (left plot), the maximum values of temperature variance observed at the capping inversion level are shifted downwards with respect to the corresponding RC extrema. In the NS case (right plot), they are shifted upwards. At the same time, the magnitudes of temperature variance inside the inversion layer are not significantly altered in the PS and NS cases compared to the reference shear-free case.

3 Discussion and Conclusions

The effect of elevated shear on the turbulent exchange across the CBL turned out to be dependent on the shear sign. We found in particular that the effect of negative elevated shear on the CBL growth is opposite to that of the positive shear. This is not consistent with shear sheltering theories we know. Our study suggests that with positive elevated shear, the thermals that penetrate into the sheared inversion are vertically squashed by the stable stratification and stretched downwind by the higher-momentum flow in the inversion layer.

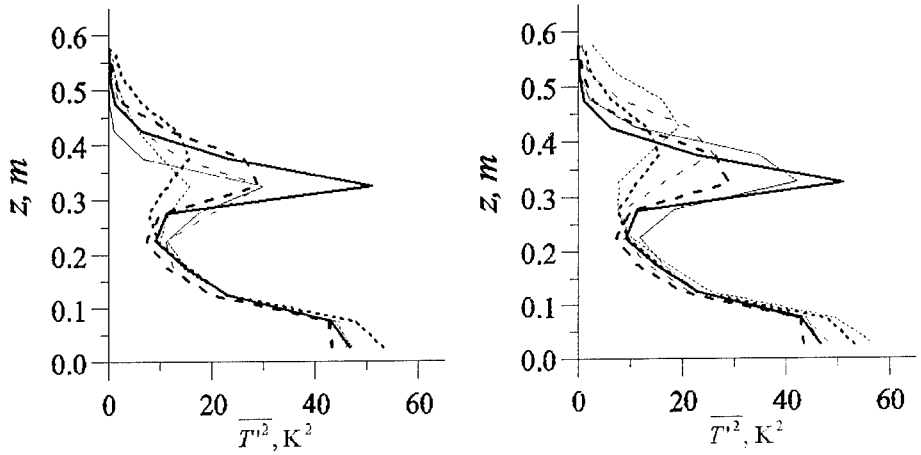


Figure 2: Temperature variance profiles in the evolving CBL at three subsequent locations along the simulation domain (wind tunnel test section): x=3.98 m (solid lines), x=5.63 m (dashed lines), and x=7.28 m (dotted lines) for the PS case (left plot, thin lines) and for the NS case (right plot, thin lines). The reference case (RC) profiles at the same locations are shown in both plots by heavy lines.

This leads to the localization of vertical motion within a comparatively shallow zone and, consequently, to the reduction of vertical turbulent exchange across the inversion layer. With negative elevated shear, the squashed penetrating thermals encounter a lateral blockage by the lower-momentum flow that brakes their horizontal transport. Such blockage induces local pressure gradients that redistribute energy from the horizontal velocity component to the vertical one. The enhanced vertical motions intensify the turbulent exchange across the inversion and lead to the faster CBL growth.

Acknowledgement: Support for the study provided by the Deutsche Forschungsgemeinschaft (Project PL 60/59) is gratefully acknowledged.

References

[1] E. Fedorovich and R. Kaiser. Wind tunnel model study of turbulence regime in the atmospheric convective boundary layer. *Buoyant Convection in Geophysical Flows*, E. J. Plate et al., Eds., Kluwer, 327–370, 1998.

[2] J.C.R. Hunt and P.A. Durbin. Perturbed vortical layers and shear sheltering. *Fluid Dyn. Res.*, 24:375–404, 1999.

[3] F.T.M. Nieuwstadt and R. A. Brost. Decay of convective turbulence. *J. Atmos. Sci.*, 43:532–546, 1986.

ADVANCES IN TURBULENCE VIII
Proceedings of the Eighth European Turbulence Conference
C. Dopazo et al. (Eds.)
© CIMNE, Barcelona 2000

On the generation of turbulence by baroclinic instability in the upper ocean

P. Ripa

Centro de Investigación Científica y de Educación Superior de Ensenada
Km. 107 carretera Tijuana–Ensenada, 22800 Ensenada, Baja California, México

Contact e-mail: ripa@cicese.mx

The upper part of the ocean is subject to vigorous forcing in the form of momentum, heat, and fresh water fluxes through the surface. These may lead to horizontal buoyancy gradients which, after partially relaxing through the radiation of Poincaré waves, attain hydrostatic and geostrophic balance with a vertically sheared current. This velocity field may be baroclinically unstable: the finite amplitude evolution triggered by the instability has important effects on the exchange of gases and other properties between the atmosphere and the deep ocean [1]. The purpose of this work is to investigate to what extent upper ocean baroclinic instability may produce turbulence. Baroclinic instability has been linked to quasi–geostrophic turbulence within the framework of Phillips two–layer model [7, 8], which has horizontal and rigid boundaries. A key element for this paper, though, is the influence of the deep ocean, which is modeled here by allowing the bottom boundary to be free (see figure 1). The first part of this work concerns the determination of saturation bounds for the perturbation to an unstable state. These bounds represent *a priori* constraints to the ergodicity of the flow, i.e. to the generation of turbulence [9, 11, 10, 12]. The second part deals with the construction of consistent few–component approximations (i.e., which conserve the integrals of motion of the full system), on a search of ergodic behavior.

The classical problems of Phillips and Eady have been extended, allowing for a free boundary and finite amplitude perturbations, by the models of Olascoaga & Ripa [2] and Ripa [5], respectively, denoted by V and D in figure 1. In both cases, changes of the state of the system can be described by two fields, say $q_\pm(x, y, t)$, where (x, y) denotes the horizontal position and t is time. In model V, q_+ and q_- are the potential vorticity fields in two homogeneous density layers, whereas in model D, q_+ and q_- are proportional to density variations at the top and bottom boundaries and potential vorticity is assumed uniform. All other variables, e.g. the streamfunction ψ or the deformation of the free boundary, are complicated functionals of $q_\pm$. Solutions of the model equations in the channel

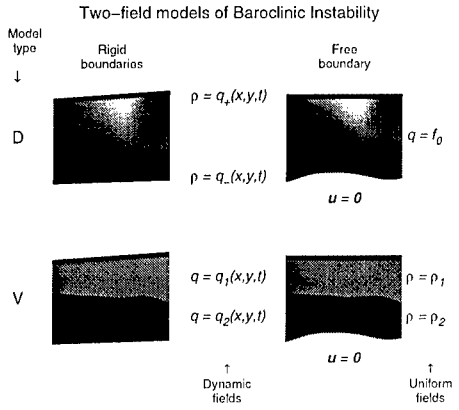


Figure 1: Vertical structure of both types of models. Left hand graphs: classical models (rigid boundaries). Right hand graphs: the top line is the ocean surface and the bottom boundary, which is free, represents the connection with the deep ocean

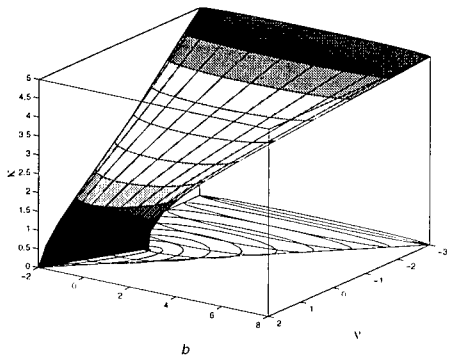


Figure 2: Instability region: κ is the wavenumber whereas b (ν) measures the competition between the stabilizing effect due to the planetary (topographic) gradient of ambient potential vorticity –the so called β effect– and the destabilizing effect of the vertical shear.

$\{x \in \mathbb{R},\ 0 < y < W\}$ are constrained by the conservation of energy, momentum, and a family of Casimirs.

Both types of systems have remarkably similar instability properties [6]. Let $q_\pm = Q_\pm(y) + \delta q_\pm(x,y,t)$, where $\{Q_\pm(y) = Q'_\pm y\}$ represents a basic state without horizontal shear ($Q'_\pm$ are constants), and the total deviation from the basic state is written as $\delta q_\pm = \delta\bar{q}_\pm(y,t) + \delta q'_\pm(x,y,t)$, with $\delta\bar{q}$ the along–channel average and $\delta q'$ the "wave". Using the integrals of motion, it follows that

$$\lambda = \frac{Q'_+ + Q'_-}{Q'_+ - Q'_-} = \frac{b+\nu}{2-\nu}$$

is such that if $|\lambda| > 1$ ($Q'_+Q'_- > 0$) the basic flow is stable, whereas if the flow is unstable then it must be $|\lambda| \leq 1$ ($Q'_+Q'_- \leq 0$). Figure 2 shows the locus of points (ν, b, κ) where the perturbation hamiltonian is indefinite in any frame; this is also the region of normal–mode unstable states (maximum growth rate is found at the center of one of the ellipses, near $(\nu, b, \kappa) = (1, -1, 0)$). The projection of the distorted cylinder over the (ν, b) covers the wedge $-2 \leq b \leq 2-2\nu$ (which implies $|\lambda| \leq 1$); outside that wedge the perturbation hamiltonian is positive definite in some frame, which implies nonlinear stability. Phillips model corresponds to the vanishing topography plane $\nu = 0$; in addition, Eady's classical problem neglects the gradient of planetary vorticity $b = 0$.

A priori bounds on the growth of both parts, $\delta q'$ and $\delta\bar{q}$, of the perturbation δq to an unstable basic state ($|\lambda| < 1$) are found to be

		Enstrophy distribution		
Least bound on		$\frac{\left\langle (\delta q')^2 \right\rangle}{\langle Q^2 \rangle}$	$\frac{\langle (\delta \bar{q})^2 \rangle}{\langle Q^2 \rangle}$	$\frac{\langle (\delta q)^2 \rangle}{\langle Q^2 \rangle}$
$\frac{\left\langle (\delta q')^2 \right\rangle}{\langle Q^2 \rangle}$	$\lvert\lambda\rvert \le \frac{1}{2}$:	$\frac{1}{1+\lambda^2}$	$\frac{1}{1+\lambda^2}$	$\frac{2}{1+\lambda^2}$
	$\lvert\lambda\rvert \ge \frac{1}{2}$:	$\frac{4\lvert\lambda\rvert(1-\lvert\lambda\rvert)}{1+\lambda^2}$	$\frac{4(1-\lvert\lambda\rvert)^2}{1+\lambda^2}$	$\frac{4(1-\lvert\lambda\rvert)}{1+\lambda^2}$
$\frac{\langle (\delta \bar{q})^2 \rangle}{\langle Q^2 \rangle}$ or $\frac{\langle (\delta q)^2 \rangle}{\langle Q^2 \rangle}$:		$\frac{4\lvert\lambda\rvert(1-\lvert\lambda\rvert)}{1+\lambda^2}$	$\frac{4(1-\lvert\lambda\rvert)^2}{1+\lambda^2}$	$\frac{4(1-\lvert\lambda\rvert)}{1+\lambda^2}$

and are illustrated in figure 3. It is clear that for slightly supercritical basic flows, $|\lambda| = 1 + 0^-$, the integrals of motion prevent the generation of turbulence. For $\lambda = 0$, on the other hand, the estimated bounds for $\left\langle (\delta q')^2 \right\rangle$, $\left\langle (\delta \bar{q})^2 \right\rangle$ and $\left\langle (\delta q)^2 \right\rangle$ are the "trivial" ones; this is taken as synonymous of maximum state space available for ergodic behavior. The condition $\lambda = 0$ corressponds to the cancellation of planetary and topographic restoring terms, $b + \nu = 0$, which yields the maximum normal modes growth rate [4].

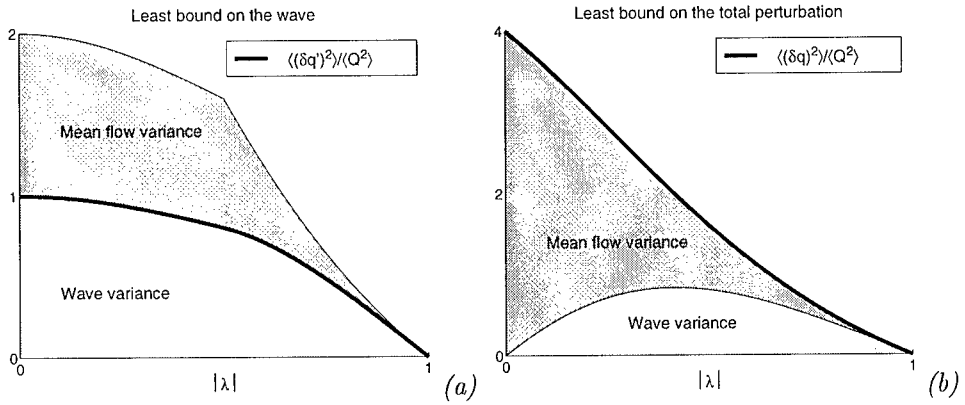


Figure 3: Bounds for the growth of the wavy part *(a)*, the mean flow variation *(b)*, or the whole perturbation *(b)*, in an enstrophy norm. The normalization is such that a trivial bound equals one *(a)* or four *(b)*, and instability of the basic flow requires $|\lambda| < 1$.

An important question is how small does $|\lambda|$ have to be in order for ergodic behavior to result from the instability. Approximate models (constructed by truncation of a Fourier series expansion of the perturbation) are found to satisfy the integral constraints of the full system. The minimal (six–component) nonlinear model is integrable (and thus non–ergodic) for all λ [3]. The *a priori* bounds for this truncated model are those of figure 3 multiplied by $6/\pi^2$

(≈ 0.61); the actual maximum perturbations are smaller than those predicted by the bounds, due to the additional constraint of energy conservation (which is different in models D and V). It is being investigated how many components have to be added and how small does λ have to be in order to realize ergodic behavior.

This work has been supported by CICESE core funding and by CONACyT (Mexico) under grant 26670-T.

References

[1] T. W. Haine and J. Marshall. Gravitational, symmetric, and baroclinic instability of the ocean mixed layer. *J. Phys. Oceanogr.*, 28:634–658, 1998.

[2] M. J. Olascoaga and P. Ripa. Baroclinic instability in a two-layer model with a free boundary and β effect. *J. Geophys. Res.*, 104:23,357–23,366, 1999.

[3] P. Ripa. A minimal nonlinear model of free boundary baroclinic instability. In *Proceedings of the 12th Conference on Atmospheric and Oceanic Fluid Dynamics*, pages 249–252. American Meteorological Society, 1999.

[4] P. Ripa. On the validity of layered models of ocean dynamics and thermodynamics with reduced vertical resolution. *Dyn. Atmos. Oceans*, 29:1–40, 1999.

[5] P. Ripa. Baroclinic instability in a reduced gravity, three-dimensional, quasi-geostrophic model. *J. Fluid Mech.*, 403:1–22, 2000.

[6] P. Ripa. Waves and resonance in free-boundary baroclinic instability. *J. Fluid Mech.*, submitted November 1999.

[7] R. Salmon. Two-layer quasi-geostrophic turbulence in a simple special case. *Geophys. Astrophys. Fluid Dyn.*, 10:1–28, 1978.

[8] R. Salmon. Baroclinic instability and geostrophic turbulence. *Geophys. Astrophys. Fluid Dyn.*, 15:167–211, 1980.

[9] T.G. Shepherd. Non-ergodicity of inviscid two-dimensional flow on a beta-plane and on the surface of a rotating sphere. *J. Fluid Mech.*, 184:289–302, 1987.

[10] T.G. Shepherd. Nonlinear saturation of baroclinic instability. Part I: The two-layer model. *J. Atmos. Sci.*, 45:2014–2025, 1988.

[11] T.G. Shepherd. Rigorous bounds on the nonlinear saturation of instabilities to parallel shear flows. *J. Fluid Mech.*, 196:291–322, 1988.

[12] T.G. Shepherd. Nonlinear saturation of baroclinic instability. Part II: Continuously stratified fluid. *J. Atmos. Sci.*, 46:888–907, 1989.

ADVANCES IN TURBULENCE VIII
Proceedings of the Eighth European Turbulence Conference
C. Dopazo et al. (Eds.)
© CIMNE, Barcelona 2000

Sensitivity of rhythmic oblique bar generation to wave-driven turbulence in the surf-zone

F. Ribas[1], A. Montoto[2] and A. Falqués [1]

[1]Dept. de Física Aplicada, Universitat Politècnica de Catalunya
c. Jordi Girona 1-3, Barcelona 08034, SPAIN
[2]Dept. de Física i Enginyeria nuclear, Universitat Politècnica de Catalunya
c. Jordi Girona 1-3, Barcelona 08034, SPAIN

Contact e-mail: cesca@fa.upc.es

1 Motivation and formulation

Nearshore hydrodynamics is highly turbulent mainly due to breaking surface waves. Besides, water motion in the nearshore is strongly coupled to morphological evolution through the sediment transport processes. However, in spite of the complexity of coastal morphodynamics, relatively regular large scale patterns dominate quite often the topography and the water motion. Rhythmic systems of transverse or oblique sand bars in the surf zone are an example of such patterns. The purpose of this work is to investigate the influence of the wave-driven turbulence on the physical mechanisms that can lead to the growth of these morphological features.

The generating mecanisms are investigated by means of a stability analysis. The governing equations are the short-wave averaged horizontal two-dimensional momentum, mass and sediment conservation equations. A basic steady equilibrium which is uniform along the shore is assumed. Then, the formation of complex topography is represented by the growth of "unstable" perturbations on this basic equilibrium. The physical mechanisms are related to the coupling between the topographic perturbations and the perturbations on the incident wave field and the longshore current (for more details see Falqués *et. al* [2]).

The breaking wave-driven turbulence comes into the model through the horizontal momentum diffusion, ν_t. According to Longuet-Higgins [3] a very simple parametrization is assumed, $\nu_t(x) = Nx\sqrt{gD}$, where x is the cross-shore distance to the coastline, D is the local water depth and N is the turbulent viscosity parameter. This is also in accordance with Battjes [1] parameterization if the appropriated wave dissipation is chosen. The aim of the present contribution is to investigate the sensitivity of the growth of morphological patterns to the parameter N. This is partially motivated by the large uncertainty existing on the

values of this parameter. For instance, recent measurements by Rodríguez *et. al* [4] show that 2HD turbulence models give values for the turbulent diffusivity that can easily be one order of magnitude greater than experimental data.

The sediment flux $\vec{q}$ is assumed to be proportional to a power m of the depth-averaged horizontal net flow with a coefficient $\alpha(x)$ that is a wave stirring function. The perturbations in the wave momentum input are included trough the perturbations in water depth (since wave height is assumed to be proportional to water depth inside the surf zone). In contrast with earlier studies, the corresponding displacement of the breaker line is taken into account.

2 Results

The results of the model are very sensitive to the sediment transport parameterization. The basic assumption is that the sediment flux is either linear or cubic ($m = 1, 3$) with the mean velocity field. The first case is representative of a wave orbital velocity much larger than the mean current whereas the cubic law fits better to the opposite situation.

In case of a cubic sediment transport formula we obtain several unstable modes when the wave incidence is oblique enough (incidence angle greater than 10 degrees). The influence of N parameter in these modes is quite strong. Figure 1 (Left) shows the growth rate curve obtained for the dominant mode, with three different values of the turbulence parameter ($N = 0.01, 0.005, 0.002$) and physically realistic values for the other parameters. When N decreases, the number of modes, their wavenumbers and their growthrate increase. Therefore, the wave-driven turbulence has a typical diffusive effect on these modes. In Figure 1 (Right) the topographic and current perturbations of the first mode can be seen in case of $N = 0.005$. These patterns are very robbust under changes of either the turbulence or the other parameters and can be recognized as a system of very oblique down-current oriented bars.

When a linear sediment transport law is used ($m = 1$), a wave-stirring coefficient either constant or increasing seaward across the surf zone can be chosen. The latter case fits better to the situation where the incident wind wave energy is dominant while the former can be representative when the significant wave energy is due to low frequency waves. In case of a constant stirring function, the N parameter has a small effect on the growth curves (see Figure 2 Left). This can be due to the fact that the perturbed flow pattern associated to the growth of these bedforms has small gradients in comparison with the case of cubic sediment transport. Figure 2 (Right) shows the topographic and current perturbation for $N = 0.005$.

When the stirring function increases (quadratically) from the shoreline up to the breaker line, the basic state is unstable only in case of a small wave incidence angle (0 to 10 degrees). For a nearly perpendicular incidence, the influence of N is not very important, and it seems to have a small diffusive effect. A typical growth rate curve for three different values of the turbulence parameter and the

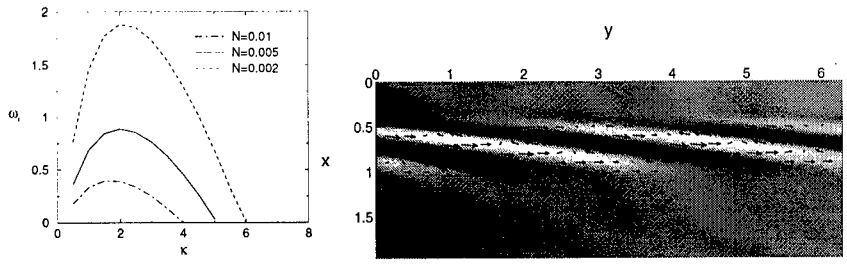


Figure 1: **Left.** Growthrate curve of the dominant mode as a function of the wavenumber in case of a cubic sediment transport formula and three different values of the turbulence parameter, N. **Right.** Topographic and current perturbations of the first mode in case of $N = 0.005$. The y axis is the coastline and the longshore current goes from the left to the right. Shoals are represented in white and pools in dark.

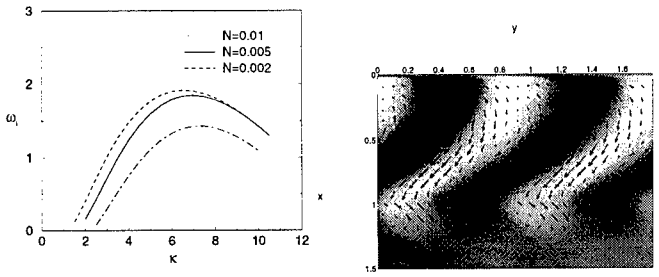


Figure 2: **Left .** Growthrate curve as a function of the wavenumber in case of a linear sediment transport formula and a constant stirring function for three different values of the turbulence parameter, N. **Right.** Topographic and current perturbations in case $N = 0.005$.

corresponding topographic and current perturbations are shown in Figure 3. In contrast, for larger incidence angle, the turbulence seems to favour the growth of the bedforms. The fact that the turbulence affects both the basic current profile and the instability may explain this anomalous behaviour. Small N values lead to very sharp profiles where the current is almost concentrated inside the surf zone (see Longuet-Higgins [3]) while the shoals and pools of this pattern tend to grow mainly on the shoaling zone. Therefore, large values of N are more conducive to the growth in this case. This explanation does not hold for small incidence angle because the flow disturbances in this former case are due directly to the waves become dominant with respect to the effects related to the current.

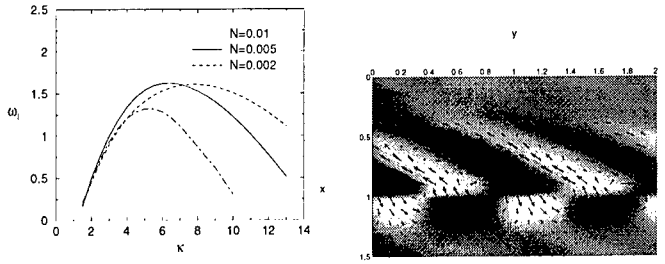


Figure 3: **Left .** Growthrate curve as a function of the wavenumber in case of a linear sediment transport formula and a quadratic stirring function for three different values of the turbulence parameter, N, and an small wave incidence angle. **Right.** Topographic and current perturbations in case $N = 0.005$.

3 Conclusions

The wave driven turbulence affects the growth of large scale morphological patterns in the surf zone in two ways: damping the instabilities by means of a typical diffusive process or modifying the profile of the longshore current itself. In general, the increase in turbulence intensity does not affect dramatically the growth which is never totally inhibited for realistic values of the viscosity parameter. Interestingly, in a rather specific situation an increase of turbulence may result in a larger growth due to the smoothing of the longshore current profile.

F. Ribas acknowledges the Generalitat de Catalunya for her FI/FIAP grant. This work is part of the SASME project which is funded by the Commission of the European Union, under contract MAS3 CT97-0081.

References

[1] J.A. Battjes. A note on modeling of turbulence in the surf zone. *Proc. Symp. Modeling Tech., ASCE*, 1: 1050–1061, 1975.

[2] A. Falqués, A., *et al.* Nearshore oblique bars. Modelling versus observations at the Truc Vert Beach *Proc. I.A.H.R. Symp. on River, Coastal and Estuarine Morphodynamics*, 1: 207–214, 1999.

[3] M.S. Longuet-Higgins Longshore currents generated by obliquely incident sea waves. *J.Geophys.Res.*, 75: 6778–6801, 1970.

[4] A. Rodríguez *et al.* Macroturbulence measurements with electromagnetic and ultrasonic sensor: a comparison under high-turbulence flows *Experiments in Fluids*, 27: 31–42, 1999.

ADVANCES IN TURBULENCE VIII
Proceedings of the Eighth European Turbulence Conference
C. Dopazo et al. (Eds.)
© CIMNE, Barcelona 2000

Laboratory modeling of geophysical turbulence

P. F. Linden[1], J. N. Hacker[2], B. M. Boubnov[3] and S. B. Dalziel[2]

1 Department of Mechanical and Aerospace Engineering,
University of California, San Diego, La Jolla, CA, USA
2 Department of Applied Mathematics and Theoretical Physics
University of Cambridge, Cambridge, UK
3 Institute of Atmospheric Physics
Moscow, Russia

Contact e-mail: pflinden@mae.ucsd.edu

1 Introduction

Oceanic and atmospheric flows may be considered as turbulent motions under the constraints of geometry, stratification and rotation. At large scales these flows tend to be along isopycnal surfaces due to the combined effects of the very low aspect ratio of the flows (the motion is confined to thin layers of fluid) and the existence of stable density stratification. The effect of the Earth's rotation is to reduce the vertical shear in these almost planar flows. The combined effects of these constraints are to produce approximately two-dimensional turbulent flows at very high Reynolds numbers — so called geophysical turbulence.

In a strictly two-dimensional flow with weak dissipation, energy input at a given scale is transferred to larger scales, because these constraints stop vortex lines being stretched or twisted. Physically this upscale energy transfer occurs by merging of vortices and leads to the production of coherent structures in the flow that contain the energy — the appearance of order from chaos [4]. This scenario is an attractive model for geophysical flows which are known to contain very energetic vortices - mesoscale oceanic eddies and atmospheric highs and lows. This upscale transfer of energy is inhibited at the Rossby deformation scale by baroclinic instability at larger scales, which accounts for the observed size of geophysical vortices.

The most famous laboratory analogue of these flows is the annulus flow, pioneered by Fultz and Hide in the 1940s and 1950s. Flow is driven in a rotating annulus by differential heating of the lateral walls of the annulus, or by internal heating of the fluid. A horizontal temperature gradient is established which drives a zonal flow via the 'thermal wind' balance. For certain values of the parameters this flow is unstable to baroclinic modes that feed on the energy

in the temperature field. At finite amplitude the instabilities can lead to large amplitude waves and vortex structures.

Many features of atmospheric flow have been identified with structures and phenomena observed in the annulus experiments, and understanding of atmospheric dynamics, in particular, has been significantly advanced. The experiments have provided new insights about the dynamics and revealed a wide range of nonlinear behavior [1].

2 Quasi-geostrophic flows

Quasi-geostrophic (QG) vortices with Rossby numbers $Ro \approx 0.1$ are primarily balanced motions with pressure gradients matched by Coriolis forces. This balance manifests itself in the aspect ratio Γ of the height H to the vortex radius R being such that the Burger number $B = NH/fR$ is order unity. In the oceans the buoyancy frequency $N \approx 10^2$ s^{-1} and the Coriolis parameter $f \approx 10^{-4}$ s^{-1}, so that the vortices are flat pancake-like structures with $\Gamma \approx 10^{-2}$. In almost all laboratory experiments $f \geq N$ and, consequently, these vortices have aspect ratios $\Gamma \geq 1$; i.e. they are tall and thin.

In a strongly stratified fluid (the ocean) dissipation is produced by horizontal vorticity associated with vertical shear of horizontal velocity [8]. In a rapidly rotating fluid (the laboratory) dissipation occurs through vertical vorticity associated with the horizontal shear of the horizontal velocity. Since dissipative processes are impossible to represent exactly, parameterizations are used. Hence, significant differences may occur between the oceans and the laboratory representations. These differences may affect the propagation and decay of laboratory vortices making extrapolations to oceanic conditions invalid.

In addition, both fission, produced by baroclinic instability, and merging of vortices are three-dimensional processes and are intimately linked to the aspect ratios of the structures. The overlapping of two pancake-like structures is different from the wrapping of two tall vortices about each other. Thus these important mechanisms are susceptible to aspect ratio changes.

The QG description of vortex motion is adequate for many purposes. In a strongly stratified fluid, $N/f \gg 1$, vertical motion is inhibited by the stratification and flow is along isopycnal surfaces. In a rapidly rotating fluid, $N/f \ll 1$, vertical shear is inhibited by the Taylor-Proudman constraint. Continuity implies the vertical velocity is zero under suitable boundary conditions, and so in many circumstances the flow is predominantly horizontal in this case also. Thus there is good reason to expect that oceanic OG flows with $N/f \gg 1$ may be modeled in the laboratory with $N/f \ll 1$ systems, simply noting the change in aspect ratio of the flows.

3 Source-sink turbulence

An alternative laboratory realization of geophysical turbulence is provided by a stratified, rotating fluid forced by an array of sources and sinks around the boundary of a tank. The sources and sinks are arranged so that the flow is forced horizontally with a minimum of vertical mixing. Vortices are produced that are dominated by their horizontal velocity and vertical vorticity. These vortices interact with one another to produce a turbulent flow in which upscale energy transfers occur, and where the effect of rotation is to produce vortices on the deformation scale - see [2, 7, 3]. This laboratory system provides a capability for studying flows with applications to the oceans and atmosphere under controlled conditions, and enables accurate measurements of the flow to be made, so that the underlying dynamics can be investigated.

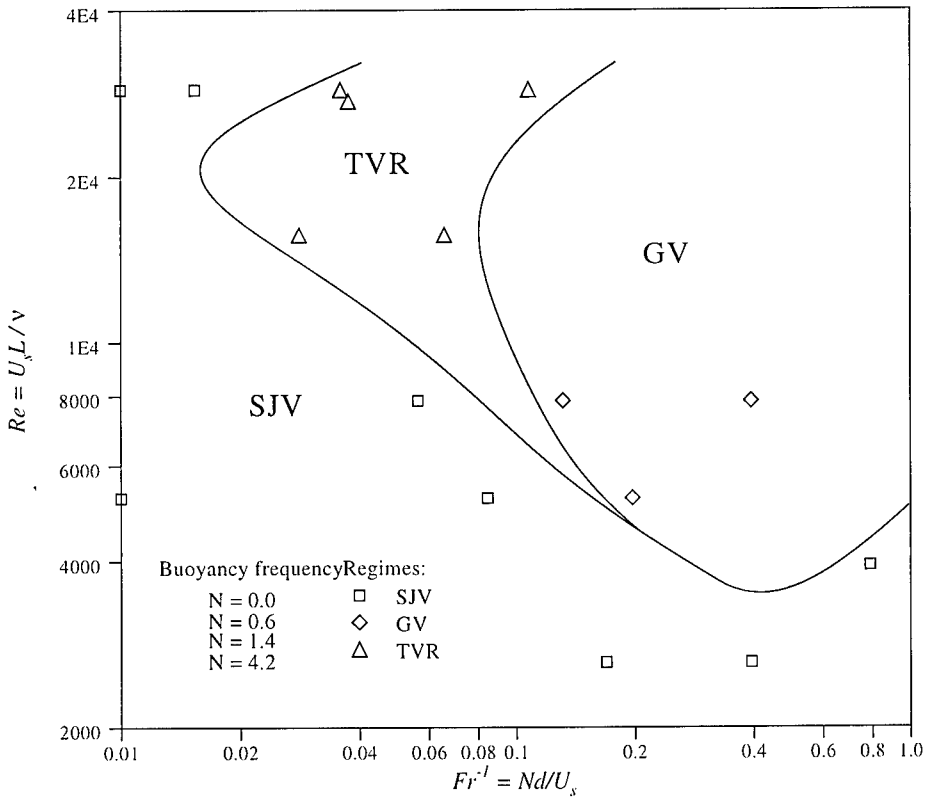


Figure 1: Regime diagram for source-sink turbulence in a stratified annulus.

Experiments in annular geometry were conducted with eight source-sink pairs positioned at regular intervals around the inner boundary at mid-depth. Three regimes occurred according to the values of Froude number $Fr = U_s/Nd$ and

Reynolds number $Re = U_s L/\nu$, based on the mean source velocity U_s, the source/sink diameter d and L the domain scale (Fig. 1). For low Re, each source produced a dipolar vortex that propagated to the outer boundary and remained stable. This regime, 'source-jet-vortices' (SJV), also occurred for larger Re and Fr, with three-dimensional turbulence becoming increasingly evident for larger Fr. For moderate Re and low Fr, the SJV interacted to form six gap-scale vortices (GV regime) of alternating sign that remained in a stable configuration. For moderate Re and moderate Fr, an intermediate regime, 'turbulent vortices' (TVR), occurred in which GV were formed but did not remain stable. The low Re branch of the SJV regime! is an essentially laminar response, with viscosity inhibiting vortex merger and upscale energy transfer. The large Fr branch of the SJV regime occurs when the radial momentum input from the source and sinks dominates the interior flow. The GV regime is of particular interest, as it indicates that the stratification can facilitate the organisation of an interior flow that is sufficiently strong to overcome the constraints of the forcing geometry. The intermediate TVR mode occurs as a result of competition between the tendency of inverse cascade to produce the GV mode, and the tendency of the forcing configuration to reassert the SJV mode. The emergence of a single domain-scale structure is considered to be a specific example of the GV mode and inverse-cascade behaviour.

Rotating flows in the annulus displayed a range of dynamic regimes, including many of the modes observed in differentially heated annulus experiments. The four basics regimes were: zonally-symmetric circulation (ZC), anticyclonic gap-scale vortices (AGV), azimuthal wave/vacillation regimes (WR), and geostrophic turbulence regimes (GT). The regimes are best displayed on a Rossby number $Ro = U_s/fL$, Ekman number $Ek = \nu/fL^2$ plot (Fig. 2). ZC occurred for low Ro. GT regimes were characterised by the production of dipoles and occurred when Ro exceeded a critical value at low Ek, indicating the importance of *ageostrophic* effects in the dipole formation process. The interaction of dipoles in the gap led to the emergence of gap-scale and azimuthally organised structures. Although eddy scales were set by the forcing parameters, the stratification played an important role in controlling dissipation levels, with eddies persisting for longer timescales as N was ! increased. AGV regimes occurred at large Ro and are thought to be similar to nonrotating GV regimes, with symmetry broken by the rotation. WR regimes occurred only for the largest value of N used and in decaying flows, at moderate Ro and Ek, and are thought to be baroclinic in origin.

4 Conclusions

These experiments reveal a rich dynamical structure and show a wide range of interesting phenomena. Examples include nonlinear vortex interactions and the development of mean flows, baroclinic instability, basin scale flows developed from localized forcing [5], spin-up and spin-down processes associated with

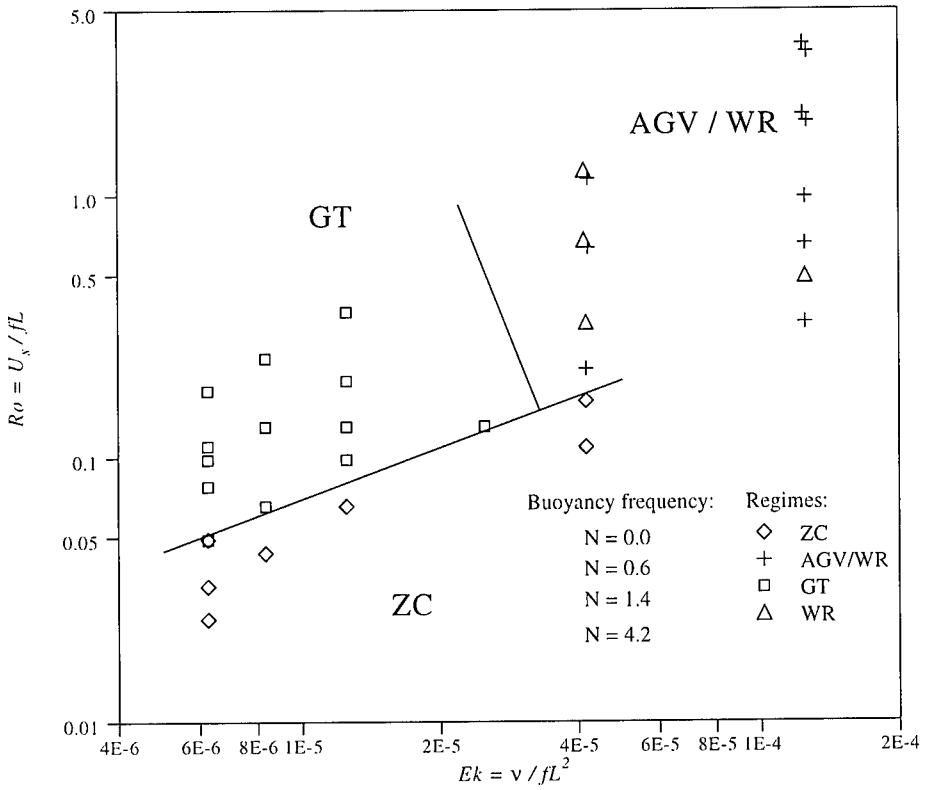


Figure 2: Regime diagram for source-sink turbulence in a rotating annulus.

vortex growth and decay and passive dispersion in flows dominated by vortex structures. There are also indications that at low Re laminar flows under strong stratification may form patterns linked to basin attractors [6] Investigation of these phenomena has given insight into the dynamical processes that occur in these constrained turbulent flows and is relevant to topical questions in oceanography. For example, the research addresses questions concerning the basin response to variable forcing and processes associated with shelf-basin transfers of mass and momentum.

These experiments provide a way of studying dynamics relevant to geophysical flows. The primary motivation is one of curiosity about the dynamics of the flows, rather than any specific geophysical problem. Further study of these experiments should result in a substantial improvement in our understanding of the large-scale dynamics of the oceans and atmosphere, and provide insights into the dynamics of constrained turbulent systems. This understanding is complementary to and extends that obtained in annulus experiments. In particular, in the source-sink experiments the forcing and the stratification are set indepen-

dently, rather than being coupled as in the annulus. This extra degree of freedom allows a significantly wider class of flows to be studied. Also, since the forcing geometry can be varied with respect to the domain geometry it is possible to study the effects of different basin geometries and/or forcing arrangements. This is particularly relevant to oceanographic prob! lems in enclosed regions such as the Mediterranean.

It is, of course, not possible to capture all the relevant physics in a single experiment. One major omission from the present experiments is the beta effect, since topographic beta (often used in experiments to represent the variation of Coriolis parameter with latitude) has limited effect in stratified flows. In this, and other, regards the experiments must be interpreted with care; e.g. applied to scales small compared to the Rhines scale. However, the experiments shows many interesting phenomena and provide a convenient environment for their study.

References

[1] Bastin, M.E. & Read, P.L.: 1998 Experiments on the structure of baroclinic waves and zonal jets in an internally heated rotating cylinder of fluid. *Phys. Fluids* ., **10**, 374–389.

[2] Boubnov, B.M. Dalziel, S.B. & Linden, P.F. 1994, Source-sink turbulence in a stratified fluid. *J. Fluid Mech.*,**261**, 273–303.

[3] De Rooij, F., Linden, P.F. & Dalziel, S.B. 1999 Experimental investigations of quasi-two-dimensional vortices in a stratified fluid with source-sink forcing. *J. Fluid Mech.*,**383**, 249–283.

[4] Flor, J.B. & Heijst, G.J.F. van 1996 Stable and unstable monopolar vortices in a stratified fluid. *J. Fluid Mech.*,**311**, 257–288.

[5] Hacker, J. N, Linden, P. F. & Dalziel, S. B. 1999 Coherent vortices produced by localised turbulent forcing of a stratified fluid. *Oceanic Fronts and Related Phenomena* (Konstantin Fedorov International Memorial Symposium). IOC Workshop Report Series, 1999, N 159, UNESCO'99.

[6] Kanda, I. & Linden, P.F. 2000 Sensitivity of horizontal flows to forcing. *J. Fluid Mech.* (submitted).

[7] Linden, P.F., Boubnov, B.M. & Dalziel, S.B. 1995 Source-sink turbulence in a rotating, stratified fluid. *J. Fluid Mech.*,**298**, 81–112.

[8] Narimousa, S., Maxworthy, T. & Spedding, G.R. 1991 Experiments on the structure and dynamics of forced, quasi-two-dimensional turbulence. *J. Fluid Mech.*,**223**, 113–133

ADVANCES IN TURBULENCE VIII
Proceedings of the Eighth European Turbulence Conference
C. Dopazo et al. (Eds.)
© CIMNE, Barcelona 2000

Large eddy simulation of turbulent, nonpremixed combustion

Parviz Moin, Charles Pierce, and Heinz Pitsch

Center for Turbulence Research, Stanford University
Stanford, California, 94305-3030, USA

Contact e-mail: moin@stanford.edu

1 Introduction

It has been pointed out that application of LES to turbulent combustion offers little advantage over RANS because chemical reactions take place at the smallest scales, which are not resolved in LES. While it was recognized that LES did provide a better description of large scale turbulent transport, it appeared that the problem of reaction source closure would not be any easier in LES. Recently it has been found that for nonpremixed combustion, LES provides significant advantages over RANS when mixture fraction or flamelet-based combustion models are considered. In this case, flamelets provide the model for the small-scale flame structure, while LES, when combined with the presumed subgrid PDF, provides a very accurate description of mixture-fraction fluctuations. Furthermore, recent work (Sec. 3,4) has produced flamelet formulations specialized for LES that have a more local description of flamelet evolution, allowing for more accurate description of phenomena such as local extinction and flame lift-off. The basic premise in LES that the small scales tend to be more universal and are governed mainly by the local large scales appears to hold for turbulent combustion.

2 Governing Equations

We consider the variable-density momentum and scalar transport equations:

$$\frac{\partial \rho \mathbf{u}}{\partial t} + \nabla \cdot (\rho \mathbf{u}\mathbf{u}) = -\nabla p + \nabla \cdot \left[2\mu(\mathbf{S} - \tfrac{1}{3}\mathbf{I}\nabla \cdot \mathbf{u})\right] \ , \tag{1}$$

$$\frac{\partial \rho \phi_k}{\partial t} + \nabla \cdot (\rho \mathbf{u} \phi_k) = \nabla \cdot (\rho \alpha_k \nabla \phi_k) + \rho w_k \ , \tag{2}$$

where, $\mathbf{S}$ is the strain-rate tensor, $\mathbf{I}$ is the identity tensor, ϕ_k is a set of one or more transported scalars, and α_k and w_k are the molecular diffusivities and

reaction sources of the scalars. One of the scalars is usually taken to be the mixture fraction, a conserved scalar:

$$\frac{\partial \rho Z}{\partial t} + \nabla \cdot (\rho \mathbf{u} Z) = \nabla \cdot (\rho \alpha \nabla Z) \ . \tag{3}$$

The present work is based on the low Mach number approximation to the flow equations. When combined with the assumption that differential diffusion is negligible at the large scales a separate energy equation is not necessary. Under the present assumptions all combustion variables are known functions of the transported scalars ϕ_k. In particular, the equation of state may be written

$$\rho = \rho(\phi_k) \ . \tag{4}$$

The continuity equation acts as a constraint on the velocity field, with the time-derivative of density as a source term:

$$\nabla \cdot (\rho \mathbf{u}) = -\frac{\partial \rho}{\partial t} \ . \tag{5}$$

This constraint is enforced by the pressure, in a manner analogous to the enforcement of the incompressibility constraint for isothermal flows.

Subgrid momentum and scalar transport terms that appear from filtering equations (1) and (2) are modeled using the dynamic approach of Moin et al.[6] Another major modeling requirement is for the nonlinear density function (4). Here, the presumed subgrid pdf is used:

$$\overline{\rho} = \int \rho(\phi_k) P(\phi_k) \, d\phi_k \tag{6}$$

For conserved scalars such as mixture fraction, the subgrid pdf can be modeled using the beta distribution [2, 4]. In this case, the subgrid mixture fraction variance is obtained dynamically using the method of Pierce and Moin [10].

3 Flamelet / Progress-Variable Approach

This approach, developed by C. Pierce [11], is based on "quasi-steady" flamelets [8], in which the local flame state undergoes unsteady evolution through a sequence of stationary solutions to the flamelet equations.

A single-parameter flamelet library is first developed for the given combustor conditions by looking for stationary solutions to the one-dimensional reaction-diffusion equations. The unstable lower branch is included so that the complete range of flame states, from completely extinguished (mixing without reaction) to completely reacted (equilibrium chemistry), is represented in the library. Arbitrarily complex chemical kinetic mechanisms as well as differential-diffusion effects can be included. The result is a complete set of flame states, given in terms of mixture fraction and a single flamelet parameter, denoted by λ:

$$y_k = y_k(Z, \lambda) \ , \quad T = T(Z, \lambda) \ , \quad \rho = \rho(Z, \lambda) \ , \quad w_k = w_k(Z, \lambda) \ . \tag{7}$$

One of the combustion variables, or some combination of the variables is chosen to serve as an overall reaction progress variable. This would be a quantity that is representative of the overall gross flame behavior and that varies monotonically with the flame state so that its value uniquely determines it.

Transport equations are solved for both mixture fraction and the progress variable, generically denoted by C:

$$\frac{\partial \overline{\rho}\widetilde{Z}}{\partial t} + \nabla \cdot (\overline{\rho}\widetilde{\mathbf{u}Z}) = \nabla \cdot (\overline{\rho}\widetilde{\alpha}\nabla\widetilde{Z}) \ , \tag{8}$$

$$\frac{\partial \overline{\rho}\widetilde{C}}{\partial t} + \nabla \cdot (\overline{\rho}\widetilde{\mathbf{u}C}) = \nabla \cdot (\overline{\rho}\widetilde{\alpha}\nabla\widetilde{C}) + \overline{\rho}\widetilde{w}_C \ . \tag{9}$$

The progress variable equation contains a reaction source term that must be closed. This is accomplished by writing

$$\widetilde{w}_C = \int w_C(Z,\lambda)\widetilde{P}(Z,\lambda)\, dZ\, d\lambda \tag{10}$$

and assuming that

$$\widetilde{P}(Z,\lambda) = \delta(\lambda - \lambda_0) \cdot \beta(Z; \widetilde{Z}, \widetilde{Z''^2}) \ . \tag{11}$$

That is, each subgrid state is represented by a single flamelet with mixture-fraction fluctuations given by the beta distribution. This is a reasonable assumption in the absence of further information about the subgrid state.

The final step is to relate λ_0 to the filtered value of the progress variable, $\widetilde{C}$, which is known from Eq. 9:

$$\widetilde{C} = \int C(Z,\lambda)\widetilde{P}(Z,\lambda)\, dZ\, d\lambda \ . \tag{12}$$

After substitution of the presumed pdf and integrating, this yields

$$\widetilde{C} = f(\widetilde{Z}, \widetilde{Z''^2}, \lambda_0) \tag{13}$$

If C is a monotonic function of λ, then the above relation can be used to eliminate λ from the problem. The final result is a closed specification of the chemical system in terms of the two variables $\widetilde{Z}$ and $\widetilde{C}$.

The forgoing process automatically creates a one-step reduced chemical system, based on stationary flamelet solutions obtained using detailed chemical kinetics. In this sense, the method is similar in concept to the intrinsic low-dimensional manifold approach of Maas and Pope [5].

4 Lagrangian-Type Flamelet Model

This approach, under development by Pitsch [12, 13] has already successfully been applied in RANS calculations of turbulent jet diffusion flames [14, 15]. The

model follows the conserved scalar approach with a presumed pdf of the mixture fraction and uses the flamelet ideas of Peters [8, 9]. Thereby the filtered values of all reactive scalars are given by an expression similar to Eq. (12). The mixture fraction pdf is presumed to be a β-function. The functional dependence of the reactive scalars on the mixture fraction required for the integration of Eq. (12) is determined by the solution of the unsteady flamelet equations.

The flamelet equation for the species mass fractions Y_i can be written as

$$\frac{\partial Y_i}{\partial \tau} - \frac{\chi}{2}\frac{\partial^2 Y_i}{\partial Z^2} - \dot{w}_i = 0\,, \tag{14}$$

where τ is a Lagrangian flamelet time and χ the scalar dissipation rate.

In Eq. (14) the Lewis numbers of all chemical species have been assumed to be unity. This assumption is discussed in great detail in Ref. [15] and seems to be valid for the present configuration.

The consideration of the time dependence certainly adds some complexity to the problem, but it has been shown that it is essential to consider the unsteadiness, if for instance radiation cannot be neglected or NO formation is considered [14].

Together with the corresponding energy equation, Eq. (14) can readily be solved, and the solution used to provide the remaining unknown quantities such as the density and temperature, provided the scalar dissipation rate is known as a function of the mixture fraction and the flamelet time τ can be related to the physical space coordinates.

The basic idea of the model is that flamelets are introduced at the inflow boundary and move downstream, essentially by convective transport. By conditionally averaging the scalars over planes of equal nozzle distance, these averages depend only on the downstream direction. Since flamelets are actually associated with the reaction zone, which is located in the vicinity of the stoichiometric mixture, the Lagrangian-type flamelet time can be related to the axial nozzle distance x by

$$\tau = \int_0^x \left\langle \widetilde{u} | \widetilde{Z}_{\mathrm{st}} \right\rangle^{-1} dx'\,. \tag{15}$$

For the evaluation of the conditional mean scalar dissipation rate, which is needed to solve the flamelet equations, a newly developed model has been used that can account for local phenomena such as the pilot flame and is described in Ref. [13].

5 Applications

The Flamelet/Progress-Variable Approach of Sec. 3 has been used for large eddy simulation of methane-air combustion in a coaxial jet combustor (Fig. 1). The configuration used corresponds to the experiment of Owen et al. [7]. An instantaneous snapshot of the mixture fraction and product mass fraction fields is

presented in Fig. 2. The simulation correctly predicts a highly unsteady, asymmetric lifted flame as was observed in the experiment. At the particular instant shown, the flame in the upper part of the flow is lifted farther down stream than the rest of the flame due to higher fuel velocity and concentration emanating from the upper part of the fuel jet. Earlier calculations with fast chemistry [2] or the steady flamelet approach [3] were unsuccessful in capturing the lifted flame phenomenon. Predictions of radial profiles of mean mixture fraction and product mass fraction ($Y_P = Y_{CO2} + Y_{H2O}$) and their comparison with experimental data are shown in Fig. 3.

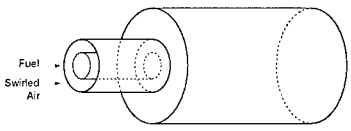


Figure 1: Schematic of a coaxial jet combustor.

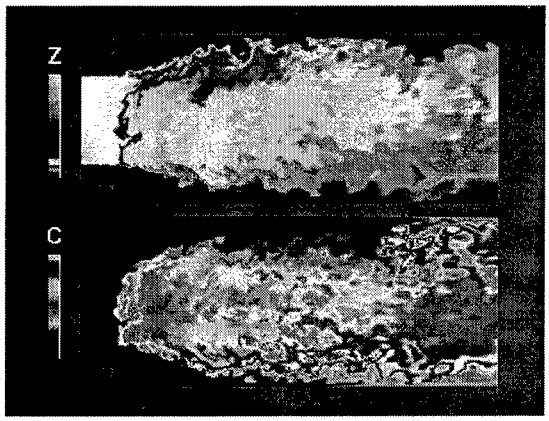


Figure 2: Instantaneous snapshot of mixture fraction (top) and product mass fraction (bottom).

The configuration used for validation of the Lagrangian flamelet model of Sec. 4 is a piloted methane/air jet diffusion flame (Sandia Flame D). The fuel is a 25 % methane, 75 % air mixture, which has been diluted with air in order to minimize the formation of polycyclic aromatic hydrocarbons and soot. The fuel nozzle is enclosed by a broad, slightly lean pilot flame and coflowing air. The Reynolds number based on the fuel stream is Re = 22400. The flame has been experimentally investigated by Barlow and Frank [1, 16], who performed Rayleigh measurements of temperature, and Raman and LIF measurements to obtain mass fractions of chemical species and the mixture fraction.

Figure 4(a) shows that the mean mixture fraction is well predicted by the simulation along the centerline until $x/D = 60$, after which the experimental data is slightly overpredicted. The mixture fraction rms (including both resolved and sub-grid contributions) is also given in Fig. 4(a). The experiment is slightly underpredicted in the far field of the jet. The underprediction for $x/D < 10$ might be attributed to experimental uncertainties, since the rms must go to zero close to the nozzle. This conclusion is supported by the temperature rms in Fig. 4(b). Figure 4(a) also indicates the subgrid-scale mixture fraction rms,

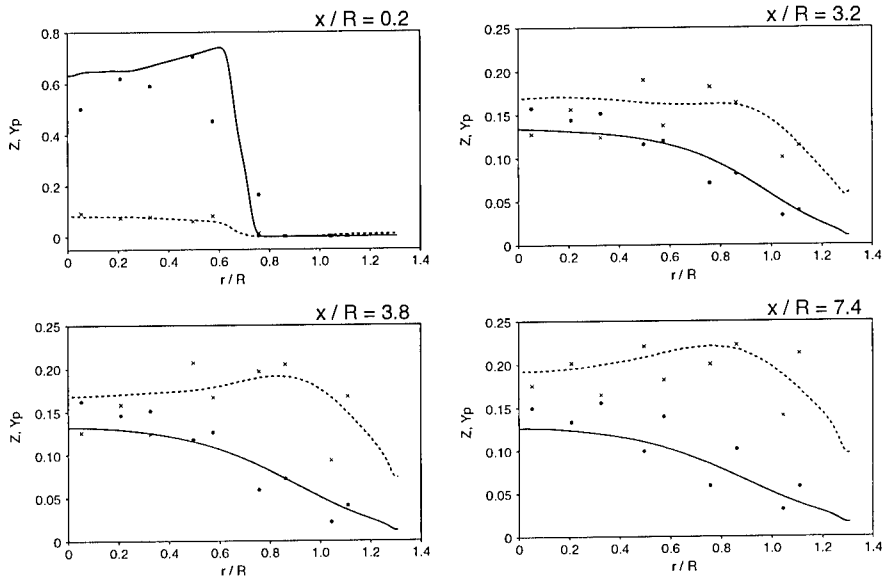


Figure 3: Radial profiles of time-average mixture fraction (—) and product mass fraction (- - -) profiles in the coaxial jet combustor and comparison with experimental data [7] (symbols) at several axial locations, x/R.

which is observed to be much smaller than the total rms, indicating that the major part of the turbulent mixture-fraction fluctuations is resolved by the LES.

The calculated mean and rms temperature along the centerline are shown in Fig. 4(b). Both agree well with the experimental data. Even the decrease in the temperature rms in the vicinity of the peak temperature is well represented by the simulation. It is interesting to note that this is not caused by heat release, but is simply due to the vanishing temperature gradient with respect to mixture fraction.

The slight overprediction in mean temperature up to $x/D = 40$ has been found to be caused by a partially premixed heat release and will be discussed below. The effect is also apparent in the experiments, but occurs in the calculations much closer to the nozzle.

The remaining figures show centerline profiles for species mass fractions of CO_2 and CO (Fig. 4(c)), and NO and OH (Fig. 4(d)). In general all profiles agree well with the experimental data. Small discrepancies beyond $x/D > 60$ can mainly be attributed to the overprediction of the mixture fraction. In the rich part of the flame ($x/D < 40$) CO_2 and CO are overpredicted. This can also be attributed to the partial premixing of the fuel with air, which causes substantial chemical reactions to occur in the rich premixed part of the jet. The OH radical mass fraction shown in Fig. 4(d) is predicted very accurately, and

the agreement of predicted and measured NO mass fractions can be considered to be very good. The analysis of the formation of nitric oxide shows that only approximately one third of the total NO is formed by the thermal path and that the N_2O path contributes approximately 10 %. The formation of NO in this case is therefore dominated by the prompt path.

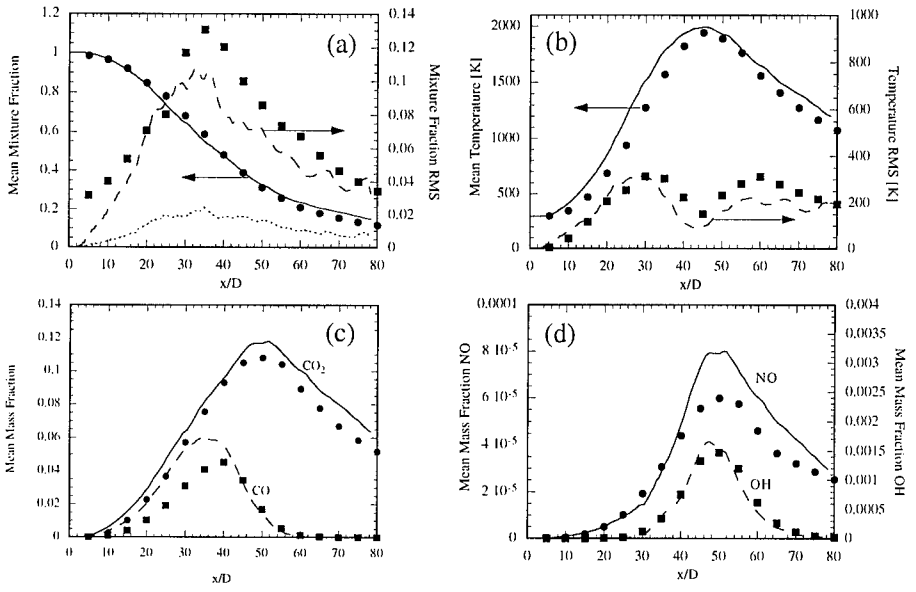


Figure 4: Comparison of calculated and experimental data along the centerline (Lines: Calculation, Symbols: Experiments).

This work has been supported by the Center for Turbulence Research, the Franklin and Caroline Johnson Fellowship at Stanford, and the Department of Energy's ASCI Program.

References

[1] R. S. Barlow and J. H. Frank. Effect of turbulence on species mass fractions in methane/air jet flames. In *Twenty-Seventh Symposium (International) on Combustion*, pages 1087–1095. The Combustion Institute (1998)

[2] A. W. Cook and J. J. Riley. A subgrid model for equilibrium chemistry in turbulent flows. *Phys. Fluids* **6**, 2868–2870 (1994)

[3] A. W. Cook, J. J. Riley, and G. Kosály. A Laminar Flamelet Approach to Subgrid-Scale Chemistry in Turbulent Flows. *Combust. Flame* **109**, 332–341 (1997)

[4] J. Jiménez, A. Liñán, M. M. Rogers, and F. J. Higuera. A-priori testing of subgrid models for chemically reacting non-premixed turbulent shear flows. *J. Fluid Mech.* **349**, 149–171 (1997)

[5] U. Maas and S. B. Pope. Simplifying Chemical Kinetics: Intrinsic Low-Dimensional Manifolds in Composition Space. *Combust. Flame* **88**, 239–264 (1992)

[6] P. Moin, K. Squires, W. Cabot, and S. Lee. A dynamic subgrid-scale model for compressible turbulence and scalar transport. *Phys. Fluids A* **3**, 2746–2757 (1991)

[7] F. K. Owen, L. J. Spadaccini, and C. T. Bowman. Pollutant formation and energy release in confined turbulent diffusion flames. Sixteenth Symposium (international) on Combustion p. 105, The Combustion Institute (1976)

[8] N. Peters. Laminar Diffusion Flamelet Models in Non-Premixed Turbulent Combustion. *Prog. Energy Combust. Sci.* **10**, 319–339 (1984)

[9] N. Peters. Laminar flamelet concepts in turbulent combustion. In *Twenty-First Symposium (International) on Combustion*, pages 1231–1250. The Combustion Institute (1987)

[10] C. Pierce and P. Moin. A dynamic model for subgrid-scale variance and dissipation rate of a conserved scalar. *Phys. Fluids* **10**, 3041–3044 (1998)

[11] C. Pierce and P. Moin. The Progress-Variable Approach for Large Eddy Simulation of Non-Premixed Combustion. *Bulletin of the Am. Phys. Soc.* vol. 44, no. 8, p. 44 (1999)

[12] H. Pitsch and H. Steiner. Large-eddy simulation of a turbulent piloted methane/air diffusion flame (Sandia flame D). submitted to *Phys. Fluids*, 2000.

[13] H. Pitsch and H. Steiner. Scalar mixing and dissipation rate in large-eddy simulations of non-premixed turbulent combustion. submitted to *Twenty-Eighth Symposium (International) on Combustion.* The Combustion Institute, 1999.

[14] H. Pitsch, M. Chen, and N. Peters. Unsteady flamelet modeling of turbulent hydrogen/air diffusion flames. In *Twenty-Seventh Symposium (International) on Combustion*, pages 1057–1064. The Combustion Institute (1998)

[15] H. Pitsch. Unsteady flamelet modeling of differential diffusion in turbulent jet diffusion flames. submitted to *Comb. Flame*, 1999.

[16] N. Smith, J. Gore, and J. Kim. www.ca.sandia.gov/tdf/Workshop.html, 1998.

XIII

Boundary Layers and Free Shear Flows

ADVANCES IN TURBULENCE VIII
Proceedings of the Eighth European Turbulence Conference
C. Dopazo et al. (Eds.)
© CIMNE, Barcelona 2000

High Reynolds number turbulent boundary-layer experiments

Jens M. Österlund and Arne V. Johansson

Department of Mechanics, KTH
SE-100 44 Stockholm, Sweden

Contact e-mail: jens@mech.kth.se

1 Introduction

The flow in a laminar boundary layer is governed by a single length scale and full similarity solutions to the boundary layer equations can be obtained. The case of the turbulent boundary layer flow is quite the opposite with a large span in both velocity and length scales. One can identify two layers with different dynamics, the inner layer where the dynamics are strongly influenced by viscous stresses and an outer layer mainly governed by inertial forces. The velocity and the length scales for the inner layer can be defined from the shear stress at the wall, $u_\tau^2 = \overline{\tau}_w/\rho$ and $\ell^* = \nu/u_\tau$, and for the outer layer as the freestream velocity U_∞ and the thickness of the boundary layer δ. At high Reynolds numbers the ratio of the two lengthscales is large and we have two distinct layers. These meet in an overlap region where the dynamics is essentially independent of lengthscale (an inertial sublayer behavior). Full similarity solutions can be sought for the inner and outer layers independently. The inner layer was treated by Prandtl [6] obtaining solutions of the form

$$\overline{U}^+ = f(y^+), \tag{1}$$

where $\overline{U}^+ = \overline{U}/u_\tau$ and $y^+ = yu_\tau/\nu$. The scaling in the inner layer has since then been verified in numerous experiments. For the outer layer several competing hypotheses for the form exist. The classical form is given by

$$\frac{\overline{U}}{U_\infty} = 1 + \frac{u_\tau}{U_\infty} F(\eta), \tag{2}$$

where $\eta = y/\delta$, see e.g. Österlund [4], ch. 2. For the most recent alternative theories the readers are referred to the works of George [2] and Barenblatt [1] and Zagarola [7].

Millikan [3] obtained the classical logarithmic scaling in the overlap region, by matching the inner and outer layer descriptions Eq. 1 and Eq. 2, here given in inner scaling

$$\overline{U}^+ = \frac{1}{\kappa} \ln y^+ + B. \tag{3}$$

George [2] and Barenblatt [1] use a different approach and arrive at a Reynolds number dependent power-law description of the overlap region although with some differences between the two.

We will here try to identify purely from experimental data, which of the hypothesis that gives the "best" description.

2 Selection criteria

We will test the following hypotheses: a) Re independent log-law, b) Re dependent log-law, c) Re independent power-law and d) Re independent power-law. There are many aspects one could look at in the different approches but the key point of interest must be whether we can identify any significant regions with log- or power-law functional behaviour, Reynolds number dependent or not. This can be done in many ways and the first idea that may spring to mind might be to make lin-log and log-log diagrams of the mean velocity. It turns out to be a rather insensitive test (see Österlund *et. al* [5]). Instead we proceed to look at a normalized gradient of the mean velocity. We define

$$\Xi = \left(y^+ \frac{d\overline{U}^+}{dy^+} \right)^{-1}, \tag{4}$$

that will be constant in a region governed by a log-law, and

$$\Gamma = \frac{y^+}{\overline{U}^+} \frac{d\overline{U}^+}{dy^+} \tag{5}$$

that will be constant in a region governed by a power-law.

To be able to identify any Reynolds number dependence we will look at Eq. 4 and Eq. 5 evaluated for individual measurements of the mean velocity at different Reynolds numbers. One should keep in mind that the scatter necessarily will be quite large when taking the derivative of measurement data.

3 Results

The measurements were carried out at the MTL wind-tunnel at the department of mechanics at KTH and are described in Österlund [4]. The data base for the mean velocity consists of 70 mean velocity profiles taken in the Reynolds number range $2500 < Re_\theta < 27300$. The data are available on the internet at: http://www.mech.kth.se/~jens/zpg/.

Here we will show a subset of the data to make the figures more readable. In figure 1 the gradient of the mean velocity is normalized according to 4 to identify regions with log-law behavior. Above $y^+ \approx 200$ the ensamble of curves flattens out around the constant value 0.38 (performing the same evaluation instead in outer scaling one finds the the outer limit of the overlap at $\eta \approx 0.15$), see Österlund *et. al* [5].

In figure 2 profiles of the mean velocity gradient normalized to identify regions governed by a power-law, are shown. From comparisons of figures 1 and 2 one can conclude that mean velocity profiles closely adhere to a log-law with von Kármán's constant $\kappa = 0.38$. One can also conclude that no significant region with power-law behaviour exists since the function Γ decreases with increasing y^+ in figure 2, for all Reynolds numbers.

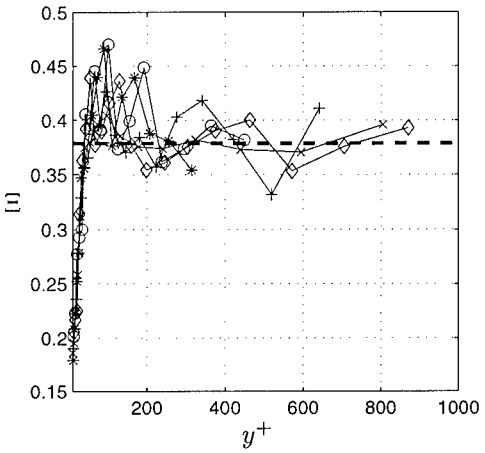


Figure 1: The gradient of the mean velocity normilized to reveal a log-law behaviour. $\eta < 0.15$. Re_θ: $*$: 9600, $\circ$: 14200, +:20560, $\diamond$:26600, $\times$:27300. Dashed line: log-law, $\kappa = 0.38$.

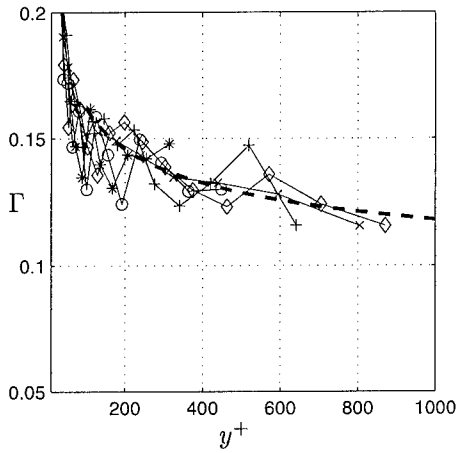


Figure 2: The gradient of the mean velocity normilized to reveal a power-law behaviour. $\eta < 0.15$. Re_θ: $*$: 9600, $\circ$: 14200, +:20560, $\diamond$:26600, $\times$:27300. Dashed line: log-law, $\kappa = 0.38$ and $B = 4.1$.

4 Conclusions

- The mean velocity profiles are best described by the log-law in the region $200 < y^+ < 0.15\delta^+$. Hence, a universal overlap region can only be expected to be found for Re_θ larger than about 6000.

- No significant Reynolds number effects were found for sufficiently high Reynolds numbers, yielding the constants $\kappa = 0.38$ and $B = 4.1$ of the log-law, Eq. 3.

Financial support from NUTEK and TFR is gratefully acknowledged.

References

[1] G. I. Barenblatt, A. J. Chorin, and V. M. Prostokishin. Analysis of experimental investigations of self-similar intermediate structures in zero-pressure boundary layers at large reynolds numbers. PAM 777, Center for Pure and Applied Mathematics, University of California at Berkeley, 2000.

[2] W. K. George, L. Castilio, and M. Wosnik. Zero-pressure-gradient turbulent boundary layer. *Applied Mech. Reviews*, 50:689–729, 1997.

[3] C. B. Millikan. A critical discussion of turbulent flows in channels and circular tubes. In *Proceedings of the Fifth International Congress of applied Mechanics*, 1938.

[4] J. M. Österlund. *Experimental Studies of Zero Pressure-Gradient Turbulent Boundary-Layer Flow.* PhD thesis, Department of Mechanics, Royal Institute of Technology, Stockholm, 1999.

[5] J. M. Österlund, A. V. Johansson, H. M. Nagib, and M. H. Hites. A note on the overlap region in turbulent boundary layers. *Phys. Fluids*, 12:1–4, 2000.

[6] L. Prandtl. Zur turbulenten Strömung in Rohren und längs Platten. *Ergebn. Aerodyn. Versuchsanst. Göttingen*, 4:18–29, 1932.

[7] M. V. Zagarola and A. J. Smits. A new mean velocity scaling for turbulent boundary layers. In *Proceedings of FEDSM'98*, 1998.

ADVANCES IN TURBULENCE VIII
Proceedings of the Eighth European Turbulence Conference
C. Dopazo et al. (Eds.)
© CIMNE, Barcelona 2000

Flow structures in high Reynolds number turbulent boundary-layers

B. Lindgren, J. Österlund and A.V. Johansson

Dept. of Mechanics, KTH, SE-100 44 Stockholm, SWEDEN

Contact e-mail: oso@mech.kth.se

1 Introduction

Distinct features of the near-wall turbulence structures have been elucidated from visualizations, measurements and direct numerical simulations (DNS) in a large number of papers, see *e.g.* [6]. Among these features we may mention a strong intermittency of turbulence production related to near-wall streak dynamics. Kline *et al.*[6] showed that a significant part of the turbulence could be described in terms of deterministic events. In close proximity of the wall the flow is characterized by alternating low and high speed streamwise streaks separated in the spanwise direction a distance $\lambda^+/2 \approx 50$. The low-speed streaks start to oscillate and suddenly they break up into "bursts". Kim *et al.* [4] showed that the intermittent bursting process is closely related to shear-layer like flow structures in the buffer region, and also that roughly 70% of the total turbulence production was associated with the bursting process. Furthermore, it has been found that there are two distinct types of turbulence production, ejection and sweeps. Ejection is characterized by a rapid outflow of low speed fluid from the wall region and sweeps are characterized by large scale motions from the outer region penetrating into the wall region.

2 Measurement technique

The present measurements were made on a flat plate with zero pressure gradient in the MTL wind-tunnel at KTH, Stockholm. The flow quality in the wind-tunnel is very good with e.g. a streamwise turbulence intensity $< 0.02\%$ and a friction velocity, u_τ, variation in the spanwise direction $< \pm 0.7\%$. The test section is 7 m long and the cross section is 1.2×0.8 m^2. The Reynolds number span in these measurements is $2530 < Re_\theta < 27300$. Two-point correlation measurements were made using a single-wire and a wall shear-stress sensor with an array of 25 hot-films. The single-wire can be traversed in the streamwise and wall normal directions and by selecting any of the hot-films the spanwise

separation can be varied in steps of 300 μm. The wall shear-stress sensor is developed by the MEMS group at UCLA/Caltec [3].

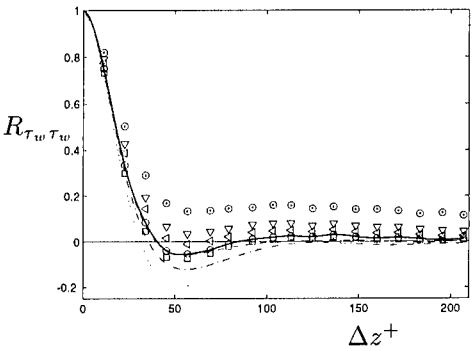


Figure 1: Spanwise correlation coefficient $R_{\tau_w\tau_w}$ vs. Δz^+, $Re_\tau = 2300$. Symbols see table. DNS of channel flow, at $y^+ = 5$, $--$: $Re_\tau = 590$, $-\cdot-$: $Re_\tau = 395$, $\cdots$: $Re_\tau = 180$.

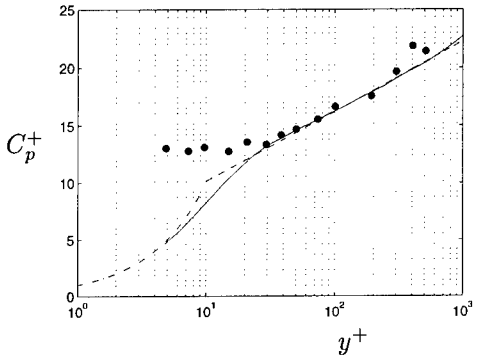


Figure 2: Propagation velocity C_p^+, •. $--$: log-law, $\kappa = 0.38$ and $B = 4.1$. $-\cdot-$: linear profile. —: mean velocity profile. $Re_\theta = 9500$.

symbol	⊙	▽	◁	○	□
f_c^+	unfiltered	1.3×10^{-3}	2.6×10^{-3}	5.3×10^{-3}	7.9×10^{-3}

3 Results

The mean spanwise separation between low-speed and high-speed streaks, usually called streak spacing, was investigated using the MEMS hot-film. This allowed for correlation measurements with 17 different spanwise separations which translates in wall units to a separation of $0 < \Delta z^+ < 210$. The Reynolds number was $Re_\theta = 9500$. The spanwise cross correlation coefficient is defined as

$$R_{\tau_w\tau_w}(\Delta z) = \frac{\overline{\tau_w(z)\tau_w(z+\Delta z)}}{\tau'^2_w}, \qquad (1)$$

where the prime denotes r.m.s value. In figure 1 the results from this calculation are represented as ⊙. At this high Reynolds number no clear minimum in the correlation coefficient function can be seen. At lower Reynolds numbers, however, there is a clear minimum in this curve as is shown for the DNS data, of [5] and [7], in figure 1. The reason for the minimum to be less clear with increasing Reynolds number is that low frequency structures, originating in the outer region, become increasingly dominant. In an attempt to exclude them a high pass filter was applied to the data before calculating the cross correlation

coefficient. Now a clear minimum appears at a spanwise separation of $\lambda^+ \approx 110$, which is similar to that for the cases with lower Reynolds numbers, see figure 1.

The wall normal space-time correlation of the wall shear stress and the streamwise velocity was measured. It is defined as

$$R_{\tau_w u}(\Delta x, \Delta y, \Delta t) = \frac{\overline{\tau_w(x,y,t)u(x+\Delta x, y+\Delta y, t+\Delta t)}}{\tau_w' u'}. \quad (2)$$

The time-shift of the correlation coefficient peaks become increasingly negative with increasing wall distance. This indicates a forward leaning structure. The propagation velocity, $C_p^+ = \frac{\Delta x^+}{\Delta t^+}$, is constant, with a value of about 13, for wall distances $y^+ < 30$. Further out it is close to the local mean velocity, see figure 2, meaning that the structures here are stretched by the mean shear.

Shear-layer events were detected using the VITA technique. By forming the short-time variance of u,

$$var(x_i, t, T) = \frac{1}{T}\int_{t-\frac{1}{2}T}^{t+\frac{1}{2}T} u^2(s)ds - \left(\frac{1}{T}\int_{t-\frac{1}{2}T}^{t+\frac{1}{2}T} u(s)ds\right)^2. \quad (3)$$

shear-layer events can be detected through a function which is 1 if $var > k\overline{u^2}$ where k is a threshold level and 0 otherwise. A chosen quantity to be studied, Q, is then conditionally averaged over all detected events through

$$\langle Q(\tau)\rangle = \frac{1}{N}\sum_{j=1}^{N} Q(t_j + \tau), \quad (4)$$

where N is the total number of detected events and τ is the time relative to the detection time t_j. Shear-layer type of events are also associated with a positive $\frac{\partial u}{\partial \tau}$ at the detection time. These events dominate over those with negative $\frac{\partial u}{\partial \tau}|_{\tau=0}$. Figure 3 (top) shows conditional average of shear-layer type of events detected at $y^+ = 15$.

To determine the governing time scale for the shear-layer dynamics in the near-wall region the frequency of occurrence of VITA events was plotted against the averaging time window size for different Reynolds numbers. Earlier Rao *et al.* [8] found the best collapse for outer scaling while Blackwelder and Haritonidis [2] found the inner scaling to be the best. In the case of turbulent channel flow Alfredsson and Johansson [1] found the mixture of inner and outer timescales, $t_m = \sqrt{t_* t_o}$, to give the best collapse. For the shortest averaging windows for the two highest Reynolds numbers, (o,+) there are non-negligible effects of finite probe size. Disregarding these data one finds that the mixed scaling also here seems to give the best collapse.

4 Conclusions

The near-wall streamwise low-speed streaks exist also for high Reynolds numbers but partially hidden in an environment where large scale motions give a

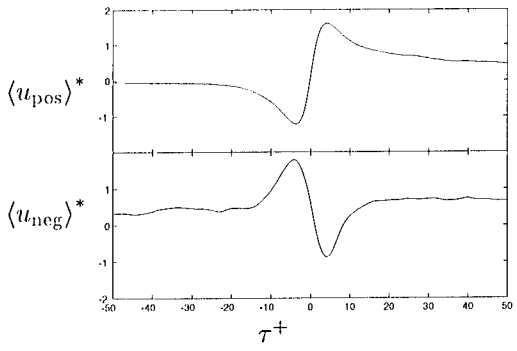


Figure 3: Conditional average of u for events with positive slope (top) and negative slope (bottom). $T^+ = 10$, $k = 1.0$ and $Re_\theta = 9700$

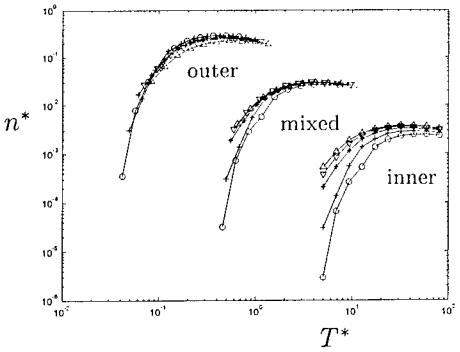


Figure 4: Frequency of occurrence of VITA events (k=1) vs. the averaging time. $y^+ = 15$, $6700 < Re_\theta < 15200$

significant contribution to the two-point correlation. By applying a proper filter the streaks are revealed. The mixed scaling seems to be the most appropriate for the frequency of occurrence of VITA events also in boundary layer flow.

References

[1] P. H. Alfredsson and Johansson. Time scales in turbulent channel flow. *Phys. Fluids A*, 27(8):1974–81, 1984.

[2] R. F. Blackwelder and J. H. Haritonidis. The bursting frequency in turbulent boundary layers. *J. Fluid Mech.*, 132:87–103, 1983.

[3] F. Jiang, Y.-C. Tai, B. Gupta, R. Goodman, S. Tung, J. B. Huang, and C.-M. Ho. A surface-micromachined shear stress imager. In *1996 IEEE Micro Electro Mechanical Systems Workshop (MEMS '96)*, pages 110–115, 1996.

[4] H. T. Kim, S. J. Kline, and W. C. Reynolds. The production of turbulence near a smooth wall in a turbulent boundary layer. *J. Fluid Mech.*, 50:133–160, 1971.

[5] J. Kim, P. Moin, and R. Moser. Turbulence statistics in fully developed channel flow. *J. Fluid Mech.*, 177:133-166, 1987.

[6] S. J. Kline, W. C. Reynolds, F. A. Schraub, and P. W. Runstadler. The structure of turbulent boundary layers. *J. Fluid Mech.*, 30:741, 1967.

[7] R. D. Moser, J. Kim, and N. N. Mansour. Direct numerical simulation of turbulent channel flow up to $Re_\theta = 590$. *Phys. Fluids*, 11(4):943–945, 1999.

[8] K. N. Rao, R. Narasima, and M.A. Badri Narayanan. The "bursting" phenomenon in a turbulent boundary layer. *J. Fluid Mech.*, 48:339–352, 1971.

ADVANCES IN TURBULENCE VIII
Proceedings of the Eighth European Turbulence Conference
C. Dopazo et al. (Eds.)
© CIMNE, Barcelona 2000

Structure of Turbulence in the Logarithmic Layer and its Mechanism

Y. Miyake, K. Tsujimoto, N. Sato, and Y. Suzuki

[1]Graduate School of Engineering of Osaka University
2-1, Yamada-oka, Suita, 565-0871, Japan

Contact e-mail: miyake@mech.eng.osaka-u.ac.jp

1 Introduction

Understanding of the structure of wall turbulence is the basis of flow control such as to reduce wall friction. Numerical simulations of turbulent flows under various novel conditions which are not realized in the experiments have given us informations of substantial importance in this regard. Today, behavior of the near-wall turbulence up to around 60 in wall unit from the wall where quasi-streamwsie vortices play dominant role has been almost fully understood. Remarkable feature of the turbulence in this layer is that it is autonomous and is little influenced by that of the top of the layer[1][2]. Meanwhile, the behaviour and the structure of turbulence in the layer further away from the wall is little understood, despite that they are as much important as those in the near-wall layer. Its time-mean distribution, however, is known to be independent on the property of wall condition, such as whether the wall is rough or smooth[3] and the magnitude of wall shear stress is the unique parameter governing the flow distribution. In this sense, the layer away from the wall is regarded as autonomous independent on lower layer. It is intended in this work to extract outstanding turbulence property in the layer away from the wall, specifically, in logarithmic layer and to get new insight into the background of this small interaction between the layers manifesting itself in the time-mean distribution, by direct numerical simulations(DNS) of channel flows.

2 Flow in logarithmic layer

2.1 Direct numerical simulation

Most of the discussions of near-wall turbulence until now are based on channel flows of low Reynolds number flows such as $Re_\tau = u_\tau H/\nu = 150 \sim 180$ where u_τ, H, ν are friction velocity, half width of the channel and kinematic viscosity, respectively, and/or of minimum channel flow data. Present authors found that developed logarithmic layer has a remarkable property that the parameter $a = -\overline{u'v'}/k$, the ratio of turbulent shear stress to turbulent kinetic energy, where u', v' are fluctuating velocity components in streamwise and wall-normal direction, stays constant across the layer[3]. Turbulent flows having this layer are realized in high Reynolds number flows and in the flow on a rough wall. Direct numerical simulations(DNS) of high Reynolds number flows have been seriously limited by computer capacity. So, in this work, a DNS of high accuracy of a channel flow of Reynolds number $Re_\tau = 395$ is conducted.

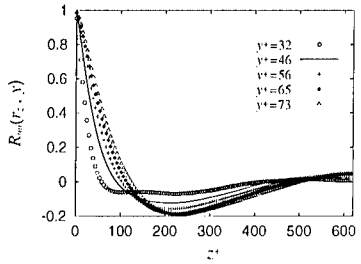


Figure 1: Spanwise correlation factor of streamwise fluctuating velocity

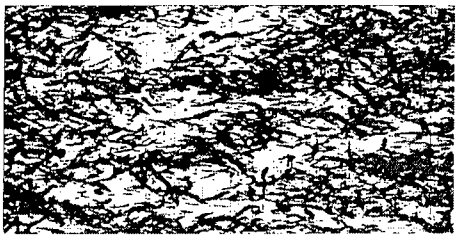
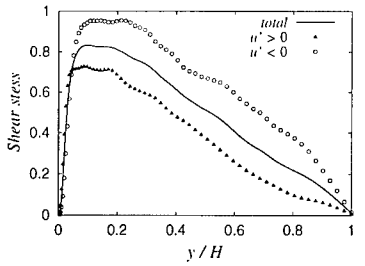


Figure 2: Plan view of coherent vortices ($Q^+ > 0.01$)

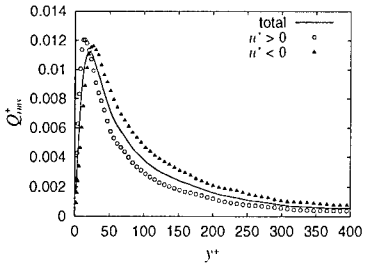
2.2 Large-scale streaks

Streaks of high and low streamwise velocity generated by quasi-streamwise vortices are notable feature of buffer layer. Meanwhile, developed logarithmic layer of high Reynolds number exhibits a remarkable feature that large-scale streaks of different nature from that in the buffer layer and of mean separation of the order of channel half width are formed. These large-scale streaks are observed in a picture of instantaneous flow field obtained by simulation and are confirmed by large negative value of spanwise correlation factor of streamwise fluctuating velocity $R_{uu}(z)$ appearing at large spanwise separation, as well, as shown in Fig.1 which is for a channel flow of $Re_\tau = 395$. The plan view seen from the central plane of a channel, of vortices visualized by threshold value $Q^+ = 0.01$ where Q^+ is the second invariant of the velocity gradient tensor $\boldsymbol{A} = \partial v_i/\partial x_j$ normalized by $(u_\tau^2/\nu)^2$ is shown in Fig.2. It is found that low speed streaks are related to the densely populated region of small-scale vortices. Experimental evidence is also available in a report by Comte-Bellot[4], though she did not give any comment on it. Large-scale streaks are also observed in a rough-wall layer of smaller Reynolds number flow, as roughness makes equivalently the Reynolds number larger[3].

In order to measure more in detail the difference of turbulence property in high and low streaks, time-mean value of turbulence in a plane parallel to the wall is taken separately in low ($u' < 0$) and high-speed ($u' > 0$) area. Figures 3 show examples of the wall-normal distribution, *i.e.*, (a) turbulent shear stress $-\overline{u'v'}$, (b) Q^+_{rms} where Q^+_{rms} is the root mean square of fluctuating component of Q^+. It is found that difference of mean velocity between each area attains $\Delta U^+ = 3.0 \sim 5.0$ which is even larger than in typical streaks in the buffer layer. In the low speed area, turbulent shear stress is higher than in the high-speed area as demonstrated in Fig.3(a), which is indicative of the fact that turbulent mixing is stronger in the former. The difference in Q^+_{rms} shown in Fig.3(b) confirms the above observation that vortices are more densely populated in low-speed area than in the other. Accordingly, turbulent kinetic energy and its production rate as well, is larger in low speed area.



(a)



(b)

Figure 3: Wall normal distribution of turbulence property in high or low speed region, (a)$\overline{u'v'}$ (b)Q^+_{rms}

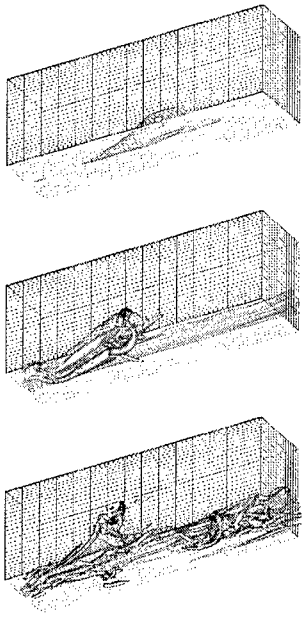


Figure 4: Time evolution of the seed extracted by LSE, (a)$T^+ = 0$, (b)$T^+ = 269$, (c)$T^+ = 537$

2.3 Simulation of formation of large-scale streaks

Simulation of evolution of a seed of a small vortex pair extracted from ordinary simulation by LSE[5], i.e., and is submerged in a shear layer near the wall which is laminar but has wall-normal velocity distribution of turbulent flow has been shown to be useful to investigate growth of hairpin vortices in near-wall turbulence[6]. In order to get an idea how the large-scale streaks are formed, this technique is applied. The initial flow containing a seed of a vortex pair is that corresponding to that of strong downwash of an initially laminar channel flow of $Re_\tau = 395$.

Evolutions from two different initial location of seed of a hair-pin vortex , i.e., center of the vortex at height from the wall y_v^+ at 50 in the first and 200, in the second, show no substantial difference. Figures 4(a) thru (c) show the development of the vortical system from an initial vortex pair for the case of $y_v^+ = 200$, for different time of $T^+ = 0, 269, 537$ from the initial instant. In the figures, vortices are visualized by iso-surface of $Q^+ = 0.001$ and the shaded area is low speed area of $\Delta U/u_\tau \leq -2.0$. In the initial stage of the development of a vortex pair, legs grow quickly and subsidial quasi-streamwise vortices are formed. As the time marches, heads of secondary, tertial, etc. hair-pin vortices

are generated and grow more and more. The upper layer farther away from the wall is being occupied by entangled fine vortices at $T^+ = 537$ which looks like resulting from the collapse of ordered structure of head of hair-pin vortices. In the case of lower Reynolds number, this collapse is not observed. To be noted is that low speed streaks are formed surounding vortices populated area. That is, as found above, low-speed streaks include many entangled fine scale vortices which is generated by a sort of instability in the layer away from the wall, basically independent on the vortices in the layer very close to the wall.

To confirm this independency, a simulation same as above except for the condition that anisotropic viscosity, larger in the spanwise direction than in other up to $y^+ = 70$ otherwise kept isotropic, is performed. This artificial condition supresses the growth of legs of lower layer. Visualized pictures give little difference as above-mentioned one, as for the development of the upper layer vortical structure, though not shown here. It is evident that the formation process of low speed-streaks is little affected by the lower layer.

3 Conclusions

- A large-scale streaks of large spanwise separation appear in the layer away from the wall, specifically in the logarithmic layer.
- Low speed streaks contains large number of entangled fine-scale vortices and as the consequence, turbulent mixing is stronger and higher turbulent shear stress is generated than in the other.
- Simulations of the development of a hair-pin vortex in a laminar but turbulent velocity distribution reveal that the large-scale streaks are formed in the upper layer little influenced by quasi-streamwise vortices in the lower layer.

References

[1] Y. Miyake, K. Tsujimoto, N. Sato and Y. Suzuki Turbulence property in the near-wall layer. *Trans.JSME, ser.B*, (in Japanese, to appear).

[2] J. Jiménez,J. and A. Pinelli. The autonomous cycle of near-wall turbulence. *J.Fluid Mech.*, 389:335–359, 1999.

[3] Y. Miyake, K. Tsujimoto and Y. Agata. A DNS of a Turbulent Flow in a Channel with a Rough Wall. *JSME Intern.J., ser.B*, (to appear), 2000.

[4] G.Comte-Bellot, "Contribution à l'étude de la turbulence de conduite" Thèse présententé à la faculté des Sciences de l'Université de Grenoble, 1963.

[5] R. J. Adrian and P. Moin. Stochastic estimation of organized turbulent structure : Homogeneous shear flow . *J.Fluid Mech.*, 190:531–559, 1988.

[6] J. Zhou, R. J. Adrian and S. Balanchandar. Autogeneration of near-wall vortical structures in channel flow. *Phys.Fluids*, 8-1:288–290, 1996.

ADVANCES IN TURBULENCE VIII
Proceedings of the Eighth European Turbulence Conference
C. Dopazo et al. (Eds.)
© CIMNE, Barcelona 2000

Kinetic energy, enstrophy and strain rate in near-wall turbulence

N.D.Sandham[1] and A.Tsinober[2]

[1]School of Engineering Sciences, University of Southampton
Highfield, Southampton SO17 1BJ, U.K.
[2]Department of Fluid Mechanics and Heat Transfer, Faculty of Engineering
Tel Aviv University, Ramat Aviv, 69978 Tel Aviv, Israel

Contact e-mail: n.sandham@soton.ac.uk

1 Introduction

The importance of vorticity stretching ($\omega_i\omega_j s_{ij}$) in turbulent flow has long been recognised. More recently Tsinober [1] has emphasised the term $s_{ij}s_{jk}s_{ki}$ which appears as a source term in the transport of strain rate magnitude $s^2 = s_{ij}s_{ij}$. Although related in the mean by a constant of proportionality, the instantaneous connections between this term and the vortex stretching term are not trivial and contain much of the geometric complexity of turbulence, as reflected in the invariants of the velocity gradient tensor. The strain rate magnitude is related to the dissipation via a constant of proportionality, so source terms in this equation can be thought of as increasing dissipation and vice versa. Previous work has focused on isotropic turbulence. Here we extend the statistical description to channel flow, using data from a direct numerical simulation at $R_\tau = 180$ [2]. The simulation uses a computational box of size 3.25 (streamwise) and 1.5 (spanwise) with lengths normalised by the channel half width. The simulation used a fully spectral method with $32 \times 32 \times 81$ points. Box size and resolution were chosen to be small (but not minimal) so as to reproduce the mean flow and turbulence statistics of [3].

All terms in the transport equations for kinetic energy, enstrophy and strain rate magnitude have been computed for turbulent flow in the channel. The transport equations for channel flow are respectively:

$$\frac{D}{Dt}(\frac{1}{2}\langle u_i u_i\rangle) \approx -\frac{\partial}{\partial x_j}\frac{\langle u_i u_i u_j\rangle}{2} + 2\nu\frac{\partial}{\partial x_j}\langle u_i s_{ij}\rangle - \langle u_i u_j\rangle S_{ij} - 2\nu\langle s_{ij}s_{ij}\rangle \quad (1)$$

$$\frac{D}{Dt}(\frac{1}{2}\langle \omega_i \omega_i\rangle) \approx \langle \omega_i\omega_j s_{ij}\rangle + \langle \omega_i\omega_j\rangle S_{ij} + \langle \omega_i s_{ij}\rangle \Omega_j - \nu\langle \frac{\partial\omega_i}{\partial x_j}\frac{\partial\omega_i}{\partial x_j}\rangle \quad (2)$$

$$\frac{D}{Dt}(\frac{1}{2}\langle s_{ij}s_{ij}\rangle) \approx -2\langle s_{ij}s_{ik}\rangle S_{kj} - \frac{1}{2}\langle \omega_i s_{ij}\rangle\Omega_j - \langle s_{ij}s_{jk}s_{ki}\rangle - \nu\langle \frac{\partial s_{ij}}{\partial x_k}\frac{\partial s_{ij}}{\partial x_k}\rangle \quad (3)$$

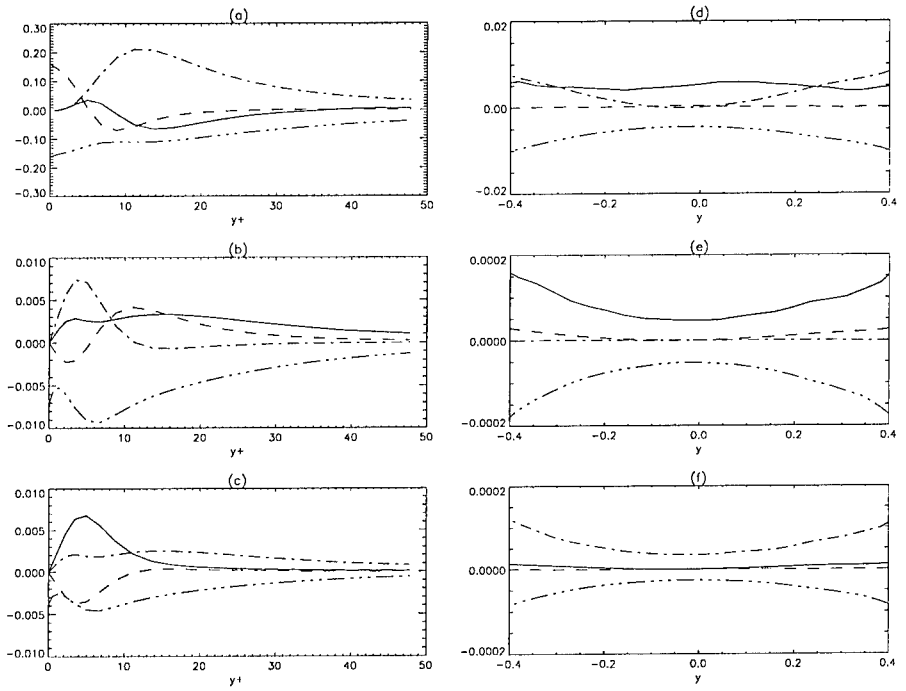


Figure 1: Budgets of from top to bottom kinetic energy, enstrophy and strain magnitude showing near-wall behaviour on the left and channel central region on the right. Solid, dashed, chain dot, and chain triple dot linestyles refer respectively to terms 1-4 on the right hand sides of equations (1), (2) and (3).

The approximate sign signifies that terms which turn out to be small in channel flow have been omitted. We will refer to the three quantities as kinetic energy, enstrophy and strain magnitude (omitting the factors of half to simplify the discussion).

2 Results

Figure 1(a-c) shows budgets in the near wall region $y^+ < 50$ while figure 1(d-f) shows the same budgets near the centre of the channel $-0.4 < y < 0.4$. The dominant terms in the enstrophy budget near the production peak $y^+ \approx 12$ are the vortex stretching by the fluctuating strain rate, vortex stretching by the mean and the destruction (terms 1, 2 and 4 on the right hand side of the above equation). The vortex stretching by the mean is never the dominant term and away from the wall ($y^+ > 40$) it becomes insignificant compared the stretching

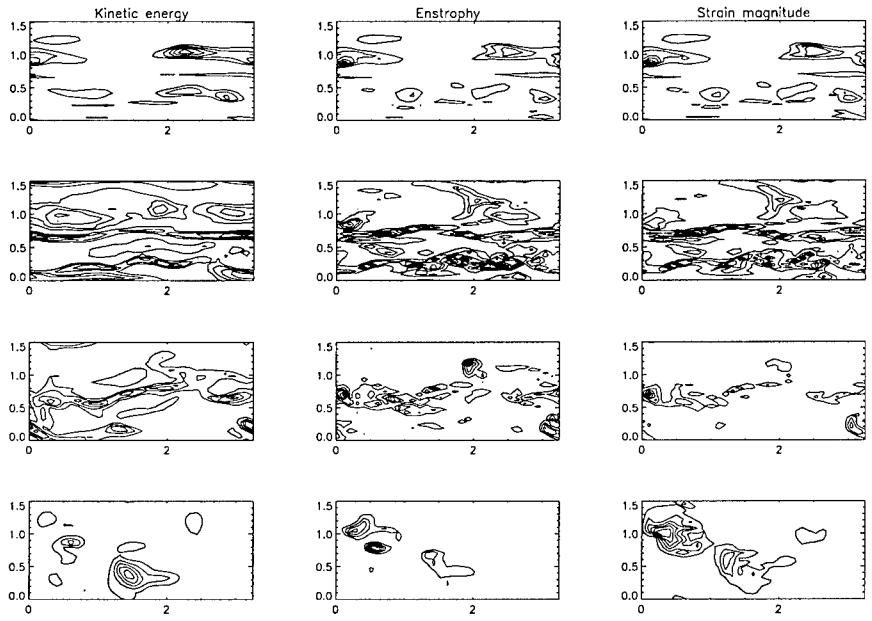


Figure 2: Instantaneous plan view of (from left to right) kinetic energy, enstrophy and strain magnitude at locations in wall units (from top to bottom) of 5.0, 16.5, 43.1, 180.0

by fluctuating strain rate. At the centre of the channel terms 1 and 4 are in balance. A similar picture emerges for strain rate magnitude. From the position of the production peak outwards the only significant terms are the triple strain correlation and the destruction term.

Examples of the instantaneous flow structure corresponding to four locations across the channel are shown on figure 2. These figures illustrate a marked change in the structure from near the wall, where the dominant flow features are the low speed streaks, to the channel centre. Near the wall there is a strong correlation of enstrophy and strain magnitude. This becomes much weaker near the channel centreline. The instantaneous flow and budget details suggest that findings relating to enstrophy stretching and strain triple product from isotropic turbulence [1] may be applicable to the region well away from the wall.

To investigate the internal structure of the turbulence in more detail we consider the enstrophy production and the triple product of strain term (the third term on the right hand side of (3)). Using weighted conditional probability density functions, it is possible to compute the relative contribution to these terms of flow with particular levels of enstrophy or strain magnitude. Figure 3 shows the result for each term at the channel centreline. In each case the solid line

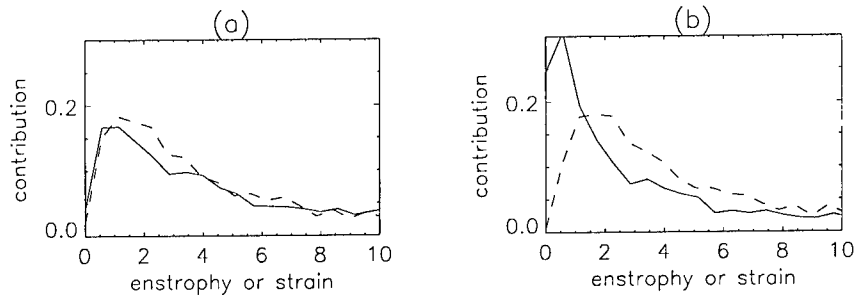


Figure 3: Conditional pdf, showing the contributions of enstrophy and strain magnitude (horizontal axis, normalised by their respective means) to (a) enstrophy production and (b) strain rate triple product (term 3 in equation (3)).

represents conditioning by enstrophy while the dashed line uses strain magnitude. With regard to enstrophy production the results are rather similar, with the peak being at slightly higher values for the strain magnitude conditioning. For the strain triple product term, however, the behaviour is different. There is a significant contribution from low values of enstrophy, which indicates that some important turbulence dynamics is occurring away from regions of high enstrophy. The contribution from strain magnitude shows a very similar variation for both terms.

3 Conclusions

Near-wall turbulence shows a strong correlation between enstrophy and strain magnitude reflecting the underlying streak structure. Nearer the channel centre there are weaker correlations and is has been shown how low enstrophy regions are important when considering the production of strain.

References

[1] Tsinober, A. Vortex stretching versus production of strain/dissipation. *Isaac Newton Institute Report NI99010-TRB*, 1999.

[2] Sandham, N.D. & Howard, R.J.A. Direct simulation of turbulence using massively parallel computers. *Parallel Computational Fluid Dynamics*, ed. D.R.Emerson et al. Elsevier Science, 1998.

[3] Kim, J., Moin, P. & Moser, R. Turbulence statistics in fully developed channel flow at low Reynolds number. 1987. *J. Fluid Mech.***177**, 133-166.

ADVANCES IN TURBULENCE VIII
Proceedings of the Eighth European Turbulence Conference
C. Dopazo et al. (Eds.)
© CIMNE, Barcelona 2000

On order and accuracy of the stochastic estimation of the flow structure associated with surface pressure events in a turbulent boundary layer

A. Naguib[1] and C. Wark[2]

[1]Department of Mechanical Engineering, Michigan State University,
East Lansing, MI-48824, USA
[2]Department of Mechanical Materials and Aerospace Engineering,
Illinois Institute of Technology, Chicago, IL-60616, USA

Contact e-mail: naguib@egr.msu.edu

1 Introduction

Recent interest in active flow control has provided a motivation for developing low-order models to link dominant flow structures to measurements of surface pressure or shear. One approach to establish such a link is through stochastic estimation (SE). Application of SE for extraction of coherent motion in turbulent flows was first proposed by Adrian [1]. Later, the approach was applied to a variety of flows such as turbulent wall-bounded flows [2] and separated flows [3]. Conceptually, the estimation is obtained from a Taylor series expansion in terms of a known condition. In most instances, the series converges satisfactorily to the conditionally averaged velocity field by keeping only the linear term. Such an estimate, known as Linear Stochastic Estimation (LSE), provides a low-order model of the average flow structure associated with some significant flow event; e.g., near-wall generation of Reynolds stresses, high wall-shear, etc.

2 Results and Discussion

In this work, SE was implemented using simultaneous measurements of the fluctuating wall pressure (p'_w) and streamwise velocity (u') in a turbulent boundary layer. The u' and p'_w probes were separated in the normal (y) but not in the spanwise or streamwise direction. To obtain the quadratic SE of the velocity ($< u' >_q$) associated with a p'_w condition, the following equation was used:

$$< u' >_q (y^+, t^+) = \frac{R_{pu}(y^+, t^+)}{p'^2_{w,rms}} p'_w + \frac{R_{ppu}(y^+, t^+)}{K_p \, p'^4_{w,rms}} p'^2_w, \qquad (1)$$

where y^+ and t^+ represent the viscous-scaled spatial and temporal offsets between u' and p'_w measurements and $p'_{w,rms}$ and K_p are the *rms* value and Kurtosis, respectively, of the fluctuating wall pressure. To obtain LSE ($< u' >_l$), only the first term in equation (1) is used. Note that the linear-term coefficient is related to the pressure-velocity correlation (R_{pu}), while the quadratic-term coefficient depends on the *squared-pressure*-velocity correlation (R_{ppu}). It is also useful to point out that the first and second terms in equation (1) are odd and even functions of p'_w, respectively.

Figure 1 shows the conditional velocity ($< u' >$), normalized by the *rms* value, as a function of the magnitude of the pressure condition. Those results are compared with LSE and quadratic estimation results for different y positions and two Reynolds numbers (Re_θ). In addition, Figure 1 includes a phase-sensitive LSE ($< u' >_{lp}$), which is obtained by replacing R_{pu} with R_{p^+u} for positive p'_w condition and R_{p^-u} for a negative one (R_{p^+u} and R_{p^-u} represent the correlation between positive and negative p'_w values, respectively, with u'). As seen from Figure 1, LSE does not capture the conditional average accurately. However, once the quadratic term is included in the estimation, a good representation of $< u' >$ is obtained for all heights and Reynolds numbers. The relative importance of the linear and quadratic terms may be assessed via inspection of the symmetry of the conditional average with respect to p'_w. At $y^+ = 20$, or close to the location of the p'_w event, $< u' >$ is neither even nor odd function of p'_w, and therefore both terms in equation (1) are needed to represent the average. As y increases, however, the conditional average becomes more symmetric (Figure 1). Thus, at locations far away from the event, only the even, or quadratic, term is needed to represent the conditional average. This suggests that the quadratic term in the stochastic estimation captures the signature of the large-scale, outer boundary layer structures, which would be absent if only LSE is used. The phase-sensitive LSE, on the other hand, seems to provide a satisfactory representation of $< u' >$ over a limited range of $-2 < \frac{p'_w}{p'_{w,rms}} < 2$.

The gradual change in the symmetry of $< u' >$, with respect to p'_w, with increasing separation from the event may also be depicted in the joint *pdf* (*jpdf*) plots given in Figure 2. As y increases, the asymmetry of the *jpdf* with respect to p'_w gradually disappears. It is also significant to note that the *jpdfs* in Figure 2 do not resemble that of a joint Gaussian distribution, which may explain the inability of LSE to represent $< u' >$ accurately, as pointed out by Brereton [4].

Finally, Figure 3 shows results similar to Figure 1 but for different t^+, rather than y^+, values and $y^+ = 20$. The general observation from Figure 1 also holds here, where the quadratic term is required for a good representation of $< u' >$ for all time offsets and Re_θ values. The exception is at t^+ = -8, which happens to correspond to the maximum negative value of R_{pu}, where $< u' >$ seems to be a linear function of p'_w at the low Re_θ. However, for the larger Re_θ, $< u' >$ deviates from this linear behavior and the quadratic term must be included. Interestingly, even the quadratic estimation does not capture the conditional average at large pressure magnitudes for this time offset. It seems that the

inclusion of a third order term may be needed here.

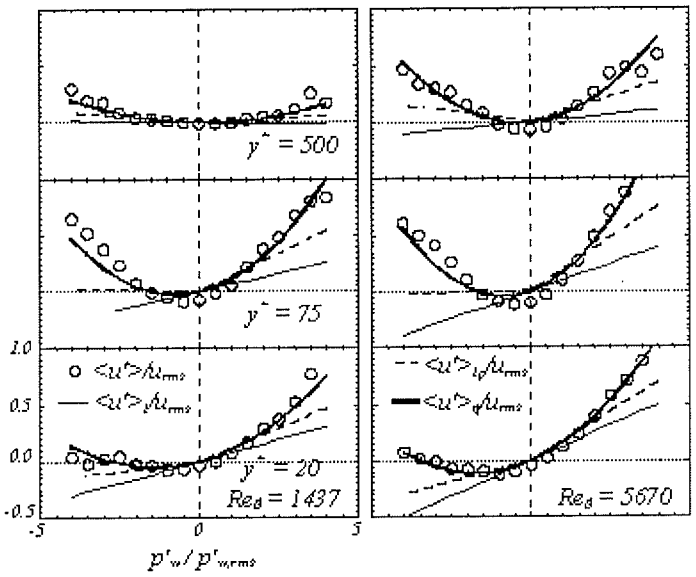


Figure 1: Comparison of the conditional average with the linear, quadratic and phase-sensitive SE for different heights and Reynolds numbers ($t^+ = 0$).

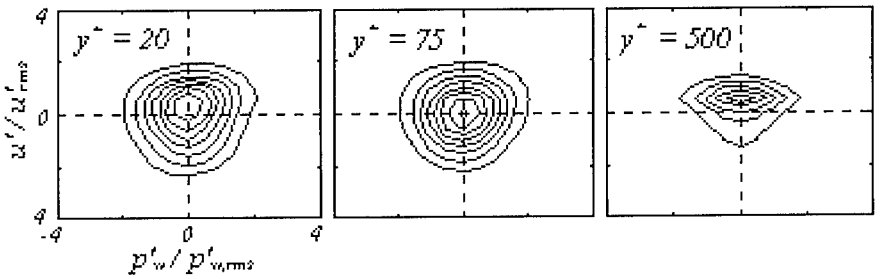


Figure 2: Joint *pdfs* for different heights and $t^+ = 0$.

3 Conclusions

Linear stochastic estimation of the velocity field based on the wall pressure does not capture the influence of the largest scales in turbulent wall-bounded flows. An improved linear estimation is obtained over a narrow range of pressures when using phase-sensitive correlation functions. However, for accurate estimation, the quadratic term must be included. The importance of the quadratic and possibly higher order terms seems to increase with increasing Reynolds number.

The authors would like to acknowledge ONR support under grant N00014-93-1-0639, monitored by Dr. Patrick Purtell.

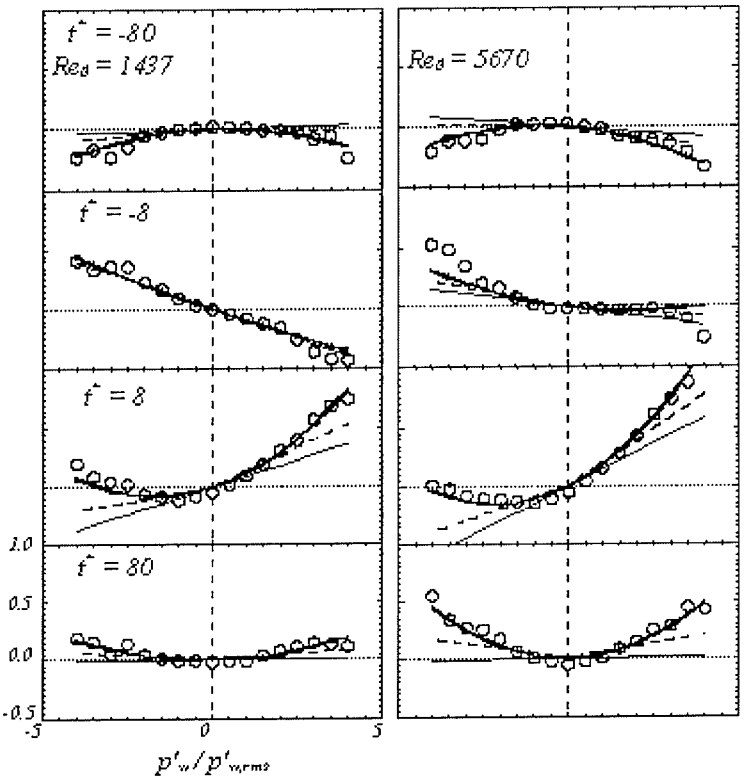


Figure 3: Comparison of the conditional average with the linear, quadratic and phase-sensitive SE for different time delays and Reynolds numbers ($y^+ = 20$).

References

[1] R. J. Adrian. On the role of conditional averages in turbulence theory. *Turbulence in liquids: proc. of the fourth biennial symposium on turbulence in liquids, edited by J. L. Zakin and G. K. Patterson, Science Press, Princton, NJ*, 323–332, 1977.

[2] Y. G. Guezennec. Stochastic estimation of coherent structures in turbulent boundary layers. *Physics of Fluids A*, 1(6):1054–1060, 1989.

[3] S. Stokes and M. Glauser. Multi-point measurement techniques used in the study of separated flows. 30^{th} *AIAA Fluid Dynamics Conference, 28 June - 1 July, Norfolk, VA, USA*, AIAA Paper no. 99-3518, 1999.

[4] G. J. Brereton. Stochastic Estimation as a Statistical Tool for Approximating Turbulent Conditional Averages. *Phys. Fluids A*, 4 (9):2046-2054, 1992.

ADVANCES IN TURBULENCE VIII
Proceedings of the Eighth European Turbulence Conference
C. Dopazo et al. (Eds.)
© CIMNE, Barcelona 2000

Reynolds-stress budgets from a wall-bounded adverse-pressure-gradient flow

G. N. Coleman[1], J. Kim[2] and P. R. Spalart[3]

[1]School of Engineering Sciences, University of Southampton
Highfield, Southampton, SO17 1BJ, UK
[2]Mechanical and Aerospace Engineering, University of California
Los Angeles, CA, 90095 USA
[3]Boeing Commercial Airplanes, Seattle, WA 98124, USA

Contact e-mail: gnc@soton.ac.uk

1 Introduction

This work is based on direct numerical simulation (DNS) of an idealized perturbed boundary layer. A spatially developing flow is emulated by straining the domain of a turbulent channel flow, replacing spatial changes with temporal ones, causing the wall-bounded turbulence to experience the deformation history of the spatial case (figure 1). This approach has the advantage of imposing the essential complexity of perturbed flows in an uncomplicated geometry. The resulting Reynolds-averaged statistics satisfy a one-dimensional unsteady problem, which provides considerable simplification for coding, analysis and modeling. Further details are provided in [2].

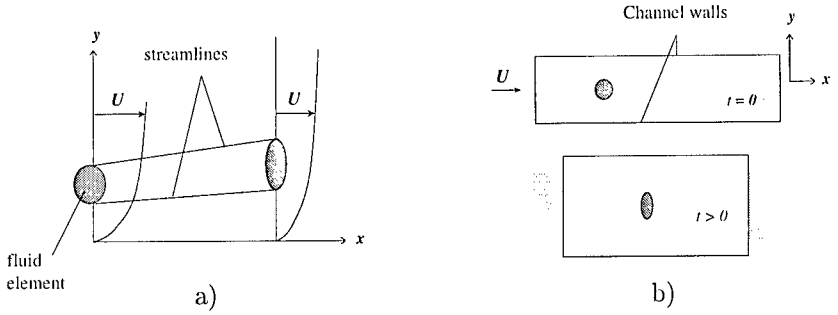


Figure 1: Side view of 2D APG boundary layer. a) Spatially developing flow. b) Initial and deformed domain of time-developing strained-channel idealization.

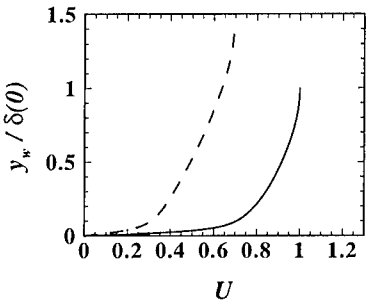


Figure 2: Mean velocity for APG strained-channel flow: ——, $A_{22}t = 0$; ----, $A_{22}t = 0.365$.

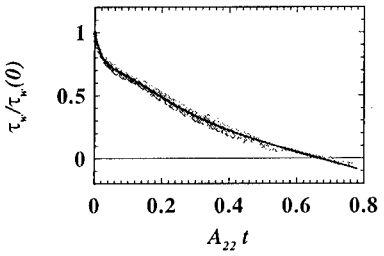


Figure 3: Mean skin-friction history: symbols from 21 independent DNS realizations; ——, equation (1) interpolant.

2 Results

We consider a strain field induced by an adverse pressure gradient (APG), with a streamwise deceleration $A_{11} \equiv \partial U/\partial x < 0$ and wall-normal stretching $A_{22} \equiv \partial V/\partial y > 0$. A relatively weak APG is assumed, with $A_{22} = -A_{11}$ chosen to be 30.7% of u_τ/δ, the ratio of initial friction velocity to channel half-width. The initial Reynolds number $Re_\tau = u_\tau\delta/\nu$ is 391, which is large enough (roughly four times that needed to sustain channel turbulence) to produce a well-defined inertial layer (cf. [4]). (The initial Reynolds number based on mean centerline velocity is 7908.) Preliminary results for this case were presented in [1]; the present study benefits from increasing the ensemble average from 4 to 21 realizations, and inclusion of Reynolds-stress budgets.

The ability of the strained-channel strategy (which combines a spatially uniform strain field with in-plane motion of the channel walls) to emulate an APG boundary layer, both near and far from the wall, is illustrated in figures 2 and 3. The time-dependent wall velocity $u_w(t)$ used to create the inner layer appropriate for an APG satisfies $\overline{u}_c(t) - u_w(t) = \overline{u}_c(0)\exp(A_{11}t)$, where $\overline{u}_c(t)$ is the mean centerline velocity (see [2]). The evolution of the mean velocity shown in figure 2 demonstrates both the reduction of the wall-shear stress and the increase of the layer thickness found in the spatial case. The skin-friction reduction is also documented in figure 3, where the symbols trace the history of the various DNS realizations. The solid curve is an interpolant, which may be useful to those wishing to compare model predictions against the DNS results. It is given by:

$$\tau_w/\tau_w(0) = \exp(a_0\sigma) + a_1\sigma^3 + a_2\exp(a_3\sigma)\sin(a_4\sigma), \qquad (1)$$

where $(a_0, a_1, a_2, a_3, a_4) = (-3.5433, -0.3127, 2.9267, -29.5295, -3.3553)$ and $\sigma = A_{22}t$.

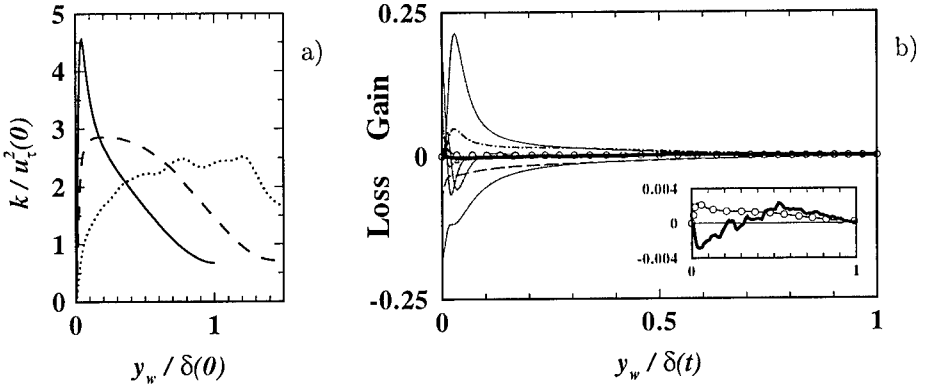


Figure 4: a) Turbulence kinetic energy k profiles: ——, $A_{22}t = 0$; ----, $A_{22}t = 0.365$; ····· , $A_{22}t = 0.77$ (single realization). b) Terms in k budget at $A_{22}t = 0.365$: —·—·—, mean-shear production; — — — —, dissipation; ----, turbulent transport; —··—, viscous diffusion; ····· , velocity pressure-gradient correlation; ∘, applied-strain production (also shown in inset with expanded vertical scale); thick-solid curve (——), sum of all terms ($\approx \partial k/\partial t$) at $A_{22}t = 0.365$ (also shown in inset). Thin-solid (——) curves denote terms at $t = 0$ (before strain). Shaded regions indicate change from unstrained initial-condition profiles. Budget terms defined as in [3].

Another feature of APG layers captured by the DNS is the simultaneous increase, in the outer layer, and decrease, near the wall, in turbulence activity. This is revealed in figures 4*a* and 5*a*, plots of turbulence kinetic energy k and turbulent shear stress $-\overline{u'v'}$, respectively. The effect of the APG strain upon the various terms in the budgets of these two quantities is also shown, in figures 4*b* and 5*b*, where the profiles at $A_{22}t = 0.365$ are compared to their initial values (the shaded regions indicate the net change induced by the APG). This time corresponds to about half that required for the flow to undergo a parallel-flow version of separation (see figure 3) – when the skin friction changes sign but without enhancing the convection away from the wall. The figure 4 and 5 results are thus representative of a non-separating APG layer (expect for the dotted curves in figure 4*a* and 5*a*, taken from a single realization at $A_{22}t = 0.77$, after the skin-friction reversal).

Figure 4*b* shows that the near-wall kinetic-energy decrease (see expanded-scale inset, which plots the net balance, approximately $\partial k/\partial t$) is accompanied by large decreases in both production and dissipation (budget terms are defined as in [3]), with the production falling most rapidly, leading to a negative imbalance. The net positive $\partial k/\partial t$ in the outer layer, on the other hand, can be traced to the $A_{11} = -A_{22}$ strain (figure 4*b* inset).

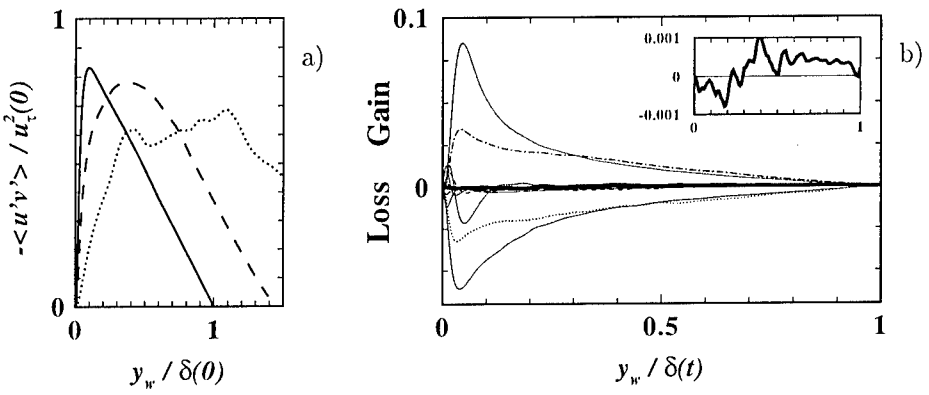


Figure 5: a) Turbulent shear-stress $-\overline{u'v'}$ profiles and b) terms in $-\overline{u'v'}$ budget at $A_{22}t = 0.365$: symbols as in figure 4.

All the terms in the $-\overline{u'v'}$ budget (figure 5*b*) become smaller near the wall, with the production $-P_{12}$ (a source of $-\overline{u'v'}$) and pressure-velocity-gradient correlation $-\Pi_{12}$ (a sink) experiencing the most obvious changes; a net decrease in $-\overline{u'v'}$ occurs since $-P_{12}$ approaches zero faster than $-\Pi_{12}$ does. A near-balance between $-P_{12}$ and $-\Pi_{12}$ also controls the outer-layer increase. The extent to which this behavior is affected by the applied strain will be explored in future work, as will the underlying sources of changes found in other budgets, along with implications for modeling APG boundary layers.

The DNS data, along with a C or Fortran model-testing code incorporating the strained-channel geometry, will be made available electronically should others wish to use them as resources for closure testing and development.

References

[1] G. N. Coleman, J. Kim and P. R. Spalart. Direct numerical simulation of decelerated wall-bounded shear flows. Eleventh Symposium on Turbulent Shear Flows, Grenoble France, 1997

[2] G. N. Coleman, J. Kim and P. R. Spalart. A numerical study of strained three-dimensional wall-bounded turbulence. To appear in *J. Fluid Mech.*

[3] N. N. Mansour,J. Kim and P. Moin. Reynolds-stress and dissipation-rate budgets in a turbulent channel flow. *J. Fluid Mech.*, 194:15–44, 1988.

[4] R. D. Moser, J. Kim and N. N. Mansour. Direct numerical simulation of turbulent channel flow up to $Re_\tau = 590$. *Phys. Fluids*, 11:943–945, 1999.

ADVANCES IN TURBULENCE VIII
Proceedings of the Eighth European Turbulence Conference
C. Dopazo et al. (Eds.)
© CIMNE, Barcelona 2000

Scaling of the near-wall layer beneath a three-dimensional turbulent separation bubble

P.E. Hancock and J.R. Hardman[1]

School of Mechanical and Materials Engineering
University of Surrey, UK
[1]Present address: Computational Dynamics, Nürnberg, Germany

Contact e-mail: p.hancock@surrey.ac.uk

1 Introduction

In two-dimensional flow the near-wall layer, which may defined as the region beneath the position of maximum reverse-flow velocity, is thin compared with height of the bubble. It exhibits 'laminar-like' features and the velocity profiles are approximately self-similar (e.g. [1]). Attention has been directed almost exclusively to the layer upstream of attachment, although there is a comparably thin layer on the downstream side.

The present flow was generated by means of a doubly-swept separation line of $\pm 10°$, formed by normal flat plates mounted on the front of a v-shape horizontal splitter plate [2]. Figure 1 shows the limiting streamlines on the splitter plate surface. The degree of three-dimensionality is 'moderate' in that the cross-flow velocity was significantly less than the free-stream velocity. The flow was about wide enough for the flows on the sides of the central region, at about $z = \pm$ 380mm, to be 'spanwise-invariant', free from the influences of the wind tunnel walls.

Pulsed-wire measurements were made of mean and fluctuating velocity and wall shear stress. The present paper is primarily concerned with the parametric dependency of the fluctuating surface shear stresses - the mean flow scaling is addressed in another paper [3]. The viscous constraint on the cross flow velocity (z-direction) extends further into the flow than it does on the streamwise (x-direction) flow. The cross-flow velocity profiles also exhibit approximate self similarity, slightly fuller than those for the streamwise flow. Wall shear stress coefficients (C_{f_x} and C_{f_z}) based on velocities (U_δ and W_δ) at the edge (δ_U, and δ_W) exhibit simple dependencies on local Reynolds numbers based upon the same edge velocities and layer thicknesses, as shown in figure 2. These relationships apply upstream and downstream of reattachment, and appear to apply reliably

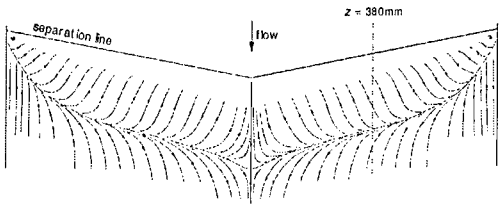


Figure 1: Surface streamlines beneath separation bubble.

across lines of zero mean stress. Other scalings proposed on the basis of two-dimensional coplanar studies do not work. There is also a striking comparability between the near-wall layer and three-dimensional turbulent boundary layers, in which the cross flow is the primary flow and the reverse (or streamwise) flow is the pressure-driven secondary flow.

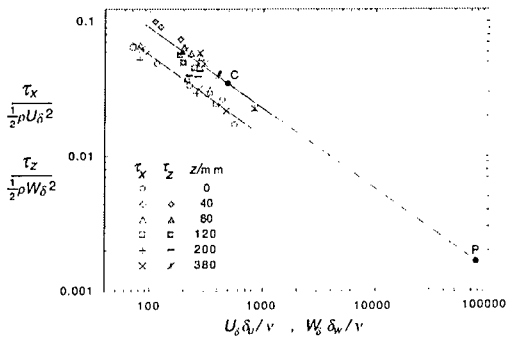


Figure 2: Local wall shear stress coefficients against local Reynolds numbers. Lines have slopes of -0.6. 'P' and 'C' denote primary and cross flow of [4].

2 Results

The r.m.s. of the wall-shear-stress fluctuations, τ_x' and τ_z', are shown in figure 3, where U_{ref} is the free-stream velocity. An example of the lateral fluctuations of velocity is given in figure 4, where in these instances the thickness, δ_U, lies in the range $\sim 0.24h_f$ to $\sim 0.38h_f$, and the thickness, δ_W, lies in the range $\sim 0.35h_f$ to $\sim 0.56h_f$. h_f is the height of the normal flat plate above the splitter plate. A simple supposition would be to suppose that the r.m.s of the fluctuating surface shear stress is proportional to the r.m.s of the (corresponding) fluctuating velocity at the edge of the near-wall layer. That is,

$$\tau_x' \approx C_x' \, \mu \, \frac{u_\delta'}{\delta_U} \quad \text{and} \quad \tau_z' \approx C_z' \, \mu \, \frac{w_\delta'}{\delta_W}$$

where u_δ' and w_δ' are $\overline{u^2}^{1/2}$ and $\overline{w^2}^{1/2}$ at $y = \delta_U$ and δ_W, respectively. Figure 5 shows, $\tau_x'\delta_U/u_\delta'$ and $\tau_z'\delta_W/w_\delta'$ normalised by $2\rho U_{ref}h_f$, where $U_{ref}h_f/\nu$ was

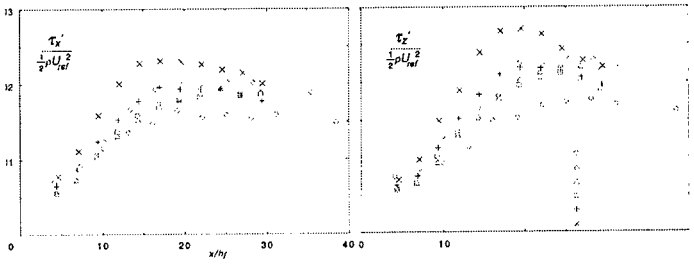


Figure 3: R.m.s. of $x-$ and $z-$direction wall shear stress fluctuations.

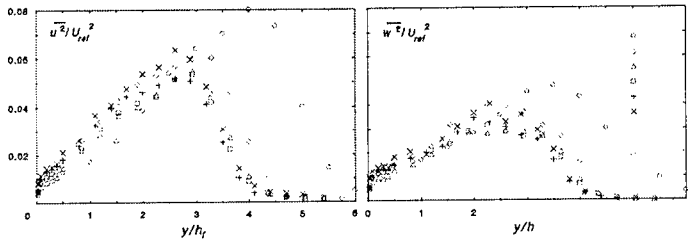


Figure 4: Mean square of $x-$ and $z-$direction velocity fluctuations, $x/X_A = 0.5$.

3900. X_A is the $x-$direction distance to the attachment line from the separation line (at z). The scatter in this figure is largely due to the difficulty in determining δ_U and δ_W accurately. The lines indicated imply values of C'_x and C'_z of about 8 and 12, respectively. The same argument can of course be applied to the mean

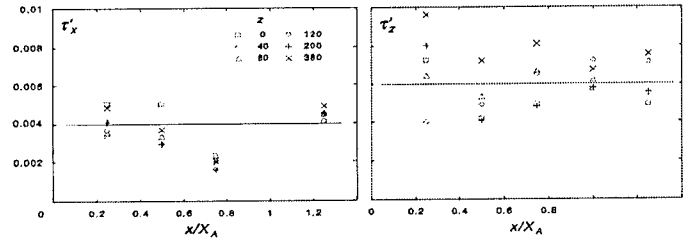


Figure 5: $\tau'_x \delta_U / u'_\delta$ and $\tau'_z \delta_W / w'_\delta$ normalised by $2\rho U_{ref} h_f$.

flow - i.e. $\tau_x \approx C_x \mu U_\delta / \delta_U$ and $\tau_z \approx C_z \mu W_\delta / \delta_W$ - where the coefficients, C_x and C_z, are about 4 and 6 - the profiles of u' and w' are fuller than those of U and W. In this argument the length scales, δ_U and δ_W, are the same for both the mean flow and the fluctuating flow, implying (reasonably) that viscous effects extend about the same distance from the surface for the fluctuations as for the mean flow. However, it should not be inferred that τ'_x and τ'_z are proportional to τ_x and τ_x since the velocity ratios u'_δ / U_δ and w'_δ / W_δ cannot in general be constant. (See also [5][6].) Figure 6 shows τ'_x and τ'_z scaled on u'_δ and u'_δ against $u'_\delta \delta_U / \nu$ and $w'_\delta \delta_W / \nu$ in analogy with the mean flow scaling of figure 2, showing

a comparably simple dependence.

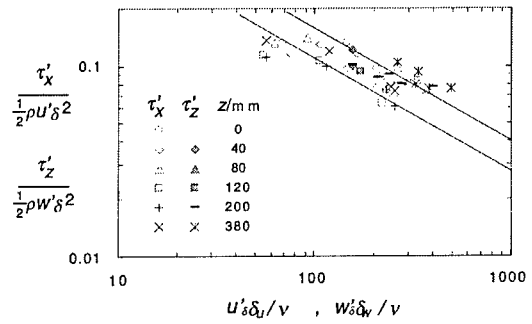


Figure 6: Local r.m.s. wall shear stress coefficients against local turbulence Reynolds numbers. Lines have slopes of -0.6.

3 Conclusions

The fluctuating wall shear stresses scale in a comparable manner to that for the mean shear stresses, but are not coupled to the mean stresses. The scalings are local, applying, it appears, through singularities of mean wall shear stress.

References

[1] R. L. Simpson. A model for the backflow mean velocity profile. *AIAA J.*, 21: 142–143, 1983.

[2] J. R. Hardman and P. E. Hancock. Moderately three-dimensional separated and reattaching turbulent flow. Proc. 2nd Int. Symp. Heat and Mass Transfer, 541–548, Delft, 1997. (Ed: H. Hanjalic and T. W. J. Peeters.)

[3] J. R. Hardman and P. E. Hancock. The near-wall layer beneath a moderately converging three-dimensional turbulent separated and reattaching flow. In preparation., 2000.

[4] P. Bradshaw and N. S. Pontikos. Measurements in the turbulent boundary layer on an 'infinite' swept wing. *J. Fluid Mech.*, 159: 105–130, 1989.

[5] P. E. Hancock. Measurements of mean and fluctuating wall shear stress beneath spanwise-invariant separation bubbles. *Expts in Fluids*, 27: 53–59, 1999.

[6] P. E. Hancock. Low Reynolds number two-dimensional separated and reattaching turbulent shear flow. *J. Fluid Mech.*, 410: 101-122, 2000.

XIV

Turbulent Reacting Flows

ADVANCES IN TURBULENCE VIII
Proceedings of the Eighth European Turbulence Conference
C. Dopazo et al. (Eds.)
© CIMNE, Barcelona 2000

A geometric criterion for non-equilibrium and triple flame domains

W. Kollmann [1], J. H. Chen [2] and H. G. Im [2]

[1]MAE Dept, University of California
Davis, CA 95616, USA
[2] CRF, SANDIA National Laboratories
Livermore, CA 94551-0969, USA

Contact e-mail: wkollmann@sweetpea.engr.ucdavis.edu

1 Introduction

Partially premixed turbulent flames can develop flow regimes where triple flames emerge consisting of essentially premixed and non-premixed zones. The description of such phenomena requires a criterion for the detection of such zones, which can be based on a wide range of variables including reaction rates, mass fractions of radicals, the sign of the product of the gradients of fuel and oxidiser mass fractions. These variables are not necessarily suitable for the derivation of sdf/pdf methods, which require transport pdes for the conditioning variables. Reaction rates are not bounded in the limit of infinitely fast reactions, the sign function is discontinuous, radical mass fractions are not necessarily present in rich and lean zones. Hence a new single scalar variable based on geometric properties of mixture fraction and non-conserved variables is constructed, that allows the detection of finite rate and, in particular, triple flame domains and remains smooth and bounded in the limit of infinitely fast reactions. It is based on the observation (see, for instance, fig.8 of Echekki and Chen [1]) that in finite rate regions the isolines of thermodynamic variables cease to be parallel to the isolines of mixture fraction.

2 Geometric criterion

The criterion to be developed rests on the following set of assumptions:

(1) The Navier-Stokes equations for the zero Mach number limit (Majda and Sethian [3]) hold.

(2) The conditions stated by Williams ([4], section 1.3) for the existence of coupling functions hold.

(3) The flow domain is open.

It follows from these conditions that the limit of infinitely fast chemistry reduces the system of thermodynamic variables governed by pdes to a single one called mixture fraction Z: Density, temperature and composition become local (not involving differential or integral expressions) functions of Z. Here the assumptions of zero Mach number and open domain are crucial since compressibility effects would make density and temperature nonlocal (i.e. via differential equations) functions of the velocity, energy and pressure fields and the zeroth order pressure would be time dependent in closed domains.

2.1 Simplified chemistry

Simplified chemistry involving only two variables (mixture fraction Z and a progress variable c, all variables are assumed dimensionless) is considered first. The angle $\gamma = \sin^{-1}(|\mathbf{n}^Z \times \mathbf{n}^c|)$ between the gradients of Z and c is according to the results of Echekki and Chen [1] close to zero for regions without significant finite rate effects and large in the flame zones. The unit normal vectors for the level surfaces of mixture fraction and progress variables are defined by

$$\mathbf{n}^Z \equiv \frac{\nabla Z}{|\nabla Z|}, \quad \mathbf{n}^c \equiv \frac{\nabla c}{|\nabla c|} \tag{1}$$

The progress variable c varies significantly near the flame zone, but can be expected to be close to zero or unity away from it. Hence, the computation of unit normal vectors may suffer from numerical inaccuracy away from the flame zones, hence

$$\mathbf{g} \equiv \frac{\nabla Z}{1 + |\nabla Z|} \times \frac{\nabla c}{\max|c| + |\nabla c|} \tag{2}$$

is used in the scalar detection function $\mathcal{F} = \mathbf{g} \cdot \mathbf{g}$. The vector $\mathbf{g}$ is proportional to the sinus of the angle between the two gradients, if $|\nabla Z| \gg 1$ and $|\nabla c| \gg \max|c|$ hold and it approaches the zero vector as one of the gradients vanishes. Hence, (2) is and the criterion for the detection of finite rate zones is then $\mathcal{F} > f_0$ where $\max \mathcal{F} \gg f_0 > 0$ is a suitable value. This definition enjoys the advantage (in contrast to reaction rates) to be smooth and bounded as the limit of infinitely fast reactions is approached.

2.2 Complex chemistry

This criterion can be generalized to partially premixed flames with complex chemistry where the local thermodynamic state is described by non-conserved variables c_i, $i = 1, \cdots, M$ and a mixture fraction variable Z. In the limit of infinitely fast reactions, all c_i become local functions of Z according to the assumptions stated above. The obvious generalisation would be to construct the scalar $\mathcal{F}$ as sum over individual products $\mathcal{F}_i$ of the form (2). This would lead to

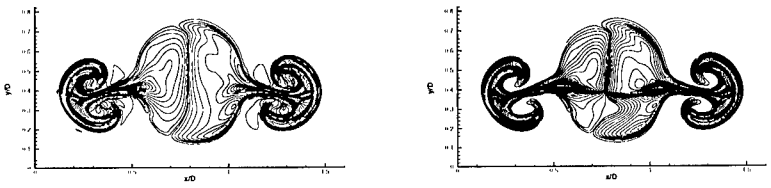


Figure 1: Isolines of $\mathcal{F} = \mathbf{g} \cdot \mathbf{g}$ for $\mathbf{g}$ constructed with mixture fraction Z and density ρ at time $t = 29$ (left) and with mixture fraction Z and mass fraction of H_2O (right) at time $t = 19$.

extreme complexity of the transport pde for $\mathcal{F}$ and defeat the purpose to produce a tool for the analysis of finite rate regions in turbulent flames. However, there is another possibility: Scalar variables such as temperature and density depend on all reaction steps in an implicit manner: The Navier-Stokes system for combustion flows in zero Mach number limit (see Majda and Sethian [3]) can be set up for the variables velocity, pressure, composition variables and internal energy, all satisfying pdes. Density and temperature follow then from local state relations, hence $\rho(v_\alpha, p, Y_1, \cdots, Y_N, u)$ and $T(v_\alpha, p, Y_1, \cdots, Y_N, u)$ with nonlocal (functional) dependence on velocity. The composition variables in turn are functions of the chemical rate parameters (Damkoehler numbers for the individual reactions), hence are density and temperature functions of these parameters. It follows that it is sufficient for complex systems of combustion reactions to consider the definition

$$\mathbf{g} \equiv \frac{\nabla Z}{1 + |\nabla Z|} \times \frac{\nabla \rho}{\max|\rho| + |\nabla \rho|} \tag{3}$$

(the dimensionless density is not necessarily positive) and $\mathcal{F} = \mathbf{g} \cdot \mathbf{g}$. This definition satisfies the requirements for the detection of finite rate regions and remains bounded as infinitely fast reactions are approached.

3 Evaluation of the criterion in 2-d flames

Im and Chen [2] investigated the structure and propagation of triple flames in partially premixed hydrogen-air mixtures using detailed chemistry. These results are used to verify the properties of the scalar variables defined in the previous sections for the detection of finite- rate regions. The case of a strong interaction with a vortex offers a suitable test case (see Im and Chen [2]) to evaluate the criterion. Figure 1 (time $t = 19$) and fig.2 ($t = 29$) show the isolines of the scalar $\mathcal{F}$ for two choices of the non-conserved scalar in the vector $\mathbf{g}$: (i) density ρ, (ii) mass fraction of H_2O. It is evident that the detailed variation of the scalar $\mathcal{F}$ within the finite rate regions is different for (i) and (ii), but the outline (level

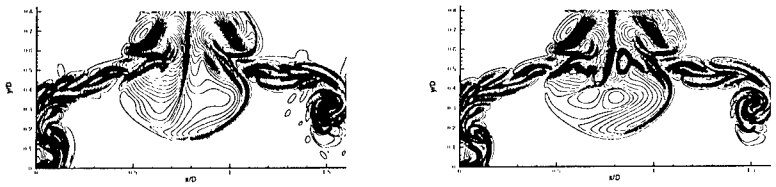


Figure 2: Same as fig.1 for time $t = 29$.

value f_0 small compared to the maximum) is essentially the same for density and mass fraction of H_2O at both times.

4 Conclusions

A new scalar variable based on geometric properties of level surfaces was constructed that allows the detection of finite rate and triple flame regions. It remains smooth and bounded in the limit of infinitely fast chemistry and can be applied to complex systems of combustion reactions. It is valid for the conditions stated in the assumptions. Evaluation of DNS results showed that various definitions of the scalar using stable mass fractions and density produce the same finite rate region but different distributions of the scalar in them.

Acknowledgements

This research was supported by the United States Department of Energy, Office of Basic Energy Sciences, Chemical Sciences Division.

References

[1] T. Echekki and J.H. Chen. Structure and Propagation of Methanol-Air Triple Flames. *Combustion & Flame* 114: 231–245. 1998.

[2] H.G. Im and J.H. Chen. Structure and propagation of triple flames in partially premixed hydrogen-air mixtures. *Combustion & Flame* 119: 436–454, 1999.

[3] A. Majda and J. Sethian. The Derivation and Numerical Solution of the Equations for Zero Mach Number Combustion. *Combust. Sci. Technol.* 42: 185–205, 1985.

[4] F.A. Williams. *Combustion Theory*, Benjamin/Cummings Publ. Comp. Inc., Menlo Park, 1985.

ADVANCES IN TURBULENCE VIII
Proceedings of the Eighth European Turbulence Conference
C. Dopazo et al. (Eds.)
© CIMNE, Barcelona 2000

Edge flame and partially premixed flamelets in nonpremixed combustion

Valérie Favier and Luc Vervisch

Institut National des Sciences Appliquées de Rouen
UMR CNRS - CORIA 6614, Avenue de l'Université - BP 8
76801 Saint Etienne du Rouvray Cedex, France

Contact e-mail: favier@coria.fr, vervisch@coria.fr

1 Introduction

Finite rate chemistry and quenching effects in diffusion flames have been the subject of multiple studies motivated by the need to understand intermediate combustion regimes observed during transition from fast chemistry to fast micromixing and quenching of the reaction zones [1]. Local flow conditions promoting quenching of diffusive-reactive layers prohibit stabilization or development of combustion. Partial extinction also modifies pollutants formation. The development of new strategies for Reynolds Averaged Simulation (RANS) or Large Eddy Simulation (LES) of turbulent combustion therefore implies a precise knowledge of both quenching mechanisms and flame structure bordering quenched locations [2, 3].

Using numerical simulations of diffusion flame quenching, it is shown that one may distinguish between conditions leading to transition from burning to quenching, and, conditions observed at a quenched location featuring different flame properties, related to partially premixed combustion.

2 Diffusion flame quenching, edge flame and partially premixed flamelets

Diffusion flames are usually parametrized using conserved scalars as the mixture fraction Z ($Z = 0$ in pure oxidizer and $Z = 1$ in pure fuel). Fundamentals of diffusion flame reveal that regions where the chemical reaction is frozen (flame quenching) appear when the local Damköhler number (Da) falls below a critical value Da_q^*. The number Da is defined as the ratio of a diffusive time τ_χ to a chemical time [4]. τ_χ may be estimated from the scalar dissipation rate $\chi = D|\nabla Z|^2$ as $\tau_\chi \approx \chi^{-1}$, where D is a diffusion coefficient. Solutions of planar flame problems for a variety of χ, called flamelet library, provide a quenching

scalar dissipation rate χ_q^*, a critical value widely used in turbulent combustion modeling [1].

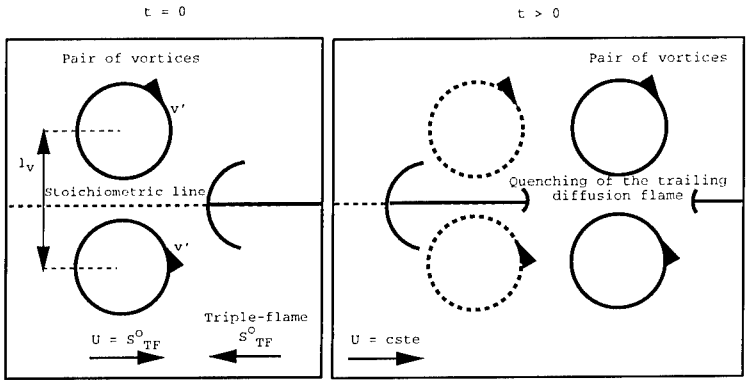


Figure 1: Schematic of the simulations of two-dimensional quenching.

To study flamelet quenching without curvature of the stoichiometric line, we have further analyzed a Direct Numerical Simulation (DNS) database initially developed to focus on triple flame / vortices interaction [5]. For strong vortices, the trailing diffusion flame is submitted to a high level of strain and scalar dissipation rate leading to quenching of the two-dimensional planar diffusion flamelet (Fig. 1). We focus on this part of the simulation where quenching appears. The diffusion flame is initially stabilized within a two-dimensional domain following a procedure proposed in [6]. The scope of the study is restricted to a zone of the computational domain where only diffusion combustion is concerned. For the simulated case, the vortices do not carry any hot gases and products remaining from their interaction with the partially premixed front and effects of unsteadiness are negligible in our analysis.

A laminar flamelet library has been constructed using the same chemistry and transport than in the full Navier Stokes simulation. The reference quenching scalar dissipation rate χ_q^*, its corresponding quenching length $\delta_q = \sqrt{D/\chi_q^*}$ and the scalar dissipation rate in the unperturbed trailing diffusion flame χ_{Diff} may be used as control parameters. The vortices are characterized by their radius R, velocity $v^{'}$ and the length l_v (Fig. 1). The reported simulations have been performed using a representative condition where diffusion flame quenching is found:

$$\frac{\chi_q^*}{\chi_{Diff}} \approx 100 \quad , \quad \frac{l_v}{\delta_q} \approx 12 \quad , \quad \frac{R}{\delta_q} \approx 5 \quad , \quad \frac{v^{'}}{\chi_q^* \, \delta_q} \approx 40 \qquad (1)$$

Varying these numbers changes the streamwise position of quenching, but do not fundamentally modified the presented results.

The studied sequence may be decomposed in three stages (Fig. 2).

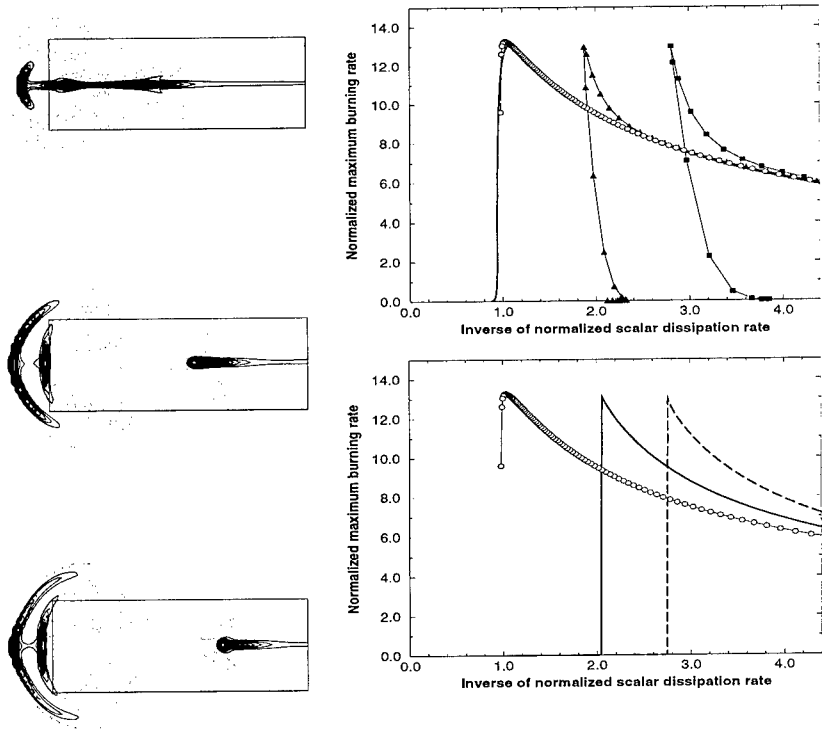


Figure 2: Three successive times of two-dimensional unsteady quenching of a planar diffusion flame pinched by a pair of vortices, configuration studied in [5]. Left, bold: iso-reaction rate, dotted: vorticity, frame: region of the flow where the centerline response of the flame versus inverse mixture fraction dissipation rate is studied. Right top, circle: 1-D flamelet library, line: top left 2-D flame, triangle: middle left 2-D flame, square: bottom left 2-D flame. Right bottom, circle: 1-D flamelet library, line: partially premixed flamelet $\phi_m = 0.16$, dash line: $\phi_m = 0.19$.

The planar diffusion flame is first squeezed by the vortices, then quenching occurs. Latter, premixed kernels develop at the reaction zone extremities. The centerline response of the burning rate shows that one should distinguish between the amount of scalar dissipation rate necessary to quench the diffusion flame χ_q, and, $\chi_{q_{Ed}}$, the value measured at the extremity of the reaction zone, featuring an edge flame [7] (Fig. 2). In these unsteady simulations, the value χ_q that should

be applied to transition from burning to quenching is found to be of the order of χ_q^* predicted by flamelet theory (Fig. 2 top right). In particular when $\chi > \chi_q^*$, quenching is observed. However, once a hole exists in the reaction zone, $\chi_{q_{Ed}}$, the level of scalar dissipation rate necessary to maintain quenching, is always lower than the reference flamelet value χ_q^*. This is explained by multi-dimensional flux of species and heat at the flame tip combined with partial premixing of the reactants in the zone bordering the quenched location.

An indicator of the local degree of partial premixing is given by ϕ_m, the product of reactants mass fractions $\phi_m = Y_F Y_O$. In a pure mixing situation:

$$\phi_m = Y_{F,o} Y_{O,o} Z(1 - Z) \tag{2}$$

where $Y_{F,o}$ and $Y_{O,o}$ are the mass fractions of fuel and oxidizer in the feeding streams. Flamelet library are usually constructed using as boundary conditions for (Y_F, Y_O, Z) the values $(0, Y_{O,o}, 0)$ and $(Y_{F,o}, 0, 1)$. These libraries may also be constructed for prescribed values of ϕ_m, leading to a family of inlet conditions $(Y_{F,o} Z_o, Y_{O,o} Z_o(1 - Z_o), Z_o)$ and $(Y_{F,o} Z_1, Y_{O,o} Z_1(1 - Z_1), Z_1)$, where Z_0 and Z_1 are functions of ϕ_m given by Eq. (2).

Fig. 2 (bottom right) suggests that steady partially premixed flamelets, parametrized with both ϕ_m and χ, reproduce the edge flame response after quenching has developed. A meaningful result for flamelet modeling of turbulent burners where strong finite rate chemistry and quenching occur, and have to be captured carefully.

References

[1] N. Peters. *Turbulent Combustion.* Cambridge University Press.

[2] V. Nayagam, R. Balasubramaniam, and P. D. Ronney. Diffusion flame holes. *Combustion theory and modelling*, 3(4):727–742, 1999.

[3] L. Vervisch and T. Poinsot. Direct numerical simulation of non-premixed turbulent flame. *Annu. Rev. Fluid Mech.*, 30:655–692, 1998.

[4] A. Liñán. The asymptotic structure of counterflow diffusion flames for large activation energies. *Acta Astronautica*, 1007(1), 1974.

[5] V. Favier and L. Vervisch. Effects of unsteadiness in edge-flames and liftoff in non-premixed turbulent combustion. In *Twenty-Seventh Symposium (International) on Combustion/The Combustion Institute*, pages 1239–1245, 1998.

[6] G.R. Ruetsch, L. Vervisch, and A. Liñán. Effects of heat release on triple flame. *Phys. Fluids*, 6(7):1447–1454, 1995.

[7] J. Buckmaster and R. Weber. Edge-flame holding. In *Proceedings of the 26th Symp. (Int.) on Combustion.* The Combustion Institute, Pittsburgh, 1996.

ADVANCES IN TURBULENCE VIII
Proceedings of the Eighth European Turbulence Conference
C. Dopazo et al. (Eds.)
© CIMNE, Barcelona 2000

The effects of combustion on turbulence in high speed mixing layers

F. Ladeinde[1], E. E. O'Brien[1] and W. Liu[2]

[1]Mechanical Engineering Dept., SUNY Stony Brook, NY 11794-2300 USA
[2]Software Engineer, Proximo, Inc. New York City, USA

Contact e-mail: ladeinde@mech.eng.sunysb.edu

1 Introduction

Three kinetic models, described fully in [1], have been studied for H_2/Air combustion in mixing layers involving convective Mach numbers of 0.5, and 0.8. The kinetic models comprise of 2-step/4-species, 8-step/7-species, and 25-step/12-species. The present paper discusses turbulence-combustion interaction, with an emphasis on the effects of chemistry on the turbulence. While studies of the effects of aerodynamics on chemistry are more common, for example, the mixing-enhancement studies, the converse problem has not received enough attention. Previous work by the authors using a Mach number of 0.2 did not show significant effects of the kinetic models on turbulence. Therefore, the present efforts focus on the two Mach number values mentioned above.

Unlike the 2-step kinetic model, which contains radicals of only the OH type, the 8-step and 25-step models include H, O, and OH in the reactions. The generation of the radicals usually involves endothermic reactions, so that temperatures that are lower than the upstream values are possible inside the mixing layer. These effects show up in the density field via the equation of state and hence in the momentum of the flow and in the turbulence. The differential temperature distribution [2] due to these kinetic models and the mass fraction probability density function (PDF) [3] have been studied. For a given Mach number, the background compressibility from high speed is similar to that of the non-reacting case for all three kinetic models. Therefore, any observed differences could roughly be attributed to the effects of the kinetic models.

In the present studies, turbulence quantities are calculated, particularly those that appear in the Reynolds stress evolution equations; their magnitudes and temporal evolution are compared for the three kinetic models. The non-reacting case is available as a reference.

2 Numerical Procedure

The present studies are of the direct numerical simulation (DNS) type, wherein the governing equations are integrated directly in space and time, with the only modeling being that of the reaction rates, in terms of the Arrhenius formula. The numerical procedure and its validation have been presented in previous work by the authors. The computations were carried out on the IBM SP2 supercomputer, to take advantage of its massive parallelization capabilities. The effects of chemistry modeling on the turbulence quantities $\overline{\rho}\widetilde{u_i''u_j''}$ (Reynolds Stress) and on the quantities

$$\mathbf{P}_{ij} = -\overline{\rho}\left(\widetilde{u_i''u_k''}\widetilde{u}_{j,k} + \widetilde{u_j''u_k''}\widetilde{u}_{i,k}\right), \qquad \mathbf{\Pi}_{ij} = \overline{p'u'_{i,j}} + \overline{p'u'_{j,i}} - \frac{2}{3}\overline{p'\theta}\delta_{ij},$$

$$\mathbf{T}_{ijk} = \overline{\rho}u_i''\widetilde{u_j''u_k''} + \left(\overline{p'u'_i}\delta_{jk} + \overline{p'u'_j}\delta_{ik}\right) - \left(\overline{u'_i\sigma'_{jk}} + \overline{u'_j\sigma'_{ik}}\right),$$

$$\overline{\rho}\epsilon_{ij} = \overline{\sigma'_{ik}u'_{j,k}} + \overline{\sigma'_{jk}u'_{i,k}}, \qquad \theta = u'_{k,k}, \qquad \sigma_{ij} = \mu\left(u_{i,j} + u_{j,i} - \frac{2}{3}u_{k,k}\delta_{ij}\right),$$

have been analyzed, where $\mathbf{P}_{ij}$ is the production, $\mathbf{\Pi}_{ij}$ the deviatoric part of the pressure-strain correlation, $\mathbf{T}_{ijk}$ the diffusive transport, ϵ_{ij} the turbulent dissipation rate tensor and $\overline{p'\theta}$ the pressure-dilatation correlation.

The details of the three kinetic models are presented in [1], as are those of the initial and boundary conditions.

3 Results and Conclusion

The evolution with the eddy turnover time of turbulence of the quantities $\mathbf{P}_{ij}$, $\mathbf{\Pi}_{ij}$, $\mathbf{T}_{ijk,k}$, $\overline{\rho}\epsilon_{ij} \equiv D_{ij}$, $\overline{\rho}\widetilde{u_i''u_j''}$, and B_{ij} were evaluated from the DNS results for the three kinetic models and Mach numbers, M_c, of values 0.5 and 0.8. In general, relative to the non-reacting situations, the 2-step reaction model did not show any significant influence on the various quantities. This was the case for $M_c = 0.5$ and 0.8. The strongest effect (not shown), although insignificant, of this kinetic model was in the D_{11} field ($M_c = 0.8$). For all three kinetic mechanisms, no significant effects were observed for $M_c = 0.5$ on any of the turbulence quantities. Furthermore, at $M_c = 0.8$, the 8-step model showed only a slightly more pronounced effect on D_{11} (Figure (a)) and $\overline{\rho}\widetilde{u_1''u_1''}$ than did the 2-step model. The figure shows the effects of the 25-step model on D_{11} (Figure (b)) and $\overline{\rho}\widetilde{u_1''u_1''}$ (Figure (f)) to be quite significant. The effects on $\mathbf{P}_{11}$ and $\mathbf{\Pi}_{11}$, and $\mathbf{T}_{22k,k}$ are also noticeable for this kinetics model ((Figures (a), (b), and (c)). The effects summarized above appear to correlate with previous observations [2,3] on the extent of reaction, as manifested in the heat production by the different reaction schemes. The concentration of radicals in the 25-step model leads to a more rigorous reaction (stronger temperature effects), which is communicated

to the velocity field and, hence, the turbulence field, via the equation of state. The relatively strong effects of the higher Mach number case is an indication of the interaction between low-speed compressibility due to chemical reaction and the compressibility induced by high-speed.

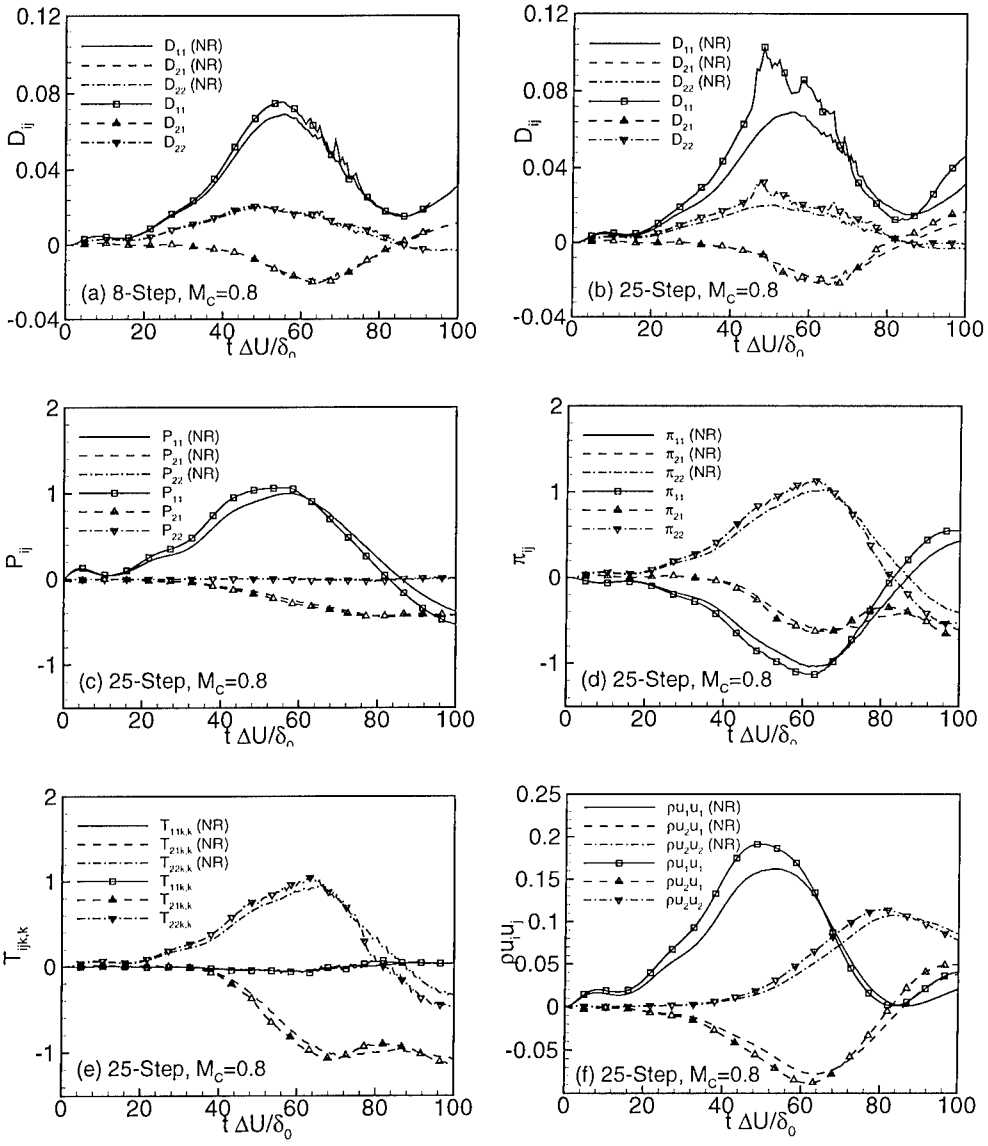
The present work was funded by the United States National Science Foundation, Grant CTS-9626413).

References

[1] W. Liu. The second moments of turbulence in reacting and non-reacting compressible mixing layers. Ph.D. Dissertation, SUNY Stony Brook, New York, 1999.

[2] F. Ladeinde, E. E. O'Brien, W. Liu, and M. Nearon. The effects of kinetics modeling on mass fraction PDF in reacting compressible mixing layers, In *"Turbulence and Shear Flow-1"*, Edit. S. Banerjee and J. K. Eaton, Pub. Begell House, Inc., pp. 321-326, 1999.

[3] F. Ladeinde, W. liu, and E. E. O'Brien. Paper # AIAA-99-0413, Aerospace Sciences Meeting and Exhibit, Reno, NV, USA, 1999.


(a) 8-Step, M_c=0.8
(b) 25-Step, M_c=0.8
(c) 25-Step, M_c=0.8
(d) 25-Step, M_c=0.8
(e) 25-Step, M_c=0.8
(f) 25-Step, M_c=0.8
$t\,\Delta U/\delta_0$
D_{ij}
P_{ij}
π_{ij}
$T_{ijk,k}$
$\rho u_i u_j$
D_{11} (NR)
D_{21} (NR)
D_{22} (NR)
D_{11}
D_{21}
D_{22}
P_{11} (NR)
P_{21} (NR)
P_{22} (NR)
P_{11}
P_{21}
P_{22}
π_{11} (NR)
π_{21} (NR)
π_{22} (NR)
π_{11}
π_{21}
π_{22}
$T_{11k,k}$ (NR)
$T_{21k,k}$ (NR)
$T_{22k,k}$ (NR)
$T_{11k,k}$
$T_{21k,k}$
$T_{22k,k}$
$\rho u_1 u_1$ (NR)
$\rho u_2 u_1$ (NR)
$\rho u_2 u_2$ (NR)
$\rho u_1 u_1$
$\rho u_2 u_1$
$\rho u_2 u_2$

ADVANCES IN TURBULENCE VIII
Proceedings of the Eighth European Turbulence Conference
C. Dopazo et al. (Eds.)
© CIMNE, Barcelona 2000

Compressibility Effects on Scalar Mixing in the Turbulent Reacting Shear Layer

C. Pantano and S. Sarkar

University of California San Diego,
Department of Mechanical and Aerospace Engineering,
La Jolla, CA 92093-0411
USA

Contact e-mail: cpantano@ucsd.edu, ssarkar@ucsd.edu

1 Introduction

Prediction of contaminant mixing as well as reacting turbulent flows requires deep understanding of the physics of turbulent mixing. The effect of compressibility associated with high-speeds, heterogeneous composition and heat release on the structure of a conserved scalar is of primary importance in advanced modeling of turbulent reacting flows. Direct Numerical Simulation is used to study the effect of these parameters in the strongly turbulent plane shear layer for the cases of a passive (mixing case) and active (reacting case) scalar. In this study, no approximation has been used for the energy equation.

An approach to modeling is based on the knowledge of the statistics of two variables; a mixture fraction variable, ζ, that represent the state of mixing and a second variable, in this case the scalar dissipation, χ, defined as $2D\nabla\zeta \cdot \nabla\zeta$, in which D is the mass diffusivity, that takes into account the rate of mixing. These models attempt to decouple the scales of turbulence from the chemical scales, usually several orders of magnitude smaller than the flow ones in real applications [1, 3, 4, 2, 5].

The convective Mach number, defined as $M_c = (U_1 - U_2)/(c_1 + c_2)$, where the velocity, density and speed of sound in stream i are U_i, ρ_i, c_i is used to quantify compressibility effects, in our case all results correspond to $M_c = 0.3$. The heat released is represented by $Ce = \Delta h^o Y_{f,-\infty}/C_p T_o(1+\phi)$, where ϕ is the equivalence ratio. The single-step, infinitely fast irreversible combustion of methane with air is considered,

$$CH_4 + 2O_2 \rightarrow CO_2 + 2H_2O \qquad (1)$$

The purpose of this work is to study the scalar statistics in a strongly turbulent flow under realistic conditions of heat release for the turbulent reacting shear layer.

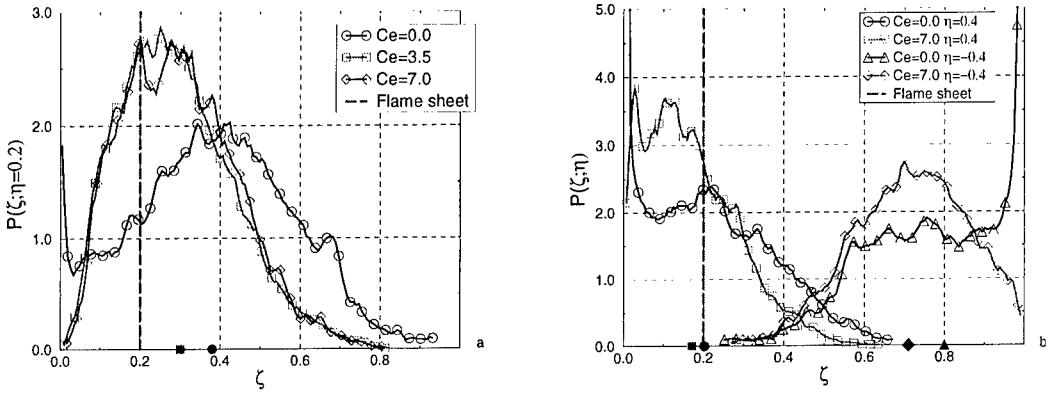


Figure 1: Scalar pdf (a) $Ce = 0$, 3.5 and 7 at $\eta = 0.2$ and (b) $\eta = \pm 0.4$.

2 Results

The problem at hand corresponds to the plane mixing layer solved in a computational domain that translates with the mean velocity of the flow. This configuration results in a flow whose statistical measurements depend on the vertical coordinate, x_2, and time. It is also known that if enough time is given, the flow approaches a self-similar state where all averages depend only on a self-similar variable defined as the ratio of the vertical coordinate to a measure of the thickness of the layer, in our case $\eta = x_2/\delta_\omega$, where δ_ω is the vorticity thickness. Simulations with grids as large as 256x192x128 and with large evolution times, required to achieves self-similarity, were performed. The Reynolds numbers based on vorticity thickness reached values of the order of 5000 at the end of the different simulations. In the cases with heat release a stoichiometric mixture fraction value of $\zeta_s = 0.2$ was fixed by diluting the fuel stream with nitrogen. Values of $Ce = 3.5$ and 7 were used in the present study. Notice that $Ce = 7$ is the value obtained for Methane-Air combustion at this stoichiometry. Furthermore, Favre averages will be used in the subsequent plots.

2.1 Scalar Pdf

Figure 1(a) shows the scalar pdf at $\eta = 0.2$ (average position of the flame) for the turbulent shear layer in cases $Ce = 0$, 3.5 and 7. The value of $P(\zeta = \zeta_s; \eta = 0.2)$ in both cases with heat release are about twice the value for the case without heat release. Figure 1(b) shows the scalar pdf at $\eta = \pm 0.4$. The pdf is no longer symmetric, since the stoichiometric value $\zeta_s = 0.2$, introduces an asymmetry in the mixing layer. Another feature of the reacting cases is that external intermittency is suppressed. These changes should be considered when

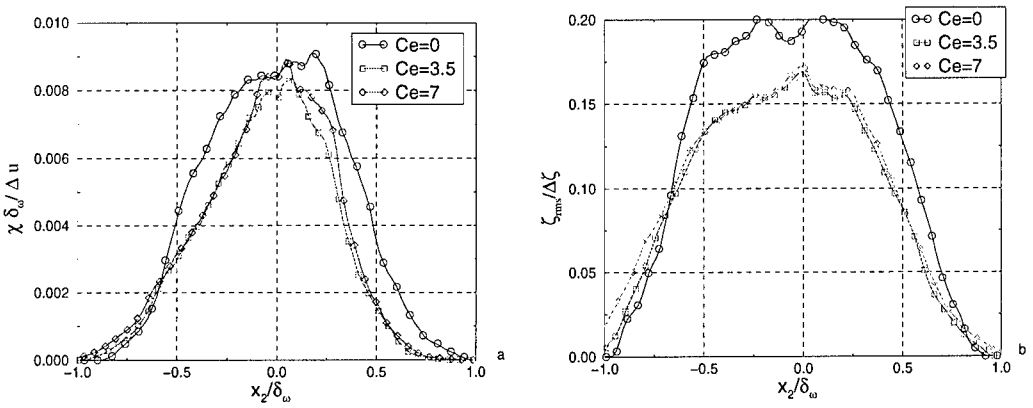


Figure 2: Scalar dissipation (a) and scalar rms (b) for $Ce = 0$, 3.5 and 7.

developing models for reacting flows. Moreover, the use of pdf measurements that correspond to non-reactive flows could lead to incorrect predictions.

2.2 Scalar Dissipation and Scalar RMS

Figure 2(a) shows the unconditional scalar dissipation, χ, normalized by vorticity thickness, as a function of the coordinate η. It can be seen that the non-reacting and reacting cases are very similar when δ_ω is used as the scaling parameter. A reduction in the thickness of the unconditional scalar dissipation profile in self-similar space is observed in the cases with heat release. Figure 2(b) shows scalar rms profiles for $Ce = 0$, 3.5 and 7. The levels of scalar rms in the heat release cases are lower than the values measured in the case without heat release.

Figure 3(a) show the center-plane scalar dissipation pdf for the three cases. Notice that the pdf is a function of $ln(\chi)$ in this case and the central region of the pdf is approximately lognormal. There is no evidence of a change in the shape of the scalar dissipation pdf at the centerplane with heat release. In Figure 3(b) the scalar dissipation pdf is calculated at different planes for the case of $Ce = 7$. We observe that the shape of the pdf does not change with η until we reach the boundaries of the mixing layer, $\eta > 0.4$.

3 Conclusions

In the case of the scalar pdf, it is observed that substantial differences between the non-reacting and reacting cases exist. The stoichiometric value of 0.2 introduces an asymmetry in the mixing layer. External intermittency is suppressed in the cases with heat release. The choice of the vorticity thickness as a normal-

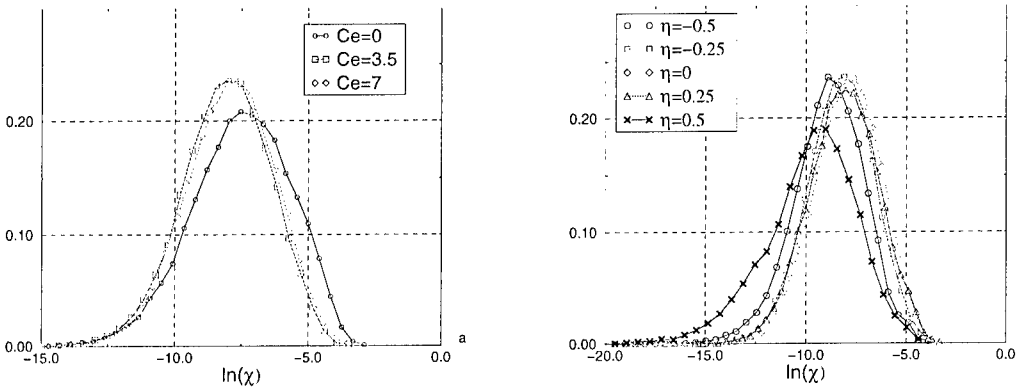


Figure 3: Scalar dissipation pdf at center-plane for $Ce = 0$, 3.5 and 7 (a) and $Ce = 7$ for different planes (b).

izing scale collapses the unconditional scalar dissipation profiles. A log-normal model for the scalar dissipation pdf seems to be correct for planes located within the mixing layer. In the intermittent region, this model seems to be no longer valid. Further studies to asses the effects of compressibility and heat release on the conditional scalar dissipation, more important from the modeling point of view, are underway.

Acknowledgement
This work was supported by AFOSR through grant F49620-96-1-0106. Computational time was provided by the CEWES and NAVO Major Shared Resource Centers and by the San Diego Supercomputer Center.

References

[1] F. A. Williams. Turbulent Mixing in Non-reactive and Reactive Flows. *(S.N.B. Murthy, Ed.), Plenum, New York*, pages 189–208, 1975.

[2] A.Yu. Klimenko. Multicomponent diffusion of various admixtures in turbulent flow. *Fluid Dynamics*, 25(3):3–10, 1990.

[3] N. Peters. Prog. Ener. Combust. Sci. 10:319–339, 1984.

[4] N. Peters. Twenty-First Symposioum (International) on Combustion. *The Combustion Institute, Pittsburgh*, pages 1231–1250, 1986.

[5] R. W. Bilger. Conditional moment closure for turbulent reacting flow. 5(2):436–444, 1993.

ADVANCES IN TURBULENCE VIII
Proceedings of the Eighth European Turbulence Conference
C. Dopazo et al. (Eds.)
© CIMNE, Barcelona 2000

Subgrid Scale Variance and Dissipation of a Scalar Field in Large Eddy Simulation Combustion Models

C. Jiménez, F. Ducros and B. Cuenot

CERFACS, 42 av. G Coriolis, 31057, Toulouse, France

Contact e-mail: carmen@cerfacs.fr

1 Introduction

Presumed probability density function (PDF) models for Large Eddy Simulations of non–premixed combustion systems [1, 2, 3] are based in the description of subgrid scale (SGS) joint statistics of reacting scalars as related to the SGS statistics of a conserved scalar, namely the mixture fraction Z. A beta–shape parametrized by the mean and variance is usually assumed for the SGS statistics of Z, assumption that appears quite appropriate in LES [2]. Prediction of reacting rates relies then in the correct estimation of the mean and variance of the PDF of the SGS fluctuations of Z, plus the filtered dissipation rate $\overline{\chi}$ that relates mixing and chemical times. The mean value coincides with the local large scale value $\overline{Z}$, and can be directly computed in a LES. Different approaches have been proposed to obtain the SGS variance and dissipation. Among them simple algebraic models are very attractive for their low cost, but they might lead to a poor representation of mixing by the introduction of non–physical relations between variance and dissipation. Adding an evolution equation for the variance plus a model for dissipation to the LES calculation would presumably better reproduce the mixing phenomena.

2 Variance definition and evolution equation

An ambiguity in the SGS variance of a scalar field as defined by a filtering operation exists, with two different expressions:

$$\overline{Z'^2} \neq \overline{Z^2} - \overline{Z}^2$$

appearing in literature.

A statistical quantity such as the variance is only properly defined in relation to a probability density function. It can be shown that while $\overline{Z^2} - \overline{Z}^2$ corresponds

to the variance of the filtered probability density function as defined by Gao and O'Brien [4], $\overline{Z'^2}$ can not correspond to any one point PDF [5].

Once the proper definition established an evolution equation for the variance $\overline{V} = \overline{Z^2} - \overline{Z}^2$ is easily obtained from the equation for Z that reads:

$$\frac{\partial \overline{V}}{\partial t} + \frac{\partial \overline{u_i} \overline{V}}{\partial x_i} = \frac{\partial}{\partial x_i}\left((D + D_T) \frac{\partial \overline{V}}{\partial x_i} \right) \underbrace{-2D \overline{\frac{\partial Z}{\partial x_i} \frac{\partial Z}{\partial x_i}}}_{\text{DISSIPATION } (\overline{\chi})} \underbrace{+2 (D + D_T) \frac{\partial \overline{Z}}{\partial x_i} \frac{\partial \overline{Z}}{\partial x_i}}_{\text{PRODUCTION}} \tag{1}$$

Subgrid scale transport of scalars has been modeled by a gradient diffusion eddy-diffusivity model giving rise to additional diffusion and production terms, while a single open term remains that represents dissipation of variance. The competition between production and dissipation represents the global variance decay by mixing. Independent models for the variance and the dissipation that do not take this into account would thus hardly be able to reproduce the physics of mixing.

3 Models for the scalar dissipation

Inspection of equation 1 shows that modeling the scalar dissipation $\overline{\chi} = \overline{2D \frac{\partial Z}{\partial x_i} \frac{\partial Z}{\partial x_i}}$ as: [3]:

$$\overline{\chi} = 2 (D + D_T) \frac{\partial \overline{Z}}{\partial x_i} \frac{\partial \overline{Z}}{\partial x_i}$$

would imply dissipation and production cancelling out, what would prevent SGS variance decay and complete mixing at the SGS level.

A simple alternative model can be proposed as an extension of the RANS modeling of dissipation in terms of a characteristic mixing time assumed proportional to the turbulent mixing time:

$$\frac{\overline{\chi}}{\overline{Z^2} - \overline{Z}^2} = C \frac{\overline{\epsilon}}{\overline{\kappa}} \tag{2}$$

where C is a parameter to be determined, $\overline{\epsilon}$ is the filtered kinetic energy dissipation rate $= \overline{\nu \frac{\partial u_i}{\partial x_j} \frac{\partial u_i}{\partial x_j}}$ and $\overline{\kappa}$ stands for the SGS kinetic energy $= 1/2 \, (\overline{u_i u_i} - \overline{u_i} \overline{u_i})$. An a priori test of this relation has been conducted by filtering results obtained from DNS of a scalar mixing in homogeneous isotropic turbulencewith box filters $f1$ and $f2$ of sizes equal to 6 and 10 times the DNS grid size resp. Results for the exact dissipation and its model as given by expression 2 are presented in figure 1. A value of $C = 1/Sc = 1/.75$ has been found to best fit the data. Even thought further tests with different Schmidt numbers are needed, for the rest of this work it is assumed that $C = 1/Sc = 1/Sc_T$.

But in a LES, quantities such as the SGS kinetic energy or its dissipation rate are not available. A practical implementation of the proposed model would then

have to use approximations of $\overline{\kappa}$ and $\overline{\epsilon}$ derived from SGS turbulence models. If a Smagorinsky–type eddy–viscosity model is used for the SGS stresses, and the Yoshizawa model is used for the SGS kinetic energy, the actual implementation of the model for $\overline{\chi}$ (assuming $C = 1/Sc_T$) would read:

$$\overline{\chi} = \frac{\left(\nu + C_S \overline{\Delta}^2 \left|\overline{S}\right|\right)}{Sc_T \, C_I \overline{\Delta}^2} \left(\overline{Z^2} - \overline{Z}^2\right), \tag{3}$$

what results a well-conditioned expression, provided that C_I and C_S are not zero.

A priori tests of this model are presented in figure 2, in which exact DNS $\overline{\chi}$ values are compared to those given by eq. 3 with constant C_I and C_S estimated by averaging. Though dynamic determination of parameters C_I and C_S should produce better estimates of $\overline{\kappa}$ and $\overline{\epsilon}$, and $\overline{\chi}$ closer to that presented in figure 1, deviation is small. Dissipation is accurately predicted both locally and on average even when roughly estimated parameters are used. Further confirmation of the adequacy of the model should be provided by LES calculations that complement these a priori tests.

References

[1] A.W. Cook and J. Riley. A subgrid model for equilibrium chemistry in turbulent flows. *Physics of Fluids*, 6:2868–2870, 1994.

[2] J. Jiménez, A. Liñán, M.M. Rogers, and F.J. Higuera. A priori testing of subgrid models for chemically reacting non-premixed turbulent shear flows. *Journal of Fluid Mechanics*, 349:149–171, 1997.

[3] Ch. D. Pierce and P. Moin. A dynamic model for subgrid variance and dissipation rate of a conserved scalar. *Physics of Fluids*, 10(12):3041–3044, 1998.

[4] F. Gao and E.E. O'Brien. A large eddy simulation scheme for turbulent reacting flows. *Physics of Fluids A*, 5:1282–84, 1993.

[5] C. Jiménez. *Modelización de flujos reactivos: El método de la función densidad de probabilidad en simulaciones de grandes escalas.* PhD thesis, Universidad de Zaragoza, 1998.

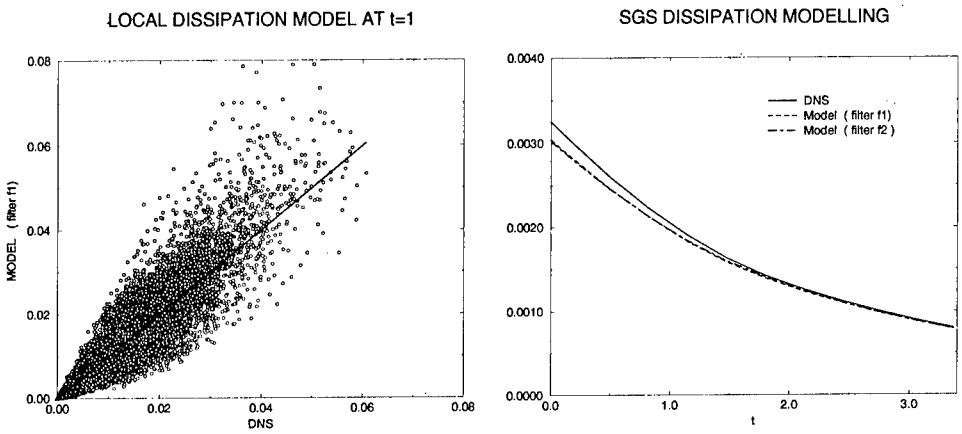


Figure 1: (left) Scatter plot of instantaneous values of $\overline{\chi}$ and its model as in equation 2 for filter f1 at $t = 1$ and (right) time evolution of their averaged values for the two filters f1 and f2. Time is non-dimensionalized by the eddy turn-over time.

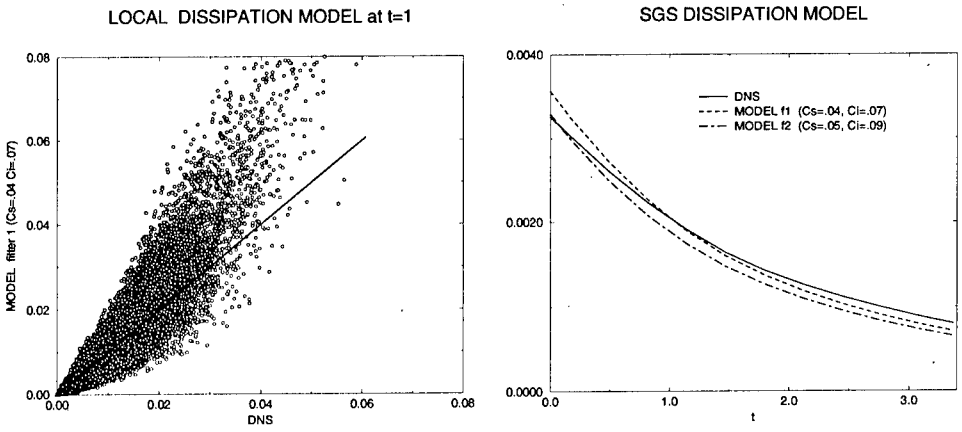


Figure 2: (left) Scatter plot of instantaneous values of $\overline{\chi}$ and its model as in equation 3 with fixed parameters for filter f1 at $t = 1$ and (right) time evolution of their averaged values for f1 and f2. Time is non-dimensionalized by the eddy turn-over time.

ADVANCES IN TURBULENCE VIII
Proceedings of the Eighth European Turbulence Conference
C. Dopazo et al. (Eds.)
© CIMNE, Barcelona 2000

Large Eddy Simulation of a Counterflow Configuration with and without Combustion: Mixing and Flowfield

A. Kempf[1], H. Forkel[2], J.-Y. Chen[3], A. Sadiki[1] and J. Janicka[1]

[1]Fachgebiet Energie- und Kraftwerkstechnik, TU-Darmstadt, Germany
[2] AEA Technology, Otterfing, Germany
[3]Department of Mechanical Engineering, UC-Berkeley, USA

Contact e-mail: akempf@gmx.net

1 Introduction

While the use of Reynolds averaged methods in the calculation of turbulent reacting counter-flows has been the focus of much work [4], the extension of LES to reacting flows in general [1 - 3, 6, 7], and to counter-flows in particular, promises a better description of turbulence and mixing. The aim of this work is to investigate the potential of LES to describe density-variable turbulent counter-flow with the view of advancing the use of LES in understanding complex combustion systems.

In the numerical method, the density is considered to be independent of pressure. The effect of heat release is included by means of a conserved scalar (mixture fraction) combustion model. Equilibrium chemistry is assumed to relate the mixture fraction to density, species concentrations and temperature. The subgrid distribution of the mixture fraction fluctuation is presumed to have the shape of a β function. To represent the sub-grid scale stresses and scalar flux, a Smagorinsky model is used [9]. The Smagorinsky coefficient is determined by the dynamic Germano procedure [3].

2 Configuration and Computational Parameters

The burner configurations studied in this work are those investigated by Mastorakos [5] and Sardi [8], in which two opposed nozzles of diameter D are arranged in line, separated by a distance H (see Figure 1). These nozzles create opposed jets. Their velocities are adjusted to balance momentum, so that the mixing layer is located at half the nozzle distance.

Two straight pipes deliver the fluid. Short upstream of the nozzles, a perforated plate excites reproduceable turbulence.

For the non-reactive case, both nozzles spend plain air. In the experiments, the mixture fraction was determined by measuring the local temperatures (One stream is heated 25 degrees over ambient). For the reactive case, one nozzle spends methane instead of air, generating an axissymmetric plane diffusion flame inbetween the nozzles. In the inert case, the coflow consists of air, for the reactive case, it was switched to Nitrogen.

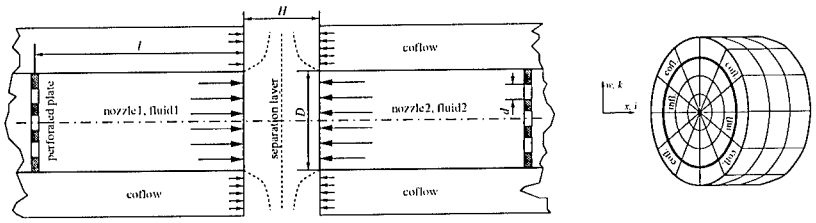


Figure 1: Opposed-Jet configuration and computational domain

In this simulation, the cylindrical domain between the nozzles was investigated. Its height is defined by the nozzle distance, its radius was set to approximately 1.5 times the radius of the pipe, so that part of the Co-flow is simulated as well. This domain is discretized by 104.000 cells (65 axial, 25 radial, 64 tangential).

The nozzles and the Co-flows were described by a Dirichlet condition for both velocity and mixture fraction and a von Neumann condition for pressure.

On the outer ring steady laminar flow is forced, whereas velocities on the inner section fluctuate corresponding to the turbulent flow out of the nozzles.

With this domain the turbulent inflow condition is of special importance for the entire flow-field, because there is no time for turbulence to develop before approaching the area of interest (centerline). Thus, it appeares to be necessary to predict the velocity fields in the wake of the perforated plate and to copy these velocities onto the inflows. The flow out of the plate holes was described by a corresponding velocity profile which was forced onto the inflow of the feeding pipes.

As boundary condition on the cylinder shell, a simple outflow condition was used (Dirichlet-condition for pressure, von Neumann-type condition for velocities and scalars). Negative outflow-velocities are cut-off to ensure stability.

3 Results, Discussions and Conclusions

For the non-reacting case, it was relied on experimental data by K. Sardi [8]. The case considered features a Reynolds-number of 7,500. The numerical solution for the mixture fraction (see Figure 2) proves that good results can be achieved by this approach. The fluctuation peak value seems to be predicted very well,

while the fluctuations out of the middle are slightly overestimated. Although the experimental data presented in Figure 2 is not really sufficient to draw such conclusions, they are confirmed by data-items acquired at an increased Reynolds-number of 10,000 (presented in [8] as well).

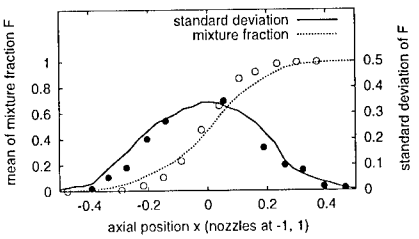


Figure 2: Axial development of Mixture fraction for the *non-reactive* case only

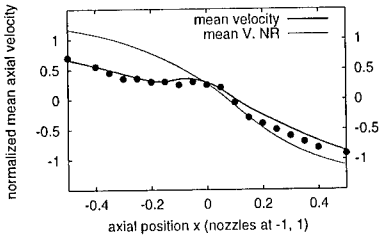


Figure 3: Axial development of the axial velocity for both *reactive* and *non-reactive (NR)* case

For the reactive case, the experimental data presented was taken from Mastorakos work [6]. The case presented here is just slightly over-critical – featuring a pipe Reynolds number of only 2,640 for the air jet. The Reynolds number of the methane jet is almost identical, so that turbulence in both jets is pretty much the same. Focusing on combustion, on turbulence-chemistry interaction in particular, a good overall agreement of the flow and mixing field is a prerequisite. The non-reactive computations (see Figure 2) proved that this can be well achieved.

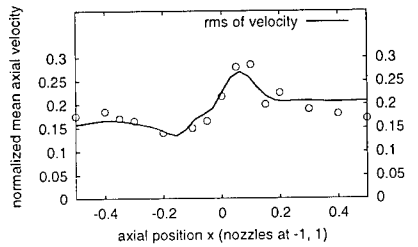


Figure 4: Standard deviation of the axial velocity for the *reactive case*

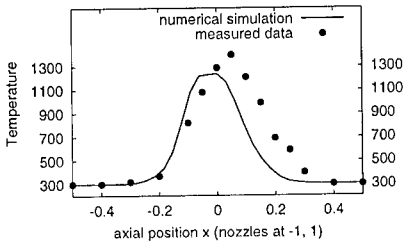


Figure 5: Axial development of the mean temperature (*reactive* case)

Figure 3 shows the axial velocities plotted along the center-line. The x-coordinate of -1 again corresponds to the left nozzle, spending air, +1 to the right one, spending methane. Obviously, the methane must stream faster to balance momentum. Comparing this curve to the numerical results for the non-reactive case (experimental data are not shown), one finds a peak at -0.1. This describes the fluid particles expansion after their ignition. Moreover, this shows how combustion influences the velocity-field. Figure 4 shows the standard deviation of the axial velocities. It is interesting to find a minimum of axial velocities

fluctuation at the location of the axial velocities peak, as determied by experiments. The maximum of fluctuation is reached on the rich side of the mixing layer. This is due to the combustion influence.

Finally, the temperature profile along the domains centerline is presented in Figure 5. Comparing the computational results to experimental data, one finds that width and temperature of the flame are underestimated and its location is computed too far at left. This confirms that the width of the mixing layer is predicted too small for the reactive case - giving a hint on insufficient turbulent mixing. Certainly, the simple chemistry model applied for this case is not capable to fully describe non-equilibrium phenomena linked to the combustion of methane. However, it could be shown that the combustion strongly influences turbulence and mixing.

Finally, it shall be stressed that the entire turbulent flow fields were computed by LES. No experimental data was used to describe the boundary conditions.

References

[1] A.W. Cook, J.J. Riley, *Subgrid-Scale Modeling for Turbulent Reacting Flows*, Combustion and Flame 112, pp. 593-606 (1998)

[2] H. Forkel, J. Janicka, *Large-Eddy Simulation of a turbulent Hydrogen Diffusion Flame*, 1st Symposium on Turbulent Shear Flow Phenomena (1999)

[3] M. Germano, U. Piomelli, P. Moin and W.H. Cabot, *A dynamic subgrid-scale eddy viscosity model*, Phys. Fluids A, 3, pp. 1760-1765 (1991)

[4] W.P. Jones, Y. Prasetyo, *Probability Density Function Modeling of Premixed Turbulent Opposed Jet Flames*, Twenty-Sixth Symposium (International) on Combustion, pp. 275-282 (1996)

[5] E. Mastorakos, A. Taylor, J. Whitelaw, *Mixing in Turbulent Opposed Jet Flows*, Ninth Symposium on Turbulent Shear Flows (1993)

[6] E. Mastorakos, *Turbulent Combustion in Opposed Jet Flows*, Ph. D. Thesis, Imperial College of Science, Technology and Medicine (1999)

[7] S.I. Möller, E. Lundgren, C. Fureby, *Large Eddy Simulation of Unsteady Combustion*, 26th Symposium (International) on Combustion, pp. 241-248 (1996)

[8] K. Sardi, A. Taylor, J. Whitelaw, *Conditional scalar dissipation statistics in a turbulent counterflow*, Journal of Fluid Mechanics, vol. 361, pp. 1-24 (1998)

[9] J.S. Smagorinsky, *General circulation experiments with the primitive equations, 1. The basic experiment*, Monthly Weather Rev.l, 91, pp. 99-164 (1963)

ADVANCES IN TURBULENCE VIII
Proceedings of the Eighth European Turbulence Conference
C. Dopazo et al. (Eds.)
© CIMNE, Barcelona 2000

Large eddy simulation of a turbulent premixed V-shaped flame

M. Boger and D. Veynante

Laboratoire E.M2.C.
C.N.R.S. and Ecole Centrale Paris
Grande Voie des Vignes, 92295 Châtenay-Malabry Cedex, France

Contact e-mail: denis@em2c.ecp.fr

1 Introduction

Large Eddy Simulation (LES) where large scale motions are resolved, appears as a very promising tool for numerical simulations in turbulent combustion because most reacting flow fields exhibit large scale coherent structures. A better description of turbulence / combustion interactions is also expected because, at any time, fresh and burnt gases regions, where turbulence may be different, are clearly identified at the resolved scale level.

The chemical reaction is described using a progress variable c ($c = 0$ in fresh gases and $c = 1$ in fully burnt ones), assuming unity Lewis number and adiabatic combustion. Applying a LES filter to the c balance equation leads to:

$$\frac{\partial \overline{\rho}\widetilde{c}}{\partial t} + \nabla \cdot (\overline{\rho}\widetilde{\mathbf{u}c}) + \nabla \cdot \overline{\rho}(\widetilde{\mathbf{u}c} - \widetilde{\mathbf{u}}\widetilde{c}) = \nabla \cdot (\overline{\rho} D \nabla \widetilde{c}) + \overline{\dot{\omega}}_c = \overline{\rho w |\nabla c|} \qquad (1)$$

where $\overline{Q}$ denotes filtered quantities and $\overline{\rho}\widetilde{Q} = \overline{\rho Q}$. D is the molecular diffusivity, $\dot{\omega}_c$ the instantaneous reaction rate and w is the propagation speed of the flame front relatively to the flow. Terms in Eq. 1 correspond respectively to unsteady effects, convection by the resolved flow field, convection due to unresolved flow motions, filtered molecular fluxes, filtered reaction rate and flame front displacement. These last four terms are unclosed and require modeling. The filtered progress variable $\widetilde{c}$ is numerically resolved using a gaussian filter larger than the computational mesh size [1].

2 Modeling

The flame front displacement may be modeled introducing the subgrid scale flame surface density Σ (i.e. the subgrid scale flame surface per unit volume):

$$\overline{\rho w |\nabla c|} = \langle \rho w \rangle_s \Sigma = \langle \rho w \rangle_s \Xi \, |\nabla \overline{c}| \qquad (2)$$

where Ξ denotes the subgrid-scale flame front wrinkling factor (i.e. the subgrid scale flame surface, divided by its projection in the resolved propagating direction). The flame displacement speed averaged along the subgrid scale flame surface, $\langle \rho w \rangle_s$ is modeled as $\langle \rho w \rangle_s = \rho_u S_L$, where ρ_u is the fresh gases density and S_L the laminar flame speed. Balance equations may be derived for Σ or Ξ but an algebraic expression is retained here [1, 2]:

$$\Sigma = 4\sqrt{\frac{6}{\pi}}\Xi\frac{\overline{c}\,(1-\overline{c})}{\Delta} \tag{3}$$

where Δ is the LES filter size. This expression is similar to the Bray-Moss-Libby expression used in RANS [3].

The unresolved scalar flux, $\overline{\rho}(\widetilde{\mathbf{u}c} - \widetilde{\mathbf{u}}\widetilde{c})$ is, unfortunatelly, non-zero for a laminar flame because of thermal expansion. For a one-dimensional steady propagating laminar flame, $\overline{\rho}(\widetilde{\mathbf{u}c} - \widetilde{\mathbf{u}}\widetilde{c}) = \rho_u S_L(\overline{c} - \widetilde{c})$ is counter-gradient and cannot be neglected. In a first step, this laminar contribution is combined with the modeled filtered reaction rate and the final equation is written [2]:

$$\frac{\partial \overline{\rho}\widetilde{c}}{\partial t} + \nabla \cdot (\overline{\rho}\widetilde{\mathbf{u}}\widetilde{c}) = \nabla \cdot \left[\left(\rho_u \frac{S_L \Delta}{16\sqrt{6/\pi}} + \frac{\mu_t}{\sigma_t}\right)\nabla \widetilde{c}\right] + 4\rho_u S_L \Xi \sqrt{\frac{6}{\pi}}\,\frac{\widetilde{c}\,(1-\widetilde{c})}{\Delta} \tag{4}$$

where μ_t is the turbulent viscosity, provided by the subgrid scale turbulence filtered Smagorinsky model, and σ_t a turbulent Schmidt number. The diffusion term, derived from a KPP analysis (see [4]) has been added in Eq. 4 to ensure a correct laminar flame propagation when turbulence vanishes and to control the resolved flame thickness [2]. Ξ could be estimated as in the G-equation context [5] from the subgrid turbulence rms velocity, u'_Δ, but, both in DNS [1] and experiments [2], the wrinkling factor has been found to remain quite low ($1 \leq \Xi \leq 1.5$, when a planar laminar flame corresponds to $\Xi = 1$) and is assumed to be constant in a first step.

3 Numerical simulations

Simulations have been performed using a fully compressible code, AVBP, based on a cell vertex finite volume scheme resolving the Navier Stokes equations [6]. The numerical configuration corresponds to a V-shaped premixed turbulent flame stabilized behing a triangular flame holder (50 % blockage ratio, inlet velocity $U_{in} = 5.75$ m/s, equivalence ratio $\phi = 0.65$) [7].

Figure 3 displays an instantaneous snapshot of the filtered progress variable $\widetilde{c}$. Averaging along time allow to recover the mean progress variable field that should be predicted by RANS simulations (Fig. 3).

Turbulent progress variable fluxes, requiring models in RANS simulations are due to the scalar transport by LES resolved motions (but unresolved in RANS) and to the unresolved LES scalar transport. The first contribution, extracted

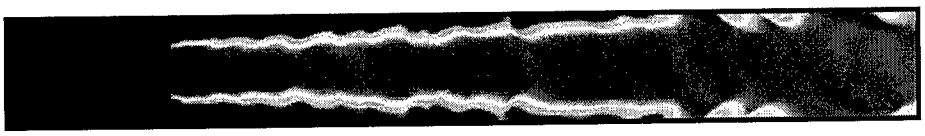


Figure 1: Instantaneous field of the reaction progress variable $\widetilde{c}$.



Figure 2: Time averaged progress variable field.

from LES, is displayed on Fig. 3. Gradient scalar transport, found close to the flame-holder, is progressively remplaced by counter-gradient features when moving downstream, as already described in [8]. This finding shows that, despite of simple subgrid scale models, LES is able to predict counter-gradient transport due to the dynamic of resolved large structures, evidencing a better turbulent combustion description than in RANS. Such a prediction would require a fully second-order turbulence fluxes modeling in RANS.

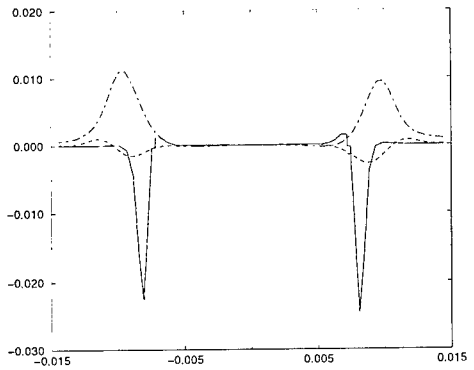


Figure 3: Transverse resolved turbulent flux profiles ($kg/m^2/s$) for various downstream locations: 2 cm (——), 6 cm (- - - -) and 10 cm (—·—) behind the flame holder. $\overline{\rho}\widetilde{u''c''} > 0$ indicates counter-gradient transport.

4 Conclusion

An algebraic flame surface density subgrid scale model is tested for large eddy simulations of a turbulent premixed flame stabilized behind a flame holder. Very promising results are achieved and show that counter-gradient transport, at least at the resolved scale level, is easily recover in LES, even using quite simple subgrid scale models. Such a prediction would be very difficult in RANS simulations, requiring a second order modeling for turbulent fluxes.

Numerical simulation have been performed at IDRIS (Institut du Développement et des Ressources en Informatique Scientifique), Orsay, France. The authors gracefully aknowledge the support of CERFACS (Toulouse, France), and especially T. Schönfeld, A. Angelberger and O. Colin, in the use of the AVBP code.

References

[1] M. Boger, D. Veynante, H. Boughanem, and A. Trouvé. Direct numerical simulation analysis of flame surface density concept for large eddy simulation of turbulent premixed combustion. In *Twenty-seventh Symposium (International) on Combustion*, pp. 917 – 925. The Combustion Institute, 1998.

[2] M. Boger. *Modélisation de sous-maille pour la simulation aux grandes échelles de la combustion turbulente prémélangée.* PhD thesis, Ecole Centrale Paris (France), 2000.

[3] K.N.C. Bray, M. Champion, and P.A. Libby. The interaction between turbulence and chemistry in premixed turbulent flames. In *Turbulent Reacting Flows*, vol. 40 of *Lecture Notes in Engineering*, pp. 541 – 563. Springer, 1989.

[4] J.M. Duclos, D. Veynante, and T. Poinsot. A comparison of flamelet models for premixed turbulent combustion. *Combust. Flame*, 95(1/2):101–118, 1993.

[5] H.G. Im, T.S. Lund, and J.H. Ferziger. Large eddy simulation of turbulent front propagation with dynamic subgrid models. *Phys. Fluids A*, 9(12):3826 – 3833, 1997.

[6] F. Ducros, F. Nicoud, and T. Schönfeld. Large eddy simulations of compressible flows on hybrid meshes. In *Eleventh Symposium on Turbulent Shear Flows*, Grenoble, France, 1997.

[7] S. Duplantier. *Etude expérimentale d'un sillage confiné se développant en aval d'un corps d'arrêt : influence de la combustion sur la structure du sillage.* PhD thesis, Université de Poitiers (France), 1995.

[8] D. Veynante, J. Piana, J.M. Duclos, and C. Martel. Experimental analysis of flame surface density model for premixed turbulent combustion. In *Twenty-sixth Symposium (International) on Combustion*, pp. 413 – 420. The Combustion Institute, 1996.

XV

Boundary Layers and Free Shear Flows

ADVANCES IN TURBULENCE VIII
Proceedings of the Eighth European Turbulence Conference
C. Dopazo et al. (Eds.)
© CIMNE, Barcelona 2000

The surface region of rough-wall boundary layers

Alison Ploss[1], Ian Castro[2] and Hong Cheng[1]

[1]EnFlo, School of Mechanical & Materials Engineering
University of Surrey, Guildford, Surrey, GU2 5XH, UNITED KINGDOM
[2]School of Engineering Sciences, University of Southampton
Highfield, Southampton, SO17 1BJ, UNITED KINGDOM

Contact e-mail: i.castro@soton.ac.uk

1 Introduction

Rough wall boundary layers have been studied in both the engineering and the atmospheric contexts for decades. In the 'inertial sub-layer' (IS), as the log-law region is sometimes called, the flow is spatially homogeneous in planes parallel to the surface, just as it is in a smooth wall boundary layer. However, there is always a region below IS in which the mean flow is horizontally inhomogeneous, with the scale and vertical extent of the inhomogeneities being dependent on the geometry of the rough surface. Much of the classical work on rough wall boundary layers in the engineering context was done using sand-grain roughness, for which the depth, d_i say, of the inhomogeneous region (the 'roughness sub-layer', RS, Raupach et al, 1991) is very small compared to the boundary layer depth and thus the RS can often be ignored.

In the atmospheric boundary layer, however, the roughness elements (height h) are frequently not very closely spaced and, furthermore, they may be quite large, covering a significant fraction of the boundary layer depth. (In extreme cases an inertial region may not exist at all). The RS may be 2-5h in depth (e.g. Rotach, 1993) and meteorological measurements are often taken in that region. There are fundamental questions about the nature of the turbulent flow in the roughness sub-layer and, indeed, above it. For example, are the turbulence statistics in the log-law region really independent of the flow in the roughness sub-layer and how do the turbulent eddies generated by the roughness elements themselves interact with (or determine) the typical eddy structures in the log-law region and above?

For roughness of very large scale (hills and mountains) it is known that although the usual log-law does not always exist, vertical mean velocity profiles may be logarithmic if, at each height, the velocity is obtained via an area average (Wood & Mason, 1993). In those circumstances, the shear velocity, u^*, deduced

from such profiles precisely reflects the total surface drag. It seems at least possible, but has never been demonstrated, that area-averaged velocity profiles in the roughness sub-layer over a flat surface covered with three-dimensional arrays of roughness elements (i.e. an urban-type surface) might also be logarithmic, blending continuously with the genuine inertial region above. The degree to which area averages of the turbulence stresses in the roughness sub-layer may be useful is unknown but it seems likely that to understand the generation and development of the surface layer eddy structures (and thus processes like pollutant dispersion from within urban canopies) consideration of local (unaveraged) turbulence energy balances will be necessary (as in the case of plant canopies, Kaimal & Finnigan, 1994).

We report results of the initial stages of a more detailed experimental study of roughness sub-layers than has previously been attempted in the laboratory.

2 Experimental Arrangements

A boundary layer was grown over 20mm hardwood cubes arranged in a staggered array (see figure 1) on the floor of the A-tunnel in the EnFlo laboratory, University of Surrey. The working section has a cross-section of 0.9 x 0.6m and most measurements were obtained some 3m downstream of the start of the roughness, which was mounted on a 6mm baseboard with a fared leading edge. Note that the flow was naturally grown so there was no confusion about the residual influence of artificial turbulence generators on details of the boundary layer structure. At the measurement location the boundary layer depth was about 160mm. Laser-doppler anemometry and 120^o included angle crossed hot wire anemometry (with high turbulence corrections) were used in order to minimise the measurement errors as far as possible.

All the anemometry was driven on-line from a Macintosh computer running comprehensive calibration and measurement routines developed in-house using the programming package LabVIEW. If hot wire data (mean velocities) differed between the beginning and end of an individual profile by more than about 1%

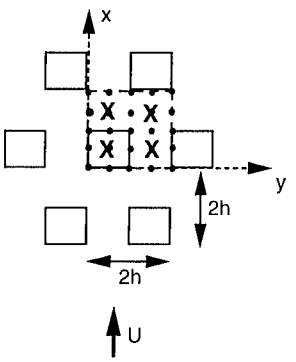


Figure 1: Geometric arrangement of the roughness array. 20mm cubes on a grid of 40mm side. Dots denote locations of the 25 vertical traverses; crosses are the locations of the four 'sample' positions.

they were rejected. Measurements of the surface's form drag were also made by fitting a special brass cube (roughness element) with numerous 0.6mm pressure taps located at appropriate positions on the front and rear faces and using a scanivalve system to obtain mean pressure data and thus the drag by integration.

3 Results

Profiles of mean velocity and Reynolds stresses through the entire boundary layer had the expected shapes and in the interests of space are not shown here. We concentrate on the region $h < z < 2.5h$, which encompassed a log-law region ($1.7h < z < 2.5h$) and a roughness sub-layer below it. Examples of the longitudinal normal stress and the shear stress are shown in figure 2, obtained at the four sampling locations shown in figure 1. The plots emphasise that spatial homogeneity is established by about z=35mm ($1.7h$), so that in this case d_i=$1.7h$, measuring d_i from z=0 - the 'ground'. Below this height the stress profiles are strongly dependent on location - just as they would be in the (unmeasured) region below the element height (i.e. $z < h = 20$mm). The mean flow profiles at these locations cannot be sensibly fitted to a log-law even using plausible values of u^* and displacement height d (see below).

To test the hypothesis that area-averaged mean flow profiles could be so fitted, and recognising the degree of variability in the mean flow within the sub-layer, a comprehensive set of vertical profiles were obtained at the 25 locations on a square mesh of grid size $h/2$ covering a single roughness array unit of side $2h$ (see figure 1). For each quantity (mean velocity and all Reynolds stresses)

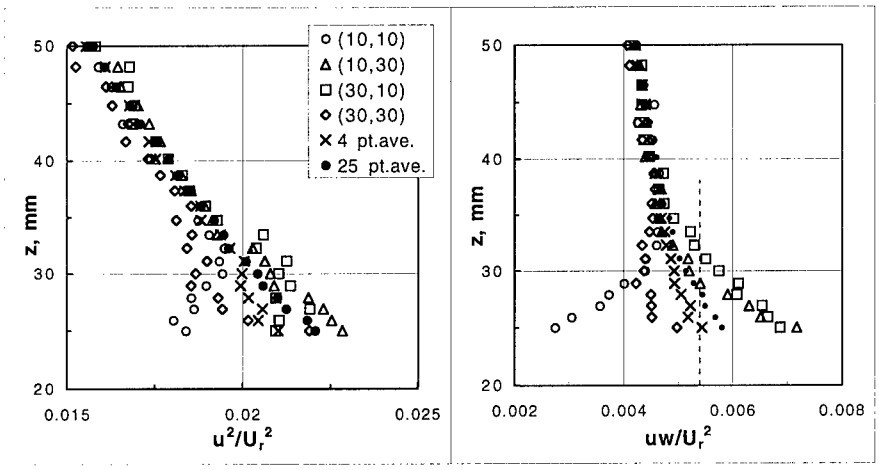


Figure 2: Reynolds stress profiles at the four sample points. Average profiles from these and from all 25 profiles are also shown. The dotted line is the wall stress deduced from the pressure drag.

the 25 values obtained at each height were then averaged. Figure 2 includes the resulting area-averaged profiles and also includes the profiles deduced by averaging just the four individual profiles shown. These two averaging methods lead to broadly similar profiles although the differences are not always insignificant.

On the assumption that the viscous contribution to the surface drag will be negligible for this surface, the profile drag data obtained from the pressure-tapped element can be used to deduce u^*. The result is included in the shear stress plot of figure 2 and it is clear that this value is significantly higher than it would be if it were deduced from the shear stress data in the inertial sub-layer ($35 < z < 50mm$). On the other hand, it is close to the value that would be deduced by vertically averaging the (averaged) shear stress profiles within the roughness sub-layer. An excellent fit to the averaged mean velocity profile was obtained up to z=50mm using the u^* deduced from the pressure data; a best-fit procedure gave d=18.5mm and a z_o of 1.22mm. Fits using alternative u^* values, like that deduced from the shear stress data in the homogeneous inertial region, are noticeably worse and imply a negative viscous contribution to the total surface drag. This seems unlikely, although it is not impossible *a priori*.

The averaged stress profiles indicate large variations in the turbulence statistics and in structure functions like $\overline{uw}/u'w'$ through the roughness sub-layer. This is of course in distinct contrast to the turbulence in the inertial sub-layer and implies that, for example, standard similarity relationships will not be sufficient for characterisation of the flow and dispersion characteristics near the surface.

4 Conclusions

The results confirm that relatively isolated measurements in urban roughness sub-layers are not adequate for proper characterisation of the surface fluxes nor even for the determination of the mean properties (u^*, d and z_o) describing the surface drag. Issues like those mentioned earlier are the subject of ongoing work. We thank the Natural Environment Research Council for their support.

References

[1] KAIMAL JC and FINNIGAN GC *Atmospheric Boundary Layer Flows*, OUP (Oxford) 1994.

[2] ROTACH MW (1993) Turbulence close to a rough urban surface. Part I: Reynolds Stress. Bound. Layer Met. 65, 1-28.

[3] RAUPACH MR, ANTONIA RA & RAJAGOPALAN S (1991) Rough wall boundary layers. Appl. Mech. Rev., 44, 1-25.

[4] WOOD N & MASON P (1993) The pressure force induced by neutral, turbulent flow over hills. Q.J.Roy.Met.Soc., 119, 1233-1267.

ADVANCES IN TURBULENCE VIII
Proceedings of the Eighth European Turbulence Conference
C. Dopazo et al. (Eds.)
© CIMNE, Barcelona 2000

Space-Time Characteristics of the Wall Shear-Stress Fluctuations in a Turbulent Boundary Layer with Transverse Curvature

Dongshin Shin[1] and Haecheon Choi[2]

[1]Department of Mechanical Engineering
Hong-Ik University, Seoul 121-791, Korea
[2]School of Mechanical and Aerospace Engineering
Seoul National University, Seoul 151-742, Korea

Contact e-mail: dsshin@wow.hongik.ac.kr

1 Introduction

The behavior of fluctuations of the wall flow variables in a turbulent boundary layer with transverse curvature is of fundamental importance in many practical applications involving flow-induced noise, drag and heat transfer. In flow-induced noise research, it is very important to know the space-time characteristics of the wall pressure and shear-stress fluctuations because they are closely related to the generation of dipole noise([1]). The instantaneous wall pressure and shear stresses are signatures of the phenomena occurring above the wall, and thus there have been many studies of the behavior of the wall flow variables for a flat turbulent boundary layer([2]) as well as an axial turbulent boundary layer([3]). Most of them, however, have focused on the wall pressure fluctuations in turbulent boundary layers, and relatively few detailed measurements of the wall shear-stress fluctuations have been made. In general, the complete wall shear-stress spectral data needed for the above mentioned research efforts are still lacking.

The main objective of this work is to compute the complete (three-dimensional) wall shear-stress spectra, as a function of streamwise and spanwise wavenumbers and frequency, using data from direct numerical simulation of turbulent boundary layer with transverse curvature.

For the direct numerical simulation, a computational mesh of $64 \times 93 \times 192$ grid points is used in the circumferential (x_1), wall-normal (x_2), and streamwise (x_3) directions, respectively. The computational box has dimensions of $2\pi\delta \times \delta \times 4\pi\delta$ in the circumferential, wall-normal, and streamwise directions, respectively,

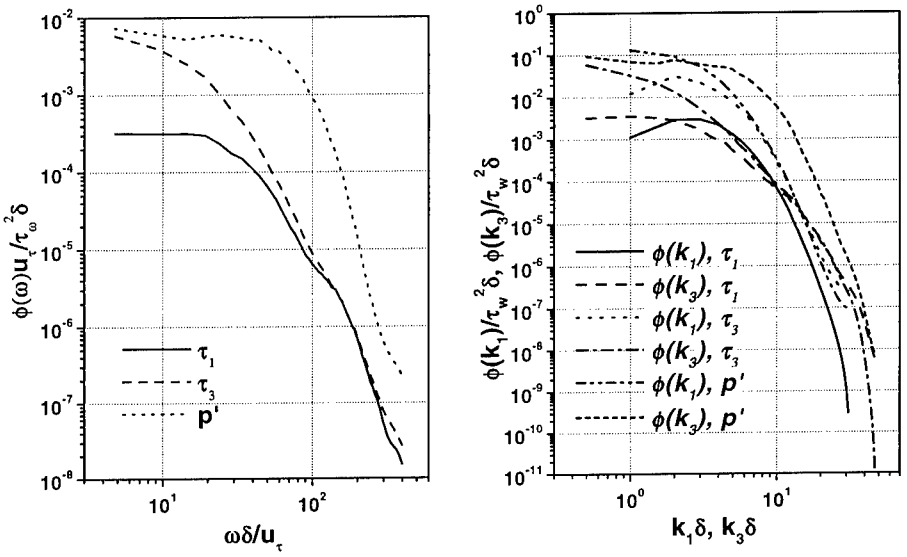


Figure 1: Spectra of the wall shear-stress and pressure fluctuations: frequency (left); streamwise and transverse wavenumbers (right).

where δ is the boundary layer thickness. The Reynolds number based on the free-stream velocity and boundary layer thickness is 3,400, and the ratio of the boundary layer thickness to the radius of curvature is 5.

2 Power spectrum

The power spectrum as a function of the frequency is calculated using a similar method as in Jeon et al.([4]). The fully developed velocity fields in a turbulent boundary layer with transverse curvature is used as an initial condition, and the Navier-Stokes equations are integrated forward in time and the shear stresses and pressure at the wall are stored every time step. The total record of $N = 1,344$ time samples is divided into 12 overlapping segments (with 50 % overlap), each containing 384 points. The shear-stress fluctuations at the wall as well as wall pressure fluctuations are Fourier transformed in space and time and the power spectral densities are computed. One- and two-dimensional power spectra are obtained by integrating the power spectral density over the remaining one or two variables. Auto-correlation functions are obtained by the inverse Fourier transformation.

Figure 1 shows the one-dimensional power spectra of the wall shear-stress

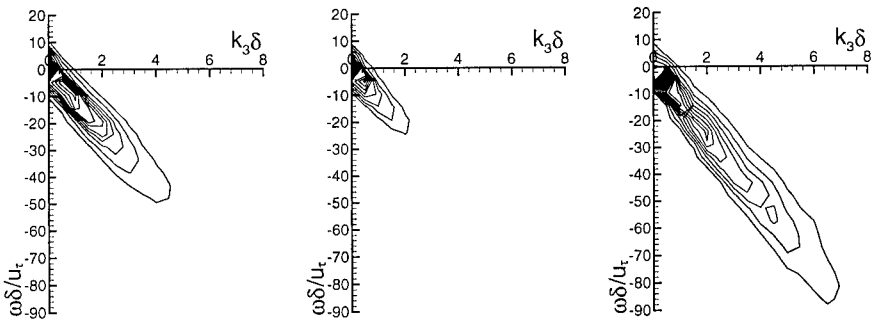


Figure 2: Contours of $\Phi(k_3, \omega)$: τ_1 (left); τ_3 (center); p_w (right). Contour levels are distributed from 10^{-9} to 10^{-6}.

and pressure fluctuations. The one-dimensional frequency power spectrum of the transverse wall shear stress (τ_1) is nearly constant at low frequencies, while that of the streamwise wall shear stress (τ_3) decreases as the frequency increases. The streamwise-wavenumber (k_3) power spectrum has similar characteristics as the frequency power spectrum. The similarity between the streamwise-wavenumber and frequency power spectra is due to the convective nature of the wall shear-stress fluctuations. On the other hand, the spanwise-wavenumber (k_1) power spectrum is very different from other power spectra in that it increases as the wavenumber increases at low wavenumbers. It is shown in Figure 1 that $\phi(k_3) > \phi(k_1)$ at low wavenumbers but $\phi(k_1) > \phi(k_3)$ at relatively high wavenumbers, indicating that large-scale fluctuations are more energetic in the streamwise direction, while small-scale fluctuations are more energetic in the transverse direction.

Figure 2 shows the frequency/streamwise wavenumber spectra $\Phi(k_3, \omega)$ of the wall flow variables. The contours are thin band-shaped and show strong convective nature of the wall variables. The contribution of large-scale fluctuations to the rms value is largest for streamwise wall shear stress, while that of small-scale fluctuations to the rms value is largest for wall pressure.

Figure 3 shows the two-point auto-correlations of the wall flow variables as functions of the streamwise and spanwise separations. It clearly shows that the spatial distributions of the wall shear-stress fluctuations are very different from that of the wall pressure fluctuations. Negative streamwise correlation occurs for wall pressure and transverse wall shear stress, but negative spanwise correlation occurs for both wall shear stresses. The instantaneous flow patterns and contour plots of correlations in space have the same characteristics. The contours of the two-point correlations of the wall flow variables in the streamwise direction and time are shaped in narrow bands and show the strong convective property of the wall flow variables.

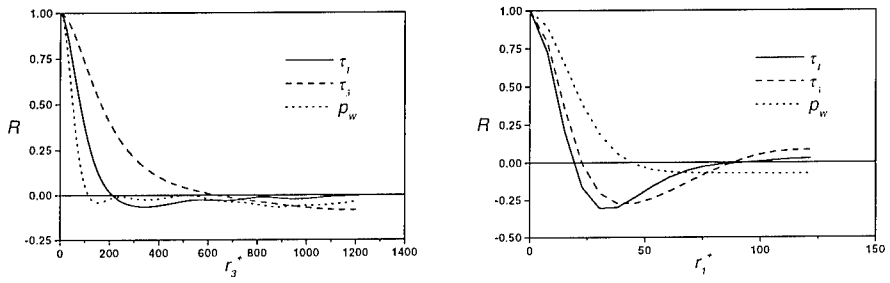


Figure 3: Two-point auto-correlations as functions of the streamwise and spanwise separation distances : r_3^+ (left); r_1^+ (right).

3 Conclusions

- At low wave numbers and frequencies, the power of τ_3 is lager than that of τ_1, while the powers of τ_3 and τ_1 are almost the same at high wavenumbers and frequencies.
- The frequency/streamwise wavenumber spectra $\Phi(k_3, \omega)$ of the wall flow variables show that large-scale fluctuations to the rms value is largest for τ_3, while that of small-scale fluctuations to the rms value is largest for p_w.
- In the two-point auto-correlations, negative correlation occurs in streamwise separations for p_w and τ_1, and in spanwise correlation for τ_1 and τ_3.

Supports from the Underwater Acoustics Research Center and the Creative Research Initiatives of the Korean Ministry of Science and Technology are gratefully acknowledged.

References

[1] W. K. Blake. *Mechanics of Flow-Induced Sound and Vibration.* Academic, London, 1986.

[2] H. Choi and P. Moin. On the space-time characteristics of wall pressure fluctuations. *Physics of Fluids A*, 2:1450–1460, 1990.

[3] J. C. Neves and P. Moin. Effects of convex transverse curvature on wall-bounded turbulence. Part 2: The pressure fluctuations. *J. Fluid Mech.*, 272:383–406, 1994.

[4] S. Jeon, H. Choi, J. Y. Yoo and P. Moin. Space-time characteristics of the wall shear-stress fluctuations in a low-Reynolds-number channel flow. *Physics of Fluids*, 11:3084-3094, 1999.

ADVANCES IN TURBULENCE VIII
Proceedings of the Eighth European Turbulence Conference
C. Dopazo et al. (Eds.)
© CIMNE, Barcelona 2000

The Influence Of Wall-Porosity Upon The Near-Wall Turbulence Dynamics

M. Uhlmann, A. Pinelli, J. Jiménez and G. Kawahara

School of Aeronautics, Universidad Politécnica de Madrid, Plaza Cardenal Cisneros 3, 28040 Madrid, Spain

Contact e-mail: uhlmann@pik-potsdam.de

1 Introduction

We investigate low-Reynolds number turbulent flow in a plane channel with one impermeable and one porous wall. Both walls satisfy the no-slip condition, but the wall-normal velocity v at the porous surface (for which $y=0$) is proportional (and of the opposite sign) to the pressure fluctuations p' with respect to the local mean at a given streamwise location, viz.

$$v(y=0) = -\beta\, p'(y=0), \text{ where } \quad p'(x,y,z) = p(x,y,z) - \overline{p}(x) \quad . \qquad (1)$$

The wall transpiration is therefore mass-less, i.e. its integral over the wall plane vanishes. This configuration is a model for a passive control device to delay boundary layer separation under adverse pressure gradients. What is required in that case is an *increase* of the local friction coefficient, which eventually results in a lower form factor, and in a more resilient boundary layer. Our purpose here is to clarify the mechanism by which the porosity of the boundary affects the near-wall turbulence statistics.

We have performed a series of direct numerical simulations at a nominal Reynolds number of 190 (based on the channel half-width h and on the friction velocity u_τ of the fully impermeable case), in boxes of size of $8.17h$ and $3.14h$ in streamwise (x) and spanwise (z) directions, respectively, and using a Fourier/-fourth-order B-spline method [1]. The spacing of the collocation points after dealiasing was less than 10×5 wall units in the homogeneous directions; the grid size ranges between $0.4 - 4$ in the wall-normal direction. Several porosity levels β were analyzed, all belonging to a regime where no noteworthy local flow reversal is observed.

2 Results

The results show a 40% increase of skin friction for an *rms* transpiration intensity of $0.17u_\tau$, a substantial increase in overall turbulence intensities, and a decrease

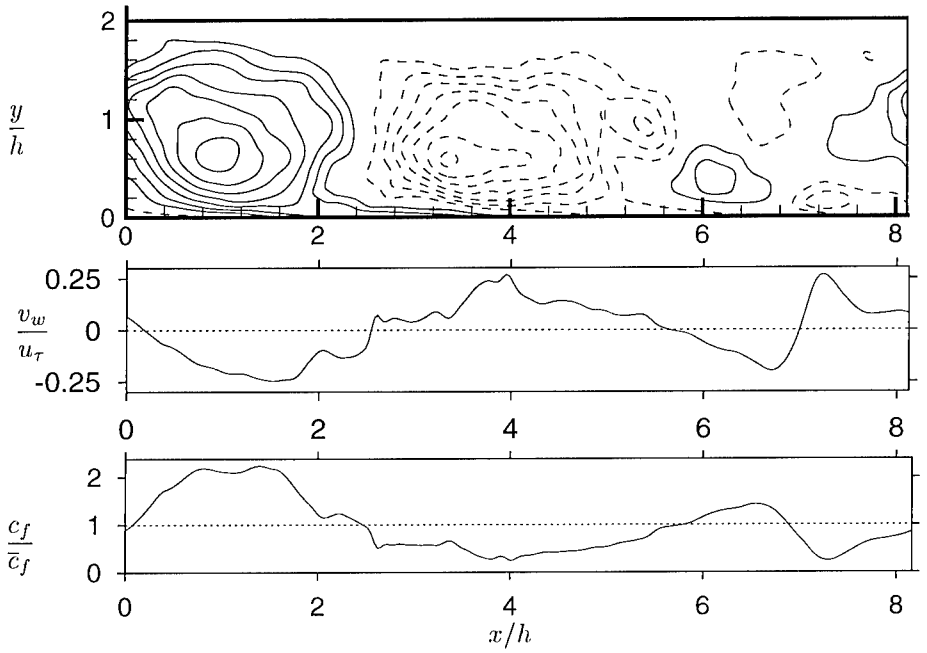


Figure 1: (Top) Instantaneous streamlines of the spanwise-averaged velocity fluctuations, (centre) spanwise-averaged wall-transpiration v_w and (bottom) spanwise-averaged skin friction c_f on the porous, lower wall of the simulated channel flow.

of the shape factor of the mean profile (cf. earlier experimental results in [2]).

Two-point autocorrelations of the velocity components reveal the presence of strong spanwise-coherent structures at large (wall-normal and streamwise) scales, of size $O(h)$. Instantaneous visualizations (figure 1) confirm that this coherent motion is formed by alternating 'roller' vortices which lag slightly with respect to the wall transpiration v_w, and which penetrate far into the core flow. Spatio-temporal correlations show that their streamwise phase velocity is of the order of $12.5\,u_\tau$ which in turn is comparable to the advection speed of the buffer layer structures [3]. The intensity of the rolls is $O(u_\tau)$ and, as a consequence, the buffer zone and the sublayer are alternately accelerated and decelerated, being periodically energized and almost laminarized along spanwise-coherent strips; the instantaneous spanwise-averaged skin friction shows a corresponding cyclic variation along the streamwise direction (figure 1). Locally, skin friction and transpiration exhibit a clear correlation which is shown in figure 2 by means of the histogram of their joint probability density. From the regression of the data it can be deduced that at points of fluid injection ($v_w > 0$) skin friction decreases by an amount that is smaller than the increase at points of equally strong suction. The non-linearity of this correlation leads to the observed increase in

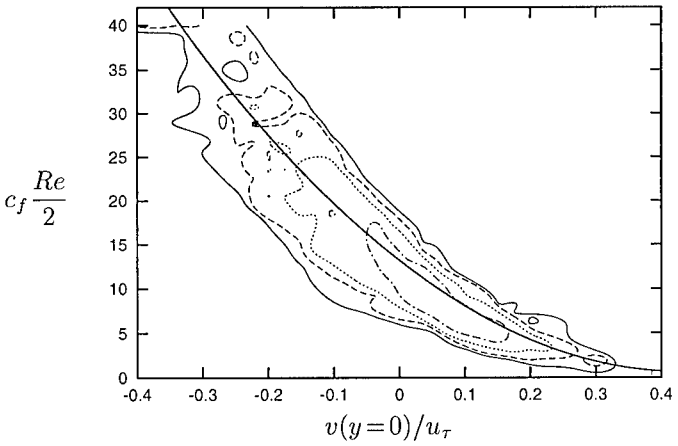


Figure 2: Histogram of the joint probability density function of the spanwise-averaged skin friction c_f and spanwise-averaged wall-transpiration $v(y=0)$. The isolines are: ——— , 10^0; - - - - , $10^{0.5}$; ····· , 10^1; —·— , $10^{1.5}$. The thick solid line is a quadratic regression obtained by a least-squares fit of the data.

overall drag. This situation is consistent with results from cases with spatially uniform suction/blowing (cf. [4] and references therein) and can be shown to hold qualitatively in the laminar regime.

The linear analysis of the mean velocity profile (taking into account 'background turbulence' through an eddy viscosity ansatz) shows that the flow near a porous wall is unstable with respect to two-dimensional eigenfunctions, whose qualitative shape and phase velocity are close to those of the fully non-linear perturbations; the basic mechanism is inviscid and similar to the instability of a plane wake, and is also present in simpler profiles, such as in a confined layer of constant shear near the wall.

We have performed further experiments in which spanwise-coherent wall transpiration, and the resulting rolls, were externally imposed (*active* control) using a simple streamwise sinusoidal distribution. They lead to quantitatively comparable increments in drag (figure 3). Note that, because the large-scale motion is the result of an intrinsic flow instability, active control requires only a net *negative* energy expenditure.

3 Conclusions

The mechanism of turbulence enhancement and drag increase at porous boundaries, with applications to separation control, was shown to be due to large-scale

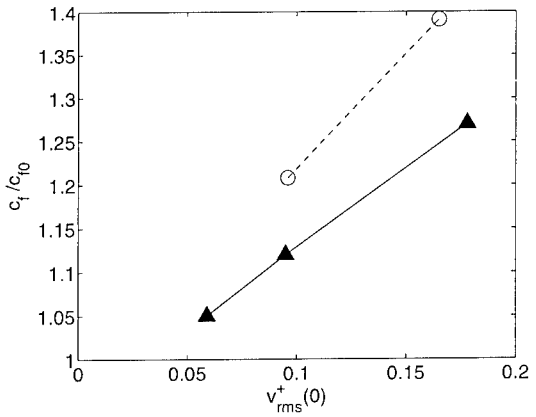


Figure 3: Increase in wall friction as a function of the r.m.s. transpiration velocity at the wall. ○ , porous wall; ▲ , sinusoidally forced ones.

spanwise-coherent structures possibly arising from an inviscid, two-dimensional instability of the mean profile. Alternatively, active generation of spanwise-coherent, streamwise-sinusoidal, mass-less transpiration can yield a similar effect. In the present strategy there is no need for fine-grained localized flow sensors. Accompanying laboratory experiments are currently being undertaken at LML, Ecole Centrale de Lille, France.

This work was supported in part by the Brite/AeroMems consortium, and by the Spanish CICYT under contract PB95-0159. G.K. received additional support from the Japanese Ministry of Education, Science and Culture.

References

[1] J. Jiménez, A. Pinelli, and M. Uhlmann. Plane channel flow simulation over porous walls. Technical Note ETSIA MF-9809, School of Aeronautics, Universidad Politécnica Madrid, Spain, 1998.

[2] F.S. Collier and J.A. Schetz. Injection into a turbulent boundary layer through porous surfaces with different surface geometries. AIAA paper no. 83-0295, 1983.

[3] J. Jiménez and P. Moin. The minimal flow unit in near-wall turbulence. *J. Fluid Mech.*, 225:213–240, 1991.

[4] Y. Sumitani and N. Kasagi. Direct numerical simulation of turbulent transport with uniform wall injection and suction. *AIAA J.*, 33(7):1220–1228, 1995.

ADVANCES IN TURBULENCE VIII
Proceedings of the Eighth European Turbulence Conference
C. Dopazo et al. (Eds.)
© CIMNE, Barcelona 2000

Similitudes in turbulent near-wall flows with injection and suction

I. I. Vigdorovich

Central Institute of Aviation Motors
2 Aviamotornaya St., Moscow 111250, RUSSIA

Contact e-mail: ivigdorovich@ciam.ru

We consider the incompressible flow in the turbulent boundary layer on a smooth flat plate in a uniform stream with a constant velocity U_e at the outer edge of the boundary layer. We assume that the injection/suction velocity, directed along the normal to the surface, is variable along the plate and $v = v_w(x)$, where x is the distance from the leading edge. The function $v_w(x)$ is assumed to vary slowly such that the parameter $\beta = |B|^{-1/2} d\ln|v_w|/d\ln x$ is of order of unity. Here, $B = v_w/U_e$ is the injection/suction parameter.

The local closure hypothesis of a general form is formulated, which implies the dependence of the shear stress on the partial derivatives of any order of the longitudinal component of the average velocity with respect to the transverse coordinate; and then the dimensional analysis is used to derive the constitutive relation [1]. An *ad hoc* change of variables is applied to the boundary layer equations, and the solution is constructed in various characteristic flow regions by the method of matched asymptotic expansions for high values of the logarithm of the Reynolds number calculated from the boundary layer thickness [1].

A universal velocity defect law for the outer region of the boundary layer is established as a generalization of the well-known defect law for an impermeable plate to the case of transpiration [2]

$$\frac{1 - u/U_e}{\sqrt{1/2c_f + B}} = f(\eta) + O(\sqrt{c_f + B}), \quad \eta = \frac{y}{\delta^*}\sqrt{1/2c_f + B}. \tag{1}$$

Here, y is the transverse coordinate and δ^* is the displacement thickness. In accordance with Eq. 1 all the velocity profiles can be represented by a single universal function $f(\eta)$ not depending on the wall conditions. Analogous representations for the shear stress and the other components of the Reynolds stress tensor also hold [2]

$$\frac{-\langle u'v'\rangle}{U_e^2(1/2c_f + B)} = 1 + \eta f(\eta) - \int_0^\eta f(\eta)\, d\eta + O(\sqrt{c_f + B}),$$

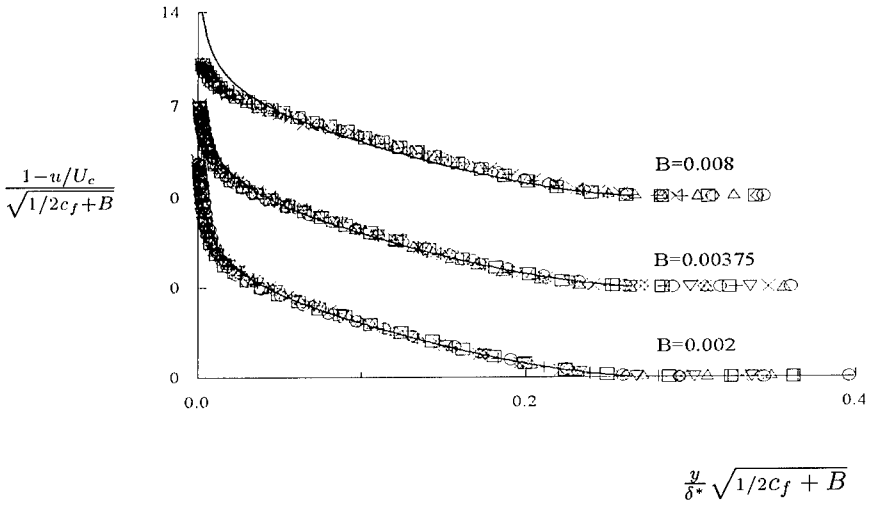


Figure 1: Experimental profiles of the velocity in a boundary layer with injection in terms of the similarity variables. Here, $R_x = 3.5 \cdot 10^5$ ($\bigcirc$), $5.4 \cdot 10^5$ ($\square$), $7.3 \cdot 10^5$ ($\triangle$), $9.2 \cdot 10^5$ ($\Diamond$), $1.1 \cdot 10^6$ ($+$), $1.3 \cdot 10^6$ ($\times$), $1.4 \cdot 10^6$ ($\triangledown$). Note the displaced origin.

$$\frac{\langle u'^2\rangle}{U_e^2(1/2c_f+B)} = G_1(\eta)+O(\sqrt{c_f+B}), \quad \frac{\langle v'^2\rangle}{U_e^2(1/2c_f+B)} = G_2(\eta)+O(\sqrt{c_f+B}).$$

Here, G_1, G_2 are universal empirical functions. The law is valid over the range of transpiration velocities from moderate suction, when the shear stress at the wall and that in the outer region are of the same order, to near-critical injection corresponding to the skin friction which is much lower than the shear stress in the outer region. In Figure 1 we have plotted, using the similarity variables, the experimental data [3] of the velocity distributions for various injection rates and Reynolds numbers. Solid lines in Figures 1 correspond to the well-known Coles empirical formula for the velocity profile in the turbulent boundary layer on an impermeable plate.

A universal friction law is established such that the skin friction coefficient distributions for various injection velocities and Reynolds numbers are described by a single universal curve [4]

$$Z^{inj}_{\left\{\begin{smallmatrix}x\\ \theta\end{smallmatrix}\right\}} = \Psi\left(\frac{\sqrt{1/2c_f}}{B}\right) + O(\sqrt{c_f+B}),$$

$$Z^{inj}_{\left\{\begin{smallmatrix}x\\ \theta\end{smallmatrix}\right\}} = B(1/2c_f+B)^{\pm 1/2}\exp\left(-\frac{2\kappa}{B}\sqrt{1/2c_f+B}\right) R_{\left\{\begin{smallmatrix}x\\ \theta\end{smallmatrix}\right\}}. \qquad (2)$$

Here, $\kappa = 0.41$ is the von Kármán constant, Ψ is a universal empirical function, R_x and R_θ are the Reynolds numbers based on x and the momentum thickness,

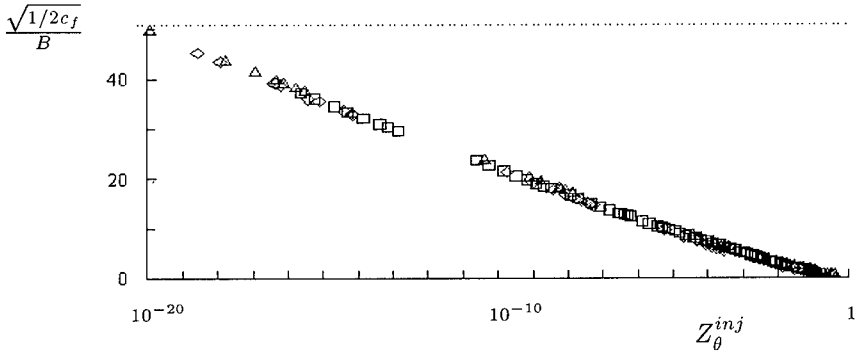


Figure 2: Skin friction over a plate with injection in universal variables for the range of $R_x \simeq 3.1 \cdot 10^4 \div 3.5 \cdot 10^6$ and $B \simeq 1.0 \cdot 10^{-3} \div 9.5 \cdot 10^{-3}$. Here, ($\triangle$) data of [5], ($\Diamond$) [3], ($\square$) [6].

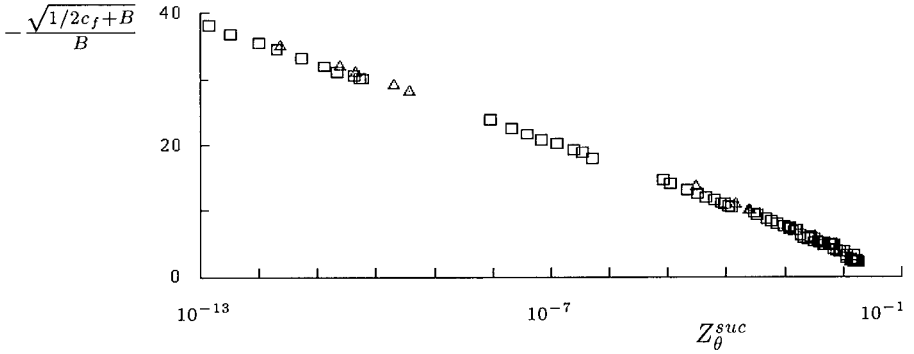


Figure 3: Skin friction over a plate with suction in universal variables for the range of $R_x \simeq 3.3 \cdot 10^5 \div 3.5 \cdot 10^6$ and $B \simeq -1.0 \cdot 10^{-3} \div -3.6 \cdot 10^{-3}$. The notation is the same as in Figure 2.

respectively. This law covers the entire range of the injection velocities from zero to the critical value corresponding to boundary layer separation. A simple criterion for boundary layer blow-off can be derived from Eq. 2. In Figure 2 we have plotted, using the similarity variables, the experimental data on skin friction over a plate for various Reynolds numbers and injection rates.

An analogous universal friction law is true for the turbulent boundary layer with suction [7]

$$Z^{suc}_{\left\{\begin{smallmatrix} x \\ \theta \end{smallmatrix}\right\}} = \Phi_{\left\{\begin{smallmatrix} x \\ \theta \end{smallmatrix}\right\}} \left(\frac{\sqrt{1/2c_f + B}}{B}, \beta \right) + O(\sqrt{c_f + B}),$$

$$Z^{suc}_{\left\{\begin{smallmatrix} x \\ \theta \end{smallmatrix}\right\}} = \sqrt{1/2c_f}\,(-B)^{\pm 1} \exp\left(2\kappa \frac{\sqrt{1/2c_f}}{B} \right) R_{\left\{\begin{smallmatrix} x \\ \theta \end{smallmatrix}\right\}}. \qquad (3)$$

Here, Φ_x, Φ_θ are universal empirical functions. However, in this case the degree of suction nonuniformity is essential, and there is a one-parameter family of curves which depend on the suction nonuniformity parameter β. The universal law given by Eq. 3 covers the entire range of suction velocities in the fully-developed turbulent boundary layer from zero to the critical value corresponding to boundary layer relaminarization [8]. In Figure 3 we have plotted, using the similarity variables, the experimental data on skin friction over a plate with suction.

One can see from Figures 1–3 that the obtained theoretical results, similitudes and asymptotic calculation formulas, are in good agreement with available experimental data.

The work was supported, in part, by a Soros Humanitarian Foundations Grant awarded by American Physical Society and by the Russian Foundation for Basic Research (projects Nos. 95-01-00988a and 98-01-00154).

References

[1] I. I. Vigdorovich. Asymptotic analysis of turbulent boundary layer flow on a flat plate at high Reynolds numbers. *Fluid Dynamics*, 28(4):514–523, 1993.

[2] I. I. Vigdorovich. Universal law for the velocity defect of a turbulent boundary layer at a plate with injection and suction. *Physics – Doklady*, 38(8):335–339, 1993.

[3] P. S. Andersen, W. M. Kays, and R. J. Moffat. The turbulent boundary layer on a porous plate: An experimental study of the fluid mechanics for adverse free-stream pressure gradients. Rep. No. HMT–15, Stanford Univ., Thermos. Div., 176 p. 1972.

[4] I. I. Vigdorovich. A universal law of friction for the turbulent boundary layer on a plate with injection. *Physics – Doklady*, 39(7):514–518, 1994.

[5] R. L. Simpson, R. J. Moffat, and W. M. Kays. The turbulent boundary layer on a porous plate: Experimental skin friction with variable injection and suction. *Int. J. Heat Mass Transfer*, 12(7):771–789, 1969.

[6] K. Depooter. The measurement of wall shear stress on a porous plate with mass transfer using a floating element technique and the investigation of various indirect measuring methods. PhD Thesis, Univ. Waterloo, Canada, 159 p. 1973.

[7] I. I. Vigdorovich. The universal law of friction for a turbulent boundary layer on a plate with suction. *Physics – Doklady*, 42(9):506–510, 1997.

[8] I. I. Vigdorovich. Turbulent boundary layer on a flat plate with strong suction. *Fluid Dynamics*, 34(3):349–362, 1999.

ADVANCES IN TURBULENCE VIII
Proceedings of the Eighth European Turbulence Conference
C. Dopazo et al. (Eds.)
© CIMNE, Barcelona 2000

Impact of localized unsteady blowing on the near wall turbulence

S. Tardu

Laboratoire des Ecoulements Géophysiques et Industriels- LEGI
B.P. 53-X 38041 Grenoble-Cédex ; France

Contact e-mail: tardu@hmg.inpg.fr

1 Introduction

The application of optimal control through suboptimal schemes (Bewley et al., 1993) or neural networks (Lee et al., 1997) and the use of DNS resulted in drag reduction of about 20-30 % and has given quite attractive insight into the near wall physics somewhat indirectly. The major shortcoming of these strategies, however, is the need of a dense distribution of MEMS requiring intervention at the wall roughly every 4 to 10 wall units in the spanwise and streamwise directions. Another method could use a linear or non-linear time-dependent forcing at the wall through a coarser distribution of intervention locations and find the optimal temporal variation of the disturbance to decrease or increase the drag. The aim is to post process the near wall turbulence before its control. Large-scale unsteady blowing/suction is already used in the control of separation, but the response and relaxation of the near wall turbulence to a localized intervention at the wall are not well understood even when the later is steady (Tardu, 1998).

2 Experimental set-up and Data reduction

An experimental model has been developed in the low-speed wind tunnel of our laboratory. The blowing and suction at the wall are done through spanwise slots of dimensions 0.6*100 mm corresponding to 10*1667 in wall units in the present working conditions. A special pulsating device has been designed for the present purpose. Quite satisfactory sinusoidal waveforms of the suction/blowing wall normal velocities have been obtained. In order to extract the deterministic and deduce the random part of the flow quantities the classical triple decomposition is used. A flow quantity $q(\vec{x},t;T)$ is decomposed into a time mean $\overline{q}$ an oscillating $\widetilde{q}$ and a fluctuating q' part, $q(\vec{x},t;T)=\overline{q}(\vec{x})+\widetilde{q}(\vec{x},t/T)+q'(t)$, where T stands for the period of the oscillating blowing. The phase average is denoted by $< q >=$

$\overline{q} + \widetilde{q}$. The results reported in this study are obtained through a *local unsteady blowing* with an imposed frequency $f^+ = 0.017$ and an amplitude $\widehat{v_0}^+ = 8$ (+ denotes values scaled with inner variables). The free stream velocity is $U = 4m/s$.

3 Results

Fig. 1a shows the cyclic modulation of the wall shear stress at $x^+ = 20$ and 40 downstream of the slit. The phase average $< \tau >$ is scaled with the time mean wall shear stress $\overline{\tau}_{SB}$ of the unmanipulated standard boundary layer. The waveform of the injection velocity (to not scale) is also shown. The striking feature of the reaction of $< \tau >$ takes place during the acceleration phase of the injection velocity. The wall shear stress decreases rapidly during this phase until it reaches the laminar limit defined as the value that a laminar Blasius boundary layer would have at the same Reynolds number. The strong modification of the wall turbulence structure is better captured in Fig. 1b which shows the phase average of the skewness $< S >_{du'/dt}$ of the time derivative of fluctuating streamwise velocity du'/dt and of the ejection frequency $< f_e^+ >$ identified by VITA through the phase averaged thresholds at $y^+ = 10$. Both the vorticity generation and production mechanisms are altered at high blowing frequency during half of the oscillation cycle. At the accceleration phase, the bursting activities together with the vortex stretching are largely suppressed. The ensemble of ingredients showing relaminarization are present near the slot at $x^+ < 40$ and during half of the cycle.

The space time evolution of the near wall flow at further downstream locations

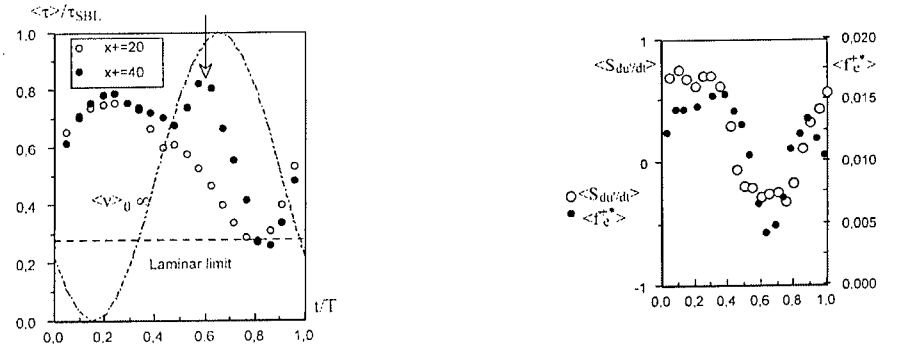


Figure 1: Phase averages of the wall shear stress (a left) at $x^+ = 20$ and 40 downstream of the injection slit. Phase averages of the time derivative skewness and the ejection frequency at $x^+ = 20$ and $y^+ = 10$ (b right)

is striking. First the velocity profiles become strongly inflectional at $x^+ = 40$ and approximately in the middle of the *deceleration* phase. Fig. 2 a shows the

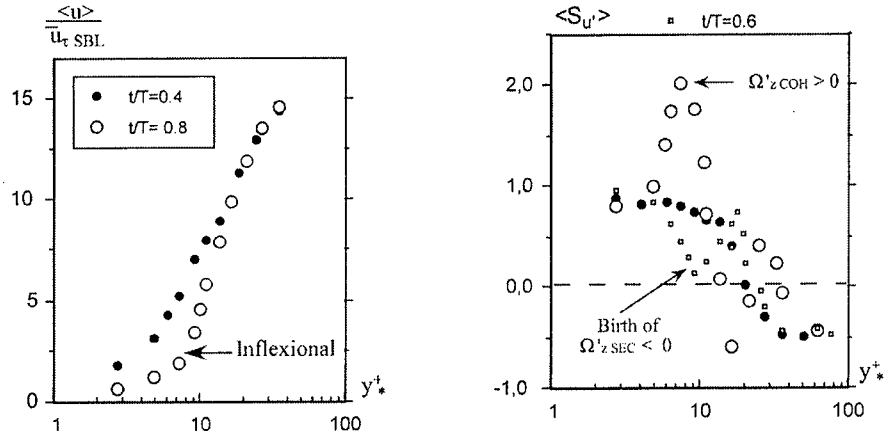


Figure 2: Velocity profiles (a left) and skewness of u' (b right) at t/T=0.4-0.8 and $x^+ = 40$. The birth of $\Omega'_{z\mathrm{SEC}} < 0$ is seen at t/T=0.6.

phase averaged velocity profiles at t/T=0.4 (for reference) and 0.8 corresponding respectively to the middle of the acceleration and deceleration phases of the injection velocity. The presence of an inflectional point at t/T=0.8 where $< \tau >$ decreases to the laminar limit (Fig.1a), is clear. It may, therefore, be argued that the *relaminarized* flow is possibly unstable to inviscid disturbances according to the Fjortoft's theorem and the observed behavior is not due to a local unsteady separation according to Moore-Sears criteria. The destabilized flow enters subsequently into *retransition* further downstream following the scheme reported by Narasimha and Sreenivasan (1973). This gives place to the accumulation and enhancement of a patch of spanwise vorticity *of the opposite sign* to the mean vorticity during the deceleration phase at t/T=0.8. The existence of this coherent patch may be clearly seen by the sudden changes in the skewness of u' shown in Fig.2b. This patch rolls up into a coherent structure $\Omega'_{z\mathrm{COH}} > 0$ approximately at $y^+ = 10$ and $x^+ = 20$. The birth of this structure,in return, gives place downstream to a secondary spanwise vortical structure near the wall with opposite sign, i.e. $\Omega'_{z\mathrm{SEC}} < 0$, because of the non slip condition. The genesis of $\Omega'_{z\mathrm{SEC}} < 0$ and its subsequent development are perfectly well localized both in time and space. The whole structure is convected downstream with an advection velocity of $7u_{\tau\mathrm{SB}}$, while $\Omega'_{z\mathrm{SEC}} < 0$ is reinforced and $\Omega'_{z\mathrm{COH}} > 0$ diffuses somewhat more rapidly. Consequently the wall shear stress increases almost in a Dirac function fashion at times and locations which are perfectly predictable as shown in Fig. 3a. The whole phenomena relaxes further downstream at $x^+ = 300$ (not shown here). This mechanism occurs in the high frequency regime, for $f^+ > 0.009$. Fig. 3b shows the phase average of the wall shear stress at $x^+ = 120$ for different imposed frequencies. It is clearly seen

that the generation of spanwise vortical structure that increases the shear takes suddenly place at this critical frequency.

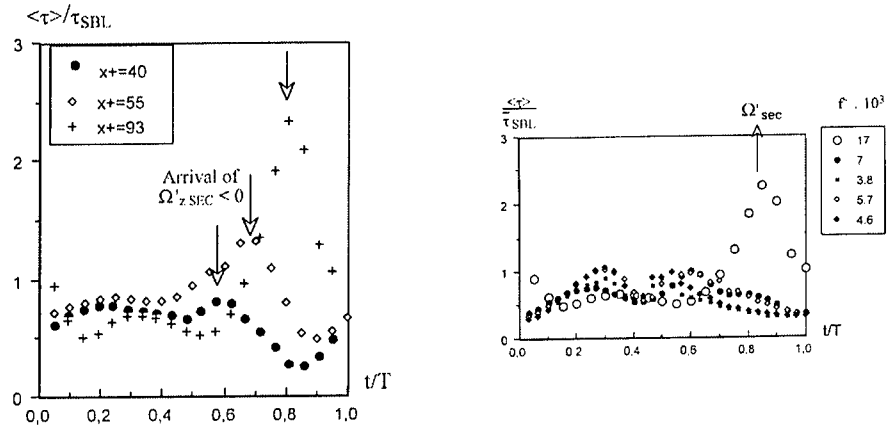


Figure 3: Phase averages of the wall shear stress at $f^+ = 0.017$ vs. x^+ (left a), and at $x^+ = 120$ vs. f^+ (left b)

4 Discussion and Conclusion

In the case of blowing there is no subtraction or addition of vorticity. The spanwise mean and fluctuating vorticity, together with *turbulent-drag* inducing quasi-streamwise vortical structures are displaced and pushed away from the wall. The removing induces a *global deficit* in the instantaneous non-slip velocity at the wall. This is subsequently corrected by the formation of a thin vortex sheet in front of the wall (and of its image) with vorticity of opposite sign to the mean vorticity. This sheet subsequently dilutes through diffusion. When the blowing is unsteady, the diffusion is constrained into a layer whose thickness varies like $l^+ \infty 1/\sqrt{f^+}$. At the critical imposed frequency where there is roll up one has $l^+ = 10$. Thus, viscous diffusion alone governs the removal of unsteady vorticity layer and the turbulence does not participate to the diffusion. Therefore, it accumulates, concentrates and rolls up.

References

[1] T. Bewley T., H. Choi , R.Temam and P. Moin Optimal feedback control of turbulent channel flow. *Annual Research Briefs, CTR*, 3–14, 1993.

[2] Narasimha R. and Sreenivasan K.R. Relaminarization in highly accelerated boundary layers flow fields. *J. Fluid Mech.*, 61:417–447, 1994.

ADVANCES IN TURBULENCE VIII
Proceedings of the Eighth European Turbulence Conference
C. Dopazo et al. (Eds.)
© CIMNE, Barcelona 2000

Changes in turbulent structure in a boundary layer due to local injection

P.-Å. Krogstad

Dept. of Mechanics, Thermo and Fluid Dynamics
Norwegian University of Science and Technology
N-7491 Trondheim, Norway

1 Introduction

Boundary layers with localized injection are found in gas turbine and boundary layer control applications, drying processes in the chemical industry and, more recently, cooling of electronics by means of injection through the printed circuit board. The flow over uniformly blown plates has been studied in some detail (e.g. [1], [2]) and it has been shown that surface blowing causes an upwards shift in the mean velocity logarithmic law. It is also found that the turbulent stresses are increased compared to the unblown case. These observations have later been confirmed numerically in Large Eddy and Direct Numerical Simulations of channel flows ([3],[4]). Sumitani and Kasagi [4] found that even small amounts of uniformly distributed injection in channel flows cause a significant increase in the turbulent production of kinetic energy. The increase was completely balanced by an increase in the dissipation rate for $y^+ > 30$. This indicates that, except very close to the surface, the structural changes in the flow may be small.

The present study investigates the effects of localized injection on the turbulent structure at much higher Reynolds numbers than are available for DNS. The injection rates were kept quite low, so that the perturbations due to the blowing were reasonably small even close to the injection area, while at the same time producing sufficient effects to significantly modify the turbulent stresses. In a previous report [5] it was shown that at blowing rates as low as $V_w = 0.003U_e$, significant effects on the turbulent structure may be observed more than 20 boundary layer thicknesses, δ, downstream of the injection area.

2 Experimental details

On a flat plate at zero pressure gradient conditions a turbulent boundary layer was initially allowed to develop over 2.35 m. It was verified that the boundary layer at this station (Reynolds number based on momentum thickness was Re_θ

= 3250) satisfied the criteria for a fully developed boundary layer (C_f, wake strength, stress levels etc.). Air was injected through a porous strip over a streamwise distance corresponding to about 2.5 times the thickness of the incoming boundary layer, δ_0. The porous strip, made of sintered stainless steel with an average hole diameter of 150 μm, spanned the entire tunnel width. The boundary layer was then allowed to relax from the perturbation for about 23 δ_0.

Mean velocity and Reynolds stress data ($\overline{u^2}, \overline{v^2}, \overline{w^2}, \overline{-uv}$ and $\overline{-uw}$) were obtained using hot wire anemometry with a range of 2.5μm and 5μm single and x-wire probes. Further details may be found in [5]. Measurements were taken for the unblown case, as well as for three injection rates $F = V_w/U_e = 0.003, 0.006$ and 0.009. Data were taken just upstream of the strip, at the strip center and at 6 stations in the relaxation region downstream.

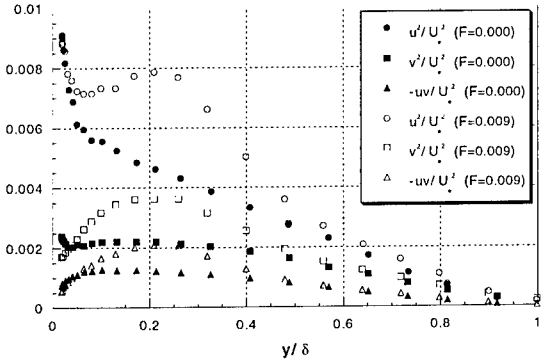


Figure 1: Stresses measured 3.5 δ downstream of the injection strip for the unblown (filled symbols) and highest blowing rate (open symbols) cases.

3 Results and discussion

Above and immediately downstream of the strip the injection causes a dramatic drop in skin friction. Although the skin friction increases again as the boundary layer develops downstream, this is a slow process which is not completed over the 23 δ covered by this investigation. Combined with the reduction in skin friction is a strong increase in turbulent mixing which affects all the turbulent stresses (see figure 1). Near the wall a new equilibrium layer is quickly re-established. Therefore, the stresses near the surface (here shown for the highest blowing rate) are very similar to the distributions found for the unblown reference case. The outer layer ($y/\delta \geq 0.6$) is not yet affected by the blowing at this station (about 3.5 δ downstream of the injection strip). In the region influenced, the stresses have been increased almost by a factor of 2.

Near the surface the production rate, $-\overline{uv}\partial U/\partial y$, for the unblown case shows the y^{-1} distribution expected for an equilibrium boundary layer (figure 2). The

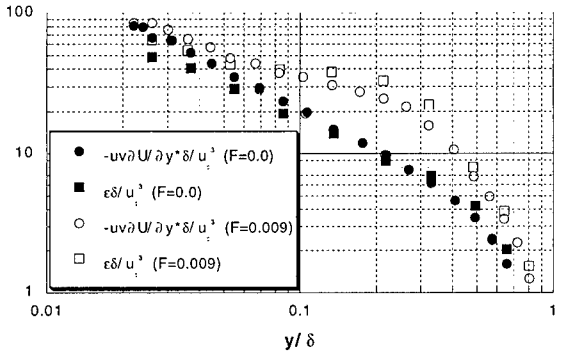


Figure 2: Production and dissipation rates measured 3.5 δ downstream of the injection strip for the unblown (filled symbols) and highest blowing rate (open symbols) cases.

blown case indicates a return to equilibrium conditions very near the wall, but for most of the inner layer the production rate is considerably increased, as observed by Sumitani and Kasagi [4] for the channel flow. With localized injection, the measurements show that the dissipation rate increases more than the rate of production, being about 35% higher at $y/\delta \approx 0.2$. (The dissipation rate was estimated from the inertial range of the power density spectrum of u). This implies a significant change in turbulent diffusion, as reported by Krogstad and Kourakine [5], and therefore suggests considerable modifications to the turbulent transport mechanism in the boundary layer when blowing is applied.

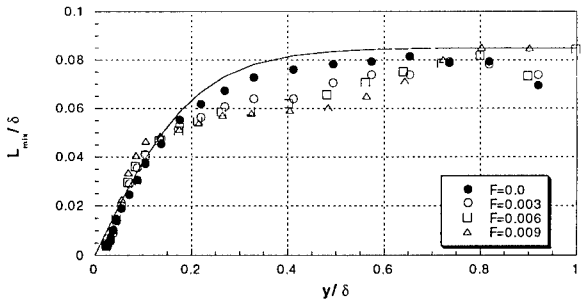


Figure 3: Mixing length distributions at 3.5 δ downstream of the injection strip. Line: Model of Michel *et al.* [6].

This affects both the small (e.g. reduced Taylor micro scale, see [5]) and the large turbulent length scales, here exemplified by the mixing length (figure 3). Krogstad and Kourakine [5] found that localized blowing led to considerable outward diffusion in the region $0.1 < y/\delta < 0.4$ which causes the mixing length to drop. This contradicts the common assumption that the mixing length scale is unaffected by surface blowing. This has been applied in all law of the walls which include injection/suction effects proposed in the literature (e.g. [1], [2]).

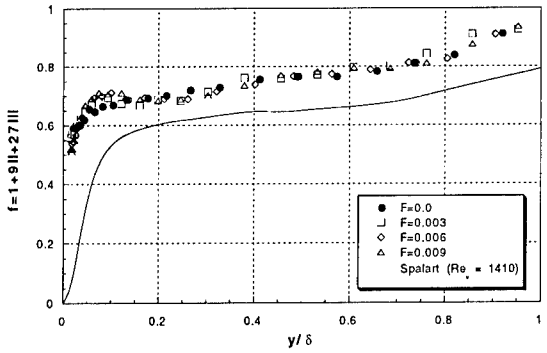


Figure 4: Invariant functions measured 3.5 δ downstream of the injection strip.

All this information suggests that the degree of flow anisotropy must have been affected by the blowing rate. However, an invariant analysis revealed that the components of the invariant tensor are hardly affected by the surface blowing. Figure 4 shows the invariant function computed from the measurements. (f=0 for two-component and 1 for isotropic turbulence). For comparison the DNS data of Spalart [7] have been included. The measurements are seen to exhibit the same y/δ dependence as the DNS data, although the level is slightly higher throughout the layer, indicating that the flow is more isotropic. This may be a Re-effect as Re for the measurements are about 3 times higher than for the DNS. However, it is evident from the plot that the degree of anisotropy is not affected by the injection rate. This implies that the observed increase in the Reynolds stresses due to the blowing affects all components by the same amount. Hence the redistribution process of the turbulent energy among the various stress components has not been affected by the changes in boundary condition.

References

[1] T.N. Stevenson, AIAA J., **6**, 553 (1968).

[2] R.J. Baker and B.E. Launder, Int. J. Heat Mass Transfer, **17**, 275 (1974).

[3] U. Piomelli, J. Ferziger and P. Moin, Phys. Fluids A, **1**, 1061 (1989).

[4] Y. Sumitani and N. Kasagi, AIAA J., **33**, 1220 (1995).

[5] P.-Å. Krogstad and A. Kourakine, In *Turbulence and shear flow - 1*, (ed. S. Banerjee and J.K. Eaton), 429 (1999).

[6] Michel, R., Quémard, C. and Durant, R, In *Proc. Computation of Turbulent Boundary Layers*, 1968 AFORS-IFP Conf., Vol. 1, (ed. S.J. Kline, M.V. Morkovin, G. Sovran and D.J. Cockrell), 195 (1969).

[7] P. Spalart, J. Fluid Mech., **187**, 61 (1988).

ADVANCES IN TURBULENCE VIII
Proceedings of the Eighth European Turbulence Conference
C. Dopazo et al. (Eds.)
© CIMNE, Barcelona 2000

Receptivity of boundary layers under centrifugal forces

N. Yurchenko

Institute of Hydromechanics, National Academy of Sciences,
8/4 Zheliabov St., Kiev, UKRAINE

Contact e-mail: yur@rdfm.freenet.kiev.ua

Introduction

Streamwise vortices developing in boundary layers precede the transition to turbulence and therefore are of primary interest from the viewpoint of fundamental knowledge and its practical applications related to the large-scale coherent structure control. Encouraging conclusions, in particular, in a form of experimentally shown advantages of longitudinal vortices to control heat transfer [1], were deduced from the analysis of the boundary-layer stability and receptivity to 3D disturbances.

A problem of natural evolution and behavior of this vortical structure under various boundary conditions can be rigorously formulated for transitional boundary layers affected by body forces (e.g. centrifugal forces or buoyancy). For the centrifugal case, this self-organized fluid motion can be analyzed in a frame of the well known Goertler stability theory describing growth and decay of vortices depending on the boundary-layer flow parameters [2, 3].

The **objective** of the present work is to reveal peculiarities of a boundary layer response to streamwise vortices generated with a given scale in a flow affected by centrifugal forces, i.e. under conditions where they are a naturally inherent and dominating structure.

Results and discussion

The work was implemented experimentally and numerically. First, the natural evolution of streamwise vortices in boundary layers over a concave wall was considered. Secondly, a flow reaction at different stages of a laminar-turbulent transition to an imposed system of counter-rotating pairs of streamwise vortices was studied.

Streamwise vortices were induced in a boundary layer with a given spanwise scale λ_g using two methods [1, 3]: (1) mechanical vortex-generator arrays placed

on a surface and (2) temperature distribution over the surface regularly varied in the spanwise, z, direction. In practice, the second method was realized with the help of streamwisily oriented electrically heated stripes flush-mounted on a test plate.

A numerical approach was based on a code developed for the direct numerical simulation of the laminar-turbulent transition in compressible subsonic boundary layers [3]. It aimed to get peculiar details both for natural and forced development of the vortical structure. For the latter case, a constant boundary condition was imposed in a form of the z-periodic surface temperature (the stripes were heated to $\Delta T = 30K$ above the (natural) adiabatic wall temperature).

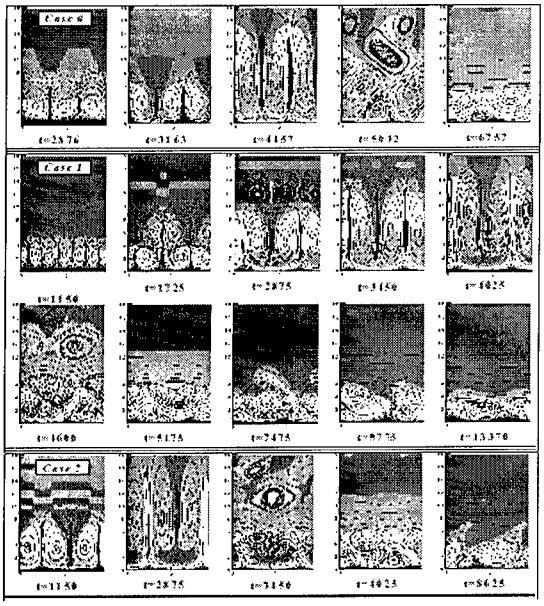


Figure 1: Calculated flow-field patterns in yz-plane in the course of natural *(Case 0)* and forced *(Cases 1,2)* evolution of streamwise vortices.

Fig. 1 shows calculated topology of a boundary-layer flow developing in time for 3 cases:

Case 1 describes permanent forcing at the wall. to excite a second mode with a non-dimensional vortex scale $\Lambda = 84$ linearly amplified according to the Goertler stability diagram, and harmonics thereof.

Case 2 corresponds to generation of a slightly irregular vortical structure that implies additional stimulation of a spectrum including the most amplified first mode, $\Lambda = 236$. In practice, *Case 2* was realized due to one of the heated stripes insignificantly shifted along z.

Case 0 is taken as a reference to the cases of forced excitation to observe laminar-turbulent transition with naturally evolving Goertler vortices. The wall was homogeneously kept thermally insulated. A very small initial pulse disturbance was introduced to keep the system in the linear regime for a very long phase. In this way, "generic" Goertler vortices could arise.

Experiments were carried out in an open low-turbulence water-channel over its bottom 25×300 cm containing a concave section with the curvature radius R=12 m at free-stream velocities within 0.05-0.2 m/s. Electro-chemical Tellurium-method (similar to the conventional hydrogen-bubble technique) was used to visualize a flow field [3]. Typical shapes of visualized $U(y)$ and, especially, of wavy $U(z)$ velocity profiles give a clear evidence of the developing vortical structure in a boundary layer (see Fig. 2), of its scale and intensity as well as the evolution downstream and normally to the surface. Space-scales of generated vortices (given by a distance between the neighboring vortex-generators or heated longitudinal stripes, λ_g) covered the range from neutral ($\Lambda_0 = 39$) to most amplified ($\Lambda \approx 100$) vortices according to the Goertler diagram.

Experimental and numerical visualization results are in a good agreement. A sequence of the flow field patterns in yz-plane (Fig. 1) enabled to restore the physical picture of the vortical structure development. Four characteristic phases of the unforced evolution process were picked out: (**a**) emergence, (**b**) growth, (**c**) breakdown, and (**d**) post-breakdown [3].

Similar events were observed in a process of the forced vortex development. However the duration of the vortex growth phase in both controlled cases is essentially larger than in the reference case. It means that compared to natural boundary layer development, the downstream distance of a developed and stably sustained vortical system extends due to the generation of vortices intrinsic to the given flow situation but having scales different from those naturally developing. This effect is especially remarkable because a weak controlling factor (ΔT) caused noticeable changes of integral boundary-layer characteristics.

Vortex scale transformation was observed not only across the boundary layer thickness but also downstream if streamwise vortices generated with a scale different from the most amplified 1st mode.

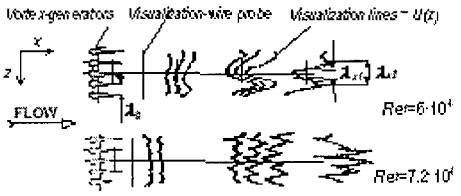


Figure 2: Boundary-layer response to vortices generated with the scales of λ_{g1}, = 3.2 cm and λ_{g2},=1.6 cm

Receptivity of a boundary layer to the scale of introduced vortices is demonstrated in Fig. 2, top view of visualized

$U(z)$ distributions. It is well seen that the flow field developing downstream of the vortex-generators depends on correlation between a spanwise scale of a disturbing factor (λ_g) and the Reynolds number, Re.

Conclusions

Both experimental and numerical studies displayed susceptibility of a boundary layer under centrifugal forces to disturbances of the type inherent to this flow, i.e. to streamwise vortices. In particular, the following was shown:

- boundary-layer selective response to the spanwise scale, λ_g, of generated vortices depending on the basic flow parameters;
- scale, λ_z, transformation of the streamwise vortices evolving downstream and normally to the wall;
- streamwise vortices can be easily manipulated what may result in their development deceleration or acceleration through the control of their growth phase.

Acknowledgements

This material is based upon work supported by the European Office of Aerospace Research and Development, AFOSR, AFRL under the Contract F61775-99-WE075. The author acknowledges with gratefulness the assistance of Drs. J. Delfs, C.Raffoul, valuable discussions with Profs. J.T.C.Liu and W. Saric.

References

[1] N. F. Yurchenko. Optimization of heat transfer control based on a receptivity approach. *Proc. of Turbulent Heat Transfer II Conference, Manchester*: P72–P81, 1998.

[2] W. S. Saric. Goertler vortices. *Annu. Rev. Fluid Mechanics*, 26: 379 – 409, 1994.

[3] N. Yurchenko, J. Delfs. Optimal control of boundary layers under body forces. *Proc. IUTAM Symposium on Laminar-Turbulent Transition, Sedona, U.S.A.*, 1999.

ADVANCES IN TURBULENCE VIII
Proceedings of the Eighth European Turbulence Conference
C. Dopazo et al. (Eds.)
© CIMNE, Barcelona 2000

The effect of long chain polymers on the structure of wall turbulence

E. De Angelis[1], C. M. Casciola[1], and R. Piva[1]

[1]Dip. di Meccanica e Aeronautica, Universitá di Roma, La Sapienza
V. Eudossiana 18, 00184 Roma, ITALY

Contact e-mail: betta@flu5.ing.uniroma1.it

1 Introduction

An attempt to achieve a better understanding of the polymer action on wall turbulence has been made through the analysis of DNS results of a 3D turbulent channel flow. The simulation has been performed using the FENE-P model for the polymer contribution to the stress tensor. Each polymer chain is modeled as a dumbbell (two massless beads connected by a non-linear spring) and characterized by a single relaxation time which takes into account the viscoelastic behavior of the solution.
We analyze here a fully coupled simulation to evaluate the respective role of the elongational and of the elastic energy redistribution in the alteration of wall turbulent structure. The solution of dilute polymers is modeled by considering that at each point of the field is attached a collection of dumbbells. The presence of the dumbells provides an extra-stress tensor T^p_{ij} in the field, given by $T^p_{ij} = n_p [F_i R_j]$, where n_p is the average number of dumbbells *per* unit volume. In the previous expression the end-to-end vector R_i represents the configuration of each dumbbell and F_i is the connector force due to the spring expressed as $F_i = kf(R^2)R_i$, where $f(R^2)$ accounts for the nonlinearity of the spring. Under the Peterlin's assumption (FENE-P), which expresses the force coefficient as a function of the average extention, the statistical behavior of the system is described by a field equation for the conformation tensor $\mathcal{R}_{ij} = [R_i R_j]$, i.e. the ensemble average of the diadic product of the end-to-end vector of the polymer. In fact, for the conformation tensor it is possible to write a frame indifferent evolution equation

$$\overset{\triangledown}{\mathcal{R}}_{ij} = -\frac{1}{De} f(\mathcal{R})\mathcal{R}_{ij} + \frac{1}{De}\delta_{ij} , \tag{1}$$

with the spring constant specified as

$$f(\mathcal{R}) = \left(R^2_{max} - 3\right) / \left(R^2_{max} - \mathcal{R}\right) , \tag{2}$$

where $\mathcal{R} = Tr(\mathcal{R}_{ij}) = [R^2]$ and R_{max} gives the maximum allowed elongation of the polymer chains. The left hand side of eq. (1) is the upper convected time derivative defined as

$$\overset{\triangledown}{\mathcal{R}}_{ij} = \frac{\partial \mathcal{R}_{ij}}{\partial t} + u_k \frac{\partial \mathcal{R}_{ij}}{\partial x_k} - K_{ir}\mathcal{R}_{rj} - \mathcal{R}_{ir}K_{jr} \tag{3}$$

where K_{ij} is the velocity gradient. The non-dimensional parameter appearing in the previous equations is the *Deborah* number $De = \tau U_0/L_0$ which is the ratio between the relaxation time of the polymer chain τ and the characteristic flow field time L_0/U_0. Equation (1) has essentially the structure of a Maxwell equation (although there is a nonlinear correction) with a relaxation parameter given by the dimensionless number De, which gives reason of the memory effects observed in these materials. The extra-stress is directly given in terms of the conformation tensor by the constitutive equation

$$T^p_{ij} = \frac{\eta_p}{De}\left(f(\mathcal{R})\mathcal{R}_{ij} - \delta_{ij}\right) \tag{4}$$

where η_p is the relative viscosity, i.e. the ratio between the contribution of the polymer molecules to the solution viscosity and the solvent viscosity. In conclusion, the basic parameters are: De, η_p and R^2_{max}.

2 Elongational viscosity vs. elastic energy

Though the effect of flexible long chain polymers on the structure of wall turbulence is well known since long ago, a definite theory that is able to fully explain this phenomenon has not been given yet. In particular the proposed theoretical models can be grouped in two main classes. A first approach was introduced by Lumley. He observed that the polymer molecules become significantly extended only when the time scale of the strain rate becomes smaller than the relaxation time of the molecules. Hence he proposed the existence of localized regions of the flow, where these events, characterized be an enhanced elongational viscosity take place leading to an overall drag reduction.
The other approach proposed by De Gennes is focused on the idea that polymer effect at small scales is described by elasticity modulus rather than by viscosity. He argued that in turbulent flows the polymers, moderately stretched, can not produce a significant change in viscosity. Whereas the major effects arise for those scales where the elastic energy stored by the partially stretched polymers becomes comparable with the turbulent energy interfering with the classical turbulent cascade.
One of the main difficulties in achieving a further comprehension of this phenomenon is due to the full knowledge of the viscoelastic quantities, which can be hardly measured in experiments. In this respect, we believe that DNS offers an unreplaceable tool of investigation. In fact, despite the problems connected

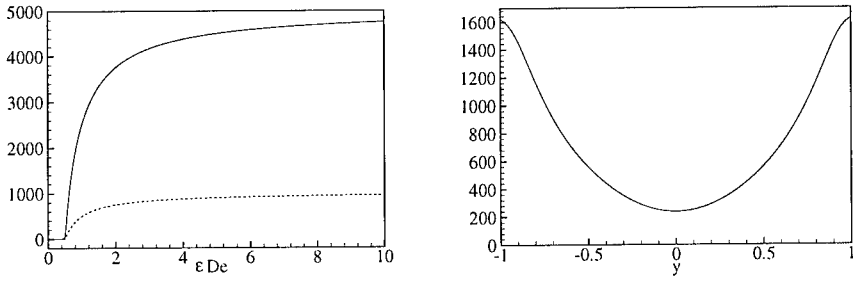


Figure 1: Left: Steady state of the elongation (solid) and of the elongational viscosity (dashed) as function of the velocity deformation. Right: Dumbbell extension given by the trace of the conformation tensor.

with the numerical simulation of a viscoelastic flow such as extreme simplicity of the affordable models or the need of an artificial diffusivity for the numerical integration [2], the simulation of a fully coupled system allows the analysis of the viscoelastic reaction and hence a deeper insight into the physics. In the following we propose a tentative evaluation, through DNS, of some of the critical issues of the two approaches.

It has been shown [6] that in an uniaxial strain, if the velocity deformation exceeds a certain value, the behavior of the dilute polymer solution is characterized by a sharp coil-stretch transition of the molecules, which, as shown in the left plot of fig.1, leads to a high value of the elongational viscosity. This should happen in localized regions of the turbulent flow, where the deformation velocity is larger, thus interfering with the regeneration events. As can be observed from the averages of the trace of the conformation tensor (right plot fig.1), the polymers never overcome the threshold in the present simulation (where the parameters are $Re = 5000, \eta_p = 0.1, De = 10$ and $R^2_{max} = 5000$). Nonetheless the present values of the parameters could reach very large values of the elongational viscosity even before coil-stretch transition. It is important at this point to analyze the role of the elastic energy. In fact, the fluid is viscoelastic and hence the transferred power is not only dissipated but also stored under the form of elastic energy, i.e. a form of energy that can be convected through the flow and released in other parts of the domain. To evaluate the role of the elastic energy redistribution, we perform a decomposition of the stress power due to the polymer which appears in the equation of the total kinetic energy

$$T^p_{ij} D_{ij} = \Phi + \frac{DE_p}{Dt} \tag{5}$$

where Φ is the viscous dissipation and the last term is the rate of elastic energy accumulation given as

$$\frac{DE_p}{Dt} = \frac{1}{2}\frac{\eta_p}{De} f(\mathcal{R}_{ii}) \frac{D\mathcal{R}_{ii}}{Dt}. \tag{6}$$

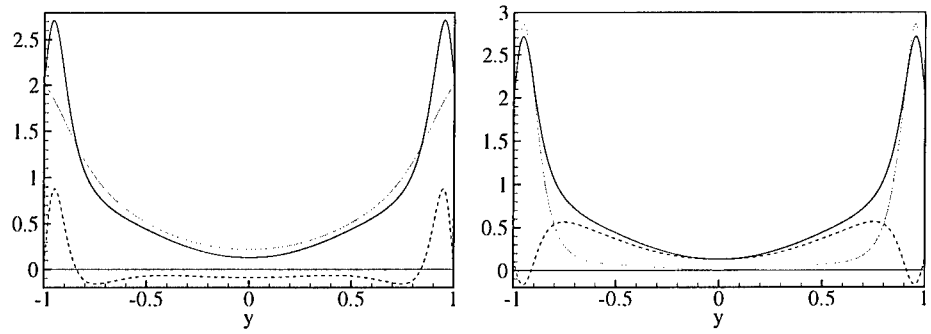


Figure 2: Left: Decomposition of the stress power due to the polymers, integrated by planes. Total stress power (solid), elastic energy rate (dashed), rate of dissipation (dotted). Right: Reynolds decomposition of the total stress power. $< T^p_{ij} D_{ij} >$(solid), $< T^p_{ij} >< D_{ij} >$ (dotted), $< T^{p'}_{ij} D'_{ij} >$ (dashed).

By a preliminary inspection of the average values, we observe regions of the domain where elastic energy is stored, namely the viscous sublayer and the buffer layer, and others where the elastic energy is released. This behavior suggests that polymers are able to drain energy from the main flow in the regions where most of the turbulence regeneration activity takes place. It is worth noticing that the decomposition of the stress power can be performed only for the terms appearing in the equation the total kinetic energy and not for the mean and fluctuating components (left part fig. 1).

References

[1] E. De Angelis, C. M. Casciola and R. Piva, Wall turbulence in dilute polymer solutions. *Computational Fluid Dynamics Journal* **9** (3) 2000.

[2] R. Sureskumar, A. N. Beris and A. H. Handler. Direct numerical simulation of the turbulent channel flow of a polymer solution. *Phys. Fluids* **9** (3) 743-755 1997.

[3] P. G. De Gennes. Towards a scaling theory of drag reduction. *Physica* **140A** 9-25 1986.

[4] J. L. De Lumley. Drag reduction in turbulent flow by polymer additives. *J. Polymer Sci., Macrom. Rev.* **7** 263-290 1973.

[5] K. R. Sreenivasan and C. M. White. The onset of drag reduction by polymer additives, and the maximum drag reduction asymptote. *Submitted to JFM*

[6] F. B. Wedgewood and R. B. Bird. From molecular models to the solution of flow problems. *Ind. Eng. Chem. Res.***27** 1313-1320, 1988.

ADVANCES IN TURBULENCE VIII
Proceedings of the Eighth European Turbulence Conference
C. Dopazo et al. (Eds.)
© CIMNE, Barcelona 2000

Direct interaction between highly-entangled polymers and small-scale coherent structures in a turbulent polymer-solution flow

Y. Hagiwara, T. Imamura, S. Takagaki, and M. Tanaka

Dept. of Mech. and System Eng., Kyoto Institute of Technology
Matsugasaki, Sakyo-ku, Kyoto 606-8585, JAPAN

Contact e-mail: yoshi@ipc.kit.ac.jp

1 Introduction

Attention has been focused on the modification of near-wall coherent structures by polymers, effective for the drag reduction of turbulent flows, to understand the mechanism of the drag reduction. Tiederman *et al.*[1] measured a decrease in the bursting rate and an increase in the average spacing of low-speed streaks caused by polymers in the buffer region of turbulent channel water flows. We demonstrated numerically that the cluster model of beads and springs, representative of highly-entangled polymers, attenuates selectively the evolution of small-scale streaks and small-scale eruptive flows in the buffer region in a turbulent channel flow (Hagiwara *et al.*[2]). This model is based on the observation of freeze-dried samples of the Polyethylene Oxide (PEO) solution (Miyamoto [3]).

In the present study, we carry out an experiment for the simultaneous visualisation of flowing entangled polymers, streamwise vortices and low-speed streaks in a turbulent channel flow to examine the direct interaction between the polymers and the small-scale coherent structures.

2 Experimental method

The test section was the fully developed region of a turbulent water flow in a horizontal channel of 2 m in length, 2 cm in height and 16 cm in width. The Reynolds number based on the centerline velocity and the duct height was 5300.

Hydrogen bubbles were used to visualise the core of hairpin vortices because the bubbles tend to be concentrated inside the vortical motion. A platinum wire for the electrode of the bubble generation was stretched between the upper and lower walls.

An aqueous solution of Rhodamine B was injected into the linear sublayer from a slot in the bottom wall to enable visualisation of the low-speed streaks. The slot was 1.0 mm wide in the streamwise direction, and the outlet was set at 45 degrees to the wall.

We developed a new technique for the visualisation of highly-entangled PEO dissolving in water using an acrylic fluorescent colour. Small pieces of colour (hereafter called colour particles) were stuck on the polymer powders through the drying of the colour. The colour particles were found to be inside the entangled polymers in observation for the dissolution of the powders in quiescent water with a microscope. A dilute solution (200ppm or 300ppm by weight) of PEO with the colour particles was injected from the other upstream slot into the buffer region. This method is similar to that used in ref.[1].

The green light of a YAG laser, expanded to a light slab of 13 mm in thickness, illuminated the main flow from above the duct. Images of the reflected light from the hydrogen bubbles and the fluorescence of Rhodamine B and the colour particles were captured through the channel side-wall by a CCD colour video camera (Sony DXC-9000). The signals from the camera were directly recorded in a PC through an image-grabber. The streamwise dimension of the observing area was $675\nu/u_\tau$. Each pixel covered a square $1.1\nu/u_\tau \times 1.1\nu/u_\tau$.

A particle-tracking-velocimetry (PTV) method was adopted for obtaining the velocities of the hydrogen bubbles and the colour particles. The images of the bubbles and the particles were covered with several pixels, which is suitable for PTV. The velocity was calculated from the displacement of each bubble or particle between five successive images.

3 Results and Discussion

Figures 1(a) and 1(b) show typical examples of the original image and the extracted red signal from the original in the case without polymer injection, respectively. The bright dots in Fig.1(a) are the hydrogen bubbles released from the wire electrode. The aligned bubbles are found in the central part of this figure ($x^+ \approx 250$). The angle of tilt of these bubbles is about 60 degrees to the horizontal. The velocity fluctuations of these bubbles from the mean velocity at $y^+ = 20$ were $u^+ = -0.57$ and $v^+ = 0.80$. This shows an upward eruptive flow in the upstream direction. This flow is similar to the outward flows induced by hairpin vortices (Zhou *et al.*[4]).

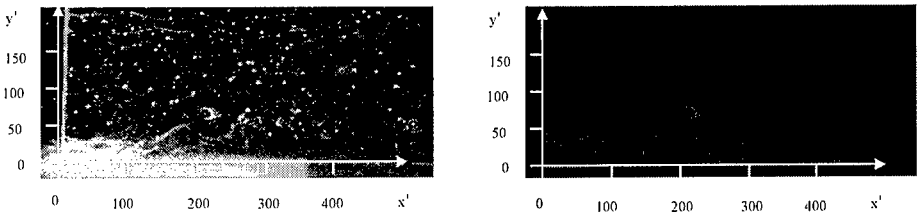
The bright area in Fig.1(b) shows the injected Rhodamine B, which is not clear in the original image in Fig.1(a). The dye reached $y^+ = 100$ after the passage of the aforementioned vortex. This represents an ejection of the low-speed streak. It was observed that the ejection was almost always followed by the passage of a streamwise vortex. The extraction of the red signal is effective for measuring the dynamics of streaks with the streamwise vortices.

Figures 2(a) and 2(b) show typical examples of the original image and the extracted red signal in the case with polymer injection. The dots in Fig.2(b)

indicate the fluorescence from the colour particles stuck on the polymers. The dimension of most entangled polymers, estimated from the distance of the dots moving together in a group, was in the range of 1.1 - 1.8 mm (16 - 27 viscous wall units).

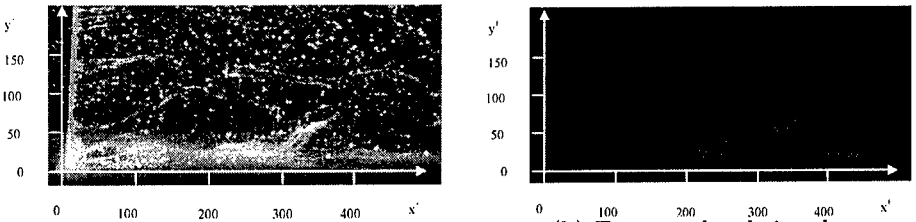
Attenuation was observed for the dynamics of the streamwise vortex and the low-speed streak due to the polymers very close to the vortex in this case. The angles of tilt of the vortex was lower than that in the case without polymer injection. The velocity fluctuations of the bubbles from the mean value at y^+=25 were $u^+ = -1.1$ and $v^+ = -0.10$. The dye reached at the highest $y^+ = 80$.

More noticeable attenuation was occasionally observed for the upward flow and the lift-up of the streaks, in particular small-scale streaks (See Figs. 3(a) and 3(b)). Aligned bubbles were not observed. Some groups of the entangled polymers happen to be transported near the streak. It is expected that the kinetic energy of the eruptive flow or small-scale streaks is not enough to lift up the polymers. This direct interaction between the entangled polymers and the coherent structures is considered to be one of the reasons for the attenuation of the dynamics of streaks.



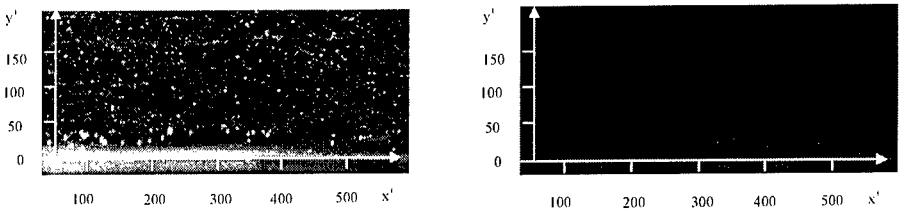
(a) Original image (b) Extracted red signal

Figure 1 Images of hydrogen bubbles and Rhodamine B



(a) Original image (b) Extracted red signal

Figure 2 Images of hydrogen bubbles,Rhodamine B and colour particles



(a) Original image (b) Extracted red signal

Figure 3 Images of hydrogen bubbles,Rhodamine B and colour particles (highly attenuated CSs)

4 Conclusions

- The new visualisation method of entangled PEO, the low-speed streaks and the streamwise vortices in a turbulent channel flow by using the colour, the Rhodamine B and the hydrogen bubbles, respectively, is effective for measuring the direct interaction between the polymers and the coherent structures.
- The entangled polymers in buffer region attenuate the eruptive flow induced by the streamwise vortices and the ejection of low-speed streaks. This may be one of the reasons for the attenuation of the dynamics of streaks.

The authors acknowledge Y. Taseda at Kyoto Inst. of Tech. for his assistance. This study is supported by the Ministry of Education, Science, Sports and Culture of Japan through the Grant-in-Aid for Scientific Research(No. 11650222).

References

[1] W. G. Tiederman, T. S. Luchik, and D. G. Bogard. Wall-layer structure and drag reduction. *J. Fluid Mech.*, 156:419–437, 1985.

[2] Y. Hagiwara, H. Hana, M. Tanaka, and S. Murai. Numerical simulation of the interactions of highly-tangled polymers with coherent structure in a turbulent channel flow. *Turbulence and Shear Flow -1*, 331–336, 1999.

[3] H. Miyamoto. Experiment for visualization of polymer chains in high-polymer aqueous solutions under shear flow regions (in Japanese) *Trans. Japan Soc. Mech. Eng., Ser. B*, 60:2038–2043, 1994.

[4] J. Zhou, R. J. Adrian, S. Balachandar, and T. M. Kendall. Mechanisms for generating coherent packets of hairpin vortices in channel flow. *J. Fluid Mech.*, 387:353–396, 1999.

XVI

Turbulent Reacting Flows

ADVANCES IN TURBULENCE VIII
Proceedings of the Eighth European Turbulence Conference
C. Dopazo et al. (Eds.)
© CIMNE, Barcelona 2000

Modeling of Mixing Processes in non–Isothermal and Combusting Flows

R. P. Lindstedt and E. M. Váos

Department of Mechanical Engineering
Imperial College of Science, Technology and Medicine
Exhibition Road, London SW7 2BX, UK

Contact e-mail: p.lindstedt@ic.ac.uk

1 Introduction

The present paper considers a transported *pdf* approach for the calculation of scalar statistics. The advantages of such methods are significant (e.g. the straightforward calculation of reaction related quantities) and have been discussed in a numbers of reviews (e.g. [2]). A common feature of transported *pdf* methods within a single–point single–time context is that modelling approximations are required to account for *mixing* processes. The latter essentially amount to transport of the *pdf* in composition space. The evolution of the joint scalar *pdf* is here examined through the use of (Lagrangian) stochastic particle methods. Two distinct cases are considered. The first features a thermal mixing layer [6] and the second considers the propagation of premixed turbulent flames. Perhaps surprisingly, no systematic study of the effects of closures for the mixing term has been performed for the latter. The standard models considered here include the classical Linear–Mean–Square–Estimate (LMSE) model (*cf.* [3]) and non–linear integral models [3, 5]. More sophisticated approaches covered include the binomial Langevin model [4]. The Langevin equation, originally proposed to simulate Brownian motion, is intuitively attractive and can readily be recovered from the Fokker–Planck equation for the special case where the drift coefficient is a linear function of the state variable and the diffusion coefficient is constant.

2 Results

Results for the cases considered here have been obtained through the use of both gradient diffusion and second moment based closures for the turbulent transport of the *pdf* in physical space. The former is based on the classical eddy diffusivity/two-equation type turbulence model, while the latter features the Generalised Langevin Model coupled with an LMSE type formulation for the

conditional turbulence intensity terms in the *pdf* equation [2, 7]. The application of different mixing models in conjunction with a gradient diffusion closure approximation leads to difficulties in the accuracy of predictions for the thermal mixing layer (Figure 1). The evolution of cross-stream profiles confirms that the observed discrepancies can be directly attributed to the transport closure. Evidently, the gradient diffusion approximation in combination with the standard value for the turbulent Prandtl number ($\sigma_\theta = 0.7$) results in an underprediction of the turbulent scalar flux in the lateral direction. In practice, compensation is typically achieved by an *expedient* case dependent re-assignment of the value of the turbulent Prandtl number (Figure 1). Results obtained for the thermal mixing layer also illustrate the need for accurate predictions of higher moments (e.g. the skewness), as indicated by Figures 2 and 3, and show that the modified Curl's model does not perform well in this respect. The result is of direct practical interest given the prevalent application of the latter.

In the present work flame structures are resolved using 200 cells with an *expected* number of 1600 weighted particles per cell ($N \simeq 320\text{x}10^3$). The thermochemistry is implemented by means of a single scalar progress variable and the instantaneous scalar reaction rate source term is extracted from unstrained CH_4/Air calculations with detailed chemistry. Results obtained for premixed turbulent flames show that even integral properties, such as the turbulent burning velocity, are strongly affected by both the choice of mixing model and the closure for the transport of the *pdf* in physical space as shown in Table 1. [1] It may thus be readily observed that under *all* conditions a gradient diffusion closure will result in reduced burning velocity values. The latter observation, combined with the unambiguous manner in which *pdf* methods allow the incorporation of scalar reaction rates, provides further evidence in relation to the concerns expressed regarding the effectiveness of gradient diffusion closures for premixed turbulent flames [7]. An example of the predictive capability of the more accurate models is shown in Figure 4.

3 Conclusions

The present study has shown that the characteristics of mixing models and closure approximations for the transport of the *pdf* in physical space have a significant influence on prediction quality. Specifically, the use of gradient approximations in the context of non–isothermal and combusting flows entails significant accuracy problems. The present study also outlines the significance of the mixing model in the evolution of the flame structure in cases where the transport of the *pdf* in the scalar space is essentially dominated by the reaction rate term. Indeed, the interaction between the mixing model and the scalar reaction rate

[1] The results shown here have been obtained through the use of a standard constant time scale ratio closure for the scalar time scale with $C_\phi = 2$. The *absolute* value of predicted turbulent burning velocities is affected by this choice. However, the *relative* behaviour with respect to mixing model and turbulent transport closure variations – examined here – is *not*.

Model	Gradient Diffusion	Second Moment Closure
Binomial Langevin [4]	1.24	1.62
Binomial Sampling [3]	0.75	1.39
Modified Curl's [5]	1.32	1.65
LMSE [4]	0.54	0.84

Table 1: Mixing model and turbulent transport closure effects on the computed turbulent burning velocity (u_T) using a "standard" constant time scale ratio. Experimental data for u_T lead to expected values around 2 m/s for the conditions considered. ($u' = 1$ m/s, $L_T = 20$ mm, $C_\phi = 2$ and $u_L = 0.385$).

is mainly confined to a region close to the "cold" boundary of the scalar space. The predominance of the reaction rate source term at high Damköhler numbers induces rapid convection towards the burnt state and thus an (almost) bimodal shape for the scalar *pdf*. A critical aspect can thus be found in the combustion initiation process. Accordingly, the predicted burning velocities will depend on the structure of turbulent transport model in scalar space (i.e. the structure of the prescribed *mixing* transition density function) and on the magnitude of the relevant (mixing) time scale. The observed differences between the LMSE and the binomial Langevin model may therefore be readily explained since the former erroneously induces only convection and not diffusion in the *pdf* scalar space. Furthermore, for the case of the binomial sampling model, homogeneous binary mixing studies may be used to show that the diffusion contribution is essentially non-operative for close to bimodal *pdf* shapes. It may be noted that the modified Curl's model performs reasonably well for source term dominated problems, but fails in the prediction of transport related quantities. The binomial Langevin model yields excellent results for the cases considered here.

References

[1] Cheng, R.K. and Shepherd, I.G. (1991), *Combust. Flame* **85**, pp. 7–26.

[2] Pope, S.B. (1985), *Prog. Energy & Comb. Sci.* **11**, pp. 119–192.

[3] Valiño, L. and Dopazo, C. (1990), *Physics of Fluids A* **2(7)**, pp.1204–1212.

[4] Valiño, L. and Dopazo, C. (1991), *Physics of Fluids A* **3(12)**, pp. 3034–3037.

[5] Janicka, J., Kolbe, W. and Kollmann, W. (1979) *Journal of Non-equilibrium Thermodynamics* **4**, p. 27.

[6] Ma, B.K. and Warhaft, Z. (1986), *Physics of Fluids A* **29(10)**, pp. 3114–3120.

[7] Lindstedt, R.P. and Vaos, E.M. (1999), *Combust. Flame* **116**, pp. 461–485.

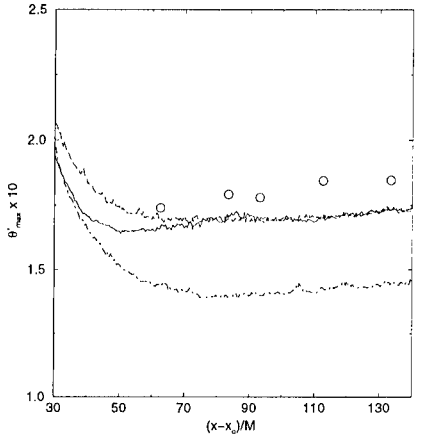


Figure 1: Predictions of the maximum normalised temperature fluctuation intensity using the binomial Langevin model. (∘) Measurements by Ma & Warhaft [6]. (—) Second moment closure; (– · –) Gradient diffusion closure with $\sigma_\theta = 0.7$ and (– –) $\sigma_\theta = 0.35$.

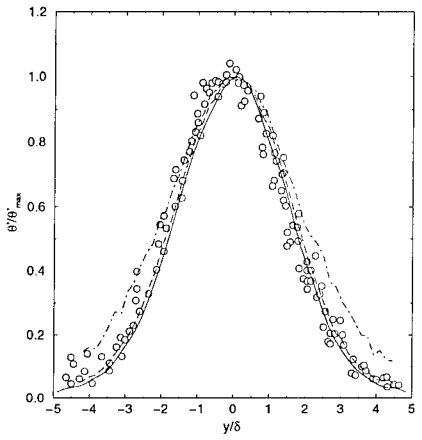


Figure 2: Predictions of normalised cross–stream temperature fluctuation intensity profiles using a second moment closure. (∘) Measurements by Ma & Warhaft [6]. (—) binomial Langevin model; (– · –) Modified Curl's model; (– –) binomial sampling model.

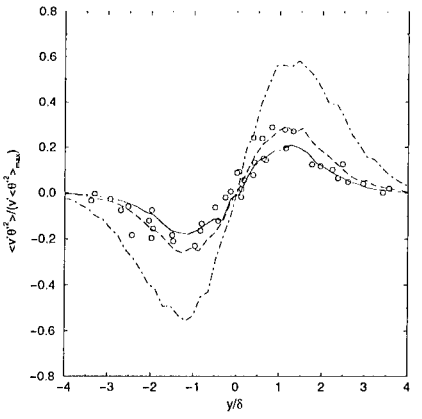


Figure 3: Normalised turbulent flux of the scalar variance. Lines and symbols as shown in Figure 2.

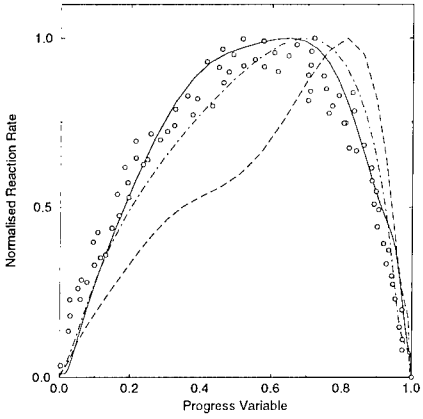


Figure 4: Normalised mean reaction rate profiles in scalar space (∘) [1]. Lines as shown in Figure 2.

ADVANCES IN TURBULENCE VIII
Proceedings of the Eighth European Turbulence Conference
C. Dopazo et al. (Eds.)
© CIMNE, Barcelona 2000

Probability Density Function Modelling of an Axisymmetric Combustion Chamber

W.P. Jones and R. Weerasinghe

Department of Mechanical Engineering
Imperial College of Science Technology and Medicine
London SW7 2BX, United Kingdom.

Contact e-mail: w.jones@ic.ac.uk

1 Introduction

Probability Density Function (pdf) transport equation methods integrated within a conventional CFD flow solver represent a rational approach for the study of turbulent combustion. The major attraction of this method is that the terms associated with chemical reaction appear in closed form, leaving only 'molecular' mixing and turbulent transport terms to be modelled. There has been considerable development in the past three decades in pdf methods and reviews can be found in Kollmann [4] and Jones and Kakhi [3].

In the present work a Lagrangian stochastic particle method is used to solve the pdf equation with the velocity field being obtained from a conventional RANS $k-\epsilon$ approach. In the pdf equation turbulent transport is treated with a conventional $k-\epsilon$ gradient transport assumption, and the Linear Mean Square (LMSE) estimation closure is used to 'molecular' mixing. The chemical reaction is described by the four step global mechanism of Jones and Lindstedt [2]. The method is applied to an axisymmetric swirl stabilised combustor burning propane, and the results are compared with experimental data and the results obtained with a conserved scalar laminar flamelet model.

2 The Governing Equations

A transport equation for the pdf can be derived using principles of mass, momentum and energy conservation and for single-phase, gaseous, low Mach number,

high Reynolds number combustion can be written:

$$\overline{\rho}\frac{\partial \tilde{P}(\underline{\psi})}{\partial t} + \overline{\rho}\tilde{U}_i\frac{\partial \tilde{P}(\underline{\psi})}{\partial x_i} + \frac{\partial}{\partial \psi_\alpha}[\overline{\rho}\dot{\omega}_\alpha(\underline{\psi})\tilde{P}(\underline{\psi})] = -\frac{\partial}{\partial \psi_\alpha}\left[\left\langle \frac{\partial J_i^\alpha}{\partial x_i}\middle|\underline{\psi}\right\rangle \tilde{P}(\underline{\psi})\right] - \frac{\partial}{\partial x_i}[\overline{\rho} < u_i''|\underline{\psi} > \tilde{P}(\underline{\psi})] \quad (1)$$

where $\tilde{P}(\psi_1, \ldots, \psi_{N+1}, \mathbf{x}, t)$ is the density weighted probability function. In equation (1) the first two terms represent the rate of change and mean convection of the pdf while the third term involves the net rate of formation, $\dot{\omega}_\alpha$ through chemical reaction. These three terms appear in exact and closed form. The terms in the right hand side of the equation comprise the turbulent transport of pdf and molecular mixing. These terms involve conditional expectations and must be modelled if the equation is to be closed.

Modelling

Turbulent transport is represented using a gradient transport hypothesis,

$$-\frac{\partial}{\partial x_k}\overline{\varrho} < u_k''|\underline{\phi} = \psi > \tilde{P}(\underline{\psi}) \approx \frac{\partial}{\partial x_k}\left[\frac{\mu_t}{\sigma_t}\frac{\partial \tilde{P}(\psi)}{\partial x_k}\right]. \quad (2)$$

where the turbulent viscosity μ_t is obtained from the $k-\epsilon$ model and where $\sigma_t = 0.7$.

For chemical reaction the global hydrocarbon-air scheme of Jones and Lindstedt is used:

$$\begin{aligned} C_3H_8 + \frac{3}{2}O_2 &\rightarrow 3CO + 4H_2, \\ C_3H_8 + 3H_2O &\rightarrow 3CO + 7H_2, \\ H_2 + \frac{1}{2}O_2 &\rightleftharpoons H_2O, \\ CO + H_2O &\rightleftharpoons CO_2 + H_2. \end{aligned} \quad (3)$$

Molecular mixing is modelled by the Linear Mean Square Estimation (LMSE) closure [1].

3 Solution Method

To obtain the fields of mean velocity, turbulence energy and dissipation rate the computer code BOFFIN was used (the code utilises a boundary fitted general curvilinear coordinate system in conjunction with a relatively standard finite-volume method. The Lagrangian form of the modelled pdf transport equation

is utilised and this is approximated by a factorisation scheme so that transport (convection and diffusion), chemical reaction and mixing can be applied separately. The pdf is then represented by an ensemble of particles and the discrete difference approximation is then simulated stochastically by a Lagrangian method in which particle positions are tracked as they move through the field according to:

$$d\mathbf{x} = \left(\tilde{\mathbf{U}} + \frac{\nabla \mu_t}{\overline{\rho}}\right) dt + \sqrt{2\frac{\mu_t}{\overline{\rho}} dt}\boldsymbol{\xi} \tag{4}$$

Here, $\boldsymbol{\xi}$ is a standard normally distributed random number vector.

The particles are allowed to react according to the reaction model, for which purpose the chemistry is tabulated

For mixing, particles are first sorted into their appropriate control volumes and mixed according to the LMSE closure whereby all particles properties are changed according to:

$$\frac{d\underline{\phi}^{(p)}}{dt} = -\frac{C_d}{2}\frac{\epsilon}{k}\left(\underline{\phi}^{(p)} - \langle\underline{\phi}\rangle\right) \tag{5}$$

4 Conclusions

The results obtained with the pdf equation method are compared with measurements and with calculations using the conserved scalar laminar flamelet model in figure 1. As can be readily observed and consistent with experiment the pdf method gives rise to a 'lifted' flame with combustion being stabilised some distance downstream of the fuel injection. In contrast the conserved scalar model predicts flame stabilisation at the fuel injection point. Figure 2 shows radial profiles of temperature and CO_2 at various axial positions through the combustor. The discrepancies which are evident are predominantly associated with limitations in the reaction mechanism being used, which incorrectly allows reaction well beyond the rich flammability limit.

References

[1] Dopazo, C. and O'Brien, E.E. An approach to the auto-ignition of a turbulent mixture. *Acta Astronautica*, 1:1239–1266, 1974.

[2] Jones, W.P. and Lindstedt, R.P. Global Reaction Schemes for Hydrocarbon Combustion. *Combustion and Flame*, 73:1–15, 1988.

[3] Jones, W.P. and Kakhi, M. Mathematical Modelling of Turbulent Flames. *Unsteady Combustion, Kluwer Academic Publishers*,1996.

[4] Kollmann, W. The PDF approach to turbulent flow. *Theoretical and Computational Fluid Dynamics*, 1:249–285, 1990.

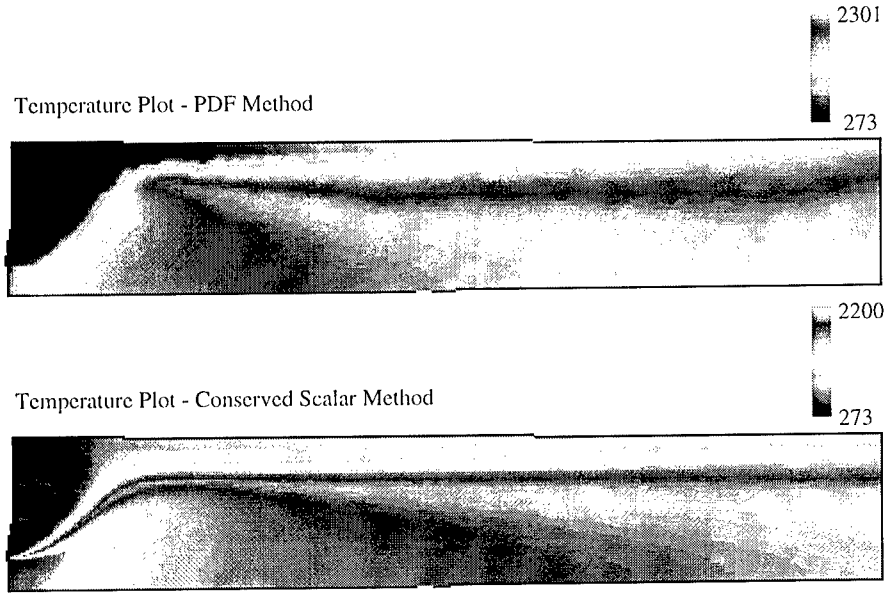
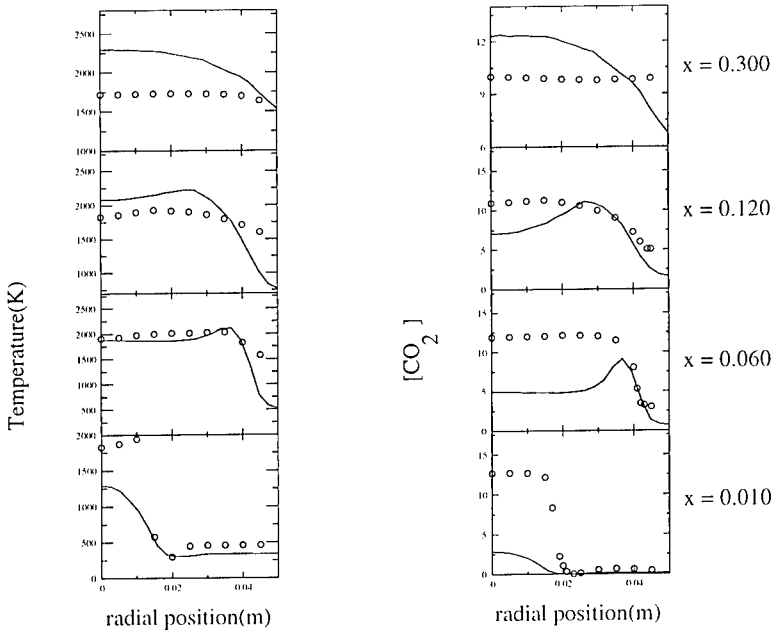


Figure1: Comparison of Temperature Plots



o measurements — PDF method

Figure 2:Temperature and CO profiles at different downstream positions

ADVANCES IN TURBULENCE VIII
Proceedings of the Eighth European Turbulence Conference
C. Dopazo et al. (Eds.)
© CIMNE, Barcelona 2000

Implementation and Validation of an Adaptive Particle PDF Transport Method

M. Pfitzner[1] and I. Romaschov[2]

[1]Methods and IT Systems, Rolls-Royce Deutschland GmbH
Eschenweg 11, D-15827 Dahlewitz, GERMANY
[2]Geschaeftsfeld Systeme, IVU Traffic Technologies AG
Bundesallee 88, D-12161 Berlin, GERMANY

Contact e-mail: michael.pfitzner@rolls-royce.com

1 Introduction

The design of low-emission combustors for aeroengines requires sophisticated CFD simulation tools to predict the gaseous emissions of combustor configurations with a high level of confidence.

The current industry standard for combustion modelling of diffusion flames in commercial CFD codes is a fast equilibrium or flamelet chemistry model coupled to an assumed probability density function (pdf) of the mixture fraction. Turbulence is modelled using two-equation k-ϵ turbulence model(s). This approach usually results in a fair prediction of temperature and NO_x emissions, but is unable to predict partially burnt combustion products like CO. More accurate NO_x predictions require higher precision in the prediction of the temperature field. The accuracy of the simulation of turbulent combustion can be significantly improved over the conventional assumed PDF method by solving a PDF transport equation for a small number of reaction progress variables.

In the current work a pdf transport algorithm using an adaptive number of pdf particles is validated using several different generic flame configurations with different gaseous fuels. The code is then applied to a 3-D simulation of the combusting flow in the pilot zone of a staged aeroengine research combustor to demonstrate the 3-D capability of the method and to explore the CPU and storage requirements relative to more conventional combustion models.

2 Implementation of PDF transport method

The composition PDF transport equation is solved using a Monte-Carlo particle method. The method locates the pdf particles in the center of the each compu-

tational cell and convection is modelled statistically (Popes 1^{st} algorithm) [1].

The method has been generalized for use of a variable number of weighted PDF particles in each CFD cell [2]. Conventionally a constant number of PDF particles of unity weight in each cell is used. Reduced chemistry is represented by an adaptive multidimensional table. The PDF particles in a computational cell representing by the same tabulation cell in composition space of reaction progress variables are lumped together, combining the weights of all lumped particles.

The method has been shown to give similar results to the conventional method with a constant number of particles within the statistical error and to be considerably less demanding in terms of computational and storage [3].

In its present form using an Eulerian algorithm for the PDF particle transport the method is strictly correct only on orthogonal grids. This puts constraints on the grid generation, particularly for 3-D cases. The pdf transport combustion model is loosely coupled to a commercial finite volume CFD code (CFD-ACE) and has been validated using several different laboratory diffusion flames, for which accurate data sets are available. The test cases encompass several different gaseous fuels [3].

The Jones-Lindstedt reduced chemistry mechanism [4] with 3 reaction progress variables (plus mixture fraction) is used. The pdf transport code has been adapted to use ILDM tables [5] provided by the University Heidelberg.

3 Results from Test Cases

The comparison of the validation cases with the experimental data shows in all cases and without tuning of parameters a consistent improvement of the prediction of the temperature and carbon monoxide (CO) fields. The improvement is small in flames at high Damkoehler numbers, where the conventional assumed mixture fraction pdf / fast chemistry approach already yields good agreement. The largest improvement is achieved in flames with medium strain like the Masri L and B flames. An overview of the local number of PDF particles in the Masri flame is given in Figure 1. At very large strain, where there is considerable local extinction, the agreement between the pdf transport method and the experiment deteriorates although there is still a large improvement over assumed pdf / fast chemistry methods. Results of similar quality are achieved for methane and propane flames.

In flames with recirculation zones it was found that the RNG k-ϵ turbulence model yields a better agreement with experiment than the standard k-ϵ model. In a disc-stabilised diffusion flame [6] the agreement with the combusting experimental flowfield is considerably improved by the pdf transport method. In this case the pdf transport method predicts correctly two stagnation points on the axis of symmetry which are not present in the fast chemistry calculation. An example of the improvement of the temperature and CO fields in case of the Garreton disc-stabilized flame is shown in Figure 2.

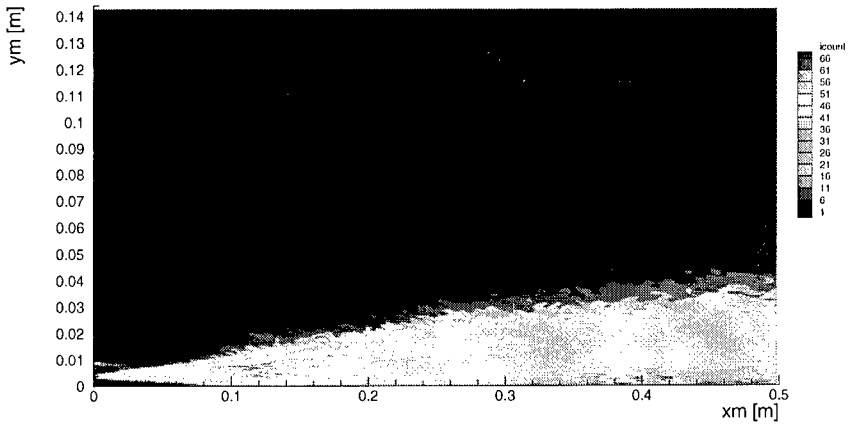


Figure 1: Masri Flame: Distribution of number of adaptive PDF particles.

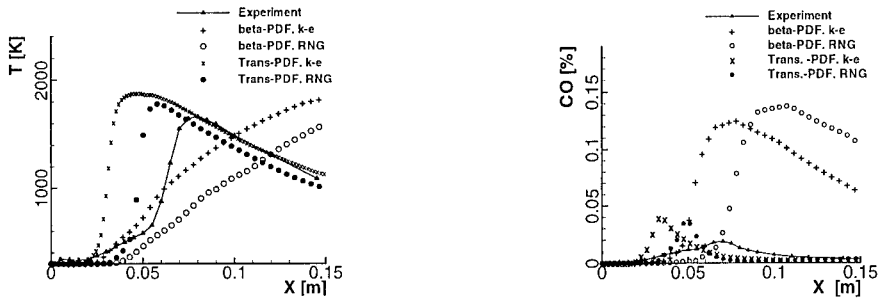


Figure 2: Garreton case: Comparison of temperature (left) and and CO on axis of symmetry.

The incorporation of the Heidelberg ILDM chemistry (using 2 reaction progress variables) results in a considerably increased risk of numerical extinction of the flame. Portions of composition space where no ILDM could be found lead to large errors in the CO field in some test cases. In parts of the flames where the ILDM data are available the agreement of the CO field with experiment is generally improved by the ILDM reduced chemistry.

The CFD code using the adaptive pdf particle method has been applied to the pilot zone of a staged research combustor. The computational grid consisted of approx. 80,000 nodes and needed 3 days to converge on a sgi R10000 workstation. This 3-D computation was only feasible with the adaptive particle method, which requires typically 5 times the resources (CPU time and storage) compared to the

conventional assumed PDF method.

4 Conclusions

- An implementation of a PDF transport method using an adaptive number of PDF particles has been successfully validated for a number of generic diffusion flame test cases
- In all cases the prediction of the temperature and CO fields are improved compared to an assumed pdf equilibrium chemistry method
- More work is required to improve the validity of the ILDM tables in all chemically relevant areas and the applicability on non-orthogonal grids before application in industrial configuration with confidence is possible

It is gratefully acknowledged that part of this work has been funded by the European Commission as part of BRITE-EURAM project BE95-1927 under contract number BRPR-CT95-0106.

References

[1] S.B. Pope. A Monte Carlo Method for the PDF Equation of Turbulent Reactive Flow. *Comb. Sci. Techn.* 25: 159, 1981.

[2] A.D. Leonard,F. Dai. Applications of a Coupled Monte Carlo PDF/Finite Volume CFD Method for Turbulent Combustion. *AIAA paper*, AIAA-94-2904, 1994.

[3] M. Pfitzner, A. Mack, N. Brehm, A.D. Leonard,I. Romaschov. Implementation and Validation of a PDF Transport Algorithm with Adaptive Number of Particles in Industrially Relevant Flows. *ASME Paper PVP-Vol.397-1* Book No. G1126A - 1999: 93–104, 1999.

[4] W. P. Jones, R. P. Lindstedt. Global Reaction Schemes for Hydrocarbon Combustion. *Combust. Flame*, 73:233–249, 1988.

[5] U.A. Maas, S.B. Pope. Simplifying chemical kinetics: Intrinsically low-dimensional manifolds in composition space. *Combust. Flame* 88 (3/4):239–264, 1992.

[6] D. Garreton, O. Simonin (Eds.). First workshop on aerodynamics of steady state combustion chambers and furnaces, Chatou, 1994.

ADVANCES IN TURBULENCE VIII
Proceedings of the Eighth European Turbulence Conference
C. Dopazo et al. (Eds.)
© CIMNE, Barcelona 2000

Simulation of turbulent spray combustion in a full-scale gas turbine combustor

S. Menon [1]

[1]School of Aerospace Engineering, Georgia Institute of Technology
Atlanta, Georgia 30332, USA

Contact e-mail: suresh.menon@aerospace.gatech.edu

1 Introduction

The structure of complex three-dimensional, swirling fuel-air mixing layers formed in a real gas combustor is very difficult to resolve using current experimental and numerical methods. Here, large-eddy simulation (LES) is used to simulate spray combustion. In LES, scales larger than the grid size are computed using a time- and space-accurate scheme, while the effect of the unresolved smaller scales (assumed to be isotropic) on the resolved motion is modeled using an eddy viscosity based subgrid model. This approach is acceptable for momentum transport since all the energy containing scales are resolved and the unresolved scales primarily provide dissipation of the energy transferred from the large scales. However, these arguments cannot be extended to reacting flows since, for combustion to occur, fuel and oxidizer species must first mix at the molecular level. Since, this process is dominated by the mixing and molecular diffusion processes in the small-scales, ad hoc eddy diffusivity concepts cannot be used except under very specialized conditions. To deal with these distinctly different modeling requirements, a new subgrid mixing and combustion model has been developed that allows for proper resolution of the small-scale scalar mixing and combustion effects [1, 2, 3]. This subgrid model is implemented within the framework of a LES approach based on an Eulerian-Lagrangian Stochastic Separated Flow (SSF) model which is capable of quantitative prediction of the effects of spray [4, 5, 6].

In this paper, application of SSF based LES modeling of spray mixing and combustion in a full-scale gas turbine engine (General Electric DLE LM 6000 derivative) is discussed.

2 Formulation

In the SSF-LES approach, the droplets are tracked in a Lagrangian manner within the Eulerian gas flow field. Full two-way coupling is included via source terms. However, a key limitation of this approach is that (due to resource constraints) only a limited range of droplet sizes are tracked and droplets below an ad hoc (pre-specified) cut-off size are assumed to vaporize and become fully mixed instantaneously. This approach has been demonstrated to be seriously flawed [5] and it has been shown that the new subgrid formulation employed here correctly takes into account the effect of all droplets below the cutoff.

In the subgrid combustion approach, all local scalar processes are simulated within a subgrid domain that resides in each LES cell. The subgrid domain is one-dimensional and is oriented in the direction of the scalar gradient. Within this 1D domain, all turbulent scales are fully resolved and the reaction-diffusion processes occur deterministically (thus, no closure for diffusion and chemical reaction rates is needed). Concurrent to this deterministic evolution of the reaction-diffusion processes, turbulent mixing of the scalars by scales ranging from the grid size to the smallest eddy (i.e., Kolmogorov scale) is explicitly implemented as a stochastic stirring process. Thus, both turbulent stirring by small-scale eddies and reaction-diffusion processes occur within each LES cell. Advection of the scalar fields across LES cells (due to eddies larger than the grid size) is carried out using a Lagrangian transport scheme. Further details of this method is given in cited references.

In the two-phase approach, the subgrid model includes the effect of the phase change and the vaporization process. The two-phase subgrid model employs a void fraction approach whereby, the fraction of the liquid phase is determined from the number of particles that drop below the cutoff scale. When combined with the SSF-LES approach, this simulation model is capable of capturing the effect of phase change and fuel-air mixing as a function of droplet volume irrespective of the droplet size. In contrast, conventional SSF approach fails to account for fuel vaporization and mixing by droplets that are below the cutoff size. Additional details of the new subgrid model is given elsewhere.

3 Results and Discussion

Analysis of the subgrid mixing process in two-phase temporal mixing layers has been carried out to investigate the impact of the cutoff size on product formation under both infinite and finite rate conditions. Figures 1 and 2 show respectively, the product density variation across the mixing layer in the conventional LES (in which droplets below cutoff are assumed to vaporize and mix instantaneously) and the new subgrid LES (denoted LES-LEM) for the infinite rate case. It can be seen that in the conventional case, increasing the cutoff size drastically changes the product formation which is incorrect since the same amount of fuel is being vaporized. However, the new approach (Fig. 2) consistently predicts the

same product formation except when the cutoff size is increased to very large values. There is a significant computational advantage of this approach since increasing the cutoff size by a factor of 4 decreases the computational cost by a factor of around 4 in-spite of the increase in computational effort due to the new subgrid model. This suggests that using an efficient parallel solver, LES-LEM of two-phase flows could be simulated in a cost effective manner.

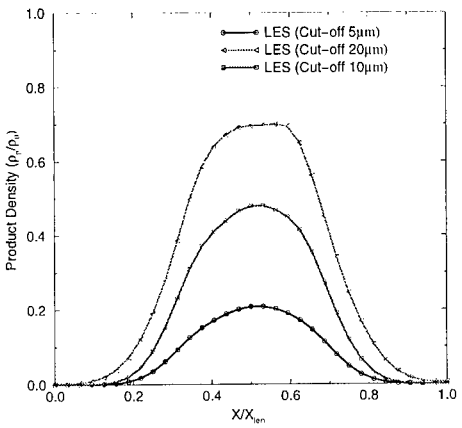


Figure 1: Product density in a temporal mixing layer as predicted by a conventional LES

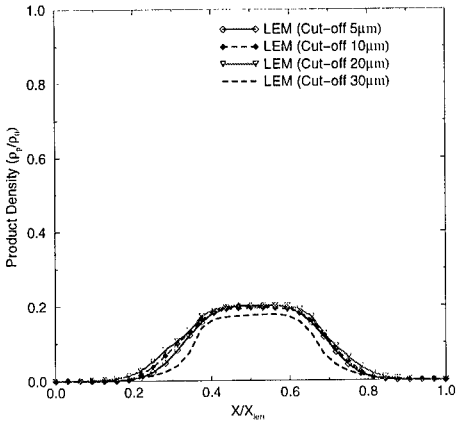


Figure 2: Product density in a temporal mixing layer as predicted by the LES-LEM

Simulations of spray mixing and combustion using both closures are being carried out in a full scale GE combustor. In this combustor, a highly swirling air flow enters the combustor at a very high Reynolds number (350,000 based on inlet diameter and axial velocity). A (log-normal) spray of methanol is injected in a 45-degree cone from the axis at the entrance of the combustor. Infinite rate kinetics with heat release is investigated. Figures 3 and 4 show respectively, the instantaneous temperature and droplet pattern in the combustor.

4 Conclusions

In this paper, the application of a new subgrid based spray vaporization and mixing model within a SSF-LES methodology is reported. It has been shown that the new subgrid model correctly predicts the product formation in shear layers even when the cutoff size is increased. Subsequently, spray vaporization, fuel-air mixing and heat release effects in a full-scale gas turbine combustor is studied to determine the impact of properly accounting for small-scale mixing effects.

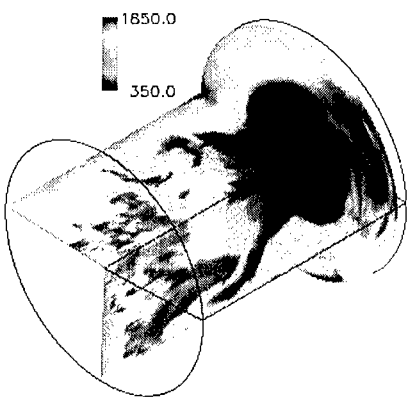


Figure 3: Instantaneous temperature contours in the GE LM 6000

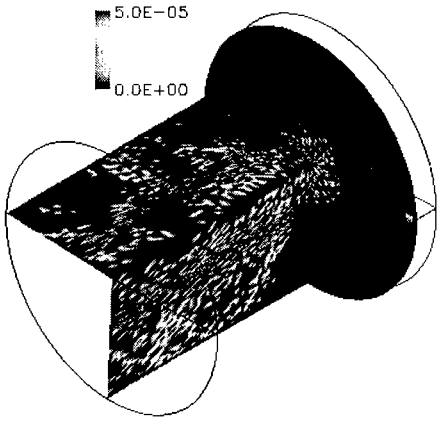


Figure 4: Instantaneous droplet spray distribution in the GE LM 6000

References

[1] S. Menon, P. A. McMurtry, and A. R. Kerstein. A linear eddy mixing model for large eddy simulation of turbulent combustion. In B. Galperin and S. Orszag, editors, *LES of Complex Engineering and Geophysical Flows*. Cambridge University Press, 1993.

[2] S. Menon and W. Calhoon. Subgrid mixing and molecular transport modeling for large-eddy simulations of turbulent reacting flows. *Twenty-Sixth Symposium (International) on Combustion*, pages 59–66, 1996.

[3] V. K. Chakravarthy and S. Menon. Modeling of turbulent premixed flames in the flamelet regime. In *Turbulence and Shear Flow -I, First International Symposium*, pages 189–194. Begel House, 1999.

[4] S. Menon and S. Pannala. Subgrid modeling of unsteady two-phase turbulent flows. *AIAA Paper No. 97-3113*, 1997.

[5] S. Menon and S. Pannala. Subgrid combustion simulations of reacting two-phase shear layers. *AIAA Paper No. 98-3318*, 1998.

[6] S. Menon and S. Pannala. Parallel simulations of turbulent reacting sprays. *AIAA-99-3438*, 1999.

ADVANCES IN TURBULENCE VIII
Proceedings of the Eighth European Turbulence Conference
C. Dopazo et al. (Eds.)
© CIMNE, Barcelona 2000

The Impact of Buoyancy and Flame Structure on Soot and Radiation Emissions from a Turbulent Flame

W. Kollmann[1], J. Auston[1], R.L. Vander Wal[2] and I.M. Kennedy[1]

[1]MAE Dept, University of California
Davis, CA 95616, USA
[2] NCMR at NASA-Glenn Research Center
21000 Brookpark Rd., Cleveland OH 44135, USA

Contact e-mail: imkennedy@ucdavis.edu

1 Introduction

It is hypothesized that the spatial structure of a turbulent nonpremixed flame plays an important role in determining the emissions of radiative energy, soot and NO_x from a combustor. This structure, manifested in the two point statistics, is influenced by buoyancy. Radiation, soot and NO_x emissions are the cumulative result of processes that occur throughout a flame. Turbulence models generally rely on a single point closure of the appropriate time averaged equations. Hence, spatial information is lost and needs to be modeled using solution variables such as turbulence kinetic energy and dissipation rate, often with the assumption of isotropy. However, buoyancy can affect the physical structure of turbulent flames and can change the spatial extent of soot bearing regions. Experiments in the NASA Glenn drop tower and LES simulations are applied for the investigation of buoyancy effects.

2 Experiments

Nonpremixed flames at atmospheric pressure are established on a 1.6 mm I.D. nozzle (length/ diameter $>$ 20) with a nonpremixed pilot flame. A regulator and fine control valve are adjusted using a mass flow meter to deliver a known fuel flow rate. The ethylene or acetylene flow through the central gas-jet tube is about 2.6 L/min giving a typical Reynolds number of around 4,000 while the fuel flow for the laminar coannular pilot flame is roughly 10 sccm. The experiments employ the 2.2s drop rig currently at NASA Glenn Research Center. A Laser Induced Incandescence (LII) configuration is used to obtain 2d maps of soot

volume fraction; Particle Imaging Velocimetry (PIV) is also used within the 2.2 s drop tower facility, using a pulsed Nd:YAG laser and video camera. Image analysis was performed using custom software developed at NASA-Glenn. For Reynolds numbers of about 4000, time separations between the two laser pulses range from 50 - 100 μs to achieve reasonable spatial resolution. Two dimensional images of soot within the turbulent flames initially at $1g$ have been obtained; the images are compared with the results of an LES simulation.

3 Modeling

The primitive variables formulation of the compressible Navier-Stokes equations in cylindrical coordinates is set up in dimensionless form consistent with the zero Mach number limit such that the incompressible equations are recovered without singularities (Hafez et al., [1]). The equations are discretized using a Fourier spectral method in azimuthal direction and high order finite difference methods in the other two spatial directions. The solver (see Auston et al. [5] for details) allows the choice of second to eighth order for first and second derivatives as explicit central difference operators or third to ninth order upwind-biased differences for the convective terms in non-conservative formulation. MUSCL and ENO schemes are available for the convective terms in conservative formulation (Wu et al. [6]). High order filters are used to provide the numerical dissipation to stabilize the system (Kennedy and Carpenter [3]). A fourth order Runge-Kutta type time integration method with minimal storage requirements (Kennedy and Carpenter [3]) is implemented. The simulation of turbulent flows requires the ability to prescribe time dependent boundary conditions for spatially evolving flows. Hence, the proper form of boundary conditions for compressible flows in domains with entrance and exit sections according to Poinsot and Lele [2] is applied.

The performance of the solver is illustrated for two axi-symmetric flows. Swirling round jets offer a significant advantage over non-swirling jets for being much shorter, hence allowing better resolution with the same number of grid points. Flows with and without combustion at the Reynolds number $Re = 1500$, the Mach number $M_0 = 0.4$ and the Swirl number $S = 141$ are simulated. The semi-infinite flow domain is mapped onto the standard domain using two-parameter exponential maps. The number of grid points was $nr \times nz = 131 \times 261$ with uniform spacing in the image domain. The sixth order accurate spatial difference operators are used with eighth order explicit filters. The initial conditions are ramped up smoothly to their full value within $\Delta t = 2$ time units. The combustion is simulated by a compressible flame sheet model for the reaction of ethylene with air. The local thermodynamic state in this model is determined by three scalar variables: Mixture fraction, density and internal energy. A simple model for soot (Kennedy et al. [4]) and radiative heat loss as described by Auston et al., [5] have been implemented.

The isotherms for cold compressible flow in fig.1 at time $t = 11.17$ and for

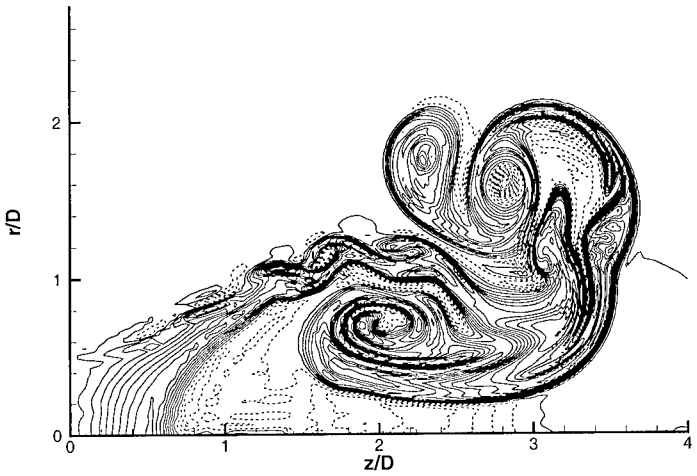


Figure 1: Isotherms in compressible cold flow for $t = 11.17$ and $Re = 1500$, $S = 1.41$

the ethylene flame in fig.2 at the late time $t = 18.44$ reflect vortex structures generated in both flows. The reacting case in fig.2 shows a distinct difference to the cold flow as can be expected. The temperature variation in the flame leads to a marked increase in viscosity, hence the flow is less complex. Furthermore, the compressible flame sheet models allow temperature change due to compression and stretching and heat loss due to radiation via soot. The soot model is not used for the present flame simulation, but the temperature reduction due to local expansion near the flame tip is visible.

4 Conclusions

A compressible Navier-Stokes solver in cylindrical coordinates was used to simulate axi-symmetric cold and reacting flows at high swirl numbers. The compressible flame sheet model shows reduction of the adiabatic flame temperature due to local expansion.

Acknowledgements

This research was supported by NASA Glenn Research Center and the Microgravity Combustion Research Program.

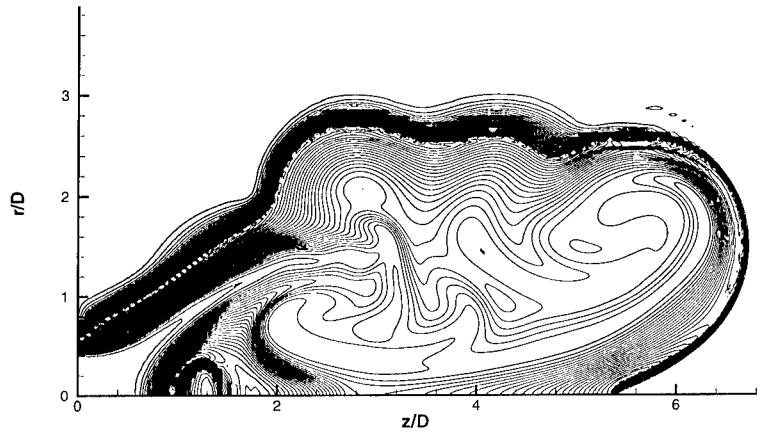


Figure 2: Isotherms in compressible flame for $t = 18.44$ and $Re = 1500$, $S = 1.41$

References

[1] Hafez, M., Soliman, M. and White, S. (1992), "A unified approach for numerical simulation of viscous compressible and incompressible flows over adiabatic and isothermal walls ", Proc. Fifth Symp. Num. and Physical Aspects of Aerodynamic Flows, Cal State Long Beach.

[2] Poinsot, T.J. and Lele, S.K. (1992), "Boundary Conditions for for Direct Simulations of Compressible Viscous Flows", J. Comput. Phys. **101**, 104-129.

[3] Kennedy, C.A. and Carpenter, M.H. (1994), "Several new numerical methods for compressible shear layer simulations", Appl. Num. Math. **14**, 397-433.

[4] Kennedy, I.M., Kollmann, W. and Chen, J.-Y. (1990), "A Model for Soot Formation in a Laminar Diffusion Flame", Combust. Flame **81**, 73-85.

[5] Auston, J.J., Kollmann, W. and Kennedy, I.M. (2000), "Impact of buoyancy and flame structure on Soot, Radiation and NO_x", AIAA 2000-0867

[6] H. Wu, L. Wang and G. Sun (1998), "Non-Existence of Third Order MUSCL Schemes, Unified Construction of ENO Schemes and a New Discontinuity Sharpenning Technique - Stiff Source Term Approach", in *Computational Fluid Dynamics Review 1998*, World Scientific, 300-317.

XVII

Direct Numerical Simulation Large Eddy Simulation

ADVANCES IN TURBULENCE VIII
Proceedings of the Eighth European Turbulence Conference
C. Dopazo et al. (Eds.)
© CIMNE, Barcelona 2000

A generalised view on mixed models

J. Meyers[1], M. Baelmans[1] and C. Lacor[2]

[1]Dep. of Mechanical Engineering - K.U.Leuven
Celestijnenlaan 300A, 3001 Heverlee, Belgium
[2]Dep. of Fluid Mechanics - V.U.B.
Pleinlaan 2, 1050 Brussel, Belgium

1 Introduction

A major research topic in LES has been the development of models that account for the interaction between resolved and unresolved scales. To this end the subgrid scale (SGS) term in the filtered momentum equations have been given special attention. Recently mixed models in combination with explicit smooth filtered Navier Stokes equations were thoroughly examined in literature. In this article, it will be shown that an explicitly smooth filtered LES formulation is equivalent to a sharp cut off filtered one. Using an idealised mixed model, both formulations are a posteriori tested and compared. For the presented test case, results are exactly the same.

2 Filtered equations

In most cases, model development and formulation are closely related to the exact SGS tensor which arises in the classical filtered Navier Stokes equations

$$\tau_{ij,sgs} = \tilde{\rho}\tilde{u}_i\tilde{u}_j - \widetilde{\rho u_i u_j}, \tag{1}$$

where in a compressible formulation $\tilde{\rho}$ is a reynolds filtered quantity, while $\tilde{u}_i$ is a favre filtered quantity. The distinction between Reynolds and Favre filtering should be clear from the context. Neither discretisation and dealiasing operations nor possible discretisation errors are considered in the above formulation. However, for consistent model development and comparison, it is important to introduce these operations formally.

Define $\overline{()}$ as the numerical cut off filter. This operation accounts for the loss of information resulting from the discretisation. It is assumed that within its resolved range all numerical operations (such as derivations) are performed error free. In case of a spectral fourier method, this filter is a sharp cut off filter with numerical cut off $k_{nc} = \pi/\Delta$, where Δ is the physical mesh spacing.

The dealiasing operation on the nonlinear term $\bar{u}_i\bar{u}_j$ equals $\overline{\bar{u}_i\bar{u}_j}$. Thus, the momentum equation can be written as

$$\frac{\partial\bar{\rho}\bar{u}_i}{\partial t}+\frac{\partial\overline{\bar{\rho}\bar{u}_i\bar{u}_j}}{\partial x_j}=-\frac{\partial\bar{p}}{\partial x_i}+\frac{\partial\bar{\tau}_{ij}}{\partial x_j}+\frac{\partial\tau_{ij,nc}}{\partial x_j}, \tag{2}$$

$$\tau_{ij,nc}=\overline{\bar{\rho}\bar{u}_i\bar{u}_j}-\overline{\rho u_i u_j}. \tag{3}$$

Here, $\tau_{ij,nc}$ is often modelled using a dynamic Smagorinsky model:

$$\tau_{ij,nc,M}=\overline{2\bar{\rho}C\Delta^2\sqrt{\overline{S_{ij}S_{ij}}}\left(S_{ij}-\frac{1}{3}S_{kk}\right)},\qquad S_{ij}=\frac{1}{2}\left(\frac{\partial\bar{u}_i}{\partial x_j}+\frac{\partial\bar{u}_j}{\partial x_i}\right). \tag{4}$$

Dealiasing operations are introduced explicitly into the model formulation using the $\overline{()}$-filter notation.

If a smooth filter $\widetilde{()}$ (such as a gaussian or top hat filter) is applied on the Navier Stokes equations, the numerical cut off filter and dealiasing operation should still be accounted for. This leads to a double filtered momentum equation:

$$\frac{\partial\widetilde{\bar{\rho}}\widetilde{\bar{u}}_i}{\partial t}+\frac{\partial\overline{\widetilde{\bar{\rho}}\widetilde{\bar{u}}_i\widetilde{\bar{u}}_j}}{\partial x_j}=-\frac{\partial\widetilde{\bar{p}}}{\partial x_i}+\frac{\partial\widetilde{\bar{\tau}}_{ij}}{\partial x_j}+\frac{\partial}{\partial x_j}\underbrace{\left(\overline{\widetilde{\bar{\rho}}\widetilde{\bar{u}}_i\widetilde{\bar{u}}_j}-\overline{\widetilde{\rho\bar{u}}_i\widetilde{\bar{u}}_j}\right)}_{\overline{\tau_{ij,sim}}}+\frac{\partial}{\partial x_j}\underbrace{\left(\widetilde{\overline{\rho\bar{u}_i\bar{u}_j}}-\widetilde{\overline{\rho u_i u_j}}\right)}_{\widetilde{\tau_{ij,nc}}} \tag{5}$$

The SGS term consists of two parts. It is readily seen that the second part equals the $\widetilde{()}$-filtered SGS term $\tau_{ij,nc}$ of eq.(3). The first part ($\overline{\tau_{ij,sim}}$) is $\overline{()}$-filtered as a result of the explicitly notated dealiasing operator on the convection term. It is clear that eq.(5) is equivalent to:

$$\frac{\partial\widetilde{\bar{\rho}}\widetilde{\bar{u}}_i}{\partial t}+\frac{\partial\widetilde{\overline{\rho\bar{u}_i\bar{u}_j}}}{\partial x_j}=-\frac{\partial\widetilde{\bar{p}}}{\partial x_i}+\frac{\partial\widetilde{\bar{\tau}}_{ij}}{\partial x_j}+\frac{\partial}{\partial x_j}\left(\widetilde{\overline{\rho\bar{u}_i\bar{u}_j}}-\widetilde{\overline{\rho u_i u_j}}\right). \tag{6}$$

Thus, the formulation of eq.(5) is formally equivalent with eq.(2) in case $\tau_{ij,sim}$ is modelled exact and $\widetilde{\tau_{ij,nc}}$ in eq.(5) is modelled similar to $\tau_{ij,nc}$ in eq.(2) by using $\tau_{ij,nc,M}\widetilde{\ }$ (cfr. eq.(4)). These conditions can be fulfilled in a practical simulation with an appropriate smooth filter. An exact deconvolution model (EDM) can then be found to reconstruct $(\bar{\rho},\bar{u}_i,...)$ from $(\tilde{\bar{\rho}},\tilde{\bar{u}}_i,...)$. These simulations will be referred to as EDM simulations.

In most mixed model formulations $(\bar{\rho},\bar{u}_i,...)$ are not available and only double filtered variables are used in the modelling of $\widetilde{\tau_{ij,nc}}$. When a Smagorinsky term is used, this leads to

$$\widetilde{\tau_{ij,nc,inv}}=\overline{2\tilde{\bar{\rho}}C\Delta^2\sqrt{\overline{S_{ij}S_{ij}}}\left(S_{ij}-\frac{1}{3}S_{kk}\right)},\qquad S_{ij}=\frac{1}{2}\left(\frac{\partial\tilde{\bar{u}}_i}{\partial x_j}+\frac{\partial\tilde{\bar{u}}_j}{\partial x_i}\right). \tag{7}$$

Simulations using the formulation of eq.(7) combined with exact deconvolution for $\tau_{ij,sim}$ will be referred to as EDMinv simulations. Furthermore, due to the equivalence between eq.(2) and eq.(5), the EDMinv simulation is analogous to an inverse Smagorinsky formulation in eq.(2). This would result in explicitly filtering the velocity field, using it in eq.(7) an defiltering $\widetilde{\tau_{ij,nc,inv}}$ afterwards.

3 Results and discussion

LES of homogeneous isotropic turbulence was performed. Reference case is a 256^3 DNS with initial $Re_\lambda \approx 90$ ([1],[2]). LES was performed on a 64 cube using three different formulations, i.e. eq.(2) combined with a Smagorinsky model (referred to as Smagorinsky), eq.(5) combined with EDM and eq.(5) combined with EDMinv. The EURANUS-code [3] was used. Here, explicit smooth filtering was performed in physical space using Padé-filters. Furthermore, sharp cut off and dealiasing operations were performed in spectral space. Results of energy spectra at three different time levels (0.33, 3.33 and 4.83) are presented in figure 1. For EDM and EDMinv simulations, the computed velocity field is first defiltered for comparison with the Smagorinsky simulation and the sharp cut off filtered DNS data. All simulations are in good agreement with DNS. LES and DNS results differ at the tail of the spectrum.

Results of the Smagorinsky and EDM simulations lie very close to each other. Negligible differences can be seen at time 4.83 in the zoomed spectrum only. These results confirm the equivalence between eq.(2) with Smagorinsky and eq.(5) with EDM. Although the magnitude of the Smagorinksy term in eq.(5) is decreased by the smooth filter operation, its dynamical influence on the smooth filtered field is thus unchanged.

Simulations with EDMinv seem to give slightly better results. However, it should be noted that this improvement only results from the reformulation of the Smagorinsky term, since the similarity term was modelled exact both for EDM and EDMinv. Although results for EDMinv are sightly better for this test case, this improvement is obtained by an ad hoc alteration of the Smagorinsky model (see discussion at the end of section 3), without any theoretical basis.

4 Conclusions

By introducing discretisation and dealiasing operators directly into the smooth filtered equations, smooth filtered LES is theoretically shown to be equivalent with sharp cut off filtered LES. Both formulations were tested in homogeneous isotropic turbulence. Numerical results confirmed that a Smagorinsky model for the sharp cut off filtered LES and an ideal mixed model (using EDM) for the double filtered equations are equivalent. When the Smagorinsky part in the mixed model is reformulated (EDMinv), results were slightly different. Most mixed models in literature use this formulation. However the slightly better results can be attributed to the reformulation of the Smagorinsky model.

References

[1] A. A. Wray. Private communications. 1998.

[2] Gregoire S. Winckelmans, A. A. Wray, and O. V. Vasilyev. Proc. of the Summer Program 1998, pages 367–388. Center for Turbulence Research, 1998.

[3] C. Lacor, Z. W. Zhu, Ch. Hirsch. AIAA-93-5023, AIAA/DGLR 5th Int. Aerospace Planes and Hypersonics Technology Conf. Mnchen, 1993

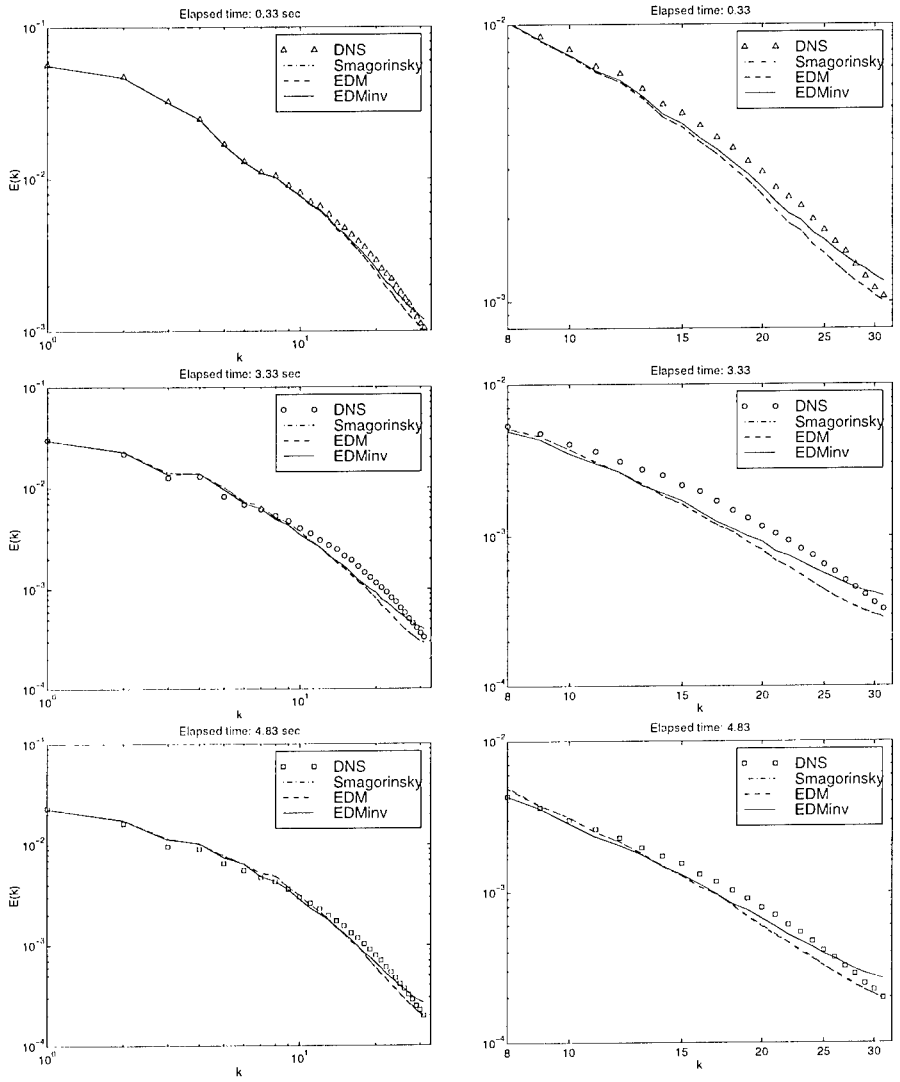


Figure 1: Spectra for homogeneous isotropic turbulence (Right column is zoom of left column) at 3 instances in time: 1^{st} row 0.33, 2^{nd} row 3.33 and 3^{th} row 4.83

ADVANCES IN TURBULENCE VIII
Proceedings of the Eighth European Turbulence Conference
C. Dopazo et al. (Eds.)
© CIMNE, Barcelona 2000

Assessment of subgrid-scale models in dissipative vortical structures

Kiyosi Horiuti

Department of Mechano-Aerospace Engineering, Tokyo Institute of Technology,
2-12-1 O-okayama, Tokyo 152-8552, Japan

Contact e-mail: khoriuti@mes.titech.ac.jp

1 Introduction

Coherent vortical structures are known to exist in various turbulent flows, e.g., the worms in the homogeneous isotropic turbulence [1]. These structures are roughly divided into the two groups: the vortex tube and sheet. Significant contributions of these structures for the dissipation of the turbulent energy has been previously shown [1]. For the sheet structures, however, there exists (at least) two kinds. One is that similar to the Burgers' vortex layer (flat sheet) generated in plane-strained flow, and the other one is the cylindrical sheet surrounding the vortex tube generated in axially-strained flow [2, 3]. The aim of the present study is to identify the structure which is most responsible for the transfer and dissipation of the turbulent energy, and conduct an assessment of the subgrid scale (SGS) models in large-eddy simulation (LES) on the accuracy for prediction of vortical structures responsible for the transfer.

2 Classification method and DNS data analysis

In order to distinguish these two sheets and tube structures, we developed a classification method, which is based on the eigenvalue solutions for the byproducts of strain rate tensor, S_{ij} and vorticity tensor, Ω_{ij} (λ_2 method [4]). To eliminate the crossover of the eigenvalues, [2, 3, 5, 6] we reordered the eigenvalues so that the eigenvalue, the eigenvector of which is most aligned with the local vorticity vector, is chosen as λ_z, and the largest eigenvalue among the remaining two eigenvalues as λ_+, and the smallest one as λ_-. Similar reordering was used to define the eigenvalues for S_{ij} as $\sigma_z, \sigma_+, \sigma_-$ [5]. We denote the corresponding eigenvectors for $\sigma_z, \sigma_+, \sigma_-$ as $\mathbf{e}_z, \mathbf{e}_+, \mathbf{e}_-$, respectively. It was shown that the cylindrical sheet region is effectively identified by imposing the condition $(\lambda_+ \geq \lambda_- \geq 0)$, and the flat sheet region by $(\lambda_+ \geq 0 \geq \lambda_-)$, and the core region of the vortex tube by $\lambda_+ < 0$ [7].

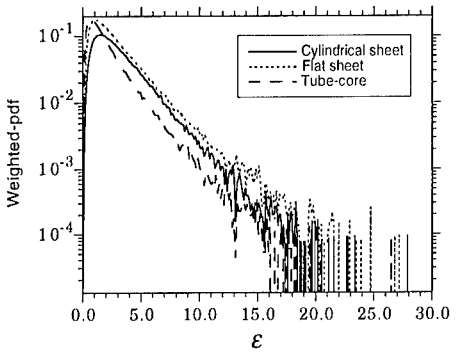


Figure 1 Weighted-pdf profiles for the dissipation rate ε

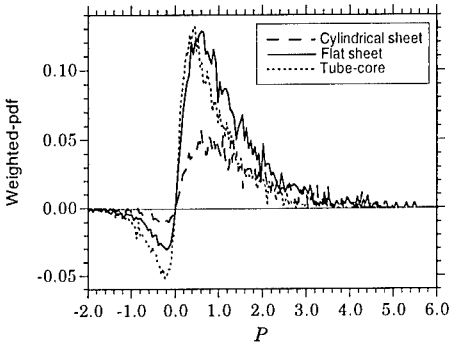


Figure 2 Weighted-pdf profiles for SGS production term P

We have utilized the incompressible decaying homogeneous isotropic turbulence DNS data which were generated with 128, 128 and 128 grid points, at $Re_\lambda = 26.8$. Figure 1 shows the weighted-probability densities ($pf(p)\Delta p$) for the dissipation rate of the turbulent energy, ε. Intense dissipation primarily occurs in the flat sheet region, the dissipation generated in the tube-core region is rather small, and the dissipation generated in the cylindrical sheet region is intermediate between them.

We examined the contribution of the structures for the energy cascade by estimating the grid scale - SGS energy transfer in LES. The energy transfer occurs through the SGS production term, $P = -\tau_{ij}\partial\overline{u}_i/\partial x_j$ (τ_{ij} is the SGS stress tensor). Positive P implies the forward scatter of the grid-scale energy into the SGS, while negative P implies the backward scatter. We obtained an estimate of the P term by applying the Gaussian filter to the DNS data, reducing 128 grid points to 32 grid points in each direction. Figure 2 shows the weighted-pdfs of P. In good correspondence with the decomposition of the dissipation rate (Fig. 1), the energy cascade (forward scatter) primarily arises in the flat sheet region, whereas the backward scatter primarily occurs in the tube-core region. Considerable occurrence of negative σ_z was found, and the backward scatter events were highly correlated with the events with negative σ_z, indicating that the backward scatter occurs along the compressed vortex tube. Figure 3 for the weighted-pdfs of the P term with conditional sampling, $\sigma_z < 0$, shows that the P term is mostly negative in the tube-core region. When $\sigma_z < 0$, $\sigma_+ > 0$, implying that the amplitude of the vorticity along σ_z, ω_z, is reduced. Figure 4 shows the scatter plot between σ_z and the vortex-stretching term, $\omega \cdot \mathbf{W}$, projected onto the eigenvector $\mathbf{e}_z$, $(\sigma_z(\mathbf{e}_z \cdot \omega)^2)$, obtained in the tube-core region of the (unfiltered) DNS data, where $\mathbf{W}$ denotes the vortex-stretching vector. It can be seen that the amplitude of the vorticity along $\mathbf{e}_z$ is reduced, in turn, the azimuthal vorticity, ω_+, is enhanced due to the backward scatter. In fact, the magnitude of the vortex-stretching term along the $\mathbf{e}_+$ was large (figure not shown). With a lapse of time, the role reversal of ω_z and ω_+ [6] will take place along the compressed tube. We note that this reversal cannot be accomplished

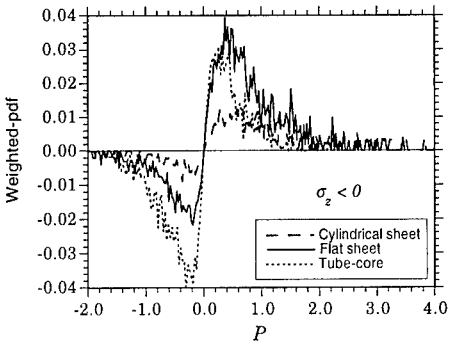


Figure 3 Weighted-pdf profiles for P with $\sigma_z < 0$

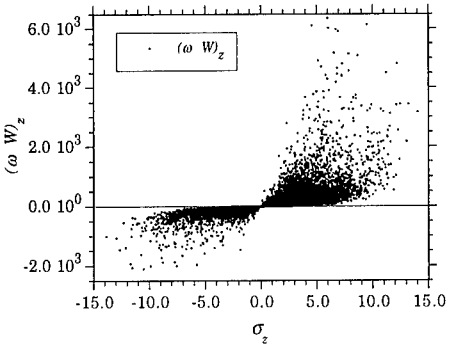


Figure 4 Scatter plot between σ_z and $\sigma_z(\mathbf{e}_z \cdot \omega)^2$

in the Burgers' vortex tube and layer models.

3 Assessment of the SGS models

As for the SGS models, we considered the Smagorinsky model, dynamic Smagorinsky model (DSM) [8, 9], dynamic mixed model ($C_B - C_S$ model [10]) and SGS estimation model. The P term estimated using the Smagorinsky model yielded good correlation with the DNS exact value (correlation coefficient (C.C.)=0.73), since the forward energy scatter primarily arised in the flat sheet region, in which the strain is dominant. DSM yielded poor correlation with the DNS data (C.C.=0.17). This poor correlation was improved to 0.73 in $C_B - C_S$ model, but the amplitude of the P term obtained using $C_B - C_S$ model was smaller than the exact value. These results were obtained because of an elimination of the effect of strain on the Smagorinsky constant, C_S, which occurred due to a cancellation of the two terms $\overline{\Delta}^2|\widetilde{\overline{S}}|\widetilde{\overline{S}}_{ij}$ and $\tilde{\overline{\Delta}}^2|\tilde{\overline{S}}|\tilde{\overline{S}}_{ij}$ (C.C. between these two terms was 0.97) contained in the $\mathcal{E}_{ij}$ term [10]. Thus, C.C. between the $\mathcal{E}_{ij}\mathcal{E}_{ij}$ term and the $S_{ij}S_{ij}$ term was lowered to 0.46. This drawback of the dynamic SGS models was circumvented in the SGS estimation model, in which high correlation with the exact value was obtained (C.C.=0.86).

These SGS models were assessed in an actual LES in which these SGS models were incorporated. Figure 5 shows the weighted-pdfs of C_S decomposed into three regions obtained using DSM. Large values of C_S primarily arise in the tube-core region, and thus the contribution of the sheet region for the energy transfer was significantly reduced, contrary to the result from the DNS data. The SGS estimation model [11] yielded the best agreement with the DNS values. Figure 6 shows the weighted-pdfs of σ_z obtained using different models. Since the generation of the azimuthal vorticity associated with the backward scatter event is not accurately captured when the Smagorinsky model is used, an evolution of the vortical structures is not well predicted by using the Smagorinsky model.

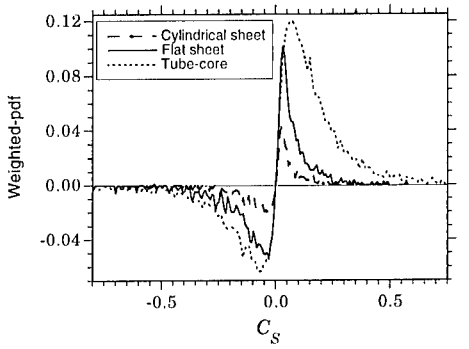


Figure 5 Weighted-pdf profiles for C_S

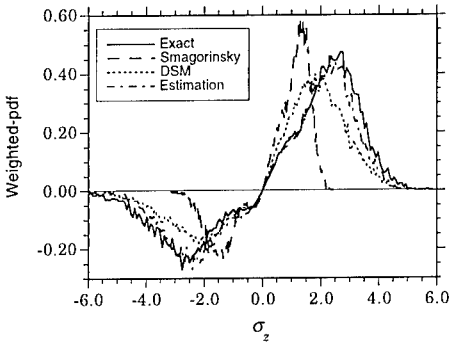


Figure 6 Weighted-pdf profiles for σ_z

DSM yielded a better prediction for the pdfs of σ_z, but the predicted structure responsible for energy transfer was different from the DNS exact one. The SGS estimation model yielded the best agreement with the DNS exact data.

4 Conclusions

Dissipation of turbulent energy and the forward scatter of the grid-scale energy into the SGS primarily took place in the flat-sheet region, and the backward scatter primarily occurred in the compressed tube-core region. Intense azimuthal vorticity was generated along the compressed tube. When the Smagorinsky constant was determined using the dynamic procedure [8], the effect of the strain on the model was reduced, and an accuracy of the prediction for the vortical structures responsible for the energy transfer was lowered.

This work was partially supported by a Grant-in-Aid from the Ministry of Education, Science and Culture, Japan (No.10650162),

References

[1] W.T. Ashurst, A.R. Kerstein, R.M. Kerr and C.H. Gibson: Phys. Fluids **30**, 2343 (1987).
[2] J. Jiménez: Phys. Fluids A **4** (1992) 652.
[3] S. Kida: Lecture Notes in Numerical Applied Analysis **12** (1993) 137.
[4] J. Jeong and F. Hussain: J. Fluid Mech. **285** (1995) 69.
[5] B. Andreotti: Phys. Fluids **9** (1997) 735.
[6] K.K. Nomura and G.K. Post: J. Fluid Mech. **377** (1998) 65.
[7] K. Horiuti: Proc. IUTAM Symposium on Geometry and Statistics of Turbulence (1999).
[8] M. Germano, U. Piomelli, P. Moin and W.H. Cabot: Phys. Fluids A **3**, 1760 (1991).
[9] D.K. Lilly: Phys. Fluids A **4**, 633 (1992).
[10] K. Horiuti: Phys. Fluids **9**, 3443 (1997).
[11] J.A. Domaradzki and K.C. Loh: Phys. Fluids **11**, 2330 (1999).

ADVANCES IN TURBULENCE VIII
Proceedings of the Eighth European Turbulence Conference
C. Dopazo et al. (Eds.)
© CIMNE, Barcelona 2000

Multifractal Scale-Similarity in Subgrid-Scale Turbulence Modeling

G.C. Burton[1,2,3], W.J.A. Dahm[1,3], D.R. Dowling[1,4] and K.G. Powell[2,3]

[1]Laboratory for Turbulence & Combustion (LTC), [2]W.M. Keck Foundation Laboratory for Computational Fluid Dynamics, [3]Department of Aerospace Engineering, [4]Department of Mechanical Engineering & Applied Mechanics
The University of Michigan, Ann Arbor, MI, 48109-2140 USA

Contact e-mail: wdahm@umich.edu

To date, most work in the field of large eddy simulation has focused on subgrid-scale modeling through a variety of dimensional reasoning, scaling assumptions, and *ad hoc* approaches in which the subgrid stress tensor τ_{ij} is related back to resolved variables. We are developing a fundamentally different approach to the modeling of subgrid-scale stresses in turbulent flow. This makes use of the significant body of experimental, numerical, and theoretical evidence which indicates that gradient quantities such as the enstrophy $\frac{1}{2}\omega\cdot\omega(\mathbf{x},t)$ exhibit multifractal scale-similarity at intermediate scales in turbulent flows (*e.g.*, Frederiksen *et al* 1997). We therefore formulate the Navier-Stokes equations solely in terms of the vorticity, leading to an integro-differential form in which the nonlinear terms appear as integrals over the vorticity field $\omega(\mathbf{x},t)$. The spatially-filtered forms of these equations then allow the subgrid-scale enstrophy to be represented by synthetically generated multifractal fields. The resulting integrals over the multifractal subgrid-scale fields can be treated analytically in terms of the underlying scale-invariant multiplier distribution $P(M_\varepsilon)$.

It may appear natural to first test this approach on the simpler problem posed by the one-dimensional Burgers equation. Differences between Burgers turbulence and hydrodynamic turbulence are widely known (*e.g.*, Kraichnan 1990; Gotoh & Kraichnan 1993; Bouchaud, Mézard & Parisi 1995). Of relevance here, Burgers equation acquires infinitely many invariants when the viscosity vanishes and contains only local interactions in the physical domain. To nevertheless mimic hydrodynamic turbulence as best possible within this simpler context, we used white-in-time correlated Gaussian-random forcing (Chekhlov & Yakhot 1995) which produces a $k^{-5/3}$ energy spectrum. Velocity fields $\mathbf{u}(\mathbf{x},t)$ were generated using high-resolution simulations with a finite-volume method over 2^{12} points. Simulations over longer times produced energy spectra $E(k)$ such as that

in figure 1*(a)*, which verifies the $k^{-5/3}$ scaling.

We then examined the resulting dissipation fields $(\partial u/\partial x)^2$ such as in figure 1*(b)*, for multifractal scale-similarity by generating the multiplier distributions $P(M_\varepsilon)$ over a wide range of scales ε. Scale-invariance in these distributions is inherent in multifractal scaling and central to the subgrid-scale modeling approach developed here. However, as the results in figure 1*(c)* clearly show, the velocity-gradient fields from our forced-Burgers simulations do not demonstrate scale-invariant multiplier distributions. At no two scales is the distribution self-similar, indicating that the field is not multifractal at any scale sampled. We also analyzed the distribution of singularity strengths $f(\alpha)$ in the dissipation fields over the same scales, which must also be scale-invariant if the field is multifractal. As with the $P(M_\varepsilon)$ distributions, the $f(\alpha)$ distributions, as seen in figure 1*(d)*, show no scale invariance, confirming that the dissipation fields cannot be multifractal.

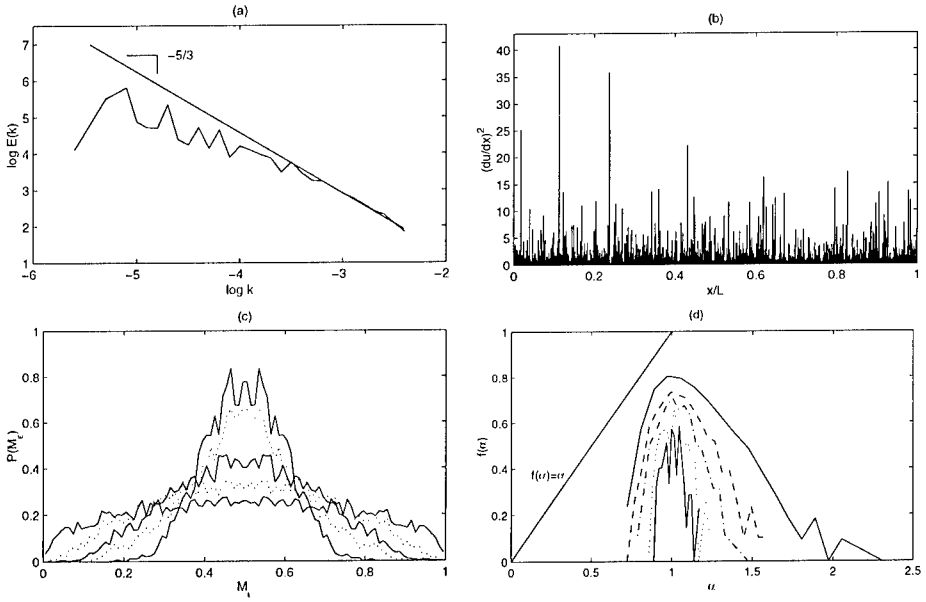


Figure 1: Results for Burgers turbulence driven by correlated Gaussian-random forcing, showing *(a)* energy spectrum for correlated-forcing regime exhibiting $k^{-5/3}$ scaling, *(b)* normalized dissipation field $(\partial u/\partial x)^2$, *(c)* multiplier distributions $P(M_\varepsilon)$ at five length scales ε from the dissipation field in *b*, *(d)* distribution of singularity strengths $f(\alpha)$ at the same five scales examined in *c*.

The lack of such scale-invariance in the $P(M_\varepsilon)$ and $f(\alpha)$ distributions was further verified in simulations of Burgers equation with random forcing without correlations (hence with a k^{-2} energy spectrum). Here Burgers systems driven by uniform-random and Gaussian-random forcing, as shown in figures 2 and 3,

also produced $P(M_\varepsilon)$ and $f(\alpha)$ distributions lacking scale-similarity at all scales sampled. This indicates that the lack of multifractal character is not connected with the correlations in the original forcing or with the particulars of any forcing scheme.

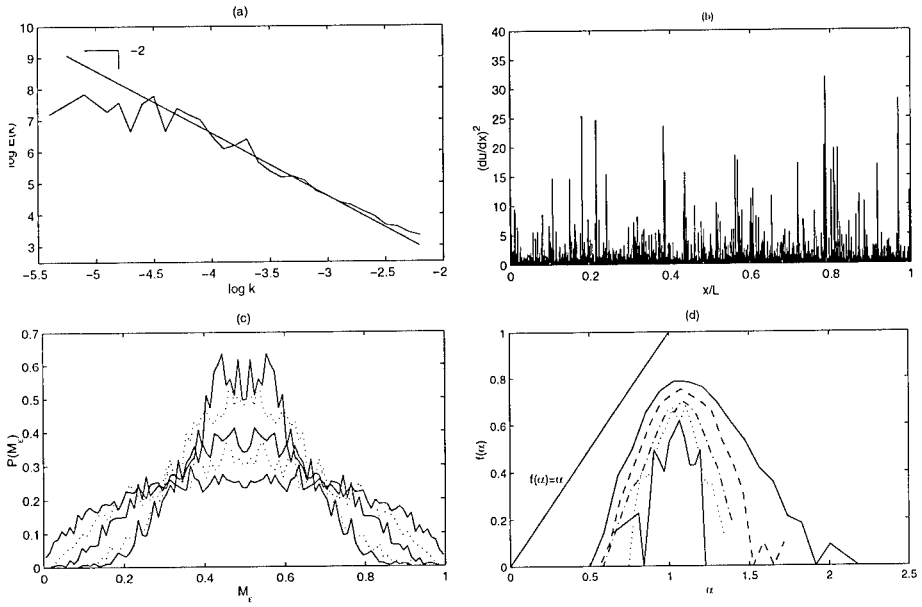


Figure 2: Similar to figure 1, but showing results for Burgers turbulence driven by uniform-random forcing. Note resulting k^{-2} scaling of energy spectrum, but lack of scale-similarity in both the $P(M_\varepsilon)$ and $f(\alpha)$ distributions, indicating that the dissipation field again lacks multifractal character.

A posteriori, the failure of the one-dimensional Burgers equation to produce scale-invariant multiplier distributions $P(M_\varepsilon)$ indicative of multifractal scale-similarity may not be surprising. The purely local nature of the dynamics in one-dimension reflects the fact that this equation involves only stretching, but no folding action such as provided by vorticity gradients in hydrodynamic turbulence. Burgers equation in one dimension thus has no mechanism to fold the fine-scale structures on which the velocity gradients are concentrated into scale-invariant fields, and thus cannot be used to test subgrid-scale models based on multifractal scaling. This is directly relevant to tests of our approach, and may extend to other subgrid-scale models based on scale-similarity (*e.g.*, Scotti & Meneveau 1997, 1999).

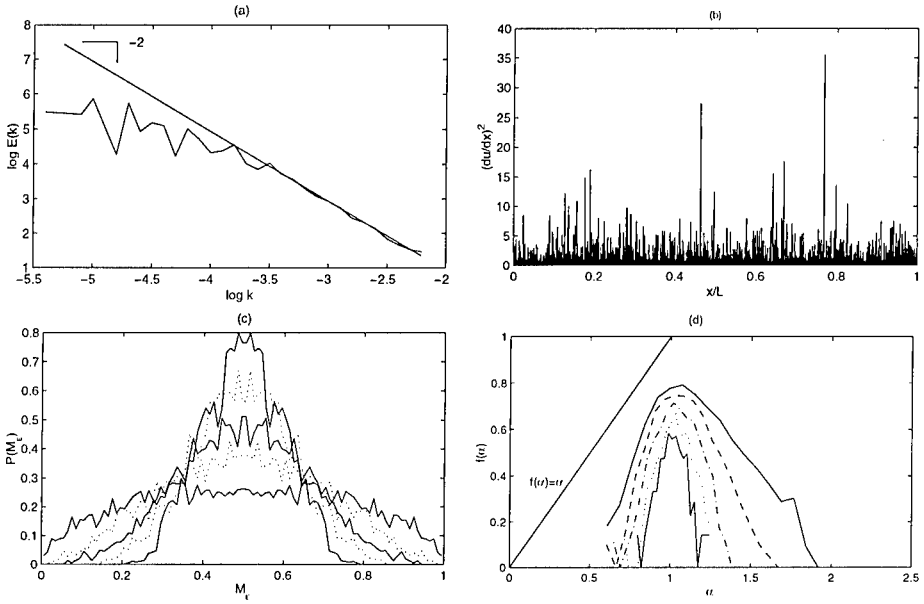


Figure 3: Similar to figures 1 and 2, but showing Burgers turbulence driven by Gaussian-random forcing. The lack of scale-similarity in both the $P(M_\varepsilon)$ and $f(\alpha)$ distributions indicates that the absence of multifractal character is not tied to the correlations in the original forcing or with the particulars of any forcing scheme.

References

[1] J.P. Bouchaud, M. Mézard, and G. Parisi. Scaling and intermittency in Burgers turbulence. *Phys. Rev. E*, 52:3656-3674, 1995.

[2] A. Chekhlov, and V. Yakhot. Kolmogorov turbulence in a random-force-driven Burgers equation. *Phys. Rev. E*, 51:R2739-R2742, 1995.

[3] R.D. Frederiksen, W.J.A. Dahm, and D.R. Dowling. Experimental assessment of fractal scale similarity in turbulent flows. Part 3. Multifractal scaling. *J. Fluid Mech.*, 338:127-155, 1997.

[4] T. Gotoh, and R. Kraichnan. Statistics of decaying Burgers turbulence. *Phys. Fluids A*, 5:445-457, 1993.

[5] R. Kraichnan. Models of intermittency in hydrodynamic turbulence. *Phys. Rev. Lett.*, 65:575-578, 1990.

[6] A. Scotti, and C. Meneveau. Fractal model for coarse-grained nonlinear partial differential equations. *Phys. Rev. Lett.*, 78:867-870, 1997.

[7] A. Scotti, and C. Meneveau. A fractal model for large eddy simulation of turbulent flow. *Physica D*, 127:198-232, 1999.

ADVANCES IN TURBULENCE VIII
Proceedings of the Eighth European Turbulence Conference
C. Dopazo et al. (Eds.)
© CIMNE, Barcelona 2000

A LES model based on the spectral decay of the kinetic energy

F. Bouchon and T. Dubois

Laboratoire de Mathématiques Appliquées, Université Blaise Pascal,
63177 Aubière, France

Contact e-mail: bouchon@ucfma.univ-bpclermont.fr

1 Introduction: the incremental unknowns

The model presented here is based on a splitting of the velocity field in the spectral space. We use the following notations for the Navier-Stokes equations for incompressible flows:

$$\frac{\partial u_i}{\partial t} - \nu \frac{\partial^2 u_i}{\partial x_j \partial x_j} + \frac{\partial}{\partial x_j}(u_i u_j) + \frac{\partial p}{\partial x_i} = f_i, \qquad \frac{\partial u_i}{\partial x_i} = 0, \tag{1}$$

The velocity field u_i is split using two sharp cut-off filters:

$$u_i = \bar{u}_i + \tilde{u}_i + u_i' \tag{2}$$

where $\bar{u}_i$ are the resolved scales (corresponding to the wavenumber $k_{n_1} = N_1/2$ in the spectral space), $\tilde{u}_i$ are the incremental unknowns (IU) (corresponding to wave-numbers from k_{n_1} to $k_{n_2} = N_2/2$), and u_i' are the smallest scales (corresponding to wave-numbers larger than k_{n_2}).

Following the concept of IU (see [2]), we write the following LES equations for $\bar{u}_i$:

$$\frac{\partial \bar{u}_i}{\partial t} - \nu \frac{\partial^2 \bar{u}_i}{\partial x_j \partial x_j} + \frac{\partial}{\partial x_j}(\bar{u}_i \bar{u}_j) + \frac{\partial \bar{p}}{\partial x_i} = \bar{f}_i - \frac{\partial \mathcal{T}_{ij}}{\partial x_j}, \qquad \frac{\partial \bar{u}_i}{\partial x_i} = 0, \tag{3}$$

where

$$\mathcal{T}_{ij} = \overline{(\bar{u}_i + \tilde{u}_i)(\bar{u}_j + \tilde{u}_j)} - \bar{u}_i \bar{u}_j \tag{4}$$

is used as an approximation of the subgrid-scale stress tensor $\tau_{ij} = \overline{u_i u_j} - \bar{u}_i \bar{u}_j$.

2 The LES model

It is a well known fact (see [4]) that the dissipative action of the smallest scales is localized on the structures of size two times larger. Thus, $\mathcal{T}_{ij} \approx \tau_{ij}$ can be considered to be valid for $N_2 = 2N_1$.

Nonetheless, u_i' has a significant dissipative action on $\tilde{u}_i$. Thus, neglecting u_i' induces an over-prediction of the kinetic energy of $\tilde{u}_i$, and an over-prediction of the dissipative action of $\tilde{u}_i$ upon $\bar{u}_i$. The large scales are then not well reproduced.

Different strategies have already been implemented to compute a SGS which provides the correct amount of dissipation on the resolved scales. It consisted in both a quasi-static approximation on the IU and a modification of the phases of the spectral coefficients of the SGS (see [1]). The numerical results were very close to those obtained with direct numerical simulations (DNS) in the context of periodic flows, but there still remained many problems to solve.

First, those strategies needed some parameters, and we had to adapt those parameters to the physics of the flows and to the cut-off levels. Moreover, those strategies were very hard to adapt to wall bounded flows.

3 Control of the spectral decay of the energy

Here, we present a multilevel model (ML) which advances in time $\bar{u}_i$ and $\tilde{u}_i$, and controls the decay of the energy spectrum of $\tilde{u}_i$ by imposing $E(k) = k^{-\alpha}$ for $k_{n_1} < k < k_{n_2}$. We first chose $\alpha = 5/3$, assuming that the cut-off level N_1 lies in the inertial range. Other values for the coefficient α were tested, and it turned out that the optimal value of α depends on the physics of the flow (particularly on the Reynolds number) and on the cut-off level N_1.

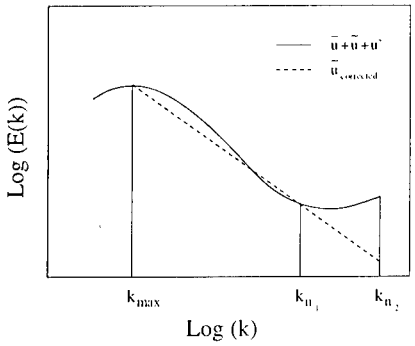


Figure 1: The dynamic procedure to control the spectral decay of the kinetic energy.

We have performed a procedure which evaluates dynamically α in terms of $\bar{u}_i$, and which does not require any *a priori* parameter. The idea is to extrapolate the decay observed between the wavenumber k_{max} and k_{n_1}, where k_{max} is the wavenumber containing the most amount of kinetic energy (see Figure 1). Thus, the decay of the energy spectrum of $\tilde{u}_i$ will depend on the cut-off level k_{n_1} and will follow the spectral decay of the resolved scales.

4 Numerical results

We have tested our model by simulating a LES of the decaying grid experiment (see [6]) for two cut-off levels and compared on Figure 2 the results with those obtained with the dynamic model (DM) of [3]. We can check that the time-decay of the kinetic energy is well reproduced and that the dynamic evaluation of α allows a correct prediction of the spectra of the large scales. This test case is particularly interesting because the Reynolds number decreases in time. Thus, the SGS dissipation decreases too. Our dynamic procedure provides values of α growing in time. A good prediction of the SGS dissipation is therefore insured.

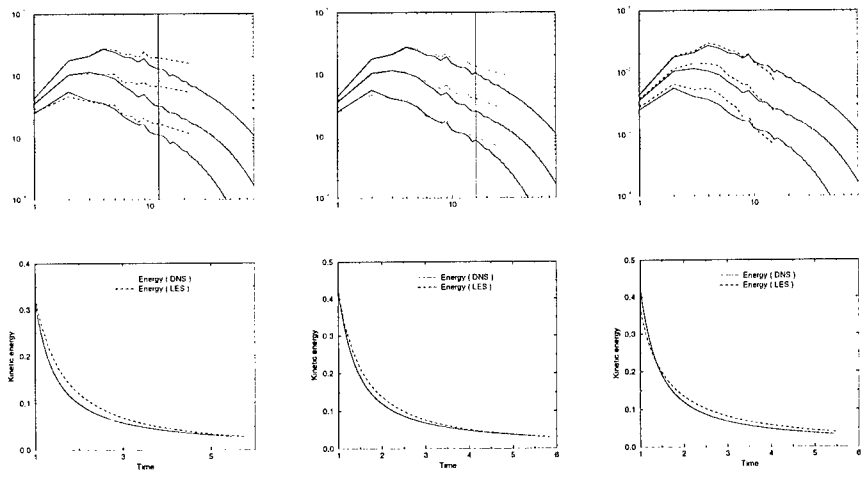


Figure 2: Energy spectra and time-decay of the filtered kinetic energy. Left: ML ($N_1 = 24$), center: ML ($N_1 = 32$), right: DM ($N = 32$). The vertical bar shows the cut-off level k_{n_1} for the ML model.

We have also adapted this procedure to wall bounded flows. Let us consider the channel flow problem, the discretization in space is done using two Fourier bases in the infinite (periodic) directions x and z, and a Chebyshev-Galerkin base is used in the normal direction y. We then implement our model in the two infinite directions, by using two cut-off levels $n_{1,x}$ and $n_{1,z}$ which correspond to the resolved scales, and two cut-off levels $n_{2,x}$ and $n_{2,z}$ corresponding to the IU. Then, for every y in the physical space, we define a coefficient $\alpha(y)$ in the same way than for the homogeneous case and use the corrected IU to compute the SGS. Here, the ability of the coefficient α to adapt to the behavior of the resolved scales is particularly useful because of the non-homogeneity of the flow. Preliminary results are presented on Figure 3 for the channel flow at Reynolds 180 (see [5]) using a cut-off level for $n_{1,x} = n_{1,z} = 24$.

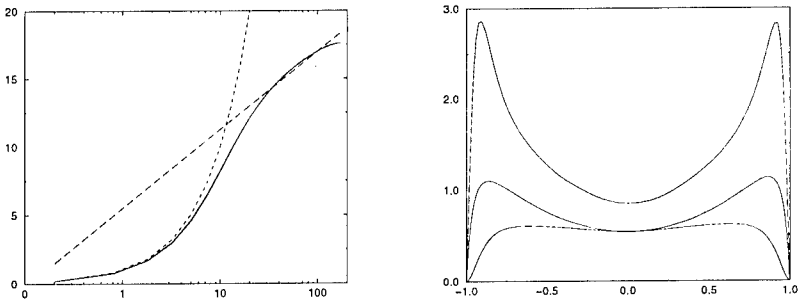


Figure 3: Mean velocity profile (left, in wall coordinates) and rms of the velocity components (right) for a LES performed with $n_{1,x} = n_{1,z} = 24$.

5 Conclusion

A new LES model has been presented. This model uses the concept of Incremental Unknowns to compute the SGS force. We have described the mechanisms used to correct the Incremental Unknowns and shown the efficiency of this method in the context of periodic flows. Preliminary results have beeń presented for wall bounded flows; we now are concentring our efforts to get breakthrues in this context.

References

[1] F. Bouchon, T. Dubois. Incremental unknowns: A tool for large eddy simulations ? *in Direct and large eddy simulation III, proceedings of the INI/ERCOFTAC Workshop*, Kluwer, 275–286, (1999).

[2] T. Dubois, F. Jauberteau, and R. Temam. Dynamic multilevel methods and the numerical simulation of turbulence. *Cambridge University Press*, 1999.

[3] M. Germano, U. Piomelli, P. Moin, and W. H. Cabot. A dynamic subgrid-scale eddy viscosity model. *Phys. Fluids*, A 3(7):1760–1765, 1991.

[4] R. M. Kerr, J. A. Domaradzki, and G. Barbier. Small-scale properties of nonlinear interactions and subgrid-scale energy transfer in isotropic turbulence. *Phys. Fluids* 8:197, 1996.

[5] J. Kim, P. Moin, and R. Moser. Turbulence statistics in fully developed channel flow at low Reynolds number. *J. Fluid Mech.*, 177:133–166, 1987.

[6] A. A. Wray. In A selection of test cases for the evaluation of large-eddy simulations of turbulent flows. *AGARD Advisory report*, 345:63–64, 1998.

ADVANCES IN TURBULENCE VIII
Proceedings of the Eighth European Turbulence Conference
C. Dopazo et al. (Eds.)
© CIMNE, Barcelona 2000

On energy and pressure backscatter in incompressible isotropic turbulence

S. Ossia and M. Lesieur

LEGI / Institut de Mécanique de Grenoble, B.P. 53,
38041 Grenoble Cedex 09, France

Contact e-mail: sepand.ossia@hmg.inpg.fr

1 Introduction

The equation for the second-order moment of the pressure (divided by the density), p, gives rise to velocity fourth-order moments. Batchelor [1] used an assumption of quasi-normality to factorize the latter into products of second-order quantities. Later, Larchevêque [2] showed that the Quasinormal (QN) and Eddy Damped Quasinormal Markovian (EDQNM) models led to same closure equations for the pressure spectrum. Making use of the QN closure, the pressure spectrum $E_{pp}(k,t)$, density in wavenumber space of $<p^2/2>$, can be related to the energy spectrum $E(k,t)$. Now, consider the infrared region $k \ll k_I$, where k_I is the spectral peak of $E(k,t)$. By means of leading-order expansions in powers of k/k_I, Lesieur *et. al* [3] showed that in incompressible isotropic turbulence,

$$E_{pp}(k,t) = A_{p_d}(t)\ k^{d-1} + O(k^{d+1}) \quad , \tag{1}$$

where d represents the dimension of space, with $A_{p_3}(t) = \frac{8}{15}\int_0^{+\infty} \frac{E^2(q,t)}{q^2} dq$ and $A_{p_2}(t) = \frac{3}{2}\int_0^{+\infty} \frac{E^2(q,t)}{q} dq$. This result is independent of both the infrared shape of $E(k,t)$ and the Reynolds number. One may question the validity of the above analysis, since it is well known that the QN model fails to predict the kinetic-energy spectrum in the ultraviolet cascade. Furthermore, large-scale intermittency and non-Gaussian effects due to the energy containing eddies, may alter the above prediction. In the next section, we will present results of 3D and 2D large-eddy simulations (LES) of decaying isotropic turbulence to elucidate these issues. The question of energy backscatter will be addressed as well.

2 Numerical Simulations

We use a standard dealiased pseudospectral code to simulate the decay of incompressible isotropic turbulence. In all simulations, the initial velocity field

is Gaussian and $E(k,0) \propto k^{s_0} \exp[-\frac{s_0 k^2}{2k_I^2}]$. Time is expressed in terms of the initial large-eddy turnover time. In the present case, the DNS display the same qualitative trends as the LES, but are limited to short times because of their high dissipativity. Only LES results will be shown hereafter.

The spectral-dynamic model of [4] has been used with 256^3 collocation points in the 3D case. The simulation on Fig. 1 starts with $s_0 = 8$ and is run up to $t = 20$. One sees the infrared kinetic-energy spectrum (IKS) immediately adopting a k^4 behaviour with positive transfer. Let us assume now that in the infrared limit, $E(k,t) = C(t)k^4$ with $C(t) \propto t^{\gamma_3}$. We recall that EDQNM computations of [5] gave $\gamma_3 = 0.16$. Chasnov [6], in LES using the plateau-peak type eddy viscosity, found an asypmtotic value of 0.25. Since $C(t)$ is proportional to the Loitsianski integral, this proves that the latter quantity is not stricto-sensu a time-invariant, although it does not vary very much at the latest stages of the computation. On the other hand, the infrared pressure spectrum (IPS) follows a k^2 law during the whole simulation and decays rapidly (no pressure backscatter). Examination of the compensated pressure spectra leads to $E_{pp}(k,t) \approx 0.63 A_{p_3}(t)k^2$, where A_{p_3} has been defined above. In fact, this result is independent of the IKS behaviour: LES starting with $s_0 = 2$ (and no energy backscatter) still behave according to the above law.

Let $t^{-\alpha_e}$ and $t^{-\alpha_p}$ approximate respectively the kinetic-energy and pressure-variance decay laws. The EDQNM model predicts that α_e be governed by s_0 [7]. Within the QN closure, Batchelor [1] showed that $\alpha_p = 2\alpha_e$. Our present LES give $\alpha_e \approx 1.40$ (value intermediate between the Kolmogorov-10/7 prediction assuming a constant Loitsianski intergral and the EDQNM-1.38 value of [5]) and $\alpha_p \approx 2.90$, in the case $s_0 \geq 4$. For $s_0 = 2$, $\alpha_e \approx 1.22$ (very close to $6/5 = 1.2$ found in [8]) and $\alpha_p \approx 2.60$. In LES, $<p^2>$ decays slightly faster than the QN prediction.

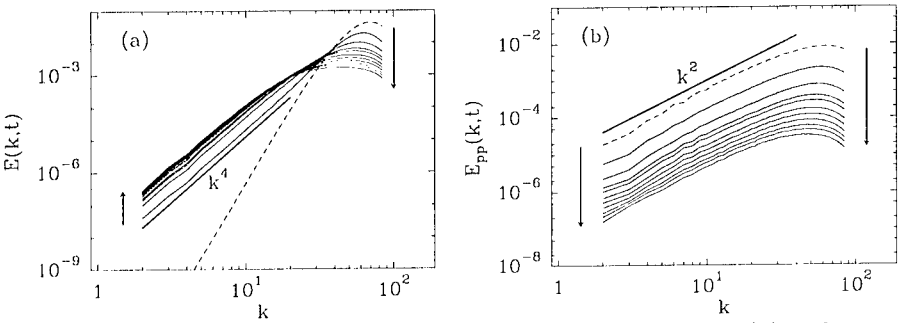


Figure 1: *3D LES at* 256^3. *Temporal evolution of kinetic-energy (a) and pressure (b) spectra (shown from* $t = 0$ *(----) to* $t = 20$ *(——) by 2). Arrows denote the direction of temporal evolution.*

In 2D, 128 independent 1024^2 simulations have been performed with a fourth-

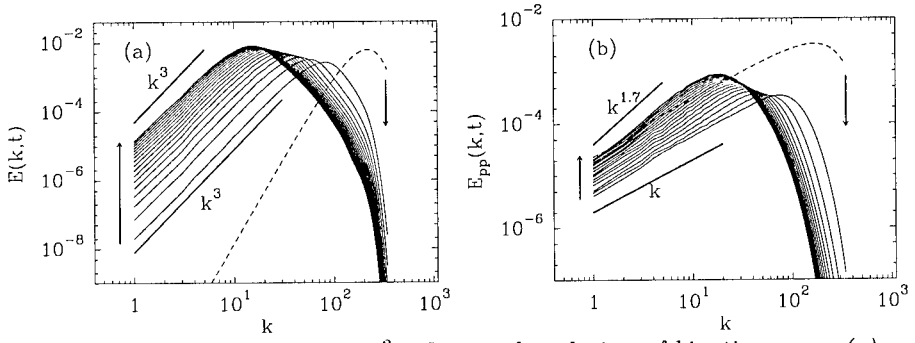


Figure 2: *2D LES at* 128×1024^2. *Temporal evolution of kinetic-energy (a) and pressure (b) spectr a. (shown from* $t = 0$ *(----) to* $t = 760$ *(——) by 40).*

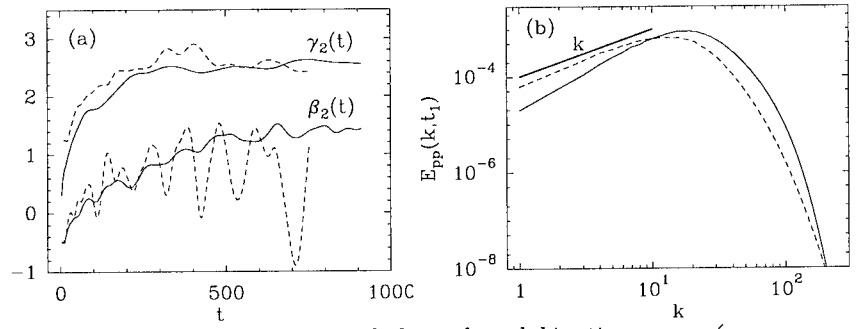


Figure 3: *(a) Growth exponent of the infrared kinetic-energy (upper curves) and pressure (lower curves) spectrum in 2D LES at* 1300×256^2 *(——) and* 128×1024^2 *(----). (b) Pressure spectra at* $t_1 = 760$, *resulting from the LES at* 128×1024^2 *points (——) and from randomizing the velocity field (----).*

order hyperviscosity. Fig. 2 shows the time evolution of $E(k,t)$ and $E_{pp}(k,t)$ for a typical run with $s_0 = 5$. One can see the k^3 backscatter of energy with a substantial growth of the infrared scales. The IPS is initially $\propto k$ and exhibits a short transient decay. It then increases in time over the whole infrared scales, departing gradually from the theoretical k-spectrum. Let us now approximate the IKS as $E(k,t) \propto t^{\gamma_2} k^3$. The exponent γ_2 can be computed by fitting the lowest modes of $E(k,t)$ to $C(t)k^s$ at two consecutive instants. Fig. 3(a) shows that γ_2 increases from 1.2 and saturates at ≈ 2.5. In 1300 realizations of 256^2-hyperviscous LES with $s_0 = 3$, γ_2 displays the same trend but the sampling fluctuations are smaller. Fig. 3(a) indicates that in an infinite domain, the strong energy backscatter of high-Reynolds-number 2D turbulence prevents the large scales from saturation. We have also computed the IPS temporal-growth exponent β_2, where $E_{pp}(k,t) \propto t^{\beta_2} k^{s'}$ (Fig 3(a)). But the data are meaningful solely for the 1300×256^2 simulations and suggest that β_2 saturate at ≈ 1.2. Finally, the velocity fields of the 128×1024^2 simulations were randomized at

$t_1 = 760$ (but the energy and zero-divergence of each 2D mode were preserved). Fig. 3(b) shows that the resulting $E_{pp}(k, t_1)$ is now $\propto k$. This indicates that the departure of the IPS from the QN prediction results from strong non-Gaussian effects associated to coherent vortices.

3 Conclusions

First, it was recalled that within the QN or EDQNM closures, the infrared pressure spectrum was always of the equipartition type (Eq. 1). In order to achieve long dynamical times together with high-Reynolds-number regimes, this result was then examined by means of LES. In 3D, the LES allowed first recovery of the k^4-infrared-spectral backscatter predicted by QN and EDQNM closures. Simultaneously, we had an infrared $E_{pp}(k, t) \propto k^2$, which exhibited a strong temporal decay. In 2D, the LES displayed the k^3 energy backscatter and showed that the infrared-temporal-growth exponent was ≈ 2.5. As for the infrared pressure spectrum, it eventually grew in time as $t^{1.2}$, while becoming steeper than k. This was certainly due to the strong non-Gaussian effects associated to the presence of coherent vortices around the spectral peak of energy.

References

[1] G. K. Batchelor. Pressure fluctuations in isotropic turbulence. *Proc. Camb. Phil. Soc.*, 47:359–374, 1951.

[2] M. Larchevêque. Pressure fluctuations and Lagrangian accelerations in two-dimensional incompressible isotropic turbulence. *Eur. J. Mech. B.*, 9:109–128, 1990.

[3] M. Lesieur, S. Ossia and O. Métais. Infrared pressure spectra in two- and three-dimensional isotropic incompressible turbulence. *Phys. Fluids*, 11:1535–1543, 1999.

[4] E. Lamballais, O. Métais and M. Lesieur. Spectral-dynamic model for large-eddy simulations of turbulent rotating channel flow. *Theor. Comp. Fluid Dyn*, 12:149–177, 1998.

[5] M. Lesieur and D. Schertzer. Amortissement similaire d'une turbulence à grand nombre de Reynolds. *J. de Mécanique*, 17:609–646, 1978.

[6] J. Chasnov. Computation of the Loitsianski integral in decaying isotropic turbulence. *Phys. Fluids A*, 5:2579–2581, 1993.

[7] M. Lesieur. Turbulence in fluids, third ed., *Kluwer*, 1997.

[8] G. Comte-Bellot and S. Corrsin. The use of a contraction to improve the isotropy of a grid-generated turbulence. *J. Fluid Mech.*, 25:657–682, 1966.

ADVANCES IN TURBULENCE VIII
Proceedings of the Eighth European Turbulence Conference
C. Dopazo et al. (Eds.)
© CIMNE, Barcelona 2000

Large-eddy simulation of turbulent mixing layers

Elias Balaras, Ugo Piomelli and James M. Wallace

Department of Mechanical Engineering, University of Maryland, College Park, MD 20742, USA

Contact e-mail: ugo@eng.umd.edu.

1 Introduction and problem formulation

Mixing layers that form between two fluid streams moving with different velocities have been studied both in experiments and simulations for about sixty years. For sufficiently high Reynolds numbers, the equations governing the development of a plane mixing layer can yield "self-similar" solutions. Self-similarity is characterized by linear growth of the layer and mean velocities and turbulent statistics independent of the downstream distance when normalized by appropriate length and velocity scales. While in the past, this self-similar state was widely believed to be unique, there is increasing experimental evidence [1, 2, 3] that mixing layers may achieve asymptotic self-preserving states that are not independent of their initial conditions, and thus are not unique. Among the factors that may influence the self-similar state are the conditions of the boundary layers at the splitter plate, and the size of the experimental apparatus. The exact mechanisms producing such differences are not well understood.

Numerical simulations, which can be conducted in an accurately controlled environment, are a valuable tool in addressing some the issues raised above by isolating each influence parameter, such as initial conditions and domain size. The present study focuses on the differences in the self-similar states caused by different initial conditions and computational domain size. In addition to an examination of the statistics of the flow field, the role of the coherent structures in the establishment of the self-similar states is also investigated.

Most numerical simulations of mixing layers to date have been temporal calculations in which the development of the layer is followed in time. The initial conditions are most commonly obtained from a given velocity profile, to which some disturbance is added. Rogers & Moser [4] (RM in the following) performed a temporal simulation starting from two different realizations of a turbulent boundary layer with their free-streams moving in opposite directions, to mimic experiments with incoming turbulent boundary layers. The present

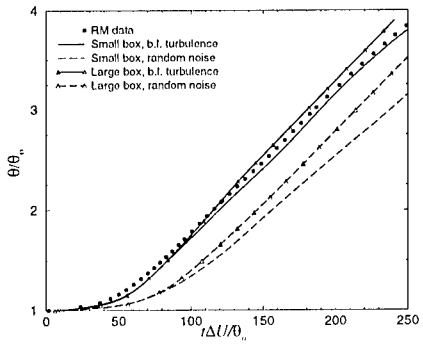


Figure 1: Time evolution of θ/θ_o.

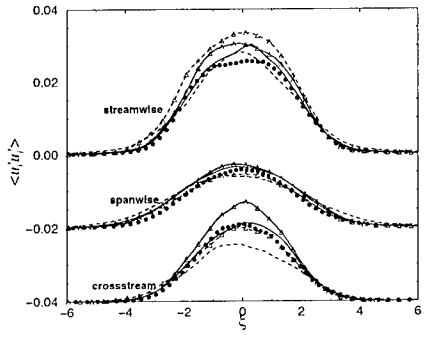


Figure 2: Velocity variances. Each set of curves is shifted downwards by 0.02 units for clarity.

study extends the RM calculations by examining the effect of domain size and initial conditions.

First, a case that matched the RM DNS was computed. Then, the initial condition was modified by imposing a field with the same mean flow of the previous case, and random perturbations with prescribed moments. Two additional calculations were performed with computational domains that were twice the size of the RM domain, both in the streamwise and spanwise directions. Since a parametric study of this sort using direct simulations would be prohibitively expensive, given the size of the computational domain, we have chosen to perform large-eddy simulations (LES).

The filtered Navier-Stokes and continuity equations, were integrated in time using an Adams-Bashforth fractional-step method. All spatial derivatives were approximated by second-order central differences on a staggered grid. The Lagrangian dynamic eddy-viscosity model [5] was used to parameterize the subgrid scale stress term τ_{ij}.

2 Results

In all cases, an initial transient was followed by a self-similar period. In Fig. 1 the evolution of the mixing-layer momentum thickness θ/θ_o (normalized by its initial value θ_o) as a function of non-dimensional time $\tau = t\Delta U/\theta_o$ is shown. After an initial transient, θ/θ_o grows linearly with time in all cases. When the domain is doubled in the streamwise and spanwise directions the initial adjustment stage is approximately the same as for the smaller domain until $\tau \simeq 90$; after this time the layer grows at a faster rate. The same trend can be seen for the calculations that start from random noise, for which, however, self-preservation is established at a later time.

While the mean velocity was not affected by the initial conditions or the

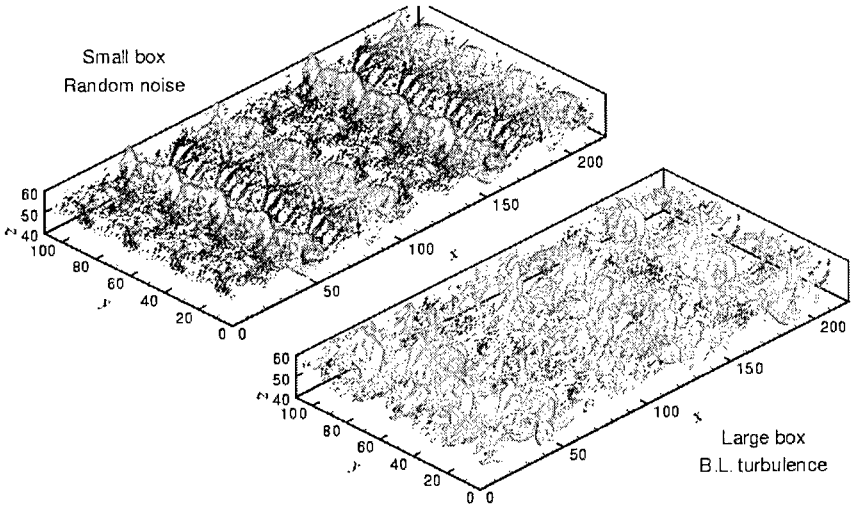


Figure 3: Iso-surfaces of P and Q during the self-similar period ($\theta/\theta_o = 2.6$).

domain size, some of the higher moments were. The large-domain calculations have higher fluctuation levels than the small-box ones (Fig. 2). In particular, there is approximately an 83% increase in the peak spanwise velocity variance for the large-domain, boundary-layer turbulence case compared to the small-domain, random noise one. These differences are an important indicator of more highly three-dimensional flow patterns in the cases initialized with boundary-layer turbulence and in the large-domain calculations.

Several methods can be used in numerical simulations to visualize the coherent eddies in a turbulent flow. In this work we have used the pressure to identify the regions of strong rotation in vortex cores, and the second invariant of the velocity-gradient tensor, $Q = -\frac{1}{2}\frac{\partial u_i}{\partial x_j}\frac{\partial u_j}{\partial x_i}$, to highlight the rib vortices. In Fig. 2, iso-surfaces of P and Q during the self-similar period at $\theta/\theta_o = 2.6$, for (a) the large domain initialized with boundary layer turbulence, and (b) the small domain initialized with random noise. The small-domain, random-noise calculation shows a fairly well-organized structure, even at this late stage of the evolution: a regular array of quasi-2D rollers can be observed, with strong rib vortices in the braid region. The large-domain, boundary-layer turbulence simulation, on the other hand, displays a much more chaotic structure: the rollers are significantly twisted, and the braid regions are essentially devoid of rib vortices; only very weak remnants of the coherent vorticity present in the ribs can be observed. The topological features of the flow support the conjecture that the more highly three-dimensional structure of the large-scale eddies in the later case is responsible for the difference in the similarity states, highlighted by the higher spanwise-velocity variances.

3 Conclusions

Large-eddy simulations of temporally evolving, turbulent mixing layers have been performed to study the effect of initial conditions and domain size on the evolution of the layer, and in particular on the self-similar states that resulted. The use a smaller domain forces the spanwise rollers to be two-dimensional during the late stages of the evolution; this results in a regular, well-ordered flow structure. The initial conditions also have a strong effect, particularly on the initial stages of the evolution. The use of random noise lets the Kelvin-Helmholtz instability emerge, leading to the early formation of a regular array of spanwise rollers. When boundary-layer turbulence is used to initiate the layer, on the other hand, the growth of the inviscid instability is inhibited by the presence of lower-wavenumber modes with significant energy content. The result is a delayed formation of the regular array and an initial structure that is more three-dimensional and with longer wavelength. The differences due to the initial conditions persist throughout the self-similar period, and are reflected in the statistics of the turbulent quantities, most notably the spanwise velocity fluctuation variances.

The main conclusion of this work is a confirmation of the experimental and theoretical findings that, although mixing layers evolve into self-similar states, these states are not unique, and may be affected by many factors. Among them, the initial conditions and the size of the domain have quite significant effects. They influence the shape of the coherent eddies of the flow and its statistics. The differences persist throughout the layer development, well into the self-similar period.

Financial support for this work was provided by the National Science Foundation under Grant CTS-961862.

References

[1] R.G. Batt. *AIAA J.* 13:245–247, 1975.

[2] P.E. Dimotakis & G.L. Brown. *J. Fluid Mech.*, 78:535–560, 1976.

[3] A.K.M.F. Hussain & M.F. Zedan. *Phys. Fluids* 21:1100–1112, 1978.

[4] M. M. Rogers & R. D. Moser. *Phys. Fluids* 6:903–923, 1994.

[5] C. Meneveau, T. S. Lund, & W. H. Cabot. *J. Fluid Mech.* 319:353–385, 1996.

ADVANCES IN TURBULENCE VIII
Proceedings of the Eighth European Turbulence Conference
C. Dopazo et al. (Eds.)
© CIMNE, Barcelona 2000

Rapid and slow contributions to the turbulent stress tensor and inverse modeling in a turbulent mixing layer

B.J. Geurts[1,2], I.C.C. de Bruin[1] and S. Sarkar[3]

[1] Faculty of Mathematical Sciences, Twente Institute of Mechanics,
University of Twente, P.O. Box 217, 7500 AE Enschede, The Netherlands
[2] Department of Engineering, Queen Mary and Westfield College,
University of London, Mile End Road, London E1 4NS, United Kingdom
[3]Department of Mechanical and Aerospace Engineering,University of California,
San Diego, 9500 Gilman Drive, La Jolla, CA 92093-0411, USA

Contact e-mail: b.j.geurts@math.utwente.nl

1 Introduction

Statistical averaging can form an alternative basis for the decomposition of the velocity field to model the turbulent stress tensor in large-eddy simulation (LES). One distinguishes 'rapid' contributions, predominantly from large scale flow-structures, next to 'slow' components arising from comparably small scales [1]. This decomposition is studied using direct numerical simulation (DNS) data of a mixing layer. We also consider the spatial filtering approach to LES [2] and focus on mixed 'subgrid' models [3], which identify a similarity model for the rapid and an eddy-viscosity model for the slow parts. Improvements in the similarity modeling due to inverse modeling [4] are illustrated.

Simulation of complex flows requires the Navier-Stokes equations to be modeled to reduce the number of degrees of freedom. In LES this traditionally involves a spatial filter and leads to the so-called turbulent stress tensor $\tau_{ij} = \overline{u_i u_j} - \overline{u_i}\,\overline{u_j}$. The over-bar denotes the filtering which introduces the decomposition $u_i = \overline{u}_i + u_i'$ of the velocity field. For turbulent flows that develop around a statistically stationairy state one can use a statistical filter as point of reference and introduce a corresponding decomposition $u_i = \langle u_i \rangle + u_i''$.

We consider the contributions to τ_{ij} in the statistical averaging context (the '$\langle u \rangle$ -formulation') and compare this to the spatial filtering context (the '$(\overline{u})$ -formulation'). The 'rapid' part involves the mean velocity gradient which is directly influenced by effects of anisotropy and inhomogeneity. Eddy-viscosity modeling may not apply and a similarity model is more appropriate. We also identify a 'slow' part which only involves the fluctuations. Differences between the $\langle u \rangle$ and the $(\overline{u})$ formulations show up in the rapid/slow decomposition.

In section 2 we introduce the mixing layer and consider correlations of the rapid and slow parts with similarity and eddy-viscosity models. The spatial structure of the turbulent stress is considered in section 3 and approximate inversion is illustrated. Some concluding remarks are collected in section 4.

2 Rapid and slow correlations in a mixing layer

We use DNS data of a spatially developing mixing layer at $Re = 200$ and $M = 0.8$. The Reynolds number is based on the upper free-stream velocity, density and viscosity and half the vorticity thickness at the inflow while the Mach number is given by the speed of sound and upper free-stream velocity. For the numerical method and treatment of the boundaries we refer to [6]. The DNS was performed at a resolution of $900 \times 192 \times 64$ grid points in the streamwise-, normal and (periodic) spanwise direction respectively in a box of size $L_1 \times L_2 \times L_3$. A snapshot of the spanwise vorticity in the long-time regime is shown in figure 1. For the analysis we coarsened to an 'LES'-grid of $225 \times 48 \times 16$ points.



Figure 1: Contours of spanwise vorticity in the fully developed long-time regime.

The spatial ($\overline{u}$) and statistical averaging ($\langle u \rangle$) settings differ in the basic filter operation that is used. For the $\langle u \rangle$ setting, we use a combined spanwise and long-time average. The spatial filtering uses the symmetric top-hat filter with filter-width Δ. Either filtering operation is denoted by L in the sequel. The turbulent stress tensor can be written as commutator of L and the product $S(f,g) = fg$, i.e. $\tau_{ij} = [L,S](u_i,u_j)$ with commutator $[L,S](f,g) = L(S(f,g)) - S(L(f),L(g))$ [4, 5]. We can write $\tau_{ij} = \tau^r_{ij} + \tau^s_{ij}$ with 'rapid' and 'slow' parts given by

$$\begin{aligned} \tau^r_{ij} &= [L,S]\Big(L(u_i),L(u_j)\Big) + [L,S]\Big(L(u_i),u'_j\Big) + [L,S]\Big(u'_i,L(u_j)\Big) \\ \tau^s_{ij} &= [L,S](u'_i,u'_j) \end{aligned} \qquad (1)$$

The 'slow' part contains contributions due to fluctuations only and the 'rapid' part contains the similarity model, and terms linear in the fluctuations.

Features of τ^r, τ^s depend on the velocity decomposition which may be relevant in subgrid-modeling. Bardina's similarity model $B_{ij} = [L,S](L(u_i),L(u_j))$ and Smagorinsky's model $M_{ij} = -2\nu_t W_{ij}$, where ν_t is the eddy viscosity and $W_{ij} = \partial_i u_j + \partial_j u_i$, are frequently used. To quantify whether B_{ij} or M_{ij} would

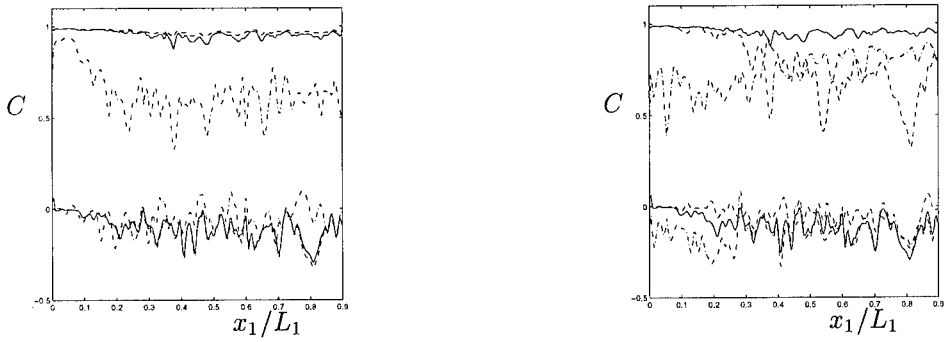


Figure 2: Correlation C of τ (solid), τ^r (dashed) and τ^s (dash-dotted) with W_{ij} (low values) and B_{ij} (high values) in the $(\overline{u})$ (left) and $\langle u \rangle$ (right) context.

be appropriate we consider the correlation in figure 2. We observe no correlation with W_{ij} in either $(\overline{u})$ or $\langle u \rangle$ setting and with either τ, τ^r or τ^s. A strong correlation between B_{ij} and τ, τ^r in the $(\overline{u})$ context, and lower but still significant correlation in the $\langle u \rangle$ context is apparent. Finally, a strongly fluctuating correlation in the range 0.3–0.7 for τ^s and B_{ij} is seen.

3 Spatial structure of turbulent stress

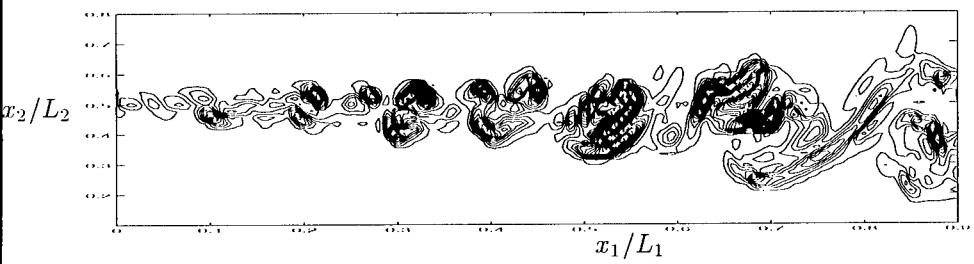


Figure 3: Snapshot of contours of τ_{12} at $\Delta = 2h$ on the coarsened grid at $x_3 = 0$.

In figure 3 we show the instantaneuous τ_{12} corresponding to figure 1. We observe a clustered structure corresponding to the vortices. The structure of τ will be compared to model-predictions. We also include the generalized similarity model $G_{ij} = [L, S](\hat{u}_i, \hat{u}_j)$ using approximate inversion [4, 5]. The reconstruction $\hat{u}_i$ considered here is only second order accurate and uses Simpson quadrature.

In figure 4 we compare τ_{12} with the similarity models. Each model follows the detailed structure of the stress tensor. Fluctuations in τ are underestimated by B_{ij} whereas G_{ij} provides too large fluctuations. An accurate, though ad hoc, model arises from averaging these two. The rapid and slow decomposition is shown in figure 4. We observe that $\tau \approx \tau^r$ in the $(\overline{u})$ context. In the $\langle u \rangle$ context we notice large excursions of τ^r, τ^s which are more complex to model.

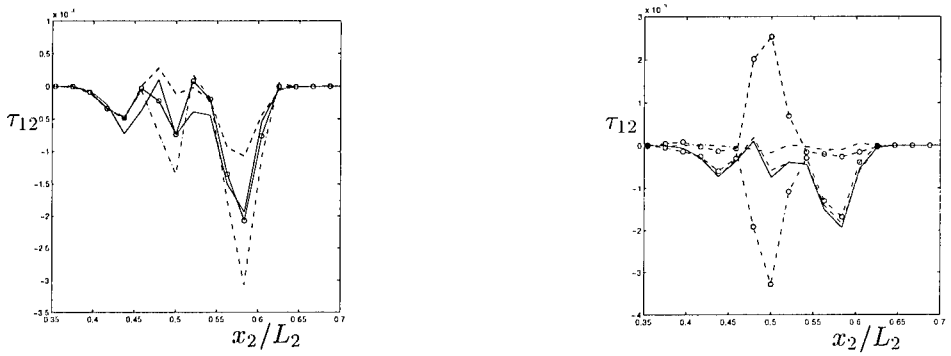


Figure 4: Left: τ_{12} (solid), B_{12} (dashed), G_{12} (dash-dotted) and $(B_{12}+G_{12})/2$ (solid; 'o'). Right: τ_{12} (solid) and in $(\overline{u})$ context: τ^r_{12} (dashed), τ^s_{12} (dash-dotted) and in $\langle u \rangle$ context: τ^r_{12} (dashed; 'o'), τ^s_{12} (dash-dotted; 'o'). Both $x_1/L_1 \approx 1/2$.

4 Concluding remarks

We compared a spatial and a statistical averaging decomposition of the turbulent velocity field and identified a 'rapid' and a 'slow' part of the turbulent stress tensor. The correlation with similarity and eddy-viscosity models and the structure of the turbulent stress tensor show large differences in the two decompositions. Generalized similarity models appear to be favored in the $(\overline{u})$ context. In the $\langle u \rangle$ context a combination with Reynolds averaged modeling is possible which avoids the 'zonal' approach and uses the RaNS prediction in the decomposition of the velocity field which appears particularly useful near walls. Connections with VLES and the statistical averaging setting will be explored in the future.

References

[1] L. Shao, S. Sarkar and C. Pantano. On the relationship between the mean flow and subgrid stresses in large eddy simulation of turbulent shear flows. *Physics of Fluids*, 11:1229–1248, 1999.

[2] M. Germano. Turbulence: the filtering approach. *J. Fluid Mech.*, 238: 325-334, 1992.

[3] A.W. Vreman, B.J. Geurts and J.G.M. Kuerten. Comparison of subgrid-models in large eddy simulation of the temporal mixing layer. *J. Fluid Mech.*, 339: 357–394, 1997.

[4] B.J. Geurts. Inverse Modeling for Large-Eddy Simulation. *Physics of Fluids*, 9:3585–3587, 1997.

[5] J.G.M. Kuerten, B.J. Geurts, A.W. Vreman and M. Germano. Dynamic inverse modeling and its testing in large-eddy simulations of the mixing layer. *Physics of Fluids*,11:3778–3785, 1999.

[6] I.C.C. de Bruin, B.J. Geurts and J.G.M. Kuerten. Statistical analysis of the turbulent mixing layer. *Proceedings Direct and Large-Eddy Simulation III*; Eds: Voke, Sandham, Kleiser, Kluwer Academic Publishers: 234–246, 1999.

ADVANCES IN TURBULENCE VIII
Proceedings of the Eighth European Turbulence Conference
C. Dopazo et al. (Eds.)
© CIMNE, Barcelona 2000

Spatial development of a 3D compressible turbulent mixing layer

L. Doris[1], C. Tenaud[1] and L. Ta Phuoc[1]

[1]Fluid Dynamics Group, LIMSI-CNRS
BP 133, 91403 ORSAY, FRANCE

Contact e-mail : laetitia.doris@limsi.fr

1 Introduction

This study deals with the simulation of high speed compressible flows, by means of large eddy simulation. The generic flow considered here is the turbulent plane 3D mixing layer spatially developing downstream of a flat plate, for which detailed experimental data are available at various convective Mach numbers. This type of flow contains no wall problem and has one inhomogeneous direction. This is why it has been chosen for the validation of large eddy simulation for compressible flows. The originality of this study stands in the fact that the spatial development of the flow starts at the trailing edge of the flat plate, including both the transitional wake and the set up of the mixing layer.

2 Subgrid modeling

The governing equations solved in this study are the full compressible Navier-Stokes equations representing the conservation of mass, momentum and total energy by unit of mass, written in a conservative form. These equations are filtered with a spatial filter combined with the Favre decomposition. $\widetilde{u}_i$ is the resolved part of the density-weighted velocity, and u_i'' its subgrid part.

In this study, the main subgrid term modeled is the subgrid stress tensor $\tau_{ij} = \overline{\rho}(\widetilde{u_i u_j} - \widetilde{u}_i \widetilde{u}_j)$. The modeling of this term is based on the concept of subgrid viscosity μ_{sg}. The model used is the Mixed Scale model adapted to compressible flows [1]. The eddy viscosity is defined as follows : $\mu_{sg} = \sqrt{\mu_\omega \, \mu_k}$ where $\mu_\omega = \overline{\rho} C_\omega \Delta^2 |\widetilde{\omega}|$ (vorticity model) and $\mu_k = \overline{\rho} C_k \Delta \sqrt{k}$ (Turbulent Kinetic Energy model), with $C_\omega = 0.01$ and $C_k = 0.126$. Δ represents the cut off length scale of the spatial filter. $\widetilde{\omega}$ is the resolved part of the vorticity. k is the subgrid kinetic energy, obtained with the scale similarity assumption, by means of a double-filtering technique.

3 Numerical approach and configuration studied

The three-dimensional domain starts at the trailing edge of the flat plate. The resolution of the governing equations has been performed through the use of a finite volume method. The numerical scheme is a spatially second-order upwind shock-capturing TVD scheme. The time integration is based on a third order Runge-Kutta method.

At the inlet, the boundary conditions are computed following the characteristics method [2]. The longitudinal velocity is prescribed to a mean boundary layer profile. The vertical and spanwise velocities are set to zero. Two white noises of amplitudes $1\%U_1$ and $0.1\%U_1$ respectively are used to perturb the longitudinal and spanwise velocities. At the upper and lower part of the domain, and at the outlet, non-reflecting conditions are applied. In the spanwise direction, a periodic condition is used.

The Reynolds number of the simulation, based on the high velocity and on the thickness of the high speed inlet boundary layer ($\delta_i = 10mm$) is $Re = 60000$. The convective Mach number is $M_c = 0.64$. The velocity ratio $r = U_2/U_1$ is 0.27, the density ratio $s = \rho_2/\rho_1$ is 0.57.

4 Results of 3D simulations

The longitudinal evolution of the vorticity thickness $\delta_\omega = \Delta U/(\partial u/\partial y)_{max}$, with $\Delta U = U_1 - U_2$, is compared to experimental data of De Bisschop [3] and of Samimy et. al [4] in the figure 1 (left). In the simulation curve, two parts can be distinguished: the first one represents the wake of the flat plate. Then, a transition occurs and the evolution becomes linear. It represents the mixing layer itself, which has reached a self-similarity behavior. If we plot a matching line of this part of the curve, its intersection with the x-axis gives X_0 the virtual origin of the mixing layer. The slope of this part of the curve matches very well the one of the experiments. However, the values of X_0 for simulation and experiment are not equal: the transition between the wake and the mixing layer occurs at $X_0 = 0.055m$ for [4], at $X_0 = 0.023m$ for [3], and at $X_0 = 0.270m$ for the simulation. This might be due to the influence of the inlet boundary conditions. In fact, the white noise perturbations, of course, do not mimic the turbulent behavior in a boundary layer.

Once the flow has reached a self-similarity state, all the dimensionless profiles should collapse. In the figure 1 (right) six non-dimensional longitudinal velocity $U^* = (u - U_2)/\Delta U$ profiles are plotted (at six different locations in the self-similarity region) as a function of the non-dimensional vertical coordinate $y^* = (y - y_0)/\delta_\omega$. y_0 is y where $u = (U_1 + U_2)/2$. The six profiles gather very well together, moreover they fit the experimental profiles satisfactorily.

Six profiles of longitudinal and vertical non-dimensional turbulence intensities ($\sigma_u = \langle u'^2 \rangle^{1/2}$) are plotted in the figure 2 at the same locations. In both cases the similarity behavior is obtained, and the shape of the curves matches

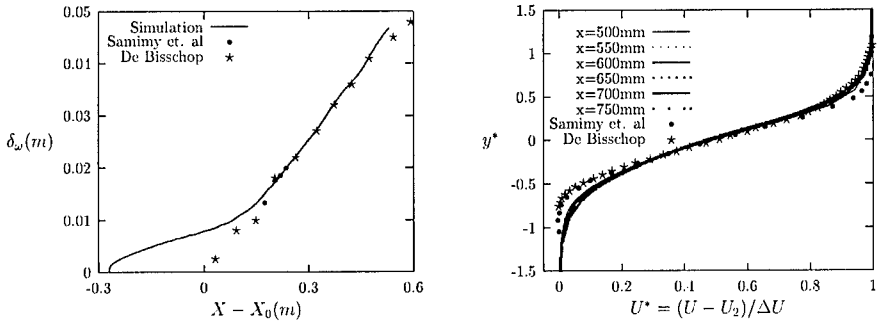


Figure 1: Longitudinal evolution of the vorticity thickness (left); longitudinal velocity profiles versus dimensionless vertical coordinate (right).

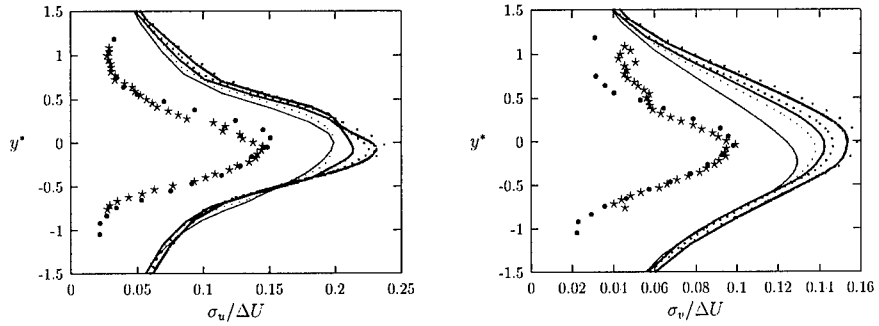


Figure 2: Turbulence intensity of longitudinal velocity (left) and of vertical velocity (right) versus dimensionless vertical coordinate. For the legend see figure 1 (right).

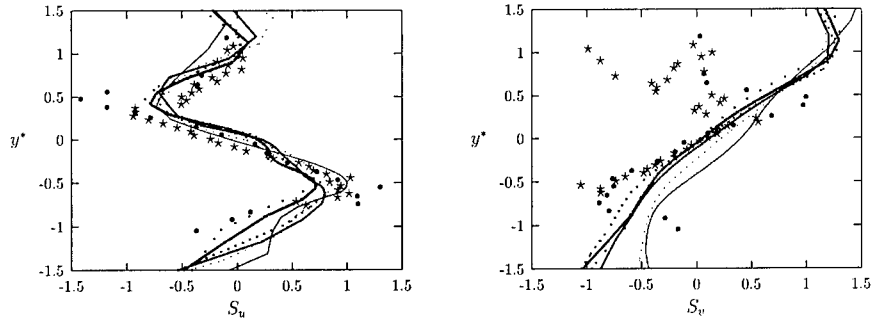


Figure 3: Skewness of longitudinal velocity (left) and of vertical velocity (right) versus dimensionless vertical coordinate. For the legend see figure 1 (right).

the experimental one. However, the intensity is overestimated by about 30% for σ_u and more than 50% for σ_v. Pellerin et. al [5], in a study concerning an incompressible mixing layer, have shown that the amplitude of the inlet white noises has a significant influence on the turbulent intensities in the mixing layer. Therefore we are currently trying to improve our results by changing the amplitude of the inlet white noises.

In the figure 3, six profiles of the skewness of u ($S_u = \langle u'^3 \rangle / \langle u'^2 \rangle^{3/2}$) and of v are plotted, as well as the experimental data. The qualitative and quantitative agreement is better than for turbulence intensity, which proves that the turbulence organization is correctly recovered even if the intensities are overpredicted.

5 Conclusion

The longitudinal evolution of the vorticity thickness as well as the non-dimensional longitudinal velocity profiles fit well the experimental data. The turbulence intensities are overpredicted. The turbulence organization seems however to be well estimated. We are currently studying the influence of the inlet perturbations on the turbulent intensities in the mixing layer. Moreover, in order to study the effects of compressibility on the mixing layer development, a simulation at a higher convective Mach number will be undertaken in the future.

Acknowledgments. The calculation time has been provided by IDRIS, CNRS. This work is financially supported by the DGA. The authors greatly acknowledge these institutions.

References

[1] L. Doris, C. Tenaud, and L. Ta Phuoc. LES of a spatial compressible mixing layer : model influence analysis. Proceedings of the Euromech 403 conference on turbulence in high speed compressible flows, Poitiers, France, 1999 (to appear).

[2] T. J. Poinsot and S. K. Lele. Boundary conditions for direct simulations of compressible viscous flows. *Journal of Computational Physics*, 101:104–129, 1992.

[3] J.-R. De Bisschop. *Comportement de la turbulence en couches de mélange supersoniques.* Thèse de doctorat, Université de Poitiers, 1993.

[4] M. Samimy and G. Elliott. Effects of compressibility on the characteristics of free shear layers. *AIAA Journal*, 28(3):439–445, 1990.

[5] S. Pellerin, A. Dulieu, L. Ta Phuoc, and C. Tenaud. Incompressible 3-D mixing layer using LES: Influences of subgrid scale models and of upstream perturbations. ISCFD'99, Bremen, Germany. To be published in CFD Journal, Vol. 9, 1, April 2000.

ADVANCES IN TURBULENCE VIII
Proceedings of the Eighth European Turbulence Conference
C. Dopazo et al. (Eds.)
© CIMNE, Barcelona 2000

A-Posteriori Tests of a New SGS Model: LES of Fully Developed Pipe Flow

C. Brun, T. J. Hüttl, and R. Friedrich

Lehrstuhl für Fluidmechanik, Technische Universität München
Boltzmannstr. 15, D-85748 Garching, GERMANY

Contact e-mail: Brun@lrz.tum.de

Standard eddy viscosity based Large Eddy Simulation (LES) approaches fail in reliably predicting turbulent wall bounded flows. Some recent studies have focused on scale similarity approaches which are able to model backward transfer of energy from small to large scales taking place *e.g.* in the buffer zone of a turbulent boundary layer. All of them ended up with a 2-part model blending both Smagorinsky and scale similarity concepts, so called mixed models [1, 5, 7]. We demonstrate that the Increment model [2] based on a new scale similarity approach is able to provide the proper spectral energy distribution within the near wall layer of a fully developed pipe flow without using any purely dissipative term.

1 The Increment SGS Model

By applying a low-pass filter to the velocity field of a turbulent flow, one obtains the resolved field $v_i = \overline{u_i}$ that one attempts to compute in LES. The SGS stress tensor which has to be modeled in the filtered Navier-Stokes equations reads: $\tau_{ij} = \overline{u_i u_j} - \overline{u_i}\ \overline{u_j}$. One can associate to each filtered quantity a $3D$ Taylor expansion with respect to the original unfiltered quantity [2]. When such an expansion is introduced into the SGS stress tensor [2, 7], and when a non-separable and non-symmetric filter is considered [1, 2], a 2^{nd} order discretisation in space applied to the $3D$ truncated Taylor expansion yields: $\tau_{ij} \approx c\ \delta u_i\ \delta u_j$, where c is related to the shape of the filter, and δu_i is the velocity increment determined at the filter size Δx_k in the k direction. This expression was the guideline for the Increment model proposed by Brun & Friedrich [2], which is based on the resolved velocity increment tensor $Q_{ij} = \delta\overline{u_i}\ \delta\overline{u_j}$ as follows:

$$\boxed{\begin{array}{c} \tau_{ij} = f\ Q_{ij} = f\ \delta v_i\ \delta v_j \\ \delta v_i = \sum_{k=1}^{3} [v_i(x_k + \Delta x_k/2) - v_i(x_k - \Delta x_k/2)] \end{array}} \quad (1)$$

Due to the strong correlation between the generalised Leonard stress tensor [2] and the SGS stress tensor τ_{ij}, a specific dynamical approach has been applied to determine the coefficient f locally. The test filter $\widehat{()}$ required has twice the size of the implicit filter $\overline{()}$ of the computation:

$$f(\underline{x},t) = \frac{1}{4}\,\frac{\widehat{v_k}\,\widehat{v_k} - \widehat{v_k}\;\widehat{v_k}}{\delta v_l\;\delta v_l} \tag{2}$$

2 Fully developed turbulent pipe flow

Three large-eddy simulations have been performed with a code based on staggered grids and second order central schemes to integrate the filtered incompressible Navier-Stokes equations in cylindrical coordinates [3]. The computational domain is a pipe section of length $L_x = 10R$, R being the radius of the pipe. The mesh is equidistant in each homogeneous direction and stretched in the wall-normal direction with the center of the wall-nearest cell being around $z^+ = 1$ (table 1). At the wall, impermeability and no-slip boundary conditions are realized. In the circumferential and axial directions periodic boundary conditions are used.

	n_x	n_φ	n_r	Δx^+	$R\Delta\varphi^+$	Δz_w^+	Re_τ	Re_b
experiment [6]	-	-	-	-	-	-	169	4922
DNS [3]	256	128	96	7.0	8.8	1.88	180	5000
LES1	32	64	96	56.3	18.0	1.88	180	4860
experiment [6]	-	-	-	-	-	-	315	9972
LES2	54	72	48	62.6	33.0	1.70	338	10380
experiment [6]	-	-	-	-	-	-	520	17773
LES3	64	160	48	81.3	20.0	2.00	520	16860

Table1: Flow and computational parameters of the 3 LES in comparison with DNS and experimental data.

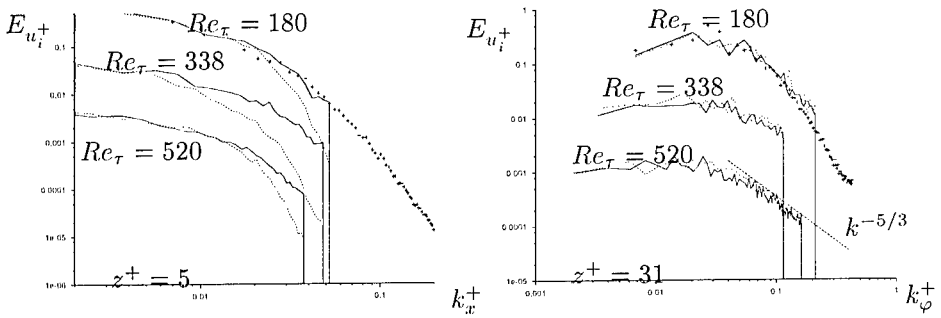


Figure 1: Velocity energy spectra in axial (left) and circumferential (right) direction (arbitrary vertical scale): + DNS [3], —— LES, - - - No Model

Figure 1 compares $1D$ spectra of turbulent kinetic energy at different Reynolds numbers. The effect of the model is to predict the right shape of the spectrum. Another information to be drawn from figure 1 is that the cutoff wavenumber in circumferential direction is too close to the energy containing scales. The mean axial velocity and the RMS velocity fluctuations in figure 2 reflect an acceptable behaviour. They are characterized by an overprediction of the axial RMS velocity fluctuations and an underprediction of the remaining two components. This is typical for most of the LES predictions. What is new here is the fact that these results have been obtained with a model that contains no explicit dissipative term.

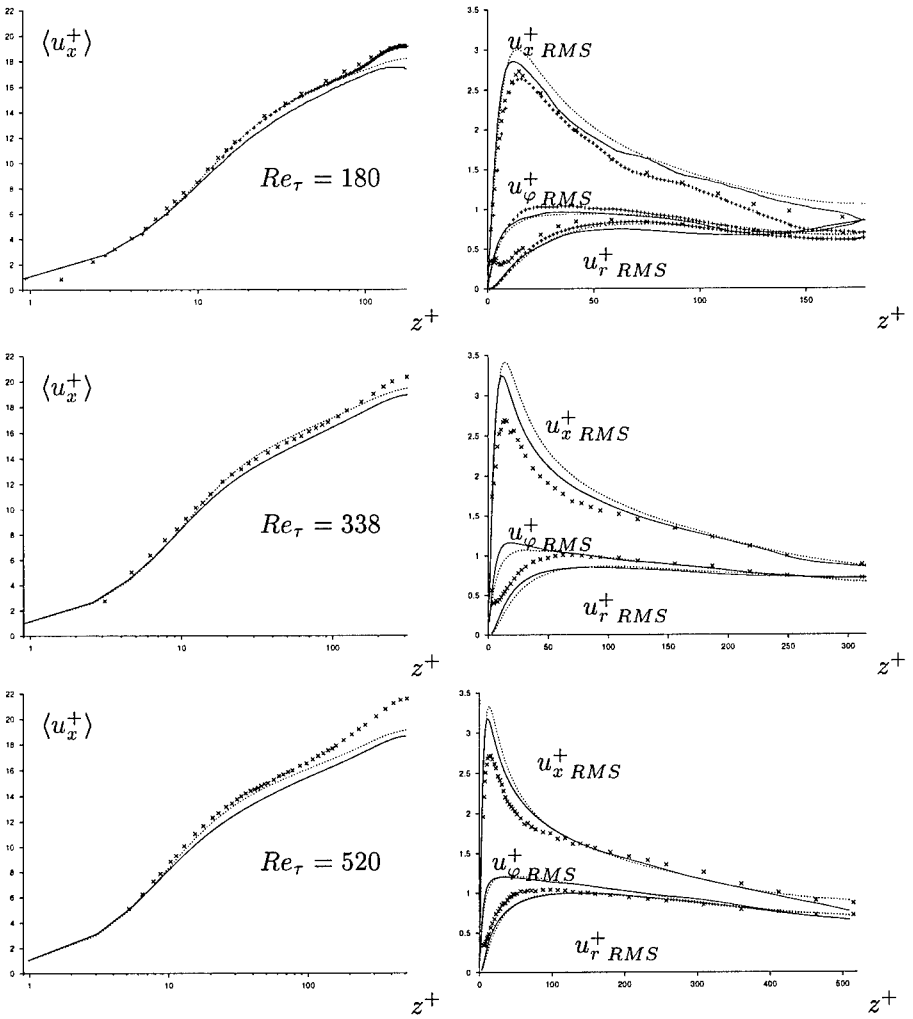


Figure 2: Profiles of the mean velocity (left) and RMS velocity fluctuations (right) for pipe flow at $Re_\tau = 180$ (top), $Re_\tau = 338$ (center) and $Re_\tau = 520$ (bottom): —— LES (Increment model), - - - No Model, + DNS [3], × experiment [6] .

3 Conclusions

We have shown that the scale similarity concept in modelling the SGS stress tensor without supplementing a Smagorinsky term allows for stable solutions. The use of a model coefficient which is determined locally in space and time with a proper dynamical procedure is a condition *sine qua non* of the success of such a model. The results presented here are promising concerning statistics as well as the energy distribution of the velocity field in spectral space. Further efforts are curently undertaken to decouple the effect of the model from the numerical errors [4].

This work was supported by the EC TMR project 'LES of complex industrial flows'. The authors want to thank Jaap M.J. den Toonder for providing the experimental data of the pipe flow.

References

[1] V. Borue and S. A. Orszag. Local energy flux and subgrid-scale statistics in three-dimensional turbulence. *J. Fluid Mech.*, 366:1–31, 1998.

[2] C. Brun and R. Friedrich. A-priori tests of SGS stress models in fully developed pipe flow and a new local formulation. *Isaac Newton Institute Symposium/ ERCOFTAC Workshop, Cambridge, Royaume Uni*, In: P.R. Voke et al. (eds.), *Direct and Large-Eddy Simulation III*, Kluwer Academic Publishers, 249–262, 1999.

[3] T. J. Hüttl. Direkte Numerische Simulation turbulenter Strömungen in gekrüm-mten und tordierten Rohren. In: *Ph.D. Thesis, TU München*, VDI Fortschritt-Berichte, Reihe 7, Nr 364, VDI-Verlag Düsseldorf, 1999.

[4] A. G. Kravchenko and P. Moin. On the effect of Numerical Errors in Large Eddy Simulations of Turbulent Flows. *J. Comp. Phys.*, 131:310–322, 1997.

[5] F. Sarghini, U. Piomelli and E. Balaras. Scale-similar models for large-eddy simulations. *Phys. Fluids*, 11(6):1596–1607, 1999.

[6] J. M. J. den Toonder and F. T. M. Nieuwstadt. Reynolds number effects in a turbulent pipe flow for low to moderate Re. *Phys. Fluids*, 9:3398–3409, 1997.

[7] G. S. Winckelmans, A. A. Wray and O. V. Vasilyev. Testing of a new mixed model for LES: the Leonard model supplemented by a dynamic Smagorinsky term. *Proc. Summer Program*, CTR, NASA Ames/Stanford Univ., 367–388, 1998.

XVIII

Two Phase Flows

ADVANCES IN TURBULENCE VIII
Proceedings of the Eighth European Turbulence Conference
C. Dopazo et al. (Eds.)
© CIMNE, Barcelona 2000

Settling velocity and clustering of particles in an homogeneous and isotropic turbulence

F. Hainaux[1], A. Aliseda[1], A. Cartellier[2] and J. C. Lasheras[1]

[1] University of California, San Diego, USA
[2]LEGI - CNRS, Grenoble, FRANCE

Contact e-mail: lasheras@mae.ucsd.edu

1 Introduction

The behavior of droplets in homogeneous and isotropic turbulence has been experimentally investigated in the case of particles smaller than the Kolmogorov scale. It is known that the average settling velocity V_z of droplets can be significantly larger than their terminal velocity V_s in still air. The difference $V_z - V_s$ depends both on the droplet inertia and on its terminal velocity. The dimensionless parameters commonly used to characterize this effect are the Stokes number, St, defined as the ratio of the particle response time τ_p to the Kolmogorov time scale τ_k, and the ratio of the droplet terminal velocity V_s to the Kolmogorov velocity u_k. Recent DNS results have shown that when $St = 1$, a maximum increase in the settling velocity is obtained for V_s/u_k between 1.5 to 2.5 [1]. Meanwhile, for $V_s/u_k = 1$ the maximum increase in settling velocity was observed for $St = 1$. Although these results are robust, they are somewhat sensitive to the value of the turbulent Reynolds number leading to a debate on the correctness of a Kolmogorov scaling [2]. They notably hold for a Stokes drag as well as for a drag corrected for weak inertial effects. In parallel, the formation of droplet clusters has also been observed for this type of flow. In these clusters, the local concentration may reach 20 to 50 times the mean value, local meaning here at a scale $(2\eta)^3$, where η is the Kolmogorov length scale. So far, little attention has been paid to the relationship between the average settling velocity and the mean concentration and between the settling velocity and the presence of droplet clusters.

2 Experimental setup and main results

In order to investigate the effect of the clustering on the settling velocity, we conducted experiments in a horizontal wind tunnel 2.5 m long and 200 mm

wide, where the droplet laden flow was created through an array of 150 air-blast atomizers. Precise measurements were carried out for a mass loading ratio ranging from 0.5% to 10%. In absence of water injection, the base flow param-

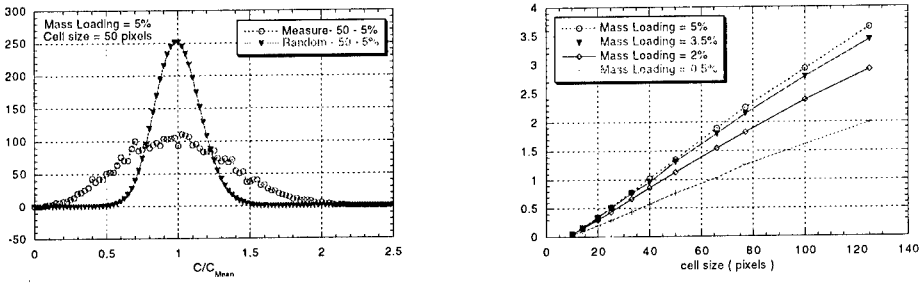


Figure 1: a) Measured and Poisson particle concentration distribution. b) Evolution of D, Deviation of the particle concentration distribution from randomness, with the cell size for different mass loading. $D = (\sigma - \sigma_{Poisson})/\lambda$, where σ and σ_{lambda} represent the standard deviation for the measured local particle concentration distribution and the Poisson distribution, and λ is the mean concentration in each box. (10 pixels correspond to one Kolmogorov length)

eters are $u = 11.2m/s$, $u_{rms} = 0.2m/s$. At a distance of 1.5 m downstream the droplet injection, the dissipation rate ϵ is $1.41m^2/s^3$, the Kolmogorov scale is $\eta = 0.22mm$, and the integral length scale is about 7 cm. The resulting droplet size has a Sauter Mean Diameter $SMD = 27\mu m$ and an arithmetic mean $D_{10} = 10\mu m$. The occurence of clustering has been analyzed using image processing techniques of planar cuts of the flow (high resolution digital camera and short exposure time). Surface concentration maps were extracted from the row images by counting droplets over square cells, ranging in size from η to 15η. The probability density function of these surface concentration was determined

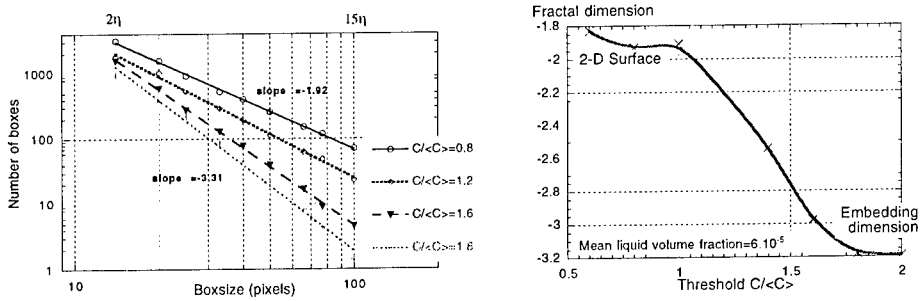


Figure 2: a) Number of cells needed to cover an iso-concentration surface. b) Evolution of the fractal dimension of cluster according to the concentration threshold.

for various mass loading ratio. These pdf were compared with the pdf of the

random distribution (fig. 1.a). Using the parameter defined by Fessler et al. [3], the deviation of the measured pdf from randomness were found to increase with the mass loading and the cell size (fig. 1.b), first indicating the role of the mean concentration in the formation of particle clusters and second that the spatial inhomogeneity is visible from a few Kolmogorov lengths up to scales one order of magnitude larger. Clusters of droplets were then identified by thresholding the concentration image. Similary to what was found in the experiments in homogeneous jets [4], the geometrical nature of iso-concentration islands evolves with the concentration threshold. Low concentration objects were found to be close to 2-D surfaces while high concentration objects consist of a multitude of small regions the dimension of which approaches the embedding dimension i.e. 3. In between, the fractal dimension evolves continuously with the concentration as shown fig. 2.b. An analog behavior has been recently observed in simulation [5]. The droplet settling velocity was measured using a PDPA. A typical result

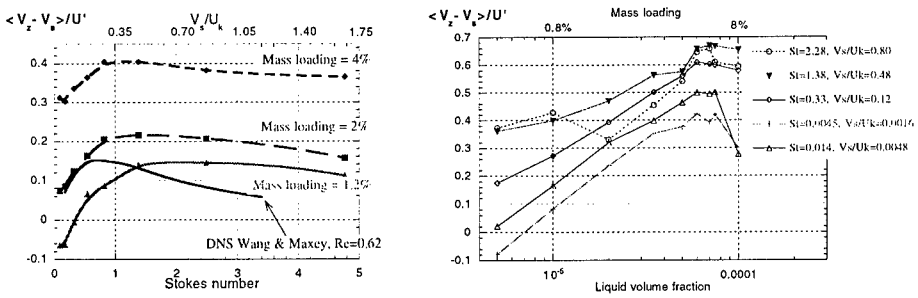


Figure 3: Increase of settling velocity a) according to the particule size. b) with the mean liquid volume fraction in the channel.

for different mass loading is shown fig. 3.a and 3.b. Clearly, $V_z - V_s$ shows a non-monotonic increase with the Stokes number which agrees qualitatively with the numerical simulations. Notably, the settling velocity of very small particles, which follow passively the turbulent eddies, is unchanged. The velocity difference reaches a maximum for a drop diameter about $25\mu m$. In the experiments, St and V_s/u_k are not independent, since they take fixed values once the droplet diameter is fixed. This provides an explanation why the maximum in fig. 3.a is located between $St = 1$ and $V_z/V_s = 1$. The second result shown here is that, for mass fractions less than 5%, for which the underlying turbulence is weakly modified by the dispersed phase, the mean settling velocity increases monotonically with the mean liquid loading (fig 3.b). Using PDPA measurement conditioned by the local concentration we were able to measure the size and the settling velocity of the droplets inside and outside the clusters. In the figure 4.a we plotted, for a given mean mass loading, the difference between the particle size pdf for a given local concentration and the initial size pdf. It shows clearly that regions of high concentration contain more particles of Stokes number around one. In parallel, the size-pdf presents an increase up to 15% compared to the initial pdf

at each extrem of the plot. Furthermore, the settling velocity for small particles were found to be up to 30% higher inside cluster than outside (fig. 4.b).

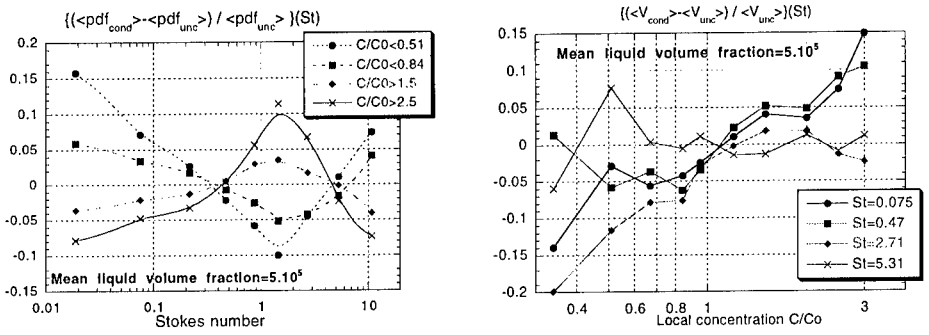


Figure 4: PDPA measurments conditioned by the local concentration: a) Difference between the particle size distribution in a given environment and the unconditional distribution. b) Increase of settling velocity in a given concentration environment compared with the unconditional settling velocity $< V_{unc} >$ for various Stokes numbers.

3 Conclusions

The main conclusions ascertained thus far are twofold : i) The particles interacting with the surrounding turbulence leads to the formation of clusters of multifractal nature, and ii) These clusters are responsible for an increase in the settling velocity. The hypothesis currently investigated here is that this increase is due to the convection velocity of dense compact droplet cluster regions which sink in the overall low concentration medium.

References

[1] L. P. Wang and M. R. Maxey (1993). Settling velocity and concentration distibution of heavy particles in homogeneous isotropic turbulence.

[2] M. S. Yang, A. E. Lei (1998). The role of the turbulent scales in the settling velocity of heavy particles in homogeneous isotropic turbulence.

[3] J. R. Fessler, J. D. Kulick and J. K. Eaton (1994). Preferential concentration of heavy particles in a turbulent channel flow.

[4] H. J. Catrakis and P. E. Dimotakis (1996). Mixing in turbuleny jets: scalar measures and isosurface geometry.

[5] C. Y. Hogan, J. N. Cuzzi and A. R. Dobrovolskis (1999). Scaling properties of particle density field in simulated turbulent flows.

ADVANCES IN TURBULENCE VIII
Proceedings of the Eighth European Turbulence Conference
C. Dopazo et al. (Eds.)
© CIMNE, Barcelona 2000

Two-way coupling effect on settling velocity of small heavy particles in homogeneous turbulence

M. Tanaka[1], N. Komai[1], Y. Maeda[2], and Y. Hagiwara[1]

[1]Dept. of Mech. and System Eng., Kyoto Institute of Tech.
Matsugasaki, Sakyo-ku, Kyoto 606-8585, JAPAN
[2]Sanyo Electric Co., Keihan-Hondohri, Moriguchi 570-8677, JAPAN

Contact e-mail: mtanaka@ipc.kit.ac.jp

1 Introduction

The study of the settling velocity of small heavy particles in turbulent flows is important for many environmental and engineering applications, such as the settling of aerosol particles in the atmosphere and the combustion of pulverized coal or liquid sprays. It is well known that the average settling velocity of particles in turbulence is greater than that in still fluid. The increase of settling velocity depends on the inertia and terminal velocity of particles, since they control the particle accumulation in low vorticity regions and the preferential sweeping of particles in downward moving fluid. Wang and Maxey [1] showed that a significant increase can occur for the particle with inertia response time and still-fluid terminal velocity comparable to the Kolmogorov scales of the turbulence. However, the above result has been confirmed only in so-called one-way coupling case, that is, at very low particle mass loadings in which the effect of particles on the turbulent flow is negligible. It is still unknown how the interaction between the particles and the turbulence (two-way coupling) influences the increase in the settling velocity.

In the present work, we investigate the two-way coupling effect on settling velocity of small heavy particles by using a direct numerical simulation of isotropic turbulence at relatively low mass loadings of particles.

2 Formulation

We consider the motions of spherical particles under the gravitational force in the x_1 direction. The particle diameter, d_p, was assumed to be small compared with the Kolmogorov length-scale, l_K, of turbulence. It is also assumed the

concentration of particles is low enough such that the effect of particle-particle interaction is negligible. Taking account of the fact that the particle (solid) density, ρ_p, is much larger than the fluid (air) density, ρ_f, only the Stokes drag and the gravitational forces were assumed to act on particles. The particle motions are then governed by the following equations,

$$\frac{\mathrm{d}\boldsymbol{u}_p}{\mathrm{d}t} = \frac{1}{\tau_p}\left\{\boldsymbol{u}(\boldsymbol{x}_p) - \boldsymbol{u}_p + V_S\widehat{\boldsymbol{e}}_1\right\} \ , \ \frac{\mathrm{d}\boldsymbol{x}_p}{\mathrm{d}t} = \boldsymbol{u}_p, \tag{1}$$

where $\tau_p = \rho_p d_p^2/18\rho_f\nu$ and $V_S = \tau_p g$ (g: gravity) denote the particle inertia and the still-fluid terminal velocity, respectively. The reaction force due to the Stokes drag was assumed to act on the carrier fluid.

The motions of the carrier fluid were solved on 64^3 grid points in a cubic box of sides of 2π by using the Fourier spectral method. The 13-point spatial interpolation method [2] was used both for the evaluation of fluid velocity at the particle position from its neighboring grid points and for the distribution to the grid points of the reaction force exerted by the particle on the fluid.

In the present study, we focus on the particles with $\tau_p/\tau_K = O(1)$ and $V_S/v_K = O(1)$ at which the increase in settling velocity due to turbulence is significant in the one-way coupling case, where τ_K and $v_K = l_K/\tau_K$ are the Kolmogorov time and velocity scales of the turbulence, respectively. A decaying run was performed starting from the random initial condition. We introduced 2^{19} particles randomly throughout the computational domain at $t = t_0$ when the turbulence had attained a fully developed state. The Taylor microscale Reynolds number at $t = t_0$ was 20.4. The particle volume fraction was as low as 6.8×10^{-5} (see Table 1). The particle and the fluid motions were simulated until $t = t_c = t_0 + 1.93T_e$, where $T_e = u_i^2/\epsilon$ (ϵ: energy dissipation rate) is the eddy turnover time.

Four additional runs were conducted for the particles with different values of d_p with the gravity, the particle's density and the volume fraction fixed (see table 1). Since the lack of stationarity would cause difficulties in the comparison between the results for different values of τ_p (or d_p), the turbulence was kept stationary by fixing the sum of the amplitude of Fourier modes within the wavenumber band of $2.5 < |\boldsymbol{k}| < 3.5$. The Taylor microscale Reynolds number in the case without particle was 33.7. The number of particles was 2^{18}.

For comparison, simulations without the reaction force were carried out for all the cases. It was found that the turbulence energy changed slightly due to the two-way coupling effect (4.0 percent increase for the decaying case, 1.0 and 10.0 percent decreases for the case2 and case4 in the stationary turbulence, respectively).

3 Results and Discussion

First, we consider the decaying case. Figure 1 shows the concentration probabilities of particles at the end of the simulation. The concentration C at any

grid point is defined as the number of particles inside a small cubic cell with the center at the grid point and its side equal to the grid spacing. The figure shows that both the regions of $C = 0$ and of large values of C are large compared with the random distribution as a result of the particle clustering. This is due to the particle accumulation in low vorticity and high strain regions [3, 1]. It is seen that the two-way coupling effect modifies the particle concentration only slightly. On the other hand, it noticeably enhances the increase in the settling velocity, $\Delta V_S = u_{p1} - V_S$. Figure 2 shows the time evolution of the mean value $\langle \Delta V_S \rangle$. The increase in the one-way coupling case is 11.9 percent of the magnitude of vertical velocity u_1', which is comparable with those in previous works [1, 4]. The relative increase of the settling velocity due to the two-way coupling effect amounts to 11.4 percent of u_1' at $t = t_e$. This is larger than the increase in u_1' itself (5.3 percent) due to the reaction force by the particles.

Figure 3 shows the settling velocity averaged over the particles inside the grid cells with the specified concentration C. The monotonous increase in settling velocity with C in the one-way coupling case corresponds to the concentration of particles to the local downward flows. It is interesting that the additional increase of settling velocity due to the two-way coupling effect also increases with C. This indicates that the particles accumulated in clusters intensify the local downward flows, which further accelerate the settling of the particles.

Finally, we examine the dependence of the settling velocity on the particle diameter. Figure 4 shows the increase in the average settling velocity for the stationary turbulence. Note that since the gravity is fixed, the still-fluid terminal velocity, $V_S (= \tau_p g \propto {d_p}^2)$, is proportional to the particle inertia τ_p. It is seen that the maximum enhancement of the increase, $\langle \Delta V_S \rangle$, occurs at $\tau_p \approx \tau_K$ in the one-way coupling case [1, 4]. The two-way coupling effect significantly enhances $\langle \Delta V_S \rangle$ for all the cases. The additional increase in $\langle \Delta V_S \rangle$ due to the two-way coupling effect seems to be maximized at $\tau_p \approx \tau_K$ as in the one-way coupling case, though its dependence on the particle diameter is relatively weak.

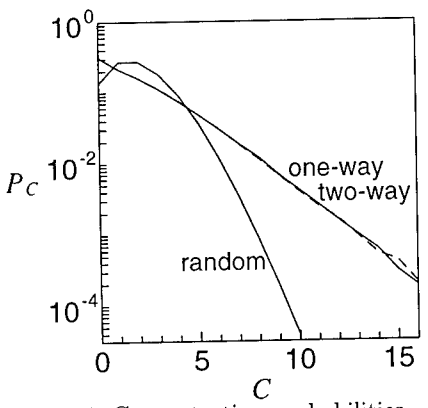


Figure 1: Concentration probabilities of particles. $\langle C \rangle = 2$.

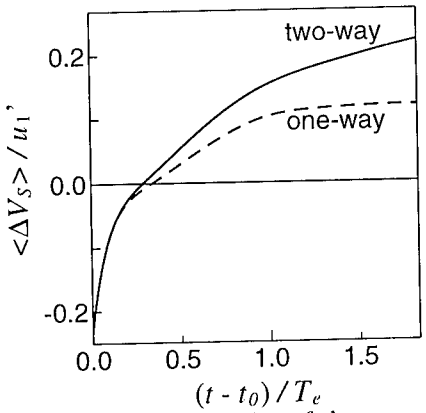


Figure 2: Time evolution of the increase in average settling velocity.

Table 1: Parameters. $k_{\max} = \sqrt{3}N/2$ $(N = 64)$.

case	d_p/l_K	τ_p/τ_k	ρ_p/ρ_f	ϕ_v	V_S/v_k	$l_K k_{\max}$
decaying $(t = t_0)$	0.16	1.43	1000	6.8×10^{-5}	0.96	0.8
decaying $(t = t_e)$	0.07	0.26	—	—	1.23	1.8
stationary (case1)	0.09	0.5	1000	6.1×10^{-5}	0.5	1.1
stationary (case2)	0.13	1.0	1000	6.1×10^{-5}	1.0	1.1
stationary (case3)	0.19	2.0	1000	6.1×10^{-5}	2.0	1.1
stationary (case4)	0.27	4.0	1000	6.1×10^{-5}	4.0	1.1

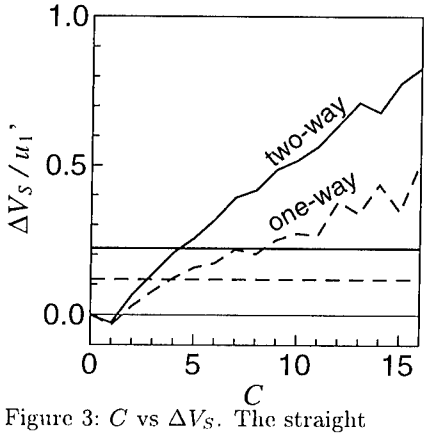


Figure 3: C vs ΔV_S. The straight lines represent the averages over all particles.

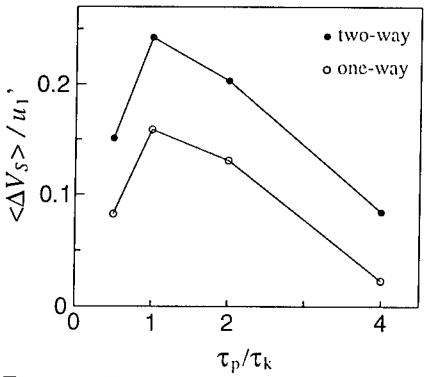


Figure 4: Increase in average settling velocity for the stationary turbulence.

References

[1] L. P. Wang and M. R. Maxey. Settling velocity and concentration distribution of heavy particles in homogeneous isotropic turbulence. *J. Fluid Mech.*, 256:27–68, 1993.

[2] P. K. Yeung and S. B. Pope. An Algorithm for Tracking Fluid Particles in Numerical Simulations of Homogeneous Turbulence. *J. Comp. Physics*, 79:373–416, 1988.

[3] K. D. Squires and J. K. Eaton. Preferential concentration of particles by turbulence. *Physics of Fluids A*, 3:1169–1178, 1991.

[4] C. Y. Yang and U. Lei. The role of the turbulent scales in the settling velocity of heavy particles in homogeneous isotropic turbulence. *J. Fluid Mech.*, 371:179–205, 1998.

ADVANCES IN TURBULENCE VIII
Proceedings of the Eighth European Turbulence Conference
C. Dopazo et al. (Eds.)
© CIMNE, Barcelona 2000

Direct numerical simulation of particle dispersion in a spatial mixing layer

Z. W. Hu, K. H. Luo and X. Y. Luo

Engineering Department, Queen Mary & Westfield College
University of London, Mile End Road, London E1 4NS, U.K.

Contact e-mail: z.hu@soton.ac.uk

1 Introduction

Particle dispersion in free shear turbulence is important for many industrial, environmental and medical processes. Direct numerical simulation(DNS) has been commonly used to study particle dispersion[2-5]. Most of the DNS work, however, are carried out in homogeneous turbulent flow, i.e., assuming the spatial particle mixing behaves the same as in a temporal developing process. To consider the possible influences of spatial developing character on the particle dispersion, this paper uses DNS to study the particle dispersion in a two dimensional spatial mixing layer. Results are compared with these of temporal mixing layer, and the effect of gravity on the particle mixing are also analyzed.

2 Computational procedure

The compressible continuity, momentum and energy equations are solved for the turbulent spatial mixing layer. They are non-dimensionalized by $U_1 (U_1 > U_2$, where U_1 and U_2 are the upper($y > 0$) and lower($y < 0$) free stream velocity, respectively), and the mixing layer vortex thickness $\delta_\omega = \frac{U_1 - U_2}{|du_0^*/dy^*|_{max}}$.

$$\frac{\partial \rho}{\partial t} = -\frac{\partial(\rho u_j)}{\partial x_j} \tag{1}$$

$$\frac{\partial(\rho u_i)}{\partial t} = -\frac{\partial(\rho u_i u_j)}{\partial x_j} - \frac{\partial p}{\partial x_i} + \frac{\partial \tau_{ij}}{\partial x_j} \tag{2}$$

$$\frac{\partial E_T}{\partial t} = -\frac{\partial[(E_T + p)u_j]}{\partial x_j} - \frac{\partial q_j}{\partial x_j} + \frac{\partial(u_i \tau_{ij})}{\partial x_j} \tag{3}$$

Assume that all particles are rigid sphere with identical diameter d_p and density ρ_p, $\rho_p \gg \rho$, where ρ is fluid density, and assume also the particle has

no influence on the fluid, we obtain the non-dimensional Lagrange motion of equation for particles:

$$\frac{d\mathbf{v}}{dt} = \frac{f_p(\mathbf{u}\text{-}\mathbf{v})}{St} + (1-\alpha)\frac{1}{S_t}\frac{\tau_p}{U_1}\mathbf{g} \tag{4}$$

The computational flow domain is chosen as in figure 1, where $L_x \times L_y = 300 \times 30$, with grid points 601×61. Non-reflecting boundary condition is applied to all boundaries. The 6th order Pade finite difference scheme[1] is used in space, and an explicit 3th order compact-storage Runge-Kutta method is used in time. The initial velocity is set to be a hyperbolic tangent profile.

3 Results

Typical parameters are: Reynolds number $R_e = \rho U_1 \delta_\omega / \mu = 200$, convective Mach number $M_c = 0.04$, and $\lambda = (U_1 - U_2)/(U_1 + U_2) = 0.25$. Figure 1 shows the vortex contour of the mixing layer at t=350.

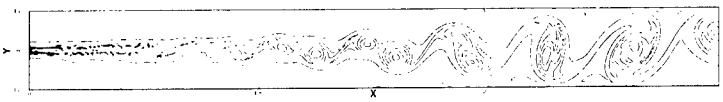


Figure 1: Vortex contour of the spatial mixing layer at t=350.

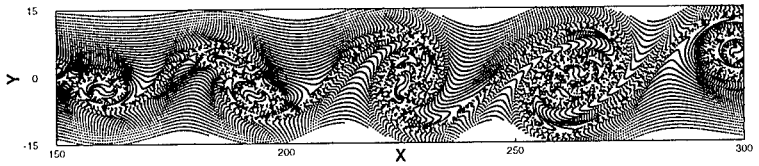
Initially, particles are put at every grid point. As the mixing layer develops, some of particles are carried out of the domain. Different from a temporal mixing layer, which let particle reenter form the opposite boundary with the same parameter, in the spatial mixing layer, new particles have to be added into the upper and lower stream separately to keep the same spatial interval.

Particles with Stokes number from 0.1 to 100 are calculated. The large-scale vortex is developed for $x \approx 0 - 90$, and has little influence on the particles. With the evolution of the mixing layer, particles are transmitted and mixed, and finally form patterns in the vortex area. Figure 2 shows some typical dispersion pattern of particles with St=0.1, 4 and 100 at x=150-300.

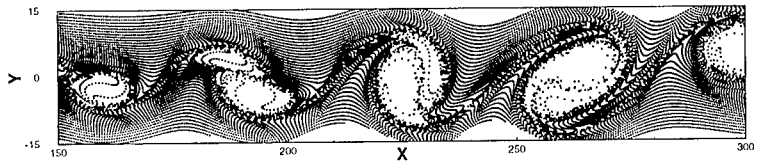
Particles with small Stokes number tend to follow the vortex of fluid, because they response much quicker to the change of fluid parameters due to their small inertia, and they stay in a near equilibrium condition with the surrounding fluid.

The response time of particles with $S_t = 1 \sim 10$ has a same order with the flow time scale. The influence of fluid through Stokes viscous drag is now comparable to the particle inertia. These particles tend to accumulate around the circumference of the two-dimensional large-scale vortex, and this trend is strengthened with the increase of particle Stokes number.

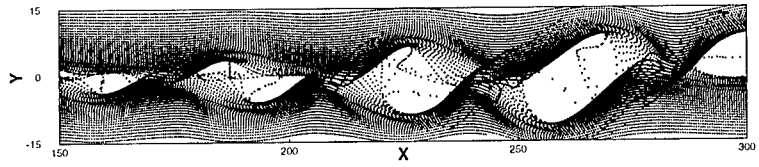
The dispersion pattern for large particles (S_t=100) is quite different. Their large particle momentum response time kept them from responding quickly to



(a) St=0.1



(b) St=4.0



(c) St=100

Figure 2: Particle dispersion pattern at t=350.

any change of fluid parameters. The results in figure 2 show that in the vortex area, particles are depleted from the core area, but do not accumulate around the circumference of vortex, their final patterns are different from the vortex structure, and is asymmetric. We note that the particle pattern is symmetric for a temporal mixing layer with the similar parameters[2]. This is because the large particles are in a non-equilibrium state with the fluid, their velocity is different from the velocity of surrounding fluid, so they will travel through different vortex of the mixing layer. This can not be presented in the temporal mixing layer which only has one vortex[2].

The root mean square of particle number per cell for each streamwise position, $N_{rms}(x)$[2], is shown in figure 3. It shows again the difference between a temporal and a spatial mixing layer.

As the ratio of gravity to Stokes viscous drag is proportional to particle response time τ_p, gravity effect is usually considered to be small and is neglected for small particles. Figure 4 gives the percentage of particles transmitted from one fluid into the other with and without gravity for relatively small particles($St = 4$). It shows that the gravity has significant influence on the particle mixing even for small particles. The gravity will reduce the number of particle transmitted from lower fluid to upper fluid, and enhance the opposite. Thus more particles tend to accumulate in the lower stream where the fluid velocity is small.

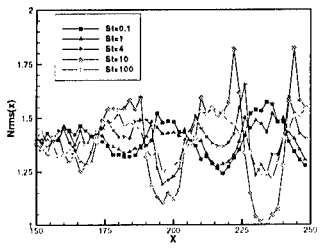


Figure 3: Nrms(x) for particles with different Stokes number

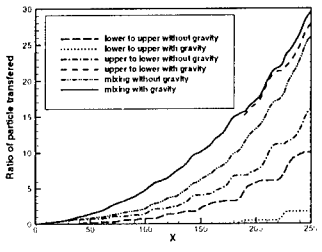


Figure 4: Influence of gravity on particle mixing.

4 Conclusion

- Particle dispersion in a two-dimensional spatial mixing layer is simulated using DNS. Results are compared with those of the temporal mixing layer, and important differences are found for particles with large Stokes number. In particular, a particle pattern which is symmetric in the temporal mixing layer becomes asymmetric in the spatial mixing layer.
- Gravity is found to have significant influence on the numbers of particles transmitted from one fluid layer into another even for small particles. With gravity, more particles tend to accumulate in the lower layer where the fluid velocity is small.

References

[1] S. K. Lele. Compact Finite Difference Schemes with Spectral-like Resolution. *J. Computational Physics*, 103:16–42, 1992

[2] W. Ling, J. N. Chung, T. R. Troutt and C. T. Crowe. Direct numerical simulation of a three-dimensional temporal mixing layer with particle dispersion. *J. Fluid Mech.*, 358:61–85, 1998

[3] B. Marcu and E. Meiburg. The effect of streamwise braid vortices on the particle dispersion in a plane mixing layer. II. Nonlinear Particle dynamics, *Phys. Fluids*, 8(3):734–753, 1996

[4] G. C. Truesdell and S. Elghobashi. On the two-way interaction between homogeneous turbulence and dispersed solid particles. II. Particle dispersion. *Phys. Fluids*, 6(3):1405–1407, 1994.

[5] L. P. WANG and M. R. MAXEY Setting velocity and concentration distribution of heavy particle in homogeneous isotropic turbulence. *J. Fluid Mech.*, 256:27-68, 1993

ADVANCES IN TURBULENCE VIII
Proceedings of the Eighth European Turbulence Conference
C. Dopazo et al. (Eds.)
© CIMNE, Barcelona 2000

Measurements and LES Modeling of Dispersion in a Turbulent Two phase round Jet

I.M. Kennedy[1], P.J. Santangelo[1] and W. Kollmann[1]

[1]MAE Dept, University of California
Davis, CA 95616, USA

Contact e-mail: imkennedy@ucdavis.edu

1 Introduction

The simulation of turbulent two-phase flows using the LES approach can be developed by extending the notion of resolved scales to the liquid/solid phase. Particle clusters (Naber and Reitz, [1]) and particle groups (Zhou and Yao, [2]) have been suggested for the related purpose of increasing the mass loading in spray simulations. An earlier paper ([3]) addressed this issue by extending the notion of LES to the discrete particle phase and developed closure models analog to SGS closures for the redundant unknowns. The idea is to treat finite subsets of discrete particles contained in a sphere as an identifyable entity, which satisfy dynamic equations similar to but different from the equations for an individual particle. This method is applied to forced homogenous turbulence and round jets.

The guiding philosophy of the experimental program was the development of accurate data on turbulent dispersion and vaporization of particles in a shear flow with well documented initial conditions. Atomizers that are frequently used in spray research involve rather complicated geometries and initial conditions difficult to set up for numerical simulations. Considerable effort has been expended to achieve well defined conditions that can be used in LES solvers for comparison.

2 Experiment

A round turbulent jet was the base flow for the experiments. Air blast atomizers yielded a spray with mass loadings up to 30%. Measurements of the dispersion of a single particle were obtained by adding a fluorescent dye to a droplet that was created by a piezo electric droplet generator. Fluorescent particles were

injected along the centerline of the spray. Fluorescence that was emitted from the particle as it passed through an Argon ion laser sheet was imaged onto a position sensing photomultiplier tube. Data from many particles were collected and averaged to yield the mean square displacement from the axis, the so-called dispersion. It was apparent that the addition of the spray had an impact on the dispersion of the tagged fluorescent particle.

Mie scattering images of the spray suggested a large scale, quasi sinusoidal motion of the spray. Details of the flow field were studied with PIV. A novel scheme was implemented to obtain these PIV data with limited optical resources. A single YAG laser was used to generate the light sheet for the velocity imaging. A double pulse with variable timing was generated with a solid state switch that had been introduced to the US market. It permitted switching of the 3 to 5 kV supply to the Pockel cell of the YAG laser within 10 ns, following a TTL input signal from a function generator. Hence, a Marx bank was not required to generate the double pulse. Furthermore, the solid state switch offered flexibility in timing as well as the possibility of using multiple pulses for Particle Tracking Velocimetry. This scheme was implemented successfully in the spray. The strong secondary background scattering from the spray outside the laser sheet necessitated image processing to remove noise via thresholding before a FFT analysis was carried out.

The instantaneous vector plot shows a large scale motion of the spray that lends credence to the notion that a helical structure may account for the increased dispersion of the tagged particle as spray is added to the jet.

3 Modeling

A particle LES model (PLES) was developed ([3]) and implemented into the Navier-Stokes solver for the spatially developing turbulent round jet. The PLES model treats spherical subdomains $D_i(t)$ of the flow field with constant radius R containing $N_i(t)$ particles as an entity (called "blobs"), that is governed by dynamic equations for position $\mathbf{X}_i(t)$ and velocity $\mathbf{v}_i(t)$ of the center of the blob i, similar to an individual particle but with non-closed terms. These additional terms represent the effect of particle motion inside the blob and particles leaving and entering it. The position $\mathbf{X}_i(t)$ and the velocity $\mathbf{v}_i(t)$ of a blob $D_i(t)$ change with time according to the differential equations

$$\frac{d\mathbf{X}_i}{dt} = \mathbf{v}_i(t) \tag{1}$$

$$d\mathbf{v}_i = \mathbf{P}_i dt + d\mathbf{Q}_i + d\mathbf{S}_i + d(\frac{d^2\mathbf{Y}_i}{dt^2}) \tag{2}$$

where (2) is regarded as a stochastic differential equation ([3]). The terms on the right side of (2) are regarded as forces acting on a blob: $\mathbf{P}_i(t)$ is the particle force computed with the centroid properties of the blob, $\mathbf{Q}_i(t)$ is the difference

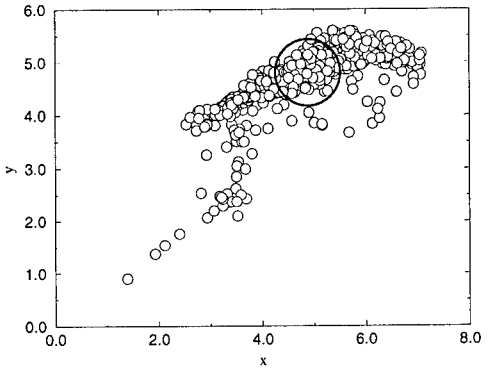


Figure 1: Individual particles (small spheres) and blob (thick sphere) in forced homogeneous turbulence (Reynolds number based on Taylor scale $Re_\lambda = 38$) at $t = 5.6$ after release.

between the average acceleration of the blob and $\mathbf{P}_i$, the third term $d\mathbf{S}_i(t)$ is the effect of particles leaving and entering the blob boundary and the last term represents the effect of the motion of the particles inside the blob relative to the position of the centre of the blob, $\mathbf{Y}_i(t)$ denoting the distance between the blob center $\mathbf{X}_i(t)$ and the centroid location $\hat{\mathbf{X}}_i(t)$ (mean value of the postion of all particles within the blob).

Closure models ([3]) have been developed for these additional terms based on integrated white-noise processes, which can be simulated using stochastic differential equations of the Ornstein-Uhlenbeck type. The closure model was tested in forced homogeneous turbulence and low Reynolds number turbulent jets. The results for forced homogeneous turbulence show that the blobs follow roughly the cloud of particles they are designed to represent. Figure 1 shows the result of a simulation of a cloud of particles and a blob in forced homogeneous turbulence. The closure model is seen to keep the blob in the center of the particle cloud as required. Computations in round jets at $Re = 4000$ have shown the possibility of similar helical instabilities that were evident in the experimental measurements of dispersion.

4 Conclusions

The notion of Large Eddy Simulations was extended to the discrete particle phase with the aim to improve the simulation of sprays based on the tracking of particle

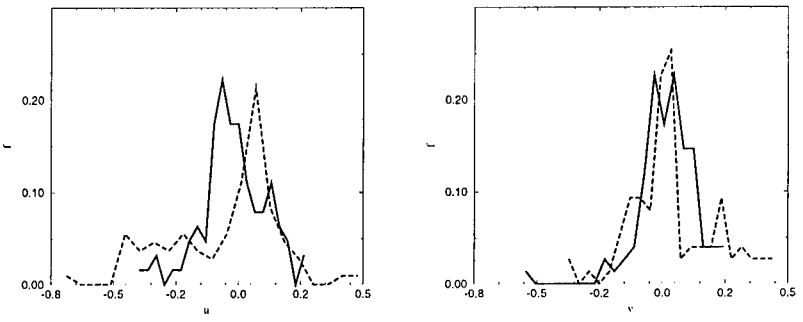


Figure 2: Pdf f of blobs (full line) and particles (dashed line) for the radial (right) and axial (left) velocity component at $x/D = 8$. Blobs and particles are released at the same location and time.

subsets called blobs. Results for particle dispersion in forced homogeneous show that the effect of the closure model for the blob dynamics is to follow the cloud of particles it represents. The application of the PLES model to turbulent round jets shows that the blob statistics are in good agreement with the results for individual particles in low mass loading.

Acknowledgements

This research was supported by the Air Force Office of Scientific Research, AFOSR Grant G-F49620-92-J-0418.

References

[1] J.D. Naber and R.D. Reitz. Modeling engine spray/wall impingement. *SAE paper* 880107, 1988.

[2] Q. Zhou and S.C. Yao. Group modeling of impacting spray dynamics. *Int. J. Heat Mass Transfer* 35: 121–134, 1992.

[3] W. Kollmann and I.M. Kennedy. LES model for the particulate phase in sprays. *AIAA* 97-0369, 1997.

ADVANCES IN TURBULENCE VIII
Proceedings of the Eighth European Turbulence Conference
C. Dopazo et al. (Eds.)
© CIMNE, Barcelona 2000

Initial distribution of bubbles injected into a turbulent water jet and its effect on the final bubble size PDF

C. Martínez-Bazán[1], J.L. Montañes[2] and J.C. Lasheras[3]

[1]Área de Mecánica de Fluidos, Universidad Carlos III de Madrid
C. Butarque 15, 28911 Leganés (Madrid) , SPAIN
[2]Dpto. de Motopropulsión y Termofluidodinámica, E.T.S.I Aeronáuticos.
Pza. Cardenal Cisneros 3, 28040 Madrid, SPAIN
[3]Mechanical and Aerospace Eng. Department, University of California, San Diego
9500 Gilman Drive, San Diego, CA, USA

Contact e-mail: carlosmb@ing.uc3m.es

1 Introduction

When a jet of air is continuously injected co-axially at the jet's centerline into a turbulent water jet, the turbulent stresses acting on the surface of the air jet result in its fragmentation into air bubbles. In this paper we have made an attempt to quantify the initial size of the bubbles resulting from the injection of an air jet into the fully developed region of a turbulent water jet as a function of the injection conditions. As these bubbles are convected by the water jet, they undergo a cascade break up until a situation is reached where the turbulent stresses from the liquid are no longer strong enough to overcome the surface tension, and a frozen bubble size *pdf* is obtained. In this paper we also address the dependence of the mean bubble size (achieved in the frozen state) with the initial bubble size. This work is a continuation of a recent study performed by the same authors, [1, 2].

2 Prediction of the initial bubble's size

We conducted a series of experiments where an air jet was injected into the fully developed region of a turbulent water jet through a very small hypodermic needle (details of the experimental facility are described in [1]). Upon exiting the needle, the air jet, which was injected at the same velocity as the local mean velocity of the water jet, is broken by the turbulent stresses acting on its surface and bubbles are formed. The characteristic size of the initial bubbles formed should be a function of the breakup time, t_b, and of the air flow rate,

Q_a, with a dependence of the form $D_0 \propto (Q_a t_b)^{1/3}$. In our experiments, the turbulent properties of the water jet at the air injection point, the air flow rate, and the needle's diameter were systematically varied to cover a wide range of flow conditions. The size of the bubbles formed was measured by analyzing

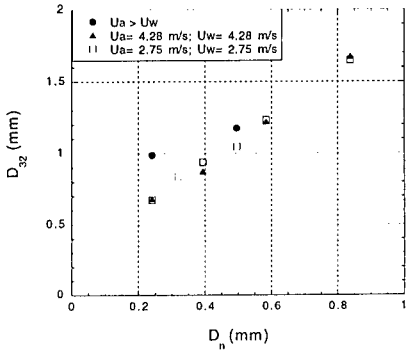


Figure 1: Measured D_{32} versus D_n.

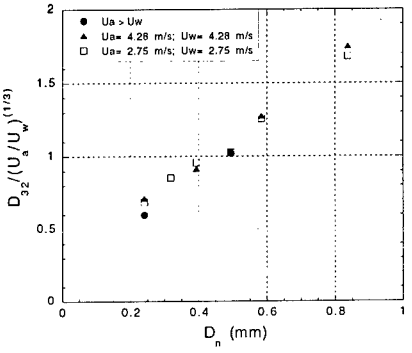


Figure 2: Dependence of D_0 with D_n.

approximately 3000 images taken with CCD cameras at a very short exposure time of 1/80,000 seconds. The mean bubble diameter was found to increase with both, the needle diameter, D_n, and the air flow rate. Furthermore, the bubble mean diameter was also found to decrease for increasing values of the root-mean-square of the water velocity at the air injection point, u'. The dependence of the Sauter Mean Diameter of the measured initial bubble size distributions, D_{32}, with the needle diameter, D_n, is shown in Fig. 1 for different values of u' and Q_a. With the turbulent breakup time defined as $t_b \propto D_n/u'$, the diameter of the bubbles resulting from the initial break up can be estimated as

$$D_0 \propto \left(\frac{6}{\pi}\frac{Q_a D_n}{u'}\right)^{1/3} = \left(\frac{3}{2}\frac{U_a}{u'}\right)^{1/3} D_n. \qquad (1)$$

When the air velocity is equal to the local value of the water jet mean velocity, U_w, which, in this particular case, is linearly proportional to u', the above equation simplifies to, $D_0 \propto D_n$, a linear dependence that is verified in Fig. 1. Notice also that, as predicted by equation 1, the values of D_{32} measured for cases where $U_a > U_w$ (solid circles) are larger than those obtained for the same needle diameter and with $U_a = U_w$. Equation 1 can also be rewritten to give

$$\frac{D_0}{\left(\frac{U_a}{u'}\right)^{1/3}} \propto D_n\,, \qquad (2)$$

This simple model is verified in Fig. 2, where we have plotted the values of the measured D_{32} divided by $(U_a/u')^{1/3}$. In the following section, we will use this simple model to study the dependence of the final bubble size PDF on D_0.

3 Dependence of the final bubble size on the initial diameter

The dependence of the maximum bubble size, D_{max}, on the local value of ϵ is given by,

$$D_{max} \propto \left(\frac{\sigma}{\rho}\right)^{-3/5} \epsilon^{-2/5} \tag{3}$$

where σ is the interfacial surface tension, and ρ the density of the continuous phase (Kolmogorov 1949, [3]). Furthermore, we have found that, in a turbulent water flow, the breakup frequency as well as the size of the daughter bubbles depend on D_0. Therefore, D_{max} can be written as a function of D_0 and the critical diameter, $D_c = (\sigma/\rho)^{-3/5} \epsilon^{-2/5}$ as,

$$D_{max} = F(D_0, D_c); \qquad \frac{D_{max}}{D_c} = F_1\left(\frac{D_0}{D_c}\right). \tag{4}$$

Particularly, in the case of a turbulent jet, the local value of the ϵ decreases with the distance from the water nozzle. During the time that a bubble of initial size D_0 takes to finish its breakup process, it will be transported to regions of values of ϵ lower than that of the injection point. If we estimate the value of ϵ as $\epsilon \propto U_J^3/D_J$, equations 3 and 4 can be expressed in nondimensional form as:

$$\frac{D_{max}}{D_J} = F_2(D_0/D_c)\ {We_n}^{-3/5}, \tag{5}$$

where $We_n = \rho\ U_J^2\ D_J/\sigma$ is the Weber number based on the nozzle's diameter, D_J, the velocity at the exit of the water jet and, U_J, and F_2 is a function which depends on D_0/D_c. To determine the function F_2 we conducted several sets

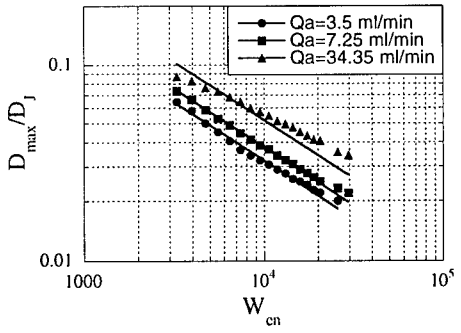


Figure 3: Variation of D_{max} with We_n.

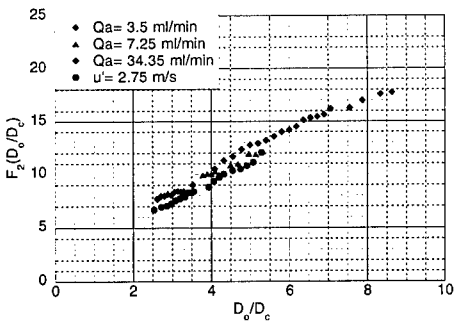


Figure 4: Evolution of F_2 with D_0/D_c.

of experiments varying the values of Q_a and ϵ. The experiments consisted of measurements of the final bubble size distribution, achieved once the break up

process had finished. In these experiments the needle's diameter was always kept constant and equal to $D_n = 0.394$ mm. Three sets of experiments were performed by increasing u' at the air injection point from 1.46 m/s to 5.12 m/s for three different values of Q_a ($Q_a = 3.6$ ml/min, $Q_a = 7.25$ ml/min, and $Q_a = 34.35$ ml/min). A last set of experiments was performed by keeping constant the water velocity at $u' = 2.75$ m/s while varying the air velocity from 0.35 m/s to 7.73 m/s. More details on the experimental conditions are given in [2]. Figure 3 shows that the maximum bubble size, measured once the break up process has concluded, decays with the Weber number with a power law almost equal to the one predicted by the simple theory given by equation 5. It is also shown that increasing values of Q_a results in increasing values of D_{max}, a consequence of the effect of Q_a on the initial bubble's size, D_0, (given by equation 1), and consequently, on F_2. From the measurements of D_{max}/D_J and W_{cn} obtained for a large range of values of ϵ and D_0, we can obtain the function $F_2(D_0/D_c)$ from equation 5. The evolution of F_2 with D_0/D_c is plotted in Fig. 4 where equation 1 has been used to estimate the values of D_0 in each case, and D_c has been calculated with the value of ϵ at the air injection point. Figure 4 shows that the dependence of F_2 on D_0/D_c is almost a linear one giving an almost perfect collapse of all the experimental data onto the same line.

4 Conclusions

When an air jet is injected into the fully developed region of turbulent water jet, air bubbles are formed with a characteristic size D_0. We have shown that D_0 is proportional to the air injection needle's diameter, D_n, and $(U_a/u')^{1/3}$. Upon injection, the initial break up is followed by a break up cascade process until, eventually, a final (unchanged) bubble's size PDF is achieved. Experimental measurements of the maximum, final bubble size (covering a large range of values of u' and U_a) show an almost linear dependence of D_{max}/D_c on D_0/D_c.

Acknowledgements : This work has been partially supported by ONR under contract # N00014-96-1-0213 and # N00014-7-1-0305, and the Spanish Ministry of Education (PB98-0142-C04-02).

References

[1] C. Martínez-Bazán, J. L. Montañes, and J. C. Lasheras. "On the breakup of an air bubble injected into a fully developed turbulent flow. Part I: Breakup frequency". *Journal of Fluid Mechanics*, 401:157 - 182, 1999.

[2] C. Martínez-Bazán, J. L. Montañes, and J. C. Lasheras. "Bubble size distribution resulting from the breakup of an air cavity injected into a turbulent water jet". *Physics of Fluids*, 1:145-148, 2000.

[3] A. N. Kolmogorov. On the breakage of drops in a turbulent flow. *Dokl. Akad. Navk. SSSR*, 66:5:825–828, 1949.

ADVANCES IN TURBULENCE VIII
Proceedings of the Eighth European Turbulence Conference
C. Dopazo et al. (Eds.)
© CIMNE, Barcelona 2000

The Breakup Time of a Droplet in a Fully-Developed Turbulent Flow

C. Eastwood[1], A. Cartellier[2] and J. C. Lasheras[1]

[1] Mechanical and Aerospace Engineering Department
University of California, San Diego
9500 Gilman Dr., LA Jolla, CA USA 92093-0411
[2]LEGI - CNRS, Grenoble, FRANCE

Contact e-mail: ceastwoo@ucsd.edu

1 Introduction

We extend the work of Martínez-Bazán *et al* [1], [2], [3], on the breakup of air bubbles in a fully-developed turbulent flow, to liquid-liquid systems. A continuous jet of an immiscible liquid is injected into the fully-developed region at the centerline of a submerged, high Reynolds number water jet. The jet of liquid is initially broken into a distribution of droplets. As these droplets are convected downstream in the water jet, they are broken into successively smaller droplets, until a state is reached in which the turbulent stresses from the water jet are no longer strong enough to overcome the confinement forces due to surface tension. At this point, a frozen size distribution is achieved. We investigate the evolution of the droplet size distribution leading up to this frozen state in order to characterize the breakup frequency (inverse of the breakup time) of the droplets based on their size and on the local dissipation rate of turbulent kinetic energy.

2 Results

We conducted a series of experiments in which heptane was continuously injected through a very small hypodermic needle into the fully developed region of a turbulent water jet (the details of the experimental facility are given in [1]). The injection conditions tested are given in Table 1. Droplet size distributions were determined by analyzing approximately 1500 images at each of 15 interrogation windows located immediately downstream of the injection point. The images were taken using a CCD camera with an exposure time of 1/80,000 seconds and a frame rate of 30 fps. The total interrogation region (all 15 windows) was approximately 2.0 cm wide and 4.5 cm tall. In all cases tested, the lateral dispersion of the heptane droplets was less than the width of the interrogation

Injection Location (X/D_j)	ID_{needle}	$Re_{waterjet}$	U_{hept}	D_{max}
25	0.394	39,000	2.4	1.12
25	0.495	39,000	2.4	1.30
25	0.584	39,000	2.4	1.57
35	0.584	52,000	2.2	1.55
40	0.584	52,000	1.9	1.53
40	0.838	52,000	1.9	2.02
40	0.838	39,000	1.4	2.07

Table 1: D_j is the diameter of the water nozzle; ID_{needle} is the inner diameter of the hypodermic needle (mm); $Re_{waterjet} = U_0 D_j/\nu$; U_{hept} is the injection velocity of the heptane (m/s); D_{max} is the largest droplet size class (mm).

window. Furthermore, the width of the interrogation window was much less than the local width of the water jet. Droplet convection, therefore, was treated as one-dimensional. Breakup frequencies based on the maximum diameter of the measured droplet size distributions (D_{max}) were determined from equation (1) (see [1] for the derivation of this equation):

$$g(x, D_{max}) = -\frac{1}{N_{D_{max}}} \frac{d(N_{D_{max}} U)}{dx}, \tag{1}$$

where $g(x, D_{max})$ is the breakup frequency, and $N_{D_{max}}$ is the number of droplets of size D_{max} at the given location. Since the dissipation rate of turbulent kinetic energy is known at each x location, we also obtain $g(\epsilon, D_{max})$. The dependence of g on ϵ for the conditions tested is shown in Figures 1 and 2.

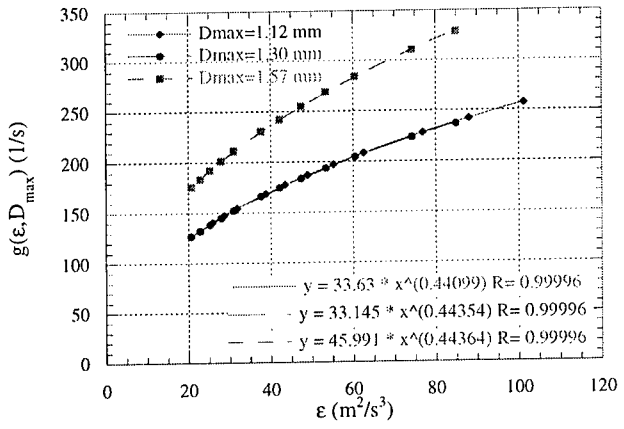


Figure 1: Breakup frequency vs. dissipation rate for injection at $X/D_j = 25$.

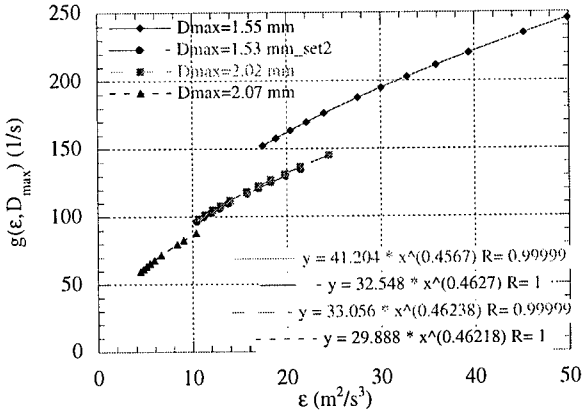


Figure 2: Breakup frequency vs. dissipation rate for injection at $X/D_j = 35$ and 40.

Figures 1 and 2 suggest that for a given value of the dissipation rate of turbulent kinetic energy, there may be a diameter for whch the breakup frequency is a maximum. Selecting $\epsilon = 20\ m^2/s^3$, a value of the dissipation rate common to a majority of the data sets, a critical diameter ($D_c = (12\sigma/(\beta\rho))^{3/5}\epsilon^{-2/5}$, see [4] and [5]) was calculated. The breakup frequency was then plotted as a function of D_{max}/D_c. The result is shown in Figure 3. The figure reveals a maximum breakup frequency at a value of D_{max}/D_c of about 1.6.

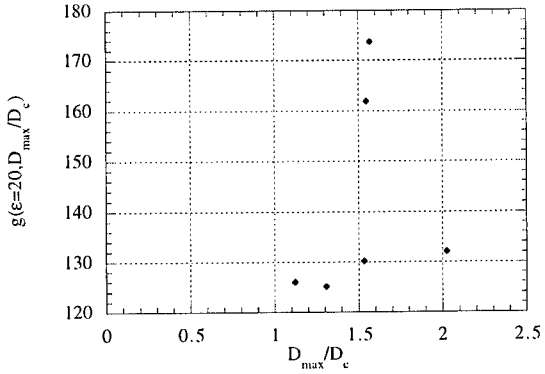


Figure 3: Breakup frequency vs. D_{max}/D_c. The figure is based on data points from Figures 1 and 2 with $\epsilon = 20\ m^2/s^3$.

3 Conclusions

When heptane is injected continuously into the fully developed region at the centerline of a high Reynolds number water jet, a droplet size distribution is formed which evolves as the droplets are convected downstream and broken by the underlying turbulence. The experimental results presented in this paper reveal two features of this breakup process:

- For the conditions tested ($We_t = \frac{\rho\overline{\Delta u^2}D}{\sigma} < 70$), the breakup frequency evolves with the dissipation rate of turbulent kinetic energy as $g(\epsilon, D_{max}) \propto \epsilon^{0.45\pm0.01}$
- A maximum breakup frequency, for $\epsilon = 20\ m^2/s^3$, is observed at a value of D_{max}/D_c of about 1.6. More data is required to confirm this result; however, the existence of a maximum breakup frequency agrees with the model proposed in [1].

References

[1] C. Martínez-Bazán, J.L. Montañes, J.C. Lasheras, "On the Breakup of an Air Bubble Injected into a Fully-Developed Turbulent Flow, Part 1: Breakup Frequency," *J. Fluid Mechanics*, **401**:157-182, 1999.

[2] C. Martínez-Bazán, J.L. Montañes, J.C. Lasheras, "On the Breakup of an Air Bubble Injected into a Fully-Developed Turbulent Flow, Part 2: Size PDF of the Resulting Daughter Bubbles," *J. Fluid Mechanics*, **401**:183-207, 1999.

[3] C. Martínez-Bazán, J.L. Montañes, J.C. Lasheras, "Bubble Size Distribution Resulting from the Breakup of an Air Cavity Injected into a Turbulent Water Jet," *Physics of Fluids*, **1**:145-148, 2000.

[4] A.N. Kolmogorov, "On the Breakage of Drops in a Turbulent Flow," *Dokl. Akad. Navk. SSSR*, **66**:5:825-828, 1949.

[5] J.O. Hinze, "Fundamentals of the Hydrodynamic Mechanisms of Splitting in Dispersion Processes," *Journal of AIChE*, **1**:3:289-295, 1955.

ADVANCES IN TURBULENCE VIII
Proceedings of the Eighth European Turbulence Conference
C. Dopazo et al. (Eds.)
© CIMNE, Barcelona 2000

Experiments on Particle-Turbulence Interaction in a Backward-Facing Step Flow

T. Vogt and U. Renz

Institute of Heat Transfer and Air Conditioning
RWTH Aachen, 52056 Aachen, Germany

Contact e-mail: vogt@wuek.rwth-aachen.de

1 Introduction

Particle-laden recirculating flows appear in many technical applications. An example may be the flow of air and coal at the outlet of a pulverized coal burner. Separating and reattaching flows are still difficult to predict especially with particles and their influence not only on the momentum transport of the gas phase but also on turbulence. In this paper, experiments on particle-turbulence interaction in a backward-facing step flow are described.

There are several ways to predict turbulent flows all of which start with the Navier-Stokes equations. For low Reynolds numbers and simple geometries it is possible to solve those in Direct Numerical Simulation (DNS) for a grid fine enough to calculate even the smallest eddies. For higher Reynolds numbers the number of nodes increases and the necessary computer storage and computer time exceed what is currently available. In this case an additional set of differential equations is necessary to model flow structures which are smaller than the grid. Differential equations for the turbulent kinetic energy and the dissipation are commonly used. They still include Reynolds stress terms (velocity cross correlations) which can be modeled by another set of differential equations or symmetry assumptions.

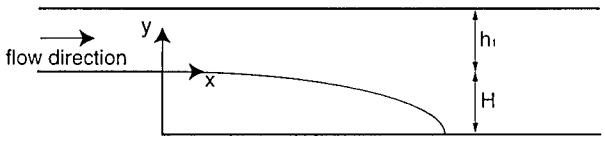


Figure 1: Geometry of the channel with expansion ratio $ER = (h_1 + H)/h_1 = 2$.

2 Experiments

Velocity measurements have been carried out in a particle-laden air flow at a backward-facing step which is a simple case of separation and reattachment. The expansion ratio of the flow at the step is ER = 2 (Figure 1) and the step Reynolds number Re = 16,000. The mean diameter of the quartz sand particles is about 150 μm ($100 < d < 200\mu m$) and their mass fraction 0.2.

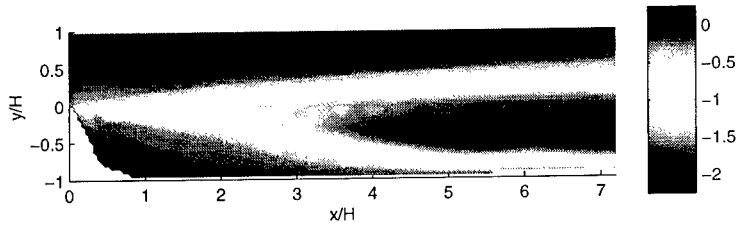


Figure 2: Cross-correlation $\overline{u'v'}$ for flow without particles.

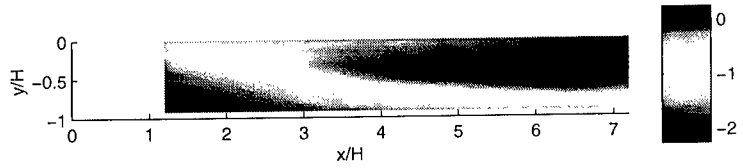


Figure 3: Cross-correlation $\overline{u'v'}$ for flow with particle mass fraction $\mu = 0.2$.

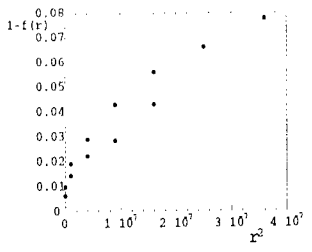


Figure 4: Spatial correlation $f(r)$ at $x/H = 4$ and $y/H = 0$ for $\mu = 0$ plotted as r^2 versus $1 - f(r)$.

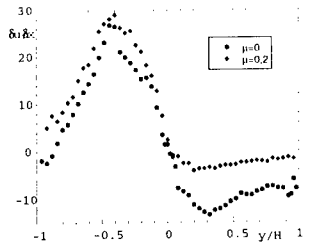


Figure 5: Gradients of u-velocity in x-direction at $x/H = 4$ for $\mu = 0$ and $\mu = 0.2$.

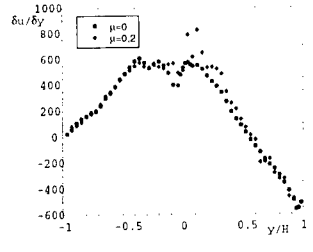


Figure 6: Gradients of u-velocity in y-direction at $x/H = 4$ for $\mu = 0$ and $\mu = 0.2$.

The detailed 3D-LDA velocity and 1D-LDA spatial velocity correlation measurements yield mean and fluctuating part, skewness, flatness, auto- and cross-

correlation, triple correlation, integral time scale and gradients of the velocities and micro and macro length scales of turbulence.

Figure 2 shows the velocity cross-correlation $\overline{u'v'}$ for the flow without particles and Figure 3 the velocity cross-correlation $\overline{u'v'}$ in the recirculating zone for the flow with a particle mass fraction $\mu = 0.2$. In Figures 4, 5 and 6 examples of spatial velocity correlations and gradients of u-velocity in x- and y-direction are given.

The spatial velocity correlations yield micro scales λ_f and λ_g and macro scales Λ_f and Λ_g. The micro scales can be estimated from expanding the correlation function $f(r)$ (or $g(r)$) in a Taylor series at $r = 0$ and neglecting terms of higher power which yields

$$f(r) = 1 - \frac{r^2}{{\lambda_f}^2}. \tag{1}$$

In a plot r^2 versus $1 - f(r)$ the initial points should lie in a straight line with a slope of $\frac{1}{\lambda^2}$ (see also Figure 4).

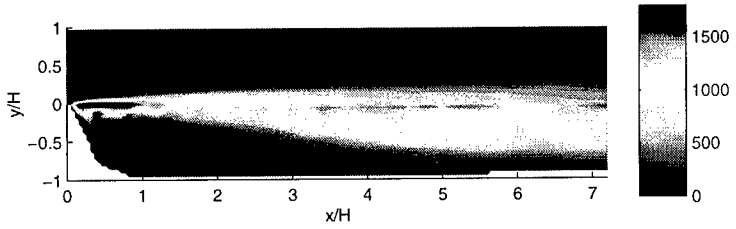


Figure 7: Production of turbulent kinetic energy for flow without particles.

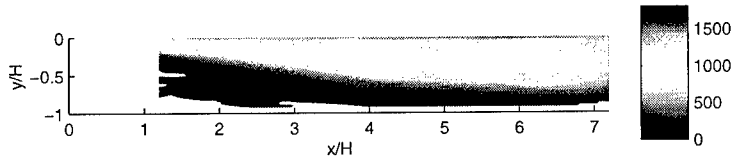


Figure 8: Production of turbulent kinetic energy in the recirculating zone for flow with $\mu = 0.2$.

Considering homogeneous shear turbulence the transport equation for the turbulent kinetic energy is

$$\frac{\partial k}{\partial t} + \overline{u_i}\frac{\partial k}{\partial x_i} = \frac{\partial}{\partial x_i}\left(\frac{\nu_t}{\sigma_k}\frac{\partial k}{\partial x_i}\right) + \nu_t\left(\frac{\partial \overline{u_i}}{\partial x_j}\frac{\partial \overline{u_j}}{\partial x_i}\right)\frac{\partial \overline{u_i}}{\partial x_j} - \varepsilon. \tag{2}$$

The first term on the left side of (2) is the change of turbulent kinetic energy in time and vanishes for stationary flows. The second term represents the convection of turbulent kinetic energy and the terms on the right side of (2) represent diffusion, production and dissipation, respectively.

All terms of (2) except of the dissipation can be calculated from the measurements, as an example Figures 7 and 8 show the production term of (2). The dissipation can then be calculated from (2) and is shown in Figures 9 and 10.

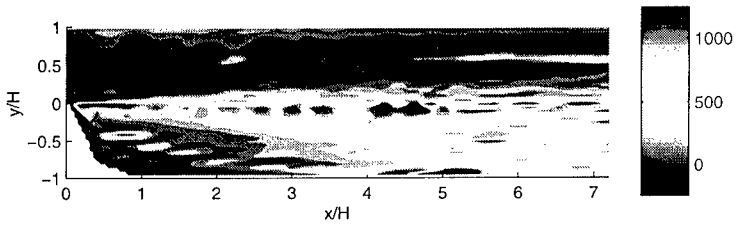


Figure 9: Dissipation of turbulent kinetic energy for flow without particles. Calculated from the transport equation of k.

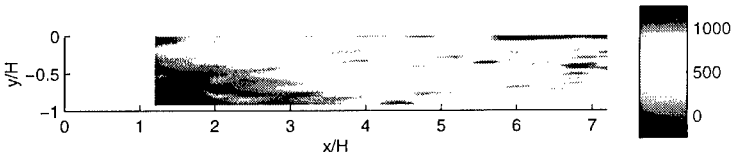


Figure 10: Dissipation of turbulent kinetic energy for flow with $\mu = 0.2$. Calculated from the transport equation of k.

3 Conclusions

Results of velocity measurements in a two-phase flow at a backward-facing step are described in this paper. Detailed 3D-LDA velocity and 1D-LDA spatial velocity measurements have been carried out. The results show increased turbulence production and a more even distribution of the dissipation in the shear zone for the particle-laden flow. The measurements help to validate numerical simulations and give the opportunity to examine different sets of equations for their validity for separating and reattaching flows.

ADVANCES IN TURBULENCE VIII
Proceedings of the Eighth European Turbulence Conference
C. Dopazo et al. (Eds.)
© CIMNE, Barcelona 2000

Partially premixed turbulent combustion in spray

J. Réveillon and L. Vervisch

LMFN - CORIA, University and INSA of Rouen
Avenue de l'Université, B.P. 8
76801 Saint Etienne du Rouvray Cdx.

Contact e-mail: reveillon@coria.fr

1 Introduction

Many industrial devices dedicated to propulsion systems or energy transformation involve the injection of liquid fuel with a gaseous oxidizer to feed the combustion chamber. To develop accurate numerical models of turbulent combustion in such devices, it is important to carefully understand the physical phenomena controlling the interactions between spray turbulent mixing and combustion. To this end, direct numerical simulations (DNS) of a turbulent spray flame are performed. The gaseous phase is captured in an eulerian context in association with a Lagrangian solver for dispersed vaporizing droplets.

Previous studies have described vaporizing turbulent spray in decaying [1, 2] or forced [3, 4] homogeneous turbulence. We report DNS results of a burning jet surrounded by a forced preheated coflow of air. For this configuration, it is shown that turbulent combustion mainly occurs in a partially premixed regime.

2 Numerical procedure

The continuous phase is a fully compressible Newtonian fluid following the equation of state for perfect gases. DNS allows us to solve exactly all the scales of the flow from the Kolmogorov up to the integral scale.

The modeling of the liquid phase [5] includes several simplifications. The droplets are assumed to be spherical without any motion in the liquid core and droplet-droplet interactions are neglected. Time and space dependant vaporization rate of droplets is computed following local properties of the gas phase (temperature, pressure, gaseous fuel mass fraction). Local saturation properties are determined through the Clausius-Clapeyron relation. A modified convective Sherwood number accounting for convection of the gas around droplets is retained.

Spatial derivatives of Eulerian equations are determined by a 6^{th} order Pade scheme [6]. Time advancement is computed with a third order Runge Kutta method used with a minimal data storage algorithm [7]. Figure 1 shows the computational configuration and the injection profile, Fig. 2 is a snapshot of the mixture fraction levels at a given time.

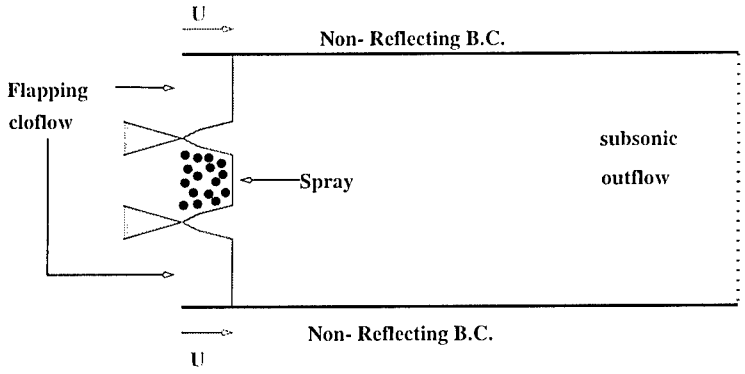


Figure 1: Computational domain.

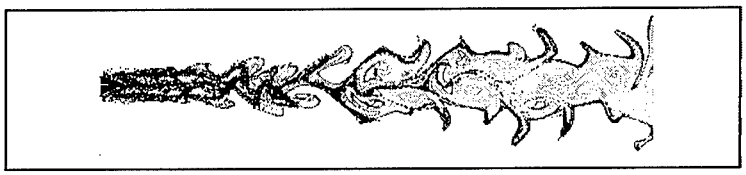


Figure 2: Snapshot of the fuel mass fraction (isolignes) and the vaporizing particles (dots), pure mixing case.

3 Flame structure at stabilization

Figure 3 is a snapshot of the flame at a representative time. The stoichiometric ratio between oxidizer and fuel corresponds to n-heptane.

Combustion starts with triple points surrounding the spray. Three flames emerge from each triple point: A rapidely vanishing lean premixed flame on the oxidizer side, a trailing diffusion flame and a rich premixed flame, both connected to the triple point. Combustion is therefore organized in an hybrid regime. The large mean vaporization time of the droplets implies the presence of the partially premixed (rich) flame along the whole droplets trajectories (Fig. 3).

Figure 4 presents the flame at two successive times. The droplets are also shown, some are crossing the computational domain without being totally vaporized. A variety of flame topologies is observed, pockets of burning droplets behind the diffusion flame (A') or multiple interaction between premixed and diffusion flames (B'). Local extinctions may be detected as well.

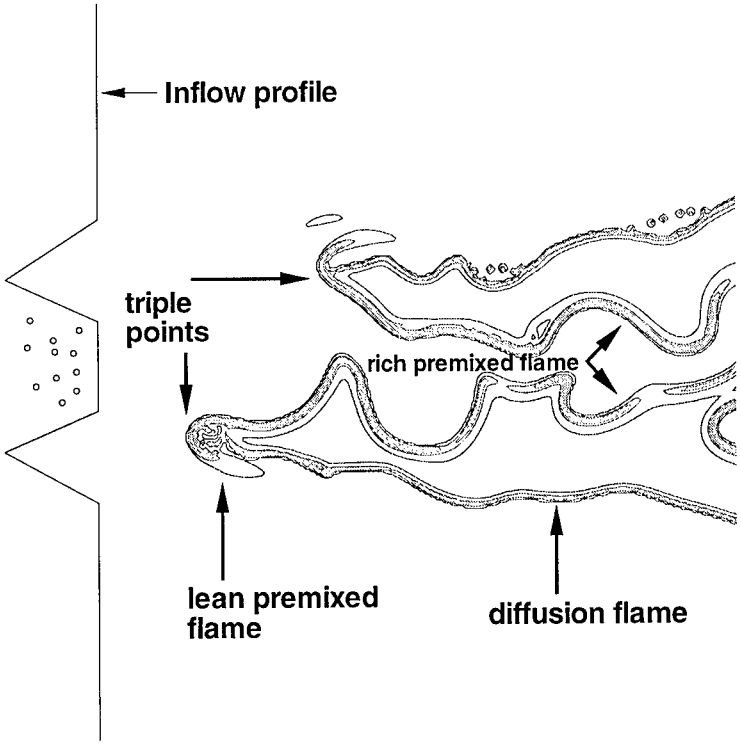


Figure 3: Structure of the turbulent flame attached to the spray.

References

[1] J. Réveillon and L. Vervisch. Accounting for spray vaporization in non-premixed turbulent combustion modeling: A single droplet model (sdm). *Combustion and Flame*, 121(1/2):75–90, 2000.

[2] J. Réveillon, K.N.C. Bray, and L. Vervisch. Dns study of spray vaporization and turbulent micro-mixing. In *AIAA 98-1028*, 36th Aerospace Sciences Meeting and Exhibit, January 12-15, Reno NV, January 1998.

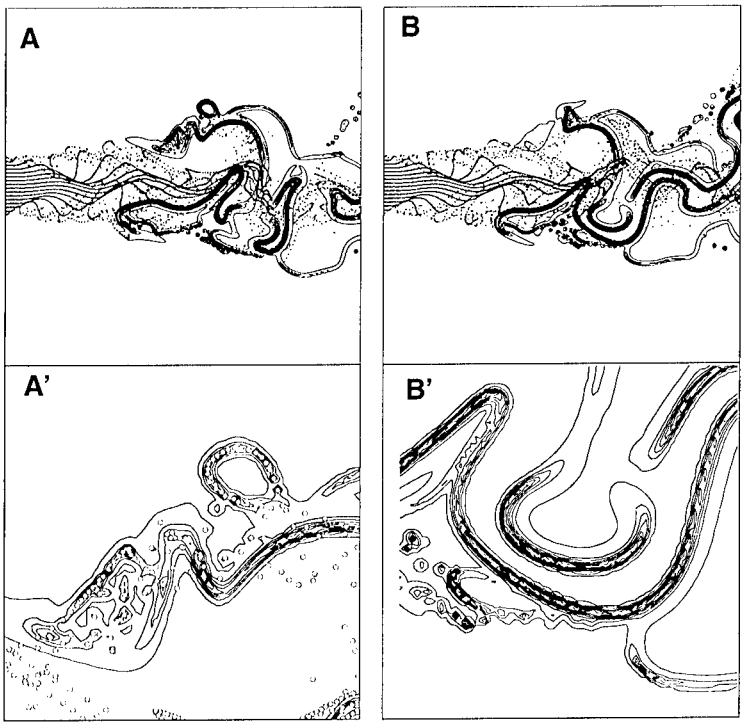


Figure 4: Two snapshots (A and B) of the energy heat release (isolignes) and the vaporizing droplets (dots). Local zooms show a burning ring of droplets (A') and flame complex interactions and extinctions (B'). (Droplets size is not representative of the computation.)

[3] F. Mashayek. Direct numerical simulations of evaporating droplet dispersion in forced low mach number turbulence. *Int. j. heat mass transfer*, 41(17):2601–2617, 1998.

[4] F. Mashayek. Simulations of reacting droplets dispersed in isotropic turbulence. *AIAA Journal*, 37(11):1420–1425, 1999.

[5] G.M. Faeth. Evaporation and combustion of sprays. *Prog. Energy Combust. Sci.*, 9:1–76, 1983.

[6] S. K. Lele. Compact finite difference schemes with spectral like resolution. *J. Comput. Phys.*, (103):16–42, 1992.

[7] A. A. Wray. Minimal storage time-advancement schemes for spectral methods. Technical report, Center for turbulence research Report, Stanford University, 1990.

ADVANCES IN TURBULENCE VIII
Proceedings of the Eighth European Turbulence Conference
C. Dopazo et al. (Eds.)
© CIMNE, Barcelona 2000

Modelling inter-particle collisions in Lagrangian approaches

P. Achim, A. Berlemont and Z. Chang

UMR 6614-CORIA, INSA de Rouen
BP 8 76131 Mont Saint Aignan cedex FRANCE

Contact e-mail: Alain.Berlemont@coria.fr

1 Introduction

Previous studies on Lagrangian approach for particle dispersion in turbulent fields have been developed from the simplest case of one-way coupling to more complicated problems involving two-way coupling with heat, mass, momentum and energy exchanges between phases (Berlemont *et al* [1] [2]). Numerical simulations of particle two-phase flows is now more focussed on particle/particle interactions. This is a four-way coupling problem which is still unsolved in its full generality, but which was the object of much effort in the recent years. The present paper concerns two particle tracking approaches, which will be described and then compared with LES results from Laviéville [3]. We found that an important parameter requires particular attention in our approaches, namely the overall (referring on the two colliding particles) particle/particle velocity correlation which is induced by the surrounding fluid.

2 Lagrangian tracking

A Lagrangian approach has been developed in Rouen for particle tracking in turbulent flows, which relies on the simulation of both fluid particle and discrete particle trajectories (Berlemont *et al* [1]). As usually for fluid particle tracking, we use a random process, in which a Gaussian p.d.f. is assumed, and complies with Lagrangian correlation laws. Rather than using a stochastic process leading to a fixed Lagrangian correlation, we choose the correlation and we adapt the random process to it. This is done through a correlation matrix, but let us note that most important remains the turbulence scale approximation since dispersion results are very sensitive to their variations. For a discrete particle, the forces acting on the particle are expressed through Maxey and Riley equation which depends on the fluid velocity at the discrete particle location. A fluid particle is simultaneously followed and the fluid velocity is transferred from the fluid

location to the particle location by use of Eulerian correlations. This process is carried out until the discrete particle leaves a correlation domain defined around the fluid particle. When the distance between the two particles is greater than a correlation length scale, a new fluid particle is considered and the process is repeated. This scheme is simulating the crossing trajectory effects in a very physical way.

3 The stochastic collision model

We are here concerned by a one particle Lagrangian approach. We thus have to use a stochastic particle/particle collision model, as described by Sommerfeld [4], which is driven through a collision frequency. By assuming that the fluctuating motion of the discrete phase can be identified to the thermal motion of molecules in gas, the kinetic theory formalism leads to an expression for the collision frequency and collision probability (Gourdel *et al* [5]). To decide whether there is a collision or not, a uniform random number (between 0 and 1) is tossed and the collision occurs when it is smaller than the collision probability. In the present work, binary perfectly elastic collisions are considered. When two particles are colliding, two uniform random numbers are used to obtain the impact location. We then move to a new coordinate system such as the first axis is on the particle center direction and momentum conservation drives the collision process.

4 The multiple particles collision model

In the multiple particles Lagrangian approach (Berlemont *et al* [8]), several particles are simultaneously followed, and suitable treatment is developed on particle pairs for collisions (only binary collisions are considered), at each time step of the particle trajectories construction. As far as the number of simultaneous trajectories is limited, simulations are carried out on 1000 successive launches of 500 particles which are initially randomly distributed in a box whose size is fixed by the desired concentration. After moving the 500 particles, we test on all the particle pairs if two particles are colliding. When a collision occurs, we move into a new reference frame where the first coordinate vector is aligned with the particle centers and the above process for the particle velocities after collision is used in the same way than for the stochastic approach.

5 Fluid/Particle correlation

We then report in Table 1 the comparisons for the particle kinetic energy between our simulation with both approaches and LES results, for ρ_p=50 kgm^{-3} and four particle volumetric fractions. As we previously observed with the multiple particles Lagrangian tracking and as Sommerfeld [4] also noticed with his stochastic approach, a decrease of the particle energy is obtained when collisions

are included in the simulations, which is not observed in the LES simulations (Laviéville *et al* [6]). It thus appears that the particle motion was insufficiently correlated to the fluid motion, due to collisions. It was deduced that during the collision process the fluid/particle correlation was partially destroyed, in both approaches but not in the same way. Each approach has thus been modified to account for the correlation between the fluctuating motion of the colliding particles through the surrounding fluid.

In the stochastic approach, the collision frequency is deduced from the kinetic theory and is linked to the particle/particle pair distribution function. When assuming that colliding particle velocities are independent (molecular chaos assumption), each particle velocity is satisfying a Gaussian distribution and the particle/particle pair distribution function is the product of the two distribution functions. But this assumption can be no more valid when the distance between the two particles is small, leading to a possible correlation between their velocities through the turbulent eddy in which they are moving. We then have to introduce a distribution function, which accounts for the fact that the two particles are driven by the same fluid. This important point has been first stated by Laviéville [3] for two identical particles, then by Pigeonneau [7] for particles with different diameters.

α_2 %	LES -	Multi part. uncorrel.	Multi part. correlated	Stochastic uncorrel.	Stochastic correlated
no col.	0.053	0.054	0.054	0.052	0.052
0,88	0,055	0,053	0,055	0,043	0,049
1,76	0,056	0,045	0,056	0,040	0,048
4,41	0,059	0,038	0,057	0,039	0,049

Table 1: Particle fluctuating energy $[m^2 s^{-2}]$

In the multiple particles collision model, when a collision occurs between a particle pair, both particle velocities are modified. Each discrete particle is followed with its own fluid particle, without any correlation between the two fluid motions, even when there are on the same location. As a consequence modifying the particle velocities during a collision is introducing a decorrelation between the discrete particle and the fluid particle on each trajectory. That behavior has been proved erroneous by LES simulations, as the overall (that means the sum on the two colliding particles) correlation remains constant during the collision. As the discrete particle velocities are fully determined through the collision process, we decided to modify each associated fluid velocity in order to respect the invariance before and after the collision. As it has been previously mentioned, the fluid/particle correlation was partially destroyed during the collision process in both approaches, but not in the same way. The above described improvements of both approaches are also quite different in their formulation. We can notice that the particle/particle correlated motion is taken into account in the stochastic approach before the colliding process itself, by introducing a corre-

lated motion between the two partners of collision. In the multiple particles approach, the modification of the process is introduced just after the collision, by forcing the constant overall fluid/particle correlation through a change of the pilot fluid particle velocity of each colliding particle. We then compared the particle kinetic energies that are obtained through the two Lagrangian models with the LES results for all the cases under study (Table 1).

A good agreement is now observed and that confirms the initial statement that the colliding particle velocities are strongly linked together by the surrounding fluid. That effect is more important as the ratio between the particle relaxation time and the fluid Lagrangian time scale decreases, since the particle motions are more and more rapidly responding to any change in the fluid velocities.

The financial support by the K.C. WONG Foundation/CNRS postdoctoral grant is gratefully acknowledged.

References

[1] A. Berlemont, P. Desjonquères, G. Gouesbet. Particle Lagrangian Simulation in Turbulent Flows. *Int. J. Multiphase Flow*, 16:19–34, 1990.

[2] A. Berlemont, M.S. Grancher, G. Gouesbet. Heat and mass transfer coupling between vaporizing droplets and turbulence using a Lagrangian approach. *Int. J. Heat Mass Transfer*, 38,16:3023–3034, 1995.

[3] J. Laviéville. Simulations Numériques et Modélisation des Interactions entre l'entrainement par la Turbulence et les Collisions Interparticulaires en Ecoulements Gaz-Solide. *PhD Thesis*, Univ. Rouen, 1997.

[4] M. Sommerfeld. The importance of inter-particle collisions in horizontal gas-solid channel flows. *Gas-Particle Flows , ASME Fluids Eng. Conf., Hiltons Head, USA,* 228:335–345, 1995.

[5] C. Gourdel, O. Simonin, E. Brunier. Two-Maxwellian Equilibrium Distribution Function for the Modelling of a Binary Mixture of Particles. *6th Int. Conf. on Circulating Fluidized Beds, J. Werther Ed.*,Germany:205–210, 1995.

[6] J. Laviéville, O. Simonin, A. Berlemont, Z. Chang. Validation of inter particle collision models based on large eddy simulation in gas solid turbulent homogeneous shear flows. *ASME Summer Meeting*, FEDSM9-3623, 1997.

[7] F. Pigeonneau. Modélisation et calcul numérique des collisions de gouttes en écoulement laminaire et turbulent. *PhD Thesis*, Univ. ParisVI, 1998.

[8] A. Berlemont, Z. Chang, G. Gouesbet. Particle Lagrangian Tracking with Hydrodynamic Interactions and Collisions. *Lyon ICMF'98-535* 1998.

XIX

Direct Numerical Simulation Large Eddy Simulation

ADVANCES IN TURBULENCE VIII
Proceedings of the Eighth European Turbulence Conference
C. Dopazo et al. (Eds.)
© CIMNE, Barcelona 2000

Application of Optimal LES

J.A. Langford, S. Völker, P. Venugopal and R.D. Moser

University of Illinois
104 S. Wright St, Urbana IL 61801, USA

Contact e-mail: r-moser@uiuc.edu

1 Introduction

In an optimal LES formulation, the subgrid is considered to be stochastic and the problem of subgrid modeling is treated as an error-minimization problem. When the error is defined as an r.m.s. measure on the instantaneous time-derivative of filtered velocity, the best subgrid model is the conditional average of the time derivative, conditioned on the current large-scale field. This is the ideal model since in addition to minimizing dynamical error, it also assures that single-time statistics of the LES field match those of the filtered real turbulence [1]. While the conditional average cannot be determined directly, it can be approximated with a relatively simple, but general class of one-point estimates, which can be computed from two-point correlation data, and which accurately reproduce the dissipation of the real system. In this paper, new results for isotropic turbulence and turbulent channel flow are discussed.

2 Isotropic Turbulence

Optimal LES of forced isotropic turbulence has already been studied for the case of a Fourier cutoff filter [1]. It has been shown that the simplest linear optimal model can be represented as a k-dependent eddy viscosity, and that much more complicated models do not perform significantly better. Further, LES using the optimal models with spectral methods produces very good agreement with filtered DNS. However, with a spectral cutoff filter and a spectral simulation, numerical errors do not play a role in the LES dynamics. For practical simulations in realspace, it is expected that numerical effects may be significant, and that numerics should be an integral part of an optimal LES formulation.

To demonstrate a practical model, an optimal LES finite volume formulation is applied to a case of forced isotropic turbulence with $\mathrm{Re}_\lambda = 167$. In a finite volume formulation, the LES state variable $w_j^{\mathbf{i}}$ is simply the real fluid velocity u_j averaged within the $\mathbf{i}_{\text{th}}$ volume element. In this case, the domain consists of 32^3 volume elements, each a cube of dimension Δ. Formulations are tested for collocated and fully staggered volume elements.

	M_{uw}	M_{ww}	$M_{du/dz}$	$M_{dw/dz}$
collocated linear	0.9965	0.9966	0.2233	0.1005
collocated quadratic local	0.2443	0.2052	0.2228	0.1002
collocated quadratic nonlocal	0.1963	0.1246	0.2172	0.0984
staggered linear	0.9965	0.9966	0.2136	0.1086
staggered quadratic nonlocal	0.2306	0.1742	0.2105	0.1072

Table 1: Relative estimation error for various finite-volume fluxes.

The finite volume LES governing equations can be written in terms of surface fluxes, which depend on unresolved velocity scales and must be modeled. For isotropic turbulence, each flux term can be constructed from rotations and reflections of 4 basic fluxes. The terms M_{ww}, M_{uw}, $M_{\partial w/\partial z}$, and $M_{\partial u/\partial z}$ will be used to denote these basic fluxes, which are integrals of ww, uw, $\partial w/\partial z$, and $\partial u/\partial z$ respectively over a plane of dimension $\Delta \times \Delta$ oriented in the z-direction and located at the boundaries of two adjacent volume elements. When these fluxes are used in a simulation, there may be cancellations from pairs on opposing faces; for this reason, error measurements are presented for estimations of fluxes in such pairs.

For each of these terms M, an estimate m is constructed as $m = A + \sum_{\mathbf{i}} B_k^{\mathbf{i}} w_k^{\mathbf{i}} + \sum_{\mathbf{i}} \sum_{\mathbf{j}} C_{kl}^{\mathbf{ij}} w_k^{\mathbf{i}} w_l^{\mathbf{j}}$, and the estimation coefficients A, B and C are chosen to minimize mean square of the error $e = M - m$. The relative error is defined as the mean square of e normalized by the mean square of M. Table 1 shows the relative errors for the different estimates of the flux terms. Interpretation of this error is subtle, since it includes the variance of the actual fluxes about the conditional average, as well as an error in estimating the conditional average. Experience with Fourier cutoff filters suggests that the "error" is dominated by the first term, which is not really an error at all. Results presented here are for global estimates, in which LES velocity data from everywhere in the domain is included. Separations in the quadratic product are restricted to $|\mathbf{i} - \mathbf{j}| = 0$ (local quadratic) and $|\mathbf{i} - \mathbf{j}| \leq 1$ (nonlocal quadratic). In the case of a fully staggered grid, a local quadratic estimate was not computed. Effects of nonglobal locality are being investigated.

Note that one can think of the finite volume LES filter as a classic tophat filter followed by a sampling operation. The sampling operation introduces a filter inhomogeneity, and it follows that the continuity equation cannot be expressed solely as a function of the LES state variables. In standard numerical methods, the pressure term is chosen to ensure that the velocity field is divergence-free. For finite-volume LES, there will be an error in performing such a procedure. We define the optimal "divergence" operator as the one that minimizes the error one would commit in making the LES field "divergence-free". This minimum error is shown in Figure 1. It is clear that continuity has a much better representation with a staggered grid, though the smallest scales still incur about a 10% error.

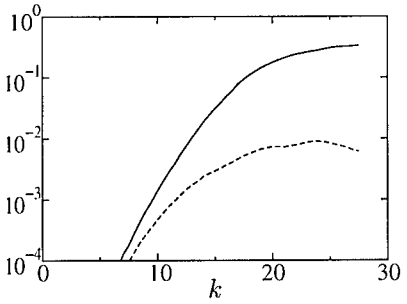


Figure 1: Spectrum of error one would commit in enforcing an optimal continuity constraint, normalized by the spectral magnitude of the LES velocity field for a collocated grid (———) and a staggered grid (- - - -).

3 Turbulent Channel Flow

In order to explore the properties of optimal LES in a wall-bounded flow, DNS data by Moser *et al.* [2] was filtered in the streamwise and spanwise directions using sharp Fourier cutoff filters. No filter was applied in the wall-normal direction. The friction Reynolds number Re_τ of the DNS is 590 with a grid resolution of $384 \times 257 \times 384$. The filtered grid has a resolution of $32 \times 257 \times 32$ grid points.

Turbulent channel flow differs from isotropic turbulence in a number of aspects. One significant difference is that in addition to being wall-bounded, channel flow has a non-zero mean. As a result, the mean model term $\overline{M}_1$ is not zero. The importance of the mean model term is indicated in Figure 2a. It shows the mean Reynolds shear stress of the DNS and the subgrid contribution to the mean shear stress. For values of $y^+ > 100$ the subgrid contribution is small (less than 10% of the total mean shear stress). However, close to the wall the subgrid contribution to the mean shear stress is significantly larger, reaching a peak of approximately 40% at $y^+ = 25$. Thus, in order for the LES to reproduce the correct flow statistics, it is crucial to predict the mean component of the optimal model accurately. From the requirement to minimize the r.m.s. error we find that the mean component of the optimal model has to be equal to $\overline{M}_1$, the mean subgrid force. Consequently, the *a priori* error in the model will be due entirely to error in predicting the fluctuating components of the model term.

Generally, since we don't have the exact mean model term available when doing an LES, we need to approximate the mean model term based on filtered velocity information. One possible approach is to use a RANS type model such as a k–ϵ model. Figure 2b shows the true mean model term and its approximations based on different k–ϵ type subgrid models. The k–ϵ model matches the actual

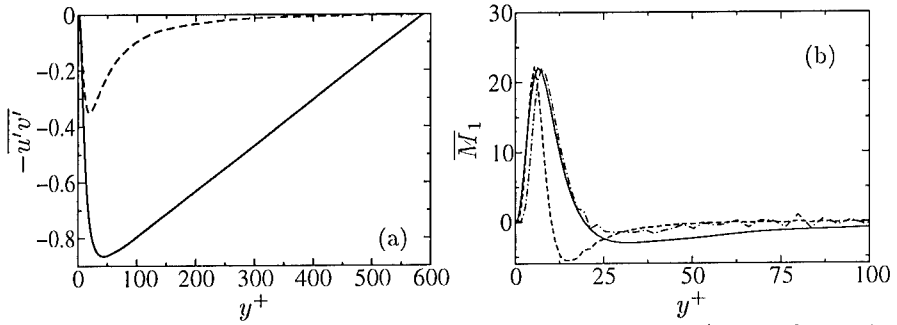


Figure 2: Mean model term of the turbulent channel flow: (y coordinate is in wall units, where the center of the channel is at $y^+ = 587$). (a) Mean Reynolds stress (———) and the subgrid contribution to the mean Reynolds stress for the given choice of filter (- - - -). (b) Mean model term (———) and its approximations using a k–ϵ model (- - - -) and a k–ϵ–v^2 model (- · - · -).

mean model term very closely near the wall up to $y^+ = 10$. However, after reaching its peak, it falls off too steeply underpredicting the mean model term. The k–ϵ–v^2 model [3] does not predict the mean as well as the k–ϵ model for small y^+ ($y^+ < 10$), but does a significantly better job for larger y^+.

4 Conclusions

While intial work with optimal LES formulations has been promising, there are a variety of complications that must be addressed before any practical models are presented. This paper presents a sampling of such complications. In the finite volume formulation of isotropic turbulence, it is shown that the introduction of a realspace numerical method introduces error into the viscous terms as well as the continuity equation, though such errors may be reduced by using a staggered grid. Optimal LES of turbulent channel flow demostrates the need for accurate prediction of the mean model component in order to correctly reproduce global statistics.

References

[1] J. Langford and R. Moser. Optimal Large-Eddy Simulation Formulations for Isotropic Turbulence. *J. Fluid Mech.* 398:321–346, 1999.

[2] R. Moser, J. Kim, and N. Mansour. Direct Numerical Simulations of Turbulent Channel Flow up to $\mathrm{Re}_\tau = 590$. *Phys. Fluids*, 11(4):943–945, 1999.

[3] P. Durbin. Constitutive Equation for the k–ϵ–v^2 model. *Proc. 6th Int. Symp. on Computational Fluid Dynamics*, 1:258-262, 1995

ADVANCES IN TURBULENCE VIII
Proceedings of the Eighth European Turbulence Conference
C. Dopazo et al. (Eds.)
© CIMNE, Barcelona 2000

Large Eddy Simulation of High Reynolds Number Flows

C. Fureby[1], and F.F. Grinstein[2]

[1] Weapons and Protection Division, Warheads and Propulsion
FOA Defence Research Establishment S-172 90, Stockholm, SWEDEN
[2] Laboratory for Computational Physics and Fluid Dynamics
Naval Research Laboratory, Washington DC 20375-5344, USA

Contact e-mail: fureby@sto.foa.se

1 Introduction

At the high Re of practical interest, direct numerical simulations (DNS) can not be used to resolve all scales of motion, and subgrid scale (SGS) modeling becomes unavoidable to provide a mechanism by which dissipation of kinetic energy at high wavenumbers can occur. The Large Eddy Simulation (LES) approach seeks to resolve most of the entrainment-dominating large-scale structures by choosing the cut-off wavelength within the inertial subrange. The challenge is to emulate the fluid dynamics near the cut-off, to ensure that proper interactions between grid scales (GS's) and SGS's are accurately simulated. The most common LES method involves low-pass filtering of the Navier–Stokes equations (NSE) followed by explicit SGS modeling using a static or dynamic Smagorinsky-type model (SMG), but other SGS models are also used, e.g. [3] and references therein. A recently proposed alternative is Monotonically Integrated LES (MILES), [1], [4], which is the main subject of this study.

2 The MILES Model

In MILES, the discretization effectively filters the NSE across the grid using an anisotropic kernel. The functional reconstruction of the convective fluxes is performed with a flux-limiting method combining a high-order flux-function with a low-order dispersion-free flux-function using a non-linear flux-limiter Γ. When basing MILES on concepts such as the FCT algorithm used here, the functional reconstruction of viscous and SGS fluxes is typically performed using linear interpolation, [4]. Similar approaches have been used by [8] and [6] involving upwind-biased and TVD schemes, respectively. Physical considerations motivating the MILES approach have been presented, [1], [4]. Formal properties

of MILES were recently documented using databases of high Re-number free flows, [4], and it was suggested that the modified equations would provide the most suitable platform for comparing LES and MILES. For the incompressible NSE the modified equations are,

$$\begin{cases} \operatorname{div} \mathbf{v} = 0 \\ \partial_t(\mathbf{v}) + \operatorname{div}(\mathbf{v} \otimes \mathbf{v}) = -\operatorname{grad} p + \operatorname{div}(\mathbf{S} + \mathbf{B}) \end{cases} \tag{1}$$

where $\mathbf{v}$ is the velocity, p the pressure, $\mathbf{S} = 2\nu\mathbf{D}$ the viscous stress tensor, and $\mathbf{B} = \mathbf{C}\mathbf{L}^T + \mathbf{L}\mathbf{C}^T + \beta^2\mathbf{L}\mathbf{d} \otimes \mathbf{L}\mathbf{d}$ is the leading order truncation error that acts as the implicit SGS model with $\mathbf{C} = \beta(\mathbf{v} \otimes \mathbf{d})$ and $\beta = \beta(\Gamma)$. Because of the tensorial nature of the SGS viscosity, MILES offers an attractive alternative to conventional SGS models when seeking improved LES for inhomogeneous flows. The insufficient stress-strain correlation in eddy-viscosity models has been identified, [2], as responsible for the fact that, at best, we can expect good approximations to the turbulent energy dissipation, but not to the SGS stress in the context of this type of models. An alternative within the classical LES formalism is to use an SGS Differential Stress Equation Model (DSEM).

3 Fully Developed Turbulent Channel Flow

Fully developed turbulent channel flow at a target Re-number of $\mathrm{Re}_\tau = 395$, for which DNS data exists, [7], have been computed with SMG, DSEM, [5], and MILES in a channel of size $6h \times 2h \times 3h$, on a 60^3 grid. At the walls no-slip conditions are used whilst boundary conditions in the streamwise and spanwise directions are periodic, and the flow is driven by a constant mass flow. In the cross-stream direction the grid is stretched, using geometrical progression, so that $y^+ = 1.0$ for the first near wall cell. As initial conditions, random finite-amplitude perturbations of a parabolic velocity profile are used. Statistics are obtained after the simulations have reached a steady state identified by approximate similarity of first and second order statistical moments of $\mathbf{v}$, after which sampling is performed for an additional $40h/u_\tau$ time units.

Figure 1 presents profiles of the mean streamwise velocity $\langle v_1 \rangle$ and the corresponding rms-fluctuations v_i^{rms}. Concerning $\langle v_1 \rangle$, only minor differences between the LES models can be observed and the von Karman-constant can be predicted with essentially no dependence on the SGS model. For v_i^{rms} the agreement between LES and DNS is still good, although variations between SGS models are beginning to appear. The MILES and DSEM models give very similar profiles — overpredicting the peak value of v_1^{rms} with 3% and underpredicting the profiles of v_2^{rms} and v_3^{rms} by about 7%, in comparison to the DNS data. SMG underpredicts the peak value of v_1^{rms} with 5% and the entire profiles of v_2^{rms} and v_3^{rms} with about 10%. This result supports many previous studies, and indicates that SMG is too diffusive, especially in the near-wall region, where the flow is anisotropic. Grid refinement gives virtually identical results.

Figure 2 presents a perspective view of the flow in the streamwise direction from MILES. The flow in the near-wall region consists of recurrent streamwise rolls of high or low-speed fluid, having a length of about $1000\delta_\tau$, where δ_τ is the viscous length scale, a radius of about $15\delta_\tau$, and a streak spacing of $100\delta_\tau$. These spanwise structures originate in a layer of vorticity, having a thickness of about $10\delta_\tau$ and situated at a distance of about $10\delta_\tau$ from the wall. Ejections of low speed fluid or inrushes of high speed fluid at a shallow angle towards the wall are observed, and away from the walls all organized structures disappear. The high-speed fluid elements are inclined with respect to the walls, this being a consequence of the action of the shear on a fluid element from the outer layer moving towards the lower wall. High pressure regions occur whenever high-speed fluid impacts on low-speed fluid forming a stagnation point. Most low-pressure regions are elongated and concur with the vortex cores. The near-wall region is densely populated by streamwise or ω_1-vortices, having an upward inclination that increase with distance from the wall. In the near-wall region ω_1-vortices often occur individually, although sporadic counter-rotating vortex-pairs may occur. Comparing visualizations from MILES, DSEM, and SMG suggests that these models essentially capture the same physics. Due to the isotropic nature of the SGS viscosity of the SMG model, processes associated with mainly spanwise topology are overly damped, resulting in weaker spanwise and cross-stream rms velocity fluctuations and lower shear stresses, due to a reduced production of small scale turbulent kinetic energy.

4 Concluding Remarks

We have demonstrated that MILES can reproduce $\langle v_1 \rangle$ and v_i^{rms} almost as accurately as the DSEM, and better than Smagorinsky-type eddy viscosity models in a fully developed channel flow. We argue that this is due to the intrinsic nature of the MILES model in which a non-linear, tensorial viscosity-type SGS model is built into the algorithm. From the simulations we conclude that SMG underpredicts v_i^{rms} by about 10% as compared to the experimental data whilst both DSEM and MILES give better agreement, with the error being about 3%. The issue of grid non-uniformity pertinent to implicit and explicit SGS modelling has not be adreesed in this study, but will be presented elsewhere.

This research is performed with support from ONR through the NRL 6.1 Computational Physics task area and computer time is provided by the DoD-HPC-MP program

References

[1] J.P. Boris, F.F. Grinstein, E.S. Oran and R.J. Kolbe. New Insights into Large Eddy Simulation. *Fluid Dyn. Res.*, 10:199, 1992.

[2] V. Borue and S.A. Orszag. Local Energy Flux and Subgrid-Scale Statistics in Three Dimensional Turbulence. *J. Fluid Mech.*, 366:1, 1998.

[3] M. Lesieur and O. Metais. New Trends in Large Eddy Simulations of Turbulence. *Annu. Rev. Fluid Mech.*, 28:45, 1996.

[4] C. Fureby and F.F. Grinstein. Monotonically Integrated Large Eddy Simulation of Free Shear Flows. *AIAA.J.*, 37:544, 1999.

[5] C. Fureby, G. Tabor, H. Weller, and A.D. Gosman. On Differential Sub Grid Scale Stress Models in Large Eddy Simulations. *Phys. Fluids*, 9:3578, 1997.

[6] E. Garnier, M. Mossi, P. Sagaut, P. Comte and M. Deville. On the Use of Shock-Capturing Schemes for Large Eddy Simulation. *J. Comp. Phys.*, 153:273, 1999.

[7] J. Kim, P. Moin and R. Moser. Turbulence Statistics in Fully Developed Channel Flow at Low Reynolds Number. *J. Fluid Mech.*, 177:133, 1987.

[8] K. Tsuboi, T. Tamura and K. Kuwahara. Numerical Study of Vortex Induced Vibration of a Circular Cylinder in High Reynolds Number Flow *AIAA 89–1824*, 1989.

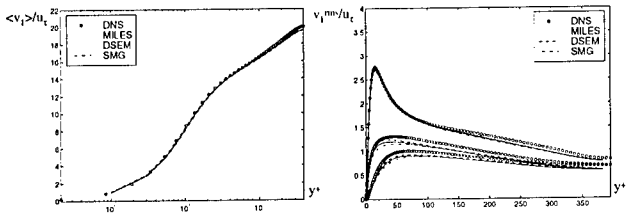


Figure 1: Fully developed turbulent channel flow at $\mathrm{Re}_\tau = 395$ from LES, MILES and DNS; profiles of $\langle v_1 \rangle$ (left) and v_i^{rms} (right, v_1^{rms} on the top).

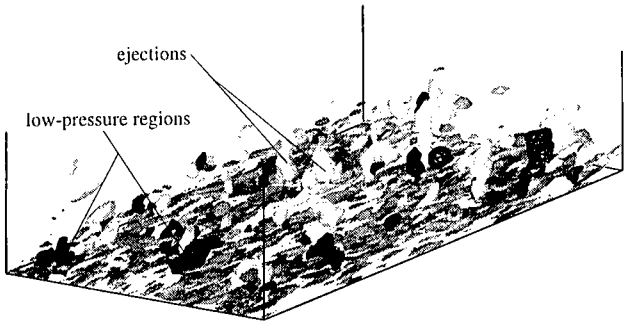


Figure 2: Volume visualization of fully developed turbulent channel flow at $\mathrm{Re}_\tau = 395$ based on MILES.

ADVANCES IN TURBULENCE VIII
Proceedings of the Eighth European Turbulence Conference
C. Dopazo et al. (Eds.)
© CIMNE, Barcelona 2000

Lagrangian methods for the tensor-diffusivity subgrid model

Piet Moeleker and Anthony Leonard

Graduate Aeronautical Laboratories
California Institute of Technology, Pasadena, CA 91125

email: piet@galcit.caltech.edu

Abstract

We consider the filtered scalar advection-diffusion equation. An infinite series expansion for the advection term was found for closure. By retaining only the first two terms in the expansion, the tensor-diffusivity subgrid model is obtained. In order to avoid problems associated with the negative diffusion of the model in one or more spatial directions, the scalar field is represented as a sum of anisotropic Gaussian particles. Numerical results in two dimensions will be presented.

1 Tensor-diffusivity subgrid model

Consider the scalar advection-diffusion equation. In order to perform numerical computations for small values of the diffusivity κ without large CPU efforts, a filtering operation is used to obtain an equation for the large scale structures in which the effects of the small scales have to be modeled. These simulations are known as large eddy simulations (LES) and the models as subgrid models.

Our research has used a Gaussian spatial filter with a characteristic length scale σ. In order to close the filtered equation, an infinite series expansion was found in terms of known variables[1, 3],

$$\widehat{\mathbf{u}\psi}(\mathbf{x},t) = \sum_{n=0}^{\infty} \frac{1}{n!} \left(\frac{\sigma^2}{2}\right)^n \frac{\partial^n \widehat{\mathbf{u}}}{\partial x_{i_1} \partial x_{i_2} \ldots \partial x_{i_n}} \frac{\partial^n \widehat{\psi}}{\partial x_{i_1} \partial x_{i_2} \ldots \partial x_{i_n}}, \qquad (1)$$

where a hat indicates a filtered quantity, $\mathbf{u}(\mathbf{x},t)$ is an incompressible velocity field, and $\psi(\mathbf{x},t)$ the (unknown) scalar function. Einstein's summation convention is implied. By retaining only the first two terms in the expansion, we end up with the filtered advection-diffusion equation closed by the tensor-diffusivity

subgrid model,

$$\frac{\partial \widehat{\psi}}{\partial t} + \widehat{\mathbf{u}} \cdot \nabla \widehat{\psi} = \kappa \nabla^2 \widehat{\psi} - \frac{\sigma^2}{2} \widehat{S}_{ij} \frac{\partial^2 \widehat{\psi}}{\partial x_i \partial x_j}, \tag{2}$$

where $\mathbf{S}$ is the strain rate tensor. The extra term can be interpreted as an added diffusivity with an effective diffusivity $-\frac{\sigma^2}{2}\widehat{S}_{ij}$, which depends on the spatial direction. It is straight forward to show that this model is material frame indifferent and will allow for backscatter.

Since $\text{trace}(\widehat{\mathbf{S}}) = \nabla \cdot \widehat{\mathbf{u}} = 0$, at least one of the eigenvalues of the strain rate tensor has to be greater than zero indicative of a direction where the subgrid model acts as negative diffusion. Computations using a finite difference or spectral method show that this can lead to growing instabilities in the scalar field.

2 Lagrangian particle method

On occasion mathematical models of physical processes lead to ill-posedness requiring some kind of regularization. Care needs to be taken in the choice of regularization, since the results can depend strongly on the approach used. Our work will regularize the problem of negative diffusion in the stretching directions by decomposing the scalar field in a collection of Lagrangian particles each of them well-behaved for large wave numbers.

Assume the scalar function can be written as a collection of N anisotropic Gaussian particles,

$$\widehat{\psi}(\mathbf{x}, t) = \sum_{k=1}^{N} \frac{a_k \sqrt{\det(\mathbf{M}_k)}}{(\sqrt{\pi}\delta_k)^d} \exp\left(-\frac{(\mathbf{x} - \mathbf{x}_k)^T \mathbf{M}_k (\mathbf{x} - \mathbf{x}_k)}{\delta_k^2} \right), \tag{3}$$

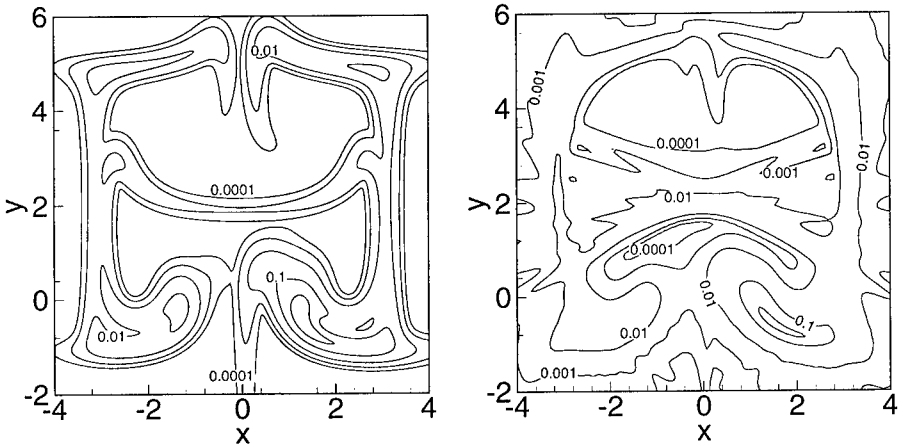
where each particle k is centered at $\mathbf{x}_k$ and d is the spatial dimension of the problem. The positive definite matrix $\mathbf{M}_k$ gives the shape of each particle.

Equations for the time evolution of $\mathbf{x}_k$ and $\mathbf{M}_k$ are obtained after substituting (3) in (2), expanding each term in a series of Hermite polynomials, and setting the lowest order coefficients equal to zero. For particle k, we end up with

$$\frac{d\mathbf{x}_k}{dt} = \overline{\mathbf{u}}^k - \frac{\sigma^2}{2} \overline{\nabla^2 \mathbf{u}}^k, \tag{4a}$$

$$\begin{aligned} \frac{d\mathbf{M}_k}{dt} = &- \overline{\nabla \mathbf{u}}^k \mathbf{M}_k - \mathbf{M}_k \overline{\nabla \mathbf{u}}^{kT} - \frac{4\kappa}{\delta_k^2} \mathbf{M}_k \mathbf{M}_k + \frac{\sigma^2}{\delta_k^2} \mathbf{M}_k \left(\overline{\nabla \mathbf{u}}^k + \overline{\nabla \mathbf{u}}^{kT} \right) \mathbf{M}_k \\ &+ \frac{\sigma^2}{2} \left(\overline{\nabla \nabla^2 \mathbf{u}}^k \mathbf{M}_k + \mathbf{M}_k \overline{\nabla \nabla^2 \mathbf{u}}^{kT} \right), \end{aligned} \tag{4b}$$

where an overline indicates a weighted average over anisotropic particle k. To obtain realistic results, we need to choose the core size δ_k larger than or equal to the filtering constant σ. Core sizes smaller than σ can lead to growing instabilities and do not correspond to a physically realizable unfiltered field.



(a) filtered DNS

(b) no subgrid model

(c) tensor-diffusivity model

(d) Smagorinsky model

Figure 1: Scalar contour lines (0.0001, 0.001, 0.01, 0.1, and 0.3) at t = 9.

Our scheme solves the diffusion term exactly (core-expansion method), which necessitates the implementation of a particle splitting or remeshing scheme to obtain accurate results[2, 5]. A novel remeshing scheme has been implemented making use of the properties of the particle method. The new particles are assumed to be all identical, axisymmetric, and spread out on a regular equidistant mesh. A least square error method is used to obtain explicit expressions for the

unknown amplitudes. Numerical experiments show good agreement between the scalar fields before and after the remeshing operation, while keeping the number of total particles reasonably small as well.

3 Numerical results

The two-dimensional incompressible velocity field with a time-dependent perturbation,

$$\begin{pmatrix} u \\ v \end{pmatrix} = \begin{pmatrix} \sin(x)\sin(y) \\ \cos(x)\cos(y) + 0.5\sin(t) \end{pmatrix} \tag{5}$$

has been used to test different aspects of the subgrid model and the numerical implementation. A Gaussian exponential located initially at $(0.3, -0.4)$ with core size 0.5 was used as an initial condition. The diffusivity was set equal to $\kappa = 0.001$ and the filtering constant $\sigma = 0.15$. In order to assess the accuracy of the model, a filtered DNS solution has been computed, which is given in figure 1(a) at $t = 9$.

The initial Gaussian has been approximated by 6504 anisotropic particles. In absence of any subgrid model, the result is given in figure 1(b). When the tensor-diffusivity model is used, the solution tracks the filtered DNS solution very well as shown in figure 1(c). This solution was remeshed every time unit. Without remeshing, the solution will break down after $t = 3$. To assess the efficiency of this model, the results using a Smagorinsky subgrid model ($C_s = 0.20$) are given in figure 1(d).

Work is currently underway to implement the model and particle method in a forced turbulence code to study the effects of mixing for high Schmidt numbers.

References

[1] Bedford, K. and W. Yeo: 1993, 'Conjunctive filtering procedures in surface water flow and transport'. In: B. Galperin and S.A. Orszag (ed.): *Large eddy simulation of complex engineering and geophysical flows.* CUP, pp. 513–537.

[2] Greengard, C.: 1985, 'The core spreading vortex method approximates the wrong equation'. *J. Comput. Phys.* **61**, 345–348.

[3] Leonard, A.: 1997, 'Large-eddy simulation of chaotic convection and beyond'. *AIAA 97-0204.*

[4] Moeleker, P. and A. Leonard: 2000, 'Lagrangian methods for the tensor-diffusivity model'. submitted to J. Comput. Phys.

[5] Rossi, L.: 1996, 'Resurrecting core spreading vortex methods: a new scheme that is both deterministic and convergent'. *SIAM J. Sci. Comput.* **17**(2), 370–397.

ADVANCES IN TURBULENCE VIII
Proceedings of the Eighth European Turbulence Conference
C. Dopazo et al. (Eds.)
© CIMNE, Barcelona 2000

Wavelet Cross-Correlation Analysis of Turbulent Mixing from Large-Eddy-Simulations

S. Sello and J. Bellazzini

Enel Research
A. Pisano 120, Pisa 56122, ITALY

Contact e-mail: sello@pte.enel.it

1 Introduction

The complex interactions existing between turbulence and mixing in a bluff-body stabilised flame configuration is investigated by means of a wavelet cross-correlation analysis on Large Eddy Simulations. The combined approach allows to better point out typical features of unsteady turbulent flows with mixing through the characterisation of the processes involved both in time and scales. The wavelet cross-correlation analysis of the time signals of velocity and mixture fraction fluctuations can be an an effective tool to study the processes involved in turbulent mixing flows which are of great interest in combustion problems.

2 Generalities on wavelet cross-correlation

The continuous wavelet transform of a function $f(t)$ is defined as the convolution between f and a dilated function ψ called wavelet mother:

$$W_f(a,\tau) = \frac{1}{\sqrt{a}} \int_{-\infty}^{+\infty} f(t)\psi^*(\frac{t-\tau}{a})dt, \tag{1}$$

where a is the dilation parameter, which plays the same role as the frequency in Fourier analysis, and τ indicates the translation parameter corresponding to the position of the wavelet in the physical space. In the present study we use the complex Morlet wavelet ($\psi(t) = e^{i\omega_0 t}e^{-t^2/2}$) as wavelet mother.
Let $W_f(a,\tau)$ and $W_g(a,\tau)$ be the continuous wavelet transforms of $f(t)$ and $g(t)$. We define the *wavelet cross-scalogram* as

$$W_{fg}(a,\tau) = W_f^*(a,\tau)W_g(a,\tau), \tag{2}$$

where the symbol $*$ indicates the complex conjugate. When the wavelet mother is complex, the wavelet cross-scalogram $W_{fg}(a,\tau)$ is also complex and can be written in terms of its real and imaginary parts:

$$W_{fg}(a,\tau) = CoW_{fg}(a,\tau) - iQuadW_{fg}(a,\tau). \tag{3}$$

It can be shown that the following equation holds if $f(t), g(t) \in \mathcal{L}^2(\Re)$

$$\int_{-\infty}^{+\infty} f(t)g(t)dt = 1/c_\psi \int_0^{+\infty} \int_{-\infty}^{+\infty} CoW_{fg}(a,\tau)d\tau da, \tag{4}$$

where $1/c_\psi$ is a constant depending on the choice of the wavelet mother.

3 Cross wavelet coherence functions

The highly redundant information from a multiscale wavelet analysis of time series must be reduced by means of suitable selective procedures and quantities, in order to extract the main features correlated to an essentially intermittent dynamics. In this study, we analysed and compared the properties of two complementary wavelet local correlation coefficents which are able to well evidence peculiar and anomalous local events associated to the vortex dynamics. More precisely, given two signals $f(t)$ and $g(t)$, we refer to the so-called *Wavelet Local Correlation Coefficent* (Buresti *et. al* [1]), defined as:

$$WLCC(a,\tau) = \frac{CoW_{fg}(a,\tau)}{\mid W_f(a,\tau) \mid\mid W_g(a,\tau) \mid}. \tag{5}$$

This quantity is essentially a measure of the phase coherence of the signals. Here we introduce the *Cross Wavelet Coherence Function* (CWCF) defined as:

$$CWCF(a,\tau) = \frac{2 \mid W_{fg}(a,\tau) \mid^2}{\mid W_f(a,\tau) \mid^4 + \mid W_g(a,\tau) \mid^4}, \tag{6}$$

which is essentially a measure of the intensity coherence of the signals. Using the polar coordinates we can write the wavelet transforms of $W_f(a,\tau)$, $W_g(a,\tau)$ and $W_{fg}(a,\tau)$ as:

$$W_f(a,\tau) = \rho_f e^{\imath\theta_f} \qquad W_g(a,\tau) = \rho_g e^{\imath\theta_g} \tag{7}$$

$$W_{fg}(a,\tau) = \rho_f \rho_g e^{\imath(\theta_g - \theta_f)}, \tag{8}$$

and the Cross Wavelet Coherence Function can be written also as:

$$CWCF(a,\tau) = \frac{2\rho_f^2 \rho_g^2}{\rho_f^4 + \rho_g^4}. \tag{9}$$

It is easy to observe the two basic properties of the function (6):

$$CWCF(a,\tau) = 0 \Longrightarrow \rho_f = 0 \qquad \text{or } \rho_g = 0 \tag{10}$$

$$0 \leq CWCF \leq 1 \qquad \forall\, a,\tau. \tag{11}$$

4 Numerical simulation

We considered a laboratory-scale axisymmetric flame of methane-air in a non confined bluff-body configuration. More precisely, the burner consists of a 5.4 mm diameter methane jet located in the center of a 50 mm diameter cylinder. Air is supplied through a 100 mm outer diameter coaxial jet around the 50 mm diameter bluff-body. The Reynolds number of the central jet is 7000 (methane velocity =21 m/s) whereas the Reynolds number of the coaxial jet is 80000 (air velocity =25 m/s). This is a challenging test case for all the turbulence models, as well documented in the ERCOFTAC report (Chatou, 1994) [2]. Moreover, due to the highly intermittent, unsteady dynamics involved and the high turbulence level, especially for the reactive case, the Large Eddy Simulation (LES) appears as the most adequate numerical approach (Sello *et. al* [3]).

5 Results and discussion

In this analysis we are mainly interested to relations existing between evolution of turbulence and mixing, for the reactive case. Previous DNS simulations on coaxial jets at different Reynolds numbers, show the ability of the wavelet cross-correlation analysis to better investigate the relations between mixing process and the dynamics of vorticity (Salvetti *et. al* [4]). Thus, the signals analysed here are velocity fluctuations (for Reynolds stress contributions) and mixture fraction fluctuations (for mixing evolution) from LES. As an example, Figure 1 shows the wavelet co-spectrum maps for a significant time interval in the pseudo-stationary regime of motion. The main contributions to the Reynolds stress are evidenced by high intensity correlations (red) and anti-correlations (blue) regions, which evolve intermittently. The dominant frequencies involved are located around 130 Hz. For the mechanisms responsable of the evolution of mixing, we note that the same regions of high Reynolds stress correspond to high correlation, or cooperation, between velocity and mixture fraction fluctuations, suggesting that, at the selected location, the same events of stretching and tilting of the vorticity layer, drive both Reynolds stress and mixing evolutions. Note that the large high value region located at low frequencies in the right map is statistically not significant if we assume a proper red noise background spectrum. To better investigate the role of the high correlation regions, we performed a cross section in the wavelet map at the frequency 160 Hz. Figure 2 (left) shows the time behaviour of the coherence functions WLCC, eq.(5), and CWCF, eq.(6). Here the phase and intensity coherence of signals are almost equivalent, but we can clearly point out an important anomalous event occurred at around t=0.19 s, corresponding to a loss of both intensity and phase coherence, followed by a change of the correlation sign. The link between this event and the dynamics of vorticity is evidenced by Figure 2 (right), which displays the wavelet map of the related vorticity signal. The higher frequency significant regions ($\approx$ 730 Hz) result strongly intermittent, with a bifurcation to lower and higher values than

average, followed by a drop of activity, in phase with the anomalous event.

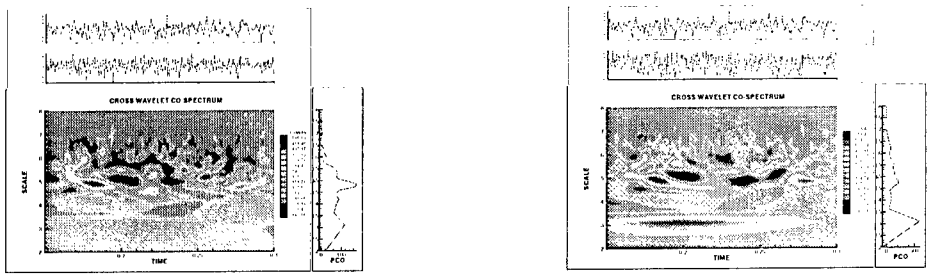


Figure 1: Cross-Wavelet co-spectrum maps for axial and radial velocity fluctuations (left) and for axial velocity and mixture fraction fluctuations (right) at a given spatial point near the edge of the central jet.

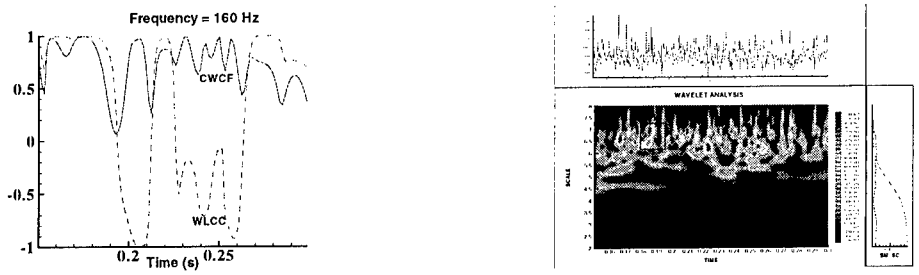


Figure 2: Coherence functions for axial velocity and mixture fraction fluctuations (left) and wavelet map of vorticity time series (right).

These few examples support the usefulness of the cross-wavelet analysis approach to better investigate turbulent mixing processes in real systems.

References

[1] G. Buresti and G. Lombardi. Application of continuous wavelet transforms to the analysis of experimental turbulent velocity signals. *Proc. of the* 1^{st} *Int. Symp. on Turb. Shear Flow Phen.*, S. Barbara USA, Sept. 1999.

[2] EDF Direction des Etudes et Researches. 1^{st} *A.S.C.F. Workshop Final Results*, Chatou, France, October 1994.

[3] S. Sello and G. Mariotti. Large eddy simulation of a bluff body stabilised flame. *Proc. of the* 4^{th} *ETMM Int. Symp.*, Ajaccio France, May 1999.

[4] M.V. Salvetti, G. Lombardi and F. Beux. Application of a wavelet cross-correlation technique to the analysis of mixing. *AIAA Jour.*, 37:1007–1009, 1999.

ADVANCES IN TURBULENCE VIII
Proceedings of the Eighth European Turbulence Conference
C. Dopazo et al. (Eds.)
© CIMNE, Barcelona 2000

Sidewall boundary layer instabilities in confined swirling flow

H. M. Blackburn

CSIRO Building Construction and Engineering
P.O. Box 56, Highett 3190, AUSTRALIA

Contact e-mail: hugh.blackburn@dbce.csiro.au

1 Introduction

The flow that is produced in a cylindrical container by a rotating endwall has been the subject of many studies, as it provides a convenient prototype for industrial and geophysical swirling flows. Much attention has been paid to aspects of vortex breakdown and stability at Reynolds numbers up to the onset of chaotic behaviour, rather less attention to describing the characteristics of the flow after the onset of turbulence.

Some recent studies of rotating flows in low aspect ratio cylindrical containers with differential endwall rotation have indicated the presence of sidewall boundary layer instabilities. In physical experiments with a rotating cylindrical tank and Kalliroscope (micro-platelet) flow visualisation, Hart & Kittelman [1] described and suggested possible mechanisms for a number of sidewall instabilities that appeared as the differential endwall co-rotation rate was raised. If the endwall rotates more slowly than the container, or counter-rotates slowly, the sidewall boundary layer flow is centrifugally stable. Lopez [2], using unsteady axisymmetric simulations of rotating tank flows with differential endwall rotation, also observed sidewall boundary layer instabilities that appear to propagate axially along the path where the axial velocity has a near-wall extremum. His simulation results show that the wall-normal profile of the axial velocity is inflectional.

Here, we study flows in a stationary cylindrical cavity with a rotating endwall, and find that sidewall boundary layer instabilities again arise. The work presented is for a cavity of height:radius ratio $H/R = 1$, with a Reynolds number $Re = \Omega R^2/\nu = 2.5 \times 10^4$. The aspect ratio was chosen so that flows with vortex breakdowns on the cylinder axis would not be observed [3]. The observed instabilities take the form of localised flow separations, with the line of separation aligned with the near-wall streamlines. For the parameters in the present work, ten separation vortices are observed, and these structures move with a slow prograde rotation around the cylinder sidewall.

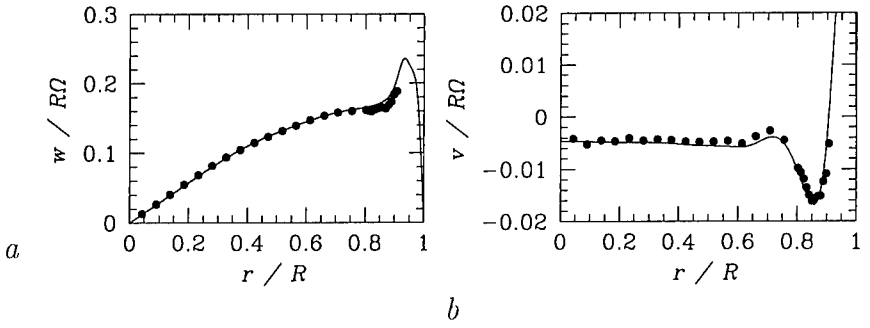


Figure 1: A comparison of computed (—) and measured (•) time-mean flow at cylinder mid-height; a: azimuthal velocity, b: axial velocity. The peak axial velocity of $v/R\Omega = 0.059$ occurs at $r/R = 0.975$.

2 Numerical and experimental techniques

Numerical simulations have been carried out using a spectral element–Fourier method, similar to that developed by Tomboulides [4]. A mesh of 100 spectral elements was used to discretise the geometry in meridional planes, with Fourier expansions in the azimuthal direction. After axisymmetric flow was fully developed, a small random perturbation was added to the fundamental Fourier mode, and the flow evolved until a statistically steady state was reached. As a check of azimuthal resolution, it was verified that the primary spectral statistics were very similar for both 96 and 128 planes of data in the azimuth.

Flow visualisation and LDV measurements of time-mean flow were obtained in a corresponding experimental apparatus with $R = 70\,\mathrm{mm}$ and with water as the working fluid. Visualisation was carried out using a low concentration of Kalliroscope platelets, while velocity measurements were obtained in pure water with a TSI 900-3 two-component system, traversed by a GMFanuc-Robotics S-10 industrial robot.

3 Results

A comparison of measured and computed time-mean velocity profiles at cylinder mid-height is presented in figure 1. The near-wall LDV measurements are unreliable, owing to a lack of spatial resolution, and have been omitted. A feature apparent in the velocity profiles is the presence of a cylindrical wall jet, which results from the diversion of the boundary layer formed on the rotating endwall. This jet flow is strongest and sharpest near the rotating endwall, and becomes weaker and more diffuse near the stationary endwall. It may be noted that the profiles for both velocity components are inflectional.

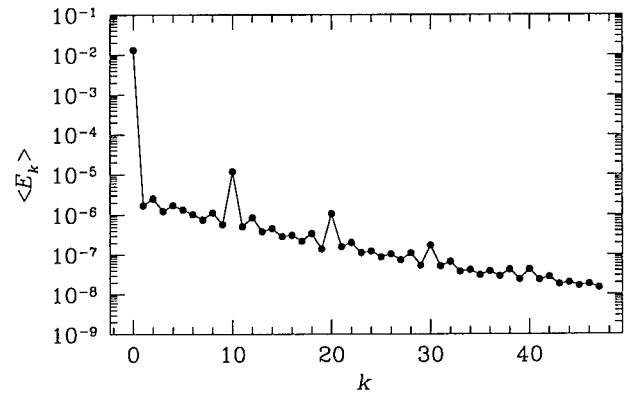


Figure 2: Spectrum of azimuthal modal energies.

Figure 2 shows the azimuthal energy spectrum, revealing significant energy in the 10th mode and its harmonics. The energy in each azimuthal Fourier mode k is given by

$$E_k = \frac{1}{2A}\rho \int_A \hat{\boldsymbol{u}}_k \cdot \hat{\boldsymbol{u}}_k^* \, r \, \mathrm{d}A,$$

where A is the area of the two-dimensional meridional semi-plane, ρ is fluid density, r is distance from the axis and $\hat{\boldsymbol{u}}_k^*$ denotes the complex conjugate of the velocity data in the kth Fourier mode. Energy of the axisymmetric base flow is represented by E_0.

A view of instantaneous contours of axial velocity on near-wall surfaces is shown in figure 3. This reveals the presence of near-wall vortical structures that are approximately aligned with the time-mean streamlines close to the cylindrical wall (i.e. with the wall traction field). From the view it can be inferred that ten of these structures exist on an azimuthal traverse, in agreement with the spectrum of figure 2. The structures have an approximately helical shape, and a slow prograde rotation (with the same sense as the rotation of the endwall), at an angular velocity $\omega/\Omega \simeq 0.09$. Each structure is associated with a local flow separation, producing reversed axial flow near the wall. The structures are not apparent at the end of the cavity near the rotating endwall. The strongest reversed flow is also the site of the highest axial–azimuthal Reynolds stress, which peaks at $r/R \simeq 0.95$, $z/H \simeq 0.5$. Examination of the time-mean flow also reveals a small separation zone around the junction of the stationary side and endwall.

4 Discussion and conclusions

This study of transitional flow in a cylindrical cavity notes the presence of sidewall boundary layer instabilities that give rise to local flow separation. It appears



Figure 3: Instantaneous contours of axial velocity on near-wall surfaces. Rotating endwall is at bottom.

that the instability is associated with the presence of a boundary layer with inflectional profile, produced by the wall-jet type flow originating on the rotating endwall. The boundary layer structures are aligned with the wall traction field, and have the appearance of an array of helices that has a slow prograde rotation.

Experimental flow visualisation studies conducted over a range of Reynolds numbers and cylinder aspect ratios suggest that the near-wall vortical structures with local separation are a characteristic feature for this flow—they maintain alignment with the wall traction field, but become smaller and more numerous as the Reynolds number increases, indicating law-of-the-wall scaling.

References

[1] J. E. Hart & S. Kittelman. Instabilities of the sidewall boundary layer in a differentially driven rotating cylinder. *Phys. Fluids*, 8(3):692–696, 1996.

[2] J. M. Lopez. Characteristics of endwall and sidewall boundary layers in a rotating cylinder with a differentially rotating endwall. *J. Fluid Mech.*, 359:49–79, 1998.

[3] M. P. Escudier. Observations of the flow produced in a cylindrical container by a rotating endwall. *Expts. Fluids*, 2:189–196, 1984.

[4] A. G. Tomboulides. *Direct and Large-Eddy Simulation of Wake Flows: Flow Past a Sphere.* PhD thesis, Princeton, 1993.

ADVANCES IN TURBULENCE VIII
Proceedings of the Eighth European Turbulence Conference
C. Dopazo et al. (Eds.)
© CIMNE, Barcelona 2000

Convective turbulence of gaseous helium in a closed domain: a look inside the cell

R. Verzicco[1] and R. Camussi[2]

[1]Politecnico di Bari, Istituto di Macchine ed Energetica, via Re David 200, 70125 Bari ITALIA.
[2]Università di Roma 'Tre', DIMI, via della Vasca Navale 79, 00146 Roma, ITALIA.

Contact e-mail: verzicco@imeapol.poliba.it

1 Introduction

Large attention has been devoted to thermal convection in the last decade owing to the advances in nonlinear dynamics and turbulence provided by this flow. This was shown recently in experiments by Castaing *et al.* (1989), Cioni, Ciliberto and Sommeria (1997), Chavanne *et al.* (1996) and Niemela *et al.* (2000) (among many others). The achievement of strongly turbulent conditions requires the experiments to be carried out in critical situations such as the use of liquid metals (mercury or sodium) or gasses at criogenic temperatures (helium at 5K). These circumstances, combined with the intrinsic difficulties of taking velocity measurement in thermal convection make very hard the experimental study of the phenomena. Within this scenario it is clear that the numerical simulations can be very helpful in the interpretation of the flow physics since quantitative measurements can be easily obtained of virtually any quantity and the hypotheses underlying theoretical models can be directly checked. This is particularly true thanks to the increasing power of computers and to the availability of parallel architectures that allow for numerical simulations at Rayleigh numbers comparable with those of experiments.

On account of the previous arguments, in this study we analyse by direct numerical simulation the convective turbulence generated in gaseous helium (Prandtl $\simeq 0.7$) in a small aspect ratio cylindrical cell (diameter–to–height ratio 0.5) heated from below and cooled from above, for Rayleigh numbers ranging from $2 \cdot 10^6 \leq Ra \leq 2 \cdot 10^{11}$. The flow conditions have been selected in such a way to replicate the experiments carried out in Grenoble by the group of B. Castaing and that by Niemela *et al.* (2000). The aim of this study is twofold: to validate our results by a comparison with the experiments and to perform those analyses which are impossible in laboratory experiments.

2 Problem and Computational Set–up

In this paper we study the flow generated by thermal convection processes in a set–up which is identical to the experimental set–up by Chavanne *et al.* (1996) and Niemela *et al.* (2000). The fluid is confined in a cylindrical cell; let d be the diameter of the cell and h the distance between the lower hot and upper cold horizontal plates, the aspect ratio of the cell $\Gamma = d/h$ is 0.5 for all the simulations. The gravity vector points downwards and is orthogonal to the upper and lower plates which are maintained at constant temperature. The lateral wall of the cell is adiabatic with the condition of zero heat flux. All the boundaries are no–slip.

The three–dimensional time–dependent Navier–Stokes equations with the Boussinesq approximation for an incompressible viscous fluid have been integrated numerically. The equations, in a cylindrical coordinate system in terms of primitive variables (velocity and pressure), have been discretized using second–order–accurate finite–difference approximations in space and in time. The solution procedure is that of Verzicco & Orlandi (1996) with the modifications described in Verzicco & Camussi (1997). Here it is enough to note that the system of discretized equations is solved by a fractional–step method and the advancement in time is performed by a third–order Runge–Kutta scheme.

The resolution requirements induced us to use a non–uniform mesh in the radial and vertical directions with the gridpoints slightly clustered close to the boundaries. Grids ranging from $65 \times 49 \times 129$ up to $193 \times 129 \times 513$, respectively, in the azimuthal, radial and axial directions were used and the mesh size was determined by the necessity of having the computational cell smaller than the kolmogorov scale at the centre of the cell and at the same time to have 8–10 gridpoints inside each thermal boundary layer.

As additional diagnostics we have placed inside the cell about 400 numerical probes (therefore not intrusive) by which we sampled in time temperature, pressure and all velocity and vorticity components. These data have been used to perform statistical analyses on quantities which can not be achieved by experiments.

3 Results and Discussion

As mentioned in the introduction the high computational cost of an unsteady three–dimensional direct numerical simulation is made up by the possibility of performing analyses which are virtually impossible in experiments. Among many, the most intuitive is the possibility of visualizing instantaneous sections of the flow in order to have a look at the flow structures inside the cell. In figure 1 we report vertical and horizontal sections of the temperature which evidence the presence of a cold descending current on the right and the hot rising counterpart on the left. This is confirmed also by the contours of vertical velocity showing separate positive and negative regions according to the temperature distribution.

The above flow maps indicate the presence of a large scale recirculation that is

persistent during the flow evolution and dominates the flow dynamics, similarly to what observed in $\Gamma = 1$ aspect–ratio cells by Verzicco & Camussi (1999). This large–scale flow can be quite effective in the heat transfer since the "winds" sweeping the horizontal plates exchange heat inside the thermal boundary layers and this heat is transferred between the plates by the vertical currents. The non–dimensional heat transfer (Nu) as function the Rayleigh number is shown in the first panel of figure 2 together with some experimental results. The first point is that the data are on a power law with exponent $1/3$ which is definitely different from the value $2/7$ commonly accepted for moderate and high Prandtl fluids. The second point is that, although the agreement with the experiments is generally good, there are small deviations with respect to the data of Chavanne *et al.* (1996). Those authors ascribed the deviation from the power law to the onset of a transition which should lead to the asymptotic regime predicted by Kraicknan (1962), This disagrees with the findings of Niemela *et al.* (2000) which, instead, found a unique power law all the way up to $Ra = 10^{17}$ without appreciable deviations.

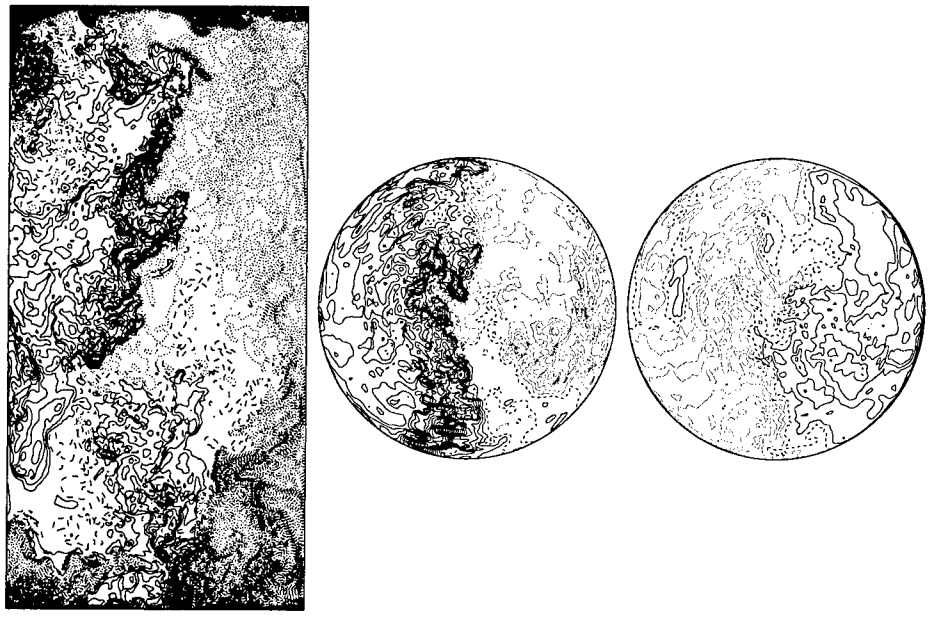


Figure 1: Instantaneous snapshots of temperature in a vertical plane through the diameter (*left*) and in a horizonthal plane midway between the plates (*centre*); $\Delta T = 5 \cdot 10^{-3}$, —— $0 \leq T < 0.5$, ····· $0.5 > T \geq 1$, ---- $T = 0.5$. (*right*) the same as (*centre*) but for the vertical velocity component; $\Delta v = \pm 0.05$, —— $0 < v \leq 0.55$, ····· $-0.55 \leq v < 0.$, ---- $v = 0$. $Pr = 0.7$, $Ra = 2 \cdot 10^{10}$.

Several numerical probes have been placed inside the flow in order to compute the statistics of the fluctuating quantities. The results for the velocity and

temperature halfway between the plates and close to the axis are shown in figure 2. Both spectra show about two decades of power law range but while the velocity follows the classical Kolmogorov scaling, the temperature behaves according to the Bolgiano prediction. This might appear very surprising, however, a direct computation of the Bolgiano and integral scales has shown that at the centre of the cell the latter is equal to the former thus explaining the velocity spectrum. In contrast, given the small value of the temperature variance dissipation, the integral scale for the temperature variance is bigger than the Bolgiano's length scale and the temperature behaves accordingly.

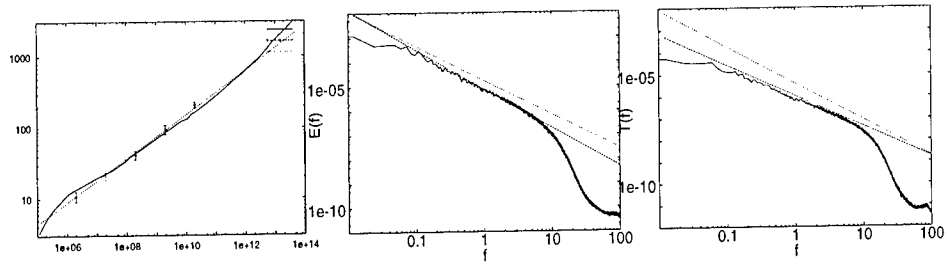


Figure 2: *left Nu vs Ra* relation, —— experimental results by Chavanne *et al.* (1996), ····· experimental results by Niemela *et al.* (2000), symbols present results. *centre* Spectrum of temperature at the cell centre and $Ra = 2 \cdot 10^{10}$, ---- -1.4 slope, ····· -1.6 slope. *right* the same as *(b)* for the velocity ---- -1.6 slope, ····· -1.4 slope.

References

[1] Castaing, B., Gunaratne, G., Heslot, F., Kadanoff, L., Libcha ber, A., Thomae, S., Wu, X.Z., Zaleski, S. and Zanetti, G. *J. Fluid Mech.*, 204, p.1, 1989.

[2] Cioni, S., Ciliberto, S. and Sommeria, J. *J. Fluid Mech.*, 335, p.150, 1997.

[3] Chavanne, X., Chillà, F, Chabaud, B., Castaing, B., Chaussy, J., and Hèbral, B. *J. of Low Temp. Phys.*, 104, p.109, 1996.

[4] Niemela, J.J., Skrbek, L., Sreenivasan, K.R. and Donnelly, R.J., *to appear in Nature.*

[5] Kraichnan, R., *Phys. Fluids* , 5, p.1374, 1962.

[6] Verzicco, R., & Camussi, R., *Phys. of Fluids*, 9, p.1287, 1997.

[7] Verzicco, R. & Orlandi, P., *J. Comp. Phys.*, 123, p.402, 1996.

[8] Verzicco, R., and Camussi, R. *J. Fluid Mech.*, 383, p.55, 1999.

XX

Modelling

ADVANCES IN TURBULENCE VIII
Proceedings of the Eighth European Turbulence Conference
C. Dopazo et al. (Eds.)
© CIMNE, Barcelona 2000

Low-order models derived from POD-Galerkin approximations for separated turbulent flows

A. Lombard[1], P. Sagaut[1], J.P. Bonnet[2] and J. Delville[2]

[1]ONERA, 29 av. de la Division Leclerc, 92322 CHÂTILLON cedex, FRANCE
[2]CEAT, 43 rte. de l'aérodrome, 86036 POITIERS cedex, FRANCE

Contact e-mail : lombard@onera.fr

1 Introduction

Fluid flows are very often governed by the dynamics of a small number of coherent structures, i.e., fluid features which keep their individuality during the evolution of the flow. The purpose of this paper is to study low-order simulations of the Navier-Stokes equations for separated incompressible turbulent flows, on the basis of the evolution of such coherent structures. One way to extract from flow simulations some basis functions which can be interpreted as coherent structures is Proper Orthogonal Decomposition (POD). Then, by means of a Galerkin projection [1], it is possible to find the system of ODEs which approximates the problem in the finite dimensional space spanned by the POD basis functions.
It is found that the low-order modeling of relatively complex flow simulations, such as the vortex sheddings from a square cylinder and from a backward facing step (which are two examples of respectively 2D and 3D separated flows behind an obstacle), provides good qualitative results compared with reference computation.

2 Theory

POD consists of searching for the preferred modes $\phi(x)$ of a flow, that is -in some average sense- as similar as possible to a set of realizations $u(x,t_i)$ of the flow. Mathematically, this problem can be written :

$$\frac{< (u,\phi)^2 >}{(\phi,\phi)} \stackrel{!}{=} Max \qquad (1)$$

where (,) is related to a scalar product, and < , > to a statistical average. Here we use the Snaphot approach of POD, first introduced by Sirovich [2], to

solve equation (1) : the preferred modes are thus found to be an infinite discrete set of orthogonal functions $\{\phi^{(n)}(x)\}_{n=1,\ldots,+\infty}$ defining a basis for the flow field u. Each realization $u(x,t_i)$ can then be decomposed using the deterministic functions $\phi^{(n)}(x)$ in the following way :

$$u(x,t_i) = \sum_{n=1}^{+\infty} a^{(n)}(t_i)\phi^{(n)}(x) \tag{2}$$

where the coefficients $a^{(n)}$, projections of u onto $\phi^{(n)}$, are calculated by using :

$$a^{(n)} = (u, \phi^{(n)}) \tag{3}$$

In order to derive a low-order model of the flow, by used of a POD basis, we first consider the Navier-Stokes equations for incompressible flows that can be written symbolically as :

$$\frac{\partial u}{\partial t} = F(u) \tag{4}$$

where F is a differential operator. An essential property of POD is that this decomposition is optimal in term of energy : this allows us to truncate the POD basis at a limited number of modes : N_{POD}, function of the rate of energy captured desired. The decomposition (2) is then introduced into (4) and by use of a Galerkin projection [1] onto the truncated POD basis, we end up with a dynamical system of ODEs constituing the low-order model of the flow :

$$\frac{da^{(n)}(t)}{dt} = \mathcal{F}^{(n)}(a^{(1)}(t), a^{(2)}(t), \ldots) \qquad n = 1, \ldots, N_{POD} \tag{5}$$

where the $\mathcal{F}^{(n)}$ are given by :

$$\mathcal{F}^{(n)} = (\phi^{(n)}, F(u)) = (\phi^{(n)}, F(\sum_m a^{(m)}(t)\phi^{(m)}(x))) \qquad n = 1, \ldots, N_{POD} \tag{6}$$

In this study, the data set of realizations available to compute the POD basis functions have been obtained by carrying out a DNS of the flow around the square cylinder and a LES of the flow over the backward facing step. The simulations were performed using a second-order accurate on both space and time numerical methods.

3 Square Cylinder ($Re = 100$)

The ensemble of realizations consists of 400 equally spaced time steps within one time-period of the lift coefficient. Two dynamical systems are derived, one from the pressure-velocity formulation of the Navier-Stokes equation (the pressure term, which cannot be expressed using POD-modes, is neglected), and another from the vorticity transport equation. Subsequently, the predicted cofficients

will be respectivly noted *apred*1 and *apred*2 and the projected coefficients *aproj*.

Figure 1 shows the energy contained by each mode : most of the fluctating energy is captured by the first two modes alone, and if eight modes are taken, the remaining energy accounts for less than 0.1% of the unsteadiness. Fig.2 illustrates for the first two modes $\phi^{(1)}$ and $\phi^{(2)}$ that POD-modes occur in pairs of almost equal energy, the corresponding coherent structures being phase-shifted in space and time. In Fig.3, predicted and projected coefficients are compared : the dynamical systems are truncated at $N_{POD} = 8$. Clearly, the low-order model derived from the vorticity transport equation gives better and more stable results : this demonstrates that the pressure term cannot be easily neglected in this case. Netherthless, if the integrated time histories for the first modes match the observed results extremely well, the amplitudes and phases of the higher modes are less accurately predicted.

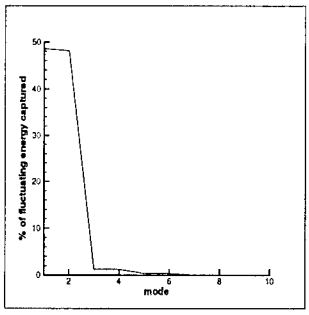


Fig.1

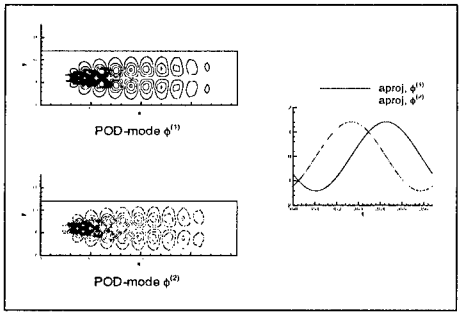


Fig.2 : Contour lines of the streamwise velocity for $\phi^{(1)}$, $\phi^{(2)}$, and corresponding projected coefficients.

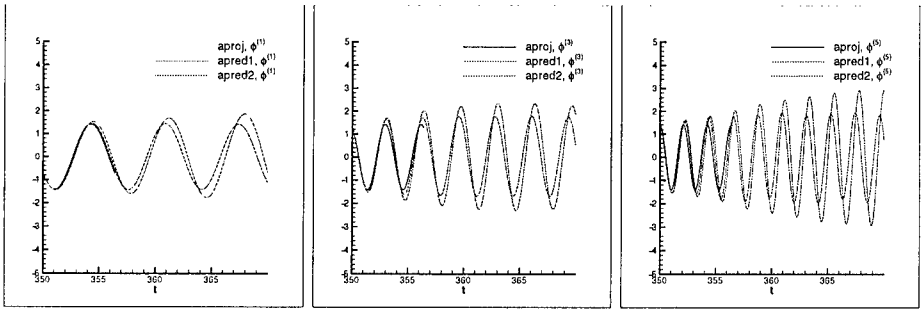


Fig.3 : Projected and predicted coefficients associated to $\phi^{(1)}$, $\phi^{(3)}$ and $\phi^{(5)}$.

4 Backward Facing Step ($Re = 9910$)

The ensemble of realizations consists of 1000 equally spaced time steps within one period of the flapping mechanism.

Figure 4 shows the energy spectrum : clearly, the highly 3D turbulence results in a flow with many more degrees of freedom (based on energy distribution) than in the 2D laminar test case. In Fig.6 are plotted the velocity vectors of the first POD-mode in a xz-plane and in a yz-plane behind the step. We recognize here the main features of a turbulent flow behind a backward facing step : high levels of fluctuations are observed in the separated shear layer and near the reattachment point; the mode is seen to be 3D, with alternated streamwise vortices. Finally, Fig. 5 shows the projected coefficients for the first two modes : same as before, they appears to be phase-shifted in time. Nethertheless, for higher modes, this parity is not so obvious than in the 2D steady-state case.

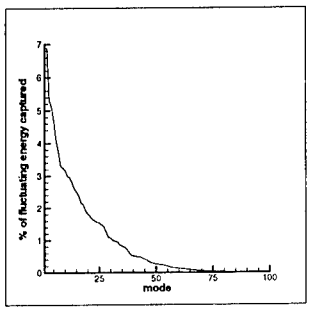


Fig.4

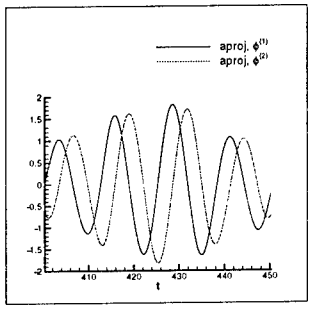


Fig.5 : projected coefficients for $\phi^{(1)}$, $\phi^{(2)}$

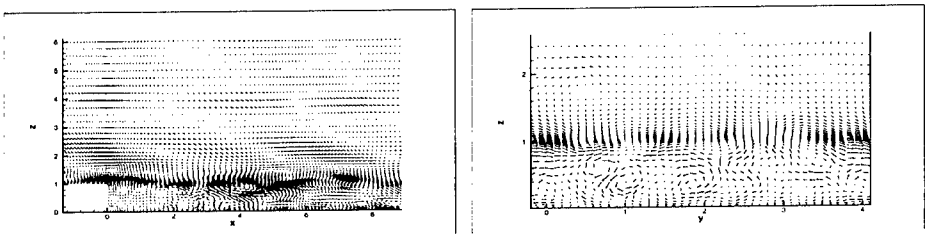


Fig.6 : Velocity vectors of $\phi^{(1)}$ in a xz-plane (left) and in a yz-plane (right).

5 Conclusion

Concerning 2D flows, low-order models derived from a POD-Galerkin method have already showed their efficency. For the flow behind a backward facing step, results show the three-dimensionnal nature of the flow : future works will deal with the POD-Galerkin analysis of the 3D case.

References

[1] C.A.J. Fletcher, *Computational Galerkin methods.* Springer Verlag, Berlin, 1984

[2] L. Sirovich, 'Turbulence and the dynamics of coherent structures. Part I : coherent structures'. *Quatterly of Applied Mathematics*, vol. XLV, n. 3, pp. 561-571, 1987.

ADVANCES IN TURBULENCE VIII
Proceedings of the Eighth European Turbulence Conference
C. Dopazo et al. (Eds.)
© CIMNE, Barcelona 2000

Geometry and statistics in Lagrangian dispersion

A. Pumir[1], B. Shraiman[2] and M. Chertkov[3]

[1]Institut Non Linéaire de Nice, CNRS
1361 route des Lucioles, 06560, Valbonne, France
[2] Bell Labs, Lucent Technologies,
700 Mountain Ave, Murray Hill, NJ 07974, USA
[3]T13 and CNLS,
Los Alamos National Laboratory, NM 87545, USA

Contact e-mail: pumir@inln.cnrs.fr

The fast mixing characteristic of fluid turbulence is very important in a number of natural or engineering contexts. The important modelling issue of predicting passive scalar transport in turbulence can be addressed by following the evolution of Lagrangian particles [1]. We address the question of how a cluster of $n = 3, 4$ particles evolves, a question relevant to the study of the multipoint correlation function. This leads us to follow both the overall scale and the shape of the object. The geometry of a cluster of points is important from a conceptual and analytical point of view [2, 3]. Newly developed methods of particle tracking[5, 6] should allow to answer many questions and in particular, to address the problem of statistical geometry of dispersing particles.

We study the problem with the help of direct numerical simulations (DNS) at moderate Reynolds numbers ($R_\lambda \leq 85$). Starting from initially regular (isotropic) clusters of points, of size R_0, we characterize the evolution of the radius of gyration, $R(t)$, and of the shape of the object. A convenient way to describe the configuration of the set of points consists in defining the moment of inertia tensor,

$$g^{ab} \equiv \sum_{i=1}^{n-1} \rho_i^a \rho_i^b \tag{1}$$

where $\vec{\rho}_i$ are $n-1$ vectors characterizing the differences between the posistions of the n points (note that the center of mass plays no role in our study). The eigenvalues of this tensor g_i ($g_1 \geq g_2 \geq g_3$; $g_1 + g_2 + g_3 = R^2$) provide a way of quantifying the shape distorsion of the set of points. The case when $g_1 \approx g_2 \approx g_3$ corresponds to a roughly isotropic object ($g_1 = g_2 = g_3$ for regular tetrahedra).

The case $g_1 \approx g_2 >> g_3$ corresponds to a very flat, pancake like object. When $g_1 >> g_2,\ g_3$, the object is very elongated, needle like. The same considerations apply for a triangle, with the restriction that $g_3 = 0$. A convenient way to describe the overall shape of the swarm consists in monitoring the ratio g_2/R^2. This ratio is less than $1/3$ $(1/2)$ for tetrahedra (triangles). The area of a triangle, $\mathcal{A} = |\vec{\rho}_1 \times \vec{\rho}_2|$, and the volume of a tetrahedron, $V = det(\vec{\rho}_1, \vec{\rho}_2, \vec{\rho}_3)$ also provide some information on the shape of the cluster. In the triangle case, g_2/R^2 and $\mathcal{A}/R^2$ are related by $g_2/R^2 = \frac{1}{2}(1 - \sqrt{1 - 4\mathcal{A}^2/R^4})$.

The evolution of $< g_2/R^2 >$ for tetrahedra as a function of time, and for the initial values of R_0 chosen, is shown in Fig.1a. A strong growth of anisotropy is initially observed, the more so as the intial size of the swarm of particles gets smaller. At very short times, all the curves corresponding to dissipative scale $(R_0 \lesssim 10\eta)$ superpose. A systematic comparison with data at lower Reynolds number demonstrates that the characteristic time in the short time, dissipation scale regime is the Kolmogorov time, $\tau_K = \nu/\epsilon$. For larger scales, our data can be superposed at early times by scaling with the time scale $\tau(R_0) = \epsilon^{1/3} R_0^{-2/3}$.

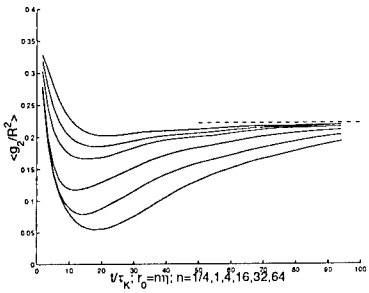


Figure 1: Evolution of the ratio $< g_2/R^2 >$ for a set of $(27)^3$ tetrahedra, initially regular, with a edge size of $r_0 = n\eta$, $n = 1/4,\ 1,\ 4,\ 16,\ 32$ and 64. The integral size is $L \sim 64\eta$; $R_\lambda \approx 83$. The dashed horizontal line shows the gaussian value, $< g_2/R^2 >_{G,4} \approx 0.222$.

At short times, and for $R_0 \lesssim 4\eta$, the volume is approximately conserved, as expected. The growth of R is related to important shape distorsions. The conditional value $< R(t)|I_2 \leq 0.1 >$ is initially significanlty larger than $< R(t) >$. Once R reaches inertial scale values, volume is no longer preserved. Small non volume preserving fluctuations induce huge volume fluctuations on highly distorted clusters. The rough aspect of the curves for small initial values of r_0 and at short times is due to the very wide tails of the pdf of volume, see Fig.1b. The number of tetrahedra followed (27^3) was not large enough to obtain a reliable

estimate of the second moment of the distribution !

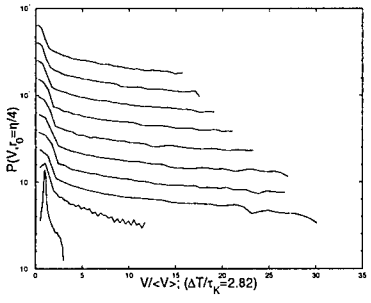


Figure 2: The pdf's of $\mid V \mid / < \mid V \mid >$ at different times, separated by $\Delta t/\tau_K = 2.8$ have been shifted upwards by a constant factor, for clarity.

To investigate the geometrical properties in the inertial range, we use the model :

$$\frac{d\rho_i^a}{dt} = \rho_i^b M_{ba} + u_i^a \tag{2}$$

$$\frac{dM_{ab}}{dt} = -\frac{M_{ab}}{\tau(R)} + \eta_{ab} \tag{3}$$

$$< \eta_{ab}(t)\eta_{cd}(t') >= C_\eta^2 \ \delta(t-t')(\delta_{ab}\delta_{cd} - \frac{1}{d}\delta_{ab}\delta_{cd})/\tau(R) \tag{4}$$

$$< u_i^a(t)u_j^b(t') >= C_v^2 \ \delta(t-t')\delta_{ij}\delta_{ab}R^2/\tau(R) \tag{5}$$

where the first term in the left hand side of Eq.2 represents the effect of advection by the velocity at scale $\sim R$, and the second term represents the effect of the small scale jitter induced by the small scales of the motion [7]. The matrix M is random, with a Gaussian distribution and a characteristic time scale $\tau(R)$, see Eq.3. The Kolmogorov scaling is imposed through the R dependence of the noise terms, see Eq.4,5. The dimensionless ratio C_v/C_η describes the relative importance of the incoherent (small scale) and of the coherent fluctuations of the velocity field.

As expected dimensionally, the scale R eventually grows as $t^{3/2}$. More importantly for our own purpose, the ratio $< I_2/R^2 >$ reaches a finite value when $t \to \infty$. The limiting value depends monotonically on the ratio C_v/C_η. As expected, the gaussian value is recovered, when $C_v/C_\eta \to \infty$, whereas the anisotropy increases without limit ($< g_2/R^2 > \to 0$) when $C_v/C_\eta \to 0$. Our results suggest that the anisotropy is constant in the inertial range.

Characterizing experimentally this anisotropy would provide an estimate on the ratio C_v/C_η, and also a constraint on the models used for turbulent mixing.

Acknowledgements

AP and BIS wish to acknowledge the hospitality of the Isaac Newton for Mathematical Sciences, where part of this work was done. The numerical calculations were carried out on the Cray C98 thanks to a grant of computer time from IDRIS (France).

References

[1] S. B. Pope, Ann. Rev. Fluid Mech. **26**, 23 (1994).

[2] L. Mydlarski et al, Phys. Rev. Lett. **81**, 4373 (1998).

[3] M. Chertkov, A. Pumir and B. I. Shraiman, Phys. of Fluids **11**, 2394 (1999).

[4] M. C. Jullien, J. Paret and P. Tabeling, Phys. Rev. Lett. **82**, 2872 (1999).

[5] G. A. Voth, K. Satyanarayan and E. Bodenschatz, Phys. Fluids **10**, 2268 (1998).

[6] J. Mann, S. Ott and J. Andersen, preprint (1999); N. Mordant and J. F. Pinton, preprint (1999).

[7] B.I. Shraiman and E.D. Siggia, C. R. Acad. Sci. **321**, 279 (1995).

ADVANCES IN TURBULENCE VIII
Proceedings of the Eighth European Turbulence Conference
C. Dopazo et al. (Eds.)
© CIMNE, Barcelona 2000

Using Rapid Distortion Theory to interpret experiments on stably stratified turbulent shear flows

D. D. Stretch[1], J. W. Rottman[2], K. H. Keller[2] and C. W. Van Atta[2]

[1]School of Civil Engineering, University of Natal, Durban, SOUTH AFRICA
[2]Department of Mechanical and Aerospace Engineering,
University of California, San Diego, La Jolla, CA, USA

Contact e-mail: stretchd@eng.und.ac.za

1 Introduction

Stably stratified turbulence occurs widely in environmental flows. Many laboratory experiments have been carried out in order to increase our understanding of the physics of these flows and to apply the results to the development of improved turbulence models. In this paper we consider the canonical problem of turbulence subjected to a uniform stable stratification and a uniform shear. The interpretation of experimental results from investigation of this flow remains controversial which has hindered progress in the application of the results to modeling. We have applied Rapid Distortion Theory (RDT) to help us to understand these flows, and report on some preliminary findings below. In particular, we use RDT to solve an idealized initial-value problem in which a homogeneous field of turbulence is suddenly subjected at time $t = 0$ to a uniform plane strain, with shear strength S, and a uniform stable stratification, with buoyancy frequency N. Some initial comparisons between RDT and the grid turbulence experiments of [4] have been previously reported by [1] and [5]. In this paper we expand on those results by analyzing the more recent and extensive experiments of [2] and [3].

Comparing idealized RDT calculations with experimental results of grid turbulence requires some care. First the initial conditions have to be properly specified to match the experimental conditions. RDT requires the velocity pertubations, the density perturbations and the statistical relationship between these two fields at the initial time.

Second, RDT is formally valid only when the distortion time (the time over which shear and stratification have a significant effect on the turbulence) is small compared with the decay time of the individual turbulent eddies. When this distortion time scale is larger than the decay time, we argue (following [6]) that

RDT can still be applied if *effective* strains ($\beta_{eff} = S\,T_L$ and $\eta_{eff} = N\,T_L$) are used instead of the *total* strains ($\beta = S\,t$ and $\eta = N\,t$). The argument is based on the idea that the decay time scale T_L of the energy containing eddies places an upper limit on the strain which these eddies can experience before losing their energy to smaller scales through nonlinear transfer. A suitable working definition is $T_L = k/\epsilon$ where k is the turbulence kinetic energy and ϵ is the dissipation rate. For the case of grid-generated turbulence without shear, it is found that the effective strain is proportional to the total strain. On the other hand, for grid-generated turbulence in sheared flows the effective strain may evolve differently from the total strain, depending on the gradient Richardson number $R_i = N^2/S^2$. Typical examples of effective strain as compared with total strain evolution are shown in Fig. 1 for the data from [2]. For $R_i \geq 0.25$ the effective strains increase with distance from the grid in proportion to the total strains. In contrast, at lower R_i the effective strains initially increase in proportion to the total strains but eventually approach constant values as the total strains continue to increase.

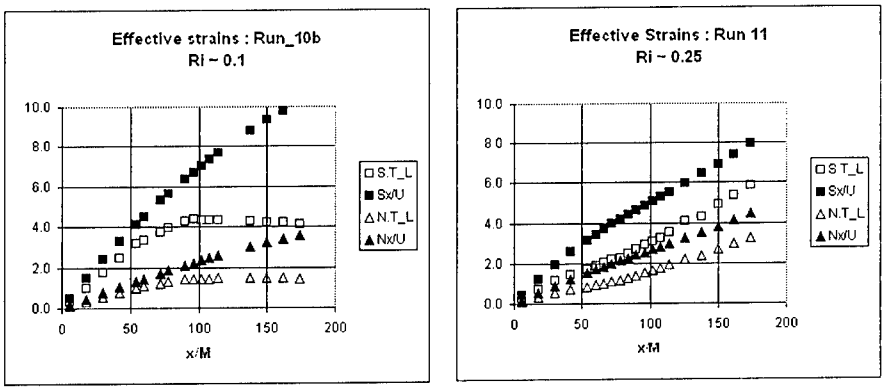


Figure 1: The evolution of the effective strains (open symbols) and the total strains (solid symbols) as a function of nondimensional distance x/M downstream of the grid, where M is the grid mesh length, for $R_i = 0.10$ and 0.25. The approximation $t = x/U$, where U is the mean flow speed at the height of the measurements, has been used to compare the spatially evolving laboratory flow with the temporally evolving RDT calculation.

2 Results

A hypothesis which has emerged from our RDT analysis is that the effects of stable stratification on certain aspects of the turbulence structure can be universally parameterized using the effective "buoyancy strain" $\eta = NT_L$. This parameter may be interpreted as the inverse of a *local* turbulence Froude number.

To test the above hypothesis we have examined various turbulence structure parameters as a function of η. A sample of these results is shown in Fig. 2. The RDT calculations are all for an initially isotropic velocity field and no initial density fluctuations.

The figure shows the calculated evolution (as a function of the buoyancy strain) of the normal stress ratio, the vertical buoyancy flux, and the density fluctuations for different values of R_i.

It can be seen from these results that RDT predicts the qualitative form of the evolution of these turbulence structure parameters reasonably well. In quantitative terms, the results are mixed. The quantitative evolution of the density fluctuations is reasonably well predicted by RDT, with a maximum occurring near $\eta = 2$. However, while the form of the flux evolution is well predicted, with a maximum at $\eta = 1$ and a reduction to low values at $\eta = 2$, RDT predicts a sign change in the flux for $\eta > 2$ which is not observed in these experiments. We note that although the flow becomes non-diffusive over times of order $2/N$ (with greatly reduced buoyancy flux), the flow remains highly dissipative. This is not consistent with a transition to an internal-wave dominated flow.

3 Conclusions

Accounting for an effective strain appropriately for the various laboratory experiments on grid-generated turbulence in stratified shear flows, we have been able to get reasonable qualitative agreement between RDT and experimental results. In particular, the evolution of the density fluctuations as well as that of the vertical density flux is correctly predicted. There are however some significant quantitative differences between theory and experiment: we attribute these mainly to RDT's tendency to overestimate the anisotropy of the turbulence due to the neglect of nonlinear effects. The results of the comparison of RDT with laboratory experiments suggests that many features of turbulence in stratified shear flows may explained by a linear interaction between the energy containing eddies and the mean shear and stratification. The nonlinear effects seem to limit this process rather than significantly modify it.

References

[1] Hunt J.C.R., Stretch, D.D. and Britter, R.E.: 1988, 'Length scales in stably stratified turbulent flows and their use in turbulence models', In *Stably Stratified Flow and Dense Gas Dispersion* , Proc. IMA Conf., Chester, UK, 9-10 April, 1986. Clarendon Press, Oxford., pp. 285–321.

[2] Keller, K.H. and Van Atta, C.W.: 1999a, 'On the evolution of turbulent kinetic and potential energies in homogeneous stratified shear turbulence', *J. Fluid Mech.* (submitted).

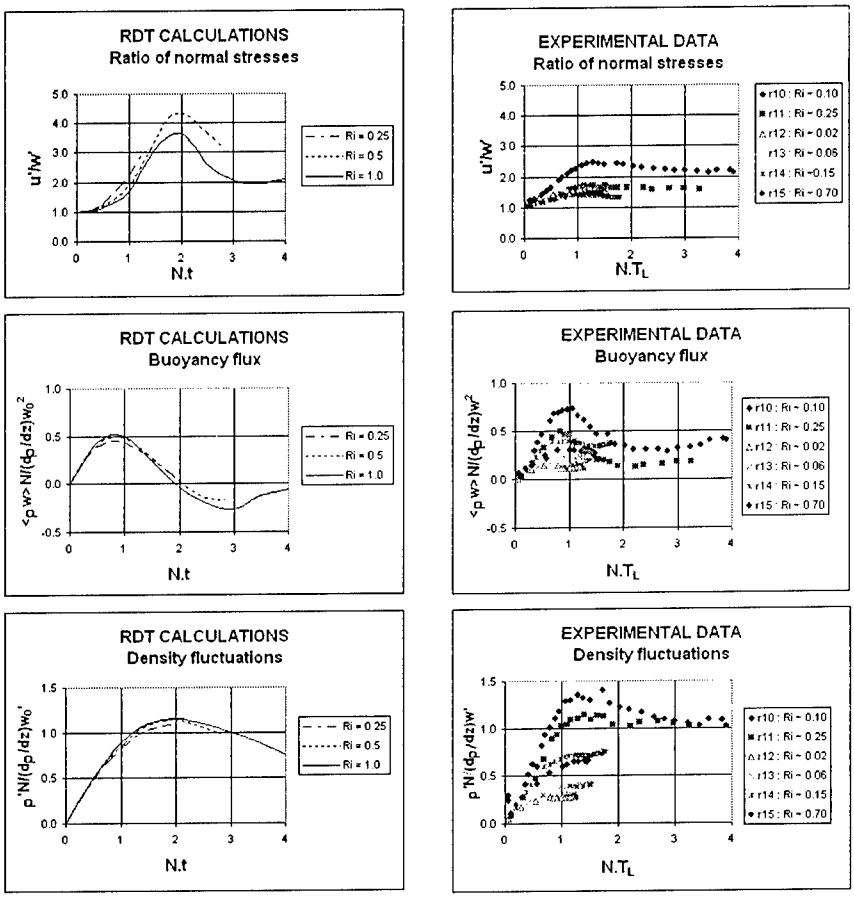


Figure 2: Comparison between RDT calculations and experimental data.

[3] Keller, K.H. and Van Atta, C.W.: 1999b, 'An experimental investigation into the vertical temperature structure of homogeneous stratified shear turbulence', *J. Fluid Mech.* (submitted).

[4] Stillinger, D.C., Helland, K.N. and Van Atta, C.W.: 1983, 'Experiments on the transition of homogeneous turbulence to internal waves in a stratified fluid', *J. Fluid Mech.* **Vol. 131**, pp. 91–122.

[5] Stretch, D.D.: 1986, *The dispersion of slightly dense contaminants in a turbulent boundary layer* . Ph.D. thesis, University of Cambridge, Cambridge, UK.

[6] Townsend, A.A.: 1976, *The structure of turbulent shear flow.* CUP.

ADVANCES IN TURBULENCE VIII
Proceedings of the Eighth European Turbulence Conference
C. Dopazo et al. (Eds.)
© CIMNE, Barcelona 2000

Nonlinear RDT theory of near wall turbulence

S.V. Nazarenko[1], N.K.-R. Kevlahan[2] and B. Dubrulle[3]

[1]Mathematics Institute, University of Warwick, Coventry CV4 7AL, UK
[2]Dept of Math and Statistics, McMaster University, Hamilton L8S 4K1, Canada
[3]CNRS URA 2052, L'Orme des Merisiers, 709, 91191 Gif sur Yvette, France

Contact e-mail: snazar@maths.warwick.ac.uk

1 Introduction

There has been lively discussion in the literature over several past years about whether near-wall turbulence has the complete similarity property, a classical picture introduced by von Karman and Prandtl [1], or whether it is characterized by an incomplete similarity as suggested by Barenblatt et al [2]. The difference between these two cases is important because the first assumption leads to the prediction a logarithmic mean velocity profile, whereas the second results in a scaling law characterized by a power-law profile. Both approaches, as well as some other recent suggestions by different authors, are based on dimensional analysis not linked directly to Navier–Stokes equations. It is becoming clear that further development of the theory is severely hindered by insufficient understanding of the relevant physical processes. This lack of understanding stems from the absence of rigorous results on the turbulence dynamics obtained directly from the Navier–Stokes equations. Indeed, even if valid only for special cases such results could provide a check on the assumptions used in less rigorous (but more general) phenomenological theories. They would identify the physically important quantities to be measured in future experiment, and essential physical mechanisms to be included into future phenomenology. The derivation of such rigorous results about near-wall turbulence directly from the Navier–Stokes equations is the main goal of the present paper. Our analytical theory has three ingredients: rapid distortion theory (RDT), the Reynolds averaged mean-flow equations, and a model for the initial vorticity that provides turbulence forcing. The first ingredient, RDT, has been a popular and powerful tool of description of shear-flow turbulence since the work of Moffatt [3] who extended the RDT approach of Batchelor and Proudman [5] to the shear-flow geometry. We will use a generalised RDT proposed in [4] to describe inhomogeneous turbulence and shear in terms of the Gabor transforms. The second ingredient, the Reynolds averaged equations is the standard way of describing the dynamics of

the mean flow subject to turbulent stresses. Our aim is to write the averaged turbulent stresses which enter into this equation in terms of the quantities used in RDT, and thus to obtain a closed coupled system of equations for the mean flow and turbulence. However, to describe turbulent shear flows one has to add yet another ingredient to ensure existence of a statistically steady state, - the turbulence forcing in the overlap region. This forcing is provided by a initial vorticity that penetrates into the overlap region in the form of the debris of the coherent structures originating in the viscous sublayer. Because the viscous sublayer is very thin compared to the overlap region these coherent structures have a scale which is smaller than the characteristic scale of the mean flow in the overlap region. Also, it is natural to think that the starting vorticity debris are weak far from the viscous sublayer because they get diluted in large volume fluid. Thus, one can assume that the turbulence forcing is weak and small-scale, which allows one to use the RDT approach and the scale separation technique. The view that the near wall turbulence is a linear driven system was originally proposed by Landahl [6] who also argued that the turbulence forcing is produced by vorticity bursts originating in the viscous sublayer and which are intermittent in space and time.

2 Dynamics of turbulence

Let us consider a velocity field in three-dimensional space that consists of a strong large-scale mean component $\boldsymbol{U}$ and a weak small-scale fluctuations $\boldsymbol{u}$

$$velocity = \boldsymbol{U}(\boldsymbol{x},t) + \boldsymbol{u}(\boldsymbol{x},t), \tag{1}$$

$$\boldsymbol{U} = \langle velocity \rangle, \qquad \langle \boldsymbol{u} \rangle = 0, \tag{2}$$

$$L \sim U/|\nabla U| \gg u/|\nabla u| \sim l, \quad U/L \gg u/l. \tag{3}$$

Averaging $\langle\cdot\rangle$ is performed over the statistics of a random force which will be introduced below. Below, we will deal with the shear-flow geometry, so that $\boldsymbol{U} = (U(y,t),0,0)$. Let us define Gabor transform (GT)

$$\hat{\boldsymbol{u}}(\boldsymbol{x},\boldsymbol{k},t) = \int f(\epsilon^*|\boldsymbol{x}-\boldsymbol{x}_0|)e^{i\boldsymbol{k}\cdot(\boldsymbol{x}-\boldsymbol{x}_0)}\boldsymbol{u}(\boldsymbol{x}_0,t)\,\mathrm{d}\boldsymbol{x}_0, \tag{4}$$

where $1 \gg \epsilon^* \gg \epsilon$ and $f(x)$ is a function which decreases rapidly at infinity, e.g. $\exp(-x^2)$. One can think of GT as a local Fourier transform taken in a box centered at $\boldsymbol{x}$ and having a size which is intermediate between L and l.

Let us substitute (1) into the Navier–Stokes equation,

$$\partial_t \boldsymbol{U} + \partial_t \boldsymbol{u} + (\boldsymbol{U}\cdot\nabla)\boldsymbol{u} + (\boldsymbol{u}\cdot\nabla)\boldsymbol{U} + (\boldsymbol{u}\cdot\nabla)\boldsymbol{u} = -\nabla p + \sigma + \nu\nabla^2\boldsymbol{U} + \nu\nabla^2\boldsymbol{u}. \tag{5}$$

Here $\sigma = \sigma(\boldsymbol{x},t)$ describes an external random forcing. In the case of wall turbulence, this term models the vorticity seeding in the outer layers due to the inner-layer vortex structures which break and penetrate into the outer layers and

serve as initial turbulence material. We now apply GT to the above equation with $k \sim 2\pi/l \sim 1 \gg 2\pi/L \sim \epsilon$ and only retain terms up to first power in ϵ and ϵ^* (we chose ϵ^* such that $\epsilon^* \gg \epsilon \gg (\epsilon^*)^2$). All large-scale terms (the first one on the LHS and the third one on the RHS) give no contribution because their Gabor transforms are exponentially small. Further, the nonlinear term $(\boldsymbol{u}\cdot\nabla)\boldsymbol{u}$ may be neglected as it is small compared to $(\boldsymbol{u}\cdot\nabla)\boldsymbol{U}$ because of the assumption (3). As a result we have (see [7] for details)

$$(\partial_t + U\partial_x + \Omega k_x\,\partial_{k_y})\hat{\boldsymbol{u}} - \mathbf{e_x}\Omega\hat{u}_y = -\frac{2\boldsymbol{k}}{k^2}\,\Omega\,\hat{u}_y k_x + \hat{\sigma}_\perp - \nu k^2\hat{\boldsymbol{u}}, \tag{6}$$

where $\Omega = -\partial_y U$ is the mean flow vorticity and $\hat{\sigma}_\perp = \hat{\sigma} - \frac{\boldsymbol{k}}{k^2}(\boldsymbol{k}\cdot\hat{\boldsymbol{\sigma}})$. Equation (6) generalizes RDT to the case of non-uniform turbulence and shear.

3 Dynamics of the mean flow

In order to derive a mean flow equation one has to filter out the small scales from the Navier–Stokes equations (5) by ensemble averaging over the statistics of the random forcing σ. We have

$$\partial_t U = -\partial_y \tau - \partial_x P + \nu\partial^2_{yy} U, \tag{7}$$

where $\tau = \langle u_1 u_2\rangle$ is the turbulent shear stress. This is the standard equation used for description of turbulent shear flows. The y and z components of the mean flow are not generated by turbulent stresses if the forcing σ is statistically symmetric with respect $z \to -z$, as we will see later.

Let us use GT to rewrite the shear stress $\tau = \langle u_1 u_2\rangle$ as follows,

$$\tau = \frac{1}{f^2(0)(2\pi)^6}\int \langle \hat{u_1}(\boldsymbol{x},\boldsymbol{k}',t)\hat{u_2}(\boldsymbol{x},\boldsymbol{k}'',t)\rangle\,\mathrm{d}\boldsymbol{k}'\,\mathrm{d}\boldsymbol{k}'', \tag{8}$$

Here we have to substitute $\hat{u}_i$ found by solving the RDT equation (6). In the limit of small viscosity and assuming statistical mirror symmetry of σ with respect to $x_1 \to -x_1$ we have (see derivation in [7]):

$$\tau = \tau_c + \tau_s, \tag{9}$$

where τ_c is an independent of y part (which does not contribute to the mean flow dynamics) and

$$\tau_s = \frac{\lambda_s}{\Omega}, \tag{10}$$

where λ_s is independent of y it is given by a rather lengthy expression which can be found in [7].

4 Steady mean profile

For stationary mean flow (7) implies

$$\tau + \nu\Omega = -(y - H/2)\,\partial_x P = (1 - 2y/H)\,u_*^2, \tag{11}$$

where we measure y as the distance from one of the walls and we took into account the fact that the total shear stress must be zero in the centre of the channel, at $y = H/2$. Because we restricted ourselves to the case $\Omega > 0$, we have $U < 0$ and $\partial_x P > 0$. Away from the wall, where viscosity is not important, (11) and (10) give

$$\frac{\lambda_s}{\partial_y U} = 2y\,u_*^2/H. \tag{12}$$

Integrating this equation, we have

$$U(y) = \frac{\lambda_s H}{2u_*^2}\log y + const. \tag{13}$$

We see that the Log law of the wall appears as an analytical solution of the dynamical equations in our approach. To obtain this solution we implicitly assumed statistical spatial uniformity of the vorticity seeding σ. Other conditions of the Log law realisability, as well as study of a more general set-up will appear in [7].

References

[1] Th. von Karman, Mechanische Aehnlichkeit und Turbulenz, *Nach.Ges.Wiss.Goettingen Math-Phys. Klasse* (1932) pp 58-76; L. Prandtl, Zur turbulenten Stroemung in Rohren und laengs Platten, *Ergeb. Aerodyn. Versuch.*, Series 4, (1932) Goettingen.

[2] G. I. Barenblatt *J. Fluid Mech* 248 (1993) 513; G. I. Barenblatt and A. J.Chorin, *Proc. Nat. Ac. Sci. USA*, 93 (1996) 6749.

[3] H. K. Moffatt, The interaction of turbulence with a strong wind shear, in: Proceedings of the URSI-IUGG International Colloquim on "Atmospheric turbulence and radio wave propagation" held in Moscow, June 1965 (ed. A.M. Yaglom and V.I. Tatarsky) Nauka Moscow 1967.

[4] S. V. Nazarenko, N.Kevlahan and B.Dubrulle, *J. Fluid Mech*, 390 (1999) 325.

[5] G. K. Batchelor and I. Proudman *Q. J. Mech. Appl. Math.* 7 (1954) 83.

[6] M.T. Landahl, *Physica D* 37 (1989) 11.

[7] S. Nazarenko, N. K.-R. Kevlahan and B. Dubrulle, Nonlinear RDT theory of near wall turbulence, to appear in Physica D, (2000); B. Dubrulle, J.-P. Laval, S. Nazarenko and N. K.-R. Kevlahan, Derivation of equilibrium profiles in plane parallel flows using a dynamic subgrid-scale model. Submitted to Phys Fluids (1999).

ADVANCES IN TURBULENCE VIII
Proceedings of the Eighth European Turbulence Conference
C. Dopazo et al. (Eds.)
© CIMNE, Barcelona 2000

Decaying two-dimensional turbulence in a bounded domain

H.J.H. Clercx and G.J.F. van Heijst

Fluid Dynamics Laboratory, Eindhoven University of Technology,
P.O. Box 513, 5600 MB Eindhoven, THE NETHERLANDS

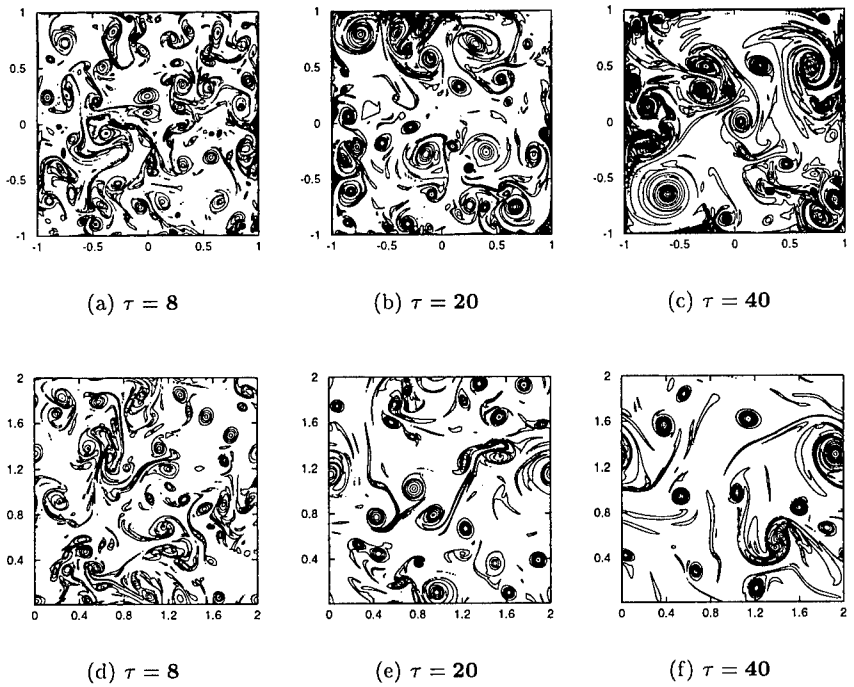
Contact e-mail: H.J.H.Clercx@tue.nl

1 Introduction

During the last decades many theoretical and numerical studies have been carried out to improve the understanding of two-dimensional (2D) turbulence. Thirty years ago the first phenomenological theory of forced 2D turbulence was presented by Kraichnan [1] and by Batchelor [2]. According to this theory, the energy spectrum shows an inverse energy cascade with a $k^{-5/3}$ inertial range for wave numbers smaller than the injection-scale wave number k_i. A direct enstrophy cascade, characterised by a k^{-3} inertial range, is predicted for $k > k_i$. Numerical studies of forced 2D turbulence with periodic boundary conditions more or less support the Kraichnan-Batchelor picture [3, 4], although steeper spectra for large wave numbers are also observed [4]. The energy spectra obtained for numerical simulations of decaying 2D turbulence with periodic boundaries show that the inverse cascade is usually not very clearly observed, and the direct enstrophy cascade is often only established as a transient state before the viscous range starts to dominate the spectrum at large wave numbers. Additionally, the appearance of coherent vortices during the decay process introduces steeper spectra for large wave numbers than predicted by Kraichnan and Batchelor.
The emergence and the temporal evolution of a hierarchy of coherent vortices in decaying 2D turbulence has been the subject of many analytical, numerical and experimental studies. One of the most remarkable theoretical results is the scaling theory put forward by Carnevale *et al.* [5]. They assumed that the total kinetic energy of the flow and the vorticity extremum of the dominant vortices are conserved. It is also supposed that the average number density of vortices, $\rho(t)$, decreases algebraically: $\rho(t) \propto t^{-\zeta}$, with ζ so far undetermined. Dimensional analysis then yields also algebraic power laws for the average enstrophy, $Z(t) \propto t^{-\zeta/2}$, for the average vortex radius, $a(t) \propto t^{\zeta/4}$, and for the average mean vortex separation, $r(t) \propto t^{\zeta/2}$. The power-law exponent is a free parameter which has to be predicted on the basis of numerical simulations.

2 Energy spectra and vortex statistics

In several studies it has been observed that vorticity produced near no-slip walls modifies the decay process of 2D turbulence in a square container considerably [6, 7]. The source of vorticity is found in the thin boundary layers at the no-slip walls, and after boundary layer detachment these filaments are either advected into the interior of the flow domain or they roll up and form new small-scale vortices. Figure 1 shows some snapshots of vorticity contour plots of a numerical simulation of decaying 2D turbulence for Re=20,000 in a container with no-slip boundaries (employing a 2D Chebyshev pseudospectral method), computed for $\tau \cong 8$, 20 and 40, respectively, (Figs. 1a-1c) and for the case with periodic boundary conditions (Figs. 1d-1f, $\tau \cong 8$, 20 and 40, respectively). In the latter case a 2D Fourier pseudospectral method has been used for the simulations. The dimensionless time $\tau = 1$ corresponds approximately with the (initial) eddy turnover time. The initial conditions of both runs are exactly the same. It can be concluded that already at early times in the flow evolution strong vortex-wall interactions can be observed and that huge amounts of small-scale vorticity are produced near the no-slip walls. Apparently, the no-slip walls, at which the flow velocity is forced to be zero, acts as a local forcing agent.
One of the tools to understand the role of the boundaries in the evolution of turbulence is by comparing the energy spectra computed for simulations with no-slip and with periodic boundary conditions. It is obvious that isotropy and homogeneity are absent when no-slip walls confine the flow. As a consequence an alternative approach has to be used to measure the energy spectra. In the present simulations 1D energy spectra are computed for runs with the two kinds of boundary conditions. An interesting observation is the following: the inertial range of the 1D energy spectrum, measured along a line parallel with one of the boundaries not too far from this boundary, shows a $k^{-5/3}$-slope up to the smallest wave numbers used in the simulations (length scales as small as the enstrophy dissipation scale are well resolved). The presence of the $k^{-5/3}$-slope for small wave numbers is due to the production of small-scale vorticity filaments near the no-slip walls. The direct enstrophy cascade is virtually absent at early times during the decay process. To illustrate this remarkable feature we have plotted in Fig. 2a the ensemble-averaged 1D energy spectra for runs with no-slip boundaries for Re=5,000, 10,000 and 20,000. The steepest inertial range spectrum corresponds to the run with Re=5,000 ($n = 2.4$). The inertial range spectrum with $n = 5/3$ corresponds with the Re=20,000 run. Present spectra are measured near the boundaries for $\tau = 4$. At later times the energy spectrum shows the build-up of a direct enstrophy cascade with a k^{-3} inertial range together with the inverse energy cascade for smaller wave numbers. The energy spectrum shows a kink, which slowly moves to smaller wave numbers. The position of the kink, which represents the injection scale k_i, can clearly be associated with the growth of an averaged local boundary-layer thickness. The spectrum as observed in these simulations differs from the well-known Kraichnan-Batchelor



(a) $\tau = 8$ (b) $\tau = 20$ (c) $\tau = 40$

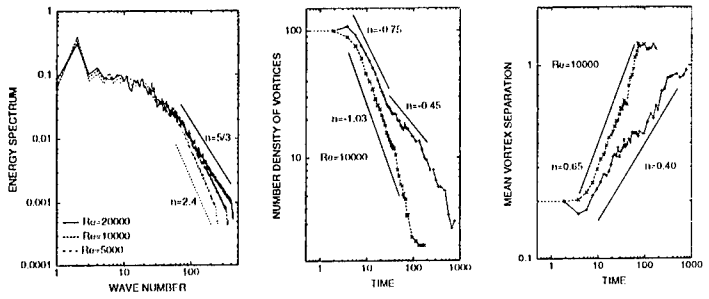
(d) $\tau = 8$ (e) $\tau = 20$ (f) $\tau = 40$

Figure 1: Vorticity contour plots of simulations for Re=20,000 with no-slip (a-c) and with periodic (d-f) boundary conditions.

picture of 2D turbulence mentioned earlier, and differs also with spectra computed from our simulations with periodic boundary conditions.
Actually, the boundaries act as generators of vortices, thus modifying the evolution of vortex statistics. Numerical studies of decaying 2D Navier-Stokes turbulence in containers with no-slip boundaries show a distinctly different evolution of vortex statistics (see Figs. 2b and 2c), at least up to integral-scale Reynolds numbers up to 20,000. It is an open question yet wether the difference in the evolution of vortex statistics for decaying 2D turbulence depends indeed on the type of boundary conditions. An additional complication, which has not been discussed here, might be the role of the initial flow field on vortex statistics.

3 Conclusions

We have shown that decaying 2D turbulence in bounded domains leave us with some intriguing results: small-scale vorticity produced near no-slip boundaries changes the k^{-3} direct enstrophy cascade into a $k^{-5/3}$ inverse energy cascade



(a) (b) (c)

Figure 2: The 1D energy spectra for the no-slip runs (a), the averaged vortex number density (b) and the mean vortex separation (c) for runs with periodic (×) and with no-slip (+) boundary conditions.

during the initial decay stage, and the evolution of vortex statistics is strongly modified for runs with Re=5,000, 10,000 and 20,000.

References

[1] R. H. Kraichnan. Inertial ranges in two-dimensional turbulence. *Phys. Fluids*, 10:1417–1423, 1967.

[2] G. K. Batchelor. Computation of the energy spectrum in homogeneous two-dimensional turbulence. *Phys. Fluids Suppl. II*, 12:233–239, 1969.

[3] U. Frisch and P. L. Sulem. Numerical simulation of the inverse cascade in two-dimensional turbulence. *Phys. Fluids*, 27:1921–1923, 1984.

[4] B. Legras, P. Santangelo, and R. Benzi. High-resolution numerical experiments for forced two-dimensional turbulence. *Europhys. Lett.*, 5:37–42, 1988.

[5] G. F. Carnevale, J. C. McWilliams, Y. Pomeau, J. B. Weiss, and W. R. Young. Evolution of vortex statistics in two-dimensional turbulence. *Phys. Rev. Lett.*, 66:2735–2737, 1991.

[6] H. J. H. Clercx, S. R. Maassen and G. J. F. van Heijst. Spontaneous spin-up during the decay of 2D turbulence in a square container with rigid boundaries. *Phys. Rev. Lett.*, 80:5129–5132, 1998.

[7] H. J. H. Clercx, S. R. Maassen and G. J. F. van Heijst. Decaying two-dimensional turbulence in square containers with no-slip or stress-free boundaries. *Phys. Fluids A*, 11:611–626, 1999.

ADVANCES IN TURBULENCE VIII
Proceedings of the Eighth European Turbulence Conference
C. Dopazo et al. (Eds.)
© CIMNE, Barcelona 2000

Some Open Computational Problems in Wall-Bounded Turbulence

Javier Jiménez

School of Aeronautics, Universidad Politécnica de Madrid
Plaza Cardenal Cisneros 3, 28040 Madrid, Spain
and
Centre for Turbulence Research, Stanford University, Stanford CA 94305.
Contact e-mail: jimenez@torroja.dmt.upm.es

1 Introduction

Wall-bounded turbulence is perhaps the last canonical incompressible turbulent flow that cannot be considered as being even approximately understood. It was given a theoretical framework during the 1940's with the logarithmic-law arguments of Von Kármán and others but, while the structural aspects of free shear flows were effectively clarified during the 1960's and 1970's, the case for wall-bounded flows is much less clear-cut. In recent years even the scaling arguments for the logarithmic profile have been challenged, leading to a resurgence of interest within the physical community. Engineering interest has also been renewed by the possibility of micromechanical manipulation of turbulent boundary layers.

It is not my purpose here to discuss wall flows in general, even if a modern review is missing for them. What I will do is to point to some open problems related to their simulation, both from the point of view of how computation can help physical understanding, and viceversa. The paper takes the form of a collection of proposed 'problems' which I personally believe to be important enough to require attention, together with short comments on their difficulty and on their present status.

2 The logarithmic layer

The arguments leading to the logarithmic velocity profile assume that the only relevant length scale, when the distance y to the wall is large in wall units but small compared with the boundary layer thickness δ, is y itself. A further assumption, based in that the shear stress $\tau/\rho = u_\tau^2$ is constant near the wall, is that the velocity scale is u_τ. The only dimensionally consistent expression for the velocity gradient is then

$$\partial U/\partial y \sim u_\tau/y, \tag{1}$$

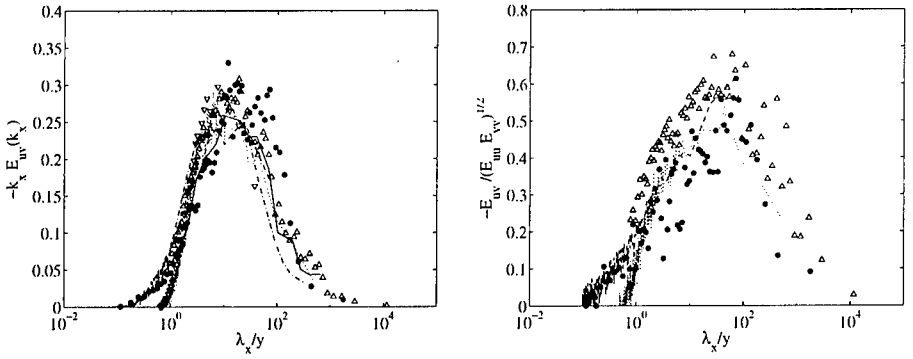


Figure 1: (Left) Pre-multiplied Reynolds stress streamwise cospectra. (Right) Spectral correlation coefficient for the u and v components. $\triangledown$, numerical channel at $Re_\tau = 590$, [18]. $y^+ = 99$. ——— , $y^+ = 100$; —·— , $y^+ = 250$. Pipe at $u_\tau R/\nu = 2100$, [15]. ····· , $y^+ = 110$; - - - - , $y^+ = 1150$. Laboratory boundary layer at $u_\tau \delta/\nu = 7050$, private communication by J. Carlier and M. Stanislas. Other symbols are from the atmospheric boundary layer [6], with $U \approx 10$ m/s at 10 m, and roughness height, $u_\tau h/\nu \approx 400$. $\delta/h \approx 5 \times 10^4$: $\triangle$, $y/h = 100$; $\bullet$, $y/h = 1000$. All spectra are approximately in the logarithmic layer, normalized by the distance to the wall and scaled to unit area.

which leads directly to a logarithm. There are several problems with this argument, even if the experimental support for the logarithmic profile is excellent [24, 19]. The main one is the possible influence of motions parallel to the wall, which are not necessarily limited in size to $O(y)$.

Very large longitudinal velocity structures, of the order of many boundary layer thicknesses, have been documented within the logarithmic layer of wall bounded flows [8, 13], roughly between $y^+ > 100$ and $y/\delta < 0.2$. It has been suggested that they scale with the boundary layer thickness [5], or at least that their streamwise lengths increase nonlinearly with y [8, 13]. This would imply that some length beyond y is involved, destroying the dimensional basis for the logarithmic profile.

Although the scaling of these u-structures is still unclear, figure 1 presents a compilation of Reynolds-stress longitudinal cospectra in the logarithmic layer, for a range of Reynolds numbers going from direct numerical simulations in the low end, to the atmospheric boundary layer. The flows represented in the figure include channels, pipes and boundary layers, both over smooth and over rough surfaces. Even if the experimental scatter is large, the fact that the stress-containing peaks of such diverse cospectra collapse reasonably well when scaled with the wall distance, strongly suggests that at least the shear stresses are consistent with the classical dimensional argument. The same is true of the wall-normal fluctuations.

It is interesting, however, that the peak of the cospectrum is at a large multiple of y, and that even wavelengths of the order of $100\,y$ appear to be necessary to capture most of the turbulent shear stress. The right-hand-side of figure 1 displays the correlation coefficient $E_{uv}/(E_{uu}E_{vv})^{1/2}$, which represents the 'efficiency' of the turbulent fluctuations in generating Reynolds stresses. It vanishes near $\lambda_x \approx y$, in agreement with the idea that eddies of that size are approximately isotropic and do not generate stresses, and increases monotonically towards a maximum near $100y$ (20δ near the edge of the logarithmic layer). These lengths are of the same order as the longest observed longitudinal velocity structures.

There are fewer data on the spanwise extent of these large-scale fluctuations, but those available from numerical simulations at moderate Reynolds numbers also suggest a linear scaling with y. The overall picture is of very large stress-producing structures whose maximum intensities are at sizes $\lambda_x \times \lambda_z \approx 10y \times 3y$, but which contain appreciable stresses up to $100y \times 10y$. At the edge of the logarithmic layer they are of the order of 20×2 times the boundary layer thickness. None of the available direct numerical simulations of wall-bounded flows, and few experiments, have been designed with those large numbers in mind.

It was noted in [8] that the dominant deformation mechanism for such large structures is the mean shear, because its associated time scale, $(\partial U/\partial y)^{-1} \approx y/u_\tau$, is shorter than the eddy turnover time λ/u_τ. In this sense they can be described by linearized perturbation equations,

$$\left[\partial_t + U(y)\partial_x - Re^{-1}\nabla^2\right] \nabla^2 v - \partial_{yy}U\,\partial_x v = 0, \tag{2}$$

$$\left[\partial_t + U(y)\partial_x - Re^{-1}\nabla^2\right] \omega_y + \partial_y U\,\partial_z v = 0. \tag{3}$$

The first of these is Orr-Sommerfeld's stability equation for the parallel flow $U(y)$, while the second one describes Squire's wall-normal modes. While the former defines an eigenvalue problem, the latter is enslaved to it. For the velocity profiles of most parallel wall-bounded flows, equation (2) has no unstable eigenvalues, but it has neutral solutions associated with translational invariances, and weakly damped ones. In particular, any strictly streamwise vortex only decays in times of $O(Re/\partial_y U)$, and forces onto equation (3) streamwise 'streaks' whose intensity grows approximately linearly over shorter periods.

The initial value problem for (2)–(3) is rapid distortion theory and, in the case of a uniform shear, also tends asymptotically to an array of alternating streamwise streaks [17].

The large scales discussed here are fascinating structures which, from figure 1, are responsible for most of the shear stress (and energy) throughout the logarithmic layer. They are crucial for the physical and technological understanding of wall-bounded flows. They suggest two problems:

Problem 1 *Clarify the relationship, in any, between the very large scales of the logarithmic layer, and the solutions of the initial value problem (2)–(3), or its quasi-neutral eigenfunctions.*

Problem 2 *Simulate any wall flow at Reynolds numbers high enough for a logarithmic layer to exist ($Re_\tau > 1,000$), in a big-enough box for the largest structures to be adequately represented ($L_x \times L_x \geq 30\delta \times 5\delta$). Note that a large eddy simulation may be able to clarify the logarithmic-layer processes, which are probably not connected with the dissipative scales.*

For a well-resolved spectral direct simulation of a plane channel, with $\Delta x^+ = 10$ and $\Delta y^+_{max} = \Delta z^+ = 6$, the minimum grid required for such a computation is $3000 \times 513 \times 800$ spectral modes. This is beyond the capacity of most present computers, although it should be possible within a few years, but the LES would be within present capabilities if a reliable wall boundary-condition could be found for the equations.

3 The near-wall region

The region closer to the wall than about 100 wall units was one of the first to be studied using numerical simulations. The local Reynolds numbers are low and the resolution requirements are less strict than for the logarithmic layer. There is strong evidence that, at least for smooth walls, this region is the seat of a regeneration cycle involving long streamwise high- and low-velocity 'streaks', and shorter quasi-streamwise vortices. It was shown in [9] that this cycle can function in a 'minimal' unit, which is a doubly periodic 'crystal' in which each identical element, $L_x^+ \times L_z^+ \approx 500 \times 100$, contains a pair of counterotating vortices, and a segment of an infinitely long streak. It was later shown in [11] that the cycle is 'autonomous', in the sense that the flow above $y+ \approx 70$ can be removed without seriously disturbing it. Attempts to maintain a working cycle in a minimal *and* autonomous unit, which would neither interact with its neighbours nor with the core flow, have failed up to now, and it is still unknown which are the minimum ingredients necessary for the self-generation of wall turbulence.

There have been many proposals for dynamical models of the cycle itself. It is fairly clear that the vortices generate the streaks by advecting the mean profile, and that the streaks are involved in the regeneration of the vortices [11], but the details of the latter are unclear. The linear instabilities of the streaks have, for example, been considered in [7, 12], but there are questions about whether the unstable eigenvalues are fast enough for the observed effects. A more complete low-dimensional model, mimicking the whole regeneration process, was discussed in [23], but it is difficult to prove that it really represents the cycle observed in fully turbulent flows. Perhaps the most suggestive recent development is [22], which identifies, in a minimal channel unit, a low-dimensional dynamical structure resembling a Silnikov-type saddle in phase space. Its stable manifold connects to the linear instability of a streak, but the saddle is nonlinear, and its faster unstable manifold merges into full turbulence. The saddle itself corresponds, in configuration space, to a bent streak similar to those educed in [9, 7] as precursors to near-wall bursts.

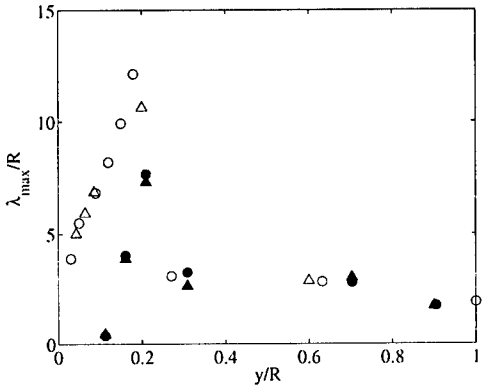


Figure 2: Locations of the maxima in the longitudinal premultiplied spectra, $k_x E_{uu}(k_x)$ [1]. ∘ , $U_{max}R/\nu = 2.6 \times 10^5$; △ , 1.2×10^5. Open symbols, smooth pipes; closed, rough pipes whose equivalent sand roughness height is $h/R = 0.008$. The jump at $y/R \approx 0.2$ switches between two local maxima.

Problem 3 *The full characterization of the near-wall turbulence cycle should by now be reasonably straightforward. The elements involved are known, and it should be possible to construct truly minimal self-sustaining wall units that can be studied as relatively low-dimensional systems, but which can also be unequivocally related to real turbulence. A strong candidate could be a set of a few, perhaps two or three, autonomous minimal units.*

Even if this is achieved, the question of the relationship between this near-wall cycle and the logarithmic and outer layers would still be open. One important question is connected with rough walls. It is generally believed that the logarithmic layer over rough walls does not differ much from those over smooth ones, even if fully developed roughness requires that the dimensionless roughness height be $h^+ > 50$–100. This would probably destroy the cycle discussed in the previous paragraphs. The experimental evidence, which *does* show some differences (figure 2), is generally at Reynolds numbers which are too low to distinguish between the true effects of roughness and those of measuring at wall distances which are moderate multiples of the physical dimensions of the roughness elements. The approximate collapse of the cospectra in figure 1, and similar results in other atmospheric boundary layers, suggest that logarithmic layers far enough from the wall become independent of the wall boundary condition.

Problem 4 *Any simulation of a rough wall, specially one containing a logarithmic region, would give insight both on the interaction of the wall with the outer flow, and on the dynamical processes of the logarithmic region. A preliminary step might be a simulation without a smooth-wall cycle, even one not corresponding to any physically realistic roughness.*

The simulation of a rough wall is even more demanding than that proposed in problem 2. Figure 2 suggests that the logarithmic layer should be at least twenty times thicker than the roughness height, which in turn should be $h^+ > 50$. This implies $Re_\tau > 5,000$ for the half channel. On the other hand a LES might be enough to understand the interaction of the logarithmic and wall layers, subject, as in the smooth case, to the identification of a reliable wall boundary condition.

4 Large-eddy simulations

We have referred twice to the problem of finding proper boundary conditions for wall-bounded large-eddy simulations of attached wall flows. It was shown in [2, 10] that LESs using present sub-grid models approximate well the mean velocity profiles only if the filter is chosen so that the fraction of the shear stresses carried by the model is negligible. Mixed models, which include a scale-similarity part, appear to work better [21], but it is unlikely that any model can be found that predicts correctly the full subgrid stresses, especially in anisotropic and inhomogeneous situations such as near walls. Some fixed fraction of the shear stress will always have to be carried by the resolved scales, and it follows from figure 1 that, for attached flows, this requires that $\Delta x \sim y$ up to the edge of the near-wall layer. The number of grid elements, even for an optimally unstructured grid using elements of volume y^3 at height y, is therefore of order

$$N \sim \int_{1/Re_\tau} y^{-3}\,\mathrm{d}y = O(Re_\tau^2). \tag{4}$$

This is an absolute lower bound if something like the integral scale is to be retained at each point (i.e. in a *Large-Eddy* simulation), and it is only slightly less stringent than the requirement for direct simulations, $N = O(Re_\tau^{9/4})$.

The trouble is with the lower limit in the integral in (4), which is Reynolds number dependent, and it can only be remedied if the grid refinement can be restricted to distances away from the wall which are fixed fractions of the outer flow scale (e.g. the pipe radius). In attached flows this means that the last grid point would be in the logarithmic layer.

Problem 5 *Find a boundary condition for the LES of attached wall flows which allows the last grid point to be located at an arbitrary location within the logarithmic layer (except perhaps for a grid point at the wall).*

This question has been the subject of extensive research in recent years, since it limits the Reynolds numbers at which LES of wall-bounded flows can be used in practice. A recent informal summary is [3]. What is required is an estimate for the wall stress, as a function of the filtered velocities, which can be implemented either by using a special sub-grid model near the wall, or by modifying the velocity boundary condition in such a way that the model used for the interior points also gives the right wall stresses. The problem is worst

in attached flows, and may actually not be relevant otherwise. Consider the momentum balance in a control volume one of whose boundaries is the wall. Assume that the volume is roughly cubical, of size $O(\ell)$, and that the filtered velocity fluctuations are $O(u'^2)$. The rate of change of momentum is the sum of the advective fluxes, which are $O(u'^2\ell^2)$, of the pressure gradients, which are at least of the same order, and of the subgrid and viscous stresses, which at the wall are $u_\tau^2\ell^2$. The latter, which are the subject of the boundary condition, are only important if $u' \leq O(u_\tau)$. This happens in attached equilibrium flows, where $u' \approx u_\tau$, and may also be true in reattaching or far from equilibrium flows, where thin and energetic boundary layers create large surface stresses that may need special treatment. It is not true in flows close to separation, where $u_\tau \ll u'$, and where even large surface stress errors may be acceptable.

In equilibrium attached flows there are also reasons to believe that the problem is tractable. The discussion of roughness in the previous section suggests that even such drastic changes in the wall boundary conditions as the change from smooth to fully rough surfaces have small effects in the flow far enough from the wall. This is especially true when the Reynolds number is high, which is the natural application of LES, but it does not mean that the boundary condition can be arbitrary. It is for example clear that, in the derivation from equation (1) of the logarithmic law

$$u^+ = \kappa^{-1} \log y^+ + A, \tag{5}$$

the logarithm itself, and probably the Kármán constant κ depend only on universal properties of turbulence, but that the additive constant A is determined by a near-wall layer where (1) no longer applies. This suggest that, if we use the wrong wall boundary condition for the LES equations, most of the flow, except for the first few grid points close to the wall, and for the additive constant in the mean velocity profile, might be correct. It might then be possible to fix the latter by the *a-posteriori* application of a suitable RANS model.

Unfortunately the issue is clouded by numerical effects. In the first place, except for very high order numerical schemes, the first few points near the wall are wrong in any case, because the effective resolution of the numerical methods is never better than a few grid points. Numerical errors get confused with modelling inadequacies. Consider the pipes and channels summarized in figure 3. The velocity profiles away from the wall can be characterized by the magnitude of their wake parameter Π, where the profile is written in the form [4]

$$u^+ - u^+_{max} \approx \kappa^{-1}[\log(y/\delta) + G(y/\delta)], \tag{6}$$

with $G(x) \equiv (1 + 6\Pi)x^2 - (1 + 4\Pi)x^3 - 2\Pi$. The open symbols in figure 3 are results either from experiments or from direct simulations. The wake parameters of pipes decrease from relatively high values at low Reynolds numbers to an asymptote above $Re_\tau \approx 10^4$. Those of channels increase from near zero at low Reynolds numbers to converge with those of the pipes at about the same Re_τ.

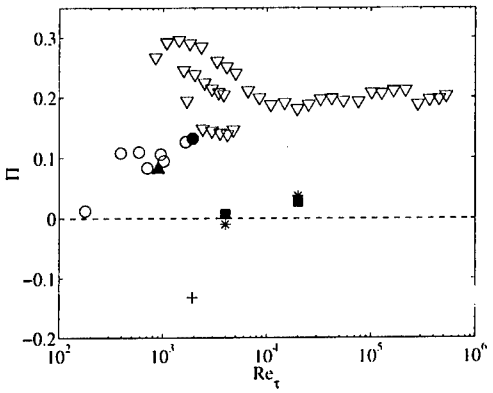


Figure 3: Wake component of mean velocity profiles. ∘ , smooth channels; ▽ , smooth and rough pipes. Solid symbols are LES of channels. ■ , 'dynamic' boundary condition, finite differences [3]; ∗, same, but with modified boundary viscosity. ▲ , resolved boundary, B-splines [14]; +, resolved boundary, finite differences filtered at $2\Delta x$ [16]. • , same, filtered at $3\Delta x$. This figure is adapted from [3].

The solid triangle, which agrees with experiments, is a LES using a high-order numerical method and a multiblock grid which resolves the near-wall layer. The two solid squares use second-order finite differences, and a fairly sophisticated wall boundary condition; they have incorrect wake parameters consistent with a lower Reynolds number. That the problem is not with the boundary conditions is suggested by the asterisks, which use the same code but a fairly different boundary condition, and still have the same incorrect profiles. An interesting experiment is represented by the solid circle and the cross [16]. These authors argue that the dynamic sub-grid model, which is the one used in all the simulations in this figure, is based on information from the last octave of the velocity spectrum, and should not be used with low-order finite-different methods. Second-order schemes, for example, have large dispersion errors in the last two thirds of their spectra, resulting in small scales which are presumably unphysical. What the authors did in [16] was to use a second-order finite difference scheme, but to filter it explicitly to discard the contaminated wavenumbers. In the simulation represent with the cross, the last half of the spectrum was discarded, which was insufficient, while for the (correct) solid circle the full contaminated two-thirds were filtered out.

This work was supported in part by the Spanish CICYT contract PB95-0159. by AFOSR grant AF F49620-97-1-0210, and by ONR grant N0014-00-1-0146. Special thanks are due to J. Carlier, R.P. Hoxey, R.D. Moser, A.E. Perry and M. Stanislas for providing their unpublished or hard-to-get data.

References

[1] C.J. Abell and A.E. Perry. Smooth and rough wall pipe flow longitudinal turbulence spectral data, *Rep. FM6.* Dept. Mech. Engng., Univ. Melbourne, 1974.

[2] J.S. Baggett, J. Jiménez and A.G. Kravchenko. Resolution requirements in large-eddy simulations of shear flows, *CTR Ann. Res. Briefs*, Stanford Univ. 51–66, 1997.

[3] W. Cabot, J. Jiménez and J.S. Baggett. On wakes and near-wall behaviour in LES with wall models and second-order finite differences, *CTR Ann. Res. Briefs*, Stanford Univ. 1999.

[4] R.B. Dean. A single formula for the complete velocity profile in a turbulent boundary layer, *ASME J. Fluids Engng.*, 98:723-727, 1976.

[5] M.H. Hites. Scaling of high-Reynolds number turbulent boundary layers in the national diagnostic facility, Ph. D. thesis, Illinois Inst. of Technology, 1997.

[6] R.P. Hoxey and P.J. Richards. Spectral characteristics of the atmospheric boundary layer near the ground, *First UK Wind Engng. Conf.* Cambridge, September 1992.

[7] J. Jeong, F. Hussain, W. Schoppa and J.Kim. Coherent structures near the wall in a turbulent channel flow, *J. Fluid Mech.* 332:185–214, 1997.

[8] J. Jiménez. The largest scales of turbulent wall flows. *CTR Ann. Res. Briefs*, Stanford Univ. 137–154, 1998

[9] J. Jiménez and P. Moin. The minimal flow unit in near-wall turbulence. *J. Fluid Mech.*, 225:213–240, 1991.

[10] J. Jiménez and R.D. Moser. LES: where are we and what can we expect?, *AIAA Paper 98-2891*, 1998 (To appear, *AIAA J.*)

[11] J. Jiménez and A. Pinelli. The autonomous cycle of near-wall turbulence, *J. Fluid Mech.*, 389:335–359, 1999.

[12] G. Kawahara, J. Jiménez, M. Uhlmann and A. Pinelli. The instability of streaks in near-wall turbulence, *CTR Ann. Res. Briefs*, Stanford U., 155–170, 1998.

[13] K.C. Kim and R.J. Adrian. Very large-scale motion in the outer layer, *Phys. Fluids*, 11:417–422, 1999.

[14] A.G. Kravchenko, P. Moin and R.D. Moser. Zonal embedded grids for numerical simulations of wall-bounded turbulent flows. *J. Comput. Phys.* 127:412–423, 1996.

[15] C.J. Lawn. The determination of the rate of dissipation in turbulent pipe flow. *J. Fluid Mech.*, 48:477-505, 1971.

[16] T.S. Lund and H.J. Kaltenbach. Experiments with explicit filtering for LES using a finite-difference method, *CTR Ann. Res. Briefs*, Stanford Univ. 91–106, 1995.

[17] M.R. Maxey. Distortion of turbulence in flows with parallel streamlines. *J. Fluid Mech.*, 124:261-281, 1982.

[18] R.D. Moser, J. Kim, and N.N. Mansour. Direct numerical simulation of turbulent channel flow up to $Re_\tau = 590$. *Phys. Fluids*, 11: 943–945, 1999.

[19] J.M. Österlund, A.V. Johansson, H.M. Nagib and M.H. Hites. A note on the overlap region in turbulent boundary layers, *Phys. Fluids*, 12:1–4, 2000.

[20] A.E. Perry, S. Henbest and M.S. Chong. A theoretical and experimental study of wall turbulence. *J. Fluid Mech.*, 165:163–199, 1986.

[21] F. Sarghini, U. Piomelli and E. Balaras. Sacle-similarity models for large-eddy simulations, *Phys. Fluids*, 11:1596–1607, 1999.

[22] S. Toh and T. Itano. Low-dimensional dynamics embedded in a plane Poiseuille flow turbulence, *IUTAM Symp. on Geometry and statistics in turbulence*, Hayama, Japan, (physics/9905012) October 1999.

[23] F. Waleffe. On a self-sustaining process in shear flow, *Phys. Fluids* 9:883–900, 1997.

[24] M.V. Zagarola and A.J. Smits. Scaling of the mean velocity profile for turbulent pipe flow, *Phys. Rev. Lett.*, 78:239–242, 1997.

ADVANCES IN TURBULENCE VIII
Proceedings of the Eighth European Turbulence Conference
C. Dopazo et al. (Eds.)
© CIMNE, Barcelona 2000

Low-Pressure Vortex: The Role in Turbulence Dynamics

S. Kida

Theory and Computer Simulation Center, National Institute for Fusion Science,
Toki, 509-5292, JAPAN

Contact e-mail: kida@toki.theory.nifs.ac.jp

1 Introduction

It has been recognized that tubular fine-scale swirling vortices exist commonly in all kinds of turbulent flows and that they play important roles in turbulence dynamics such as the enhancement of diffusion and mixing. The characterization and definition of such vortices, however, are not unique but there have been proposed a lot of identification methods (see [1, 2, 3, 4] and references therein). Although different in detail, the objects identified by different methods share some common features. They are localized in elongated tubular regions of high vorticity, the length of which is of order of the integral scale and the diameter of the cross-section is several times the Kolmogorov length. The Reynolds number dependence of the intensity of vorticity and circulation associated with vortices were also examined in some detail [1].

In this paper we discuss further the physical properties of tubular vortices and their dynamical roles in terms of the low-pressure vortex which we have recently introduced [3, 5, 6]. The concept of low-pressure vortex is recapitulated in §2. Their physical structures are anatomized for a forced isotropic turbulence in §3. The role of vortices in turbulent diffusion process is discussed in §4.

2 Low-Pressure Vortex

In view of the importance of tubular swirling vortices in turbulence it is highly desirable to find the way to capture the real image of them. They accompany with (i) high vorticity, (ii) low pressure, and (iii) swirling motions around them. The first of these characteristics has been frequently stressed by many authors to visualize tubular vortices with the iso-surface representation of high vorticity in various kinds of turbulence. Not to mention that the isosurface representation often gives completely different pictures of the structure depending upon the level of threshold, the 'structure' of high-vorticity magnitude is not necessarily

parallel to the vorticity vector therein. This deviation problem is not so apparent for a strong vortex in isotropic turbulence of vanishing mean vorticity, but may become serious in strongly sheared turbulence. In the latter, the vorticity tends to orient to the mean shear vorticity irrespective of the direction of vortices. Recall that the vorticity does not necessarily represent a swirling motion though it certainly represents rotation of a fluid element.

The second and third of the above features are taken by Miura and Kida [3]. They introduced the low-pressure vortex, the axis of which is defined by the sectional minimum lines of pressure with a swirl condition. See Refs. [5, 6] for its application to isotropic and uniformly sheared turbulence, which includes the skeleton representation of turbulent flows, the comparison with other visualization methods, an automatic chasing scheme of a particular vortex, the physical and dynamical properties of the vortex itself. In the following new analyses related with the low-pressure vortex are presented.

Since the axis of a low-pressure vortex is defined by the sectional minimum lines of pressure, it may be natural to define the core as the region in which pressure is concave in radial directions, i.e. $\partial^2 p/\partial r^2 > 0$. [1] A Burgers vortex tube, which is realized in an axi-symmetric stagnation flow ($u_r = -\frac{1}{2}\alpha r$, $u_\theta = 0$, $u_z = \alpha z$, where α is a positive constant), has only the z component of vorticity,

$$\omega_z = \frac{\alpha\Gamma}{4\pi\nu}\exp\left[-\frac{\alpha r^2}{4\nu}\right], \tag{1}$$

and the second derivative of pressure with respect to r is given by

$$\frac{1}{\rho}\frac{\partial^2 p}{\partial r^2} = -\frac{1}{4}\alpha^2 + \left(\frac{\Gamma}{2\pi}\right)^2 \frac{3}{r^4}\left\{\left(1+\frac{\alpha r^2}{3\nu}\right)\exp\left[-\frac{\alpha r^2}{4\nu}\right] - 1\right\}\left(1-\exp\left[-\frac{\alpha r^2}{4\nu}\right]\right). \tag{2}$$

In order that the pressure may take a minimum on the vortex axis, eq. (2) must be positive at $r = 0$, that is, the vortex Reynolds number $\Gamma/\nu > 4\pi$. This means that a Burgers vortex of $\Gamma/\nu \leq 4\pi$ is not be able to be captured as a low-pressure vortex. The boundary surface of the vortex core is given by r_c on which $\partial^2 p/\partial r^2 = 0$. It is a function of Γ/ν and shown in Figure 1. In the limit of large Reynolds number $\Gamma/\nu \to \infty$, we find $r_c \to 1.48\sqrt{\nu/\alpha}$ ($= r_{c\infty}$, say), which corresponds to that of the Oseen decaying vortex. The azimuthal velocity u_θ takes a maximum at $r_* \approx 2.24\sqrt{\nu/\alpha}$ which is 1.51 times of $r_{c\infty}$. Incidentally, the $e^{1/2}$-fold radius of vorticity is $r_B = \sqrt{2\nu/\alpha} \approx 0.96 r_{c\infty}$.

[1] This definition of core size is different from [5], where a swirl condition is used for simplicity.

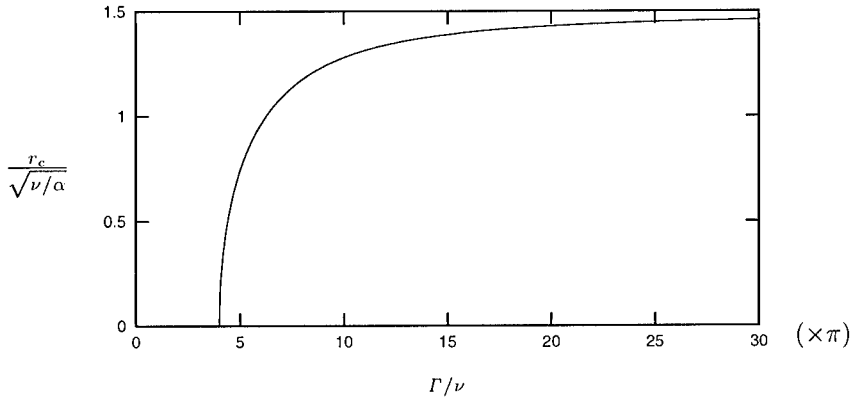


Figure 1: Dependence of the radius r_c of a Burgers vortex on the vortex Reynolds number Γ/ν.

3 Structure of low-pressure vortex

Here, we examine the physical properties of low-pressure vortices in a forced numerical turbulence of an incompressible viscous fluid. It is simulated by the spectral method in a periodic box with period 2π in three orthogonal directions. The flow is forced by keeping the magnitude of the Fourier coefficients at small wavenumbers ($|\mathbf{k}| \leq \sqrt{8}$) constant in time but by allowing their phases to change. The resolution of the simulation is $N^3 = 256^3$. Starting with an arbitrary initial condition, the simulation is performed over several ten characteristic times ($= \mathcal{E}/\epsilon$, where $\mathcal{E}$ and ϵ are respectively the turbulence energy and its dissipation rate per unit mass) so that the velocity field is in a statistically stationary state of fully developed turbulence with the Reynolds number $Re_\lambda = 57$, the Taylor micro-scale length $\lambda = 1.9\Delta x$, and the Kolmogorov length $l_K = 1.3\Delta x$, where Δx is the grid width. In Figure 2 we show a snapshot of low-pressure vortices in a one-eighth of the simulation box. There are 413 vortices in this domain. The axes are represented by black lines. The cores of five longest vortices are drawn by gray surfaces. The diameter of the core cross-section distributes around $10\Delta x$. The length of the longest vortex is about $140\Delta x$.

Inside of each vortex core the vorticity is more or less parallel to the axis. A strong vortex tube, on the other hand, may generate vortex layers of high cross-axial component of vorticity around it by stretching, tilting and wrapping of surrounding background vorticity [7]. In Figure 3 we plot the axial and cross-axial components of vorticity in a cross-section of a low-pressure vortex which is the longest one drawn in figure 3. The axial component of vorticity is dominant around the vortex core, whereas the cross-axial component takes large values in an annular region surrounding the core. Low intensity of the cross-axial component at the center is due to the viscous canceling of it enhanced by the

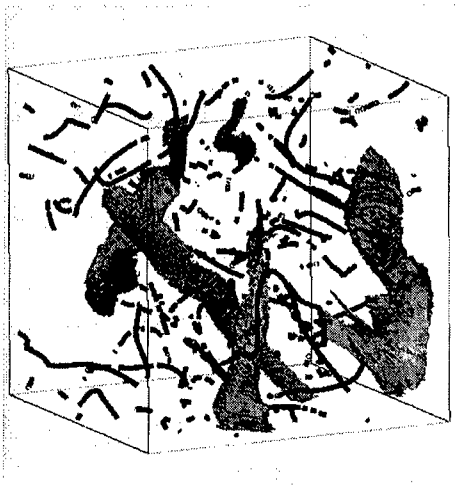


Figure 2: Low-pressure vortices in a forced turbulence. All the vortex axes and five selected cores are shown respectively by black lines and gray surfaces in a one-eighth of the simulation box. The side-length of the cube spans over $170l_K$. $Re_\lambda = 57$

strong swirling shear, which is the phenomenon known as the expulsion of normal vorticity [7]. The volume in which the cross-axial component of vorticity takes significant values is wider than that of the axial component. It is anticipated that this trend is augmented more and more at larger values of Reynolds number and that the cross-axial component may eventually give a dominant contribution in energy dissipation in the large Reynolds number limit [8].

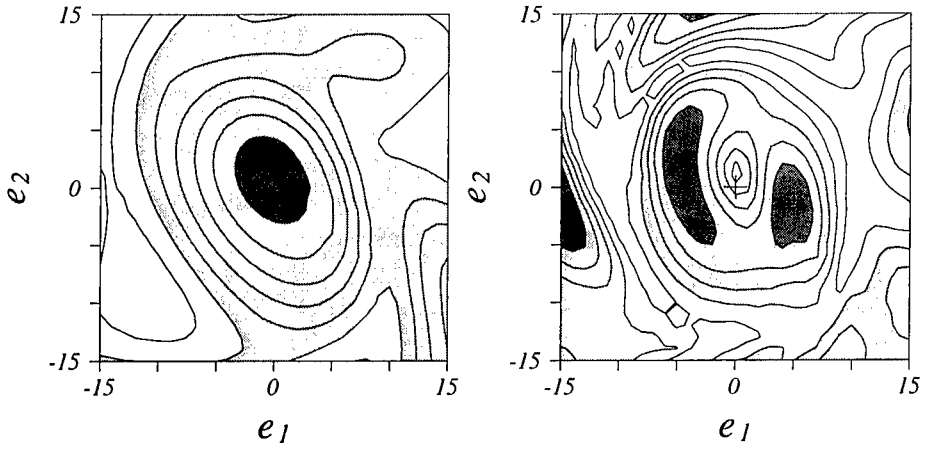


Figure 3: Structure of a low-pressure vortex. (left panel) Contours of axial component of vorticity in a cross-section of the longest vortex in Figure 2. The threshold is greater than 10 in the dark shade, and negative in white. (right panel) Same as the left panel for cross-axial component of vorticity. The threshold is greater than 2.5 in the dark shade, and less than 1 in white. Note that a hole of small values.

4 Relative diffusion and low-pressure vortices

Relative diffusion of a pair of particles is fundamental in the diffusion problem. It is expected by a purely statistical argument that the mean distance $\sqrt{\langle r^2 \rangle}$ between two particles increases in time exponentially as $\log\sqrt{\langle r^2 \rangle} \propto \sqrt{\epsilon/\nu}\, t$ if $\sqrt{\langle r^2 \rangle}$ is in the dissipation scale, algebraically as $\sqrt{\langle r^2 \rangle} \propto \epsilon^{1/2} t^{3/2}$ if $\sqrt{\langle r^2 \rangle}$ is in the inertial scale, and increases as $\sqrt{\langle r^2 \rangle} \propto (\mathcal{E}/\epsilon^{1/2})\, t^{1/2}$ if $\sqrt{\langle r^2 \rangle}$ is greater than the integral scale.

In order to investigate the role of tubular swirling vortices in the relative diffusion we performe a direct numerical simulation of passive particles in a forced turbulence described in the preceding section but with less resolution $N^3 = 128^3$. A fully developed turbulence is used for the initial condition of this study. Trajectories of 128^3 particles are integrated numerically starting at all the grid points. The probability density function (PDF) of the distance of pairs of particles which were located at grid points nearest to each other at the initial instant is calculated. The initial delta function of the PDF spreads in time. It is nearly Gaussian both at the early stage of evolution in which the mean distance is of order of the Kolmogorov length and at the late stage in which it is beyond the integral scale. Between these two stages the PDF is skewed from a Gaussian and has a longer tail on the small distance side. The temporal evolution of the mean distance is drawn in Figure 4. The time and length are normalized by $\mathcal{E}/\epsilon = 4.4$ and $l_K = 0.03$. The behavior mentioned above is actually realized.

Tubular vortices induce swirling shear motions around them, which should affect the diffusion properties. Particles near a vortex may stay sometime rotating around it. Therefore relative movement of tubular vortices themselves may give substantial influences to the diffusion process. One of the influences of the tubular vortices at earlier stages of evolution is demonstrated in Figure 5. Here, the positions of pairs of particles whose distance is less than the mean by three

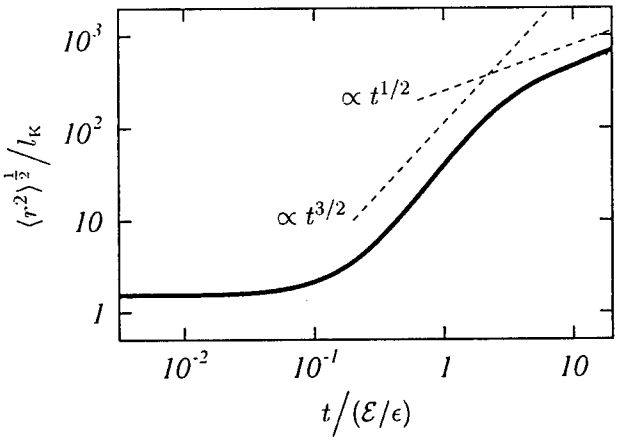


Figure 4:Temporal evolution of the mean distance between pairs of particles. $\langle\ \rangle$ denotes the average over all particles. The initial separation distance of all the pairs is $1.5 l_K$. $Re_\lambda = 55$.

times the standard deviation are plotted. The vortices play important roles in diffusion by trapping pairs of particles and advect them together.

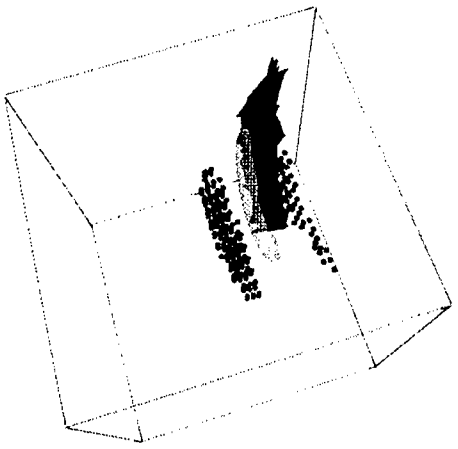


Figure 5: Trapped pairs of particles. The core of a low-pressure vortex, the iso-surface of the Laplacian of pressure, and the positions of pairs of close particles are shown by black and light-gray surfaces and dark-gray points, respectively. The side-length of the cubic box is 30 meshes.

The author would like to express his hearty gratitude to Dr. S. Goto for his cooperation in the simulation study presented in §4.

References

[1] J. Jiménez, A.A. Wray, P.G. Saffman and R.S. Rogallo. The structure of intense vorticity in isotropic turbulence. *J. Fluid Mech.*, 255:65-90, 1993.

[2] J. Jeong and F. Hussain. On the identification of vortex. *J. Fluid Mech.*, 285:69-94, 1995.

[3] H. Miura and S. Kida. Identification of tubular vortices in turbulence. *J. Phys. Soc. Japan*, 66:1331-1334, 1997.

[4] M. Tanahashi, T. Miyauchi and J. Ikeda. Scaling law of coherent fine structure in homogeneous isotropic turbulence. *Proc. 11th Symp. on Turbulent Shear Flows*, 1:4-17 - 4-22, 1997.

[5] S. Kida and H. Miura. Identification and analysis of vortical structures. *Eur. J. Mech. B/Fluids*, 17:471-488, 1998.

[6] T. Adachi, H. Miura and S. Kida. Automatic Chase of Low-Pressure Vortex Axes. *J. Plasma and Fusion Res. Ser. Vol. 2. Proc. 9th Int. Toki Conf.* 339-342, 1999.

[7] G. Kawahara, S. Kida, M. Tanaka and S. Yanase. Wrap, tilt and stretch of vorticity lines around a strong thin straight vortex tube in a simple shear flow. *J. Fluid Mech.*, 353:115-162, 1997.

[8] G. Kawahara, S. Kida, S. Yanase. and M. Tanaka. Energy dissipation in spiral vortex layers. in *this Volume,* 2000.

XXI

Direct Numerical Simulation Large Eddy Simulation

ADVANCES IN TURBULENCE VIII
Proceedings of the Eighth European Turbulence Conference
C. Dopazo et al. (Eds.)
© CIMNE, Barcelona 2000

Appearance and Alignment with Strain Rate of Coherent Fine Scale Eddies in Turbulent Mixing Layer

M. Tanahashi[1], S. Iwase[1] and T. Miyauchi[1]

[1]Department of Mechano-Aerospace Engineering, Tokyo Institute of Technology, 2-12-1 Ookayama, Meguro-ku, Tokyo 152-8552, Japan

Contact e-mail: mtanahas@mes.titech.ac.jp

1 Introduction

With the transition to turbulence, many fine scale eddies appear in turbulent mixing layer[1]. Our previous studies[2] show that these fine scale eddies show tube-like features and their properties such as diameter and azimuthal velocity well coincide with those of the fine scale eddies in homogeneous isotropic turbulence[3][4][5]. The most expected diameter and maximum azimuthal velocity of the fine scale eddies are 8η and $0.5u_{\rm rms}$. Since mean shear exists in the turbulent mixing layer, there is a possibility that strain rate on the fine scale eddies is quite different from that in homogeneous isotropic turbulence. The investigations of their appearance and the alignment with the strain rate would lead to an understanding of the detailed mechanism of the transition to turbulence.

2 Strain rate on coherent fine scale eddies

The DNS of a temporally developing turbulent mixing layer has been conducted by using spectral methods in all directions. Calculation domain was selected to be $4\Lambda \times 6\Lambda \times 8/3\Lambda$ and grids points are $216 \times 325 \times 144$, where Λ is the most unstable wavelength for initial mean velocity distribution. We analyzed the DNS data at different time: $t = 65$, 85, 105, 125, where $t = 65$ corresponds to the onset of mixing transition. At the fully-developed state ($t = 125$), Reynolds number based on momentum thickness is 1048.

Figure 1 shows the contour surface of positive second invariant ($Q = (W_{ij}W_{ij} - S_{ij}S_{ij})/2$) at different time. On the occasion of transition to turbulence, the number of the fine scale eddies is obviously increasing. The high density region of the fine scale eddies corresponds to so-called large scale coherent structure in the turbulent mixing layer[6]. By applying a new identification scheme based on local flow pattern[2], we identified center of the coherent fine scale eddies

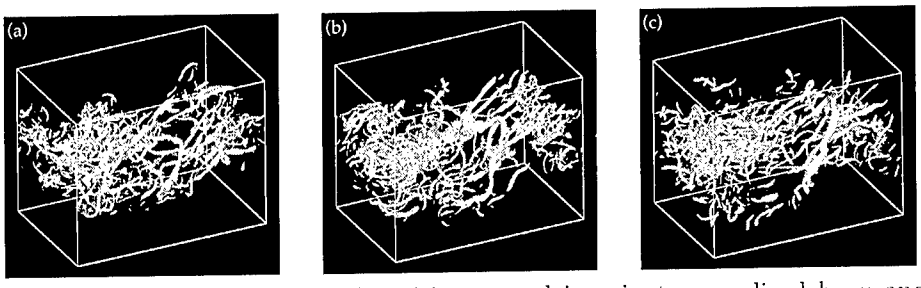


Figure 1: Contour surfaces of positive second invariant normalized by η and $u_{\rm rms}(Q^* = 0.03)$. (a): $t = 85$, (b): $t = 105$ and (c): $t = 125$.

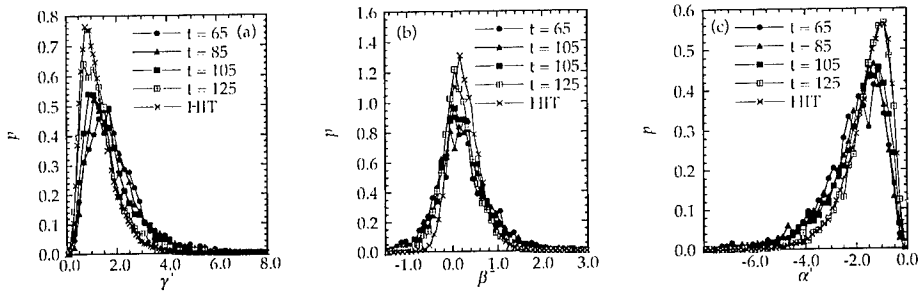


Figure 2: Probability density functions of strain rates at the center of coherent fine scale eddy.

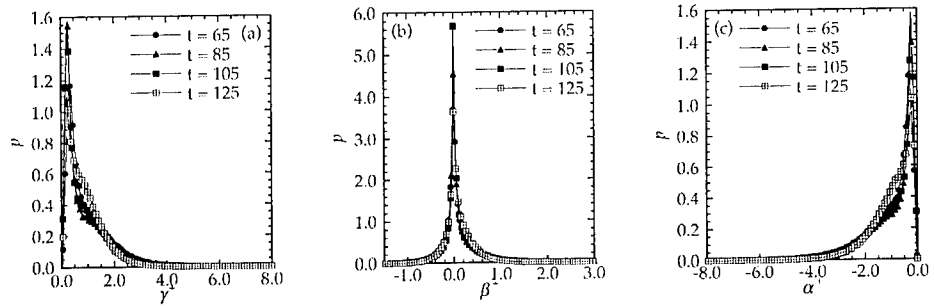


Figure 3: Probability density functions of strain rates in the whole region.

and calculated the eigen values of strain rate tensor at the center of coherent fine scale eddies. Figure 2 shows the probability density function of the eigen values. The eigen values α, β and γ denote the maximum, intermediate and minimum eigen value respectively and HIT shows the result obtained in homogeneous isotropic turbulence with $Re_\lambda = 87.9$. All eigen values are normalized by Taylor micro scale (λ) and $u_{\rm rms}$, which is denoted by +. In the case of turbulent mixing layer, λ and $u_{\rm rms}$ at the center of the mixing layer are used. For comparison, the pdfs of the eigen values in the whole region are shown in Fig. 3. The pdfs of the eigen values in the whole region denote that the turbulence

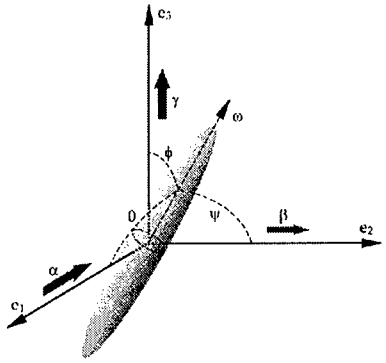


Figure 4: Definition of angles between rotating axis and eigen vectors of strain rate.

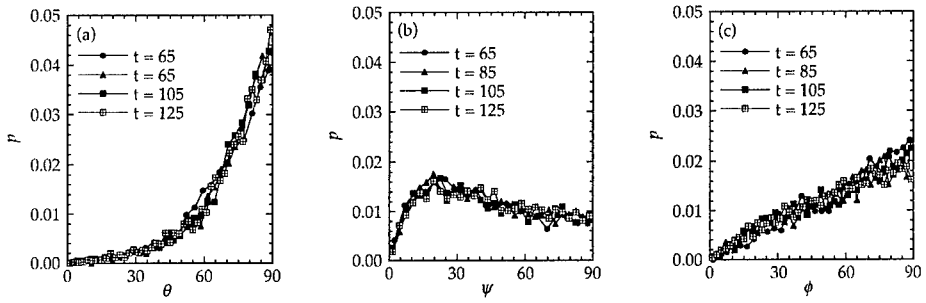


Figure 5: Probability density functions of the angles between axis and eigen vectors at the center of coherent fine scale eddies.

field are dominated by a plane shear. However, at the center of the coherent fine scale eddies, particular behavior of the eigen values can be observed. With the transition to turbulence, the most expected γ^+ decreases and reaches to 1.0 and that of α^+ tends to increase, although, the most expected γ^+ and α^+ in whole region is about 0.25 and -0.25 respectively (Fig. 3(a)(c)). This means that at the center of coherent fine scale eddies, large strain rates which are four times of mean strain rate act on the coherent fine scale eddy. The pdf of β^+ skews into the positive portion. The pdfs in the fully-developed state well coincide with those in homogeneous isotropic turbulence where the eigen values can be scaled by λ and $u_{\rm rms}$.

The angles between the eigen vectors of the strain rate and rotating axis are defined in Fig. 4, where e_1, e_2 and e_3 represents the eigen vectors of α, β and γ respectively. The pdfs of these angles are shown in Fig. 5. For comparison, same plots for the angles between vorticity vector and eigen vectors in the whole region are shown in Fig. 6. At the center of the coherent fine scale eddies, possibilities for $\theta = 90°$ and $\psi = 20°$ are pronounced. This tendency does not depend upon time, which implies that coherent fine scale eddies that appears in

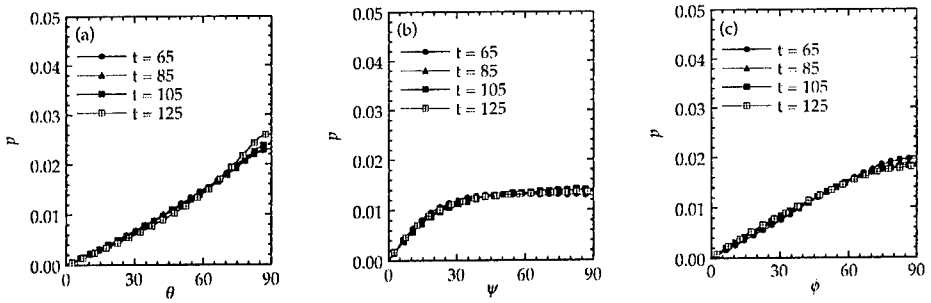


Figure 6: Probability density functions of the angles between vorticity vectors and eigen vectors of strain rate in the whole flow field.

the early state of the transition have quite similar characteristics with those in the fully-developed state.

3 Conclusions

In this study, strain rate acting on coherent fine scale eddies in turbulent mixing layer is investigated. At the center of coherent fine scale eddies, eigen values of the strain rate tensor are of the order of $u_{\rm rms}/\lambda$. With the transition to turbulence, the most expected maximum and minimum eigen value slightly increases and decreases respectively. The eigen vector of the minimum eigen value tends to be perpendicular to the axis and the most expected angle between rotating axis and eigen vector of intermediate eigen value is about 20 degrees. In the fully-developed state, these characteristics of coherent fine scale eddies in turbulent mixing layer are well coincide with that of homogeneous isotropic turbulence.

References

[1] R. D. Moser and M. M. Rogers. Mixing transition and the cascade to small scales in a plane mixing layer. *Physics of Fluids A*, 3:1128–1134, 1991.

[2] M. Tanahashi, T. Miyauchi and K. Matsuoka. Coherent fine scale structures in turbulent mixing layers. *Turbulence, Heat and Mass Transfer*, 2:461–470, 1997.

[3] J. Jimenez, A. A. Wray, P. G. Saffman and R. S. Rogallo. The structure of intense vorticity in isotropic turbulence. *J. Fluid Mech.*, 255:65–90, 1993.

[4] M. Tanahashi, T. Miyauchi and S. Iwase. Statistics of Coherent Fine Scale Eddies in Homogeneous Isotropic Turbulence. *Bulletin of the American Physical Society*, 43-9:1975, 1998.

[5] M. Tanahashi, S. Iwase, J. Ikeda and T. Miyauchi. to be submitted to JFM.

[6] G. L. Brown and A. Roshko. On density effects and large structure in turbulent mixing layers. *J. Fluid Mech.*, 64:775–816, 1974.

ADVANCES IN TURBULENCE VIII
Proceedings of the Eighth European Turbulence Conference
C. Dopazo et al. (Eds.)
© CIMNE, Barcelona 2000

DNS of flow around a circular cylinder at a subcritical Reynolds number with cartesian grids

F. Tremblay, M. Manhart and R. Friedrich

Lehrstuhl für Fluidmechanik, Technische Universität München
Boltzmannstr. 15, D-85748 Garching, Germany

Contact e-mail: fred@flm.mw.tum.de

A new method for direct numerical simulation (DNS) of turbulent flow over arbitrarily shaped bodies, based on cartesian grids, is used to compute the flow around a circular cylinder. Several test cases computed with this approach show good agreement with calculations performed with body fitted grids. DNS data of the flow around a cylinder at a Reynolds number of 3900 are presented and compared with numerical and experimental data of other authors.

1 Motivation

Flow across a circular cylinder is one of the classical flow problems which are not understood in all details. At a Reynolds number based on freestream velocity and diameter of 3900, which is low for most technical applications, the flow is already very complex, see fig. 1. It is characterized by laminar separation, transition to turbulence in the free shear layers leaving the body and shedding of large-scale vortices. All these flow features can be properly resolved and predicted in an efficient manner by a Navier-Stokes code based on cartesian grids.

The possibility to predict flows over arbitrarily shaped bodies with cartesian grids is very attractive, since typically a cartesian code is between 10 to 30 times more economical in terms of both CPU time and memory requirements when compared to a code for general curvilinear coordinates [7]. One can thus afford to do a computation with higher grid resolution and still achieve appreciable savings in computational resources. Another important aspect is the complete elimination of the need to produce a body-fitted grid, a task that is not trivial and in general consumes an important amount of time.

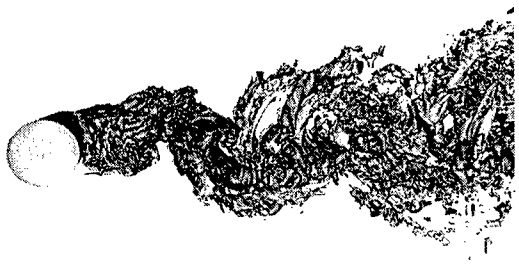


Figure 1: Instantaneous spanwise velocity isosurface

2 Numerical approach

The code MGLET, used here, is based on a finite volume formulation of the Navier-Stokes equations on a staggered cartesian non-equidistant grid. The spatial discretization is central and of second order accuracy for the convective and diffusive terms. For the time advancement of the momentum equations, an explicit second-order time step is used. The pressure solver uses a multigrid method based on a point-wise velocity-pressure iteration.

The present cartesian grid method [10] uses the following algorithm to treat an arbitrary body. The pressure cells crossed by the surface of the body are "blocked" and do not contribute to the computation. Also, the velocity components defined on the surfaces of these cells are blocked. To represent the influence of the body onto the fluid, the blocked velocity components are interpolated/extrapolated using Lagrangian polynomials and satisfying the no-slip and impermeability conditions at the surface to a desired degree of accuracy. At each time step, the blocked velocity components are re-interpolated/extrapolated and act as Dirichlet boundary conditions.

The explicit time advancement scheme for the momentum equations permits us to treat the blocked cells in the same way as the other cells i.e. all velocity cells are advanced in time in the same manner. For each open pressure cell, a pressure correction is computed so that the divergence is driven to zero. For the blocked pressure and velocity cells, no correction is applied. The total overhead in computational time produced by the introduction of the present method is less than 10%.

The method has been validated for a number of laminar cases. Second order accuracy has been demonstrated for the cylindrical Couette flow, and excellent agreement with other numerical experiments was obtained for steady and unsteady flows over a cylinder as studied by Schäfer et al. [9]

3 DNS of flow around a cylinder at Re = 3900

The flow around a cylinder at Re=3900 has been investigated experimentally by Ong and Wallace [8], and Lourenco and Shih [5]. Recently, a DNS was performed

by Ma et al. [6]. LES computations were presented by Breuer [2], Fröhlich et al. [3], Beaudan and Moin [1] and by Kravchenko and Moin [4].

Our computational domain is 20 diameters long in the streamwise direction, with the center of the cylinder being 5 diameters downstream of the inflow plane. In the normal direction, the domain size is also 20 diameters. The spanwise dimension of the domain was chosen to be πD, which corresponds to the size used by previous authors. A uniform inflow is prescribed, and periodicity is used in the normal and spanwise directions. A zero-gradient outflow condition is prescribed. The mesh was generated such that its size is of the same order of magnitude as the average Kolmogorov length scale in the plane normal to the cylinder axis. Around 425000 cells are needed in this plane. In the spanwise direction, 112 cells were used, so that the total number of cells is around 48 million. The explicit leap-frog method was used to advance the flow field in time with a maximum Courant number of about 0.3. The calculation was performed on 8 processors of the Fujitsu VPP700. With a mean performance of 7 GFlops, each time step requires 10 seconds. Starting from a uniform flow field, the solution was advanced for 100 problem times, based on the diameter and the inflow velocity. Statistics were then gathered for about 300 additional problem times. The results are presented for first and second order statistics.

The upper left diagram of fig.2 contains the mean streamwise velocity along the centerline. There is excellent agreement of our DNS data with the experiment in the near and far wake. The vertical profile of the variance of the streamwise velocity fluctuation at $X \approx D$ (upper right) reflects the proper peak values in the free shear layers and agrees well with the profile obtained by Ma et al. [6]. The Reynolds shear stress profiles at two downstream positions (lower left and right diagrams) reveal the right structural changes of the mean flow in the near wake region. At $X \approx D$, the overall shape of the shear stress is in agreement with the experiment and the results of Ma et al. [6]. The LES data of [4] on the other hand underpredict the peak Reynolds stresses.

4 Conclusion

A DNS of the transitional/turbulent flow over a cylinder at Re = 3900 has been conducted. It demonstrates the capability of the cartesian method to provide reliable solutions in an efficient way for flows around bodies of arbitrary shape. If one takes into account certain deficiencies in the experimental data (lack of symmetry), the present DNS data provide an accurate prediction of the flow and are in close agreement with the DNS data of Ma et al. [6].

References

[1] Beaudan, P. and P. Moin: 1994, 'Numerical Experiments on the Flow Past a Circular Cylinder at Sub-Critical Reynolds Number'. Report No. TF-62, Thermosciences Division, Department of mechanical engineering, Stanford University.

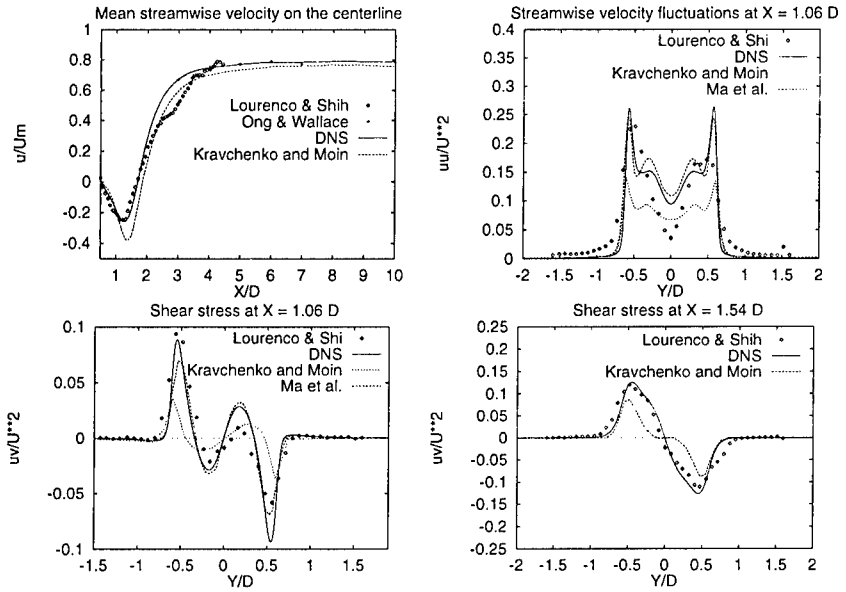


Figure 2: First and second order statistics in the near wake region

[2] Breuer, M.: 1998, 'Large eddy simulation of the subcritical flow past a circular cylinder: numerical and modeling aspects'. *Int. J. Numer. Meth. Fluids* **28**, 1281–1302.

[3] Fröhlich, J., W. Rodi, P. Kessler, S. Parpais, J. Bertoglio, and D. Laurence: 1998, 'Large Eddy Simulation of Flow around Circular Cylinders on Structured and Unstructured Grids'. In: E. Hirschel (ed.): *Notes on Numerical Fluid Mechanics*. pp. 319–338.

[4] Kravchenko, A. and P. Moin: 1998, 'B-Spline Methods and Zonal Grids for Numerical Simulations of Turbulent Flows'. Report No. TF-73, Flow Physics and Computation Division, Department of mechanical engineering, Stanford University.

[5] Lourenco, L. and C. Shih: 1993, 'Characteristics of the plane turbulent near wake of a circular cylinder, a particle image velocimetry study'. private communication, data taken from [4].

[6] Ma, S., G.-S. Karamanos, and G. Karniadakis: 1999, 'Dynamics and Low-Dimensionality of the Turbulent Near-Wake'. *J. Fluid Mech. (To appear)*.

[7] Manhart, M., G. Deng, T. Hüttl, F. Tremblay, A. Segal, R. Friedrich, J. Piquet, and P. Wesseling: 1998, 'The minimal turbulent flow unit as a test case for three different computer codes'. In: E. Hirschel (ed.): *Vol. 66, Notes on numerical fluid mechanics*. Braunschweig: Vieweg-Verlag, pp. 365–381.

[8] Ong, L. & Wallace, J.: 1996, 'The Velocity Field of the Turbulent Very Near Wake of a Circular Cylinder'. *Experiments in Fluids* **20**, 441–453.

[9] Schäfer, M. and S. Turek: 1996, 'Benchmark Computations of Laminar Flow Around a Cylinder'. In: E. Hirschel (ed.): *Notes on Numerical Fluid Mechanics*. pp. 547–566.

[10] Tremblay, F. and R. Friedrich: 2000, 'A cartesian-grid method for flows with arbitrary solid surfaces'. *(in preparation)*.

ADVANCES IN TURBULENCE VIII
Proceedings of the Eighth European Turbulence Conference
C. Dopazo et al. (Eds.)
© CIMNE, Barcelona 2000

Reynolds number effect on turbulent structures in a pipe flow via DNS

S. Satake[1] and T. Kunugi[2] and R. Himeno[3]

[1]Department of Mechanical and Intellectual Systems Engineering,
Toyama University, 3190 Gofuku, Toyama 930-8555, Japan
[2]Department of Nuclear Engineering,
Kyoto University, Yoshida, Sakyo, Kyoto 606-8501, Japan
[3]RIKEN,
Dept. of Computer and Information. 2-1 Hirosawa, Wako, Saitama,351-0198

Contact e-mail: ssatake@eng.toyama-u.ac.jp

1 Introduction

Turbulent transport computations for fully-developed turbulent pipe flow were carried out by means of a direct numerical simulation (DNS) procedure. To investigate the effect of Reynolds number on the turbulent sturcures, the Reynolds number based on a friction velocity and a pipe radius was set to be $Re_\tau = 150, 180, 360, 500, 1050$. The number of maximum computational grids used for $Re_\tau = 1050$ is $1024 \times 512 \times 768$ in the $z-$, $r-$and ϕ -directions, respectively. The friction coefficients are in good agreement with the empirical correlation. The turbulent quantities such as the mean flow, turbulent stresses, turbulent kinetic energy budget, and the turbulent statistics were obtained by previous our DNS(Satake et al., 1999)[6]. It is found that the turbulent structures are dependent at these Reynolds numbers.

2 Numerical Procedure

The DNS code can numerically solve the incompressible Navier-Stokes and continuity equations described in cylindrical coordinate using a second-order finite volume discretization scheme with the radial momentum flux formulation. These equations are integrated in time by using the fractional-step method with Crank-Nicholson and a modified third-order Runge-Kutta scheme. In our previous study regarding the turbulent pipe flow (Satake and Kunugi,[4],[5]), this DNS code has been shown in good agreement with the existing DNS results.

3 Computational conditions

The computational domain of the fully developed turbulent pipe flow is shown in Fig. 1. The number of grid points, the Reynolds number and grid resolutions summarized in Table 1. To perform a DNS with a highest Reynolds number in this study, a highest grids size of 1024 × 512 × 768 is adopted for 84GB main memory as 64 PEs on a vector-parallel computer Fujitsu VPP 700E at RIKEN.

4 Results and Discussions

In comparison with previous DNS and experimental data, the mean velocity profiles are shown in Fig. 2. At Re_τ=180 (Re_b = 5300), the present DNS are in excellent agreement with those of DNS by Eggels et al. (1994) and with the experimental data by Durst et al. (1996). The present results except Re_τ=1050 also agree with the experimental data obtained by Durst et al. (1996). At Re_τ = 1050 (Re_b =40000), the present DNS is in excellent agreement with those of the experimental data by Laufer (1954). Figure 3 shows the contour of the low speed streaky structures (u^+ <-3.5)and second invariant of velocity gradient tensor (Q^+ <0.008). Its are normalized by n and ut. The volume visualized obtained as cutting volume (z^+ =985,$y^+ = R^+ - r^+$ =1050,$r^+\phi$=536) for Re_τ =1050 from full computational volume (L_z^+ =15750,$y^+ = R^+ - r^+$ =1050, $L_r^+\phi$=6597). The many tube like structures and large streaky structures exist in this volume. The width of the large streaky structures are larger than $r^+\phi$=100, located at away from the wall. A few streaks merged as plate like structures at y^+=200 from the wall. The second invariant of velocity gradient tensor (Q^+ <0.008), the ejection ($-U_z^+V^+$ <0, V^+ >0, $V^+ = -u_r^+$) and the sweep ($-U_z^+V^+$ <0, V^+ <0, $V^+ = -u_r^+$) for $Re_\tau = 180, 360, 500, 1050$ in the cross section perpendicular to the circumferential direction are shown in Fig. 4 (a)-(d), respectively. In low Reynolds number (Re_τ =180), the ejection and the sweep are observed very small region, located around vortical structures. However, in high Reynolds number (Re_τ = 360, 500, 1050), the structures seem to be rather different from the one in low Reynolds number. A characteristic size of the ejection and the sweep are even larger than the half of the pipe radius. Almost large structures located in y^+ >200, correspond to the wake region in the mean velocity profile. In the region, the scales of the fluid motion are different from the near wall region.

References

[1] Durst, F., Kikura, H., Lekakis, I., Jovanovic and Ye, Q., Wall shear stress determination from near-wall mean velocity data in turbulent pipe and channel flows," *Experiments in Fluids* Vol.20, pp. 417–428,1996.

Table 1: Computational condition

Case	Grid numbers	Δz^+	$R^+\Delta\phi$	Δr^+_{wall}	Δr^+_c
$Re_\tau = 150$	256 × 128 × 128	8.78	7.36	0.24	0.86
$Re_\tau = 180$	256 × 128 × 128	10.5	8.84	0.29	1.04
$Re_\tau = 360$	384 × 256 × 256	14.0	8.83	0.11	1.1
$Re_\tau = 500$	512 × 384 × 384	14.6	8.18	0.1	2.6
$Re_\tau = 1050$	1024 × 512 × 768	15.4	8.59	0.163	4.16

[2] Laufer, J. , The structure of turbulence in fully developed pipe flow, *NACA report 1174*,1954.

[3] Eggels, J.G.M., Unger, F., Weiss, M.H., Westerweel, J. Adrian, R.J., Friedrich, R., and Nieuwstadt, F.T.M., Fully developed turbulent pipe flow: comparison between direct simulation and experiment, *J. Fluid Mech., Vol. 268*, pp. 175–209,1994.

[4] Satake, S. and Kunugi, T. *Direct numerical simulation of turbulent pipe flow, Bulletin JSME Vol.64(in Japanense)*, pp. 65–70,1998.

[5] Sakate, S. and Kunugi, T. *Direct numerical simulation of an impinging jet into parallel disks, Int. J. Numerical Methods for Heat and Fluid Flow*, 8, 768–780, 1998.

[6] Sakate, S. , Kunugi, T. and Himeno, R. *DNS of turbulent pipe flows with high Reynolds number, 3th Computational Fluid Dynamics Conf. in Japan*, p.68, 1999.

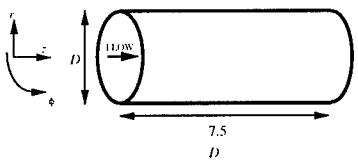


Figure 1: The computational domain

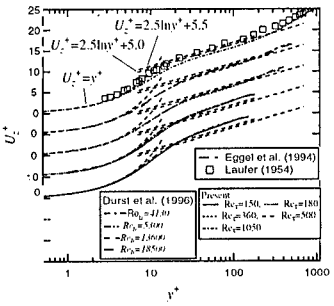


Figure 2: Mean velocity profiles

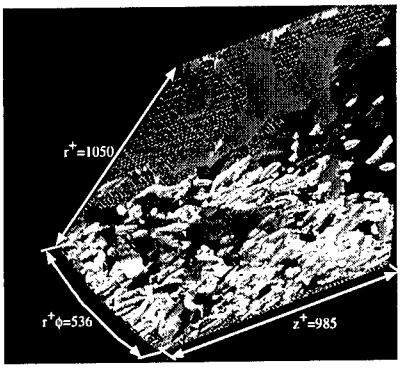


Figure 3: The contour of the low speed streaky structures (u^+ <-3.5); Blue and second invariant of velocity gradient tensor (Q^+ <0.008), White. $Re_\tau = 1050$

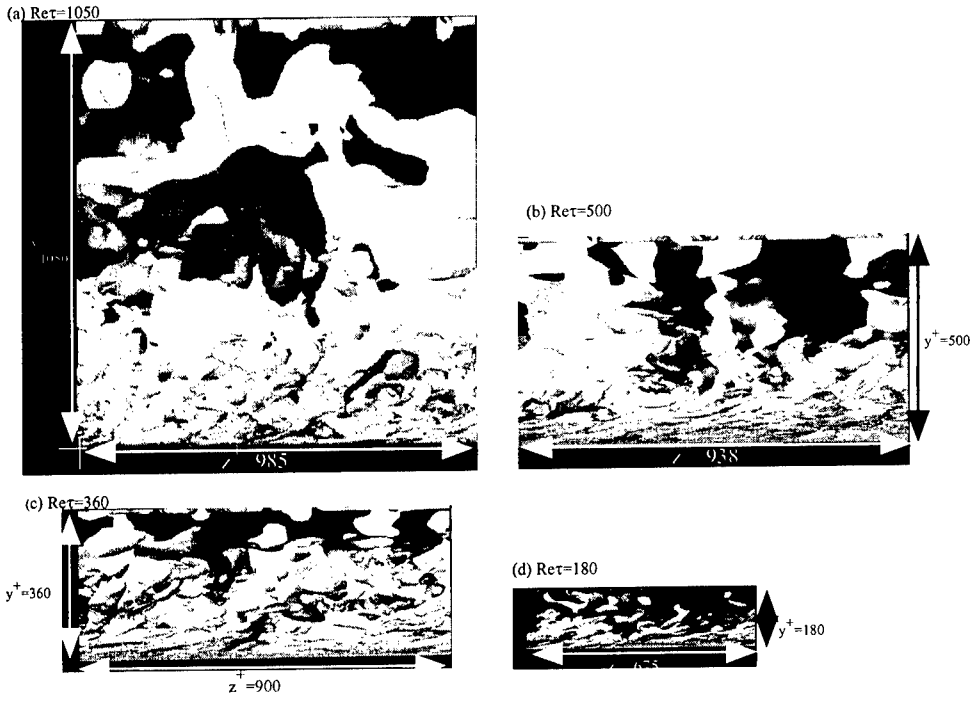


Figure 4: The second invariant of velocity gradient tensor (Q^+ <0.008), White, the ejection ($-U_z^+V^+$ <3.5, V^+ >0, $V^+ = -u_r^+$); Yellow and the sweep($-U_z^+V^+$ <3.5, V^+ <0, $V^+ = -u_r^+$); Green for $Re_\tau = 180, 360, 500, 1050$ in the cross section perpendicular to the circumferential direction

ADVANCES IN TURBULENCE VIII
Proceedings of the Eighth European Turbulence Conference
C. Dopazo et al. (Eds.)
© CIMNE, Barcelona 2000

The directional dissipation scale: a criterion for grid resolution in direct numerical simulations

M. Manhart

Lehrstuhl für Fluidmechanik
Technische Universität München
GERMANY

Contact e-mail: michael@flm.mw.tu-muenchen.de

1 Introduction

While there is a considerable amount of experience on grid resolution issues for DNS of turbulent channel and boundary layer flow, no experience is available for more complex flow situations, where empirical measures based on wall shear stress fail. The most conservative method to guarantee a sufficient grid resolution is to perform grid resolution studies, which are very expensive. In homogeneous or periodic directions, wavenumber spectra can provide enough information to decide whether a grid resolution was fine enough. From a theoretical point of view, a DNS has to resolve all relevant length scales including the large scales and the dissipation scales. The isotropic dissipation scale is determined by the Kolmogorov microscale η

$$\eta = \left(\frac{\nu^3}{\epsilon}\right)^{\frac{1}{4}}, \tag{1}$$

which does not account for anisotropy of the small scales appearing in low Reynolds number turbulent flows (Antonia et al. [1]). The anisotropy in the small scales is usually reflected in anisotropic grid spacings. An example for this is the turbulent boundary layer (Spalart [4]) or channel flow (Kim et al. [2]). We propose a directional dissipation scale η_{ij} which is able to keep track of the anisotropy of the small scales in strongly anisotropic flow situations.

$$\eta_{ij} = \left(\frac{\nu^2}{< (\partial u_i'/\partial x_j)^2 >}\right)^{\frac{1}{4}} \quad \text{(no summation!)}. \tag{2}$$

2 Present investigation

If a one-point measure has to be used as a resolution indicator, it has to meet two requirements. On the one hand it has to be reliable in a sense, that it is insensitive to grid resolution itself. On the other hand, it has to provide reliable information in any flow situation. In order to check these requirements, we selected as a test case a fully turbulent boundary layer subjected to an adverse pressure gradient until separation occurs. In the subsequent nearly zero-pressure gradient region, the flow reattaches and slowly relaxes to a canonical boundary layer. Before the pressure gradient is imposed, a zero pressure gradient region at a Reynolds number of about $Re_\theta \approx 800$ (based on the inlet momentum thickness) is applied to establish a well defined inflow condition. In this region, our findings can be compared with empirical measures for grid resolution in this kind of flow.

The test simulation has been performed with a finite volume code based on second order central differencing (see Manhart and Friedrich [3]). The grid parameters based on inner scaling of the oncoming boundary layer are $\Delta x^+ = 26.4$ in streamwise, $\Delta y^+ = 12.4$ in spanwise and $\Delta z^+ = 3.3$ in wall normal direction. These grid spacings are relatively coarse for the zero pressure gradient region but sufficient for the adverse pressure gradient and separated region. A more detailed description of the simulation is published in [3].

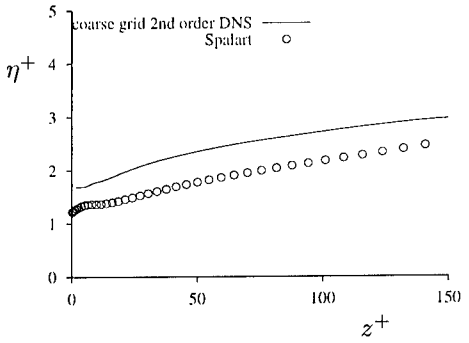


Figure 1: Kolmogorov microscale in a zero pressure gradient boundary layer predicted with a spectral method (Kim et al., [2]) and coarse grid DNS

Reliability. The ability of predicting small scale characteristics, like dissipation length scales, with a coarse numerical grid is essential for the usefulness of the dissipation scale as an indicator for correct grid resolution. In order to investigate this, we show in figure 1 the Kolmogorov length scale in the zero pressure gradient region (where the grid resolution of the present simulation is not really sufficient) and compare it with that predicted by a spectral code (Spalart [4]). It can be concluded, that the prediction of η is very robust concerning the grid resolution. The error introduced by the coarse grid is smaller than 25%.

Relevance. In figure 2, the directional dissipation scales of the streamwise velocity component (which are the smallest) are compared to the Kolmogorov microscale in the zero pressure gradient boundary layer. The minima are about $\eta_{1j} = 4.4$, 2.2 and 1.5 wall units in streamwise, spanwise and wall-normal direction, respectively. The required grid resolution in streamwise and spanwise direction are roughly twice the minima of the directional dissipation scales in the corresponding direction. In wall-normal direction, immediately at the wall, a resolution of η_{13} seems to be required. These findings are fully consistent with results from a well resolved DNS of plane channel flow (not shown here).

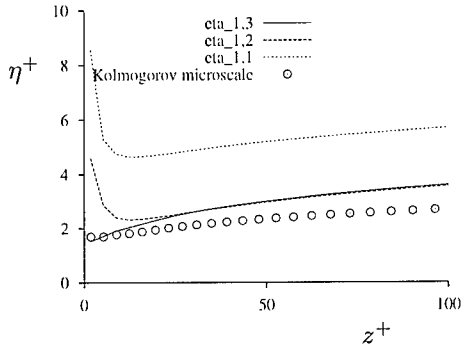


Figure 2: Directional dissipation scales η_{1j} in a turbulent boundary layer ($Re_\theta = 800$) compared to Kolmogorov microscale

Behaviour in complex flow situations. A further check for the ability of the directional dissipation length scale as a resolution criterion is done by relating it to wavenumber spectra. If a wavenumber spectrum in a DNS drops off by a certain order of magnitude, we consider the DNS as sufficiently resolved in that direction. In the present study, we are using spanwise spectra in the separating turbulent boundary layer at different locations during the separation process ($x = 3.0$ indicating the zero pressure gradient phase, $x = 40.0$ the separation region and $x = 60.0$ the reattachment region). As one can see in figure 3, the directional dissipation scale η_{ij} always indicates the spatial resolution at which the spectrum would exhibit a sufficient drop-off. At $x = 3.0$ where the spanwise grid resolution captured only a spectral drop-off by one orders of magnitude, the directional dissipation scale would indicate a resolution fine enough to capture more than three orders of magnitude. During the separation process, the length scales are increasing, which is displayed in the spectra at $x = 40$ and $x = 60$. Here, the directional dissipation scale clearly follows this behaviour showing that in this region a much coarser grid could have been applied in spanwise direction.

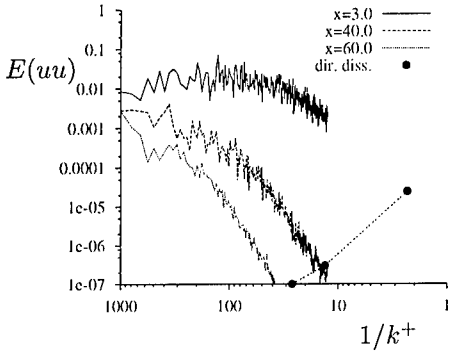


Figure 3: Spanwise spectra in a separating and reattaching turbulent boundary layer. Streamwise positions (from top to bottom): zero pressure gradient phase ($x = 3.0$), separation region ($x = 40.0$) and reattachment region ($x = 60.0$). The full circles indicate the directional dissipation scale η_{12} at the corresponding positions.

3 Conclusions

The study shows that the directional dissipation scale is a suitable criterion for grid resolution in DNS of geometrically complex flows. The robustness of the dissipation scale against grid resolution itself makes it possible to estimate the appropriate resolution by a simulation with a coarse grid without the need of extensive resolution studies. In a zero pressure gradient turbulent boundary layer, the empirically found values for proper grid resolution coincide with about twice the dissipation scale in the corresponding direction. In complex flow situations, like separation or reattachment, the dissipation scale is able to indicate the length scale at which the wavenumber spectrum shows a sufficient drop off.

References

[1] R.A. Antonia, J. Kim, and L.W. Browne. Some characteristics of small-scale turbulence in a turbulent duct flow. *J. Fluid Mech.*, 233:369–388, 1991.

[2] J. Kim, P. Moin, and R. Moser. Turbulence statistics in fully developed channel flow at low Reynolds number. *J. Fluid Mech.*, 177:133–166, 1987.

[3] M. Manhart and R. Friedrich. Towards DNS of separated turbulent boundary layers. In P.R. Voke, N.D. Sandham, and L. Kleiser, editors, *Direct and Large-Eddy Simulation III*, pages 429–440. Kluwer Academic Publishers, Dordrecht, 1999.

[4] P.R. Spalart. Direct simulation of a turbulent boundary layer up to $R_\theta = 1410$. *J. Fluid Mech.*, 187:61–98, 1988.

ADVANCES IN TURBULENCE VIII
Proceedings of the Eighth European Turbulence Conference
C. Dopazo et al. (Eds.)
© CIMNE, Barcelona 2000

Analysis of coherent structures in turbulent channel flow using the orthogonal wavelet representation.

D. C. Dunn and J. F. Morrison

Department of Aeronautics, Imperial College of Science, Technology and Medicine, London, SW7 2YB, United Kingdom.

1 Introduction

In large eddy simulation of turbulent flows, the large-scale (resolved) motions are computed by solving the filtered Navier-Stokes equations, and the small-scale (subgrid) motions are modelled. Most subgrid-scale models are based on the eddy-viscosity hypothesis and are therefore anisotropic with the energy drain being unidirectional in the same sense as the conventional cascade ("forward scatter"). However, recent *a priori* studies of DNS data for wall-bounded turbulence (e.g. Härtel & Kleiser [1], Piomelli *et. al.* [2], Westbury *et. al.* [3]) have shown that transfer of energy from the subgrid scales to the resolved scales ("backscatter") occurs at up to 50% of the grid points, and in fact backscatter dominates the energy transfer in the buffer region. Therefore it is important to develop accurate models of the subgrid-scale motions thus permitting simulations at high Reynolds numbers using 'off the surface' boundary conditions.

The present work investigates a possible connection between bursting events in wall-bounded turbulence and both forward scatter and backscatter, the ultimate objective being to develop a structure based subgrid scale model. Experimental work by Morrison *et. al.* [4] suggests that in the logarithmic region 'ejections' ($u < 0, v > 0$) and 'sweeps' ($u > 0, v < 0$) are the main contributors to the turbulent shear stress and effect most of the universal part of the spectral transfer of energy. In a conventional spectral analysis of DNS data at $Re_\tau = 180$ Westbury *et. al.* [3] have shown that in the viscous sublayer, sweeps are the main contributors to backscatter while ejections are the primary contributors to forward scatter. Therefore these structures provide the starting point into the investigation of spatial variations in forward scatter and backscatter (while these terms are filter-specific, we use them loosely for the present). Moreover, it appears that not only are the physical-space structures quite small and therefore 'local' in physical space, the spectral transfer associated with them is also 'local'

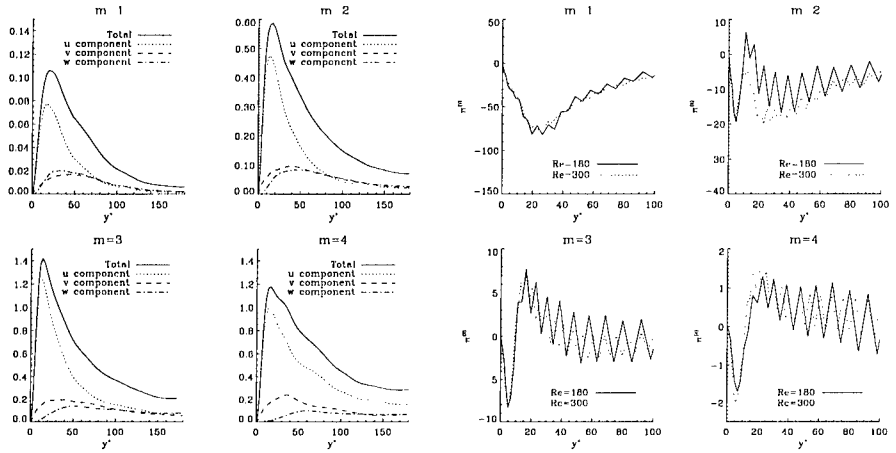


Figure 1: Plot of the components of the kinetic energy for $Re_\tau = 300$.

Figure 2: Mean values $\pi^{(m)}$ for both Reynolds numbers.

in wave-number space. Meneveau [5] uses an orthonormal wavelet representation to examine the energy transfer in turbulent velocity signals. The wavelet representation retains information about spatial location as well as scale, and is ideally suited to studying the effect of spatially localised structures on energy transfer. In this paper some preliminary results are given which indicate a qualitative relationship between subgrid scale flux and uv.

2 Results

An orthonormal wavelet analysis has been applied to DNS data of turbulent channel flow, due to Sandham & Howard [6]. Data is available for $Re_\tau = 180$ and 300. The decomposition has been carried out in two-dimensional homogeneous planes, parallel to the wall. The wavelet decomposition gives information about discrete scales of characteristic size $r_m = 2^m h_1 h_3$, at increasingly coarse spatial resolution. Here h_1 and h_3 are the grid spacings in the streamwise and spanwise directions respectively. Figure (1) shows the components of kinetic energy for $Re_\tau = 300$. In this and all subsequent plots all quantities are given in wall units, e.g. $y^+ = yu_\tau/\nu$, $u^+ = u/u_\tau$. Most of the turbulence production feeds the streamwise direction goes into the streamwise velocity component, and the streamwise component, as well as the total kinetic energy attain maxima in the buffer region.

Meneveau [5] defines the quantities $t^{(m)}[\mathbf{i}]$, which represents the transfer of energy to the scale r_m from all other scales, and $\pi^{(m)}[\mathbf{i}]$, which represents both the spatial flux of energy through a region of characteristic size r_m and the flux of energy through the scale r_m. It is defined such that a decrease in energy of

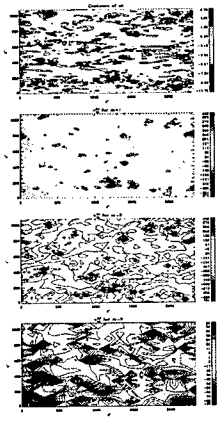


Figure 3: Contours of uv and $\pi_{sg}^{(m)}$ for a plane in the buffer region, for $Re_\tau = 180$.

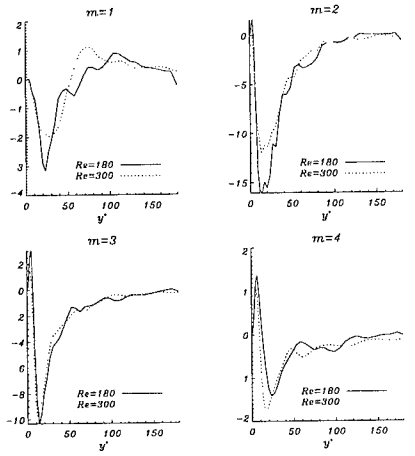


Figure 4: Plots of the mean values of $\pi_{sg}^{(m)}$ as a function of y^+, for $m = 1, \ldots, 4$ for each Reynolds number.

the large scales corresponds to positive flux. Figure (2) shows the mean values of $\pi^{(m)}[\mathbf{i}]$ as a function of distance from the wall. At each scale $\pi^{(m)}$ reaches a local negative minimum in the sublayer. For the smaller scales it is negative in the buffer region, whereas in the larger scales it is positive. A negative value of $\pi^{(m)}$ does not strictly correspond to backscatter since it includes a spatial flux due to the 'sweeping' of small eddies by the large ones. The spatial flux is therefore more apparent at larger y^+. Dunn & Morrison [7] have used the VISA+LEVEL conditional sampling scheme to investigate the relationship between $\pi^{(m)}$ and sweeps and ejections, and shown that there is little correlation. However, Figure (3) indicates a qualitative correspondence between large negative values of fluctuating uv and $\pi^{(m)}$ in the buffer region, for both Reynolds number values considered here.

Meneveau [5] defines the 'subgrid' flux, $\pi_{sg}^{(m)}$, which represents the flux of energy to scale r_m, due only to interactions with scales smaller than r_m. It is this quantity that is best compared with the subgrid transfer, T^{fs}, of Härtel & Kleiser [1]. Figure (4) shows the mean value of $\pi_{sg}^{(m)}$ as a function of distance from the wall. At all scales in the wavelet representation $\pi_{sg}^{(m)}$ is negative in the buffer region, indicating that the flux is from the small to the large scales on average. For the larger scales $\pi_{sg}^{(m)}$ resembles T^{fs}, reaching a local maximum in the sublayer and a local minimum in the buffer layer. The former is consistent with an unsteady Couette flow dominated by vortex stretching. Only the smallest scale exhibits positive $\pi_{sg}^{(m)}$ over a significant part of the channel, suggesting that the Reynolds number is so low that genuine inertial transfer occurs close

to the viscous cut-off. It is unlikely therefore that there is a genuine inertial subrange, the usual range of wave numbers in which a filter is likely to be used. This result also suggests that there is some significant viscous spectral transfer not included in $\pi_{sg}^{(m)}$.

3 Conclusions

Qualitatively, it is clear that close to the wall $\pi_{sg}^{(m)}$ is localised in regions in which the uv field is breaking up. Given the prevalence of quasi-streamwise vortices in this region, it is clear that more sophisticated vortex eduction techniques are required such as λ_2 (Jeong *et. al.* [8]) or cubic discriminant (Cantwell *et. al.* [9]) for assessing their contributions to energy transfer.

Acknowledgements. The first author is supported by EPSRC grant GR/M31187. The authors are indebted to Charles Meneveau for assistance with implementing the wavelet code, and to Neil Sandham and Philippa Westbury for preliminary work which has led to this paper.

References

[1] Härtel, C. & Kleiser, L.. Analysis and modelling of subgrid-scale motions in near-wall turbulence. *J.Fluid Mech.*, 356:327-352, 1998.

[2] U. Piomelli, Y. Yu & R. J. Adrian. Subgrid-scale energy transfer and near-wall turbulence structure. *Phys. Fluids*, 8:215-224, 1996.

[3] P. S. Westbury, N. D. Sandham & J. F. Morrison. Bursts and subgrid-scale energy transfer in turbulent wall-bounded flow. in *Advances in Turbulence VII*, pages 23-26, Kluwer, 1998.

[4] Morrison, J. F., Subramainian, C. S., & Bradshaw, P. Bursts and the law of the wall in turbulent boundary layers. *J. Fluid Mech.*, 241:75-108, 1992.

[5] Meneveau, C. Analysis of turbulence in the orthonormal wavelet representation. *J. Fluid Mech.*, 232:469-520, 1991.

[6] Sandham, N. D. & Howard, R. J. A. Statistics databases from direct numerical simulation of fully-developed channel flow. *QMW Report QM-EP-1111*, 1996.

[7] Dunn, D. C. & Morrison, J. F. Energy transfers in wall turbulence. *Imperial College Aero Report 00-01*, 2000.

[8] Jeong, J., Hussain, F., Schoppa, W. & Kim, J. Coherent structures near the wall in a turbulent channel flow. *J. Fluid Mech.*, 332:185-214, 1997.

[9] Cantwell, B. J., Chacin, J. M. & Bradshaw, P. On the dynamics of turbulent boundary layers. In *Self-sustaining mechanisms of wall turbulence* (ed. R. L. Panton), Computational Mechanics Publications, Southampton, UK and Boston USA, 365-384.

ADVANCES IN TURBULENCE VIII
Proceedings of the Eighth European Turbulence Conference
C. Dopazo et al. (Eds.)
© CIMNE, Barcelona 2000

Near-wall structures in turbulent rotor-stator flow

M. Lygren and H. I. Andersson

Division of Applied Mechanics
Norwegian University of Science and Technology
N-7491 Trondheim, NORWAY

Contact e-mail:helge.i.andersson@mtf.ntnu.no

1 Introduction

Several investigations of three-dimensional turbulent boundary layers (3DTBLs) have shown that the three-dimensionality affects the turbulence statistics and structure (see e.g. ref. [1]). In a 3DTBL the Reynolds shear stress vector is generally not aligned with the mean velocity gradient vector, and the ratio of the magnitude of the shear stress vector to the turbulent kinetic energy is reduced relative to a 2DTBL. This reduction indicates that the three-dimensionality reduces the efficiency of the turbulence in extracting energy from the mean flow.

The reason why the three-dimensionality seems to stabilize the turbulence is not yet completely understood. A common assumption is that the answer is to be found in the underlying vorticity structure near the wall. Littell and Eaton [5] performed an experiment of the flow over a rotating disk and found asymmetric velocity profiles in the spanwise direction near strong stress-producing events. They concluded that the three-dimensionality reduced the strength of the ejections produced by Case 1 streamwise vortices while the Case 2 vortices produced weak sweeps. A streamwise vortex with the induced near-wall velocity being in the direction of the crossflow is here labelled "Case 1", the vortex rotating in the opposite sense is labelled "Case 2"; see figure 1(a). Kang *et al.* [4] performed a similar experiment, but concluded that the asymmetries in the conditional averages of Littell and Eaton were not related to the coherent vortical structures. The aim of this study is to expand the understanding of how the three-dimensionality affects the coherent vortical structures near the wall.

2 Numerical approach and results

A direct numerical simulation (DNS) of the fully turbulent flow between a disk rotating with angular frequency ω and a stationary disk was performed. The

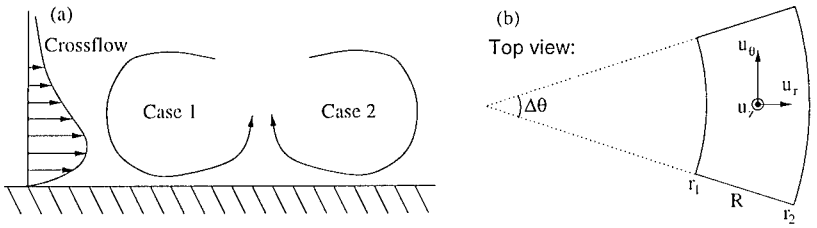


Figure 1: (a) Vortex definitions. (b) Sketch of the computational domain.

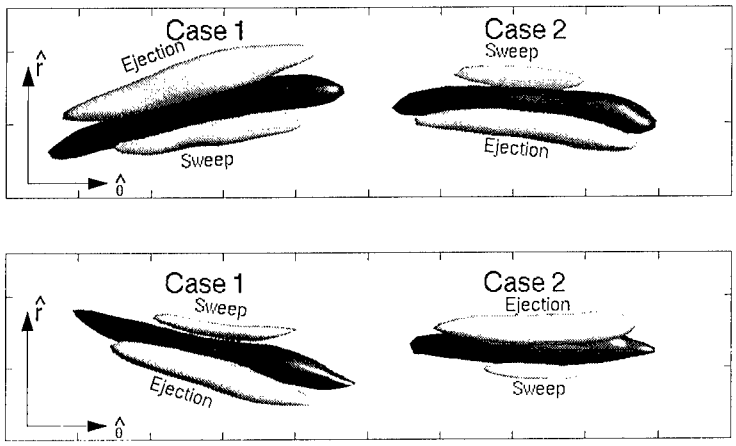


Figure 2: Isosurface plots (top view) of the ensemble-averaged coherent structures near the rotating (upper plot) and the stationary disk (lower plot). Dark shading represents $\langle\lambda_2\rangle$, indicating the shape of the vortices, light shading represents the associated stress $\langle u_\theta u_z\rangle$. Tickmarks are 50 wall-units apart. The crossflow is in $+\hat{r}$-direction near the rotor and in $-\hat{r}$-direction near the stator.

incompressible Navier-Stokes equations were solved in an angular section $\Delta\theta$ between the two radial surfaces r_1 and r_2, see figure 1(b). Periodic boundary conditions were applied in the tangential direction while quasi-periodic conditions were used between r_1 and r_2. No-slip conditions were imposed at both disks. The DNS was performed at a rotational Reynolds number $Re_R = R^2\omega/\nu = 4{\cdot}10^5$ and gap ratio $s/R = 0.02$ where s is the distance between the disks. Further details on the numerical approach as well as the time-averaged statistics are reported in [6].

Ensemble-averaging of quasi-streamwise vortices in the 3DTBLs near the two disks was performed, based on the procedure by Jeong *et al.* [2]. The vortices were detected using the λ_2 criterion proposed by Jeong and Hussain [3], their extent was required to exceed 130 wall-units in tangential direction. Figure 2 shows isosurface plots of the ensemble-averaged vortices and their associated

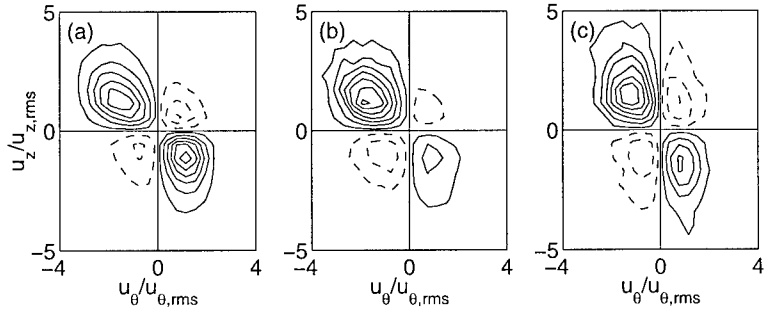


Figure 3: Weighted joint PDFs of u_θ and u_z near the rotating disk ($z^+ = 30$). (a) No conditioning. (b) Conditioned on $\omega_\theta < -1.5\omega_{\theta,rms}$ (Case 1). (c) $\omega_\theta > -1.5\omega_{\theta,rms}$ (Case 2).

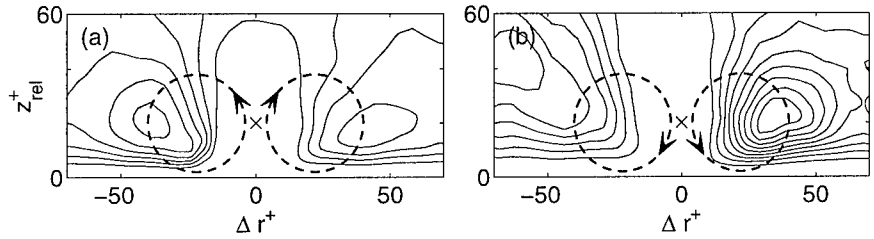


Figure 4: (a) Q4 contributions to the $\overline{u_\theta u_z}$ stress near strong ejections ($u_\theta u_z > 3\overline{u_\theta u_z}$ and $u_z > 0$). (b) Q2 contributions to $\overline{u_\theta u_z}$ near strong sweeps ($u_\theta u_z > 3\overline{u_\theta u_z}$ and $u_z < 0$). The locations of the strong events are marked by $\times$.

positive contribution to the shear stress. Near both disks the Case 1 coherent vortex is of greater extension than Case 2. It is also noticeable that both vortices produce very weak sweeps compared to ejections. The coherent structures educed in ref. [2] in a 2DTBL did not show this pronounced feature.

Joint probability-density functions (PDFs) of the u_θ-u_z fluctuations are displayed in figure 3. The PDFs were weighted with $u_\theta u_z$ in order to show how each velocity component contributes to $\overline{u_\theta u_z}$. By conditioning on the tangential component of the vorticity vector it can be seen how vortices of different sign contribute to this Reynolds stress. Near the rotating disk both positive and negative vortices were more closely connected with Q2 (quadrant 2) events (ejections) than with Q4 events (sweeps). This was also seen near the stationary disk. The PDFs therefore support the conclusions from the ensemble-averages in that streamwise vortices produce stronger ejections than sweeps.

Following Kang *et al.* [4], the velocity field near strong ejections and sweeps was examined by averaging about these high-shear-stress locations. A quadrant analysis of the averaged field was also performed. Since coherent structures are associated with Q2 and Q4 events, figure 4 shows the contours of Q4 contributions to $\overline{u_\theta u_z}$ near strong ejections and Q2 contributions near strong sweeps.

As indicated in the figure, the peaks around the detection points are signatures of a pair of vortices generating the high-stress events. Since the highest peak near the strong ejections is to the left of the ejection, it is concluded that the left vortex (Case 1) is responsible for generating the majority of the strong ejections. Near the strong sweep, the vortex to the right (Case 1) produces most of the strong sweeps. A corresponding analysis near the stationary disk led to the same conclusions. Figure 4 clearly supports Littell and Eaton [5] in that asymmetries in the conditionally averaged fields are associated with vortical motions.

3 Concluding remarks

The mean-flow three-dimensionality near the rotating disk is caused by the centrifugal force being larger than the inward pointing pressure gradient. Near the stationary disk the three-dimensionality can be considered driven by the pressure gradient alone. The observed differences between the present coherent structures and those found in 2DTBLs are therefore most likely effects of the mean-flow three-dimensionality. Based on the ensemble average, PDFs and the quadrant analysis, it is concluded that the three-dimensionality causes the coherent structures to produce very weak sweeps compared to ejections. In addition, Case 1 coherent vortices produce both more strong sweeps and ejections than Case 2 vortices, the reason could possibly be that Case 1 vortices are of larger streamwise extent. It is believed that the reduction in the strength of the sweeps near the coherent structures is the reason for the reduced efficiency of the mean flow to produce Reynolds shear stress.

References

[1] J. K. Eaton. Effects of mean flow three dimensionality on turbulent boundary-layer structure. *AIAA Journal*, 33:2020–2025, 1995

[2] J. Jeong, F. Hussain, W. Schoppa, and J. Kim. Coherent structures near the wall in a turbulent channel flow. *J. Fluid Mech.*, 332:185–214, 1997.

[3] J. Jeong and F. Hussain. On the identification of a vortex. *J. Fluid Mech.*, 285:69-94, 1995.

[4] H. S. Kang, H. Choi, and J. Y. Yoo. On the modification of the near-wall coherent structure in a three-dimensional turbulent boundary layer on a free rotating disk. *Phys. Fluids*, 10:2315–2322, 1998.

[5] H. S. Littell and J. K. Eaton. Turbulence characteristics of the boundary layer on a rotating disk. *J. Fluid Mech.*, 266:175–207, 1994.

[6] M. Lygren and H. I. Andersson. Turbulent flow between a rotating and a stationary disk. *In preparation.*

ADVANCES IN TURBULENCE VIII
Proceedings of the Eighth European Turbulence Conference
C. Dopazo et al. (Eds.)
© CIMNE, Barcelona 2000

Triadic interaction of vorticity, strain rate, and scalar gradient in stably stratified homogeneous sheared turbulence

K.K. Nomura and P.J. Diamessis

Department of Mechanical and Aerospace Engineering
University of California, San Diego, La Jolla, CA 92093-0411, U.S.A.

Contact e-mail: knomura@ucsd.edu

1 Introduction

An important aspect of turbulence is vortex stretching, that is, the interaction of vorticity ω and rate-of-strain S. Direct numerical simulations (DNS) of homogeneous turbulence have revealed various properties of ω and S and the presence of distinct small-scale structure (see, e.g., review in [1]). The dynamic interaction of ω and S is effectively described in the principal strain basis [1] which distinguishes vortex stretching and rotation of the principal axes of S. In the case of homogeneous shear [2], these mechanisms are influenced by the imposed mean ω and S. As a consequence, the spatial orientation of ω, principal axes of S, and associated structures (Fig. 2a) may exhibit distinct preferences. In the presence of stratification (mean density gradient), ω and S will influence the behavior of the fluctuating density gradient, $\boldsymbol{G} \equiv \nabla\rho'$. When buoyancy effects are significant, the fluid density ρ is an active scalar and the dynamics of $\boldsymbol{G}$ will feedback on ω and S. Previous DNS studies [3] of stratified homogeneous shear flow considered the structure of ω and showed increasingly horizontal ω with increasing stratification. In the case of strong (supercritical) stratification, the associated vortex structures collapse towards the horizontal plane (Fig. 2b). In order to provide a more complete description of the behavior of ω in stratified turbulence, we investigate the fully coupled triadic interaction between ω, S, and $\boldsymbol{G}$. Detailed results of our work are presented elsewhere [4]. Here, we present some further results and a general description of the interaction.

2 Analysis and Discussion

Results from DNS of homogeneous sheared turbulence with uniform stable stratification [4] are used in this analysis. In these flows, the significance of strat-

ification, $\overline{G}_3 = d\overline{\rho}/dx_3$, is characterized by the gradient Richardson number, $Ri = N^2/S^2 = (-g\,\overline{G}_3\,/\,\rho_0)/S^2$, where N is the Brunt-Vaisala frequency, S is the mean shear, and g is the acceleration of gravity. Here, we present results from two simulations, one with no buoyancy, i.e., $g = 0$ ($Ri = 0$, NB), and one with strong buoyancy ($Ri = 1$, HB). In both flows, the initial microscale Reynolds number is $Re_{\lambda_\circ} = 24$ and the shear number is $Sh_\circ = 3.2$. In order to effectively study the complex dynamics, conditional sampling based on the invariants of the velocity gradient tensor is employed. In particular, regions of high-amplitude positive ($II > 0$) and negative ($II < 0$) second invariant, where $II = (\boldsymbol{\omega}^2/2 - \mathsf{S}^2)/2$, are considered. This assists in distinguishing various mechanisms by considering the relative significance of rotation versus strain.

The dynamics of $\boldsymbol{\omega}$, S, and $\boldsymbol{G}$ are described by their evolution equations which are derived from the Navier-Stokes (with Boussinesq approximation) and scalar transport equations (written here without diffusion terms for brevity):

$$\frac{D\omega_i}{Dt} = \underbrace{S_{ik}\,\omega_k}_{\text{vortex stretching}} \quad \underbrace{-\tfrac{g}{\rho_0}\epsilon_{ij3}\,G_j}_{\text{baroclinic torque}} \quad , \tag{1}$$

$$\frac{DS_{ij}}{Dt} = -S_{ik}S_{kj} \underbrace{-\tfrac{1}{4}(\omega_i\omega_j - \delta_{ij}\omega_k\omega_k)}_{\text{strain gen./rot.}} - \tfrac{1}{\rho}\tfrac{\partial^2 p}{\partial x_i \partial x_j} \underbrace{-\tfrac{g}{2\rho_0}\,(G_j\,\delta_{i3} + G_i\,\delta_{j3})}_{\text{differential acceleration}} \quad , \tag{2}$$

$$\frac{DG_i}{Dt} = \underbrace{-\,S_{ik}\,G_k}_{\text{straining}} \quad \underbrace{+\tfrac{1}{2}\,\varepsilon_{ijk}\,\omega_j\,G_k}_{\text{rotation}} \quad . \tag{3}$$

Interaction between $\boldsymbol{\omega}$ and S in (1)-(2) includes vortex stretching (VS) and strain generation and axes rotation (SR). Influence of $\boldsymbol{\omega}$ and S on $\boldsymbol{G}$ is through gradient amplification/reorientation by S (GS) and reorientation by $\boldsymbol{\omega}$ (GR) as described in (3). In the presence of buoyancy, there is direct feedback of $\boldsymbol{G}$ on $\boldsymbol{\omega}$ through baroclinic torque (BT) and on S through differential acceleration (DA).

The early development ($St < 1$) of the NB and HB flows is similar. Since there is no initial $\boldsymbol{G}$ imposed, interaction between the flow and density fields is initiated by the generation of $\boldsymbol{G}$. In rotation-dominated ($II > 0$) regions, $\boldsymbol{G}$ is generated primarily by rotation of $\overline{G}_3$ by $\boldsymbol{\omega}$ (GR). Through this mechanism, the correlations $\langle\omega_2\,G_1\rangle < 0$ and $\langle\omega_1\,G_2\rangle > 0$ are established which, as described by (3), promote $+G_3$. The positive correlation between ω_1 and G_2 at early times is reflected in the conditional expectation $\langle\omega_1|_{G_2}\rangle$ shown in Figs. 1a,b. In the HB flow, BT is generated which is of *opposite sign* to the $\boldsymbol{\omega}$ which gave rise to the corresponding G_i component. This tends to reverse the correlations between ω_i and G_i, as indicated in Fig. 1b, and effectively attenuates the magnitudes of ω_1 and ω_2. Furthermore, the presence of $\pm G_3$ components will promote $\mp S_{33}$ through DA (2) which represents, e.g., enhancement of vertical compressive straining due to high density fluid occuring over low density fluid (Fig. 2c). DA is also observed in strain-dominated $II < 0$ regions as will be discussed below. In the case of $II > 0$ regions, due to strong GR, significant $+G_3$ occurs.

The enhanced $S_{33} < 0$ in these regions results in an enhanced attenuation of ω_3 by vortex contraction. The effects of shear tend to maintain horizontal $\boldsymbol{\omega}$ and the net result is an overall predominance of horizontal $\boldsymbol{\omega}$ in the HB flow. In strain-dominated ($II < 0$) regions of NB and HB, $\boldsymbol{G}$ is initially generated through GS which establishes a positive correlation between S_{33} and G_3 at early time (Figs. 1d,e). In the HB flow, the effect of DA is to counteract the existing strain, that is, $+G_3$ promotes $-S_{33}$ and $-G_3$ promotes $+S_{33}$, which tends to reverse the correlation (Fig. 1e). The response of GS is a positive feedback in the former and negative in the latter. In addition, since $|G|$ is significant in high strain regions, BT may be significant and generate $\boldsymbol{\omega}^2$.

Overall, the triadic interaction can be considered in terms of the direct coupling of mechanism pairs (underbraced terms in (1)-(2)) and influential secondary effects. Interaction of $\boldsymbol{\omega}$ and $\boldsymbol{G}$ involves an inherent negative feedback between BT and GR. Probability distributions of the BT term in the $\boldsymbol{\omega}^2$ equation, $-\epsilon_{ij3}\omega_i G_j$ (Fig. 1c), show a tendency for negative values in $II > 0$ regions, i.e., baroclinic torque acts as a sink for $\boldsymbol{\omega}^2$. Interaction of S and $\boldsymbol{G}$ is characterized by a predominantly negative feedback between DA and GS. Probability distributions of the DA term in the S^2 equation, $-S_{ij}(G_j\,\delta_{i3} + G_i\,\delta_{j3})$ (Fig. 1f), show a tendency towards negative values in $II < 0$ regions, i.e., differential acceleration acts as a sink for S^2. The interaction of $\boldsymbol{\omega}$ and S is characterized by the coupling of VS and SR [1, 2]. These mechanisms are weakened and/or impeded as a result of BT, DA, and the associated attenuation of $\boldsymbol{\omega}$ and S [4].

The physical implications of these dynamics are evident in the small-scale structure of the flow. In the NB flow and early times in HB, high-amplitude $II > 0$ regions are characterized by tube-like spatial structures (Fig. 2a). These structures are responsible for significant overturning motion, i.e., they tend to wrap around isopycnal surfaces establishing significant $+G_3$ in the core of the vortex (Fig. 2c). With strong buoyancy (HB), the associated dynamics lead to a predominance of horizontal $\boldsymbol{\omega}$ with diminished amplitude. In general, the nature of the flow differs and high-amplitude events are characterized by comparable $\boldsymbol{\omega}^2$ and S^2 ($II \sim 0$) which tend to form sheet-like spatial structure [4]. These effects manifest themselves as *collapsed* or flattened vortex structures (Fig. 2b). The weakened structures, in turn, exhibit reduced overturning motion and wrapping of the isopycnal surfaces.

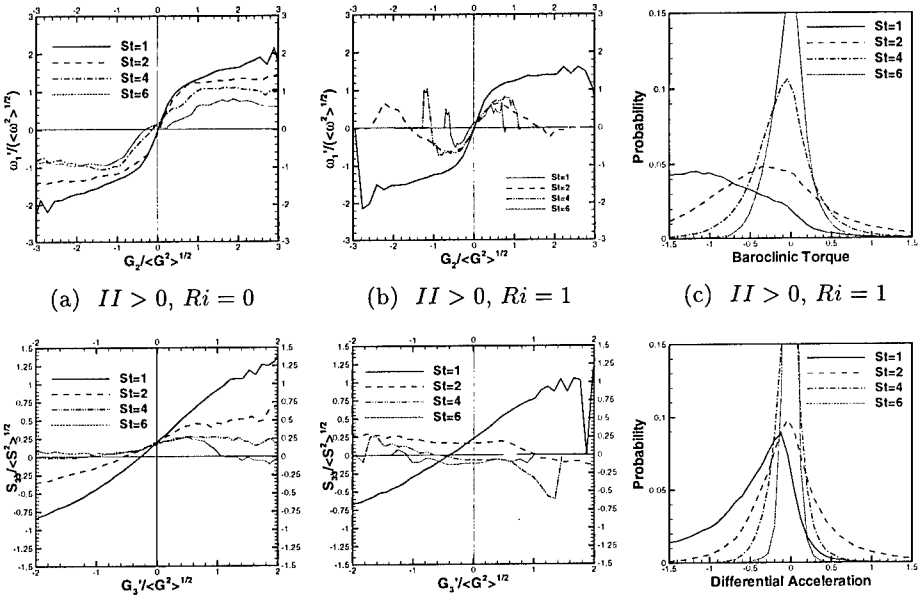
References

[1] K. K. Nomura and G. K. Post, The structure and dynamics of vorticity and rate of strain in incompressible homogeneous turbulence. J. Fluid Mech. **377**, 65 (1998).

[2] K. K. Nomura and P. J. Diamessis, The interaction of vorticity and rate of strain in homogeneous sheared turbulence. To appear in Phys. Fluids.

[3] T. Gerz, in *Evolution of coherent vortex structures in sheared and stratified homogeneously turbulent flows* (Eighth Symposium on Turbulent Shear Flows, Munich, Germany, 1991).

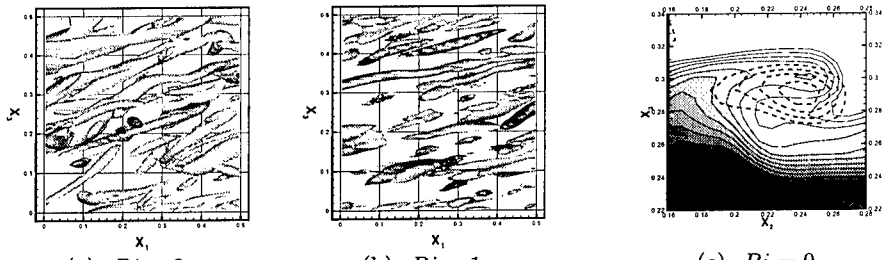
[4] P. J. Diamessis and K. K. Nomura, Interaction of vorticity, rate of strain, and scalar gradient in stratified homogeneous sheared turbulence. To appear in Phys. Fluids.



(a) $II > 0$, $Ri = 0$ (b) $II > 0$, $Ri = 1$ (c) $II > 0$, $Ri = 1$

(d) $II < 0$, $Ri = 0$ (e) $II < 0$, $Ri = 1$ (f) $II < 0$, $Ri = 1$

Figure 1: Top row - $II > 0$ regions: (a),(b) expected value of ω_1 conditioned on G_2, (c) probability distributions of baroclinic torque term in ω^2 equation. Bottom row - $II < 0$ regions: (d),(e) expected value of S_{33} conditioned on G_3, (f) probability distributions of differential acceleration term in S^2 equation.



(a) $Ri = 0$ (b) $Ri = 1$ (c) $Ri = 0$

Figure 2: (a),(b) Three-dimensional visualizations (64^3 subdomain of computational grid) of high-amplitude rotation-dominated ($II > 0$) regions in NB and HB flows at time $St = 6$ (side view shows streamwise (x_1) and vertical (x_3) directions). (c) Close-up of cross-section in x_2-x_3 plane shows instantaneous density contours (dark=high ρ, light=low ρ) in vicinity of vortex tube (dotted lines are contours of $II > 0$).

XXII

Modelling

ADVANCES IN TURBULENCE VIII
Proceedings of the Eighth European Turbulence Conference
C. Dopazo et al. (Eds.)
© CIMNE, Barcelona 2000

Spectral reduction: a statistical description of turbulence

John C. Bowman[1], B. A. Shadwick[2] and P. J. Morrison[3]

[1]Department of Mathematical Sciences
University of Alberta, Edmonton, Alberta T6G 2G1 Canada
[2]The Institute for Advanced Physics, Conifer C0 80433-7727 USA
[3]Department of Physics
The University of Texas at Austin, Austin TX 78712-1081 USA

Contact e-mail: bowman@math.ualberta.ca

1 Introduction

Over the past forty years, much effort has been devoted to the development of a satisfactory statistical theory of turbulence. For example, statistical closures were developed in an attempt to find closed expressions for the unknown triplet correlation function that arises upon averaging the Navier–Stokes equation. Familiar examples include Kraichnan's direct-interaction approximation [1, 2] and Lagrangian-history direct-interaction approximation [3]. Unfortunately, there is considerable arbitrariness in the formulation of statistical closures. Moreover, it is generally believed that low-order statistical theories are not capable of capturing the effects of coherent structures [4, 5]. But probably the greatest weakness of these methods is that there exists neither an error estimate nor a control parameter that can be varied to increase the accuracy of the solution.

Recently, a method called spectral reduction has been proposed [6] for calculating statistical moments of turbulent quantities by introducing a coarse-graining in Fourier space. A notable feature of this model is the existence of a control parameter (bin size) that can be varied to increase the accuracy of a solution. The method exploits the fact that statistical moments are much smoother functions of wave number than are the underlying stochastic amplitudes. Collections of Fourier amplitudes are represented by nonuniformly spaced sample modes that interact via enhanced coupling coefficients. By assigning most of these sample modes to the scales of greatest physical interest, the technique makes optimal use of limited computational resources. The approximation reduces to the exact Navier–Stokes equation as the number of fundamental wave numbers associated with each sample mode tends to one. Even at large values of this parameter, the statistics of the full dynamics may be accurately recovered from the time-averaged predictions of the theory.

2 Spectral reduction

We restrict our attention to homogeneous and isotropic incompressible turbulence in two dimensions, for which the Fourier-transformed Navier–Stokes vorticity equation takes the form

$$\frac{\partial \omega_{\mathbf{k}}}{\partial t} + \nu_{\mathbf{k}}\omega_{\mathbf{k}} = \int_{\mathcal{D}} d\mathbf{p} \int_{\mathcal{D}} d\mathbf{q}\, \frac{\epsilon_{\mathbf{kpq}}}{q^2}\omega^*_{\mathbf{p}}\omega^*_{\mathbf{q}}. \tag{1}$$

Here $\nu_{\mathbf{k}}$ models time-independent linear dissipation and the interaction coefficient $\epsilon_{\mathbf{kpq}} \doteq (\hat{z}\cdot\mathbf{p}\times\mathbf{q})\,\delta(\mathbf{k}+\mathbf{p}+\mathbf{q})$ is antisymmetric under permutation of any two indices. As a consequence of the antisymmetry of $\epsilon_{\mathbf{kpq}}$, Eq. (1) conserves the energy $\frac{1}{2}\int_{\mathcal{D}} d\mathbf{k}\,|\omega_{\mathbf{k}}|^2/k^2$ and enstrophy $\frac{1}{2}\int_{\mathcal{D}} d\mathbf{k}\,|\omega_{\mathbf{k}}|^2$ in the inviscid limit $\nu_{\mathbf{k}} = 0$.

We introduce an arbitrary coarse-grained grid on $\mathcal{D}$, to which we associate new variables $\Omega_{\mathbf{K}} \doteq \Delta_{\mathbf{K}}^{-1}\int_{\mathbf{K}} \omega_{\mathbf{k}}\, d\mathbf{k}$, where $\Delta_{\mathbf{K}}$ is the area of bin $\mathbf{K}$. The exact evolution of $\Omega_{\mathbf{K}}$ is given by

$$\frac{\partial \Omega_{\mathbf{K}}}{\partial t} + \langle \nu_{\mathbf{k}}\omega_{\mathbf{k}}\rangle_{\mathbf{K}} = \sum_{\mathbf{P},\mathbf{Q}} \Delta_{\mathbf{P}}\Delta_{\mathbf{Q}} \left\langle \frac{\epsilon_{\mathbf{kpq}}}{q^2}\omega^*_{\mathbf{p}}\omega^*_{\mathbf{q}} \right\rangle_{\mathbf{KPQ}}, \tag{2}$$

where $\langle\cdot\rangle_{\mathbf{K}}$ denotes a bin average and the operator

$$\langle f\rangle_{\mathbf{KPQ}} \doteq \frac{1}{\Delta_{\mathbf{K}}\Delta_{\mathbf{P}}\Delta_{\mathbf{Q}}} \int_{\mathbf{K}} d\mathbf{k} \int_{\mathbf{P}} d\mathbf{p} \int_{\mathbf{Q}} d\mathbf{q}\, f, \tag{3}$$

depends only on the bin geometry. The geometric factors $\langle f\rangle_{\mathbf{KPQ}}$ can be efficiently computed using a combination of analytical and numerical methods[7, 8, 9]; being independent of both time and initial conditions, they need only be computed once for each new wave-number partition. The reality condition $\Omega_{\mathbf{K}} = \Omega^*_{-\mathbf{K}}$, where $-\mathbf{K}$ denotes the inversion of bin $\mathbf{K}$ through the origin, will be respected for partitions that possess inversion symmetry.

Equation (2) is unfortunately not closed. If $\omega_{\mathbf{k}}$ were naively approximated by its bin-averaged value $\Omega_{\mathbf{K}}$, one would obtain

$$\frac{\partial \Omega_{\mathbf{K}}}{\partial t} + \langle \nu_{\mathbf{k}}\rangle_{\mathbf{K}}\,\Omega_{\mathbf{K}} = \sum_{\mathbf{P},\mathbf{Q}} \Delta_{\mathbf{P}}\Delta_{\mathbf{Q}} \left\langle \frac{\epsilon_{\mathbf{kpq}}}{q^2} \right\rangle_{\mathbf{KPQ}} \Omega^*_{\mathbf{P}}\Omega^*_{\mathbf{Q}}. \tag{4}$$

In the inviscid limit, Eq. (4) conserves the coarse-grained enstrophy $\frac{1}{2}\sum_{\mathbf{K}} |\Omega_{\mathbf{K}}|^2\Delta_{\mathbf{K}}$ since $\langle \epsilon_{\mathbf{kpq}}/q^2\rangle_{\mathbf{KPQ}}$ is antisymmetric in $\mathbf{K} \leftrightarrow \mathbf{P}$. However, the coarse-grained energy $\frac{1}{2}\sum_{\mathbf{K}} |\Omega_{\mathbf{K}}|^2\Delta_{\mathbf{K}}/K^2$ is not conserved since $\langle \epsilon_{\mathbf{kpq}}/q^2\rangle_{\mathbf{KPQ}}/K^2$ is not antisymmetric in $\mathbf{K} \leftrightarrow \mathbf{Q}$ (here K denotes the magnitude of some characteristic wave number in bin $\mathbf{K}$). However, both of these desired symmetries can be reinstated by replacing the factor $\langle \epsilon_{\mathbf{kpq}}/q^2\rangle_{\mathbf{KPQ}}$ in Eq. (4) with the slightly modified coefficient $\langle \epsilon_{\mathbf{kpq}}\rangle_{\mathbf{KPQ}}/Q^2$. The relative error introduced by this modification is

negligible in the limit of small bin size, being on the order of the squared relative variation in the wavenumber magnitude over a bin. The result,

$$\frac{\partial \Omega_{\mathbf{K}}}{\partial t} + \langle \nu_{\mathbf{k}} \rangle_{\mathbf{K}} \, \Omega_{\mathbf{K}} = \sum_{\mathbf{P},\mathbf{Q}} \Delta_{\mathbf{P}} \Delta_{\mathbf{Q}} \frac{\langle \epsilon_{\mathbf{kpq}} \rangle_{\mathbf{KPQ}}}{Q^2} \Omega^*_{\mathbf{P}} \Omega^*_{\mathbf{Q}}, \tag{5}$$

is a more acceptable alternative as a closure of Eq. (2) since it conserves both energy and enstrophy.

The time-averaged (or ensemble-averaged) moments of Eq. (5) satisfy equations that closely approximate the equations governing the exact bin-averaged statistics. A time average (denoted by an over-bar) of the bin-averaged enstrophy equation derived from Eq. (1) leads to

$$\frac{1}{2} \overline{\frac{\partial \left\langle |\omega_{\mathbf{k}}|^2 \right\rangle_{\mathbf{K}}}{\partial t}} + \mathrm{Re} \left\langle \nu_{\mathbf{k}} \overline{|\omega_{\mathbf{k}}|^2} \right\rangle_{\mathbf{K}} = \mathrm{Re} \sum_{\mathbf{P},\mathbf{Q}} \Delta_{\mathbf{P}} \Delta_{\mathbf{Q}} \left\langle \frac{\epsilon_{\mathbf{kpq}}}{q^2} \overline{\omega^*_{\mathbf{k}} \omega^*_{\mathbf{p}} \omega^*_{\mathbf{q}}} \right\rangle_{\mathbf{KPQ}}. \tag{6}$$

If the true vorticity is a continuous function of wave number, there will exist a wave number κ in bin $\mathbf{K}$ such that $\Omega_{\mathbf{K}} = \omega_\kappa$. Furthermore, time-averaged quantities such as $\overline{|\omega_{\mathbf{k}}|^2}$ are generally smooth functions of the wave number $\mathbf{k}$. We thus deduce that $\overline{|\Omega_{\mathbf{K}}|^2} = \overline{|\omega_\kappa|^2} \approx \overline{|\omega_{\mathbf{k}}|^2}$ for all $\mathbf{k}$ in bin $\mathbf{K}$. Similarly, the triplet correlation $\overline{\omega^*_{\mathbf{k}} \omega^*_{\mathbf{p}} \omega^*_{\mathbf{q}}}$ is a smooth function of $\mathbf{k}$, $\mathbf{p}$, $\mathbf{q}$ when restricted to the surface defined by the triad condition $\mathbf{k} + \mathbf{p} + \mathbf{q} = \mathbf{0}$.

To good accuracy the statistical averages in Eq. (6) may therefore be evaluated at the characteristic wave numbers $\mathbf{K}$, $\mathbf{P}$, $\mathbf{Q}$ of each bin. Hence, to the extent that the wave-number magnitudes vary slowly over a bin, Eq. (6) may be reduced to the (nonlinearly conservative) approximation

$$\frac{1}{2} \overline{\frac{\partial |\Omega_{\mathbf{K}}|^2}{\partial t}} + \mathrm{Re} \, \langle \nu_{\mathbf{k}} \rangle_{\mathbf{K}} \, \overline{|\Omega_{\mathbf{K}}|^2} = \mathrm{Re} \sum_{\mathbf{P},\mathbf{Q}} \Delta_{\mathbf{P}} \Delta_{\mathbf{Q}} \frac{\langle \epsilon_{\mathbf{kpq}} \rangle_{\mathbf{KPQ}}}{Q^2} \overline{\Omega^*_{\mathbf{K}} \Omega^*_{\mathbf{P}} \Omega^*_{\mathbf{Q}}}, \tag{7}$$

which is precisely the evolution equation for the time-averaged enstrophy obtained from Eq. (5). Similar arguments for the higher-order statistical moments can also be made, suggesting that spectral reduction can indeed provide an accurate statistical description of turbulence, even when each bin contains many statistically independent modes. As the partition is refined, one expects the solutions of Eq. (7) to converge to the those of Eq. (6).

In Fig. 1, we demonstrate the excellent agreement obtained with forced-dissipative pseudospectral simulations for a two-dimensional fluid containing coherent structures. We also compare to the predictions of the realizable test field model (RTFM) [9]. In Fig. 2 we illustrate the scaling with distance r of the angular average $S_{10}(r)$ of the tenth moment of velocity increments $\overline{|\mathbf{v}(\mathbf{r}) - \mathbf{v}(\mathbf{0})|^{10}}$.

Spectral reduction has been used to confirm the existence of logarithmic corrections to the high-order structure functions in the two-dimensional enstrophy cascade. The inviscid version of the model has also been shown to satisfy a Liouville theorem and to yield statistical equipartition solutions [6].

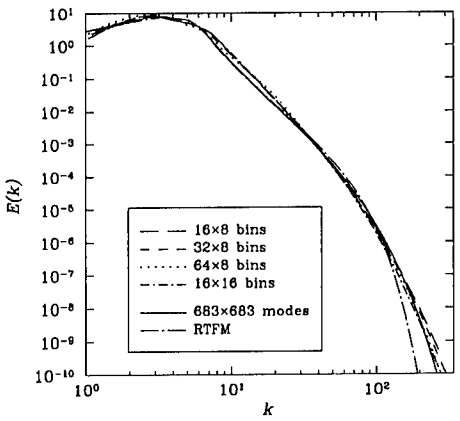


Figure 1: Comparison of the energy spectra obtained with several (radial × angular) wave-number partitions, the RTFM, and a 683×683 dealiased pseudospectral simulation.

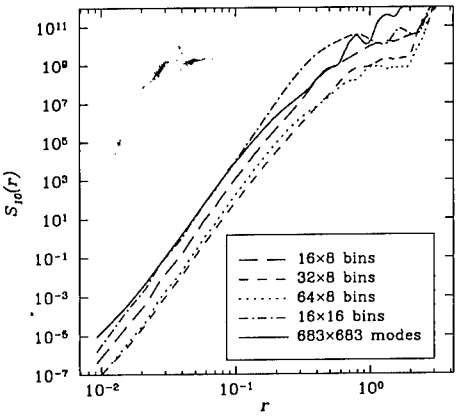


Figure 2: Angle-averaged structure function $S_{10}(r)$.

3 Conclusions

Spectral reduction appears to be a promising candidate as a statistical description of turbulence. We propose that it could be used to assess the effect of various dissipation mechanisms in large-eddy simulations, as a subgrid model, or even as a substitute for full simulation of high-Reynolds number turbulence.

References

[1] R. H. Kraichnan, J. Fluid Mech. **5**, 497 (1959).

[2] R. H. Kraichnan, J. Math. Phys. **2**, 124 (1961).

[3] R. H. Kraichnan, Phys. Fluids **8**, 575 (1965).

[4] J. C. McWilliams, J. Fluid Mech. **146**, 21 (1984).

[5] J. R. Herring, J. Fluid Mech. **153**, 229 (1985).

[6] J. C. Bowman, B. A. Shadwick, and P. J. Morrison, Phys. Rev. Lett. **83**, 5491 (1999).

[7] J. C. Bowman, Ph.D. thesis, Princeton University, Princeton NJ, USA, 1992.

[8] J. C. Bowman, J. Sci. Comput. **11**, 343 (1996).

[9] J. C. Bowman and J. A. Krommes, Phys. Plasmas **4**, 3895 (1997).

ADVANCES IN TURBULENCE VIII
Proceedings of the Eighth European Turbulence Conference
C. Dopazo et al. (Eds.)
© CIMNE, Barcelona 2000

A spectral closure applied to anisotropic inhomogeneous turbulence

H. Touil, J.P. Bertoglio and S. Parpais
Laboratoire de Mécanique des Fluides et d'Acoustique, UMR CNRS 5509
Ecole Centrale de Lyon, 36 avenue Guy de Collongue, 69 130 Ecully, France.

Contact e-mail: touil@mecaflu.ec-lyon.fr

1 Introduction

Two-point statistical closures for homogeneous turbulence were proposed several decades ago and their formal extensions to inhomogeneous fields were considered as early as in the 70's (Kraichnan [1]). However, very little applications of two-point theories to flows of real practical interest exist, the prediction of these flows remaining essentially relying on the use of classical one-point models, such as $k-\varepsilon$ or second order moment closures. This situation essentially results from the complexity of the formulation of two-point models for inhomogeneous turbulence. Indeed, before being applied to real flows at an affordable computational cost, two-point closures have to be simplified. The approach followed in the present paper is to propose a model that is simple enough for applications to wall bounded flows, but that retains the advantage of two-point closures that directly take into account an information on different turbulent length scales, up to the Kolmogorov scale.

A first version of the model was proposed in Parpais and Bertoglio [2]. The basic quantity in this version was the turbulent kinetic energy spectrum $E(\vec{X}, K, t)$ and consequently, although a spectral information was retained, the anisotropic properties of turbulence were only grossly accounted for. In the present paper the approach is extended to a tensorial description of the spectra. Examples of results show that the model leads to satisfactory predictions of flows with separation and reattachement, and provides a detailed spectral information.

2 The model

The basic quantity in the model is the spectrum φ_{ij} defined as the average over the directions of wave-vector $\vec{K}$ of the spectral tensor Φ_{ij}:

$$\varphi_{ij}(\vec{X}, K, t) = \int_{\Sigma(K)} \Phi_{ij}(\vec{X}, \vec{K}, t)\, d\Sigma$$

in which Φ_{ij} is the Fourier transform of the velocity correlation at two points:

$$\Phi_{ij}(\vec{X},\vec{K},t) = FT_{\vec{r}}(< u_i(\vec{X}-\vec{r}/2,t).u_j(\vec{X}+\vec{r}/2,t) >)$$

The equation for φ_{ij} reads:

$$\left(\frac{\partial}{\partial t}+\overline{U}_l\frac{\partial}{\partial X_l}\right)\varphi_{ij}(\vec{X},K,t) = \left(-2\nu K^2+\frac{\nu}{2}\nabla^2\right)\varphi_{ij}(\vec{X},K,t) - \left(\frac{\partial \overline{U}_i(\vec{X},t)}{\partial X_n}\varphi_{nj}(\vec{X},K,t)+\frac{\partial \overline{U}_j(\vec{X},t)}{\partial X_n}\varphi_{in}(\vec{X},K,t)\right) + p^L_{ij}(\vec{X},K,t)+t_{ij}(\vec{X},K,t)+D_{ij}(\vec{X},K,t)$$

in which the first term of the right hand side is the viscous contribution, including the dissipation, which can be evaluated exactly. The second term is also a term which is not requiring a closure (production term). The other terms, p^L_{ij}, t_{ij} and D_{ij}, respectively stand for the rapid part of the pressure-strain spectrum, the spectral transfer and the inhomogeneous transport term. These terms are closed introducing assumptions. One of the basic ingredients in the model is the use of the EDQNM theory to express the trace of the non-linear transfer term accounting for the energy cascade to the small scales (Orszag 1970 [3]). The rapid part of the pressure-strain term is expressed using invariant theory [4, 5]:

$$\begin{aligned} p^L_{ij}(\vec{X},K,t) = c_b & \left(\frac{\partial \overline{U}_i}{\partial X_n}\varphi_{nj}(\vec{X},K,t)+\frac{\partial \overline{U}_j}{\partial X_n}\varphi_{in}(\vec{X},K,t)-\frac{2}{3}\delta_{ij}\frac{\partial \overline{U}_m}{\partial X_n}\varphi_{mn}(\vec{X},K,t)\right) \\ +(8c_b-6) & \left(\frac{\partial \overline{U}_n}{\partial X_i}\varphi_{nj}(\vec{X},K,t)+\frac{\partial \overline{U}_n}{\partial X_j}\varphi_{in}(\vec{X},K,t)-\frac{2}{3}\delta_{ij}\frac{\partial \overline{U}_m}{\partial X_n}\varphi_{mn}(\vec{X},K,t)\right) \\ +(\tfrac{11}{5}-3c_b) & \left(\frac{\partial \overline{U}_i}{\partial X_j}+\frac{\partial \overline{U}_j}{\partial X_i}\right)\varphi_{nn}(\vec{X},K,t) \end{aligned}$$

The inhomogeneous transport term is modeled via a diffusive form [5]:

$$D_{ij}(\vec{X},K,t) = \frac{\partial}{\partial X_l}\left(\nu_{ts}(\vec{X},t)\frac{\partial \varphi_{ij}}{\partial X_l}(\vec{X},K,t)\right)$$

The wall effect is modeled, as in [2], by introducing a spectral cut-off at large scales.

Finally, the Reynolds averaged Navier-Stokes equation is closed by expressing the Reynolds stress as: $\overline{u_iu_j} = \int_0^\infty \varphi_{ij}(K,\vec{X})\,dK$.

3 Results

When the model is applied to homogeneous turbulence submitted to a uniform shear, the turbulent kinetic energy is found to increase exponentially with time, in agreement with experimental data [6]. Satisfactory results are also obtained



Figure 1: $\overline{u_1^2}$ and mean streamlines for the ERCOFTAC diffuser test case.

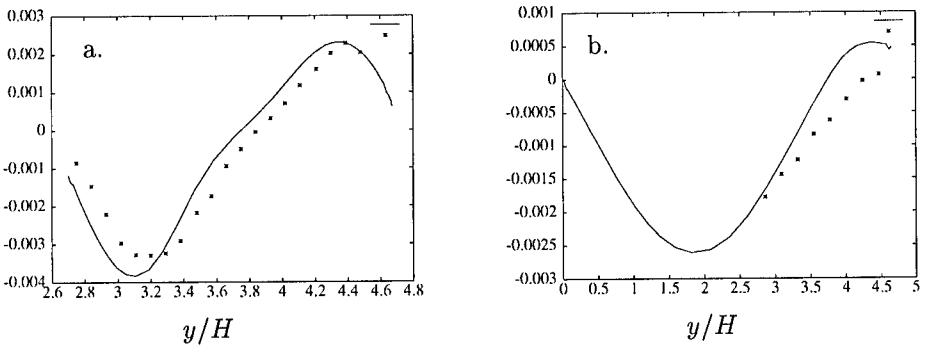


Figure 2: $\overline{uv}$ at $x = 6H$(a) and $x = 33H$(b): – present model, * experiment.

in the case of a plane channel flow and the flow over a backward facing step. In figure 1, results obtained in the case of an asymmetric diffuser are plotted. Comparisons with experiment [7], presented in [8], show that separation and reattachement are correctly predicted. Figure 1 shows Reynolds stress profiles in two sections respectively corresponding to the beginning and the end of the recirculation zone. The model was also applied to the flow around an airfoil with an angle of attack $\alpha = 13^o$ at which separation is experimentally detected (figure 3). In figure 4b, kinetic energy spectra along a mean streamline are plotted. It is observed that the compensated spectra are found to collapse into a single curve in the wake region. These spectra are however not corresponding to an equilibrium Kolmogorov spectrum, as appears when compared to the spectrum obtained in the case of a uniform shear flow at the same Reynolds number (figure 4a).

References

[1] R. H. Kraichnan. Test Field Model for inhomogeneous tubulence. *J. Fluid Mech.*, 56(2):287-304, 1972.

[2] S. Parpais and J. P. Bertoglio. A spectral closure for inhomogeneous turbulence applied to turbulent confined flow. *ETC VI*, Siena, 1996.

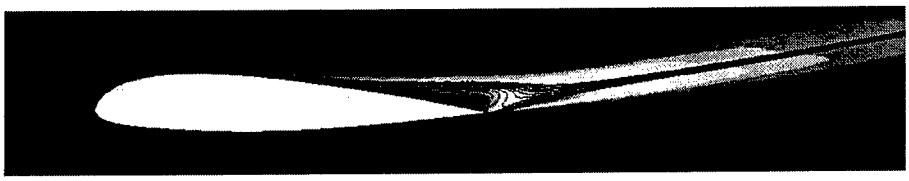


Figure 3: Turbulent kinetic energy and mean streamlines; F2A airfoil.

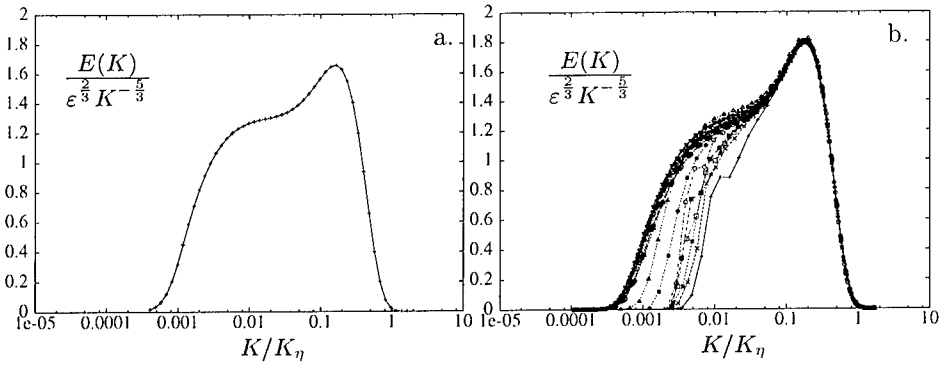


Figure 4: Compensated kinetic energy spectra: comparison between the airfoil wake (b) and homogeneous shear flow (a) at $Re_\lambda = 150$.

[3] S. Orszag. Analytical theories of turbulence. *J. Fluid Mech.*, 41(2):363–386, 1970.

[4] C. Cambon, D. Jeandel, and J. Mathieu. Spectral modeling of homogeneous non isotropic turbulence. *J. Fluid Mech.*, 104:247-262, 1981.

[5] D. C. Besnard, F. H. Harlow, R. M. Rauenzahn, and C. Zemach. Spectral transport model for inhomogeneous turbulence. *Technical Report LA-11821-MS*, Los Alamos National Laboratory, 1990.

[6] S. Tavoularis and U. Karnik. Further experiments on the evolution of turbulent stresses and scales in uniformly sheared turbulence. *J. Fluid Mech.*, 204:457-478, 1989

[7] C. U. Buice and J. K. Eaton Experimental investigation of flow through an asymmetric plane diffuser. *Report No. TSD-107. Thermosciences Division*, Dep. of Mech. Eng., Stanford Univ., 1997.

[8] H. Touil, S. Parpais and J. P. Bertoglio. Flow through an asymmetric plane diffuser. *Ercoftac/Iahr/Cost Workshop on Ref.Turb.Model.*, Report 127, Helsinki Univ. of Tech.,1999.

ADVANCES IN TURBULENCE VIII
Proceedings of the Eighth European Turbulence Conference
C. Dopazo et al. (Eds.)
© CIMNE, Barcelona 2000

A numerical algorithm for efficiently solving spectral closure equations

T. Gotoh[1] and Y. Kaneda[2]

[1]Department of Systems Engineering
Nagoya Institute of Technology
Showa-ku, Nagoya 466-8555, Japan
[2]Department of Computational Science and Engineering
Graduate School of Engineering, Nagoya University
Chikusa-ku, Nagoya, 464-8603, Japan

Contact e-mail: gotoh@system.nitech.ac.jp

1 Introduction

Lagrangian renormalized approximation (LRA) is one of the spectral closure theories of turbulence. It is derived from the Navier-Stokes (NS) equation in a fully systematic way without introducing any ad hoc parameter, and keeps various desirable properties of the exact dynamics[1]. The LRA yields the Kolmogorov spectrum $E(k) = K\bar{\epsilon}^{2/3}k^{-5/3}$ with $K = 1.72$[2], the frequency spectrum $\Phi_L(\omega) = C_L\bar{\epsilon}\omega^{-2}$ with $C_L = 0.94$[4] in the inertial subrange, and so on in good agreement with the experiments and numerical simulations [5, 6, 7, 8, 9]. However, as has been widely recognized, it is not easy to solve the equations of the closure theories. From the computational point of view, the major obstacles lie in (1) the evaluation of the convolution sum over the wavevectors arising from the nonlinear term of the NS equation and (2) that of the time integral over the Lagrangian history of fluid particle, and (3) the high-dimensionality for inhomogeneous case[5, 7, 10]. In order to extract further knowledge of turbulence from the LRA, we need development of efficient methods to solve the spectral closure equations numerically.

2 LRA equations for two-dimensional turbulence

The LRA gives a set of closed evolution equations for the Lagrangian velocity correlation and response functions[1]. For homogeneous turbulence in two dimensions, they are of the form

$$Q_{ij}(\boldsymbol{k},t,s) = P_{ij}(\boldsymbol{k})Q(\boldsymbol{k},t,s), \quad G_{ij}(\boldsymbol{k},t,s) = P_{ij}(\boldsymbol{k})G(\boldsymbol{k},t,s), \qquad (1)$$

in the wavevector space, where $P_{ij}(\boldsymbol{k}) = \delta_{ij} - k_i k_j / k^2$ is the projection operator.

One of the characteristics of the LRA is that the fluctuation dissipation relation for the Lagrangian velocity correlation function holds exactly as

$$Q(\boldsymbol{k}, t, s) = G(\boldsymbol{k}, t, s) Q(\boldsymbol{k}, s, s), \quad t \geq s. \tag{2}$$

A variant of the LRA, called MLRA, is obtained by assuming the Markovianized fluctuation dissipation relation

$$Q(\boldsymbol{k}, t, s) = G(\boldsymbol{k}, t, s) Q(\boldsymbol{k}, t, t), \quad t \geq s. \tag{3}$$

The MLRA satisfies the realizability condition, i.e., the non-negativity of the energy density[5].

3 Simplified MLRA equations

In order to achieve high computational efficiency of the MLRA equations, we simplify the MLRA equations. The simplified MLRA equations may be written in the form

$$\left(\frac{\partial}{\partial t} + 2\kappa k^2 \right) Q(\boldsymbol{k}, t) = D(\boldsymbol{k}, t) + D(-\boldsymbol{k}, t), \tag{4}$$

$$\left(\frac{\partial}{\partial \tau} + \nu k^2 + \mu(\boldsymbol{k}, t)\tau \right) \mathcal{G}(\boldsymbol{k}, t, \tau) = 0, \quad \tau \geq 0, \tag{5}$$

$$\mathcal{G}(\boldsymbol{k}, t, 0) = 1, \tag{6}$$

where $D(\boldsymbol{k}, t)$ is the energy transfer function among the wavevector components arising from the nonlinear term of the NS equation and $\mu(\boldsymbol{k}, t)$ is the nonlinear eddy damping. $D(k, t)$ and $\mu(\boldsymbol{k}, t)$ are functions of Q and $\mathcal{G}$. They are, in general, of the form of time integral of the wavevector convolution sum over the Lagrangian history of fluid particle

$$S(\boldsymbol{k}) = \int_0^t ds \overset{\triangle}{\sum_{\boldsymbol{p},\boldsymbol{q}}} A(\boldsymbol{p}, s) B(\boldsymbol{q}, s) C(\boldsymbol{k}, s), \tag{7}$$

where $S(\boldsymbol{k}, t)$ denotes $D(\boldsymbol{k}, t)$ or $\mu(\boldsymbol{k}, t)$[1, 8].

4 Convolution sum and time integral

For the convolution sum in the wavevector space, a novel method using the fast Fourier transform (FFT) has been developed by the present authors[8]. The sum of (7) is computed by transforming $A(\boldsymbol{p})$ and $B(\boldsymbol{q})$ by FFT, and multiplying them in physical space and again transforming the result, $A(\boldsymbol{x})B(\boldsymbol{x})$, back into the Fourier space.

In order to reduce computational work for the time integral, we have used the Padé approximation for the nonlinear terms[10]. The idea is simple. Let us write (7) as $D(t) = \int_0^t H(t,s)ds$. By expanding H in $\tau = t - s$ as $H(t,\tau) = H_0(t) + H_1(t)\tau + H_2(t)\tau^2 + \cdots$, we seek an approximation to $H(\tau)$ in the form of rational function

$$H(\tau) \approx \frac{D_N(\tau)}{D_M(\tau)} \equiv P_{[N/M]}(\tau), \tag{8}$$

where t is suppressed and $D_M(x)$ is a polynomial function of the order M. Coefficients of the polynomials are so determined that the coefficients of the Taylor expansion of the rational function coincide with those of the original expansion of H up to the order $N + M$[11].

Suppose that the two dimensional wavevector space is discretized by $N_k \times N_k$ grid points, and the number of time steps is T. The present method then requires $O(T(N + M)N_k^2 \log_2 N_k)$ arithmetic operations, which is much smaller than $O(T^2 N_k^6)$ required in the direct method, where N and M are the order of the Padé approximant.

5 Numerical comparison

We have compared the results of two sets of the spectral equations with those of DNS. One is the MLRA equations without Padé approximation (but with FFT), and the other is the simplified MLRA equations with both Padé approximation and FFT. Time integration along the Lagrangian history is done by the trapezoidal rule. The comparison was made for the decaying turbulence with an initially isotropic energy spectrum $E(k) = Ck^4 \exp(-(k/k_0)^2)$ with $k_0 = 8$, where the Reynolds number at $t = 0$ is 59, and $N_k = 2^8$, the wavenumber discretization $\Delta k = 3$, the minimum and maximum wavenumbers $k_{min} = \Delta k, k_{max} = 320$, the time discretizations $\Delta t = 0.005, d\tau = 0.01$, the kinematic viscosity $\nu = 3 \times 10^{-3}$ and $u_0 k_0 t_{max} = 6.86$ (u_0 is the characteristic velocity of the energy containing range). One advantage of the present method compared to the DNS is that Δk may be taken larger than the one required in the DNS. In fact, it was found that the present method is very insensitive to the width Δk.

Figures 1 and 2 show the comparison of evolution of the total enstrophy and the average rate of enstrophy dissipation with DNS. $[N/M]$ denotes the order of the Padé approximant used in the computation. The agreement of the MLRA_{Pade} is quite good. Figures 3 and 4 are the comparison of the enstrophy and enstrophy transfer spectra at the final time. Again the agreement of the simplified MLRA_{Pade} is satisfactory. The CPU time and memory size for the present method were found to be reduced to about1/10 on SX3 (NEC) machine.

The results of the comparison are very satisfactory and seem to be encouraging for further applications of the present method to anisotropic turbulence.

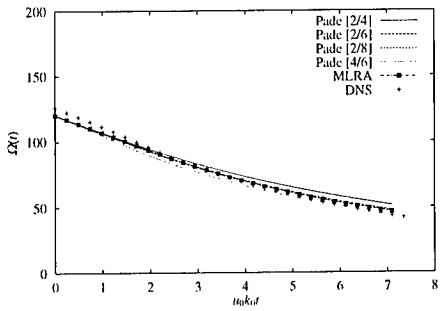


Figure 1: Evolution of the total enstrophy.

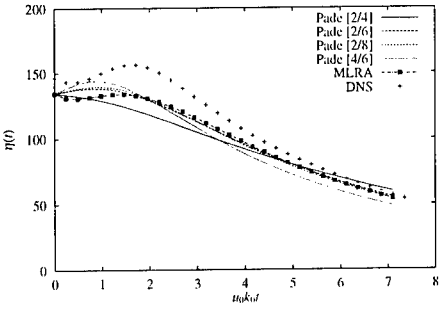


Figure 2: Evolution of the total enstrophy dissipation rate.

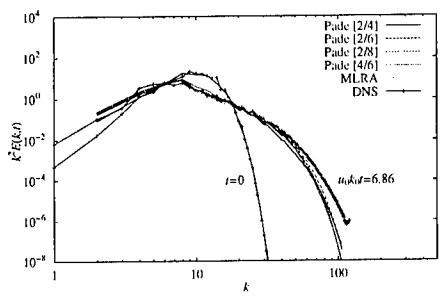


Figure 3: Comparison of $k^2E(k,t)$ at $u_0k_0t = 0$ and 6.86.

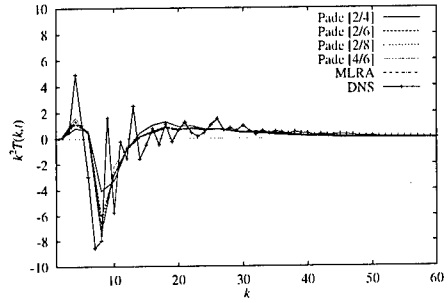


Figure 4: Comparison of $k^2T(k,t)$ at $u_0k_0t = 6.86$.

References

[1] Y. Kaneda. J. Fluid Mech. **107**, 131 (1981).

[2] Y. Kaneda. Phys. Fluids. **29**, 701 (1986).

[3] K. R. Sreenivasan. Phys. Fluids **7**, 2778 (1995).

[4] Y. Kaneda. Phys. Fluids A **5**, 2835 (1993).

[5] T. Gotoh, Y. Kaneda and N. Bekki. J. Phys. Soc. Jpn. **57**, 866 (1988).

[6] T. Gotoh. J. Phys. Soc. Jpn. **58**, 2365 (1989).

[7] Y. Kaneda and T. Gotoh. Phys. Fluids A **3**, 1924 (1991).

[8] T. Gotoh and Y. Kaneda. Phys. Fluids A **3**, 2426 (1991).

[9] T. Gotoh, J. Nagaki and Y. Kaneda. Phys. Fluids **12**, 155 (2000).

[10] W. P. Dannevik. J. Sci. Comput. **1**, 151 (1986).

[11] C. M. Bender and S. A. Orszag: *Advanced Mathematical Methods for Scientists and Engineers.* (McGraw-Hill Publishing Company), (1978).

ADVANCES IN TURBULENCE VIII
Proceedings of the Eighth European Turbulence Conference
C. Dopazo et al. (Eds.)
© CIMNE, Barcelona 2000

Local Energy Transfer theory in forced and decaying isotropic turbulence

W.D. McComb and A.P. Quinn

Department of Physics & Astronomy, University of Edinburgh
King's Buildings, Mayfield Road, Edinburgh EH9 3JZ, SCOTLAND

Contact e-mail: W.D.McComb@ed.ac.uk

1 Introduction

Local Energy Transfer (LET) theory [1] [2] is a two-point, two-time closure currently applied to incompressible, homogeneous, isotropic turbulence. Based on renormalized perturbation theory, LET produces a closed set of integro-differential equations with no free parameters. LET occupies a unique position as the only Eulerian closure compatible with Kolmogorov's $k^{-5/3}$ law. In terms of the Fourier transformed velocity correlation $Q(k;t,t')$ and a propagator function $H(k;t,t')$ the LET equations are

$$Q(k;t,t') = H(k;t,t')Q(k;t',t'),$$
$$\left\{\frac{\partial}{\partial t} + \nu k^2\right\} Q(k;t,t') = P(k;t,t'),$$
$$\left\{\frac{\partial}{\partial t} + 2\nu k^2\right\} Q(k;t,t) = 2P(k;t,t),$$

with an inertial transfer term $P(k;t,t')$ given by

$$P(k;t,t') = \int d^3j L_{kj\mu} \left\{ \int_0^{t'} dsH(k;t',s)Q(j;t,s)Q(|\mathbf{k}-\mathbf{j}|;t,s) - \int_0^t dsH(j;t,s)Q(k;s,t')Q(|\mathbf{k}-\mathbf{j}|;t,s) \right\},$$

where $L_{kj\mu}$ is a geometrical factor (see [1] for details).

As part of an ongoing investigation, the LET equations have been solved numerically and their predictions compared with ensemble-averaged output from multiple runs of an established Direct Numerical Simulation (DNS) code [3].

2 Numerical Procedures

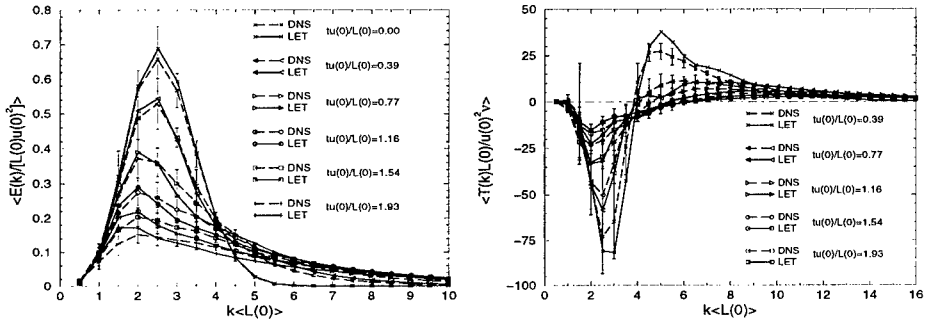
Use of different initial velocity fields in the DNS, all conforming to the required initial energy spectrum, leads to variations in the data and 'error bars' have been constructed for the DNS results indicating this range of variation. These 'error bars' are defined as $\pm$ 3 standard deviations of the ensemble-average. To study the performance of LET in freely decaying turbulence, four standard test problems [1] were investigated. These all used a common initial energy spectrum but employed different viscosity values in order to achieve a range of Taylor-Reynolds numbers from $R_\lambda(0) \simeq 3$ to $R_\lambda(0) \simeq 130$. A new test of LET theory has also been made using forced turbulence. Forcing is accomplished by injecting energy into the $k = 1$ wavenumber mode of the system at a constant rate. This is effected by a modification of the Fourier transformed correlation functions. Using a new Time History Integral Truncation approximation to economize on computer memory requirements, fully evolved stationary turbulent systems have been developed. Forced LET has been calculated for evolved Taylor-Reynolds numbers $R_\lambda \simeq 90$ and $R_\lambda \simeq 230$. These results are compared to DNS, theoretical predictions and experimental data.

3 Results

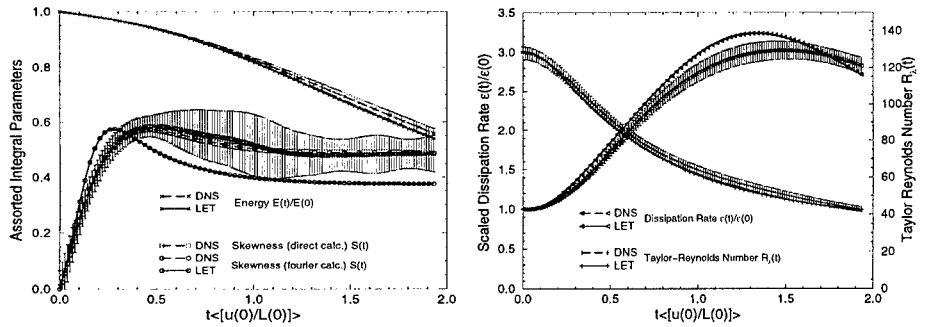
Figures $1A$ and $1B$ illustrate the energy and transfer spectra at a number of times in a free decay with initial Taylor-Reynolds number $R_\lambda(0) \simeq 130$. In both cases, the LET results lie close to or within the error bar bounds. Figures $2A$ and $2B$ illustrate a range of integral parameters from the same run. Agreement is generally good although the LET velocity derivative skewness value is a little low in comparison to DNS. This under-estimation of energy transfer is also seen in Kraichnan's DIA [4]. This matter is still under investigation. Figure $3A$ shows a comparison of an evolved energy spectra from a forced LET calculation, an analogous DNS calculation and the theoretical form proposed by Qian [5]. Agreement is good for intermediate and high wavenumbers. Figure $3B$ shows the same LET and DNS spectra compared with our own calculation of Kraichnan's DIA and Kida & Goto's Lagrangian DIA [6]. Figure 4 shows one-dimensional energy spectra from forced LET runs at two different evolved Taylor-Reynolds numbers $R_\lambda \simeq 90$ and $R_\lambda \simeq 230$ compared with a range of experimental findings. Agreement is excellent.

4 Conclusions

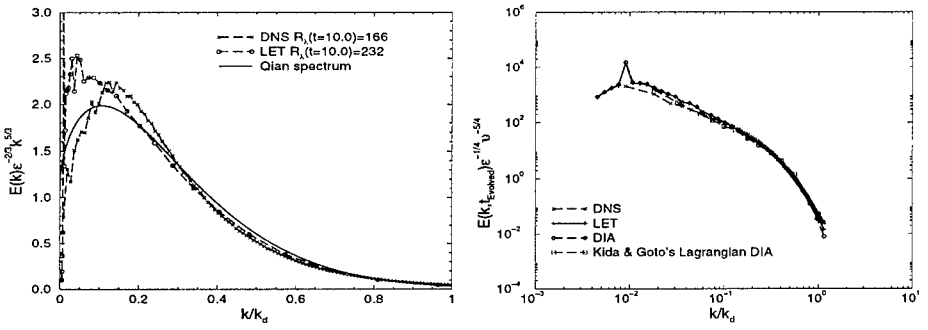
Computational solutions of the Local Energy Transfer theory equations for both freely decaying and forced isotropic turbulence agree well in general with other sources of turbulence data.



Figures 1*A* & 1*B*: Energy & Transfer Spectra at various times during a free decay: Comparison of LET with DNS at $R_\lambda(0) \simeq 130$



Figures 2*A* & 2*B*: Integral parameter evolution during a free decay: Comparison of LET with DNS at $R_\lambda(0) \simeq 130$



Figures 3*A* & 3*B*: Forced LET and DNS evolved energy spectra in comparison with *A*) Qian spectrum *B*) Kraichnan's DIA and Kida & Goto's Lagrangian DIA

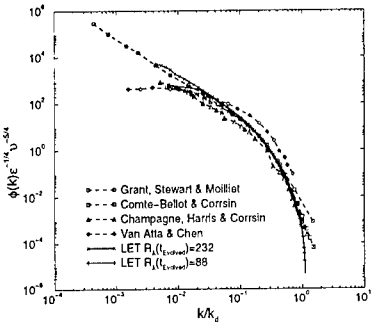


Figure 4: One-dimensional forced LET evolved energy spectra compared with a selection of experimental findings

Computational facilities were provided by the Edinburgh Parallel Computing Centre. A. P. Quinn would like to acknowledge the financial support of the Engineering and Physical Sciences Research Council.

References

[1] W.D.McComb. *The Physics of Fluid Turbulence.* Clarendon Press, Oxford, 1990.

[2] W.D.McComb, M.J.Filipiak, and V.Shanmugasundaram. Rederivation and further assessment of the LET theory of isotropic turbulence, as applied to passive scalar convection. *J.Fluid Mech.*, 245:279–300, 1992.

[3] A.J.Young. *Investigation of renormalization group methods for the numerical simulation of isotropic turbulence.* PhD thesis, University of Edinburgh, 1999.

[4] R.H.Kraichnan. Decay of isotropic turbulence in direct-interaction approximation. *Phys. Fluids*, 7(7):1030–1048, 1964.

[5] J.Qian. Universal equilibrium range of turbulence. *Phys. Fluids*, 27(9):2229–2233, 1984.

[6] S.Kida and S.Goto. A Lagrangian direct-interaction approximation for homogeneous isotropic turbulence. *J. Fluid Mech.*, 345:307–345, 1997.

ADVANCES IN TURBULENCE VIII
Proceedings of the Eighth European Turbulence Conference
C. Dopazo et al. (Eds.)
© CIMNE, Barcelona 2000

Consolidated expansions used in modeling anisotropic turbulence in a channel flow

S. T. Smith[1] and K. Santy-Ateyaba[1]

[1]Department of Mechanical Engineering
Howard University, Washington, DC, USA

Contact e-mail: sonya@vortex.eng.howard.edu

1 Introduction

Wyld's[1] diagram and the hypothesis that Reynolds stresses can be decomposed into isotropic and anisotropic (or rapid and slow) components expansion method are the starting points of this analysis. The isotropic component has been investigated intensely and shown to be amenable to the universal scaling law as referred to by Kolmogorov [2] for locally isotropic turbulence. The anisotropic component is more variant with respect to the flow conditions.

Wyld [1] truncated his series at the first order to get a solution of the integral equations for homogeneous isotropic turbulence. However, this turbulence model is not optimal to represent the turbulence in sheared or bounded flows since for these conditions, anisotropy is observed to be part of the coherent structure. The authors present an extension of the diagram method to study anisotropic turbulence and a provide a numerical solution of the closure equations.

The model will be applied to fully developed turbulent flow of an incompressible fluid in a channel. The coordinate in the direction of the mean flow (streamwise direction) is x_1 while x_2 is the direction normal to the channel walls. The two walls are identical. The origin of x_3, the coordinate in the spanwise direction, is taken at the middle of this channel whose width is $2\,h$. Since the flow is fully developed, the mean flow is two-dimensional and is a function of x_2 only. Similarly the second order correlation tensor with Cartesian components

$$Q_{ij}\left(x,t;x',t'\right) \;=\; \left\langle u_i(x,t)\, u_j\left(x',t'\right)\right\rangle \tag{1}$$

is a function of five variables only, namely

$$x_1 - x_1',\;\; x_2,\;\; ,x_2',\;\; x_3 - x_3',\;\; t - t' \tag{2}$$

The non-dimensional governing equations of incompressible fluid flow in this coordinate system are given by:

$$\frac{\partial u_i}{\partial x_i} = 0 \tag{3}$$

$$\frac{\partial u_i}{\partial t} + \frac{\partial}{\partial x_j}(u_i\, u_j) = \frac{\partial P}{\partial x_i} + \frac{1}{Re}\nabla^2 u_i + \delta_i 1. \tag{4}$$

where δ_{ij} is the Kronecker delta and (2 is the Laplacian operator and Einstein summation convention is used. No-slip boundary conditions are applied at both walls.

2 New Formulation

The correlation tensor is composed of two components; namely, the isotropic and anisotropic parts. The spectral shape of the individual components is conserved; thus any manipulation preserves that characteristic. This was validated by L'vov and Procaccia[3] who found that perturbative theory does not violate the Kolmogorov scaling law. Although the diagram method is a perturbation theory, this study does not consider the anisotropic velocity component as a perturbation induced by the mean strain. It arises from the action of the anisotropic forcing term and satisfies the following equation:

$$S^{-1}(k_x, l, k_z, \omega)\, \hat{u}_i^{(1)}(k_x, l, k_z, \omega) =$$

$$\hat{f}_i^{(1)}(k_x, l, k_z, \omega) - \frac{i}{2}\frac{p_{ijm}(k_x, l, k_z, \omega)}{\nu_T^{1/2}} \sum \hat{u}_i^{(1)}(k_x, l, k_z, \omega)\, \hat{u}_j^{(1)}(k_x, l, k_z, \omega) \tag{5}$$

The variables of primary importance are the correlation tensors $Q^{(0)}$,$Q^{(1)}$. The superscripts 0 and 1 denote the isotropic and anisotropic components, respectively. Formulation of an evolution equation for these correlation tensors is accomplished by formal diagram expansion and consolidation. What is new in the author's approach is the extension of the diagram expansion to a tensor from a scalar functions. Thus, construction of these diagrams follows rules similar to the general rules of the Feynman diagrams, modified to account for anisotropy. Henceforth, the following notation-out convention is used:$k = (k_x, l, k_z, \omega)$

The diagram expansion is constructed by the definition of a Green's function (propagator) S, an unperturbed isotropic velocity (with upper script 0), and an unperturbed anisotropic velocity (with upper script 1) defined as follows:

$$S(k) \equiv \left[\frac{1}{i\omega - \frac{1}{Re}k^2 + \hat{D}_y^2}\right] \tag{6}$$

$$u_0^{(0)}(k) = S(k) f^{(0)} \tag{7}$$

$$u_0^{(1)}(k) \;=\; S(k) f^{(1)} \tag{8}$$

Then, the evolution equations for the isotropic and anisotropic velocity components are derived as:

$$u^{(0)}(k) \;=\; u_0^{(0)}(k) \;+\; S(k)\,\frac{g}{\nu_T^{1/2}} \sum_{k = k_1 + k_2} u^{(0)}(k_1)\, u^{(0)}(k_2) \tag{9}$$

$$u_i^{(1)}(k) \;=\; u_{i0}^{(1)}(k) \;+\; S(k)\,\frac{g}{\nu_T^{1/2}} \sum_{k = k_1 + k_2} u_i^{(1)}(k_1)\, u_j^{(1)}(k_2) \tag{10}$$

where g captures the pressure effects. The velocity is then considered as a power series of the parameter g and is used to calculate the velocity correlation tensor

$$Q_{ij}\,(x,t;x',t') \;=\; \langle u_i(x,t)\, u_j\,(x',t') \rangle \tag{11}$$

The perturbation series by themselves are of course not useful as an approximation scheme for turbulence closure. Rules are developed to generalize and consolidate the diagrams which result in the anisotropic correlation function, generalized vertex function, and propagator shown in Figure 1. The correspondence principle applied to these diagrams and their isotropic counterpart produces a set of six simultaneous integral equations which make up the turbulence closure model. The closure equations are solved numerically and selected results, applied to turbulent flow in a channel are shown in figures 2 and 3. These results are in good agreement with reported results of Kim et. al.[4]

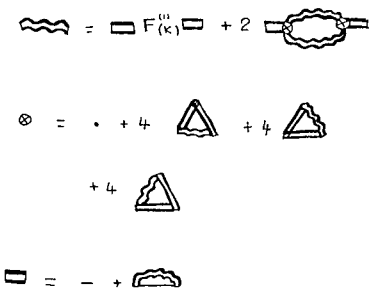


Figure 1: Integral equations for the anisotropic correlation spectrum, generalized vertex function, and propagator

3 Conclusions

The key contributions have been the extension of diagram method to include the anisotropic tensor representation of the turbulent velocity correlation function and the application of this model to numerical simulations of turbulent

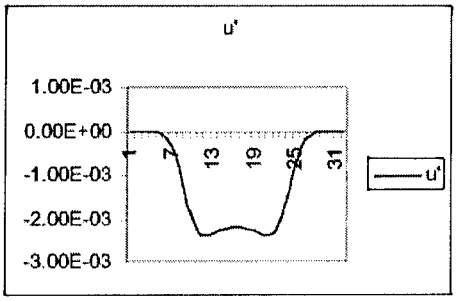


Figure 2: Disturbance profile at Re=3850

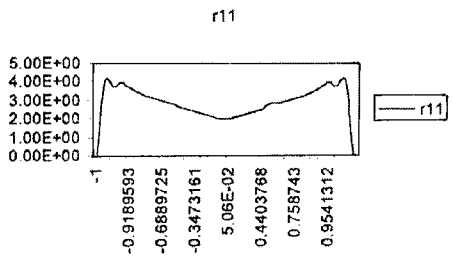


Figure 3: profile at Re=3850

flows. Additionally, the definition of new variables and consolidation rules are proposed for the analysis of mixed scalar and tensor elements. The analysis is done systematically and all the variables have a physical representation. The propagator S(k) is the diffusion operator, the vertex function, $\Gamma(k,k)$, describes pressure effects, and the scalar representation of the correlation tensor $Q_{ij}(k)$ is the kinetic energy of the flow. Owing to this characteristic, this approach is useful for a closure scheme.

The first author gratefully acknowledges the U.S. Army High performance Computing Center and NASA Langley Research Center.

References

[1] Wyld. "Formulation of the theory of turbulence in an incompressible fluid." Annals of physics,**14** 143-165 (1961)

[2] Kolmogorov, A.N. "Equations of turbulent motion of an incompressible fluid." *Izvestiya AN SSSR*, Ser. fiz., **6**, No. 1-2, 56-58 (1942).

[3] Victor L. and I. Procaccia. "Exact resummation in the theory of hydrodynamics turbulence." Physica A, **257**, (1998) pp. 165-196.

[4] Moin P. and J. Kim: "Numerical investigation of turbulent channel flow." Journal of Fluid Mechanics 118,341 (1982).

XXIII

Compressible Turbulence

ADVANCES IN TURBULENCE VIII
Proceedings of the Eighth European Turbulence Conference
C. Dopazo et al. (Eds.)
© CIMNE, Barcelona 2000

Compressibility effects in grid generated turbulence

Yiannis Andreopoulos

Experimental Aerodynamics and Fluid Mechanics Laboratory
Department of Mechanical Engineering
The City College of the City University of New York
New York, New York 10031 USA
Tel: 212-650-5206

Contact e-mail: andre@me-mail.engr.ccny.cuny.edu

1 Introduction

The effects of compressibility in a nearly homogeneous and nearly isotropic flow of decaying turbulence have been investigated experimentally by carrying out high resolution measurements (of the order of 7 to 26 Kolmogorov viscous length scales) in a large scale shock tube research facility. The measurements were carried outinside the induced flow behind the traveling shock wave. Time-dependent measurements of one, two or three velocity components have been carried out. Measurements of the vorticity vector and the full dissipation tensor at limited locations inside the flow have been also attempted for the first time in compressible flows.

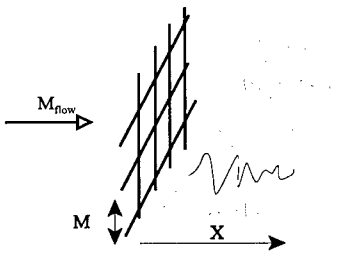


Figure 1: Flow schematic

A variety of grids of rectangular pattern of differentmesh size was used to generate the flow field. The Reynolds number of the flow based on the mesh size, Re_M , ranged from 50,000 to 400,000 while the turbulent Reynolds number Re based on Taylor's microscale was between 200 and 700 whichconstitutes one of the highest scale ever achieved in laboratory flow. The range of Mach number of the flows investigated was between 0.3 and 0.6 which was low enough to assure a shock free flow and reasonably high enough to contain compressibility effects.

2 Results

The effects of compressibility can be classified into two categories. The first category includes those effects which have a direct impact on the flow. Compressible dissipation, for instance, is a typical example of a quantity which expresses a direct effect of compressibility on total dissipation. The indirect effects comprise the second category. This include effects which change the local or global behaviorof the flow and therefore may cause significant changes of the incompressible part of the flow. Increasing the Mach number of the flow, for instance, can change the level of turbulent fluctuations in the flow which may subsequently affect the dissipation rate, particularly the incompressible part which accounts for most of the total dissipation in cases like the present subsonic flow. Direct effects of compressibility on turbulence may be described by the turbulent Mach number M_t , while indirect effects on turbulence may be characterized by the flow Mach number M_{flow}, andthe Reynolds number Re_M.

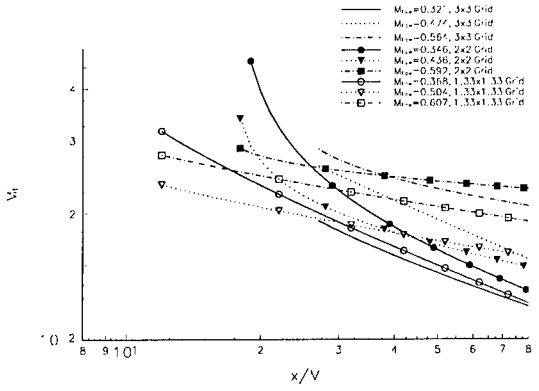


Figure 2: Decay of Mach number fluctuations

The parameters M_t , M_{flow} and Re_M,however, are not completely independent from each other. A change in any of the three may cause a change in the other two. In that respect, the effects which each of the nominally independent variables impose on the flow may be difficult to distinguish. An attempt has been made here to identify the effects of M_{flow} and Re_M on homogeneous and isotropic turbulence.

The isotropy of the present flow was verified experimentally and it was found to be within the range reported for incompressible flows. In fact, it was established for the first time that isotropic compressible turbulence at moderate subsonic Mach numbers can be setup experimentally.

The decay of Mach number fluctuations shown in figure 2 was found to follow a power law behavior similar to that describing the decay of incompressible isotropic turbulence

$$M_t^2 = B[x/M - (x/M)_0]^{-n}$$

where B, $(x/M)_0$ and n are constants depending on the flow Mach numberas well as on the Re_M and grid. These constants have been determined concurrently so that the residual deviation fromthe original data is minimized. This approach represents a departure from previous practices where one of the three parameters was fixed and the other two were determined through a best fit of the data

procedure. In that context, direct comparison of the present data with previously obtained values of any of the three constants may not be feasible. A direct consequence of the procedure followed in this investigation may be the fact that the exponent n has been found to reach values below 1, which indicates, in principle, a slower decay rate than that found in many previous cases under the assumption that one of the three unknown constants should be fixed.

Figures 3 and 4 show the power spectral density of the turbulent kinetic energy $1/2u_iu_i$ and enstrophy $1/2\omega_i\omega_i$ weighted by the wavenumber $k_1 = 2\pi/\lambda$ asmeasured in the present investigation for the case ofthe 2x2 grid. The streamwise wavenumber $k_1 = 2\pi f/U_1$ was computed by assuming the local longitudinal mean velocity as the convection velocity (Taylor s hypothesis). Wavenumbers have been non- dimensionalized by the mesh size M. In the case of $M_{flow} = 0.308$ which is shown in figure 3, the maximum value of the spectral density of turbulent kinetic energy occurs at approximately $k_1M = 4.5$ while the maximum value of the spectral density of enstrophy occurs at about $k_1M = 7$. This difference in the maxima of spectral energies indicates a shift towards higher wavenumbers of enstrophy fluctuations which suggests that they are mainly a result of a greater proportion of contributions by the smaller scales whereas the kinetic energy comes from relatively larger eddies.

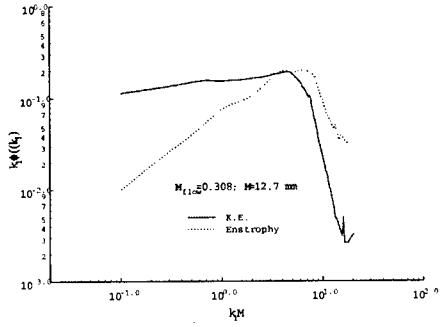


Figure 3:

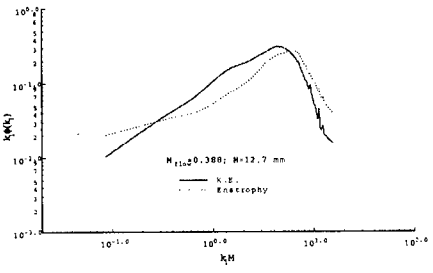


Figure 4:

Weighted power spectral densities for turbulent kinetic energy and enstrophy

In the case of $M_{flow} = 0.388$, shown in figure 4, the maximum energy of T.K.E. is found to occur at about the same wavenumber as in the case of $M_{flow} = 0.308$ i.e. at $k_1M = 4.5$, while the maximum energy of enstrophy occurs at a lower wavenumber $k_1M = 5.8$. Once more, thedata show that there is a shift towards higher wavenumbers in the case of enstrophy maxima. However, it appears that increasing M_{flow} reduces the difference between the wavenumbers where the maxima of kinetic energy and enstrophy occur. If one considers that the peak in T.K.E. represents the size of large energy containing eddies and that the peak in enstrophy represents mostly small energy dissipating eddies then it would be expected that this difference or shift increases with increasing

Reynolds number. The fact that this shifts decreases with Mach number in the present case indicates that the effect of M_{flow} in reducing this difference becomes stronger than the effect of Reynolds in increasing it.

3 Conclusions

An attempt has been made to measure all time-dependent velocity gradients involved in vorticity, its stretching, enstrophy and dissipation rates with adequately spatial and temporal resolution. This allowed estimates of dilatation s_{kk}, compressible dissipation s_{kk}^2 and compressible stretching $\omega_i s_{kk}$ to be obtained. These quantities aredirectly associated with compressibility effects. A common feature of all these quantities is that their fluctuations properly normalized by M and U_1, increase with increasing Mach number of the flow. Although this behavior maybe expected, if one considers that in compressible shear layers increasing M_{flow} suppresses turbulent fluctuations then this conclusion is surprising.

The results of the present investigation have also shown that enstrophy fluctuations which comprise the solenoidal part of dissipation are reduced with increasing M_{flow}, a conclusion which is also verified by the results ofdissipation obtained through the decay rate of turbulent kinetic energy for the case of coarse grids.

The time-dependent signals of enstrophy $\omega_k\omega_k$, dilatation s_{kk}, compressible dissipation s_{kk}^2 , and the three components of the stretching vectors $\omega_i s_{ki}$ and $\omega_i s_{kk}$ indicated a highly intermittent behavior which is characterized by bursts of high amplitude followed by less violent periods of time. The results also show that the mean values of all these quantities are considerably smaller than their r.m.s. values which suggests that time-averaged vorticity transport equations are of very limited value in understanding vorticity related phenomena.

The financial support provided by NASA Grant #NAG-1590 and by AFOSR Grant #F49620-98-0358 is greatly acknowledged. This paper is based on the PhD theses by G. Briassulis (1996) and J. Agui (1998).

References

[1] Andreopoulos, Y., Agui, J. H., and Briassulis, G., 2000, Shock Wave-Turbulence Interactions Annu. Rev.Fluid Mech., vol. 32:309-345.

[2] Briassulis, G., 1996, Interaction of Isotropic an Homogeneous Turbulence with Shock Waves, PhD Thesis,City University of New York.

[3] Agui, J.H., 1998, Shock Wave Interactions with Turbulence and Vortices, PhD Thesis, City University ofNew York

ADVANCES IN TURBULENCE VIII
Proceedings of the Eighth European Turbulence Conference
C. Dopazo et al. (Eds.)
© CIMNE, Barcelona 2000

Large Eddy Simulation of a Mach 0.9 turbulent jet

B.J. Boersma[1] and S.K. Lele[2]

[1] Department of Mechanical Engineering
Delft University of Technology
2628 AL Delft, The Netherlands
[2] Center for Turbulence Research
Stanford University
Stanford CA, 94305, USA

Contact e-mail: b.j.boersma@wbmt.tudelft.nl

1 Introduction

Over the next decade a significant reduction of the acoustic emissions of jet engines of commercial airliners will be needed to meet the ever increasing airport noise regulations. In order to make this reduction possible, it is necessary to develop prediction methods which are capable of predicting the noise emitted by a jet.

Traditional jet mixing noise predictions are based on a statistical description of turbulent flow which may be obtained form a Reynolds averaged calculation. Some interesting aspects of the jet noise may be obtained from such a method, but it requires the acoustic sources to be modeled. Recently, with increasing computer power, it has become possible to calculate the acoustic field of a jet using Direct Numerical Simulation (DNS) ([3]). However, DNS of jet flows is limited to low Reynolds numbers. Practical jets have rather high Reynolds numbers and thus the turbulence within such jets has a wide range of spatial and temporal scales. Furthermore the energy-containing scales themselves chance by a large factor from regions near the nozzle to the end of the potential core. Evidently, DNS of a high Reynolds number jet would be prohibitively expensive.

Another attractive simulation technique is the so-called Large Eddy Simulation in which the large scales are resolved on the computational grid and the small scales are modeled with a rather simple model. The justification behind this is that the small scales are not very important for the overall flow statistics and that they do not contain much energy. The advantage of the LES method is that it is possible to calculate flows with high Reynolds numbers, but there may be some uncertainty in the results, especially those related to small scale motions.

2 The filtered equations

Conventional LES methods for compressible flows use the Favre averaged (or density) weighted equations [1] . The resulting equations are rather simple and no model term appears in the density equation. However, the non-linear term in the continuity equation can give rise to an instability and damping by the LES model can be necessary. Therefore we use in this study the non-Favre averaged set of LES equations. They read:

$$\frac{\partial \overline{\rho}}{\partial t} + \frac{\partial \overline{\rho}\ \overline{u}_i}{\partial x_i} = -\frac{\partial}{\partial x_i}\left(\overline{\rho u_i} - \overline{\rho}\ \overline{u}_i\right),$$

$$\frac{\partial \overline{\rho}\ \overline{u}_i}{\partial t} + \frac{\partial \overline{\rho}\ \overline{u}_i\ \overline{u}_j}{\partial x_j} = -\frac{\partial \overline{p}}{\partial x_i} + \frac{\partial \overline{\sigma}_{ij}}{\partial x_j} - \frac{\partial}{\partial x_j}\left(\overline{\rho u_i u_j} - \overline{\rho}\ \overline{u}_i\ \overline{u}_j\right) - \frac{\partial}{\partial t}\left(\overline{\rho u_i} - \overline{\rho}\ \overline{u}_i\right)$$

In which $\overline{\rho}$ is the LES filtered density, $\overline{p}$ the LES filtered pressure, $\overline{u}_i$ the LES filtered velocity and $\overline{\sigma}_{ij}$ is the Newtonian stress tensor

$$\overline{\sigma}_{ij} = \overline{\mu}\left(\frac{\partial \overline{u}_i}{\partial x_j} + \frac{\partial \overline{u}_j}{\partial x_i} - \frac{2}{3}\delta_{ij}\frac{\partial \overline{u}_k}{\partial x_k}\right)$$

The LES filtered equation for the total energy reads

$$\frac{\partial \overline{E}}{\partial t} + \frac{\partial}{\partial x_i}[\overline{E}\ \overline{u_i} + \overline{u_i}\ \overline{p}] = -\frac{\partial q_i}{\partial x_i} + \frac{\partial}{\partial x_i}\overline{u_i}\ \overline{\sigma}_{ij} - \frac{\partial}{\partial x_i}\left(\overline{Eu_i} - \overline{E}\ \overline{u_i} + \overline{pu_i} - \overline{p}\ \overline{u_i}\right).$$

$$q_i = -\overline{\kappa}\frac{\partial \overline{T}}{\partial x_i}$$

In which T is the temperature, and κ the thermal diffusivity. The subgrid terms are modeled with simple models based on a gradient hypothesis. For instance

$$m_i = \overline{\rho u_i} - \overline{\rho}\ \overline{u}_i = -C_\rho \Delta^2 |\overline{S}| \frac{\partial \overline{\rho}}{\partial x_i}$$

In which Δ is the filter width of the LES filter, and C_ρ a coefficient which is obtained from the dynamic procedure [1] and S is the strain rate tensor defined as

$$S_{ij} = \frac{1}{2}\left(\frac{\partial u_i}{\partial x_j} + \frac{\partial u_j}{\partial x_i}\right).$$

For the subgrid stresses we can use again a model based on the Boussinesq hypothesis [1]

$$\overline{\rho u_i u_j} - \overline{\rho}\ \overline{u}_i\ \overline{u}_j = \overline{\rho} C_s \Delta^2 |\overline{S}| \overline{S}_{ij} = \overline{\rho}\nu_t \overline{S}_{ij}$$

In which C_s is the well known Smagorinsky coefficient which is evaluated using the dynamic procedure and ν_t the so-called eddy viscosity.

With the help of the equation of state we can rewrite the subgrid term in the energy equation as

$$\left(\overline{\rho u_i T} - \overline{\rho}\ \overline{u_i}\ \overline{T} + \frac{1}{2}\overline{\rho u_i u_k u_k} - \frac{1}{2}\overline{\rho}\ \overline{u_i}\ \overline{u_k}\ \overline{u_k}\right)$$

The triple correlation is assumed to be small. The remaining term has been modeled with the following model:

$$\overline{\rho u_i T} - \overline{\rho}\ \overline{u_i}\ \overline{T} = -\overline{\rho} C_T \frac{\partial \overline{T}}{\partial x_i}$$

In which C_T is again a model coefficient which is calculated dynamically.

The numerical scheme is the same as used by [3]. The Favre filtered LES equations are solved in a cylindrical system using 6th order compact differences in radial and axial direction and a Fourier method in the tangential direction. Time integration is accomplished by a 4th order Runga-Kutta method.

3 Results

In this section we will present some results of a LES simulation on a grid which consisted of 256 × 150 points in the axial radial and circumferential direction respectively. The Reynolds number based on the orifice velocity and jet diameter was equal to 50,000. The length of the computational domain is equal to 22.5 jet diameters. In Figure 1 we show a snapshot of the resolved density and the resolved total vorticity in the jet. In the first 10 diameters the flow is axis-symmetric. Farther downstream the flow becomes fully three dimensional.

4 Future work

The aim of this project is to calculate the sound field of the jet. Until now we have put most of our effort in the calculation of the flow itself. In the near future we will put more emphasis on the acoustics.

References

[1] P. Moin, K. Squires, W. Cabot and S. Lee, 1991, A dynamic subgrid-scale model for compressible turbulence and scalar transport, *Phys. Fluids* **A 3**, 11, pp 2746-2757, 1991.

[2] J.L. Stromberg, D.K. McLaughlin and T.R. Troutt, Flow field and acoustic properties of a Mach number 0.9 jet at low Reynolds number, *J. of Sound and Vib.*, **72**, pp 159-176, 1980.

[3] J.B. Freund, P. Moin and S.K. Lele, Compressibility effects in a turbulent annular mixing layer, Technical Report TF-72, Stanford University, 1997.

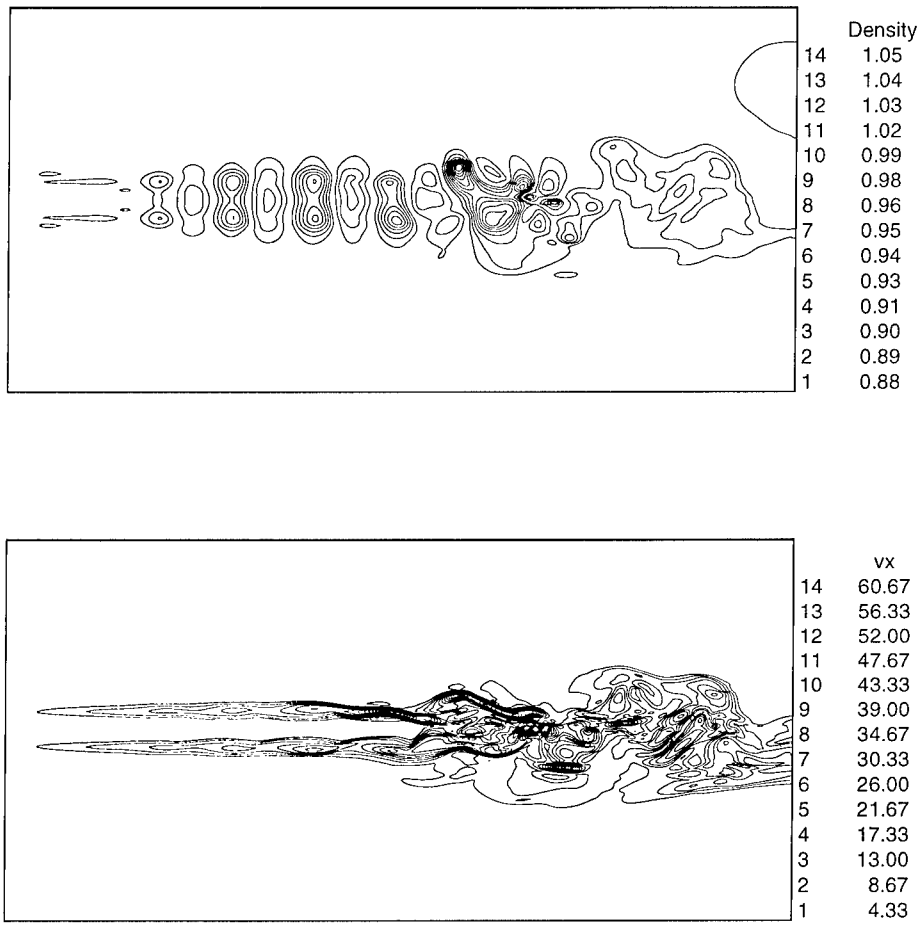


Figure 1: Top: The resolved density field. Bottom the total vorticity ω multiplied by the axial distance to the jet nozzle.

ADVANCES IN TURBULENCE VIII
Proceedings of the Eighth European Turbulence Conference
C. Dopazo et al. (Eds.)
© CIMNE, Barcelona 2000

LES of Shock-Boundary-Layer Interaction with the Approximate Deconvolution Model

S. Stolz, N. A. Adams and L. Kleiser

Institute of Fluid Dynamics, ETH Zürich, Switzerland

Contact e-mail: stolz@ifd.mavt.ethz.ch

1 Introduction

Large-eddy simulation (LES) has matured to be a tool for studying simple turbulent flows at flow parameters which render Direct Numerical Simulation (DNS) infeasible. For physically and geometrically complex flows, however, proper subgrid-scale modeling still poses a considerable challenge. In this contribution we address the LES of supersonic compression corner flow, which exhibits considerable physical complexity due to the interaction of shock, separation, and turbulence in an ambient inhomogeneous shear flow.

Recently we have developed a new approach for LES, the Approximate Deconvolution Model (ADM), which is based on a repeated filtering to approximately deconvolve the dependent variables [1]. Excellent *a posteriori* agreement with DNS was demonstrated with this approach for the LES of turbulent channel flow [2]. *A priori* tests of a supersonic compression ramp flow show correlations well exceeding 95% for all relevant subgrid scale terms [3].

2 Subgrid-scale modeling

We write a generic (one-dimensional, for notational simplicity) transport equation as $\partial u/\partial t + \partial F(u)/\partial x = 0$. By applying the primary filter operation $\overline{u}(x) = G*u(x) = \int_\Omega G(\mathbf{x}-\mathbf{x}')u(\mathbf{x}')d\mathbf{x}'$ we obtain the filtered transport equation

$$\frac{\partial \bar{u}}{\partial t} + G * \frac{\partial F(u)}{\partial x} = 0 \,. \tag{1}$$

Common practice is to gather non-closed terms in eq. (1), which arise from the non-linearity in $F(u)$, as source terms σ on the right-hand side

$$\frac{\partial \bar{u}}{\partial t} + \frac{\partial F(\bar{u})}{\partial x} = \frac{\partial F(\bar{u})}{\partial x} - G * \frac{\partial F(u)}{\partial x} =: \sigma \,. \tag{2}$$

In eq. (2), σ is unclosed due to the unknown unfiltered solution u, and requires modeling. For the generalized coordinates used with the ramp configuration we use discrete filters with a commutation error of third order [4].

If the filter G has an inverse it can be expanded as an infinite series. We truncate the series at N and obtain Q_N as an approximation of G^{-1} :

$$G^{-1} \approx Q_N = \sum_{\nu=0}^{N} (I - G)^{\nu} \ , \tag{3}$$

where I is the identity operator. The series on the right-hand side converges if $||I - G|| < 1$. Since all practically relevant filter kernels G are not invertible, only a regularized inverse can be obtained. From eq. (3) it is obvious that such an approximate inverse is given by Q_N which is bounded by $||Q_N|| \leq N + 1$. We point out that the series (3) has first been employed for image reconstruction [5]. According to our experience $N = 3$ is sufficient for acceptable results and $N > 7$ does not improve the results significantly. For the results in section 3 we use $N = 5$.

In our approach, the nonlinear term in eq. (1) is approximated directly by replacing the unfiltered quantities u in $F(u)$ with their approximate deconvolution $u^{\star} = Q_N * (G * u) = \overline{u} + (\overline{u} - \overline{\overline{u}}) + (\overline{u} - 2\overline{\overline{u}} + \overline{\overline{\overline{u}}}) + \cdots$. This implies that

$$\sigma \approx \frac{\partial F(\bar{u})}{\partial x} - G * \frac{\partial F(u^{\star})}{\partial x} \ . \tag{4}$$

The effect of non-represented scales beyond the numerical cut-off wave number $\xi_n = \pi/h$, h being the grid spacing, cannot be represented by the above procedure and requires an additional regularization to account for the energy transfer from scales with wave numbers $|\xi| < \xi_n$ to non-represented scales $|\xi| \geq \xi_n$. This is achieved adding a relaxation term $-(I - Q_N * G) * \bar{u}/T$ to the right-hand side of eq. (1) which acts only on the scales $\xi_c < |\xi| < \xi_n$. We found that the method is rather insensitive to the relaxation parameter T which can be dynamically estimated from the instantaneous filtered solution [4]. The order of this secondary filter is the given by the order of the primary filter multiplied by $N + 1$. To summarize, the equation which is solved instead of eq. (2) is given by

$$\frac{\partial \bar{u}}{\partial t} + G * \frac{\partial F(u^{\star})}{\partial x} = -\frac{1}{T} (I - Q_N * G) * \bar{u} \ . \tag{5}$$

3 LES of shock-boundary-layer interaction

The turbulent boundary layer along a compression ramp with a deflection angle of 18^o at a free-stream Mach number of $M = 3$ and a Reynolds number of $Re_\theta = 1685$, based on free-stream quantities and mean momentum thickness at inflow, was computed by LES with the Approximate Deconvolution Model. The resolution of the LES was $250 \times 30 \times 90$, while $1000 \times 80 \times 180$ grid points were used for the DNS [6] in the streamwise (x_1), spanwise x_2 and wall-normal x_3

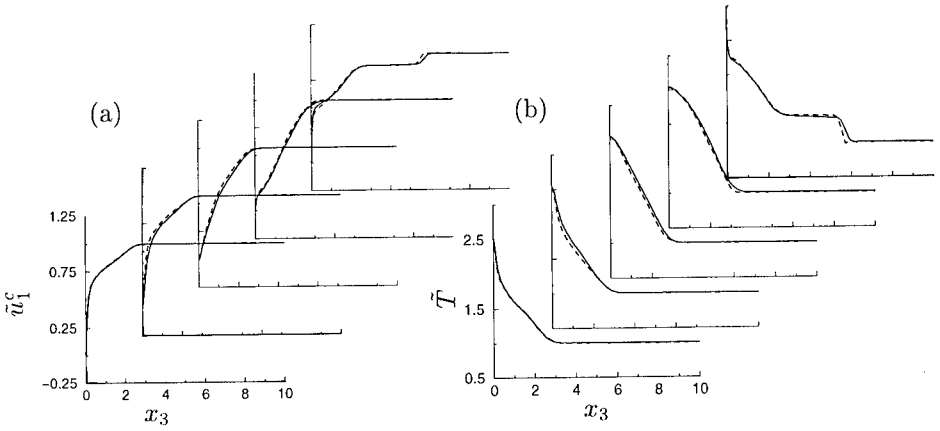


Figure 1: Mean profiles. (a) $\tilde{u^c}$, and (b) $\tilde{T}$; ——filtered DNS and ----LES.

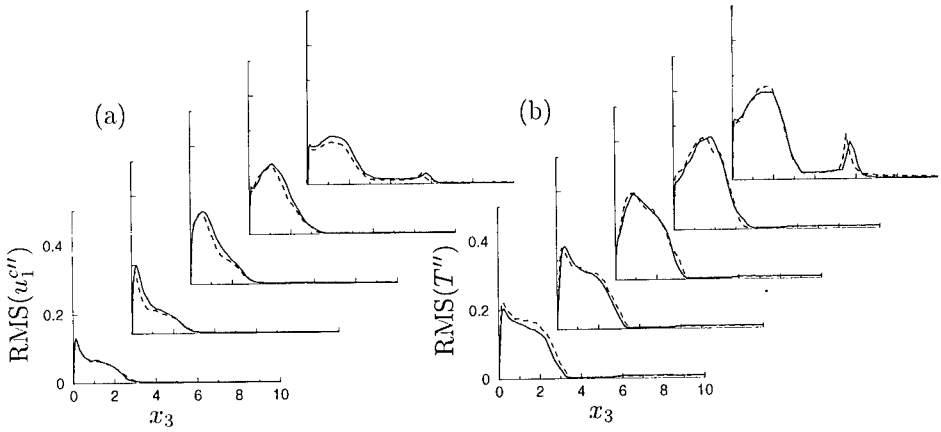


Figure 2: Root-mean-squares of fluctuations. (a) RMS($u_1^{c\prime\prime}$), and (b) RMS(T''); ——filtered DNS and ----LES.

directions. Hence, the computational effort for the LES was approximately one percent of that for the DNS.

Unlike in the DNS, in LES flow discontinuities are explicitly filtered, and the filtered discontinuities can be resolved on the mesh. Accordingly, no shock-capturing scheme is needed and a centered 6th order compact finite-difference scheme [7] is used for the spatial discretization in the LES. Further details on the mathematical model and the boundary condition implementation can be found in [8, 4].

The mean-flow profiles of the Favre-averaged contravariant downstream velocity $\tilde{u}_1^c$ and temperature $\tilde{T}$ are shown in figure 1 along computational mesh lines for five different downstream stations. Averaging is performed in time and over the homogeneous spanwise direction. We find a very good agreement

between the LES and filtered DNS data.

In figure 2 the root-mean-square of the Favre-fluctuations of the contravariant velocity RMS($u_1^{c\prime\prime}$) and of the temperature RMS(T'') are shown for the same downstream stations. Although our results have to be considered as preliminary and additional statistical samples would improve the smoothness of the profiles, the agreement between LES and filtered DNS data is remarkably good.

4 Conclusions

We have introduced the approximate deconvolution model (ADM) for the LES of supersonic compression ramp flow. The model does not use *a priori* assumptions and is parameter free except for the choice of the deconvolution order N. According to our experience $N = 5$ is sufficient for all flow configurations we have investigated so far. We would like to point out that the model also performed well in LES of incompressible turbulent channel flow [2] and of compressible decaying isotropic turbulence [1].

References

[1] S. Stolz and N. A. Adams. An approximate deconvolution procedure for large-eddy simulation. *Phys. Fluids*, 11:1699–1701, 1999.

[2] S. Stolz, N. A. Adams, and L. Kleiser. The approximate deconvolution procedure applied to turbulent channel flow. In P. Voke, N. D. Sandham, and L. Kleiser, editors, *Direct and Large-Eddy Simulation III*. Kluwer, 1999. To appear.

[3] S. Stolz, N. A. Adams, and L. Kleiser. Analysis of sub-grid scales and sub-grid scale modeling for shock-boundary-layer interaction. In S. Banerjee and J. Eaton, editors, *Turbulence and Shear Flow I*, pages 881–886. Begell House, 1999.

[4] S. Stolz. PhD thesis, Eidgenössische Technische Hochschule Zürich, 2000. Report in preparation.

[5] P. H. van Cittert. *Z. Phys.*, 69:298–308, 1931.

[6] N. A. Adams. Direct simulation of the turbulent boundary layer along a compression ramp at $M = 3$ and $Re_\theta = 1685$. 2000. To appear.

[7] S. K. Lele. Compact finite difference schemes with spectral-like resolution. *J. Comp. Phys.*, 103:16–42, 1992.

[8] N. A. Adams. Direct numerical simulation of turbulent compression corner flow. *Theor. Comp. Fluid Dyn.*, 12:109–129, 1998.

ADVANCES IN TURBULENCE VIII
Proceedings of the Eighth European Turbulence Conference
C. Dopazo et al. (Eds.)
© CIMNE, Barcelona 2000

Relaxation of super/hypersonic boundary layer behind interaction with shock wave/expansion fan

A.V. Starov and M.A. Goldfeld

Institute of Theoretical and Applied Mechanics, SB RAS
4/1 Institutskaya, Novosibirsk 630090, Russia

Contact e-mail: gold@itam.nsc.ru

1 Introduction

The hypersonic boundary layer development and its structure under the influence of disturbing factors present one of the most complicated problems of fluid mechanics. Such factors affecting the boundary layer are the adverse and/or favourable pressure gradient, roughness, gas injection, cooling, etc. A specific case of this problem is the study of the flow with successive impact of pressure gradients on the boundary layer. Though these factors are intensely studied, the question of their joint effect on the boundary layer still remains open. Different authors have carried out numerous and experimental investigations of the boundary layer structure and its properties when it is affected by a single shock and by an expansion fan in versatile flow conditions. Similar studies when the boundary layer is sequentially affected by adverse and favourable pressure gradients in an arbitrary combination are more scarce. At the same time, such flows can be often occur in the flow around elements of super and hypersonic flying vehicles (inlets, nozzles, etc.).

Conducted experimental investigation of a turbulent boundary layer include the study of the shock wave and/or expansion fan action upon the boundary layer, its separation and relaxation. Complex events of paired interactions and the flow on compression convex-concave surfaces was studied. **The main aims** of the investigation were: **a.** separation and relaxation of boundary layer; **b.** skin friction and integral parameters; **c.** pulsation characteristics; **d.** successive interaction and mutual effects; **e.** effect of relaminarization.

2 Models and Results

Scheme of models, test conditions and types of measurements are shown in Figure 1. Two groups of models were studied: 2D and 3D models (#1–#4) with shock

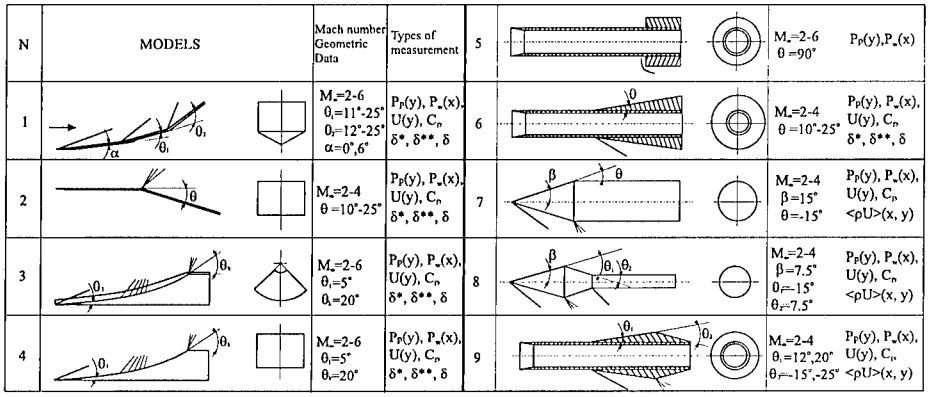


Figure 1: Models and test conditions.

waves or expansion fan and with distributed pressure gradient; a large group of axisymmetric models with shock and expansion waves. These groups includ also complex interactions (expansion fan+shock wave or shock wave+expansion fan). Models #3 and #4 can be also assigned to this group. The tests was performed at Reynolds numbers from 8 to 80 million per meter. It should be noted that the boundary layer relaxation was studied in detail over a large distance behind the interaction region (from 20 to 200 boundary layer thicknesses – δ_0). The separation conditions and separation region structure were studied in all cases.

Some boundary layer characteristics are discussed below. The changes of the momentum thickness decreases by more than 2.5 times in a separated flow over the length of up to 16 boundary layer thicknesses (Figure 2). The changes of the boundary layer thickness and displacement thickness are of the same order. The increase of the skin friction coefficient behind the shock wave was also large. The relaxation region length was larger at the Mach number equal to 3, when the boundary layer separation was observed. The length of this region is roughly twice as small in flow without separation at the Mach number equal to 4.

The influence of the favourable pressure gradient on the boundary layer state is also very substantial, despite the absence of developed separation. The flow behind the corner point, however, is also very complicated. A local separation behind the corner point was observed in experiments on the axisymmetric and 2D models. The changes of the boundary layer thickness behind the expansion fan, unlike the flow behind the shock wave, increases by factor of three over the length of about 150 δ_0 (Figure 3). The Reynolds number effect can also be seen. It was most significant immediately behind the expansion fan (up to 25 δ_0). This character of changes is typical of the entire Mach numbers range from 2 to 6. The boundary layer relaxation length behind the expansion fan was also found to be much larger than behind the shock wave, and the boundary layer remains

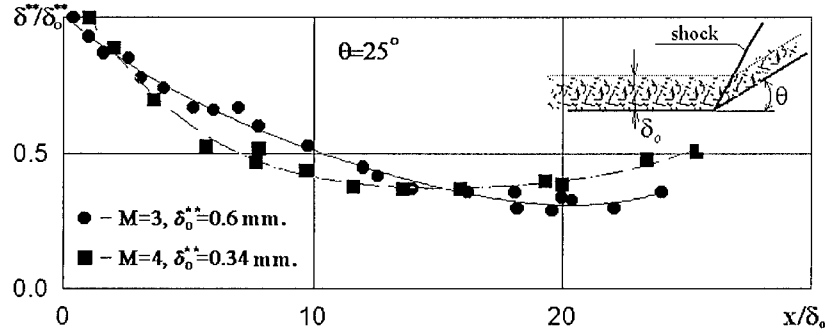


Figure 2: Momentum thicknesses behind shock wave.

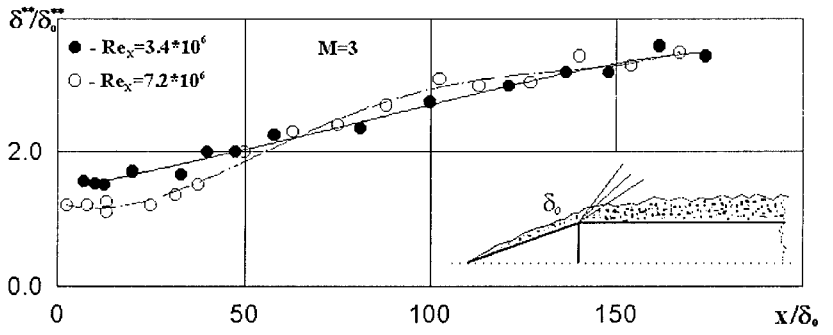


Figure 3: Momentum thicknesses behind expansion fan.

kinematically non-equilibrium (in the sense of Klauser) over the length of up to 200 δ_0. This can be related to specific features of the flow structure behind the expansion fan and to a possibility of complete or partial relaminarization of the boundary layer behind the corner point. Relaminarization was studied on 2D and axisymmetric models.

The increase of relaxation region was also confirmed by the measurement of mass flow fluctuations. Flow fluctuations decreased behind the expansion fan and was most considerable in the middle part of the layer. Mass flow fluctuations started to increase behind relaminarized region. This increase was most intense in the near-wall part of the boundary layer. It is very important to know the difference in separation properties of the boundary layer affected by the shock wave or expansion fan. The action is different in these two cases. It was found in experiments that the fullness of the boundary layer velocity profile behind the shock wave rapidly increases and grows downstream. The velocity profile

fullness behind the expansion fan, on the contrary, decreases downstream. The power exponent in the power law allows one to evaluate the fullness of velocity profile. For comparison Figure 4 and Figure 5 show the power exponent in the power law for the boundary layer velocity profile. It is seen that the values of

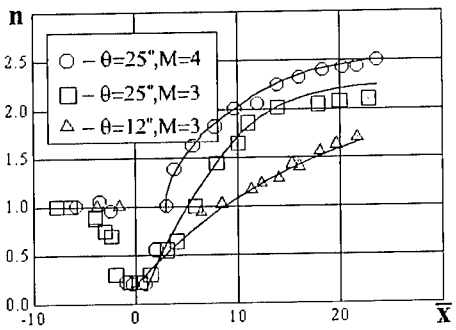


Figure 4: Power exponent behind shock wave.

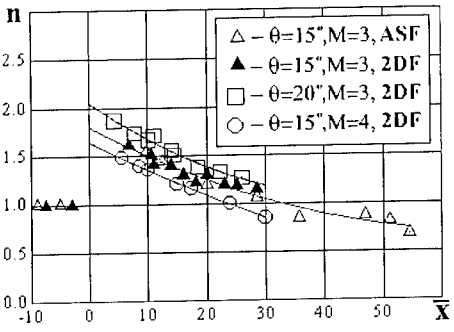


Figure 5: Power exponent behind expansion fan.

"**n**" are different behind the shock wave and expansion fan and have the opposite evolution tendencies. As a consequence, the boundary layer properties are also different. After a repeated action of the shock wave, the separation region disappears or significantly decreases in size, whereas the separation was large after the first action of the shock wave. The reverse result was obtained for the flow behind the expansion fan. Turbulization of the boundary layer and its better ability to withstand separation follow the shock (adverse pressure gradient), whereas the boundary layer relaminarization occurs after the expansion fan, its separation properties becoming worse.

3 Conclusions

- The action of the shock wave and expansion fan leads to considerable changes of structure, integral thicknesses of the boundary layer and skin friction.
- The length of the boundary layer relaxation behind the shock wave and expansion fan is considerably different (20 and 150 boundary layer thicknesses).
- Complex interactions cannot be considered as a simple superposition of two individual actions. The process is substantially nonlinear and depends on a wide range of parameters.

XXIV

Vortex Dynamics

ADVANCES IN TURBULENCE VIII
Proceedings of the Eighth European Turbulence Conference
C. Dopazo et al. (Eds.)
© CIMNE, Barcelona 2000

Multipolar instability of a vortex in a deformed cylinder

C. Eloy, P. Le Gal and S. Le Dizès

Institut de Recherche sur Les Phénomènes Hors Equilibre
CNRS UMR 6594, Universités Aix-Marseille I et II
12 avenue Général Leclerc, F-13003 Marseille, FRANCE

Contact e-mail: eloy@marius.univ-mrs.fr

1 Introduction

Filaments in turbulent flows are known to exhibit complex behavior such as splitting and undulation. These dynamics have been related to the presence of Kelvin modes on the filaments by Arendt et al. [1]. Besides, vortices in turbulent fields are subject to external strain fields which deform, at first order, their streamlines into ellipses [2]. This deformation leads to the *elliptic instability* whose proper modes are precisely combinations of Kelvin modes [3, 4, 5].

Gledzer et al. [6] first evidenced experimentally the elliptic instability using a rigid cylinder of elliptic cross section filled with water which was sharply stopped after solid body rotation was reached. Later, Malkus & Waleffe [7] used the boundary to drive the flow inside a deformable cylinder in order to avoid the transient effects of Gledzer et al's experiment. In the present work, new experiments are carried out with a set-up similar to Malkus' one and the instability is generalized to azimuthal symmetries of higher order.

2 Experimental set-up and theoretical analysis

The core of the experiment is a transparent plastic extruded cylinder of radius $R = 2.75\,\mathrm{cm}$ and variable length $H = 8$–$22\,\mathrm{cm}$. The small thickness of its wall ($0.5\,\mathrm{mm}$) allows to deform it with two or three rolls parallel to its axis as shown on Fig. 1. This deformed cylinder is rotated by a 300 W variable speed electric motor at a chosen angular speed $\Omega = 0.5$–$10\,\mathrm{rad\,s^{-1}}$. The cylinder is filled with water seeded by anisotropic particles and a laser sheet is formed in a plane containing the cylinder axis for visualisation.

When the cylinder is rotated and after the transient phase of spin-up, the basic flow is approximatively described, in cylindrical coordinates (r, θ, z), by the streamfunction:

$$\psi = -\frac{1}{2}r^2 + \frac{\varepsilon}{n}r^n \sin(n\theta), \qquad (1)$$

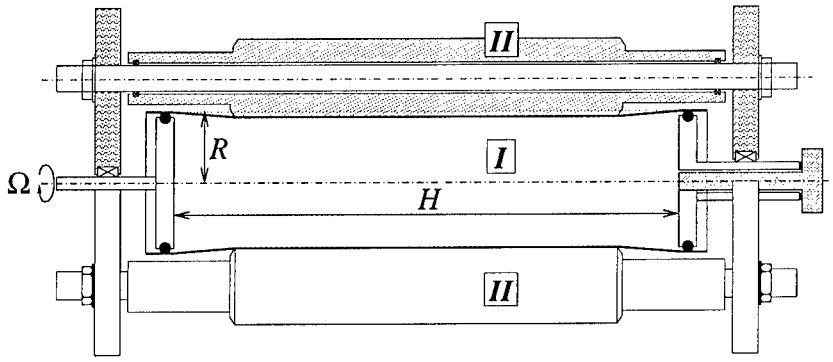


Figure 1: Experimental set-up: (I) Plastic elastic cylinder; (II) rolls.

n	mode	$\omega_{\text{th.}}$	$\omega_{\text{exp.}}$	$\lambda_{\text{th.}}$	$\lambda_{\text{exp.}}$	Fig.
2	$(-1,1,1)$	0.00	0.00	3.98	3.98	2a
2	$(-1,1,2)$	0.00	0.00	1.91	1.87	2b
2	$(1,3,1)$	2.04	2.0	2.07	2.03	2c
3	$(-1,2,1)$	0.66	0.65	1.71	1.70	3a
3	$(0,3,1)$	1.61	1.5	1.21	1.27	3b

Table 1: Theoretical prediction of frequency $\omega_{\text{th.}}$ and wavelength $\lambda_{\text{th.}}$ of few principal modes compared to experimental measurements $\omega_{\text{exp.}}$ and $\lambda_{\text{exp.}}$.

where ε measures the deformation of the streamlines and n is the degree of azimuthal symmetry of the flow or equivalently the number of rolls deforming the elastic cylinder. Here, the variables are non-dimensionalized using the characteristic length R and time Ω^{-1}. The streamfunction (1) provides a two-dimensional flow of constant vorticity with an n-fold symmetry which is a generalization of the elliptical flow. Using global techniques (as done in [3, 4]), the flow (1) was shown to be unstable for $n = 2$, 3 or 4 [5, 8], giving rise to what we shall call the *multipolar instability.*

The unstable modes of the instability are shown to be combinations of two Kelvin modes of same axial wavenumber, same frequency and azimuthal wavenumbers m_1 and m_2 such that $m_2 - m_1 = n$ [5]. However, few combinations are significantly more unstable than others; they are named *principal modes* and noted (m_1, m_2, i), where i is an integer which is an increasing function of the axial wavenumber. These principal modes form standing waves of given wavelength λ and frequency ω as given in table 1. Principal modes can be selected by viscosity (for low Reynolds numbers, $Re = \Omega R^2/\nu$, the modes with the largest wavelengths are selected) and by the aspect ratio H/R (the wavelength must satisfy $l\lambda = 2H/R$, with l an integer).

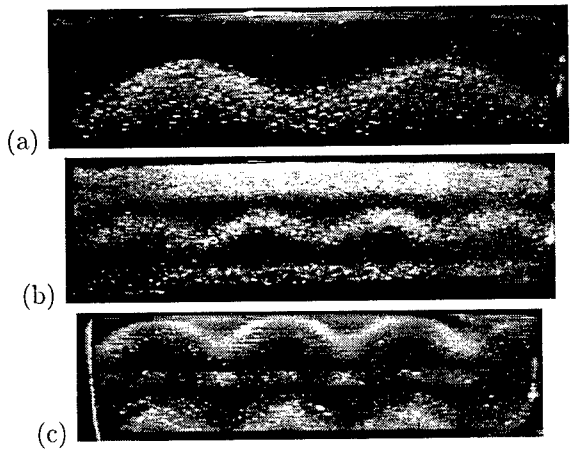


Figure 2: Visualisations of the flow for $n = 2$, $Re = 2500$ and: (a) $H/R = 7.96$; (b) 7.49; (c) 7.13. It corresponds to the principal modes $(-1, 1, 1)$, $(-1, 1, 2)$ and $(1, 3, 1)$ respectively.

3 Results and discussion

The selection of principal modes by the aspect ratio is illustrated on Figs. 2a–c, for $n = 2$. Depending on the length of the cylinder, three different principal modes have been observed for the same Reynolds number. Their wavelengths λ are such that $H/R = 2\lambda$, 4λ and 3.5λ respectively. These wavelengths are in good agreement with the theoretical predictions, as shown in table 1. The principal modes associated with Figs. 2a and 2b are steady. This is in agreement with the prediction for the modes $(-1, 1, i)$. However, the mode visualized on Fig. 2c is time periodic. Its frequency, measured by image analysis ($\omega = 2.0\Omega$), agrees with the prediction for mode $(1, 3, 1)$ (see table 1).

For triangular deformations of the cylinder, similar experiments have been carried out. For small aspect ratios, two different modes have been evidenced. Fig. 3 displays visualisations of the flow for $H/R = 3.4$ and 3.8 and $Re = 1200$. Again, the measurements of wavelengths and frequencies, given in table 1, compare well with predictions.

The experimental results reported in this paper characterize, for the first time, oscillating modes in the elliptic and triangular geometries, as predicted by theoretical stability analysis. These results extend the previous observations restricted to steady modes in the elliptic geometry [6, 7]. For Reynolds numbers below 4000, the multipolar instability has been visualized in its saturated regime. Above this value, the vortex breaks up and the flow enters a cycle of disordered and laminar states. More details on mode selection, instability threshold, nonlinear behavior and secondary instability are given in refs. [8, 9].

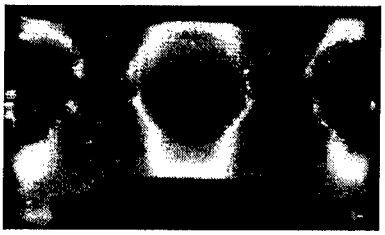
(a)  (b) 

Figure 3: Visualisations of the flow for $n = 3$, $Re = 1200$ and: (a) $H/R = 3.4$; (b) 3.8. It corresponds to the principal modes $(-1, 2, 1)$ and $(0, 3, 1)$ respectively.

References

[1] S. Arendt, D. C. Fritts, and Ø. Andreassen. Kelvin twist waves in the transition to turbulence. *Eur. J. Mech.* B/*Fluids*, 17:595–604, 1998.

[2] H. K. Moffatt, S. Kida, and K. Ohkitani. Stretched vortices -the sinews of turbulence; large-Reynolds-number asymptotics. *J. Fluid Mech.*, 259:241–264, 1994.

[3] D. W. Moore and P. G. Saffman. The instability of a straight vortex filament in a strain field. *Proc. R. Soc. London Ser. A*, 346:413–425, 1975.

[4] C.-Y. Tsai and S. E. Widnall. The stability of short waves on a straight vortex filament in a weak externally imposed strain field. *J. Fluid Mech.*, 73(4):721–733, 1976.

[5] C. Eloy and S. Le Dizès. Stability of Rankine vortex in a multipolar strain field. *Submitted to Phys. Fluids.*

[6] E. B. Gledzer, F. V. Dolzhanskiy, A. M. Obukhov, and V. M. Ponomarev. An experimental and theoretical study of the stability of motion of a liquid in an elliptical cylinder. *Izv. Acad. Sci. USSR Atmos. Oceanic Phys.*, 11(10):617–622, 1975.

[7] W. V. R. Malkus and F. A. Waleffe. Transition from order to disorder in elliptical flow: a direct path to shear flow turbulence. In A. V. Johansson and P. H. Alfredsson (editors), *Advances in turbulence III.* Springer, Berlin, 1991.

[8] C. Eloy. *Instabilité multipolaire de tourbillons.* PhD thesis, Université Aix-Marseille II, 2000.

[9] C. Eloy, P. Le Gal and S. Le Dizès. Experimental study of the multipolar vortex instability. *Submitted to Phys. Rev. Lett..*

ADVANCES IN TURBULENCE VIII
Proceedings of the Eighth European Turbulence Conference
C. Dopazo et al. (Eds.)
© CIMNE, Barcelona 2000

Decay of perturbations near the centre of a strong vortex

K. Bajer[1], A. P. Bassom[2] and A. D. Gilbert[2]

[1]Institute of Geophysics, Warsaw University
ul. Pasteura 7, 02-093 Warszawa, POLAND
[2]School of Mathematical Sciences, University of Exeter
Exeter EX4 4QE, U.K.

Contact e-mail: kbajer@fuw.edu.pl

1 Introduction

The spiral wind-up and diffusive decay of a passive scalar in circular stream lines is considered. The shear–diffuse mechanism operates to destroy scalar fluctuations on a time scale of order $P_e^{1/3}$ times the turnover time, where P_e is a Péclet number. The mechanism relies on differential rotation, that is a non-zero gradient of angular velocity. However if the flow is smooth, the gradient of angular velocity necessarily vanishes at the centre of the stream lines, and the time scale becomes greater there. The behaviour at the centre is analysed and it is found that scalar at the origin is only destroyed by the shear–diffuse mechanism on a longer time scale of order $P_e^{1/2}$. Similar results are obtained for magnetic field and for weak vorticity, an active scalar.

In the presence of shear the diffusion of passive scalars and weak magnetic fields, both governed by the advection-diffusion equation, is considerably enhanced. The principle of this phenomenon is the continuous decrease of the characteristic length-scale of the advected quantity whose growing gradients cause accelerated diffusion. Weak vorticity perturbations are also subject to this mechanism although the evolution equation has an extra term in this case. The wind-up of the vorticity perturbations has an important effect even in the diffusionless (inviscid) flow. The vorticity perturbation is not annihilated but, due to the wind-up, the corresponding velocity perturbation in the far field of the vortex decays rapidly [3].

2 Passive scalar and magnetic fields

Particularly interesting is the shear-diffusion process near a strong coherent vortex. Then the scalar isolines, the magnetic field lines or the contour levels of

the vorticity perturbations are wound up into increasingly tight double spirals. The spirals are double because, as we move radially outwards from the centre of the vortex, the arms have alternating sign of the perturbation. This is easiest to visualise for the wind-up of the uniform magnetic field where the field has opposite direction in the neighbouring arms of the spiral and is annihilated by diffusion. This combination of the spiral wind-up and diffusion is known as flux expulsion [7] [1].

When the vortex is axially symmetric we consider Fourier modes $\mathrm{e}^{in\theta}$ which are independent of each other due to the linearity of the problem. We can easily write the solution for the case of pure advection (vanishing diffusivity) and then systematically calculate the diffusive corrections. This expansion [6] [7] is valid where the angular velocity of the flow changes with radius, i.e. $\omega'(r) \neq 0$. The expansion shows that the fluctuations decay on a time-scale $\epsilon^{-1/3}t_o$, where t_o is the turnover time and ϵ is the appropriate non-dimensional diffusivity, e.g. for the passive scalar problem $\epsilon = Pe^{-1}$, Pe being the Péclet number. When $\epsilon \ll 1$ this is considerably faster than the normal diffusive time-scale $\epsilon^{-1}t_0$.

The shear-diffuse mechanism relies on differential rotation. However, if the flow having stream function $\Psi(R)$ is smooth, the gradient of angular velocity $\alpha'(r)$ necessarily vanishes at the vortex centre where $\alpha(r) = -r^{-1}\partial_r\Psi$ typically has a parabolic profile. Taking the passive scalar concentration $\Sigma(r,\theta,t)$ in the form

$$\Sigma(r,\theta,t) = \Re e\left(\sigma(r,t)\mathrm{e}^{\mathrm{i}n\theta}\right), \tag{1}$$

we obtain from the non-dimensionalised advection-diffusion equation

$$\partial_t\sigma + \mathrm{i}n\alpha(r)\sigma = \epsilon\Delta\sigma \qquad (\Delta \equiv \partial_r^2 + r^{-1}\partial_r - n^2r^{-2}). \tag{2}$$

For a parabolic profile,

$$\alpha(r) = \alpha_0 + \alpha_1 r^2, \tag{3}$$

we found an interesting exact solution to this problem in the form

$$\sigma = \sigma_0 r^n \mathrm{e}^{-\mathrm{i}n\alpha_0 t - \mathrm{i}f(t)r^2 - g(t)}. \tag{4}$$

The functions $f(t)$, $g(t)$ then satisfy the equations

$$f' = n\alpha_1 - 4\mathrm{i}\epsilon f^2, \qquad g' = 4\mathrm{i}\epsilon(n+1)f, \tag{5}$$

which can be solved as

$$f(t) = (1-\mathrm{i})\sqrt{\frac{n\alpha_1}{8\epsilon}}\tanh\tau, \qquad g(t) = (n+1)\log\cosh\tau, \tag{6}$$

with $\tau = (1+\mathrm{i})t\sqrt{2\epsilon n\alpha_1}$. A similar solution to a related problem involving a plane jet is discussed by Brunet and Haynes [5].

The exact solution (4) captures two regimes with different time-scales. For $t \ll \epsilon^{-1/2}$ we may expand

$$f = n\alpha_1 t - 4\mathrm{i}n^2\alpha_1^2\epsilon t^3 + O(\epsilon^2 t^5), \tag{7}$$

$$g = 2(n+1)(\epsilon n^2 t + \mathrm{i}\epsilon n\alpha_1 t^2 + 2\epsilon^2 n^2\alpha_1^2 t^4/3 + O(\epsilon^3 t^6). \tag{8}$$

Then we obtain

$$\sigma(r,t) \sim \sigma_0 r^n \mathrm{e}^{-\mathrm{i}n(\alpha_0+\alpha_1 r^2)t}\mathrm{e}^{-4\epsilon n^2\alpha_1^2 r^2 t^3/3} \qquad (t \ll \epsilon^{-1/2}), \tag{9}$$

which is the general asymptotic form of the shear-diffuse mechanism [7] [8]. The characteristic time-scale of this process is $t = O(\epsilon^{-1/3})$ compared with the much slower time-scale $t = O(\epsilon^{-1})$ of the ordinary diffusion in stationary fluid.

For $t \gg \epsilon^{-1/2}$ we have different expansion,

$$f(t) \sim (1-\mathrm{i})\sqrt{n\alpha_1/8\epsilon}, \qquad g(t) \sim (n+1)((1+\mathrm{i})t\sqrt{2\epsilon n\alpha_1} - \log 2), \tag{10}$$

which leads to

$$\sigma(r,t) \sim \sigma_0 r^n \sqrt{2}\mathrm{e}^{-(1+\mathrm{i})r^2\sqrt{n\alpha_1/8\epsilon}}\mathrm{e}^{pt}, \tag{11}$$

where $p = -\mathrm{i}n\alpha_0 - (n+1)(1+\mathrm{i}\sqrt{2\epsilon n\alpha_1} - \log 2)$. This represents the process near the vortex centre where the gradient of angular velocity vanishes. The time-scale is $t = O(\epsilon^{-1/2})$, intermediate between the shear-diffusion and ordinary diffusion. This is the time-scale on which the azimuthal gradients decay and the distribution of a passive scalar near the vortex centre becomes axisymmetric.

The same analysis can be repeated for the *weak* magnetic field perpendicular to the vortex. The magnetic flux function plays the role of the passive scalar and $\epsilon = Rm^{-1}$ where Rm is the magnetic Reynolds number. Then $t = O(\epsilon^{-1/2})$ would be the time-scale on which the initially uniform magnetic field survives near the centre of an eddy.

3 Vorticity

We now consider evolution of *weak* background vorticity $\omega(r,\theta,t)$ under the influence of a strong localised axisymmetric vortex with vorticity $\Omega(r) = -\Delta\Psi(r)$. The weak vorticity is an *active* scalar satisfying the linearised Navier-Stokes equation,

$$\partial_t\omega + J(\omega,\Psi) + J(\Omega,\psi) = \epsilon\nabla^2\omega, \qquad \omega = -\nabla^2\psi \qquad (\epsilon \equiv \mathrm{Re}^{-1}), \tag{12}$$

where Re is the Reynolds number. We take the parabolic angular velocity profile (3) and write ω in the form such as to separate the uniform rotation α_0,

$$\omega(r,\theta,t) = \omega_0 r^n \mathrm{e}^{\mathrm{i}n(\theta-\alpha_0 t)}X(r,t), \qquad \psi = \omega_0 r^n \mathrm{e}^{\mathrm{i}n(\theta-\alpha_0 t)}Y(r,t). \tag{13}$$

This gives coupled equations for X and Y,

$$\partial_t X + \mathrm{i}n\alpha_1 r^2 X + 8\mathrm{i}n\alpha_1 Y = \epsilon\Delta_n X, \qquad -X = \Delta_n Y, \tag{14}$$

with $\Delta_n = \partial_r^2 + (2n+1)r^{-1}\partial_r$.

In the inviscid case, $\epsilon = 0$, the solution was given by Bassom and Gilbert [3]. Quite remarkably an exact solution can also be found for arbitrary Reynolds number. It is expressed in terms of Kummer functions. The evolution of the passive scalar outlined in the previous section is a guide to the asymptotic analysis of the behaviour of vorticity but the details are too long for this brief report. Similarly to the passive scalar case the time-scale for the axisymmetrisation of vorticity near the centre of an eddy is longer than that for shear diffusion in the region of finite differential rotation.

The parabolic angular velocity profile considered here is a local approximation near the centre of an axisymmetric vortex. More realistic modeling of the decay of the azimuthal gradients must take into account vortices deformed by shear or strain [4] [2] .

This work was supported by the State Committee for Scientific Research (KBN) grant no 2 P03B 135 17 and by the British/Polish Joint Research Programme of the British Council and KBN.

References

[1] K. Bajer. Flux expulsion by a point vortex. *Eur. J. Mech. B/Fluids*, 17:653–664, 1998.

[2] K. Bajer and H. K. Moffatt. Theory of non-axisymmetric Burger's vortex with arbitrary Reynolds number. In: *Dynamics of Slender Vortices* (eds. E. Krause & K. Gersten), pp. 193–202. Kluwer, 1998.

[3] A. P. Bassom and A. D. Gilbert. The spiral wind-up of vorticity in an inviscid planar vortex. *J. Fluid Mech.* 371:109–140, 1998.

[4] A. P. Bassom and A. D. Gilbert. The spiral wind-up and dissipation of vorticity and a passive scalar in a strained planar vortex. *J. Fluid Mech.* 398:245–270, 1999.

[5] G. Brunet and P. Haynes. The nonlinear evolution of disturbances to a parabolic jet. *J. Atmos. Sci.* 52:464–477, 1995.

[6] T. S. Lundgren. Strained spiral vortex model for turbulent fine structure. *Phys. Fluids*, 25:2193–2203, 1982.

[7] H. K. Moffatt and H. Kamkar. On the time-scale associated with flux expulsion. In: *Stellar and Planetary Magnetism* (ed. A. M. Soward), pp. 91–97. Gordon & Breach, 1983.

[8] P. B. Rhines and W. R. Young. How rapidly is a passive scalar mixed within closed streamlines? *J. Fluid Mech.* 133:133–145, 1983.

ADVANCES IN TURBULENCE VIII
Proceedings of the Eighth European Turbulence Conference
C. Dopazo et al. (Eds.)
© CIMNE, Barcelona 2000

Energy dissipation in spiral vortex layers wrapped around a diffusing straight vortex tube

G. Kawahara[1], S. Kida[2], S. Yanase[3], and M. Tanaka[4]

[1]Department of Mechanical Engineering, Ehime University
Matsuyama 790–8577, Japan
[2]Theory and Computer Simulation Center, National Institute for Fusion Science
Toki 509–5292, Japan
[3]Department of Mechanical Engineering, Okayama University
Okayama 700–8530, Japan
[4]Department of Mechanical and System Engineering, Kyoto Institute of Technology
Kyoto 606–8585, Japan

Contact e-mail: kawahara@dpc.ehime-u.ac.jp

1 Introduction

Tube-like structures of concentrated high vorticity have commonly been observed in various classes of turbulent flows, and a relatively large portion of turbulence kinetic energy is dissipated by tubular structures. Another candidate for typical dissipative structures in turbulence is double spiral layers of vorticity, although spiral structures in turbulence have been less understood. There are two possible generation mechanisms of spiral structures. If a vortex layer winds up into a row of vortex tubes through the Kelvin–Helmholtz instability, the original layer forms double spirals around the tube (see Lundgren [1]). If a vortex tube exists in a weaker background vorticity field, the tube wraps and stretches vorticity lines around itself to form double spiral vortex layers (see Moore [2]; Kawahara *et al.* [3]). In the former mechanism the vorticity in the spirals aligns with the tube, while in the latter the vorticity component perpendicular to the tube becomes dominant because of vorticity stretching and intensification. Recently, in their direct numerical simulation of isotropic turbulence, Kida *et al.* [4] have found the real existence of double spiral vortex layers with the dominant perpendicular compoment of vorticity, i.e. the latter case.

In this paper, we investigate analytically the energy dissipation in spiral vortex layers that are formed through wrap and stretch of vorticity lines of a uniform shear flow around a longitudinal diffusing straight vortex tube. The structures of a viscous dissipation rate around the vortex tube and their contribution to

total dissipation are discussed. The effect on the dissipation of a small tilt of the tube from the streamwise direction is also discussed.

2 Dissipation in tube and spiral layers

We consider a straight vortex tube of circulation Γ in a uniform shear flow $Sy\,\boldsymbol{e}_x$ (see Figure 1), where S (> 0) is a shear rate which is constant in space and time. The central axis of the tube is tilted on the plane $y = 0$ at a small angle α from the x-direction. For $\alpha > 0$ (or < 0) the z-component of the tube vorticity has the same (or opposite) sign as the uniform shear vorticity. The vortex tube of $\alpha > 0$ (or < 0) is referred to as a cyclone (or anti-cyclone). When the tube starts with a vortex filament at time $St = 0$, it diffuses while wrapping and stretching vorticity lines of the uniform shear flow to form double spiral vortex layers with high azimuthal vorticity of alternating sign (Moore [2]; Kawahara *et al.* [3]; see the left panel in Figure 2). In the limit of $St|\alpha| \ll 1$, the asymptotic solution to the Navier–Stokes equation is obtained at finite as well as large Reynolds numbers Γ/ν, where ν is the kinematic viscosity of fluid.

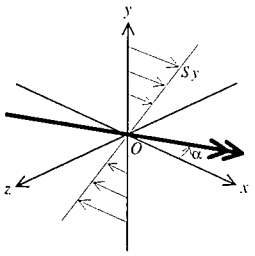


Figure 1: Flow configuration. The thick double arrow denotes a vortex tube.

Figure 2 shows the spatial distributions on a plane perpendicular to the vortex tube of the magnitude of perpendicular vorticity (the left panel) and energy dissipation rate per unit mass (the right panel), respectively. It can be seen that the dissipation rate is composed of two contributions from a swirling flow induced by the vortex tube (the circular ring region near the center) and from an axial flow induced by the wrapped vortex layers (the two spiral regions around the ring). The leading-order contribution of the diffusing vortex tube to the total energy dissipation, which is exactly expressed as $(\Gamma^2/8\pi)\,t^{-1}$, decreases with time t. On the other hand, the leading contribution of the vortex layers, which is asymptotically evaluated to be $3^{-2/3}\pi\Gamma(\frac{1}{3})\nu^2 S^2\,(\Gamma/2\pi\nu)^{4/3}\,t$ for $\Gamma/\nu \gg 1$, increases with t. Thus, there may exist critical time t_c after which the contribution of the layers is greater than that of the tube.

The critical time is shown in Figure 3 against the Reynolds number. At finite Reynolds numbers the critical time roughly stays around $St_c = 2$. For $\Gamma/\nu \gg 1$, the critical time is well described in terms of the large-Reynolds-

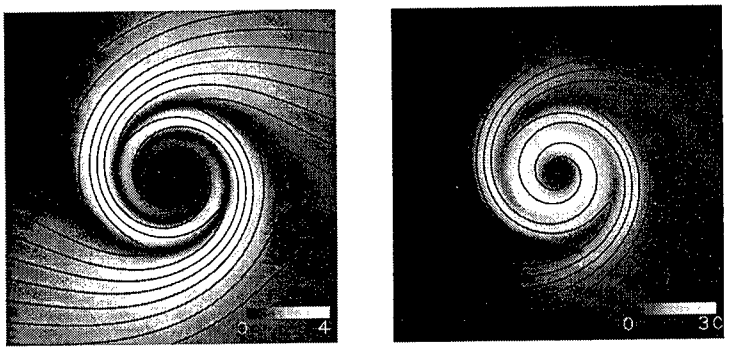


Figure 2: Spatial distributions on a plane perpendicular to the vortex tube of the magnitude of perpendicular vorticity (left) and energy dissipation rate (right) at the critical time $St_c = 2.94$ (see Figure 3) for $\Gamma/(2\pi\nu) = 100$ and $\alpha = 0$. The vorticity magnitude and the dissipation rate are scaled by S and νS^2, respectively. The bright parts represent a large value. The contribution of the uniform shear flow to the dissipation rate has been subtracted. The solid lines denote the projection of a vorticity line on the perpendicular plane. The vortex tube rotates counter-clockwise.

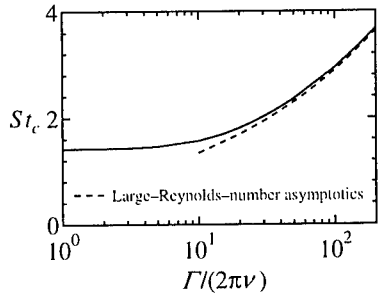


Figure 3: Reynolds number dependence of the critical time after which the contribution of the spiral vortex layers to the total dissipation exceeds that of the vortex tube.

number asymptotics $St_c = 0.623\,(\Gamma/2\pi\nu)^{1/3}$. In turbulence, wrapped vortex layers around a tubular structure are conjectured to be a dominant contributor to the energy dissipation instead of the tube itself in a later stage of their time evolution.

3 Effect of tube tilt on dissipation

Next, we discuss the effect on the energy dissipation of a small tilt of a vortex tube from the x-direction. Figure 4 shows the spatial distribution of energy

dissipation rate for a cyclone of $\alpha = 0.2$ (the left panel) and for an anti-cyclone of $\alpha = -0.2$ (the right panel) in the same way as in Figure 2 (cf. the right panel for $\alpha = 0$ in Figure 2). When the tube is tilted, the wrapped double spiral vortex layers are sheared in different ways depending on the sign of the tilt angle α. If $\alpha > 0$ (a cyclone), the radial thickness of the outermost strong spirals widens, so that the azimuthal vorticity and the corresponding viscous dissipation rate are reduced. If $\alpha < 0$ (an anti-cyclone), on the other hand, the thickness of the spirals tightens, which leads to an enhancement of the azimuthal vorticity and the dissipation rate. These local reduction and enhancement can affect the total energy dissipation at a higher order. The primary effect of the tilt of the tube on the total dissipation is expressed asymptotically as $-\frac{1}{4}\alpha\nu S^3 \Gamma \ln(\Gamma/2\pi\nu)\, t^2$ at large Reynolds numbers $\Gamma/\nu \gg 1$.

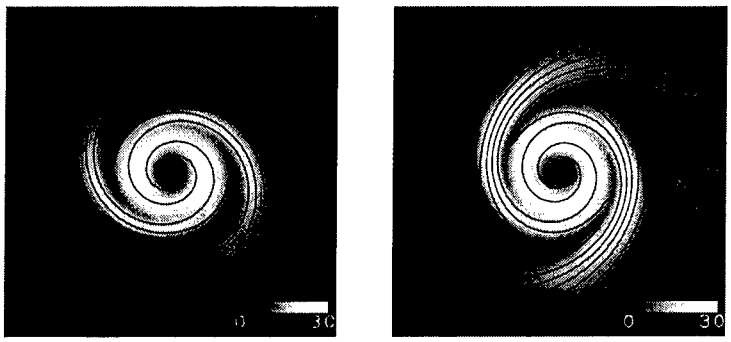


Figure 4: Same as Figure 2 but for spatial distribution of dissipation rate in the cases of a cyclone at $\alpha = 0.2$ (left) and of an anti-cyclone at $\alpha = -0.2$ (right).

References

[1] T. S. Lundgren. Strained spiral vortex model for turbulent fine structure. *Phys. Fluids*, 25: 2193–2203, 1982.

[2] D. W. Moore. The interaction of a diffusing line vortex and aligned shear flow. *Proc. R. Soc. Lond.*, A 399: 367–375, 1985.

[3] G. Kawahara, S. Kida, M. Tanaka, and S. Yanase. Wrap, tilt and stretch of vorticity lines around a strong thin straight vortex tube in a simple shear flow. *J. Fluid Mech.*, 353: 115–162, 1997.

[4] S. Kida, H. Miura, and T. Adachi. Spatiotemporal structure of tubular vortices in turbulence. *Extended Abstracts of IUTAM Symposium on Geometry and Statistics of Turbulence*, 4–5, 1999.

ADVANCES IN TURBULENCE VIII
Proceedings of the Eighth European Turbulence Conference
C. Dopazo et al. (Eds.)
© CIMNE, Barcelona 2000

Vortex-wave conversion in high shear flows

G. D. Chagelishvili,[1,2] A. G. Tevzadze,[1,3] G. Bodo[4],
P. Rossi[4] and G. T. Gogoberidze[1]

[1] Abastumani Astrophysical Observatory, Tbilisi, Georgia
[2] Space Research Institute, Moscow, Russia
[3] Centre for Plasma Astrophysics, K.U.Leuven, Belgium
[4] Osservatorio Astronomico di Torino, Pino Torinese, Italy

Contact e-mail: georgech@mx.iki.rssi.ru

1 Introduction

Excitation of waves in the hydrodynamic medium is one of the principal problems in fluid mechanics. The theory of aerodynamic sound production has been introduced in the classical papers by Lighthill [1]. Qualitatively new approach to the problem has been developed recently: the phenomenon of an abrupt emergence of acoustic waves from vortices in flows with velocity shear has been found and investigated in papers [2, 3]. This linear mechanism is non-resonant by nature and differs in principle from the Lighthill's stochastic mechanism.

We report on this mode conversion phenomenon and present the numerical study of the dynamics of initially excited vortex mode disturbances in shear flows. Particularly, evolution of individual spatial Fourier harmonics (SFH) (Sec. 2.1) as well as localized package of vortex disturbances (Sec. 2.2) is described.

2 Physical approach and numerical results

We study the phenomenon in 2D unbounded compressible inviscid flow with uniform density and constant shear of velocity: $\mathbf{U_0} = \mathbf{U_0}(Ay, 0)$. Considered system sustains two different modes of disturbances – wave mode that corresponds to the acoustic oscillations and vortex mode that corresponds to the aperiodic vortical motions. The phenomenon of the conversion of the vortex to the acoustic wave mode is closely related to the non-normality of the linear dynamics of disturbances in shear flows and is best interpreted in the framework of the nonmodal approach – by tracing of linear dynamics of SFH of vortex disturbances in time. Therefore, we present numerical calculations of the linear dynamics of SFH of vortex disturbances together with the exact numerical

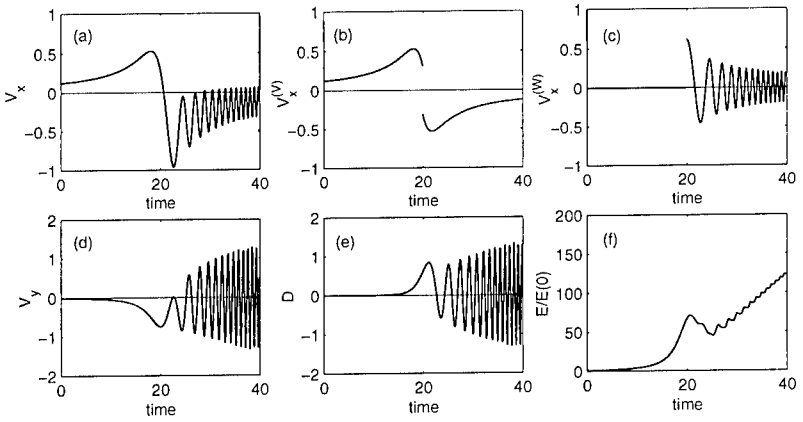


Figure 1: The evolution of the velocity $V_x(t)$, $V_y(t)$, density $D(t)$ and total energy of disturbances $E(t)/E(0)$ are shown on the a, d, e, and f graphs, respectively. The aperiodic (vortical) $V_x^{(V)}(t)$ and oscillating $V_x^{(W)}(t)$ parts of the V_x are shown on b and c graphs, respectively. Here $k_y(0)/k_x = 8$ and $R \equiv A/k_x c_s = 0.4$. Purely vortex mode SFH (without admixed acoustic wave one) is taken initially. Emergence of the oscillations clearly occurs at $\tau^* = t^*/k_x c_s = 20$.

solution of the 2D compressible hydrodynamic equations with initial values of physical quantities composed by the superposition of the shear flow and localized vortex mode disturbances.

2.1 Dynamics of vortex SFH

In the nonmodal approach, the effect of the shearing background on the wave crests of linear disturbances is described by the temporal variation of the wavenumbers ($k_x = \text{const.}$, $k_y(t) = k_y(0) - k_x At$) of the SFH defined as follows: $\psi(x,y,t) = \tilde{\psi}(k_x, k_y(t), t)\exp(ik_x x + k_y(t)y)$, where $\psi(x,y,t) \equiv (v_x', v_y', \rho', p')$, and $\tilde{\psi}(k_x, k_y(t), t) \equiv (V_x, V_y, D, P)$. We show the results of the numerical calculations that demonstrate the vortex-wave mode conversion phenomenon on Fig. 1. The linear dynamics of the vortex SFH, involving conversion to the wave SFH proceeds as follows [2]: Initially, following the linear drift of wavenumbers the vortex SFH gains shear flow energy and is amplified. Therewith, disturbances remain aperiodic till $k_y(t)/k_x > 0$. At the point in time $t^*/k_x c_s = 20$ when $k_y(t^*) = 0$, the vortex SFH abruptly gives rise to the corresponding SFH of the acoustic wave. Fig. 1.b,c separately show the vortex $V_x^{(V)}$

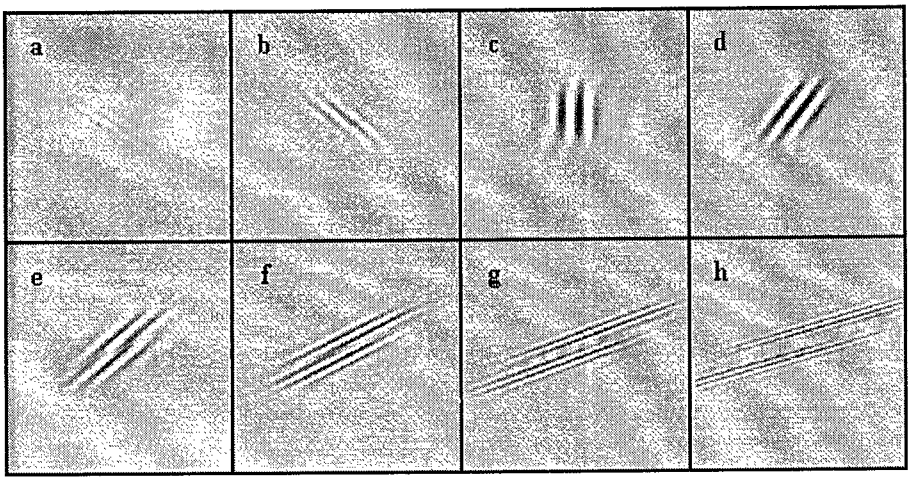


Figure 2: Evolution of the shear flow density is shown at times $\tau = t/(k_x c_s) = 2, 6, 10, 14, 16, 20, 24, 28$ on the a,b,c,d,e,f,g and h graphs, respectively. The X and Y axis are directed horizontally and vertically, respectively. Initial flow is composed by the constant shear flow with $R \equiv A/k_{xc}c_s = 0.5$ and the package of the vortex mode disturbances localized in the **k**-space in point $k_{yc} = 2k_{xc} = 0.02$ (without acoustic admixes). Characteristic scales of the localization of the package along X and Y axis (in the **r**-space) and along k_x axis (in the **k**- space) are $D_r = 1/D_k = 2/k_{xc}$. The package is prolonged in the co-ordinate space along the line $y = -(k_{xc}/k_{yc})x$ (see Fig.2a) and in the **k**-space along the line $k_y = (k_{yc}/k_{xc})k_x$, initially.

and acoustic wave $V_x^{(W)}$ components of the V_x: $V_x = V_x^{(V)} + V_x^{(W)}$. These graphs clearly demonstrate the abrupt character of the phenomenon. Only the aperiodic vortex mode disturbance is occurred initially: $V_x^{(v)}|_{t<t^*} \neq 0$ and $V_x^{(W)}|_{t<t^*} = 0$ (see Fig. 1.a-c). While oscillations of the acoustic wave SFH are emerged at $t = t^*$: $V_x^{(W)}|_{t\geq t^*} \neq 0$ (see Fig. 1.c). In short, it turns out that the vortex mode disturbances are able to excite acoustic waves in the linear regime due to the mean flow velocity shear. This phenomenon strongly depends on the value of effective shear parameter $R \equiv A/k_x c_s$. It becomes noticeable at R=0.2 and even at R=0.3 it dominates in the shear flow dynamics. At low parameters of velocity shear, amplitude of the generated wave SFH is largely reduced and in the normalized form may be estimated by the following approximate equation: $V_x(t^*)/\Omega = 1/(1.2R)\exp(-1/1.2R)$, where

$\Omega \equiv k_y(t)V_x(t) - k_x V_y(t) + AD(t) = \text{const.}$ is the conserved vorticity in **k**-space.

2.2 Dynamics of vortex package

Results of the numerical simulations of the 2D *compressible* shear flow with vortex disturbances are presented on Fig. 2. The initial conditions are composed from the superposition of the constant shear flow and a package of the vortex mode disturbances localized in both, wave-number as well as in the co-ordinate spaces. In the beginning ($\tau < 10$), vortex disturbances gain the mean flow energy and remain aperiodic in time. Wave crests are turning around due to the effect of the shearing background. Therewith, the package remains localized as much as the group velocity of the vortex disturbances is zero. Disturbance dynamics is qualitatively different after the $\tau > 10$. At $\tau = 10$, the central part of the package of vortex mode disturbances, which drifts horizontally in the **k**-space, crosses the $k_y(\tau) = 0$ line and gives rise to the acoustic wave mode disturbances. Disturbances acquire the acoustic wave features – have non-zero group velocity and are able to transport the energy. As a result the wave crests, in addition to the turning around a fixed point, undergo a translational motion. The widening of the wave-crest becomes apparent at longer times (see Figs. 1.e-h). This explicitly demonstrates the acoustic wave generation phenomenon. This phenomenon may be also well seen from the package velocity field: the initial package of the mainly vortical (nonpotential) disturbances acquire the potential (acoustic) wave one features.

The phenomenon of the vortex-wave mode conversion is essentially linear and its occurance is not restricted by a threshold value of the shear parameter. This phenomenon deals with fundamentals of the wave generation theory, should be universally realized in the hydrodynamic flows with high shear of velocity and should make acoustic waves a *natural ingredient* of the turbulence in shear flows.

A.G.T. would like to acknowledge the financial support of the "FWO Vlaanderen", project G.0335.98. This research has been supported in part by the INTAS grant GE97-0504.

References

[1] M. J. Lighthill. On sound generated aerodynamically I. General theory. Pros. Roy. Soc. Lond. A, 211:564-587, 1952; II. Turbulence as a source of sound. Pros. Roy. Soc. Lond. A, 222:1-32, 1954.

[2] G. D. Chagelishvili, A. G. Tevzadze, G. Bodo and S. S. Moiseev. Linear mechanism of wave emergence from vortices in smooth shear flows. Phys. Rev. Letters, 79:3178-3181, 1997.

[3] G. D. Chagelishvili, A. G. Tevzadze, G. Bodo, P. Rossi, and G. T. Gogoberidze. Vortex-Wave Linear Conversion in Smooth Shear Flows. (to be published).

ADVANCES IN TURBULENCE VIII
Proceedings of the Eighth European Turbulence Conference
C. Dopazo et al. (Eds.)
© CIMNE, Barcelona 2000

Experimental study of large-scale coherent structures with helical symmetry of vorticity

S.V. Alekseenko, I.S. Cherny, and S.I. Shtork

Institute of Thermophysics SB RAS, Lavrentyev Ave. 1, 630090 Novosibirsk, Russia

Contact e-mail: aleks@itp.nsc.ru

1 Introduction

As known, the characteristics of a turbulent flow are determined by behavior of the coherent organized structures representing vortices of various scales. The large-scale stationary vortices obtained in our previous studies are seen as convenient objects for studying the properties of coherent structures. It was shown that such vortices possess a universal property of helical symmetry whose parameters can be used as characteristics of the whole swirl flow [1]. The present work is devoted to the further study of helical vortices with a concentrated field of vorticity possessing an explicit helical symmetry.

2 Experimental technique and results

The experiments were conducted in a vortex chamber with a controlled design swirl parameter. Concentration of vorticity is achieved by orificing of the chamber outlet. The base structure with a rectilinear vortex axis is formed by an axisymmetric diaphragm and horizontal bottom (Figure 1a). Introduction of any asymmetry at the chamber ends, for example, a shift of the orifice from the chamber center, leads to formation of a stationary (immobile) helical vortex (Figure 1b). By transition from the plane to the two-slope bottom at the diaphragm with a central hole, we obtained a mode with two entangled spiral vortices (Figure 1c). This structure differs from the previous one by its helical symmetry sign. Vortices in the double helix are twisted along the direction of flow rotation (in this case - clockwise), and for a single helix - counterclockwise. By varying the degree of asymmetry at the chamber ends, it is possible to generate vortices with different parameters of helical symmetry.

One of the methods for determination of helical symmetry parameters is based on finding the shape of projection of the vortex axis, which can be made

visible by means of tiny air bubbles collected on it. Using two projections from two perpendicular directions, we can recover the spatial shape of the vortex axis. The flow pattern was registered by a video camera, then the video fragments were digitized and processed by a PC. The image-processing algorithm consists of the following steps:

a) Preliminary image processing on the basis of well-known techniques [2].

b) Image vectorization using original algorithm [3].

c) Recognition of the air filament, created by the air bubbles, concentrated in the vortex core. The recognition algorithm uses the sum of brightness of picture pixels - a filament with a maximum brightness is chosen.

d) Determination of the pitch and radius of the vortex axis with the standard interpolation algorithm.

The final step of helical vortex image processing, the build-up of the "tree" and finding the vortex axis shape, are shown in Figure 2a.

In Figure 3a projections of the vortex helical axis on the orthogonal vertical planes as well as projection on the bottom chamber restored from the vertical ones are shown. As seen from the bottom view, the helical character of vortex defined by the upper boundary condition is broken near the lower chamber end. The most upper part of the vortex structure (points 5-14) has left-handed symmetry, (the vortex axis is screwed against the flow rotation) at which a backward flow exists along an axis of the channel. The lower part of the vortex axis (points 1-5) tends to transit to the right-handed structure with axis screwing in a direction of flow rotation. The right-handed vortex is generated at the upward flow along an axis of the channel. Namely such condition takes place at vortex interacting with the surface. On the bottom projection, the point 5 corresponding to the junction of these two structures is clearly seen. In our previous experiments it was possible to generate the combined vortex [1], in which the lower right-handed part was amplified by declination of the bottom, and the upper left-handed part was also organized by displacement of an output orifice. In Figure 3b three projections of such structure, formed in a shorter chamber, are presented. The horizontal plane passing through the point 8 divides symmetrical parts of the vortex structure.

Figure 2b represents the dependencies of helical vortex pitch h (the spatial period) and its radius R (distance from the helical axis to the chamber axis) for the left-handed structures as a functions of the shift of diaphragm center δ. The data demonstrate that the helix pitch is almost independent on a degree of chamber asymmetry. The dependence for the radius takes a step-like character, indicating a jump transition from a weakly curved vortex to the helix with a large radius. Such an effect occurs in a phenomenon called the breakdown of a vortex, when the axisymmetric vortex suddenly transfers into a spiral vortex.

The influence of the lower boundary conditions has different characters. For example, the variation in the bottom declination gives not only a change in amplitude of vortex axis perturbation with the right-handed symmetry, but also a change in space pitch. So, at a slope angle of bottom planes relative to horizon

$\beta = 34°$, we observed a vortex with $R = 16\ mm$, $h = 169\ mm$ (Figure 1c). The increase of angle up to value $\beta = 50°$ results in formation of a double helix with parameters $R = 32\ mm$ and $h = 239\ mm$.

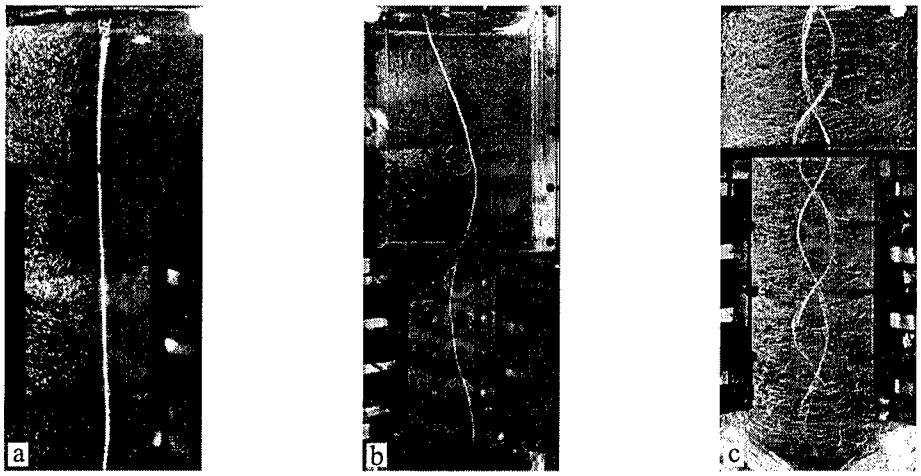


Figure 1: Stationary vortex structures with the helical symmetry: a - axisymmetrical vortex, b - single helix, c - double helix.

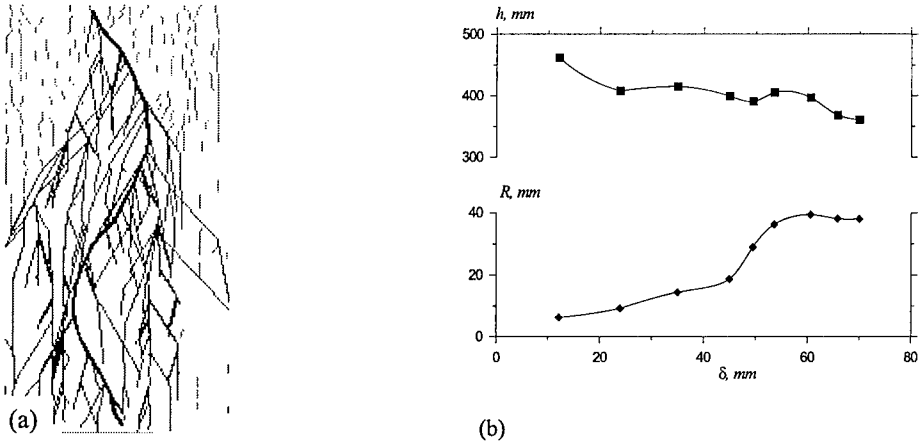


Figure 2: Results of the image processing for a single helix structure: a - final step of the obtaining of the vortex axis projection; b - geometrical characteristics of the helical vortex vs. distance between the centers of the outlet orifice and the vortex chamber.

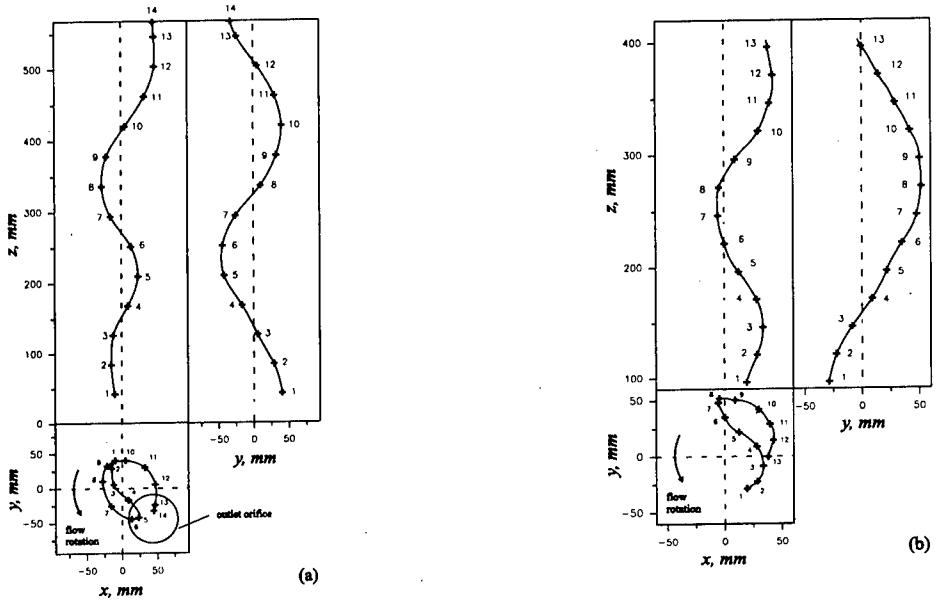


Figure 3: 3-D form of the stationary helical structures: a - left-handed vortex, b - combined vortex with various signs of helical symmetry.

3 Conclusions

Thus, in the given work the new large-scale coherent structures with helical symmetry, generated in swirling flows, has been experimentally studied. The quantitative data on the influence of boundary conditions, responsible for the formation of these vortices, on parameters of a helical symmetry are obtained. The essentially different influence of introduced asymmetry degree for the right and left helical structures is discovered. The jump like change of perturbation amplitude in the form of left-handed vortex is revealed at an increase of asymmetry degree on the upper boundary.

References

[1] S. V. Alekseenko, P. A. Kuibin, V. L. Okulov, and S. I. Shtork. Helical vortices in swirl flow. *J. Fluid Mech.*, 382:195–243, 1999.

[2] W. K. Pratt. Digital Image Processing. *Willey-Interscience publication*, 1978.

[3] I. S. Cherny. Study of swirl flows structure by the computational processing of videoimages. *In N.V. Medvetskaya and R.S. Gromadskaya (eds.). The Physics of Heat Transfer in Boiling and Condensation, Institute for High Temperature, Russian Academy of Sciences, Moscow*, 515–517, 1997.

ADVANCES IN TURBULENCE VIII
Proceedings of the Eighth European Turbulence Conference
C. Dopazo et al. (Eds.)
© CIMNE, Barcelona 2000

Coherent Vortex Simulation (CVS) of a two–dimensional mixing layer

Kai Schneider[1] and Marie Farge[2]

[1] ICT, Universität Karlsruhe (TH)
Kaiserstr. 12, 76128 Karlsruhe, Germany.
[2] LMD, Ecole Normale Supérieure
24 rue Lhomond, 75231 Paris Cedex 05, France.

Contact e-mail: schneider@ict.uni-karlsruhe.de

1 Introduction

We propose a new turbulence model, called Coherent Vortex Simulation (CVS) [1, 3], for computing fully developed turbulent flows. This new approach for CFD is based on the observation that turbulent flows contain both an organized part (the coherent vortices) and a random part (the incoherent background flow). In classically used LES methods the Navier–Stokes equations are low–pass filtered and only the evolution of the large scales of the flow is deterministically computed, while the effect of the small scales onto the large scales is statistically modelled [4]. Hence, the intermittent behaviour of the flow is only partially taken into account due to the lack of small scales. The CVS method is based on the computation of the coherent part of the vorticity (characterized by a non–Gaussian multiscale behaviour with long–range correlation and responsible for the flow intermittency), while the influence of the incoherent background flow is statistically modelled (characterized by Gaussian statistics with short–range correlation and likewise multiscale although it is non–intermittent).

2 Coherent Vortex Simulation

We filter the 2d Navier–Stokes equations in vorticity–velocity formulation using the nonlinear wavelet filter proposed in [1] and obtain an evolution equation for the coherent vorticity ω_C:

$$\begin{aligned} \partial_t \omega_C + \nabla \cdot (\omega_C \, \vec{V}_C) - \nu \nabla^2 \omega_C &= \nabla \times \vec{F}_C - \nabla \cdot \tau \\ \nabla \cdot \vec{V}_C &= 0 \quad , \end{aligned} \tag{1}$$

including an unknown term, $\tau = (\omega\ \vec{V})_C - \omega_C\ \vec{V}_C$, to be modelled. This incoherent stress term describes the effect of the discarded incoherent terms onto the resolved coherent terms. Its role is to compensate the loss of enstrophy of the wavelet filtering. This is done using a forcing term defined in wavelet space, as proposed in [5], which is conditionally applied in the region of strong nonlinear activity. In contrast to LES, where the underlying computational grid is static, the CVS method employs regridding which dynamically adjusts to the flow evolution by refining in regions of strong gradients (cf. Fig. 2).

3 Two–dimensional mixing layer

As example we compute a temporally growing two–dimensional mixing layer using the CVS method (cf. Fig. 1). To validate the approach we compare the results with DNS data obtained using a classical pseudo–spectral method. We observe that with CVS all scales of the flow are well resolved (cf. Fig. 3), although it uses 14 times less degrees of freedom than the pseudo–spectral DNS with resolution 256^2 (cf. Fig. 4). The compression thus obtained using CVS increases with the resolution, because more scales are available in the flow better the efficiency of the wavelet compression.

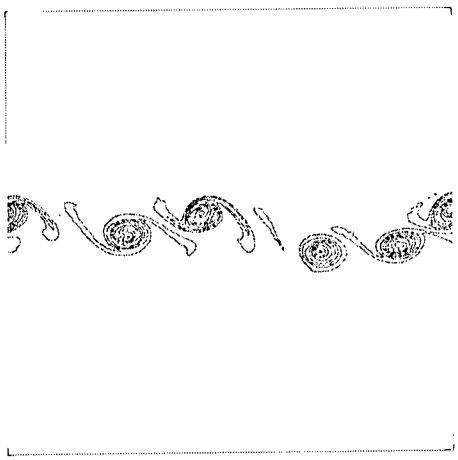


Figure 1: CVS computation of a two–dimensional mixing layer. Isolines of vorticity at $(0.1, 0.4, 0.7, 1.0, 1.3, 1.6)$.

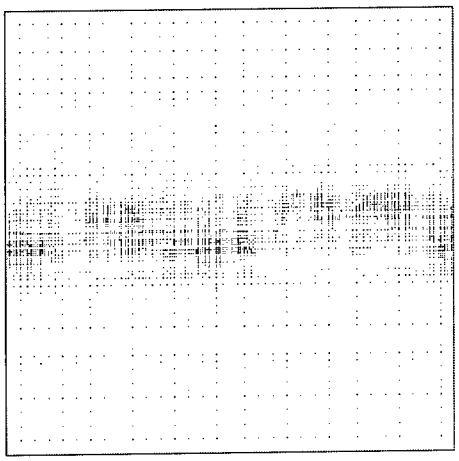


Figure 2: Adaptive grid in physical space. Note that the grid dynamically adapts to the flow evolution in scale and space.

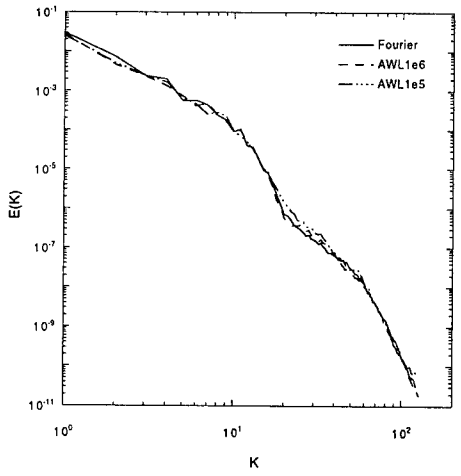


Figure 3: Comparison of corresponding energy spectra between CVS and DNS computations.

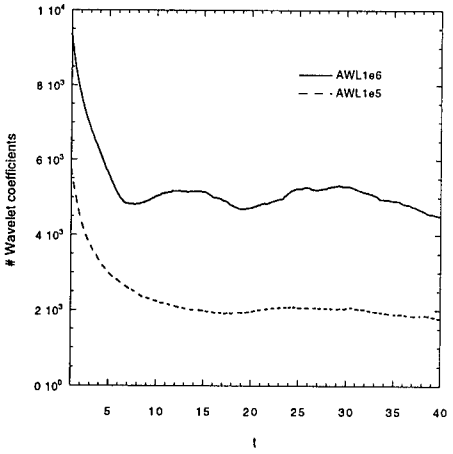


Figure 4: Time evolution of the number of grid points. Note that at $t = 37.5$ only 4700 grid points are used in CVS method, while DNS uses 65538.

4 Conclusion

We have proposed the CVS method to compute fully–developed turbulent flows in the regime where coherent vortices have been formed. This new approach combines a deterministic integration of the coherent part of the flow, done in an adaptive wavelet basis, with a wavelet forcing, which statistically models the effect of the discarded incoherent background flow onto the coherent part. The adaptive wavelet integration is based on an Eulerian projection of the vorticity field and a Lagrangian strategy in order to adapt the basis at each time step in order to resolve the regions of strong gradients. Contrarily to classical methods, such as LES, the role of the turbulence model is not to damp the nonlinear instabilities, but to model the stochastic forcing that the incoherent background flow induces onto the coherent vortex motions. Therefore in absence of turbulent model the CVS method looses a small quantity (less than 2%) of the total enstrophy, while other methods tend to diverge as soon as the Reynolds number is large. Recently, we have shown [2] that the wavelet representation also allows to extract coherent vortices (in this case vortex tubes) in three dimensional turbulence. This motivates the extension of the CVS method to compute 3D turbulent flows.

Acknowledgements:
The authors gratefully acknowledge financial support from the French-German program Procope (contract n.99090), the European TMR program (contract n.FMRX–CT 98–0184) and the program PPF of ENS Paris (contract n.15407).

References

[1] M. Farge, K. Schneider and N. Kevlahan. Non–Gaussianity and Coherent Vortex Simulation for two–dimensional turbulence using an adaptive orthonormal wavelet basis. *Phys. Fluids*, **11**(8), 2187–2201, 1999.

[2] M. Farge, K. Schneider and G. Pellegrino. Vortex tube extraction in three–dimensional turbulence using orthonormal wavelets. 8th European Turbulence Conference, Barcelona, June 2000.

[3] M. Farge and K. Schneider. Coherent Vortex Simulation (CVS), a semi–deterministic turbulence model using wavelets. *Flow, Turbulence and Combustion*, submitted March 2000.

[4] J.H. Ferziger. Large Eddy Simulation. *Simulation and modeling of turbulent flows (Eds. M.Y. Hussaini & T. Gatski)*, Cambridge University Press, 1995.

[5] K. Schneider and M. Farge. Wavelet forcing for numerical simulation of two–dimensional turbulence. *C. R. Acad. Sci. Paris Série II* **325**, 263–270, 1997.

[6] K. Schneider and M. Farge. Numerical simulation of a mixing layer in an adaptive wavelet basis. *C. R. Acad. Sci. Paris Série II*, in press.

XXV

Intermittency and Scaling

ADVANCES IN TURBULENCE VIII
Proceedings of the Eighth European Turbulence Conference
C. Dopazo et al. (Eds.)
© CIMNE, Barcelona 2000

The structures which cause intermittency

Adrian Daniel Staicu and Willem van de Water

Technische Universiteit Eindhoven, Physics Dept.
P.O. Box 513, NL-5600 MB Eindhoven, The Netherlands.

Contact e-mail: a.d.staicu@tue.nl

The anomalous scaling behavior of strong turbulence is now well established, both in experiments and in numerical simulations. It is a property of the two-point structure function $\langle[(\boldsymbol{u}(\boldsymbol{x}+\boldsymbol{r})-\boldsymbol{u}(\boldsymbol{x}))\cdot\widehat{\boldsymbol{e}}]^p\rangle$, whose inertial range behavior is $\sim r^{\zeta_p}$. In the definition of the velocity increment the measured component of the velocity $\boldsymbol{u}\cdot\widehat{\boldsymbol{e}}$ and the separation vector may not point in the same direction. The exponents are anomalous as they deviate from Kolmogorov's self-similar $\zeta_p = p/3$. Because only information in two points of the velocity field is involved, these quantities reveal little information about the structures which cause intermittency.

More about structure can be learned from multipoint measurements. Our instrumentation consists of an array of 10 hot-wire probes, each with a size of 200 μm, small enough to resolve the Kolmogorov scale. The array is oriented perpendicular to the mean flow direction. Thus we are measuring the velocity field $u(y)$ along a line. Strong turbulence with rather high Reynolds number ($R_\lambda \approx 800$) is generated by a grid (0.7×0.8 m, 0.1 m mesh size) in a recirculating wind tunnel. Long (10^9 samples) time series of velocity readings along a line were registered.

These time series contain extremely strong localized events. An average over the 200 strongest events (probability 2×10^{-6}) is shown in figure 1. The average was measured over velocity profiles which had a large transverse velocity increment over two closely-spaced probes.

A striking observation is that over a mere separation of 3.7 mm, the maximum average velocity increment is 4.3 m s^{-1}, which is four times the size of the rms velocity fluctuations and can be compared to the mean velocity $U = 12.1$ m s^{-1}. The avererage velocity profile bears a remarkable resemblance to that of a slender vortex tube with a core diameter smaller than the separation $y/\eta = 18$ of the closest probes. In the figure, the signature $y/(x^2+y^2)$ [3] of an irrotational vortex with its axis pointing in the vertical (z) direction can be recognized. We believe that the structure which is seen is the ensemble average over vortices that intersect our line-measurement with random orientations. Intense slender

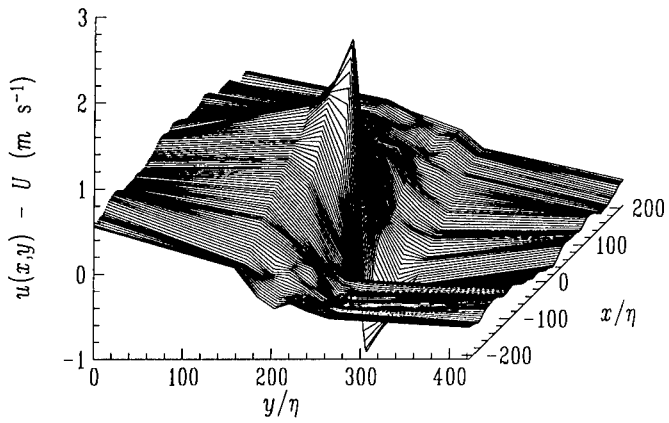


Figure 1: Average velocity profile of the 200 largest events in a times series of 10^9 velocity samples. It is conditioned on transverse $\Delta u \equiv u(x, y_4) - u(x, y_3)$ with $y_4 - y_3 = 3.7$ mm $= 18\eta$ and with x shifted to $x = 0$. The coordinates used are such that the mean flow is in the $x-$direction with the probes in the $y-$direction. The probes are at $y_1 \ldots y_8$.

vortex tubes have also been found in numerical simulations [1] and have been visualized in experiments [2].

We have devised statistical tests to verify that our conditional averages are genuine. The problem is that conditional averages such as shown in Fig. 1 may be determined by the imposed condition, and not by an indigenous property of turbulence. A test is to perform the same conditional average on pseudo turbulence, that is a random velocity signal which has the same (low–order) statistical properties as turbulence. Such pseudo turbulence was constructed by Fourier transforming a measured turbulence signal, randomizing the phases (such that the Fourier transform remains real), and performing the inverse Fourier transform. The resulting velocity field has the same second–order structure function and the same turbulence characteristics as the original turbulence signal, but it is not turbulence.

For the transverse case this procedure gave a similar average structure as shown in Fig. 1, but with a size that was a factor 2 smaller. The quest for strong events in the *longitudinal* case where the vectors $\widehat{\boldsymbol{e}}$ and $\boldsymbol{u}$ both point in the streamwise direction, produced the same average structure, both in the true and in the pseudo–turbulent signal. We conclude that the events conditioned on

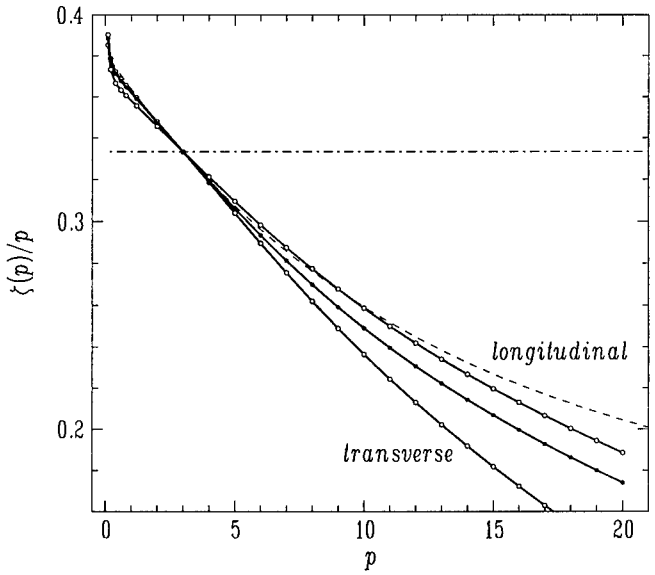


Figure 2: Open circles: scaling exponents ζ_p/p of longitudinal and transverse structure functions. Closed dots: scaling exponents of the transverse structure function, but now with the strongest events removed from the data. The scaling anomaly now tends to the longitudinal case. The dash–dotted horizontal line is Kolmogorov's 1941 self–similar prediction, the dashed line is the prediction of the log–Poisson model [5].

the transverse velocity increment are genuine, whereas those in the longitudinal case are probably artefacts of the imposed condition.

A key question is whether scaling anomaly is reduced when the strong events of the figure are removed from the data before the standard two–point structure functions are computed. Figure 2 shows the scaling exponents ζ_p of a grid–generated turbulent flow. They are plotted in a way that most vividly demonstrates the scaling anomaly. The self–similar Kolmogorov 1941 case corresponds to the horizontal line $\zeta_p/p = 1/3$. The transverse exponents ζ_p^T are more anomalous than the longitudinal ones, in agreement with our earlier findings [4]. After deletion of the 1000 strongest transverse events, a significant reduction of the scaling anomaly of the transverse exponents is seen. This number of events corresponds to a probability of 10^{-5} (0.3 % of the data, including the event's environment).

This result is remarkable because we remove events that are strong in the *dissipative* range ($r/\eta < 20$), whereas scaling exponents pertain to the *inertial range* ($r/\eta > 30$) behavior of structure functions. Thus we have identified structures that cause intermittency.

We gratefully acknowledge financial support by the "Nederlandse Organ-

isatie voor Wetenschappelijk Onderzoek (NWO)" and "Stichting Fundamenteel Onderzoek der Materie (FOM)". We are indebted to Gerard Trines and Gerald Oerlemans for technical assistance.

References

[1] J. Jimenez, A.A. Wray, P.G. Saffman, and R.S. Rogallo, J. Fluid Mech., **255**, 65 (1993).

[2] S. Douady, Y. Couder, and M.E. Brachet, Phys. Rev. Lett. **67**, 983 (1991).

[3] A. Noullez, G. Wallace, W. Lempert, R.B. Miles, and U. Frisch, J. Fluid Mech. **339**, 287 (1997).

[4] W. van de Water and J.A. Herweijer, J.Fluid Mech. **387**, 3-37 (1999).

[5] Z-S She, and E. Leveque, 1994 Phys. Rev. Lett. **72**, 336 (1994).

ADVANCES IN TURBULENCE VIII
Proceedings of the Eighth European Turbulence Conference
C. Dopazo et al. (Eds.)
© CIMNE, Barcelona 2000

Remarkable features of multiplier distributions in turbulence

P. Chainais, E. Lévêque, P. Abry and Ch. Baudet

Laboratoire de Physique, CNRS UMR 5672
Ecole Normale Supérieure de Lyon
46 Allée d'Italie, 69364 Lyon Cedex 07, FRANCE

Contact e-mail: pchainai,eleveque,pabry,baudet@ens-lyon.fr

Multiplicative cascades provide a general framework to describe intermittency properties of turbulent fluctuations [1–3]. The locally (spatially) averaged energy dissipation rate ε_r is a fluctuating quantity of special interest. The issue consists in relating fluctuations of ε_r at different scales r_1 and $r_2 \leq r_1$. A common approach is based on the introduction of a random multiplier W_{r_1,r_2}, connecting events $\varepsilon_{r_1}(x_1)$ and $\varepsilon_{r_2}(x_2)$ at location x_1 and x_2:

$$\varepsilon_{r_2}(x_2) = W_{r_1,r_2}\ \varepsilon_{r_1}(x_1). \tag{1}$$

The statistics of the multiplier W_{r_1,r_2} (or $\log W_{r_1,r_2}$) characterize the cascade properties of ε_r. In the present study, we concentrate on the (arbitrary) case of centered events, i.e. $x_1 = x_2 = x$ in eq.(1). We describe the statistics of $\log W_{r_1,r_2}$ within the framework of a new parametric model.

We analyse hot-wire velocity measurements in a turbulent jet ($R_\lambda \sim 600$) [4]. The integral scale, estimated as the velocity correlation length, is $L \simeq 2000\eta$ where $\eta \simeq 120\mu$m denotes the Kolmogorov scale. Data have been resampled by use of a local Taylor's hypothesis. The one-dimensional surrogate of energy dissipation is used. The multiplier is defined by

$$0 \leq W_{r_1,r_2} = \frac{\varepsilon_{r_2}(x)}{\varepsilon_{r_1}(x)} \leq \frac{r_1}{r_2} \quad \text{with} \quad \varepsilon_r(x) = \frac{1}{r}\int_{x-r/2}^{x+r/2} \varepsilon(x')dx'. \tag{2}$$

For any pair of scales (r_1, r_2), satisfying $\eta \lesssim r_2 \leq r_1 \lesssim L$, we propose to describe the statistics of $\log W_{r_1,r_2}$ by considering $W = \alpha\beta^w$, where

$$w = \frac{\log W_{r_1,r_2} - \log \alpha_{r_1,r_2}}{\log \beta_{r_1,r_2}} \geq 0 \tag{3}$$

has a probability density function (pdf) of the form

$$\mathrm{pdf}(w) \propto \frac{\lambda_{r_1,r_2}^w}{\Gamma(w+1)}. \tag{4}$$

This pdf may be viewed as a continuous generalization of the standard Poisson law of parameter λ used in [5]. Our choice is arbitrary but suitably captures the main features of the experimental pdfs (displayed in Fig. 1a): the Poisson distribution of parameter λ accounts for the dissymmetry, the large-amplitude cut-off of the pdf is given by $\log \alpha$ and β is an amplification factor. The parameters are estimated as follows

$$\widehat{\log \alpha} = \max(\log W_{r_1,r_2}) = \log(\max W_{r_1,r_2}) \quad (5)$$

$$\widehat{\beta} = \exp\left\{ \frac{\ll \log W - \widehat{\log \alpha} \gg}{\langle \log W - \widehat{\log \alpha} \rangle} \right\} = \exp\left\{ \frac{\ll \log(\frac{W}{\max W}) \gg}{\langle \log(\frac{W}{\max W}) \rangle} \right\} \quad (6)$$

$$\widehat{\lambda} = \frac{\langle \log W - \widehat{\log \alpha} \rangle}{\widehat{\log \beta}} = \frac{\langle \log(\frac{W}{\max W}) \rangle^2}{\ll \log(\frac{W}{\max W}) \gg}, \quad (7)$$

where $\langle . \rangle$ and $\ll . \gg$ denote respectively the estimated mean and variance. This procedure has been applied for $500\eta \leq r_1 \leq 6000\eta$ and $\eta \leq r_2 \leq r_1$. The agreement between the experimental pdfs and the model is very satisfactory (see Fig. 1a). Some discrepancies are observed only as r_2 approaches the limiting scales η and r_1. Furthermore, α, β and λ display remarkably simple laws (see Fig. 1b-d):

$$\widehat{\log \alpha}_{r_1,r_2} \simeq -0.7 \log \frac{r_2}{r_1}, \quad \text{for all } r_2/r_1, \quad (8)$$

$$\hat{\beta}_{r_1,r_2} \simeq 0.12 \log \frac{r_2}{r_1} + 0.92, \quad \text{for all } r_2/r_1, \quad (9)$$

$$\hat{\lambda}_{r_1,r_2} \simeq -2 \log \frac{r_2}{r_1} + 5.4 \quad \text{for } 10\eta \lesssim r_2 \lesssim r_1/3. \quad (10)$$

These results clearly show that $\log r_2/r_1$ appears as the relevant quantity to describe the scale dependence of $\widehat{\log \alpha}$, $\hat{\beta}$ and $\hat{\lambda}$. This is not a trivial effect since the estimation procedure uses no *a priori* assumption on the functional dependencies of the parameters with r_1 and r_2. We have noticed that these laws are valid in a wider range of scales r_2 than that where the agreement between experimental and theoretical pdfs was observed.

We now intend to compare these experimental observations with the predictions of the Log-Poisson / She-Lévêque model (LP/SL) [5, 6], which has recently received much interest. In this model, the variables $\log W_{r_1,r_2}$ are independent and satisfy eq.(3) where w is a (discrete) Poisson variable of parameter λ^{LP}.

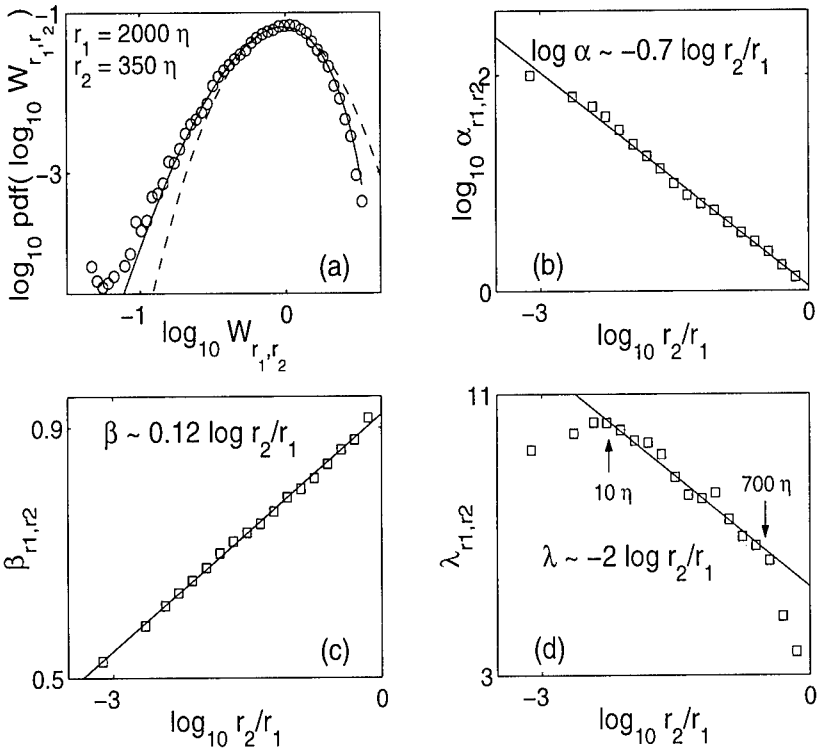


Figure 1: (a): Experimental pdf is well described by (3) and (4) (solid line). Note that the Log-Normal pdf (dashed line) is ruled out. (b-d): Evolution of the parameters with scale r_2. Solid line indicates a characteristic behavior. Remark that $\lim_{r_2 \to r_1} \alpha_{r_1,r_2} = 1$ and $\lim_{r_2 \to r_1} \beta_{r_1,r_2} \simeq 1$; this is consistent with $W_{r_1,r_1} = 1$.

Moreover, α^{LP}, β^{LP} and λ^{LP} satisfy for all r_2/r_1

$$\log \alpha^{LP} = -\frac{2}{3} \log \frac{r_2}{r_1}, \tag{11}$$

$$\beta^{LP} = \frac{2}{3}, \tag{12}$$

$$\lambda^{LP} = -2 \log \frac{r_2}{r_1}, \tag{13}$$

where the values of the constants are derived from physical arguments in [6]. The SP/SL process is multiplicative and log-infinitely divisible (see [5–7]). It yields power-law scaling for the moments of W_{r_1,r_2}:

$$\log \mathbb{E}\left[W^q_{r_1,r_2}\right] = q \log \alpha^{LP} - \lambda^{LP}\left(1 - \left(\beta^{LP}\right)^q\right) = \log \frac{r_2}{r_1} \cdot H(q), \tag{14}$$

with $H(q) = -2/3q + 2(1 - (2/3)^q)$. The key feature of eq.(14) lies in the separation of the $\log r_2/r_1$ and q dependencies.

The agreement between this model and our estimations is excellent for $\widehat{\log \alpha}$ and $\hat{\lambda}$. Our experimental results support both the $\log r_2/r_1$ dependence and the numerical values of the constants. For $\hat{\beta}$ a significant discrepancy is observed. Our results show a clear $\log r_2/r_1$ behaviour while the LP/SL model involves a constant value $\beta^{LP} = 2/3$. We observe that $0.5 \lesssim \hat{\beta} \lesssim 1$ but the specific value 2/3 cannot be singled out. The (r_1, r_2)-dependence of β is not consistent with the separation of the variables $\log r_2/r_1$ and q in $\log \mathbb{E}\left[W^q_{r_1,r_2}\right]$. Therefore, it *excludes* the possibility of a log-infinitely divisible cascade and *a fortiori* the power-law scaling hypothesis [7, 8].

We experimentally observe that the statistics of the multipliers W_{r_1,r_2} for the energy dissipation ε_r are suitably described by a continuous generalisation of the usual Log-Poisson model. The estimated parameters exhibit very simple behaviours as affine functions of $\log r_2/r_1$. This supports one of the main assumptions of the LP/SL model, i.e., that $\log(\max W_{r_1,r_2})$ behaves as $\log r_2/r_1$. Importantly, it also implies that log-infinite divisibility with independent multipliers, usually involved in the modeling of the energy dissipation cascade, should be dropped out.

References

[1] Frisch, U.: 1995, *Turbulence. The legacy of A. Kolmogorov.* Cambridge, UK: Cambridge University Press.

[2] Chhabra, A. B. and Sreenivasan, K. R.: 1992, *Phys. Rev. Lett.* **68**(18), 2762.

[3] Pedrizzetti, G., Novikov, E. A. and Praskovsky, A. A.: 1996, *Phys. Rev. E* **53**(1), 475.

[4] Baudet, C., Michel, O. and Williams, W. J.: 1999, *Physica D* **128**, 1.

[5] Dubrulle, B.: 1994, *Phys. Rev. Lett.* **73**, 959 – She, Z. S. and Waymire, E. C.: 1995, *Phys. Rev. Lett.* **74**(2), 262.

[6] She, Z. S. and Lévêque, E.: 1994, *Phys. Rev. Lett.* **72**(3), 336.

[7] Castaing, B., Gagne, Y. and Hopfinger, E.: 1990, *Physica D* **46**, 177.

[8] Chainais, P., Abry, P. and Pinton, J.-F.: 1999, *Phys. Fluids* **11**(11), 3524.

ADVANCES IN TURBULENCE VIII
Proceedings of the Eighth European Turbulence Conference
C. Dopazo et al. (Eds.)
© CIMNE, Barcelona 2000

On the complete statistical characterization of velocity increments in turbulence

St. Lück[1], Ch. Renner[1], J. Peinke[1] and R. Friedrich[2]

[1]FB-8 Physics, Universität Oldenburg,
D-26125 Oldenburg, GERMANY
[2]Institut für Theoretische Physik, Universität Stuttgart,
D-70550 Stuttgart, GERMANY

Contact e-mail: peinke@uni-oldenburg.de

1 Introduction

A fundamental issue in the investigation of isotropic turbulence is the statistics of velocity increments $v_r(x) = 3Du(x+r) - u(x)$ on different length scales r. Usually, the scaling behaviour of the n-th order moments $< (v_r(x))^n >$ are investigated, which leads to the definition of multiaffine scaling indices. On the other hand, probability density functions $P_r(v_r)$ are considered. The probability density function $P_r(v_r)$ stronlgy changes its shape from a near gaussian behaviour at large scales to a strechted exponential behaviour at small r, as can be seen from Fig. 1. This effect, which is related to multiaffine scaling behaviour of the moments, is called intermittency.

2 New Formulation

In the present article we present a new method to analyze the intermittent signature of the statistics of turbulent fields in more detail. Analyzing experimental data of a free jet-flow and of a wake-flow for different Re-numbers, we have verified that the scale dependence of the statistics of the increment v_r can be understood as a Markovian process. This stochastic process evolves in the scale varable r. As long as the step size in r is larger than a certain value: L_{mar} [1], multiple conditioned probability distributions $p(v_1, r_1|v_2, r_2; ..; v_N, r_N)$ coincide with the conditional probability distribution $p(v_1, r_1|v_2, r_2)$, which is a necessary condition for Markovian behaviour.

The length L_{mar} is of the order of the Taylor microscale. It can be seen in analogy with the finite collision time of molecules in the case of Brownian diffusion processes, c.f. [2]. We interpret the existence of the Markovian properties as a direct verification of a turbulent cascade connecting large scale properties

(in v_r) with small scale features via an iteration of an elementary process. L_{mar} marks a finite step size. It is important to note that L_{mar} turns out to be independent of the scale r.

For step sizes larger than L_{mar}, the Markovian process leads to an equation characterizing the evolution of the probability density functions $P_r(v_r)$ with r, which is called the Kramers-Moyal expansion. Furthermore we have found [3, 4] that it can even be reduced to a Fokker-Planck equation

$$-\frac{\partial}{\partial r}P_r(v_r) \quad = 3D \quad \left\{ -\frac{\partial}{\partial v_r} D_1(v_r, r) + \frac{\partial^2}{\partial v_r^2} D_2(v_r, r) \right\} P_r(v_r).$$

The coefficient D_1 is called the drift term and determines the deterministic part of the process, D_2, the diffusion term, describes the noisy part. The reduction to the Fokker-Planck equation means that the noise term actually is a white noise process. Central quantities in our analysis are conditional probability distributions $P(v_{r_2}, r_2|v_{r_1}, r_1)$, where $r_2 \leq r_1$. They can be determined accurately for different scales r_i from our experimental data. The velocity increments are evaluated at the same reference point x for different $r_i$values. Knowing the conditional probabilities the drift and diffusion coefficient are estimated by taking the limit $r_2 \to r_1$, which means $L_{mar} \to 0$. To verify the accuracy of our result we recalculate the sequence of probability distributions $P_r(v_r)$ throughout the inertial range (see Fig.1), as well as, conditional probability distributions by solving the obtained Fokker-Planck equation. Excellent agreements is found.

We remind the reader that due to the Markovian property the Fokker-Planck equation provides the complete information on the statistics. As a consequence, n-point increment probability distributions can be predicted, too [3]. A similar analysis has been performed for the energy cascade [6] using the dissipation rate $\epsilon(r)$.

Finally, we want to mention that our approach is not restricted to the case of isotropic turbulence. There is ample evidence that it works for inhomogeneous turbulence [5] as well. For velocity data of a turbulent wake behind a cylinder we found interesting effects in the behaviour of the drift term D_1 of the stochastic process containing signatures of large scale counterrotating vortices close to the cylinder. Increasing the distance to the cylinder a structural change in the deterministic part D_1 of the stochastic process shows up indicating a change of the underliing statistical properties due to the dissapearance of vortices.

3 Conclusions

We have presented a novel method for analysing the statistics of small scale turbulence. This method is based on the identification of stochastic processes generating the fluctuations of the turbulent velocity increments as a function of scale r. Mathematically, the stochastic process is formulated in terms of a Fokker-Planck equation. On the other hand, one can formulate the corresponding Langevin equation, which can be taken as starting point for the development of successful subgrid models.

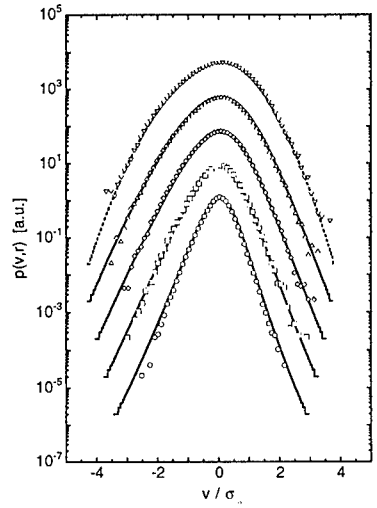


Figure 1: Probability density functions $P(v, L)$ determined from the experimental data of the free jet (bold symbols) and calculated pdfs (lines) by the numerical iteration with the experimentally determined Fokker-Planck equation (1) . The length scales $r = 3DL_0$, $0.6L_0$, $0.35L_0$, $0.2L_0$ and $0.1L_0$ going from up to down. For the numerical iteration as initial condition, an empirical fitting function for the large scale pdf was used which is shown by a broken line. For clarity of presentation the pdfs were shifted in y-direction.

References

[1] R. Friedrich, J. Zeller and J. Peinke. A note on three point statistics of velocity increments in turbulence. *Europhys. Lett.*, 41:153, 1998.

[2] H. Risken. The Fokker - Planck Equation. (Springer, Berlin 1989).

[3] R. Friedrich and J. Peinke. Description of a Turbulent Cascade by a Fokker-Planck Equation. *Phys. Rev. Lett.*, 78: 863, 1997.

[4] R. Friedrich and J. Peinke. Statistical Properties of a Turbulent Cascade. *Physica D*, 102: 147, 1997.

[5] St. Lück, J.Peinke, and R. Friedrich. Experimental evidence of a Phase Transition to Fully Developed Turbulence in a Wake Flow. *Phys. Rev. Lett.*, 83: 5495 , 1999.

[6] A. Naert, R. Friedrich, and J. Peinke. A Fokker-Planck Equation for the Energy Cascade in Turbulence. *Phys. Rev. E*, 56: 339 , 1997.

ADVANCES IN TURBULENCE VIII
Proceedings of the Eighth European Turbulence Conference
C. Dopazo et al. (Eds.)
© CIMNE, Barcelona 2000

Exit time of turbulent signals.

L. Biferale[1], M. Cencini[2], D. Vergni[2] and A.Vulpiani[2]

[1]Dipartimento di Fisica and INFM, Università di Roma "Tor Vergata",
Via della Ricerca Scientifica 1, I-00133 Roma, Italy
[2]Dipartimento di Fisica and INFM, Università di Roma "La Sapienza",
P.le A. Moro 2, I-00185, Rome, Italy

Contact e-mail: biferale@roma2.infn.it

1 Introduction

In isotropic turbulence, the most studied statistical indicators of intermittency are the structure functions, i.e. moments of the velocity increments $S_p(\tau) = < [(v(t+\tau) - v(t)]^p >$. For time increment corresponding to the inertial range, $\tau_d \ll \tau \ll T_0$, structure functions develop an anomalous scaling behavior: $S_p(\tau) \sim \tau^{\zeta(p)}$, where $\zeta(p)$ is a non linear function, while far inside the dissipative range, $\tau \ll \tau_d$, they show the laminar scaling: $S_p(\tau) \sim \tau^p$.
Beside the huge amount of theoretical, experimental and numerical studies devoted to the understanding of velocity fluctuations in the inertial range (see [1] for a recent overview), only few -mainly theoretical- attempts have focused on the Intermediate Dissipation Range (IDR), introduced in [2] (see also [3, 4]). By IDR we mean the range of scales, $\tau \sim \tau_d$, between the inertial and the dissipative range. A non-trivial IDR is connected to the presence of intermittent fluctuations in the inertial range, for details on the derivation within the multifractal model see [2, 1, 5].

Here we propose, and measure in experimental and synthetic data, a set of observable which are able to highlight the IDR properties [5]. The main idea is to take a one-dimensional string of turbulent data, $v(t)$, and to analyze the statistical properties of the exit times from a set of defined velocity-thresholds. Roughly speaking a kind of *Inverse* Structure Functions [7] (Inverse-SF).
A similar approach has already been exploited for studying the particle separation statistics [6]. Recently, exit-time moments have also been studied in the realm of shell model [7].

2 Exit Times moments and the Intermediate Dissipative Range

Fluctuations of viscous cut-off are particularly important for all those regions in the fluid where the velocity field is locally smooth. It is natural, therefore, to look for observable which feel mainly laminar events. A possible choice is to measure the *exit-time* moments through a set of velocity thresholds. More precisely, given a reference initial time t_0 with velocity $v(t_0)$, we define $\tau(\delta v)$ as the first time necessary to have an absolute variation equal to δv in the velocity data, i.e. $|v(t_0) - v(t_0 + \tau(\delta v))| = \delta v$. By scanning the whole time series we recover the probability density functions of $\tau(\delta v)$ at varying δv from the typical large scale values down to the smallest dissipative values. Positive moments of $\tau(\delta v)$ are dominated by events with a smooth velocity field, i.e. laminar bursts in the turbulent cascade. Let us define the Inverse Structure Functions as:

$$\Sigma_p(\delta v) \equiv <\tau^p(\delta v)> \ . \tag{1}$$

According to the multifractal description [5] we suppose that, for velocity thresholds corresponding to inertial range values of the velocity differences, $\delta_{\tau_d} v \equiv v_m \ll \delta v \ll v_M \equiv \delta_{T_0} v$, the following dimensional relation is valid: $\delta_\tau v \sim \tau^h \ \rightarrow \ \tau(\delta v) \sim \delta v^{1/h}$. The probability to observe a value τ for the exit time is given by inverting the multifractal probability, i.e. $P(\tau \sim \delta v^{1/h}) \sim \delta v^{[3-D(h)]/h}$. Made this ansatz, the prediction for the Inverse-SF, $\Sigma_p(\delta v)$ evaluated for velocity thresholds within the inertial range is:

$$\Sigma_p(\delta v) \sim \int_{h_{min}}^{h_{max}} dh \ \delta v^{[p+3-D(h)]/h} \sim \delta v^{\chi_{sp}(p)} \tag{2}$$

where the RHS has been obtained by a saddle point:

$$\chi_{sp}(p) = \min_h \{[p + 3 - D(h)]/h\} \ . \tag{3}$$

Let us now consider the IDR properties.
For each p the saddle point evaluation (3) selects a particular $h = h_s(p)$ where the minimum is reached. Let us also remark we can estimate the minimum value assumed by the velocity in the inertial range given a certain singularity h as [5]: $v_m(h) = \delta_{\tau_d(h)} v \sim \nu^{h/(1+h)}$. Therefore, the smallest velocity value at which the scaling $\Sigma_p(\delta v) \sim \delta v^{\chi_{sp}(p)}$ still holds depends on both ν and h. Namely, $\delta v_m(p) \sim \nu^{h_s(p)/1+h_s(p)}$. The most important consequence is that for $\delta v < \delta v_m(p)$ the integral (2) is not any more dominated by the saddle point value but by the minimum h value still dynamically alive at that velocity difference, $1/h(\delta v) = -1 - \log(\nu)/\log(\delta v)$. This leads for $\delta v < \delta v_m(p)$ to a pseudo-algebraic law:

$$\Sigma_p(\delta v) \sim \delta v^{[p + 3 - D(h(\delta v))]/h(\delta v)} \ . \tag{4}$$

The presence of this p-dependent velocity range, intermediate between the inertial range, $\Sigma_p(\delta v) \sim \delta v^{\chi_{sp}(p)}$, and the far dissipative scaling, $\Sigma_p(\delta v) \sim \delta v^p$, is

the IDR signature. Then, it is easy to show that Inverse-SF should display an enlarged IDR. Indeed, for the usual *direct* structure functions the saddle point $h_s(p)$ value is reached for $h < 1/3$. This pushes the IDR to a range of scales very difficult to observe experimentally [4]. On the other hand, as regards the Inverse-SF, the saddle point estimate of positive moments is always reached for $h_s(p) > 1/3$. This is an indication that we are probing the laminar part of the velocity statistics. Therefore, the presence of the IDR must be felt much earlier in the range of available velocity fluctuations. Indeed, if $h_s(p) > 1/3$, the typical velocity field at which the IDR shows up is given by $\delta v_m(p) \sim \nu^{h_s(p)/(1+h_s(p))}$, that is much larger than the Kolmogorov value $\delta v_{r_d} \sim \nu^{1/4}$.

The expression (4) predicts the possibility to obtain a data collapse of all curves with different Reynolds numbers by rescaling the Inverse-SF as follows [2, 3]:

$$\frac{\ln(\Sigma_p(\delta v))}{\ln(Re)} \quad vs. \quad \frac{\ln(\delta v/U)}{\ln(Re)}, \tag{5}$$

where U is an adjustable dimensional parameter.

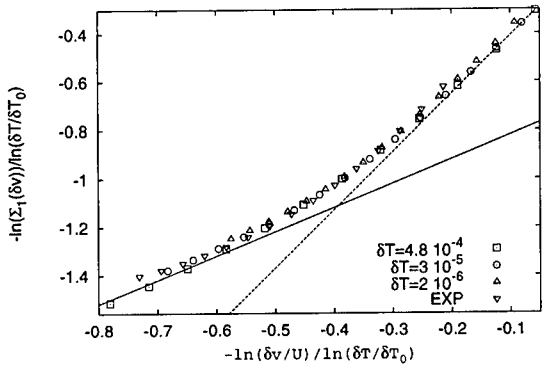


Figure 1: Data collapse of the Inverse-SF, $\Sigma_1(\delta v)$, obtained by the rescaling (5) for the smoothed synthetic signals at different Reynolds numbers (for details see [5]) and the experimental data (EXP). The two straight lines have the dissipative (solid line) and the inertial range (dashed) slope.

The rationale for the rescale (5) stems from the observation that, in the IDR, $h_s(p)$ is a function of $\ln(\delta v)/\ln(Re)$ only. This rescaling was originally proposed as a possible test of IDR for direct structure functions in [2] but, as already discussed above, for the latter observable it is very difficult to detect any IDR due to the extremely small scales involved [4].
Fig. 2 shows the rescaling (5) of the Inverse-SF, $\Sigma_1(\delta v)$, for the synthetic field at different Reynolds numbers and for the experimental signals. As it is possible to see, the data-collapse is very good for both the synthetic and experimental signal.

3 Conclusions

In conclusions we have shown that exit-time moments, $\Sigma_p(\delta v)$, are dominated by the laminar part of the energy cascade: they depend only on the part of $D(h)$ which falls to the right of its maximum , i.e. $h > 1/3$. These h's values are not testable by the direct structure functions. Inverse-SF are the natural tool to test any model concerning velocity fluctuations less singular than the Kolmogorov value $\delta v \sim \tau^{1/3}$.
By analyzing high-Reynolds data and synthetic fields, we have proved that the extension of the IDR for $\Sigma_p(\delta v)$ is magnified. The rescaling (5) based on the multifractal assumption gives a good data collapse for different Reynolds numbers. This is a clear evidence of the IDR.

We acknowledge useful discussions with R. Benzi, G. Boffetta, A. Celani, M.H. Jensen, P. Muratore Ginanneschi, M. Vergassola. We also thank Y. Gagne for the access to the experimental data. This work has been partially supported by INFM (PRA-TURBO) and by the EU network (FMRX-CT98-0175).

References

[1] U. Frisch, Turbulence. The legacy of A.N. Kolmogorov. Cambridge University Press, Cambridge 1995.

[2] U. Frisch and M. Vergassola, *Europhys. Lett*, 14:439–444, 1991.

[3] M.H. Jensen, G. Paladin and A. Vulpiani, *Phys. Rev. Lett.* 67:208–211, 1991.

[4] Y. Gagne and B. Castaing, *C. R. Acad. Sci. Paris* 312:441–443, 1991.

[5] L. Biferale, M. Cencini, D. Vergni and A. Vulpiani *Phys. Rev. E* 60:R6295–R6299, 1999.

[6] G. Boffetta, A. Celani, A. Crisanti and A. Vulpiani, *Europhys. Lett.* 46:177–181, 1999.

[7] M.H. Jensen, *Phys. Rev. Lett.* 83:76–80, 1999.

[8] L. Biferale, G. Boffetta, A. Celani, A. Crisanti and A. Vulpiani, *Phys. Rev. E* 57:R6261-R6264, 1998.

[9] E. Aurell, G. Boffetta, A. Crisanti, G. Paladin and A. Vulpiani, *Phys. Rev. Lett.* 77:1262–1266, 1996.

ADVANCES IN TURBULENCE VIII
Proceedings of the Eighth European Turbulence Conference
C. Dopazo et al. (Eds.)
© CIMNE, Barcelona 2000

A Langevin equation for turbulent velocity increments

P. Marcq[1] and A. Naert[2]

[1] Institut de Recherche sur les Phénomènes Hors Equilibre,
12 avenue du Général Leclerc, 13003 Marseille, France
[2] Laboratoire de Physique, Ecole Normale Supérieure de Lyon,
46 Allée d'Italie, 69364 Lyon Cédex 07, France

Contact e-mail: marcq@marius.univ-mrs.fr

1 Introduction

One important characterisation of high Reynolds number, incompressible hydrodynamic flows is the probability distribution function $P(v_r, r)$ of longitudinal velocity increments $v_r = u(x + r) - u(x)$ at scale r, where $u(x)$ is the velocity component along the x-axis (see, e.g., [1] for a recent review). Recent work on experimental velocity signals indicates that $P(v_r, r)$ is the solution of a Fokker-Planck equation, where the usual time variable is replaced by the scale [3]. The velocity increment v_r is well described by a continuous stochastic process in scale, *Markov* for large enough scales where viscous effects are negligible.

Our objective is to further investigate the stochastic process v_r by studying the stochastic differential equation which governs its trajectories in scale. We wish to emphasize that no attempt is made here to "model" velocity intermittency: our results are based on the statistical analysis of experimental data.

2 Langevin equation

We study a turbulent velocity signal recorded in an axisymmetric jet in air, characterised by a microscale Reynolds number $R_\lambda \simeq 430$, a Kolmogorov scale $\eta \simeq 175$ μm, and an integral scale $L = 140$ mm, or 800 η (see [2] for further details). The following Langevin equation for v_r is "read" from experimental data:

$$-\frac{\mathrm{d}v_r}{\mathrm{d}r} = D_1(v_r, r) + \sqrt{2D_2(v_r, r)}\,\xi(r), \tag{1}$$

where the minus sign on the left hand side accounts for the physical direction of the cascade, from large to small scales. We use Ito's conventions for stochastic

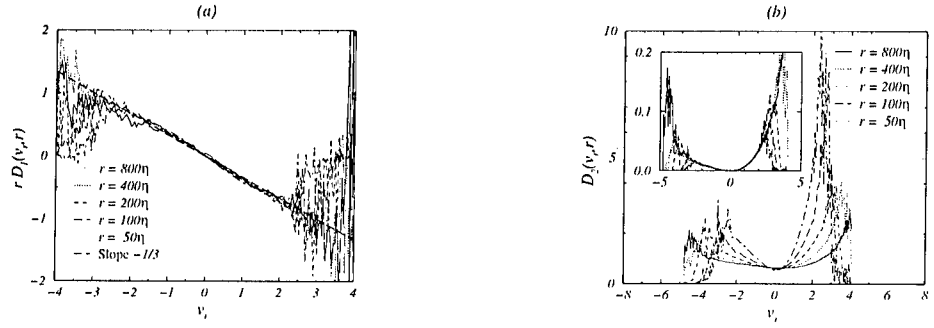


Figure 1: Graph (a): Drift coefficient $D_1(v_r, r)$. The slope of $rD_1(v_r, r)$ vs. v_r is consistent with $\gamma = -1/3$. Graph (b): Diffusion coefficient $D_2(v_r, r)$. Insert: $r(D_2(v_r, r) - d_0 + d_1 v_r)$ can be fitted by $d_2 v_r^2 + d_3 v_r^3$ ($d_0 = 0.56$ ms^{-2}, $d_1 = 0.045$ s^{-1}, $d_2 = 0.0057$; $d_3 = 0.0015$ m^{-1}s).

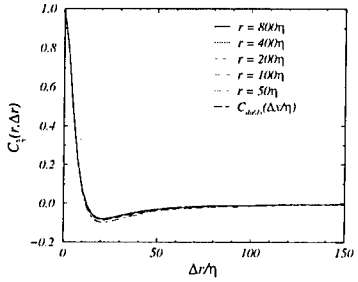


Figure 2: Normalised autocorrelation function of the random force $\xi(r)$ and of the velocity derivative $\mathrm{d}u/\mathrm{d}x$.

calculus. The drift and diffusion coefficients are measured as:

$$\begin{aligned} D_1(v_r, r) &= -\left\langle \tfrac{\mathrm{d}v_r}{\mathrm{d}r} \mid v_r \right\rangle, \\ D_2(v_r, r) &= \tfrac{1}{2} \left\langle \left(\tfrac{\mathrm{d}v_r}{\mathrm{d}r} + D_1(v_r, r) \right)^2 \mid v_r \right\rangle, \end{aligned} \tag{2}$$

We find (see Fig. 1): $D_1(v_r, r) \simeq -v_r/3r$ and $D_2(v_r, r) \simeq d_0 - d_1 v_r + d_2 v_r^2/r + d_3 v_r^3/r$ (see the caption for numerical values of d_0, d_1, d_2 and d_3).

3 A Markov process

We proceed to evaluate the random force $\xi(r)$:

$$\xi(r) = -\frac{1}{\sqrt{2D_2(v_r, r)}} \left(\frac{\mathrm{d}v_r}{\mathrm{d}r} + D_1(v_r, r) \right). \tag{3}$$

The autocorrelation function $C_\xi(r, \Delta r) = \langle \xi(r)\xi(r + \Delta r) \rangle$ decays rapidly as a function of Δr (see Fig. 2). The process v_r is indeed Markov because the

correlation scale ρ of the noise $\xi(r)$ (of the order of a few times η) is much smaller than $L = 800\ \eta$. This means in practice that $C_\xi(r, \Delta r)$ can be safely approximated by a δ-function for scales large compared to ρ, *i.e.* in the inertial range. The scale ρ quantifies the locality of the turbulent cascade process.

We checked that $\langle v_r\ \xi(r)\rangle \simeq 0$ within statistical error. Using Eq. (3), this implies that the random variable $\xi(r)$ is statistically equivalent to the derivatives $\mathrm{d}v_r/\mathrm{d}r \simeq \mathrm{d}u/\mathrm{d}x$, where $u(x)$ is the longitudinal velocity component. Indeed, Fig. 2 shows that the (spatial) autocorrelation function of $\mathrm{d}u/\mathrm{d}x$ is identical to $C_\xi(r, \Delta r)$.

A straightforward physical explanation for the Markov character of the cascade follows. The random force $\xi(r)$ is "rapid" compared to the "slow" variable v_r because the longitudinal velocity $u(x)$ is correlated over distances much larger than the correlation length of its spatial derivative $\mathrm{d}u/\mathrm{d}x$.

4 Structure functions

We checked that, since $P(\mathrm{d}u/\mathrm{d}x)$ is non-Gaussian (see, e.g., [1]), the probability distribution function of $\xi(r)$ is also non-Gaussian. However, a Gaussian approximation of the random force $\xi(r)$ allows to compute analytically the scale-dependence of the structure functions $\langle v_r^n\rangle$ in the inertial range.

Since the asymmetry of $P(v_r)$ is weak, evolution equations for even-order moments read ($\alpha_{2p} = 2p\ ((1/3) - (2p-1)d_2)$:

$$\frac{d}{dr}\langle v_r^{2p}\rangle = \frac{\alpha_{2p}}{r}\langle v_r^{2p}\rangle - 2p(2p-1)\ d_0 L\ \langle v_r^{2p-2}\rangle. \tag{4}$$

Supplemented with initial conditions at large scale $\langle v_L^{2p}\rangle$, the hierarchy (4) is exactly solvable for all p: structure functions are expressed as a finite linear combination of power laws of r with different exponents. Noticing that $d_0 L \simeq 0.07$ is a small parameter, we give below the expression of $\langle v_r^{2p}\rangle$ at order $(d_0 L)^1$:

$$\begin{aligned}\langle v_r^{2p}\rangle = \quad & \langle v_L^{2p}\rangle \left(\tfrac{r}{L}\right)^{\alpha_{2p}} \\ - \quad & d_0 L\ \langle v_L^{2p-2}\rangle\ \tfrac{2p(2p-1)}{1+\alpha_{2p-2}-\alpha_{2p}} \left(\left(\tfrac{r}{L}\right)^{1+\alpha_{2p-2}} - \left(\tfrac{r}{L}\right)^{\alpha_{2p}}\right) + \mathcal{O}((d_0 L)^2).\end{aligned} \tag{5}$$

Fig. 3 shows that expression (5) is in excellent agreement with experimental data in the inertial range.

Similar arguments yield analytic expressions for odd-order moments $\langle v_r^{2p+1}\rangle$, as a finite linear combination of power laws of r with different exponents. We find a linear scale-dependence for the third moment $\langle v_r^3\rangle \propto r$, in agreement with Kolmogorov's four-fifth law.

5 Conclusion

Our approach yields a quantitatively accurate description of the cascade process. In particular, Eq. (5) gives a quantitative assessment of how inertial range be-

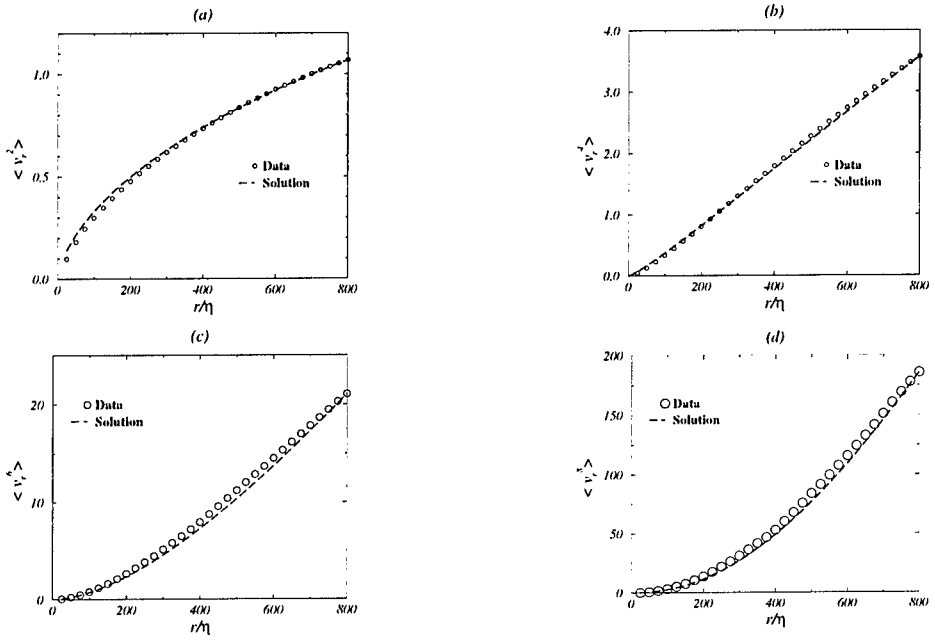


Figure 3: Even-order moments $\langle v_r^{2p} \rangle$, $p = 1$ to 4, are compared to the solutions (5) in the inertial range ($\alpha_2 = 0.66$, $\alpha_4 = 1.26$, $\alpha_6 = 1.83$, $\alpha_8 = 2.35$, $d_0 L = 0.07$). The size of symbols used for the moments gives the statitical error bars.

haviour depends upon large scale fluctuations, through the integral scale L and the moments $\langle v_L^n \rangle$. The physical picture which emerges is the following: Kolmogorov's scaling ($\langle v_r^n \rangle \propto r^{n/3}$) corresponds to a "classical path" ($D_2 = 0$) for trajectories of v_r: $\mathrm{d}v_r/\mathrm{d}r = v_r/(3r)$, while finite Reynolds number corrections amount to fluctuations around this path.

References

[1] K.R. Sreenivasan and R.A. Antonia. The phenomenology of small-scale turbulence. *Ann. Rev. of Fluid Mech.*, 29:435–472, 1997.

[2] C. Baudet, O. Michel and W.J. Williams. Detection of coherent vorticity structures using time-scale resolved acoustic spectroscopy. *Physica D*, 128:1–17, 1999.

[3] R. Friedrich and J. Peinke. Description of a turbulent cascade by a Fokker-Planck equation. *Phys. Rev. Lett.*, 78:863–866, 1997.

ADVANCES IN TURBULENCE VIII
Proceedings of the Eighth European Turbulence Conference
C. Dopazo et al. (Eds.)
© CIMNE, Barcelona 2000

Intermittent structure functions and coherent structures in fully developed turbulence

R. Camussi [1] and R. Verzicco [2]

[1]Università Roma 'Tre', DIMI
Via della Vasca Navale 79, 00146 Roma, ITALY
[2]Politecnico di Bari, Istituto di Macchine ed Energetica
Via Re David 200, 70125 Bari, ITALY

Contact e-mail: camussi@uniroma3.it

1 Introduction

The intermittent nature of the small-scale fluctuations in fully developed turbulence, is reflected by the non-Gaussian statistics of the rate of turbulent energy dissipation ϵ and the anomalous scalings of the q-order velocity structure functions:

$$S_q = < \delta V_r^q > \sim \overline{\epsilon}^{q/3} L^{q/3} \left(\frac{r}{L}\right)^{\zeta(q)} \quad \text{with } \zeta(q) \neq \frac{q}{3}. \tag{1}$$

The experimental evidence of the $\zeta(q)$ anomalous behavior (see e.g. [1]) has motivated the formulation of many so-called phenomenological models in order to predict the non-linear dependence of $\zeta(q)$ on q. This aspect has received further attention in the last years due to the connection between intermittency and the presence of organized structures. The new aspect here concerned, is that coherent structures of different size affect not only the small scales statistics but also the fluctuations at intermediate scales. This feature might be taken into account by the analysis of the local kinetic energy $e_r(x) = \delta V_r(x)^2$.

Our physical idea is that coherent structures responsible for intermittency are statistically independent inducing exponential-like PDFs of $e_r(x)$ at fixed r, with no influence of their shape, whereas the energy cascade mechanism is reflected by a power law dependence of e_r upon r. It is therefore possible to determine the q-order moments of $e_r(x)$, both in terms of r and of x:

$$< e_r(x)^q > \; = C_q \; < e_r(x) >^q \; \left(\frac{r}{L}\right)^{\gamma(q)} \tag{2}$$

$$< e_r(x)^q > \; = \frac{q}{\alpha_r} < e_r(x)^{q-1} > \quad , \tag{3}$$

where C_q is a non dimensional constant, $\gamma(q)$ is the scaling exponent which retains the effects of intermittency and α_r denotes the (positive) magnitude of the exponential decay of the PDF. By combining the above equations and taking into account the exact condition $\zeta(3) = 1$, the following equation is obtained ([2]):

$$\zeta(p) = \zeta(p-1) + \frac{log(p)}{log(6)} \cdot (1 - 3\zeta(1)) + \zeta(1) \quad . \tag{4}$$

Eq.(4) represents the recursive formula which yields the scaling exponents. We remind that this equation has been obtained with no assumptions on the shape of the coherent structures responsible for intermittency.

2 Validation of the model

The only free parameter left unknown in eq. (4) is $\zeta(1)$. From the experimental or numerical side, the $\zeta(1)$ computation may be performed with a relatively limited amount of samples since it is related to the moment of order one. On the other hand, the appropriate value of $\zeta(1)$ may be found by fitting the whole curve $\zeta(p)$ *vs.* p on previous experimental or numerical results. Using this approach, by comparison with previous experimentally estimated $\zeta(p)$ in homogeneous and isotropic turbulence ([3]) it is found $\zeta(1) = 0.38$. As indicated in Fig. 1, results are in good agreement with previous $\zeta(p)$ estimates.

An analysis of the sensitivity of the predicted $\zeta(p)$ with respect to the $\zeta(1)$ magnitude has shown that an increase in magnitude of $\zeta(1)$ leads to an increase of the intermittency corrections also for larger p (i.e. smaller magnitude of the $\zeta(p)$ for $p > 3$). Therefore, with a proper value of $\zeta(1)$, the present model may be able to predict the scaling exponents for non homogeneous turbulent flows where a larger intermittency may be observed, as in cases of wall turbulent flows. When the magnitude of $\zeta(1)$ is instead decreased, the intermittency corrections also decrease and a curve $\zeta(p)$ closer to the Kolmogorov prediction is obtained. Also this aspect may have physical implications since there might be flow conditions where the non-homogeneity leads to a decrease of intermittency (e.g. [5]). As an example, in Fig. 2 we report a comparison of present prediction with previous results in non homogeneous conditions. The agreement is good in both cases showing that present model may give appropriate approximations of the $\zeta(p)$ for both homogeneous and non-homogeneous conditions, provided the $\zeta(1)$ is properly selected.

3 Behavior at very large p

The validity of the model is mainly related to the robustness of the hypothesis of exponential PDFs of the kinetic energy fluctuations. This limitation is reflected in the analytical form of the recursive formula (eq. 4) which, for very large p ($p \geq 349$) produces negative exponents with no physical meaning. A

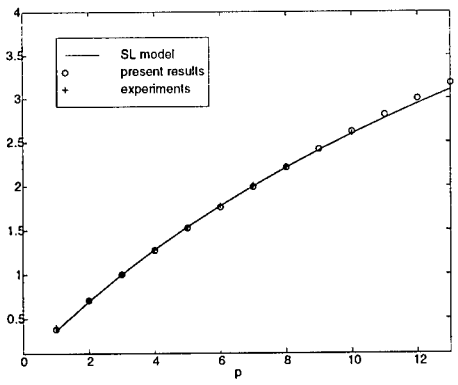


Figure 1: Present predicted $\zeta(p)$ (using $\zeta(1) = 0.38$) compared with previous theoretical ([4]) and experimental ([3]) results

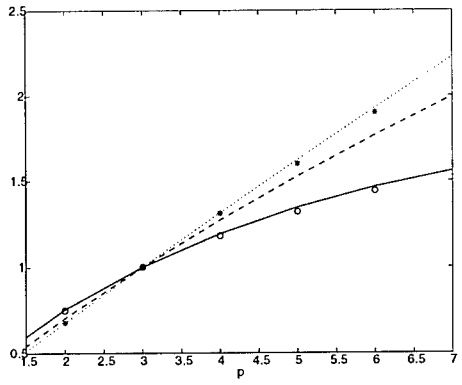


Figure 2: Present predicted ζ_p computed using $\zeta_1 = 0.35$ (solid line) and $\zeta_1 = 0.44$ (dotted line) compared with numerical results achieved in a channel flow ($\circ$, [6]) and experimental data taken close to a grid ($*$, [5]). Present predicted ζ_p obtained with $\zeta_1 = 0.38$ are also reported (dashed line).

suitable asymptotic form of eq. (4) for $p \to \infty$, cannot be obtained conserving the hypothesis of exponential PDFs of e_r. Indeed, the analysis of very large p corresponds to consider events so rare that they cannot be characterized by a simple PDF. A possibility to retrieve the correct behavior for large p, is to perform a suitable fit of the experimental PDF, by combining the exponential decay with other more complicate functional forms. For example, if a stretched

exponential is assumed (e.g., [7]). the PDF of the energy should have the form $p(e) = Aexp\left(-\alpha x^{\beta}\right)$. Then, repeating the procedure presented above, it is possible to obtain the following final formula:

$$\zeta(q) = \zeta(q-1) + \frac{1-2P\zeta(1)}{3-2P} + \frac{3\zeta(1)-1}{3-2P}\frac{1}{ln\left(\frac{h}{k}\right)}\left\{ln\left(\frac{1}{hk}\right) + 2ln\left[\frac{\Gamma\left(\frac{q+1}{\beta}\right)}{\Gamma\left(\frac{q}{\beta}\right)}\right]\right\} \tag{5}$$

where

$$h = \frac{\Gamma\left(\frac{2}{\beta}\right)}{\Gamma\left(\frac{1}{\beta}\right)}, \quad k = \frac{\Gamma\left(\frac{3}{\beta}\right)}{\Gamma\left(\frac{2}{\beta}\right)} \quad \text{and} \quad P = \frac{ln\left[\left(\frac{1}{hk}\right)^{1/2}\frac{\Gamma\left(\frac{4}{\beta}\right)}{\Gamma\left(\frac{3}{\beta}\right)}\right]}{\left(\frac{1}{hk}\right)}$$

where $\Gamma(x)$ represents the *Gamma* function. The different functional form adopted affects only the largest order moments. This explains why the present model fails the prediction of the larger order structure function exponents. On the other hand, the assumption of a stretched exponential instead of a pure exponential, does not lead to a simple recursive relation like that given in the present work. In addition, it must be noted that the stretching parameter β is not uniquely determined but it is rather obtained by an empirical fit of experimental data; this would introduce an additional tuning parameter in the model which would make it less general.

References

[1] Van der Water W. and Herweijter J., "High-order structure funtions of turbulence", J. Fluid Mech. **387**, 3-37, 1999.

[2] Camussi R. and Verzicco R., "Anomalous scaling exponents and coherent structures in high *Re* fluid turbulence", to appear on Phys. of Fluids.

[3] Benzi R., Ciliberto S., Tripiccione R., Baudet C., Massaioli F. and Succi S., "Extended self-similarity in turbulent flows", Phys. Rev. E, **48**, 29-32, 1993.

[4] She Z.S. and Levesque E., "Universal Scaling Laws in Fully Developed Turbulence", Phys. Rev. Lett. **72**, 336-338, 1994.

[5] Camussi, R. , Barbagallo, D. , Guj, G. , Stella, F., Transverse and longitudinal scaling laws in non-homogeneous low Re turbulence, Phys. of Fluids 8 (5) 1181-1191, 1996.

[6] Amati, G. , Benzi, R., Succi, S., Extended self similarity in boundary layer turbulence, Phys Rev E, Vol. 55, N; 6, 6985-6988, 1997.

[7] Kailasnath P., Sreenivasan K.R. and Stolovitsky G., "Probability density of velocity increments in turbulent flows", Phys. Rev. Lett. **68**, 2766-2769, 1992.

ADVANCES IN TURBULENCE VIII
Proceedings of the Eighth European Turbulence Conference
C. Dopazo et al. (Eds.)
© CIMNE, Barcelona 2000

Disentangling Scaling Properties in Anisotropic and Inhomogeneous Turbulence

Irene Mazzitelli[1], Itai Arad[2], Luca Biferale[3,4], and Itamar Procaccia[2]

[1]Department of Applied Physics, University of Twente,
P.O. Box 217 7500 AE, Enschede, The Netherlands.
[2]Department of Chemical Physics, The Weinzmann Institute of Science,
Rehovot 76100, Israel.
[3]Dipartimento di Fisica, Universitá di Tor Vergata,
Via della Ricerca Scientifica 1, I-00133 Roma, Italy.
[4]INFM-Unitá di Tor Vergata,
Via della Ricerca Scientifica 1, I-00133 Roma, Italy.

Contact e-mail: i.mazzitelli@tn.utwente.nl

1 Introduction

Most of the available data analysis and theoretical ideas about the universal statistics of the small scale structure of turbulence assume the existence of an idealized model of homogeneous and isotropic flow. In fact most realistic flows are neither homogeneous nor isotropic. The traditional analysis of such flows disregards the inhomogeneities and anisotropies and assumes that the results pertain to homogeneous and isotropic flows.
We present here a different approach to the problem that takes the anisotropies explicitly into account by decomposing the relevant statistical objects into their isotropic and anisotropic contributions, and estimating the degree of universality of each component separately [1].

2 The $SO(3)$ decomposition.

We address scaling in inhomogeneous and anisotropic turbulent flows by decomposing structure functions into their irreducible representations of the SO(3) symmetry group which are designated by (j, m) indices [1, 2].

Employing a direct numerical simulation of a turbulent channel flow with $\mathrm{Re}_\lambda \approx 40$, we measure directly the longitudinal structure functions:

$$S^{(p)}(\mathbf{r^c}, \mathbf{R}) = \langle [(\mathbf{u}(\mathbf{r^c} + \mathbf{R}) - \mathbf{u}(\mathbf{r^c} - \mathbf{R})) \cdot \hat{\mathbf{R}}]^p \rangle \qquad (1)$$

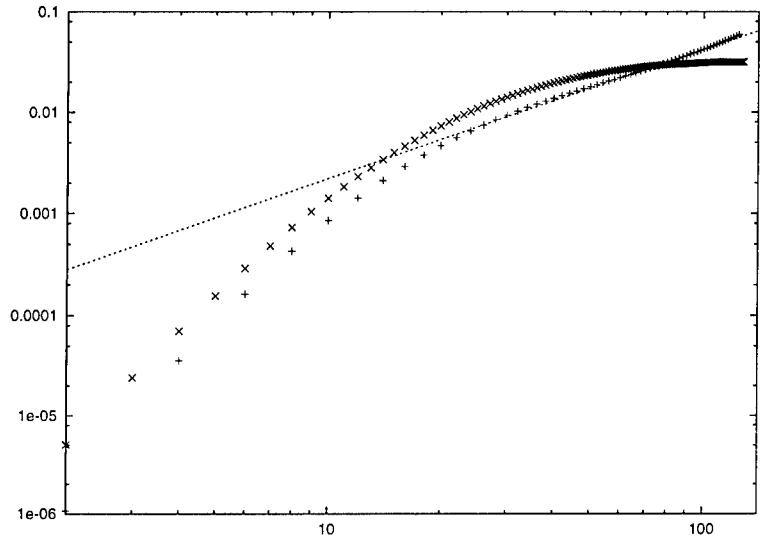


Figure 1: Log-log plot of the isotropic sector of the 4th order structure function $S^{(4)}_{0,0}$, vs. R, with $\mathbf{r^c}$ in the central plane of the channel (+). The data represented by (×) correspond to the undecomposed longitudinal structure function, $S^{(4)}(\mathbf{r^c}, R\hat{x})$ with $\mathbf{r^c}$ in the central plane of the channel. The dashed line represents the intermittent isotropic exponent $\zeta(4) = 1.28$.

Where the two velocity fields are measured at the extremes of the diameter of a sphere of radius R centered at $\mathbf{r^c}$. Due to the inhomogeneity this function depends explicitly on $\mathbf{r^c}$. Due to the anisotropy the function depends on the orientation of the separation vector $\mathbf{R}$ as well as on its magnitude. Having computed $S^{(p)}(\mathbf{r^c}, \mathbf{R})$ we decompose it into the irreducible representations of the SO(3) symmetry group according to:

$$S^{(p)}(\mathbf{r^c}, \mathbf{R}) = \sum_{j,m} S^{(p)}_{j,m}(\mathbf{r^c}, |\mathbf{R}|) Y_{j,m}(\hat{\mathbf{R}}) \ . \tag{2}$$

We expect that when scaling behavior sets in (presumably at high enough Re) we should find:

$$S^{(p)}_{j,m}(\mathbf{r^c}, |\mathbf{R}|) \sim a_{j,m}(\mathbf{r^c}) |R|^{\zeta_j(p)} \tag{3}$$

One of the main results that we want to underline is that by applying the SO(3) decomposition we seem to improve significantly the quality of the scaling behavior. In Fig.1 we show (i) the log-log plot of the undecomposed structure function with $p = 4$ measured on the central plane with the vector $\mathbf{R}$ in the streamwise direction, $\mathbf{R} = R\hat{x}$, and (ii) the fully isotropic sector $S^{(4)}_{0,0}(\mathbf{r^c}, |\mathbf{R}|)$ with the average in (1) taken on the sphere centered on the central plane of the channel. It appears that already at this fairly low Reynolds number the $j = 0$ sector shows quite good scaling behavior as a function of R. This is in marked

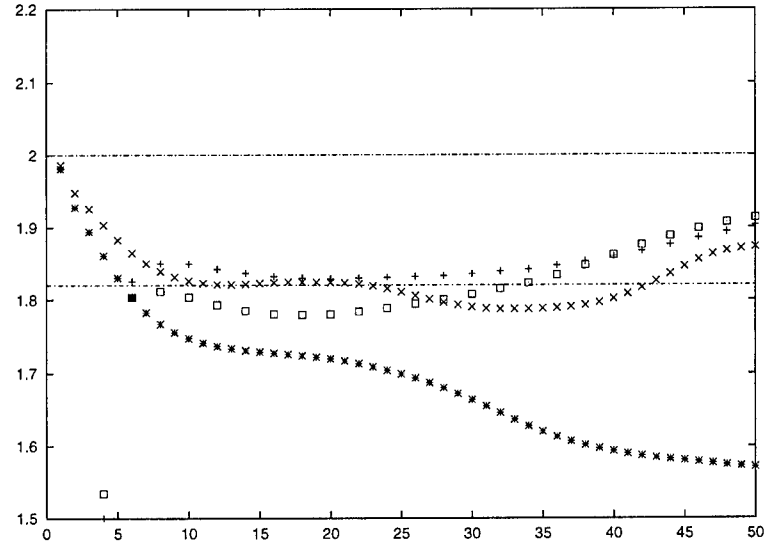


Figure 2: Logarithmic local slopes of the ESS plot of the undecomposed structure function of order 4 versus the undecomposed structure function of order 2 at the center of the channel (crosses), at 1/4 of the channel's height (stars) and of the $j = 0$ projection at the center (pluses), and at 1/4 of the channel (squares). Also two flat straight lines corresponding to the high-Reynolds number limit, 1.82, and to the K41 non-intermittent value, 2, are shown.

contrast with the undecomposed structure function for which no scaling behavior is detectable. It is remarkable that the $j = 0$ exponent agrees extremely well with measurements of the scaling exponents at high Re.
On the other hand, in order to extract scaling properties from the undecomposed structure functions it is necessary to resort to 'extended-self-similarity" (ESS) [4].
Moreover, undecomposed structure functions showed intermittent corrections strongly dependent on the distance from the walls [3]. In order to better understand the possible non-universal properties as a function of the anisotropic effects we have also applied the SO(3) decomposition with a sphere centered at one fourth of the channel.

In Fig.2 we show the *logarithmic local slopes* of the undecomposed structure functions $S^{(4)}(\mathbf{r^c}, R\hat{x})$ *vs* $S^{(2)}(\mathbf{r^c}, R\hat{x})$ with the center $\mathbf{r^c}$ both at the center and at one fourth of the channel's height. Also the *logarithmic local slopes* of the projections on the $j = 0$ sector at the same two distances from the walls are presented.
As it is evident, the undecomposed structure function at the center of the channel and the two $j = 0$ sectors are in good agreement with the high Reynolds number estimate $\zeta(4)/\zeta(2) = 1.82$, while a clearly spurious departure is seen for

the undecomposed structure function at 1/4 of the channel.

The interpretation of this result is that the *amplitude* of the isotropic sector depends strongly on the local degree of anisotropy and inhomogeneity. This component is dominant in fixing the scaling law of the total structure function only at the center of the channel, where there's the highest degree of homogeneity and isotropy.
The application of the $SO(3)$ decomposition to anisotropic flows is limited by the fact that this method is non-local, so the closest region to the boundaries, where the gradients of the velocity field are stronger, i.e. the anisotropies and inhomogeneities are higher, can not be analyzed.

3 Conclusions

- A new approach to anisotropic turbulence is presented that explicitly takes into accounts the anisotropies and gives an interpretation of the variations in the scaling exponents observed upon changing the position in which the analysis is performed.
- By decomposing the longitudinal structure functions into the irreducible representations of the $SO(3)$ symmetry group one finds that the scaling behavior is better defined in separated (j, m) sectors. This is in contrast with the undecomposed structure function which fails to exhibit any scaling, but in the ESS sense.
- The isotropic $(0, 0)$ component of the structure functions exhibits a *universal* scaling exponent, independently from the spatial location in the flow and the distance from the walls.

References

[1] I. Arad, L. Biferale, I. Mazzitelli and I. Procaccia, Phys. Rev. Lett. **82**, p. 5040 (1999)

[2] I. Arad, V.S. L'vov and I. Procaccia, Phys. Rev. E, **59** 6 p. 6753 (1999)

[3] F. Toschi, G. Amati, S. Succi, R. Benzi and R. Piva, Phys. Rev. Lett. **82**, p. 5044 (1999)

[4] R. Benzi, S. Ciliberto, R. Tripiccione, C. Baudet, F. Massaioli and S. Succi, Phys. Rev. E **48** R29 (1993)

ADVANCES IN TURBULENCE VIII
Proceedings of the Eighth European Turbulence Conference
C. Dopazo et al. (Eds.)
© CIMNE, Barcelona 2000

Scaling laws and vortical structures in homogeneous shear flow

P. Gualtieri*, C. M. Casciola*, G. Amati† and R. Piva*

*Dipartimento di meccanica e aeronautica universitá di Roma La Sapienza
Via Eudossiana 18, 00184 Roma ITALY
†C.A.S.P.U.R.
Piazzale Aldo Moro 5, 00185 Roma ITALY

Contact e-mail: p.gualtieri@caspur.it

1 Introduction

Recent numerical simulations of wall bounded turbulent flows have confirmed the growth of intermittency towards the wall where a large population of coherent structures develops in high shear regions.

A quantitative description of the statistical properties of the flow is achieved by considering the moments of the longitudinal increments of streamwise velocity, $\delta V = V(x+r) - V(x)$. In the context of homogeneous isotropic turbulence, the Kolmogorov-Obukhov refined similarity (RKSH) provides a scaling law, for large Reynolds number, in terms of the separation r. Assuming as independent variable the third order structure function instead of separation [1], in the spirit of extended self similarity (ESS), scaling laws emerge also at the relatively small values of the Reynolds number that can be achieved by DNS. The RKSH in its extended form,

$$< \delta V^p > \quad \propto \quad \frac{< \epsilon_r^{p/3} >}{< \epsilon >^{p/3}} < \delta V^3 >^{p/3}, \tag{1}$$

has been extensively checked against most of the available data.

In the near wall region the leading process is the momentum transfer occurring in the wall normal direction, due to the large local mean shear S, which corresponds to production of turbulent kinetic energy via Reynolds stresses, $S < uv >$. Based on this analysis, a new form of scaling law has been proposed [2] for the wall region,

$$< \delta V^p > \quad \propto \quad \frac{< \epsilon_r^{p/2} >}{< \epsilon >^{p/2}} < \delta V^2 >^{p/2}, \tag{2}$$

in terms of the structure function of order two.

To reproduce a similar dynamics under simplified conditions we consider here a flow with a constant mean shear rate in absence of solid walls. The homogeneous shear flow presents two main advantages with respect to wall bounded flows. Namely it isolates the effect of the shear from other concurrent effects such as the suppression of wall-normal fluctuations [3], and the non uniform momentum flux across adjacent layers. Moreover it improves the statistical analysis by exploiting homogeneity in all the spatial directions. Clearly the possibility to reach a stationary state [4] is a necessary prerequisite.

2 Homogeneous shear flow

We consider a periodic box with an imposed mean velocity gradient, as already done by Lee *et al.* [3], Kida and Tanaka [5] and Pumir [4] following the approach proposed by Rogallo.

In order to analyze the statistical features of the flow we have computed, by using ESS, the scaling exponents of the structure functions. As shown in figure 1 a departure from the values typical of isotropic turbulence is quite clear. The effect of the mean shear over the fluctuations of turbulence is usually evaluated by means of the non dimensional parameter $S^* = Sq^2/\epsilon$ with q the rms value of velocity and ϵ the mean dissipation [3]. This parameter may be interpreted as the ratio between an inertial scale $l_d = q^3/\epsilon$ and the shear scale defined as $L_s = \sqrt{\epsilon/S^3}$. By using dimensional arguments the dynamics induced by the shear is relevant at scales $r \gg L_s$, a condition that can be achieved when $S^* = (l_d/L_s)^{2/3} \gg 1$. In our calculation we have $S^* = 7$.



Figure 1: Left: $< \delta V^6 >$ vs. $< \delta V^3 >$: isotropic turbulence (triangles) and their fit (slope 1.78). Shear flow (filled circles) and their fit (slope 1.7). Right: Scaling exponents ζ_p, K41 (solid line), isotropic turbulence (triangles), shear flow (filled circles).

For this flow let us check the validity of the two forms of similarity laws i.e. equations (1) and (2). We can observe, figure 2, a quite clear failure of the classical RKSH form (1) in the homogeneous shear flow, while the new scaling

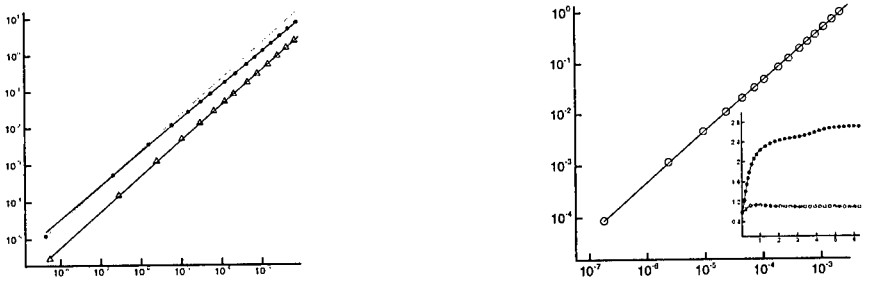


Figure 2: Left: $< \delta V^6 >$ vs. $< \epsilon^2 >< \delta V^3 >^2$. Isotropic turbulence (triangles) and their fit (solid line with slope 0.98). Shear flow (filled circles) and their fits in two regions $r^+ \in [1,5]$ and $r^+ \in [5,60]$, dotted line with slope 0.99 and solid line with slope 0.90 respectively. Right: $< \delta V^4 >$ vs. $< \epsilon^2 >< \delta V^2 >^2$ in shear flow. The solid line (slope 0.99) gives the fit in the whole range. In the inset compensated plot for eq. (1) vs. r (filled circles) and corresponding plot for eq. (2), (circles).

law (2) holds in the whole range of available scales. This results is consistent with the role played by the Reynolds stress term $S < uv >$ as occurs for wall turbulence.

Both ESS and RKSH results clearly indicate how the homogeneous shear flow presents many features quite similar to wall bounded flows. The scaling exponents ζ_p show a departure from isotropic values while the failure of RKSH indicates the role of the production term, with respect to isotropic nonlinear energy transfer, on the energy cascade. These observations suggest to analyze in more details the anisotropy and its possible persistence at small scales.

In order to attempt a scale by scale analysis of anisotropy we have applied a sharp low-pass filter with cut-off wave number k_f to the DNS data and we have computed the anisotropy indicator $b_{ij} =< u_i u_j > / < u^2 > -1/3\delta_{ij}$ shown in figure 3. The anisotropy is essentially built up from the contribution of the largest scales ($r > L_s$) where the effect of shear is predominant. By adding the finest scales ($r < L_s$), the anisotropy of the flow saturates up to an asymptotic value different from zero which is the value of the global field. Actually, in the present calculation, the shear wave number is $k_s = 2\pi/L_s \sim 8$ while the saturation of b_{ij} occurs at $k_f \sim 10$. This observation doesn't necessarily imply small scale isotropy, at least for small value of the Reynolds number. In fact, in the present conditions, the anisotropy, injected at large scales, is essentially inherited at the smaller ones.

In order to get a deeper insight into the feature of small scale anisotropy, we have performed a further analysis, local in wave number space, computing the indicator E_{12}/E_{ii}, where E_{12} and E_{ii} are respectively the energy cospectrum

and the energy spectrum of the velocity field. This indicator vanishes for wave numbers where isotropy is reached. From the plot in figure 3 we observe a trend towards a saturation which corresponds to a common behavior of the two spectra. This result resembles the theoretical prediction given in [6] about the common k^{-1} scaling for shear dominated scales in wall turbulence. On the other hand, according to this theory, isotropy may be recovered as confirmed by well established experimental results [7] for quite large distances from the wall ($y^+ \simeq 10^3$). In these conditions the ratio $S_c^* = S(\nu/\epsilon)^{1/2} = (\eta/L_s)^{2/3}$ is very small of the order of 10^{-2}. Such a large separation of scales provides enough space for the setting up of local isotropy. Close to the wall, instead, the value of S_c^* increases and anisotropy is expected to persist up to the smallest scales. In these last conditions the new RKSH, equation (2), is observed to hold both for wall bounded [2] and for homogeneous shear flow [8].



Figure 3: Left: anisotropy indicator b_{ij} as a function of the cut-off wave number k_f. Right: ratio E_{12}/E_{ii} as a function of wave number k.

References

[1] Benzi, Biferale, Ciliberto, Struglia, Tripicccione, Phys. D., **96**, 162-181, 1996.

[2] Benzi, Amati, Casciola, Toschi, Piva, Phys. Fluids, **11**(6), 1-3, 1999.

[3] Lee, M.J., Kim, J., Moin, P., J. Fluid Mech., **216**, 561-583, 1990.

[4] Pumir, A., Phys. Fluids, **8**(11), 3112-3127, 1996.

[5] Kida, S., Tanaka, M., J. Fluid Mech., **274**, 43, 1994.

[6] Nikora, V., To appear on Phys. Rev Lett.

[7] Saddoughi, S.,G. Veeravalli, S.,V., J. Fluid Mech., **268**, 333, 1994.

[8] Piva, R., Casciola, C.,M., Amati, G., Gualtieri, P., Proc. IUTAM Symp. on Geometry and Statistics of Turbulence, (T. Kambe ed.) Tokyo Nov. 1999

ADVANCES IN TURBULENCE VIII
Proceedings of the Eighth European Turbulence Conference
C. Dopazo et al. (Eds.)
© CIMNE, Barcelona 2000

Self similarity and intermittency in a turbulent non-homogeneous wake

O.B. Mahjoub[1,2], J.M. Redondo [2], and A. Babiano [3]

[1]Département de Physique
Faculté de Sciences et Techniques de Tanger, Morocco
[2]Departamento de Física Aplicada
Univ. Politècnica de Catalunya, Barcelona, Spain
[3]LMD, Ecole Normale Supérieure
24 rue Lhomond, F-75005 Paris, France

Contact e-mail: redondo@fa.upc.es

1 Introduction

Many studies have been devoted to the interpretation of the anomalous scaling of the velocity structure functions in non-homogeneous and non-isotropic turbulent flows. Progress in this domain relies on the property called "Extended Self Similarity" [1], that has received attention in numerical studies performed by [2] and [3]. Following the methodology proposed in Babiano *et al.* [2] and Babiano [3], used in the study of non-homogeneous *numerical* two-dimensional turbulence, we were led to a more detailed investigation of Gaudin *et al.* [4] experimental data by analyzing the anomalous behavior of the third-order longitudinal structure function at different locations in the turbulent wake, as was done for grid turbulence in [5]. We propose that *ESS* is more than a simple experimental methodology, useful for defining with greater accuracy the *inertial* range according to Kolmogorov's theory. It is in fact a fundamental property sustained by the natural link between the energy transfer among the various scales of motion and the non-linear term in the Navier-Stokes equation, where the third order longitudinal velocity increments seem to play a fundamental role.

2 The methodology

The methodology proposed by Babiano *et al.* [2], based on the statistical properties of the absolute energy transfer at scale l, is related to the non-linear term of the Navier-Stokes equation. For a given length-scale l, the instantaneous absolute value of the energy transfer assured by the non-linear term of the equation

of motion of an incompressible flow is given by

$$\sigma_l = \frac{1}{V_l}\left| \int_{S_l} (u^2 + v^2 + P) u ds_l \right|, \tag{1}$$

where $u = \vec{V}.\vec{n}$ is the component longitudinal to $\vec{l}$ of the velocity $\vec{V}$, which is also normal to the element ds_l of surface S_l containing the control volume defined at scale l and centered at the space-position $\vec{x} + \vec{l}/2$, P is the pressure and v is the transversal component of $\vec{V}$, ($\mid \vec{V} \mid^2 = u^2 + v^2$).

The energy transfer hierarchy is defined as:

$$H(p,l) = \frac{\langle \sigma_l^{p+1} \rangle}{\langle \sigma_l^p \rangle} \sim l^{-\delta_p}, \tag{2}$$

where δ_p is a local scaling exponent which may also depend on the length-scale l in a non-homogeneous case. The transfer hierarchy has two limits $\sigma_l^0 = \lim_{p\to 0} H(p,l) \sim l^{-\delta_0}$ and $\sigma_l^\infty = \lim_{p\to\infty} H(p,l) \sim l^{-\delta_\infty}$, characterizing respectively the relative contribution of the least or most intermittent fluctuations of σ_l at given scale l. We consider valid in the non-homogeneous case the generalized similarity hypothesis

$$\frac{|\delta u_l^3|}{\langle |\delta u_l^3| \rangle} \stackrel{\text{law}}{=} \frac{\sigma_l}{\langle \sigma_l \rangle}, \tag{3}$$

where $\stackrel{\text{law}}{=}$ means that the terms have the same scaling properties. Then, from (3) the relative scaling exponents ζ_p/ζ_3, defined in the framework of the ESS, are given by

$$\frac{\zeta_p}{\zeta_3} = \frac{p}{3} + \Delta \left[I(p/3) - \frac{p}{3} \right], \tag{4}$$

where $I(p) = \sum_{q=0}^{p-1} h(q)$, and $\Delta = \frac{\delta_\infty - \delta_0}{\zeta_3}$. More details may be found in [5]

3 Experimental results

Figure 1a shows the behavior of the third order scaling exponent ζ_3 at different downstream distances X/D from the cylinder at the lateral distance $Y/D = -0.8$, where D is the diameter of the cylinder. The curve clearly illustrates the anomalous behavior of the third-order structure function. Near the cylinder, where the flow dynamics is nonlocal, ζ_3 shows maximum values in an average sense. Furthermore, ζ_3 decreases up to a minimum closer to 1, corresponding to the most explored regions in the cylinder wake. Figure 1b shows the hierarchy for $p = 0$ and $p = 5$ as a function of non dimensional length-scale l/η, where η is Kolmogorov's length scale, for already explored positions near the cylinder, up to $X/d = 15$, corresponding to the same section $Y/d = -0.8$. All quantities are normalized by their maximum values at small scale. Near the cylinder, δ_0 shows

a minimum value at all length-scales l/η and saturates far from the cylinder. At the same time, δ_∞ remains almost stationary. Consequently, $(\delta_\infty - \delta_0)$ is maximum near the cylinder where the flow dynamics is strongly nonlocal.

In the framework of the laboratory measurements described here, the absolute scale-to-scale energy transfer defined in (1) is approximated by

$$\sigma_l^* \approx \frac{1}{l} < |u^3(\vec{x}) - u^3(\vec{x} + \vec{l})| >, \tag{5}$$

where $< . >$ now refers to the time average using locally Taylor's hypothesis to obtain the spatial dependence.

The newly defined quantity Δ^*, which is calculated via the hierarchy described in (2) using instead σ_l^*, exhibits a universal behavior as a function of the non-dimensional scale l/η. This is shown as an example for the lateral distance $Y/d = -0.8$ at different downstream distances X/d from the cylinder in figure 1c. In the experiments described in his paper, Δ^* shows a remarkably good scale-invariance in a large range, even when both the absolute scaling exponents ζ_3 and $\delta_\infty - \delta_0$ depend clearly on the separation distance l/η. This explains the compensation effect which operates in (1), consolidating the application of the ESS property even in non-homogeneous flows. These results are also consistent with the numerical investigations of non-homogeneous two-dimensional turbulence performed in [2] and [3], and consolidates the idea that both the unmasked properties in non-homogeneous flows and the proposed tool are well sustained independently of the particular flow geometry, as seen in [5] where a similar behavior was found in a jet flow and in grid induced turbulence.

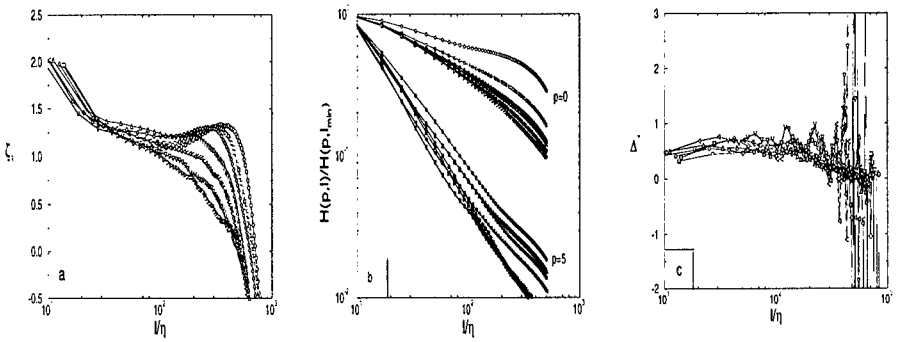


Figure 1: The behavior of ζ_3 (a), $\frac{H(p,l)}{H(p,l_{min})}$ (b) and $\Delta^* = \frac{\delta_\infty - \delta_0}{\zeta_3}$ (c) as function of non-dimensional scale l/η at different downstream distance X/D from the cylinder, for the lateral distance $X/D = -0.8$ ($X/d = 2$ ($\circ$), $X/d = 3$ ($\square$), $X/d = 4$ ($\diamond$), $X/d = 7$ ($\triangle$), $X/d = 10$ ($\triangleleft$), $X/d = 15$ ($\triangledown$), $X/d = 20$ ($\triangleright$))

4 Conclusions

- Even if the local scaling exponents $(\delta_\infty - \delta_0)$ and ζ_3 depend on the separation distance l, the quantity Δ and its close approximation Δ^* show scale-invariant properties and seem universal. This experimental results may explain why the ESS property applies in non-homogeneous and non-isotropic turbulence.
- The non-uniqueness of ζ_p/ζ_3 seems affected by the localness of the flow dynamics generated by the coherent structures traveling in the wake behind the cylinder. In fact, the intermittency is not uniformly distributed in the flow. The regions near the cylinder, where the coherent structures are more concentrated and the dynamics is nonlocal, are strongly intermittent. Far from the cylinder the turbulence is quasi-homogeneous, even if the turbulence has decayed.
- Due to the experimental difficulties of measuring transversal velocity components and their scaling, taking into consideration the local symmetry, we have ignored their contribution to σ_l^*. We would like to stress the non-universality of ζ_p/ζ_3, apparent in non-homogeneous turbulence while at the same time there appears to be universality of Δ. Other experiments are needed to asses whether ζ_p/ζ_3 is different and Δ constant in various types of flows, and whether this behavior is dependent on the Reynolds number.

This work was financed by the European Science Foundation (TAO grant) and by European Union projects MAS3- CT950016 and MAS3-CT960049 (UE95-0016). We thank J. Wojciechowski, E. Gaudin and J. E. Wesfreid for their comments.

References

[1] R. Benzi, S. Ciliberto, R. Tripiccione, C. Baudet, F. Massaioli, S., Succi. Extended self-similarity in turbulent flows. *Phys. Rev. E*, 48:R29–R32, 1993.

[2] A. Babiano, B. Dubrulle and P. Frick. Some properties of two-dimensional inverse energy cascade dynamics. Phys. Rev. E, 55: 2693–2706, 1997.

[3] A. Babiano. On the non-homogeneous two-dimensional inverse cascade. *Phys. of Fluids*, submitted, 1999.

[4] E. Gaudin, B. Protas, S. Goujon-Durand, J. Wojciechowski, J. E. Wesfreid. Spatial properties of velocity structure functions in turbulent wake flows. *Phys. Rev. E*, 57:9–12, 1998.

[5] O. B. Mahjoub, J. M. Redondo and A. Babiano. Structure Functions in Complex Flows. *Applied Scientific Research*, 59:299–313, 1998.

ADVANCES IN TURBULENCE VIII
Proceedings of the Eighth European Turbulence Conference
C. Dopazo et al. (Eds.)
© CIMNE, Barcelona 2000

Asymmetry of Velocity Increments in a Turbulent Channel Flow

G. Iuso [1] and M. Onorato [2]

[1]Dip. di Ingegneria Aerospaziale, Politecnico di Torino
Corso Duca degli Abruzzi 24 - 10129 Torino, ITALY
[2]Dip. di Fisica Generale, Universitá di Torino
Via Pietro Giuria 1,10125 Torino, ITALY

Contact e-mail: iuso@polito.it

1 Introduction

Recently a number of papers on the intermittency properties of the streamwise velocity component in turbulent channel flow have been published (Onorato et al. [1], Benzi et al. [2], Antonia et al. [3], Toschi et al. [4]). A major finding consistent with all the work published is that, moving towards the wall, it is observed a growth of the intermittency that indicates a dependence of the scaling exponent on y^+ (the distance from the wall adimensionalized with the viscous length). In this paper, our aim is to give a contribution in understanding the intermittency features of the longitudinal velocity close to the wall. We consider hot wire experimental data of the streamwise velocity component in a fully developed turbulent channel flow. The experiment has been carried out in a rectangular cross section channel, 7 m long, 70 mm high and 300 mm wide. The Reynolds number based on the friction velocity is Re_τ =510. Longitudinal velocity measurements have been performed using a single subminiature hot wire sensor characterized by 2 μm of diameter and 0.45 mm long, which corresponds to 6.6 wall units.

2 PDF and "plus and minus" structure function

In Figures 1 and 2 we show the PDFs of the streamwise velocity increments respectively at y^+ =218 and y^+=15, for different values of the separation distance r^+(variations in time are converted into space variations with the Taylor hypothesis). The PDF continually changes its character as the separation r^+ varies: from a nearly Gaussian curve, when r^+ is comparable to the integral scale, to some curve with wider tails for smaller r^+. The behavior of the PDF at y^+=15 (Fig. 2) is strongly asymmetric for small r^+: the left tail becomes

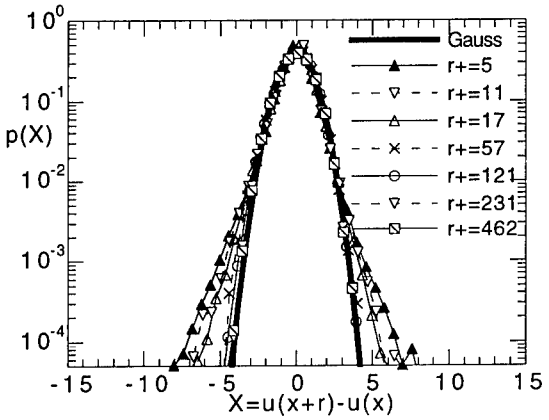


Figure 1: PDF of the streamwise velocity difference at y^+=218.

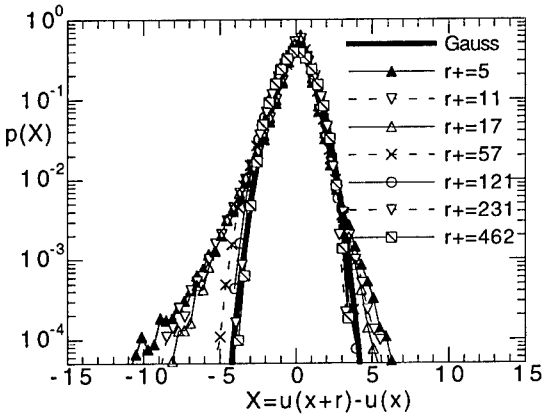


Figure 2: PDF of the streamwise velocity difference at y^+=15.

wider with respect to the right one. In order to quantitatively investigate on this asymmetry we consider the " plus and minus structure function " defined as [5]:

$$S_p^{\pm}(r) = < \left[\frac{1}{2}(|\Delta u_r| \pm \Delta u_r)\right]^p >, \qquad (1)$$

where $\Delta u_r = u(x+r) - u(x)$. We used the extended self similarity (ESS) [6] in order to compute the local slopes of the plus and minus increments. In Figures 3 and 4 we consider respectively the ESS local slopes, dS_4^-/dS_3^- and dS_4^+/dS_3^+, at different distances from the wall, in the buffer layer ($y^+ = 7, 10, 15, 28$ and 35) and in the higher log region ($y^+ = 218$ and 310). It is evident from Fig. 3 the different behavior of the slope in the two regions: while in the log layer the values of the slope are almost constant and consistent with the one of the

homogeneous isotropic turbulence ($dS_4/dS_3 = 1.28$), in the buffer layer the values of dS_4^-/dS_3^- are always lower and weakly dependent on the separation r^+. For the plus structure function (Fig.4) the slope dS_4^+/dS_3^+, for all distances from the wall, seems to collapse on a single curve characterized by an almost constant value comprised between 1.25 to 1.28.

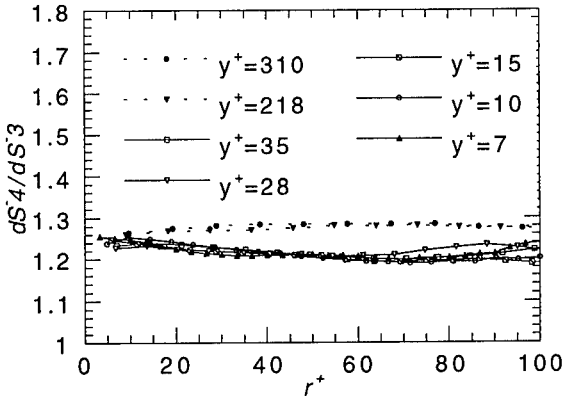


Figure 3: ESS local slope for the minus structure function at different y^+.

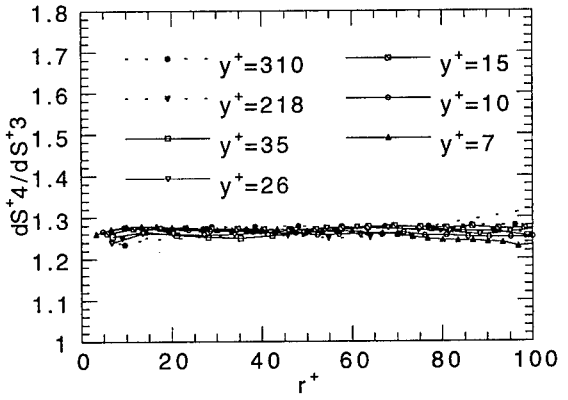


Figure 4: ESS local slope for the plus structure function at different y^+.

Summarizing, the main result shown here is that, while the relative local slope for the minus structure function is a function of y^+ and is in agreement with the value of the scaling exponent of the full structure function (see, e.g. [1]), the plus structure function seems to be much less affected by the presence of the wall. An interpretation of these experimental results in terms of simple phenomenological model of wall bounded flows will be given in the next section.

3 Discussion

It is well known that the buffer region is populated by elongated structures (*high* and *low* speed streaks) characterized by high and low velocities with respect to the mean flow. The "head" and the "tail" of a low speed streak exhibit respectively positive and negative longitudinal velocity gradients (strong streamwise velocity gradients are also present whenever the streaks are not perfectly straight). Due to the differences of velocity between the mean flow and the streaks, the highest longitudinal velocity gradients occur presumably more often at the tail of the low speed streak where $\partial u/\partial x < 0$. An analogous argument can be applied to high speed streaks: in this case the highest gradients are always negative but now are located at the head of the structure. As a consequence, for small r^+, higher negative velocity differences are more probable to occur with respect to the positive ones, giving rise to the skewed PDF (Fig. 2) and to the different behavior of the relative slopes of the plus and minus structure functions (Fig. 3 and 4). Outside the buffer region the streaky structure is weakened rendering the statistics of the ! velocity differences more similar to the homogeneous and isotropic flow. These results confirm our previous findings [1] that the intermittency is affected by the wall structures dynamics.

References

[1] M. Onorato, R. Camussi and G. Iuso, "Small Scale Intermittency and Bursting Process in a Turbulent Channel Flow", Phys. Rev. E **61**, 29 (2000).

[2] R. Benzi, G. Amati, C.M. Casciola, F. Toschi and R. Piva, "Intermittency and scaling laws for wall bounded turbulence", Phys. of Fluids, **11**, 6 (1999).

[3] R. A. Antonia, P. Orlandi and G.P. Romano, "Scaling of longitudinal velocity increments in a fully developed turbulent channel flow", Phys. Fluids **10**, 12 (1999).

[4] F. Toschi, G. Amati, S. Succi, R. Benzi, and R. Piva "Intermittency and Structure Functions in Channel Flow Turbulence", Phys. Rev. Lett., **82**, 25 (1999) pp.5044-5047.

[5] S. I. Vainshtein and K.R. Sreenivasan, "Kolmogorov's 4/5th law and intermittency in turbulence ", Phys. Rev. Lett., **73**, 23 (1994) pp.3085-3088.

[6] R. Benzi, S. Ciliberto, R. Tripiccione, C. Baudet, F. Massaioli and S. Succi, "Extended self-similarity in turbulent flows", Phys. Rev. E, **48**, R29 (1993).

XXVI

Vortex Dynamics

ADVANCES IN TURBULENCE VIII
Proceedings of the Eighth European Turbulence Conference
C. Dopazo et al. (Eds.)
© CIMNE, Barcelona 2000

Alignment properties in Fourier and wavelet filtered forced two-dimensional turbulence

Bartosz Protas[1,2], Kai Schneider[3] and Marie Farge[4]

[1]Department of Aerodynamics, Institute of Aeronautics and Applied Mechanics,
Warsaw University of Technology
ul. Nowowiejska 24, 00-665 Warsaw, Poland
[2]Laboratoire de Physique et Mécanique des Milieux Hétérogènes,
École Supérieure de Physique et Chimie Industrielles
10 rue Vauquelin, 75231 Paris Cedex 05, France
[3] I.C.T., Universität Karlsruhe (TH)
Kaiserstraße 12, 76128 Karlsruhe, Germany
[4] L.M.D.-CNRS, Ecole Normale Supérieure,
24 rue Lhomond, 75231 Paris cedex 05, France

Contact e-mail: bprotas@meil.pw.edu.pl

1 Introduction

The paper discusses the structural properties of the fields obtained with the Fourier and Wavelet filtering methods. In turbulence modeling these methods are used to split the turbulent field into the *resolved* part, which is computed deterministically, and the *unresolved* part whose average effect is accounted for by some model. The Fourier filtering is based on the separation between low and high wavenumber modes and is characterized by a given cut-off wavenumber. This classical approach relies on the assumption of scale-separability of the turbulent flow dynamics. The validity of this hypothesis is still debated and in the present work we propose and analyze a different method of filtering which no longer requires this assumption. By means of nonlinear wavelet filtering (see [1], [2]) we separate the field into the coherent and incoherent parts corresponding to strong and weak wavelet coefficients, respectively. Both components are multiscale, but exhibit distinct statistical behaviors. The coherent contribution corresponds to localized vortices which are characterized by non-Gaussian vorticity PDFs and long-range correlations. On the other hand, the incoherent contribution corresponds to filamentary debris which exhibit Gaussian vorticity PDFs and short-range correlations [2]. In 2D the wavelet filtering method consists in projecting the vorticity field ω onto a two-dimensional orthogonal wavelet basis spanned by the wavelets ψ_λ, with the multi–index λ characterizing the scale,

position and direction of each basis function [1], and reconstructing the coherent vorticity field taking only the wavelet coefficients with absolute value larger than $\tilde{\omega}_T = (2Z \log_{10} N)^{-1/2}$. This threshold in wavelet space depends only on the total enstrophy Z, which is the L^2-norm of vorticity, and on the resolution N, without any *ad hoc* adjustable parameter. In the Large Eddy Simulation (LES) method the *resolved* components are the low wavenumber modes, while for the Coherent Vortex Simulation (CVS) method (see [2]) the coherent modes are *resolved*. The *unresolved* parts correspond to the high wavenumber in the LES method and the incoherent modes in the CVS method, respectively.

The objective of the present paper is to compare the two filtering methods in terms of the dynamical passivity of the unresolved modes. In this we focus on the structural properties of the resolved and unresolved parts and their mutual interaction. We examine the geometrical statistics (see e.g. [3], [4], [5]) to analyze the dynamical and structural properties of the filtered fields. In the context of 2D turbulence the issue of central interest is the interaction of thin, elongated filaments with the strain field generated by the coherent vortices. The unresolved part can be regarded as dynamically passive as long as its evolution is constrained by the resolved part. In this case the unresolved part follows the strain field of the resolved part which is reflected in the alignment properties of the vorticity gradient with the corresponding rate of strain. As shown in [6], this phenomenon is described by evolution of vorticity gradients $\boldsymbol{\nabla\omega}$. Using the Weiss criterion, it can be shown (see [7]) that in the hyperbolic (i.e. strain dominated) parts of the flow the dynamics of vorticity gradient is determined by the angle between $\boldsymbol{\nabla\omega}$ and the compressing eigenvector $\mathbf{d_2}$ of the rate of strain tensor. Vorticity gradients are steepened by the strain field when they lie within the range of $\frac{\pi}{4}$ from $\mathbf{d_2}$, and are suppressed otherwise.

2 Results

In [7] it was shown that 2D forced turbulence exhibits, in the mean, preferential alignment of the vorticity gradient with the principal direction of compression $\mathbf{d_2}$. Magnitude of this alignment was shown to depend on the Reynolds number and the dissipation model (Newtonian or hyperviscous). Herein we use the same diagnostics to explore the internal structure of the vorticity fields obtained with the two different filtering methods. We analyze 2D vorticity fields at resolution 256^2 obtained from the solution of the incompressible Navier-Stokes system in a box with periodic boundary conditions and Fourier space forcing at the wavenumber $k_i = 4$ (see [2] for details). For both filtering methods the split was made so that the resolved part contains 0.7% of the total number of modes. In the case of the Fourier filtering (FF) we consider the alignment property observed in the fields corresponding to high wavenumbers (FH), low wavenumbers (FL) and the *cross*-alignments between vorticity gradients in the high-pass filtered field and the strain related to the low wavenumbers (FHvsL). Similarly, for the case of the Wavelet filtering (WF) we analyze the alignments in the co-

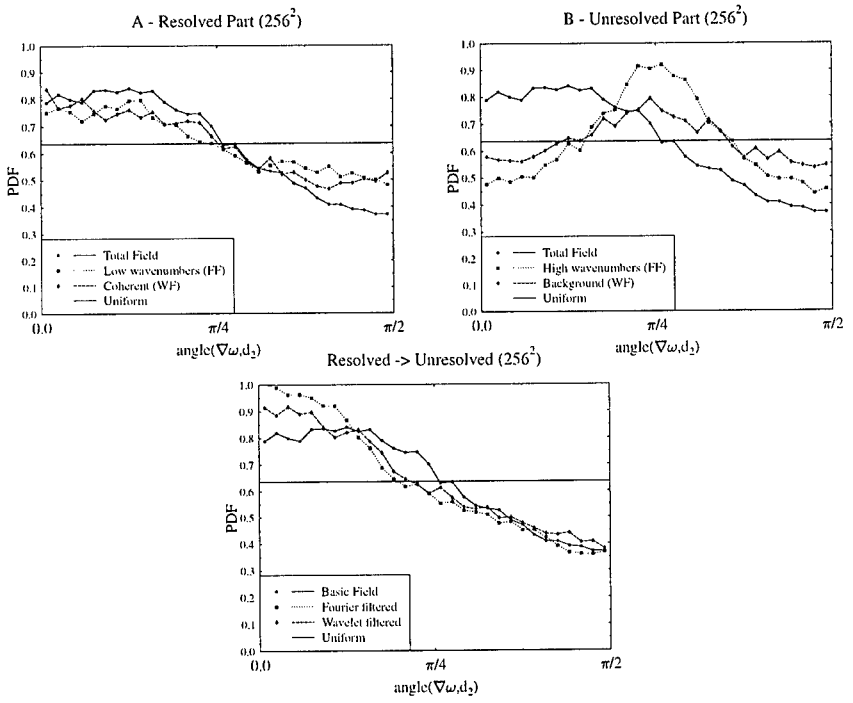


Figure 1: PDF's of the alignment angle α in the resolved part of the flow (A - top left), the unresolved part (B - top right), and between the vorticity gradient of the unresolved part and the strain field of the resolved part (C - bottom).

herent part (WC), the background part (WB) and the *cross*-alignments for the background part against the strain field induced by the coherent part (WBvsC). We also provide results concerning the basic field which was analyzed (B).

Interesting information is revealed by the PDF's of the alignment angle α computed for the different fields. In Fig. 1A we show the PDFs of the alignment angle in the resolved parts, i.e. for the Fourier Low-pass filtered field (FL), the Wavelet-Coherent field (WC) and, for comparison, the basic field (B). We see that the PDF corresponding to Wavelet filtering follows more closely that of the basic field. This implies that Fourier filtering removes some structural information from the field. Now we turn to the analysis of the unresolved parts obtained with the two methods of filtering. In Fig. 1B we present the PDFs of the alignment angle for the the Fourier High-pass filtered field (FH), the Wavelet-Background field (WB) and the basic field (B) for reference. The first two PDFs have bumps around the angle $\frac{\pi}{4}$. They correspond to the idealized situation when a single vorticity filament is embedded in its own strain field. Then the principal directions of strain are always at the angle of $\frac{\pi}{4}$ with respect to the filament axis. Nevertheless, the PDF of the Wavelet filtered field is significantly

closer to the uniform distribution which implies that it is more *structureless* than the Fourier filtered field. Flat PDF is what one would expect of a completely random field and this result suggests that the Fourier-filtered field still contains some structurally important information. Next we go on to the analysis of the *cross*-alignment PDFs. In Fig. 1C we show that the alignment angle α between vorticity gradient of the unresolved parts (i.e. Fourier High-pass filtered and Wavelet-Background fields) and the strain field of the resolved parts (i.e. Fourier Low-pass filtered and Wavelet-Coherent fields). Good agreement is observed for angles corresponding to suppression of vorticity gradients. Conversely, in the range of angles corresponding to amplification agreement is worse, with Wavelet filtering resulting in stronger alignment than in the basic field. The meaning of this is an open question and analysis of fields at higher resolution is necessary to clarify this issue.

3 Conclusions

In this work we apply the concept of geometrical statistics to quantify the efficiency of the Fourier and Wavelet filtering methods. The preliminary results shown here imply that the two methods give comparable results. The unresolved part is more structureless in the case of the Wavelet filter, the cross-alignments however show that the unresolved part aligns more closely with the strain field of the resolved part in the case of the Fourier filtering. In order to get further insight into these phenomena fields at higher resolution need to be analyzed.

Acknowledgments: We thankfully acknowledge partial support from the French-German Program Procope (contract 99090) and the Polish-French Program POLONIUM (contract 99158).

References

[1] M. Farge. Ann. Rev. of Fluid Mech., **24**, 395–457, 1992.

[2] M. Farge, K. Schneider and N. Kevlahan. Phys. Fluids, **11** (8), 2187–2201, 1999.

[3] P. Constantin, SIAM Review, **36**, 73 (1994).

[4] A. Tsinober, Eur. J. Mech. B/Fluids, **17** (4), 421-449 (1998).

[5] W. T Ashurst, A. R. Kerstein, R. M. Kerr, C. H. Gibson, Phys. Fluids, **30** (8), 2343 (1987).

[6] J. Weiss, Physica D **48**, 273 (1991).

[7] B. Protas, A. Babiano, N. K.-R. Kevlahan, Physica D **128**, 169-179, (1999).

ADVANCES IN TURBULENCE VIII
Proceedings of the Eighth European Turbulence Conference
C. Dopazo et al. (Eds.)
© CIMNE, Barcelona 2000

Vortex tube extraction in three–dimensional turbulence using orthogonal wavelets

Marie Farge[1], Kai Schneider[2] and Giulio Pellegrino[2]

[1] LMD, Ecole Normale Supérieure
24 rue Lhomond, 75231 Paris Cedex 05, France.
[2] ICT, Universität Karlsruhe (TH)
Kaiserstraße 12, 76128 Karlsruhe, Germany.

Contact e-mail: farge@lmd.ens.fr

1 Introduction

The importance and the role of coherent structures (coherent vorticity tubes) in three–dimensional turbulence have been established largely by high resolution numerical simulations, e.g. in [5]. In the past we have developed a wavelet method to extract coherent vortices in two–dimensional turbulent flows [2, 3], at which the remaining background flow exhibits Gaussian statistics. In this paper we propose a new wavelet based method to seperate three-dimensional flows into an organized part, corresponding to the coherent vorticity tubes, and a random part, corresponding to the incoherent background flow.

2 Vortex tube extraction

As an example we consider DNS data of statistically stationary three–dimensional homogenous and isotropic turbulence. The flow has been computed by Meneguzzi & Vincent [5] using a pseudo-spectral scheme with resolution $N = 240^3$ corresponding to a microscale Reynolds number of 150. We project each component of the vorticity vector field $\vec{\omega}$ onto a three–dimensional orthogonal wavelet basis. Then we reconstruct the coherent vorticity field ($\vec{\omega}_C$) from those wavelet coefficients for which the modulus of the wavelet coefficient vector is larger than $(2Z \log_{10} N)^{1/2}$ (where Z denotes the total enstrophy and N the number of grid points), while the incoherent background flow ($\vec{\omega}_I$) is reconstructed from the weak coefficients. We find that only 3% of the coefficients represent the coherent vortex tubes (cf. Fig. 1) and retain 73% of enstrophy. The remaining 97% of the coefficients represent the unorganized background flow (cf. Fig. 2) containing

27% of the enstrophy, which is quasi–homogeneous. The energy spectra (Fig. 3) show that both components ($\vec{\omega}_C$ and $\vec{\omega}_I$) are multiscale, although the coherent part only differs at high wavenumbers from the original field ($\vec{\omega}$), which confirms the fact that vorticity tubes are multiscale. We also observe that the coherent part, as well as the total flow, are long–range correlated, while the incoherent part is on the contrary short–range correlated. The PDF of vorticity (Fig. 4) for the coherent part is very similar to the original PDF, which confirms the fact that most of the statistical information is preserved by the wavelet filtering. The PDF of the background field is not exactly Gaussian as in the two–dimensional case, however its variance is strongly reduced.

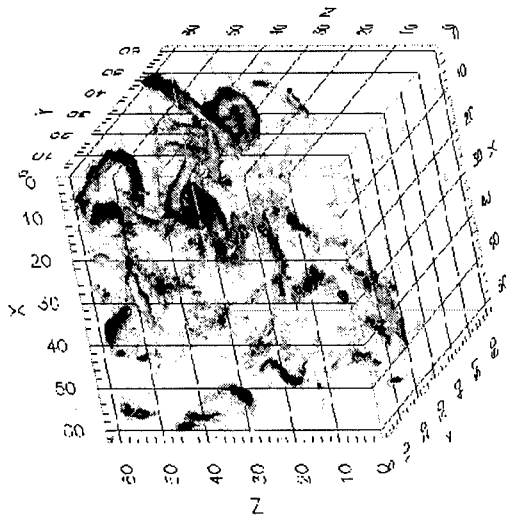


Figure 1: Isosurfaces of coherent vorticity field $\vec{\omega}_C$ reconstructed from 3% of the wavelet coefficients. Note that the coherent vorticity is nearly indistinguishable from the orginal field $\vec{\omega}$.

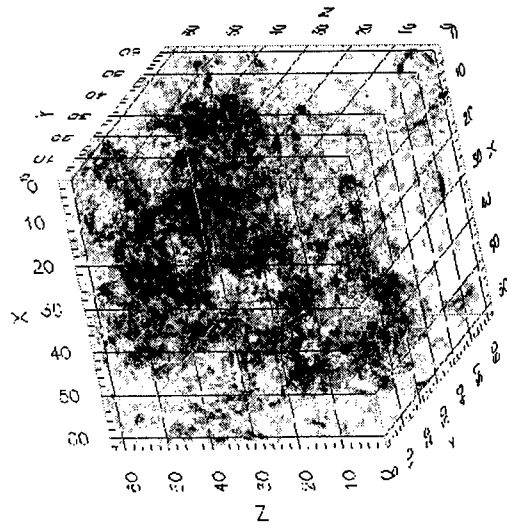


Figure 2: Isosurfaces of background vorticity $\vec{\omega}_I$ reconstructed from 97% of the wavelet coefficients.

3 Conclusions

The motivation for the above approach is the development of a new turbulence model, called Coherent Vortex Simulation (CVS) [3], for simulating fully–developed turbulent flows. Therein the evolution of the coherent vorticity tubes is calculated in an adaptive wavelet basis, which dynamically adjusts to the flow evolution, while the influence of the incoherent background flow onto the coherent vortices is statistically modelled. This has been applied for two–dimensional turbulent flows and is currently being extended for three–dimensional turbulent flows. In contrast to classical turbulence models, the CVS method ensures that the incoherent background flow is actually quasi–homogeneous, quasi–Gaussian and short–range correlated, hence its effect onto the coherent part can be more easily taken into account by the turbulence model.

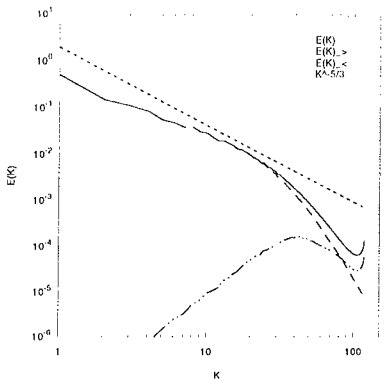


Figure 3: Energy spectra of the total field $\vec{\omega}$, of the coherent field $\vec{\omega}_C$ and of the background field $\vec{\omega}_I$.

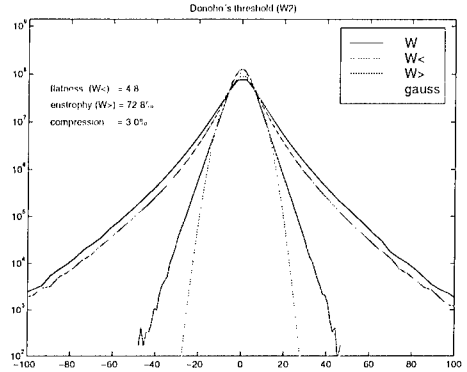


Figure 4: Pdf of vorticity of the total field $\vec{\omega}$, of the coherent field $\vec{\omega}_C$ and of the background field $\vec{\omega}_I$.

Acknoledgements: We thank Maurice Meneguzzi for providing us the DNS data. We also acknowledge partial financial support from the French–German program Procope (contract n.99090), the European program TMR (contract n.FMRX–CT 98–0184) and the program PPF of ENS Paris (contract n. 15407).

References

[1] M. Farge, Wavelet Transforms and their Applications to Turbulence, *Ann. Rev. of Fluid Mech.*, 24:395–457, 1992.

[2] M. Farge, K. Schneider and N. Kevlahan. Coherent structure eduction in wavelet–forced two–dimensional turbulent flows. *IUTAM Symposium on Dynamics of slender vortices (Ed. E. Krause and K. Gersten)*, Kluwer Academic Publishers, 65–83, 1998.

[3] M. Farge, K. Schneider and N. Kevlahan. Non–Gaussianity and Coherent Vortex Simulation for two–dimensional turbulence using an adaptive orthonormal wavelet basis. *Phys. Fluids*, **11**(8), 2187–2201, 1999.

[4] K. Schneider and M. Farge. Wavelet approach for modelling and computing turbulence. *Lecture Series 1998–05 Advances in turbulence modelling*, von Karman Institute for Fluid Dynamics, Bruxelles, 132 pages, 1998.

[5] A. Vincent, M. Meneguzzi. The spatial structure and statistical properties of homogeneous turbulence. *J. Fluid Mech.*, Vol. 225, pp. 1–20, 1991.

ADVANCES IN TURBULENCE VIII
Proceedings of the Eighth European Turbulence Conference
C. Dopazo et al. (Eds.)
© CIMNE, Barcelona 2000

Flow and Reynolds Number Dependencies of Turbulent Vorticity Fluctuations

R. A. Antonia and T. Zhou

Department of Mechanical Engineering
University of Newcastle, N.S.W., 2308 Australia

Contact e-mail: meraa@cc.newcastle.edu.au

1 Introduction

Significant attention has been given to the evolution of various characteristics of turbulent velocity and scalar fields with R_λ, the Taylor microscale Reynolds number. The major impetus for this was the refined hypothesis of Kolmogorov [1]. Wyngaard & Pao [2] noted that the measured pdf and spectra of $\partial u/\partial x$, where u is the velocity fluctuation in the streamwise (x) direction, depended on R_λ in ways consistent with this hypothesis. A compilation of the dependence on R_λ of the low-order normalised moments of $\partial u/\partial x$ was presented in [3], where the predictions, based on different vortical models, were also reviewed. The advent of direct numerical simulations has provided information about the shape of the intense vortical structures and their dependence on R_λ [4]. Recently, the R_λ dependence of low-order moments of the longitudinal and transverse velocity structure functions was investigated for a wide range of flows, Reynolds numbers and separations, r [5]. The Kolmogorov-normalised moments exhibited a significant dependence on R_λ. There was also strong evidence that the moments were flow dependent and, in any particular flow, location-dependent in the plane of mean shear. The present paper is an attempt to extend the study to flow and R_λ dependencies of the vorticity characteristics. Specifically, we present statistics of the transverse vorticity component, ω_z, in three flows, i.e. decaying grid turbulence ($R_\lambda = 30 - 100$), the centreline of the 2-D wake of a circular cylinder ($R_\lambda = 40 - 230$) and of a plane jet ($R_\lambda = 550 - 1000$).

2 Experimental Details

Measurements in grid and wake turbulence were carried out in the same blower type open-circuit wind tunnel. Details of the experimental facility for grid turbulence can be found in [6]. Four kinds of cylinders of diameters 6.35 mm to

24.5 mm were used to generate the wake turbulence [7]. Measurements in the plane jet were carried out at a distance of $36h$ downstream from the exit, where the flow is approximately self-preserving [5].

A 1-component vorticity probe, consisting of one X-wire straddled by a pair of parallel hot wires, was used to measure ω_z. A 3-component (four X-wires) vorticity probe was also used in grid ($R_\lambda = 50$) [8] and wake ($R_\lambda = 40$) flows [9]. The separation between the two parallel wires of the 1-component probe is about $2-4\eta$ while, for the 3-component probe, the separation of the opposite X-wires, which lie either in the $x-y$ plane or $x-z$ plane, is about $4-5\eta$. The signals from the anemometers were low-pass filtered at a cut-off frequency f_c close to the Kolmogorov frequency, $f_K \equiv U/2\pi\eta$. The sampling frequency was set at $2f_c$ with a record duration of 60–300 s.

Grid turbulence provides an important calibration of the measurement since both $\langle\omega^2\rangle$ (angular brackedts denote time averaging) and its streamwise decay can be determined with relatively good accuracy. The streamwise decay of the turbulent energy $\langle q^2\rangle$ yielded a value of $\langle\omega^2\rangle$ within 10% of that directly estimated from the 3-component vorticity probe [8].

3 Results and Discussion

The Kolmogorov-normalised mean square values of u, v and ω_z are shown in Figure 1, an asterisk denoting normalisation by Kolmogorov length scale η and/or velocity scale u_K. Both $\langle u^{*2}\rangle$ and $\langle v^{*2}\rangle$ exhibit a linear increase with respect to R_λ. This is consistent with the assumption of local isotropy (LI), i.e. $\langle\epsilon\rangle = 15\nu\langle(\partial u/\partial x)^2\rangle$. The R_λ dependence of $\langle u^{*2}\rangle$ follows from $\langle u^{*2}\rangle \equiv \langle u^2\rangle/u_K^2 = \langle u^2\rangle/\nu^{1/2}\langle\epsilon\rangle^{1/2} = R_\lambda/15^{1/2}$. The data in Figure 1 are in close agreement with this result. For $\langle v^{*2}\rangle$, we have $\langle v^{*2}\rangle = (\langle v^2\rangle/\langle u^2\rangle)R_\lambda/15^{1/2}$. The $\langle v^{*2}\rangle$ data for any given flow also show a linear dependence on R_λ but this cannot be universal since the ratio $\langle v^2\rangle/\langle u^2\rangle$, which represents a measure of the global (large scale) anisotropy, varies from flow to flow. In particular, this ratio is much closer to 1 in the wake than in the other two flows. If the turbulence is homogeneous, $\langle\epsilon\rangle = \nu\langle\omega^2\rangle$ and $\langle\omega^{*2}\rangle = 1$, independently of R_λ. For LI, $\langle\omega_x^2\rangle = \langle\omega_y^2\rangle = \langle\omega_z^2\rangle$, so that $\langle\omega_z^{*2}\rangle = 1/3$. The present values of $\langle\omega_z^{*2}\rangle$ (Figure 1) confirm closely with this (the average value is estimated to be 0.36 ± 0.04). Checks of LI have been made in the three flows, grid and wake turbulence showing closer agreement with LI; for these flows, the measured spectra (Figure 2) of ω_x, ω_y and ω_z agree quite well with calculations based on isotropy [8].

The pdfs of ω_z, p_{ω_z}, when normalised in the usual way, i.e. $p(\omega_z/\omega_z')$ vs ω_z/ω_z' (the prime denotes the rms value), evolve with R_λ in a manner similar to that previously reported, for example, for $p[(\partial u/\partial x)/(\partial u/\partial x)']$. As R_λ increases, the tails of the pdfs tend to spread out further whereas near the origin, the shape contracts and the amplitude increases. The previous behaviour seems unaffected when the pdf is Kolmogorov-normalised (Figure 3). The area under each curve remains equal to 1 but there is no range of ω_z^* over which the three distributions

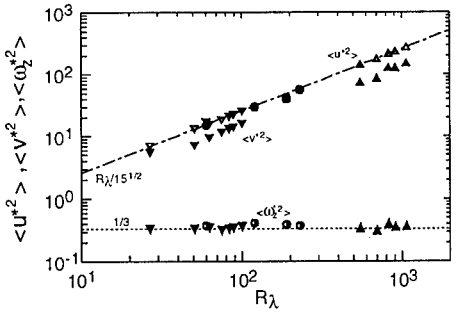


Figure 1: Dependence of $\langle u^{*2}\rangle$, $\langle v^{*2}\rangle$ and ω_z^{*2} on R_λ. Grid : ∇. Wake : $\circ$. Jet : $\triangle$. Open symbols are for $\langle u^{*2}\rangle$; filled symbols are for $\langle v^{*2}\rangle$; half-filled symbols are for ω_z^{*2}.

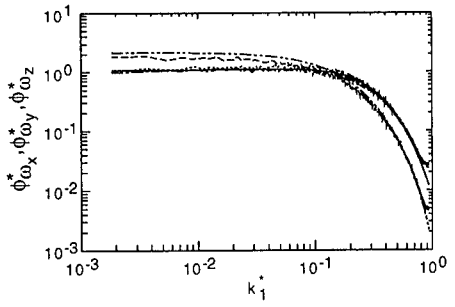


Figure 2: Comparison of measured and calculated spectra of ω_x, ω_y and ω_z in grid turbulence. Measured : – –, $\phi^*_{\omega_x}$; - - -, $\phi^*_{\omega_y}$; — - —, $\phi^*_{\omega_z}$. Calculated : — - - —, $\phi^*_{\omega_x}$; —, $\phi^*_{\omega_y}$ or $\phi^*_{\omega_z}$.

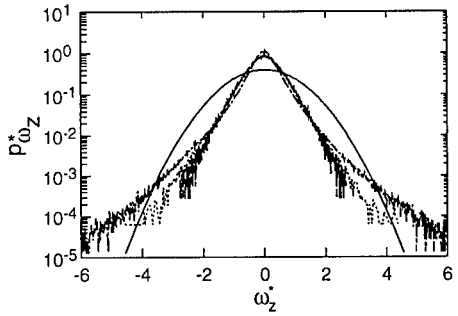


Figure 3: Kolmogorov-normalized pdf of ω_z. – –, grid ($R_\lambda = 27$); - - -, wake (60); — - —, jet (550); —, Gaussian distribution.

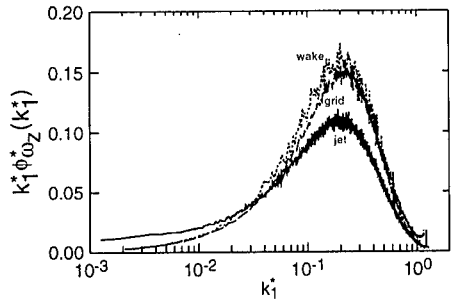


Figure 4: Kolmogorov-normalized spectra of ω_z weighted by k_1^*. - - -, grid ($R_\lambda = 27$); – –, wake (60); —, jet (550).

of $p(\omega_z^*)$ collapse.

The distributions of $k_1^*\phi^*_{\omega_z}(k_1^*)$ in Figure 4 show a peak near $k_1^* \simeq 0.2$, as previously noted in both numerical [10] and experimental studies [11], possibly indicating that the most energetic vortices have a diameter of about 5η. The magnitude of the peak is about 30% smaller in the plane jet than in either the grid or wake flows. We suspect that the jet peak may have been affected by a spurious increase in $\phi^*_{\omega_z}(k_1^*)$ at low wavenumbers. Since the contribution from $\partial v/\partial x$ in the low wavenumber region is small, the increase of $\phi^*_{\omega_z}$ in this region mainly reflects the contribution from $\partial u/\partial y$. We verified that the increase is not a spurious artefact of the use of the vorticity probe since the spectrum $\phi^*_{\partial u/\partial y}$ agrees quite well with that obtained using only a pair of parallel wires for which

the flow interference was deemed negligible. (It should also be noted that the vorticity probe and a single X-wire probe yielded essentially the same v spectra). We cannot discount a possibility of the low wavenumber distortion caused by the fact that the wall and ceiling of the laboratory were only about two half widths of the jet away from the centreline. Notwithstanding this discrepancy, there are discernible differences between flows, in terms of the shape of the distributions. It would obviously be desirable to compare vorticity statistics for the three flows at the same R_λ. Unfortunately, there is no overlap in R_λ between the jet and wake but a comparison can be made between the wake and grid turbulence at $R_\lambda \approx 60$. The distributions in the wake and grid turbulence exhibit differences : there is more energy contribution to $k_1^* \phi_{\omega_z}^*(k_1^*)$ at low wavenumbers in the wake than in the grid. We have checked that these differences appear to be more important than those arising through a variation of R_λ in a particular flow. A possible implication is that there are morphological differences in the fine scale structure between the three flows. A more likely possibility is that the influence of the large scale motion on the vorticity spectrum may not be discounted, at least in the case of the jet and wake. The features of the organised large scale motion are well documented for these two flows. The frequency corresponding to this motion has been identified in the present jet and wake v-spectra.

4 Conclusion

The present study suggests that Kolmogorov-normalized pdfs and spectra of the spanwise vorticity fluctuations appear to be more dependent on the nature of the flow than on R_λ.

The support of the Australian Research Council is gratefully acknowledged.

References

[1] Kolmogorov, A. N. 1962. *J. Fluid Mech.*, **13**, 82.
[2] Wyngaard, J. C. & Pao, Y. H. 1972. *Lecture Notes in Physics*, **12**, 384.
[3] Van Atta, C. W. & Antonia, R. A. 1980. *Phys. Fluids*, **23**, 252.
[4] Jimenez, J. Wray, A. A., Saffman, P. G. & Rogallo, R. S. 1993. *J. Fluid Mech.*, **255**, 65.
[5] Pearson, B. R. & Antonia, R. A. 2000. *J. Fluid Mech.* (submitted)
[6] Zhou, T. & Antonia, R. A. 2000. *J. Fluid Mech.*, **406**, 81.
[7] Antonia, R. A., Zhu, Y. & Shafi, H. S. 1996. *J. Fluid Mech.*, **323**, 173.
[8] Antonia, R. A., Zhou, T. & Zhu, Y. 1998. *J. Fluid Mech.*, **374**, 29.
[9] Zhu, Y. & Antonia, R. A. 1999. *Expts. in Fluids*, **27**, 21.
[10] She, Z. S., Chen, S., Doolen, G., Kraichnan, R. H. & Orszag, S. A. 1993. *Phys. Rev. Lett.*, **70**, 3251.
[11] Antonia, R. A., Shafi, H. S. & Zhu, Y. 1996. *Phys. Fluids*, **8**, 2196.

ADVANCES IN TURBULENCE VIII
Proceedings of the Eighth European Turbulence Conference
C. Dopazo et al. (Eds.)
© CIMNE, Barcelona 2000

Two-dimensional breakdown of a Burgers vortex subject to a rotating strain field

S. Le Dizès

Institut de Recherche sur les Phénomènes Hors Équilibre,
12, avenue Général Leclerc, F-13003 Marseille, France.

Contact e-mail: ledizes@marius.univ-mrs.fr

The discovery of concentrated vorticity filaments in turbulent flows and their possible connection to fundamental properties of turbulence has renewed the interest in vortex dynamics. Direct numerical simulations suggest that filaments resemble Burgers vortices. In order to understand the dynamical properties of filaments, it is then natural to construct and analyse asymptotic solutions close to this model. In this framework, Moffatt *et al.* [1] (hereafter referred to as MK0) recently extended the Burgers model to account for a non-axisymmetric correction generated by a stationary external strain field. In this talk, MKO analysis will be generalized by considering a vortex subject to an external strain field rotating around the vortex axis. This extension is needed in practice as the external strain field of a given vortex is generally created by other vortices rotating around it due to their mutual interactions. The main objective is to understand in which conditions the vortex can deform to remain in equilibrium with the external field and to analyse the main characteristics of the equilibrium state [2].

The vorticity maximum and the radius of Burgers vortex are used to non-dimensionalized time and spatial variables, such that the problem depends on three parameters: the strain rate ε of the external field, its angular frequency Ω and the Reynolds number $Re = 1/\nu$ (ν being the kinematic viscosity). The analysis is performed in the limit of small ε and large Reynolds numbers.

The results can be summarized as follows. When Ω is not in the range of the angular velocity of the vortex, i. e. $\Omega < 0$ or $\Omega > 1/2$, a stationary equilibrium, which does not depend on the Reynolds number (if sufficiently large) is shown to exist. As in MKO, the correction to Burgers vortex is governed by a linear inviscid equation. When $0 \leq \Omega \leq 1/2$, the vortex correction has a different structure, which strongly depends on the Reynolds number. The main difference is due to the presence of a critical point singularity at the radial location where the local angular velocity of the vortex equals the angular frequency of the strain.

This singularity is smoothed by introducing higher order effects such as viscosity or nonlinearity. The nature of the critical layer, which depends on the parameter $h = 1/(Re\,\varepsilon^{3/2})$, is found to govern the entire structure of the correction. Figure 1 shows the streamlines in the vortex core for the two extreme values of h and a fixed value of Ω. Note that the elliptic vortex core is oriented at 45 degrees with respect to the direction of external stretching in the nonlinear case but not in the viscous case.

It is also worth mentioning that the critical point singularity implies that the vorticity correction is much larger than the strain field that has generated it. Its maximum scales as $\omega_{\max} = F_v(\Omega)Re^{1/3}\varepsilon$ in the viscous regime ($h \gg 1$), and $\omega_{\max} = F_{nl}(\Omega)\sqrt{\varepsilon}$ in the nonlinear regime ($h \ll 1$). The variations of $F_v(\Omega)$ and $F_{nl}(\Omega)$ are displayed in Fig. 2. In the viscous regime, the results are in good agreement with the viscous numerical simulations by Lingevitch & Bernoff [3]. In the nonlinear regime, the vorticity maximum of the equilibrium solution blows up for a particular frequency $\Omega^{nl} \approx 0.16$. This breakdown could be the signature of a strongly time-dependent response of the vortex to the external strain. Our conjecture is that, for this particular frequency, inertial waves would have to be generated to avoid vorticity blow up. These waves are associated with the spiral wind-up of vorticity [4] which has been observed in both experiments and numerical simulations [5], particularly during vortex interactions before merging. The existence of an angular frequency for which the vortex breaks down would provide a simple explanation for the spontaneous spiral wind-up of vorticity leading to vortex merging.

References

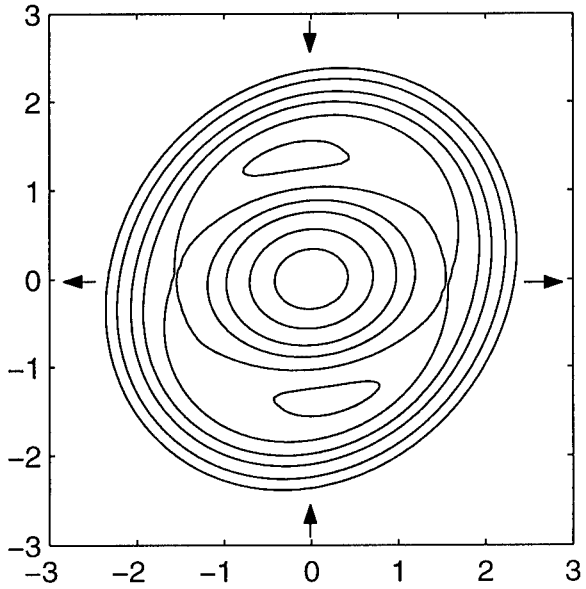
[1] H. K. Moffatt, S. Kida, and K. Ohkitani. Stretched vortices -the sinews of turbulence; large-Reynolds-number asymptotics. *J. Fluid Mech.* **259**, 241–264, 1994.

[2] S. Le Dizès. Non-axisymmetric vortices in two-dimensional flows. *J. Fluid Mech.*, **406**, 175–198, 2000.

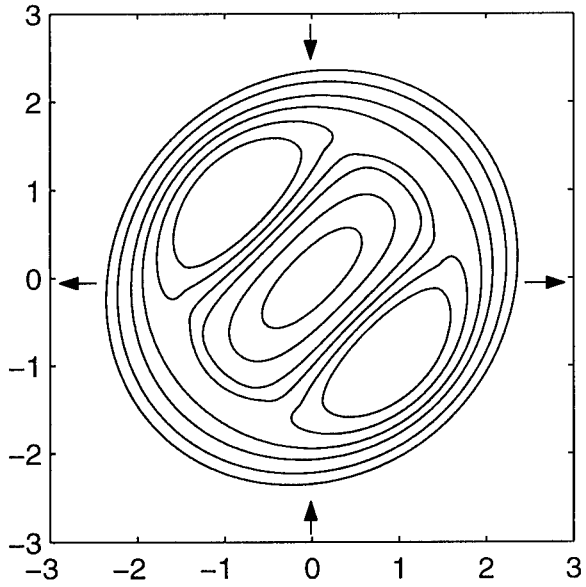
[3] J. F. Lingevitch and A. J. Bernoff. Distortion and evolution of a localized vortex in an irrotational flow. *Phys. Fluids* **7**(5), 1015–1026, 1995.

[4] T. S. Lundgren. Strained spiral vortex model for turbulent fine structure. *Phys. Fluids* **25**(12), 2193–2203, 1982.

[5] A. P. Bassom and A. D. Gilbert. The spiral wind-up of vorticity in an inviscid planar vortex. *J. Fluid Mech.*, **371**, 109–140, 1998.



(a)



(b)

Figure 1: Streamlines of the strained Burgers vortex in a co-rotating frame for $\Omega = 0.2$ and $\varepsilon = 0.01$. The arrows indicate the principal directions of the external strain field. (a) Viscous critical layer regime ($h \gg 1$), (b) Nonlinear critical layer regime ($h \ll 1$).

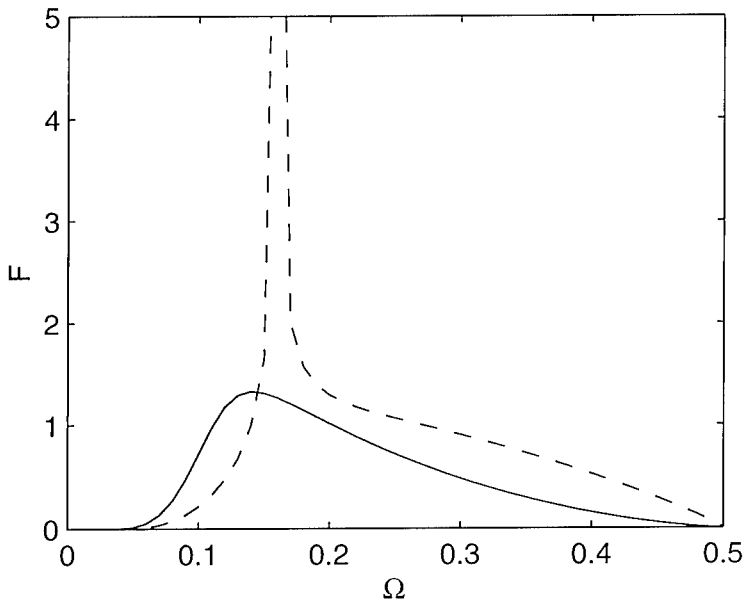


Figure 2: Maximum amplitude of the vorticity correction as a function of the angular frequency Ω. Solid line: $F_v(\Omega)$ (viscous regime); Dashed line: $F_{nl}(\Omega)$ (nonlinear regime).

ADVANCES IN TURBULENCE VIII
Proceedings of the Eighth European Turbulence Conference
C. Dopazo et al. (Eds.)
© CIMNE, Barcelona 2000

The Axisymmetric Vortex Breakdown Phenomenon

Z. Rusak

Department of Mechanical Engineering, Aeronautical Engineering and Mechanics
Rensselaer Polytechnic Institute, Troy, New York 12180-3590 USA

Contact e-mail: rusakz@rpi.edu

1 Abstract

The paper reviews the recent theoretical studies of the author and co-workers on the axisymmetric vortex breakdown phenomenon. The theory is built of a global analysis of the steady Euler equations which describe the motion of an axisymmetric and inviscid swirling flow in a pipe and of linear stability analyses of the various steady-state solutions. Asymptotic studies are also used to explore the effects of viscosity, pipe divergence, and inlet vorticity perturbations on the flow behavior. It is shown that the present study provides a consistent explanation of the physical mechanism leading to the axisymmetric vortex breakdown phenomenon as well as the conditions for its occurrence. Calculations of the breakdown conditions of various vortices in a pipe as well as of the leading-edge vortices above slender delta wings are also summarized.

2 Introduction

Vortex breakdown is a remarkable phenomenon in fluid dynamics which is referred to the abrupt change in structure that suddenly occurs in vortex flows with an axial flow component and where the swirl level is high. It is usually characterized by a sudden deceleration of the axial flow over a relatively short distance and the formation of a free stagnation point in the flow, followed by a large separation zone and turbulence behind it. Several breakdown patterns have been observed, ranging from asymmetric spiral waves to almost axisymmetric disturbances. Controlling the vortex breakdown phenomena may have applications in the aeronautical and mechanical engineering technologies of high angles of attack aerodynamics, combustion chambers, hydrocyclone separators, and chemical mixing processes.

The scientific interest to explain this strongly non-linear phenomenon has led to many experimental, numerical and theoretical studies, and several review papers on this subject have been presented, including the reports by Hall [1], Leibovich [2, 3], Escudier [4] and Sarpkaya [5]. Although there has been an extensive research, these phenomena still remain largely unexplained as to their fundamental nature from both the experimental as well as the theoretical stand points.

This paper concentrates on the axisymmetric breakdown phenomenon in a swirling flow in a streamtube. The various theoretical analyses and numerical computations of this phenomenon suggested several explanations of vortex breakdown. However, a consistent description of this complicated phenomenon has not been provided. Also, it is found that the relations between the various theoretical and numerical solutions is not fully clear.

This paper presents a review of the recent work of the author and co-authors on this topic [6 – 14]. The present study provides a consistent explanation of the physical mechanism leading to the axisymmetric vortex breakdown phenomenon as well as the conditions for its occurrence.

3 Summary of Recent Theoretical Studies

The approach of Wang and Rusak [6] – [14] is based on a rigorous study of the dynamics of swirling flows in a finite-length streamtube as described by the axisymmetric and unsteady Navier-Stokes equations. Certain boundary conditions that may reflect the physical situation in the experiments are used. In the inviscid flow limit, the analysis studies the growth rate of an initial perturbation as it relates to the special stability characteristics found by Wang and Rusak [7, 8] as well as the relation of the flow time-asymptotic behavior to steady-state solutions [6]. It is found that there exist two critical swirl ratios of the incoming flow to the pipe, ω_0 and ω_1, where $\omega_0 < \omega_1$. Columnar flows with a swirl ratio less than the threshold level, ω_0, are unconditinally stable to any axisymmetric disturbance. In the range $\omega_0 < \omega < \omega_1$ the flow may evolve into one of two steady states, depending on the size of the initial disturbances. When disturbances are sufficiently small they decay in time and the flow returns to be columnar but, when disturbances are large, they grow and evolve into a large and steady, semi-infinite stagnation zone, similar to the breakdown states found in very high Reynolds number flows [5]. When $\omega > \omega_1$, any initial disturbance grows and evolves into a breakdown zone.

These special stability characteristics are related to the upstream propagation of both small- and large-amplitude disturbances and their interaction with the flow conditions downstream of the vortex generator. The disturbances tend to propagate upstream with a speed that increases with ω. When $\omega < \omega_1$, small

disturbances are convected by the axial flow out of the pipe and the columnar flow is, therefore, stable. However, when $\omega > \omega_1$, small disturbances tend to move upstream. Since the flow out of the vortex generator at steady operation is fixed, the disturbances cannot move through it. They are trapped, grow, and stabilize as a large and steady stagnation zone. These large-amplitude zones also tend to grow and move upstream as ω changes. However, when $\omega < \omega_0$, they are convected by the axial flow out of the pipe and the flow returns to be columnar.

These results clarify the mechanism leading to the axisymmetric vortex breakdown in high Reynolds number flows. As the incoming swirl ratio is increased above ω_0, and is near or above ω_1, the columnar vortex loses its stability to axisymmetric disturbances and evolves into a breakdown state. The theory explains the sudden and abrupt nature of the process, specifically around ω_0, where a large separation zone may suddenly appear in the flow as swirl increases. It also clarifies the role of the critical state at ω_1 where a columnar vortex becomes unstable as swirl increases, and that at ω_0 where axisymmetric breakdown states become unstable as swirl decreases. Therefore, ω_0 is a threshold level for breakdown states and $\omega > \omega_0$ is a necessary condition for a steady and stable axisymmetric breakdown. $\omega > \omega_1$ is a sufficient condition for breakdown. The numerical studies of Rusak et al. [9]. demonstrate these results as well as describe the evolution of the perturbations to breakdown states.

Analysis of the effect of slight viscosity on the flow dynamics shows [10] that when the Reynolds number (Re) is sufficiently high the inviscid instability/transition mechanism is dominant. This dynamical behavior matches the Navier-Stokes simulations [15 – 18] for high Reynolds number laminar flows. The establishment of long and nearly stagnant breakdown zones as Re increases is also found in the simulations. However, when Re is less than a certain value, both the analysis [6] and the simulations [15 – 18] show that the instability mechanism disappears and the breakdown develops as a disturbance that gradually grows with the increase of the incoming swirl ratio. Also, the simulations [16] demonstrate that the separation zone becomes a closed bubble with an internal flow structure as Re decreases, similar to the states found in laminar flow experiments [2 – 5].

The effects of an adverse pressure gradient and of inlet vorticity perturbations on the vortex flow dynamics show [11, 12] a similar behavior. The inviscid instability mechanism is dominant when these effects are small. However, above a certain limit level, these effects dominate and breakdown develops as a disturbance that gradually grows with the increase of the incoming swirl ratio. The combined effects of Re, adverse pressure, and vorticity perturbations can also be estimated for both the analysis of vortex flows or the control of the breakdown phenomenon.

Finally, the theoretical approach was recently applied to various model vortices such as the Burgers' vortex, the Q-vortex, and leading-edge vortices above slender delta wings at high angles of attack [13, 14]. The breakdown condi-

tions for these vortices were estimated and the calculated results showed good agreement with available experimental data. Specifically, it was found that free vortices may breakdown when the swirl ratio (maximum of circumferential speed to maximum axial speed) is above about 0.6.

This research was carried out with the support of the USA National Science Foundation under Award No. CTS-9804745.

References

[1] M.G. Hall, *Annual Review of Fluid Mechanics,* **4**, 195-217, 1972.

[2] S. Leibovich, *Annual Review of Fluid Mechanics,* **10**, 221-246, 1978.

[3] S. Leibovich, *AIAA Journal,* **22**, 1192-1206, 1984.

[4] M.P. Escudier, *Progress in Aerospace Sciences,* **25**, 189-229, 1988.

[5] T. Sarpkaya, AIAA paper 95-0433, 1995.

[6] S. Wang and Z. Rusak, *Journal of Fluid Mechanics,* **340**, 177-223, 1997.

[7] S. Wang and Z. Rusak, *Physics of Fluids*, **8**, 4, 1007-1016, 1996.

[8] S. Wang and Z. Rusak, *Physics of Fluids*, **8**, 4, 1017-1023, 1996.

[9] Z. Rusak, S. Wang and C. Whiting, *Journal of Fluid Mechanics,* **366**, 211-237, 1998.

[10] S. Wang and Z. Rusak, *Physics of Fluids* **9**, 7, 1914-1927, 1997.

[11] Z. Rusak, K.P. Judd and S. Wang, *Physics of Fluids,* **9**, 8, 2273-2285, 1997.

[12] Z. Rusak, *Physics of Fluids,*, **10**, 7, 1672-1684, 1998.

[13] Z. Rusak, C.H. Whiting and S. Wang, *AIAA Journal,* **36,** 10, 659-667, 1998.

[14] Z. Rusak and D. Lamb, *Journal of Aircraft,* **36**, 4, 659-667, 1999.

[15] P.S. Beran and F.E.C. Culick, *Journal of Fluid Mechanics,* **242**, 491-527, 1992.

[16] J.M. Lopez, *Physics of Fluids*, **6**, 11, 3683-3693, 1994.

[17] P.S. Beran, *Computers Fluids*, **23**, 7, 913-937, 1994.

[18] D.L. Darmofal, *Computers Fluids*, 1996.

ADVANCES IN TURBULENCE VIII
Proceedings of the Eighth European Turbulence Conference
C. Dopazo et al. (Eds.)
© CIMNE, Barcelona 2000

Confined Vortex Breakdown in a Conical Cavity

R. K. M. Seah, T. T. Lim, B. C. Khoo and J. M. Lopez*

Department of Mechanical and Production Engineering
National University of Singapore
10 Kent Ridge Crescent, S119260, SINGAPORE.

*Department of Mathematics
Arizona State University
Tempe, AZ85287-1804, USA.

Contact e-mail: mpelimtt@nus.edu.sg

1 Introduction

Vortex breakdown is a phenomenon, which is characterized by an abrupt change in the structure of the vortex core. It is of technological importance in the area of aerodynamics and in combustion processes where vortex breakdown acts as an efficient mixer and stabiliser. Although considerable progress in our understanding of vortex breakdown (see for example Faler and Leibovich (1977), Escudier (1984), Lugt and Abboud (1987), Lopez and Perry (1992), Khoo *et. al* (1995)) has been made in recent years, much of the flowfield remains unclear. In this paper, we study the generation of vortex breakdown in a conical cavity. The objective here is to examine how changes in the boundary conditions affect the generation and the characteristics of the vortex breakdown. This may lead to a better understanding of the mechanisms involved in the vortex breakdown.

2 Experimental Setup

Figure 1 shows a schematic drawing of the apparatus used. Two test sections, with cone angles of 8^o and 13.4^o, were fabricated using perspex rod. Since the conical cavities can be inverted, a total of four cavity configurations were studied. In all cases, the Reynolds number (Re) is defined as $Re = \frac{r^2\omega}{\nu}$, where r is the radius of the disc, ω, its rotational velocity and ν, the kinematic viscosity of the fluid.

The fluid medium used is a solution of glycerine in distilled water with a 50:50 ratio by weight. In all the tests, steady state operating temperature was at approximately a constant value with a temperature variation of less than

2.5 percent. To visualize the flow, neutrally buoyant florescin dye was used in conjunction with a thin sheet of laser sheet, and the flow images are captured using either a CCD video camera or a still camera.

3 Results and Discussion

Right Cylinder
For the purpose of calibrating our set-up, we repeated Escudier (1984) experi-

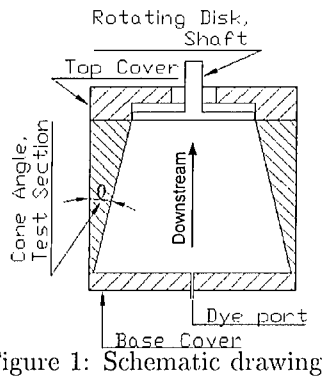
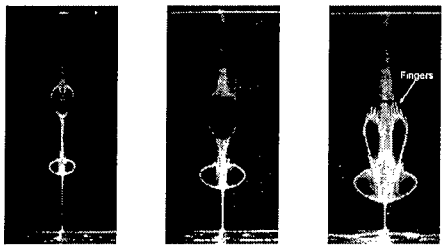


Figure 1: Schematic drawing of one of the test sections used



Re=1800 *Re*=2000 *Re*=2500

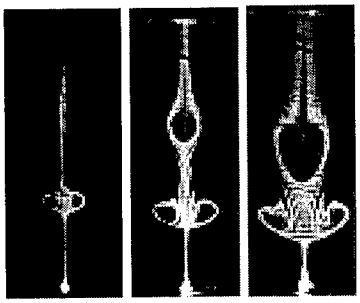
Figure 2: Vortex breakdown for right cylinder with increasing Reynolds numbers

ments for the aspect ratio of 2.5, although the physical dimensions of our apparatus are slightly smaller. Figure 2 shows the results obtained using a straight cylindrical cavity for the Reynolds numbers of 1800, 2000 and 2500. They are in good agreement with those of Escudier's (1984), thus giving us confidence about our set-up.

Positive Angle Conical Cavity (PACC)
For ease of reference in the following discussion, a conical cavity with its outer boundaries diverging from the rotating disk is defined as a positive angle conical cavity (henceforth referred to as PACC), and the opposite configuration is defined as a negative conical angle cavity (henceforth referred to as NACC).

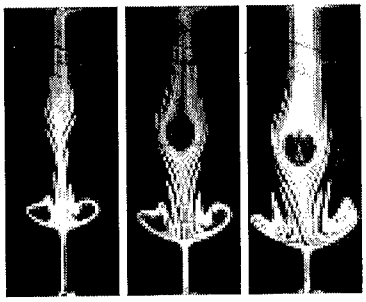
Figure 3 shows the results obtained using PACC. The obvious difference between these pictures and those presented in Figure 2 is the Reynolds number at which the vortex breakdown is initiated. For the right cylinder, the breakdown occurs at a Re $\approx$ 1700, whereas for the 8^o PACC and 13.4^o PACC, it occurs much earlier at Re of approximately 1536 and 1359, respectively. In both cases, the upstream breakdown occurs first, follows by the downstream breakdown. And the folding of the unstable streaklines causes the appearance of 'fingers' (see also Lopez and Perry (1992)).

The prominence of these fingers was found to distort and define the shape of the upstream bubble. It is of interest to note that in the numerical study of



1607 1822 2143

Figure 3: Vortex breakdown for 8^o PACC with increasing Reynolds numbers



1607 1822 2143

Figure 4: Vortex breakdown for 13.4^o PACC with increasing Reynolds numbers

Lopez and Perry (1992), the fingers are apparent only when $Re > 2500$, and they are accompanied by two modes of oscillation. In our study for the 8^o PACC, the fingers are present as soon as the breakdown is initiated and there is no evidence of any oscillation for $Re < 2250$. However, for $Re > 2250$, the oscillation of the finger tips can be clearly seen at the downstream end, near the rotating disk. Video replay shows that the oscillatory motion affects the upstream region as well as distorting the vortex bubble as Reynolds number increases.

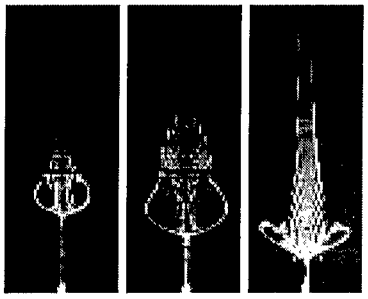
For the *downstream* bubble, it is noticeably smaller and the shape is heart-like as in Fig. 3 for the 8^o PACC at moderate Re and is more rounded for 13.4^o PACC in Fig. 4.

Negative Angle Cone Cavity (NACC)
With NACC, the most obvious difference compared to the reference case is the absence of the downstream vortex breakdowns. Also, the breakdown occurs much earlier at Reynolds number of approximately 1613 and 1481 for the 8^o NACC and 13.4^o NACC, respectively.

During the initial stage of the vortex breakdown, the bubble is small and rounded and is accompanied by an enlargement of the emptying tail at its downstream end. With a larger cone angle, the enlargement at the downstream side of the breakdown decreases (see Fig.5). However, as Re increases, the overall diameter of the breakdown increases, which subsequently "flattens" into a saucer shape (see Fig. 6).

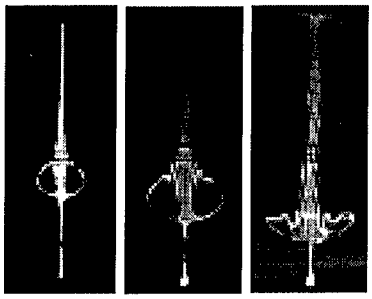
At moderate Reynolds number of about 2700, the tail has thickened and the fingers are aligned in the flow direction. As soon as the bubble begins to take on the shape of a saucer, the fingers are progressively pointed outward from the axis of symmetry. In addition, separation distance between individual fingers appears to increase.

Attempts were made to see if the stagnation point undergoes oscillation like in the reference case by increasing the Reynolds number progressively to 4000, but



1700 2000 2900

Figure 5: Vortex breakdown for 8^o NACC with increasing Reynolds numbers



1700 2000 2900

Figure 6: Vortex breakdown for 13.4^o NACC with increasing Reynolds numbers

there is no evidence of the oscillation. Instead, the size of the bubble decreases until it collapses inwards to form a small pitched spiral vortex.

4 Conclusion

The vortex breakdown in a conical cavity has been studied experimentally using dye visualization technique. Comparison with the reference case shows that the breakdown in the conical cavities differs significantly from that of a right cylinder. The most notable differences are the stability of the upstream stagnation point with respect to axial oscillation of its location, the variation in the number of breakdowns and the prominence of the streakline fingers defining the breakdown form.

References

[1] Escudier, M. P. 1984. Observations of the flow produced in a cylindrical container by a rotating endwall. *Expts Fluids.* **2**, 189-196.

[2] Faler, J. H.; Leibovich, S. 1977. Disrupted states of vortex flow and vortex breakdown. *Phys. Fluids.* **20**, 1385-1400.

[3] Lopez, J. M.; Perry, A. D. 1992. Axisymmetric vortex breakdown. Part 3. Onset of periodic flow and chaotic advection. *J. Fluid Mech.* **234**, 449-471.

[4] Khoo, B. C.; Yeo, K. S.; Lim, D. F.; He, X. 1997. Vortex breakdown in an unconfined vortical flow. *Expt Therm. Fluid Sci.* **12(2)**, 131-148.

ADVANCES IN TURBULENCE VIII
Proceedings of the Eighth European Turbulence Conference
C. Dopazo et al. (Eds.)
© CIMNE, Barcelona 2000

Modelling of the turbulent vortex breakdown as a transition from column to conical helical vortices

T.O. Murakhtina, V.L. Okulov

Institute of Thermophysics, Novosibirsk, Russia

Contact e-mail: okulov@itp.nsc.ru

1 Introduction

The vortex breakdown has being observed during study of slender vortex in pipe flows with high swirl. In the low Re regimes $Re < 35000$, there are well-known numerous types of vortex breakdown: double helix, bubble and spiral [2]. Recent progress in the understanding of the phenomenon [4] shows that it may be explained as a spontaneous transition from the right- to left-handed helical symmetry of the vorticity field (see Fig. 1, a). The difference between vortex structures with right- and left-handed helical symmetry is governed by the sign of torsion or helical pitch of the vortex lines. In this modeling the breakdown possibility is determined by existence of two or more different columnar helical vortices with the parameters (Γ is the vortex circulation; w_0 and p_0 are the axial velocity and pressure; ε is the vortex core radius; $2\pi l$ is the helical pitch of a vortex) under the same flow characteristics (flow rate - Q; flow circulation - G; axial fluxes of angular momentum - L, momentum - S and energy - E). The pairs of the columnar helical vortices described flows before and after breakdowns were found [4] for the each six regimes of swirl flows from [3]. Sarpkaya was the first to show that vortex breakdown in non-cavitating swirling flows in tubes at $Re > 100000$ is significantly different from the low Re types. In this case the conical breakdown is born from a few spirals that are rotating at very high speeds. At higher Reynolds numbers [5], the breakdown became more like an axisymmetric cone. The objective of this work is to generalize the phenomenon modeling on the case with transition from the right-handed columnar helical vortex to left-handed hollow helical vortex (see Fig.1,b).

2 Transition from columnar to hollow vortex

For high Reynolds numbers, analyzing of a diagram of the vorticity distribution and the velocity profiles, measured upstream and downstream position of the

vortex breakdown [5] showed impossibility to approximate the flow with the simplest modeling of the columnar helical vortex only [1]. Indeed, the vorticity distribution after the breakdown has the shape of hollow cone.

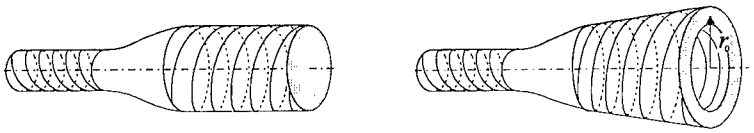


Figure 1: Changes in helical symmetry of vorticity during vortex breakdown at low (a) and high (b) Re.

For this reason a hollow helical vortex with the vorticity distributed into the annular section: $r_0 - \varepsilon < r < r_0 + \varepsilon$ and with the swirl (w_φ) and axial (w_z) velocity was constructed:

$$\omega_z = \frac{2\Gamma\varepsilon^2}{\left(\varepsilon^2 + (r-r_0)^2\right)^2}; \omega_\varphi = \frac{r\omega_z}{l}; w_\varphi = \frac{\Gamma}{r} f(r,\varepsilon,r_0); w_z = w_0 - \frac{r}{l} w_\varphi, \quad (1)$$

$$f(r,\varepsilon,r_0) = \frac{r(r-r_0)}{(r-r_0)^2 + \varepsilon^2} + \frac{r_0}{\varepsilon}\left[arctg\left(\frac{r-r_0}{\varepsilon}\right) + arctg\left(\frac{r_0}{\varepsilon}\right)\right].$$

A good approximation of the data obtained by [5] with the hollow vortex (1) are shown in the Fig.2 with vortex parameters from the table:

TABLE. Parameters of the approximated and calculated vortices

		Γ	w_0	l	ε	r_0	p_0
before breakdown	approximation	0.18	2.6	0.10*	0.5	0	0
after breakdown	approximation	0.05	0	-0.20*	0.20	0.24	-
after breakdown	modeling	0.03	-0.7	-0.08*	0.24	0.44	5.5

* the sign of l denotes the right- or left-handed helical vortex.

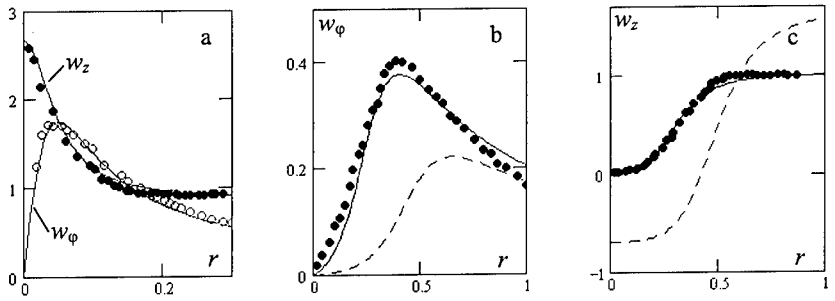


Figure 2: The velocity profiles before (a) and after (b, c) vortex breakdown for $Re = 230000$: a comparison of the data (points) obtained by [5] with the annular vortex model (solid-lines are the approximations; dash-lines are the modeling).

The hypothesis about a jumping transition from a columnar vortex with a right-handed helical symmetry to a hollow vortex with left-handed one during the vortex breakdown will be true if these vortex structures may exist under the same flow characteristics:

$$Q = 2\pi\rho \int_0^R w_z r dr; \quad G = R w_\varphi (R); \quad L = 2\pi\rho \int_0^R w_\varphi w_z r^2 dr;$$

$$J = 2\pi\rho \int_0^R \left(w_z^2 + \left(\int_0^r \frac{w_\varphi^2}{\sigma} d\sigma + \frac{p_0}{\rho} \right) \right) r dr; \tag{2}$$

$$E = 2\pi\rho \int_0^R \left(\frac{w_z^2 + w_\varphi^2}{2} + \left(\int_0^r \frac{w_\varphi^2}{\sigma} d\sigma + \frac{p_0}{\rho} \right) \right) w_z r dr;$$

$$B = 2\pi\rho \int_0^R \left(\frac{w_\varphi^2 + w_z^2}{2} + \left(\int_0^r \frac{w_\varphi^2}{\sigma} d\sigma + \frac{p_0}{\rho} \right) \right) \omega_z r dr$$

where B is an axial vortex flux of energy which was expressly considered as additional invariant characteristic for the vortex flow without losses with fluid density - ρ in a tube with radius - R. The equation system for the parameters (Γ, l, ε, r_0, w_0, p_0) was found after substituting (1) into (2) and equating it to the flow characteristics (Q, G, L, J, E, B) before the vortex breakdown. After expressing w_0, l, Γ, p_0 as functions of ε and r_0:

$$\Gamma = \frac{G}{\bar{f}}; w_0 = \frac{Q\Gamma b_0^2 - L b_0^1}{\pi\Gamma \left[b_0^2 - \left(b_0^1 \right)^2 \right]}; l = \pi\Gamma^2 \frac{b_0^2 - \left(b_0^1 \right)^2}{L - Q\Gamma b_0^1}; p_0 = \frac{J}{\pi} - \frac{w_0 Q}{\pi} - \frac{L}{\pi l} - 2\Gamma^2 b_1^0$$

the system was reduced to study of two non-linear equations for ε and r_0:

$$w_0 \left[J - \frac{w_0}{2} Q + \frac{\pi\Gamma^2}{2l^2} b_0^2 + \pi\Gamma^2 \bar{b}_2 \right] + \pi \frac{\Gamma}{l} \left[p_0 b_0^1 + \Gamma^2 \bar{b}_3 + \frac{\Gamma^2}{2l^2} b_0^3 + 2\Gamma^2 b_1^1 \right] = E$$

$$\Gamma\varepsilon^2 \left[\left(w_0^2 + 2p_0 \right) d_0^0 + 2w_0 \frac{\Gamma}{l} d_0^1 + \frac{\Gamma^2}{l^2} d_0^2 + \Gamma^2 \left(\bar{d} + 2d_1^0 \right) \right] = \frac{B}{2\pi} \tag{3}$$

Where $\bar{f}(\varepsilon, r_0) = f(1, \varepsilon, r_0); \quad \bar{d}(\varepsilon, r_0) = \int_0^1 \frac{f(x, \varepsilon, r_0)^2}{x \left[\varepsilon^2 + (x - r_0)^2 \right]^2} dx$

$$b_j^i (\varepsilon, r_0) = 2^{1-j} \int_0^1 x P^j (x, \varepsilon, r_0) f^i (x, \varepsilon, r_0) dx, \; i = 0, 1, 2, 3; \; j = 0, 1;$$

$$\bar{b}_i (\varepsilon, r_0) = \int_0^1 \frac{f^i (x, \varepsilon, r_0)}{x} dx, \; i = 2, 3; \quad P (x, \varepsilon, r_0) = \int_0^x \frac{f (s, \varepsilon, r_0)^2}{s^3} ds;$$

$$d_j^i(\varepsilon, r_0) = \int_0^1 \frac{x f^i(x, \varepsilon, r_0) P^j(x, \varepsilon, r_0)}{\left[\varepsilon^2 + (x - r_0)^2\right]^2} dx, i = 0, 1, 2; j = 0, 1;$$

and values of Γ, l, ε, r_0, w_0, p_0, Q, G, L, J, E in (3) are referred as non-dimensional values in accordance with $\Gamma/R*U$, l/R, ε/R, r_0/R, w_0/U, $p_0/\rho * U^2$, $Q/\rho * U * R^2$, $G/R * U$, $L/\rho * U^2 * R^3$, $J/\rho * U^2 * R^2$, $E/\rho * U^3 * R^2$, $B/\rho * U^3 * R$ (U is mean axial velocity). The two different solutions of the system (3) were founded for the set (Q; G; L; J; E; B) corresponded to the cross-section of the flow upstream of the turbulent vortex breakdown [5]. The first solution is right-handed helical columnar vortex with $r_0 = 0$ and jet-like profile of axial velocity. The second solution is left-handed helical hollow vortex with $r_0 \neq 0$ and wake-like profile of axial velocity. The first vortex precisely coincides with the approximation of the flow before the breakdown, and the second vortex corresponds to the flow after the breakdown (see Table and Fig.2). The additional distinction of the solutions consists in the different values of the pressure drop and right- or left-handed helical vortices will be selected by the axial pressure gradient that takes place in the tube. In this case (high Re) the modeling profiles were largely differ from experimental data in contrast of the low Re [4]. That was expected result for the laminar model, which does not take into account turbulent pulsation.

3 Conclusion

For the first time an existence of the helical symmetry for a vortex field in the flow with the turbulent vortex breakdown was established and the possibility of the transition under the same integral flow characteristics from a slender right-handed helical vortex to a hollow (conical) vortex with the left-handed helical symmetry was modeled. Thus the hypothesis [4], that the phenomenon of a vortex breakdown is associated with a transition from right- to left-handed symmetry in the helical vortex structure, was supported during analysis of the turbulent vortex breakdown too.

References

[1] S. V. Alekseenko, P. A. Kuibin, V. L. Okulov and S. I. Shtork. Helical vortices in swirl flow. *J. Fluid Mech.*, 382:195–243, 1999.

[2] J. H. Faler and S. Leibovich. Disrupted states of vortex flow and vortex breakdown. *Phys. Fluids.*, 20(9):1385–1399, 1977.

[3] A. K. Garg and S. Leibovich. Spectral characteristics of vortex breakdown flow fields. *Phys. Fluids.*, 22:2053–2064, 1979.

[4] V. L. Okulov. Transition from right to left helical symmetry during vortex breakdown. *Tech. Phys. Lett.*, 22(10):798–800, 1996.

[5] T. Sarpkaya and F. Novak. Turbulent vortex breakdown at high Reynolds numbers. *AIAA 99-0135*, 1-19, 1999.

ADVANCES IN TURBULENCE VIII
Proceedings of the Eighth European Turbulence Conference
C. Dopazo et al. (Eds.)
© CIMNE, Barcelona 2000

DNS of vortex breakdown in swirling jets

W. Kollmann[1], A. Ooi[2], M. S. Chong[3] and J. Soria[4]

[1]MAE Dept, University of California
Davis, CA 95616, USA
[2] Defence Science Technology Organisation
Fishermens Bend, Vic. 3207, Australia
[3] MAME Dept, University of Melbourne
Parkville, Vic. 3052, Australia
[4] ME Dept, Monash University
Clayton, Vic. 3168, Australia

Contact e-mail: kollmann@sweetpea.engr.ucdavis.edu

1 Introduction

A numerical study is conducted to investigate the flow structure of vortex breakdown in swirling free jets found in the experiments carried out by Billant *et al.* [1]. Data obtained from direct numerical simulations (DNS) reveal the structure of the conical jet layer and its break up into three-dimensional vortex structures for moderate Reynolds numbers of [1]. Axi-symmetric and three-dimensional flows for swirl numbers at and above the threshold value observed experimentally are considered.

2 Numerical method

A hybrid spectral finite-difference method numerical scheme has been used to solve the Navier-Stokes equations. Solutions are obtained using a fifth order upwind biased scheme (Li[4]) for the convective terms and a fourth order central difference scheme for the other terms in the axial and radial directions and periodic Fourier series have been used for discretisation in the azimuthal direction. The numerical formulation carefully considers the variation of the azimuthal Fourier modes close to the $r = 0$ axis and exploits the symmetry and pole conditions described by Lewis and Bellan[2] and Shen[3].

A fourth order Runge-Kutta type time integration method is used to advance the simulation in time. Helmholtz equations for the streamfunction and the pressure modes are solved using LU decomposition and deferred corrections to minimize the bandwidth of the coefficient matrices.

3 Results and discussion

Both axi-symmetric and fully three-dimensional (3-d) swirling jet flows were computed. Only the 3-d simulations carried out at Reynolds number $Re = 626$ and swirl number (as defined by Billant *et al.* [1]) of $S = 1.33$ will be presented in this paper. The predicted data show the emergence of helical, counter-rotating vortices in the wake of a conical jet region close to the nozzle exit. Figure 1 shows isosurfaces of azimuthal vorticity for only one half of the computational domain. The darker isosurfaces have positive azimuthal vorticity and the lighter isosurfaces indicates negative azimuthal vorticity. It is evident that the conical shear layer consists of azimuthal vorticity of both signs. Further upstream, the conical shear layer breaks up and produces counter- rotating vortex structures.

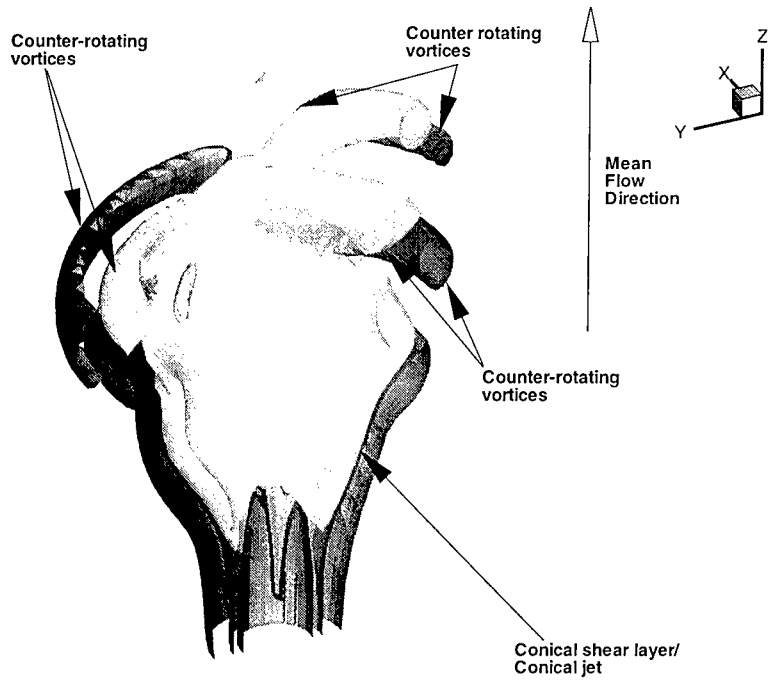


Figure 1: Isosurfaces of azimuthal vorticity for simulation at $Re = 626$ and $S = 1.33$. The darker isosurfaces has an isovalue of $\Omega_\theta/|\Omega_\theta|_{max} = +0.25$ and the lighter isosurfaces has an isovalue of $\Omega_\theta/|\Omega_\theta|_{max} = -0.25$. The isosurfaces are cut with a plane $\theta = 0/\theta = \pi$. Only isosurfaces in the $0 \leq \theta \leq \pi$ domain are shown.

It is possible to construct a simplified analytical model for the conical shear layer to explain the vortical structure present in the simulation. Consider an axisymmetric inviscid flow near the slip surface given by

$$r = R(z) \equiv R_0 + zM_1 \tag{1}$$

where r and z are the radial and axial coordinates respectively. This surface represents a cone if both R_0 and M_1 are assumed to be positive constants. The axial velocity, v_z, is assumed to be uniform within the cone and zero outside

$$v_z(r,z) = \begin{cases} \frac{C}{R(z)^2} & \text{for } 0 \le r \le R(z) \\ 0 & \text{for } r > R(z) \end{cases} \tag{2}$$

and C is a positive constant. The radial velocity, v_r, which follows from mass balance is

$$v_r(r,z) = \begin{cases} \frac{CM_1 r}{R^3(z)} & \text{for } 0 \le r \le R(z) \\ \frac{CM_1}{rR(z)} & \text{for } r > R(z). \end{cases} \tag{3}$$

The azimuthal vorticity, Ω_θ, generated by this flow field is then given by

$$\Omega_\theta = \frac{\partial v_r}{\partial z} \tag{4}$$

for $r \neq R(z)$ and by

$$\Omega_\theta = \frac{C}{R^2(z)}\delta(r - R(z)) - \frac{CM_1^2}{R^3(z)} \tag{5}$$

at the slip surface $r = R(z)$. Hence we obtain the following expression for Ω_θ

$$\Omega_\theta = \begin{cases} -\frac{CM_1^2 r}{R^4(z)} & \text{for } 0 \le r < R(z) \\ \frac{C}{R^2(z)}\delta(r - R(z)) - \frac{CM_1^2}{R^3(z)} & \text{for } r = R(z) \\ \frac{-CM_1^2}{rR^2(z)} & \text{for } r > R(z). \end{cases} \tag{6}$$

This simple argument shows that negative vorticity is created inside the cone. Positive vorticity is generated at the slip layer ($r = R(z)$) because the positive contribution of the Dirac pseudofunction outweighs the negative contribution in (6). Outside the cone, negative vorticity is present. It is clear that the negative vorticity is a result of the axial variation of the radial velocity which in turn is a consequence of mass balance. If the cone angle M_1 approaches zero, the negative vorticity contributions vanish and the standard model for a mixing layer concentrated in a cylindrical slip surface is recovered.

This property of the conical shear layer is detected in the simulations. Figure 2 shows the instantaneous velocity and vorticity profiles at the stations $z/D = 1.5$ and $z/D = 2.5$ for $t = 30.7$. It is evident that both negative and positive azimuthal vorticity are present. The structure of the conical shear layer

is closer to a jet than a mixing layer, which is due to the velocity field created by the vortex ring structures downstream. The jet character of the shear layer is prominent even further downstream at $z/D = 2.5$, but the flow is now genuinely three dimensional. Hence, we conclude that the dominant feature next to the entrance boundary is a conical jet.

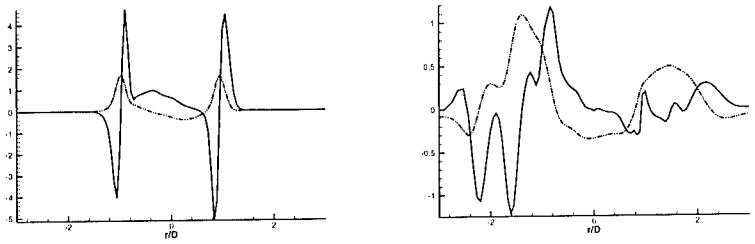


Figure 2: Instantaneous axial velocity, $3v_z$ (dashed dot line), and azimuthal vorticity Ω_θ (solid line) profiles at $z/D = 1.5$ (left) and $z/D = 2.5$ (right).

4 Conclusions

The flow visualisations of Billant et al.[1] showed the development of a conical shear layer in swirling jets. Using a simplified analytical model, it can be shown that this conical shear layer produces sheets of azimuthal vorticity of both signs. ¿From DNS data, this conical shear layer is demonstrated to have a spatial structure similar to a conical jet. The break up of this conical jet produces counter-rotating vortices.

References

[1] P. Billant, J. Chomaz and P. Huerre. Experimental study of vortex breakdown in swirling jets. *J. Fluid Mech*, 376: 183–219, 1999.

[2] H.R. Lewis and P.M. Bellan. Physical constraints on the coefficients of Fourier expansions in cylindrical coordinates. *J. Math. Phys.* 31: 2592–2596, 1990.

[3] J. Shen. Efficient spectral-galerkin methods III: polar and cylindrical geometries. *SIAM J. Sci. Comput* 18(6):1583–1604, 1997.

[4] Li, Y. Wavenumber Extended High-Order Upwind-Biased Finite Difference Schemes for Convective Scalar Transport. *J. Comput. Phys.* 133: 235-255, 1997.

ADVANCES IN TURBULENCE VIII
Proceedings of the Eighth European Turbulence Conference
C. Dopazo et al. (Eds.)
© CIMNE, Barcelona 2000

Lagrangian LES and vortex dynamics of forced unsteady round jets and colliding vortices

H. Ishikawa, S. Izawa and M. Kiya

Division of Mechanical Science, Graduate School of Engineering
Hokkaido University, Sapporo, 060-8628, Japan

Contact e-mail: ishi@eng.hokudai.ac.jp

1 Introduction

Core spreading is a method of incorporating effects of the molecular viscosity into Lagrangian vortex methods. In two-dimensional flows the core spreading accurately approximates the diffusion of vorticity but the vorticity is advected by an average velocity field rather than by the local velocity [1]. Nevertheless the core spreading method is attractive in engineering applications because this method requires less number of vortex elements than the methods which correctly incorporate the molecular viscosity [2, 3]. Moreover, the core-spreading algorithm is simple. Thus it is worth examining the extent to which the core spreading method approximates the exact solution of Navier-Stokes equations within accuracy which can be accepted in the applications.

In this paper, a turbulence model based on the core spreading is proposed. This model, which is based on Leonard & Chua's [4] nonlinear core spreading, employs the subgrid scale eddy viscosity of Smagorinsky type to represent the rate of core spreading by small-scale turbulence. The linear combination of this model and the molecular core spreading model constitutes a Largangian turbulence model which includes Reynolds-number effects. Simulations are made of an impulsively started round jet, and of interaction between a vortex ring and a vortex tube to show that the turbulence model seems to yield reasonable results for evolution of large-scale vortices.

2 Turbulence model

A Lagrangian vortex method calculates evolution of a region of distributed vorticity by subdividing the region into a collection of vortex blobs with overlapping cores. A vortex blob is characterized by the position, vorticity, volume, and the cut-off radius which is a length scale of a smoothing function for vorticity distribution around the blob [5]. The evolution of position and

vorticity of a vortex blob is described by the Biot-Savart law and the vorticity equation.

The molecular diffusion of vorticity is approximated by the core spreading $d\sigma^2/dt = 4\nu$, where σ is the cut-off radius of a vortex blob and ν is the kinematic viscosity [6, 7]. This will be referred to as the linear model. The diffusion by small-scale turbulence is also modelled by $d\sigma^2/dt = 4\nu_{SGS}$, where the subgrid eddy viscosity is approximated by $\nu_{SGS} = c^2\sigma^2\omega^{-1}|d\omega/dt|$, where c is a numerical constant and ω is the modulus of vorticity vector, on the basis of Smagorinsky eddy viscosity $\nu_{SGS} = c^2\Delta^2(s_{ij}s_{ij})^{1/2}$, where Δ is the grid size and s_{ij} is the rate-of-strain tensor [4]. The value of $c = 0.17$, which is recommended for free turbulent shear flows, is employed. This will be referred to as the nonlinear model. Thus the combined model

$$d\sigma^2/dt = 4(\nu + \nu_{SGS}) \tag{1}$$

can be interpreted as a Lagrangian turbulence model which includes Reynolds-number effects. It may be noted that ,within the framework of core spreading, results by the linear model should be interpreted as the benchmark with which results by the other models are to be compared.

3 Numerical procedure

Numerical simulations are made for impulsively started jets issuing from a round nozzle of radius R, and a vortex ring interacting with a vortex tube.

The jet is forced by a sinusoidal disturbance to fix the position of rolling up of the initial shear layer. This is because, in the unforced jet, the rolling-up position can be influenced by numerical noises, making it difficult to compare vortex structures in the jet simulated by the three core spreading models. The disturbance is such that the longitudinal velocity fluctuation at the exit of the nozzle is of the form $u = 2a\cos(m\phi)\cos(2\pi ft)$, where a and f are the amplitude and frequency of forcing, respectively, and ϕ is the azimuthal angle. This is a combination of two helical modes of the same strength and the modes $m = 1$ and $m = -1$. The maximum disturbance is fixed at the positions $\phi = 0$ and π. The forcing frequency is chosen as the fundamental frequency of instability in the initial shear layer of the unforced jet, which is $f = 0.56U/R$, U being the time-mean velocity at the centre of the nozzle exit. The amplitude of each mode is $a = 0.025U$, which is near the upper limit of linear growth of infinitesimal disturbances in free shear layers.

In the second simulation, a vortex ring of radius R, core radius $b(= 0.155R)$ and circulation Γ_r interacts with a vortex tube of the same core radius and circulation Γ_f. The ratio Γ_r/Γ_f is varied in a range of 0.5-2.0.

In order to maintain the spatial resolution, a vortex blob is divided into two blobs, if its length becomes greater than twice the initial value.

Reynolds number Re is 2,000 and 20,000 for the jet, based on the diameter and the exit velocity U, while that for the vortex interaction is 300 and 3,000, based on the diameter and the initial convection velocity of the vortex ring.

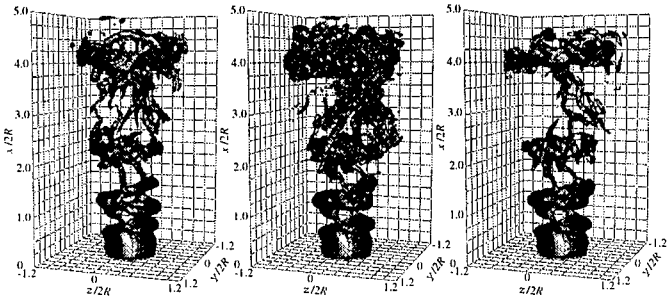


Figure 1: Isosurfaces of magnitude of vorticity for (a) non-linear model, (b) linear model (Re = 20,000) and (c) combined model (Re = 20,000) at $Ut/2R = 10.7$ from start of flow.

4 Results and discussion

Figure 1 shows isosurfaces of magnitude of vorticity in the jet calculated by the three models at Re = 20,000. The initial shear layer rolls up at the same distance from the nozzle exit; the vortical structures in the range $x/2R < 1.0$ is almost the same. This is because the growth of the cut-off radius of vortex blobs by the molecular viscosity (for the linear model) and by the vortex stretching (for the nonlinear and combined models) is small in this region.

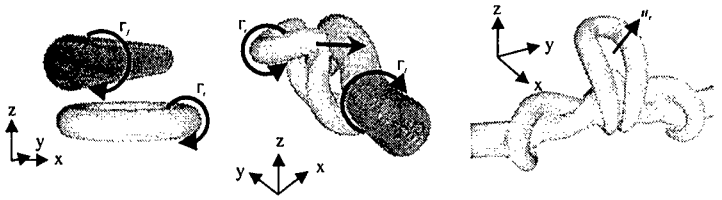
The linear model yields small-scale vortices in the region $x/2R > 2.0$, which are superposed on large-scale vortices. This indicates that the flow in this region is turbulent. The vortical structure of the nonlinear model is such that the structure of the linear model (the benchmark) is spatially filtered to eliminate the small-scale structures. This structure is further modified by the molecular viscosity to yield the structure of the combined model. On the other hand, the vortical structures at the lower Reynolds number of 2,000 (not shown) were basically the same for the linear and combined models.

The above comparison of the vortical structures suggests that the combined model can be a reasonable turbulence model although more detailed examination should be made quantitatively on the basis of statistical properties such as time-mean velocities and Reynolds stresses.

Figure 2 shows the interaction of the vortex ring and the vortex tube with $\Gamma_r/\Gamma_f = 0.5$ at Re = 300. The vortex ring is seen to wrap around the vortex tube which is also deformed by the interaction. For $\Gamma_r/\Gamma_f = 1.0$ the cut-and-reconnection occurs between a part of the vortex ring and a part of the vortex tube (Figure 3). The vortex ring was found to pass through the vortex tube for Γ_r/Γ_f greater than approximately 1.5 (not shown).

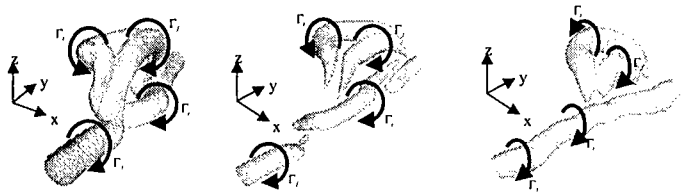
References

[1] C. Greengard. The core spreading vortex method approximates the wrong equation. *J. Comput. Phys.*, 61:345–347, 1985.



(a) (b) (c)

Figure 2: Isosurfaces of magnitude of vorticity for interacting vortex ring and vortex tube with $\Gamma_r/\Gamma_f = 0.5$ and $Re = 300$ calculated by combined model at (a) $\Gamma_r t/R^2 = 0.0$, (b) 3.50,and (c) 9.75.



(a) (b) (c)

Figure 3: Isosurfaces of magnitude of vorticity for interacting vortex ring and vortex tube with $\Gamma_r/\Gamma_f = 1.0$ and $Re = 300$ calculated by combined model at (a) $\Gamma_r t/R^2 = 7.0$, (b) 12.0, and (c) 22.0. Intitial positions of vortices are the same as in Figure 2.

[2] A. J. Chorin. Numerical study of slightly viscous flow. *J. Fluid Mech.*, 579:785–796, 1973.

[3] P. Degond and S. Mas-Gallic. The weight particle method for convection-diffusion equations. Part 1: The case of an isotropic viscosity. *Math Comput.*, 53:485–507, 1989.

[4] A. Leonard and K. Chua. Three-dimensional interactions of vortex tubes. *Physica.*, D37:490–496, 1989.

[5] G. S. Winckelmans and A. Leonard. Contributions to vortex particle methods for computation of three-dimensional incompressible unsteady flows. *J. Comput. Phys.*, 109:247–273, 1993.

[6] K. Kuwahara and H. Takami. Numerical studies of two-dimensional vortex motionby a system of points. *J. Phys. Soc. Japan*, 34:247–253, 1973.

[7] A. Leonard. Vortex methods for flow simulation. *J. Comput. Phys.*, 37:289–335, 1980.

XXVII

Intermittency and Scaling

ADVANCES IN TURBULENCE VIII
Proceedings of the Eighth European Turbulence Conference
C. Dopazo et al. (Eds.)
© CIMNE, Barcelona 2000

Intermittency in turbulent boundary layers

F. Toschi[1], E. Levêque[2] and G. Ruiz-Chavarria[3]

[1]University of Twente, Department of Applied Physics,
P.O. Box 217, 7500 AE Enschede, The Netherlands and
INFM, Unitá di Tor Vergata, Roma, Italy.
[2]Laboratoire de Physique CNRS, ENS de Lyon,
69364 Lyon cedex 07, France.
[3]Departamento de Física, Facultad de Ciencias,
UNAM, 04510 Mexico D.F., Mexico.

Contact e-mail: f.toschi@tn.utwente.nl

Much efforts have been devoted in the recent past towards a better understanding of intermittency in homogeneous and isotropic turbulence. Intermittency refers here to the anomalous scaling behavior of velocity structure functions (see [1]). Here we address the problem of how non homogeneities of the flows influence intermittency (see [2]). We concentrate on turbulent boundary layers and write the usual Reynolds decomposition for the fluctuating velocity, v':

$$D_t v_i'(r;t) + \mathcal{S}_{ij}(r) v_j' + \left(v_j' \nabla_j\right) v_i' = -\nabla_i p' + \nu \nabla^2 v_i' \tag{1}$$

where $D_t = (\partial_t + \overline{v}_j \partial_j)$ and $\mathcal{S}_{ij} = \partial_i v_j$ is the shear. Starting from this equation we define the following Integral Structure Functions (ISF):

$$\tilde{S}_p(r) = \left\langle (\delta v(r)^3 + r \cdot \mathcal{S} \cdot \delta v(r)^2)^{p/3} \right\rangle \tag{2}$$

The rationale behind these structure functions being that the energy, in presence of shear, $\mathcal{S}$, is not only transferred to small scales (non linear term, eqn. 1) but also is advected spatially by means of the average velocity ($\mathcal{S}v'$ term, eqn. 1).

On general dimensional grounds, we expect that there will be a length scale (shear length scale, $L_\mathcal{S}$) at which the two contributions will be of the same order of magnitude (see [3]). In general:

$$\tilde{S}_p(r) \simeq S_p(r) \qquad \text{for} \quad r \ll L_s \tag{3}$$

$$\tilde{S}_p(r) \simeq (r\mathcal{S})^{p/3} S_{2p/3}(r) \quad \text{for} \quad r \gg L_s \tag{4}$$

The shear length scale, $L_\mathcal{S}$, defined by the condition $\frac{\delta v(L_\mathcal{S})}{L_\mathcal{S}} = \mathcal{S}$ can be estimated (neglecting intermittency) as $L_\mathcal{S} = \left(\epsilon/\mathcal{S}^3\right)^{1/2}$ (ϵ being the energy dissipation rate).

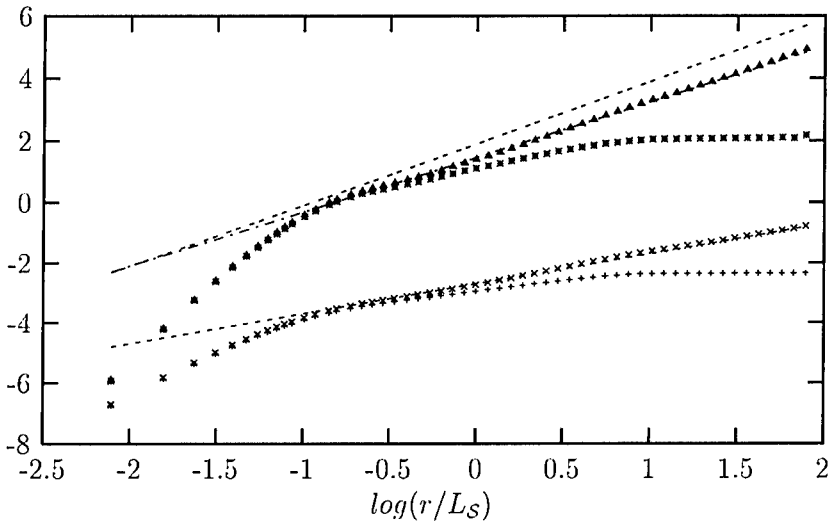


Figure 1: In the turbulent boundary layer at the distance $y^+ = 102$. In log-log scale, S_3 (+) and S_6 ($\star$) are compared with $\tilde{S}_3$ ($\times$) and $\tilde{S}_6$ ($\triangle$). The scale r has been renormalized by the characteristic shear length-scale L_s. The solid lines passing through $\tilde{S}_3$ and $\tilde{S}_6$ indicate the expected *homogeneous and isotropic* power-laws, respectively $\zeta_3 = 1$ and $\zeta_6 = 1.78$. For comparison, the dashed line has slope 2.

Here we report some tests performed on experimental data coming from the recirculating wind tunnel of ENS-Lyon (for details on the experiment, see [4]).

We have computed the ordinary structure functions, $S_p(r)$, and the ISF, $\tilde{S}_p(r)$, for several distances from the wall. The value of the shear $\mathcal{S}$ was estimated as the derivative of the well-established log-law for the average velocity in a turbulent boundary layer:

$$\langle v^+(y^+) \rangle = (1/\kappa) \log(y^+) + B.$$

where quantities are expressed in non dimensional units, $\kappa \simeq 0.4$ and $B \simeq 5.26$ (see also [4]).

In Figure 1 we show, in log-log scale, the SF and ISF of order 3 and 6 measured at a distance $y^+ = 102$ from the wall. While the SF do not display a clean scaling over the full range, the ISF present scaling exponents in remarkable agreement with the ones of homogeneous and isotropic turbulence. In particular notice that we are able also to keep into account intermittency on order 6.

This finding lead us to generalize the Refined Kolmogorov Hypothesis in presence of a shear flow, as follows:

$$\tilde{S}_p(r) \sim \left\langle \epsilon(r)^{p/3} \right\rangle r^{p/3}$$

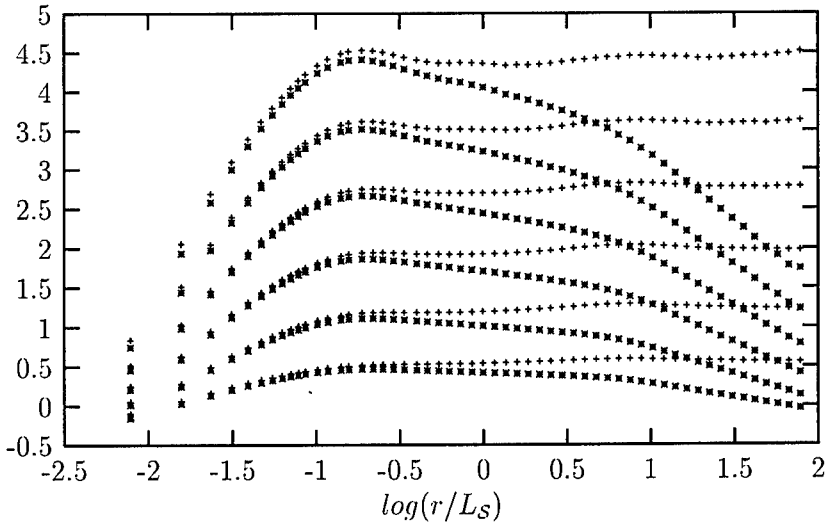


Figure 2: From experimental data at $y^+ = 102$. From bottom to top, in log-log scale, $\tilde{S}_p(r)/r^{\zeta_p}$ (+ symbols) as compared to $S_p(r)/r^{\zeta_p}$ ($\star$ symbols) , for p=1...6.

A stronger test of this relation is presented in Figure 2, where we compensate the SF and the ISF by the expected homogeneous/isotropic power law: $S_p(r)/r^{\zeta_p}$ and $\tilde{S}_p(r)/r^{\zeta_p}$, respectively.

While $S_p(r)/r^{\zeta_p}$ show a definite tendency to decrease at inertial range separations, the $S_p(r)/r^{\zeta_p}$ show a clear *plateau*.

As is it evident from Figure 2 the change of the statistic of the energy dissipation is negligible at this distance from the wall. The "strange" scaling behavior of the SF can fully be understood in terms of the relevance of the shear: Integral Structure Functions being completely able to account for it.

Another test of our proposed formalism consists in checking the dependency from the distance from the wall, y^+. In Figure 3 we show several SF of order 3, $S_3(r, y^+)$, as compared to ISF, $\tilde{S}_3(r, y^+)$, for different values of y^+. The SF show a strong dependence from y^+ and do never display a scaling exponents equal to 1 (this is not surprise as the turbulence we are considering is not homogeneous and isotropic, hence Howart-Von Karman equation does not apply).

On the other side ISF collapse and, regardless of the value of y^+, they show a scaling exponent equal to 1 (as if we were dealing with homogeneous and isotropic turbulence).

From this evidences we conclude that in our experiment the presence of a large scale shear was able to change drastically the scaling exponents of ordinary structure functions. Using the correct observable (i.e. ISF) we are able to recover scaling in very good agreement with homogeneous and isotropic turbulence. In

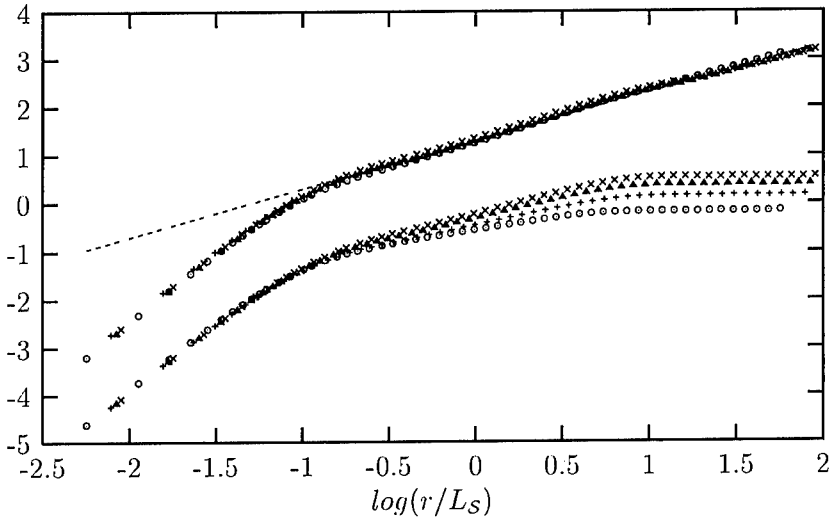


Figure 3: Third-order structure functions at various distances from the wall: $y^+ = 32$ ($\circ$), $y^+ = 102$ ($+$), $y^+ = 168$ ($\triangle$) and $y^+ = 233$ ($\times$). The scaling properties of S_3 (SF, lower curves) do depend on the distance y^+. On the opposite, $\tilde{S}_3$ (ISF, upper curves) displays the same scaling behavior for all y^+. The dashed line has slope 1. The curves have been shifted vertically for convenience.

other words ISF are able to smoothly abridge between the two limiting behavior of equations (3) and (4).

Acknowledgments: G. R.-C. and E. L. acknowledge the ECOS committee and CONACYT for their financial support under the project No M96-E03. G. R.-C. also acknowledge DGAPA-UNAM for partial support under the project IN-107197.

References

[1] U. Frisch, *Turbulence: the legacy of A. N. Kolmogorov*, Cambridge University Press, Cambridge (England) (1995).

[2] F. Toschi, E. Levêque, G. Ruiz-Chavarria, *Shear Effects in Non-Homogeneous Turbulence*, submitted to Phys. Rev. Lett. (2000).

[3] F. Toschi, G. Amati, S. Succi, R. Benzi and R. Piva, Phys. Rev. Lett., **82**, 5044 (1999).

[4] G. Ruiz-Chavarria, S. Ciliberto, C. Baudet and E. Lévêque, *Scaling Properties of the Streamwise Component of Velocity in a Turbulent Boundary Layer*, submitted to Physica D (1999).

ADVANCES IN TURBULENCE VIII
Proceedings of the Eighth European Turbulence Conference
C. Dopazo et al. (Eds.)
© CIMNE, Barcelona 2000

Turbulent mixing of a passive scalar: Statistics of the cliffs

F. Moisy[1], H. Willaime[1], J. S. Andersen[2], and P. Tabeling[1]

[1]Laboratoire de Physique Statistique, École Normale Supérieure,
24 rue Lhomond, 75231 Paris Cedex 05, FRANCE
[2]Centre for Chaos and Turbulence Studies, Niels Bohr Institute,
Blegdamsvej 17-19, DK-2100 København Ø, DENMARK

Contact e-mail: moisy@physique.ens.fr

The small scale persistence of anisotropy in turbulent mixing of a passive scalar is known to be related to the presence of cliffs [1], large-scale scalar jumps concentrated over small separations. However the link, if any, between cliffs and inertial range anomalous scaling remains far from clear. We report here a detailed study of cliff statistics, obtained from one-point temperature time series in a high-Reynolds number turbulence experiment in low temperature helium gas. We will focus on statistics of spatial organization of high temperature gradients, giving evidence of self-similar clustering for inertial range separations.

The flow takes place in a cylindrical vessel, 20 cm in diameter, and is generated between two coaxial disks, 13 cm apart [2], rotating in the same direction. The fluid is helium gas at a temperature of 8 K and at pressures ranging from 0.3 to 3 bar. Thermal fluctuations, of typically 50 mK, are induced by the means of a heated grid, and temperature measurements are performed at a position 30 mesh sizes downstream. The hand-made thermometers are 7 μm diameter carbon fiber, working in constant current mode, with a resolution of 100 μK.

For this first study of temperature measurements we restrict ourself to a range of microscale Reynolds numbers R_λ from 100 to 300. The turbulence parameters are determined from velocity measurements at the same point and in the same flow configuration. The integral length scales of temperature (θ) and velocity (u) fluctuations are respectively $\Lambda_\theta = 0.7$ cm and $\Lambda_u = 1.0$ cm, with no noticeable R_λ dependence, and the Kolmogorov scale η lies between 185 and 39 μm.

The thermal cliffs are defined from a simple threshold on the temperature derivative,

$$|\partial\theta/\partial x| > s\,\langle(\partial\theta/\partial x)^2\rangle^{1/2},$$

where s is an arbitrary constant, in the range 3–20. Spatial derivatives are obtained from temporal ones using the Taylor hypothesis. Figure 1a shows a magnification of a cliff, concentrating a temperature jump of about 5 standard

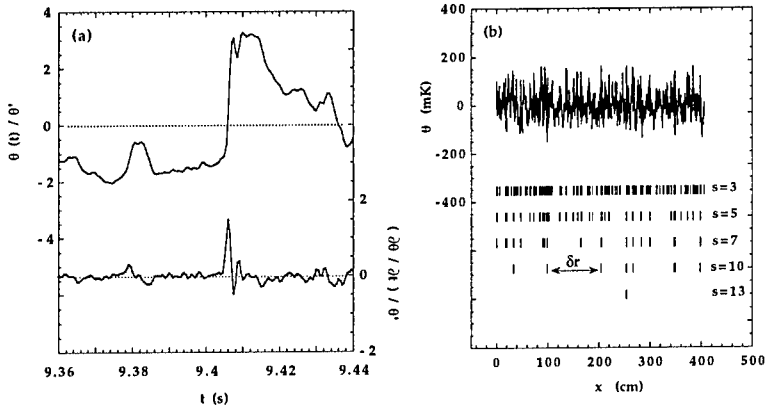


Figure 1: (a) Detail of a typical cliff on the temperature signal, and its corresponding time derivative. (b) Long recording of temperature fluctuations; the bars indicate the positions of the cliffs, for different thresholds, revealing the hierarchical organization of cliffs.

deviations. The cliff width, Δ, is defined such that the temperature derivative takes values exceeding 90 % of its local maximum. Distributions of this width are shown in figure 2a, for three different thresholds, at a Reynolds number $R_\lambda = 280$. It is clear that no threshold dependence appears, giving confidence in our detection method. Figure 2b shows the mean cliff width divided by the Kolmogorov scale for different Reynolds number from 100 to 300. We can see a well defined plateau,

$$\langle \Delta \rangle = (13 \pm 3)\eta.$$

Although a $\lambda \sim R_\lambda^{-1}$ scaling cannot be ruled out because of the small range of Reynolds numbers spanned here, our data suggest that the $\eta \sim R_\lambda^{-3/2}$ scaling is more likely. This observation indicates that the highest scalar jumps, whose amplitude is a few temperature standard deviations, are concentrated over distances scaling as the Kolmogorov scale, the "smallest available lengthscale" of the flow.

In order to investigate the occurrence of cliffs in the temperature signal, we now focus on the statistics of intervals between cliffs. In figure 1b we show a long recording of temperature fluctuations together with the positions of the cliffs, indicated by vertical bars for different thresholds. From this plot, a hierarchical organization of cliffs appears: the strongest gradients (highest s) are surrounded by weaker ones (smaller s). This clustering trend appears more clearly if we plot the probability density function (pdf) of these interval lengths, as shown in figure 3a. These pdfs are very wide, so we have used width-varying bins to compute the histograms. For long separations, the pdf is well fitted by an exponential decay, a signature of uncorrelated events. The characteristic length

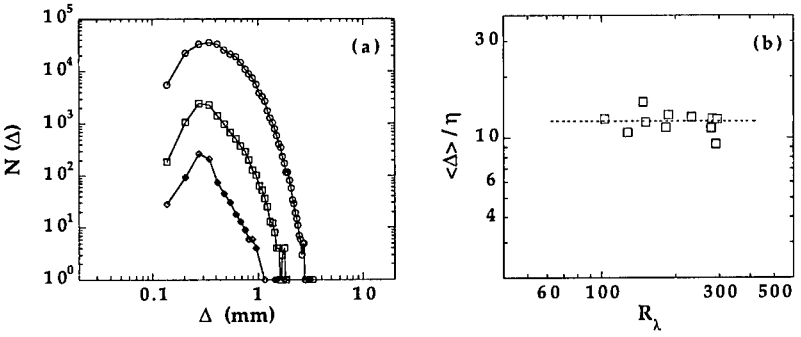


Figure 2: (a) Histograms of cliff width Δ, defined with thresholds s=3, 7 and 13. (b) Mean cliff width, divided by the Kolmogorov scale η, as a function of R_λ.

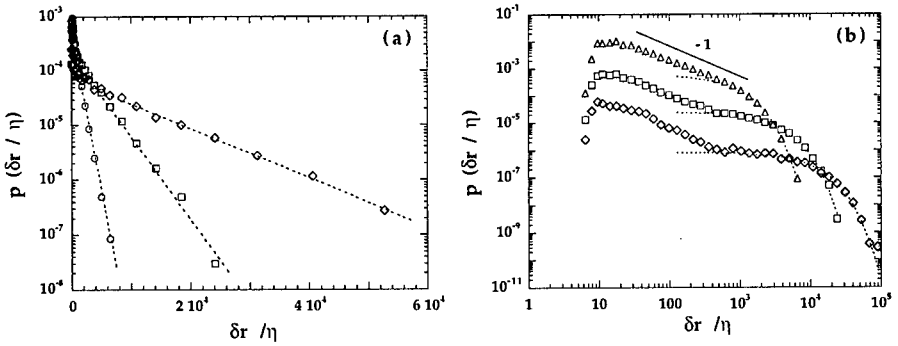


Figure 3: Distribution of interval between fronts for different thresholds s=3, 7 and 13, in log-linear (a) and log-log (b) coordinates. The dashed lines are exponential fit for $\delta r/\eta > 500$.

scale of this exponential behavior is related to the ratio of events selected by the threshold s.

For smaller separations, the pdf shows an algebraic decay,

$$p(\delta r) \sim \delta r^{-\mu},$$

clearly visible in figure 3b, with an exponent μ close to -1. The logarithmic derivative of this pdf gives a local exponent $\mu = 0.98 \pm 0.05$ for $30 < \delta r/\eta < 300$, with no variation with the threshold s. For higher thresholds, fewer events are selected and the exponential contribution dominates the algebraic one. The cross-over between these two regimes is $L_c \simeq (2.4 \pm 0.1)\Lambda_\theta$, again with no threshold dependence.

This algebraic distribution of waiting times between cliffs strongly suggests a self-similar clustering, in which the only characteristic size appears to be the

upper bound of the inertial range. One consequence of such a law is that the mean interval between cliffs, $\langle \delta r \rangle$, is fixed by the large scale. Together with the mean cliff width $\langle \Delta \rangle \sim \eta$ mentioned above, we note that this result is in good agreement with the constant $\sim o(1)$ skewness of temperature derivative observed at high Reynolds numbers.

Algebraic distributions of waiting times between intense events have been observed for other turbulent quantities. Thresholds on pressure drops in the turbulent flow between counter-rotating disks [3] reveal an algebraic distribution for short waiting times, with an exponent $\mu \simeq 1.6$ up to separations close to the integral scale. Waiting times between successive intense velocity bursts in the near field of a turbulent jet [4] also show algebraic distributions. For thresholds performed on longitudinal velocity derivative [5], we observe algebraic distributions with an exponent μ increasing from 0.5 to 1 for $R_\lambda < 400$ (in agreement with earlier observations [6] at moderate Reynolds numbers), and saturating at the value $\mu \simeq 1$ for higher R_λ (up to 2000).

Such distributions reveal the hierarchical organization of the small scale structures of turbulent flows, highlighting the intermittent behaviour of energy and scalar dissipation. An exciting issue is the universality of the $p(\delta r) \sim \delta r^{-1}$ law of waiting times, for both scalar and velocity derivatives, and its link with the inertial range anomalous scaling of scalar and velocity structure functions.

References

[1] Z. Warhaft. Passive scalars in turbulent flows. *Annu. Rev. Fluid. Mech.*, 32:203–240, 2000.

[2] F. Moisy, H. Willaime and P. Tabeling. Kolmogorov equation in a fully developed turbulence experiment. *Phys. Rev. Lett.* 82(20):3994–3997, 1999.

[3] P. Abry, S. Fauve, P. Flandrin and C. Laroche. Analysis of pressure fluctuations in swirling turbulent flows. *J. Phys. II France* 4:725–733, 1994.

[4] R. Camussi and G. Guj. Experimental analysis of intermittent coherent structures in the near field of a high Re turbulent jet flow. *Phys. Fluids* 11(2):423–431, 1999.

[5] F. Moisy. *Etude expérimentale des fluctuations de vitesse, de température et de pression en turbulence développée.* PhD thesis, Université Paris 6, France, 2000.

[6] Y. Gagne. *Etude expérimentale de l'intermittence et des singularités dans le plan complexe en turbulence développée.* Thesis, Université Grenoble, France, 1987.

ADVANCES IN TURBULENCE VIII
Proceedings of the Eighth European Turbulence Conference
C. Dopazo et al. (Eds.)
© CIMNE, Barcelona 2000

Velocity-acceleration structure function and Kolmogorov's 4/5 law

Søren Ott and Jakob Mann

Risø National Laboratory P.O. Box 49, DK4000 Roskilde, Denmark.
soeren.ott@risoe.dk

1 Introduction

Kolmogorov's 4/5 law [1] states that

$$\langle \delta v_{\parallel}{}^3 \rangle = -\frac{4}{5} \langle \varepsilon \rangle \, r \tag{1}$$

where $\delta\mathbf{v}(\mathbf{r}) = \mathbf{v}(\mathbf{z}+\mathbf{r}) - \mathbf{v}(\mathbf{z})$ is the velocity difference between two points separated by the vector $\mathbf{r}$, $\delta v_{\parallel} = \delta\mathbf{v}(\mathbf{r}) \cdot \mathbf{r}/r$, ε is the energy dissipation and brackets denote ensemble averages. The result is valid under certain symmetry assumptions in the infinite Reynolds number limit, where it is assumed that $\langle\varepsilon\rangle$ is fixed as $\nu \to 0$. The law was discussed by Frisch [2] who gave a proof based on global homogeneity, stationarity and isotropy. The law is fundamental in the sense that the coefficient $\frac{4}{5}$ is exact, and Frisch [2] argue that symmetries can be expected to be restored at high R_λ, so that is should be sufficient to assume stationarity and the existence of an infinite Reynolds number limit. It has indeed been found that the symmetry assumptions can be relaxed. Thus Hill [3] argue that it is sufficient to assume *local* homogeneity and gives a proof based on the assumption that mean values of terms containing a factor $\delta\mathbf{v}$ or δP can be ignored. This can be considered a strong version of local homogeneity. Mann, Ott & Andersen [4] give a proof based on a weaker form of local homogeneity involving statistics formed only from the local velocity field $\delta\mathbf{v}$ and found that the assumption of *local* stationarity was necessary. No isotropy assumption was found necessary when averaging over all directions of the separation vector $\mathbf{r}$ was included in the definition of the structure function. These results are discussed further below.

Measurements in the atmospheric surface layer by Dhruva *et al.* [5] have verify the 4/5 law at high Reynolds numbers ($R_\lambda \sim 10^4$). Experimentally the ratio $K(r) \equiv -\frac{\langle \delta v_{\parallel}{}^3 \rangle}{\langle\varepsilon\rangle r}$ increases with r to a plateau very close to $\frac{4}{5}$ and decreases for larger r. However, even for $R_\lambda \sim 10^4$ the width of the plateau is quite

small. At more moderate Reynolds numbers ($R_\lambda \sim 10^2 - 10^3$) the maximum is generally considerably lower than $\frac{4}{5}$ (e.g. [8], [6], [7], [4]).

The question is what causes the deviations from (1) at moderate R_λ. We have reviewed both the derivation of the 4/5 law and the definition of local homogeneity searching for terms which could be important at moderate R_λ.

2 Defining Local Homogeneity

We prefer to define local homogeneity by means of a local frame of reference attached to a fluid particle. For a particular point $\mathbf{z}$ we follow the trajectory $\zeta(t)$ passing through $\mathbf{z}$ at time t_0 and define a local coordinate system $(\mathbf{y}, s)$ where $\mathbf{y} = \mathbf{x} - \zeta(t)$ is the local position (or separation) and $s = t$ is the local time variable. The following connection exists between partial derivatives in local system $(\mathbf{y}, s)$ and the laboratory system $(\mathbf{x}, t)$

$$\frac{\partial}{\partial y_i} = \frac{\partial}{\partial x_i} \quad , \quad \frac{\partial}{\partial s} = \frac{\partial}{\partial t} + v_j(\zeta(t), t)\frac{\partial}{\partial \zeta_j}$$

We define *local quantities* as quantities that can be constructed from the local velocity field $\delta\mathbf{v}(\mathbf{y}, s) = \mathbf{v}(\zeta + \mathbf{y}, s) - \mathbf{v}(\zeta, s)$ and partial derivatives of $\delta\mathbf{v}$ with respect to the *local* coordinates $\mathbf{y}$ and s. The local quantities constitute the information available to an observer in a local coordinate system. Taking ensemble averages of local quantities for $t = t_0$ we get a set of local statistics for the point $\mathbf{z}$. Local homogeneity means that local statistics are independent of $\mathbf{z}$.

This definition is slightly different from the one given by Monin & Yaglom [9], who allow pressure differences as well as $\delta\mathbf{v}$ in the definition of local quantities. Our definition implies that simple flow fields that are linear in $\mathbf{x}$ are locally homogeneous. A rotating flow can be made by applying an instantaneous force field of the form $f_i = A_{ij}x_j\delta(t)$, where $A_{ij} = -A_{ji}$, to a globally homogeneous turbulent flow. Using our definition this flow is locally homogeneuos even for $t > 0$.

We note that $\frac{\partial}{\partial t}$ generally produces non-local quantities, which have zero averages by stationarity. $\frac{\partial}{\partial s}$ can be used to define local stationarity meaning that $\left\langle \frac{\partial Q}{\partial s} \right\rangle = 0$ for any local quantity Q. We emphasize that global stationarity does not imply local stationarity.

In local coordinates the Navier-Stokes equation becomes

$$\frac{\partial \delta v_i}{\partial s} + \delta v_j \frac{\partial \delta v_i}{\partial y_j} = -\frac{\partial q}{\partial y_i} + \nu \frac{\partial^2 \delta v_i}{\partial y_j \partial y_j} \tag{2}$$

where $q(\mathbf{y}) \equiv p(\zeta + \mathbf{y}) - p(\zeta) + \mathbf{a}(\zeta)\cdot\mathbf{y}$ and $\mathbf{a} \equiv \partial\mathbf{v}/\partial t + \mathbf{v}\cdot\nabla\mathbf{v}$ is the acceleration. Thus the Navier-Stokes equation is unchanged even if the local system is not an inertial system. There is no way to detect from local observations of the flow that q is not the real pressure (pressure sensitive dye is not allowed). Note that the left hand side of (2) can be written as $\delta\mathbf{a} = \mathbf{a}(\zeta + \mathbf{y}) - \mathbf{a}(\zeta)$.

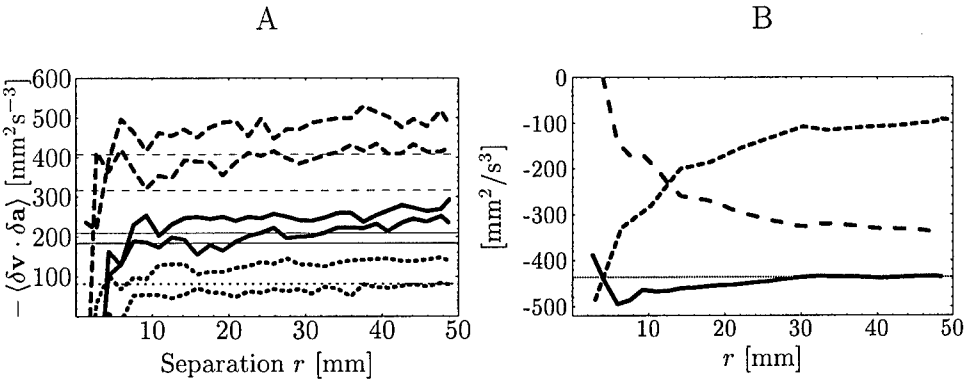


Figure 1: A: $\langle \delta \mathbf{v} \cdot \delta \mathbf{a} \rangle$ for six runs. The short dashed curves are runs with a grid frequency of 2 Hz, the solid 3 Hz, and the long dashed 3.5 Hz. The horizontal lines are values of $2\langle \varepsilon \rangle$ derived from second order velocity structure function. B: The local energy budget (cf. (4)). The long dashed curve is local kinetic energy decay rate, the short dashed curve is the local energy flux divergence, and the solid curve is $\langle \delta \mathbf{v} \cdot \delta \mathbf{a} \rangle$.

The following incompressibility relations hold

$$\frac{1}{3} G_{ii} r^2 = r \frac{\partial \left\langle \delta \mathbf{v}_\parallel^2 \right\rangle}{\partial r} + 3 \left\langle \delta \mathbf{v}_\parallel^2 \right\rangle - \langle \delta \mathbf{v}^2 \rangle ,$$

and

$$\frac{r^3}{15} \left(2F_{ii} - \frac{\partial G_{ii}}{\partial s} \right) = r \frac{\partial \left\langle \delta \mathbf{v}_\parallel^3 \right\rangle}{\partial r} + 4 \left\langle \delta \mathbf{v}_\parallel^3 \right\rangle - 3 \langle \delta \mathbf{v}_\parallel \delta \mathbf{v}^2 \rangle$$

where $G_{ii} = \left\langle \frac{\partial v_j(\mathbf{x}')}{\partial x_i'} \frac{\partial v_j(\mathbf{x})}{\partial x_j} \right\rangle$ and $F_{ik} = \left\langle \frac{\partial v_j(\mathbf{x}')}{\partial x_k'} \frac{\partial a_j(\mathbf{x})}{\partial x_j} \right\rangle$ are constants independent of $\mathbf{x}$ and $\mathbf{x}'$. Since $\mathbf{x}$ and $\mathbf{x}'$ can be chosen to be far apart we may expect $G_{ii} \sim 0$ and $F_{ik} \sim 0$, at least when the mean flow is not strained or rotating.

3 $\langle \delta \mathbf{v} \cdot \delta \mathbf{a} \rangle$ and the 4/5 law

Using the above definition of local homogeneity Mann, Ott & Andersen [4] show that

$$\langle \delta \mathbf{v}(\mathbf{y}) \cdot \delta \mathbf{a}(\mathbf{y}) \rangle = \nu \frac{\partial^2 \left\langle \delta \mathbf{v}^2(\mathbf{y}) \right\rangle}{\partial y_j \partial y_j} + 2\nu \langle G_{ii} \rangle + F_{ik} y_i y_j - 2 \langle \varepsilon \rangle$$

The two first terms on the right hand side vanish as $\nu \to 0$ and they can be neglected for separations larger than a few Kolmogorov length scales. The third term cannot be ruled out in general and it could play a role for large separations.

Figure 1A shows direct measurements of $\langle \delta \mathbf{v} \cdot \delta \mathbf{a} \rangle$ in turbulence generated by two oscillating grids made by us [4] with $R_\lambda \sim 100$. It appears that $\langle \delta \mathbf{v} \cdot \delta \mathbf{a} \rangle$ is almost constant over a range of separations much wider than the inertial range.

Furthermore, the constant value agrees well with estimates of $\langle\varepsilon\rangle$ obtained from the second order structure function. We have also find that $\langle\delta\mathbf{v}\cdot\delta\mathbf{a}\rangle$ is nearly independent of the direction of the separation vector $\mathbf{y}$. In other words the experiments are consistent with the simple relation

$$\langle\delta\mathbf{v}\cdot\delta\mathbf{a}\rangle = -2\,\langle\varepsilon\rangle \tag{3}$$

Integrating both sides of over a ball of radius r, (3) is turned into a kinetic energy budget

$$\frac{\partial}{\partial s}\int\limits_{|\mathbf{y}|<r} \mathrm{d}^3y\,\left\langle\frac{1}{2}\delta\mathbf{v}^2(\mathbf{y})\right\rangle + \int\limits_{|\mathbf{y}|=r} \mathrm{d}^2y\,\left\langle\delta\mathbf{v}_{\|}(\mathbf{y})\frac{1}{2}\delta\mathbf{v}^2(\mathbf{y})\right\rangle = -\frac{8\pi\,\langle\varepsilon\rangle}{3} \tag{4}$$

If the first term is ignored we get the so-called 4/3 law, and, using the incompressibility relations, the 4/5 law follows with no need for additional assumptions (cf. [4] for details). The crucial step is therefore to assume that the local kinetic energy $\left\langle\frac{1}{2}\delta\mathbf{v}^2\right\rangle$ is stationary. The assumption is daring because there is no production term in (4) to compensate for the dissipated energy. Figure 1B shows experimental results for the three terms. For small separations the contribution from local energy decay (long dashed curve) is indeed small, but for quite moderate separations, where (3) is valid, the local energy decay becomes the leading term on the left hand side of (4). In other words the energy cascade is maintained by feeding on the local kinetic energy, and we conclude that this is the main reason for the deviations from the 4/5 law observed at moderate Reynolds numbers.

References

[1] A. N. Kolmogorov. Dokl. Akad. Nauk SSSR,**30**: 4, 1941.

[2] U. Frisch. Cambridge University Press, Cambridge 1995

[3] R. Hill. Journal of Fluid Mechanics,**353**: 67–81, 1997.

[4] J. Mann, S. Ott and J. S. Andersen. Risø National Laboratory. Risø–R–1036(EN), 1999.

[5] B. Dhruva, Y. Tsuji and K. R. Sreenivasan. Phys. Rev. E, **56**: R4928–4930, 1997

[6] F. Moisy, P. Tabeling and H. Williame Phys. Rev. Lett., **82**: 3994-3997, 1999.

[7] S. G. Saddoughi and S. V. Veeravalli. J. Fluid Mech., **268**: 333–372, 1994.

[8] L. Mydlarski and Z. Warhaft. J. Fluid Mech., **330**: 331–368, 1996.

[9] A. S. Monin and A. M. Yaglom. The MIT Press, 1975.

ADVANCES IN TURBULENCE VIII
Proceedings of the Eighth European Turbulence Conference
C. Dopazo et al. (Eds.)
© CIMNE, Barcelona 2000

Scaling behavior of the vertical velocity field and of the intensity field in the solar photosphere

F. Lepreti[1], B. Bavassano[2], F. Berrilli[3], R. Bruno[2],
V.Carbone[1], G. Consolini[2], and E. Pietropaolo[4]

[1]Dip. Fisica and I.N.F.M., Univ. della Calabria, I-87036 Rende, Cosenza, ITALY
[2]I.F.S.I.–CNR, I-00133, Roma, ITALY
[3]Dip. Fisica, Univ. di Roma "Tor Vergata", I-00133, Roma, ITALY
[4]Dip. Fisica, Univ. di L'Aquila, I-67010, L'Aquila, ITALY

Contact e-mail: carbone2@fis.unical.it

1 Introduction

The overshooting of convective motions in the stable layers of the solar atmosphere produces observable velocity and intensity patterns. The characterization of these photospheric structures is extremely relevant for the understanding of the energy transport in the outer layers of the Sun. The solar photosphere is also a natural laboratory where it is possible to study pattern formation in driven out of equilibrium systems [1]. Recently many studies claimed that a turbulent cascade process could be a starting point for the comprehension of these patterns [2]. Moreover previous analyses of photospheric velocity and intensity field have evidenced the presence of scaling features and intermittency phenomena [3, 4].

Here, using Extended Self Similarity (ESS) [6] analysis and multifractal analysis [7], two methods used in the past years to characterize intermittency effects in MHD and fluid turbulence, we investigate the anomalous scaling features of the velocity and intensity field at the solar photosphere.

2 Data analysis

This study is based on a set of velocity and intensity fields obtained from monochromatic and white light images acquired by the THEMIS-IPM monochromator [8] in the '99 observative campaign. The observed field refers to a quiet solar region at the disk center, and velocity and intensity images have been computed from the observation of three spectral lines, C I 538.0 nm, Fe I 537.9 nm, Fe I 557.6 nm, forming at three different photospheric heights, $\simeq$ 60 km,

$\simeq$ 200 km and $\simeq$ 370 km respectively. In order to study only the convective pattern, the images, corrected for standard instrumental effects, have been filtered to remove the 5-minutes acoustic waves (p-modes) by means of a subsonic filter. The field of view of the corrected images is about 30 "×30 " (21.5 Mm×21.5 Mm on the solar surface). The spatial resolution of the acquired images is of the order of 0.4 ". In the case of velocity and intensity fields, calculated from the monochromatic images, the resolution was decreased of a factor $\simeq$ 2 (0.8 ").

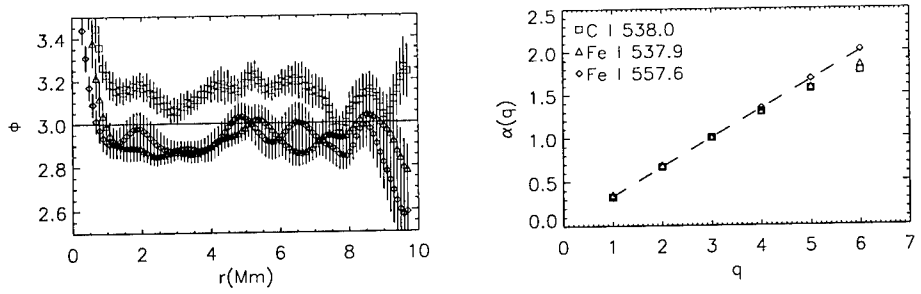


Figure 1: Left: flatness vs. scale for velocity fluctuations at three photospheric heights. Squares, triangles and diamonds refer, respectively, to the C I 538.0, Fe I 537.9 and Fe I 557.6 velocity fields. The error bars have been obtained from the scatter among 16 13" × 13" sub-images. Right: relative scaling exponents $\alpha(q)$ for vertical velocity structure functions at three different photospheric heights. The dashed line represents the linear relation $\alpha(q) = q/3$ from the K41 theory.

To investigate the occurrence of scaling laws in the vertical photospheric velocity field we analyze the structure functions $S_q(r) = \langle |v_\parallel(\mathbf{x}+\mathbf{r}) - v_\parallel(\mathbf{x})|^q \rangle = \langle \delta v_\parallel(r)^q \rangle$ where $\langle\ \rangle$ denotes the spatial average and $v_\parallel(\mathbf{x}) = v_\parallel(x,y)$ is the vertical velocity field, that is the line of sight component of the velocity field. To obtain a simple measure of intermittency of the $\delta v_\parallel(r)$ distribution function we calculate its flatness Φ, that is $S_4(r)/S_2(r)$, at three different photospheric heights. For a Gaussian distribution $\Phi \simeq 3$, while it is $\Phi > 3$ in presence of intermittency effects. As it can be seen in Figure 1, we find that the velocity fluctuations are nearly gaussian, as already reported by Lawrence et al. [5], with values sligthly higher for the C I line. The occurrence of scaling invariance can be studied through the scaling relations $S^q(r) \sim r^{\zeta(q)}$ where the scaling exponents $\zeta(q)$ are linearly related to the moment order in absence of intermittency. In our case it is not easy to define a sufficiently good scaling region in the structure functions. Benzi et al. [6] have introduced a new concept, the Extended Self Similarity, which allows to analyze the scaling properties of the structure functions in a different way. In this method, the relative scaling exponents $\alpha(q)$ are determined from the scaling laws $S^q(r) = \left[S^3(r)\right]^{\alpha(q)}$. In this work we calculate the exponents $\alpha(q)$ of the vertical velocity field at three different photospheric heights, for

six values of the moment order q ($1 \leq q \leq 6$). In Figure 1 we show $\alpha(q)$ vs. the moment order q. It can be seen that the scaling exponents for the C I 538.0 nm and the Fe I 537.9 nm velocity fields show a non linear dependence from the moment order, while a linear dependence is found for the Fe I 557.6 nm velocity field. This suggest that some intermittency effects in the vertical velocity field could be generated by the convective pattern at lower altitudes.

The intermittent nature of the dissipation of passive scalar fluctuations in fluids has been evidenced in some past papers [9]. Here, we study the photospheric intensity as a passive scalar defining a dissipation field $\Gamma(x, y)$ as

$$\Gamma(x, y) \simeq |\nabla I|^2 = \left(\frac{\partial I}{\partial x}\right)^2 + \left(\frac{\partial I}{\partial y}\right)^2 , \qquad (1)$$

where $I(x, y)$ is the intensity field. It can be seen that $\Gamma(x, y)$ is intermittent, showing large variations at the boundaries of the convective cells. To investigate the intermittency properties of the dissipation field we can try to obtain anomalous scaling laws through a multifractal analysis [7]. To this aim we introduce a probability measure $\varepsilon_i(r) = \chi_i(r)/\chi(L)$, where $\chi_i(r) = \int_{D_i(r)} \Gamma(x, y) dx\, dy$, beeing $D_i(r) \subset D(L)$ a hierarchy of disjoint squares of size r, covering the whole square $D(L)$ of size L. The anomalous scaling laws can be obtained from the relation $\langle \varepsilon^q \rangle \sim r^{(q-1)D_q}$ where D_q are the generalized dimensions. The singularity spectrum $f(\alpha)$, that is the fractal dimension of the set of points where the probability measure scales as $\varepsilon(r) \sim r^{\alpha}$, can be calculated from a Legendre transform of the variables (q, D_q) [7]. In Figure 2 we show the $f(\alpha)$ curves for the

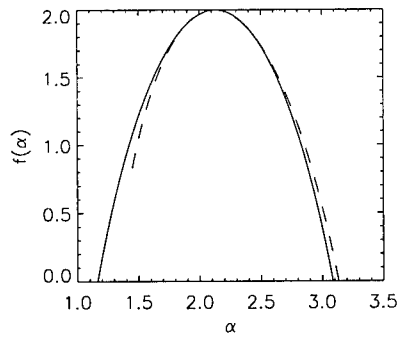


Figure 2: The $f(\alpha)$ curves for the dissipation of continuum intensity fluctuations (dashed line) and for Fe I 557.6 nm line core intensity fluctuations (solid line).

intensity dissipation field. These curves show that the intensity dissipation field is more intermittent in the higher photosphere than in the lower photosphere.

3 Conclusions

We have shown that the photospheric vertical velocity fluctuations are nearly gaussian with a possible presence of intermittency effects at lower altitudes. We have analyzed also the scalar dissipation field obtained from the intensity fields. Using the multifractal geometry we have found that the dissipation is more intermittent in the higher photosphere.

This work is based on observations obtained with the Italian Panoramic Monochromator mounted at the THEMIS telescope operated on the island of Tenerife by THEMIS/CNRS-INSU/CNR in the Spanish Observatorio del Teide of the Instituto de Astrofisica de Canarias. We thank the THEMIS staff for the efficient support in the observations. Special thanks are due to C. Briand and G. Ceppatelli for their operational support.

References

[1] U. Frisch. Turbulence: The Legacy of A. N. Kolmogorov. Cambridge University Press, Cambridge, 1995.

[2] O. Espagnet, R. Muller, T. Roudier, and N. Mein. Turbulent power spectra of the solar granulation. *Astron. Astrophys.*, 271:589–600, 1993.

[3] G. Consolini, V. Carbone, F. Berrilli, R. Bruno, B. Bavassano, C. Briand, B. Caccin, G. Ceppatelli, A. Egidi, I. Ermolli, A. Florio, G. Mainella, and E. Pietropaolo. Scaling behavior of the vertical velocity field in the solar photosphere. *Astron. Astrophys.*, 344:L33–L36, 1999.

[4] F. Lepreti, V. Carbone, E. Pietropaolo, G. Consolini, R. Bruno, B. Bavassano, F. Berrilli. Multifractal structure of the dissipation field of intensity fluctuations in the solar photosphere. *Physica A*, 280:88–92, 2000.

[5] J. K. Lawrence, A. C. Cadavid, and A. A. Ruzmaikin. Characteristic scales of photospheric flows and their magnetic and temperature markers. *Astrophys. Jour.*, 513:506–515, 1999.

[6] R. Benzi, S. Ciliberto, R. Tripiccione, C. Baudet, F. Massaioli, and S. Succi. Extended self-similarity in turbulent flows. *Phys. Rev. E*, 48:R29–R32, 1993.

[7] G. Paladin and A. Vulpiani. Anomalous scalig laws in multifractal objects. *Phys. Rep.*, 156:147–225, 1987.

[8] F. Cavallini. The Italian Panoramic Monochromator. *Astron. Astrophys. Suppl. Ser.*, 128:589–598, 1998.

[9] R. R. Prasad, C. Meneveau, and K. R. Sreenivasan. Multifractal nature of the dissipation field of passive scalars in fully turbulent flows. *Phys. Rev. Lett.*, 61:74–77, 1988.

ADVANCES IN TURBULENCE VIII
Proceedings of the Eighth European Turbulence Conference
C. Dopazo et al. (Eds.)
© CIMNE, Barcelona 2000

An inner scale for dissipation of helicity in turbulence

P. D. Ditlevsen[1] and P. Giuliani[2]

[1]Niels Bohr Institute, Geophysical Department
Juliane Maries Vej 30, DK-2100 Copenhagen O, Denmark
[2]Dipartimento di Fisica and Istituto Nazionale di Fisica della Materia
Università della Calabria, 87036 Rende (CS), Italy

Contact e-mail: pditlev@gfy.ku.dk

1 Helical turbulence

The existence of a second quadratic inviscid invariant, the helicity, besides the energy, in a helical turbulent flow leads to coexisting cascades of energy and helicity [1]. An equivalent of the four-fifth law for the longitudinal third order structure function, which is derived from energy conservation, is easily derived from helicity conservation [2, 3]. This is a scaling relation for the third order correlator associated with the spectral flux of helicity, $\langle \delta \mathbf{v}_{\parallel}(l) \cdot [\mathbf{v}_{\perp}(r) \times \mathbf{v}_{\perp}(r+l)] \rangle = (2/15)\overline{\delta} l^2$, where $\overline{\delta}$ is the mean dissipation of helicity. This relation is called the 'two-fifteenth law' due to the numerical prefactor. The two-fifteenth law establishes another non-trivial scaling relation for velocity differences in a turbulent helical flow.

The ratio of dissipation of helicity to dissipation of energy in spectral space is proportional to the wave-number k. This is leading to a different inner – or Kolmogorov scale for helicity than for energy [5]. The Kolmogorov scale η for energy dissipation is obtained from $\overline{\varepsilon} \sim \delta u_\eta^3/\eta \sim \nu \delta u_\eta^2/\eta^2 \Rightarrow \eta \sim (\nu^3/\overline{\varepsilon})^{1/4}$, where δu_l is a typical variation of the velocity over a scale l and $\overline{\varepsilon}$ is the mean energy dissipation. The Kolmogorov scale ξ for dissipation of helicity is obtained by balancing the helicity dissipation and the spectral helicity flux. With dimensional counting we have $\overline{\delta} \sim \nu \delta u_\xi^3/\xi^2$ and using $\delta u_l \sim (l\overline{\varepsilon})^{1/3}$ we obtain the inner scale ξ for helicity dissipation,

$$\xi \sim (\nu^3 \overline{\varepsilon}^2/\overline{\delta}^3)^{1/7}, \tag{1}$$

where ν is the kinematic viscosity, $\overline{\varepsilon}$ the mean energy dissipation and $\overline{\delta}$ the mean helicity dissipation. The inner scale for helicity is always larger than the Kolmogorov scale for energy so in the high Reynolds number limit the flow will always be helicity free in the small scales, much in the same way as the flow

will be isotropic and homogeneous in the small scales. However, as is the case for the enstrophy, we must have a blow up of helicity for high Reynolds number flow in order to permit the energy to cascade to the dissipation scale since the spectral helicity density dimensionally dominates with a factor k over the spectral energy density. Helicity is, in contrast to enstrophy, an inviscid invariant in 3D turbulence so the only way there can be a blow up of helicity is if there is a detailed balance between positive and negative helicity production in the range $K_H < k < K_E$. So the situation in 3D turbulence with cascades of energy and helicity is very different from the situation in 2D turbulence since helicity is not a positive quantity. In 2D turbulence, where enstrophy is a positive inviscid invariant, the cascade of enstrophy prohibits a forward cascade of energy.

2 Model simulation

The idea is illustrated in a shell model of turbulence. Shell models are toy-models of turbulence which by construction have second order inviscid invariants similar to energy and helicity in 3D turbulence. The advantage of shell models is that they can be investigated numerically for very high Reynolds numbers, in contrast to the Navier-Stokes equation. Shell models lack any spatial structures so we stress that only certain aspects of the turbulent cascades have meaningful analogies in the shell models. This should especially be kept in mind when studying helicity which is intimately linked to spatial structures, and the dissipation of helicity to reconnection of vortex tubes [4]. So the following only concerns the spectral aspects of the helicity and energy cascades. The most well studied shell model, the GOY model [6, 7], is defined from the governing equation,

$$\dot{u}_n = ik_n(u_{n+2}u_{n+1} - \frac{\epsilon}{\lambda}u_{n+1}u_{n-1} + \frac{\epsilon-1}{\lambda^2}u_{n-1}u_{n-2})^* \\ -\nu k_n^2 u_n + f_n \qquad (2)$$

with $n = 1, ..., N$ where the u_n's are the complex shell velocities. The wave-numbers are defined as $k_n = \lambda^n$, where λ is the shell spacing. The second and third terms are dissipation and forcing. The model has two inviscid invariants, energy, $E = \sum_n E_n = \sum_n |u_n|^2$, and 'helicity', $H = \sum_n H_n = \sum_n (\epsilon-1)^{-n}|u_n|^2$. The model has two free parameters, λ and ϵ. The 'helicity' only has the correct dimension of helicity if $|\epsilon - 1|^{-n} = k_n \Rightarrow 1/(1-\epsilon) = \lambda$. In this work we use the standard parameters $(\epsilon, \lambda) = (1/2, 2)$ for the GOY model.

Figure 1 shows two shell model simulations, one with a helicity free forcing and one with coexisting cascades of energy and helicity. The spectral fluxes of energy and helicity are plotted against wave-number. The helicity flux (diamonds) in the case of a helical forcing shows a crossover between a regime with a constant cascade of helicity and a regime dominated by balanced dissipation of positive and negative helicity (for even – and odd numbered shells). The scaling in this regime is governed by the dissipation of helicity $D_n \sim \nu k_n^3 |u_n|^2 \sim \nu k_n^{7/3}$.

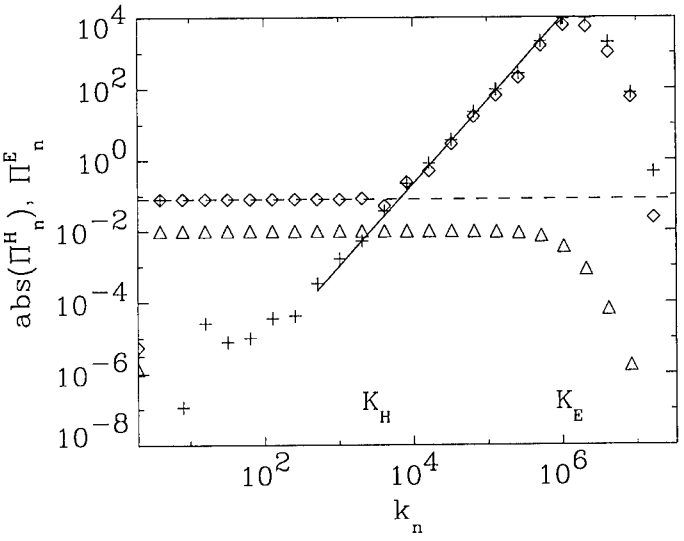


Figure 1: The absolute values of the helicity flux $|\langle\Pi_n^H\rangle|$ (diamonds) show a crossover from the inertial range for helicity to the range where the helicity is dissipated. The line has a slope of 7/3 indicating the helicity dissipation. The dashed lines indicate the helicity input $\overline{\delta}$. The crosses is the helicity flux in the case $\overline{\delta} = 0$ where there is no inertial range and K_H coincides with the integral scale. The triangles are the energy flux $\langle\Pi_n^E\rangle$.

The crossover defines the inner scale $\xi = K_H^{-1}$ for helicity dissipation. In the first regime both the four-fifth - and the two-fifteenth' law applies, in the second regime only the four-fifth law applies. The position of the inner scale K_H depends on the input of helicity $\overline{\delta} = 0$. Figure 2 shows a set of simulations performed with different helicity inputs. When scaling the wave number with K_H and the helicity flux with $\overline{\delta} = 0$ a clear data collapse between the different simulations is seen, confirming the scaling (1).

3 Conclusions

The role of helicity in 3D turbulence is different from the role of enstrophy in 2D turbulence. In 3D helical turbulence the helicity is dissipated within the inertial range of energy cascade. Thus there exist two inertial ranges in helical turbulence, a range smaller than K_H with coexisting cascades of energy and helicity where both the four-fifth - and the two-fifteenth law applies, and a range between K_H and K_E where the flow is non-helical and only the four-fifth law

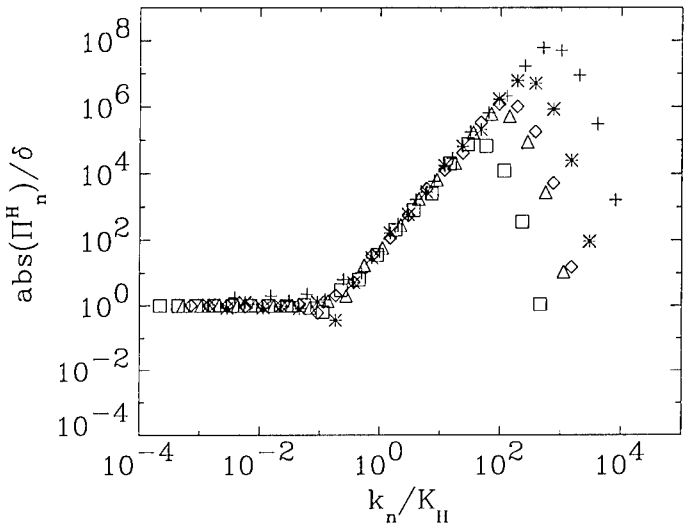


Figure 2: Five simulations with constant viscosity $\nu = 10^{-9}$, constant energy input $\overline{\varepsilon} = 0.01$ and varying helicity input $\overline{\delta} = (0.0001, 0.001, 0.005, 0.01, 0.08)$ are shown. The absolute values of the helicity flux $|\langle \Pi_n^H \rangle|$ divided by $\overline{\delta}$ is plotted against the wave number divided by $K_H = (\nu^3 \overline{\varepsilon}^2 / \overline{\delta}^3)^{-1/7}$, which is obtained from (1) neglecting $O(1)$ constants.

applies. In this range there is a detailed balance between positive and negative helicity associated with the structures where the energy is dissipated.

References

[1] M. Lesieur, 'Turbulence in Fluids', Third edition, Kluwer Academic Publishers, 1997.

[2] V. S. L'vov et al. chao-dyn/9705016 (unpublished).

[3] O. Chkhetiani, JETP Lett., 63, 808, 1996.

[4] E. Levich, L. Shtilman and A.V. Tur, Physica A, 176, 241, 1991.

[5] P. D. Ditlevsen and P. Giuliani, chao-dyn/9910013.

[6] E. B. Gledzer, Sov. Phys. Dokl, 18, 216, 1973.

[7] L. Kadanoff et al., Phys. Fluids, 7, 617, 1995.

ADVANCES IN TURBULENCE VIII
Proceedings of the Eighth European Turbulence Conference
C. Dopazo et al. (Eds.)
© CIMNE, Barcelona 2000

A universal law for tails of density pdf's in multi-dimensional Burgers turbulence

J. Bec[1,2], U. Frisch[1,2], K. Khanin[3] and B. Villone[4]

[1]Observatoire de la Côte d'Azur, Lab. G.D. Cassini
B.P. 4229, F-06304 Nice Cedex 4, FRANCE
[2]CNLS - Theoretical Division, LANL, Los Alamos, NM 87545, USA
[3]Isaac Newton Institute for Mathematical Sciences
20 Clarkson Road, Cambridge CB3 0EH, UK
[4]CNR - Istituto di Cosmogeofisica, 10133 Torino, ITALY

Contact e-mail: bec@obs-nice.fr

Abstract

Extending work of E, Khanin, Mazel and Sinai [1] on the one-dimensional Burgers equation, we show that density pdf's have universal power-law tails with exponent -7/2. This behavior stems from singularities, other than shocks, whose nature is quite different in one and several dimensions. We briefly discuss the possibility of detecting singularities of Navier–Stokes turbulence using pdf tails.

1 Introduction

In recent years there has been considerable interest in probability density functions (pdf) for Navier–Stokes turbulence. Similar questions can be asked for random solutions of Burgers equation ("burgulence"). We are interested here in the tail behavior of the pdf of the density ρ for solutions to the d-dimensional Burgers equation in the limit of vanishing viscosity ($\nu \to 0$):

$$\partial_t \mathbf{v} + (\mathbf{v}\cdot\nabla)\mathbf{v} = \nu\nabla^2\mathbf{v}, \quad \mathbf{v} = -\nabla\psi, \tag{1}$$

$$\partial_t \rho + \nabla\cdot(\rho\mathbf{v}) = 0. \tag{2}$$

The initial potential $\psi_0(\mathbf{r}_0)$ and the initial density $\rho_0(\mathbf{r}_0)$ are random functions of the space variable. This problem arises, for example, in the study of large-scale structures in the Universe (see Ref. [2] and references therein). As is well known, the Burgers equation leads to shocks in which the density of matter is infinite. Yet, large but finite densities do not necessarily occur in the neighborhood of shocks. E *et al.* [1] considered a related problem of determining the pdf of the velocity gradient for the one-dimensional Burgers equation with large-scale and white-in-time random forcing. They showed that large negative gradients

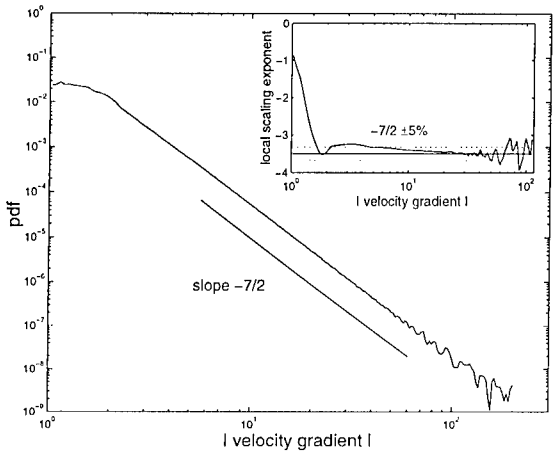


Figure 1: Pdf of the velocity gradient at negative values in log-log coordinates, for one-dimensional kicked burgulence. A power law with exponent $-7/2$ is obtained over two decades. Simulation uses a modification of the Fast Legendre Transform algorithm of Ref. [5].

come from "preshocks" (nascent shocks) which contribute a power-law tail with exponent -7/2 to the pdf. Preshocks correspond to fast fluid particles catching up for the first time with slow ones. They constitute discrete events in (Eulerian) space time. We have shown that the -7/2 law for the pdf of (negative) velocity gradients in one dimension applies also (i) for decaying (unforced) "burgulence" with smooth (i.e. large-scale) random initial conditions [3] and (ii) for the case of a deterministic time and space-periodic force which is a sum of delta functions in time with smooth space dependence [4]. For this "kicked burgulence", the -7/2 law was also obtained numerically (see Fig. 1).

2 "Kurtoparabolic" points and the -7/2 law

We turn now to the multi-dimensional problem (1)-(2) with smooth and random initial conditions (for details see Ref. [2]). As is known, the one or multi-dimensional viscous Burgers equation can be solved explicitly by means of the Cole–Hopf transformation. ¿From this, by taking the limit $\nu \to 0$, a "maximum representation" can be derived for the velocity potential

$$\psi(\mathbf{r},t) = \max_{\mathbf{r}_0} \left(\psi_0(\mathbf{r}_0) - \frac{|\mathbf{r}-\mathbf{r}_0|^2}{2t} \right). \qquad (3)$$

The maximum is achieved at a point at which the gradient of the r.h.s. vanishes, leading to $\mathbf{r} = \mathbf{r}_0 + t\mathbf{v}(\mathbf{r}_0, 0)$. From this it follows that $\mathbf{r}_0$ is a Lagrangian

coordinate. The "naive" Lagrangian map $\mathbf{r}_0 \mapsto \mathbf{r}$ given by this relation is however not invertible, except for short times. The requirement that the maximum in (3) is *global* can be recast in geometrical terms by introducing the Lagrangian potential $\varphi(\mathbf{r}_0, t) \equiv t\psi_0(\mathbf{r}_0) - |\mathbf{r}_0|^2/2$ and the "proper" Lagrangian map $\mathbf{r}_0 \mapsto \mathbf{r} \equiv -\nabla\varphi_c(\mathbf{r}_0, t)$, where φ_c is the convex-hull of φ with respect to $\mathbf{r}_0$. For example, in one dimension, the graph of φ_c is obtained by tightly pulling a string over the graph of φ. The graph of φ_c coincides with that of φ at regular points, wherever fluid particles have not yet fallen into shocks. It also contains linear and ruled manifolds associated to the different types of shocks: segments when $d = 1$, triangles and ruled surfaces when $d = 2$, etc. Conservation of mass implies that the density is given, at regular points, by $\rho(\mathbf{r}, t) = \rho_0(\mathbf{r}_0)/J(\mathbf{r}_0, t)$, where J is the Jacobian of the Lagrangian map. (The density is infinite in shocks.) Since the Jacobian is (up to a factor $(-1)^d$) equal to the Hessian of the Lagrangian potential (determinant of the matrix of second space derivatives), it follows that large densities are typically obtained only near parabolic points. However, arbitrarily close to a parabolic point there are generically hyperbolic points where the surface defined by φ crosses its tangent (hyper)plane and which, therefore, do not belong to its convex hull. Yet, there exist in general exceptional "kurtoparabolic" points which are parabolic and belong to the boundary of the set of regular points. Near such points, arbitrarily large densities are obtained. In one dimension, the only kurtoparabolic points are the preshocks which are discrete space-time events in both Eulerian and Lagrangian coordinates. In two and more dimensions, kurtoparabolic points are also born at preshocks but persist in general for a finite time (see Fig. 2). In Eulerian space, they are associated to boundaries of shocks (e.g. end points of shock lines for $d = 2$).

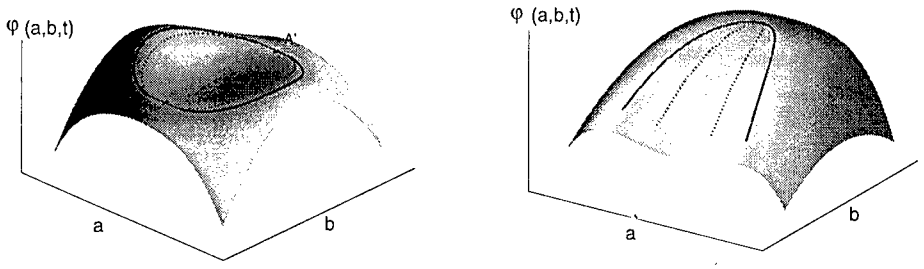


Figure 2: The Lagrangian potential in two dimensions, just after a preshock (left) and in the neighborhood of a kurtoparabolic point (right). Continuous lines: separatrices between the regular part and the ruled surface of the convex hull; dotted lines: vanishing of the Jacobian of the Lagrangian map. A and A' are a pair of kurtoparabolic points born with the shock.

We just indicate general ideas involved in the determination of the density

pdf for random initial conditions (which need not be homogeneous). The determination of the large-ρ tail of the cumulative probability distribution of the density is equivalent to finding the fraction of Eulerian space-time where ρ exceeds a given value. The latter is determined by changing from Eulerian to Lagrangian coordinates and using a suitable normal form (i.e. a Taylor expansion to the relevant order) of the Lagrangian potential near a kurtoparabolic point. The theory is rather different in one dimension and higher dimensions, because kurtoparabolic points are persistent only in the latter case. However, the scaling law for the resulting pdf, namely $\propto \rho^{-7/2}$, is the same in all dimensions. In fact, when $d \geq 2$, two orthogonal spatial directions play the same role as space and time in one dimension.

3 Detecting Navier–Stokes singularities

It is clear that the algebraic tail of the pdf of velocity gradients or of density for burgulence comes from identified singularities. Measurements of pdf's for space or time derivatives of Eulerian velocities for incompressible three-dimensional Navier–Stokes turbulence have not revealed power law tails, but such tails may just have been, so far, "lost in the experimental noise". There has indeed been considerable speculations about singularities of the Navier–Stokes equations in the inviscid limit. If singularities with divergent gradients are present, they will give power-law tails, at least as intermediate asymptotics when the viscosity is small (the converse is however not true, since statistical effects not related to singularities can also give power laws). The confirmed absence of power laws would probably rule out singularities.

References

[1] W. E, K. Khanin, A. Mazel and Y.G. Sinai. Probability distribution functions for the random forced Burgers equation. *Phys. Rev. Lett.*, 78:1904–1907, 1997.

[2] U. Frisch, J. Bec and B. Villone. Singularities and the distribution of density in the Burgers/adhesion model. *Physica* D, submitted, 1999. e-print: cond-mat/9912110.

[3] J. Bec and U. Frisch. Probability distribution functions of derivatives and increments for decaying Burgers turbulence. *Phys. Rev.* E, 61:1395–1402, 2000.

[4] J. Bec, U. Frisch and K. Khanin. Kicked Burgers turbulence. *J. Fluid Mech.*, submitted, 1999. e-print: chao-dyn/9910001.

[5] A. Noullez and M. Vergassola. A fast algorithm for discrete Legendre transforms. *J. Sci. Comp.*, 9:259–281, 1994.

XXVIII

Miscellaneous

ADVANCES IN TURBULENCE VIII
Proceedings of the Eighth European Turbulence Conference
C. Dopazo et al. (Eds.)
© CIMNE, Barcelona 2000

Fossils of turbulence and non-turbulence in the primordial universe: the fluid mechanics of dark matter

Carl H. Gibson

Departments of Mechanical and Aerospace Engineering
and Scripps Institution of Oceanography
University of California at San Diego, La Jolla, CA 92093-0411, USA Contact
e-mail:cgibson@ucsd.edu, http://www-acs.ucsd.edu/~ ir118

1 Introduction

Was the primordial universe turbulent or non-turbulent soon after the Big Bang? How did the hydrodynamic state of the early universe affect the formation of structure from gravitational forces, and how did the formation of structure by gravity affect the hydrodynamic state of the flow? What can be said about the dark matter that comprises 99.9% of the mass of the universe according to most cosmological models? Space telescope measurements show answers to these questions persist literally frozen as fossils of the primordial turbulence and nonturbulence that controlled structure formation, contrary to standard cosmology which relies on the erroneous Jeans 1902 linear-inviscid-acoustic theory and a variety of associated misconceptions (e. g., cold dark matter). When effects of viscosity, turbulence, and diffusion are included, vastly different structure scenarios and a clear explanation for the dark matter emerge [1]. From Gibson's 1996 theory the baryonic (ordinary) dark matter is comprised of proto-globular-star-cluster (PGC) clumps of hydrogenous planetoids termed "primordial fog particles"(PFPs), observed by Schild 1996 as "rogue planets ... likely to be the missing mass" of a quasar lensing galaxy [2]. The weakly collisional non-baryonic dark matter diffuses to form outer halos of galaxies and galaxy clusters [3].

2 Fluid mechanics of structure formation

Before the 1989 Cosmic Microwave Background Experiment (COBE) satellite, it was generally assumed that the fluid universe produced by the hot Big Bang singularity must be enormously turbulent, and that galaxies were nucleated by density perturbations produced by this primordial turbulence. George Gamov 1954 suggested galaxies were a form of "fossil turbulence", thus coining a very

useful terminology for the description of turbulence remnants in the stratified ocean and atmosphere, Gibson 1980 – 1999. Other galaxy models based on turbulence were proposed by von Weizsacker 1951, Chandrasekhar 1952, Ozernoi and colleagues in 1968 – 1971, Oort 1970, and Silk and Ames 1972. All such theories were rendered moot by COBE measurements showing temperature fluctuation values $\delta T/T$ of only 10^{-5} at 300,000 years compared to at least 10^{-2} for the plasma if it were turbulent. At this time, the opaque plasma of hydrogen and helium had cooled to 3,000 K and become a transparent neutral gas, revealing a remarkable photograph of the universe as it existed at 10^{13} s, with spectral redshift z of 1100 due to straining of space at rate $\gamma \approx 1/t$.

Why was the primordial plasma before 300,000 years not turbulent? Steady inviscid flows are absolutely unstable. Turbulence always forms in flows with Reynolds number $Re = \delta v L/\nu$ exceeding $Re_{cr} \approx 100$, where ν is the kinematic viscosity of a fluid with velocity differences δv on scale L, Landau-Lifshitz 1959. Thus either ν at 10^{13} s had an unimaginably large value of 9×10^{27} m^2 s^{-1} at horizon scales $L_H = ct$ with light speed velocity differences c, or else gravitational structures formed in the plasma at earlier times and viscosity plus buoyancy forces of the structures prevented strong turbulence.

3 Fossils of first structure (proto-supervoids)

The power spectrum of temperature fluctuations δT measured by COBE peaks at a length 3×10^{20} m which is only 1/10 the horizon scale ct, suggesting the first structure formed earlier at 10^{12} s (30,000 years). The photon viscosity of the plasma $\nu = c/n\sigma_\tau$ was 4×10^{26} m^2 s^{-1} then, with free electron number density $n = 10^{10}$ m^{-3} and σ_τ the Thomson cross section for Compton scattering. The baryon density ρ was 3×10^{-17} kg m^{-3}, which matches the density of present globular-star-clusters as a fossil of the weak turbulence at this time of first structure. The fragmentation mass $\rho(ct)^3$ of 10^{46} kg matches the observed mass of superclusters of galaxies, the largest structures of the universe. Because $Re \approx Re_{crit}$, the horizon scale $ct = 3 \times 10^{20}$ m matches the Schwarz viscous scale $L_{SV} = (\gamma\nu/\rho G)^{1/2}$ at which viscous forces $F_V = \rho\gamma L^2$ equal gravitational forces $F_G = \rho^2 G L^4$, and also the Schwarz turbulence scale $L_{ST} = \varepsilon^{1/2}/(\rho G)^{3/4}$ at which inertial-vortex forces $F_I = \rho\varepsilon^{2/3}L^{8/3}$ equal F_G, where ε is the viscous dissipation rate [1]. Further fragmentation to proto-galaxy scales is predicted in this scenario, with the nonbaryonic dark matter diffusing to fill the voids between constant density proto-supercluster to proto-galaxy structures for scales smaller than the diffusive Schwarz scale $L_{SD} = (D^2/\rho G)^{1/4}$, where D is the diffusivity of the nonbaryonic dark matter [1]. Fragmentation of the nonbaryonic material to form superhalos implies $D = 10^{28}$ m^2 s^{-1}, from observation of present superhalo sizes L_{SD} and densities ρ [3], trillions of times larger than D for H-He gas with the same ρ.

4 Fossils of the first condensation (as "fog")

Photon decoupling dramatically reduced viscosity values to $\nu = 3 \times 10^{12}$ m^2 s^{-1} in the primordial gas of the nonturbulent 10^{20} m size proto-galaxies, with $\gamma = 10^{-13}$ s^{-1} and $\rho = 10^{-17}$ kg m^{-3}, giving a PFP fragmentation mass range $M_{SV} \approx M_{ST} \approx 10^{23} - 10^{25}$ kg, the mass of a small planet. Pressure decreases in voids during fragmentation as the density decreases, to maintain constant temperature from the perfect gas law $T = p/\rho R$, where R is the gas constant, for scales smaller than the acoustic scale $L_J = V_S/(\rho G)^{1/2}$ of Jeans 1902, where V_S is the sound speed. However, the pressure cannot propagate fast enough in voids larger than L_J so they cool. Hence radiation from the warmer surroundings can heat such large voids, increasing their pressure and accelerating the void formation, causing a fragmentation within proto-galaxies at the Jeans mass of 10^{35} kg, the mass of globular-star-clusters. These proto-globular-cluster (PGC) clumps of PFPs provide the materials of construction for everything else to follow, from stars to people. Leftover PGCs and PFPs thus comprise present galactic dark matter inner halos which typically have expanded to about 10^{21} m (30 kpc) of the core and exceed the luminous (star) mass by factors of $10-30$.

5 Observations

Observations of quasar image twinkling frequencies reveal that the point mass objects which dominate the mass of the lens galaxy are not stars, but "rogue planets... likely to be the missing mass", Schild 1996, independently confirming this prediction of Gibson 1996. Other evidence of the predicted primordial fog particles (PFPs) is shown in Hubble Space Telescope photographs, such as thousands of 10^{25} kg "cometary globules" in the halo of the Helix planetary nebula and possibly like numbers in the Eskimo planetary nebula halo. These dying stars are very hot (100,000 K versus 6,000 K normal) so that many PFPs nearby can be brought out of cold storage by evaporation to produce the 10^{13} m protective cocoons that make them visible to the HST at 10^{19} m distances.

6 Summary and conclusions

The Figure summarizes the evolution of structure and turbulence in the early universe, as inferred from the present nonlinear fluid mechanical theory. It is very different, very early, and very gentle compared to the standard model, where structure formation in baryonic matter is forbidden in the plasma epoch because L_J is larger than $L_H = ct$ and galaxies collapse at 140 million years (redshift z=20) producing 10^{36} kg Population III superstars that explode and re-ionize the universe to explain the missing gas (sequestered in PFPs). No such stars, no galaxy collapse, and no re-ionization occurs in the present theory. To produce the structure observed today, the concept "cold dark matter" (CDM)

was invented; that is, a hypothetical non-baryonic fluid of "cold" (low speed) collisionless particles with adjustable L_J small enough to produce gravitational potential wells to drive galaxy collapse. Cold dark matter is unnecessary in the present theory. Even if it exists it would not behave as required by the standard model. Its necessarily small collision cross section requires $L_{SD} \gg L_J$ so it would diffuse out of its own well, without fragmentation if $L_{SD} \gg L_H$. The immediate formation of "primordial fog particles" from all the neutral gas of the universe emerging from the plasma epoch permits their gradual accretion to form the observed small ancient stars in dense globular-star-clusters known to be only slightly younger than the universe. These could never form in the intense turbulence of galaxy collapse in the standard model because L_{ST} scales would be too large.

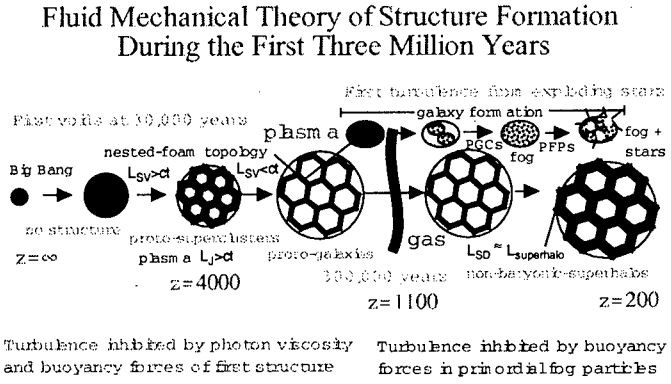


Figure 1: Evolution of structure and turbulence in the early universe

References

[1] C. H. Gibson. Turbulence in the ocean, atmosphere, galaxy, and universe. *Applied Mechanics Reviews*, 49:299–315, 1996.

[2] R. E. Schild. Microlensing variability of the gravitationally lensed quasar Q0957+561 A,B. *Astrophysical Journal*, 464:125–130, 1996.

[3] J. A. Tyson and P. Fischer. Measurement of the mass profile of Abell 1689. *Astrophysical Journal*, 446:L55–L58, 1995.

ADVANCES IN TURBULENCE VIII
Proceedings of the Eighth European Turbulence Conference
C. Dopazo et al. (Eds.)
© CIMNE, Barcelona 2000

Power fluctuations in confined turbulence, analogy with finite size critical phenomena

J.-F. Pinton[3], P.C.W. Holdsworth[3], R. Labbé[4]
S.T. Bramwell[1] and J.-Y. Fortin[2]

[1]Univ. College London
[2]Univ. Washington, Seattle
[3]École Normale Supérieure de Lyon
[4]Univ. de Santiago de Chile

Contact e-mail: jean-francois.pinton, peter.holdsworth@ens-lyon.fr

1 Power fluctuations in a confined turbulent flow

In the study of turbulence, much work has been devoted to the description of small scale properties. Experimental data and models have been concerned with the scaling of local quantities such as the velocity increment $\delta u(r) \equiv < u(x+r) - u(x) >_x$. It has then been shown that a key feature is the statistics of the energy transfer rate from the integral to the dissipative scale. However in the development of a statistical description of turbulence it will be necessary to link these observations to the behaviour of global quantities, as is done in statistical thermodynamics and dynamical systems driven far from equilibrium [1]. In particular, little is known about the global power consumption P of a fully turbulent flow. The standard phenomenology assumes that P is constant in time, or that it has very small Gaussian fluctuations. Recent studies, both experimental [2], and numerical [3] have shown that this is not always so, at least for finite Reynolds numbers. We present experimental measurements of $P(t)$ in the case of a closed flow, in an experiment that covers two decades in Reynolds number. The flow is confined in a cylinder and driven by two counter-rotating coaxial disks. The power consumption of the flow is measured from the voltage and current consumption of the motors driving the disks [2]. Using gases of varying molecular weights, Reynolds numbers between 15000 and 500,000 are achieved [4].

The power consumption $P_1(t)$ and $P_2(t)$ of the motors driving the two disks are shown in Fig 1, where simultaneous power drops can be seen over a wide range of amplitudes. The data illustrates that coherent fluid motion occurs over the entire flow and that the coherent flow structure is responsible for power

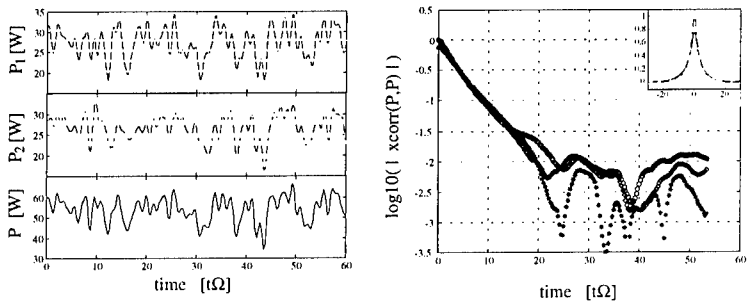


Figure 1: (a) Variation with time (measured in units of the discs rotation period) of the injected power (measured in Watts, for each disk and total), (b) cross-correlation ($*$) and auto-correlation ($\circ, \square$) functions in time of P_1 and P_2.

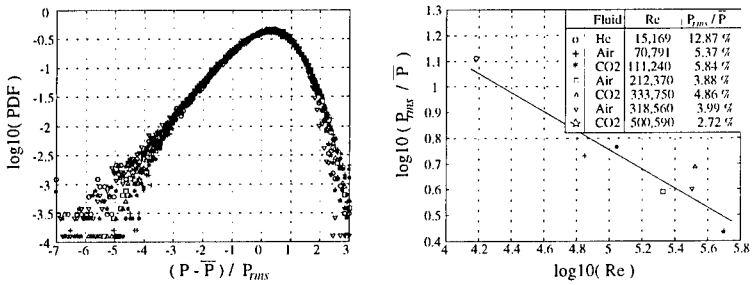


Figure 2: (a) PDF of normalized power fluctuations over the entire range of explored Re. (b) Evolution of the rms fluctuation intensity $P_{rms}/\overline{P}$. The conditions and plot symbols for both plots are given in the inset of figure (b).

fluctations over the whole range of observed variation. A results of this spatial correlation is that one cannot expect the power fluctuations to obey Gaussian statistics as the system cannot, at any instant, be divided into statistically independent parts. The PDFs for the power consumption, normalized to the rms intensity, are shown in figure 2(a), for experiments that span almost two orders of magnitude in Re. We observe that when plotted in normalized units $(P - \overline{P})/P_{\rm rms}$, all the measurements collapse onto a single curve. There is no evidence that, as Re increases, the power fluctuations will eventually reduce to Gaussian behaviour.

The variation of the relative intensity of the power fluctuations is also of interest. We first note that the mean value of the power consumption is set by the rate at which kinetic energy is supplied at large scales. Dimensional analysis yields $\overline{P} = K\rho L^2 U^3$. As for the value of the rms fluctuations, the standard turbulence phenomenology would assume that $P_{rms}/\overline{P}$ should decrease with increasing Re as the square root of the effective number of degrees of freedom, i.e. as $Re^{-9/8}$. The variation measured in our experiment is plotted in figure 2(b). We observe [4] a very slow decrease of $P_{rms}/\overline{P} \sim Re^{-\alpha}$ with $\alpha = 0.33 \pm 0.05$, although a logarithmic behavior cannot be ruled out.

2 Magnetization in the critical 2DXY model

These results can all be put into the context of critical phenomena where the diverging correlation length ensures the same property: systems, whatever their size, can never be divided into statistically independent mesoscopic regions. We have observed [5] that power fluctuations in confined turbulence and the global fluctuations in the magnetization of the 2DXY spin model at a critical temperature share same PDF, despite the systems being so utterly dissimilar. We show here that this PDF which can be calculated analytically for the spin model is universal in the sense that it does not depend on system size.

In the spin wave limit, the Hamiltonian of the 2DXY model reads $H = -J\sum_{\langle i,j\rangle}\left[1-(\theta_i-\theta_j)^2/2\right]$ where J is the near neighbour exchange constant for angular variables θ_i that occupy a square lattice with periodic boundary conditions. The magnetization is defined as $m = 1/N\sum_i \cos(\theta_i - \overline{\theta})$, where $\overline{\theta}$ is the instantaneous mean orientation. This model is critical at all temperatures and for an infinite system has algebraic correlations on all length scales. In the finite system the lattice constant a and the system sizes $L = a\sqrt{N}$ define a natural inertial range. The model can be diagonalized in Fourier space, which makes it very convenient for analytical work. The PDF of the magnetization $P(m)$ can be expressed as the Fourier transform of a sum over its moments. In Ref. [6] it was shown that the moments are given by $\mu_n = g_n(g_2/2)^{-n/2}\sigma^n$, where σ^2 is the variance and the $g_k (k = 2, 3, 4...)$ are sums related to the lattice Green function in Fourier space $G(\mathbf{q})$: $g_k = \sum_{\mathbf{q}} G(\mathbf{q})^k/N^k$. The fact that $\mu_n \propto \mu_1^n$ means that a change of N or T is equivalent to a linear transformation of the variate m; hence, the PDF can be expressed in a universal form. As shown in [6] the moment series can be resummed to give the following expression, exact to leading order in N:

$$P(y) = \int_{-\infty}^{+\infty} \frac{dx}{2\pi\sigma} \exp\left[iyx + \sum_{k=2}^{\infty} \frac{g_k}{2k}\left(ix\sqrt{\frac{2}{g_2}}\right)^k\right]. \tag{1}$$

Here $y = (m - \langle m\rangle)/\sigma$ and $\langle m\rangle$ is the mean of the distribution. Including only g_2 in (1) would give a Gaussian PDF with variance σ^2. However the terms for $k > 2$ cannot be neglected and $\Pi(y) = \sigma P(y)$ is a non-Gaussian.

Asymptotically we find [8] $\Pi(y) \propto |y|\exp(+\frac{\pi}{2}by)$ for $y \ll 1$ and $\Pi(y) \propto \exp(-\frac{\pi}{2}e^{b(y-s)})$ for $y \gg 1$, with $b = 8\pi\sqrt{g_2/2} \simeq 1.105$ and $s = 0.745$. The asymptotic forms are an accurate approximation to Eqn. (1) for large $|y|$; they also suggest for $\Pi(y)$ the following functional form

$$\Pi(y) = K\left(e^{x-e^x}\right)^a; x = b(y-s),\ a = \pi/2. \tag{2}$$

This function must obey the three conditions of unit area, zero mean and unit variance, which fixes b, s and K to values slightly different to those found analytically: $b = 0.938$, $s = 0.374$, $K = 2.14$. An alternative approach is to

choose the parameters in the generalized function $Ne^{a(b(y-s)-e^{b(y-s)})}$ such that the first four Fourier coefficients match Eqn.(1). In this case we find $a = 1.58$, $K = 2.16$, $b = 0.934$, $s = 0.373$, in satisfying agreement with the previous estimates. The ratios of the higher order Fourier coefficients differ from unity only very slowly, showing that Eqn. (2) is an accurate approximation to $\Pi(y)$. This has been accurately confirmed by numerical simulation [8]. In Fig. 3 we show that Eqn. (2) does indeed give an excellent fit to the power consumtion data from the turbulence experiment, thus confirming our analogy with a critical system of finite size. Finally we note that note Eqn.(2) is reminiscent of Gumbel's first asymptote from extremal statistics [7]. However, our finding that $a = \pi/2$ rather than an integer value suggests that the fluctuations are not dominated by single variables; rather, it is the collective excitations of the whole system that are responsible [8].

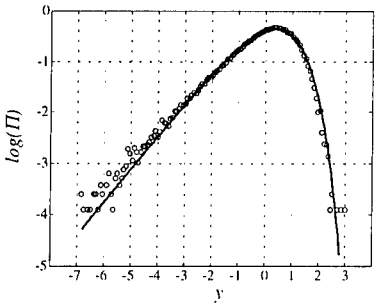


Figure 3: The PDF $\Pi(y)$ as found from a numerical Fourier transform of Eqn. (1) (long dash), from Eqn. (2) (solid) and by Molecular Dynamics simulation of a system of $N = 1024$ classical rotors (dotted).

References

[1] Gallavotti G., Cohen E.D.G., *Phys. Rev. Lett.*, **74**, 2694-2697, (1995).

[2] Labbé R., Pinton J.-F., Fauve S., *J. Phys. II France* **6**, 1099 (1996).

[3] Pumir A., it Phys. Fluids A **8**, 3112 (1996).

[4] Pinton J.-F., Holdsworth P.C.W., Labbé R., *Phys. Rev. E.*, **60**, R2452, (1999).

[5] Bramwell S., Holdsworth P., Pinton J.-F., *Nature*, **396**, 552-554, (1998).

[6] P. Archambault *et al.*, *J. Appl. Phys.* **83**, 7234-7236 (1998).

[7] E.J. Gumbel *Statistics of Extremes*, Columbia University Press, (1958).

[8] S.T. Bramwell *et al.*, *Phys. Rev. Lett.*, to appear (2000).

ADVANCES IN TURBULENCE VIII
Proceedings of the Eighth European Turbulence Conference
C. Dopazo et al. (Eds.)
© CIMNE, Barcelona 2000

Reduction and long time behaviour of homogeneous turbulence under spatially constant mean-velocity gradient

M. Oberlack[1] and M. Barakat[2]

[1]Institut für Technische Mechanik, RWTH Aachen
Templergraben 64, 52056 Aachen, Germany
[2]Lehrstuhl B für Mathematik, RWTH Aachen
Templergraben 64, 52056 Aachen, Germany

Contact e-mail: M.Oberlack@itm.rwth-aachen.de

1 Introduction

Since the early studies of von Kármán & Howarth [3] on isotropic turbulence and of Batchelor [1] and Chandrasekhar [2] on axisymmetric turbulence research on homogeneous flows has in recent years focused on flows with non-zero mean velocity gradient where

$$\frac{\partial \bar{u}_i}{\partial x_j} = \bar{B}_{ij}(t) \quad \text{and} \quad \frac{\partial \bar{u}_k}{\partial x_k} = \bar{B}_{kk}(t) = 0 \tag{1}$$

i.e. $\bar{B}_{ij}$ is at most a function of time. These type of flows are of great importance due to their exemplary character for practical flows.

As for the von Kármán-Howarth and the Chandrasekhar equation it is known that homogeneous flows tend to self-similar states as $t \to \infty$. Several of these limiting states have been implemented into common RANS models.

Subsequently we derive the complete set of *all* those $\bar{B}_{ij}(t)$ by utilizing group theoretical methods (Lie groups) which allow for a reduction of the dependent variables and a self-similar states as $t \to \infty$.

2 Multi-point correlation equation for homogeneous flows

In the analysis to follow we will only investigate the two-point correlation equation. However, it is important to note that all results to follow are consistent with *all* multi-point correlation equations up to infinite order. In the limit $Re \to \infty$

and for sufficient large correlation distances, i.e. $|r| \gg \eta$ where η is the Kolmogorov length, the two-point correlation equation may be written as

$$\frac{\partial R_{ij}}{\partial t} = -R_{kj}\,\bar{B}_{ik}(t) - R_{ik}\bar{B}_{jk}(t) - \bar{B}_{kl}(t)r_l\,\frac{\partial R_{ij}}{\partial r_k} + \frac{\partial \overline{pu}_j}{\partial r_i} - \frac{\partial \overline{u_i p}}{\partial r_j} + \frac{\partial}{\partial r_k}\left[R_{(ik)j} - R_{i(jk)}\right] - 2\,\Omega_k\,\left[e_{kli}R_{lj} - e_{klj}R_{il}\right]\ , \tag{2}$$

where R_{ij} is the two-point correlation tensor, $\overline{pu}_j$ is the pressure-velocity vector and $R_{(ik)j}$ is the two-point triple correlation tensor.

Viscosity is only of leading order for the dissipation term $-2\nu\frac{\partial^2 R_{ij}}{\partial r_k \partial r_k}$ and $|r| = \mathcal{O}(\eta)$. Since the dissipation term is "driven" by the large eddies we can deduce that once a solution for R_{ij} in (2) is obtained the dissipation term may be obtained by matching the correlation functions in the limit $r \to 0$. In other words dissipation may be derived from the one-point correlation equation.

3 Symmetries and scaling laws of homogeneous turbulence

Origin from the Navier-Stokes equations in the limit of infinite Reynolds number we may expect the maximum symmetry group for equation (2) to comprise two scaling groups X_{s_1} (scaling of space) and X_{s_2} (scaling of time), three rotation groups $\mathrm{X}_{r_{12}}$, $\mathrm{X}_{r_{23}}$ and $\mathrm{X}_{r_{31}}$ and translation in time X_t. Since the symmetry groups constitute a linear vector space we may write the linear combination

$$\mathrm{X}_{IIT} = k_t\mathrm{X}_t + k_{r_{12}}\mathrm{X}_{r_{12}} + k_{r_{23}}\mathrm{X}_{r_{23}} + k_{r_{31}}\mathrm{X}_{r_{31}} + k_{s_1}\mathrm{X}_{s_1} + k_{s_2}\mathrm{X}_{s_2}, \tag{3}$$

where the k_i are arbitrary constants. Representation details on the X_i are given in Oberlack [4].

For mathematical convenience we separate $\bar{B}_{ij}$ into a symmetric and an anti-symmetric part $\bar{S}_{ij}$ and $\bar{A}_{ij}$ respectively. Without loss of generality we may rotate the coordinate system as such that $\bar{S}_{ij}$ is diagonal. Hence we obtain

$$\bar{B}_{ij} = \underbrace{\begin{pmatrix} \bar{S}_1 & 0 & 0 \\ 0 & \bar{S}_2 & 0 \\ 0 & 0 & -(\bar{S}_1+\bar{S}_2) \end{pmatrix}}_{\bar{S}_{ij}} + \underbrace{\begin{pmatrix} 0 & \bar{A}_{12} & -\bar{A}_{31} \\ -\bar{A}_{12} & 0 & \bar{A}_{23} \\ \bar{A}_{31} & -\bar{A}_{23} & 0 \end{pmatrix}}_{\bar{A}_{ij}}\ . \tag{4}$$

Cases with $\bar{B}_{ij} = 0$ will not be considered here since they have exhaustively been discussed in the literature [1, 2, 3]. In isotropic turbulence all three rotation groups are considered simultaneously while axisymmetric turbulence encompass only one rotation group.

For $\bar{B}_{ij} \neq 0$ two general cases need to be distinguished: constant $\bar{B}_{ij}$ and time-dependent $\bar{B}_{ij}$. Due to space limitations only parts of the results can be presented. Details may be taken from [4].

3.1 Constant $\bar{B}_{ij}$

For any combination of parameters $\bar{B}_{ij}$ and and system rotation rate Ω_k scaling of time is always broken and hence $k_{s_2} = 0$. Physically speaking this is due to the external time scale $t_{\bar{B}} = 1/\|\bar{B}_{ij}\|$ or $t_\Omega = 1/|\Omega_k|$ which precludes an arbitrary scaling of time. In addition it is shown that at most *one* rotation group is admitted. This is if $\bar{S}_{ij}$ describes axisymmetric expansion or contraction and if $\bar{A}_{ij}$ and Ω_k represent rotation about the same axis. If at least two of $\bar{S}_{ij}$, $\bar{A}_{ij}$ and Ω_k are non-zero and deviate from this alignment no rotation group is admitted.

The corresponding reduction for the long-time behaviour is due to the new coordinates

$$\tilde{r}_k = r_k \exp\left(-\frac{k_{s_1}}{k_t}t\right) \quad , \quad R_{ij} = \exp\left(2\frac{k_{s_1}}{k_t}t\right)\tilde{R}_{ij}(\tilde{r}), \tag{5}$$

independent of the fact whether a rotation group is admitted or not.

3.2 Time-dependent $\bar{B}_{ij}$

For the present case $\bar{B}_{ij}$ will not be separated into $\bar{S}_{ij}$ and $\bar{A}_{ij}$. Using symmetry group analysis it turned out that the maximum number of symmetries are admitted by equation (2) if $\bar{B}_{ij}$ is a solution of the equation

$$\frac{\mathrm{d}\bar{B}_{ij}}{\mathrm{d}t}(k_{s_2}t + k_t) = -k_{s_2}\bar{B}_{ij} + k_{r_{il}}\bar{B}_{lj} - \bar{B}_{il}k_{r_{lj}} \ . \tag{6}$$

In contrast to the previous cases where the group parameter k_i were merely determined by the form of $\bar{B}_{ij}$ all constants in (6) can be chosen freely. Due to space limitation we cannot give all possible solutions of (6) and will restrict to the case when $k_{r_{ij}} \neq k_t \neq 0$ and k_{s_2} is either zero or non-zero:

$$\begin{aligned}
\bar{S}_{ij} \ = \ & \Theta(t)\Big\{ \bar{S}^0_{ij}\cos(2\,\mathsf{k}_r\,t_*) + \left(e_{ikl}\check{k}_{r_l}\bar{S}^0_{kj} + e_{jkl}\check{k}_{r_l}\bar{S}^0_{ki}\right)\frac{\sin(2\,\mathsf{k}_r\,t_*)}{2\,\mathsf{k}_r} \\
& + \left(\check{k}_{r_i}\check{k}_{r_k}\bar{S}^0_{kj} + \check{k}_{r_j}\check{k}_{r_k}\bar{S}^0_{ki} - \frac{2}{3}\,\delta_{ij}\,\check{k}_{r_k}\bar{S}^0_{kl}\check{k}_{r_l}\right)\frac{\cos(\mathsf{k}_r\,t_*) - \cos(2\,\mathsf{k}_r\,t_*)}{\mathsf{k}_r^2} \\
& + \left(\check{k}_{r_i}e_{klj}\check{k}_{r_k}\bar{S}^0_{lm}\check{k}_{r_m} + \check{k}_{r_j}e_{kli}\check{k}_{r_k}\bar{S}^0_{lm}\check{k}_{r_m}\right)\frac{\sin(2\,\mathsf{k}_r\,t_*) - \sin(\mathsf{k}_r\,t_*)}{2\,\mathsf{k}_r^3} \\
& + \left(\check{k}_{r_i}\check{k}_{r_j} + \frac{2}{3}\delta_{ij}\right)\check{k}_{r_k}\bar{S}^0_{kl}\check{k}_{r_l}\,\frac{3 + \cos(2\,\mathsf{k}_r\,t_*) - 4\cos(\mathsf{k}_r\,t_*)}{2\,\mathsf{k}_r^4}\Big\}
\end{aligned} \tag{7}$$

and

$$\begin{aligned}
\bar{A}_{ij} \ = \ & \Theta(t)\Big\{ \bar{A}^0_{ij} + \left(\check{k}_{r_i}\bar{A}^0_{jk}\check{k}_{r_k} - \check{k}_{r_j}\bar{A}^0_{ik}\check{k}_{r_k}\right)\frac{1 - \cos(\mathsf{k}_r t_*)}{\mathsf{k}_r^2} \\
& + \left(\bar{A}^0_{ik}e_{kjl}\check{k}_{r_l} - e_{ikl}\check{k}_{r_l}\bar{A}^0_{kj}\right)\frac{\sin(\mathsf{k}_r t_*)}{\mathsf{k}_r}\Big\} \ .
\end{aligned} \tag{8}$$

where

$$\Theta(t) = 1 \ , \qquad t_* = \frac{t}{k_t} \qquad \text{for} \quad k_{s_2} = 0 \ , \tag{9}$$

$$\Theta(t) = \frac{k_t}{k_{s_2}\, t + k_t} \ , \quad t_* = \frac{1}{k_{s_2}} \ln\left(\frac{k_{s_2}\, t + k_t}{k_t}\right) \quad \text{for} \quad k_{s_2} \neq 0 \ , \tag{10}$$

$$\check{k}_{r_i} = \frac{1}{2} e_{ijk}\, k_{r_{jk}} \ , \quad \mathsf{k}_r^2 = k_{r_{12}}^2 + k_{r_{23}}^2 + k_{r_{31}}^2 \tag{11}$$

and $\bar{S}_{ij}^0$ and $\bar{A}_{ij}^0$ denote initial conditions. For brevity the corresponding reduction for the long-time behaviour is given in short form

$$\tilde{r}_k \propto \theta_1(t)\,\{\cdot\} \ , \quad R_{ij} \propto \theta_2(t)^2\,\{\cdot\}\,, \tag{12}$$

where

$$\theta_1(t) = \exp\left(\frac{k_{s_1}}{k_t} t\right) \ , \quad \theta_2(t) = \exp\left(\frac{k_{s_1}}{k_t} t\right) \qquad \text{for } k_{s_2} = 0, \tag{13}$$

$$\theta_1(t) = \left(t + \frac{k_t}{k_{s_2}}\right)^{\frac{k_{s_1}}{k_{s_2}}} \ , \ \theta_2(t) = \left(t + \frac{k_t}{k_{s_2}}\right)^{\frac{k_{s_1}}{k_{s_2}} - 1} \quad \text{for } k_{s_2} \neq 0, \tag{14}$$

and the terms in curly brackets are trigonometric function of time (see [4]).

It should be noted that from the constants in (13) and (14) only the group parameter corresponding to scaling of space (k_{s_1}) cannot be determined freely and will adjust due to the flow.

4 Summary and conclusion

Systematic symmetry reductions have been carried out for the two- and multipoint correlation equations leading to equations analogous to the von Kármán-Howarth equation. It is important to note that since group theory has been used the analysis is complete in the sense that no other than those $\bar{B}_{ij}$ derived above exist which lead to reductions in the correlation equations.

References

[1] G. K. Batchelor. The Theory of Axisymmetric Turbulence. *Proc. Roy. Soc. A*, 186:480–502, 1946.

[2] S. Chandrasekhar. The Theory of Axisymmetric Turbulence. *Phil. Trans. Roy. Soc. Lond. A*, 242:557–577, 1950.

[3] T. von Kármán, L. Howarth. On the Statistical Theory of Isotropic Turbulence. *Proc. Roy. Soc. A*, 164:192–215, 1938.

[4] M. Oberlack. Symmetrie, Invarianz und Selbstähnlichkeit in der Turbulenz. *Habilitation thesis, RWTH Aachen, Germany*, 2000.

ADVANCES IN TURBULENCE VIII
Proceedings of the Eighth European Turbulence Conference
C. Dopazo et al. (Eds.)
© CIMNE, Barcelona 2000

Interaction of worm-like micelles with turbulent flow

Z. Chara and J. Myska

Institute of Hydrodynamics,AS CR
Pod Patankou 5, Prague 6, CZECH REPUBLIC

Contact e-mail: chara@ih.cas.cz

1 Introduction

There are two main types of additives that could considerably reduce the friction - polymers and surfactants. Long chain polymers are very efficient at concentrations even less than 1 ppm, but their main disadvantage is their non-reversible degradability when passing through pumps or other region with shear stress exceeding a critical level. On other hand, molecules of surface-active agents (surfactants) dissolved in water form large aggregates - micelles. Many geometrical shapes of the micelles can be found but under some specific conditions the worm-like geometry is formed. With additional increase of surfactant concentration the worm-like micelles start to build up hyper-structures that are aligned in flow direction under shear flow. They can considerably damp the turbulence, which results in a decrease of pressure losses in turbulent flows. When the flow shear rate exceeds a critical value, the drag reduction effectiveness is temporally lost, but decreasing the shear rate below a critical value the original drag reduction efficiency is regained. The present paper deals with experimental investigation of turbulent structure of drag reducing worm-like surfactant systems. We have investigated two types of surfactant aqueous solutions - a cationic surfactant CTAC (cetyl trimethyl ammonium chloride) with NaSal (Sodium salicylate) as counterion (concentration 0.4/0.5 g/l) and a biologically degradable zwitterionic surfactant SPE98330 (N-cetylbetaine in mixture with Na-dodecylbenzenesulphonate, product of Akzo Chemicals, Sweden, concentration 1.1 g/l).

2 Experimental set-up

The experiments were done in a horizontal smooth glass pipe DN 40 (inner diameter 40 mm). The measurements were performed by means of LDA technique. We have used two-component fibre LDA system 60X (Dantec) with two BSA (Burst Spectrum Analyzer) to evaluate primary Doppler signals. Inductive flow

meter and differential transducer Hottinger-Baldvin were used to measure bulk velocities and pressure losses, respectively. Velocity measurements were made in the distance $265D$ from entering section. Both surfactants were dissolved in tap water and according to the recommendation of the producer, Trilon A (Nitriloacetic acid, Na salt) was added to the SPE98330 solution. Apparent viscosities measured on a capillary viscometer at 20^oC were 1.2 mPas (SPE98330) and 1.87 mPas (CTAC/NaSal).

3 Results and discussion

Influence of temperature on turbulent friction behaviour is shown in Fig.1, where Colebrook-White friction factor is plotted versus Reynolds number. Here, the solvent viscosity was used to calculate the Reynolds number. Blasius curve and Virk's maximum drag reduction asymptote for polymers [3] are plotted in full lines. Friction factors of both surfactants (mainly for higher temperature) are well bellow the polymer asymptote which indicates that the turbulence behaviour of the surfactants is different compared to polymers and drag reduction effectiveness is even higher than 90 per cents [1].

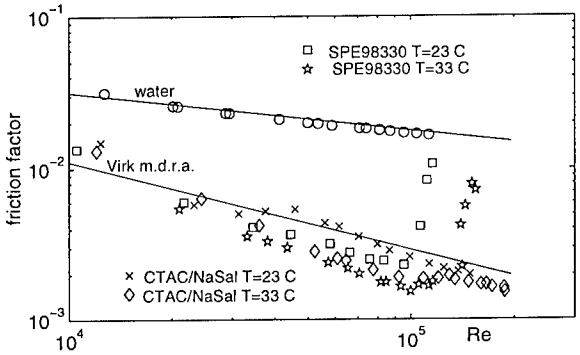


Figure 1: Influence of temperature on friction factor of SPE98330 and CTAC/NaSal.

Fig. 2 and 3 show the dependence of maximum to mean velocity ratio and turbulence intensities of longitudinal velocity component measured in the centre of the pipe on the Reynolds number. The ratio of maximum to mean velocity is much higher than that in water flow and its decrease with Re is more abrupt.When the critical stress is achieved (SPE98330), the micelle network structure is broken down and the maximum velocity is approaching the mean velocity. The turbulence intensities of both surfactants are decreasing with increasing Reynolds number, minimum values are reached just before the micelle network breaks, Fig.3.

Non-dimensional velocity profiles of SPE98330 (Re=79200, T=33^oC), CTAC /NaSal (Re=79400, T=23^oC) and water (Re=79700, T=23^oC) expressed in the wall units (y^+, u^+) are presented in Fig. 4. The velocity data of surfactant

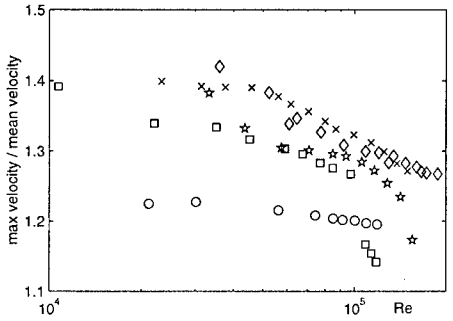


Figure 2: Ratio of maximum to mean velocity versus Reynolds number. Symbols as in Fig.1.

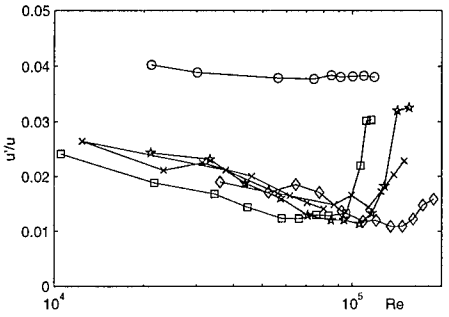


Figure 3: Turbulence intensities of longitudinal velocity component. Symbols as in Fig.1.

solutions exhibit very interesting behaviour. SPE98330 data follow the viscous sublayer up to the value $y^+ = 28$, then continue in the steep buffer zone (the slope of SPE98330 is the steepest one we have ever measured) and finally reach core part of the pipe, where the velocities are practically constant. The velocity profile in the buffer zone of SPE98330 can be approximated by the equation $u^+ = 64.5 \log y^+ - 65.3$.

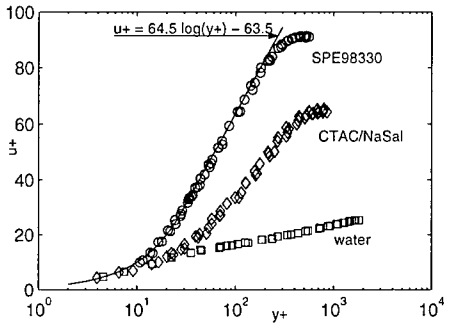


Figure 4: Dimensionless velocity profiles.

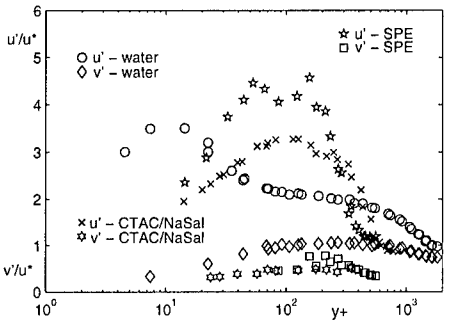


Figure 5: Dimensionless profiles of longitudinal and radial velocity fluctuations.

Profiles of the longitudinal and radial velocity fluctuation components (dimensionless by friction velocity) are shown in Fig. 5 for the same values of Reynolds numbers as in Fig. 4. The maximum of longitudinal fluctuations, which corresponds to the value $y^+ = 11 - 13$ for water flows, is shifted to higher wall distance (about $y^+ = 70 - 100$) and with increasing drag reduction the maximum level is also increasing. On the other hand, radial components are always lower than water data. Due to the great difference of radial and longitudinal components, the turbulence field can not be considered as isotropic even in the pipe centre where such an assumption could be done for water flow. Reynolds

stresses are practically zero in the whole cross section of the pipe, see Fig. 6 that indicates decoupling of u' and v'. To satisfy momentum balance it was confirmed that Reynolds stress deficit (elastic stresses) occurs [2]. This stress deficit can be regarded as mean flow energy interacting with micelle structure. The values of Reynolds stress deficit are shown in Fig. 7 for SPE98330.

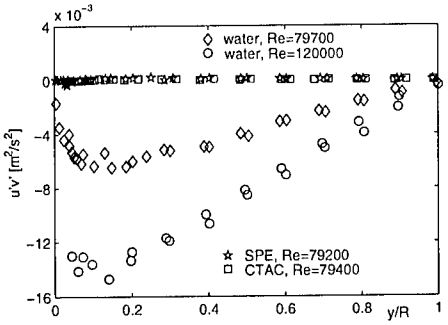


Figure 6: Reynolds stress versus normalized distance y/R.

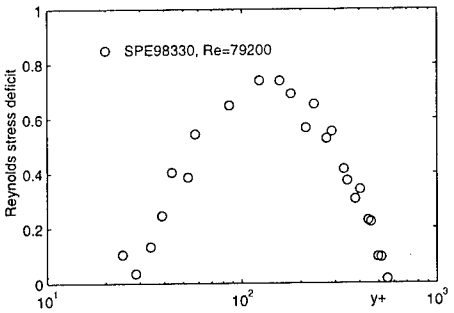


Figure 7: Reynolds stress deficit versus non-dimensional wall distance.

4 Conclusions

Based on the measurements of turbulence characteristics in worm like surfactants following conclusion could be drawn:

- Ratio of maximum to mean velocity is higher than in pure water.
- Turbulence intensities in the centre of the pipe are decreasing with increasing Reynolds number.
- Large amount of mean flow energy is probably consumed on the interaction with micelle network structures.

This research was supported in part under Grant No. A2060804 of the Grant Agency of the ASCR.

References

[1] J. Myska and Z. Chara. New view of the surfactant drag reduction ability. *11th European Drag Reduction Meeting*, Prague, Czech Republic, 32–33,1999.

[2] P. Schummer and W. Thielen. Structure of turbulence in viscoplastic fluids. *Chem. Eng. Commun.*, 4:593–606,1980.

[3] P. S. Virk, H. S. Mickley and K. A. Smith. The ultimate asymptote amd mean flow structures in Toms phenomenon. *ASME, J. Appl. Mech.*, 37:488,1970.

ADVANCES IN TURBULENCE VIII
Proceedings of the Eighth European Turbulence Conference
C. Dopazo et al. (Eds.)
© CIMNE, Barcelona 2000

Numerical Simulations and DPIV Measurements of Pulsatile Flow in Large Stenosed Arteries

A. Borg and L. Fuchs

Department of Heat and Power Engineering/Fluid Mechanics
Lund Institute of Technology, SE-221 00 Lund, Sweden

Contact e-mail: aborg@ms.vok.lth.se

Abstract

Pulsatile flow in an axi-symmetric constricted pipe with a cross-sectional area reduction of 75%, approximating a moderately stenosed artery is studied by numerical simulations and DPIV measurements. Our studies have shown that the general behaviour of the post-stenotic flow-field is the generation of a starting vortex in the early acceleration phase followed by strething of this vortex due to the presence of the wall and eventually a roll-up of additional vortices behind the starting vortex. At higher flow-rates the jet core break down if the Reynolds number is high enough and generation of turbulence occurs. The occurence and extent of the above described events are strongly modulated by the Reynolds number and the Strouhal number. The present work describes the post-stenotic flow field for moderate stenoses in the largest vessels of the arterial tree. Focus is on describing the temporal and spatial distribution in wall shear stress in different stages of the flow cycle.

1 Introduction

A better knowledge of pulsatile flow in constricted pipes is important for the understanding of the impact of stenoses on the local hemodynamic conditions in man. Interesting fluid mechanical parameters include: pressure drop over the constriction, wall shear stress distribution, and turbulent stresses in the flow. It is believed that the local changes in wall shear distribution in an already stenosed artery are of significance for the progress of the disease and for the formation of more serious conditions like post-stenotic dilation [1].

In the largest arteries the peak Reynolds number varies from 600 to 4000, ($Re_p = U_p D/\nu$, U_p is the peak cross-sectional velocity, D the diameter of the artery, and ν the kinematic viscosity of the fluid). In a constricted artery the

local Reynolds number can reach over 10000, generating turbulence in the post-stenotic region. We have studied constrictions with a diameter reduction of 50% or equivalently an area reduction of 75%. Clinically this is considered as a moderate constriction, but the local hemodynamic impact of such a constriction is significant, particularily for high Reynolds numbers. Velocity, vessel diameter and frequency variations are limited in the arterial tree. The period is set by the heart, the diameters range from O(mm) to O(cm) and the peak velocity is O(0.1-1 m/s). According to [4] the flow-rate in the first branches of the systemic circulation is proportional to the square of of the diameter, i.e. the peak and mean velocity is fairly constant. If the heart rate is fixed this leads to that the peak Reynolds is linearly related to the Strouhal number ($Re_p = kSt$), ($St = \omega D/U_p$) where ω denotes angular frequency.

We have studied numerically the properties of constricted pipe flows for a half-sinusoidal flow-rate pulse for Reynolds numbers in the range 1500-3000, and Strouhal numbers between 0.1-0.2. Furthermore the numerical method is validated for steady flow through a 75% constriction with $Re = 2000$ and is shown to capture the essence of the flow both qualitatively and quantitatively. A similar case is studied for a higher Reynolds number ($Re_p = 8560$) both numerically and experimentally (DPIV).

2 Methods

The fluid is treated as an incompressible Newtonian fluid, and is governed by the Navier-Stokes equations. The equations are discretized with finite differences on a three-dimensional Cartesian grid. Details on the numerical method can be found in [5]. The time-step is changed during the pulsatile cycle to approximately hold a maximum constant CFL number. In all simulations this is set between 1 to 3. Properties of the cases investigated are outlined in table 1. The geometric data for the stenosis referred to as "Cosine" is given in [2] and for "piecewise linear" in [3]. The flow-rate pulse is modelled as a half sine profile which is a reasonable approximation for the largest arteries. In all the pulsatile cases investigated the inlet velocity profile is flat placed at three diameters upstream of the throat corresponding to entry flow. For the stationary case (Case 1) the inlet profile is parabolic. In all simulations a Neumann condition for all velocity components is applied at the outlet. Details about the case studied by DPIV (Case 6) are given in [3].

3 Results and Conclusions

The first case is used as a validation case for the numerical method and as a reference case for the structure of the flow field close to peak flow-rate in the pulsatile cycle. Figure 1a shows contours of the mean axial velocity field behind the constriction between $(x - x_0)/D = -1$ and $(x - x_0)/D = 6$ (x_0 is at the

constriction center). Figure 1b shows a comparison between numerical results for three different grids together with the experiments by [2], for the time averaged streamwise velocity along the centerline, and the rms values of the fluctuation velocity in the streamwise direction . Figure 1c shows the rms of the fluctuations in the circumferential direction along the centerline and the mean wall shear stress behind the stenosis (Quantities in Fig. 1 are non-dimensionalized with the mean inlet velocity).

Table 1: Cases studied

Case nr.	Re_p	St	L/D	x0	Constriction shape
1	2000	0	12	3	Cosine
2	1500	0.096	12	3	Cosine
3	2000	0.128	12	3	Cosine
4	3000	0.192	12	3	Cosine
5	400	0.128	12	3	Cosine
6	8560	0.114	12	3	Piecewise Linear

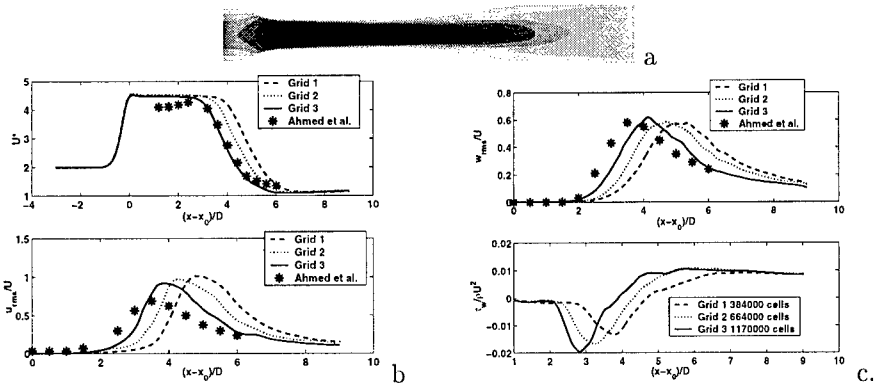


Figure 1: a. Contours of mean streamwise velocity (Case 1), b. Mean streamwise velocity along the centerline (Upper frame) and fluctuating streamwise velocity (Lower frame), c. Fluctuating circumferential velocity along the centerline (Upper frame), and mean wall shear stress (Lower frame)

In the pulsatile case we focus on the flow at two time instants. The first is when the flow-rate is half of its maximum value in the acceleration phase (T1) and the second is at peak flow rate (T2). At T1 the flow is characterized by a leading vortex and the generation of additional vortices behind this vortex. Figure 2 shows vector fields at this instant for the different cases and Fig. 3a shows wall shear stress behind the stenosis (Quantities in Fig. 3 are non-dimensionalized with the inlet velocity at peak flow). The leading vortex generates large negative wall shear stress values compared to those in front of the vortex for the high Reynolds number cases in contrast to the low Reynolds case (Case 5). For Case 3 we see that the negative wall shear stress induced by this vortex at T1 is larger than the fully developed downstream value for the stationary case (Case 1). For the peak phase we compare properties of Case 3 with those of Case 1. For Case 3 the mean and rms values have been obtained by averaging over 12 cycles. The main conclusion that can be drawn from Figure 3 b and c is that the properties of

the flow at peak flow-rate are similar to those at steady flow with the Reynolds number equal to that at peak flow-rate.

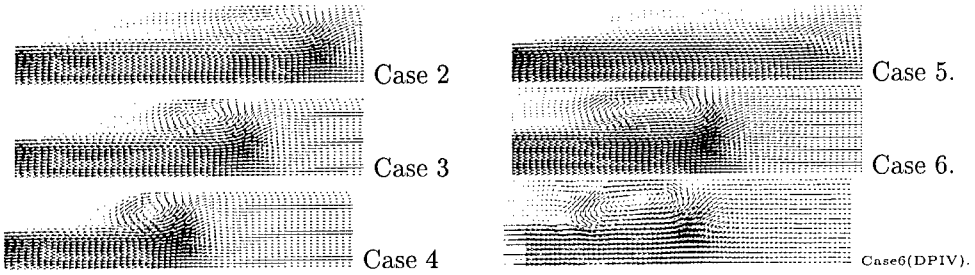


Figure 2: Vector fields in the acceleration phase at the time instant corresponding to half of the maximum flow-rate (T1)

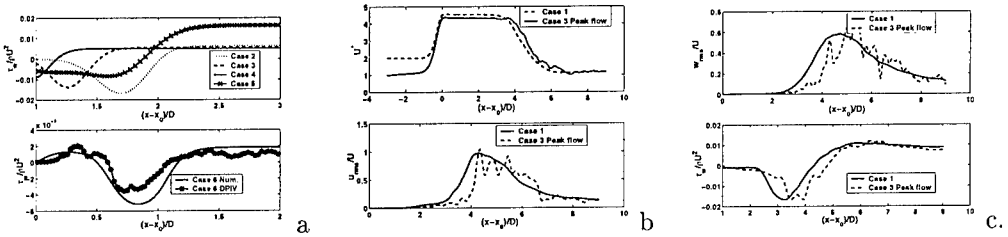


Figure 3: a. Wall shear stress behind the stenosis at T1, b. Averaged streamwise velocity along the centerline at T2 (Upper frame) and fluctuating streamwise velocity at T2 (Lower frame), c. Fluctuating circumferential velocity along the centerline a T2 (Upper frame), and normalized mean wall shear stress at T2 (Lower frame)

References

[1] M. R. Roach. An experimental study of the production and time course of post-stenotic dilation in the femoral and Carotid arteries of adualt dogs *Circ. Res*, 13:537–551, 1963.

[2] S. A. Ahmed and D. P. Giddens. Velocity measurements in steady flow through axisymmetric stenoses at moderate Reynolds numbers. *J. Biomech*, 7:505–516, 1983.

[3] A. Borg, J. Bolinder, and L. Fuchs. DPIV measurements of pulsatile flow in a constricted pipe at high Reynolds numbers. *Ninth International Symposiym on Laser Techniques and Fluid Mechanics*, Paper 29.2, 1998.

[4] M. Zamir, P. Sinclair, and T. H. Wonnacot. Relation between diameter and flow in major branches of the arch of the aorta *J. Biomech.*, 25:11:1303–1310, 1992.

[5] X .S. Bai, and L. Fuchs Fast multigrid method for 3-D turbulent incompressible flows. *Int. J. Num. Meth. Heat Fluid Flow*, 2:127-137, 1992 .

ADVANCES IN TURBULENCE VIII
Proceedings of the Eighth European Turbulence Conference
C. Dopazo et al. (Eds.)
© CIMNE, Barcelona 2000

Quantification of anisotropy in an oscillating grid flow

Jakob Mann and Søren Ott

Risø National Laboratory
DK-4000 Roskilde, Denmark

Contact e-mail: jakob.mann@risoe.dk

1 Introduction

A particle tracking system is used to measure three-dimensional velocities in the turbulent flow between two oscillating grids. We show that particle tracking can be used for quantification of the anisotropy of the turbulence in terms of an expansion of the velocity structure tensor in spherical harmonics. The tensors of rank two and four quickly becomes isotropic as the separation decreases, while the behavior is obvious for the tensor of rank three.

2 A particle tracking experiment

Specially prepared polystyrene particles with diameters in the range 500–600 μm and with relative densities of 1 ± 10^{-4} are used for 3D particle tracking in a $0.32 \times 0.32 \times 0.5$ m water tank with two oscillating grids producing turbulence. Four CCD cameras synchronized with a stroboscope record continuously the

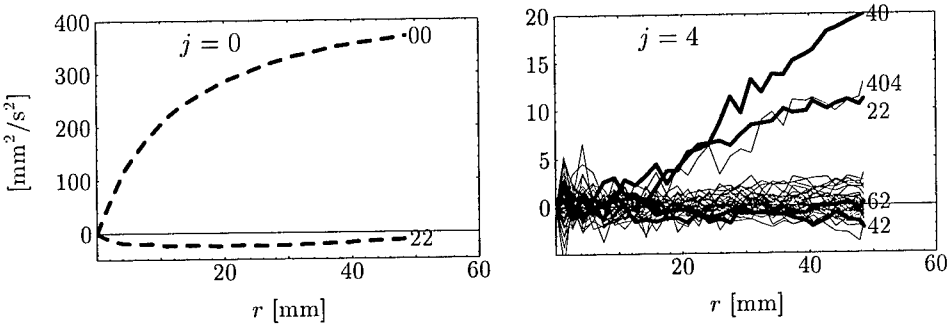


Figure 1: Coefficients C_{jlsm} for $j = 0$ and 4 as functions of r for the structure tensor of rank two. All isotropic (dashed curves) and axisymmetric coefficients (solid thick curves) are labeled with the quantum numbers l and s, and selected non-axisymmetric coefficients (thin curves) are labeled with the numbers l, s and m.

positions of more than 500 particles with a precision of the order of 60 μm in each dimension. The experiment has been used to study diffusion of particle pairs in three dimensional turbulence [2, 3]. Experiments analysed here have $R_\lambda \approx 100$, a Kolmogorov scale of 0.25 mm and an integral scale of 22 mm. The measurements can be used to calculate the Eulerian velocity structure tensor of, in principle, any order.

3 Expansion of the Eulerian velocity structure tensor

It is clear that the two-grid flow is not isotropic, but how anisotropic is it?

One way of answering this question is to decompose the second order structure tensor $\langle \delta v_p(\boldsymbol{r}) \delta v_q(\boldsymbol{r}) \rangle$ using spherical harmonics.

The decomposition of the second order structure tensor looks like this

$$\langle \delta v_p(\boldsymbol{r}) \delta v_q(\boldsymbol{r}) \rangle = \sum_{j=0}^{\infty} \sum_{s=0}^{2} \sum_{l=|j-s|}^{j+s} \sum_{m=-j}^{j} C_{jlsm}(r)\, Y_{pq}^{jlsm}(\theta, \phi), \tag{1}$$

where j, l, s, and m are integers (also called quantum numbers) specifying uniquely the spherical harmonic functions Y_{pq}^{jlsm}, which constitute an orthonormal basis, i.e. $\int_{4\pi} Y_{pq}^{jlsm} Y_{pq}^{j'l's'm'} \mathrm{d}\Omega = \delta_{jj'}\delta_{ll'}\delta_{ss'}\delta_{mm'}$. The $2j+1$ functions Y_{pq}^{jlsm} with $m = -j, ..., j$ form a rotation invariant subspace.

Velocity structure tensors of higher rank, e.g. $\langle \delta v_p(\boldsymbol{r}) \delta v_q(\boldsymbol{r}) \delta v_r(\boldsymbol{r}) ... \rangle$ can be expanded in similar ways. The basis functions $Y_{pqr...}^{jlsm}$ become more cumbersome to construct and the summation over s in (1) has to go from zero to the rank.

The structure tensor has two properties which make some of the coefficients C_{jlsm} zero. Interchanging the two points defining the velocity difference $\delta \boldsymbol{v}(\boldsymbol{r}) \equiv \boldsymbol{v}(\boldsymbol{x}+\boldsymbol{r}) - \boldsymbol{v}(\boldsymbol{x})$, is equivalent to multiplying by the factor $(-1)^R$, where R is the rank. Since the parity of $Y_{pqr...}^{jlsm}$ is $(-1)^l$, this implies that even rank Cs are zero for l odd, and odd rank Cs are zero for l even. In addition to this, symmetry in the indices implies that all even rank coefficients with s odd, and odd rank coefficients with s even are zero. Arad *et al.* [1] discuss a similar expansion, but for the less symmetric case of the correlation function.

The squared norm is

$$\int_{4\pi} \langle \delta v_p \delta v_q \rangle^2 \,\mathrm{d}\Omega = \sum_{jlsm} |C_{jlsm}|^2$$
$$= \underbrace{\sum_{j=0} |C_{jlsm}|^2}_{\text{isotropic}} + \underbrace{\sum_{\substack{m=0 \\ j>0}} |C_{jlsm}|^2}_{\text{axi-symmetric}} + \sum_{\text{the rest}} |C_{jlsm}|^2 \tag{2}$$

Table 1: Number of index symmetric basis functions $Y^{jlsm}_{pq\ldots}$ with parity $(-1)^R$. All basis functions used in this paper are indicated. The number of axi-symmetric functions are also shown.

	rank 2		rank 3		rank 4	
j	#	axi-symm.	#	axi-symm.	#	axi-symm.
0	2	2	2	2	3	3
1	3	1	6	2	5	2
2	20	4	25	5	35	7
3	14	2				
4	36	4				

and there are similar expressions for the tensors of rank 3 and 4 etc. In (2) we split $\int_{4\pi} \langle \delta v_p \delta v_q \rangle^2 \, \mathrm{d}\Omega$ into just three parts: the isotropic part, the axi-symmetric part and the rest. Figure 1 shows one of the few examples where a $j > 0$ and $m \neq 0$ coefficient is significantly different from zero. We believe this is caused by the quadratic cross section of our tank which introduces a departure from exact axi-symmetry.

Experimentally it becomes very difficult to measure things as j and m increase. We have not attempted to go beyond $j = 4$ for the second order structure function. There are 75 coefficients with $j \leq 4$. For the rank 3 and rank 4 tensors we limit ourselves to $j \leq 2$, giving 33 and 44 coefficients, respectively, see table 1.

4 Results

Disregarding anomalous scaling the isotropic coefficients are supposed to be proportional to $(\varepsilon r)^{R/3}$, where R is the rank. In the analysis of the effects of shear on anisotropy of atmospheric surface layer turbulence Wyngaard and Coté [4] proposed that $\langle \delta v_1(x_1) \delta v_3(x_1) \rangle \propto \frac{\mathrm{d}U_1}{\mathrm{d}x_3} \varepsilon^{1/3} r^{4/3}$, where $\mathrm{d}U_1/\mathrm{d}x_3$ is the mean vertical shear. This correlation is zero in isotropic turbulence. We propose that in general anisotropic coefficients scale as $\mathcal{T}^{-1} \varepsilon^{\frac{R-1}{3}} r^{\frac{R+2}{3}}$, where $\mathcal{T}$ is a time scale characterising the anisotropy. The squared isotropic and axisymmetric coefficients in (2) thus scale as 4/3 and 8/3 for rank 2, 2 and 10/3 for rank 3, and 8/3 and 4 for $R = 4$. Figure 2 shows that this is not far off for $R = 2$ and $R = 4$, but for $R = 3$ the scaling fails for our low R_λ flow.

References

[1] I. Arad, V. S. L'vov, and I. Procaccia. Correlation functions in isotropic and anisotropic turbulence: The role of the symmetry group. *Phys. Rev. E*, 59(6):6753–6765, June 1999.

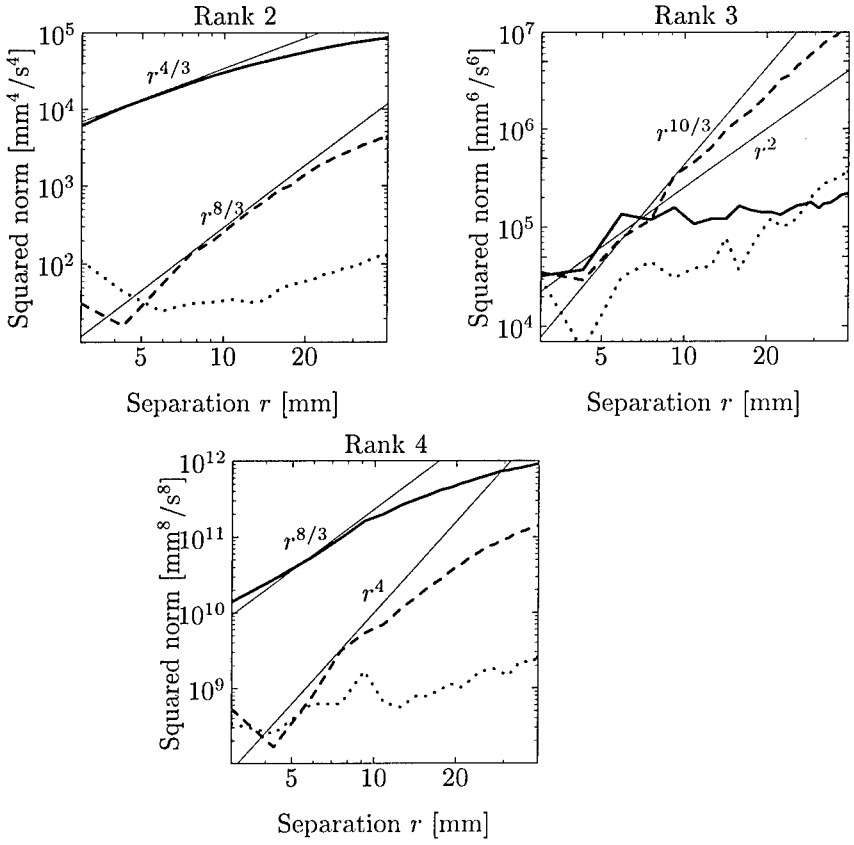


Figure 2: Squared isotropic (solid curve) and axi-symmetric (dashed curve) coefficients as functions of rank and separation. Also shown are expected inertial subrange scalings (thin lines) and the sum of squared coefficients that are neither isotropic nor axi-symmetric (dotted curve).

[2] Jakob Mann, Søren Ott, and Jacob Sparre Andersen. Experimental study of relative, turbulent diffusion. Technical Report Risø–R–1036(EN), Risø National Laboratory, 1999.

[3] Søren Ott and Jakob Mann. An experimental investigation of the relative diffusion of particle pairs in three dimensional turbulent flow. *J. Fluid Mech.*, 2000. Submitted.

[4] J. C. Wyngaard and O. R. Coté. Cospectral similarity in the atmospheric surface layer. *Q. J. R. Meteorol. Soc.*, 98:590–603, 1972.

ADVANCES IN TURBULENCE VIII
Proceedings of the Eighth European Turbulence Conference
C. Dopazo et al. (Eds.)
© CIMNE, Barcelona 2000

Anomalous Scaling Laws in Turbulence

R. Benzi

Dipartimento di Fisica universitá di Roma *Tor Vergata*
Via Della Ricerca scientifica 100, 00133 Roma ITALY
Sezione INFM Univ. Roma "Tor Vergata".

Contact e-mail: r.benzi@aipa.it

1 Introduction

One of the challenging question in physics is to describe and to undestand the statistical properties of turbulence at large Reynolds number *Re*. In the last few years, the use of Direct Numerical Simulations, the continuous refinement of laboratory experiments as well as new theoretical ideas allowed a real breakthrough in our understanding of turbulence at least for what concerns the delicate issue of intermittency. It is the aim of this paper to review part of this work.
Let me consider an observable $Q(s)$ where s is the "scale" of the observable Q (for the time being the definition of the scale is arbitrary and does not play any role in what follows). I assume that Q is a random field with probability distribution $P_s(Q)$. Moments of Q are defined as $F_n(s) = \int P_s(Q)Q^n dQ$ (note that the integral is not made with respect to s). If $F_n(s)$ satisfy the scaling relation:

$$F_n(s) = A_n s^{\alpha(n)} \tag{1}$$

in the interval $s = (\eta_A, L_A)$, then the knowledge of $(A_n, \alpha(n))$ completely defines the probability distribution of Q and its scale dependence. Scaling laws like(1) have played an important role in our understanding of many complex physical phenomena as well as in fully developed turbulence. An important remark on scaling (1) can be made by rewriting (1) in the following form:

$$F_n(s) = C_{n,m} F_m(s)^{\beta(n,m)} \tag{2}$$

where $C_{n,m} = A_n(1/A_m)^{\beta(m,n)}$ and $\beta(n,m) = \frac{\alpha(n)}{\alpha(m)}$. If $\beta(n,m) = n/m$, then scaling (2) satisfies dimensional counting. When dimensional counting is broken, then $\beta(n,m) \neq n/m$ are called anomalous exponents. Anomalous scaling implies that dimensioless quantities, like the skewness and the kurtosis for instance, have non trivial behavior in s. Because of the condition $\alpha(0) = 0$, which is satisfied for any random field with decent support in s, anomalous scaling also implies that $\alpha(n)$ is a convex non linear function of n. From a theoretical point of view, scaling (2) can be considered a more general scaling relation with respect to (1).

In terms of equation (2), the probabibiliy distribution $P_s(Q)$ is determined by the set $(C_{m,n}, \beta(m,n)$ and the behavior of one of the moments of Q, say m, i.e. by the function $f(s) = F_m(s)$. The relevant remark is that (2) can be true even if (1) is never observed. In particular one can show REFERENZAfisicaD96 that it is possible to define in a rigorous mathematical sense random fields which obey to scaling (2), with anomalous exponents, and do not satisfy scaling (1). I consider this (theoretical) result important because it opens up a new way to investigate scaling laws in complex physical systems. The first systematic investigation of scaling law (2) in turbulence was proposed by Benzi *et. al.* [1].

2 Extended Self Similarity

In fully developed turbulence there are many possible and well defined physical observables which can be used for defining the scale dependence statistical properties of the turbulent flows. Among them, a relevant role is played by the so called structure functions, $S_n(r)$, defined as $S_n(r) =< (\delta V(r))^n >$ where $\delta V(r) = \delta \vec{V}(vecr) \cdot \vec{r}/r$ and $\delta \vec{V}(\vec{r}) = \vec{V}(\vec{x}+\vec{r}) - \vec{V}(\vec{x})$. As it is known, S_3 and S_2 are linked by the Kolmogorov 4/5 law for homogeneous and isotropic turbulence, namely

$$S_3(r) = -\frac{4}{5}\epsilon r + 6\nu \frac{dS_2(r)}{dr} \tag{3}$$

where ϵ is the mean rate of energy dissipation and ν the kinematic viscosity. For large Re and for r in the inertial range ($\eta << r << L$, where $\eta = (\nu^3/\epsilon)^{\frac{3}{4}}$), the second term on r.h.s. can be neglected and one can derive the scaling relation $S_3(r) \propto \epsilon r$. In the same regimes (large Re and r in the inertial range), one is interested to understand whether the scaling relation:

$$S_n(r) \propto r^{\zeta(n)} \tag{4}$$

holds. There are three main questions concerning the scaling exponents $\zeta(n)$, namely: (1) whether the scaling exponents $\zeta(n)$ are anomalous or not; (2) their dependence, if any, on Re; (3) the degree of universality, that is to say whether the scaling exponents are different for different flow geometry or different forcing mechanisms. Because $\zeta(3) = 1$, the exponents $\zeta(n)$ are anomalous if they differ from the Kolmogorov prediction $\zeta(n) = n/3$. The difficulty in answering the above questions can be understood by looking at fig. (1) left where a log-log plot of $S_6(r)$ is shown as function of r for three rather different cases, namely a DNS of homogeneous and isotropic turbulence ($Re_\lambda \propto 50$), a turbulent flow behind a cylnder ($Re_\lambda \propto 100$) and jet turbulence ($Re_\lambda \propto 1000$), where Re_λ is the Reynold number based on Taylor microscale. As one can see, only at rather large Re it is possible to state that a scaling region is observed, namely for the case of jet turbulence (note that observing scaling region in DNS seems almost hopeless). The situation changes dramatically if we choose to investigate the generalized scaling (2) for the structure functions. Because $\zeta(3) = 1$, it is

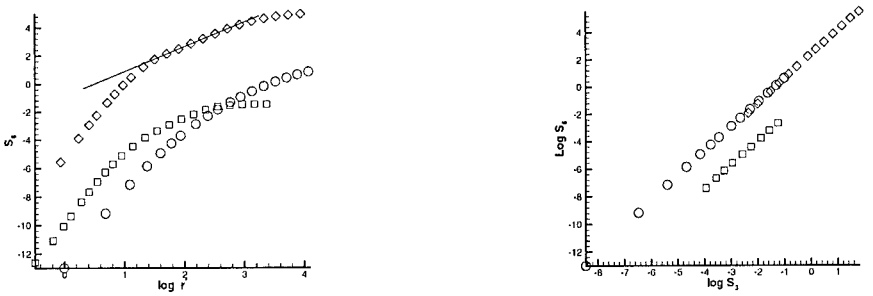


Figure 1: Left: S_6 vs. r/η The straight line corresponds to the best fit with anomalous exponents $\zeta_6 = 1.78$ for experimental data at $Re_\lambda \propto 1000$. Right: S_6 vs. $< |\delta V(r)|^3 > (\propto S_3)$ for the same data set.

natural to look at the generalized scaling in the form:

$$S_n(r) \propto S_3(r)^{\beta(n)} \tag{5}$$

where $\beta(n) = \zeta(n)$ in the region where scaling (4) holds. In fig.(1) right, it is shown a log-log plot of S_6 versus S_3 for the same data set of figure (1) right. Actually, instead of S_3 we use the quantity $< |\delta V(r)|^3 >$ in order to increase the statistical accuracy, taking into account that the relation $S_3 \propto < |\delta V(r)|^3 >$ is extremely well satisfied for the cases shown in figure (1). By inspecting figure (1), one can immediately understand that the generalized is well observed at small, moderate and large Re. The quality of the scaling relation shown in

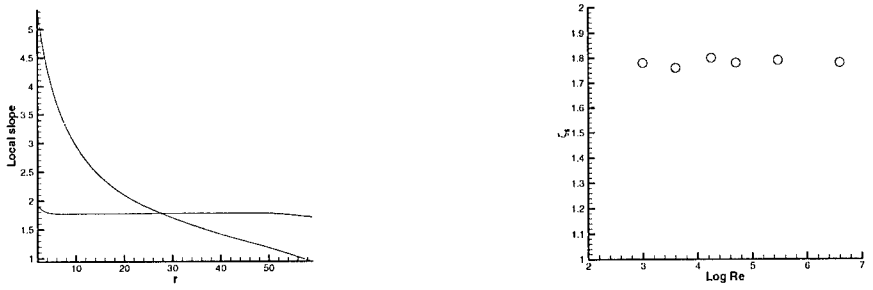


Figure 2: Left : Local slopes of S_6. The curve going from 6 to 1 corresponds to $dlogS_6/dlogr$. The other curve, almost a constant, corresponds to $dlogS_6(r)/dlogS_3(r)$. Right: experimental values of ζ_6 computed using ESS for different Re.

figure (1) can be better understood by looking at the so called local slope of the scaling, namely the quantity $\beta(6,r) = \frac{dlogS_6(r)}{dlogS_3(r)}$, shown in figure (2) on the left

for the DNS data reported in figure (1). As one can see, the anomalous local scaling extends from few grid points up to 60 grid points, while scaling with respect to r never holds. Let me remark that for small r, the scaling cannot be anomalous simply because in the dissipation region $\delta V(r) \propto r$. Figures (1) and (2) tell us that the generalized scaling (5) extends the usual concept of scaling both at low and moderate Re and at small scales. For this reason, scaling (5) has been called Extend Self Similarity. One of the most imporant point on ESS is that it allows an accurate measurements of the scaling exponents at low Re. It is therefore possible to compare scaling exponents at different Reynolds number and for different (experimental and/or numerical) flow configuration. It turns out that for large Re we find that $\beta(n) = \zeta(n)$. Moreover, for homogeneous and isotropic turbulence there is good evidence that the anomalous exponents are universal, i.e. independent of the forcing mechanism which produces the turbulence. Finally, and somehow more important, the anomalous exponents are Re independent. Figure (2) right shows the value of $\beta(6)$ for different Re (from $Re = 1000$ up to $Re = 10^6$): no dependence on Re is observed. Recently, an accurate investigation on $\beta(2)$ has been performed in order to check whether a Re dependence may be observed as proposed by some theoretical arguments. Even if the value of the anomalous exponents $\beta(2) = 0,7$ is very close to $2/3$, the accuracy of the ESS scaling is good enough to show that $\beta(2)$ does not change by changing Re, see [2]. The ESS scaling can be also applied to many other statistical observables in turbulent flows, like for instance velocity circulation and energy dissipation. In particular, it is interesting to consider energy dissipation on scale r defined as:

$$\epsilon_r = \frac{1}{B(r)} \int_{B(r)} \epsilon(x) dr^3 \tag{6}$$

where $B(r)$ is the volume of integration. The quantity ϵ_r played an important role in developing phenomenological theories of intermittency since it is often assumed that the refined Kolmogorov hypothesis (RKH) holds, namely:

$$S_n(r) = < (\epsilon_r)^{n/3} > r^{n/3} \tag{7}$$

The RKH implies that anomalous fluctuations in turbulent flows are closely linked to the fluctuations of non linear energy transfer among scales which can measured, locally in space, by the local fluctuating rate of energy dissipation, i.e. ϵ_r. Benzi *et.al.* [3] suggested that the RKH should be reformulated in the following way:

$$S_n(r) = \frac{< (\epsilon_r)^{n/3} >}{\epsilon} S_3(r)^{n/3} \tag{8}$$

This form of the RKH is not deducable by the ESS scaling although it is somehow a natural generalization of the original proposal in the ESS language. In figure (3) left, the generalize form of the RKH is shown for the experimental data at$Re_\lambda \propto 1000$ previously considered. The quality of the scaling predicted by equation (8) is somehow striking. What is impressive is that the generalized

RKH scaling holds not only in the region where ESS is observed but also at very small scales and with the intercept. This means that (8) is working independent of the effect of dissipation. This results is not at all simple to understand since it requires the effect of energy dissipation enters in turbulent flows in a rather special way. Let me also remark that it is not straightforward to include in existing theories of multifractal fluctuations for turbulent flows the result shown in figure (3). An attempt in this direction can be found in Benzi *et.al.* [3].

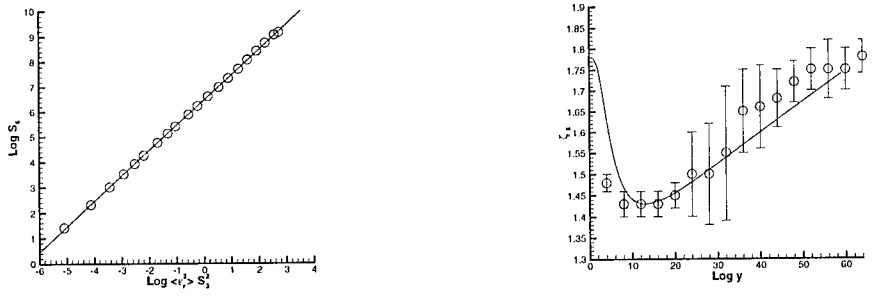


Figure 3: Left: log-log plot S_6 vs $< \epsilon_r^2 > S_3^2$. Right : values of the local exponents ζ_6 as function of the grid points (1 grid point = 2.5 y^+) in turbulent boundary layers.

3 Application to turbulent boundary layers

The problem of characterizing the complex phenomena arising in the near-wall region, and their relation to the lack of isotropy has been analyzed in depth by several authors (see Arad et. al. [4] and references therein). Here, I want to analyse the spatial behaviour of the scaling exponents and their link to coarse-grained features of the flow in the near-wall region, using ESS. The analysis discussed in this section are taken by the Toschi *et. al.* [5] and Benzi *et.al.* [6] which used a data set obtained by a direct numerical simulation with high statistical accuracy about 10^3 in time units U_0/h, where U_0 is the centerline velocity and h is the channel half-width). In the following I use wall units defined as $y^+ = y/\delta$ and $v^+ = v/v^*$ where v^* is the friction velocity and $\delta = \nu/v^*$ is the typical boundary layer thickness. To study intermittency in the channel, let me introduce the following y-dependent longitudinal streamwise structure functions: $S_n(r^+, y^+) =< |(v_x(x^+ + r^+, y^+, z^+) - v_x(x^+, y^+, z^+)|^n >$. The average is taken at a fixed y^+ value (the normal to wall coordinate). The quantities $S_n(r^+, y^+)$ have been measured for each value of y. Follwing the discussion of the previous section, the use of ESS may enable us to understand the statitical properties of turbulence even if the simulation are performed at relatively low Re and the analysis is done in a region of the flow where strong dissipative effect should

be active. The analysis performed in Toschi *et. al* [5] shows that indeed ESS scaling is observed. However the physical interpretation of what is happening is not trivial. There are two regions in y^+, hereafter referred to as region H ("Homogeneous") and region B ("Boundary") respectively, where well defined constant local slopes for the scaling exponents can be detected. Region H is close to the center of the channel ($y^+ \geq 100$) while region B is close to the viscous sublayer ($20 \leq y^+ \leq 50$). In region H, the scaling exponents $\zeta_n(H)$ are found to be approximately the same as the ones measured in homogeneous and isotropic turbulence. On the other hand, in region B the scaling exponents $\zeta_n(B)$ have been found to be much smaller than $\zeta_n(H)$. In the intermediate region between region H and region B, it is difficult to identify a range in r where a scaling exponent can be defined with enough confidence. In fig. (3) right, the quantity ζ_6/ζ_3 is plotted as a function of r with the associated error bars (large error bars in the region $50 \leq y^+ \leq 100$ indicates the local slopes are poorly defined). The result shown in figure (3) indicates that there is a transition in the nature of intermittency between region H and region B. In order

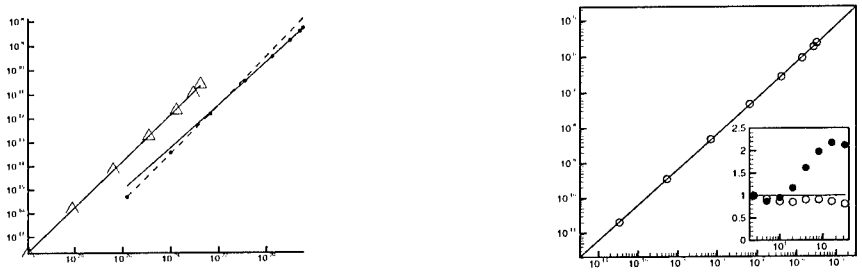


Figure 4: Left: check of eq.(8) for $n = 2$ for turbulent boundary layer. The tringles refer to data in region H while the black dot to data in region H. Right : check of equation (9) for $n = 2$ in rgion B. In the insert it is shown the compensated plot of (8) for $n = 2$ in homogeneous and isotropic turbulence and of (9) for $n = 2$ in region B of the turbulent boundary layer.

to understand why we observe stronger intermittency in region B with respect to region H, let me consider figure (4) left where a chek of the generalized RKH is shown in both region H and B. While in region H RKH holds quite well, in region B a clear breaking of the generalized RKH is observed. This result seems to suggest there is a relationship between the failure of the RKH and the increase of intermittency near the wall region. To this aim, let me recall that RKH is somehow linked to the 4/5 Kolmogorov equation and it tells us that the energy flux, represented by $(\delta V(r))^3$, fluctuates with the same probability distribution of ϵ_r. However, in the presence of strong shear we should expect that a new term, proportional to $\partial_z U(\delta V(r))^2$, enters the estimate of the energy flux at scale r. Such a new term indeed appears in the analysis performed for

homogeneous shear flows (see for instance [7]). If this term becomes dominant one is led to assume that the fluctuations of the energy flux in the inertial range are proportional to $A(r)(\delta V(r))^2$ where $A(r)$ is a non fluctuating quantity. It follows that in this case $\epsilon_r \propto (\delta V(r))^2$. Therefore a new form of RKH should hold namely:

$$< (\delta V(r))^n >= \frac{< (\epsilon_r)^{n/2} >}{< \epsilon >^{n/2}} < (\delta V(r))^2 >^{n/2} \tag{9}$$

The above expression of the new RKH is given in terms of the structure function of order two, without explicit reference to the separation r, in the same spirit of the generalized RKH. In figure (4) right we check the new form of RKH and compared it against the usual form. A quite clear agreement with the predicted new form of RKH is observed. By using the same argument, is possible to define a scale L_s above which one should expect that the new form of RKH holds. A simple algebraic computation gives $L_s = (\epsilon/\Gamma^3)^{1/2}$, Γ being the shear strenght. A detailed analysis shows that the breaking of RKH starts near by the scale L_s, as predicted. By using the new form of RKH is is now possible to explain the increase of intermittency near the wall region. Indeed, let us introduce the scaling exponent $\tau(n)$ of the local energy dissipation ϵ_r, i.e. $< (\epsilon_r)^n > \propto r^{\tau(n)}$. The original form of RKH gives us a relationship between $\tau(n)$ and $\zeta(n)$; namely $\tau(n) = \zeta(3n) - n\zeta(3)$. By using ESS the last relationship is written as

$$\nu(n) = \beta(3n) - n \tag{10}$$

where $\nu(n) = \tau(n)/\zeta(3)$. The new form of RKH predicts:

$$\nu(n) = \beta(2n) - \frac{n}{2}\beta(2) \tag{11}$$

In figure (5) the two form of $\nu(n)$ are reported for the B region as well as the

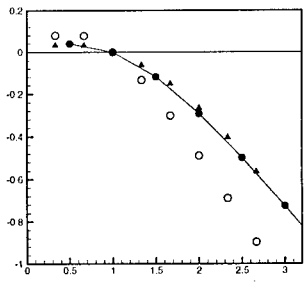


Figure 5: Computation of $\nu(n)$ using eq. (10), circles, and (11), triangles. The continuos curve represents the values obtained using data for homogeneous and isotropic turbulence.

values of $\nu(n)$ as computed for the homogenous and isotropic turbulence. While in region B eq. (10) predicts a value of $\nu(n)$ showing an increase of intermittency with respect to homogenous and isotropic turbulence, equation (11) predicts ,in the same region, values of $\nu(n)$ rather close to the values observed in the homogenous and isotropic case. This result shows that turbulence in the B region is characterized by nearly the same probability distribution (in the ESS form) for the local energy dissipation. Because of the new form of the RKH, the anomalous scaling exponents of velocity structure functions appears to be more intermittent. A final remark is due to understand what happens in the intermediate region, i.e. in between region H and B. Following the analysis so far presented, one should expect that the scaling exponents, if any, emerge from a complex blending of these two basic behaviors, i.e. the two possible form of the RKH. Recently, Toschi *et.al.* [8] proposed to use a generalized form of structure functions $Z_n(r) =< ((\delta V(r))^3 + \alpha\Gamma r(\delta V(r))^2)^{n/3} >$ for shear flow turbulence, where α is a constant independent of r . The structure functions Z_n should be characterized by the same set of anomalous scaling exponents independent of the scale r and of the shear intesity. Application of this idea in boundary layer turbulence shows the predicted behavior with very good accuracy.

References

[1] Benzi, Biferale, Ciliberto, Struglia, Tripicccione, Phys. D., **96**, 162-181, 1996.

[2] Benzi, Ciliberto, Baudet, Ruiz-Chavarria Physica D,127, 111-112 1999.

[3] Benzi, Ciliberto, Baudet, Ruiz-Chavarria Physica D, **80**, 385-398, 1995.

[4] Arad, Biferale, Mazzitelli, Procaccia Phys. Rev. Lett., **82**, 5044, 1999.

[5] Toschi, Amati, Succi, Piva, Benzi, Phys. Rev. Lett., **82**, 5040, 1999.

[6] Benzi, Amati, Casciola, Toschi, Piva, Phys. Fluids, **11**(6), 1-3, 1999.

[7] O.J. Hinze, Turbulence, (Mc Graw-Hill) New York 1969

[8] Toschi, Leveque, Ruiz-Chavarria Preprint, December, 1999.

ADVANCES IN TURBULENCE VIII
Proceedings of the Eighth European Turbulence Conference
C. Dopazo et al. (Eds.)
© CIMNE, Barcelona 2000

Nonlinear self-sustained structures in shear flows

Patrick Huerre

Laboratoire d'Hydrodynamique (LadHyX)
CNRS – École polytechnique
F-91128 Palaiseau cedex, France

Contact e-mail: huerre@ladhyx.polytechnique.fr

According to experimental and numerical observations, spatially developing shear flows such as mixing layers with a sufficiently large counterflow, hot jets, wakes at Reynolds numbers above the onset of the Kármán vortex street, typically behave as *flow oscillators* with a well defined frequency that is insensitive to low levels of external noise. Such self-sustained time-periodic states are described in terms of so-called *global modes*, i.e. extended wavepackets that live in the underlying spatially developing flow and display the same global frequency at all streamwise stations [1]. The global frequency satisfies an eigenvalue problem in the streamwise direction : the eigenfunction distribution along the stream is composed of a collection of spatially evolving waves which must be suitably combined in order to comply with specific upstream and downstream boundary conditions. Global frequency selection criteria are then derived which, in many instances, only involve the local instability properties at a single streamwise station. This particular station then effectively acts as a wavemaker which imposes its frequency to the entire flow. The objective of the lecture is to review our current understanding of such self-sustained structures in the *fully nonlinear régime.*

Until recently, *global mode* formulations had been developed within the framework of linear theory, first on Ginzburg-Landau evolution models [2, 3] and then on real flows governed by the Navier-Stokes equations [4]. Two configurations have been distinguished. In *infinite media*, the complex global frequency is given by a saddle point condition applied to the local linear dispersion relation in the space of complex wavenumber and streamwise coordinate. This criterion provides a satisfactory prediction of the shedding frequency in flat-plate wakes [5]. In *semi-infinite media* that are most absolutely unstable at the upstream boundary, the complex global frequency is simply the local absolute frequency prevailing at the upstream boundary point.

In the last few years, the same line of thought has been followed to investigate the fully non-linear régime, the main goal being the determination of nonlinear frequency selection criteria valid for *finite-amplitude global modes.* General

definitions of nonlinear absolute/convective instability have been proposed by Chomaz [6], which formally extend the usual linear concepts.

The analysis of various Ginzburg-Landau model equations in *semi-infinite spatially uniform media*, say $0 < x < \infty$, carried out by Couairon and Chomaz [7, 8, 9] have firmly established the intimate connection existing between nonlinear absolute/convective instability, front velocity selection in pattern formation problems [10, 11] and the onset of nonlinear global modes In all the examples studied so far, global mode onset in the streamwise domain $0 < x < \infty$ is found to coincide with the appearance of nonlinear absolute instability. More specifically, at global instability onset, a front separating the bifurcated state from the rest state succeeds in travelling upstream against the oncoming flow before it is stopped in its motion by the boundary point $x = 0$. The global mode structure is therefore dominated by a stationary front pinned near $x = 0$. Two cases must then be distinguished. If the stationary front is *linearly determined* [10], the appearance of a nonlinear global mode coincides with the onset of linear absolute instability at $x = 0$. At global onset, the global frequency is then given by the linear absolute frequency at the boundary $x = 0$. Furthermore the healing length Δx, which measures the streamwise distance from $x = 0$ necessary to reach a fully saturated state, is predicted to scale as $\varepsilon^{-1/2}$, where ε is the supercriticality parameter. This scaling law has been observed to effectively apply in numerical simulations of Rayleigh-Bénard convection with through flow [12] and of Taylor-Couette flow with superimposed axial flow [13]. If the front is *nonlinearly determined* [11], the appearance of a nonlinear global mode no longer coincides with the onset of linear absolute instability and the healing length Δx is predicted to scale as $ln(1/\varepsilon)$. This scenario of global bifurcation in a medium that is still linearly convectively unstable has recently been observed and validated in the case of the Kelvin-Helmholtz instability in a Hele-Shaw cell [14].

The above nonlinear studies all pertain to global modes in spatially uniform semi-infinite media, e.g. for Ginzburg-Landau models with constant coefficients. Most shear flows however are non-uniform along the stream. In order to take this effect into account, the analysis of Ginzburg-Landau models with *spatially varying coefficients* has therefore been undertaken. In the case of a *semi-infinite medium* $0 < x < \infty$, the selected global frequency is still given near global onset by the linear absolute frequency at $x = 0$, provided that the front structure is linearly determined. The streamwise structure of nonlinear global modes is then shown to agree with numerical simulations of wake flows [15]. In the case of an *infinite medium* with spatially varying instability properties, two types of nonlinear global modes have been identified. *Soft global modes* [16] evolve slowly over a typical wavelength and are governed by a nonlinear frequency selection criterion: the global frequency satisfies a saddle point condition enforced on the nonlinear dispersion relation with respect to both the wavenumber and the streamwise coordinate. Such nonlinear states are only likely to be observed for weak basic flow advection. *Steep global modes* [17, 18] are the infinite-medium counterparts of

the global modes encountered in semi-infinite media. They display a stationary front at the streamwise station separating the upstream convectively unstable region from the central absolutely unstable region. The steep global frequency is then given by the real absolute frequency that prevails at the front station, where the medium exhibits a transition from convective to absolute instability. Such steep nonlinear global modes have recently been identified in direct numerical simulations of a family of spatially developing wakes [19]. The numerically computed frequency is found to be satisfactorily predicted by the marginal absolute/convective instability criterion (see the contributed lecture of Pier and Huerre entitled "A resonance principle for spatially developing wakes" in this volume).

References

[1] Huerre, P. and Monkewitz, P.A. Local and global instabilities in spatially developing flows. *Ann. Rev. Fluid Mech.* 22:473-537, 1990.

[2] Chomaz, J.M., Huerre, P. and Redekopp, L.G. A frequency selection criterion in spatially developing flows. *Stud. Appl. Math.* 84:119-144, 1991.

[3] Le Dizès, S., Huerre, P., Chomaz, J.M. and Monkewitz, P.A. Linear global modes in spatially developing media. *Phil. Trans. R. Soc. Lond. A* 354:169-212, 1996.

[4] Monkewitz, P.A., Huerre, P. and Chomaz, J.M. Global linear stability analysis of weakly non-parallel shear flows. *J. Fluid Mech.* 254:1-20., 1993.

[5] Hammond, D.A. and Redekopp, L.G. Global dynamics of symmetric and asymmetric wakes. *J. Fluid Mech.* 331:231-260., 1997.

[6] Chomaz, J.M. Absolute and convective instabilities in nonlinear systems. *Phys. Rev. Lett.* 69:1931-1934, 1992

[7] Couairon, A and Chomaz, J.M. Absolute and convective instabilities, front velocities and global modes in nonlinear systems. *Physica D* 108:236-276, 1997.

[8] Couairon, A and Chomaz, J.M. Pattern selection in the presence of a cross flow. *Phys. Rev. Lett.* 79:2666-2669, 1997.

[9] Couairon, A and Chomaz, J.M. Fully nonlinear global modes in slowly varying flows. *Phys. Fluids* 11:3688-3703, 1999.

[10] van Saarloos, W. Front propagation into unstable states : marginal stability as a dynamical mechanism for velocity selection. *Phys. Rev. A* 37:211-229, 1988.

[11] van Saarloos, W. Front propagation into unstable states. II. Linear versus nonlinear marginal stability and rate of convergence *Phys. Rev.* A 39:6367-6390, 1989.

[12] Müller, H.W., Lücke, M. and Kamps, M. Transversal convection patterns in horizontal shear flow. *Phys. Rev. A* 45:3714-3726, 1992.

[13] Büchel, P., Lücke, M., Roth, D., and Schmitz, R. Pattern selection in the absolutely unstable regime as a nonlinear eigenvalue problem : Taylor vortices in axial flow. *Phys. Rev. E* 53:4764-4777, 1996.

[14] Gondret, P., Ern, P., Meignin, L. and Rabaud, M. Experimental evidence of a nonlinear transition from convective to absolute instability. *Phys. Rev. Lett.* 82:1442-1445, 1999.

[15] Zielinska, B.J.A. and Wesfreid, J.E. On the spatial structure of global modes in wake flows. *Phys. Fluids* 7:1418-1424., 1995

[16] Pier, B. and Huerre, P. Fully nonlinear global modes in spatially developing media. *Physica D* 97:206-222, 1996.

[17] Pier, B., Huerre, P., Chomaz, J.M. and Couairon, A. Steep nonlinear global modes in spatially developing media. *Phys. Fluids* 10:2433-2435, 1998.

[18] Pier, B., Huerre, P. and Chomaz, J.M. Bifurcation to fully nonlinear synchronized structures in slowly varying media. Submitted to *Physica D*, 2000.

[19] Pier, B. and Huerre, P. Nonlinear self-sustained structures and fronts in spatially developing wake flows. Submitted to *J. Fluid Mech.*, 2000.

XXIX

Small Scale Features

ADVANCES IN TURBULENCE VIII
Proceedings of the Eighth European Turbulence Conference
C. Dopazo et al. (Eds.)
© CIMNE, Barcelona 2000

Geometrical statistics in the atmospheric turbulent flow at Re_λ=10^4

M. Kholmyansky, A. Tsinober, and S. Yorish

Department of Fluid Mechanics and Heat Transfer
Faculty of Engineering, Tel Aviv University, Tel Aviv 69978 Israel

Contact e-mail: kholm@eng.tau.ac.il

1 The experiment

We report first results obtained in a field experiment (see Table 1 for the basic data) in which we measured all the three velocity componets and all the nine componenets of the velocity gradients tensor. This was done by implementation in the field of techniques used by [3, 4] in laboratory experiments. Several essential technological innovations were introduced in the manufacturing process of the 20 hot-wire probe in view of specific requirements of a field experiment. A special high precision calibration unit was designed and manufactured for computer controlled three-dimensional calibration of the probe. More details on the experiments are given in [1].

Table 1. Basic information on the experimental run.

U_1	u_1'	u_2'	u_3'	λ	η	$r_{u_1u_3}$	C	Re_λ	$S_{\alpha\alpha}$	$S_{ij}(i\neq j)$
m/s	m/s	m/s	m/s	m	m					
7.0	1.0	1.0	0.6	0.14	$8\cdot10^{-4}$	-0.33	0.53	10^4	0.7	$0.05\div0.1$

The notations are: x_1 - horizontal streamwise, x_2 - horizontal spanwise, and x_3 - vertical coordinates respectively; u_i - corresponding components of velocity fluctuations, u_i' - their rms values; $r_{u_1u_3}=\langle u_1u_3\rangle/(u_1'u_3')$ - correlation coefficient between the streamwise and vertical components of velocity fluctuations; C - Kolmogorov constant; $S_{\alpha\alpha}$ - skewness of velocity derivative $\frac{\partial u_\alpha}{\partial x_\alpha}$ ($\alpha=1,2,3$, no summation), $S_{ij}(i\neq j)$ - skewness of velocity derivative $\frac{\partial u_i}{\partial x_j}$.

2 Geometrical statistics

Geometrical statistics exhibits important aspects of dynamics and structure of turbulent flows which are essentially beyond phenomenology. The PDFs of the cosine of the angle between vorticity $\boldsymbol{\omega}$ and the eigenvectors $\boldsymbol{\lambda}_i$ of the rate of strain tensor $\cos(\boldsymbol{\omega},\boldsymbol{\lambda}_i)$ exhibit the same behaviour as in flows at moderate Reynolds numbers $\mathrm{Re}_\lambda\sim10^2$. This is clearly seen from Figure 1*a*.

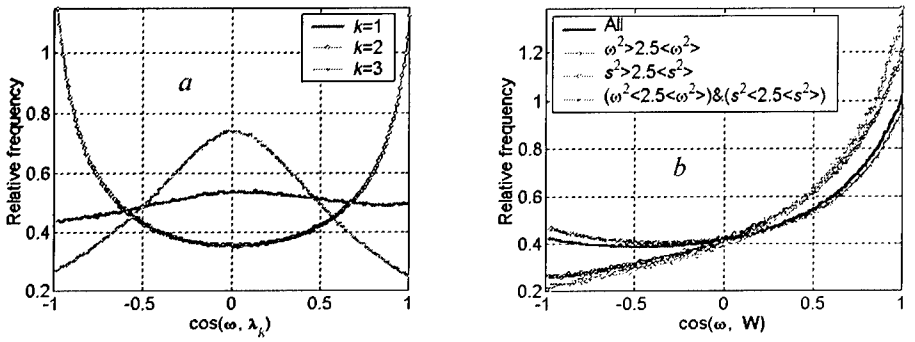


Figure 1: PDFs of the cosine of the angle between vorticity $\boldsymbol{\omega}$ and a) the eigenvectors $\boldsymbol{\lambda}_k$ of s_{ij}, $\cos(\boldsymbol{\omega}, \boldsymbol{\lambda}_k)$; b) the vortex stretching vector, $\cos(\boldsymbol{\omega}, \mathbf{W})$.

Table 2. Contribution of terms associated with the eigenvalues Λ_k of s_{ij} to the mean enstrophy generation $\langle \omega_i \omega_j s_{ij} \rangle = \langle \omega^2 \Lambda_k \cos^2(\boldsymbol{\omega}, \boldsymbol{\lambda}_k) \rangle$, its rate, and vortex stretching $\langle W^2 \rangle = \langle \omega^2 \Lambda_k^2 \cos^2(\boldsymbol{\omega}, \boldsymbol{\lambda}_k) \rangle$ and its rate. The last row shows the means of the eigenvalues of the rate of strain tensor, Λ_k; $s^2 = s_{ij} s_{ij} = \Lambda_1^2 + \Lambda_2^2 + \Lambda_3^2$.

$\langle \omega^2 \Lambda_1 \cos^2(\boldsymbol{\omega}, \boldsymbol{\lambda}_1) \rangle$	$\langle \omega^2 \Lambda_2 \cos^2(\boldsymbol{\omega}, \boldsymbol{\lambda}_2) \rangle$	$\langle \omega^2 \Lambda_3 \cos^2(\boldsymbol{\omega}, \boldsymbol{\lambda}_3) \rangle$
1.437	0.467	-0.904
$\langle \Lambda_1 \cos^2(\boldsymbol{\omega}, \boldsymbol{\lambda}_1) \rangle$	$\langle \Lambda_2 \cos^2(\boldsymbol{\omega}, \boldsymbol{\lambda}_2) \rangle$	$\langle \Lambda_3 \cos^2(\boldsymbol{\omega}, \boldsymbol{\lambda}_3) \rangle$
2.275	0.472	-1.748
$\langle \omega^2 \Lambda_1^2 \cos^2(\boldsymbol{\omega}, \boldsymbol{\lambda}_1) \rangle$	$\langle \omega^2 \Lambda_2^2 \cos^2(\boldsymbol{\omega}, \boldsymbol{\lambda}_2) \rangle$	$\langle \omega^2 \Lambda_3^2 \cos^2(\boldsymbol{\omega}, \boldsymbol{\lambda}_3) \rangle$
0.517	0.125	0.358
$\langle \Lambda_1^2 \cos^2(\boldsymbol{\omega}, \boldsymbol{\lambda}_1) \rangle$	$\langle \Lambda_2^2 \cos^2(\boldsymbol{\omega}, \boldsymbol{\lambda}_2) \rangle$	$\langle \Lambda_3^2 \cos^2(\boldsymbol{\omega}, \boldsymbol{\lambda}_3) \rangle$
0.499	0.089	0.412
$\langle \Lambda_1 \rangle / \langle s^2 \rangle^{1/2}$	$\langle \Lambda_2 \rangle / \langle s^2 \rangle^{1/2}$	$\langle \Lambda_3 \rangle / \langle s^2 \rangle^{1/2}$
0.474	0.058	-0.532

The most dynamically important alignment is the one between vorticity $\boldsymbol{\omega}$ and the vortex stretching vector $\mathbf{W}$, $W_i = \omega_j s_{ij}$, since the cosine of the angle between the two is the normalized enstrophy production $\omega_i \omega_j s_{ij} / (|\boldsymbol{\omega}| \cdot |\mathbf{W}|)$. The PDF of the cosine of this angle, $\cos(\boldsymbol{\omega}, \mathbf{W})$, is positively skewed in full accordance with the predominance of vortex stretching over vortex compressing (Figure 1b). This asymmetry is preserved at very low level of enstrophy and total strain, which is a clear indication that there are no regions in the turbulent flow exhibiting Gaussian behaviour and/or which are 'structureless'. An important aspect is that the asymmetry of $\cos(\boldsymbol{\omega}, \mathbf{W})$ and corresponding process of predominant production of enstrophy is associated with two qualitatively different regions of turbulent flow. The first one is where vorticity tends to be aligned with $\boldsymbol{\lambda}_1$, the eigenvector corresponding to the largest eigenvalue, Λ_1, of s_{ij}. The second region is where vorticity tends to be aligned with $\boldsymbol{\lambda}_2$, the eigenvector corresponding to the intermediate eigenvalue, Λ_2, of s_{ij} ($\Lambda_1 > \Lambda_2 > \Lambda_3$). It is interesting that the contribution to the enstrophy production and other nonlinearities from the first

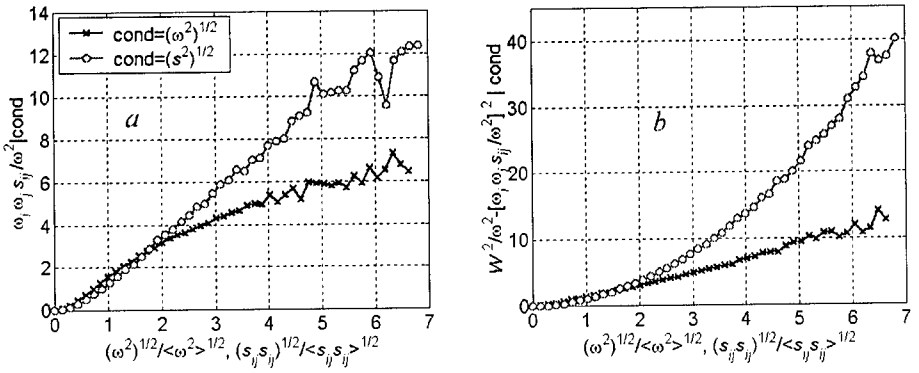


Figure 2: Conditional averages of *a*) $\omega_i\omega_j s_{ij}/(\omega^2)$ and *b*) $W^2/(\omega^2) - \{\omega_i\omega_j s_{ij}/(\omega^2)\}^2$ in slots of ω and s.

region is two times larger than from the second region in spite of the general tendency for alignment between vorticity and $\boldsymbol{\lambda}_2$ (see Table 2). This happens because Λ_1 is almost order of magnitude larger than Λ_2 (see the last row in the Table 2). The asymmetry in the PDF of $\cos(\boldsymbol{\omega}, \mathbf{W})$ is much stronger in regions dominated by strain, $s^2 \equiv s_{ij}s_{ij}$ than in regions with large enstrophy, ω^2. This corresponds to reduction of nonlinearity in the regions with large enstrophy as compared with regions dominated by strain.

3 Reduction of nonlinearity

This is understood here in the sense of the works [2, 5]. Namely, all the physically meaningful nonlinearities appear to be much smaller in the regions with concentrated vorticity (large enstrophy) than in the regions dominated by strain. This is true of such quantities as $\omega_i\omega_j s_{ij}$, $\omega_i\omega_j s_{ij}/(\omega^2)$, $s_{ij}s_{jk}s_{ki}$, $s_{ij}s_{jk}s_{ki}/(s^2)$, W^2 ($W_i \equiv \omega_i s_{ij}$), $W^2/(\omega^2)$ and $W^2/(\omega^2) - \{\omega_i\omega_j s_{ij}/(\omega^2)\}^2$. All these quantities appear in the equations for vorticity, ω_i, enstrophy, ω^2, total strain, $s^2 = s_{ij}s_{ij}$, etc. The quantity $W^2/(\omega^2) - \{\omega_i\omega_j s_{ij}/(\omega^2)\}^2$ is the inviscid rate of change of direction of the vorticity vector. It appears in the equation for the unit vector of vorticity, $\widetilde{\omega}_i = \omega_i/\omega$, i.e. it is responsibe for tilting of vorticity. In Figure 2 we show two examples clearly demonstrating the phenomeneon of reduction of nonlinearity. It is noteworthy that this behaviour is observed also for the nonlinearity, $N_i = u_k\partial u_i/\partial x_k$ in the Navier-Stokes equation as seen from the Figure 3*a*), whereas the behaviour of the Lamb vector $\boldsymbol{\omega} \times \mathbf{u}$ is opposite (Figure 3*b*).

4 Conclusions

The results obtained in this research are the first ones in which explicit information is obtained on the field of velocity derivatives (all the nine components of the tensor $\frac{\partial u_i}{\partial x_j}$) and velocity differences along with all the tree components of

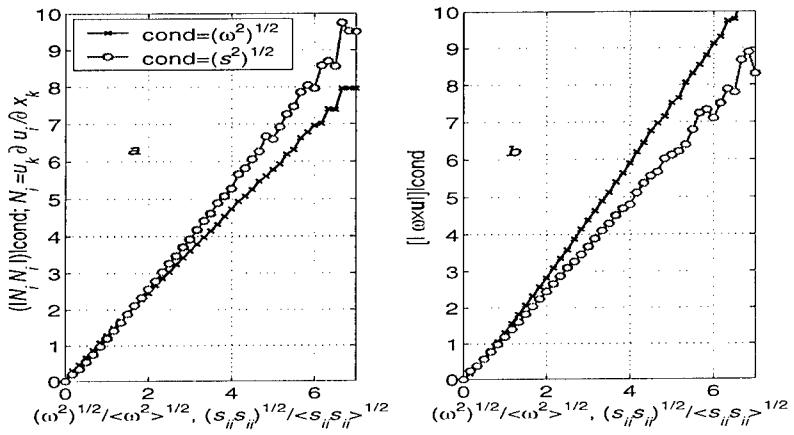


Figure 3: Conditional averages of *a*) N^2 and *b*) $\boldsymbol{\omega} \times \mathbf{u}$ in slots of ω and s.

velocity fluctuations at Reynolds number as high as $\mathrm{Re}_\lambda \sim 10^4$. Up to present the field of velocity derivatives was accessible at $\mathrm{Re}_\lambda \sim 10^2$.

Our main conclusion is that the the basic physics of turbulent flow at high Reynolds number $\mathrm{Re}_\lambda \sim 10^4$ at least qualitatively is the same as at moderate Reynolds numbers, $\mathrm{Re}_\lambda \sim 10^2$. This is true of such basic processes as enstrophy and strain production, geometrical statistics, the role of concentrated vorticity and strain, and reduction of nonlinearity.

References

[1] M. Kholmyansky, and A. Tsinober. On the origins of intermittency in real turbulent flows. *in: Intermittency in Turbulent Flows and Other Dynamical Systems, Isaac Newton Institute, Cambridge, June 21-24, 1999, in press.*.

[2] A. Tsinober. Vortex stretching versus production of strain/dissipation. Isaac Newton Institute for Mathematical Sciences, Preprint NI99010-TRB, 11 June 1999. To be published in the Proceedings of the Symposium on *Turbulence structure and vortex dynamics*, held at Isaac Newton Institute, Cambridge, March 15-19, 1999.

[3] A. Tsinober, E. Kit, and T. Dracos. Experimental investigation of the field of velocity gradients in turbulent flows. *J. Fluid Mech.*, 242:169–192, 1992.

[4] A. Tsinober, L. Shtilman, and H. Vaisburd. A study of vortex stretching and enstrophy generation in numerical and laboratory turbulence. *Fluid Dyn. Res.*, 21:477–494, 1997.

[5] A. Tsinober, M. Ortenberg, and L. Shtilman. On depression of nonlinearity in turbulence. *Phys. Fluids*, 11:2291–2297, 1999.

ADVANCES IN TURBULENCE VIII
Proceedings of the Eighth European Turbulence Conference
C. Dopazo et al. (Eds.)
© CIMNE, Barcelona 2000

Improvements to hot-wire measurements of turbulence energy dissipation

J.-J. Lasserre, M. Coantic and F. Anselmet

I.R.P.H.E., Universités d'Aix-Marseille I & II, CNRS,
12, Av. Général Leclerc, F-13003 Marseille, France.

Contact e-mail: lasserre@marius.univ-mrs.fr

1 Introduction

In turbulent flows where the relative turbulence intensity is not too high, hot-wire anemometry is the most practical and most used experimental technique for the measurement of ϵ, the mean dissipation rate of the kinetic energy of turbulence into heat. Only in the academic isotropic case, ϵ can be obtained from a single hot wire measurement of the longitudinal velocity derivative, using Taylor's hypothesis. In the much more frequent homogeneous anisotropic situations, the determination of ϵ requires the nine variances of velocity component derivatives $\overline{(\partial u/\partial y)^2}$ to be known, so that probes with several wires are needed. In a first step, two-wire probes (X and parallel) are used to evaluate the influence of anisotropy in the determination of ϵ. However, the measurement of the fine scales of turbulence which govern the above variances still raises many problems such as the spatial integration through the finite probe size (Wyngaard [6], Elsner et al. [2]) and the anemometer signal-to-noise ratio in the high frequency range (Freymuth [4]). In addition, the spacing between parallel wires has to be optimized for accurate measurements of velocity transverse derivatives (Mestayer and Chambaud [5]).

Our first objective is to improve the spectral measurements of ϵ_{iso} with a single hot-wire, while the second is to identify the reasons for the "explosion" phenomenon of derivative estimates from two closely spaced parallel wires. Measurements were performed on the axis of a fully-developed 0.25 m diameter pipe flow where turbulence can be considered as locally isotropic, for velocities between 1 ms^{-1} and 30 ms^{-1} corresponding to a large Kolmogorov scale range, 1 mm $\geq \eta \geq O.14$ mm . The Dantec Streamline anemometer system was used together with, first, spot-soldered Tungsten wires 1.25 mm long and 5 μm in diameter and, then, Wollaston Tungsten wires 0.5 mm long and 2.5 μm in diameter.

2 Corrections to the spectral measurements of ϵ_{iso}

To avoid integration effects (Zhu and Antonia [7]), it would be desirable that the probe dimensions do not exceed the Kolmogorov scale, which is not feasible in general. The correction methods are generally based on Wyngaard's assumptions which state that the sensitivity to velocity fluctuations is uniformly distributed along the hot wire length and Pao's isotropic spectral model can be used. Figure 1 shows that the resulting high-frequency correction is too important, so that ϵ_{iso} obtained from the spectrum derivative is overestimated by about 10%. We, therefore, choose to follow Elsner et al's suggestion after which the wire sensitivity should be taken as proportional to its local excess temperature, so that the cooling effect of the probe prongs reduces the effective length of the wire. In addition, a new semi-empirical Reynolds-number-dependent model taking into account the "bump" phenomenon due to an energy pileup at the right end of the inertial plateau in "compensated" high-Reynolds number turbulence spectra (Coantic and Lasserre [1]) has been adopted. The final result is compared with the first one and it appears clearly that the integration effect is better corrected. Here, for the spot-soldered Tungsten wires 1.25 mm long and 5 μm in diameter, the effective wire length is only about 80% of the wire length.

Electronic noise is known as the limiting factor for the high frequency range which can be covered by hot-wire anemometry. As a consequence, Kolmogorov scales are generally buried within the noise during high Reynolds number experiments, and an accurate determination of ϵ_{iso} is impossible. We have checked from our constant-temperature anemometers that the noise spectra follow a reproducible close to f^2 behavior with an amplitude agreeing with Freymuth's theory (figure 2). Signal and noise being not correlated, this leads to the following correction procedure : i) a dissipation spectrum is measured up to frequencies such that only noise is important, ii) this allows determining the amplitude of a f^4 noise contribution to the dissipation spectrum that we extrapolate down to the lowest frequencies and subtract from the original dissipation spectrum as shown in figure 1.

3 On the divergence of $\overline{(\Delta u/\Delta y)^2}$

The measurement of $\overline{(\partial u/\partial y)^2}$ using closely spaced parallel wires is handicapped by two conflicting requirements: very small separations are necessary to avoid spatial averaging, and an increasing divergence appears due to noise when this separation decreases [5]. Wyngaard suggested that the optimum value of Δy should be in the range . Considerable experimental, numerical and theoretical effort has been done during the last two decades to explain this phenomenon [3]. Some studies suggest that an electrical or thermal crosstalk exists between the two wires in addition to the aerodynamic disturbance caused by the probe [3].

Others ignore as not reliable the results obtained at small separations and perform an extrapolation from the largest to the smallest separations ([7], [3]). We have carried out a spectral study of this phenomenon with the view to find the origin of this "noise". In fact, experiments in laminar flow for different mean velocities and wire separations show that the noise spectrum of the signal difference is just the sum of the noises from the two anemometers, and therefore important only for the highest frequencies. On the contrary, experiments in turbulent situations have demonstrated the presence of an additional "noise" of much larger amplitude extending down well in the energy-containing frequency range (figure 2). Since that contribution does not vary much for the smallest separations, the $(\Delta u/\Delta y)$ spectra tend to "explode" when Δy is very small, as shown on figure 3. To find the noise spectrum and the corresponding spectral correction for the turbulent case, we assume that signal and noise are not correlated. We can thus write for each frequency and for the three smallest separations Δy : $E_{\Delta u}^{meas} = B(f) + S(f).(\Delta y)^2$, where $B(f)$ is the noise spectrum, and the slope $S(f)$ is the corrected spectrum. Then, $S(f) = E_{\Delta u}^{corr} = (E_{\Delta u}^{meas} - B(f))/(\Delta y)^2$ (figure 3). Using the three smallest separations to determine a corrected spectrum enables us to avoid the phenomenon of spatial integration. Figure 4 furthermore shows that the relative level of this "noise" appears as unaffected by the wire overheat : this test therefore denies the possibility of electrical or thermal cross-talk. Moreover, such a divergence is observed in the measurements of the transverse gradient of temperature, using cold wire anemometry. It is important to note that the phenomenon is similar at different Reynolds numbers, the variance being a unique function of the separation when plotted using Kolmogorov's scaling. In addition, the Δu pdfs for the smallest separations tend to be gaussian.

4 Conclusion

We first showed that the traditional Wyngaard correction using Pao's spectrum tends to overestimate eiso by approximately 10%, whereas Elsner et al.'s suggestion combined with a new semi-empirical Reynolds dependent model gives a better result in comparison with experiments. Moreover, using Freymuth's theory about the electrical noise, we suggest an original correction of the longitudinal spectrum of the dissipation. The final objective was to identify the reasons for the divergence of the derivative variance estimates $\overline{(\Delta u/\Delta y)^2}$ from two closely spaced parallel wires. A spectral study has demonstrated the presence of an additional "noise" between the laminar and turbulent cases, the level of which appears as unaffected by the wire overheat. A spectral correction method is proposed. The ensemble of our experimental results suggests to associate the problem only with the aerodynamic disturbances of the probes. This opens the way to interesting speculations and new investigations. (Supports of PSA Peugeot-Citroën and of Electricité de France are gratefully acknowledged.)

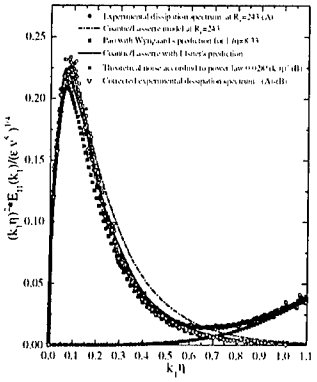


Figure 1

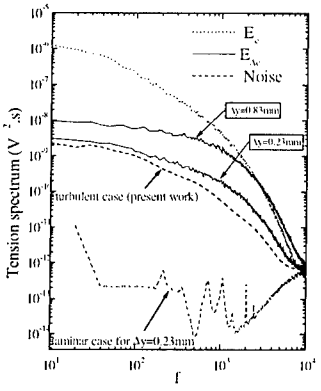


Figure 2

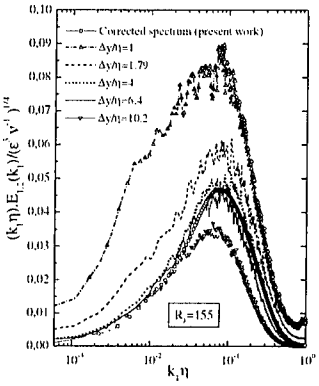


Figure 3

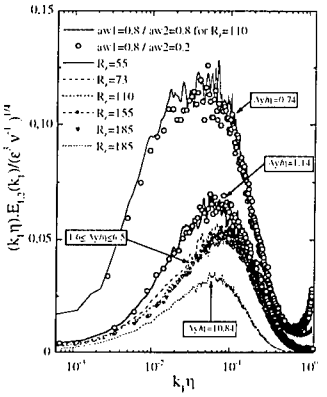


Figure 4

Figure 1 : Different corrections of dissipation spectrum for a large R_λ.
Figure 2 : Noise in the determination of $\overline{(\Delta u/\Delta y)^2}$.
Figure 3 : Correction of the "explosion " phenomenon.
Figure 4 : Spectral behavior of $(\Delta u/\Delta y)$ for both various R_λ and overheats.

References

[1] M. Coantic and J.-J. Lasserre. *Eur. Jour. Mech.-B/Fluids*,6, 1027-1047, 1999.
[2] J. W. Elsner, P. Domagala and W. Elsner. *Meas. Sci. Technol.*, 4, 517-523, 1993.
[3] J. W. Elsner and W. Elsner. *Meas. Sci. Technol.*, 7, 1334-1348, 1996.
[4] P.Freymuth. *Rev. Sci. Instr.*, 10, 550-557, 1968.
[5] P. Mestayer and P. Chambaud. *Boundary Layer Met.*, 16, 311-329, 1979.
[6] J.C. Wyngaard. *Jour. Sci. Instr.*,2, 1, 1105-1108, 1968.
[7] Y. Zhu and R.A .Antonia. *Meas. Sci. Technol.*,7, 1349-1359, 1996.

ADVANCES IN TURBULENCE VIII
Proceedings of the Eighth European Turbulence Conference
C. Dopazo et al. (Eds.)
© CIMNE, Barcelona 2000

Turbulent energy scale–budget equations in a fully developed channel flow

L. Danaila[1], F. Anselmet[1], T. Zhou[2] and R.A. Antonia[2]

[1] I.R.P.H.E.
C.N.R.S.- Université d'Aix Marseille, 13003 Marseille, FRANCE
[2]Department of Mechanical Engineering
University of Newcastle, N.S.W., 2308, AUSTRALIA

Contact e-mail: ldanaila@marius.univ-mrs.fr

1 Introduction

Kolmogorov's equation (homogeneous and isotropic relation linking the second– and third–order moments of velocity increment) provides a simple method for estimating the mean energy dissipation rate $\langle\epsilon\rangle$ [1]. When investigating low and moderate Reynolds numbers, Kolmogorov's equation is usually not verified. The aim of this study is to identify the origin of this shortcoming, in the specific context of what happens on the centreline of a turbulent channel flow. In this case, a generalized form of Kolmogorov's equation is written which includes an additional term reflecting the large-scale turbulent diffusion acting from the walls through the centre of the channel. We verify our predictions using hot–wire measurements in a fully developed turbulent channel flow ($R_\lambda \geq 36$), analyzed using values of the mean energy dissipation rate inferred from direct numerical simulation (DNS) data [2], for the same flow and Reynolds numbers. We point out that, for moderate Reynolds numbers, the mean turbulent energy transferred at a scale r also contains a large–scale contribution, reflecting the non–homogeneity of these scales.

2 Theory and Results

The determination of the mean energy dissipation rate $\langle\epsilon\rangle$ with relatively high accuracy is a major challenge in experimental turbulence research, since the definition of $\langle\epsilon\rangle$, $\equiv \frac{1}{2}\nu\langle(\frac{\partial u_i}{\partial x_j}+\frac{\partial u_j}{\partial x_i})^2\rangle$, includes all velocity component derivatives. Here, repeated indices indicate summation, ν is the kinematic viscosity of the fluid, u_i is the fluctuating velocity component in the i-th direction, and angular brackets denote time averaging.

Estimating $\langle\epsilon\rangle$ directly from this definition represents a formidable task to the experimenter since velocity spatial derivatives are very difficult to obtain accurately. Additional hypotheses on the flow properties are then necessary. Homogeneity leads to $\langle\epsilon\rangle \equiv 3\nu\langle(\frac{\partial u_i}{\partial x_1})^2\rangle$, whilst isotropy leads to $\langle\epsilon\rangle_{iso} \equiv 15\nu\langle(\frac{\partial u_1}{\partial x_1})^2\rangle$, where u_1 is the longitudinal (streamline) velocity component. A simpler way of estimating $\langle\epsilon\rangle$ is to focus on the larger scales of the flow. Starting from the Navier–Stokes (N–S) equations, using homogeneity and isotropy, Kolmogorov's equation is obtained [1]:

$$-\langle(\Delta u_1)^3\rangle + 6\nu\frac{d}{dr}(\Delta u_1)^2 = \frac{4}{5}\langle\epsilon\rangle r, \tag{1}$$

where the increment $\Delta u_1(r) \equiv u_1(x_1+r) - u_1(x_1)$ is measured along the streamwise direction x_1. Writing Eq.(1) as $A+B=C$, term C, directly proportional to the dissipation rate $\langle\epsilon\rangle$, is associated with the energy transferred at any scale r. Relation (1) indicates that the mean energy transferred at a scale r is composed of both the energy lost through the turbulent advection (term A) and the energy lost by molecular destruction (term B). Therefore, equation (1) provides in principle a practical means of obtaining $\langle\epsilon\rangle$, since the second– and third–order moments can be inferred from single hot–wire measurements via Taylor's hypothesis. It was experimentally demonstrated that relation (1) is verified only for the small scales, when the Taylor microscale Reynolds number R_λ is moderate [3] (see also our Fig. 1), ($R_\lambda \equiv u_1'\lambda/\nu$, where u_1' is the longitudinal velocity RMS, and $\lambda \equiv u_1'/[\langle(\partial u_1/\partial x_1)^2\rangle]^{1/2}$ is the longitudinal Taylor micro-scale). For very small scales, Eq. (1) reduces to the isotropic form of $\langle\epsilon\rangle$.
A slightly more general relation between second and third–order velocity moments has been obtained in [4], viz:

$$-\langle\Delta u_1(\Delta u_i)^2\rangle + 2\nu\frac{d}{dr}\langle(\Delta u_i)^2\rangle = \frac{4}{3}\langle\epsilon\rangle r. \tag{2}$$

An analogy between this equation and Yaglom's equation for temperature increments is discussed. Equation (2), which reduces for very small scales to the homogeneous form of $\langle\epsilon\rangle$, is also verified for only the small scales, despite its more general character.

There is no physical reason why Eqs. (1) and (2) should not be verified, since they characterize the equilibrium state of the flow. Our objective is then to understand more about the mathematical form and the physical significance of the differences between the left and right sides in various forms of Kolmogorov's equation, for moderate Reynolds numbers. It is reasonable to think that one (or more) additional term has to be taken into account in a 'complete' form of these equations. This term plays the role of a 'forcing' term, and its contribution would be mainly to re–establish the balance for the large scales.
Kolmogorov's equation with an additional forcing term has been introduced in a generic form by Frisch, [5], re-discussed in the wider context of local homogeneity and isotropy, by Hill [6], and further investigated by [7], [8], [9].

In the present paper, we identify the origin of the imbalance between the different terms in Eqs. (1) and (2) for relatively small Reynolds numbers, on the centreline of a channel flow. Channel flow does not decay, but it is characterized by lateral diffusion in the direction x_3, normal to the wall. We take into account this (large–scale) non–homogeneity when deriving Kolmogorov's equation, but continue to use local isotropy for terms such as turbulent advection and molecular diffusion. The generalized form of Kolmogorov's equation is then:

$$-\langle(\Delta u_1)^3\rangle + 6\nu\frac{d}{dr}\langle(\Delta u_1)^2\rangle - \frac{6}{r^4}\int_0^r y^4\partial_{x_3}\langle u_3(\Delta u_1)^2\rangle(y)dy = \frac{4}{5}\langle\epsilon\rangle r, \qquad (3)$$

where y is a dummy variable, representing the separation along the x_1 direction. The third term on the left reflects the flow non–homogeneity since it contains derivatives with respect to x_3. Similarly, it is possible to generalize Eq. (2):

$$-\langle\Delta u_1(\Delta u_i)^2\rangle + 2\nu\frac{d}{dr}\langle(\Delta u_i)^2\rangle - \frac{2}{r^2}\int_0^r y^2\partial_{x_3}\langle u_3(\Delta u_i)^2\rangle(y)dy = \frac{4}{3}\langle\epsilon\rangle r, \quad (4)$$

where y is also considered along the x_1 direction. Equation (4) is then written in a dimensionless form as $A + B + NH = C$ ($C = \frac{4}{3}r/\eta$, $\eta = (\nu^3/\langle\epsilon\rangle)^{1/4}$). NH expresses the non–homogeneity of the flow and takes into account all velocity components. Figure (1) contains all the terms in (4) for $R_\lambda = 36$. Note that in

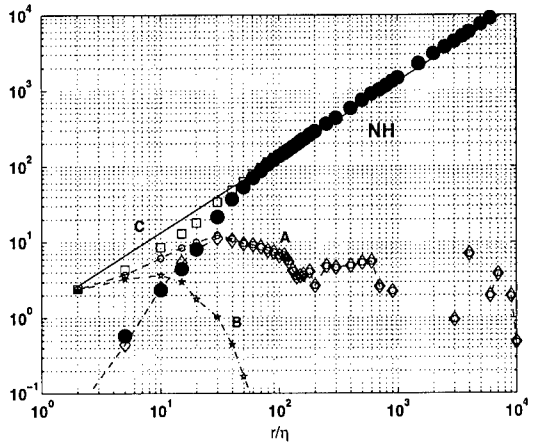


Figure 1: Terms in Eq. (4): term A ($\diamond$), B ($\star$), $A + B$ ($\circ$), NH ($\bullet$). Term $A + B + NH$ ($\square$) is to be compared with C (continuous line).

equations (3) and (4), the non–homogeneous terms are not isotropic, since they retain an information about the 3–D large scale motion. However, these terms have been estimated using measurements [2] and a weak form of local isotropy, which has been experimentally tested.

3 Conclusions

We have incorporated in Kolmogorov's equation an additional term (NH), important for large scales, and of diminishing importance as the scales decrease. For the intermediate scales ($5\eta \leq r \leq 30\eta$), equation (4) is verified with an accuracy of $\pm 15\%$, presumably because of the lack of isotropy. For the larger scales, the equation is very well verified, indicating that the main phenomenon responsible for the equilibrium state of the flow is indeed the large–scale non–homogeneity. Equation (4) is better verified (not shown here) than (3) (especially for the very large scales), indicating that all velocity components play a different role in the energy budget.

The support of the Australian Research Council is gratefully acknowledged. L.D. warmly thanks Prof. M. Coantic and J.J. Lasserre for useful discussions.

References

[1] A. S. Monin and A. M. Yaglom. Statistical fluid mechanics, vol. 2. *Cambridge, Mass., MIT Press*, 1975.

[2] R. A. Antonia, T. Zhou and G. P. Romano. Second– and third– order longitudinal velocity structure functions in a fully developed turbulent channel flow. *Phys. of Fluids*, 9:3465–3471, 1997.

[3] R. A. Antonia, A. J. Chambers and L. W. Browne. Relations between structure functions of velocity and temperature in a turbulent jet. *Experiments in Fluids*, 1:213–219, 1983.

[4] R. A. Antonia, M. Ould–Rouis, F. Anselmet and Y. Zhou. Analogy between predictions of Kolmogorov and Yaglom. *J. Fluid Mech.*, 332:395–409, 1997.

[5] U. Frisch. Turbulence: The Legacy of A.N. Kolmogorov. *Cambridge University Press*, 1995.

[6] R. J. Hill. Applicability of Kolmogorov's and Monin's equations of turbulence. *J. Fluid Mech.*, 353:67–81, 1997.

[7] P. G. Saffman. Lectures on homogeneous turbulence. *Topics in Nonlinear Physics*, Ed. N. Zabusky, 485–614, 1968.

[8] E. Lindborg. Correction to the four–fifths law due to variations of the dissipation. *Physics of Fluids*, 11:510–512, 1999.

[9] L. Danaila, F. Anselmet, T. Zhou and R. A. Antonia. A generalization of Yaglom's equation which accounts for the large–scale forcing in heated decaying turbulence. *J. Fluid Mech.*, 391:359–372, 1999.

ADVANCES IN TURBULENCE VIII
Proceedings of the Eighth European Turbulence Conference
C. Dopazo et al. (Eds.)
© CIMNE, Barcelona 2000

Energy and Temperature Dissipation Rates in a Cylinder Wake and Grid Turbulence

T. Zhou and R. A. Antonia

Department of Mechanical Engineering
University of Newcastle, N.S.W. 2308 Australia

Contact e-mail: metz@cc.newcastle.edu.au

1 Introduction

The enstrophy ω^2, the turbulent energy dissipation rate ϵ and the temperature dissipation rate ϵ_θ are important small-scale turbulence characteristics. For example, ϵ_r and ϵ_{θ_r}, the locally averaged values of ϵ and ϵ_θ, feature in the refined similarity hypothesis [1] and its extension [2, 3] when scalar fluctuations are present. The small-scale characteristics of the scalar field are not only influenced by ϵ_θ, but also by the correlation between ϵ and ϵ_θ. While determinations of ω^2, ϵ and ϵ_θ are feasible in direct numerical simulations (DNS), there have not yet been any attempts to measure these quantities simultaneously. It was shown [4, 5] that intense ω^2 occurs in vortex tubes and ϵ is strongly correlated with these tubes. The regions where ϵ_θ is the largest are dissociated from these tubes and occur as large flat sheets. This implies a good correlation between ϵ and ω^2 but a poor correlation between ϵ_θ and ω^2 (or ϵ). The main objective of this paper is to examine the correlations between ω_3^2, ϵ and ϵ_θ using data obtained from simultaneous measurements of one vorticity component and two components of the temperature dissipation rate in grid and wake flows. This study represents an attempt at simultaneously measuring what are believed to be more reasonable approximations to ϵ and ϵ_θ than $\epsilon_{iso} \equiv 15\nu\, u_{1,1}^2$ and $\epsilon_{\theta_{iso}} \equiv 3\kappa\, \theta_{,1}^2$ [where u_1 is the velocity fluctuation in the streamwise (x_1) direction, ν and κ are the kinematic and thermal diffusivities, $\alpha_{,1} = \partial\alpha/\partial x_1$].

2 Experimental Details

Measurements in the grid (the Taylor microscale Reynolds number R_λ is about 50) and wake ($R_\lambda = 40$) turbulence were carried out in the same working section of the blower type open-circuit wind tunnel. Details of the experimental facility

for grid turbulence can be found in [6]. A circular cylinder of diameter $d = 6.35$ mm is electrically heated to generate temperature fluctuations. The measurement location is at $x_1/d = 240$, where the flow is self-preserving. A probe consisting of four hot-wires (one X-wire straddled by a pair of parallel wires) and a pair of parallel cold-wires is used to measure ω_3 and ϵ_θ (two components : $\theta_{,1}$ and $\theta_{,2}$) simultaneously. The separations Δx_2 between the parallel hot wires and Δx_3 between the two inclined wires of the X-wire respectively, are 1.6 mm, corresponding to 4.8η in the grid and 2.5η on the centreline of the wake (η is the Kolmogorov length scale). The separation Δx_c between the parallel cold wires is 1.95 mm. All wires were etched from Wollaston (Pt-10% Rh) wires. The active lengths were about $800d_w$ and $200d_w$ for the cold and hot wires respectively (d_w is the diameter of the wire and equal to 0.63 μm for the cold and 2.5 μm for the hot wires). The output signals from the anemometers were passed through buck and gain circuits and low-pass filtered at a cut-off frequency f_c close to the Kolmogorov frequency $f_K (\equiv U_1/2\pi\eta$, U_1 is the local mean velocity).

3 Results and Discussion

Since three of the nine velocity derivatives that make up ϵ are measured simultaneously, assuming local isotropy and homogeneity, ϵ is approximated using continuity, $\epsilon \simeq \nu(6u_{1,1}^2 + 3u_{1,2}^2 + 2u_{2,1}^2 + 2u_{1,2}u_{2,1})$. ϵ_θ can be approximated using the temperature derivatives via $\epsilon_\theta \simeq \kappa(\theta_{,1}^2 + 2\theta_{,2}^2)$. The previous relations have been verified in grid turbulence [6] by comparing the measured values of $\langle\epsilon\rangle$ and $\langle\epsilon_\theta\rangle$ with those inferred from the streamwise decay rates of $\langle q^2\rangle$ and $\langle\theta^2\rangle$.

The measured values of $\langle\epsilon\rangle$ and $\langle\epsilon_\theta\rangle$ in the wake, normalized by the half-width L, velocity defect U_0 and the mean temperature ΔT relative to ambient, are shown in Figure 1(a,b) with those in [7, 8, 9]. Because of the spatial resolution, the measured (uncorrected) values of $\langle\epsilon\rangle$ (Figure 1a) are 30% smaller than those of [7]. Spectral corrections [8] to the velocity derivatives result in an increase of 10% for $\langle\epsilon\rangle$. The corrected values of $\langle\epsilon\rangle$ agree favourably with those obtained using a 3-D vorticity probe [8], indicating the appropriateness of the above approximation. The magnitude of $\langle\epsilon\rangle_{iso}$ departs from the corrected value of $\langle\epsilon\rangle$, especially near the edge of the wake, reflecting an increased departure from local isotropy. The present approximation for $\langle\epsilon_\theta\rangle$ (Figure 1b) is consistently smaller than those in [9] in the central region of the wake. The difference between $\langle\epsilon_\theta\rangle_{iso}$ and $\langle\epsilon_\theta\rangle$ is similar to that between $\langle\epsilon\rangle_{iso}$ and $\langle\epsilon\rangle$ (Figure 1a).

The correlations between ω_3^2, ϵ and ϵ_θ can be quantified with the correlation coefficient, $\rho_{\alpha,\beta}$ [$\equiv (\alpha - \langle\alpha\rangle)(\beta - \langle\beta\rangle)/\sigma_\alpha\sigma_\beta$, σ_α and σ_β are the standard deviations of α and β]. They are shown in Figure 2(a,b). The large values of $\rho_{(\omega_3^2)_r,\epsilon_r}$ and the small values of $\rho_{(\omega_3^2)_r,\epsilon_{\theta_r}}$ in both flows indicate a high correlation between enstrophy and energy dissipation rate but a small correlation between enstrophy and temperature dissipation rate. The values of $\rho_{\epsilon_r,\epsilon_{\theta_r}}$ are larger than those of $\rho_{(\omega_3^2)_r,\epsilon_{\theta_r}}$, indicating that the temperature dissipation field is more correlated with the energy dissipation field than with the enstrophy field.

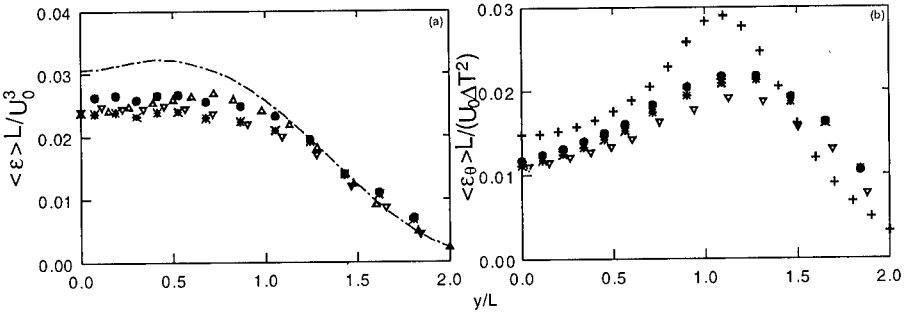


Figure 1: Distributions of $\langle\epsilon\rangle$ and $\langle\epsilon_\theta\rangle$ across the wake. (a) $\langle\epsilon\rangle$; (b) $\langle\epsilon_\theta\rangle$. Present: •, corrected; $*$, uncorrected; ∇, isotropic values. [7]: — - —. [8]: $\triangle$. [9]: +.

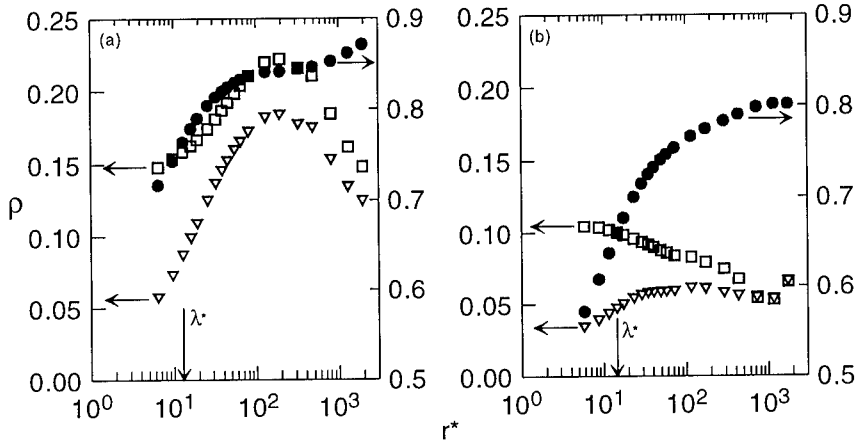


Figure 2: Correlation coefficients between locally averaged values of ω_3^2, ϵ and ϵ_θ. The asterisk denotes normalization by the Kolmogorov length scale $\eta \equiv (\nu^3/\langle\epsilon\rangle)^{1/4}$. (a) wake; (b) grid. •, $\rho_{(\omega_3^2)_r,\epsilon_r}$; ∇, $\rho_{(\omega_3^2)_r,\epsilon_{\theta_r}}$; $\square$, $\rho_{\epsilon_r,\epsilon_{\theta_r}}$.

The magnitudes of $\rho_{\alpha,\beta}$ are larger in the wake than in grid turbulence, possibly reflecting the organized large-scale structures in the former flow, which are identifiable in the u_2 spectrum. Away from the centreline, the influence on $\rho_{\alpha,\beta}$ from these structures increases, resulting in an increase in $\rho_{\alpha,\beta}$.

Jpdfs between $(\omega_3^2)_r$ and either ϵ_r or ϵ_{θ_r} for $r = \lambda$ (λ is the Taylor microscale) on the centreline of the wake are shown in Figure 3(a,b). Large fluctuations of $(\omega_3^2)_r$ are mainly associated with large values of ϵ_r and vice versa. The main axis of the contours is about 45°. The results indicate that high vorticity regions may contain large energy dissipation rates. Figure 3b indicates that large values of $(\omega_3^2)_r$ occur when ϵ_{θ_r} is small and vice versa. These results (Figures 2 and 3) support the DNS-based observations [4, 5].

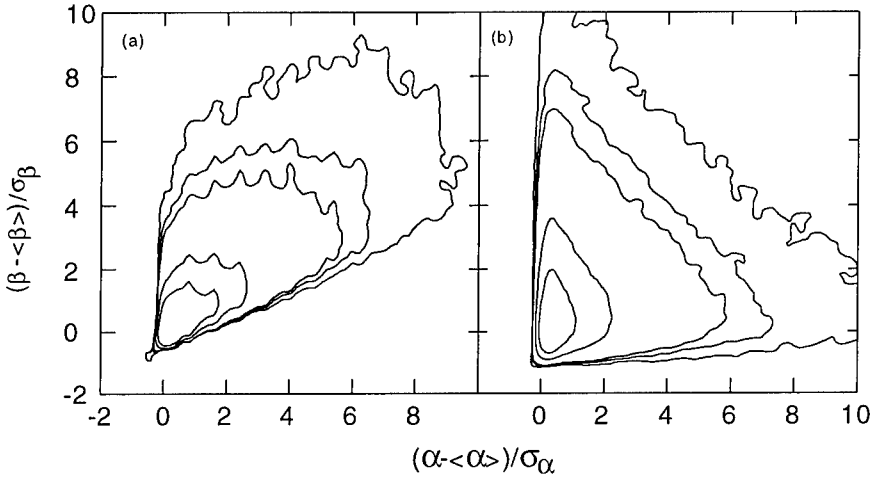


Figure 3: Jpdfs of $(\omega_3^2)_r \sim \epsilon_r$ and $(\omega_3^2)_r \sim \epsilon_{\theta_r}$ in the wake for $r = \lambda$. (a) $\alpha = (\omega_3^2)_r$, $\beta = \epsilon_r [\rho_{(\omega_3^2)_r, \epsilon_r} = 0.77]$; (b) $\alpha = (\omega_3^2)_r$, $\beta = \epsilon_{\theta_r} [\rho_{(\omega_3^2)_r, \epsilon_{\theta_r}} = 0.09]$. Outer to inner contours : 0.001, 0.005, 0.01, 0.1, 0.3.

4 Conclusions

Using data obtained in grid and wake turbulence, the correlation between ω^2 and ϵ is found to be much higher than that between ω^2 and ϵ_θ, in accord with DNS-based investigations [4,5]. The increased magnitudes of these correlations in the wake are likely due to the presence of the organized large-scale motion.

The support of the Australian Research Council is gratefully acknowledged.

References

[1] Kolmogorov, A. N. 1962. *J. Fluid Mech.*, **13**, 82.
[2] Stolovitzky, G., Kailasnath, P. & Sreenivasan, K. R. 1995. *J. Fluid Mech.*, **297**, 275.
[3] Zhu, Y., Antonia, R. A. & Hosokawa, I. 1995. *Phys. Fluids*, **7**, 1637.
[4] Ruetsch, G. R. & Maxey, M. R. 1991. *Phys. Fluids A*, **3**, 1587.
[5] Pumir, A. 1994. *Phys. Fluids*, **6**, 3974.
[6] Zhou, T. & Antonia, R. A. 2000. *Phys. Fluids*, **12**, 335-344.
[7] Browne, L. W. B., Antonia, R. A. & Shah, D. A. 1987. *J. Fluid Mech.*, **179**, 307.
[8] Zhu, Y. & Antonia, R. A. 1999. *Expts. in Fluids*, **27**, 21.
[9] Antonia, R. A. & Browne, L. W. B. 1986. *J. Fluid Mech.*, **163**, 393.

XXX

Miscellaneous

ADVANCES IN TURBULENCE VIII
Proceedings of the Eighth European Turbulence Conference
C. Dopazo et al (Eds.)
© CIMNE, Barcelona 2000

Oscillatory binary fluid convection in finite containers

O. Batiste[1], M. Net[1], I. Mercader[1] and E. Knobloch[2]

[1]Departament de Física Aplicada, UPC
[2]Department of Physics, UC Berkeley

Thermal convection in a binary fluid mixture heated from below provides an ideal system for the study of complex spatio-temporal dynamics. For sufficiently negative separation ratios this system undergoes an oscillatory bifurcation from the conduction state resulting in a rich variety of behavior close to onset, including extended or localized traveling wave states in annular geometry, and the so-called "chevron" and "blinking"' states in rectangular containers of moderately large aspect ratio. In the latter geometry the presence of sidewalls destroys the translation invariance present in an annulus, with important consequences for the dynamics even in large aspect ratio containers [1, 2].

To elucidate the effects of the presence of sidewalls in such containers we have calculated [3] the critical Rayleigh number R_c and oscillation frequency ω_c at the onset of oscillatory convection in a two-dimensional domain with no-slip, no-mass-flux boundary conditions for different values of the separation ratio S, the Prandtl number σ, the Lewis number τ, and of the aspect ratio Γ of the container, assuming fixed temperature along the horizontal boundaries and insulating sidewalls. The parameter values used correspond to experiments performed with normal ^{3}He-^{4}He mixtures [4] and water-ethanol mixtures [5] in narrow rectangular containers. In all cases the first unstable mode has either odd or even parity under left-right reflection, and has the form of a "chevron" pattern, consisting of a pair of waves (usually) propagating outwards from the cell center. These eigenfunctions describe rolls that are continually born in the middle of the container, and travel towards the walls where they disappear (fig. 1). Thus quite complex, albeit temporally periodic behavior, with sources and sinks, is readily described by linear eigenfunctions.

To study the nonlinear saturation of the first unstable mode we have integrated numerically the governing nonlinear partial differential equations in two dimensions for small values of $\epsilon \equiv (R-R_c)/R_c$. We find that nonlinear chevrons resembling those in fig. 1 are stable only in a very narrow range of R and S, cf. [6], and that they lose stability via a subcritical secondary Hopf bifurcation to a state consisting of waves that travel back and forth in the cell, i.e., a blinking state. This observation is consistent with the expected effects of breaking

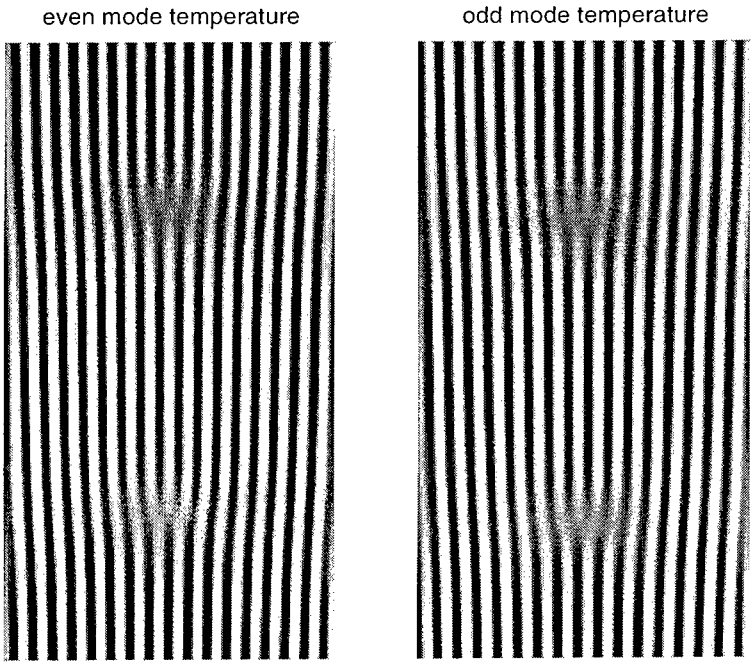


Figure 1: Space-time plots of the midplane temperature for the first two critical modes in a $\Gamma = 34$ container, with time increasing upwards and x horizontally. The parameter values $\sigma = 0.6$, $\tau = 0.03$, $S = -0.021$ correspond to a normal ^{3}He-^{4}He mixture [4]. The critical Rayleigh numbers and frequencies (in vertical thermal diffusion times) are (a) $R_c = 1828.461$, $\omega_c = 2.077$ (odd mode), (b) $R_c = 1829.961$, $\omega_c = 2.062$ (even mode).

translation symmetry due to distant walls [1, 7]. Depending on the parameters and the aspect ratio we find blinking states that evolve regularly or irregularly in time, in accord with both experimental results [5] and theory [8]. For other parameters, for which the chevrons are subcritical and hence unstable, an initial chevron-like disturbance grows exponentially from random initial conditions but does not saturate. Instead, it begins to blink [9] but since the blinking states are also unstable the resulting state collapses to small amplitude, before a new chevron-like disturbance emerges from the collapsed state (see fig. 2). Repeated transients of this type have been observed experimentally in water-ethanol mixtures [5]. The top panel (fig. 2a) shows the distribution of the concentration at a particular instant in time (indicated by a vertical arrow), and confirms that the growing pattern is an even chevron as predicted by linear theory. Fig. 2b shows a long but apparently nonperiodic sequence of repeated transients using the vertical velocity $v_z(x = 0.13L, z = 0.5)$ as a point indicator of the dynamics of the system. This measure is analogous to the point measure employed by Kolodner

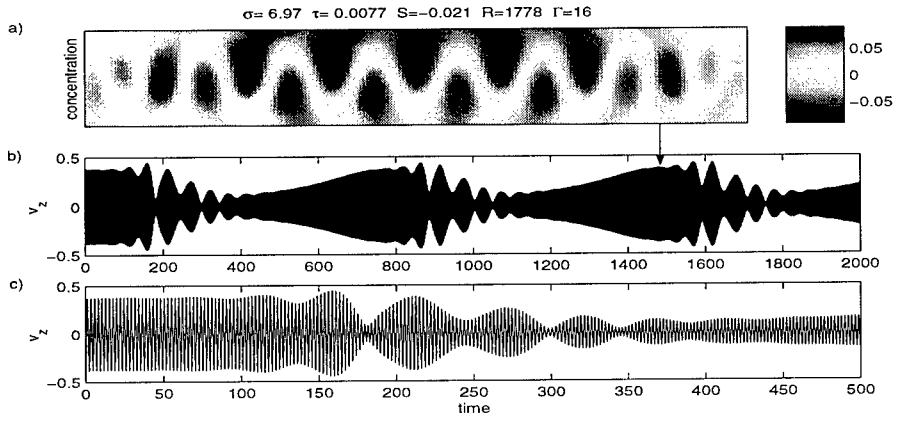


Figure 2: Repeated transients for a water-alcohol mixture in a $\Gamma = 16$ container at $\epsilon = 2.6\,10^{-4}$. The first unstable mode is an even chevron with $R_c = 1777.528$, $\omega_c = 2.854$. Fig. (a) shows the concentration field at the instant indicated, revealing substantial concentration fluctuation even at these small values of ϵ. Figs. (b,c) show $v_z(x = 0.13L, z = 0.5, t)$ over 7.8 horizontal thermal diffusion times, and a detail that shows the onset of blinking followed by collapse. The detailed appearance of the time series depends on the location x.

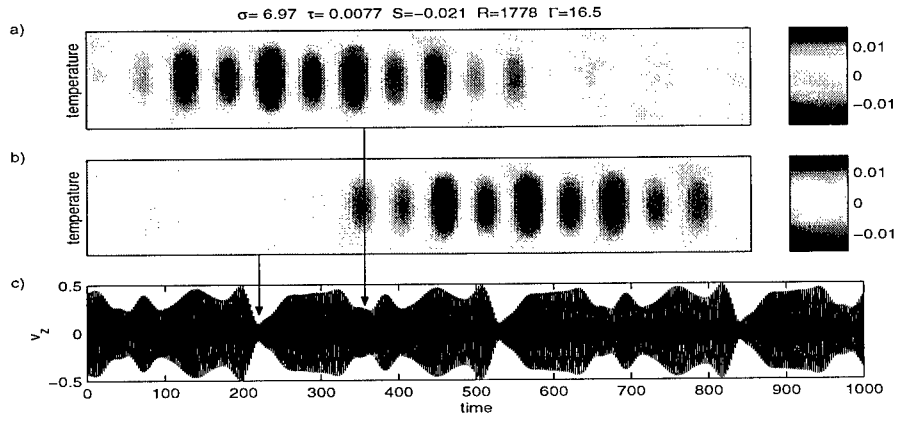


Figure 3: Periodic blinking states for a water-alcohol mixture in a $\Gamma = 16.5$ container at $\epsilon = 8.4\,10^{-4}$. For these parameter values $R_c = 1776.505$, $\omega_c = 2.785$. Figs. (a,b) show the temperature field at the two instants indicated by the vertical arrows; fig. (c) shows $v_z(x = 0.13L, z = 0.5, t)$ after transients have died out. The blinking period is approximately 1.1 horizontal thermal diffusion times.

in his experiments. Fig. 2c shows a detail of the onset of the blinking phase and the subsequent collapse. In fig. 3 we show a time-periodic blinking state at a slightly higher value of ϵ. Figs. 3a,b show the temperature field at two times separated by approximately half the period of a blink. These figures show waves that are localized in opposite parts of the container. The resulting solution may be understood as an oscillation between the amplitudes of the constituent left- and right-traveling waves; the waves themselves do not reverse their direction of propagation. Such an oscillation results in a lateral oscillation of the "source" from which the waves appear to be emitted (cf. fig. 1). The corresponding time series (fig. 3c) shows that despite the complex dynamics the "reversals" are periodic in time. The behavior shown in figs. 2 and 3 occurs in a regime in which the conduction state is unstable to one mode only, and consequently represents the result of secondary bifurcations from a (stable or unstable) small amplitude chevron state [1, 7]. The associated timescale is therefore necessarily long compared with the basic Hopf frequency, as observed. We were unable to reproduce the bursts observed by Sullivan & Ahlers [4] for the parameters of fig. 1.

References

[1] G. Dangelmayr and E. Knobloch. Hopf bifurcation with broken circular symmetry. *Nonlinearity*, 4:399–422, 1991.

[2] A.S. Landsberg and E. Knobloch. Oscillatory bifurcation with broken translation symmetry. *Phys. Rev. E* 53:3579–3600, 1996.

[3] O. Batiste, I. Mercader, M. Net and E. Knobloch. Onset of binary fluid convection in finite containers. *Phys. Rev. E* 59:6730–6741, 1999.

[4] T.S. Sullivan and G. Ahlers. Nonperiodic time dependence at the onset of convection in a binary liquid mixture. *Phys. Rev. A* 38:3143–3146, 1988.

[5] P. Kolodner. Repeated transients of weakly nonlinear traveling-wave convection. *Phys. Rev. E* 47:1038–1048, 1993.

[6] T. Clune and E. Knobloch. Mean flow supression by endwalls in oscillatory binary fluid convection. *Physica D* 61:106–112, 1992.

[7] P.C. Hirschberg and E. Knobloch. Complex dynamics in the Hopf bifurcation with broken translation symmetry. *Physica D* 90:56–78, 1996.

[8] E. Knobloch. System symmetry breaking and Shil'nikov dynamics, in *Pattern formation: Symmetry Methods and Applications*, J. Chadam, M. Golubitsky, W.F. Langford and B. Wetton (eds). Fields Inst. Comm. 5:271–279, 1996.

[9] L. Ning, Y. Harada and H. Yahata. Modulated traveling waves in binary fluid convection in an intermediate-aspect-ratio rectangular cell. *Prog. Theor. Phys.* 97:831–848, 1997.

ADVANCES IN TURBULENCE VIII
Proceedings of the Eighth European Turbulence Conference
C. Dopazo et al. (Eds.)
© CIMNE, Barcelona 2000

From Hard Turbulence to the Ultimate Regime in a Rough Rayleigh-Bénard cell

P.M. Roche[1], B. Castaing[1,2], B. Chabaud[1] and B. Hébral[1]

[1]Centre de Recherches sur les Très Basses Températures
BP 166, 38042 Grenoble Cedex 9, FRANCE
[2]École Normale Supérieure de Lyon,
46 Allée d'Italie, 69364, Lyon Cedex 07, FRANCE

Web page: http://www-crtbt.polycnrs-gre.fr/hydrodyn/HYDRO/
Contact e-mail: philippe@polycnrs-gre.fr

1 Introduction

A Rayleigh-Bénard experiment is performed with cryogenics helium in a monodisperse rough surface cell. The fluid is enclosed in a $h = 20$ cm high cylindrical cell of aspect ratio $\phi/h = 0.5$. A 110 microns deep 90 deg V-shape groove covers all the interior of the cell. Roughness aside, geometry, materials and measuring apparatus are similar to the smooth surface (a few microns roughness) Rayleigh-Bénard experiment described in [1, 2]. The cell is successively filled with 5 different densities. For each density, the mean temperature and the temperature difference is varied within the Boussinesq approximation given by the $\alpha.DT < 30$ % criterion, where α is the thermal expansion coefficient. The Rayleigh (Ra) and Nusselt (Nu) numbers presented are corrected for the adiabatic gradient [3].

2 Hard turbulence

Figure 1 gathers the data of Chavanne and al [3] (smooth surface cell) and ours. From $Ra = 10^7$ up to $Ra = 2.10^{11}$, in the hard turbulence regime, the Prandtl (Pr) number remains close to 0.9 (± 0.25) in both experiments. According to the well validated $\lambda = \frac{h}{2.Nu}$ formula, the thermal boundary layer thickness λ is always at least 1.5 times larger than the roughness in the rough cell. Within the data uncertainty, there is no clear difference between the results from both experiments. This qualitative result was already obtained by others [4, 5] but on a much smaller range of Rayleigh numbers. This result validates the intuitive idea that turbulent heat transfer in the hard turbulence regime is not affected by sub-boundary layer roughness.

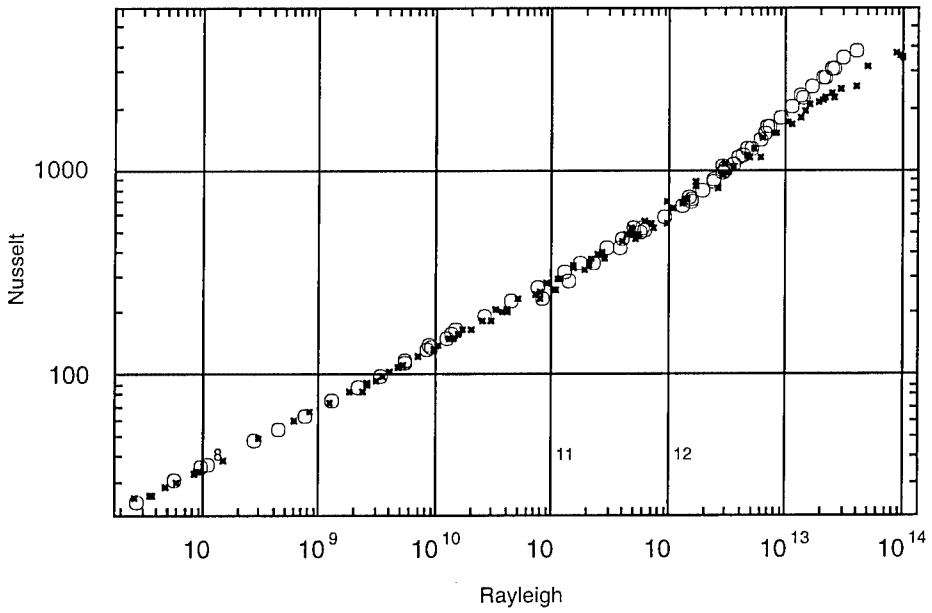


Figure 1: Nusselt number versus Rayleigh number for (circles) the rough surface cell and (crosses) the smooth surface one [3].

3 New regime

From $Ra = 2.10^{11}$ up to $Ra = 2.10^{12}$, $\lambda \leq 110$ microns and no clear difference appears between both sets of data. Within data uncertainty, the rising of the new regime first observed in [3] is indeed not affected by the roughness.

Above $Ra = 2.10^{12}$ ($\lambda < 110$ microns), the new regime in our rough cell can be fitted by a power law $Nu \sim Ra^{\beta}$ with $\beta = 0.51 \pm 0.01$. This exponent optimises the compensated plots $\frac{Nu}{Ra^{\beta}}$ versus Ra for the three different Pr numbers (1.45, 3.65, 4.9) explored above $Ra = 2.10^{12}$ (see second plot). The two lowest Pr numbers were obtained for a density of 39.8 kg/m^3 and Pr=4.9 for a density of 66.3 kg/m^3. The Pr dependence of the prefactor is weak : around a 10 % increase for more nearly 240 % increase of the Pr number. The data are robust to a tilt of the cell (5 deg) and to a non-symmetrical bottom plate heating [6].

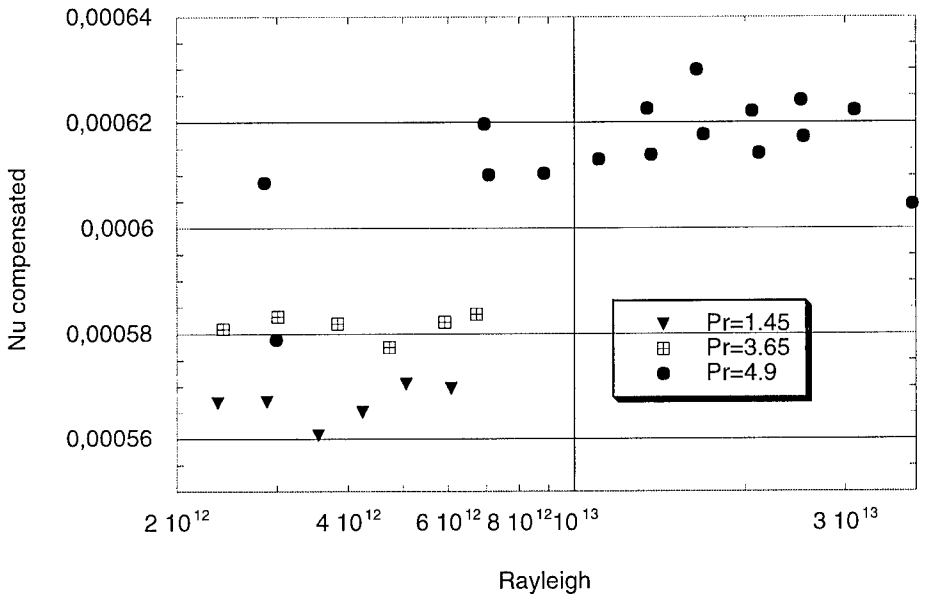


Figure 2: Compensated Nusselt number $\frac{Nu}{Ra^{0.5}}$ versus Rayleigh number for three different Prandtl numbers.

4 Discussion

The β exponent found is in perfect agreement with the Kraichnan prediction [7]. It also validates Chavanne prediction that an appropriate roughness allows to observe the 0.5 exponent for Rayleigh numbers as low as $Ra = 2.10^{12}$ [1]. A recall of [3] results is preferable to understand this last prediction. In this paper a new turbulent regime was found for $Ra > 2.10^{11}$. The β exponent between $Ra > 2.10^{12}$ and the highest Rayleigh numbers obtained (2.10^{14}) was 0.38. This new regime was identified with the ultimate regime predicted by Kraichnan in 1962 [7]. This ultimate regime is characterised by turbulent boundary layers and an exponent $\beta = 0.5$, but the variation of the boundary layer thickness add a logarithmic correction to β for the lower Nu numbers. An experimental approach to observe the $\beta = 0.5$ exponent for Rayleigh numbers as low as $Ra = 2.10^{12}$ is to cancel the logarithmic term. A 110 microns roughness imposes a lower bound to the turbulent boundary layer thickness. According to the formula mentioned previously, $\lambda = 110$ microns for $Ra = 2.10^{12}$ which means that above this Rayleigh number, the logarithmic correction is cancelled and the experimental

observation of the 0.5 exponent becomes possible.

Another interpretation can't however be discarded. If the boundary layer remains laminar up to the highest Rayleigh numbers, the effective surface seen by the fluid will increase as the boundary layer gets thinner than the roughness. This would result in an increase of the Nusselt number compatible with our data. The measurement of an effective exponent β of 0.51 ± 0.01 over more than one decade would then be pure coincidence.

5 Conclusion

From calorimetric measurements in a rough surface Rayleigh-Bénard cell,

- we validated over 4 to 5 decades the statement that sub-boundary layer roughness in Rayleigh-Bénard cells doesn't affect global heat transfer in the hard turbulence regime.

- we report the first observation of a $Nu \sim Ra^{0.5}$ power law above $Ra = 2.10^{12}$. This regime may be identified with Kraichnan ultimate convection regime.

References

[1] Chavanne, X. (1997). PhD Thesis,C.R.T.B.T., C.N.R.S. Grenoble, France, Universit Joseph Fourier.

[2] Chavanne, X., F. Chilla, and al. (1996). *Journal of Low Temperature Physics*, 104(1/2): 109-129.(1962).

[3] Chavanne, X., F. Chilla, and al. (1997). *Physical Review Letter*, 79: 3648-3651.

[4] Du, Y.-B. and P. Tong. (1998). *Physical Review Letters*, 81: 987-990.

[5] Cilberto, S. and C. Laroche. (1999). *Physical Review Letters*, 82: 3998-4001.

[6] Roche, P.M. and al. to be published.

[7] Kraichnan, R. H.. (1962). *Phys. Fluids*, 5: 1374.

ADVANCES IN TURBULENCE VIII
Proceedings of the Eighth European Turbulence Conference
C. Dopazo et al. (Eds.)
© CIMNE, Barcelona 2000

The phase diagram of Rayleigh-Benard turbulence

Siegfried Grossmann[1] and Detlef Lohse[2]

[1] Univ. of Marburg, FB Physik, Renthof 6, 35032 Marburg, Germany
[2] Univ. of Twente, Applied Physics, P. O. Box 217, 7500 AE Enschede, Netherlands

Contact e-mail: lohse@tn.utwente.nl

Rayleigh-Benard turbulence is one of the classical problems of hydrodynamics. After the experiments by Libchaber and coworkers [2] it was generally believed that in the high Rayleigh number regime the Nusselt number scales as

$$Nu \sim Ra^{\gamma} \tag{1}$$

with $\gamma = 2/7$. For many further experiments which seem to confirm this point of view and for theoretical explanations we refer to the review article by Siggia [8].

Various recent experimental measurements of the Nu number as a function of both Ra and the Prandtl number Pr increase more and more doubts whether eq. (1) is the end of the story, as: (i) Low Prandtl number measurements by Cioni et al. [4] (mercury, $Pr = 0.025$) and by Horanyi et al. [6] (sodium, $Pr = 0.005$) reveal smaller scaling exponents, namely $\gamma = 0.26 \pm 0.02$ and 0.25, respectively. Also the Pr dependence of Nu (for fixed Ra) was unexpected. (ii) The experiments by Chavanne et al. [3] with turbulent thermally driven helium beyond $Ra = 10^{11}$ showed a much stronger increase of Nu with increasing Ra than previously thought. (iii) Very recent measurements by Niemela et al. [7] with extremely high Ra up to 10^{17} reveal a scaling exponent of $\gamma = 0.309 \pm 0.004$ in eq. (1). (iv) The experiments of the Ahlers group [10] achieve utmost precision and reveal that the dependence of Nu on Ra cannot be discribed by a single power law. All these puzzling observations can be resolved within a recently suggested systematic and unifying theory for scaling of Nu and of the large scale wind Reynolds number Re in strong Rayleigh-Benard convection [5].

The key idea of the theory [5] is to split the total kinetic energy dissipation rate ϵ_u and the total thermal dissipation rate ϵ_θ, for which exact expressions as a function of Nu, Ra, and Pr exist [8], into boundary layer (BL) and bulk contributions,

$$\epsilon_u = \frac{\nu^3}{L^4}(Nu-1)RaPr = \epsilon_{u,BL} + \epsilon_{u,bulk}, \tag{2}$$

$$\epsilon_\theta = \kappa\frac{\Delta^2}{L^2} = \epsilon_{\theta,BL} + \epsilon_{\theta,bulk}. \tag{3}$$

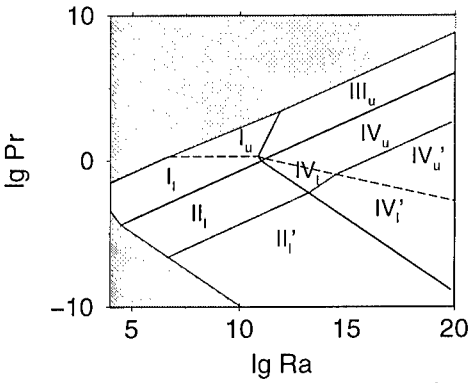


Figure 1: Thermal convection phase diagram in the $Ra - Pr$ plane.

regime	dominance of	BLs	Nu	Re
I_l	$\epsilon_{u,BL}$, $\epsilon_{\theta,BL}$	$\lambda_u < \lambda_\theta$	$0.27Ra^{1/4}Pr^{1/8}$	$0.037Ra^{1/2}Pr^{-3/4}$
I_u		$\lambda_u > \lambda_\theta$	$0.33Ra^{1/4}Pr^{-1/12}$	$0.039Ra^{1/2}Pr^{-5/6}$
II_l	$\epsilon_{u,bulk}$, $\epsilon_{\theta,BL}$	$\lambda_u < \lambda_\theta$	$0.97Ra^{1/5}Pr^{1/5}$	$0.47Ra^{2/5}Pr^{-3/5}$
III_l	$\epsilon_{u,BL}$, $\epsilon_{\theta,bulk}$	$\lambda_u < \lambda_\theta$	$6.43 \cdot 10^{-6}Ra^{2/3}Pr^{1/3}$	$5.24 \cdot 10^{-4}Ra^{2/3}Pr^{-2/3}$
III_u		$\lambda_u > \lambda_\theta$	$3.43 \cdot 10^{-3}Ra^{3/7}Pr^{-1/7}$	$6.46 \cdot 10^{-3}Ra^{4/7}Pr^{-6/7}$
IV_l	$\epsilon_{u,bulk}$, $\epsilon_{\theta,bulk}$	$\lambda_u < \lambda_\theta$	$4.43 \cdot 10^{-4}Ra^{1/2}Pr^{1/2}$	$0.036Ra^{1/2}Pr^{-1/2}$
IV_u		$\lambda_u > \lambda_\theta$	$0.038Ra^{1/3}$	$0.16Ra^{4/9}Pr^{-2/3}$

Table 1: The power laws for Nu and Re of the theory or ref. [5], including the prefactors which are adopted to four pieces of experimental information.

This kind of thinking immediately suggests the existence of four main regimes:
(I) Both ϵ_u and ϵ_θ are dominated by their BL contributions;
(II) ϵ_θ is dominated by $\epsilon_{\theta,BL}$ and ϵ_u is dominated by $\epsilon_{u,bulk}$;
(III) ϵ_u is dominated by $\epsilon_{u,BL}$ and ϵ_θ is dominated by $\epsilon_{\theta,bulk}$;
(IV) both ϵ_u and ϵ_θ are bulk dominated.

The estimates for the individual contributions on the rhs of eqs. (2) and (3) are based on the dynamical equations in the bulk and in the boundary layers. The crucial assumption for those estimates is the existence of a large scale "wind of turbulence". This wind of turbulence was doubtlessly detected in various experiments [1, 9, 2]. Therefore we consider the assumption as weak and in particular also as controllable.

Further ingredients are the widths of the kinetic and the thermal BLs, $\lambda_u \sim L/\sqrt{Re}$, $\lambda_\theta \sim L/Nu$. The estimates for the individual rhs contributions in eqs. (2) and (3) differ depending on whether the thermal BL is nested into the kinetic one or vice versa, splitting the phase space into an upper (large Pr, $\lambda_u > \lambda_\theta$) and a lower domain (small Pr, $\lambda_u < \lambda_\theta$) which we mark with indices "u" and "l", respectively. Note that for the kinetic BL we assumed a *laminar* BL (i.e.,

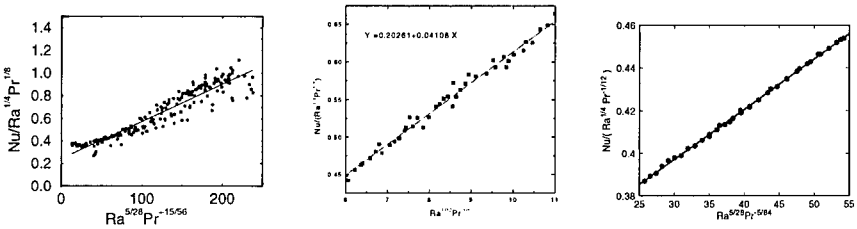


Figure 2: To test whether an eq. of type (4) is consistent with experimental data, we plot $Nu/(Ra^{\alpha_1}Pr^{\alpha_2})$ vs $Ra^{\alpha_3-\alpha_1}Pr^{\alpha_4-\alpha_2}$. Left: for the helium data by Chavanne et al. [3] where regimes I_l and III_u are the relevant regimes, center: for the helium data by Niemela et al. [7] where regimes I_l and IV_u are the relevant ones, and right: for the aceton data by Xu et al. [10] where regimes I_u and III_u are the relevant ones. Note that Pr is not constant in (left).

a BL of Blasius type). This assumption is justified as long as Re relatively low. Only for the very large Ra we expect the laminar BL to become turbulent which will lead to a transition in the phase diagram from II to II', etc.

Limitations of the theory are towards very large Pr as there Re becomes too small and the flow therefore viscous as well as towards very small Pr as there $Nu = 1$, i.e., only molecular heat transport.

The phase diagram resulting from the theory [5] is shown in figure 1, the corresponding power laws in table 1. The prefactors in the respective regimes are adopted to very few experimental information, see ref. [5]. The tiny regime right of regime I_l is regime III_l. On the dashed line it is $\lambda_u = \lambda_\theta$. In the shaded regime for large Pr it is $Re \leq 50$, in the shaded regime for low Pr we have $Nu = 1$. The dotted line indicates the onset of turbulence in the laminar kinetic BL. The scaling in regime II_l' is therefore as in the bulk dominated regime IV_l.

The most striking feature of the phase diagram figure 1 is that it is decomposed into many subdomains. Therefore one cannot expect to observe clean scaling over several orders of magnitude in Ra or Pr. Neighboring regimes will always matter. Therefore, rather than the pure scaling law (1) one should consider superpositions of neighboring regimes,

$$Nu = aRa^{\alpha_1}Pr^{\alpha_2} + bRa^{\alpha_3}Pr^{\alpha_4}, \tag{4}$$

$$Re = a'Ra^{\alpha_1'}Pr^{\alpha_2'} + b'Ra^{\alpha_3'}Pr^{\alpha_4'}, \tag{5}$$

with the α_i, α_i' depending on what the relevant regimes are, i.e., on Ra and Pr.

The best way to test eqs. (4) and (5) is to plot $Nu/(Ra^{\alpha_1}Pr^{\alpha_2})$ vs $Ra^{\alpha_3-\alpha_1}Pr^{\alpha_4-\alpha_2}$ and $Re/(Ra^{\alpha_1'}Pr^{\alpha_2'})$ vs $Ra^{\alpha_3'-\alpha_1'}Pr^{\alpha_4'-\alpha_2'}$. If eqs. (4) and (5) hold, this should result into straight lines. This kind of plot is done in figure 2.

Indeed, in all cases a straight line results.

Note that with our theory [5] the power law $Nu \sim Ra^{2/7}$ does not result in any domain of the phase space. However, a linear combination of the $1/4$ and the $1/3$ power laws for Nu with Ra, $Nu = 0.27Ra^{1/4} + 0.038Ra^{1/3}$ (the prefactors follow from experiment), mimicks a $2/7$ power law exponent in a regime as large as ten decades [5].

Acknowledgement: We are grateful to K. R. Sreenivasan and G. Ahlers for various discussions and for letting us reproduce their experimental data. This work was supported by FOM.

References

[1] A. Belmonte, A. Tilgner, and A. Libchaber. Temperature and velocity boundary layers in turbulent convection. *Phys. Rev. E*, 50:269–279, 1994.

[2] B. Castaing, G. Gunaratne, F. Heslot, L. Kadanoff, A. Libchaber, S. Thomae, X. Z. Wu, S. Zaleski, and G. Zanetti. Scaling of hard thermal turbulence in Rayleigh-Benard convection. *J. Fluid Mech.*, 204:1–30, 1989.

[3] X. Chavanne, F. Chilla, B. Castaing, B. Hebral, B. Chabaud, and J. Chaussy. Observation of the ultimate regime in Rayleigh-Benard convection. *Phys. Rev. Lett.*, 79:3648–3651, 1997.

[4] S. Cioni, S. Ciliberto, and J. Sommeria. Strongly turbulent Rayleigh-Benard convection in mercury: comparison with results at moderate Prandtl number. *J. Fluid Mech.*, 335:111–140, 1997.

[5] S. Grossmann and D. Lohse. Scaling in thermal convection: A unifying view. *J. Fluid. Mech.*, 407:27–56, 2000.

[6] S. Horanyi, L. Krebs, and U. Müller. Turbulent Rayleigh-Benard convection in low Prandtl number fluids. *Int. J. of Heat Mass Transfer*, 42:3983–4003, 1999.

[7] Niemela, L. Skrebek, K. R. Sreenivasan, and R. Donelly. To appear in *Nature*, 2000.

[8] E. D. Siggia. High Rayleigh number convection. *Annu. Rev. Fluid Mech.*, 26:137–168, 1994.

[9] Y. B. Xin, K. Q. Xia, and P. Tong. Measured velocity boundary layers in turbulent convection. *Phys. Rev. Lett.*, 77:1266–1269, 1996.

[10] X. Xu, K. M. S. Bajaj, and G. Ahlers. Heat transport in turbulent Rayleigh-Benard convection. Submitted to *Phys. Rev. Lett.*, 2000.

ADVANCES IN TURBULENCE VIII
Proceedings of the Eighth European Turbulence Conference
C. Dopazo et al. (Eds.)
© CIMNE, Barcelona 2000

Cryogenic Ultra-High Rayleigh Number Turbulence

J.J. Niemela[1], L. Skrbek[1], K.R. Sreenivasan [2] and R.J. Donnelly[1]

[1]Cryogenic Helium Turbulence Laboratory, University of Oregon
Eugene, Oregon 97403, USA
[2]Department of Mechanical Engineering, Yale University
New Haven, Connecticut 06520, USA

Contact e-mail: joe@vortex.uoregon.edu

Turbulent thermal convection can be described by three dimensionless parameters: the Rayleigh number, $Ra = \alpha g \Delta T L^3/\nu\kappa$, Prandtl number $Pr = \nu/\kappa$, and aspect ratio, $\Gamma = D/L$, where g is the acceleration of gravity, ΔT is the vertical temperature difference across the fluid layer of height L, and α, ν and κ are respectively the thermal expansion coefficient, kinematic viscosity and thermal diffusivity of the fluid. D is a characteristic horizontal length scale; for a cylindrical cell it is the diameter. We report heat transfer measurements in turbulent thermal convection using helium gas in the temperature and pressure ranges $4.3K < T < 6K$ and 0.1 mbar$< P <$3 bar, contained in a large Rayleigh-Benard cell of height $L = 1m$, covering 11 decades in Ra, $10^6 \leq Ra \leq 10^{17}$ [1]. Our data overlap previous measurements [2, 3] without relying on the divergence of fluid properties near the critical point, resulting in nearly constant Pr and negligible non-Boussinesq effects in the overlap region. To facilitate comparison with [2, 3], we retain the aspect ratio $\Gamma = 1/2$.

It is of considerable importance to predict the efficiency of heat transport at large Ra, represented by the Nusselt number, Nu, defined as the total heat flux normalized by its conductive contribution. Simple scaling arguments and experiments have suggested $Nu \sim Ra^\beta$. As summarized in [4], marginal stability arguments and dimensional reasoning produced the "classical" result: $\beta = 1/3$, while the so-called asymptotic "Kraichnan regime" suggests $\beta = 1/2$. Helium gas experiments of Wu [2] up to 10^{14} yielded exponents closer to 2/7 and somewhat higher for aspect ratio 0.5 (see below) stimulating other scaling theories, also reviewed in [4].

In contrast to [2], cryogenic helium experiments by Chavanne et al.[3] displayed a continual increase in β with increasing Ra, attaining a value close to 0.4 at $Ra \approx 10^{14}$. This was attributed to a transition to the asymptotic regime; however, it has not been observed in recent Hg experiments up to $Ra \approx 10^{11}$ [5], nor in recent SF_6 experiments [6], where (for constant Pr) a power law with $\beta = 0.3 \pm 0.03$ is reported for all Ra up to 10^{14}.

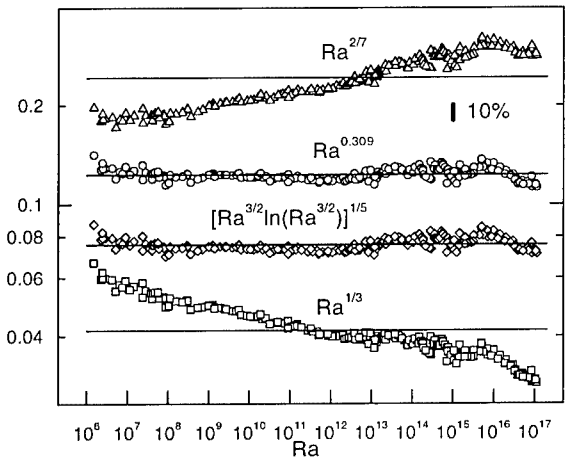


Figure 1: The log-log plot of Nu normalized by different scaling functions.

Our measurements in a $\Gamma = 1/2$ cell [1] also do not show any transition to an asymptotic regime, and yield an overall exponent for developed thermal turbulence $\beta \approx 0.31$ (preliminary data in a $\Gamma = 1$ cell are consistent with this scaling) over the whole range $10^6 \leq Ra \leq 10^{17}$. Our results are shown normalized to various expressions in figure 1. It includes the least-squares fit $Nu = 0.124Ra^{0.309\pm0.004}$, where the three significant figures result from the fitting procedure alone. Our data can be equally well described by a 'mean-field' result [7] $Nu \sim (Ra^{3/2}lnRa^{3/2})^{1/5}$, with only one adjustable parameter (the prefactor) instead of two for the simple power law. Exponents 1/3 and 2/7 are ruled out: the latter perhaps could be applied to a narrow region up to $Ra \approx 10^8$.

We remark on the newer theory of Grossman and Lohse [8]. They propose a superposition of power laws $Nu = 0.27Ra^{1/4}Pr^{1/8} + 0.038Ra^{1/3}$ that can mimic a single power law over many decades of Ra. It can be satisfactorily fitted to our data with slightly different prefactors (approximately 0.2 and 0.04).

To first order, β does not change significantly if one or more decades of Ra in the developed turbulence range are removed from the fitting procedure. It can depend, however, on the fluid properties used to evaluate Nu and Ra. The currently accepted property values [9] have changed significantly from the older ones [10], used to evaluate Ra and Nu in Wu's original experiments[2]. By far the most significant change is a decrease by $(5-10)\%$ in the thermal conductivity. We have recalculated Wu's original $\Gamma = 0.5$ data to take into account all changes in property values as well as a small correction due to the adiabatic gradient.

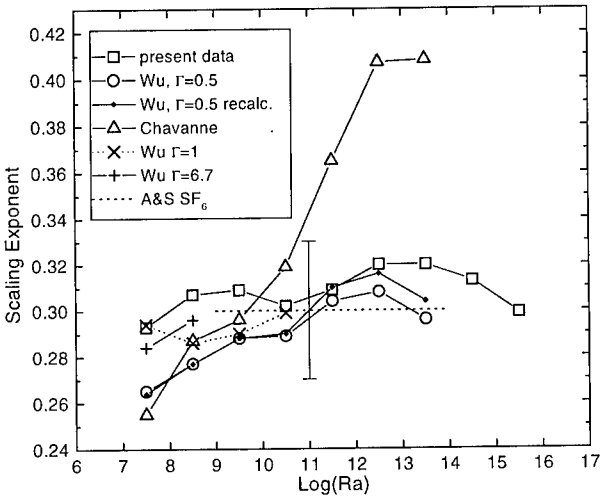


Figure 2: Figure 2. Local $Nu - Ra$ scaling exponents for successive 3-decade intervals, plotted against Ra at the mid-point of each interval.

The scaling for Wu's $\Gamma = 0.5$ data is affected primarily for $Ra > 10^{10}$, where the fractional change in thermal conductivity between [9] and [10] begins to vary significantly - otherwise Nu is simply shifted up with no change in slope.

Although the $Nu - Ra$ scaling for our data can be described to a good approximation by a single exponent 0.31 over the entire range of Ra, we examine it "microscopically" in figure 2, along with similar analysis for helium data of Wu [2] and Chavanne [3]. The local scaling exponents are calculated from least-squares fits over 3-decade intervals in Ra and are plotted versus Ra that corresponds to the middle of each interval. The first interval covers the range $10^6 \leq Ra \leq 10^9$. From the tabulated values of Nu and Ra in Chavanne's Thesis [3], only those points determined to be Boussinesq by the author's prescription were used. Included in the plot are data points derived from the recalculated $Nu - Ra$ data of Wu [2] for the $\Gamma = 0.5$ cell, as well as for the $\Gamma = 1$ and $\Gamma = 6.7$ cells. We note that the local exponent corresponding to the highest Ra for each data set was calculated from an interval slightly less than 3 decades. The recent SF_6 data [6] are represented as a horizontal dotted line with an associated error bar. Although we hesistate to extract too much information from this kind of detailed analysis, we can nonetheless make a few general observations.

First, the use of revised fluid properties [9] to recalculate Wu's $\Gamma = 0.5$ data results in a clear increase in the scaling exponent above $Ra \approx 10^{10}$, as expected

from considerations above, and closely matches our results. Indeed, the scaling relation derived from Wu's re-analyzed data yields $Nu = 0.146Ra^{0.299}$ for all $Ra > 5x10^7$, where the turbulence is presumably fully developed. This scaling exponent is significantly greater than the previously reported value 0.290 ± 0.005.

Second, it appears that the 2/7 law can be applied over narrow regions for most data sets. It is indeed not inconsistent with our data over the limited range $10^6 < Ra < 10^9$ where the calculated exponent is 0.29.

Third, the scaling exponents derived from Wu's and our helium experiments display a spread of values that are more or less consistent with the size of the error bar for the SF_6 experiments [6]. In accord with the discussion above, those from Chavanne's data show significant differences from the others for $Ra > 10^{11}$.

The authors acknowledge valuable discussions with many colleagues during various stages of this research, supported by NSF grant DMR-9529609.

References

[1] J. J. Niemela, L. Skrbek, K. R. Sreenivasan and R. J. Donnelly. Turbulent convection at very high Rayleigh numbers. Accepted for *Nature*, 2000.

[2] X. Z. Wu. Along a Road to Developed Turbulence: Free Thermal Convection in Low Temperature Helium Gas. *Ph.D. Thesis*, U. Chicago, 1991.

[3] X. Chavanne, F. Chilla, B. Castaing, B. Hebral, B. Chaubaud, and J. Chaussy. Observation of the ultimate regime in Rayleigh-Benard convection. *Phys. Rev. Lett.*, 79, 3648-3651, 1997. X. Chavanne *Ph.D. Thesis*, University of Grenoble, France 1997.

[4] E. D. Siggia. High Rayleigh number convection. *Annual Reviews of Fluid Mechanics*, 26, 137-168 1994.

[5] J. A. Glazier, T. Segawa, A. Naert, and M. Sano Evidence against 'ultrahard' thermal turbulence at very high Rayleigh numbers. *Nature*, 398, 307-310 1999.

[6] S. Ashkenazi, V. Steinberg. High Rayleigh number turbulent convection in a gas near the gas-liquid critical point. *Phys. Rev. Lett.*, 83, 3641-3644, 1999.

[7] F. H. Busse. Nonlinear properties of thermal convection. *Reports on Progress in Physics*, 41, 1930-1967, 1978.

[8] S. Grossman and D. Lohse. Scaling in thermal convection: A unifying theory. *Journal of Fluid Mechanics*, in press, 2000.

[9] V. D. Arp and R. D. McCarty. The properties of critical helium gas. Technical report, University of Oregon, 1998.

[10] R. D. McCarty. Thermophysical Properties of Helium-4 from 2 to 1500 K with Pressures to 1000 Atmospheres. NBS Technical Note 631, 1972.

ADVANCES IN TURBULENCE VIII
Proceedings of the Eighth European Turbulence Conference
C. Dopazo et al. (Eds.)
© CIMNE, Barcelona 2000

Turbulence in liquid helium

D. Kivotides[1], C.F. Barenghi[1] and D.C. Samuels[1]

[1]Mathematics Department, University of Newcastle,
Newcastle-upon-Tyne, NE1 7RU ENGLAND

Contact e-mail: c.f.barenghi@ncl.ac.uk

1 Introduction

Recent experiments at ENS Paris and at the University of Oregon by Tabeling, Donnelly and coworkers have showed that turbulence in helium II is very similar to turbulence in a classical fluid. For example, measurements of the decay of vorticity produced by a towed grid gave the same decay rate in helium II as in a classical fluid [1]. Furthermore, the same Kolmogorov 5/3 spectrum of classical turbulence was observed [2] in helium II. These experiments have renewed theoretical work in the hydrodynamics of helium II. Additional interest arises from the cryogenics engineering applications.

According to Landau's model [3], helium II can be described as the intimate mixture of two fluid components, the superfluid and the normal fluid, each having its own velocity and density field. The superfluid, which is inviscid, is like a classical Euler fluid. The normal fluid, which is viscous, is like a classical Navier Stokes fluid. The relative proportion of normal fluid and superfluid depends on the absolute temperature T. At absolute zero helium II is entirely superfluid; if T is increased then the relative amount of normal fluid increases until, at the phase transition temperature $T = 2.17\ K$, there is no superfluid component left and helium II becomes helium I, which is a classical Navier Stokes fluid.

What makes helium II particularly interesting is that superfluid vorticity exists only in the form of long thin vortex filaments [4] around which the circulation is quantized according to the rule

$$\int_{\mathcal{C}} \mathbf{v}^s \cdot \mathbf{dl} = \Gamma, \tag{1}$$

where $\mathbf{v}^s$ is the superfluid velocity field, $\mathcal{C}$ is a circular path around the vortex core and $\Gamma = 9.97 \times 10^{-4}\ cm^2/sec$ is the quantum of circulation (Plank's constant divided by the mass of the helium atom). Since the vortex core region (where quantum effects dominate) is of microscopic size ($\approx 10^{-8}\ cm$) while the length

of a vortex filament is macroscopic, the classical Euler theory of inviscid vortex filaments of infinitesimal thickness [5] applies well to helium II. The evolution of a superfluid vortex line is therefore determined, first of all, by the Biot-Savart law, which says that the self-induced velocity of a vortex filament at the point $\mathbf{r}$ is

$$\mathbf{v}^s_{self}(\mathbf{r}) = \frac{\Gamma}{4\pi} \int \frac{(\mathbf{r}' - \mathbf{r}) \times \mathbf{dr}'}{|\mathbf{r}' - \mathbf{r}|^3}, \tag{2}$$

where the integral extends over the entire vortex configuration. The second ingredient which determines the evolution is the occurrence of vortex reconnections. These events are introduced *ad hoc* in our numerical simulations based on (2), but have been studied using the Bose - Einstein Condensate model of superfluidity at $T = 0$. The microscopic BEC model yields the nonlinear Schroedinger equation

$$i\frac{\partial \psi}{\partial t} = -\nabla^2 \psi + |\psi|^2 \psi, \tag{3}$$

where the superfluid density and velocity are given respectively by the amplitude and the gradient of the phase of the wave function ψ. Finally, the third ingredient which determines the evolution of a vortex line is the mutual friction force which the superfluid vortex lines and the normal fluid exert on each other [6]. At finite temperatures, therefore, the friction force couples the normal fluid and the superfluid components.

2 Turbulence at absolute zero

If the temperature of helium II is reduced below 1 K there is so little normal fluid left that helium II can be considered a pure superfluid. Vortex tangles in this regime were studied by Nore, Abid and Brachet [7] using equation (3). They found, surprisingly, the classical 5/3 Kolmogorov energy spectrum. The same spectrum was observed experimentally by Maurer and Tabeling [2] at $T = 1.4\ K$, a temperature at which the normal fluid fraction is only about 7%.

To investigate the vortex structures which develop in a pure superflow (that is to say in the absence of normal fluid and friction) we study the evolution of four initial vortex rings in a periodic box. The same initial condition (but for viscous vortex rings) was studied by Kiya and Ishii [8]. In our case we find that the initial rings become distorted by the Biot-Savart interaction, vortex waves develop and reconnections take place (see Figures 1a and b). It is thought that vortex waves and (probably more important) vortex reconnections are the major processes which generate sound and dissipate organized kinetic energy at absolute zero [9]. Work is in progress to analyze the results in terms of curvature and energy spectra (see Figure 2a and b).

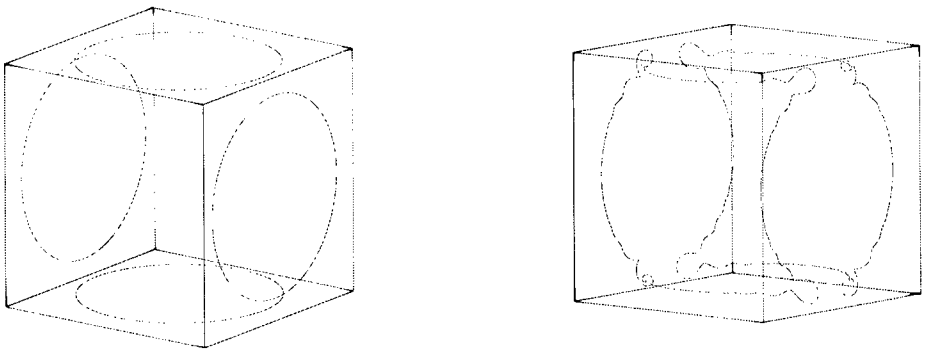


Figure 1: Evolution of four initial vortex rings.

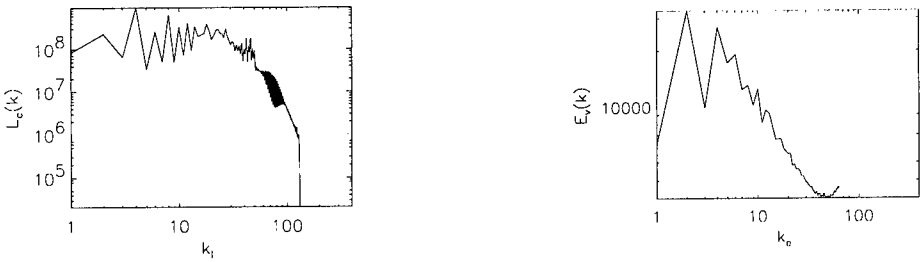


Figure 2: Spectra of the curvature and the energy.

3 Turbulence at finite temperatures

If the temperature is raised above 1 K then the normal fluid component and the friction play an important role. Until very recently the full implications of the friction interaction between the normal fluid and the superfluid vortices in the context of turbulence has not been fully appreciated. In particular, very little is known about the motion of the normal fluid induced by the presence of superfluid vortex lines. The evidence from the experiments is that there is a strongly coupled regime. For example, pressure drops in pipes and channels at high Reynolds numbers obey classical rules; moreover, the same circulation was observed in both the superfluid and normal fluid components of vortex rings.

To investigate the effect which superfluid vortex lines have on the normal fluid, and viceversa, we have developed the first fully 3D calculation of the coupled motion of vortex lines and normal fluid. Our approach combines vortex dynamics (equation 2) with a Navier Stokes solver for the normal fluid, modified by the introduction of mutual friction terms. Because of the importance of vortex rings in the study of helium II, we consider what happens to a superfluid vortex ring set in the normal fluid initially at rest. We find that the interaction creates vorticity structures in the normal fluid which propagate with the superfluid ring

in a coherent way, see Figure 3.

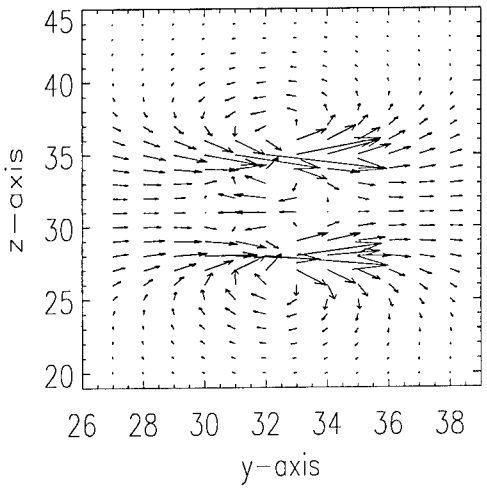


Figure 3: Cross section of normal fluid velocity field generated by a superfluid vortex ring travelling to the right.

D.K. gratefully acknowledges the support of the Leverhulme Trust.

References

[1] M.R. Smith, R.J. Donnelly, N. Goldenfeld and W.F. Vinen, *Phys. Rev. Lett.*,**71**, 2583, 1993.

[2] J. Mauerer and P. Tabeling, *Europhysics Letters*, **43**, 29, 1998.

[3] L. Landau and E. Lifchitz, *Mécanique des Fluides*, MIR, Moscow 1971.

[4] R.J. Donnelly, *Quantized vortices in helium II*, Cambridge University Press, 1991.

[5] P.G. Saffman, *Vortex dynamics*, Cambridge University Press, 1992.

[6] C.F. Barenghi, R.J. Donnelly and W.F. Vinen, *J. Low Temp. Phys.* **52** 189, 1983.

[7] C. Nore, M. Abid and M.E. Brachet, *Phys. Rev. Lett.* **78**, 3896, 1997.

[8] M. Kiya and H. Ishii, *Fluid Dynamics Research*, **8**, 73, 1991.

[9] D.C. Samuels and C.F. Barenghi, *Phys. Rev. Lett.* **81**, 4381, 1998.

ADVANCES IN TURBULENCE VIII
Proceedings of the Eighth European Turbulence Conference
C. Dopazo et al. (Eds.)
© CIMNE, Barcelona 2000

Decay of Grid Generated Classical and Superfluid Turbulence

L. Skrbek and Steven R. Stalp

Cryogenic Helium Turbulence Laboratory, Department of Physics
University of Oregon, Eugene, OR 97403, USA

Contact e-mail: ladik@vortex.uoregon.edu

1 Introduction

Decay of nearly homogeneous and isotropic (HIT) grid generated turbulence is one of the most important and extensively explored problems in turbulence. Most of the experimental work is related to wind tunnels, where the turbulence is studied as it decays downstream (e.g., [1-3]). Turbulence without a mean flow, generated by using an oscillating grid and by towing a grid through a stationary sample of fluid has also been studied [4, 5]. A general theory describing the decay of turbulence based on first principles has not yet been developed. However, experimental data containing information about the turbulent energy spectra provide a solid foundation for a phenomenological approach first outlined in [1, 6], as the generally accepted forms of the three-dimensional turbulent energy spectra uniquely determine the temporal decay of turbulence. We generalize this approach taking into account the finite size of the turbulence box, intermittency and viscosity effects and discuss the final period of decay. In particular, we show that distinctly different decay regimes exist due to the physical restriction that eddies larger than the size of the turbulent box cannot exist[3, 4].

By re-analyzing some old data from various authors, we provide an improved understanding of decaying HIT, a subject where there is sometimes little agreement even after several decades of investigation. We include our recent experimental results obtained in superfluid helium, also referred to as He II, where second sound attenuation technique provides a tool to directly probe several orders of decaying vorticity. He II has already proven to be a very useful fluid for these complementary studies, although care must be taken when applying the classical turbulence model to He II flows[7].

2 Spectral Decay Model

We developed several variants of a model describing decaying HIT based on different forms of the three-dimensional energy spectra. For HIT it is generally

accepted that for small wavenumbers $E(k) = Ak^m$ where A is a dimensional constant. For larger k we adopt an inertial range with refined Kolmogorov scaling, $E(k) = C\varepsilon^{2/3}k^{-5/3}\,(kL)^{-\mu}$ where E is the total turbulent energy per unit mass, $\varepsilon = -dE/dt$ is the dissipation rate, L is the integral length scale, C is the dimensionless three dimensional Kolmogorov constant and μ is the intermittency exponent. We further assume that for HIT the integral and the energy containing length scale are equivalent: $\ell_e \approx L$. Associated with the energy containing eddy length scale is the wavenumber $k_e\,(t) = 2\pi/\ell_e\,(t)$, around which most of the turbulent energy resides. A novel aspect of our model is that we truncate the spectrum at $k_c = 2\pi/d$, where d is the dimension of the containing vessel. As an example, in a wind tunnel this dimension is associated with the width of the tunnel and eddies larger than this width cannot exist in the turbulent flow. We take into account viscous dissipation by truncating the spectrum at an effective Kolmogorov length scale $k_\eta = \gamma\left(\varepsilon/\nu^3\right)^{1/4}$, where ν stands for kinematic viscosity and γ is a numerical factor of order unity. The total turbulent energy is evaluated by integrating the 3D spectrum over all wavenumbers. Evaluating the integral leads to a differential equation for decaying turbulent energy, as the expression for energy contains ε. Applying condition valid for HIT, $\varepsilon = \nu\omega^2$, one gets differential equation for decaying vorticity ω. Although the general case is not analytically soluble, under some approximations on the 3D energy spectrum one obtains analytical solutions that predict various regimes of decay and shed light on decaying HIT. The detailed calculation will appear elsewhere [3].

3 Discussion

We have applied the predictions of the model to a broad variety of experimental data including our own recent studies on decaying superfluid turbulence [3]. Here the available space only allows to summarize and classify our findings depending on the geometry where the nearly HIT was created and decays.

We first consider the simplest case where the size of the turbulence box can be approximated as being infinite and are interested only in the part of the decay at sufficiently high Re, say, of order of several hundred. The energy (vorticity) decay at times sufficiently longer than the virtual origin time can be described by a single power law $E \propto t^{-6/5}$ [6], $(\omega \propto t^{-11/10})$, while the energy containing length scale grows as $\ell_e \propto t^{2/5}$. The value of the virtual origin depends on the intermittency coefficient and viscosity, but was always found to be within a few mesh lengths of the grid[3]. As Re_λ decreases during the decay, the influence of the finite viscosity of the fluid gradually starts to play a more important role. The decay speeds up and can not be expressed by a simple power law anymore. The growth of ℓ_e also becomes faster. The Kolmogorov microscale grows faster than ℓ_e and thus the inertial range of the energy spectrum shortens as HIT decays. At some point the concept of the Kolmogorov microscale does not hold any more and a diffusive length scale $(\nu t)^{1/2}$ is used to characterize the final

period of decay with a predicted $E \propto t^{-3/2}$, in agreement with [6]. We have found convincing experimental evidence that this regime was indeed observed in the wind tunnel experiments [2]. However, some experimental data originally claimed as evidence for the observation of the final period of decay, e.g., [5], are better explained by the saturation of ℓ_e (see below).

If the turbulent fluid is confined in a box of the characteristic size, d, eddies larger than d cannot exist and the energy spectrum is naturally truncated at the smallest physically significant wavenumber $2\pi/d$. Again the simplest case is the part of the decay at sufficiently high Re_λ. If the starting value of $\ell_e << d$, the decay essentially behaves as described above. However, as ℓ_e starts to approach the size of the box, the decay is affected by the truncation of the spectrum at $2\pi/d$. The rate of vorticity decay gradually decreases where just before saturation it follows the power law $\omega \propto t^{-5/6}$. This power law originates from the broad maximum in the 3d energy spectrum in the vicinity of ℓ_e. As it grows and approaches $2\pi/d$ the low wave number part of the spectrum effectively becomes $E(k) \cong Ak^m$ with $m \to 0$. Power law $\omega \propto t^{-5/6}$ is clearly experimentally documented by Figure 1 for the decay of He II vorticity in a finite channel. Note the absence of a corresponding simple power law for decaying energy, due to the additional time-independent term in the differential equation for decaying energy that disappears when differentiating with respect to time. This results

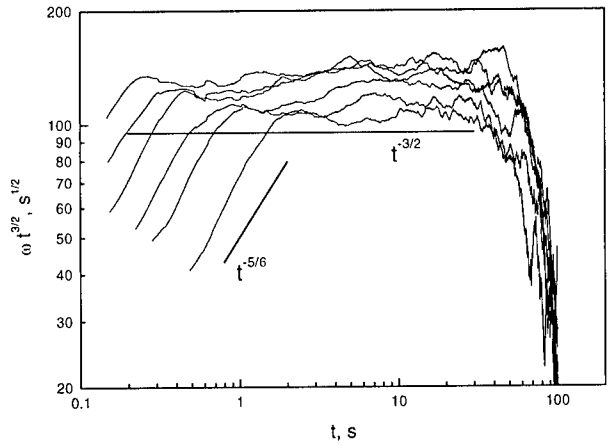


Figure 1: Vorticity decay data multiplied by $t^{3/2}$ obtained at T=1.75 K and mesh Re, from left to right, $2 \cdot 10^5$, $1.5 \cdot 10^5$, 10^5, $6 \cdot 10^4$, $4 \cdot 10^4$, and $2 \cdot 10^4$, where t is the experimental time. Solid lines represent vorticity decay power laws.

in the above simple power law solution for decaying vorticity.

At the saturation time, a distinctly different decay regime takes over, with a predicted universal time dependence at long times, assuming the influence of the finite viscosity is still negligible:

$$E(t) \cong \frac{27C^3}{2}\left(\frac{d}{2\pi}\right)^2 t^{-2}; \omega(t) \cong \frac{(3C)^{3/2}}{\sqrt{\nu}}\left(\frac{d}{2\pi}\right) t^{-3/2}$$

This regime is clearly documented in both classical and He II experimental data [4] . The influence of the finite viscosity after saturation is similar in that the decay rate gradually speeds up [3], see Figure 1 .

By applying our model to a number of different sets of experimental data obtained for nearly HIT, in most cases we have found agreement between the shape of the energy spectrum and the observed decay. In particular, we have not found any decay data that would contradict the validity of Saffman invariant[6]. It should be emphasized that our study includes decay of He II turbulence. We find it remarkable that it is so well described by this entirely classical approach. Superfluid turbulence is a very fascinating field that deserves the attention of the turbulence community and can largely contribute to our understanding of turbulence in general.

The authors wish to thank R. J. Donnelly, G. L. Eyink, J.J. Niemela, K. R. Sreenivasan, W.F. Vinen for suggestions and discussions at various stages of this work. This research was supported by NSF under grant DMR-9529609.

References

[1] G. Comte-Bellot and S. Corrsin. The Use of a Contraction to Improve The Isotropy of Grid-Generated Turbulence. *J. Fluid Mech.* 25: 657, 1966.

[2] C. Bennett and S. Corrsin. Small Reynolds Number Nearly Isotropic Turbulence in a Straight Duct and a Contraction. *Phys. Fluids* 21: 2129, 1978.

[3] L. Skrbek, S. R. Stalp. On the Decay of Homogeneous Isotropic Turbulence. *Submitted to Phys. Fluids.*

[4] S.R. Stalp, L. Skrbek, and R. J. Donnelly. Decay of Grid Turbulence in a Finite Channel. *Phys. Rev. Lett.* 82: 4831-4, 1999.

[5] I. P. D. De Silva and H. J. S. Fernando. Oscillating Grids as a Source of Nearly Isotropic Turbulence. *Phys. Fluids* 6: 2455, 1994.

[6] P.G. Saffman. The Large-Scale Structure of Homogeneous Turbulence. *J. Fluid Mech.* 27: 581, 1967. Note on Decay of Homogeneous Turbulence. *Phys. Fluids* 10: 1349, 1967.

[7] W.F. Vinen. Classical Character of Turbulence in Quantum Liquid. *Phys. Rev.* B 61: 1410-20, 2000.

ADVANCES IN TURBULENCE VIII
Proceedings of the Eighth European Turbulence Conference
C. Dopazo et al. (Eds.)
© CIMNE, Barcelona 2000

Modeling of quantum turbulence in superfluid ^{4}He

Tomasz Lipniacki

Institute of Fundamental Technological Research
Polish Academy of Sciences, Warsaw, Świętokrzyska 21

Contact e-mail: tlipnia@ippt.gov.pl

1 Introduction

The variety of the dynamic phenomena exhibited by superfluid ^{4}He involves the appearance and motion of quantized vortices. Due to the existence of these singularities the superfluid component is coupled dissipatively with the normal component. At low velocities He II (superfluid ^{4}He) flows in the frictionless, presumably laminar manner consistent with the ideal fluid description. When the counterflow (the relative velocity of the two helium components) $v_{ns} = v_n - v_s$ becomes sufficiently large, however, the superfluid laminar flow develops into superfluid turbulent flow in which the quantum vortices form a chaotic tangle.

The aim this work is to model the homogeneous quantum turbulence (vortex tangle) and derive the evolution equation for vortex line-length density L. In the proposed approach the special attention is paid to reconnections of vortex lines. The vortex line evolution is analyzed in the localized induction approximation, supplemented by the assumption that when two vortex lines cross, they undergo a reconnection.

Let us recall that if the curve traced out by a vortex filament is specified in the parametric form $s(\xi, t)$, then in superfluid reference frame the instantaneous velocity of a given point of the filament is given by the equation (in scaled units in which the elementary circulation around vortex line equals to unity)

$$\dot{s} = s' \times s'' + \alpha s'' + \alpha s' \times v_{ns} \ , \tag{1}$$

where dot and prime denote instantaneous derivatives with respect to the scaled time τ and arc length ξ, respectively, α is the nondimensional friction coefficient and v_{ns} the counterflow.

The line-length of vortex filament $l = \int d\xi$, which motion is given by (1), satisfies the equation

$$\frac{\partial l}{\partial \tau} = \int \Big(\alpha v_{ns} \cdot (s' \times s'') - \alpha |s''|^2 \Big) d\xi \ . \tag{2}$$

Let us note, that just after the reconnection, close to the reconnection point, the two vortices have the binormals $(s' \times s'')$ opposite to each other. In the result the first term in Eq. (2) when integrated over two lines resulting from reconnection gives no contribution to total line length change. Because the second term of Eq. (2) is always negative the total length of resulting vortices decreases in the beginning. However, during the further evolution, the characteristic curvatures (and so the absolute value of second term) get smaller, and the two vortices turn so that the average value of $v_{ns} \cdot (s' \times s'')$ becomes positive. In the result the total length of vortices starts growing. It can be shown that after the idealized reconnection of two straight vortex lines the summary line-length change ΔS of two vortices resulting from the reconnection can be approximated in the following form [1,2]

$$\Delta S(\tau) = -a\ \tau^{1/2} + b\ \tau^{3/2} v_{ns}^2\ , \tag{3}$$

where $a > 0$, $b \geq 0$ are the nondimensional coefficients depending on the friction coefficient α and the specific reconnection configuration (which may be described by the relative angles between two reconnecting lines and the counterflow velocity v_{ns}). Let us notice that the coefficients a, b determine the characteristic nondimensional time $\tau^* = \tau v_{ns}^2 = a/b$ for which the line-length change is zero.

2 The model

Equation (3) gives one a hint to the explanation how the vortex tangle is sustained: for the steady-state turbulence, the average line-length change between reconnections have to be zero. If for a given value of the counterflow v_{ns}, the line density is smaller then the equilibrium one, the reconnections occur less frequently, and so, the characteristic time between reconnections is longer; hence according to Eq. (3) the line-length change between reconnections becomes positive. In the result the line density of vortex tangle grows up until the equilibrium is restored. Inversely, when the line density is too large, the reconnections are much frequent, so the decaying term in Eq. (3) prevails and the line density gets smaller.

In the proposed approach the dynamics of vortex tangle will be considered as a sequence of reconnection followed be a "free" evolution of vortex lines resulting from each reconnection.

Let the instantenous line-length density be L, this gives one the characteristic spacing between lines l_o and the characteristic (average) line curvature $< |s''| >$

$$l_o = L^{-1/2}\ , \qquad < |s''| > = 1/l_o = L^{1/2}\ . \tag{4}$$

Let us divide the vortex lines into segments with length l_o. Because the length l_o is equal to the spacing between lines we may expect that each segment moves (more or less) as a unity, but the motions of the neighboring segments are not strongly correlated. Moreover, because the length of segments is equal to the

characteristic radius of curvature, when consider collisions, the segments can be roughly treated as straight ones. It is assumed that any collision of vortex segments leads to a reconnection; such assumption is justified by numerical simulations of Schwarz [3]. For the sake of simplicity we assume that all segments move with the same speed v_o which can be estimated basing on (1):

$$v_o =< |\dot{s}| >= \sqrt{L(1+\alpha^2) + \frac{2}{3}(\alpha v_{ns})^2} \ . \tag{5}$$

Having v_o and l_o (i.e. the number of segments per unit volume $n = L/l_o = L^{3/2}$) one can estimate the reconnection frequency (per unit volume) f_r,

$$f_r = \frac{v_o L^2}{2} \ , \tag{6}$$

and the average time between reconnections of line segments

$$\tau_c = \frac{1}{L^{1/2} v_o} \ . \tag{7}$$

The estimation of f_r needs some algebra since the cross section for collision of two given segments depends on their direction angles and the direction of their relative velocity. The time derivative of line-length density is then

$$\frac{dL}{d\tau} = f_r \ < \Delta S(\tau_c) > \ , \tag{8}$$

where $< \Delta S(\tau_c) >$ is the average line-length change due to a single reconnection and is given in the form of Eq. (3) with coefficients $a_o =< a >$, $b_o =< b >$, which must be calculated in numerical simulations. The resulting evolution equation is

$$\frac{dL}{d\tau} = -a_o \alpha^{1/2} \ L^{7/4} \ v_o^{1/2} + b_o \alpha^{3/2} \ L^{5/4} \ v_o^{-1/2} \ v_{ns}^2 \ , \tag{9}$$

with v_o given by Eq. (5).

The obtained evolution equation (9) differs from the classical Vinen equation

$$\frac{\partial L}{\partial t} = -\beta_v L^2 \ + \ \alpha_v |v_{ns}| L^{3/2} \ , \tag{10}$$

where α_v and β_v temperature dependent coefficients. For $\alpha \ll 1$ Eq. (9) simplifies to the so called alternative Vinen equation in which the second "generation" term is proportional to v_{ns}^2 rather then to $|v_{ns}|$.

To determine a_o, b_o in Eq. (9) one should average ΔS over all possible reconnection configurations. Numerically it is rather impossible, hence to do the calculations we assume that every line in the moment of reconnection has to be parallel or antiparallel to one of 3 "main" directions: $\hat{x}, \hat{y}, \hat{z}$ and that the direction of v_{ns} is $(1, 1, 0)$ in Cartesian coordinates. In principle, this means that there are 12 possible reconnection configurations, but it is not difficult to check

that only 3 of them are essentially different. The average line-length change $\Delta S(\tau)$ is then estimated by averaging over these configurations. In the result we get $a_o = 1.17, b_o = 0.257$.

The experimental data is not enough precise to chose between Vinen, alternative Vinen equation, or the Eq. (9). It makes sense only to compare with experimental data the steady-state value of L following from (9) i.e. L_∞

$$L_\infty = v_{ns}^2\Big(\sqrt{\frac{\alpha^4}{9} + 8\big(\frac{b_o\alpha}{\pi a_o}\big)^2} - \frac{\alpha^2}{3}\Big) \tag{11}$$

In a broad range of α ($\alpha \in (0.01, 1)$) the value of L_∞ predicted by (11) generally agrees with experimental data and Schwarz [4] numerical simulations of steady-state turbulence.

Equation (9) may be confronted with data from Schwarz and Rosen[5]. The authors analyzed in numerical simulation of non-equilibrium turbulence the large transients when the line-length density grows from small to large values and found that the coefficients in Vinen equation are not constant. Their data are considerably better fitted by Eq. (9) then by the classical Vinen equation.

This work was supported by KBN grant 7T07A 018 17.

References

[1] T. Lipniacki, Dynamics of quantum vortices in superfluid ^{4}He *Arch. Mech.*, 50:467-482, 1998.

[2] T. Lipniacki, Evolution of quantum vortices following reconnection - accepted for publication in *European Journal of Mechanics, B/Fluids*, 2000.

[3] K. W. Schwarz, Three-dimensional vortex dynamics in superfluid ^{4}He: Line-line and line-boundary interactions, *Phys. Rev. B*, 31:5782-5804, 1985.

[4] K. W. Schwarz, Three-dimensional vortex dynamics in superfluid ^{4}He: Homogenous superfluid turbulence, *Phys. Rev. B*, 38:2398-2417, 1988

[5] K. W. Schwarz, J. R. Rosen, Transient behavior of superfluid turbulence in a large channel, *Phys. Rev. B*, 44:7563-7576, 1991.

Posters

Numerical study of bifurcations for the two-dimensional Poiseuille flow

Pablo S. Casas[1] and Àngel Jorba[2]

[1]Departamento de Matemática Aplicada I, Universidad Politécnica de Cataluña
Diagonal, 647; 08028 Barcelona. Spain
e-mail: pablo@vilma.upc.es
[2]Departamento de Matemática Aplicada y Análisis, Universidad de Barcelona
Gran Via, 585; 08007 Barcelona. Spain

Contact e-mail: angel@maia.ub.es

In this work we firstly compute, for several values of the wave number α, the branch of time-periodic unstable solutions that bifurcate from the laminar flow: they are steady in moving axes because of the translational symmetry of the channel. We confirm previous results with regard to the existence of two Hopf bifurcations for several values of α, from which emanates a family of quasi-periodic solutions such that, due to symmetry, are periodic flows when the observer is moving at an appropriate speed c. We follow the bifurcating branches of quasi-periodic orbits, searching for fixed points of a suitable Poincaré map of the flow, what allows us to find stable and unstable flows. The stability can be studied through the spectrum of the Poincaré map linearization.

Nonlinear dynamics in a rapidly rotating annulus

D. Pino, I. Mercader, J. Sánchez and M. Net

Departament de Física Aplicada. Universitat Politécnica de Catalunya. Barcelona. Spain.

One of the main subjects in geophysical and astrophysical fluid dynamics is the study of the features related with thermal convection at very high Taylor numbers. A widespread model configuration, less expensive than fully three-dimensional calculations, is a fast rotating cylindrical annulus with radial gravity and heating, and the top and bottom boundaries of the annulus slightly sloped. In this case, if the rotation rate is high enough, solutions are two dimensional, independent of the coordinate parallel to the rotation axis.

Fixing $\sigma = 0.7$, we have studied the nonlinear quasi–geostrophic drifting solutions (thermal Rossby waves), their linear stability by using a Floquet parameter, and the bifurcating solutions, that appear for different rotation rates and radius ratios.

Reentrant squares in Rayleigh-Bénard convection

A. Demircan and N. Seehafer

Institut für Physik, Universität Potsdam
PF 601553, 14415 Potsdam, GERMANY

Contact e-mail: demircan@agnld.uni-potsdam.de

We numerically investigate nonlinear square patterns in Boussinesq convection in a horizontal fluid layer with stress-free boundaries at a Prandtl number of 6.8. The patterns appear via the skewed varicose instability of rolls. The time-independent nonlinear state is generated by two different wave numbers and their nonlinear interaction. As the bouyancy forces increase the interacting modes give rise to bifurcations leading to a periodic alternation between a nonequilateral hexagonal pattern and the square pattern or to different kinds of standing oscillations. For still higher Rayleigh numbers chaotic solutions are found to coexist with a roll pattern with traveling waves along the roll axis.

The research of laminar–turbulent transition in hypersonic three-dimensional boundary layer

M.A. Goldfeld

Institute of Theoretical and Applied Mechanics, SB RAS
4/1 Institutskaya, Novosibirsk 630090, Russia

Contact e-mail:gold@itam.nsc.ru

Results of experimental research of structure and laminar-turbulent transition in 3D flow with distributed pressure gradient including the flow with local boundary layer separation are presented. The development of boundary layer and transition were researched on the 3D model with lengthwise-transverse curvature and on the 2D model with similar lengthwise curvature. The experiments were conducted at the Mach numbers from 4 to 6 and unit Reynolds numbers from 10 to 60 million. The comparison of the data has shown that in 3D flow the length of transition area is approximately two times less than in 2D flow. It was ascertained strong influence of pressure gradient and separation on structure, characteristics of boundary layer and its non-equilibrium state and transition.

Stability of a helium II flow

S. P. Godfrey, C. F. Barenghi and D. C. Samuels

Dept. of Mathematics, University of Newcastle upon Tyne, Newcastle, NE1 7RU, UK

Contact e-mail: s.p.godfrey@ncl.ac.uk

The determination of the stability of any helium II flow is complicated by the fact that we must consider the interaction of two fluids: the normal fluid component and the superfluid component. We consider 2-D channel flow and concentrate on the stability of the normal fluid velocity profile under a mutual friction forcing from the superfluid. The addition of the mutual friction force modifies the Orr-Sommerfeld linear stability calculation. We find that the addition of the mutual friction force has a slight stabilizing effect on the standard instability of the channel flow, but that this force causes an entirely new instability to occur at very low wavenumbers. By raising the magnitude of the forcing, the new instability can occur at arbitrarily low Reynolds numbers.

Interactions of Three-dimensional Instabilities in Plane Mixing Layers

Jordi Estevadeordal

Innovative Scientific Solutions Inc.
2766 Indian Ripple Rd., Dayton, OHIO, 45440, USA

Contact e-mail: jordi@innssi.com

Detailed measurements of the roll-up, first and second vortex pairing of a large plane mixing layer reveal that excitation of several three-dimensional (3D) instability modes occurs. It is shown that the two-dimensional (2D) rollers first become 3D as they approach each other and that the linear growth of at least two instability waves involving core instabilities leads to a spanwise periodic first pairing. The second pairing is characterized by instabilities involving non-axisymmetric modes which amplify into snake, spiral, and double-helical forms. Refs.: Physics of Fluids, Vol. 11, Issue 6, June 1999, pp 1688-1693); Experiments in Fluids, Vol. 27, Issue 4, 1999, pp 378-390.

Holographic flow visualization for study of 3D vortex and flow instabilities

J. Estevadeordal [1], S. Gogineni [1], L. Goss [1], H. Meng [2] and M. Roquemore [3]

[1]Innovative Scientific Solutions Inc.
2766 Indian Ripple Rd., Dayton, OHIO, 45440, USA
[2]Mechanical and Aerospace Eng. Dpt.
SUNY at Buffalo, NY, USA
[3]Air Force Research laboratory
Wright-Patterson Air Force Base, OHIO, 45433, USA

Contact e-mail: jordi@innssi.com

Holographic Flow Visualization (HFV) has the capability of three-dimensional (3D) representation of spatial objects and particle ensembles. The technique provides a novel means of studying spatially and temporally evolving complex flow structures marked by scalars. Experimental results in several fluid flows and flames demonstrate the effectiveness of HFV using different types of seeding in flows undergoing different instabilities: 1) a vortex ring generated by a falling drop of polymer suspension in water, 2) cascade of a bag-shaped drop of milk in water, and 3) internal flow structures of a jet diffusion flame. Ref.: Physics of Fluids, Vol. 9 , 1997; International Journal of Visualization of Japan, 1998.

Anisotropic zero-modes for a kinematic MHD model

A. Lanotte[1] and A. Mazzino[2,3]

[1] CNRS, Observatoire de Nice, BP 4229, 06304 Nice Cedex 4, France
[2] INFM and Dipartimento di Fisica, Via Dodecaneso 33, 16142 Genova, Italy
[3] Niels Bohr Institute, Blegdamsvej 17, DK-2100 Copenhagen, Denmark

Contact e-mail: mazzino@fisica.unige.it

We analyze, through non-perturbative calculations, the effects of anisotropy on anomalous scaling exponents of the second-order magnetic field correlations, within a kinematic magneto-hydrodynamics (MHD) problem. Here, the source of anisotropy for the magnetic field statistics is a mean field $\mathbf{B}^o$. As the advecting velocity field that we consider is δ-correlated in time, analytical approach is possible: the main result we have obtained is that the anomalous scaling exponent, ζ_0, associated to the isotropic contribution is dominant with respect to the anisotropic ones, ζ_j. In addition, the entire set of anisotropic scaling exponents, ζ_j, is given, showing the existence of a hierarchy related to the degree of anisotropy j, such that: $\zeta_0 < \zeta_2 < \cdots$.

Helical and Chiral Dynamo

O. Chkhetiani[2], E. Golbraikh[1], V. Pungin[2] and S. Moiseev[2]

[1]Center for MHD Studies, Ben-Gurion University of the Negev, Beer-Sheva, Israel
[2]Space Research Institute, RAS, Moscow, Russia

Contact e-mail: golbref@bgumail.bgu.ac.il ; moiseev@mx.iki.rssi.ru

We present results of the study of mechanisms of mean helicity H and chirality appearance and generation in various turbulent flows and their role in the dynamo of mean vortical and magnetic fields. At $H \neq 0$ the medium becomes unstable with respect to weak external large-scale disturbances, which leads to an "inverse energy cascade" over the spectrum. The presence of helicity leads to a decrease in turbulent viscosity. It is shown that either rotation or an external homogeneous constant magnetic field is sufficient for mean helicity generation The strongest generation is observed in media with a shear of mean velocity in an external homogeneous magnetic field. On the other hand, electromagnetic fields with violated mirror symmetry induce chiral properties of plasma. In this case $j = \sigma E + \sigma_k \mathrm{rot} E$. At the motion of plasma electrons in stochastic electromagnetic fields, the growth rate for mean magnetic field is $\gamma_{1,2} = -c^2 k^2 (\sigma + \sigma_* k^2) / \left(4\pi(\sigma + \sigma_* k^2)^2 - \sigma_k^2 k^2\right)$.

Vortex evolution in helical turbulence flow

A. Kapusta, B. Mikhailovich, E. Golbraikh

Center for MHD Studies, Ben-Gurion University of the Negev, Beer-Sheva, Israel

Contact e-mail: borismic@bgumail.bgu.ac.il

The increase in the lifetime of vortical structures in a turbulent MHD flow in a wake behind a bluff body (Karman's vortices) is observed in our laboratory experiments in an external homogenous coaxial magnetic field. Within the framework of semiempirical "external friction" model (A. Kapusta et al., AIAA, 182,1998) the system of equations for vortex evolution is derived. The key parameter of this model ε, which determines flow regimes, is equal to a unity. This correspondence to a strong turbulence with nonzero mean helicity and intense energy transfer (H. Branover et al., Turbulence and Structures, 1999). A good agreement of the proposed mathematical model with laboratory experimental data is obtained.

Characterization of the intermittency in 2–D magnetohydrodynamic through the scaling properties of the PDFs of the turbulent fluctuations

L. Sorriso-Valvo [1,2], V. Carbone [1], P. Veltri [1], H. Politano [2] and A. Pouquet[2]

[1]Dipartimento di Fisica and Istituto Nazionale per la Fisica della Materia, Università della Calabria, I-87036 Rende (Cosenza), ITALY
[2]Laboratoire G. D. Cassini, CNRS UMR 6529, OCA Observatoire de Nice B. P. 4229, 06304 Nice Cedex 04, France

Contact e-mail: sorriso@fis.unical.it

Intermittency in plasma turbulence has been analysed through the probability distribution functions (PDFs) of the fields fluctuations. The PDFs show a peculiar behavior, that is their shape depend on the scale at which we calculate the fluctuations, so that they are gaussians at large scales, but the tails become higher as the scale decreases, showing a strong non-gaussian behavior. We used a simple model due to Castaing et al. (1990), introducing a single parameter to characterize the intermittency, to fit the PDFs of the magnetic field intensity, bulk speed and Elsässer fields fluctuations, obtained from high resolution 2–D magnetohydrodynamic numerical simulations. We found the typical scaling behavior of intermittent systems.

Response of the solar wind to incoming thermal or magnetic perturbations

R. Grappin, J. Léorat and A. Buttighoffer

Observatoire de Paris-Meudon, 92195 Meudon, France

Contact e-mail: grappin@obspm.fr

The solar wind is a flow with open boundaries, represented here by numerical solutions of the axisymmetric MHD equations, integrated in the meridian of a spherical shell. The boundary conditions are imposed via characteristics. We consider the problem of the instability of cold streams in the accelerating region, in the absence of magnetic field: the distance of turbulent mixing is shown to depend on the mean temperature, i.e., on the location of the sonic point. We also consider the propagation of Alfvén waves in presence of cold channels and a current sheet: the waves retain properties close to obser ved within the channels, suggesting that channels are a main constituent of the wind. Finally, waves are strongly dissipated by phase mixing in the vicinity of the current sheet.

Modification of a two-dimensional vortex street by a polymer additive

W.I. Goldburg*, J.R. Cressman and Q. Bailey

Department of Physics and Astr., Univ. of Pittsburgh, Pittsburgh, PA 15260, USA

*Contact e-mail: goldburg+@pitt.edu

We have studied the shedding of vortices produced by a rod several mm in diameter that penetrates a vertically flowing soap film. A high molecular weight polymer was then added to the soap solution. Measurements were made of $\sigma(Y')$, the rms fluctuation of the horizontal velocity component as a function of the distance Y' below the rod. The polymer strongly broadens the power spectrum of the velocity fluctuations and reduces the energy injected into the vortex street created by the rod. It will be argued that this result is due to the elongation of the boundary layer by the polymer. The polymer has the effect of broadening the power spectrum $S(f)$ of the transverse velocity variations and enhancing the elongational viscosity of the film.

Controlling a Separating Flow using Piezoelectric-Actuators

Y. Yokokawa [1], Y. Fukunishi [2] and S. Kikuchi [3]

[1]Graduate school of Tohoku University
Aramaki-Aoba 01, Aoba-ku, Sendai 980-8579, Japan
[2]Department of Mechanical Engineering, Tohoku University
Aramaki-Aoba 01, Aoba-ku, Sendai 980-8579, Japan
[3]Institute of Fluid Science, Tohoku University
2-1-1 Katahira, Sendai 980-8577, Japan

Contact e-mail: fushi@fluid.mech.tohoku.ac.jp

An attempt to control the spanwise phase of the velocity fluctuation in the flow over a cavity is carried out. The long-term objective of this research is to suppress the aerodynamic noise generated from a separating flow. In order to achieve an active flow control, two types of piezoelectric-devices are tested. The first type is the uni-morph type actuator. It expands or shrinks parallel to the surface. The other is the bi-morph type actuator, which moves its ends vertical to its plane. Experimental results show that the flow field with a wavy structure, 180 degree out of phase in the spanwise direction, can be generated using either type of the actuators. As a result of controlling the flow, the suppression of the aerodynamic noise was also achieved.

The numerical solution of the equation for one-point probability density function of a scalar in homogeneous turbulence

A.D. Chorny, V.A. Sosinovich

Academic Scientific Complex "A.V. Luikov Heat and Mass Transfer Institute"
National Academy of Sciences, Minsk, Belarus

Contact e-mail: vl-bond@ns1.hmti.ac.by

In paper the closed system of the equations for one-point probability density function of the uniformly distributed scalar in a turbulent flow is resulted. The task is ill-posed owing to the negative member describing transfer in phase space of scalar fluctuations. It causes instability of known numerical procedures at finding of the decision of the equation for one-point probability density function. In paper the method of building steady difference schemes for ill-posed evolutionary tasks from positions of the regularisation principle for difference schemes and their asymptotic stability is used.

New development of the LMSE mixing model with accounting for intermittency

M.Gorokhovski [1] and V.Sabel'nikov [2]

[1]CORIA UMR 6614 CNRS University of Rouen, France
[2]UPR 9028 CNRS, Poitiers, France;
Central Aerodynamic Institute, Zhukovsky-3, Russia

Contact e-mail: Gorokhovski@coria.fr

The objective is to derive and verify a new mixing model that accounts for the interaction between scalar mixing and time scales of turbulent eddies. This new model is a further development of the classical LMSE mixing model. The basic idea behind it is to represent the scalar mixing as a linear stochastic relaxation to the conditionally mean concentration at the given value of mixing frequency. The effect of intermittency appear in the model through the Obukhov's log-normality hypothesis. The equation for conditional PDF of concentration at the given mixing frequency is derived and numerically solved. The behavior of non-conditional PDF of concentration and of scalar variance was shown with variation of the Reynolds number, the turbulent integral time scale and the mean mixing time scale. Further, a modified PDF-equation was proposed where injection of unmixed concentrations is taken into account and the plug-flow reactor mixing was analyzed.

Iso-scalar surfaces in a Direct Numerical Simulation of isotropic turbulence with scalar injection

M. Elmo [1], J. P. Bertoglio [1] and V. A. Sabel'nikov [2]

[1]Laboratoire de Mécanique des Fluides et d'Acoustique UMR 5509
Ecole Centrale de Lyon, 36 Av. Guy de Collongue, 69130 Ecully, FRANCE
[2]TSAGI, Zhukovsky, Moscow Region 140160, RUSSIA

Contact e-mail: elmo@mecaflu.ec-lyon.fr

The geometry of iso-scalar surfaces is an important parameter for the description of turbulent reacting flows. In a D.N.S. of isotropic turbulence, in which scalar fluctuations are injected periodically in time using the technique proposed in Elmo, Bertoglio and Sabel'nikov -TSFP, Santa Barbara 1999-, the area density $A(\Gamma)$ is evaluated using: $A(\Gamma) =< |\nabla c|/c = \Gamma > P(\Gamma)$ in which $< .|c = \Gamma >$ denotes a conditional average and $P(\Gamma)$ is the p.d.f. of c.
The ratio of the area densities $A(\Gamma = 0)$ observed at two scales, l_1 and l_2, when plotted as a function of $\frac{l_1}{l_2}$ shows a similarity behaviour over half a decade. The same behavior is observed in a higher Reynolds number L.E.S., the similarity region being then observed over more than one decade. In both cases the similarity dimension is found to be 2.6 in reasonable agreement with the theoretical prediction $\frac{8}{3}$.

Mean-field theory of a passive scalar advected by a random velocity field with finite renewal time

T. Elperin [1], N. Kleeorin [1], I. Rogachevskii [1] and D. Sokoloff [2]

[1]Department of Mechanical Engineering, Ben-Gurion
University of the Negev, Beer-Sheva 84105, P. O. Box 653, Israel
[2]Department of Physics, Moscow State University, 117234 Moscow, Russia

We derived a mean-field equation for number density of particles advected by a random velocity field with a finite correlation time and showed that this equation is integro-differential equation. The finite correlation time of random velocity field results in the appearance of the high-order spatial derivatives in the equation for a number density of particles. The finite correlation time and compressibility of the velocity field can cause a depletion of turbulent diffusion and a modification of an effective mean drift velocity. The effective mean drift velocity is caused by a compressibility of particles velocity field and results in formation of large-scale inhomogeneities in spatial distribution of particles.

Effects of compressibility and finite renewal time of a random velocity field to intermittency of passive scalar fluctuations

T. Elperin [1], N. Kleeorin[1], I. Rogachevskii[1] and D. Sokoloff[2]

[1]Department of Mechanical Engineering, Ben-Gurion University of the Negev, Beer-Sheva 84105, P. O. Box 653,Israel
[2]Department of Physics, Moscow State University, 117234 Moscow, Russia

We showed that very small compressibility ($\sim 1/\mathrm{Re}$) of a random velocity field causes an anomalous scalings of passive scalar fluctuations in the inertial range of a random velocity field. In a random velocity field with finite correlation time turbulent diffusion is determined by the field of Lagrangian trajectories which is compressible even if the velocity field is incompressible. We showed that the finite correlation time of a random compressible velocity field causes an excitation of the small-scale instability of fluctuations of number density of particles and formation of small-scale inhomogeneties of a passive scalar distribution. This implies that the second and higher moments of a passive scalar can grow in time exponentially.

Two-particle dispersion in Kinematic Simulations

J.Dávila [1], E. Bravo-León [1], and J.C. Vassilicos [2]

[1]Grupo de Mecánica de Fluidos, University of Seville
Camino de los Descubrimientos s/n, E-41092 Sevilla, SPAIN
[2]Department of Applied Mathematics and Theoretical Physics
University of Cambridge, CB3 9EW Cambridge, UK.

Contact e-mail: davila@eurus2.us.es

We have calculated the mean square distance between two fluid or inertial particles, $\langle \Delta^2 \rangle(t)$, in an isotropic and homogeneous turbulent-like flow generated by using Kinematic Simulations. This study is based on the "locality assumption". Hence $\langle \Delta^2 \rangle(t) = G_\Delta \epsilon t^3$, where ϵ is the dissipation of energy and G_Δ the Richardson's constant. We have studied the dependence of G_Δ on the ratio of the outer scale, L, to the inner scale, η, and on the dimensionless parameters that determine the characteristics of the particles, i.e., the settling velocity of the particles in still fluid, V_T, and the characteristic viscous response time of the particles, τ_p. We have related this result with the power-law of the number of stagnation points per unit volume $n_s = C_s(L/\eta)^2$, where C_s is a function of V_T.

Measurement of Passive Scalar Statistics through Use of Compensated Cold Wires

J. Lemay [1], J. S. Blais [1], A. Benaïssa [2] and B. Fleck[2]

[1] Département de génie mécanique, Université Laval
Ste-Foy (Québec) Canada G1K 7P4
[2] Department of Mechanical Engineering, Royal Military College of Canada
PO Box 17000 Stn Forces, Kingston (Ontario) Canada K7K 7B4

Contact e-mail: Jean.Lemay@gmc.ulaval.ca

The statistics of temperature fluctuations θ are studied in terms of the validity of the different limitations or assumptions involved in their measurement process. The effect of the limited frequency response of a cold-wire probe, relative to the Kolmogorov frequency, and the use of Taylor's hypothesis are the main points under investigation in a turbulent round jet ($R_\lambda \simeq 170$). Particular attention is paid to the effect of the amplitude and phase corrections applied to the cold-wire signals. The statistics being analysed are: *i)* $\overline{\epsilon_\theta}$, the average dissipation rate of $\overline{\theta^2}/2$; *ii)* p.d.f. and moments of θ; *iii)* the moments of the temperature derivatives $\overline{(\partial\theta/\partial x_i)^n}$ and the j.p.d.f. between θ and ϵ_θ; and *iv)* the structure functions $\overline{(\Delta\theta(x))^n}$ and $\overline{(\Delta\theta(r))^n}$ (with $n = 2$, 3 and 4).

Statistics of a high Schmidt number passive scalar in the far-wake

H. Rehab, R. A. Antonia and L. Djenidi

Department of Mechanical Engineering
University of Newcastle, N.S.W, 2308, AUSTRALIA

Temporal statistics of the concentration fluctuation c of a high Schmidt number passive scalar ($Sc \approx 2000$) are measured in the far-wake of a circular cylinder using a single point laser induced fluorescence technique. The statistics of c are compared with those of θ, the temperature fluctuation ($Sc \approx 0.7$), at the same x/d and Re. The centreline pdf of c deviates from Gaussianity; this becomes less pronounced as Re increases while the pdf of θ has reached a homogeneous state underlining the importance of molecular diffusion. The pdfs of the increments of c at small separations indicate the uniformity of the scalar as Re increases. The spectra of c shift systematically towards high wavenumbers as Sc increases but the $\phi(k_1) \sim k_1^{-1}$ prediction, for $Sc \gg 1$, of Batchelor (1959) is not observed.

Mixing and coherent structures in jets in crossflow

A. Rivero[1], J.A. Ferré[1], F. Giralt[2]

[1]Department of Mechanical Engineering, University Rovira i Virgili.
[2]Department of Chemical Engineering, University Rovira i Virgili

Several studies (numerical simulations and experiments in a wind tunnel and in a water tunnel) have been performed in a jet in crossflow at Re=6600 and 2700. The results obtained by means of the pattern recognition analysis of X-wire data display the prototypical threedimensional vorticity field of the turbulent jet. PLIF visualizations with several lobulated nozzles (4 and 8 lobes) demonstrate that mixing is enhanced significantly (40%) only in one of the five configurations tested. Another aspect that has been investigated is the influence of the nature (laminar/turbulent) of boundary layer that interects with the jet. Finally the numerical simulation shows the influence of cross-flow over the vorticity formed in the nozzle of the jet and its deflection.

A Comparative Study of Heat and Mass Transfer by Impinging Jets on Flat and Curved Surfaces

H. Stapountzis[1], D. Tsipas[1],and A. Stamatellos[2]

[1] Mechanical Engineering Dept.,
Univ.of Thessaloniki, Greece 540 06
[2]Mechanical and Industrial Engineering Dept.,
Univ. of Thessaly, Greece 383 34

Contact e-mail: erikos@eng.auth.gr

An experimental study was undertaken in order to investigate the effect of solid surface curvature and flow geometry on the heat transfer and mass transfer (water paint material dissolution and surface erosion by solid particles) which was induced by turbulent impinging jets. Transport coefficients (for heat and mass) were optimimum, if the jet nozzle - surface separation distance was about half the length of the potential core of the jet in unconfined conditions. The max. in the Nu number occured off the stagnation point. The optimum angles of incidence for max. Nu were between 90 deg. (normal impingement) and 75 deg. while for dissolution mass transfer between 35 and 60 deg. Surfaces of ductile material were eroded at different impingement angles than surfaces of brittle material. Curved surfaces exhibited better transport coefficients in the immediate region of the stagnation point than flat surfaces.

Characterization of trailing vortex structures in stirred tanks

Jos Derksen[1],John McLaughlin[2] and Konstantinos Kontomaris[3]

[1] Kramers Laboratorium, Delft University of Technology
2628 BW Delft, The Netherlands
[2] Department of Chemical Engineering, Clarkson University
Potsdam, New York, 13699-5705, USA
[3] DuPont Central Research and Development
Wilmington, Delaware, 19880-0304, USA

Contact e-mail: jos@klft.tn.tudelft.nl

Turbulent flow in stirred tanks is used in industry to bring initially separated species into intimate contact. From a modeling point of view, the turbulence characteristics of the flow are difficult to assess because of its intrinsically transient and 3-D nature. In the present work, direct and large-eddy simulations on turbulent stirred tank flow have been performed, thereby focusing on the vortex system generated by the revolving impeller. A high level of detail could be reached in the simulations by making use of a lattice-Boltzmann scheme. The simulations accurately predicted the way the vortices are formed as well as the way they are swept into the tank. Associated with the vortex cores are regions of concentrated turbulent activity. It will be demonstrated that by slightly adapting the impeller geometry the vortex structure can be strongly influenced, which might have implications for process design.

Experimental assessment of stress-strain relation for coaxial jets

F. Schmitt, Ch. Hirsch and B. K. Hazarika

Department of Fluid Mechanics, Vrije Universiteit Brussel
Pleinlaan 2, B-1050 Brussels

Contact e-mail: francois@stro.vub.ac.be

We performed 2D LDA measurements of the coaxial jets generated by a double annular burner, with an axisymmetry better than 2%. The measurements have been taken on a very fine grid (5,500 grid points) in order to be able to numerically compute the gradients of the mean velocity field. This provides an experimental determination of the strain tensor S, and since the stress tensor T is also given by the measurements, Boussinesq's hypothesis, which is at the basis of classical k-ϵ modeling, can be experimentally tested. We show that this hypothesis, corresponding to a linear relation between T and S, is invalid, and we experimentally check a nonlinear generalisation involving the tensors $SW - WS$ and S^2, where W is the vorticity tensor. We also compute inrariants of the flow.

Effect of an accelerating co-flow on a turbulent jet

A. Califano[1], A.K. Prasad[2] and J. Westerweel[3]

[1]University of Rome 'La Sapienza,' Italy
[2]University of Delaware, U.S.A.
[3]Delft University of technology, The Netherlands

Contact e-mail: J.Westerweel@wbmt.tudelft.nl

A turbulent jet entrains ambient fluid at a rate given by $U_e = \alpha U_c$ where U_e is the entrainment velocity, U_c the local centerline velocity and α the entrainment coefficient. For axisymmetric jets, the value of α is given as 0.05. Sreenivas & Prasad proposed a model [1] which predicts the variation of α when a jet is subjected to (i) off-source volumetric heating, and (ii) an accelerating co-flow. Entrainment predictions by this model for case (i) have been verified by experiment [2]. PIV measurements were taken for a jet in an accelerating co-flow to verify the model for case (ii). A water jet issues from a 1 mm nozzle at Re$\sim 10^3$ into a quiescent chamber. After the jet flow is established, the water in the chamber is accelerated by a pump. Results include the variation of entrainment as a function of acceleration and the effect of acceleration on the vortex dynamics of the coherent structures at the jet boundary.

A Comparative Experimental Investigation of a Turbulent Axisymmetric Zero-Net-Mass Flux Jet and a Continuous Jet

J. Cater and J. Soria

Monash University, Melbourne, Australia

A comparative study between an axisymmetric zero-net-mass flux (ZNMF) jets and the equivalent continuous jets is presented. Cross-correlation digital particle image velocimetry was employed to measure the instantaneous velocity field in the far-field of the jet. The Reynolds number for both jets ranged between $3120 < Re_{U_0} < 9380$ and the Strouhal number for the ZNMF jets was $St_{U_0} = 0.0032$. The growth rate is linear at a distance greater than 130 x/D_0 for both cases and the growth rate of the ZNMF jet is aprroximately 1.8 times larger. In this region the ZNMF jet has a mean centerline velocity that is approximately 1/3 that of the equivalent continuous jet. The results indicate that the structure and dynamics of these jets are different and depend strongly on the initial jet formation.

Development of large-scale structures in confined jet shear layer

S. Alekseenko, A. Bilsky, D. Markovich and V. Vasechkin

Institute of Thermophysics, Siberian Branch of RAS Lavrentyev Ave., 1, Novosibirsk, 630090, Russia

Contact e-mail: dmark@itp.nsc.ru

This work is devoted to the study of instabilities evolution during submerged round jet impingement under the action of low-amplitude periodical forcing. The main results are obtained with the aid of electrodiffusion method for measuring velocity and wall shear stress and also by the DANTEC Particle Image Velocimeter. The behaviour of fundamental and subharmonics was tested including phase velocity of the structures and radial symmetry loss. The technique of conditional sampling (phase averaging) allowed us to measure the instantaneous pattern of the flow, averaging only by broad-band turbulence. The contribution of coherent and broad band components of pulsations into the turbulent kinetic energy was also obtained. The local back flows in the near-wall region were observed. Two regions with local flow separations have been found - stagnation point region and zone where propagating large-scale structure initiates the local positive pressure gradients.

Experimental investigation of wall effects on the initial region of turbulent round jets

A. Benaissa [1], B. A. Fleck [1], A. Pollard [2], and J.F. Morrison[3]

[1]Department of Mechanical Engineering Royal Military College of Canada
Kingston, CANADA
[2]Department of Mechanical Engineering
Queens University, Kingston, Ontario, CANADA
[3]Department of Aeronautics,
Imperial College, London, ENGLAND

Contact e-mail: benaissa-a@rmc.ca

The effect of wall proximity on the development of an axisymmetric air jet is studied experimentally. The effect of wall presence on large coherent structures is dominant since it modifies their shape and conditions their evolution. Flow visualization, velocity and wall pressure measurements, space-time correlation and spectra of wall pressure indicate a discrete frequency for the primary instability and roll-up of the mixing layers. The pressure velocity correlations reveal and localize the horseshoe vortices and show clearly their inclination and evolution in the direction of the main flow. This work supports the idea that the primary vortex, upon interacting with a wall, produces a horseshoe-type structure persisting to x/D = 5 for a jet height of H/D=1

Evaluating the accuracy of the LSE-POD technique in an axisymmetric shear layer.

D. Ewing[1] and S. Woodward[2]

[1]Department of Mechanical Engineering, McMaster University
Hamilton, Ontario, CANADA
[2]Department of Mechanical and Aerospace Engineering,
University of Buffalo Amherst, New York, USA.

Contact e-mail: ewingd@mcmaster.ca

Investigating the dynamics of the large structures in turbulent flows experimentally is challenging because it requires the simultaneous sampling of the velocity over the entire region of interest. Recently, Bonnet *et al.* (*Expts. in Fluids*, 17: 307–314, 1994) proposed a simplified technique where the velocity was measured at a few points in a region and estimated at the remaining points. They showed this technique could be used with the POD to accurately recover the dynamics of the structures in some flows. However, this could only be shown by measuring the full field and comparing the results. Analytical expressions to evaluate the accuracy of the LSE-POD technique *a priori* are outlined here and their use is demonstrated for the axisymmetric shear layer.

A study of turbulent transport processes in the near wake of cylinder under controlled inflow oscillation

A. Jarża , M. Podolski

Institute of Thermal Machinery, Technical University of Częstochowa

Contact e-mail: alicja@imc.pcz.czest.pl, podolski@imc.pcz.czest.pl

The near wake of circular cylinder has been studied in order to provide experimental informations on the turbulent energy transfer processes in flow considered. The lock-on phenomenon resulting from the inflow periodical perturbations has also been discussed as potential way of active wake control.

The instantaneous velocity-time series measured by means of multichannel DISA 55MCTA System made it possible to obtain statistics of streamwise and lateral velocity components in the near wake region. Phase averaging technique, proper for the flows containing the periodical velocity component was applied.

The present experimental set-up offered the possibility to evaluate all terms of turbulent kinetic energy budget except the diffusion treated as a closing quantity.

A numerical investigation of momentumless turbulent wake dynamics in a linearly stratified medium

G. G. Chernykh [1], B. B. Ilyushin [2], O. F. Voropayeva [1]

[1]Institute of Computational Technologies, Russian Academy of Science SD, Lavrentjev ave. 6, Novosibirsk 630090, Russia
[2]Institute of Thermophysics, Russian Academy of Science SD, Lavrentjev ave. 1, Novosibirsk 630090, Russia

Contact e-mail: chernykh@lchd.ict.nsc.ru

To describe the flow in a far turbulent wake of self-propelled body of revolution in a linearly stratified medium the parabolized three-dimensional system of the averaged equations for the motion, continuity and incompessibility in the Oberbeck-Boussinesq approach is used. This system of equations is nonclosed. In the present work we consider the hierarchy of closed mathematical models of second order. A comparison with the experimental data of Lin and Pao (1979) has been carried out. One succed in obtaining a satisfactory description of the anisotropic decay of wake characteristics only by using the modified algebraic relationships for determination of triple velocity field correlations. This model takes into account the anisotropic damping effect by a stable stratification. The work has been supported by INTAS (Grant No. 97-2022).

A spatial structure of a flow in a axisymmetric sudden expansion

Noriyuki Furuichi [1], Yasushi Takeda [1] and Yasuhiro Ozaki [2]

[1]Paul Scherrer Institut, 5232 Villigen PSI, Switzerland
[2]Keio University, Hiyoshi 3-14-1, Kohoku-ku, Yokohama 233-8522, Japan
Contact e-mail: Noriyuki.Furuichi@psi.ch

A flow structure in a channel with a symmetric sudden expansion has been studied in the past as it is frequently encountered in engineering practice. A basic structure around a separated shear layer and reattachment region is seen to be similar to that of the two-dimensional backward-facing step flow. However, in the axisymmetric sudden expansion flow, the structure of the separated shear vortex might be more complex because it is generated as an angular structure and is not uniform to azimuthal direction. In this experiment, we used a ultrasonic velocity profiler to measure spatio-temporal velocity field on the streamwise direction in the axisymmetric sudden expansion. We report here a behavior of the time dependent velocity field and clarify the spatial structure, especially of the azimuthal structure of the separated shear vortex by spatial cross correlation functions.

Instability waves in separated swirling flows at bluff bodies

S. P. Bardakhanov

Institute of Theoretical and Applied Mechanics
Siberian Branch of Russian Academy of Sciences
Novosibirsk, 630090, Russia

In present work it was the aim to investigate the development of controlled disturbances in three-dimensional swirling separated flows existed on upper surface of delta wing at high angle of attack and at the end of rectangular wing at the angle of attack. During laminar separation natural periodical disturbances are observed in conical flow. The measurements had shown that at the initial region of disturbance's development their frequency depends from freestream velocity and the angle of attack. These disturbances have linear, nonlinear and turbulent stages during the flow development. Imposition of artificial disturbances influences the development of these stages. The vortex surface has the layer structure and the number of layers grows downstream. The spectral components of the excited disturbance develop in the different layers of the vortex surface. Measurements were also made in turbulent separation regime with vortex "breakdown". The artificial disturbances introduced in the flow results into eigen disturbances or coherent structures.

Enstrophy and Dissipation Within Flow Regions of a Turbulent Channel Flow

S. Wade [1], J. Soria [1], A. Ooi [2] and M. S. Chong[3]

[1]Department of Mechanical Engineering
Monash University, Clayton, Victoria, AUSTRALIA
[2]DSTO, Melbourne, Victoria, AUSTRALIA
[3]Department of Mechanical Engineering University of Melbourne, Melbourne, Victoria, AUSTRALIA

The enstrophy and dissipation of flow regions within a wall bounded flow are investigated using a direct numerical simulation (DNS) of a fully developed channel flow at $Re_{u_\tau} = 180$. It is shown that only 5.5% of the volume integrated enstrophy and dissipation comes from the viscous sublayer, compared with 75% from the region $20 < y^+ < 100$. This region is also shown to be responsible for most of the dissipation of kinetic energy within the flow. 85% of enstrophy is contained in focal regions and 57% is contained in both focal regions and in the spatial region $20 < y^+ < 100$. These focal regions are also responsible for 66% of dissipation of kinetic energy. The contribution of the focal regions in the region $20 < y^+ < 100$ to the total dissipation of kinetic energy is 43%.

Flow visualization of turbulent flow in an open channel with 2D fixed bed forms

Joselina Espinoza[1] and Jorge Rojas[2]

[1]Instituto Mexicano de Tecnología del Agua, Jiutepec, Mor. MEXICO
[2]Centro de Investigación en Energía, UNAM, A.P. 34, Temixco, Mor. MEXICO

Contact e-mail: jrm@mazatl.cie.unam.mx

Three visualization techniques, dye, hydrogen bubble and solid particles, were implemented to identify the flow structures over two dimensional fixed bed forms in a 20 meters open channel with $Re = 18,400$. The macro flow structures behind the bed forms were interpreted as: 1) Kelvin- Helmholz waves, 2) Boils o Kolks, 3) Vertical vortices, 4) Funnel vortices and 5) Recirculating flow. The velocity field was estimated with a particle tracking technique. It was clearly distinguished an upper fast flow and a lower, behind the crest, slow fluid motion with velocity magnitude two to three times different. The combination of three flow visualization techniques gave valuable information of the formation, evolution and destruction of some turbulent boundary layer flow structures.

Experimental Investigation of Secondary Currents Using High-Temporal Resolved PIV

J. von Lukowicz, T. Rosenstein, T. Baur and J. Köngeter

Institute of Hydraulic Engineering and Water Resources Management
Aachen University of Technology (RWTH Aachen)
Kreuzherrenstr., 52056 Aachen, Germany

Contact e-mail: lukowicz@iww.rwth-aachen.de

Natural rivers are characterised by compound open-channel flows, where secondary currents are produced not only in river benches but also from the anisotropy of turbulence. The poster presents experimental results from PIV-measurements of secondary currents in planes perpendicular to the main velocity component of a test flume. A camera with high-temporal resolution is used to provide a time-series view on the time-dependent flow field. Instantaneous velocities and related flow quantities like Reynolds stress, anisotropy of turbulence and vorticity are evaluated. Vortices moving towards the main channel indicate the temporal resolved substructures of secondary currents. The latter flow phenomena cause a reasonable mass and momentum transfer between main channel and flood plains.

Scaling the outer profiles of turbulent boundary layers

L. Castillo[1] and W.K. George[2]

[1]Department of Mechanical Engineering, Aeronautical Engineering
Rensselaer Polytechnic Institute, Troy, NY 12180 USA
[2]Department of Mechanical and Aerospace Engineering
State University of New York at Buffalo, Buffalo, NY 14260 USA

The outer velocity scale determined from the RANS equations using similarity analysis, U_∞, provides physical insight on the flow development downstream and it provides implications on flow control which are not possible with any other velocity scale. Furthermore, defining equilibrium flows with $\Lambda = \delta/\rho(U_\infty^2)dP_\infty/dx = constant$ (from which it follows that $\delta \sim U_\infty^{-1/\Lambda}$) leads to three profiles in turbulent boundary layers regardless of the strength of the pressure gradient: one for favorable pressure gradient (FPG) with $\Lambda = -1.915$, one for adverse pressure gradient (APG) with $\Lambda = 0.22$, and for zero pressure gradient (ZPG) with $\Lambda = 0$. Finally, the Zagarola & Smits scale, $U_\infty(\delta_*/\delta)$, removes all Reynolds dependence (which arise from the upstream conditions) even for flows near separation, and it yielded three profiles: one for FPG, one for APG and one for ZPG.

Simulation of the intrusion of coherent free-stream perturbations in a subsonic boundary layer

H.C. de Lange and R.J.M. Bastiaans

Energy Technology and Internal Combustion Engines
Eindhoven University of Technology, P.O. Box 513, 5600 MB Eindhoven, THE NETHERLANDS

Contact e-mail: R.J.M.Bastiaans@wtb.tue.nl

Direct numerical simulation is used to study the fluctuation penetration process in a boundary layer and the subsequent formation of spots. In this study a numerical code has been developed for the DNS of compressible subsonic flows. The code is based on higher order compact schemes, with a Runge Kutta time integration, the acoustics are treated in a separate sub time-step integration. A spatial boundary layer is simulated with initial profiles given by the Blasius solution for Re_δ equal to 400 and a Mach number of 0.2. The stream-wise velocity at the inflow is perturbed by an oscillating structure with size 4δ at the edge of the boundary layer. First results show the formation of a flow structure with characteristics similar to those of turbulent spots.

Analysis of the Interactions between Large-Scale Streamwise EHD Structures and a Turbulent Boundary Layer

C. Marchioli[1], A. Soldati[1] and M.V. Salvetti[2]

[1]Dept. of Chemical Science and Technology, Università di Udine, V. Cotonificio 108. 33100 Udine, Italy.
[2]Dept. of Aerospace Engineering, Università di Pisa, V. Diotisalvi 2, 56100 Pisa, Italy.

Contact e-mail: mv.salvetti@ing.unipi.it

The interactions between large-scale electro-hydrodynamic (EHD) streamwise structures and a turbulent boundary layer, which may lead to significant drag reduction, are analyzed. The data from DNS of a turbulent channel flow with different intensities and configurations of the electrostatic forcing flow are used. A filtering procedure based on the wavelet cross-correlation analysis is proposed to identify and educe the EHD flow from the background turbulence. Usual analysis techniques are then applied to the filtered velocity fields to study turbulence modifications. Moreover, the the wavelet cross-correlation analysis is also used to understand the mechanisms leading to drag reduction, since it gives the local contribution to the Reynolds stress of each flow scale.

Interaction of Endothermic and Exothermic Regions with a Turbulent Hypersonic Boundary Layer

M. Pino Martín and Graham V. Candler

Aerospace Engineering and Mechanics
University of Minnesota, Minneapolis, MN 55455

Contact e-mail: pino@aem.umn.edu

The boundary layer on proposed hypersonic vehicles will be turbulent and chemically reacting. Understanding the interaction between turbulent flow and reactions in the boundary layer is important, since the behavior of the flow near the wall affects the vehicle aerodynamics. Thus, we perform DNS of boundary layers at Mach 4 and $Re_\theta = 7000$ with finite-rate chemical reactions. For the isothermal case, we find an increase in the range of turbulent scales, magnitude of temperature fluctuations, turbulent kinetic energy, and structure inclination angle. This is a result of exothermic reactions occurring near the wall and feeding the turbulent modes of motion. The opposite is found for the adiabatic simulation, as the reactions occur at the expense of the turbulent fluctuations.

Correlation intervals of sea turbulence velocity field

G. A. Fedotov

Science and Engineering Centre, Granit-7 Company
Gospitalnaya st. 3, Saint-Petersburg 191014, RUSSIA

Contact e-mail:fedotov@GF4766.spb.edu

On the basis of the classical expressions for the spectral tensor and the three-dimensional energy spectrum of a sea turbulence velocity field the exact values of the longitudinal and transverse correlation intervals are obtained in a dimensionless form. Four types of the correlation intervals, namely, integral, absolute, quadratic, and maximal correlation intervals are evaluated. The exact values of the longitudinal and transverse normalized spatial correlation functions, when their arguments are equal to the correlation intervals, are computed. The new effective modifications of the difference method for the sea turbulence energy determination using mobile (especially high-speed) carriers of hydrophysical instrumentation are proposed.

Turbulence structure and mixing near gas-liquid interface

Derek Stretch and Mosa Chaisi

School of Civil Engineering, University of Natal, Durban, South Africa

Understanding the structure of turbulence near gas-liquid interfaces and mechanisms of mixing and transport across them has important environmental and industrial applications. The coupling of turbulence across a flat interface is analyzed using Rapid Distortion Theory and kinematic simulations. Our analysis predicts the coupled motions at the interface as a function of the fluid properties, turbulence velocity and length scales far from the interface. Aspects of these predictions are compared with results from DNS computations with encouraging results.

On Tracers And Potential Vorticities In Ocean Dynamics

Michael V. Kurgansky[1] and Ettore Salusti[2]

[1]Institute of Atmospheric Physics, Russian Academy of Sciences
Pyzhevsky 3, 109017 Moscow, Russia
[2]INFN - Phys. Dept., University of Rome "La Sapienza"
Piazzale A.Moro 2, Roma, Italy

The Ertel potential vorticity for stratified viscous fluids in a rotating system, considering also external forcings, is here analyzed: the conservation laws corresponding to novel invariants are obtained. These invariants do not have a classical form: indeed one example is mere classical potential vorticity multiplied by a time function. It has to be stressed that similar relations hold not only for marine water density but also for a wide class of conserved quantities such as salt, entropy, tracers, etc. So a set of "tracers", i.e. materially conserved scalar quantities, and the corresponding Ertel's potential vorticities in this study are applied to various cases of physical interest as current marked by radioactive tracers, fronts and thermoaline currents. These ideas are then used for an "absolute field" determination in a realistic case of large-scale slow oceanic currents.

Large Eddy Simulation of Flow Phenomena in Lakes and Reservoirs

K. Rettemeier [1], O. Bergen [2] and J. Koengeter [1],

[1]Institute of Hydraulic Engineering and Water Resources Management,
Aachen University of Technology
Mies van der Rohe Str. 1, 52064 Aachen, GERMANY
[2]IMS Ingenieurgesellschaft
Stadtdeich 5, 20097 Hamburg, GERMANY
Contact e-mail: rettemeier@iww.rwth-aachen.de

The presented poster shows the application of a finite element model to simulate the flow and turbulence in natural geometries such as lakes and reservoirs which are very complex and in most cases fully three-dimensional. This is due to the irregular boundaries, the large volume of the water body and the variability of the external forces on the water body. Numerical models must at least be able to model the large scale processes as well as the influence of wind forces, momentum induced by in- and outflow and the coriolis force. Another problem is the large spectrum of turbulence with strong anisotropic flow characteristics. Standard statistic models are widely used, but it is very difficult to model the whole spectrum correctly thus a very promising approach is the Large-Eddy-Simulation technique.

GOTM, a model for simulating dissipation measurements in estuaries and open ocean

M. R. Villarreal [1], H. Burchard [2], K. Bolding [3] and P. P. Mathieu[3]

[1]Grupo de Física Non Lineal, University of Santiago de Compostela
15706 Santiago de Compostela, SPAIN. E-mail: uscfmmrv@ds.cesga.es
[2]Institut für Meereskunde University of Hamburg
Troplowitzstr.7, D-22529 Hamburg, GERMANY
[3]Joint Research Center, Space Applications Institute, Marine Environment Unit
I-21020 Ispra (VA), Italy

GOTM, General Ocean Turbulence Model is a one-dimensional water column model that allows for different combinations of momentum and tracer equations and a choice between some standard turbulence parametrizations. Different test cases have been prepared and implemented to be run with GOTM, including some situations where direct measurements of turbulence dissipation rate are available. The actual forcings in the site are estimated from measurements and turbulent magnitudes are prognosed and compared with the available dissipation rate measurements. Different turbulence models, stability functions and parametrizations of internal wave and shear instability mixing will be applied and compared. GOTM is a freeware code available under the GNU license in http://www.gotm.net

Experiments on flow characteristics and resistance in vegetated channels

A. Bateman[1], J.M. Redondo[2], D. Velasco[1] and J.P. Martín Vide[3]

[1]Technical University of Catalunya. Hydraulic and Hydrological Section
[2]Technical University of Catalunya. Applied Physics Department
[3]Technical University of Catalunya. (Currently at University of Illinois)

Contact e-mail: bateman@etseccpb.upc.es

The present paper tries to advance in the behavior of the flow through plants. The purpose is to obtain the friction factor of flexible vegetated channels and to describe the influence of turbulence in it. The experimental set up is a 20 m long, 1 meter wide 1 meter high flume with a mild slope made with gravel. Plastic strips were used to represent river plants (common reed) in a scale model. A Sontek flowmeter was used to measure flow velocities. The Darcy Weisbach friction factor (f) shows good agreements with the approach by Kouwen (Kouwen, 1992). We show the behavior of the friction factor versus the density of the plants. We present some results showing a relationship between shear and slip velocities (just over the plants). The vertical distribution of velocities has been measured and compared in dimensionless form.

SAR Observations of the Gibraltar Oceanographic and Environmental Features

J.J. Martinez Benjamin, A. Platonov and J.M. Redondo

Dept. de Fisica Aplicada Univ. Politecnica de Catalunya,
B5, Campus Nord, Barcelona E-08034, SPAIN

Contact e-mail: benjamin@fa.upc.es

The Synthetic Aperture Radar (SAR) is a usefull tool that may be used to study both marine water dynamics and its pollution. Oil spills and Natural sliks and fronts may be detected and procesed with advanced computer techniques to reveal vortex dynamics and turbulence spectral characteristics of the complex eddy and current interaction in the ocean surface. It is also posible to detect changes in the thermocline and internal wave activity. We analise in detaill frontal features asociated with maximal exchange flow in the Strait of Gibraltar and present some statistics of vortices during 1996-1998. We conclude from the observations that:

- The upwelling features are consistent with a small composite Froude number
- The vortical structures seem generated by coastal canyons

Mixing Regimes in Gaseous Diffusion Flames

A. Cavaliere [1], D. Pappa [1] and R. Ragucci [2]

[1]Dip. Ing. Chimica, Università di Napoli, Federico II
[2]Instituto Ricerche sulla Combustione, CNR, Napoli

A mixing classification is presented, in which stirring and mixing evolution is taken into account on the ground of evaluation of four quantities, namely the average virtual mixing layer thickness, the minimum ?dissipative? length scale, the maximum fluid-dynamic length scale and the average interface separation distance. The feasibility of the measurements of the quantities needed to identify the different regimes is assessed too. For such purpose an optical diagnostics procedure, based on the Reactive Scattering Technique, has been developed for the quantitative evaluation of the mixing layer thickness in the inert and reactive mixing layers. It consists in the detection of TiO_2 microparticles formed during the diffusion of a gaseous $TiCl_4$ tracer in a water-saturated second reactant. Assessment of the sensitivity of the technique is presented and discussed in relation to measurements in laminar and highly stretched mixing layers.

Effect of chemical reactions and phase transitions on turbulent transport

T. Elperin, N. Kleeorin and I. Rogachevskii

Department of Mechanical Engineering, Ben-Gurion University of the Negev, Beer-Sheva 84105, P. O. Box 653, Israel

We showed that turbulent diffusion can be strongly depleted by chemical reactions or phase transitions. We found that there exist additional turbulent fluxes of number density of particles (effect of turbulent mutual diffusion of admixtures) and additional turbulent heat flux which is proportional to the gradient of number density of particles in flows with chemical reactions or phase transitions. We determined the existence of the turbulent cross-effects similar to those in irreversible thermodynamics. The analyzed effects may result in the excitation of a large-scale instability which causes formation of large-scale inhomogeneities in the spatial distributions of temperatures and number densities of admixtures.

Reduced Kinetic Mechanisms in Time Dependent Numerical Simulations of Nonpremixed Flames

J. Hsu and S. Mahalingam

Joint Center for Combustion and Environmental Research
Department of Mechanical Engineering
University of Colorado at Boulder
Boulder, CO 80309-0427, USA

Contact e-mail: hsuj@colorado.edu

It is of great theoretical interest to investigate the interaction between flames and vortices as a model problem to study turbulent combustion. The goal of this study is to understand the limits of applicability of progressively more accurate reduced kinetic schemes for methane-air flames using time dependent numerical simulations in a two–dimensional flow field. Nonpremixed one–, three– and four–step reduced kinetic methane–air flame structure and flame response to interaction between a pair of counterrotating vortices and an initially laminar unstrained flame is studied. Both continuous burning and local extinction of the flame by the vortex pair have been observed for one– and three–step reduced kinetic schemes in the numerical experiments carried out to date.

DNS of turbulent Couette flow and its comparison with turbulent Poiseuille flow

K. Shingai[1], H. Kawamura[1], and Y. Matsuo[2]

[1]Department of Mechanical Engineering, Science University of Tokyo
Noda-shi, Chiba 278-8510, JAPAN
[2]National Aerospace Laboratory
Chofu-shi, Tokyo 182-8522, JAPAN

Contact e-mail: kawa@rs.noda.sut.ac.jp

A direct numerical simulation (DNS) of turbulent plane Couette flow (CF, hereafter) is performed. This employs two calculation domains of $3.2h \times h \times 1.6h$ and $24h \times h \times 6h$ to examine the effect of box size. Reynolds numbers based on the friction velocity and channel half width is $Re_\tau = 180$ and 128, respectively. The obtained statistical quantities are compared with those of turbulent Poiseuille flows (PF) with Reynolds numbers of $Re_\tau = 180$, 395 and 640. The comparison revealed that the CF can simulate better the turbulence characteristics of the turbulent boundary layer with a higher Reynolds number than PF because the total shear stress in CF stays constant across the channel width.

Generation of Turbulent Inflow Data without Temporal Correlations

A. Spille and H.-J. Kaltenbach

Hermann-Föttinger-Institut für Strömungsmechanik,
Sekretariat HF 1, Technische Universität Berlin, D-10623 Berlin

Contact e-mail: spille@prandtl.pi.tu-berlin.de

Simulation of spatially developing turbulent flows using DNS or LES requires specification of unsteady inflow data. Several methods for generating turbulent inflow data have been proposed which introduce a temporal periodicity (e.g. Lund *et al.* [J. Comp. Phys. 140 (1998)]) that can interfer with low-frequency flow dynamics. On the other hand, inflow generation methods based on random numbers are known to require an extended spatial development region, see e.g. Le *et al.* [J. Fluid Mech. 330 (1997)]. We propose to accelerate the adjustment process by using body forces in the framework of closed-loop control in order to increase the shear stress magnitude until it reaches its equilibrium profile in a turbulent boundary layer.

A priori and a posteriori tests of subgrid scale models for scalar transport

C. Jiménez[1,*], C. Dopazo[1,2] and L. Valiño[2]

[1] Fluid Mechanics Area. University of Zaragoza. Spain
[2] LITEC. CSIC. Spain.
[*] Present Affiliation: CERFACS. France

Contact e-mail: carmen@cerfacs.fr

A priori tests of SGS models for the transport of scalars by turbulence ($\tau_i = \overline{u_i Y} - \overline{u_i}\,\overline{Y}$) are performed, by studying the transfer of scalar fluctuations between resolved and subgrid scales, identified by a term $\epsilon_{\overline{Y}SGS} = 2\tau_i \frac{\partial \overline{Y}}{\partial x_i}$, in the equation of large and subgrid scale fluctuations. Physical analysis suggest that both forward and backward transfer occur and a priori tests performed with data issued of a DNS of a mixing layer confirm that. Mixed models (eddy–diffusivity + scale similarity) appear in that tests as the most adequate. However in a posteriori tests it is shown that eddy diffusivity models, even if only able to dissipate fluctuations from large to small scales, give very similar results at final times, probably due to the decay of the backward transfer relative magnitude.

A-posteriori test of LES closure models for free surface flows.

R. Broglia[†], L. Bognetti[*], A. Di Mascio[†] and B. Favini[*]

[†] INSEAN, Roma, via di Vallerano 139, 00128 Roma, Italy
[*] Dip. Meccanica e Aeronautica, Universiti Roma, La Sapienza
via Eudossiana 18, 00184 Roma, Italy

Contact e-mail: r.broglia@insean.it

Naval hydrodynamics is characterized by very high Reynolds number regimes, peculiar geometry conditions as free surface and juncture flows, and, in some circustances, decaying conditions. Along with the turbulence intensity reduction occurring in decaying process, the flow field suffers a transition from three-dimensional to two-dimensional topology. Numerical simulations have been performed for several test cases as free-surface channel flows and juncture geometries. Comparison between a low order standard technique and an high order spectral accurate method are presented. Beside that, large eddy simulations for the same cases with dynamic closure techniques are performed and analyzed.

Large Eddy Simulations of the flow around a square cylinder

E. Védy and P. R. Voke

S.M.M.E., The University of Surrey, Guildford, Surrey, GU2 5XH
UNITED KINGDOM

Contact e-mail: e.vedy@surrey.ac.uk

We present the results of Large Eddy Simulations of the flow around a square cylinder at a Reynolds number of 21400. The first simulations, designed to investigate the meshing requirements in all three spatial directions, make use of a Smagorinsky model (Smagorinsky, 1963) with a near wall damping function. In the second serie of simulations, we compare different subgrid scale models: the Smagorinsky model, the dynamic Smagorinsky model (Germano, 1991), Sagaut's mixed model (Sagaut, 1998) and the Velocity Increment model (Brun, Friedrich, 1999), on two types of grids, using $192 \times 144 \times 64$ and $224 \times 160 \times 64$ points in the mean flow, crossflow and spanwise directions, respectively. A more detailed analysis of the flow dynamics, using a higher resolution simulation ($256 \times 240 \times 64$), is also presented.

Large-eddy simulation of flow around a rectangular obstacle in fully developed turbulent boundary layer – The effects of turbulence on a separation bubble –

K. Nozawa [1] and T. Tamura [2]

[1]Izumi Research Institute, Shimizu Corporation
Chiyoda-ku, Tokyo, JAPAN
[2]Department of Environmental Science and Technology,
Tokyo Institute of Technology, Midori-ku, Yokohama, Kanagawa, JAPAN

Contact e-mail: nozawa@ori.shimz.co.jp

The applicability of large-eddy simulation to the flow around a rectangular obstacle mounted in fully turbulent boundary layer is discussed compared with the case in laminar boundary layer. Especially, the effect of turbulence on a separation bubble formed on the rectangular obstacle is focused on. The time dependent turbulent inflow was generated by the method of Lund et al. [J. Comp. Phys. 140(1998)]. In the case of turbulent flow, the pressure distribution is characterized by a low-pressure peak near the separation point followed by rapid recovery towards the reattachment point. The fast growth of vortical thickness shows that the separated flow was clearly affected by turbulence.

Large Eddy Simulation of a turbulent flow in a heated duct

M. Salinas Vázquez and O. Métais

LEGI, Institut de Mécanique de Grenoble,
Intitut Polytechnique de Grenoble, BP 53, 38041 Grenoble CEDEX 9, FRANCE

Contact e-mail: Martin.Salinas@hmg.inpg.fr

Large Eddy Simulations of a compressible turbulent square duct at low Mach number are described. First, the isothermal case with all the walls at the same temperature is considered. Good agreement with previous incompressible DNS results is obtained both for the mean and turbulent statistics. The heated duct with a larger temperature prescribed at one wall is then considered. In the vicinity of the heated wall, we observe a drastic modification of the near-wall structures with the creation of one big ejection around the wall bisector. The latter is accompanied by an amplification of the mean secondary flow, a decrease of the turbulent fluctuations in the near wall region and, conversely, an enhancement of the latter in the outer region. These large scale flow modifications are analyzed with the aid of various statistical tools analysis and various three-dimensional flow visualisation techniques.

A Multi-domain/Multi-resolution Method with Application to Large-eddy Simulation

P. Quéméré[1], P. Sagaut[1], V. Couaillier[1] and F. Leboeuf[2]

[1]ONERA
29 av. de la Division Leclerc, B.P. 72, F-92322 Châtillon cedex, FRANCE
[2]Ecole Centrale de Lyon
36 av. Guy de Collongue, B.P. 163, F-69131 Ecully cedex, FRANCE

Contact e-mail: quemere@onera.fr

The use of a multi-domain approach in LES appears as an appropriate mean to reduce CPU costs. From a theorical point of view, it leads meanwhile to sudden changes of resolution at the interfaces, since LES lays on space step to determine the characteristic lengths. Thus, for two sub-domains having different resolutions, the resolved flow representation has to be discontinuous along the interface. In the aim to take into account this discontinuity, a reconstruction procedure is proposed both for the resolved flow (restriction and enrichment procedure) and for the associated subgrid-scale viscosity ('rescaling').
The calculations performed in a subsonic plane channel and compared with monodomain results, show the efficiency of this multi-domain/multi-resolution method while diminushing strongly the CPU costs.

Large-Eddy Simulation of an oscillatory boundary layer

V. Armenio [1] and G. Vittori [2]

[1]Dipartimento di Ingegneria Civile , Universitá degli Studi di Trieste
Piazzale Europa 1, 34127, Trieste-Italy
[2]Dipartimento di Ingegneria Ambientale, Universitá degli Studi di Genova
via Montallegro 1, 16145 Genova-Italy.

Contact e-mail: armenio@univ.trieste.it

LES of an oscillating boundary layer is performed using mixed and eddy viscosity dynamic models (Armenio *et al*, Proc. ERCOFTAC Workshop, Cambridge 1999) as well as the Smagorinsky model. The results are compared with the reference data of Vittori and Verzicco (*J. Fluid Mech., 371*) at $Re_\delta = 800$. As expected, the Smagorinsky model damps the energy content of the velocity fluctuations of approximately 50% and the wall stress is not well predicted, particularly during the decelerating parts of the cycle. Conversely, the dynamic models are found to compare well with DNS. In the simulations performed, the energy content is approximately the same using both models. The scale similar part of the mixed model drains approximately 50 % of the available energy.

On the relation between coherent structures and grid/subgrid-scale energy transfer in transitional and turbulent shear flows

C. B. da Silva

LEGI, Institut de Mécanique de Grenoble, B.P. 53, 38041 Grenoble Cedex 09, France

Contact e-mail: Carlos.Silva@hmg.inpg.fr

DNS of spatially developing plane jets were used to analyze the influence of coherent structures in the local grid/subgrid-scale interactions. In 1) Transition, 2) emergence of strong longitudinal vortices between Kelvin-Helmholtz pairs and 3) merging of a pair of Kelvin-Helmholtz vortices, the transport equations for the grid and subgrid-scale tensors ($u_i^< u_j^<$ and τ_{ij}) were analyzed trough the application of a localized top-hat filter. The most important stresses were identified as well as their role in the inter-scale interactions. A-*priori* tests were conducted in the DNS with the a) Smagorisnky, b) Filtered structure function, c) Dynamic Samgorisnky-Lilly, e) Spectral-dynamic, f) Scale similarity and g) increment SGS models.

Turbulence modification by particles; Experimental verification of a theoretical model

G. Ooms, J. Pietryga, C. Poelma and J. Westerweel

J.M. Burgerscentrum, Delft University of Technology
Laboratory for Aero- and Hydrodynamics,
Rotterdamseweg 145, 2628 AL Delft, The Netherlands

Contact e-mail: C.Poelma@wbmt.tudelft.nl

An experimental verification has been made of a theoretical model developed for the calculation of the turbulence surpression by small particles. To that purpose, a systematic literature study was carried out to find all published relevant experimental data, which was then compared with predictions made with the model. It was found, that for the same values of the relevant dimensionless parameters, the experimental data can differ considerably, thus making a verification of the model difficult. Recently, a new project was started to gain experimental data. The experiments focus on water flows with high particle loading. Their aim is obtaining the velocity fields and spectra of both the fluid phase and the particle phase.

Near wall effects on particles in a turbulent channel flow

P. Rambaud[1,2], A. Tanière[2], B. Oesterlé[2] and M.L. Riethmuller[1]

[1]von Karman Institute for fluid Dynamics (VKI),
Chaussée de Waterloo, B-1640 Rhode saint Genèse, BELGIUM
[2]Laboratoire Universitaire de Mécanique et d'Energétique de Nancy (LUMEN),
Rue Jean Lamour, F-54500 Vandoeuvre-lès-Nancy, FRANCE

Contact e-mail: rambaud@vki.ac.be

A one-way coupling particle laden flow is computed by the mean of direct simulation in Eulerian/Lagrangian frame. The geometry is a classical channel flow with a Reynolds number based on bulk velocity and half channel width equal to 2800. The particle equation include: the wall corrected drag, the lift force due to the particle rotation and an attempt is made to consider an electrostatic force. High care has been devoted to gas velocity interpolation at the location of the particle. At this purpose a fully 3D-Hermitian interpolation, second order type even on stretched and staggered grid, is proposed. Lagrangian statistics for several particle diameters are proposed. Visualisation of wall vorticity structures and particle concentration is done.

Optimisation of two-equation turbulence models

H. Bézard

ONERA
Office National d'Études et de Recherches Aérospatiales
Aerodynamics and Energetics Modelling Department
BP 4025 - 31055 Toulouse Cedex 4 - FRANCE

Contact e-mail: bezard@onecert.fr

In order to improve the prediction of standard k-ε and k-ω turbulence models, a numerical optimisation process has been used to optimise the modelling constants so as to predict correctly self-similar flows such as free shear flows and equilibrium boundary layers. Constraints were prescribed to satisfy the decay of isotropic turbulence, the logarithmic law equilibrium and the behaviour at the edge of a turbulent region. Optimal models exhibit better comparisons with experiments than standard models. Particularly the plane jet / round jet anomaly is solved without any additional terms and the prediction of APG boundary layers is greatly improved even by the optimal k-ε model which constants are: $C_{\varepsilon_1} = 1.48$, $C_{\varepsilon_2} = 1.97$, $\sigma_k = 0.58$, $\sigma_\varepsilon = 1.14$. The study was performed within the European AVTAC project.

A $k-\omega$ /Rapid Distortion Model applied to unsteady wall flows

P. da Costa and S. Tardu

Laboratoire des Ecoulements Géophysiques et Industriels- LEGI
B.P. 53-X 38041 Grenoble-Cédex ; France

Contact e-mail: tardu@hmg.inpg.fr

The $k-\omega$ model is combined with the rapid distortion scheme to develop effective unsteady closures in non-equilibrium wall flows subjected to oscillating shear. The phase averaged eddy viscosity is related to the modulation of the effective strain parameter $< \alpha_{\text{eff}} >$ (Maxey, JFM, 124, 261;1982) by $< \nu_T >= \dfrac{< k >}{\partial < u > /\partial y} F(< \alpha_{\text{eff}} >)$ and the function $F(< \alpha_{\text{eff}} >)$ is obtained by the bench data of the steady channel flow. The transport equation for $< \alpha_{\text{eff}} >$ is complete:

$$\frac{\partial < \alpha_{\text{eff}} >}{\partial t} = -\frac{< \alpha_{\text{eff}} >}{T_d} + \frac{\partial < u >}{\partial y} + \frac{\partial}{\partial y}\left[< D(y) > \frac{\partial < \alpha_{\text{eff}} >}{\partial y}\right] + \frac{\partial}{\partial y}[< V \alpha_{\text{eff}} >]$$

where we consider both a gradient type diffusion and convection by large-scale $< V >$ motions. This last effect is necessary to understand the very high imposed frequency regime.

Effect of inlet turbulence on convective flow between two vertical walls : k-ϵ low Reynolds turbulence model

R. Bennacer[1], T. Hammami[1] and A.A. Mohamad[2]

[1]Laboratoire Matériaux et Sciences des Constructions Rue d'Eragny, 95031 Neuville sur Oise, FRANCE
[2]Department of Mechanical Engineering 2500 University Drive, Calgary, Alberta, Canada T2N 1N4

The natural convection flow in an asymmetrically moderately heated vertical channel of finite length was simulated using Low Reynolds number k-ϵ model [Perez Sagara *et al.* 1995]. This air flow is related to many application in industry and civil engineering cooling systems. The experimental configuration of Miyamoto (1986) with a constant flux generation left wall and an adiabatic right wall with a modified $Gr^* = 2.2\ 10^8$ was considered. In order to trigger transition inlet turbulence is introduced and we study its influence on the flow. This noise intensity seems mesh dependent and affect the transition point location. In any case the transition between entirely laminar flow solution and turbulent one is somewhat brutal and needs an inlet intensity greater than a threshold value. In contrast to the kinetic energy k which is overestimated The wall temperature evolution especially the transition point position is well predicted for the above experience.

Thermodynamically Consistent Turbulence Modeling of Turbulent Flows with Variable Mass-density

A. Sadiki

Energy and Power plant Technology, Darmstadt University of Technology, Mechanical Engineering Dpt., Petersenstr. 30, 64287 Darmstadt, Germany
Contact e-mail: sadiki@hrz2.hrz.tu-darmstadt.de

The validity of the Favre regrouping procedure has been verified for thermodynamically closed systems and for "mass conserving" open sytems only. Implementation of the second law of thermodynamics expressed by an entropy inequality based on extended thermodynamics leads to thermodynamically compatible second order closure assumptions valid for turbulent flows far from equilibrium. Thermodynamical constraints on model coefficients are derived to ensure physically admissible real processes. Using the Maxwellian iteration scheme, nonlinear algebraic expressions are deduced and new results are presented. Thermodynamically compatible subgrid scale closure assumptions for LES are also evaluated and thermodynamic consistency of existing SGS-models are discussed.

Prediction of the Reynolds stresses and higher moments in a developed turbulent flow in an axially rotating pipe

B. B. Ilyushin [1,2] and S. N. Yakovenko [2,3]

[1] Laboratory of Aerodynamics Fundamentals of Power Engineering,
Institute of Thermophysics SB RAS, 630090 Novosibirsk, RUSSIA
[2] Physics Department, Novosibirsk State University, 630090 Novosibirsk, RUSSIA
[3] Laboratory of Modeling of Turbulent Flows, Institute of Theoretical and
Applied Mechanics SB RAS, 630090 Novosibirsk, RUSSIA
Contact e-mail: yakovenk@itam.nsc.ru

The computation results for mean velocities and Reynolds stresses, as well as skewness and flatness factors have been obtained in stationary and rotating cylindrical pipe flows. Third-moment closing assumptions usually used and corrected for mean shear terms with the tangential velocity were applied in the Reynolds-stress model. In the rotating flow the corrected model gives, on the whole, better description for triple correlations and visible improvement for the second moments than those for standard models. Model of fourth-order cumulants reproduces the measured data for the radial flatness factor in the most part of the non-rotating flow and some its features in the rotating flow.

This research has been supported by the INTAS-OPEN-97-2022 Grant.

Predictions of higher moments by a transported pdf model

D. Lentini

Dipartimento di Meccanica e Aeronautica
Università degli Studi di Roma "La Sapienza"
Via Eudossiana 18, I-00184 Roma, Italy

The joint pdf (probability density function) transport approach for turbulent flows features the unique capability, unparalleled in other approaches, to recover monovariate and joint pdf's, as well as moments of any order, thus enabling full comparison with experimental data (when such quantities are measured), and a thorough insight into the causes of possible disagreement. In the present paper an original computational algorithm of this kind is presented, based on a Langevin model for velocity components and a Poisson equation solver, replacing solution of the continuity equation. It is applied to a test case of a jet flow (Hussein *et al.*, *J. Fluid Mech.* 258:31, 1994), for which measurements of moments up to the third order are reported.

Full velocity-scalar PDF approach for wall-bounded flows and computation of thermal boundary layers

J. Pozorski[1] and and J. P. Minier[2]

[1]Institute of Fluid Flow Machinery, Polish Academy of Sciences
Fiszera 14, 80952 Gdańsk, POLAND
[2]Groupe Mécanique des Fluides et Transferts Thermiques, Electricité de France
6 quai Watier, 78400 Chatou, FRANCE

Contact e-mail: jp@imp.pg.gda.pl

Turbulent flows with temperature treated as a passive inert scalar variable are computed with the probability density function (PDF) method. Wall boundary conditions for scalar variable are developed and tested in the full (velocity, turbulent frequency and scalar) joint PDF approach. The boundary conditions are formulated in terms of instantaneous particle variables; conditions for velocity are those for the logarithmic region of the wall layer, and new proposal is put forward for the instantaneous temperature of stochastic particles crossing the boundary. Mean temperature profile across the channel with given heat flux as well as higher-order moments of joint (velocity-scalar) PDF distribution have been computed and compared with available DNS results.

Asymptotic models for slow dynamics and anisotropic structure of turbulence in a rotating fluid

F.S. Godeferd, J.F. Scott and C. Cambon

Lab. de Mécanique des Fluides et d'Acoustique,
UMR 5509, École Centrale de Lyon,
BP 163, 69131 Ecully, France

The present work deals with weakly nonlinear statistical two-point models of homogeneous turbulence with solid body rotation. It follows previous theories based on anisotropic EDQNM models that have been applied to cases of rotating as well as stably stratified turbulent flows, of interest both in industrial and geophysical engineering contexts. A theory is developped to describe the asymptotic limit of strong rotation. Since it only deals with integrals over resonant surfaces, the resulting model is simpler than a full nonlinear approach. It has also suggested an improvement of the Markovianisation procedure used in the full model thus rendering the latter valid in both the weak and strong rotation limits. Comparisons are performed between the asymptotic model, the full model, and results from DNS.

Assessment of turbulence models of second order for the prediction of near-field aircraft plumes

A. Sadiki, A. Maltsev and J. Janicka

Institute of Energy and Power Plant Technology, Darmstadt University of Technology
Petersenstr. 30, 64287 Darmstadt, Germany

Contact e-mail: maltsev@hrzpub.tu-darmstadt.de

The main objective of this study is to explore the assessment of transport equation turbulence and mixing models for the prediction of near-field jet exhaust plumes. Turbulence is modelled with three different models (two different linear second order moment closures and k-Epsilon model). The scalar fluxes are modeled by corresponding transport equations. Chemical reaction mechanism is the finite rate chemistry. Simulations were carried out for two types of initial and boundary conditions. Calculation results are compared with results of different authors as well as different turbulent models are validated. The performance of the model choice for the temperature predictions and for major nitrogen species is pointed out.

Influences of Buoyancy on Turbulence for Conditions of Heat Transfer by Combined Forced and Free Convection to Air in a Vertical Tube

J.D. Jackson and Jiankang Li

School of Engineering, University of Manchester
M13 9PL, UK
Contact e-mail: jdjackson@man.ac.uk, jkl@fs1.eng.man.ac.uk

A comprehensive programme of experiments to study buoyancy-influenced turbulent heat transfer in a tube has recently been completed by the authors. Computational simulations of the experiments were then performed using a low Reynolds number $k - \varepsilon$ turbulence model. The results reproduced observed behaviour closely. The success of these simulations encouraged the authors to examine the results with a view to obtaining a better understanding of the mechanisms involved in buoyancy-induced impairment of heat transfer. The velocity profiles were strongly modified by buoyancy and the consequences in terms of turbulence were clearly evident. The shear stress was drastically reduced and the viscous sublayer thickness increased by a factor of about three.

Validation of the subgrid modelling by simulating a compressible turbulent flow in a 3D channel

L. Coquart, C. Tenaud and L. Ta Phuoc

This study deals with the **L**arge **E**ddy **S**imulation of unsteady compressible internal flow at high Reynolds number, for turbomachinery appplications. To validate the subgrid scale modelling in a realistic configuration, where shock-wave/boundary layer interaction and separation occur, the simulation of a compressible flow through a 3D convergent-divergent channel is performed (Delery, ONERA). The subsonic flow at the inlet is accelerated in the convergent part and reaches the sonic conditions at the throat. A shock-wave interacts with the boundary layer in the divergent leading to a large separation. The isentropic Mach distributions, the mean velocity and the Reynolds stress profiles are compared to experiments and $R_{ij} - \varepsilon$ simulations. The different results obtained by LES are in good agreement with experiments and will be presented on the Poster.

Study of wake, vortex-shedding, and shock in a Transonic Compressor

J. Estevadeordal [1], S. Gogineni [1], L. Goss [1], W. Copenhaver [2] and S. Gorrell [2]

[1]Innovative Scientific Solutions Inc.
2766 Indian Ripple Rd., Dayton, OHIO, 45440, USA
[2]Air Force Research laboratory
Wright-Patterson Air Force Base, OHIO, 45433, USA

Contact e-mail: jordi@innssi.com

The instantaneous wake-shock-blade interactions occurring in a high-through-flow, axial-flow transonic compressor are studied using Digital Particle Image Velocimetry (DPIV). In the present study a system was developed to obtain high-resolution velocity data from the high-through-flow, axial-flow transonic compressor located in the Compressor Aerodynamic Research Laboratory (CARL) at Wright-Patterson AFB. The coherent structures interactions with the potential field of the leading edge of the blades and the shock as a function of the blade position is presented. Chopping of the wake due to blade passage is evident and the shock location and motion can be calculated from the DPIV velocity field at different instants. Ref.: AIAA 00-0378, Reno , NV, January 2000

Anisotropic Scaling Anomaly in Isotropic Turbulence

B. R. Pearson and W. v. d. Water

Fluid Dynamics Laboratory, University of Technology, Eindhoven
P. O. Box 513. 5600MB Eindhoven, THE NETHERLANDS

Contact e-mail: w. v. d. water@tue.nl

The inertial range (IR) structure of turbulence is investigated in a perforated plate flow over a considerable range of R_λ ($200 < R_\lambda < 1200$). At $x/M = 40$,the flow has good global isotropy in the normal transverse direction $(\langle v^2 \rangle / \langle u^2 \rangle \sim 1.1)$ and high anisotropy in the spanwise transverse direction $(\langle w^2 \rangle / \langle u^2 \rangle \sim 1.7)$. ESS is used to measure the IR scaling exponents $\zeta_u(n)$, $\zeta_v(n)$ and $\zeta_w(n)$. $\zeta_v(n)$ are close to, but distinct from, $\zeta_u(n)$. Both are R_λ independent. $\zeta_w(n)$ are more anomalous than $\zeta_v(n)$ and slightly R_λ dependent with asymptotic values very different to $\zeta_v(n)$. The turbulence produced by a simple geometry highlights the dependence of IR scaling on anisotropy generated by initial conditions.

Effects of shear on small-scale properties in a Kolmogorov flow

I. San Gil [1,2], S. Chen [2,3] and K. R. Sreenivasan [1]

[1]Mason Lab. Yale University
9 Hillhouse Ave., New Haven, CT 06520, USA
[2]Center for non-linear studies, Los Alamos Natl. Lab.
TA-3, Bldg. 1690, Los Alamos, NM 87545, USA
[3]Mech. Eng. Dept. John Hopkins University
200 Latrobe Hall, 3400 North Charles St. Baltimore, MD 21218, USA

Contact e-mail: inigo.sangil@yale.edu

We study the effects of shear on some small-scale properties in the Kolmogorov flow for different Reynolds numbers and shear rates. Several DNS of the Kolmogorov flow are obtained using pseudospectral techniques with sinusoidal forcing. In particular, we characterize the influence of shear on the second moment of the longitudinal velocity difference. The PDF of Δu_r^2 conditioned on the large scale velocity shows a curvature, in agreement with the behavior observed in high-Reynolds data. The PDF of the enstrophy is stretched out to higher values than for the energy dissipation. Second and fourth moments of the locally averaged fields also show a more intermittent character of enstrophy, and showing a second order effect with the shear.

Fractal skins of turbulence

D. Queiros-Conde

Department of Applied Mathematics and Theoretical Physics
University of Cambridge, Silver Street, Cambridge CB3 9EW, United Kingdom

A new geometrical structure is proposed in order to describe intermittency in fully developed turbulence. An hierarchy of fractal structures Ω_p of dimension Δ_p ranging from $\Delta_\infty = 1$ to $\Delta_0 = d = 3$ linked by $\gamma = (\Delta_{p+1} - \Delta_\infty)/(\Delta_p - \Delta_\infty)$ where $\gamma = ((1 + 3/\sqrt{8})^{1/3} + (1 - 3/\sqrt{8})^{1/3})^{1/3} \approx 0.68$ is introduced (D. Queiros-Conde, C. R. Acad. Sci. Paris, t.327, Serie IIb, p. 385, 1999). This allows a determination without adjustable parameters of the scaling exponents ζ_p and τ_p of velocity and energy dissipation structure functions. This is obtained by the introduction of an entropy jump defined at the scale r, $\Delta S_p(r) = (\Delta_{p+1} - \Delta_p) ln(r/r_0)$, characterizing the order level of each sub-structure Ω_p and verifying a linear relation $\Delta S_p(r)/\Delta S_{p-1}(r) = \gamma$.

Turbulent wakes of 3-D fractal grids

D. Queiros-Conde and J.C. Vassilicos

Department of Applied Mathematics and Theoretical Physics
University of Cambridge, Silver Street, Cambridge CB3 9EW, United Kingdom

We have measured turbulence fluctuations and various velocity profiles at distances in the wakes of 3-D fractal grids where the turbulence has had the time to travel for a large number of turnover times. We have four 3-D fractal grids at our disposal, all identical except for their fractal dimensions which are 2.05, 2.17, 2.40 and 2.75. Our main result is that velocity structure functions are slower varying functions of two-point separation for larger fractal grid dimensions. However, mean shear rates decrease as the fractal grid dimension increases. Furthermore, the relative exponent ζ_2/ζ_3 determined by Extended Self-Similarity increases with fractal grid dimension. For more details see Queiros-Conde, D. & Vassilicos, J.C. 2000 In *Intermittency in Turbulent Flows*, CUP.

Temporal structures in Shell Models

F. Okkels

Dept. of Optics and Fluid Dynamics, Risø National Laboratory, Denmark
and
Center for Chaos and Turbulence Studies, The Niels Bohr Institute, University of Copenhagen, Denmark.

Contact e-mail: okkels@nbi.dk

Among the reduced models of fully developed turbulence the GOY shell model has been particular successful. The temporal statistics of the model nicely reproduce the intermittency corrections found in experimentally measured turbulence. In this work we view the GOY model as a dynamical system and show that the dynamics consist of a unique pattern of a burst followed by a relaxation. It turns out that the local coupling in the model causes the temporal evolution to follow a 3 dimensional "local attractor". The "local attractor" is used to explain the self-organisation and the intermittent nature of the bursts.

This work indicates how the intermittency corrections in turbulence can be generated by a low-dimensional dynamical system.

Wavelet Analysis of Intermittent Behavior of Pressure Fluctuations in Separated and Reattaching Flows

Inwon Lee [1] and Hyung Jin Sung [1]

[1] Flow Control Laboratory, Department of Mechanical Engineering
Korea Advanced Institute of Science and Technology
373-1, Kusong-dong, Yusong-ku, Taejon 305-701, KOREA

Time-dependent characteristics of wall pressure fluctuations in separated and reattaching flows over a backward-facing step were investigated by means of continuous wavelet transform. Emphasis was placed on the combination of time-localized analyses of wavelet transform and multi-point measurements of pressure fluctuations. Synchronized wavelet maps revealed the evolutionary behavior of pressure fluctuations and gave further insight into the modulated nature of large-scale vortical structures. It was found that there exist two modes of shed vortices: one is the global oscillation and the other is the vortex convection. The two alternating modes are synchronized with the flapping frequency component of pressure fluctuations.

The Scalings of Scalar Structure Functions in a Velocity Field with Coherent Vortical Structures

Md. Amirul Islam Khan and J. Christos Vassilicos

Department of Applied Mathematics and Theoretical Physics,
University of Cambridge, Silver Street, Cambridge CB3 9EW, United Kingdom
Contact e-mail: maik2@damtp.cam.ac.uk and jcv10@damtp.cam.ac.uk

In a two dimensional (2-D) turbulence modelled as an isotropic and homogeneous collection of 2-D non-interacting compact vortices, the structure functions $\mathcal{S}_p(r)$ of an advected and diffusing passive scalar field (initially on-off) have the following scaling behaviour in the limit where the Péclet number $Pe \to \infty$:

$$\mathcal{S}_p(r) \sim constant + log\left(\frac{r}{lPe^{-1/3}}\right) \text{ for } lPe^{-1/3} < r < l,$$

$$\mathcal{S}_p(r) \sim \left(\frac{r}{lPe^{-1/3}}\right)^{6(1-D)} \text{ for } lPe^{-1/2} < r < lPe^{-1/3}$$

where l is a large scale and D is the fractal co-dimension of the spiral scalar structures generated by the vortices ($1/2 < D < 1$). Note that $lPe^{-1/2}$ is the scalar Taylor microscale which stems naturally from our analytical treatment of the advection-diffusion equation.

Coherent structures in shell models for passive scalar advection

L. Biferale[1], I. Daumont[2], T. Dombre[3] and A. Lanotte[4]

[1] Dept. of Physics and INFM, Univ. di Tor Vergata
Via della Ricerca Scientifica 1, I-00133 Roma, Italy
[2]Laboratoire de Physique, URA-CNRS 1325, ENS Lyon
46 allée d'Italie, 69364 Lyon cedex 07 France.
[3]Centre de Recherche sur les Très Basses Températures-CNRS,
BP 166, 38042 Grenoble Cedex 9, France.
[4]Laboratoire Cassini- CNRS, Observatoire de Nice, BP 4229, 06304 Nice France
Contact e-mail: idaumont@ens-lyon.fr

We consider a shell model version of Kraichnan's passive scalar problem and study its anomalous scalings in terms of singular coherent structures. The role played by fluctuations with local exponent h in the original physical space model is replaced by the formation of pulse-like structures, growing self-similarly as they propagate from large towards small scales. Arguying that the most intermittent events are well-captured by configurations of optimal Gaussian weight, we are able to compute numerically with instanton techniques the distribution $f(h)$ of the multifractal set of scaling exponents h. We find that the asymptotic properties of the scalar field statistics are well reproduced.

Passive temperature pdf's in fully developped turbulence

C. Auriault[1], Y. Gagne[1] and B. Castaing[2]

[1]LEGI/IMG-CNRS, B.P.53X,
38041 Grenoble Cedex 9, France.
[2]ENS Lyon, URA 1325 CNRS, 46 allée d'Italie,
69364 Lyon Cedex 7, France.

Contact e-mail: gagne@hmg.inpg.fr

Passive temperature fluctuations θ (measured in axysimmetric jet, boundary layer, "chunk" turbulence, with $400 \leq R_\lambda \leq 2000$) show:

- Depending on the scalar injection, the θ pdfs are skewed following a unique scheme. Fluctuations coming from the rare outer flow events and mixed by the flow are quasi exponentially skewed whereas fluctuations due to the temperature field of the flow itself are always quasi gaussian.
- On the contrary, pdfs of the increments $\delta\theta(\ell_0)$ measured at the integral scale ℓ_0 result of the convolution of θ by its symetric $(-\theta)$ and thus have always two quasi exponential wings. When the separation ℓ decreases the $\delta\theta(\ell)$ pdfs are more and more skewed as long as the local velocity temperature correlation $< \delta u(\ell).\delta\theta(\ell) >$ is not zero.

From a Vortex Gas Model of Turbulence to Mellin Functions

P. Borgnat[1], O. Michel[1], C. Baudet[2] and P. Flandrin[1]

[1] Laboratoire de Physique, École Normale Supérieure de Lyon
46, allée d'Italie 69364 Lyon Cédex 07, FRANCE
[2] LEGI, INPG-Université J. Fourier
1025, rue de la Piscine, 38400 Saint-Martin-d'Hères, FRANCE

Relying upon a description of turbulent flows as a "gas of objects", we study Lundgren's small scale turbulence model. This approach describes turbulence as a statistical diluted distribution of stretched aging spiral vortices. We found that direct estimates of vorticity and velocity spectra evidence a Kolmogorov's inertial range but that details are blurred out by the core of the spiral, in both cases of simulated velocity measures and fractal-based geometrical studies (*à la* Vassilicos). Because such tools are not adequate to capture properties of the unsteady objects, we propose to use mixed representations, either in time-Fourier domain where a certain lack of universality is observed, or in a time-scale domain on the basis of scale-invariant Mellin functions.

The Scalings of Scalar Structure Functions in a Velocity Field with Coherent Vortical Structures

Md. Amirul Islam Khan and J. Christos Vassilicos

Department of Applied Mathematics and Theoretical Physics,
University of Cambridge, Silver Street, Cambridge CB3 9EW, United Kingdom

Contact e-mail: maik2@damtp.cam.ac.uk and jcv10@damtp.cam.ac.uk

In a two dimensional (2-D) turbulence modelled as an isotropic and homogeneous collection of 2-D non-interacting compact vortices, the structure functions $\mathcal{S}_p(r)$ of an advected and diffusing passive scalar field (initially on-off) have the following scaling behaviour in the limit where the Péclet number $Pe \to \infty$:

$$\mathcal{S}_p(r) \sim constant + log\left(\frac{r}{lPe^{-1/3}}\right) \text{ for } lPe^{-1/3} < r < l,$$

$$\mathcal{S}_p(r) \sim \left(\frac{r}{lPe^{-1/3}}\right)^{6(1-D)} \text{ for } lPe^{-1/2} < r < lPe^{-1/3}$$

where l is a large scale and D is the fractal co-dimension of the spiral scalar structures generated by the vortices ($1/2 < D < 1$). Note that $lPe^{-1/2}$ is the scalar Taylor microscale which stems naturally from our analytical treatment of the advection-diffusion equation.

The definition and identification of a vortex revisited

B. Herrera 1[1], F.X. Grau 2[2] and Francesc Giralt[3]

[1]Departament d'Enginyeria Informàtica i Matemàtiques
Universitat Rovira i Virgili, Tarragona, SPAIN
[2]Department d'Enginyeria Mecànica
Universitat Rovira i Virgili, Tarragona, SPAIN
[3]Departament d'Enginyeria Química
Universitat Rovira i Virgili, Tarragona, SPAIN

Contact e-mail: bherrera@etse.urv.es

Several techniques and algorithms have been proposed in the past to identify vortexes and to visualize them (Hunt, Chong, Jeon&Hussain, Michard, Cucitore). One of the difficulties for defining and identifying vortexes is to characterize its boundaries. Up to now, all existing definitions either are ambiguous in defining the vortex boundary or fail in cases as clear as the Hill vortex. In this work we propose an unambiguous definition of a vortex boundary that works in cases where the previous definitions fail. Our definition in given by: the points p that $f(p) = \|\omega\|^2 S(v,v) - \|v\|^2 S(\omega,\omega) = 0$, with $\nabla f \| (v \times \omega)$; where $\nabla \mathbf{v} = S + \Omega$.

Inhomogeneous turbulence near a large scale vortex

C. Simand, F. Chillà and J.-F. Pinton

Laboratoire de physique, École normale supérieure de Lyon
46, allée d'Italie, 69364 Lyon cedex 07, FRANCE

Contact e-mail: csimand@ens-lyon.fr

We study the statistics of turbulent velocity fluctuations in the neighbourhood of a strong large scale vortex. The Reynolds number is about 10^5 so that the flow is turbulent but strongly anisotropic and inhomogeneous. We study the third order moment of velocity differences at differents locations in the flow and consider it as a measurement of the energy transfer. We find that in a situation in which the vortex is stable the skewness is small and negative far away from the axis of rotation and becomes positive near the vortex core: there, energy is accumulated in the large scale where it stabilizes the dynamics of the vortex. In a situation in which the vortex is largely unstable, the skewness exhibits values similar to those of isotropic homogeneous turbulence.

Computation of equilibria between two corotating nonuniform vortices.

U. Ehrenstein [1] and M. Rossi [2]

[1]Laboratoire J.-A. Dieudonné
Université Nice-Sophia Antipolis
Parc Valrose, F-06108 Nice Cedex, FRANCE
[2]Laboratoire de Modélisation en Mécanique
Université de Paris VI
4, Place Jussieu, F-75252 Paris Cedex 05, FRANCE

Contact e-mail: maur@ccr.jussieu.fr

Nonlinear equilibria between vortices are generally obtained in the context of uniform vorticity (Dritschel,JFM 293, 1995). We compute the equilibria between two nonuniform vortices. Constraints imposed on the vorticity field of an inviscid equilibrium, are introduced into a branch following algorithm. This latter method determines nonlinear branches as fixed points, starting from a given initial solution. As an input, we use two Lamb vortices located far apart. The continuation parameter is the distance between vortices L. A whole family of equilibrium states is thus computed step by step by decreasing the continuation parameter L. Different cases are considered according to the circulation ratio, core radius and parameter characterizing the vortex non-uniformity.

Experiments on the vortex structure of a wake behind a torus

S. Yamashita and Y. Inoue

Dept. Mech. & Systems Eng., Gifu University
1-1 Yanagido, Gifu 501-1193, JAPAN

Contact e-mail: yinoue@mech.gifu-u.ac.jp

We research the spatiotemporal structure of a wake behind a torus by using an ultrasonic velocity profile monitor (UVP). A torus has a cross-sectional diameter d and a center-line diameter D, and two tori of $D/d = 3$ and 5 are used in this study. Experiments are performed in a uniform flow, and the Reynolds number based on the diameter d remains constant at 1500. Spatiotemporal contour maps of the fluctuating velocity component in the radial direction clearly show the flow patterns in the space-time field. The proper orthogonal decomposition is applied to these data. It is clear that the flow structures are considerably different between the wakes of $D/d = 3$ and 5, and this discrepancy in the flow structure seems to be associated with the solidity of the torus.

Topological complexity of a vortex tangle

C. F. Barenghi, A. Marsden and D. C. Samuels

Dept. of Mathematics, University of Newcastle upon Tyne, Newcastle, NE1 7RU, UK

Contact e-mail: c.f.barenghi@ncl.ac.uk

In this work we study the time evolution of the topological complexity of a turbulent tangle of vortex filaments which move according to the Biot-Savart law. Reconnections of vortex filaments occur frequently and are important to the evolution of the structure of the vortex tangle. Since topology preservation of the vortex filaments is broken by the reconnections, the vortex line topology is therefore a dynamically varying quantity, and we attempt to characterize the changes in the topological complexity of the vortex tangle. The advantage of this model is that the structure of the turbulence is defined in a simple and non-ambiguous way.

Length scales in turbulent superfluid vortex line tangles

D. C. Samuels and D. Kivotides

Dept. of Mathematics, University of Newcastle upon Tyne, Newcastle, NE1 7RU, UK

Contact e-mail: d.c.samuels@ncl.ac.uk

Turbulence in a superfluid consists of a tangle of quantised vortex filaments coupled to a normal fluid flow (a low viscosity fluid interpenetrating with the zero viscosity superfluid). We show that the coupling of superfluid turbulence with the normal fluid causes a new length scale, ℓ_{sd}, to appear. The coupling between the two fluids allows energy exchange between the components. For superfluid vortex structures with length scales below ℓ_{sd} this energy exchange can only occur in one direction, from the superfluid to the normal fluid, so that the superfluid loses energy below this length scale. In this sense, ℓ_{sd} acts as a dissipation length scale for the superfluid turbulence.

Coherent Vortex Simulation (CVS) to compute two-dimensional turbulent flows using wavelets

M. Farge[1], K. Schneider[2] and N. Kevlahan[3]

[1]Ecole Normale Superieure, Paris, France
[2]ICT, Universitat Karlsruhe, Germany
[3]Department of Mathematics and Statistics,
Mc Master University, Hamilton, Canada

We propose a new method, called Coherent Vortex Simulation (CVS), to compute the time evolution of fully-developed turbulent flows. For this we decompose each flow realization into two orthogonal components: - A coherent, inhomogeneous, intermittent and non-Gaussian contribution, corresponding to the vortices, - An incoherent, homogeneous, non-intermittent and Gaussian contribution, corresponding to the background flow excited by the nonlinear vortex interactions. The two components have different probability distributions and different correlations, hence different scaling laws.

The CVS method combines a deterministic computation and a statistical model.

Dimension of the Attractor of Turbulence revisited: statistical mechanics considerations

E. Segre[1] and L. Rondoni[2]

[1]Dipartimento di Ingegneria Aeronautica e Spaziale, Politecnico di Torino, Italy
[2]Dipartimento di Matematica, Politecnico di Torino, Italy

Contact e-mail: segre@athena.polito.it

A recent theory due to Gallavotti and Cohen links entropy production in nonequilibrium, stationary dynamical systems with microscopic chaos. 2D Navier–Stokes (NS) turbulence is viewed in this framework. Numerically, we find a dynamical equivalence of steady states of the NS dynamics, and of those of a time-reversible counterpart (GNS) which constrains some global quantity, and lets the viscosity vary in time. GNS fluctuations obey to the "Gallavotti-Cohen formula"; Lyapunov spectra of NS of GNS coincide and appear to obey a pairing rule characteristic of dissipated Hamiltonian systems. Predictions regarding the dimension of the attractor and its connection with global fluctuations can thus be compared with experimental facts, established for either NS or GNS.

Self-amplification of the field of velocity derivatives in quasi-isotropic turbulence

B. Galanti [1] and A. Tsinober[2]

[1]Department of Chemical Physics
Weizmann Institute of Science, 76100 Rehovot, Israel
[2]Department of Fluid Mechanics and Heat Transfer
Faculty of Engineering, Tel Aviv University, Tel Aviv 69978, Israel

Contact e-mail: barak.galanti@weizmann.ac.il

One of the most basic phenomena and distinctive features of three-dimensional turbulence is the predominant vortex stretching, which is manifested in positive net enstrophy generation, $\langle \omega_i \omega_j s_{ij} \rangle > 0$. It is commonly believed that this process is mainly due to *self-amplification*. The main purpose of this communication is a straightforward check of this belief by means of direct numerical simulations of the Navier-Stokes equations.

The key result is that the quantities $\langle \omega_i \omega_j s_{ij} \rangle$ and $\langle -s_{ij} s_{jk} s_{ki} \rangle$ in the equations for ω^2 and s^2 are three orders of magnitude larger than the corresponding terms associated with forcing, $\omega \cdot curl\ \mathbf{f}$ and $s_{ij} f_{ij}$. That is indeed the process of production of the field of velocity derivatives - both vorticity and strain is a *self-amplification* process.

On the calculation of streamwise derivatives from single-point measurements

C.F. Stein [1], A. Bakchinov[2], J. Bergh [1] and L. Löfdahl[2]

[1]Department of Mathematics, Chalmers University of Technology,
S-412 96 Göteborg, SWEDEN
[2]Thermo and Fluid Dynamics, Chalmers University of Technology,
S-412 96 Göteborg, SWEDEN

Contact e-mail: stein@math.chalmers.se

The measurement of streamwise gradients of fluctuating quantities is a long-standing and frequently encountered problem in fluid dynamics. For instance in hot-wire measurements Taylor's hypothesis is used to convert temporal derivatives into spatial ones. Unless the turbulence level is low, the Heskestad formula must be invoked in the conversion. Unfortunately, the validity of this formula may be questioned. On the current poster we present an extended method, which is based on less restrictive assumptions. Results from the two methods are compared using measurements in a boundary layer with a moderate pressure gradient.

Instantaneous frequency of the near wall singularities

S. Tardu

Laboratoire des Ecoulements Géophysiques et Industriels- LEGI
B.P. 53-X 38041 Grenoble-Cédex ; France

Contact e-mail: tardu@hmg.inpg.fr

The wavelet coefficients $\Omega(k,t)$ are expressed as

$$\Omega(k,t) = r(k,t)\cos\left[\int_0^t \omega_i(k,t)dt\right]$$

where $r(k,t)$ stands for the instantaneous amplitude and $\omega_i(k,t)$ is the instantaneous angular frequency at scale k. The random phase $\psi(k,t)$ is deduced from $\omega_i(k,t) = \omega_c(k) + \frac{\partial\psi(k,t)}{\partial t}$ where $\omega_c(k)$ is the optimum carrier frequency. The Rice canonical representation is used. The near wall turbulent signals behave as a frequency shift key process with random phase discontinuities. The arrivals of coherent structures are merely constant phase events. The jumps in frequency with the *same* fraction of ω_c are often and repetitively observed and that can be related to the multifractal nature of the cascade process.

Large scales features of the flow induced by precession of a rotating cylinder

J. Léorat [1], P. Lallemand [2], J.L. Guermond [3] and F. Plunian [4]

[1]Observatoire de Paris-Meudon, 92195-Meudon, France
[2]ASCI, CNRS, Bat.506, 91400-Orsay, France
[3]LIMSI, CNRS, BP133, 91403 - Orsay, France
[4]LEGI, INPG, BP53, 38041- Grenoble, France

Contact e-mail: leorat@obspm.fr

We examine the problem of precession in the context of the experimental fluid dynamo (for the Earth dynamo, the issue was first settled by W. Malkus, Science, Vol.160,P.259,1968). A driving mechanism for the flow at large scales is needed for such a device, and precession of the container may be considered as an efficient alternative to the use of impellers or turbines. We present numerical simulations at Reynolds numbers of a few thousands in cylindrical geometry. They show that the optimal precession rate is around 0.1, with comparable azimutal and meridional velocities. An experimental setup designed for the study of precession at larger Reynolds is presented. One presents also preliminary numerical results of the kinematic dynamo problem using the computed precessing flow.

Mean field hydrodynamics for turbulent flows subjected rotation

A.S. Petrosyan and D.V. Tsygankov

Space Research Institute, Russian Academy of Sciences,
Profsoyuznaya 84/32, Moscow, 117810, Russia

The present study is concerned with Reynolds Averaged Navier-Stokes equations for rotating system with and without convection. Our prime interest here is to find nontrivial parameterizations of Reynolds stresses describing contribution of turbulence subjected to rotation to the large-scale momentum flux. For this purpose we use statistical perturbation methods to analyse the way the basic flow is modified by a weak large-scale perturbation. We consider model homogeneous turbulence as an initial basic state in Reynolds stresses computations. It has been found that the presence of the rotation leads to the additional terms in the Reynolds stress tensor. These terms cause an additional wave-like transport of momentum. In the presence of convection, described in Boussinesque approximation, we found the possibility for decreasing turbulent viscosity value in comparison with the rotating system without convection.

Computation of turbulent flow around periodic obstacles using a Krylov-spectral method based on Brinkman penalization

A. Cherhabili and N. K.-R. Kevlahan

Department of Mathematics and Statistics, McMaster University,
1280 Main Street West, L8S 4K1, Hamilton, Ontario, CANADA

A major difficulty in computing engineering flows is the need of non-uniform grids adapted to solid boundaries that may be moving or changing shape. As an alternative to this problem, we use a penalization method based on Brinkman law for porous medium (Angot *et al.*, *Numerische Mathematik* **81**, 1999). This method models the flow as a porous medium, where the porosity is infinite in the fluid part and tends to zero in the solid part. For Numerical purposes, a time-evolution based on a Krylov method (stiffly stable) is used (Edwards *et al.*, JCP **110**, 1994). This combination (Krylov Method + Brinkman penalization) should provide an efficient tool to study a wide of variety of flows in complex geometries. As a test-case we study the flow around a circular cylinder.

Buoyancy generated turbulent flows in semi-enclosed regions: applications to oil-production technology

M.K. Neophytou, R.E. Britter

Computational Fluid Dynamics Laboratory, Cambridge University Engineering Department, Trumpington Street, Cambridge CB2 1PZ, UK

We introduce a novel approach entailing the complementary use of laboratory experiments, semi-analytical modelling and Computational Fluid Dynamics (CFD) in order to address a diphasic buoyancy driven turbulent flow in a semi-enclosed region. Inclined at 45 degrees to horizontal, the flow consists of a dispersed oil phase in water continuum with a recirculating mass flux of oil which this work aims to predict. The diphasic flow was studied experimentally using Particle Tracking Velocimetry (PTV); the oil phase was modelled using suitably chosen solid particles. A semi-analytical model based on integral arguments was developed to predict the recirculating flux in the diphasic and a corresponding single-phase problem; to close the diphasic model, a particle-size parameter is required. The closure is made by employing CFD to simulate the single-phase flow that presents the same recirculating motions as those in the diphasic case. The model results are compared with the available PTV data of the diphasic flow.

On the role of the divergence of the velocity for variable density flows in mixed or natural convection

C. Rey

Université d'Aix-Marseille III and
Institut de Recherche sur les Phnomènes Hors d'Equilibre IRPHE,
UMR 6594 du CNRS, Technopôle de Château Gombert, F-13451 Marseille Cedex 20,
FRANCE
Contact e-mail: claude.rey@VMESA12.U-3MRS.FR

The writing of the mass balances (for a material and not for a volume) and the introduction of the $\Theta = -ln(\rho/\rho_r)$ variable allows to develop a new analysis of the variable density flows. Navier-Stokes equation is written using this new variable, with application to heated gas or liquid flows, or gas mixing, in natural or mixed convection. For each case, the density variations are notable (ρ_r is a reference value, constant, for density) and the velocity is moderate so that $p'/\overline{P} \ll 1$ (p' is the pressure fluctuation). This new formulation leads to equations where density effects are isolated and clearly identified, no simplification is carried out, especially the divergence of the velocity is not zero. A comparison between each case of flow is made, in terms of similarity limitation.

Cryogenic High Reynolds Experiment

B. Chabaud[1], B. Hebral[1], S. Pietropinto[1], P. Roche[1], C. Baudet[2], Y. Gagne[2], E. Hopfinger[2], C. Poulain[2], B. Castaing[3], Y. Ladam[3], O. Michel[3], A. Naert[3], A. Bezaguet[4], J.-P. Dauvergne[4], P. Lebrun[4] and R. Van-Weelderen[4]

[1]Centre de Recherches sur les Très Basses Températures (CRTBT) - Grenoble
[2]Laboratoire des Ecoulements Géophysiques et Industriels (LEGI) - Grenoble
[3]Laboratoire de Physique de l'Ecole Normale Supérieure (ENSL) - Lyon
[4]Laboratoire Europeen pour la Physique des Particules (CERN) - Gèneve

We are developing a new open jet experiment that will use the large liquid Helium facilities at the LEP-LHC, in CERN. 5 K Helium gas will be supplied from a 6 kW cold power refrigerator. Flow rates as high as 300 g/s of Helium will feed the jet, that will develop inside an experimental chamber 1.1 m in diameter and 2.5 m high. At the nozzle (25 mm in diameter), the gas velocity can reach up to c/2, where c = 100 m/s is the sound velocity. This should allow to reach Taylor-based Reynolds numbers as high as $R\lambda = 5500$. Furthermore, thanks to the possibility to adjust the kinematic viscosity via the gas pressure, a large range of Reynolds numbers can be continuously explored. Local gas velocity or temperature fluctuations will be measured from cryogenic sensors, and spectral vorticity field will be obtained from the Doppler diffusion of ultrasonic waves.

Experimental and numerical investigation of the transition convective motion in a cylinder

Minerva Vargas[1], Fernando Sierra[2], Andrey Avramenko[2] and Eduardo Ramos[2]

[1]Instituto Tecnológico de Zacatepec
Av. Tecnológico 27 Zacatepec, Mor. Mexico
[2]Centro de Investigación en Energía UNAM
Ap.34, 62580 Temixco, Mor. Mexico

We present an experimental and numerical study of the natural convection in a cylinder of aspect ratio (height/diameter) two with water as a working fluid. The upper and lower walls of the cylinder are isothermal with the lower one held at a higher temperature. Two thermocouples monitor the temperature as a function of time inside the cell. Flow visualization is made by videotaping the image of tracers suspended in the fluid and illuminated with a green laser sheet. The numerical solution of the convective motion under study was obtained using a code FLUENT V5.0 The flow observed in the experiments displays a changing pattern that goes from one single convective cell that covers most of the volume of the cavity, to up to eight identifiable small cells that compete with each other.

Experimental investigation and numerical simulation of the flow around a high speed train

N. Paradot[1], C. Talotte[1], H. Garem[2], J. Delville[2] and J.-P. Bonnet[2]

[1]SNCF, Research and Technology Department
Physics of the Railway System and Comfort Unit
45 rue de Londres, F-75379 Paris Cedex 08, FRANCE
[2]Laboratoire d'Etudes Aérodynamiques, UMR CNRS 6609 / Université de Poitiers
CEAT, 43 route de l'aérodrome, F-86036 Poitiers, FRANCE

Contact e-mail: nicolas.paradot@sncf.fr

Numerical computations are carried out at SNCF, to understand the structure of the flow surrounding a high speed train, and to improve the knowledge of drag and its distribution into the different elements of the train . The numerical methodology developed consists in building the complete topology of a train with three blocks, and in setting the results of a block at the entrance of the computation domain of the further block. Experimental data required for validation are obtained through wind tunnel tests on a five coaches configuration TGV model. Velocity measurements are performed by hot-wire anemometry in the boundary layer and in the wake of the mok-up, and the drag coefficient is measured for each coach. Results from experiments and first computations are presented.

AUTHOR INDEX

Abid, M., 15
Abry, P., 755
Achim, P., 585
Adams, N.A., 715
Afanasyev, Y., 283
Airiau, C., 157
Alberghi, S., 315
Alekseenko, S.V., 741, 958
Aliseda, A., 553
Amati, G., 779
Amielh, M., 239
Andersen, J.S., 835
Andersson, H.I., 675
Andreopoulos, Y., 707
Angele, K., 349
Anselmet, F., 239, 899, 903
Antonia, R.A., 801, 903, 907, 954
Arad, I., 775
Argentini, S., 315
Armenio, V., 976
Auriault, C., 988
Auston, J., 509
Avramenko, A., 999
Ayrault, M., 235, 333

Babiano, A., 783
Baelmans, M., 515
Bailey, Q., 950
Bajer, K., 729
Bakchinov, A., 113, 995
Balaras, E., 535
Barakat, M., 865
Bardakhanov, S.P., 961
Barenghi, C.F., 929, 945
Bassom, A.P., 729
Bastiaans, R.J.M., 964
Bateman, A., 968
Batiste, O., 913
Baudet, C.,755, 998, 988
Baur, T., 963
Bavassano, B., 843
Bec, J., 851
Bellazzini, J., 603
Benaïssa, A., 954, 959
Bennacer, R., 979
Benzi, R., 881
Bergen, O., 967
Berggren, M., 205
Bergh, J., 995
Berlemont, A., 585
Berrilli, F., 843
Bertoglio, J.P., 689, 952
Bezaguet, A., 998
Bézard, H., 978
Biferale, L., 763, 775, 987
Billant, P., 19
Bilsky, A., 958
Binchun, Feng, 333
Blackburn, H.M., 607
Blais, J.S., 954
Bockhorn, H., 355
Bodo, G., 737
Boersma, B.J., 711
Boffetta, G., 171
Boger, M., 449
Bognetti, L., 973
Bolding, K., 968
Bonnet, J.-P.,617, 999
Borg, A., 873
Borgnat, P., 988
Borodulin, V.I., 149
Boubnov, B.M.,
Bouchon, F., 527
Bountin, D.A., 153
Bowman, J.C., 685
Bramwell, S.T., 861
Branover, H., 57, 61, 303
Bravo-León, E., 953
Brethouwer, G., 133
Britter, R.E., 997
Broglia, R., 973
Brun, C., 547
Bruno, R., 843
Bukasa, T., 219
Bullard, C., 41
Burchard, H., 968
Burton, G.C., 523
Buttighoffer, A., 949

Califano, A., 957
Cambon, C., 981
Camussi, R., 611, 771
Candler, G.V., 965
Carbone, V., 843, 948
Carlotti, P., 307
Cartellier, A., 553, 573
Casas, P.S., 943
Casciola, C.M., 83, 483, 779
Castaing, B., 125, 917, 988, 998
Castiglione, P., 175
Castillo, L., 963

Castro, I., 455
Cater, J., 958
Cavaliere, A., 970
Cencini, M., 763
Chabaud, B., 125, 917, 998
Chagelishvili, G.D., 67, 737
Chainais, P., 755
Chaisi, M., 966
Chanal, O., 125
Chang, Z., 585
Chara, Z., 869
Chavanne, X., 125
Chen, J.-Y., 445
Chen, J.H., 425
Chen, S., 984
Cheng, H., 455
Cherhabili, A., 997
Cherny, I.S., 741
Chernykh, G.G., 960
Chertkov, M., 621
Chillá, F., 990
Chkhetiani, O., 57, 947
Choi, Haecheon, 105, 459
Choi, Joonhyuk, 105
Chomaz, J.-M., 19
Chong, M.S., 821, 962
Chorny, A.D., 951
Chung, Yongmann M., 109
Ciraolo, G., 341
Clercx, H.J.H., 633
Coantic, M., 899
Coleman, G.N., 415
Consolini, G., 843
Copenhaver, W., 983
Coquart, L., 983
Couaillier, V., 975
Cressman, J.R., 23, 950
Cuenot, B., 441

da Silva, C.B., 93, 976
de Bruin, I.C.C., 539
de Lange, H.C., 964
Dahm, W.J.A., 523
Dalziel, S.B., 379
Danaila, L., 187, 903
Darabi, A., 201
Dauchot, O., 79
Daumont, I., 987
Dauvergne, J.-P., 998
Dávila, J., 953
Davis, S.A., 97
Dawes, W.N., 213
De Angelis, E., 483
Deane, A.E., 287
Delville, J., 617, 999
Demircan, A., 944
Derksen, J., 956
Di Cicca, G.M., 345
Di Mascio, A., 973
Diamessis, P.J., 679
Ditlevsen, P.D., 847
Djenidi, L., 954
Dombre, T., 987
Donnelly, R.J., 925
Dopazo, C., 183, 223, 973
Doris, L., 543
Dowling, D.R., 523
Dubois, T., 527
Dubrulle, B., 629
Ducros, F., 441
Dunn, D.C., 671
Duplat, J., 179

Eckhardt, B., 71
Eidelman, A., 57, 61, 303
Elmo, M., 952
Eloy, C., 725
Elperin, T., 952, 953, 970
Espinoza, J., 962
Estevadeordal, J., 945, 946, 983
Ewing, D., 959

Falqués, A., 375
Farge, M., 745, 793, 797
Favier, V., 429
Favini, B., 973
Fedorovich, E., 367
Fedotov, G.A., 966
Fernholz, H.-H., 253, 321
Ferré, J.A., 955
Fischer, P.F., 287
Flandrin, P., 988
Fleck, B.A., 954, 959
Forkel, H., 445
Fortin, J.-Y., 861
Friedrich, R., 547, 659, 759
Frisch, U., 851
Fuchs, L., 873
Fukunishi, Y., 950
Fureby, C., 595
Furuichi, Noriyuki, 961

Gad-el-Hak, M., 113
Gagne, Y., 988, 998
Galanti, B., 994
Gao, Ge, 277
Garem, H., 999
George, W.K., 963
Gerlinger, W., 355
Geurts, B.J., 539
Gibson, C.H., 857
Gilbert, A.D., 729
Giralt, F., 249, 955
Giuliani, P., 847
Glezer, A., 97
Godeferd, F.S., 981
Godfrey, S.P., 945
Gogineni, S., 946, 983
Gogoberidze, G.T., 737
Golbraikh, E., 57, 947, 948
Goldburg, W.I., 23, 950
Goldfeld, M.A., 719, 944
Gordienko, S., 303

Gorokhovski, M., 951
Gorrell, S., 983
Goss, L., 946, 983
Gotoh, T., 693
Grappin, R., 949
Grebenev, V., 359
Grek, G.R., 121
Grinstein, F.F., 595
Grossmann, S., 921
Gualtieri, P., 779
Guermond, J.L., 996
Guixiang, Cui, 333
Gutmark, E., 101

Haber, L., 101
Hacker, J.N.,
Hagiwara, Y., 487, 557
Hahn, Seonghyeon, 105
Hainaux, F., 553
Hammami, T., 979
Hancock, P.E., 419
Hanifi, A., 157
Hanjalić, K., 53
Hardman, J.R., 419
Hazarika, B.K., 957
Hébral, B., 125, 917, 998
Henningson, D.S., 157, 205
Himeno, R., 663
Hirsch, Ch., 957
Hodson, H.P., 213
Holdsworth, P.C.W., 861
Hopfinger, E., 998
Horváth, V.K., 23
Hsu, J., 971
Hu, Z.W., 561
Huerre, P., 27, 889
Hunt, J.C.R., 307
Huppertz, A., 253
Hüttl, T.J., 547
Hyers, R.W., 41

Ilyushin, B.B., 363, 980
Im, H.G., 425
Imamura, T., 487
Ishikawa, H., 825
Iuso, G., 345, 787
Iwase, S., 655
Izawa, S., 825

Jackson, J.D., 982
Janicka, J., 445, 982
Jarża, A., 960
Jiménez, C., 223, 441, 973
Jiménez, J., 463, 637
Johansson, A.V., 395, 399
Johansson, P., 113
Jones, W.P., 497
Jorba, À., 943
Jullien, M.-C, 175
Jürgens, W., 273

Kachanov, Y.S., 149
Kaltenbach, H.-J., 269, 273, 972
Kaneda, Y., 693
Kapusta, A., 948
Kawahara, G., 463, 733
Kawamura, H., 972
Keller, K.H., 625
Kempf, A., 445
Kenjereš, S., 53
Kennedy, I.M., 509, 565
Kevlahan, N.K.-R., 629, 997
Khan, Md.A.I., 989
Khanin, K., 851
Kholmyansky, M., 895
Khoo, B.C., 813
Khotyanovsky, D., 161
Khujadze, G.R., 67
Kida, S., 647, 733

Kikuchi, S., 950
Kim, J., 415
Kivotides, D., 929
Kiya, M., 825
Kleeorin, N., 952, 953, 970
Kleiser, L., 715
Knobloch, E., 913
Koengeter, J., 967
Kollmann, W., 425, 509, 565, 821
Komai, N., 557
Köngeter, J,. 963
Kontomaris, K., 956
Kopp, G.A., 249
Koptsev, D.B., 149
Kostas, J., 265
Kozlov, V.V., 121
Krogstad, P.-Å., 475
Kudryavtsev, A., 161
Kumar, S., 31
Kunugi, T., 231, 663
Kurgansky, M.V., 967

Labbé, R., 861
Lacor, C., 515
Ladam, Y., 998
Ladeinde, F., 433
Lallemand, P., 996
Langford, J.A., 591
Lanotte, A., 947, 987
Lasheras, J.C., 553, 569, 573
Lasserre, J.-J., 899
Le Dizès, S., 725, 805
Le Gal, P., 725
Leboeuf, F., 975
Lebrun, P., 998
Lee, I., 986
Lele, S.K., 711
Lemay, J., 954
Lentini, D., 980
Leonard, A., 599

Léorat, J., 949, 996
Lepreti, F., 843
Lesieur, M., 531
Lévêque, E., 755, 831
Leweke, T., 15
Li, H., 245
Li, Jiankang, 982
Lim, T.T., 813
Linden, P.F., 379
Lindgren, B., 399
Lindstedt, R.P., 493
Lipniacki, T., 937
Liu, W, 433
Löfdahl, L., 113, 995
Lohse, D., 921
Lombard, A., 617
Lominadze, J.G., 67
Lopez, J.M., 193, 813
Lourenco, L., 201
Lück, St., 759
Lumley, J.L., 3
Luo, K.H., 561
Luo, Kai. H., 109
Luo, X.Y., 561
Lygren, M., 675

Maeda, Y., 557
Maekawa, H., 87
Mahalingam, S., 971
Mahjoub, O.B., 783
Makita, H., 291, 337
Mallier, R., 49
Maltsev, A., 982
Manhart, M., 659, 667
Mann, J., 839, 877
Manneville, P., 75
Manuilovich, S.V., 117
Marchioli, C., 964
Marcq, P., 767
Markovich, D., 958
Marques, F., 193
Martínez-Bazán, C., 569
Martín, J., 183
Martín Vide, J.P., 968
Martinez Benjamin, J.J., 969
Maslov, A.A., 153
Mastrantonio, G., 315
Mathieu, P.P., 968
Matsunaga, S., 291
Matsuo, Y., 972
Mazzino, A., 947
Mazzitelli, I., 775
McComb, W.D., 697
McGuirk, J.J., 227
McLaughlin, J., 956
Medeiros, M.A.F., 197
Meinke, M., 329
Meng, H., 946
Menon, S., 505
Mercader, I., 913, 943
Meunier, P., 15
Meyers, J., 515
Michel, O., 998, 988
Mikhailovich, B., 948
Minier, J.P., 219, 981
Mironov, D.V., 299
Miyake, Y., 403
Miyauchi, T., 655
Moeleker, P., 599
Moez, Y., 87
Mohamad, A.A., 979
Moin, P., 385
Moiseev, S., 57, 61, 303, 947
Moisy, F., 835
Montañes, J.L., 569
Montoto, A., 375
Morrison, J.F., 671, 959
Morrison, P.J., 685
Moser, R.D., 591
Muhammad-Klingmann, B., 349
Murakhtina, T.O., 817
Mydlarski, L., 187
Myska, J., 869

Naguib, A., 411
Nazarenko, S.V., 629
Neophytou, M.K., 997
Net, M., 913, 943
Nicolleau, F., 167, 295
Niemela, J.J., 925
Nieuwstadt, F.T.M., 133
Nishizawa, A., 337
Nomura, K.K., 679
Nozawa, K., 974

Oberlack, M., 865
O'Brien, E., 433
Oesterlé, B., 977
Okkels, F., 986
Okulov, V.L., 817
Olivieri, A., 83
Onorato, M., 345, 787
Ooi, A., 821, 962
Ooms, G., 977
Orellano, A., 257
Ossia, S., 531
Österlund, J.M., 395, 399
Ott, S., 839, 877
Ozaki, Yasuhiro, 961

Pappa, D., 970
Paradot, N., 999
Parpais, S., 689
Paschereit, C.O., 101
Pearson, B.R., 984
Peinke, J., 759
Pellegrino, G., 797
Petrosyan, A.S., 996
Pfitzner, M., 501
Pier, B., 27
Pierce, C., 385
Pietri, L., 239
Pietropaolo, E., 843
Pietropinto, S., 998
Pietryga, J., 977
Pinelli, A., 463

Pino Martín, M., 965
Pino, D., 943
Pinton, J.-F., 861
Piomelli, U., 535
Pitsch, H., 385
Piva, R., 83, 483, 779
Platonov, A., 969
Ploss, A., 455
Plunian, F., 996
Podolski, M., 960
Poelma, C., 977
Politano, H., 948
Pollard, A., 959
Poulain, C., 998
Pouquet, A., 948
Powell, K.G., 523
Pozorski, J., 219, 981
Pralits, J.O., 157
Prasad, A.K., 957
Prigent, A., 79
Procaccia, I., 775
Protas, B., 793
Pumir, A., 621
Pungin, V., 947

Queiros-Conde, D., 985
Quéméré, P., 975
Quinn, A.P., 697

Réveillon, J., 581
Ragucci, R., 970
Rambaud, P., 977
Ramos, E., 999
Reau, N., 209
Redondo, J.M., 783, 968, 969
Rehab, H., 954
Renner, Ch., 759
Rettemeier, K., 967
Rey, C., 998
Ribas, F., 375
Riethmuller, M.L., 977
Ripa, P., 371
Ritchie, B.D., 97
Rivero, A., 955
Roche, P., 125, 917, 998
Rogachevskii, I., 952, 953, 970
Rojas, J., 962
Romano, G.P., 341
Rondoni, L., 994
Roquemore, M., 946
Rosenstein, T., 963
Rossi, P., 737
Rottman, J.W., 625
Ruiz-Chavarria, G., 831
Rusak, Z., 809
Rütten, F., 329

Sætran, L., 261
Sabel'nikov, V., 951, 952
Sadiki, A., 445, 979, 982
Sagaut, P., 617, 975
Salinas Vázquez, M., 975
Salvetti, M.V., 964
Samuels, D.C., 929, 945
San Gil, I., 984
Sandham, N.D., 407
Santangelo, P.J., 565
Santy-Ateyaba, K., 701
Sarkar, S., 437, 539
Sassa, K., 291
Satake, S., 663
Sato, N., 403
Savill, A.M., 213
Schmidts, M., 325
Schmiegel, A., 71
Schmitt, F., 957
Schneider, K., 355, 745, 793, 797
Schober, M., 321
Schröder, W., 329
Schumacher, J., 45
Scott, J.F., 981
Seah, R.K.M., 813
Seehafer, N., 45, 944
Segre, E., 994
Seitzman, J.M., 97
Sello, S., 603
Sen, M., 113
Serizawa, A., 231
Shadwick, B.A., 685
Shen, J., 193
Shin, Dongshin, 459
Shingai, K., 972
Shiplyuk, A.N., 153
Shraiman, B., 621
Shtork, S.I., 741
Sidorenko, A.A., 153
Sierra, F., 999
Simoëns, S., 235
Skrbek, L., 925, 933
Smith, S.T., 701
Sokoloff, D., 952, 953
Soldati, A., 964
Soria, J., 265, 821, 958, 962
Sorriso-Valvo, L., 948
Sosinovich, V.A., 951
Spalart, P.R., 415
Spazzini, P.G., 345
Spille, A., 972
Sreenivasan, K.R., 925, 984
Staicu, A.D., 751
Stalp, S.R., 933
Stamatellos, A., 955
Stapountzis, H., 955
Starov, A.V., 719
Stein, C.F., 995
Stolz, S., 715
Stretch, D., 966
Stretch, D.D., 625
Sung, Hyung Jin, 109, 986
Suzuki, Y., 403

Tabeling, P., 175, 835

Takagaki, S., 487
Takeda, Yasushi, 961
Talotte, C., 999
Tampieri, F., 315
Tamura, T., 974
Tanahashi, M., 655
Tanaka, M., 487, 557, 733
Tang, G., 227
Tanière, A., 977
Tardu, S., 471, 995, 978
Tenaud, C., 543, 983
Tevzadze, A.G., 737
Thäter, J., 367
Theofilis, V., 35
Thomson, D.J., 167
Toschi, F., 831
Touil, H., 689
Trapaga, G., 41
Tremblay, F., 659
Tsinober, A., 407, 895, 994
Tsipas, D., 955
Tsujimoto, K., 403
Tsygankov, D.V., 996
Tufo, H.M., 287
Tumin, A., 209

Valiño, L., 183, 223, 973
Van Atta, C.W., 625
van de Water, W., 751, 984
Van-Weelderen, R., 998
Vander Wal, R.L., 509
Váos, E.M., 493
Vargas, M., 999
Vasanta Ram, V., 325
Vasechkin, V., 958
Vassilicos, J.C., 167, 295, 953, 985, 989
Védy, E., 974
Velasco, D., 968
Veltri, P., 948
Venås, B., 261
Venugopal, P., 591
Vergni, D., 763
Vernet, A., 249
Vervisch, L., 429, 581
Verzicco, R., 611, 771
Veynante, D., 449
Vicedo, J., 213
Vigdorovich, I.I., 467
Villarreal, M.R., 968
Villermaux, E., 179
Villone, B., 851
Vilmin, S., 213
Vinçont, J.-Y., 235
Viola, A., 315
Vittori, G., 976
Voke, P.R., 145, 974
Völker, S., 591
von Ellenrieder, K., 265
von Lukowicz, J., 963
Voropayeva, O.F., 960
Vulpiani, A., 763

Wallace, J.M., 235, 535
Wark, C., 411
Weerasinghe, R., 497
Wengle, H., 257
Westerweel, J., 957, 977
Willaime, H., 835
Woodward, S., 959
Wu, X.L., 23
Wygnanski, I., 201

Yakovenko, S.N., 980
Yamamoto, K., 87
Yamamoto, Y., 231
Yanase, S., 733
Yang, Z.Y., 145, 227
Yokokawa, Y., 950
Yong, Yan, 277
Yorish, S., 895
Yurchenko, N., 479

Zhou, T., 801, 903, 907
Zhou, Y., 245
Zilitinkevich, S., 311